Transesophageal Echocardiography Multimedia Manual

A Perioperative Transdisciplinary Approach

EDITED BY
André Y. Denault
Pierre Couture
Jean Buithieu
Jean-Claude Tardif

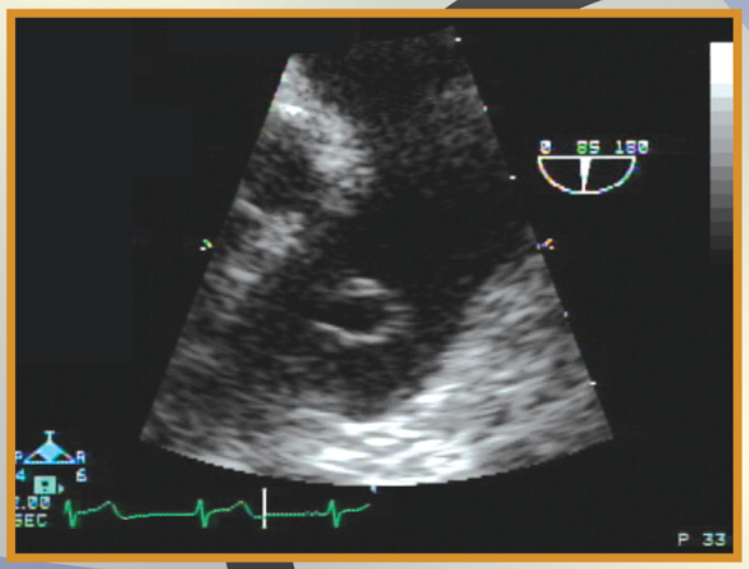

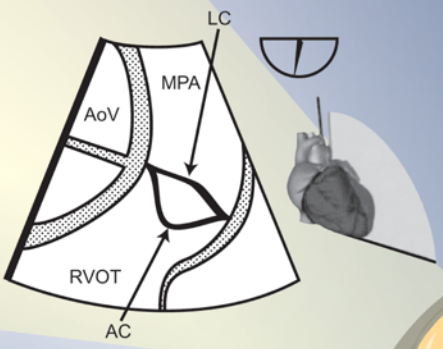

Transesophageal Echocardiography Multimedia Manual

Transesophageal Echocardiography Multimedia Manual

A Perioperative Transdisciplinary Approach

Edited by

André Y. Denault
Montreal Heart Institute
Centre Hospitalier de l'Université de Montréal
Montréal, Québec, Canada

Pierre Couture
Montreal Heart Institute
Montréal, Québec, Canada

Jean Buithieu
McGill University Health Center
Montréal, Québec, Canada

Jean-Claude Tardif
Montreal Heart Institute Research Center
Montréal, Québec, Canada

Taylor & Francis
Taylor & Francis Group
New York London

Published in 2005 by
Taylor & Francis Group
6000 Broken Sound Parkway NW, Suite 300
Boca Raton, FL 33487-2742

© 2005 by Taylor & Francis Group, LLC

No claim to original U.S. Government works
Printed in the United States of America on acid-free paper
10 9 8 7 6 5 4 3 2 1

International Standard Book Number-10: 0-8247-2353-8 (Hardcover)
International Standard Book Number-13: 978-0-8247-2353-8 (Hardcover)

This book contains information obtained from authentic and highly regarded sources. Reprinted material is quoted with permission, and sources are indicated. A wide variety of references are listed. Reasonable efforts have been made to publish reliable data and information, but the author and the publisher cannot assume responsibility for the validity of all materials or for the consequences of their use.

No part of this book may be reprinted, reproduced, transmitted, or utilized in any form by any electronic, mechanical, or other means, now known or hereafter invented, including photocopying, microfilming, and recording, or in any information storage or retrieval system, without written permission from the publishers.

For permission to photocopy or use material electronically from this work, please access www.copyright.com (http://www.copyright.com/) or contact the Copyright Clearance Center, Inc. (CCC) 222 Rosewood Drive, Danvers, MA 01923, 978-750-8400. CCC is a not-for-profit organization that provides licenses and registration for a variety of users. For organizations that have been granted a photocopy license by the CCC, a separate system of payment has been arranged.

Trademark Notice: Product or corporate names may be trademarks or registered trademarks, and are used only for identification and explanation without intent to infringe.

Library of Congress Cataloging-in-Publication Data

Catalog record is available from the Library of Congress

Taylor & Francis Group is the Academic Division of T&F Informa plc.

Visit the Taylor & Francis Web site at
http://www.taylorandfrancis.com

This book is dedicated to

my wife Denise and children Jean-Simon, Gabrielle, and Julien who have supported me with love and patience (André Y. Denault);

Frédéric, Noémi, Manon, Jacob and also Jean and Nicole (Pierre Couture);

my parents, Tuong and Thai (Jean Buithieu)

Michele, Jean-Daniel, and Pier-Luc, who have been so supportive and so patient with me. (Jean-Claude Tardif);

our family and teachers who have prepared us for this work;

our students;

and above all our patients for whom we hope and believe that transesophageal echocardiography will improve their care

Jean-Claude Tardif André Y. Denault Jean Buithieu Pierre Couture

Foreword

The use of transesophageal echocardiography (TEE) has literally exploded in recent years, especially in the Operating Room and in the Intensive Care Unit. Several years ago, TEE was reserved to a community of experts and visionaries but, nowadays, TEE is becoming a valuable and essential tool in a growing number of conditions and procedures such as during cardiac anesthesia. Several reasons explain this success. First, the equipment has improved. Probes and TEE machines have become smaller while providing images of better quality. Second, and most important, TEE provides highly relevant information that allows clinicians to optimize the decision-making process. The ability to visualize, in real-time, anatomical structures and their functional status is a unique feature of TEE in comparison to all other bedside monitoring devices available at present.

Unfortunately, expertise in TEE comes at a price. The technique remains relatively complex and one must take the time required to go through the proper training process. The capacity to conceptualize the heart in its three dimensions (3D) from two-dimensional tomographic planes while manipulating the TEE probe is not innate. Thus, some formal learning and significant hands-on training in the field are extremely valuable in mastering the technique. While a book such as the one prepared by André Denault, Pierre Couture, Jean Buithieu, and Jean-Claude Tardif cannot replace the latter, this is how close it gets. The efforts put into the visual aspects of the "book" (printed material and DVD) are commendable. The learning aids presented by the authors will, most certainly, help newcomers to TEE, such as myself, to "see" the heart in 3D by presenting correlations between anatomy (normal or pathologic), orientation of the TEE probe and TEE images. So, while the learning curve remains steep, I suspect this book will help considerably.

Jean-Francois Hardy, MD, FRCPC
Chairman
Department of Anesthesiology
University of Montreal
Canada

Preface

I remember there was once a dream, or a vision, that perioperative transesophageal echocardiography would become an important, and even essential, tool in the management of patients with heart disease or who were hemodynamically unstable. This dream is now a reality. Eleven years after Pierre Couture and I introduced perioperative transesophageal echocardiography in the Department of Anesthesia at our Hospital in 1993, we were contacted by the editors of Marcel Dekker to produce this manual.

Since our first echocardiographic exam was performed, significant advances in the field of perioperative echocardiography have occurred. An important aspect was the recognition of perioperative transesophageal echocardiography as a special field of competence. This was accomplished by the creation of an exam on perioperative transesophageal echocardiography by the National Board in 1998. We have decided to base our training, our teaching and our book on the objectives of the National Board. Each author was asked to orient his own chapter towards the objectives of the National Board of Echocardiography.

As a clinician, I think that perioperative transesophageal echocardiography performed in the Operating Room or in the Intensive Care Unit is a superb complement to the history taking, physical findings, hemodynamic data, and other imaging modalities used at the bedside. This is the reason why the manual will emphasize the role of perioperative transesophageal echocardiography in patient care and why some of the complementary information will be presented to give the perspective of a clinician trained in perioperative transesophageal echocardiography. This transdisciplinary book is unique in that it contains the experience of individuals trained in anesthesiology, cardiology, critical care, internal medicine, cardiac and vascular surgery, lung and hepatic transplantation, radiology, pathology, physics, and computer technology.

"An image is worth a thousand words," but what about a video? Transesophageal echocardiography is a dynamic process and most of our two-dimensional examples will be presented in their original video format accompanied by sketches, three-dimensional orientation, Doppler-related information, hemodynamic, radiologic and anatomical correlation in a user-friendly companion DVD. Such work would not have been possible without the collaboration of several individuals. First Pierre and I had the privilege to work with Jean Buithieu and Jean-Claude Tardif, who agreed to collaborate and share their expertise with us in the creation of this manual. My assistant, Denis Babin, with his knowledge and talent in organizing, digitalizing, and facilitating this work also contributed to making the dream a reality. My thanks also go to my anesthesiology colleagues from Notre Dame Hospital and the Montreal Heart Institute and to their former chiefs, Dominique-Camille Girard and Jean Taillefer, who supported Pierre and me for all these years. I am grateful to the surgical teams of both hospitals who have always been supportive in sharing their knowledge and calling me when they had interesting cases and anatomical observations were made. Finally, my appreciation is beyond words for the contribution and passion of the current chief of cardiac surgery at the Montreal Heart Institute, Michel Pellerin, in teaching us surgical anatomy and sharing his video material.

There are several other individuals in addition to the anesthesiology and surgical team in the operating room who have collaborated in the creation of this book by suggestions on chapter content, figures, video clips, and DVD creation which greatly facilitated our work. Their names are listed on the following page. Financial support for the DVD which accompanies this book was provided by Pierre deGuise, through an educational grant from the Montreal Heart Institute, and by the Montreal Heart Institute Foundation. An educational sponsorship from Philips has allowed us to insert their brilliantly educating transesophageal echocardiography three-dimensional normal exam in our work and this has already delighted several of our trainees. Finally a grant from Organon through the Anesthesiology department of the University of Montreal was pivotal in the creation of our digitalization station.

I hope that this book will help you to offer better care to your patients and become part of your teaching.

André Y. Denault, MD, FRCPC

Acknowledgments

We would like to thank the following individuals who have contributed in improving this manual through their corrections, suggestions, figures, pictures, live images captured in the operating room, technical and financial support.

Denis Babin,
Arsène Basmadjian,
Yanick Beaulieu,
Luce Begin,
François A. Béïque,
Pierre Beaulieu,
Robert Blain,
Isabelle Borduas,
Denis Bouchard,
Michèle Brault,
Monique Brouillard,
Diane Campeau,
Michel Carrier,
Raymond Cartier,
Pierre-Guy Chassot,
Jennifer Cogan,
Annie Coté,
Geneviève Coté,
Stéphane Coutu,
Philippe Demers,
Vincent Denault,
Sylvain Durocher,
Amélie Gariepy,
Alain Girard,
François Haddad
Yves Hébert,
Gisèle Hemmings,
Stuart Herd,
Christian Jodoin,
Suzanne Kaprélian,
Philippe Lallier,
Jean Leclerc,
Tack Ki Leung,
Patrick Limoges,
Francois Marcotte,
Ariane Marelli,
Avrum Morrow
Raymond Martineau,
Pierre Pagé,
Michel Pellerin,
Guy Pelletier,
Louis Perrault,
Nancy Poirier,
Baqir Qizilbash,
Catherine Roy,
Philippe Sahab,
Sophie St-Onge
Jean Taillefer,
France Thériault,
Pierrette Thivierge,
Normand Tremblay,
Patricia Ugolini,
Ann Wright,
Les inhalothérapeutes du bloc opératoire de l'ICM
Association des Anesthésiologistes du Québec,
Bourse Organon du département d'anesthésiologie de l'Université de Montréal (Educational grant),
Canadian Institutes of Health Research
Edwards Lifesciences (Educational grant),
Fond de la Recherche en Santé du Québec,
The Montreal Heart Institute Foundation (Educational grant),
Nicolas Bussières from BUZE productions,
Pierre deGuise from the Montreal Heart Institute (Educational grant),
Richard Maheu from the Montreal Heart Research Center,
Simon Bergeron,
Francine Tardif and Gina Kelley from Philips (Equipment grant),

Contents

Foreword Jean-Francois Hardy . . . . . *vii*
Preface . . . . . *ix*
Acknowledgments . . . . . *xi*
Contributors . . . . . *xv*
Abbreviations . . . . . *xix*
How to Use the Transesophageal Echocardiography Multimedia Manual . . . . . *xxv*

1. Principles of Ultrasound
   Alain Gauvin, Guy Cloutier *1*
2. Basic Principles of Doppler Ultrasound
   Pierre-Guy Chassot *23*
3. Transducers
   François Haddad, Bradley I. Munt, John Bowering *41*
4. Normal Anatomy and Flow
   George N. Honos, Jean Buithieu, Nicolas Dürrleman, André Y. Denault *55*
5. Quantitative Echocardiography
   Jean Buithieu, André Y. Denault *89*
6. Imaging Artifacts and Pitfalls
   Robert Amyot, Maria Di Lorenzo, Réal Lebeau, Claude Sauvé *121*
7. Equipment, Complications, Infection Control, and Safety
   Geneviève Côté, André Y. Denault *141*
8. Segmental Ventricular Function and Ischemia
   Ady Butnaru, Anique Ducharme, Jean-Claude Tardif *157*
9. Global Ventricular Function and Hemodynamics
   André Y. Denault, Pierre Couture, Jean Buithieu *185*

10. Cardiomyopathy
Vicky Soulière, Philippe L.-L'Allier, Anique Ducharme 215

11. Pericardium
Yan-Fen Shi, André Y. Denault, Jean-Claude Tardif 241

12. Aorta
Ivan Iglesias, Daniel Bainbridge, John Murkin, Alan Menkis 261

13. Echocardiography During Cardiac Surgery
Pierre Couture, André Y. Denault, Raymond Cartier 285

14. Perioperative Role of TEE in Mechanical Circulatory Assistance
Yanick Beaulieu, Denis Bouchard 315

15. Native Aortic Valve
François A. Béïque 329

16. Perioperative Evaluation of Aortic Valve Surgery
Jean G. Dumesnil, Philippe Pibarot 363

17. Mitral Valve
André Saint-Pierre, Stéphane Coutu, Pierre Couture, André Y. Denault, Jean Buithieu 383

18. Mitral Valve Replacement and Repair
Arsène-J. Basmadjian, Michel Pellerin 417

19. Pulmonic and Tricuspid Valves
François Marcotte, Denis Bouchard 447

20. Heart Transplantation
Pierre Couture, Michel Carrier 471

21. Lung Transplantation
André Y. Denault, Pasquale Ferraro 481

22. Liver Transplantation
François Plante, Stéphane Busque 491

23. Intracavitary Contents
Maria Di Lorenzo, Robert Amyot, Réal Lebeau, Claude Sauvé 497

24. Congenital Heart Disease
Jean-Marc Côté, Dany Côté, Alain Cloutier 525

25. Indications for Perioperative Transesophageal Echocardiography
André Martineau, Marie Arsenault 555

Index 569

Contributors

Robert Amyot, MD, FRCPC *Assistant Professor, Department of Medicine, Division of Cardiology, Hôpital du Sacré-Coeur de Montréal, University of Montreal, Montreal, Canada*

Marie Arsenault, MD, FRCPC *Department of Medicine, Division of Cardiology, Quebec Heart Institute/Laval Hospital, Laval University, Quebec City, Canada*

Daniel Bainbridge, MD *Assistant Professor of Anesthesiology and Perioperative Medicine, London Health Science Center, Department of Anesthesiology University of Western Ontario, London, Ontario, Canada*

Arsène-J. Basmadjian, MD, MSc, FRCPC, FACC *Associate Professor, Department of Medicine, Division of Cardiology, Montreal Heart Institute, University of Montreal, Montreal, Canada*

Yanick Beaulieu, MD FRCPC *Clinical Instructor, Department of Medicine, Division of Cardiology and Critical Care, Hôpital du Sacré-Coeur de Montréal, University of Montreal, Montreal, Canada*

François A. Béïque, MD, FRCPC *Director of Cardiac Anesthesia, Sir Mortimer B. Davis Jewish General Hospital, Associate Professor, Department of Anesthesiology, McGill University, Montreal, Canada*

Denis Bouchard, MD, FRCSC *Assistant Professor in Cardiac Surgery, Department of Cardiac Surgery, Montreal Heart Institute, University of Montreal, Montreal, Canada*

John Bowering, MD, FRCP *Associate Professor, Department of Anesthesiology, Providence Health Care, University of British Columbia, Vancouver, British Columbia, Canada*

Jean Buithieu, MD, FRCPC *Director of Echocardiography and Non-Invasive Cardiology, McGill University Health Center, Assistant Professor, Department of Medicine, Division of Cardiology, McGill University, Montreal, Canada*

Stéphane Busque, MD, FRCSC *Associate Professor, Department of Surgery, Stanford University, Palo Alto, California, USA*

Ady Butnaru, MD *Cardiology Fellow, Montreal Heart Institute, Department of Medicine, Division of Cardiology, University of Montreal, Montreal, Canada*

Michel Carrier, MD, FRCSC *Program Director, Associate Professor, Department of Cardiac Surgery, Montreal Heart Institute, University of Montreal, Montreal, Canada*

Raymond Cartier, MD, FRCSC *Professor of Cardiac Surgery, Department of Cardiac Surgery, Montreal Heart Institute, University of Montreal, Montreal, Canada*

Pierre-Guy Chassot, MD *Head of Cardiovascular Anesthesia, Department of Anesthesiology, Centre Hospitalier Universitaire Vaudois (CHUV), Lausanne, Switzerland*

Alain Cloutier, MD, FRCPC *Professor, Department of Pediatrics, Division of Pediatric Cardiology, Laval University, Quebec City, Canada*

Guy Cloutier, Eng., PhD *Director Laboratory of Biorheology and Medical Ultrasonics, Professor, Department of Radiology, University of Montreal, Montreal, Canada*

Dany Côté, MD, FRCPC *Department of Anesthesiology, Hôpital Enfant-Jésus, Laval University, Quebec City, Canada*

Jean-Marc Côté, MD, FRCPC *Associate Professor, Department of Pediatrics, Division of Pediatric Cardiology, Laval University, Quebec City, Canada*

Geneviève Côté, MSc, MD, FRCPC *Clinical Instructor, Department of Anesthesiology, Ste-Justine Hospital, University of Montreal, Montreal, Canada*

Stéphane Coutu, MD, FRCPC *Clinical Instructor, Department of Anesthesiology, University of Sherbrooke, Sherbrooke, Canada*

Pierre Couture, MD, FRCPC *Chief of the Cardiac Anesthesiology Department, Montreal Heart Institute, Assistant Professor, Department of Cardiac Anesthesiology, University of Montreal, Montreal, Canada*

André Y. Denault, MD, FRCPC *Cardiac Anesthesia Fellowship Program Director, Associate Professor, Department of Cardiac Anesthesiology, Montreal Heart Institute, Division of Critical Care of the Department of Medicine, Centre Hospitalier Universitaire de Montréal (CHUM), University of Montreal, Montreal, Canada*

Maria Di Lorenzo, MD, FRCPC *Clinical Instructor, Department of Medicine, Division of Cardiology, Hôpital du Sacré-Coeur de Montréal, University of Montreal, Montreal, Canada*

Anique Ducharme, MD, MSc, FRCPC *Director of the Heart Failure Clinic, Montreal Heart Institute, Associate Professor of Medicine, Department of Medicine, Division of Cardiology, University of Montreal, Montreal, Canada*

Jean G. Dumesnil, CQ, MD, FRCPC, FACC *Professor of Medicine, Quebec Heart Institute/Laval Hospital, Department of Medicine, Division of Cardiology, Laval University, Quebec City, Canada*

Nicolas Dürrleman, MD *Cardiac Surgical Fellow, Montreal Heart Institute, Department of Cardiac Surgery, University of Montreal, Montreal, Canada*

Pasquale Ferraro, MD, FRCSC *Surgical Director of the Lung Transplantation Program, Associate Professor, Department of Surgery, Division of Thoracic Surgery, Centre Hospitalier Universitaire de Montréal (CHUM), University of Montreal, Montreal, Canada*

Alain Gauvin, MSc, MCCPM, DABR, DABMP *Clinical Instructor, Physicist, Department of Radiology, University of Montreal, Montreal, Canada*

François Haddad, MD, FRCPC *Cardiologist, Montreal Heart Institute, Department of Medicine, Division of Cardiology, University of Montreal, Montreal, Canada*

George N. Honos, MD, FRCPC, FACC *Director of Echocardiography, Sir Mortimer B. Davis Jewish General Hospital, Associate Professor, Department of Medicine, Division of Cardiology, McGill University, Montreal, Canada*

Ivan Iglesias, MD *Assistant Professor of Anesthesiology and Perioperative Medicine, London Health Science Center, Department of Anesthesiology, University of Western Ontario, London, Ontario, Canada*

Philippe L.-L'Allier, MD, FRCPC *Assistant Professor, Department of Medicine, Division of Cardiology, University of Montreal, Montreal, Canada*

Réal Lebeau, MD *Assistant Professor, Department of Medicine, Division of Cardiology, Hôpital du Sacré-Coeur de Montréal, University of Montreal, Montreal, Canada*

François Marcotte, MD, FRCPC, FACC, FASE *Assistant Professor, Department of Medicine, Division of Cardiology, Montreal Heart Institute, University of Montreal, Montreal, Canada*

André Martineau, MD, FRCPC *Department of Anesthesiology, Quebec Heart Institute/Laval Hospital, Laval University, Quebec City, Canada*

Alan H. Menkis, MD, FRCSC *Professor and Chair, Department of Cardiac Surgery, St-Boniface General Hospital, University of Manitoba, Manitoba, Canada*

Bradley I. Munt, MD, FRCPC *Clinical Instructor, Department of Medicine, Division of Cardiology, Providence Health Care, University of British Columbia, Vancouver, British Columbia, Canada*

John Murkin, MD, FRCPC *Professor of Anesthesiology, Department of Anesthesiology and Perioperative Medicine, London Health Science Center, University of Western Ontario, London, Ontario, Canada*

Michel Pellerin, MD, FRCSC *Chief of the Department of Cardiac Surgery, Montreal Heart Institute, Associate Professor, Michael and Renata Chair in Cardiac Surgery, University of Montreal, Montreal, Canada*

Philippe Pibarot, DVM, PhD, FACC *Director of the Canada Research Chair in Valvular Heart Disease, Research Center of the Quebec Heart Institute/Laval Hospital, Associate Professor of Medicine, Department of Medicine, Division of Cardiology, Laval University, Quebec City, Canada*

François Plante, MD, FRCPC *Associate Professor, Department of Anesthesiology, Centre Hospitalier Universitaire de Montréal (CHUM), University of Montreal, Montreal, Canada*

André Saint-Pierre, MD, FRCPC *Department of Anesthesiology, Quebec Heart Institute/Laval Hospital, Laval University, Quebec City, Canada*

Claude Sauvé, MD, FRCPC *Assistant Professor, Department of Medicine, Division of Cardiology, Hôpital du Sacré-Coeur de Montréal, University of Montreal, Montreal, Canada*

Yan-Fen Shi, MD *Cardiologist, Research Center of the Montreal Heart Institute, Department of Medicine, Division of Cardiology, University of Montreal, Montreal, Canada*

Vicky Soulière, MD, FRCPC *Clinical Instructor, Department of Medicine, Division of Cardiology, Hôpital du Sacré-Coeur de Montréal, University of Montreal, Montreal, Canada*

Jean-Claude Tardif, MD, FACC, FRCPC *Director of the Montreal Heart Institute Research Center, Associate Professor, Department of Medicine, Division of Cardiology, University of Montreal, Montreal, Canada*

Abbreviations

λ	wavelength
ρ	the concentration of masse or weight kg/cm^3
2D	two-dimensional
A	anterior
AA	apical anterior
ACC	American College of Cardiology
ACT	activated clotting time
AHA	American Heart Association
AI	apical inferior
AL	anterolateral
AL	apical lateral
AML	anterior mitral leaflet
Ao	aorta
AoV	aortic valve
AP	anteroposterior
AR	aortic regurgitation
AR	atrial reversal
AS	anteroseptal
AS	aortic stenosis
AS	apical septal
ASA	American Society of Anesthesiology
ASD	atrial septal defect
ASE	American Society of Echocardiography
AVA	aortic valve area
AVR	aortic valve replacement
BA	basal anterior
BAL	basal anterolateral
BAS	basal anteroseptal
BIL	basal inferolateral
BIS	basal inferoseptal
c	propagation speed

CNS	central nervous system
CO	cardiac output
COLD	chronic obstructive lung disease
CPB	cardiopulmonary bypass
CS	coronary sinus
CSA	cross-sectional area of the orifice
CT	computed tomography
CVA	cerebrovascular accident
CW	continuous wave
CXR	chest radiograph
d	depth
D	diastolic
DBP	diastolic blood pressure
DT	deceleration time
EAS	epiaortic scanning
ECMO	extra-corporeal membrane oxygenation
EDA	end-diastolic area
EE	epiaortic echocardiography
EF	ejection fraction
EOA	effective orifice area
Eq	equation
ERO	effective regurgitant orifice
EROA	effective regurgitant orifice area
ESA	end-systolic area
ET	ejection time
f	frequency
FAC	fractional area change
FS	fractional shortening
HOCM	hypertrophic obstructive cardiomyopathy
HPS	hepatopulmonary syndrome
HR	heart rate
Hz	Hertz
I	intensity cm^2
I	inferior
ICA	internal carotid artery
ICU	Intensive Care Unit
IOE	intraoperative echocardiography
IRI	ischemia-perfusion injury
IS	inferoseptal
IVC	inferior vena cava
IVCT	isovolumic contraction time
IVRT	isovolumic relaxation time
IVST	interventricular septal thickness
J/s	Joule per second
k	compressibility
LA	left atrium
LAA	left atrial appendage
LAD	left anterior descending
LAX	long axis
LCX	left circumflex
LIJV	left internal jugular vein
LLPV	left lower pulmonary vein
LPA	left pulmonary artery
LSCV	left subclavian vein

LUPV	left upper pulmonary vein
LV	left ventricle
LVD	left ventricular diameter
LVEDA	left ventricular end-diastolic area
LVEDD	left ventricular end-diastolic diameter
LVEDP	left ventricular end-diastolic pressure
LVEDV	left ventricular end-diastolic volume
LVESA	left ventricular end-systolic area
LVESD	left ventricular end-systolic diameter
LVESP	left ventricular end-systolic pressure
LVESV	left ventricular end-systolic volume
LVET	left ventricular ejection time
LVNC	left ventricular noncompaction
LVOT	left ventricular outflow tract
LVPEP	left ventricular pre-ejection period
LVSW	left ventricular stroke work
MA	mid-anterior
MAL	mid anterolateral
MAP	mean arterial pressure
MAR	mitral annuloplasty ring
MAS	mid-anteroseptal
MAV	mitral annular velocities
mDT	mitral deceleration time of the *E* velocity
MI	mechanical index
MI	mid-inferior
MIS	mid-inferoseptal
ML	mediolateral
MPA	main pulmonary artery
MPAP	mean pulmonary artery pressure
MPI	myocardial performance index
MR	mitral regurgitation
MRI	magnetic resonance imaging
MS	mitral stenosis
MV	mitral valve
MVA	mitral valve area
MVR	mitral valve replacement
NYHA	New York Heart Association
OHT	othotopic heart transplantation
OLT	othotopic liver transplantation
OR	Operating Room
Pa	Pascal
PAC	pulmonary artery catheter
PACS	picture archiving and communication systems
PAEDP	pulmonary artery end-diastolic pressure
Paop	pulmonary artery occlusion pressure
PD	pulse duration
PDA	patent ductus arteriosus
Pe	pericardial effusion
PFO	patent foramen ovale
PG	pressure gradient
PHT	pressure half-time
PHT	pulmonary hypertension
PISA	proximal isovelocity surface area

PML	posterior mitral valve leaflet
Ppa	pulmonary artery pressure
PPH	primary pulmonary hypertension
PPHTN	portopulmonary hypertension
Pra	right atrial pressure
PRF	pulse repetition frequency
PRP	pulse repetition period
Prv	right ventricular pressure
PRS	post-reperfusion syndrome
PS	pulmonic stenosis
PV	pulmonic valve
PVD	peripheral vascular disease
PVF	pulmonary venous flow
PW	pulsed wave
PWT	posterior wall thickness
Q	quality factor
Q	cardiac output
RA	right atrial, right atrium
RAA	right atrial appendage
RCA	right coronary artery
RICA	right internal carotid artery
RIJV	right internal jugular vein
RLPV	right lower pulmonary vein
RPA	right pulmonary artery
RUPV	right upper pulmonary vein
RV	right ventricle
RVEDD	right ventricular end-diastolic diameter
RVEDP	right ventricular end-diastolic pressure
RVOT	right ventricular outflow tract
RWMA	regional wall motion abnormalities
S	systolic
SAM	systolic anterior motion
SAP	systolic arterial pressure
SAX	short axis
SBP	systolic blood pressure
SEC	spontaneous echo contrast
SPL	spatial pulse length
SPPA	spatial peak pulse average
SPTA	spatial peak/temporal average
SV	stroke volume
SVC	superior vena cava
SWT	septal wall thickness
T	transmitted intensity
TEE	transesophageal echocardiography
TG	transgastric
TGA	transportation of the great arteries
TGC	time gain control
TI	thermal index
TIA	transient ischemic attack
TMF	transmitral flow
TR	tricuspid regurgitation
TS	tricuspid stenosis
TTE	transthoracic echocardiography

TTF	transtricuspid flow
TV	tricuspid valve
TVI	time velocity integral
UE	upper esophageal
V_{max}	maximal velocity
VSD	ventricular septal defect
W	Watt
WMSI	wall motion score index
WS	wall stress
Z	acoustic impedance (rayls)

How to Use the Transesophageal Echocardiography Multimedia Manual

The manual was designed to facilitate the learning of transesophageal echocardiography (TEE). To this end, TEE images are accompanied by explanatory two-dimensional (2D) diagrams and 3D icons for spatial orientation. Both diagram and icon borders share a unique thick black line meant to allow the reader to exactly realign the 2D diagram on the 3D icon. Superposition of both lines gives the spatial orientation of the TEE image.

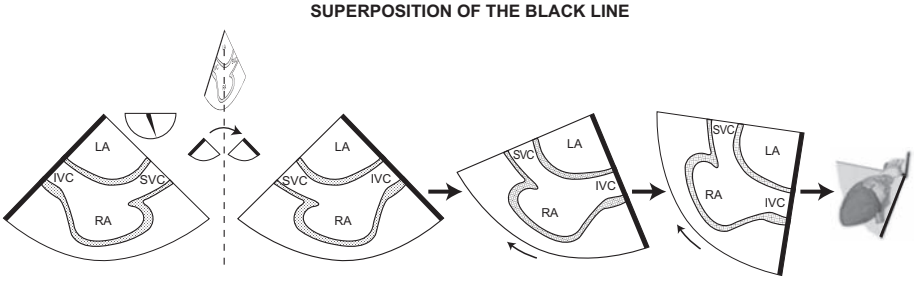

.

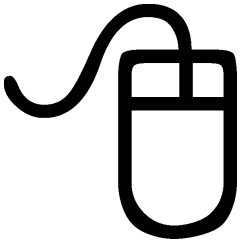

This symbol used in the legend indicates the presence of additional videoclips in relation to the figure available on the accompany DVD.

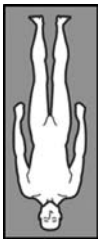

The human body icon indicates how the patient was positioned relative to the camera when intraoperative images or videos were obtained.

The manual is accompanied by a DVD-ROM where all the figures and the related-video clips are stored. Several figures are accompanied by echocardiographic, hemodynamic, radiological, anatomical/surgical data, and other videoclips. Moreover, 3D animations are provided to clarify the spatial orientation of the TEE images. As anatomical variations can occur between patients, the suggested 3D planes represent our best understanding of the images orientation. To maximize the learning experience with this multimedia manual, we strongly recommend that reading be performed with simultaneously running the DVD.

1

Principles of Ultrasound

ALAIN GAUVIN, GUY CLOUTIER
University of Montreal, Montreal, Canada

I. Principles of Ultrasound 1
A. Nature: Compression and Rarefaction 1
B. Frequency, Wavelength, Propagation Speed in Biological Tissues 3
1. Frequency 3
2. Wavelength 3
3. Propagation Speed 3
C. Other Properties of Ultrasound Waves 4
1. Amplitude 4
2. Power 4
3. Pressure 4
4. Intensity 4
D. Specular Reflection 6
1. Acoustic Impedance 6
2. Angle Dependence 6
3. Acoustic Impedance Mismatch 7
E. Scattering, Refraction, and Attenuation 8
1. Scattering 8
2. Refraction 8
3. Attenuation 9
II. Imaging 11
A. Advantages and Limitations of A-, B-, and M-Mode Ultrasonography 11
1. A Mode 11
2. B Mode 13
3. M Mode 14
4. Other Modes 14
B. Instrumentation 14
1. Transducers 14
2. Transmitting/Receiving Electronics 15
3. Scan Converters 16
C. Signal Processing, Image Resolution, and Display 16
1. Time Gain Control 16
2. Image Resolution 16
3. Display 17
D. Related Factors 17
1. Pulsing Characteristics 17
2. Frame Rate and Time to Generate One Frame 18
3. Number of Lines per Frame 19
4. Depth 19
5. Temporal Resolution 20
6. Pixels 20
III. Conclusion 21
Bibliography 21

I. PRINCIPLES OF ULTRASOUND

A. Nature: Compression and Rarefaction

Ultrasound consists of mechanical sound waves whose frequencies are above the audible range, that is, $\gtrsim$20,000 Hz (Hz stands for the number of wave cycles per second). Ultrasound can also be defined as a mechanical wave that propagates in a medium. The mode of propagation of ultrasound is related to successive molecular compressions and rarefactions occurring in that medium

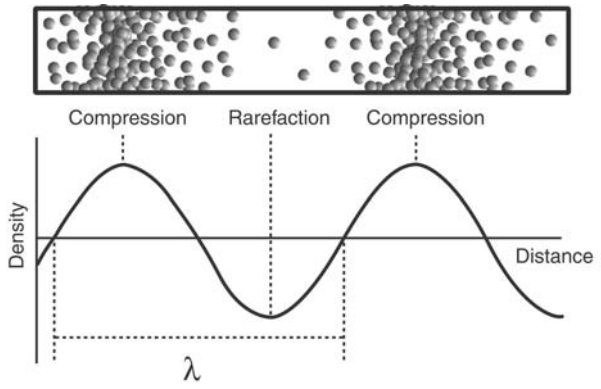

Figure 1.1 Ultrasound wave. Representation in terms of alternating molecular compressions and rarefactions. Corresponding 2D plot of density as a function of distance along the propagation direction. The wavelength (λ) is the distance corresponding to one cycle of the longitudinal wave.

(Fig. 1.1). Isotropic solids can experience both *transverse* (or *shear*) and *longitudinal* waves. An example of a transverse wave is the vertical motion of a boat on the surface of the ocean as the wave passes underneath. Ultrasound in fluids and gases only experiences longitudinal propagation because of the lack of strong coupling between the molecules. Consequently, transverse waves do not play an important role in medical ultrasound imaging. However, recent research suggests that shear waves may become clinically useful to characterize the visco-elastic properties of biological tissues.

In order to understand ultrasound production, one can imagine a small transducer driving an oscillating surface in contact with gas molecules, as illustrated in Fig. 1.2. As the surface moves forward, it pushes gas molecules in front of it, creating a zone of compression, as seen in Fig. 1.2(A). The oscillating surface then retracts, during which time the newly created zone of compression moves forward. However, this backward motion of the surface causes a rarefaction of local gas molecules, as shown in Fig. 1.2(B). In the time elapsed between Fig. 1.2(A) and Fig. 1.2(B), the zone of increased density initially created moves forward at propagation speed denoted as *c*. If the oscillation of this surface, which can be referred to as the *source*, is sustained, a continuous traveling wave made by alternating compressions and rarefactions is established.

At a given point in space, the rarefactions and compressions are accompanied by local oscillation of molecules in a direction parallel to the axis of propagation of the wave. During the transition from compression to rarefaction, molecules, initially located in a compressive region, move on average backwards (with respect to the direction of propagation of ultrasound) so that the local density of molecules is reduced. The velocity of the

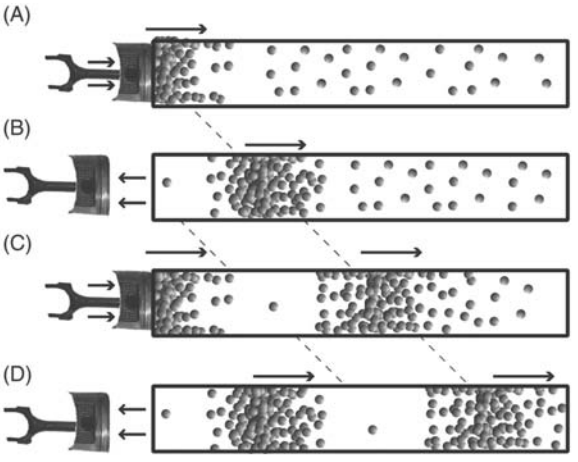

Figure 1.2 Generation of ultrasound wave. Representation of the density of gas molecules subjected to the oscillation of a column of gas from a small transducer at one end. (A) The surface has moved forward with respect to its rest position, creating a zone of increased molecule density (compression). (B) The surface has retracted behind its rest position, and now leaves a zone of decreased density (rarefaction). The initial zone of compression created in *A* has moved forward. (C) The surface is back to the same position as in *A* and it has created a new zone of compression. The compression from *A* has traveled even further, and the rarefaction from *B* has also traveled. (D) The situation of *B* is repeated, again with all previous compressions and rarefactions correspondingly displaced forward.

molecules reaches a maximum when the local density is half that of the maximum density, for a sinusoidal wave which occurs midway between a maximum and a minimum density. Molecules eventually come to a stop, at which point their local density is at its minimum, right in the middle of the rarefaction zone. Motion then resumes, and the velocity reaches a maximum midway in the transitory period, just as it did previously. Finally, molecules again come to rest when the density is at its highest. Therefore, at any given point in space, molecules experience all density states at different times, as illustrated in Fig. 1.2.

Such waves are said to be *longitudinal*. The process repeats itself as long as the surface is in oscillating motion. It is, therefore, the *momentum* (or the mechanical motion of molecules initially at rest) that propagates, not the molecules themselves which merely oscillate back and forth when insonified.

In conclusion, these compressions and rarefactions are made possible by the elastic nature of the material, arising from intermolecular interactions. It is this elasticity, together with the density of the material, which mainly governs the properties of the medium with respect to wave propagation.

Table 1.1 Various Parameters for Describing Waves

Parameters	Basic units	Units	Mainly determined by
Period	Time	s, μs	Sound source
Frequency	1/time	s^{-1}, Hz	Sound source
Amplitude	Acoustic	Pressure, voltage	Sound source
Power	Work/time	W	Sound source
Pressure	Force/area	Pa	Sound source
Intensity	Power/area	W/cm^2	Sound source
Wavelength	Distance	mm, cm	Source and medium
Propagation speed	Distance/time	m/s	Medium

B. Frequency, Wavelength, Propagation Speed in Biological Tissues

Ultrasound can be described by the following: period, frequency, amplitude, power, pressure, intensity, wavelength, and propagation speed. These variables can be determined by the sound source or the medium in which they travel (Table 1.1).

1. *Frequency*

Once a traveling wave is established, a given spatial position (Fig. 1.2) will find itself crossed by alternating compressions and rarefactions, at a pace determined by the *frequency* (f) (a unit of $1/s = s^{-1}$ also termed Hertz, abbreviated Hz, where s signifies second). It represents the number of cycles per second (a cycle being a complete back-and-forth motion) of the oscillating surface that gives rise to the mechanical waves. The frequency, symbolized by f, is determined by the source, that is, the oscillating surface in this case. The frequency-dependent attenuation of the medium and nonlinear propagation can modify the shape and frequency of the transmitted waves.

The time interval, or the duration of a cycle, is the *period*, which is inversely related to the frequency (Fig. 1.3). The frequency of ultrasound used for medical imaging usually ranges from 2 to 15 MHz, although it can be higher for some special imaging techniques, such as endovascular ultrasound and ultrasound biomicroscopy.

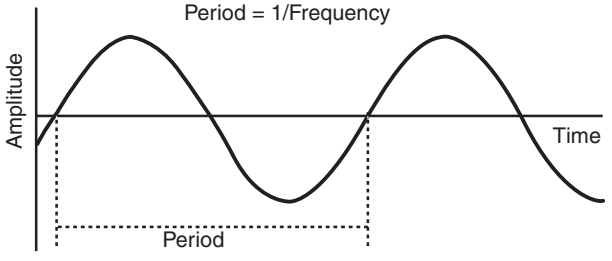

Figure 1.3 Ultrasound period. Plot of the amplitude of the wave as a function of time. The period is the longitudinal variable between corresponding and adjacent points along this plot; for instance, in this example the abscissa crossing of the ascending portion of the wave. Note that the abscissa represents time rather than distance, in contrast to Fig. 1.1.

2. *Wavelength*

The wavelength (λ) corresponds to the distance separating two adjacent maximums or minimums of a wave, as shown in Fig. 1.1. Therefore, λ in Fig. 1.1 represents the *spatial* spacing of points of similar intensity along the wave at a given instant, while the period in Fig. 1.3 represents the *temporal* spacing of points, also with similar intensity, at a given location.

3. *Propagation Speed*

A given location in space is crossed by a number of cycles per second given by f, these cycles being spaced by a distance given by λ. The product of both values yields the propagation speed of the wave.

$$c = f\lambda \tag{1.1}$$

An analogy would be evenly spaced cars driving on a highway at the same speed; the speed is the distance between each car multiplied by the number of cars per time unit passing an observer at rest along the road. The propagation speed c is generally a property of the medium, and independent of the frequency. It is determined by the compressibility (k) or elasticity and density (ρ) of the medium, through the equation (Eq.)

$$c = \sqrt{\frac{k}{\rho}} \tag{1.2}$$

Compressibility is the reduction in volume of a material by external pressure. For example, air is compressible, bone is not. Stiffness is the opposite of compressibility. Density is the concentration of mass or weight and the units are kg/cm^3. It is a property of the medium through which sound travels. As f is mainly determined by the ultrasound source, specifying its value and the nature of

the medium generally determines the wavelength, through the use of Eq. (1.1).

The speed of sound c is typically a few hundred m/s for gases (330 m/s in air), and between 1000 and 2000 m/s for liquids (1480 m/s in pure water at 20°C). In soft biological tissues, its value is generally assumed to be 1540 m/s (see Table 1.2 for speed values in different materials). The actual speed at a given point can vary a few percent above or below this accepted value depending on the local density and compressibility of the tissue. According to Eq. (1.2), the value of c is inversely proportional to the density of the material. It is of note that the speed of sound in air (low density) is much lower than that observed in solids (high density). This is because the relative difference in compressibility of air compared with solids is much more important than their relative density differences.

C. Other Properties of Ultrasound Waves

1. Amplitude

Longitudinal waves are characterized by the traveling of mechanical perturbations within a medium. The *amplitude* of these perturbations can be defined as the range of change of a certain property of the medium around its mean value, which is the density of molecules in the case of Fig. 1.3. Acoustic amplitude in the context of ultrasound usually has units of pressure or voltage. An amplitude of zero generally corresponds to the average value of the property. It also represents the normal value of the property when no perturbation exists. In other words, the amplitude is the *deviation* of the property around its mean value.

2. Power

As already discussed, a medium crossed by ultrasound will undergo localized compressions and rarefactions of the density of its molecules. In order for compressions to occur locally, supplementary energy must be provided, so a sound wave constitutes a form of energy transport, that energy being carried from the source into the medium. It is possible to characterize the *power* of the source, or the amount of energy it transfers to the medium per unit of time [in the International Unit System, the energy of the source is given in Joules per second (J/s) or Watt (W)]. In medical imaging, the power is influenced by many operating parameters and its value is generally difficult to measure but is proportional to the intensity defined in the following text.

3. Pressure

Compressions and rarefactions accompany the propagation of a sound wave and can be described as density differences along the direction of the wave propagation. However, varying densities also correspond to different pressures, which can be defined by the force per unit area. Thus, one can also describe the manifestation of a longitudinal wave by the higher-than-average and lower-than-average pressure. The unit of pressure is Pascal, or Pa.

The pressure (P) is related to the intensity of the beam (I) by the proportionality relationship:

$$I \propto P^2 \tag{1.3}$$

4. Intensity

The power was previously described as the energy per unit of time transferred from the source to the medium. The source (the *transducer* in an actual ultrasound imaging system) has a certain area. When the ultrasound energy is transmitted from the source, the amount of power crossing a certain area varies considerably with respect to the position of the transducer, due to the directional dependence of ultrasound emission and attenuation. Intensity is the parameter used to describe that spatial dependence, and it is defined as the energy per unit of time (or power) that crosses a small surface, in cm^2, located at the point where intensity is sought.

For concerns related to the safety of diagnostic ultrasound the intensity, or pressure, of the sound wave are important parameters to consider. However, other parameters that pertain to patient safety can be displayed on the screen of medical ultrasound instruments: the *thermal index* and the *mechanical index.* Different forms of thermal indices are proposed in the ultrasound literature. In general terms, thermal index can be defined as

Table 1.2 Ultrasound Properties in Some Common Materials

Material	Density (g/cm^3)	c (m/s)	Z (rayls $\times 10^{-5}$)	Attenuation coefficient (dB/cm at 1 MHz)
Air	0.0000012	331	0.0004	12
Fat	0.95	1450	1.38	0.63
Muscle	1.1	1580	1.70	0.5–1.0
Skull bone	1.91	4080	7.80	20

Note: c, speed of sound; Z, acoustic impedance which is the product of density and speed of sound.

the ratio of the transmitted ultrasonic power to the power required to raise the temperature of the medium by 1°C in the same conditions. Mechanical index is a parameter that reflects the potential for *cavitation*, or bubble formation in zones of rarefactions, which has been hypothesized as a potential mechanism for biologically harmful effects. The mechanical index increases together with the transmitted power of the transducer and is inversely related to frequency. More specifically, it is given by the rarefactional peak pressure at a point along the ultrasound beam axis where the pulse intensity is maximum, divided by the square root of the transmitted frequency. For safety reasons, it is more relevant to measure the mechanical index than the power of the source. It is common for instruments to display mechanical index, as it allows the operator to understand the effect of common operating parameters, such as the transmitting power on the mechanical index (Fig. 1.4). In a similar fashion, thermal index can often be visualized on some instruments, and it is influenced by similar factors (Fig. 1.5).

Depending on the type of clinical scan (obstetric, cardiac, peripheral, etc.), the maximum values of mechanical and thermal indices are usually limited by the instrument. Consequently, the potential for harmful effects is limited, and possibly nonexistent. However, epidemiological demonstrations of noncausality are very difficult to obtain, and the existence of such risk should not be ruled out.

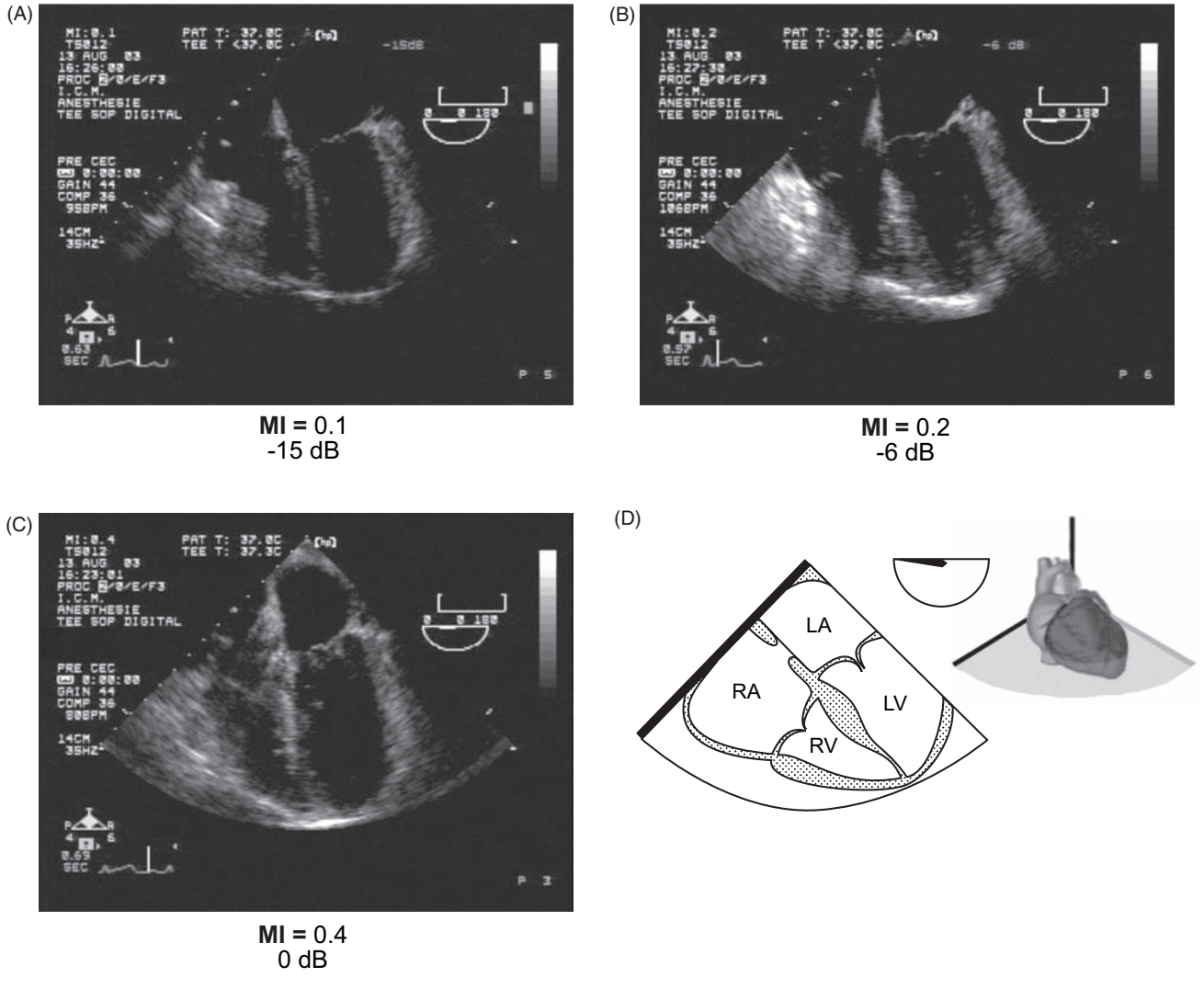

Figure 1.4 Transmitting power and mechanical index. (A–D) The mechanical index (MI) decreases when transmitting power is reduced [expressed in negative decibel (dB)]. A value of 0 dB means that the emitting source is at 100% of its power (LA, left atrium; LV, left ventricle; RA, right atrium; RV, right ventricle).

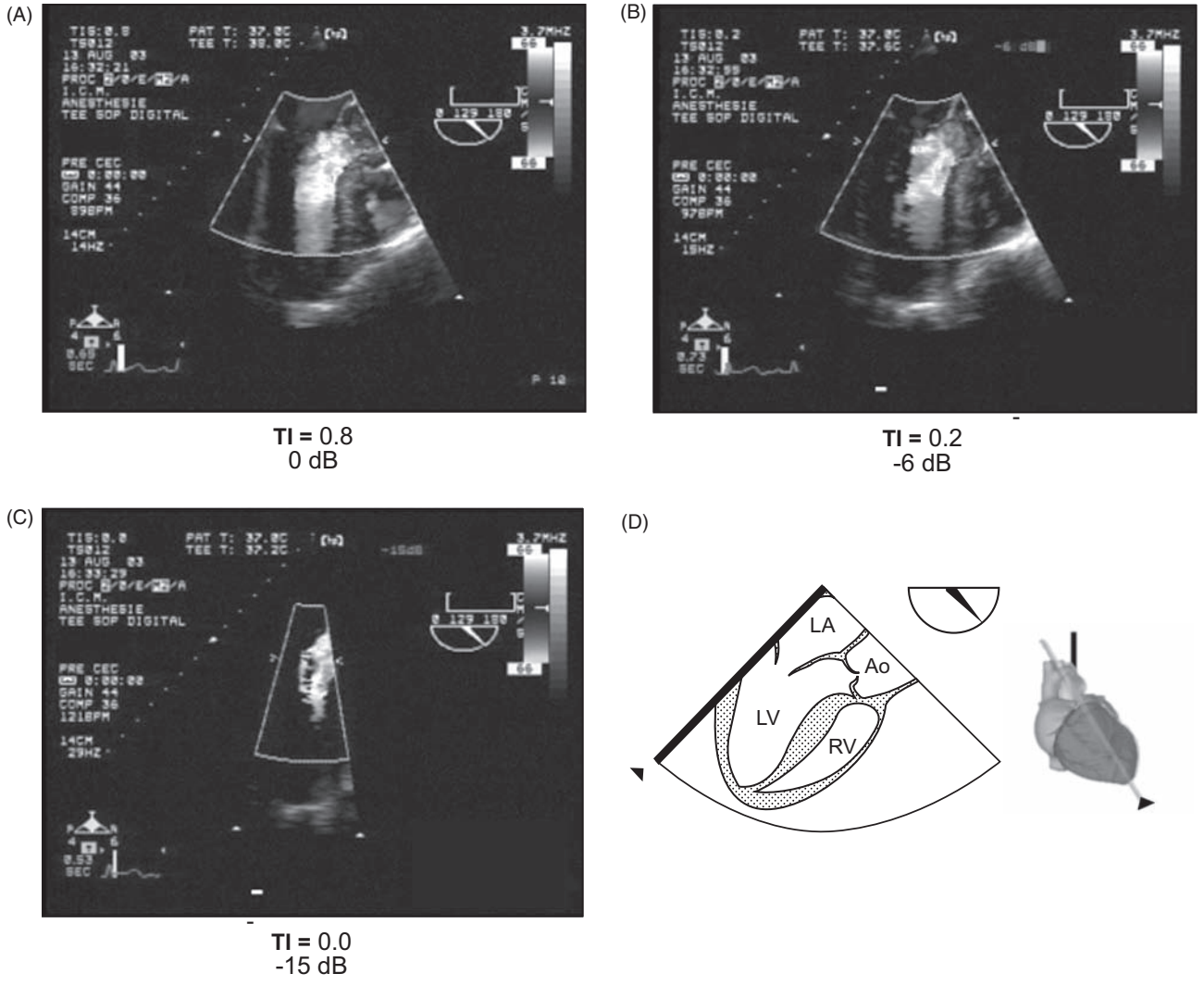

Figure 1.5 Transmitting power and thermal index. (A–D) The thermal index (TI) decreases when transmitting power is reduced [expressed in negative decibel (dB)]. A value of 0 dB means that the emitting source is at 100% of its power (Ao, aorta; LA, left atrium; LV, left ventricle; RV, right ventricle).

D. Specular Reflection

1. Acoustic Impedance

The acoustic impedance (Z) is a characteristic of the interaction between an ultrasound wave and the medium. It can also be defined as the product of ρ and c.

$$Z = \rho \times c \tag{1.4}$$

As both ρ and c are constants of a material, so is Z [Eq. (1.4)]. When ultrasound propagates from one medium to another, the impedance generally changes at the interface between the media. When the boundary is perpendicular to the direction of propagation, part of the incoming ultrasound energy is reflected back, whereas the remainder penetrates the new medium and pursues its course. The relative amount of reflected energy depends on the impedance difference, as described later in this chapter. When the ultrasound λ is much smaller than the size of the interface, this phenomenon is termed *specular reflection.* On the other hand, when the ultrasound λ is much larger than the size of the interface, it is termed *nonspecular reflection* or *scattering*.

2. Angle Dependence

With any angle of incidence θ with respect to the impedance boundary, the reflected beam is oriented with the same angle of incidence θ. This more general case of *specular* reflection is illustrated in Fig. 1.6. Ultrasound imaging is based on the detection of the reflected

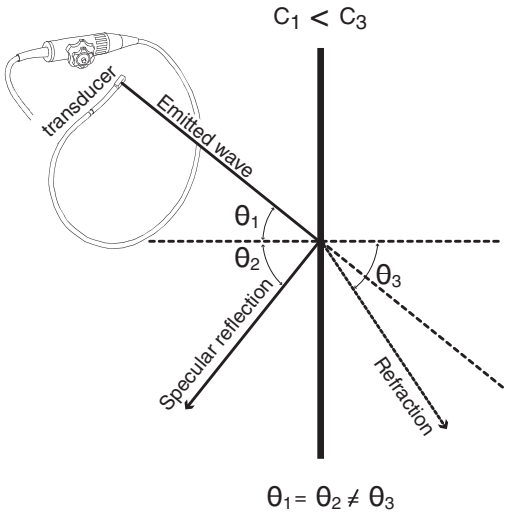

Figure 1.6 Refraction. A wave reflected at a boundary on either side of which are two different impedance values is reflected with an incidence angle (θ_2) identical to the one of the incoming beam (θ_1), but away from the transducer. However, part of it penetrates the second medium, but changes propagation direction or angle (θ_3) according to Snell's law (C, propagation speed).

ultrasound energy from internal boundaries and structures, as these generally have different impedance values. A smooth structure at 90° with respect to the incident beam yields specular reflection and is, therefore, seen on the image. If, on the other hand, the same structure has a different orientation, specular reflection will not be returned to the transducer. Given the largely complex shapes of boundaries inside the human body, it might, therefore, seem like specular reflection alone would not yield much information, as surfaces are generally not perpendicular with respect to the incident beam. However, most surfaces also have a structural pattern that can be described on a scale smaller than the macroscopic boundary of the organ to which they belong. Consequently, this microstructural pattern gives rise to *nonspecular* reflections that cover a broad angular distribution, thus allowing imaging of the interfaces even if the angle of incidence differs from 90° (90° still being the optimal angle to obtain the maximal amount of energy reflected back to the transducer). This explains why *nonspecular* reflections, known as *scattering*, play the biggest role in the generation of ultrasound images. It is also relevant to mention that in practice, by using a range of incident angles, one can detect perfect flat specular reflectors due to the complex pattern of intensities and divergence of ultrasound beam (see Chapter 3).

Nonspecular reflection allows the return of ultrasound to the transducer through multiple paths, each with a varying number of scatter interactions and also allows for destructive and constructive interferences of ultrasound reaching the transducer. This produces the *speckle appearance of ultrasound images*, for which a relatively uniform tissue, such as the liver, gives a nonuniform pattern, as illustrated in Fig. 1.7. Speckle is artifactual and does not directly reflect the location of scatters from which echoes seem to arise.

3. *Acoustic Impedance Mismatch*

When ultrasound crosses a boundary, either side of which acoustic impedance differs, the intensity of the reflected ultrasound depends on the difference between acoustic impedance of the two media: this is termed the acoustic-impedance mismatch. With a 90° angle of incidence, the proportion of the transmitted intensity that is reflected back (R), at the interface is given by:

$$R = \left(\frac{Z_2 - Z_1}{Z_2 + Z_1}\right)^2 \tag{1.5}$$

where Z_1 and Z_2 represent the impedance of the medium before and after the boundary. Therefore, the transmitted

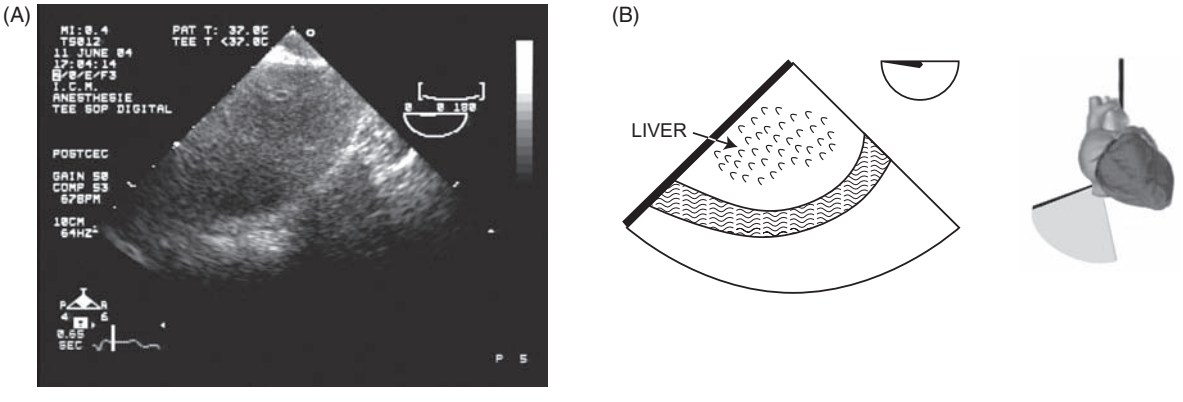

Figure 1.7 Speckle reflection. Transgastric ultrasound image of the liver which shows the presence of speckle reflections.

intensity (T) is simply the remaining fraction of the initial intensity value, or

$$T = 1 - R = 1 - \left(\frac{Z_2 - Z_1}{Z_2 + Z_1}\right)^2 = \frac{4Z_1Z_2}{(Z_2 + Z_1)^2} \qquad (1.6)$$

According to the aforementioned definitions of the reflected and transmitted signal intensities, some examples can be given to understand better the mechanisms of ultrasound propagation in the human body. For instance, let us consider the impedance of air Z_1 (0.004×10^{-5} rayls) that is much smaller than that of fat Z_2 (1.38×10^{-5} rayls). Consequently, the reflected intensity at this interface will be close to one and such a boundary essentially reflects all incoming ultrasound energy [T is close to zero, see Eq. (1.6)] (Fig. 1.8). Another interface involving a large reflected fraction of the incoming wave is that of bone/tissue. This particular situation poses a special problem for cardiac imaging, as the heart is "shielded" by the rib cage during transthoracic echocardiography (TTE).

E. Scattering, Refraction, and Attenuation

1. *Scattering*

As ultrasound interacts with a medium, most of the energy is absorbed and the rest is reflected or scattered. When ultrasound interacts with structures much smaller than the wavelength *nonspecular* reflection or *scattering* occurs, as described previously. Such interaction involves the absorption of ultrasound, followed by its reemission in all directions. In ultrasound imaging, this situation is typical of parenchymal tissue, in which complex structures exist at a microscopic level.

2. *Refraction*

Refraction is a change in the direction of travel of an ultrasound wave as it moves into a different medium (Fig. 1.6). When applied to light, the same phenomenon causes the distorted appearance of objects that are partly immersed in water (Fig. 1.9).

Refraction therefore implies a deviation of the beam from its original direction of propagation. Fundamental

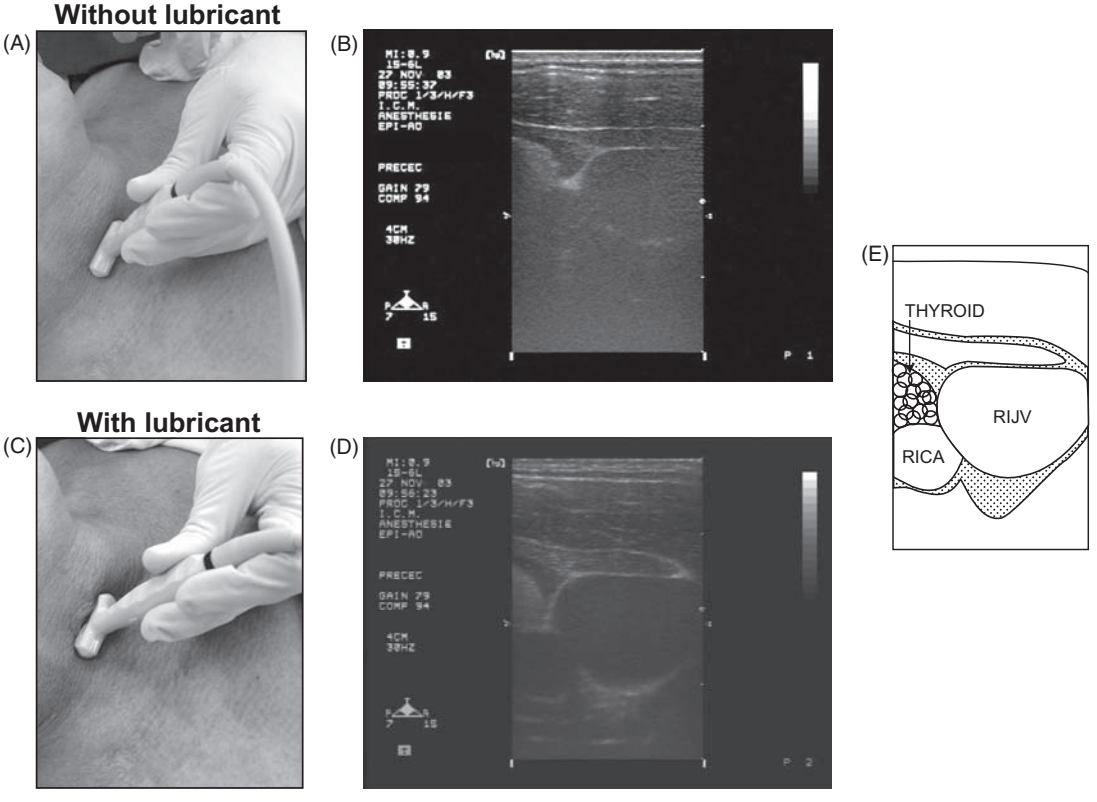

Figure 1.8 Acoustic mismatch. Different acoustic mismatch obtained with a 10 MHz transducer for insertion of a central venous catheter. (A, B) Image without lubricant. (C, D) Image with lubricant. The lubricant reduces the acoustic impedance mismatch because the impedance of the lubricant is much higher than air. Therefore, the amount of transmitted intensity is increased and the ultrasound image is clearer (RICA, right internal carotid artery; RIJV, right internal jugular vein).

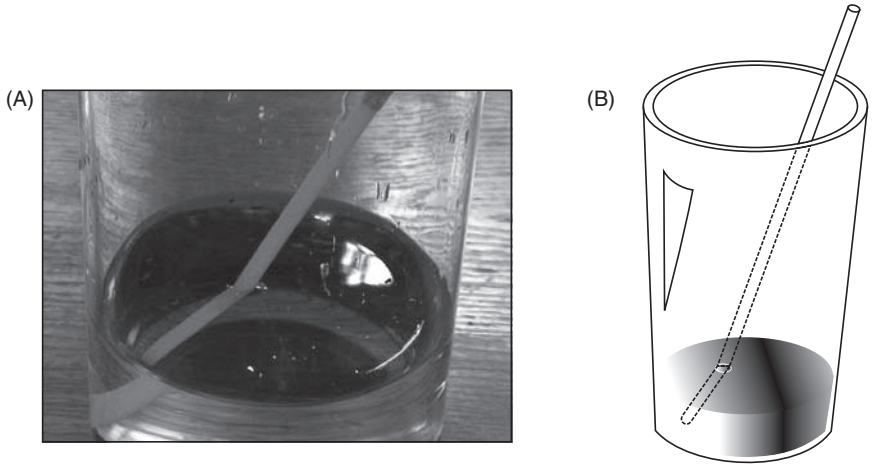

Figure 1.9 Refraction phenomenon. The visible light from the immersed part of the straw follows a different path then the light from the non-immersed part: air and water are two different media in this case. The refraction creates the illusion of a broken straw.

to the understanding of refraction is the fact that frequency does not normally change when ultrasound passes from one medium to the next, as it is determined by the source. As seen previously, small velocity differences, however, do exist, and in order for Eq. (1.1) ($c = f\lambda$) to be true, wavelength must be modified by the medium change (Fig. 1.10). This, in turn, can only hold true if one considers a change in the orientation of the beam at an interface, as illustrated in Fig. 1.6.

$$\frac{\sin\theta_1}{\sin\theta_3} = \frac{c_1}{c_3} \tag{1.7}$$

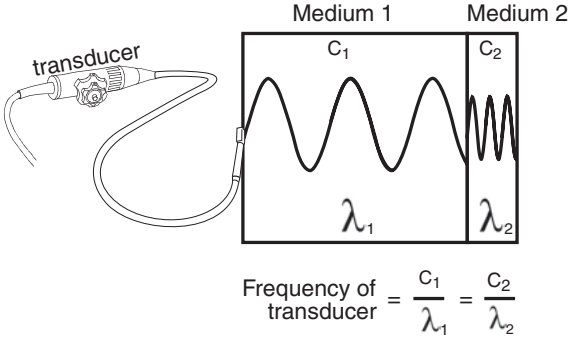

Figure 1.10 Ultrasound characteristics in different medium. Two different media are shown with their own velocity of propagation (c_1 and c_2). The frequency (f) does not change when ultrasound passes from one medium to the next, as it is determined by the source. Wavelength (λ), however, will be modified by the medium change according to the formula $f = c/\lambda$.

Equation (1.7) represents Snell's law, which quantifies the deviation of the penetrating beam in Fig. 1.6. In ultrasound imaging, it is generally assumed that the beam is traveling in a straight line with respect to the source and refraction can cause structures to be spatially positioned at the wrong location, thereby causing image artifacts.

3. Attenuation

Typical media are not perfectly elastic, which implies that some energy is converted to heat. The ultrasound beam is therefore *attenuated*, through the loss of energy in the medium, a mechanism termed absorption. Another mechanism of attenuation in biological tissues is due to scattering, or dispersion, of the energy in all directions when the mechanical wave hits particles smaller than the wavelength. As a part of the energy is removed from the beam, the intensity decreases as ultrasound travels and undergoes attenuation, so density difference between maximum and minimum amplitudes is correspondingly decreased (Fig. 1.11). At a given frequency, the amount of energy loss per distance traveled through the medium can vary depending on the human tissues of concern. For example, the attenuation in muscle is twice that of liver and soft biological tissues. The frequency of the ultrasound beam is another important parameter to consider. As the frequency is increased, so is the attenuation. This explains why ultrasound images are more attenuated as a function of depth at higher frequencies. It is interesting to note that attenuation due to scattering actually decreases with increasing frequency. However, the decrease in attenuation scattering is not sufficient to compensate for the increase in absorption at higher frequencies. Therefore,

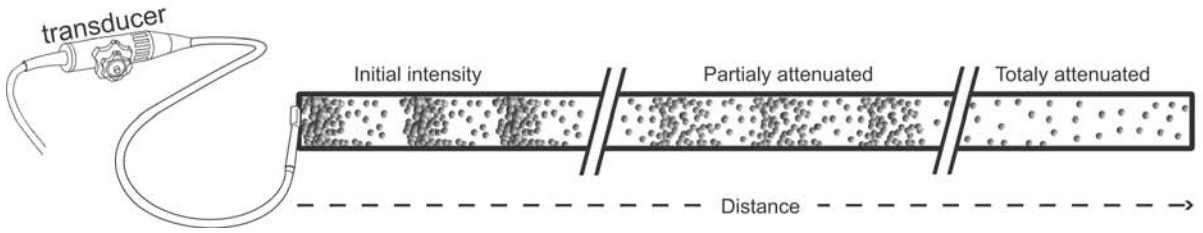

Figure 1.11 Attenuation. As the wave travels through the medium and undergoes attenuation, the relative difference of density between compressions and rarefactions, or intensity, decreases.

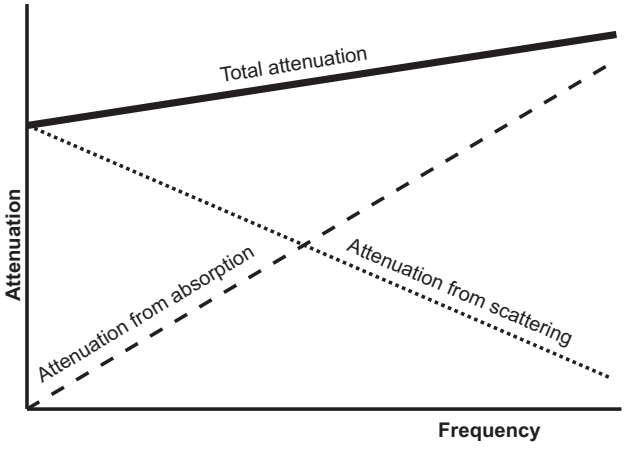

Figure 1.12 Components of attenuation. Total attenuation arises from both absorption and scattering, which are modified by a frequency change. With increasing frequency, attenuation due to absorption increases (worsens) while that secondary to scattering decreases (improves). Overall, the effect of absorption predominates such that overall attenuation increases with imaging frequency.

the total attenuation increases with frequency, as illustrated in Fig. 1.12.

In order to describe attenuation, it is possible to look at the ratio of intensities at two points along the beam. As intensity changes can span a very large range, it is convenient to express it in the logarithm scale,[1] as this mathematical operation considerably compresses the range of values that can be met. For instance, intensity changes from 1000 to 10 (ratios of attenuation) can be expressed as 3 and 1, respectively, on a logarithmic scale (Table 1.3).

There is a convention to indicate that a given attenuation has been obtained from the log of a ratio rather than the ratio itself, and consists of converting the ratio in units of "bel." Generally, the prefix "deci" is applied

[1]The computation of the logarithm (abbreviated as log) of a certain value can be interpreted as answering the following question: "Which power of 10 would give the value for which a logarithm is sought?" For example, the log of 100 is 2 (10 elevated to the power 2 is 100), whereas the log of 1000 is 3 (10 elevated to the power of 3 is 1000).

Table 1.3 Relative ultrasound intensity changes for various decibel values, both negative and positive

dB	Relative intensity
−40	0.0001
−30	0.001
−20	0.01
−10	0.1
−3	0.5
−2	0.63
−1	0.79
0	1.0
1	1.26
2	1.59
3	2.00
10	10
20	100
30	1000
40	10,000

on the "bel," and the resulting unit, the decibel, is used with the abbreviation dB. From this discussion, the calculation of attenuation in decibel is given by:

$$\text{Attenuation (dB)} = 10\log\left(\frac{I_2}{I_1}\right) \tag{1.8}$$

where I indicates the intensity. The attenuation in decibel has a negative value and is expressed as a function of depth (e.g. -0.5 dB/cm). If the pressure is considered instead of the intensity, the multiplicative factor of 20 should be used instead of 10, as in Eq. (1.3):

$$I \propto P^2$$

The attenuation in human tissue is fairly constant per unit of depth, being about 0.5 dB/cm at 1 MHz (see Table 1.2 for attenuation values of different materials). Multiple attenuations in decibel can be arithmetically added to yield the overall attenuation. Therefore, one can simply obtain the overall attenuation of a beam crossing a

certain thickness (th) measured in centimeters (cm), using

$$\text{Attenuation (th)} = 0.5\frac{\text{dB}}{\text{cm}} \times \text{th(cm)} \tag{1.9}$$

To account for frequency, a first-order approximation can be used by considering a linear relationship between attenuation and frequency. Consequently, Eq. (1.9) can be rewritten, for all frequencies (measured in MHz), as

$$\text{Attenuation } (f, \text{th}) = 0.5\frac{\text{dB}}{\text{MHz} \cdot \text{cm}} \times \text{th(cm)} \times f(\text{MHz}) \tag{1.10}$$

When working with depth on the screen of an ultrasound scanner, one has to take into account that ultrasound has to travel from the probe to the target point, and back to the probe, so the resulting attenuation as a function of depth (d) is

$$\text{Attenuation } (f, d) = 0.5\frac{\text{dB}}{\text{MHz} \cdot \text{cm}} \times 2d(\text{cm}) \times f(\text{MHz}) \tag{1.11}$$

Consequently, attenuation can be approximated as being proportional to both depth and frequency (Fig. 1.13).

II. IMAGING

The imaging process can be presented in several modes of data acquisition and display. This includes A-, B-, C-, M-mode and three-dimensional (3D) imaging (Fig. 1.14).

A. Advantages and Limitations of A-, B-, and M-Mode Ultrasonography

1. A Mode

Transducers, which are described in greater detail in Chapter 3, are driven by an electrical signal (voltage) to produce ultrasound waves. An interesting feature of transducers is their bifunctionality allowing them not only to emit but to also receive ultrasound and create an electrical signal from it, although the voltage involved in that process is much weaker than that used for emission.

The bidirectional mode of operation of a transducer is fundamental to the process of ultrasound image formation, of which *mode A* (for *amplitude* mode) is the most elementary form [Fig. 1.14(D)]. In mode A, a transducer releases

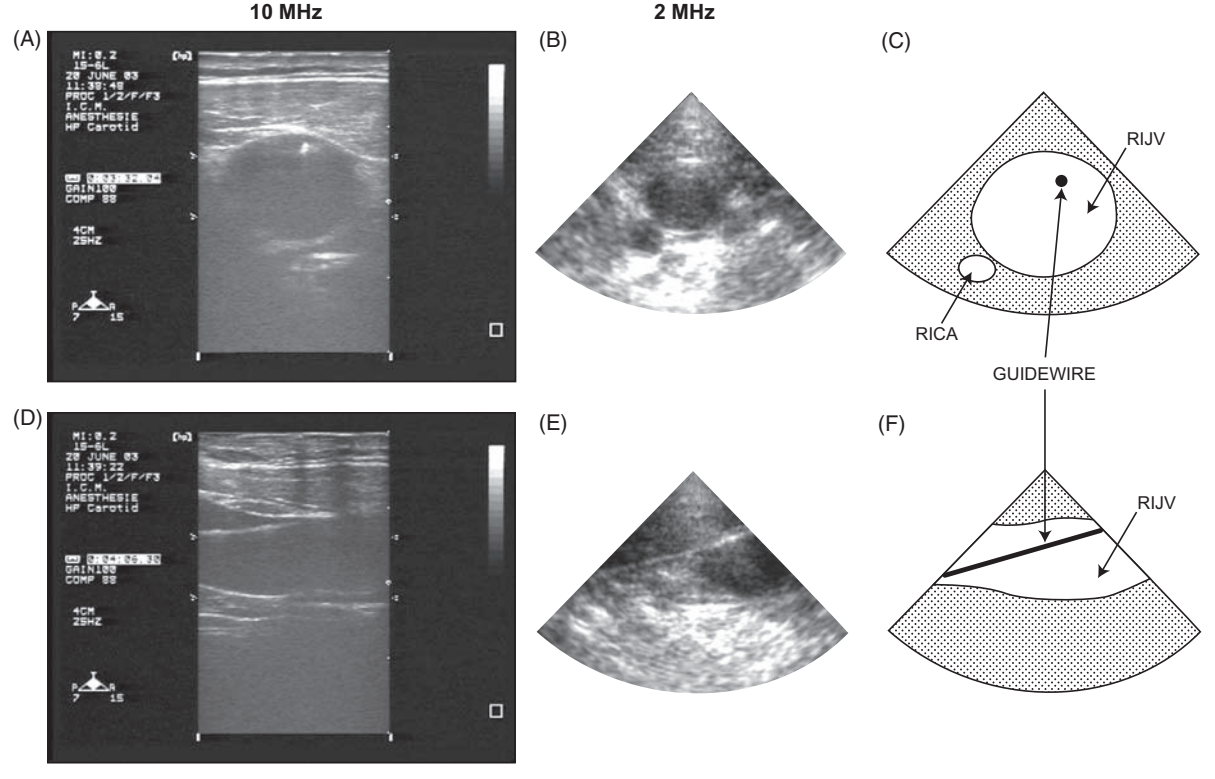

Figure 1.13 Imaging ultrasound frequency. (A–C) Transverse plane. (D–F) Longitudinal plane of right internal jugular vein (RIJV) and right internal carotid artery (RICA). The selection of the probe frequency determines the relative importance of either better resolution or improved penetration for structural imaging. The image obtained with the 10 MHz transducer provides more anatomical details but the deeper carotid artery is not as clearly seen as with the 2 MHz probe because attenuation is increased with higher frequency.

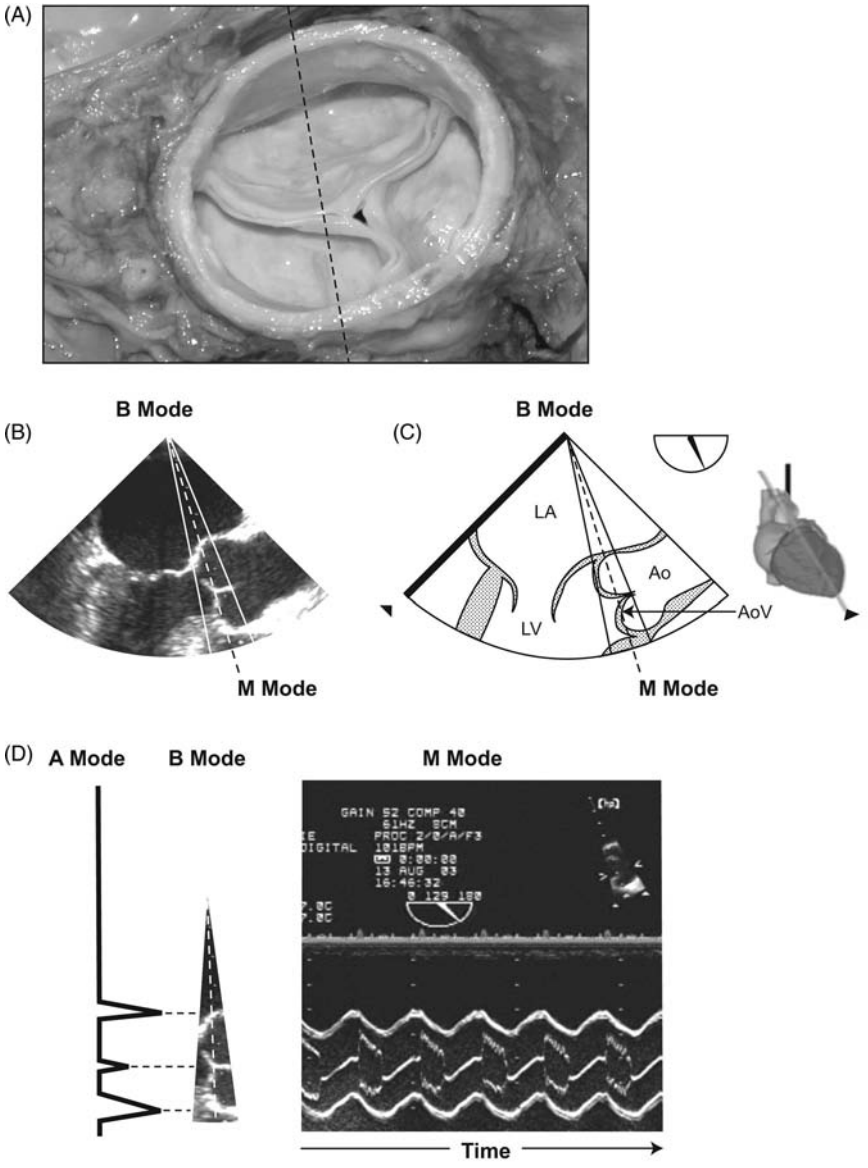

Figure 1.14 Ultrasound imaging modes. B (brightness), M (motion), and A (amplitude) modes are illustrated. (A) The real object, an aortic valve, is displayed. (B, C) Brightness mode displays the intensity of the echo signals on a bidimensional map. (D) The amplitude mode (or A-mode) displays each ultrasound boundary reflector as a peak corresponding to the strength of the reflected ultrasound. In M-mode, a small slice of the 2D object is displayed on a 2D format where the abscissa represents the time dimension and the ordinate represents the spatial dimension. This allows motion of the anatomical structures to be displayed (Ao, aorta; AoV, aortic valve; LA, left atrium; LV, left ventricle). (Photo (A) courtesy of Dr Nicolas Dürrleman.)

a *pulse*, or a small sequence of successive compressions and rarefactions created by the oscillating surface of the transducer. The oscillating surface then comes to rest, putting itself in "listening" mode, while the rarefaction and compression waves travel away from the transducer. The wavefront eventually meets a reflector, or a zone of acoustic impedance difference, which returns a fraction of the incident ultrasound wave energy (thus creating an *echo*), while the nonreflected component pursues its course. As further reflectors are met, the same process is repeated, with more echoes being returned to the transducer, until echoes from the maximum depth (set as an operating parameter) are received. At this point, a new pulse is released and a new series of echoes is received.

In the ultrasound scanning system (Fig. 1.15), the transducer spends relatively little time emitting ultrasound, and is most of the time listening for returning echoes. The amplitude mode (or A-mode) owes it name to the fact

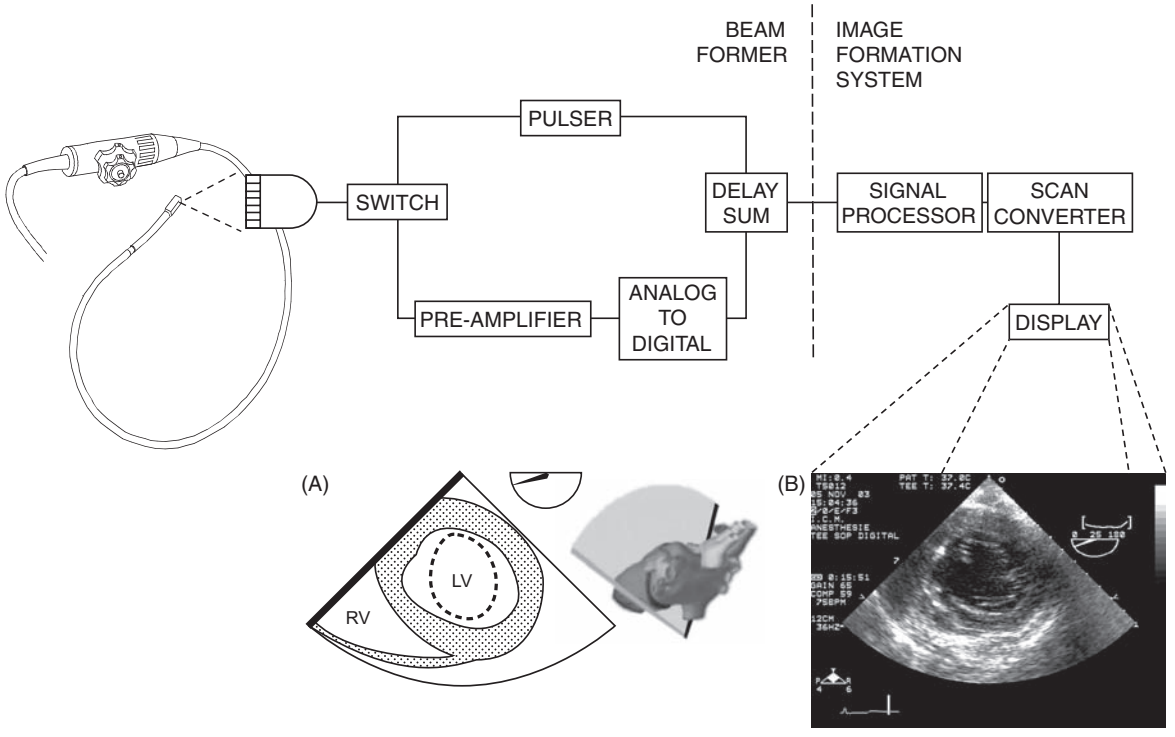

Figure 1.15 Ultrasound scanning system. Schematics of an ultrasound scanner, divided in two subgroups: the beam former and the image formation system. On the beam former side, the electronics illustrated exist for each element of the transducer array, and connect to the delay/sum module. The latter then connects to the image formation modules (LV, left ventricle; RV, right ventricle).

that it displays each ultrasound boundary reflector as a peak corresponding to the amplitude of the reflected ultrasound echo envelope. The A-mode allows identification of changes in echogenicity (or the presence of ultrasound reflecting structures) of a patient. However, the information is unidimensional as only the depth and relative strength (itself an indication of the impedance difference) of reflecting structures can be determined (Fig. 1.14). No precise determination of the shape of these structures can be achieved. With the exception of ophthalmology and research applications in tissue characterization, A mode is rarely used in medical imaging.

Such an *echo train* of returning periodic echoes is detected by the transducer which converts it to an electrical signal. Successive electrical signals are then created, and are separated by time intervals corresponding to the time taken by ultrasound pulses to travel between those reflectors, also termed *time-of-flight.* The relationship between the time-of-flight (t), propagation speed (c), and the distance (d) traveled by ultrasound is given by

$$d = ct \tag{1.12}$$

The time of arrival of an echo at the transducer is related to the depth at which the reflecting structure is located. To determine the depth of a reflecting structure, it is important to take into account the fact that the ultrasound echo has to accomplish a round trip and consequently twice the time is required.

Equation (1.12) also expresses the need to know precisely the propagation speed of ultrasound in order for an accurate value of depth to be calculated. Fortunately, propagation speeds in most tissues are closely represented by an accepted average value of 1540 m/s, and this is necessary to allow ultrasound images to be relatively free of geometrical distortion. In fact, most large geometrical distortions occur from other causes, for example, refraction.

2. *B Mode*

The brightness mode (or B mode) represents each ultrasound boundary reflector as a luminous dot whose brightness is proportional to the strength of the received echo. The B-mode can allow for 2D echogenicity maps to be acquired. It can be obtained by juxtaposing multiple B-mode lines, where each one is plotted on an image matrix with an intensity proportional to the echo strength, as shown in Fig. 1.14 (a matrix is a 2D arrangement of values positioned in rows and columns, as in Fig. 1.16). The ultrasound beam for B-mode imaging is kept narrow enough by focussing so that the interrogated tissue (the

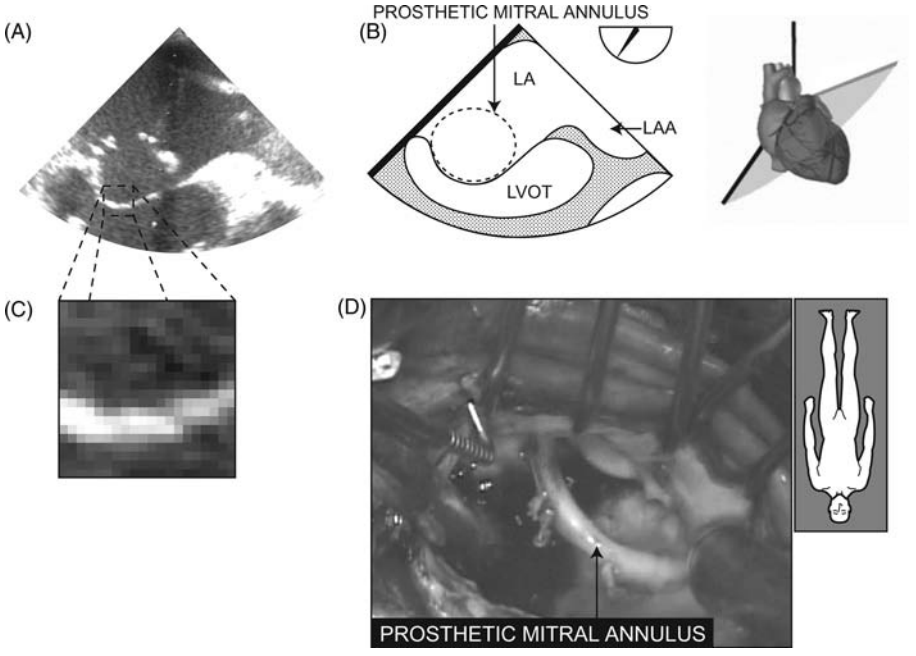

Figure 1.16 Matrix representation of an ultrasound image. (A–C) A matrix is a 2D arrangement of rows and columns of pixels, easily evident on higher magnification in (C). (D) Anatomical correlation (LA, left atrium; LAA, left atrial appendage; LVOT, left ventricular outflow tract). (Photo (D) courtesy of Dr Michel Pellerin.)

tissue that returns an echo) is confined laterally for a given scan line. By moving the scan line mechanically or electronically, 2D maps of echo strength can be obtained. During the receiving of a given scan line, all echoes are assumed to originate from points along that line, whose precise distance from the transducer can be determined using Eq. (1.12). The vast majority of contemporary B-mode systems now direct the beam by using a nonmechanical technique in a manner that will be described in detail in Chapter 3.

3. M Mode

In M-mode (motion mode), an A line is displayed on a 2D B-mode map (image matrix) with brightness indicating the echo strength or the amplitude [Fig. 1.14(D)]. However, the other dimension direction corresponds to time rather than lateral distance, as in A- or B-mode. Consequently this mode is used to show the motion of reflectors as a function of time by continuously retracing a line such as is acquired in B-mode, but maintaining the location to which this line corresponds with respect to the patient, hence insonifying the same column of tissue every time (in a true B-mode image acquisition, that line in swept in the patient). Each of these lines is traced vertically in the image, and shifted laterally on the screen from one line to the next. Once the full width of the image has been swept in this way, the process is repeated for a new image. This mode is commonly used for dimensional measurements at specific time of the cardiac cycle and for the analysis of valve leaflets, wall and abnormal structure motions.

4. Other Modes

Other modes of imaging, such as C-mode, duplex, Doppler, and 3D imaging are not described here and are beyond the scope of this chapter.

B. Instrumentation

1. Transducers

Whatever the type of transducer used, a 2D scanner image involves the gathering of multiple B-mode lines to construct the final image. Modern transducers are actually made of many crystal elements disposed as an array within a portable assembly. Each element is selectively fired using a scheme described in Chapter 3. It is common to refer to the assembly as the *probe*. Modern transducers can generate a narrow beam of ultrasound, and direct it in a selectable direction, in a manner compatible with the description of B-mode acquisition given earlier. The term "narrow" in the previous sentence applies to both the lateral (or "in-plane") and axial (or "in the beam") directions.

2. Transmitting/Receiving Electronics

The dual use of the transducer for both ultrasound transmitting and receiving implies that some switching must take place. In addition, the different signal strengths involved between transmission and reception imply that different electronics must be used for each role. The beam former is the first stage of the transmitting/receiving electronics, and handles output/input to/from the transducer elements. As represented in Fig. 1.15, switching allows for the selection of the proper module within the beam former, depending on whether the system is transmitting or receiving.

When the system is in transmitting mode, the beam former generates the signal to be sent to the different transducer elements. Focusing of the transmitted beam can be achieved by correctly selecting the delays of the electrical impulses fired by each crystal element. The output for each element has to be amplified so that a large voltage (typically 100–200 V) can be applied to the transducer elements, a task performed by the "pulser," which connects to the switching module.

When the system is in receiving mode, the weak voltage detected must first be amplified using a preamplifier. That amplification process is weighted as a function of the time-of-flight, increasing the applied gain as greater time-of-flight implies greater attenuation that needs to be compensated for. The signal is then converted into digital form, as most modern systems do most processing in such format. Further processing is applied to combine the signal from the different transducer elements (or individual crystals) to form a single A-mode scan line, a step termed "focusing." It involves the summing of the signals from many transducer elements, each of those signals being applied at a variable time delay prior to recombination. Delays for each element are typically time variable, so as to allow "dynamic focusing" with time delays best suited for each depth at which an echo is detected. Adiposization also is performed by most beam former. This refers to the process that consists of multiplying the echo of each element of the array by a "weight." This allows performance shaping of the ultrasound beam and modification of the size of the side lobes. The scan line is the final product of the beam former stage.

The stage following the beam former is the signal processor, which first applies time gain control (TGC) to amplify the scan line increasingly as a function of depth. The TGC settings are normally user-adjustable (Fig. 1.17).

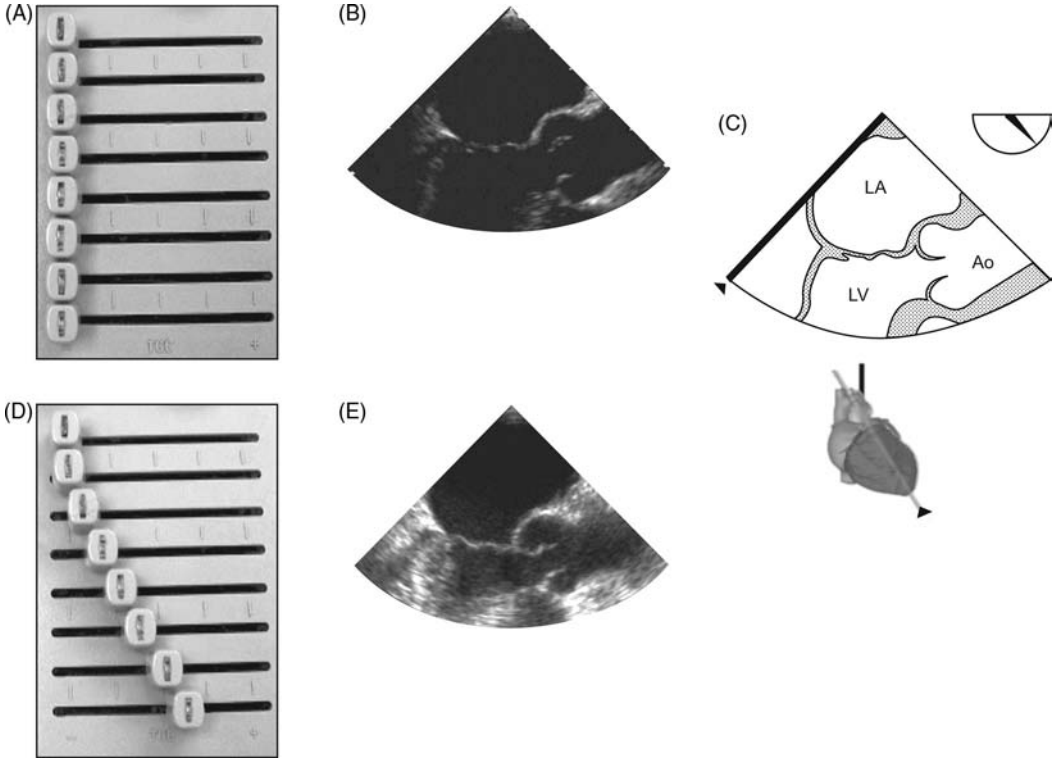

Figure 1.17 Time gain compensation. Effect of the time gain compensation (TGC) adjustments to obtain a mid-esophageal long axis view of the aortic valve. A given TGC control slider is assigned to determine depth range. (A–C) The TGC control sliders are set to the left at 0. As the depth increases towards the bottom, the image brightness is less because of attenuation. (D–E) TGC adjustments are made to adjust the brightness to that of the near field, creating a more homogenous image (Ao, aorta; LA, left atrium; LV, left ventricle).

The signal is then converted to its logarithm form, which effectively compresses the range of signal values encountered. This procedure allows the display of both large amplitude echoes from reflectors and weak scattering from small cellular elements on a single 2D display. The signal is then rectified, and the envelope of the signal is obtained. An overall description of a typical ultrasound scanner is provided in Chapter 3.

3. Scan Converters

The scan lines have to be stored and combined so that a 2D image can be obtained and displayed. This task is left to the *scan converter*, a device which represents the overall image as a matrix. Interpolation between the various A-lines of data has to be performed to obtain a matrix of typically 512 × 512 pixels. Modern scan converters also support a variety of postacquisition image processing, and are integrated with storage and transmission peripherals (e.g. network card).

C. Signal Processing, Image Resolution, and Display

1. Time Gain Control

There are two sets of gain control for the receiving amplifier: the overall gain control (Fig. 1.18), which affects all echoes equally, and the TGC (Fig. 1.17), which modifies the performance of the amplifier as a function of depth.

The TGCs are divided into two types. The first TGC amplification of the received signal is weighted according to the time-of-flight. The gain applied between the nearest and farthest echoes may be linear or follow a predetermined non-linear function to emphasize, for example, the echo signals away from the transducer. This step is also used to adjust the dynamic range of the displayed images. For this purpose, the maximum and minimum gains in decibels applied as a function of depth can be predetermined. This allows limiting the range of echo strengths to display the B-mode images, and consequently the echo contrasts, which may help emphasizing diagnostic features.

The second type of TGC consists of a series of cursors (also known as sliders or potentiometers) that are usually available beside the monitor to modulate the amplification as a function of depth (or time-of-flight). These cursors are easily accessible and their positions are changed by the clinician or technician according to the physiological structures being investigated (Fig. 1.17).

2. Image Resolution

Resolution is the ability to distinguish small objects located close to each other. The resolution of ultrasound imaging systems is best analyzed as separate components

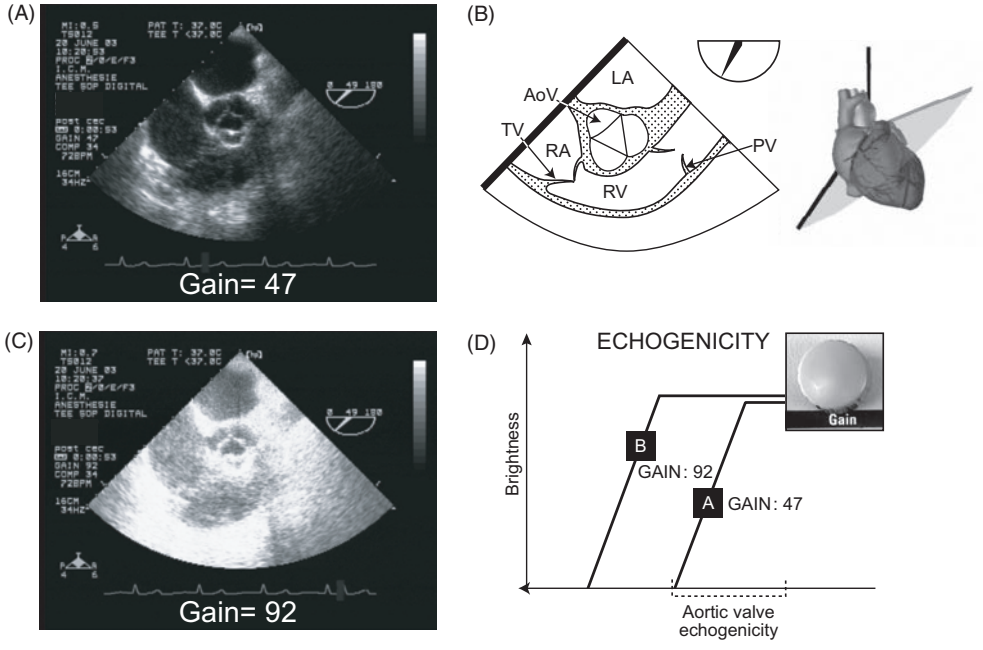

Figure 1.18 Overall gain control. (A, B) Mid-esophageal short axis view of the aortic valve. The effect of varying gain is shown. Gain = 47. (C) Higher gain at 92. (D) Adjusting total gain modifies the relative position of the center of the slope with respect to the available range. Brightness is therefore enhanced within that range. However, echo signals below the chosen minimal threshold will appear as black pixels, while those exceeding the maximal range will be uniformly displayed as dense white pixels (AoV, aortic valve; LA, left atrium; PV, pulmonic valve; RA, right atrium; RV, right ventricle; TV, tricuspid valve).

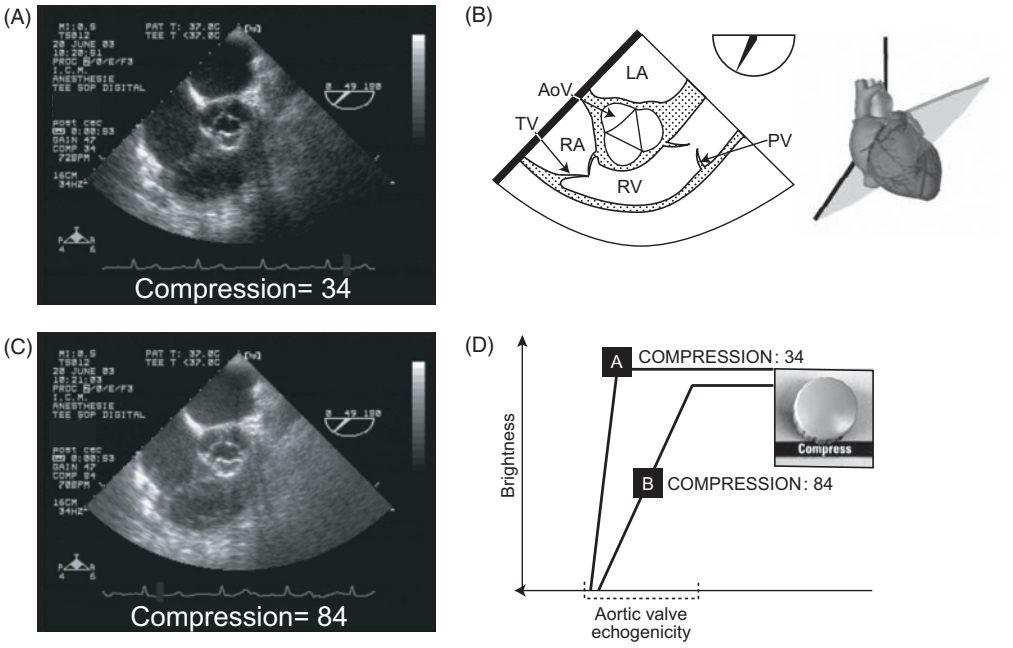

Figure 1.19 Dynamic range compression. (A, B) Mid-esophageal short axis view of the aortic valve. The effect of varying compression is shown. Compression = 34. (C) Higher compression at 84. (D) Compression range modifies the slope of the relationship between brightness and echo strength. Secondarily, it also alters the range of echo signal strength which can be displayed by the scale of brightness. Contrast is therefore enhanced within that range. For instance, the brightness difference between blood and aortic valve is more pronounced with lower compression (slope A). Reducing compression range increases the slope such that larger difference in brightness will occur for the same difference in echo strength. Increasing compression range reduces the perceived difference in brightness because the slope is more flat (AoV, aortic valve; LA, left atrium; PV, pulmonary valve; RA, right atrium; RV, right ventricle; TV, tricuspid valve).

of the overall resolution, that is the axial resolution (along the direction propagation of ultrasound), and the lateral resolution (perpendicular to it). For most systems, the axial resolution, which is of the order of 1 mm, is better than the lateral resolution. Image resolution is largely influenced by the design of the transducer, and the beam former in both transmission and reception. Resolution is further discussed in Chapter 3.

3. Display

The ultrasound image is displayed on a computer monitor, which allows for the viewing of the real-time representation of the ultrasound image. Dynamic range compression determines the range of echo strength used to display ultrasound echo intensities and may affect overall image contrast (Fig. 1.19). For each new frame acquired by the system, the display is refreshed with the new image data. This is repeated many times per second, allowing for a real-time update of the image. Digital processing and storage capability are today available with most ultrasound systems.

D. Related Factors

1. Pulsing Characteristics

Pulsed-waves can be characterized by the following parameters: pulse duration (PD), pulse repetition period (PRP), pulse repetition frequency (PRF), duty factor, and spatial

Table 1.4 Various Parameters for Pulsed Ultrasound

Parameters	Basic units	Units	Determined by	Common values
Pulse repetition period	Time	s, μs	Sound source	0.1–1.0 ms
Pulse repetition frequency	1/time	1/s, Hz	Sound source	1–10 kHz
Pulse duration	Time	s, ms	Sound source	0.5–3.0 μs
Duty factor	None	None	Sound source	0.001–0.01
Spatial pulse length	Distance	mm, cm	Source and medium	0.1–1.0 mm

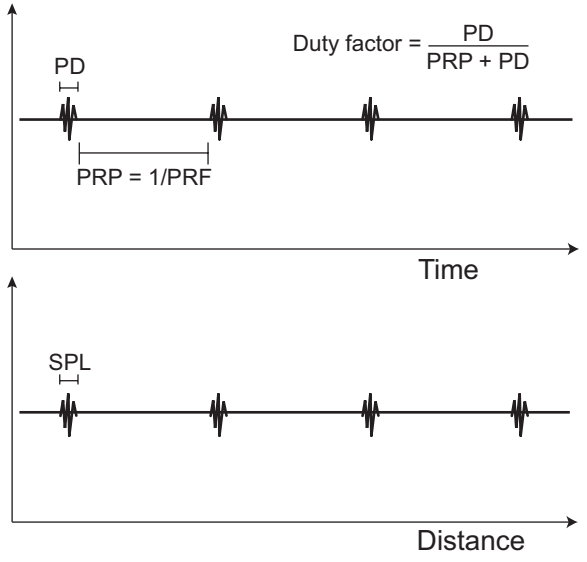

Figure 1.20 Pulsed Doppler wave characteristics (see Table 1.4). (PD, pulse duration; PRP, pulse repetition period; PRF, pulse repetition frequency; SPL, spatial pulse length).

pulse length (SPL) (Table 1.4). The pulse duration and the PRP are illustrated in Fig. 1.20. The duty factor is the fraction of time that the ultrasound machine is producing a pulse. It corresponds to the ratio of the PD to the PRP. Duty factors are important in relation to the average intensity.

The PRF can be defined as the number of pulses emitted by the transducer per unit of time, or $1/\text{PRP}$ and it depends on the maximum depth $d_{\max}$ and velocity of propagation (c) according to the following equation:

$$\text{PRF} = \frac{c}{2d_{\max}} \tag{1.13}$$

Thus, it is clear that the number of pulses per time unit depends on the maximum depth for which echoes are to be measured (Fig. 1.21).

2. Frame Rate and Time to Generate One Frame

The exact number of lines from which the image (also called a *frame*) is made can vary, and this number is referred to as N_{line}. The number of frames per second (or frame rate) f_{frame} is given by

$$f_{\text{frame}} = \frac{\text{PRF}}{N_{\text{line}}} \tag{1.14}$$

This explains why a small sector (lower N_{line}) will result in a higher frame rate, and why an increase in PRF will be associated with a shallower (less time is required to wait for distal echoes) image with an increased frame rate (Fig. 1.22). By combining Eqs. (1.13) and (1.14), the latter can be rewritten as

$$f_{\text{frame}} = \frac{c}{2d_{\max}N_{\text{line}}} = \frac{154\,000\ \text{cm/sec}}{2d_{\max}N_{\text{line}}} \tag{1.15}$$

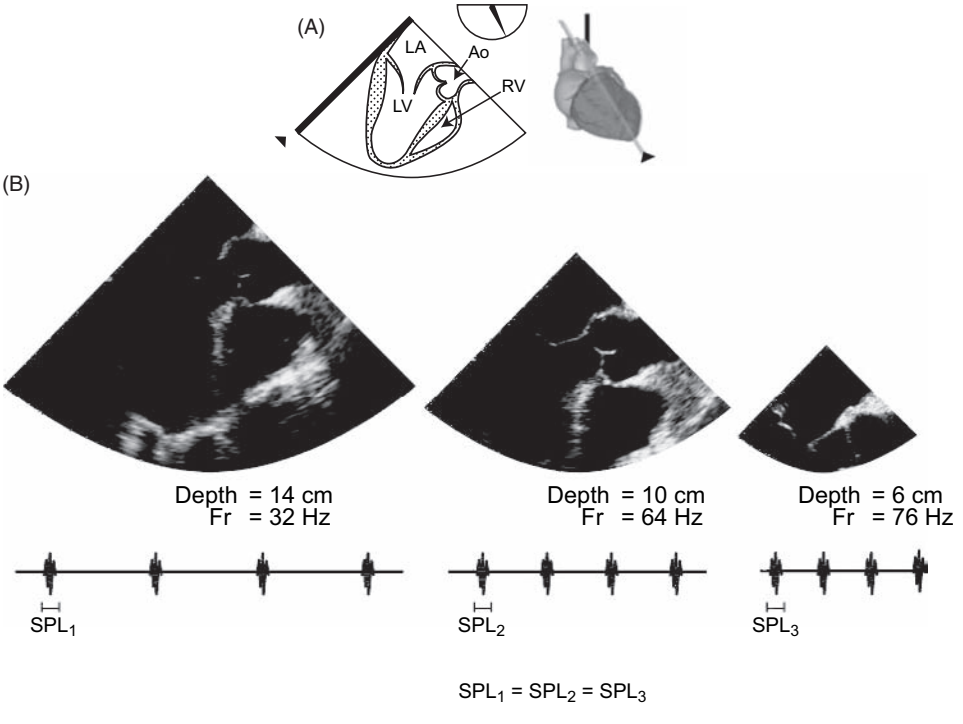

Figure 1.21 Maximal imaging depth as a function of the pulse repetition frequency (PRF). As depth is decreased, the PRF increases with associated increase in frame rate (Fr) from 32 to 64 and 76 Hz. Spatial pulse length (SPL) is left identical between the three cases (Ao, aorta; LA, left atrium; LV, left ventricle; RV, right ventricle).

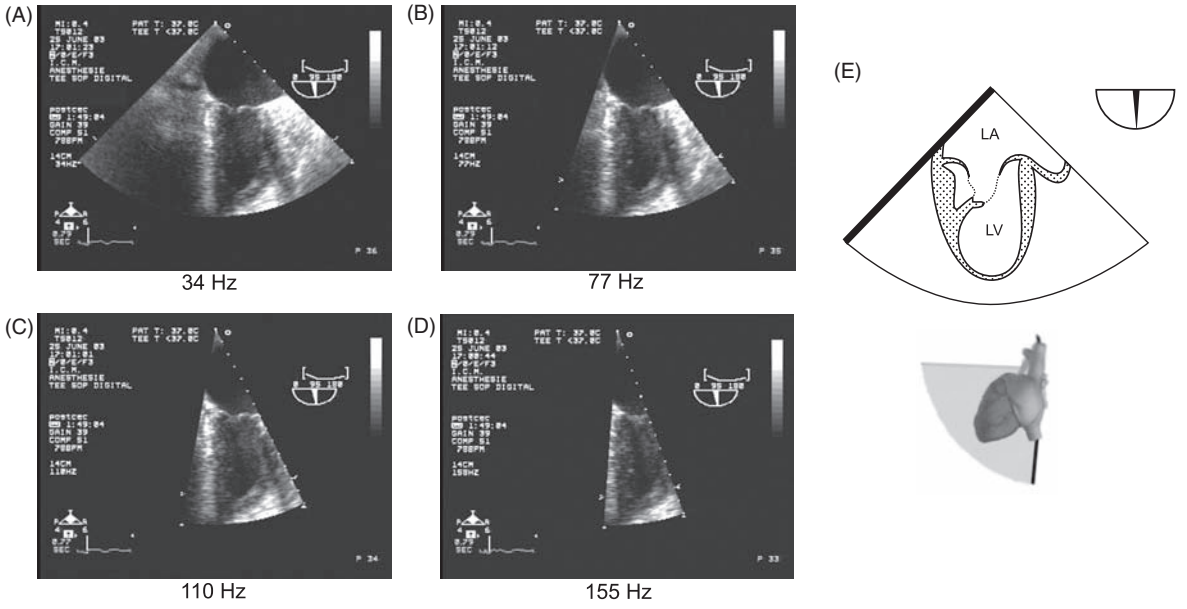

Figure 1.22 Width of the sector scan and frame rate. Mid-esophageal two-chamber view of the left ventricle (LV). (A–D) As the operator narrows the width of the sector scanned, the system takes less time to sweep the sector and thus refreshes the image more often. Thus, a narrower sector yields a higher frame rate. (LA, left atrium).

The average speed of ultrasound in tissues has been introduced in the second part of Eq. (1.15) to convert distance units to time units. The parameter $d_{\max}$ is the maximum depth of the image and is expressed in centimeters. The frame rate is typically displayed as a parameter on the monitor of ultrasound systems.

The time to generate one frame T_{frame} is simply

$$T_{\text{frame}} = \frac{1}{f_{\text{frame}}} = \frac{N_{\text{line}}}{\text{PRF}} \tag{1.16}$$

and one can use again Eqs (1.15) and (1.16) to rewrite Eq. (1.17):

$$T_{\text{frame}} = \frac{2d_{\max}N_{\text{line}}}{c} = \frac{2d_{\max}N_{\text{line}}}{154\,000\ \text{cm/sec}} \tag{1.17}$$

where $d_{\max}$ is again expressed in centimeters. As the depth decreases, less time is spent waiting for returning echoes, and T_{frame} decreases, while f_{frame} increases (Fig. 1.21). Decreasing the number of lines per image has the same effect (Fig. 1.22).

3. *Number of Lines per Frame*

The number of lines per frame can be rewritten from Eqs. (1.16) and (1.17):

$$N_{\text{line}} = \frac{154\,000\ \text{cm/sec}}{2f_{\text{frame}}d_{\max}} = \frac{1{,}54{,}000T_{\text{frame}}}{2d_{\max}} \tag{1.18}$$

If the depth increases, less lines can be acquired if a given frame rate is to be maintained. The number of lines covering a given area in an image influences the lateral resolution, which increases with the density of such lines. However, if the number of lines is modified with corresponding change of spatial coverage (scanning sector) to maintain the scan line density, lateral resolution is not affected, but the time to acquire a frame will be modified, as indicated by Eq. (1.17), with a corresponding change in frame rate (Fig. 1.22).

4. *Depth*

As the ultrasound beam travels away from the transducer, it not only undergoes multiple reflections, but also becomes attenuated. Therefore, there is less and less power available downstream from the transducer for remote reflectors to return an echo, so echo intensity decreases with the depth from which it originates. Although distal echoes are more amplified than proximal ones, due to the TGC control, this only works up to a point, when the echo signal is so weak that its electrical signal becomes similar in strength to electrical noise, the presence of which is unavoidable in any electronic system. This, therefore, defines a maximum range for an ultrasound beam, which depends on the capability of the system to detect small echoes, and the frequency employed, through the influence of the latter on attenuation (Fig. 1.13). It is also possible to increase the time resolution by decreasing the image

depth, as indicated on the screen by an increase in the frame rate (Fig. 1.21).

5. Temporal Resolution

The temporal resolution is given by Eq. (1.17) and is the time taken to generate one frame. As T_{frame} increases, the motion in the image field is not correctly rendered as structures seem to move in a discontinuous fashion from one frame to the next. Temporal resolution is, therefore, possibly gained at the expense of lateral resolution (number of lines) and maximum depth from which echoes are measured. In cases where temporal resolution is called for, such as during TTE, this provides a strong incentive to bring the probe as close as possible to the anatomy of interest, thereby decreasing the maximum exploration depth (with respect to the probe). This is precisely what is done in transesophageal ultrasound.

6. Pixels

A pixel is the smallest element of a digital picture. Image data gathered from an ultrasound imaging system ultimately end up being represented as a matrix, typically of 512×512 pixels, which is then displayed on a computer screen in real time. As the acquired lines do not follow the columns or rows of the matrix, an interpolation process needs to be used in order to resample the image

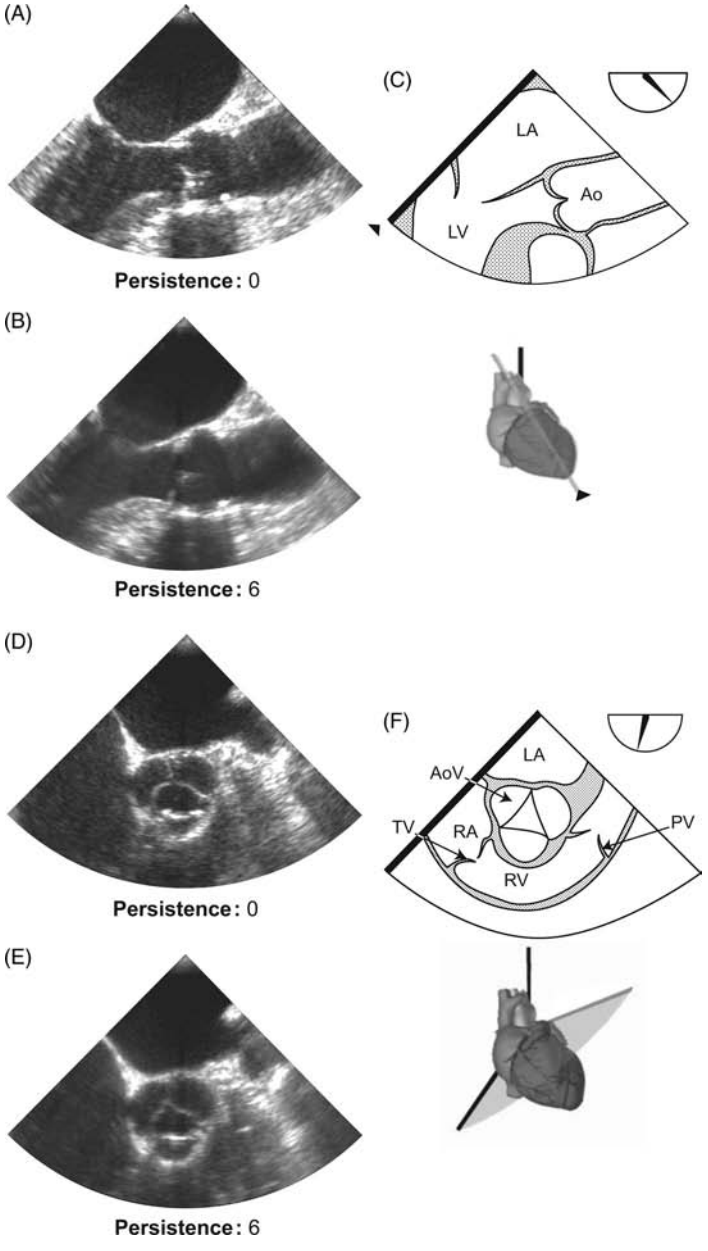

Figure 1.23 Persistence. Mid-esophageal long (A–C) and short axis (D–F) view of the aortic valve. Digital post-processing can substantially impact image appearance. By averaging multiple images (persistence) in (B) and (E), the image appears smoother, at the cost of reduced time resolution (Ao, aorta; AoV, aortic valve; LA, left atrium; LV, left ventricle; PV, pulmonic valve; RA, right atrium; RV, right ventricle; TV, tricuspid valve).

to the image pixels. The number of available pixels is normally such that no resolution loss is incurred from that process. Such *digital images* lend themselves well to post processing which can sometimes enhance the appearance of images, and make important details more conspicuous (Fig. 1.23).

The image is normally displayed with the points located in the vicinity of the probe on top on the monitor image. Simple ultrasound images are generally displayed as grayscale, with a pixel value in the range of 0–255 (8 bits). However, a narrower range is generally selected for display, through *windowing* which allows for that narrower range of pixel values to be represented by the full brightness range of the monitor, at the expense of contrast for pixel values outside of that range, which are either black or white. However, Doppler images need to be represented in color. To accomplish this, such images are rendered using 16–24 bits.

The Dicom standard allows for images to be sent in digital form to an external device over conventional, non proprietary networks. This is accomplished via the use of the common TCP/IP transmission protocol (often referred to as the Internet protocol) over that network. This group of protocols enables devices from different manufacturers to exchange images, including all attached demographic data and other acquisition information that accompany images. Image management systems, such as picture archiving and communication systems (PACS), can then take over the distribution, display and archival of images. Both static and dynamic images can be sent using Dicom, although dynamic data such as obtained in echocardiography requires a considerable amount of disk storage space, and this constitutes an emerging challenge for PACS.

III. CONCLUSION

The operation of ultrasound imaging systems is based on principles directly derived from the Physics and technology of medical ultrasound. A proficient use of such systems strongly depends on mastering these principles.

BIBLIOGRAPHY

Kremkau FW. Diagnostic Ultrasound: Principles and Instruments. 6th ed. Philadelphia: WB Saunders, 2002.

Bushberg JT, Seibert JA, Leidholt EM, Boone JM. The Essential Physics of Medical Imaging. 2nd ed. Philadelphia: Lippincott Williams & Wilkins, 2002.

Zagzebski JA. Essentials of Ultrasound Physics. St. Louis: Mosby-Year Book, 1996.

McDicken WN. Diagnostic Ultrasonics. 3rd ed. New York: Churchill Livingstone, 1991.

2

Basic Principles of Doppler Ultrasound

PIERRE-GUY CHASSOT

Centre Hospitalier Universitaire Vaudois (CHUV), Lausanne, Switzerland

I. Doppler Effect 23
II. Instrumentation 25
III. Aliasing 26
IV. Continuous- and Pulsed-Wave Doppler 27
V. Spectral Display 30
VI. Color Doppler 31
VII. Doppler Tissue Imaging 37
VIII. Artifacts 37
IX. Clinical Applications 39
Acknowledgments 39
References 39

I. DOPPLER EFFECT

The Doppler effect is a well-known phenomenon: the sound of a train whistle has a higher pitch when the train is traveling towards the listener than when moving away, although the emitting frequency remains the same. In 1842, the Austrian physicist Johann-Christian Doppler, studying the direction of movement of stars, described mathematically this shift of frequency of recorded waves, when a luminous or acoustic source, in relative motion, is compared with the stationary observer. The velocity of traveling waves (C), such as light, sound or ultrasound, is constant through a determined medium, and depends on the characteristics of this medium. When the emitting source is in motion, regardless of its speed, the sound waves are "compressed" in front of the transmitter, which is "catching up" with the transmitted waves it has produced [Fig. 2.1(A)]. After generating an ultrasound wave, the source moves slightly before emitting the next wave. The two waves peaks are then closer together when they reach the receiver (observer), where the wavelength is shortened and the frequency increased (1). This happens because the product of wavelength (λ) and frequency (f) is constant:

$$C = f \times \lambda \tag{2.1}$$

If the source moves away, the opposite occurs: the wavelength increases and the frequency decreases. The Doppler shift is the difference between the frequency generated by the source (f_0) and the frequency observed by the listener (f_1):

$$\Delta f = f_1 - f_0 \tag{2.2}$$

This shift is proportional to the ratio of the speed of the object (v) to the velocity of the sound (c) and to the generated frequency (f_0), but is independent of the amplitude of the wave:

$$\Delta f = \frac{v \times f_0}{c} \tag{2.3}$$

The formula can be rearranged to determine the velocity of the object:

$$v = \frac{c \times \Delta f}{f_0} \tag{2.4}$$

The same phenomenon occurs if the moving object is the target of an ultrasound wave emitted by a fixed source: the emitted ultrasound wave and the echo reflected wave returning to the transducer have different frequencies (Fig. 2.2). They are also linked by the previous Doppler

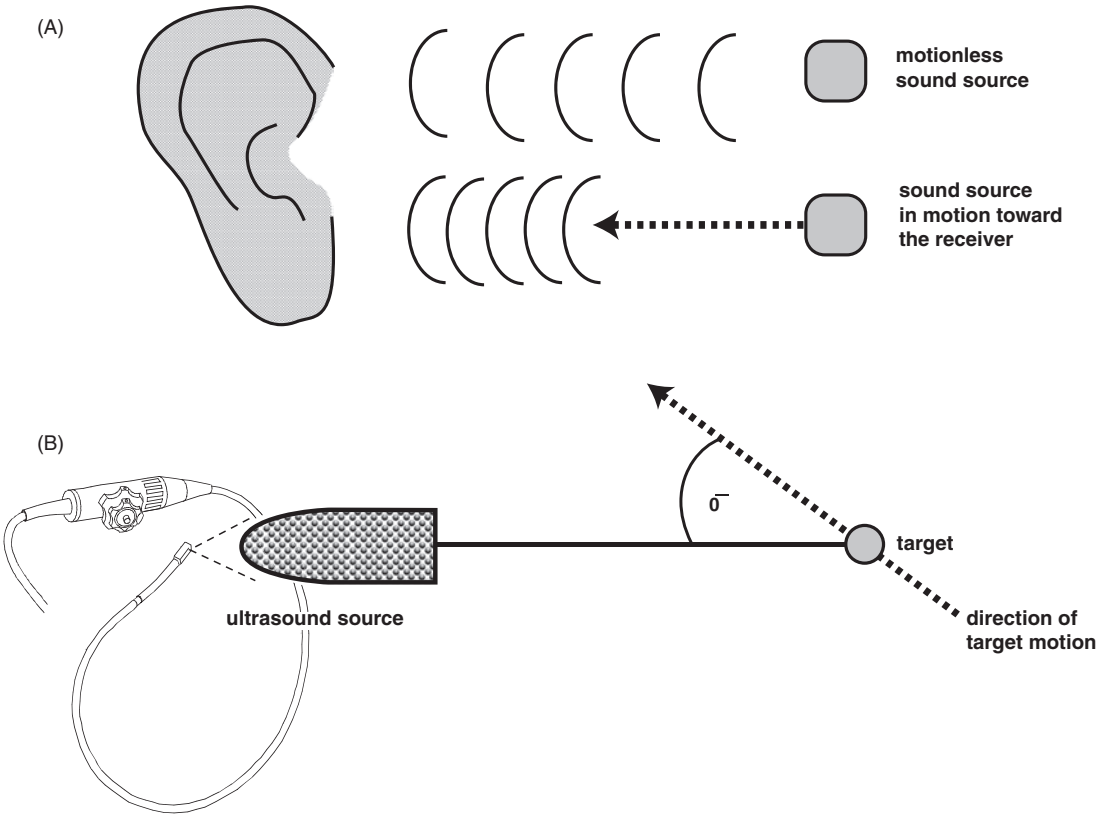

Figure 2.1 Doppler effect. (A) When a sound source is in motion towards the observer, its emitting frequency is increased compared with the same sound wave emitted from a stationary source. (B) Illustration of the angle (θ) between the direction of the interrogating Doppler beam and the direction of target motion.

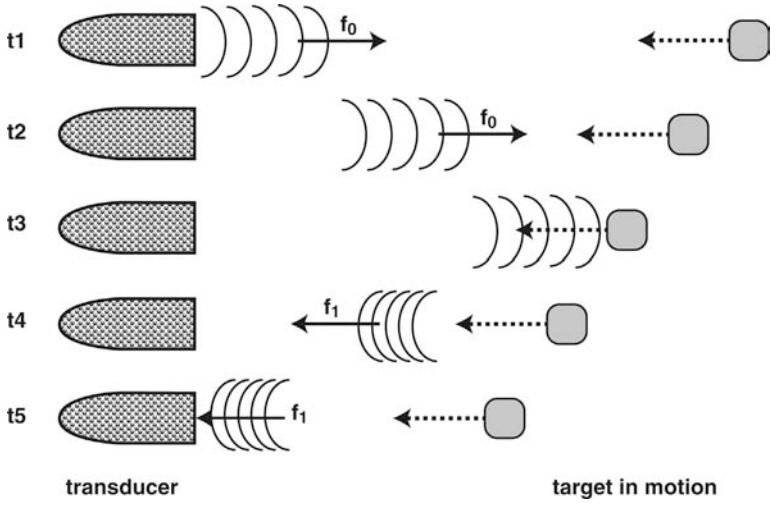

Figure 2.2 Doppler effect. The target in motion towards the transducer reflects the emitted sound wave of frequency (f_0) with an increased frequency (f_1). The delay of the time (t) sequence (t1 to t5) of the events determines the depth (distance) of the target.

equation, but the frequency shift occurs twice, in the emitted and in the reflected wave:

$$\Delta f = f_1 - f_0$$
$$\Delta f = \frac{v}{c} \times 2f_0 \quad (2.5)$$

The velocity of ultrasound in human soft tissues is constant; it lies between 1540 and 1580 m/s (2); in blood, the acknowledged value is 1540 m/s. The frequency shift can be positive or negative, depending on whether the target is moving towards or away from the receiver. The formula is completed by an angle correction, and can be rearranged to determine the velocity of the target:

$$v = \frac{c \times (\pm \Delta f)}{2f_0 \cos \theta} \quad (2.6)$$

where θ is the angle between the direction of the target and the interrogating ultrasound beam, v is the speed of the target (e.g. moving red blood cells), c is the ultrasound speed (1540 m/s), and f_0 is the emitting frequency of the ultrasound transducer.

The angle (θ between the direction of the target and the interrogating beam) has to be introduced in the formula, the maximal shift being observed when the transducer's orientation is parallel to the blood flow: if the angle is zero, the cosine is 1 [Fig. 2.1(B)]. On the other hand, perpendicular orientation of the interrogating beam to the axis of the flow gives no Doppler shift, because the cosine of 90° equals zero. Up to 20° (cosine 0.94), the underestimation induced by this angle in the velocity measurement is <6% (~5 cm/sec), and considered as negligible for clinical purposes (1). Increasing the angle to 30° (cosine 0.87) increases the error to 13%. Although ultrasound systems can perform a correction for the angle of incidence in the Doppler formula calculation, this correction is done only in the displayed bidimensional (2D) plane. Therefore, this angle correction is not recommended because it creates false precision (3).

With respect to the usual blood flow velocities (0.2–6.0 m/s), the speed of the ultrasound in tissues (1540 m/s), and emitting frequencies of the cardiac transducers (2–10 MHz), the Doppler shift falls within the human audible range (4–10 KHz) and can be heard through a loudspeaker. This sound is mathematically reproduced by addition or multiplication of emitted and received waves. The product of this operation is a new wave with a frequency equal to the Doppler shift (4). Echocardiography is based on the time delay measurement between the emission of a short pulse of ultrasound and the detected echo. Bidimensional echo is essentially based on variations in amplitude (or intensity) of returning waves, whereas Doppler echo analysis is based principally on variations in frequency (Fig. 2.2). Doppler analysis and 2D display require different conditions for optimal results. The best 2D image is obtained with a high-frequency transducer (>5 MHz), and an interrogating beam perpendicular to the structure. The Doppler shift is maximum when the ultrasound beam is parallel to the flow and when the emitting frequency is low (1–2 MHz) (5). In clinical practice, the set-up of the echocardiographic machine has to be properly adjusted for each function.

All moving structures and elements can induce a Doppler shift when hit by an ultrasound wave. Blood cell velocities represent a high-frequency, low-amplitude signal compared with the surrounding tissues which are characterized by high-amplitude (>80 dB) and low-frequency (<200 Hz) echoes. They are dense signals and move slower compared with blood. Echoes from heart structures are considered as "noise" in conventional Doppler systems and are eliminated by a high-pass filter. New systems of Doppler tissue imaging on the other hand are devoted to the analysis of the information contained in the low-frequency band of velocities as tissue velocities are rarely >10 cm/sec (6). In the following discussion, however, we will concentrate on blood flow. Unless mentioned otherwise, Doppler analysis concerns blood cells exclusively.

II. INSTRUMENTATION

Two Doppler systems are used for blood flow evaluation, both of which have specific characteristics: continuous-wave (CW) and pulsed-wave (PW) Doppler. Their analysis can be displayed on the screen following two different modes: spectral display and color flow mapping. The beam axis, the sampling volume, and the color image are overlayed on the regular 2D images (duplex scanning) in order to isolate, anatomically, the targeted blood flow. To spare computer working time being shared between the different modes, the 2D images are renewed at a much lower rate than the Doppler sampling rate. Three technical concepts have to be explained before embarking further on the description of instruments: the pulse repetition frequency (PRF), the frame rate, and the Nyquist limit. The PRF is the number of times a PW Doppler instrument transmits and receives pulses of ultrasound in 1 s; the rate of the emitting–receiving cycles is 1000–6000 s^{-1}. The PRF decreases with increasing depth of analysis, because returning echoes take more time to reach the transducer from a remote target. It also decreases with increased transducer emitting frequency as described in the Doppler formula, where Δf and f_0 vary reciprocally for the same target velocity. The frame rate is the frequency of image renewal on the screen; it varies from 6 to 120 images per second. It depends on the number of scan lines used for investigating the field (the larger the

field the slower the frame rate), and on the additional data processing such as simultaneous color Doppler and bidimensional images (7). The Nyquist limit is linked to a phenomenon called "aliasing."

III. ALIASING

Any pulsating system observing an oscillating object will record anomalous images if its sampling rate is close to the vibration frequency of the observed structure. The Doppler effect generated by the moving blood cells (Δf = 4000–10,000 cycles per second) has an oscillating frequency approaching the PRF of the observing instrument (PRF = 1000–6000 impulses per second). This proximity induces an artifact due to insufficient sampling, called "aliasing." It is well illustrated by the apparent counter-rotation of a carriage wheel in a Western movie, when the number of rotations per second is superior to the number of images per second taken by the movie camera (8). When the wheel revolution rate is much slower than the camera frame rate, the image is accurate. When the wheel rotates at a speed which is half the camera frame rate, the direction of rotation is no longer discernible, because the wheel spokes are at 180° on each movie frame. If the rotation rate equals the sampling rate, the film will catch the spokes of the wheel at the same place in each cycle and the wheel will appear motionless. Finally, when the rotation rate exceeds the sampling rate, the wheel will appear to be counterrotating at an inaccurate and slow speed (Fig. 2.3).

This sampling phenomenon introduces a limit above which the precision of movement reporting is lost. The maximum frequency shift measurement is equivalent to one-half of the sampling frequency. This limit is called the "Nyquist limit":

$$\text{Nyquist limit} = \text{PRF}/2 \tag{2.7}$$

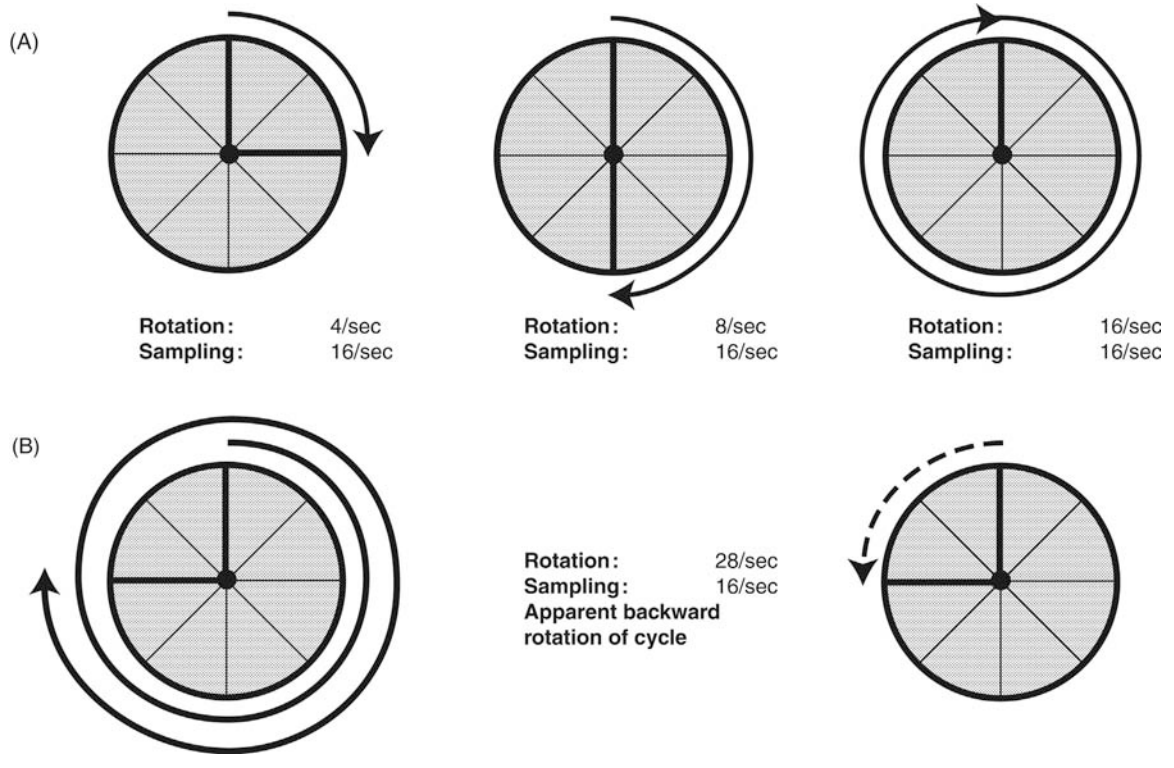

Figure 2.3 Aliasing in movie image. (A) The rotating speed of the wheel is increasing from 4, 8, and 16 rotations per second, whereas the sampling rate of the camera is fixed at 16 images per second. In the left case, the wheel rotates at a rate equal to one-fourth of the camera sampling rate: the index spoke has thus turned one-fourth of a complete rotation with each camera image and moved from the 12 h to the 3 h position. In the center case, the wheel rotates at a rate equal to one-half of the camera sampling rate: the index spoke has completed one-half of a turn with each image from the 12 h to the 6 h position. However, it is not possible to tell if that movement's direction was clockwise or counterclockwise. In the right case, both the wheel and the camera have the same rate and the wheel has done a complete turn with each camera image, but seems immobile because each camera frame always finds the wheel in the same position. (B) Aliasing occurs when the sampling rate of the camera (16 s^{-1}) is lower than the rotating rate of the wheel (28 s^{-1}). The wheel has performed one and three-quarters rotation during the time elapsed between two camera images. However, the index spoke looks as though it has moved slowly backwards from the 12 h to the 9 h position.

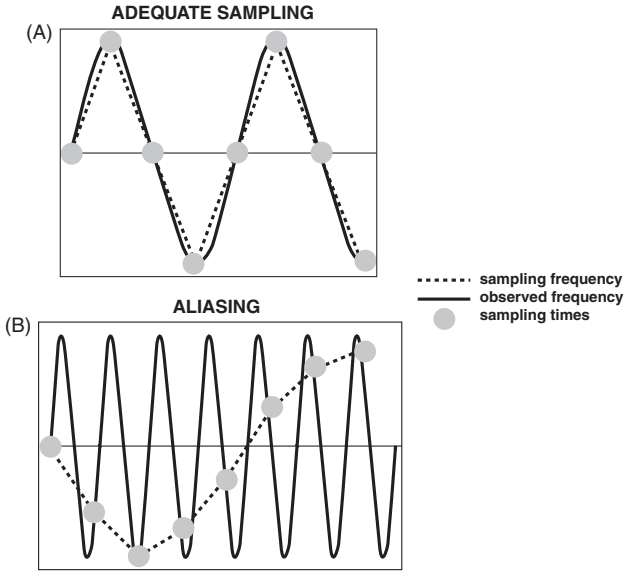

Figure 2.4 Aliasing in computer sampling. (A) The computer sampling rate (gray dots) is more than twice the observed wave frequency; it is adequate to reproduce a wave which has a similar frequency. (B) With the same sampling rate as in (A), the frequency calculated by the computer (dotted lines) is completely different from the actual frequency of the wave (solid line), the latter frequency being markedly superior to the sampling rate; the recorded frequency is out of phase and much lower, creating aliasing.

To represent a corrected frequency signal (fs), it must be sampled at least twice for each cycle of the signal; the PRF of the computer must be superior to two oscillating periods of the observed wave, in this instance the Doppler shift Δf (9):

$$\text{PRF} \geq 2 \text{ fs} \quad \text{or} \quad \text{PRF} \geq 2\Delta f \tag{2.8}$$

If the Doppler frequency shift is superior to one-half of the PRF, aliasing occurs (Fig. 2.4). The instrument reports a spurious value equal to the true Doppler shift minus the PRF: on the spectral frame, the velocity curve appears as artificially reversed on the opposite side of the baseline (Fig. 2.5). In color flow, aliasing appears as an area of reversed color (Fig. 2.6). By increasing the PRF, the Nyquist limit can be raised, and the ability to obtain high velocity recordings is also increased. This is done by the technique called high-PRF PW Doppler which is, however, less precise than the CW instrument (CW Doppler). The use of CW Doppler is mandatory for accurately analyzing high velocities. The maximum velocity ($V_{\max}$) that can be measured without aliasing is given by this formula (4):

$$V_{\max} = \frac{(\text{PRF}) \times C}{4f_0 \cos\theta} \tag{2.9}$$

Aliasing can be limited by reducing the emitting frequency of the transducer (f_0) or increasing the PRF. The presence of aliasing flow does not signify turbulence but translates as increased velocity. The flow may stay laminar.

IV. CONTINUOUS- AND PULSED-WAVE DOPPLER

The CW Doppler equipment transmits and receives the ultrasound signal continuously and simultaneously through two separate crystals: one for emission and one for reception (Fig. 2.7). It records all velocities in the area of overlap between the emitted and the returning beams at any depth and at any frequency shift. No limitation for analysis of high velocities is present because its emission is continuous and has therefore an infinite PRF. However, it lacks the spatial resolution necessary to know the exact depth at which the measurement is obtained. Since emission and reception are continuous, the computer cannot define when or where the emitted waves are reflected by the moving target.

In the PW Doppler, the transducer emits a short burst of ultrasound waves (three to six waves) and waits for the return of the reflected waves (Fig. 2.7). As the transducer alternates between transmitting and receiving bursts of ultrasound energy, it is able to calculate the time delay for the echoes to reach back and interrogate the blood flow in a specific region (Fig. 2.2). It waits until the echo from a specific location reaches the transducer whereupon it opens an electronic gate to read the signal. The gate then shuts for a fixed duration after reading the signal (10). The duration of gate opening determines the length of the exploring window, or sample volume (Fig. 2.7). This volume appears as a box that can be moved along the Doppler cursor on the screen (depth of the sample) and its size can be modified (duration of echo listening). The sensitivity rises when the dimension of the window increases because a larger sample volume contains more blood cells and produces stronger signals, but the axial resolution is lessened because the location is less precise. The delay (Δt) defines the depth (D) of the target; it is the time necessary for the ultrasound of known speed (c) to make a round-trip between the transmitter and its target:

$$D = c \times (\Delta t/2)$$

This precision in the location of the source of frequency shift has a drawback: it limits the velocity range that

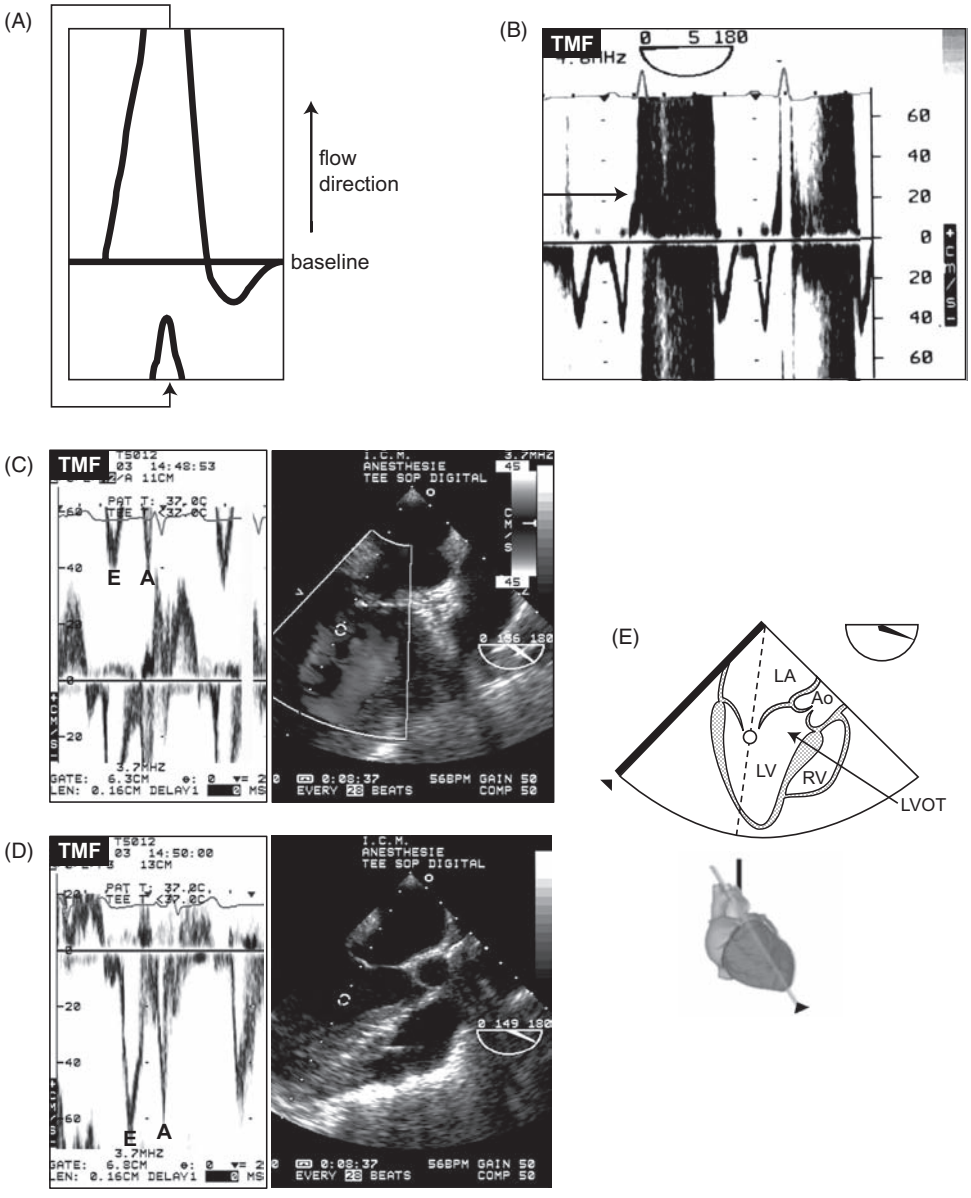

Figure 2.5 Flow reversal on spectral display (aliasing). (A) Schematic drawing of spectral display. By lowering the baseline, the tip of the curve can be readjusted into the forward direction and maximal velocity can be calculated. (B) Pulsed-wave Doppler image of mitral flow with mitral regurgitation. The velocity of the forward flow is correctly estimated (0.45 cm/sec) but the high-velocity jet of regurgitation (5–6 m/s) is buried in the aliasing signal (arrow). The maximal velocity is unrecordable. (C) Mid-esophageal long axis view of the mitral valve. The scale on the left is lower than the maximum mitral velocity. (D) This aliasing is eliminated by increasing the scale through baseline elevation. (E) Site of the transmitral pulsed-wave Doppler sampling (Ao, aorta; LA, left atrium; LV, left ventricle; LVOT, left ventricular outflow tract; RV, right ventricle; TMF, trans-mitral flow).

the instrument can read. Three facts explain this phenomenon:

- the sampling rate: the frequency overlap between PRF and Doppler shift giving rise to aliasing, as explained earlier;
- the emitting frequency of the probe: for the same Doppler shift, the transducer must sample twice as fast for a 5.0 MHz as for a 2.5 MHz probe; at the same PRF, the maximum recordable velocity with a 5.0 MHz probe is half the velocity determined by a 2.5 MHz probe (7);
- the depth of the sampling gate: the deeper the interrogated target, the longer the elapsed time between two pulse emissions; the maximum recordable velocity is lessened when the PRF decreases (2.3 m/s at 8 cm with a 2.5 MHz probe and 0.65 cm/sec at 16 cm with a 5.0 MHz) (5).

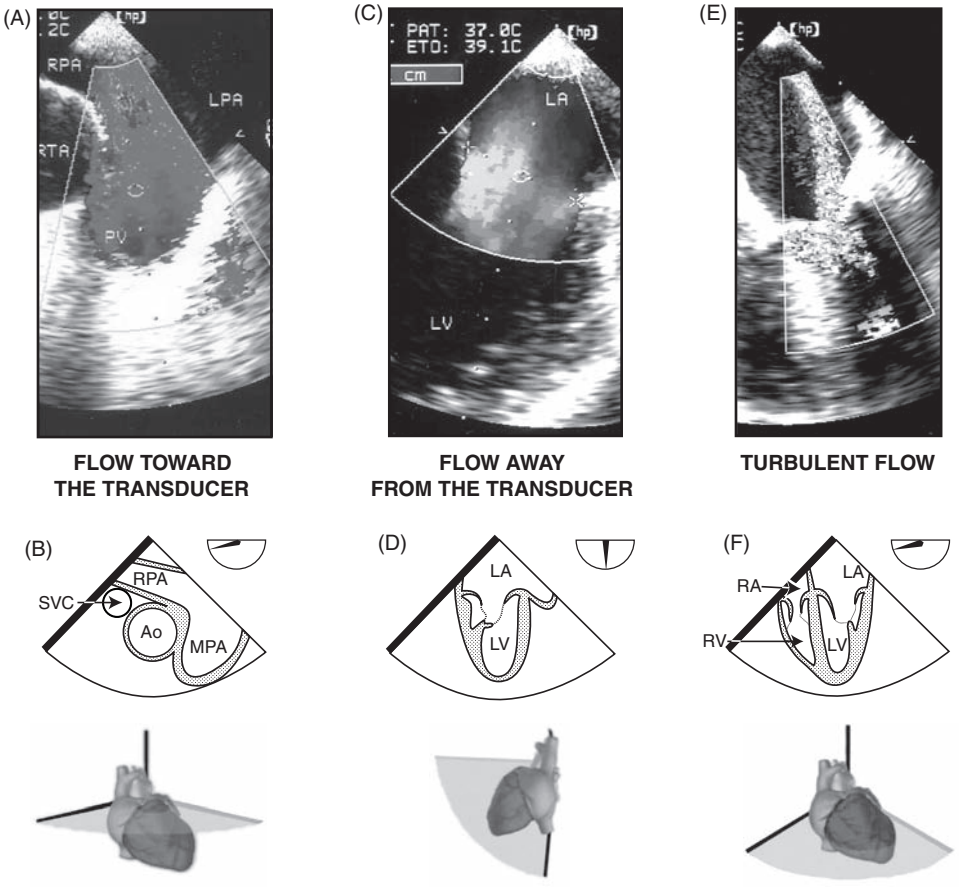

Figure 2.6 Standard color mapping. Illustration of the standard colors attributed to flow. (A, B) Red: towards the transducer in an upper esophageal short axis aortic view. (C, D) Blue: away from the transducer in a mid-esophageal two chamber view. (E–F) Mosaic: red and blue mixture due to aliasing from high velocity mitral regurgitation (Ao, aorta; LA, left atrium; LPA, left pulmonary artery; LV, left ventricle; MPA, main pulmonary artery; RPA, right pulmonary artery; RA, right atrium; RV, right ventricle; SVC, superior vena cava).

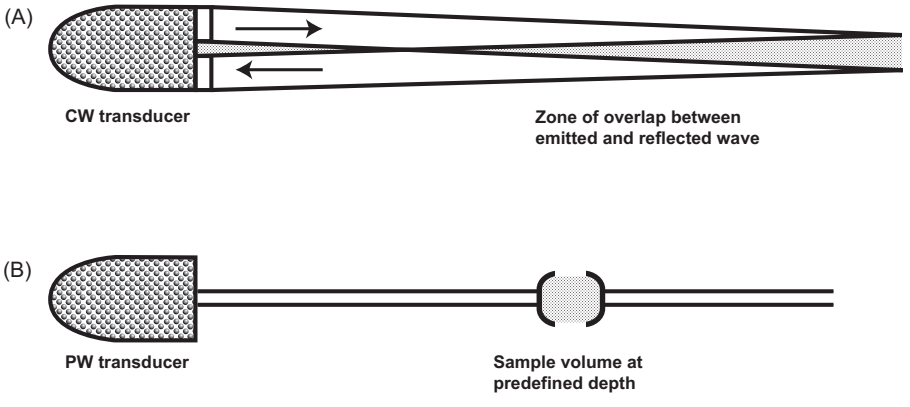

Figure 2.7 Transducer Doppler mode. (A) Continuous-wave (CW) mode transducer with emitting and receiving beams; the area explored is the opacified area of overlap between the two beams. (B) Pulsed-wave (PW) mode transducer: the Doppler effect is analyzed in a small zone of predefined depth and volume called the sample volume (opacified area). Depth is defined by the position of the cursor along the axial beam; the sample volume is chosen by widening or narrowing the window.

In order to enable the measurement of higher velocities, a modification called "high-PRF" has been implemented on most echo machines. In this system, the PRF is multiplied by 2, 3, or 4: a new burst of ultrasound waves is sent before the electronic receiving gate is opened to returning echoes. It, therefore, raises the number of sampling sites but introduces a "range ambiguity" because the computer is unable to identify the origin of the echo (1). Fortunately, the gates are pictured on the 2D images and the examiner can assume that the sampling volume lies where the recorded flow velocity is expected. The actual PRF is determined by the most proximal sample volume but the most distal PRF is used for sampling flow in the zone of interest (3).

An additional problem occurs with the PW technology. The bursts of ultrasound waves are produced at a certain rhythmic time period introducing an additional frequency in the emission. The frequency of bursts of an ultrasound wave (f_0) is also Doppler-shifted by the moving blood. The resultant velocity profile is not as precise as CW Doppler and is affected by a significant spectral broadening (11).

V. SPECTRAL DISPLAY

To display the Doppler information, the apparatus must reproduce the spectrum of the frequency shifts. This spectrum must be updated regularly during a cardiac cycle. The Doppler signal is a complex wave, containing information about the motion of all blood cells and tissue moving at different velocities. The received signal is a wave, out of phase with the original emitted signal. In the spectral mode, this shift is visually displayed as a power spectrum of frequencies against time. The ultrasound echoes go through a logarithmic amplifier which increases the amplitude of the weaker signals more than the stronger signals, so that amplitudes become comparable. The signal is processed in segments of 1–5 ms duration by the computer and a mathematical calculation, called fast Fourier transform, is performed on each segment to resolve the Doppler signal into its individual component frequencies. This spectrum represents the relative magnitude of each frequency component. The calculation of velocity (Doppler equation) is done automatically by the computer from these frequency shifts. Each segment of time is assigned a stack of vertical bins whose intensity is proportional to the strength of the signal or to the number of blood cells moving within the range of velocities represented by each bin (Fig. 2.8) (8). A trade-off exists between temporal and frequency resolution: the time period represented by each time slice is correlated with the ability to distinguish between two Doppler shifts.

The spectral display of the Doppler trace has time on the horizontal axis and flow velocity on the vertical axis. The gray scale is proportional to the number of blood cells moving at a certain speed: the darker the trace, the greater the number of blood cells. Usually, 16–32

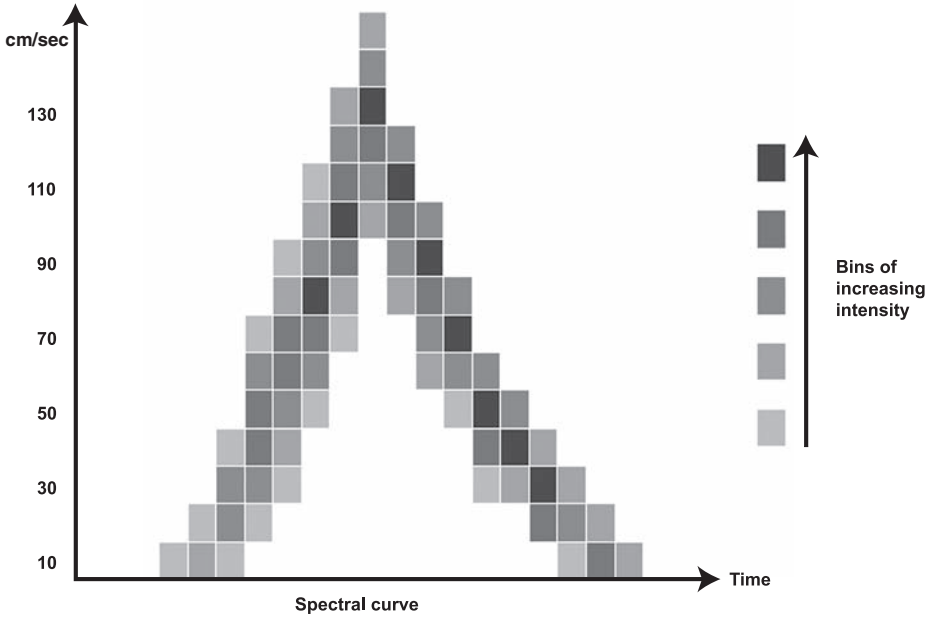

Figure 2.8 Spectral display. Construction of a spectral curve with vertical stacks of bins of varying intensity where the shade of gray is proportional to the quantity of blood cells moving at a corresponding velocity. The width of the curve corresponds to the spectrum of the different velocities of blood cells.

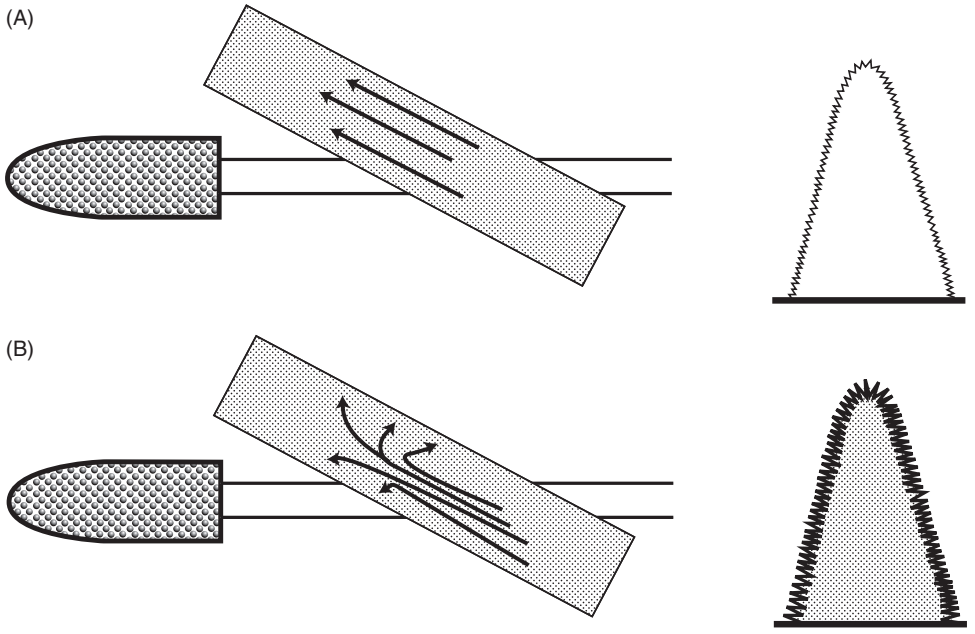

Figure 2.9 Laminar and turbulent flows. (A) Spectral curve of a laminar flow with fine and clear-cut envelope; most of blood cells are moving at the same velocity. (B) Spectral curve of turbulent flow with blood cells moving at different velocities and directions inside the vessel. The spectral display shows no envelope but a dark filled curve of different velocities.

shades of gray are used because human eye resolution is no more than 32 shades of gray. The width of the trace is proportional to the spread of frequency. With little difference in velocity, the band is narrow and the flow laminar whereas multiple velocities produce a wide spectral spread and a large trace on the screen with a turbulent flow (Figs. 2.9 and 2.10). By convention, the flow towards the transducer is depicted above the baseline and the flow away from it is below. A filtering technique removes the echoes of high intensity but low frequency ($<$200 Hz) due to the movements of the cardiac walls and valves. On the spectral frame, the CW Doppler appears as a filled gray curve, showing all the velocities encountered on the ultrasound beam, whereas the PW velocity curve has a thin envelope representing the blood flow at a determined sampling site (Fig. 2.11). The maximal velocity measurement must be done at the outer edge of the trace. In order to display the entire flow curve, it is frequently necessary to displace the baseline in the direction opposite to flow. In case of aliasing, the velocity curve appears artificially reversed on the opposite side of the baseline (Fig. 2.5). For blood flow towards the transducer, it will be plotted below the zero line as a negative shift. For high velocities, the wrapping-around may occur many times, so that the peak of the spectrum is buried in the superposed traces, and the maximal velocity impossible to determine (Fig. 2.5). By repositioning the base line in the direction opposite to flow, some degree of aliasing may be unwrapped because higher velocities can be recorded in the flow direction.

VI. COLOR DOPPLER

The PW Doppler analyzes the complete spectrum of blood flow velocities in a single sampling site. The technique can be expanded to the analysis of several samples along a line of information. This multigate Doppler technique allows "flow mapping" by measuring returning echoes sequentially at different successive times after transmission of a single burst of ultrasound. The scan line is interrogated many times, ranging from 3 to 16. The amount of time each line is sampled is called the "packet size" and is selected by the examiner or provided by the instrument (12). After having interrogated one scan line, the beam direction is changed to the next scan line and so on for the entire field. Every time a scan line is interrogated, an algorithm stores the Doppler data at each sample site along the line. Depending on the ultrasound system, the spacing between scan lines can be modified. This spacing is called "line density." Spatial resolution increases with greater density of scan line, but the frame rate decreases simultaneously because processing times are longer. The number of sample sites per scan line varies amongst manufacturers while the number of scan

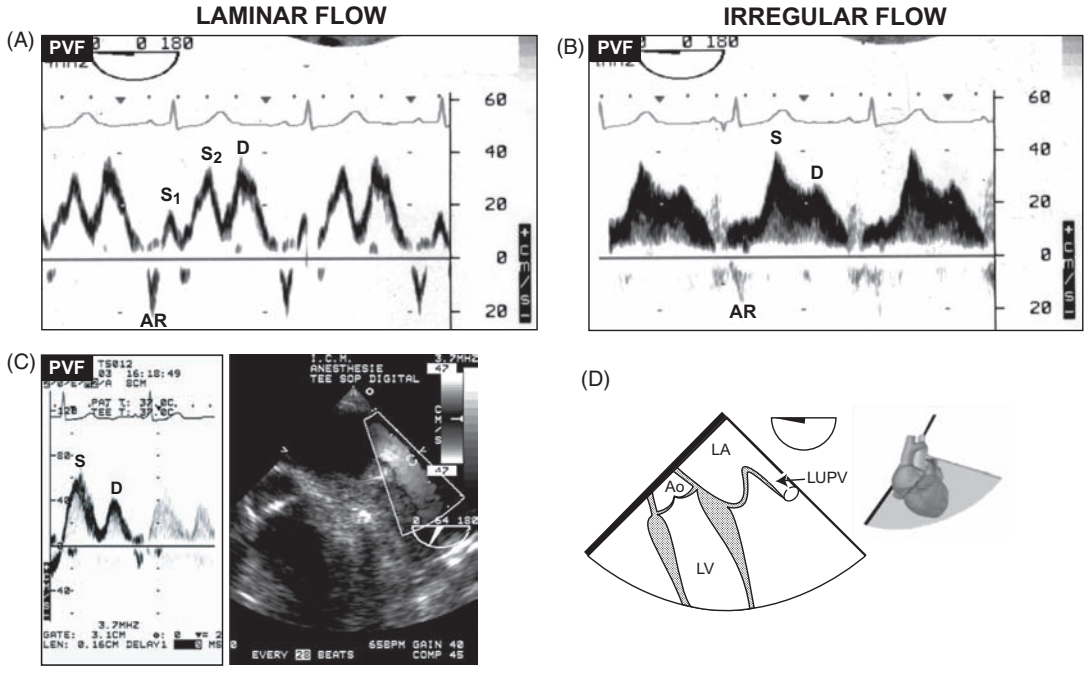

Figure 2.10 (A) Laminar flow: in the center of the vessel almost all the blood cells are traveling at the same velocity. The spectral display shows a well-defined narrow envelope. (B) Irregular flow: near the wall of the vessel many different velocities occur; the PW Doppler records a larger spectrum of velocities and the envelope is replaced by a large band of different speeds occurring simultaneously because the sample volume was placed close to the vessel wall. (C–D) Mid-esophageal short axis view with interrogation of left upper pulmonary vein (LUPV). The flow moves from a laminar to irregular pattern as the sampling volume moves from the center to the side of the LUPV (Ao, aorta; AR, atrial reversal; LA, left atrium; LV, left ventricle; PVF, pulmonary venous flow).

lines is determined by the color sector width and the line density.

Despite the power of recent microprocessors, this large amount of information significantly lowers the frame rate of the images displayed on the screen. Therefore, instead of determining the complete spectrum of frequencies, as in PW spectral display, an autocorrelator analyzes the resultant phase shift between the emitted and received waveforms in order to generate a modal frequency representing the velocity of the majority of blood cells (13). If the packet size comprises eight pulses, for example, the first pulse travels the scan line and returns to the transducer. It is followed by the second pulse whose recorded frequency is slightly out of phase with the first pulse because the target is moving. The calculation is repeated for the eight pulses on the scan line (Fig. 2.12). If pulse

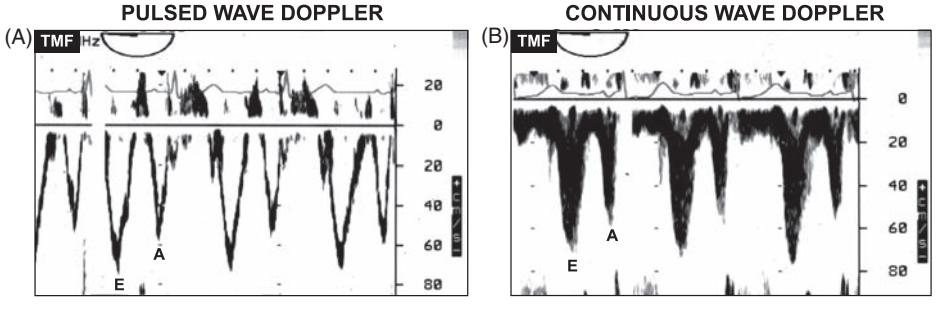

Figure 2.11 Pulsed-wave (PW) and continuous-wave (CW) Doppler flow. (A) Pulsed-wave (PW) Doppler examination of the mitral valve inflow. The flow is interrogated at a specific location by placing the sample volume between the tip of the mitral leaflets. Because the flow is laminar at this sampling site, most blood cells are travelling at the same velocity and the envelope is narrow and well-defined. (B) CW Doppler examination of the mitral valve inflow. Since all velocities are recorded along the interrogating beam, there is an envelope with significant spectral broadening, that is, a curve filled with different velocities. The maximal velocity is assumed to be at the narrowest area, that is, between the tips of mitral leaflets (TMF, transmitral flow).

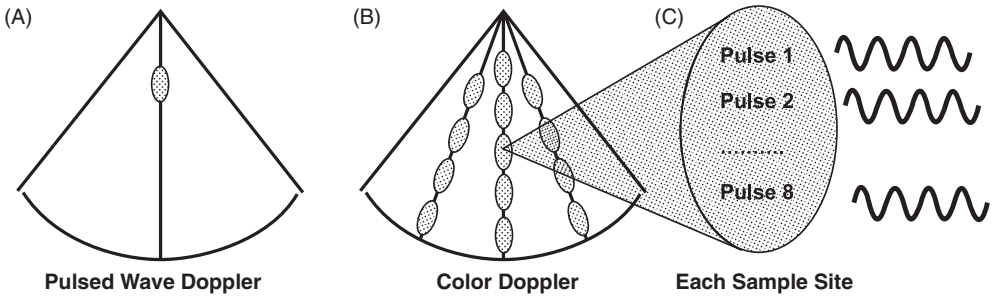

Figure 2.12 Color Doppler principle. (A) Pulsed-wave Doppler: one site is sampled on one scan line. (B) Color flow imaging: several hundred sites are sampled on many scan lines. (C) Each area of the scanning lines is interrogated successively eight times according to the packet size. Each successive wave is slightly out of phase compared with the preceding one; one number, the mean velocity, is stored by an algorithm at each sample site. The algorithm processes the phase shift between the waves of the eight pulses, estimates the mean velocity by derivation at each sample and assigns a color to each area. The larger the packet size, the more precise the results, but the lower the frame rate.

two is ahead of pulse one, the target is moving towards the transducer and if pulse two lags behind pulse one, the target is flowing away. Echoes from subsequent pulses are correlated with echoes from previous pulses to determine the mean Doppler shift and its "variance," which is the difference between the highest and the lowest returning frequencies or the frequency spread of the spectrum. Averaging, by repetitive sampling, is performed to improve the statistics. The modal frequency can be used in the Doppler equation to determine mean velocities and variance. For laminar flows, the value of the mean velocity is approximately the same as the peak velocity (14).

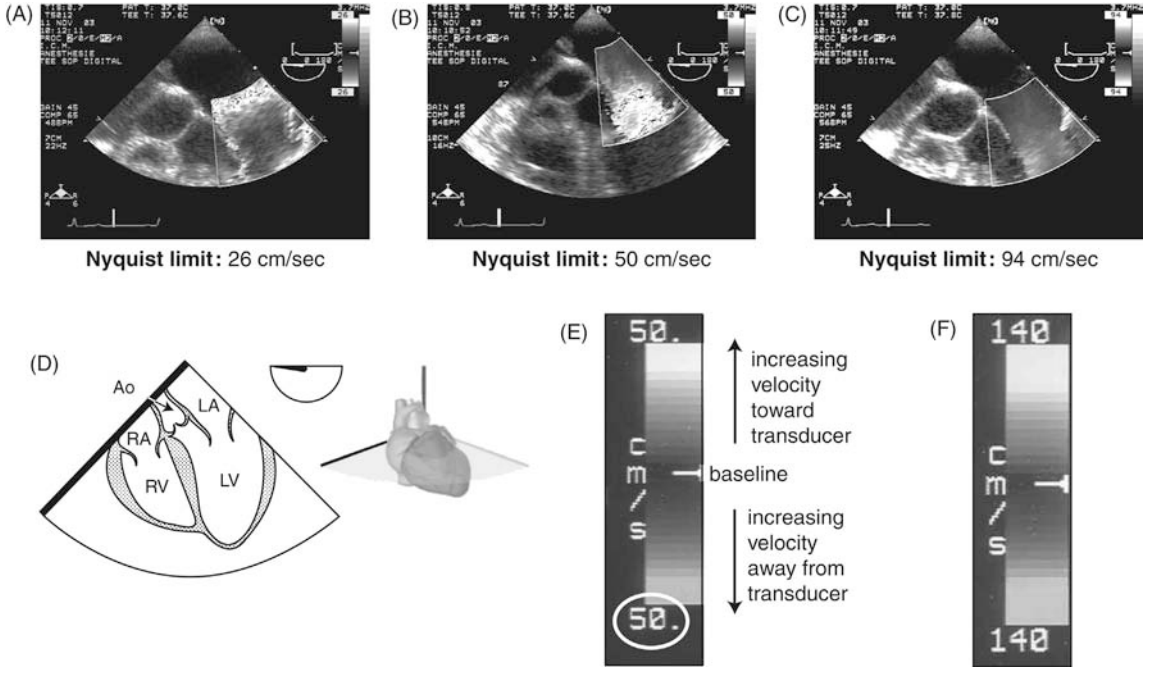

Figure 2.13 Color code displayed on the screen. (A–D) Mid-esophageal five-chamber view using color Doppler interrogation of the mitral valve inflow. The upper limit of the color coded scale is progressively increased from 26 cm/sec (A), 50 cm/sec (B), and 94 cm/sec (C). Aliasing is reduced by increasing the Nyquist limit. (E) Color flow. Flow towards the transducer is red at low velocity, progressively yellow at higher velocity and blue when away from the transducer with increasingly clear color at higher velocity. The number 50 indicates that the upper limit of mean velocity readable without aliasing is 50 cm/sec under the present conditions (Nyquist limit). (F) Increased Nyquist limit. By increasing the pulse repetition frequency and/or decreasing the depth of the color field, the upper limit of velocity readable without aliasing can be significantly increased (in the present case: 140 cm/sec) (Ao, aorta; LA, left atrium; LV, left ventricle; RA, right atrium; RV, right ventricle).

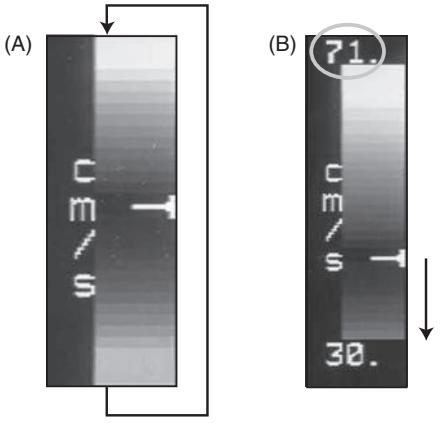

Figure 2.14 To prevent or induce aliasing, the baseline of the color bar can be shifted in the direction of flow or opposite to it. The maximal velocity recordable without aliasing is increased in one direction (71 cm/sec) but decreased in the opposite (30 cm/sec).

By converting the calculated values of mean velocity into colors, the blood flow velocity image can be overlayed onto a 2D gray-scale display. Blood flow moving towards the transducer is usually displayed in red and blood flow moving away from the transducer in blue (Fig. 2.13). Color maps identify the pattern of colors in use, and are shown by a color bar appearing on the screen. It displays the color properties such as hue (amount of primary colors red, blue, or green), saturation (amount of white contained) and intensity (brightness). Lower velocities are displayed in dark colors located closer to the color bar's baseline. Higher velocities are displayed in brighter tones near the end of the scale. In "enhanced" color maps, the red gradually changes to yellow and the blue changes to an intense luminous shade as the velocity increases (Fig. 2.13). This display is useful in operating rooms because it increases the contrast with the surrounding light. The numbers seen at both ends of the color scale bar represent the limit of the recordable mean velocity, or Nyquist limit, rather than peak velocity estimates as in PW or CW Doppler (Fig. 2.13). Above this limit, aliasing appears as color reversal: the blood flowing towards the transducer, for example, changes abruptly from yellow to bright blue. By moving the color bar baseline towards the flow, the recordable velocity is increased in the flow direction but diminished in the opposite direction (Fig. 2.14).

As laminar flow appears as a homogeneous smooth pattern of red or blue, turbulent flow is displayed in a disorganised multicolored pattern called "mosaic," representing the many different velocities and directions of each sample site. The severity of turbulence is illustrated with an orthogonal color, usually green, and can be laid

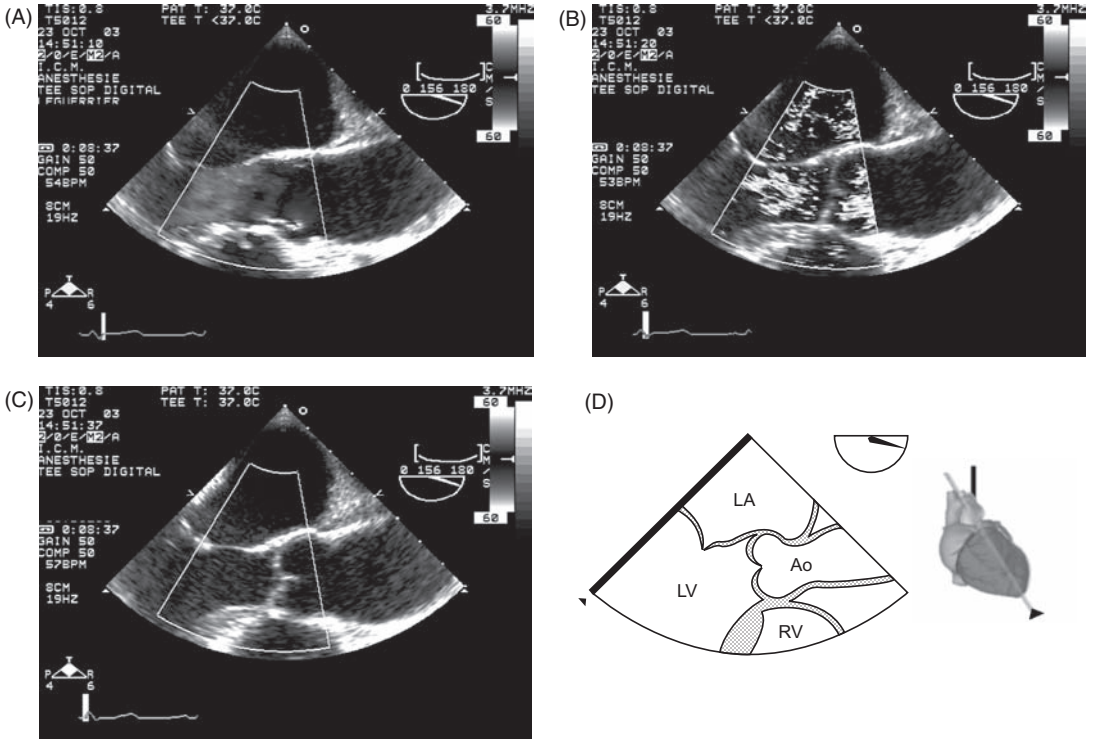

Figure 2.15 (A–D) Mid-esophageal long axis view color Doppler interrogation of the aortic valve in a 57-year-old woman. (A) Optimal gain setting. (B) Suboptimal higher (C) or lower gain (Ao, aorta; LA, left atrium; LV, left ventricle; RV, right ventricle).

across the standard red and blue velocity bars. An algorithm calculates the variance between individual velocities at each sampling site and adds the green if the irregularity is above a predetermined level. This particuliar display offers the advantage of "mapping" the turbulent areas inside the color flow. Under normal circumstances, intracardiac flows are laminar. Turbulent flow appears if there are pathological flows or abnormally high velocities.

The extent of calculations imposed by data processing are dependant on the dimensions of the field of investigation. With a wide sector, more lines are sampled. With a deeper sector, greater time is required for the echoes to return to the transducer. Decreasing the sector width and depth decreases the processing time and increases the frame rate which consequently varies from 6 to 90 images per second. This is critical for patients with rapid heart rates because important information can be missed if the frame rate is too low. Moreover, a minimum frame rate of 15 images per second is required to achieve the blending of images into smooth motion by the human eye. Therefore, it is always an advantage to keep the color sector as small as possible. Another method of raising the frame rate is to decrease the packet size, or to increase the PRF by adjusting the color scale to a higher mean velocity. Nevertheless it decreases the system's sensitivity to low velocity blood flow (Fig. 2.13). Using a transducer of lower frequency (<5 MHz), or reducing the emitting frequency, of the probe will increases the PRF and the maximum velocity measurement capability at any depth. This decreases tissue attenuation because lower frequencies lose less energy than high-frequency waves while traveling through the organ. The depth at which transmission can interrogate the number of scan lines, the probe frequency, the PRF and the frame rate are interdependent. It is up to the observer to find the optimal combination between these settings to obtain the most accurate flow information.

Sometimes, the interrogating beam can record frequency shift caused by wall motion, and colors can be assigned to moving structures. This phenomenon is called "ghosting." It is minimized by a filtering process named "clutter filter" which attenuates the signals of low velocity and high intensity corresponding to tissues. However, it may eliminate the low-velocity blood flow images. This drop-out in low-velocity flow can also occur when using a high PRF, because it increases the lowest readable flow velocity. These phenomena lead to a smaller sized color flow jet, and make it appear smaller than it actually is.

Color gain has to be properly adjusted. Setting the gain control too low prevents detection of low-amplitude signals, and blood flow patterns appear smaller than they are. A gain set too high causes a lot of color noises, which appear as random multicolored specks sprayed over cardiac chambers and tissues. Adequate gain is obtained by adjusting the control until noise becomes obvious and then reducing it to a point where noise is just disappearing (Fig. 2.15). The gray-scale gain which displays the 2D tissue image over which the flow is superimposed must be kept low. If not, noise is generated restricting the dimensions of the color flow. Like all Doppler data, color flow accuracy is dependent on the angle between the flow direction and the beam axis. If this angle is too wide ($>20^\circ$), the speed is misinterpreted as being too low. If the beam and the flow are perpendicular, there is no Doppler effect and no color picture. The adjustment of the transducer's focal zone is important in multigate Doppler systems because distal sensitivity and spatial resolution decreases as the focal zone is set in the near field. The distal area of flow can appear larger than it actually is because Doppler data are collected in the divergent part of the ultrasound beam. When using color

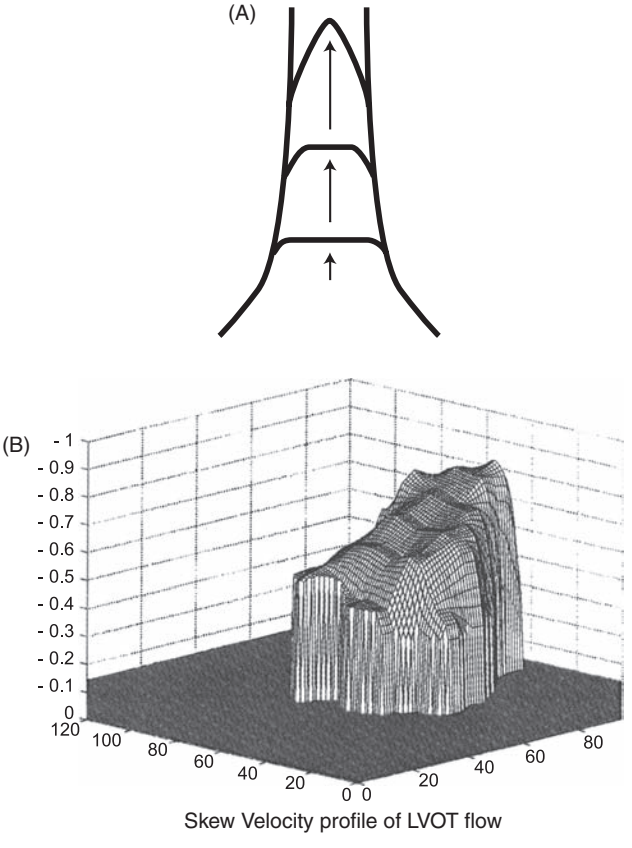

Figure 2.16 Flow profiles. (A) In a vessel, the flow front presents an aspect of increasing central acceleration with a parabolic profile. The flow front is flat at the origin of the vessel, where the flow is convergent. (B) Three-dimensional aspect of the systolic flow in the left ventricular outflow tract (LVOT); the flow front is complex and skewed with increasing speed near the septum. [With permission from Berg et al. (15).]

flow, the focal zone must be kept at or below the interrogated area (1).

By displaying flow patterns, color provides an indicator for adequate positioning of the beam in order to perform quantitative spectral Doppler measurements. As the images obtained are 2D, it is important to visualize the flows in different planes to reconstitute the 3D structure of a given flow jet. A flow in a vessel crossing the entire screen, although uniform, will appear under different colors as the angle of the flow with the different scan lines changes along its visible course. For instance, on a 90° image of the descending thoracic aorta, the flow will be colored in red on the right-hand side of the screen where it comes toward the transducer but in blue on the left part of the screen, where it moves away from the transducer.

It is important to remember that color flow display is a velocity mapping and not an actual blood volume measurement. Area and brightness on the screen are determined only by the speed of blood, which is the result of an instantaneous pressure gradient between upstream and downstream cavities (7). A small mitral regurgitation (MR) orifice, in the context of a normal left ventricular function, will create a high-velocity jet (6 m/s) into the left atrium (LA) appearing larger than the real regurgitant blood volume. This is due to the sweeping of left atrial blood by the regurgitant jet. Color image in severe mitral insufficiency with poor left ventricular function will underestimate the amount of regurgitant blood because of smaller pressure gradient. Moreover, the velocity measured in a precise vessel does not take into account the real flow profile (which is not flat except closer to the root of great vessels or when convergent). Most of the time flow profile is parabolic or displays zones of acceleration near the curvatures (Fig. 2.16) (15). This limits the accuracy of velocity measurements, particularly when integrated into calculations such as cardiac output. Various positioning of the Doppler sample volume in the main pulmonary artery cross sectional area, for example, introduces errors of ±35% in

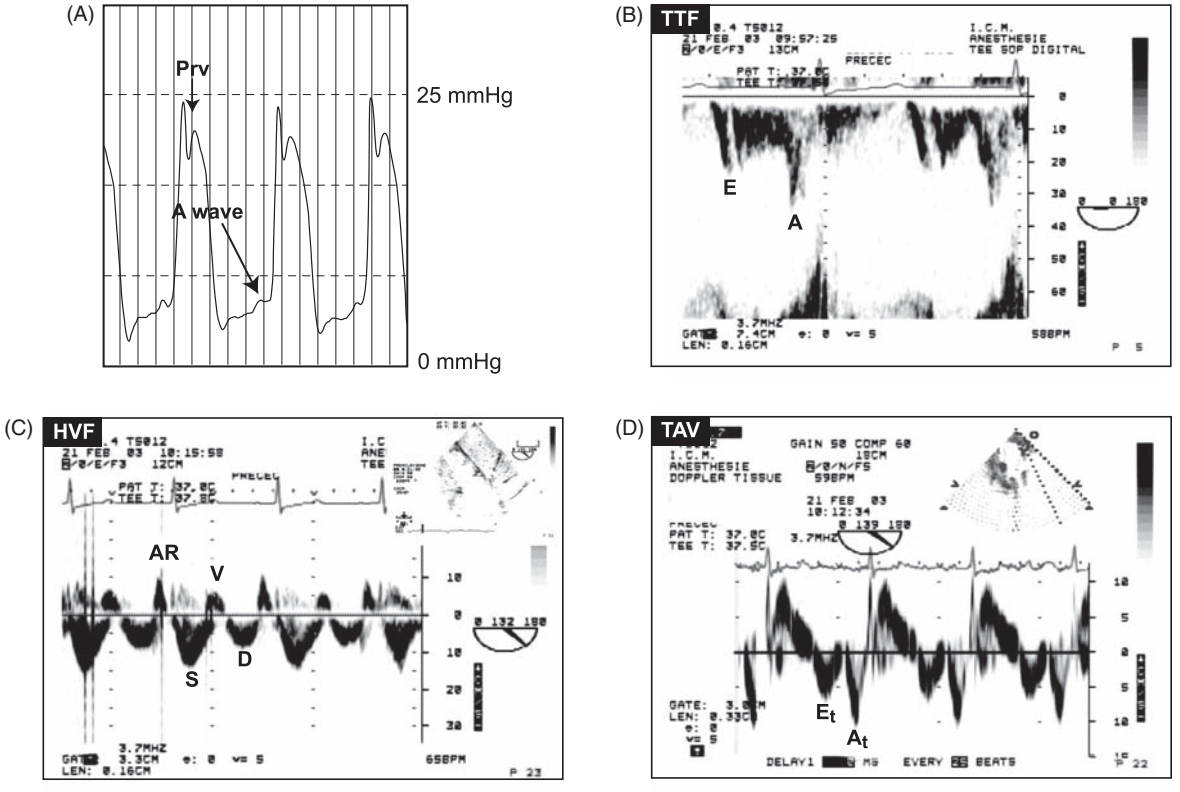

Figure 2.17 Clinical application of Doppler. A 70-year-old woman before coronary revascularization and aortic valve replacement. (A) The right ventricular hemodynamic pressure waveform is shown with an end-diastolic "A" wave. (B) The trans-tricuspid flow (TTF) Doppler waveform: abnormal E to A ratio with predominant A wave. (C) Doppler hepatic venous flow (HVF): S wave superior to the D wave. (D) Tissue Doppler interrogation of the tricuspid annulus: abnormal Et to At ratio with predominant At wave. This is consistent with right ventricular diastolic dysfunction (AR, atrial reversal; Prv, right ventricular pressure; TAV, tricuspid annular velocity).

cardiac output measurements (16). In turbulent flows, random swirls and eddies appear, where there are wide fluctuations in direction and velocity of flow components. They are spread amongst a slow varying, forward motion of blood. Consequently, the measured velocity corresponds to the mean flow velocity.

VII. DOPPLER TISSUE IMAGING

Doppler signals are generated not only by flowing red blood cells but also by cardiac walls and valvular motion. Tissues induce stronger backscatter echoes at lower frequency but these are usually filtered to improve the blood flow image. These echoes appear only when color gain is too high or when filters are set too low. However, this drawback can be used to identify parietal movements and wall kinetics if the low-amplitude, high-frequency signals of blood cells are properly filtered (high-pass filtering system and low-clutter filter setting). With this technique, called "tissue Doppler," velocities as low as 0.1 cm/sec are recorded. Depth resolution is inferior to that of conventional Doppler because velocity mapping requires longer pulses to be transmitted and longer gate times (6).

A myocardial velocity mapping can be obtained. It assesses the regional myocardial velocity contraction patterns (17). Subepicardial layers usually have velocities lower than subendocardial ones. These instantaneous velocity gradients within the walls present different patterns for normal, ischemic, or dysfunctional myocardial muscle. Encoded in color, they appear in shades of red for positive transmural gradients (thickening), and blue for negative ones (thinning). Frame rate can be increased by sampling a single line in color M-mode. A spectral display of PW analysis of a single sample can be used to identify local movements, such as mitral ring displacement or the evaluation of diastolic function (Fig. 2.17).

VIII. ARTIFACTS

Numerous artifacts, due to physical properties of ultrasounds or instrument ajustments, can mislead the examiner (see Chapter 6). Aliasing and ghosting have already been mentioned. Strong reflectors, like prosthetic material or

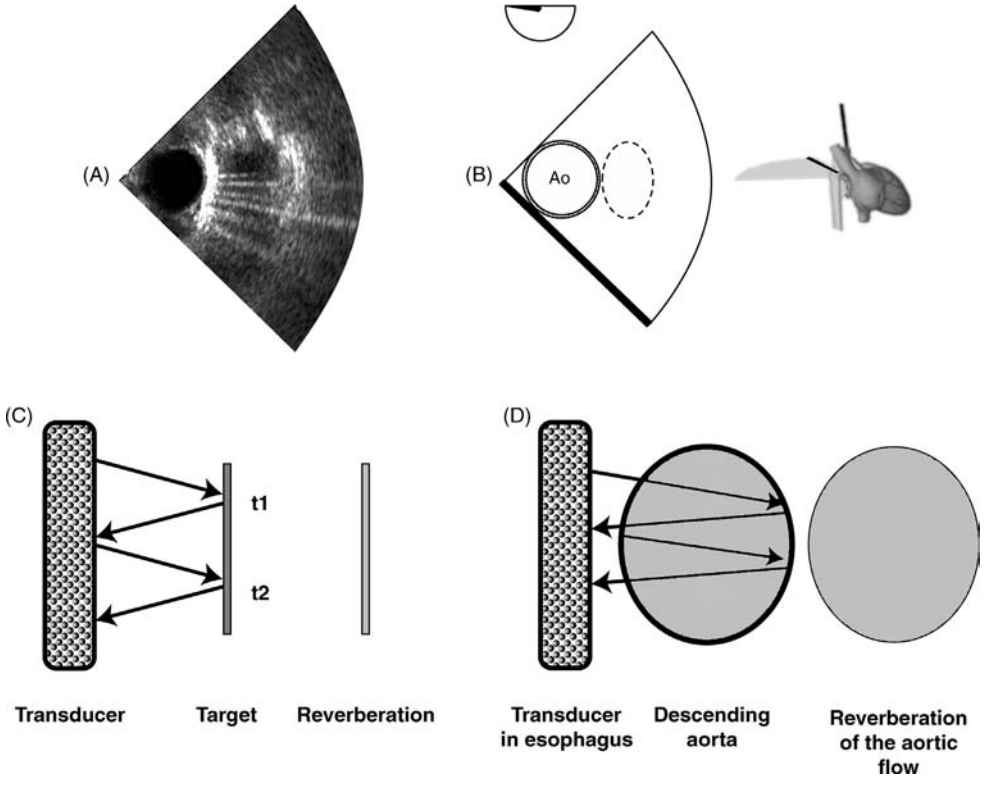

Figure 2.18 Reverberation. (A–B) Mid-esophageal short axis view of the aorta (Ao). (C–D) When a strong reflector is close to the transducer, the high-energy echo beam giving the image at the initial time (t1) is reflected on the front part of the transducer and then rerouted toward the reflector for a second time (t2). It gives a second image interpreted by the computer as being at a double distance of the first target, since t2 is twice t1.

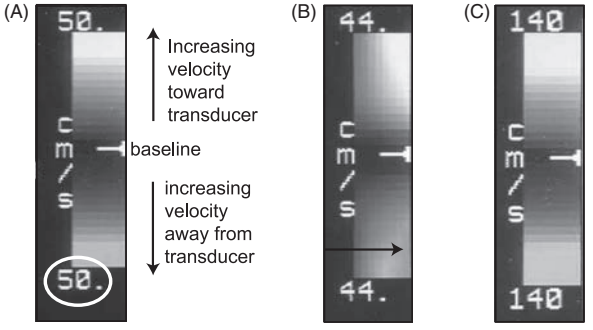

Figure 2.19 Color-coded mapping variations. (A) Enhanced color. Flow towards the transducer is red at low velocity, progressively yellow at higher velocity and blue when flow is away from the transducer with increasingly clear color and increasing velocity. The number 50 indicates that the upper limit of mean velocity readable without aliasing is 50 cm/sec under the present conditions (Nyquist limit). (B) Variance: green (green arrow) is superimposed on the previous colors to illustrate the presence of turbulence, characterized by a large amount of variance within the velocities. (C) Increased Nyquist limit: by increasing the pulse repetition frequency and/or decreasing the depth of the color field, the upper limit of velocity readable without aliasing can be significantly increased (in the present case: 140 cm/sec).

calcium deposits, can mask structures located behind them and create "shadowing." Close to the transducer, an acoustic noise is generated by high-amplitude oscillations of the piezoelectric elements and prevents visualization of reflectors; this is called "near-field clutter" (7). More important are "reverberations": when an ultrasound beam is strongly reflected by a nearby object, the near side of the anatomic wall or the transducer itself may function as another reflecting surface. The echo beam is then sent back to the object being hit a second time by the same ultrasound. This second wave travels with the same burst and produces a second signal. It is interpreted as a second object at twice the distance from the first. It is displayed on the screen in a straight line from the transducer and the real object (Fig. 2.18). This pattern can be repeated two or three times and can also occur between strong reflectors deeper in the field. When the source of reverberation is moving, its amplitude of motion may be twice as great as that of the original echo. Color Doppler is subject to the same artifact: the flow of a sclerotic descending aorta, very close to the esophagus, might be reproduced a second time in front of the aorta, as if a second vessel was present with the same arterial pulse.

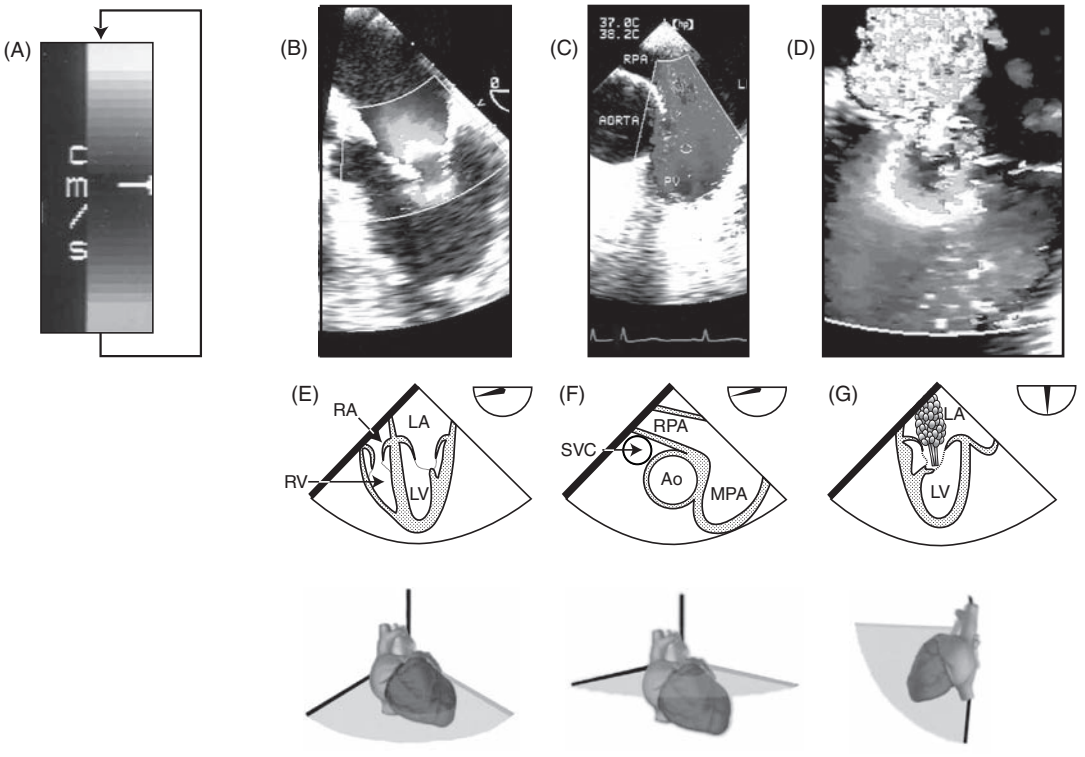

Figure 2.20 (A) Color reversal with aliasing. As soon as the velocity is above the Nyquist limit, the color suddenly jumps from clear blue to bright yellow. (B) and (E) Accelerating flow through a restricted mitral valve orifice. (C) and (F) Central acceleration zone in a pulmonary artery. (D) and (G) Proximal flow acceleration convergence zone on the ventricular side of a mitral regurgitation jet (Ao, aorta; LA, left atrium; LV, left ventricle; MPA, main pulmonary artery; PV, pulmonic valve; RA, right atrium; RPA, right pulmonary artery; RV, right ventricle; SVC, superior vena cava).

Usually, these artifacts can be recognized because they have features independent of actual heart structure characteristics. They cross anatomical walls and cavities without any relationship with natural borders and flow appears in areas where there is no vessel. They usually disappear with readjustment of the depth, angle, and the emitting frequency of the transducer.

IX. CLINICAL APPLICATIONS

In the clinical setting, the Doppler has two main applications: detection and quantitation of normal and disturbed blood flow. The technique has high detection sensitivity and specificity. Color Doppler allows fast localization of abnormal flows and provides a spatial display in two dimensions (Fig. 2.19). Quantification is, however, better performed with PW and CW Doppler and spectral display. The PW Doppler is primarily used for specific flow sampling in definite areas such as cardiac valves or large arteries and veins. Most normal velocities are within its range of measurement without aliasing (Fig. 2.20). The CW Doppler must be utilized for measurement of high velocities across restrictive orifices like stenotic or regurgitant valves. It is more precise for hemodynamic calculations and should be used for all velocities >1.2 m/s (see Chapter 5).

ACKNOWLEDGMENTS

The author is particularly grateful to Dr. Dominique Bettex (University Hospital Zürich, Switzerland) and Mrs Cristine Dardel (CHUV, Lausanne, Switzerland) for their invaluable help in correcting the manuscript.

REFERENCES

1. Labovitz AJ, Williams GA. Doppler Echocardiography. The Quantitative Approach. 3rd ed. Philadelphia: Lea & Febiger, 1992.
2. Goldman DE, Jueter DF. Tabular data of the velocity and absorption of high-frequency sound in mammalian tissues. J Acoust Soc Am 1956; 28:35–37.
3. Quinones MA, Otto CM, Stoddard M et al. Recommendations for quantification of Doppler echocardiography: a report from the Doppler Quantification Task Force of the Nomenclature and Standards Committee of the American Society of Echocardiography. J Am Soc Echocardiogr 2002; 15:167–184.
4. Sehgal CM. Principles of ultrasonic imaging and Doppler ultrasond. In: St John Sutton MG, ed. Textbook of Echocardiography and Doppler in Adults and Children. Cambridge: Blackwell Science, 1996:3–30.
5. Chassot PG. Principes physiques de l'échocardiographie. In: Bettex D, Chassot PG, eds. Echocardiographie transoesophagienne en anesthésie-réanimation. Paris: Masson, 1997:13–39.
6. Garcia-Fernandez MA, Zamorano J, Azevedo J. Doppler Tissue Imaging in Ischemic Heart Disease. In: Doppler Tissue Imaging Echocardiography. Madrid: McGraw-Hill, 1998:7–21.
7. Feigenbaum H. Instrumentation. In: Feigenbaum H, ed. Echocardiography. Philadephia: Lea & Febiger, 1994:1–67.
8. DeMaria E. Cardiac Doppler: The Basics. Andover, MA: Hewlett Packard Co, 1984:1–35.
9. Bom K, de Boo J, Rijsterborgh H. On the aliasing problem in pulsed Doppler cardiac studies. J Clin Ultrasound 1984; 12:559–567.
10. Baker DW, Rubenstein SA, Lorch GS. Pulsed Doppler echocardiography: principles and applications. Am J Med 1977; 63:69–80.
11. Cannon SR, Richards KL. Principles and physics of Doppler. In: Markus M, ed. Cardiac Imaging: A Companion to Braunwald's Heart Disease. Philadelphia: W.B. Saunders Co, 1991:365–373.
12. Pandian N. Cardiac Doppler: color flow imaging. Andover, MA: Hewlett-Packard Co, 1993:1–34.
13. Wells PNT. Colour flow mapping: principles and limitations. In: Roelandt JRTC, Sutherland GR, Iliceto S, Linker DT, eds. Cardiac Ultrasound. Edinburgh: Churchill Livingstone, 1993:43–51.
14. Nanda NC. Basics in Doppler echocardiography. In: Nanda NC, ed. Atlas of Color Doppler Echocardiography. Philadelphia: Lea & Febiger, 1989:1–5.
15. Berg S, Torp H, Haugen BO, Samstad S. Volumetric blood flow measurement with the use of dynamic 3-dimensional ultrasound color flow imaging. J Am Soc Echocardiogr 2000; 13:393–402.
16. Muhiudeen IA, Kuecherer HF, Lee E et al. Intraoperative estimation of cardiac output by transesophageal pulsed Doppler echocardiography. Anesthesiology 1991; 74:9–14.
17. Sutherland GR, Stewart MJ, Groundstroem KW et al. Color Doppler myocardial imaging: a new technique for the assessment of myocardial function. J Am Soc Echocardiogr 1994; 7:441–458.

3

Transducers

FRANÇOIS HADDAD
University of Montreal, Montreal, Canada

BRADLEY I. MUNT, JOHN BOWERING
Providence Health Care, University of British Columbia, Vancouver, British Columbia, Canada

I. The Piezoelectric Principle 41
II. The Structure of the Transducer 42
A. The Structure of a Single Element Transducer 42
B. Assembly and Array 43
III. The Mode of Operation of Transducers 43
A. The Emission of Ultrasound Energy 44
1. Mode of Generation of the Electrical Impulse 44
2. Operating Frequency 44
3. Frequency Bandwidth 44
4. Transducer Damping 45
5. Impedance Matching 45
6. Electrical Matching 45
B. The Ultrasound Beam, Focusing, and Scanning 45
1. Structure 46
2. Main Beam 46
3. Focusing 46
4. Side Lobes 48
5. Image Scanning 49
C. Generation of the Image 49
IV. The Structural and Functional Classification of Transducers 49
V. The Image Quality 50
A. Resolution 50
1. Detail Resolution 50
2. Contrast Resolution 51
3. Temporal Resolution 52
B. Attenuation and Penetration 53
VI. The Recent and Future Transducer Technology 53
References 54

A transducer is a device capable of converting one form of energy into another. Ultrasound transducers convert electrical energy into ultrasound energy or *vice versa* (Fig. 3.1). In this chapter, we will study the structure and operation of transducers as they relate to clinical echocardiography.

I. THE PIEZOELECTRIC PRINCIPLE

Ultrasound transducers operate according to the piezoelectric principle. Piezoelectric is derived from the Greek words piezo meaning to press and electron meaning amber, which refers to the fossilized organic plant resin

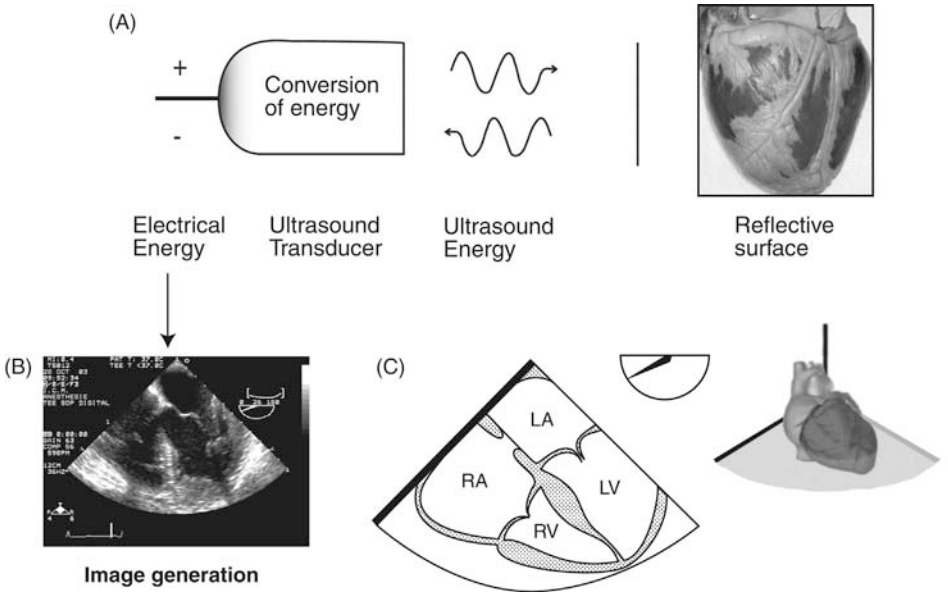

Figure 3.1 The concept of an ultrasound transducer. (A–C) An ultrasound transducer converts electrical energy into ultrasound energy and *vice versa*. The heart represents the reflective surface. The image is generated from the incoming electrical energy (LA, left atrium; LV, left ventricle; RA, right atrium; RV, right ventricle).

that was used in early electrical studies (1). The piezoelectric effect is the phenomenon whereby some materials (quartz, ceramics, lithium sulfate, and others) are able to generate an electric current when deformed by mechanical pressure or stress (1,2). The same materials, when submitted to an alternating electrical current, change shape and can be made to vibrate and deform, that is, the opposite of the first principle (Fig. 3.2). This is the basis of the transducer's construction and function. When we apply this principle to clinical echocardiography, we can understand how a piezoelectric element can be used to generate ultrasound waves from electrical stimulation and how an electrical current can be generated from the mechanical stimulation caused by the returning ultrasound echoes.

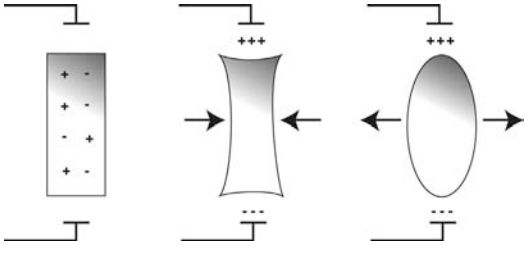

Figure 3.2 The piezoelectric principle. The arrows represent pressure, while (+) and (−) represent electrical charges.

II. THE STRUCTURE OF THE TRANSDUCER

A. The Structure of a Single Element Transducer

The most simple transducer is composed of a single piezoelectric element or crystal. In practice, single crystals are used for A- and M-mode recordings. The transducer contains seven important components (5) (Fig. 3.3):

1. The piezoelectric element which generates acoustic pulses and electrical signals when submitted to electrical or mechanical stimulation.
2. The electrodes which transmit the electric current to and from the piezoelectric element and record the voltage generated by the returning echoes.
3. The backing material which shortens the time during which the crystal vibrates following excitation, thus shortening the spatial pulse length, and improving axial resolution. It is usually composed of a mixture of tungsten and rubber.
4. The matching layer which reduces the acoustic impedance mismatch between the patient and the transducer thereby attenuating reflected ultrasound waves at the transducer–patient interface.
5. The acoustic insulation which prevents the transmission of vibration to the housing of the transducer.

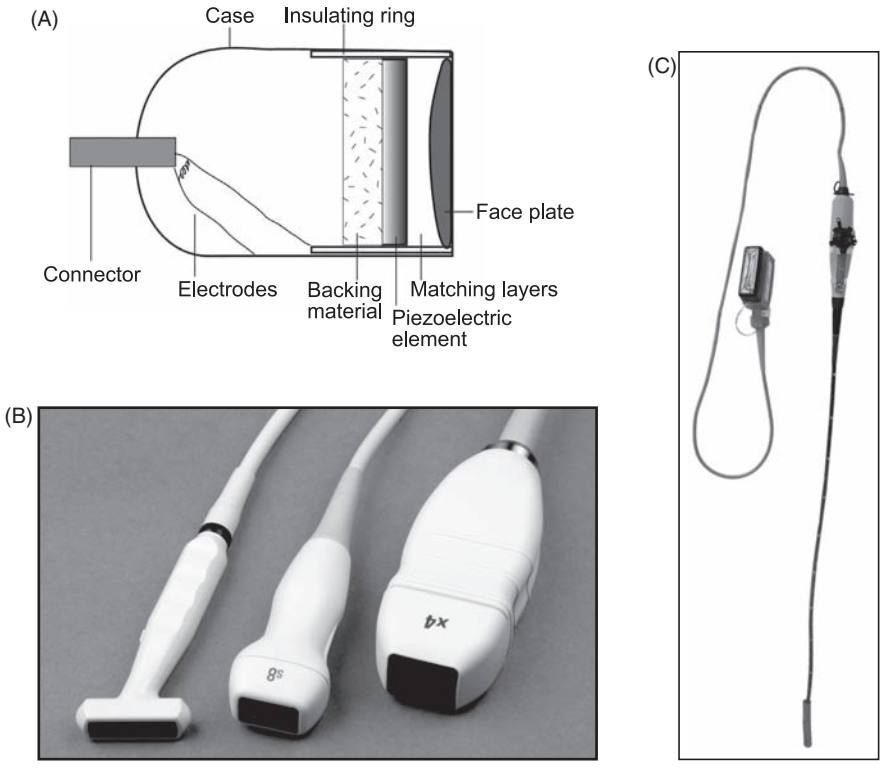

Figure 3.3 (A) The structure of a simple disk-shaped transducer. See text for details. (B) Example of transducers: epiaortic, transcutaneous cardiac, three-dimensional. (C) Transesophageal multiplane transducer.

6. The face plate which allows for improved contact of the probe with the patient.
7. A casing which provides protection for all the probe components.

B. Assembly and Array

A transducer assembly is a transducer composed of an element or a set of piezoelectric elements with damping and matching material in a case (1). A transducer array represents an assembly containing many elements in a given configuration (1,3). Almost all imaging transducers used in clinical echocardiography today are transducer arrays. If the elements are placed side by side, the transducer is referred to as a linear array. When the elements are placed along a curved line, the term convex or curved array is used. Finally, in an annular array the elements are ring shaped rather than rectangular and arranged concentrically (Fig. 3.4). The term phasing is applied to array transducers (phased array) and implies both focusing and steering of the ultrasound beam (see following text). Transesophageal echocardiography (TEE) transducers are phased-array transducers comprising from 64 to 256 piezoelectric elements.

III. THE MODE OF OPERATION OF TRANSDUCERS

This section answers three questions:

1. How does a transducer emit or capture (receive) an ultrasound wave (transducer operation)?

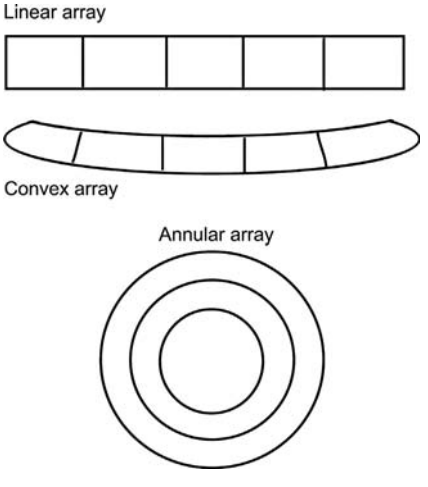

Figure 3.4 The configuration of arrays: linear, convex, and annular.

2. What are the main characteristics of an ultrasound beam (structure and focus)?
3. How can a good quality ultrasound image be generated by combining a set of focused beams (the principle of scanning and steering)?

A. The Emission of Ultrasound Energy

To understand the fundamental principles of transducer function, one has to keep in mind the important characteristics of an ultrasound wave as illustrated in Fig. 3.5 (see also Chapter 1).

1. Mode of Generation of the Electrical Impulse

Transducers can operate in two different generation modes: burst excited or shock excited. In the burst excited mode, transducers convert an alternating electrical voltage burst into an ultrasound pulse by inducing conformational changes in the piezoelectric elements. The transducer can also convert incoming ultrasound echoes into alternating electrical voltage bursts. Most modern transducers operate in burst excited mode because this provides the possibility of selecting the operating frequency from the bandwidth. Typically, transducers are driven by one to three cycles of alternating current in order to generate an image. In the shock excited mode, a transducer converts a uniphasic voltage impulse into ultrasound pulses while returning echoes are converted into alternating electrical voltage bursts.

2. Operating Frequency

The operating, or resonant, frequency of the system is the preferred vibrating frequency of the transducer that provides the maximum efficiency of operation. This frequency depends on two factors:

1. the piezoelectric element thickness which corresponds to one-half of the pulse wavelength and
2. the propagation speed of the crystal.

As wavelength and frequency are reciprocal, the thinner the element the higher the transducer frequency. The typical thickness for a piezoelectric element is between 0.2 and 1 mm (1).

$$\text{Propagation speed} = \text{wavelength} \times \text{frequency}$$

$$\text{Element thickness} = \frac{1}{2} \times \text{wavelength}$$

Therefore

$$\text{Frequency} = \frac{\text{propagation speed}}{2 \times \text{element thickness}} \qquad (3.1)$$

3. Frequency Bandwidth

Under ideal circumstances, when a transducer produces a pulse, its frequency will equal the operating frequency. In reality, however, a pulse contains different frequencies. The bandwidth refers to the range of frequencies in which amplitude exceeds a given value, contained in the ultrasound pulse. The bandwidth is inversely related to spatial pulse length. Therefore, sound pulses with a short duration (shorter spatial pulse length) are composed of

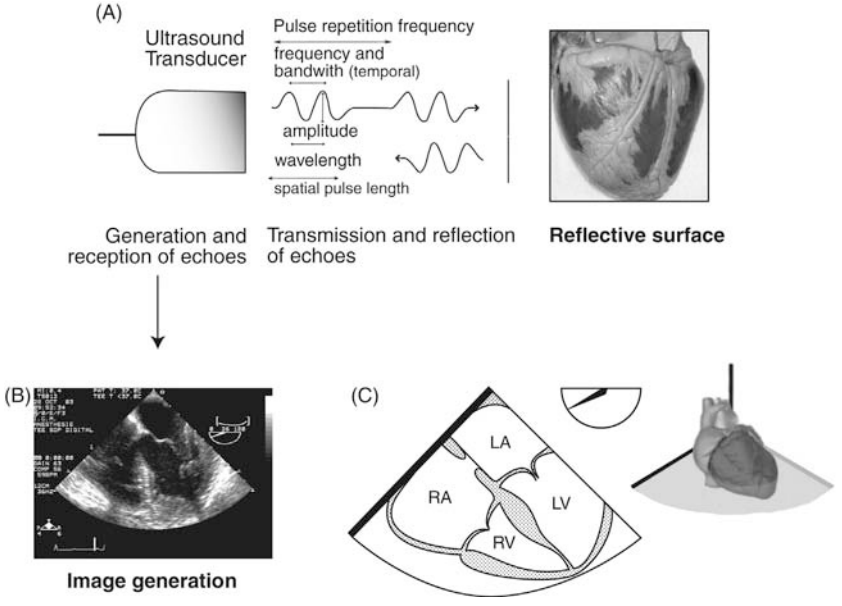

Figure 3.5 The generation and transmission of ultrasound waves. (A–C) This figure illustrates the important characteristics of ultrasound waves leading to the generation of an image (LA, left atrium; LV, left ventricle; RA, right atrium; RV, right ventricle).

more frequencies than pulses with greater spatial length which have fewer frequencies. The range of frequencies can also be described by the quality factor, Q:

$$Q = \frac{\text{operating frequency}}{\text{bandwidth}} \tag{3.2}$$

A lower Q factor generates images with better detail resolution. A transducer with a high (wide) bandwidth can, under certain circumstances, operate at different frequencies. This property provides the advantage of choosing the appropriate operating frequency depending on the desired axial resolution and penetration (a compromise). The bandwidth concept is also important for new imaging modalities such as harmonic imaging, which will be briefly discussed at the end of the chapter.

4. Transducer Damping

Transducer damping is the process in which the number of cycles in each pulse is reduced (Fig. 3.6). This is achieved by placement of specific backing material behind the piezoelectric crystal. The advantage of damping is to improve detail resolution by reducing the spatial pulse length. However, damping has the disadvantage of decreasing the ultrasound amplitude, which reduces the ability of the system to detect weak returning echoes and decreases its sensitivity. A system which has poorly damped crystals will have a higher sensitivity, but lower detail resolution and a smaller bandwidth.

5. Impedance Matching

The transducer element has an acoustic impedance ~25 times greater than that of the human body (4). This acoustic impedance mismatch can generate a large reflective loss at the transducer–skin interface. To reduce this loss, a matching layer is placed between the skin and the transducer which has an impedance intermediate between those of the crystal and tissue. Its thickness is equal to one-quarter of the wavelength of the transducer's center frequency (5). This specific thickness provides constructive interference in the layers, thereby improving sound transmission. Multiple matching layers have the advantage of increasing sensitivity as well as bandwidth.

When the ultrasound wave is emitted from the transducer and strikes air, which has a low impedance, the difference in impedance between the two interfaces is such that most of the ultrasound wave would be reflected away from the patient. This is minimized by use of a coupling medium such as aqueous gel (see Chapter 1, Fig. 1.8).

6. Electrical Matching

Electrical matching represents the electrical compatibility between the transducer and the diagnostic instrument. Suboptimal electrical matching could lower the transducer sensitivity and explain why a particular transducer performs better in a certain electrical environment (on a different pulser machine). Electrical matching is accomplished by tuning the transducer's impedance to that of the pulse/receiver of the diagnostic machine. This tuning is not a user-variable function and has to be designed into the transducer based on a good understanding of the pulse/receiver characteristics of the echographic instrument (5).

B. The Ultrasound Beam, Focusing, and Scanning

Ultrasound waves propagate in the acoustic medium as part of a beam. The ultrasound beam determines the area of the heart from which returning echoes will be recorded.

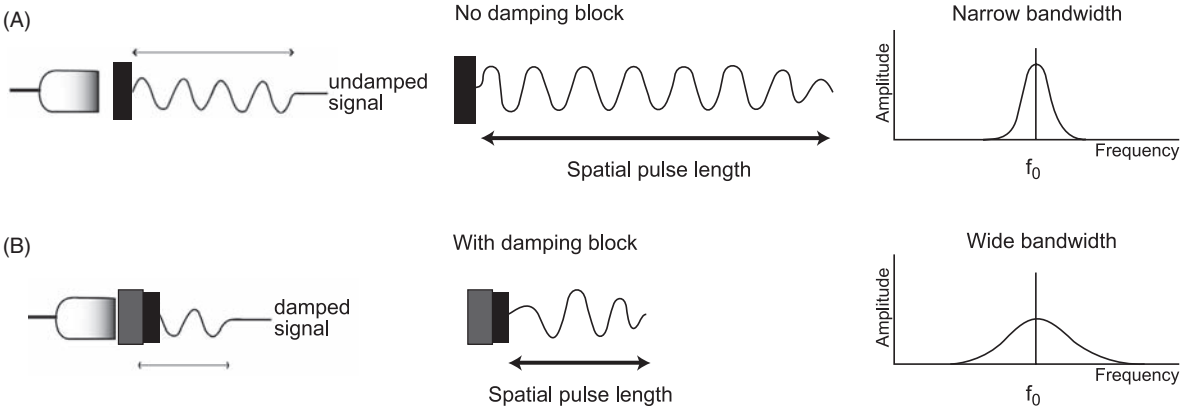

Figure 3.6 The role of damping material. (A) No damping block. (B) Damping block. This reduces the spatial pulse length which improves detail resolution. It also increases the frequency (f) bandwidth. However, it decreases the ability of the system to detect weak distal echoes through a reduction of the amplitude.

1. Structure

The ultrasound beam is composed of a main beam or central beam, which generate the desired image as well as side lobes or grading lobes, which can be responsible for artifact imaging. The main beam represents the part in which the intensity of the acoustic wave is greater than a determined percentage of a spatial peak value (1). The side lobes represent weaker beam of sounds that propagate in a different direction than that of the main beam. Its intensity is smaller than the determined percentage of the spatial peak value.

2. Main Beam

In a simple disk transducer, the convergent portion of the beam is referred to as the near or Fresnel zone. The point where the beam begins to diverge is the transition zone. Beyond the transition zone lies the far or Fraunhofer zone (Fig. 3.8). The shape of the ultrasound beam is important because it determines the area from which echoes can be recorded as well as the intensity and lateral resolution of the system (5).

As the pulse travels through the near zone, its diameter decreases; as it travels through the far zone, its diameter increases (1). The length of the near zone is determined by the operating frequency and the diameter of the transducer element(s) also known as the aperture. Both an increase in the operating frequency and diameter (aperture) of the transducer will increase the near zone length (Fig. 3.9). At a sufficient distance from the near zone, increasing the operating frequency or the aperture can decrease the beam diameter. Therefore, the width of the ultrasound beam depends on (1) the distance from the element, (2) the diameter of the piezoelectric element, and (3) the wavelength and the operating frequency. Figure 3.9 displays how both frequency and aperture affect the length and width of the ultrasound beam. The concept of beam width is important because objects that are imaged at the end of the near zone where the beam width is narrow will generate images with a better lateral resolution. Beam width can be further reduced through focusing.

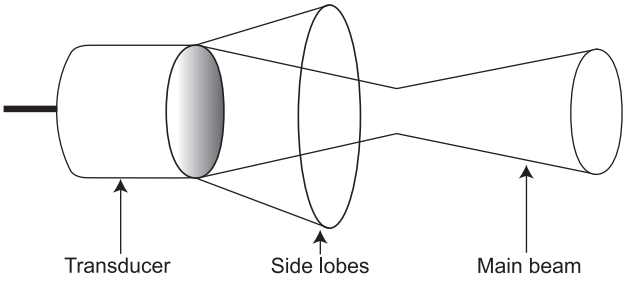

Figure 3.7 The ultrasound beam components: main beam and side lobes.

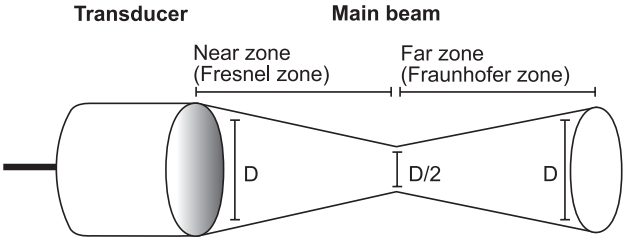

Figure 3.8 The near (Fresnel) and far (Fraunhofer) zones of the main beam. The diameter (D) of the near zone decreases until it reaches a value of one-half its initial D ($D/2$) in the transition zone. It then increases in the far zone until it reaches its original diameter at twice the near zone length.

Although the ultrasound beam is often displayed in two dimensions, it has a three dimensional volume. The thickness of the ultrasound beam, called also the z-axis or elevation axis, is important because it determines the extent of section thickness artifact. This artefact occurs when the third dimension of the beam is collapsed to zero (1). These off-axis echoes often disappear when changing the position of the scan plane. These thickness artifacts can sometimes be seen when imaging the aotic arch and should not be confused with abnormal thickness of the aortic wall.

3. Focusing

Focusing consists of concentrating the beam to a smaller cross-sectional area—the focal region, to improve resolution. This process brings the end of the near zone closer to the transducer. The focal length, defined as the distance from the transducer to the focal region, is equal to or

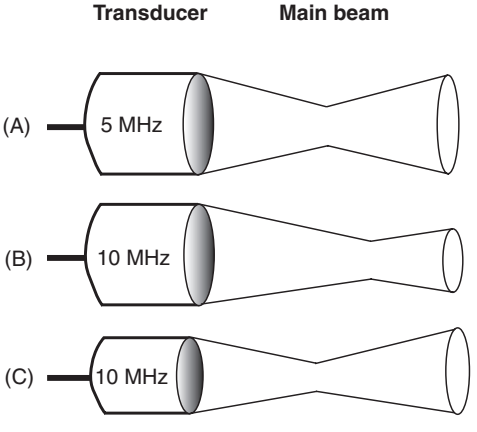

Figure 3.9 The dynamic relationship of beam width determinants. Main beam of (A) 5 MHz transducer and (B) 10 MHz transducer: the near field is lenghtened. (C) Decreasing the size of the transducer results in a smaller field diameter with a reduced near-field length.

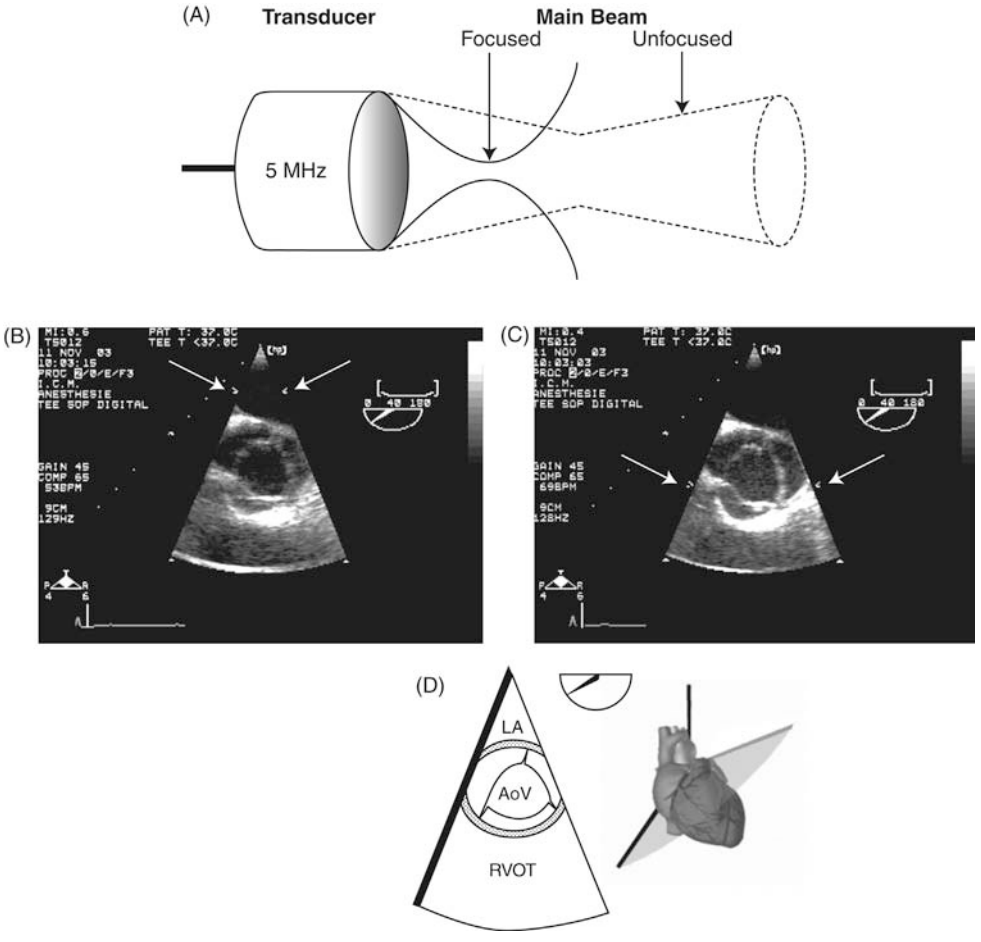

Figure 3.10 Beam focusing. (A) Focusing reduces beam diameter in the near zone, increases beam diameter in the far zone and moves the transition zone closer to the origin of the transducer. (B–D) Examples of two images with different focus location. Note the difference in (B) when the focus zone is not centered on the structure of interest, the aortic valve (AoV), compared with (C), where it is positioned over the AoV. The detail resolution is improved at that level (LA, left atrium; RVOT, right ventricular outflow tract).

shorter than the near-zone length of the unfocused beam. The beam width decreases from the transducer to the focal region but increases beyond in the far zone (Fig. 3.10). Beam focusing can be achieved by either mechanical or electronic means.

Mechanical

With simple disk transducers, two methods of focusing have been described. *Internal* focusing is achieved by applying a radius of curvature to the piezoelectric crystal. In the *external* focusing method, the piezoelectric element is kept flat while a concave acoustic lens is placed in front of the crystal (Fig. 3.11).

Electronic Focusing by Phasing

Using multiple piezoelectric elements organized in a transducer array, focusing is achieved by electronic phasing. Electronic phasing consists of the successive activation of the different elements of the transducer array following a specific time delay pattern. Varying activation time pattern creates different specific focus regions and allows the generation of multiple foci regions without modifying the curvature of a mechanical element. The diagram on the top in Fig. 3.12 shows a long delay in activation of the elements. This results in a greater curvature moving the focus region closer to the transducer. In the adjacent diagram, the delay between element activation is decreased, producing a narrower curvature and moving the focus region further away.

It is important to note that beam width changes as the focal length is increased. In order to maintain the same focal width, the number of elements activated has to change according to the focal length. For short focal lengths, a small number of the elements are activated, while for a focus placed further from the transducer, a larger percentage of the elements must be activated. The ability to change the number of activated elements is

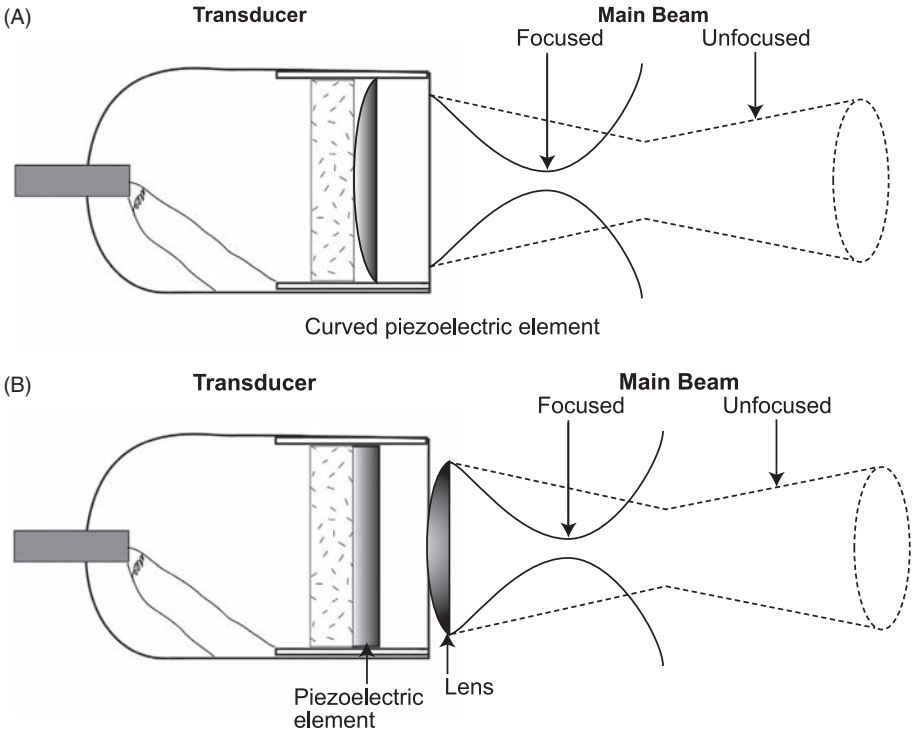

Figure 3.11 Mechanical methods of ultrasound beam focusing. (A) Curved piezoelectric crystal. (B) Flat crystal with a concave lens.

referred to as variable or dynamic aperture. Likewise, the concept of dynamic reception focus refers to the ability to adjust the focus of the "listening" capability of the transducer to a given depth. This is analogous to the automatic focusing device in movie cameras which changes the focus while tracking a moving object.

4. Side Lobes

As mentioned previously, side lobes represent weaker beams of sound that propagate in a direction different from that of the main beam originating from a single element. Grading lobes also represents weaker beams of

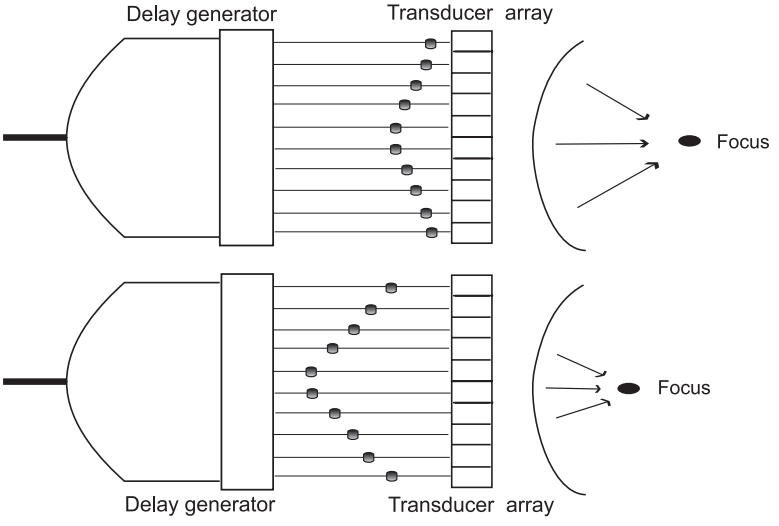

Figure 3.12 Electronic methods of ultrasound beam focusing. The time delay pattern is illustrated in the middle, resulting in specific focus point.

sound that propagate in a direction different from that of the main beam, but in contrast to side lobes, they originate as a result of the multi-element structure of the transducer array (1). If the side lobe or grading lobe beam encounter a strong reflector, their echoes may be imaged, especially if they propagate in a poorly echogenic region. Because the system assumes that the echos originate from the main beam, the image is displayed in a position that differs from its true location and usually cross anatomical boundaries (side lobes or grading lobes artifacts).

In transducer array, grading lobe artefacts can be minimised by dividing the elements into smaller pieces, a process known as subdicing (6). Further reduction of this artifact is achieved by applying different voltages to these subdiced elements. They usually disappear with readjustment of depth, angle, emitting frequency of the transducer, or by adjusting the mode of harmonic imaging.

5. Image Scanning

Scanning (or steering) is the process through which pulses are sent through the many paths required to generate the cross-sectional image (1). The cross-sectional image is then assembled from the reconstruction of the focused ultrasound beams. Ultrasound beam scanning can be achieved by mechanical steering, electronic scanning, and electronic phasing. Mechanical steering is accomplished by oscillating or rotating a transducer element. This method is used with the intravascular ultrasound probe, where the ultrasound beam is made to turn 360 by rotating either the crystal or an ultrasound reflector or mirror. In electronic scanning (Fig. 3.13), the ultrasound beam scanning is created by successively activating different subsets of transducer elements within an array, where each subset acts as a larger transducer element. Phasic scanning (Fig. 3.13) uses small time differences (phases) in stimulating piezoelectric element activity to generate beams with various orientations. Nowadays, modern echographic transducers operate using mostly electronic scanning and phasing.

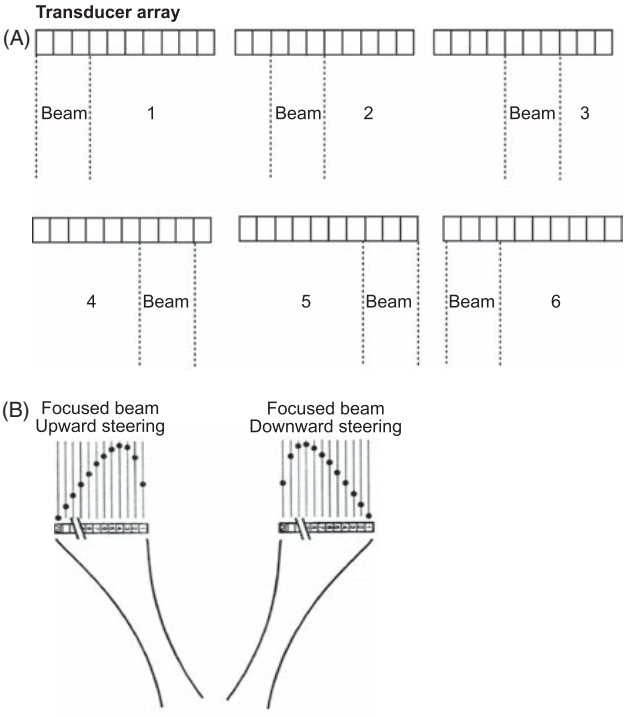

Figure 3.13 Difference between electronic scanning and phasing. (A) With electronic scanning, only a subset of piezoelectric crystals are successively activated. (B) During electronic phasing, sequential activation of the piezoelectric allows steering of the ultrasound beam.

C. Generation of the Image

The initial step of ultrasound image generation involves the application of a short pulse of voltage to the electrodes of the piezoelectric crystal, resulting in vibration and a pulse wave of very short duration. The ultrasound pulse waves are then propagated into the surrounding medium where they will be both reflected and transmitted by the tissue interfaces encountered. The portion of sound energy returned to the transducer (the echo) causes conformational changes in the piezoelectric crystal, generating in turn an electrical charge on its surface. Because of its weak strength, this signal is then amplified. The receiver circuit can then determine the amplitude of the echo, its total travel time away from the transducer as well as the depth of the reflecting tissue. The amplitude of the echo determines the shade of gray it is assigned in the image. Each pulse produced by the ultrasound machine creates a single line of information. Only one pulse is required for each scan line, but with multifocus beam systems and color Doppler, numerous pulses can be used to generate each scan line. In order to produce an adequate image, 128 lines of information are normally used (Fig. 3.14).

To reduce the flicker of the image, 20–30 frames of information are required per second of viewing. The term pulse repetition frequency (PRF) is applied to the number of pulses generated in 1 s. Most modern transducers emit several thousand pulses per second. All echoes from one pulse must be received by the transducer before subsequent pulses can be emitted.

IV. THE STRUCTURAL AND FUNCTIONAL CLASSIFICATION OF TRANSDUCERS

Table 3.1 classifies the transducer arrays according to their configuration, scanning, focusing, and image properties. One of the most common transducer arrays used in

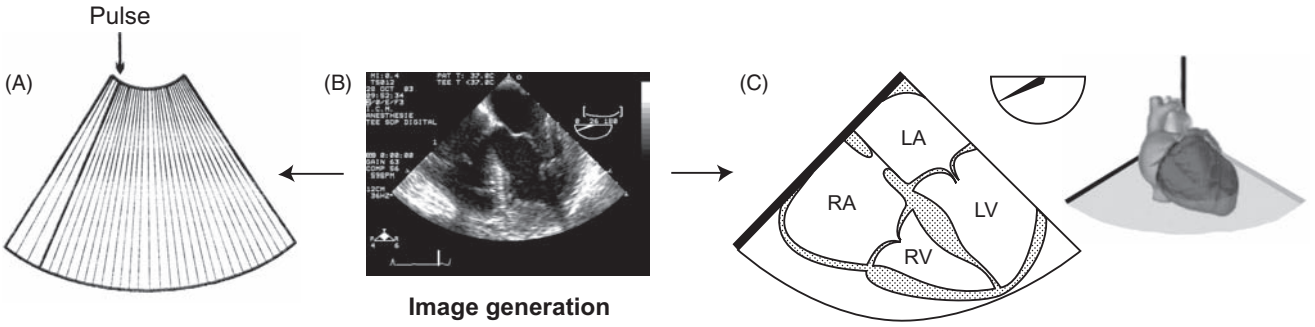

Figure 3.14 Image generation. (A–C) Each line in the image is created by a pulse. Summation of all the pulses creates the final two-dimensional image (LA, left atrium; LV, left ventricle; RA, right atrium; RV, right ventricle).

echocardiography is the vector array, in which phasing is applied to a linear sequenced array to generate focused pulses in different directions.

V. THE IMAGE QUALITY

Resolution is a characteristic that describes the quality of the image. It allows echoes to be distinguished in terms of space, intensity, and time. These are known as detail, contrast, and temporal resolution, respectively (Fig. 3.15).

A. Resolution

1. Detail Resolution

Detail or linear resolution refers to the ability of the imaging system to represent two closely related but spatially distinct objects (ultrasound reflectors) as separate (or resolved) nonoverlapping echoes. As resolution is the minimum reflector separation required to discriminate between two objects, the smaller the value of resolution, the better the imaging system. There are two aspects to detail resolution: axial and lateral.

Axial

Axial resolution is the ability to separate two objects spatially along the direction of the ultrasound beam (scan line). It is affected by the spatial pulse length, that is, the length that a pulse takes up, equal to the product of wavelength by the number of cycles in the pulse.

$$\text{Axial resolution} = \frac{1}{2} \times \text{spatial pulse length} \qquad (3.3)$$

Therefore, axial resolution is improved by decreasing both the wavelength and the number of cycles per pulse. The latter is determined by the damping material in the transducer and cannot be currently modified by the user. On the other hand, wavelength can be reduced by increasing the transducer imaging frequency, an operation which is easily accessible to the imaging system operator (Fig. 3.16). However, the drawback in increasing frequency for better resolution is higher attenuation with imaging depth and consequently a reduction in penetration capability.

Lateral

Lateral resolution represents the ability to discriminate between two objects lying perpendicular to the ultrasound beam direction (scan line). It is determined by the beam width: if the spatial separation between two objects is greater than the beam width, two different echoes can be generated and resolved as the beam is scanned across

Table 3.1 Transducer Arrays

Transducer array	Scanning or steering	Focusing	Image display
Mechanical sector	Motor drive	Curved lens or element	Sector
Linear array	Electronic sequencing	Electronic phasing	Rectangular
Phased linear array	Electronic sequencing	Electronic phasing	Parallelogram
Convex array	Electronic sequencing	Intrinsic property due to its configuration	Sector
Phased convex array	Electronic sequencing	Electronic phasing	Sector
Annular array	Motor drive	Electronic phasing	Sector
Vector array	Electronic sequencing and electronic phasing	Electronic phasing	Sector

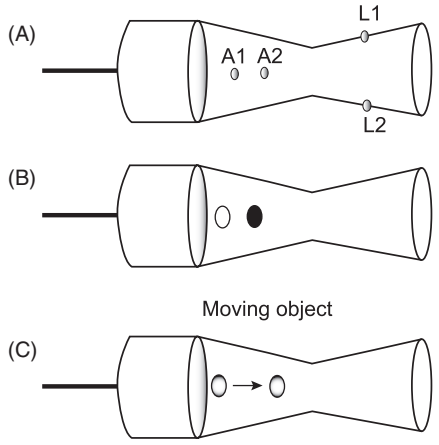

Figure 3.15 Types of resolution. (A) Detail resolution with axial A1 and A2 and lateral L1 and L2 resolution. (B) Contrast resolution. (C) Dynamic time resolution. (See text for explanations.)

them.

$$\text{Lateral resolution} = \text{beam width} \tag{3.4}$$

Because beam width changes with the distance from the transducer, so, too, does lateral resolution. In an unfocused beam, the best lateral resolution is seen at the transition zome. Lateral resolution can be improved by reducing the beam diameter through focusing. In the focused beam, the highest lateral resolution will be found at the focal point.

The relationship between Axial and Lateral Resolution

Axial and lateral resolutions are not independent of each other. Indeed, beam width, and therefore lateral resolution, is influenced by the pulse bandwidth which is related to spatial pulse length, a determinant of axial resolution (1). For a more complete discussion, the reader is referred to the excellent book on the physical principles of ultrasound by Frederick W. Kremkau (1).

2. Contrast Resolution

Contrast resolution refers to the ability to discriminate subtle echo-strength (or intensity) differences between two adjacent reflectors. Depending on the respective difference in amplitude signal of separate echoes, the echographic system assigns a different shade of gray, i.e., a different number of bits per pixel. Weak echoes are assigned darker shades of gray while strong reflectors are placed at the white end of the scale. Contrast resolution will be improved by increasing the number of bits per pixel, or by having a greater number of gray shades available.

Compression is an operator-adjustable function that can adjust the dynamic range of signal amplitude, i.e., it can change the value assigned to the highest and lower value

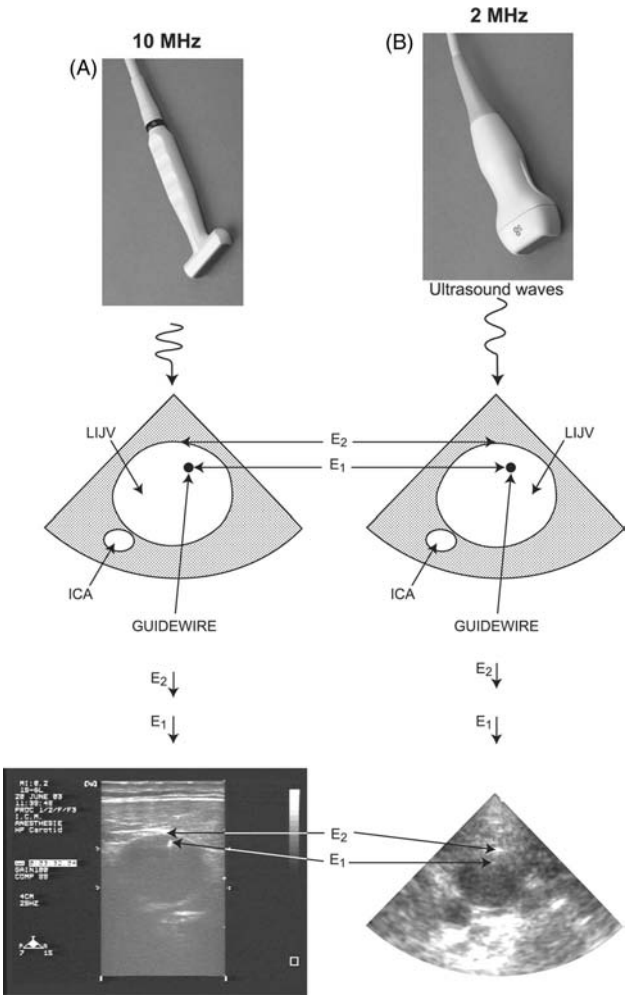

Figure 3.16 The influence of imaging frequency on axial resolution results in separate echoes of closely spaced reflectors. In this example, the 10 MHz probe (A) allows better discrimination of the left internal jugular vein (LIJV) and the guidewire compared with the 2 MHz transducer (B) (E, echocardiographic reflector; ICA, internal carotid artery).

of the returning signal amplitude. By adjusting the level of compression, the operator can choose the best dynamic range in order to optimize the contrast resolution of the image. As the dynamic range is decreased, a smaller

Table 3.2 Axial Resolution, Penetration, and Frequency

Frequency (MHz)	Depth (cm)	Axial resolution (mm)
2.0	30	0.77
3.5	17	0.44
5.0	12	0.31
7.5	8	0.20
10.0	6	0.15
15.0	4	0.10

Table 3.3 Typical Operating Frequencies Used with Different Transducers

Transducer type	Usual probe frequency (MHz)
Transthoracic probe	
New born	7.5–12
Child	5–7.5
Adult	2.5–3.5
Transesophagal probe	5–7.5
Intravascular ultrasound	10–40

difference in intensity is required to be assigned a different shade of gray. Contrast resolution has a direct influence on detail resolution because it influences the recognition of overlapping pulses. With better contrast, a system can recognize important wave overlap. Therefore, the better the contrast resolution, the greater the detail resolution.

3. Temporal Resolution

Temporal resolution refers to the ability of the echographic system to discriminate between two closely related events

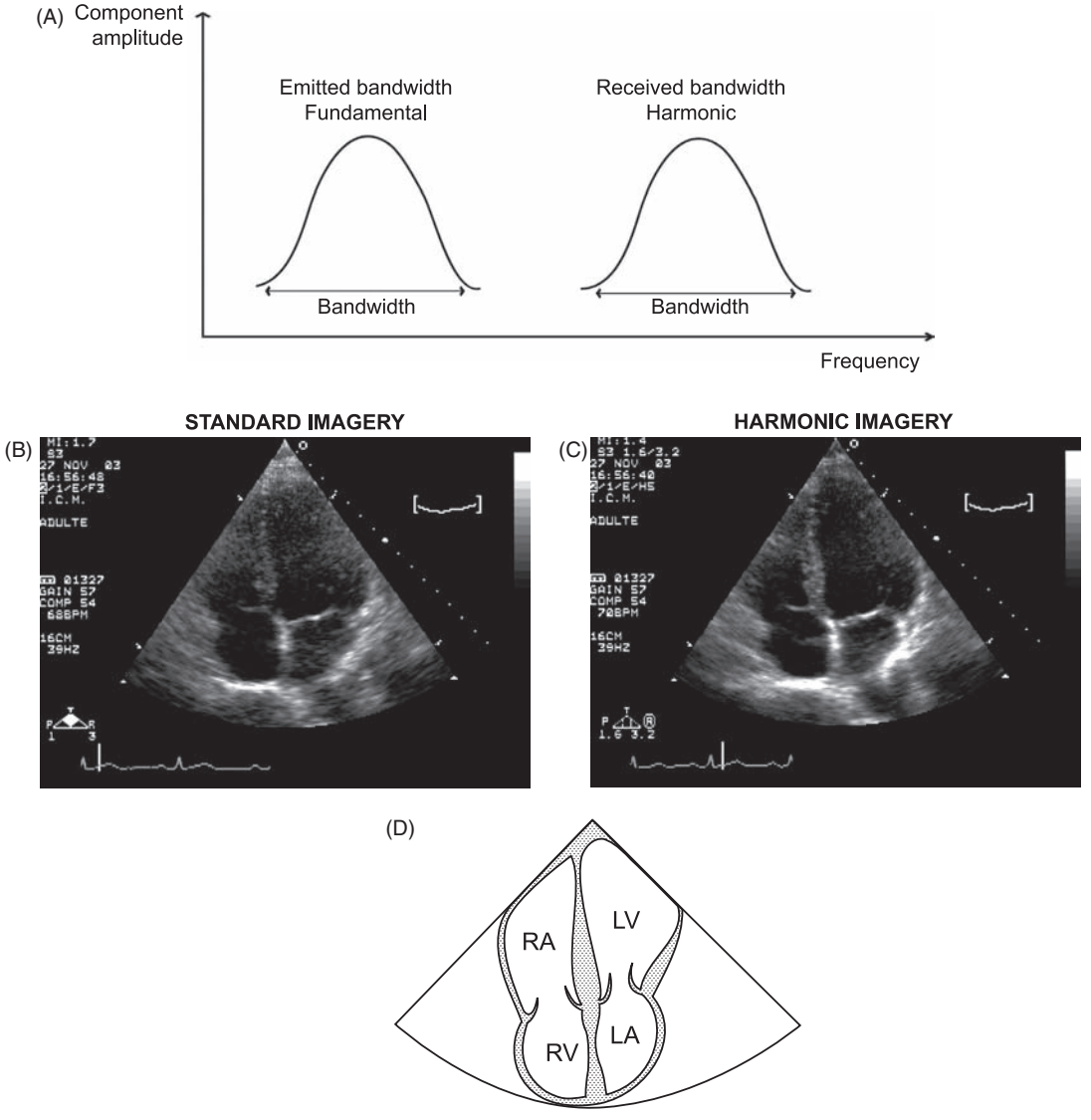

Figure 3.17 Harmonic imaging principle. (A) An ultrasound beam is emitted at a fundamental frequency but reflected echoes are selectively received at harmonics (multiples) of the fundamental frequency. This results in improved detail resolution because of the higher frequency. (B–D) Transthoracic apical four-chamber view showing the difference between fundamental in (B) and harmonic imaging in (C) (LA, left atrium; LV, left ventricle; RA, right atrium; RV, right ventricle).

in time. Without temporal resolution, imaging of valve motion or heart contraction would be impossible. Temporal resolution is directly related to frame rate, which represents the number of sonographic images (frame) stored by seconds. As frame rate increases, the temporal resolution improves. Because each frame is made of scan lines, the pulse repetition frequency (PRF) required will depend on the number of focuses, lines per frame, and the frame rate (1). In order to improve temporal resolution, the operator can reduce the width of the sector image or the number of focus areas.

B. Attenuation and Penetration

As ultrasound propagates in tissue, it progressively loses energy and attenuation occurs. The mechanisms involved in attenuation include the conversion of ultrasound energy to heat (a process called absorption), as well as reflection and scattering (7). Attenuation is frequency dependent, with the lower frequencies having a greater depth of penetration than higher frequencies.

$$\text{Penetration} = \frac{1}{\text{operating frequency}} \tag{3.5}$$

In clinical echocardiography, the transducer frequency is chosen to provide the best axial resolution while maintaining ultrasound penetration to a desirable depth. Table 3.2 lists the typical imaging depth and axial resolution of two-cycle pulses in tissue. Table 3.3 lists the typical operating frequencies used with different transducers.

VI. THE RECENT AND FUTURE TRANSDUCER TECHNOLOGY

Improvement in transducer technology has made tissue harmonic imaging possible (Philips Inc. Internet site: www.medical.philips.com/ and General Electrics Inc. Internet site: www.gemedicalsystem.com/). The imaging system emits an ultrasound signal at a broad band of low fundamental frequencies. The signal is reflected back to the system by target objects and structures (echoes), but also resonates off tissues at twice (and more) the transmitted fundamental frequency: these multiples of the fundamental frequency are called harmonics. In tissue harmonic imaging, a bandpass receiving filter is set specifically to receive harmonic frequencies while filtering out the fundamental frequencies.

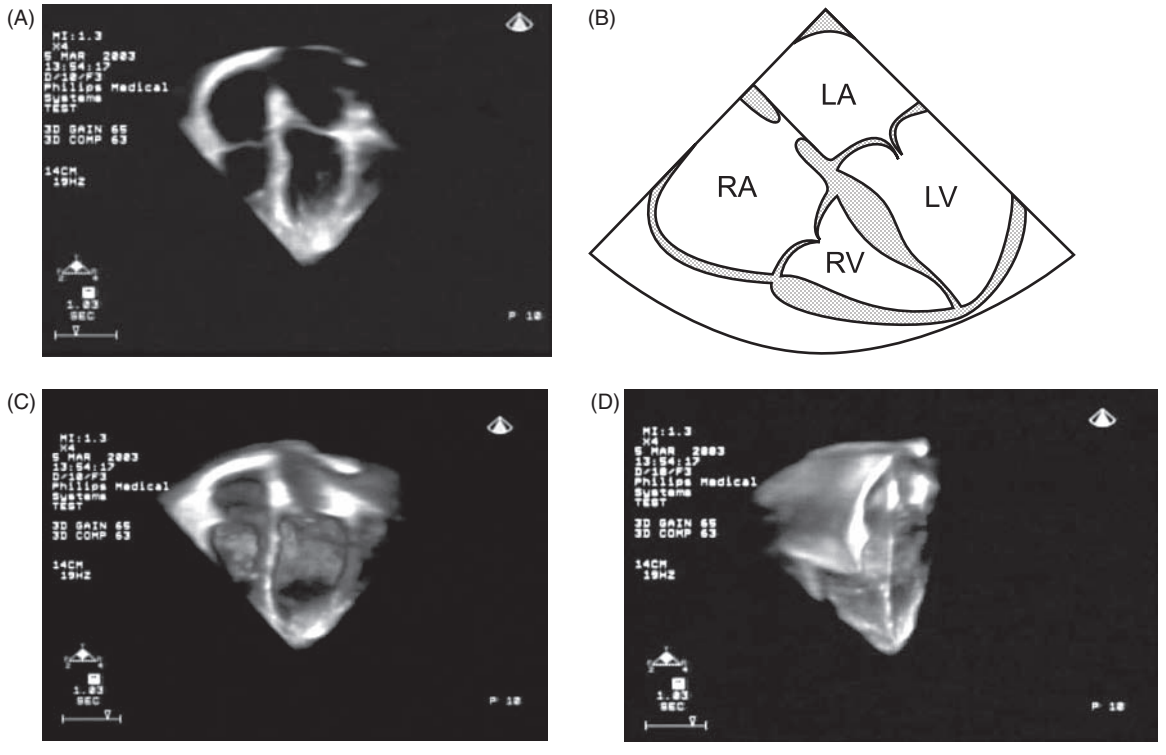

Figure 3.18 (A–B) Two-dimensional four-chamber view of the heart. (C–D) Equivalent view in three-dimensional echocardiography (LA, left atrium; LV, left ventricle; RA, right atrium; RV, right ventricle).

This method significantly improves the image quality in several ways. First, the source of harmonic frequencies is the target object and not the transducer. The travel distance to the receiver is, therefore, halved, reducing the potential for signal degradation. Most of the artifacts generated in the near field (such as superficial reverberation), before the ultrasound beam from the transducer reaches the object, are also eliminated. Moreover, grating lobe artifacts (additional side beams emitted from multiple-element array transducers) caused by strong reflectors are eliminated as those side beams are not sufficiently powerful to generate harmonic frequencies. Finally, because the minimum power required to generate harmonics will be reduced to the higher-intensity portion of the ultrasound beam, the resulting "harmonic-generating" beam will have a smaller beam width, improving resolution (Fig. 3.17).

Changes in traditional ultrasound probe design are expected to result in improved imaging capabilities. The recent advent of two-dimensional array technology with smaller element assembly within a probe (xMATRIX^{TM}, Philips Medical Systems) provides data acquisition in a volumetric rather than in a tomographic fashion, enabling real-time three-dimensional ultrasound imaging (Fig. 3.18). Future developments in computer processing power, elements assembly, probe design, and ultrasound emission and reception paradigms are currently being sought to improve detail and temporal image resolution.

REFERENCES

1. Kremkau FW. Diagnostic Ultrasound, Principles and Instruments. 6th ed. Philadelphia: WB Saunders, 2002.
2. Ballato A. Piezoelectricity: old effect, new thrusts. IEEE Trans Ultrason Ferroelectrics Freq Control 1995; 42:916–926.
3. Hill CR. Physical Principles of Medical Ultrasonics. Chicester, England: Ellis Horwood, 1986.
4. Duck FA. Physical properties of tissue. Acoustic Properties of Tissue at Ultrasonic Frequencies. New York: Academic Press, 1990.
5. Weyman AE. Principles and Practice of echocardiography. Philadelphia: Lea & Febiger, 1994.
6. Otto CM. Principles of echocardiography image acquisition and Doppler analysis. In: Otto CM, ed. Textbook of Clinical Echocardiography. St-Louis: WB Saunders, 2000:1–28.

4

Normal Anatomy and Flow

GEORGE N. HONOS, JEAN BUITHIEU
McGill University, Montreal, Canada

NICOLAS DÜRRLEMAN, ANDRÉ Y. DENAULT
University of Montreal, Montreal, Canada

I. Normal Anatomy and Flow During the Complete Examination 56
A. Systematic Transesophageal Echocardiography Examination and Imaging Planes 56
1. TEE Probe Manipulation 56
2. Conventions of Image Display 57
3. Views and Structures 57
4. Four-Chamber View (0–20°, Retroflexion) 61
5. Transgastric Views (0°, 90°, and 135°) 61
6. Thoracic Aorta Views (0°, 90°) 62
B. Anatomy and Physiology 64
1. Cardiac Chambers 64
2. Cardiac Septae 65
3. Cardiac Appendages 69
4. Veins 69
5. Arteries 72
6. Valves 77
II. Doppler Flow Profiles for Normal and Abnormal Physiology 81
A. Phases of the Cardiac Cycle (Systole vs Diastole/Four Phases) 81
B. Normal Pressures in Cardiac Chambers and Great Vessels 83
C. Mitral Valve 83
1. Mitral Regurgitation 83
2. Mitral Stenosis 83
D. Left Ventricular Inflow 83
1. Abnormal Relaxation 83
2. Restrictive Filling 83
E. Tricuspid Valve 84
F. Aortic Valve 85
1. Aortic Regurgitation 85
2. Aortic Stenosis 85
G. Pulmonic Valve 85
1. Pulmonic Regurgitation 85
2. Pulmonic Stenosis 85
H. Left Ventricular Outflow Tract 86
I. Pulmonary Vein 86
J. Hepatic Vein 86
K. Ascending Aorta 86
L. Descending Aorta-Flow Reversal and Aortic Regurgitation 86
M. Coronary Sinus 86
N. Pulmonary Artery 87
III. Conclusion 87
References 87

I. NORMAL ANATOMY AND FLOW DURING THE COMPLETE EXAMINATION

A. Systematic Transesophageal Echocardiography Examination and Imaging Planes

1. TEE Probe Manipulation (Fig. 4.1)

Following successful insertion into the patient's esophagus, the operator manipulates the Transesophageal Echocardiography (TEE) Exam probe to obtain the desired cross-sectional images of the heart (1). Because of individual variation in the anatomic relationship between the esophagus and the heart, manipulation must be individualized and based on the images that unfold on the echo system's display. Moreover, unlike for comprehensive transthoracic imaging, where a systematic approach is generally preferred, a TEE study should be tailored to address the clinical question first, followed by acquisition of the other standard views and Doppler information. This initial targeted approach is prudent in order to ensure that the study is diagnostic even in the event that the exam must be terminated quickly or postponed due to patient discomfort or clinical instability (e.g. suspected aortic dissection) (2).

Transesophageal echocardiography transducer manipulation options include (Fig. 4.1)

- Advancement/withdrawal, (to view inferior or superior structures, respectively)
- Rotation (clockwise to view rightward structures and counterclockwise to view leftward structures)

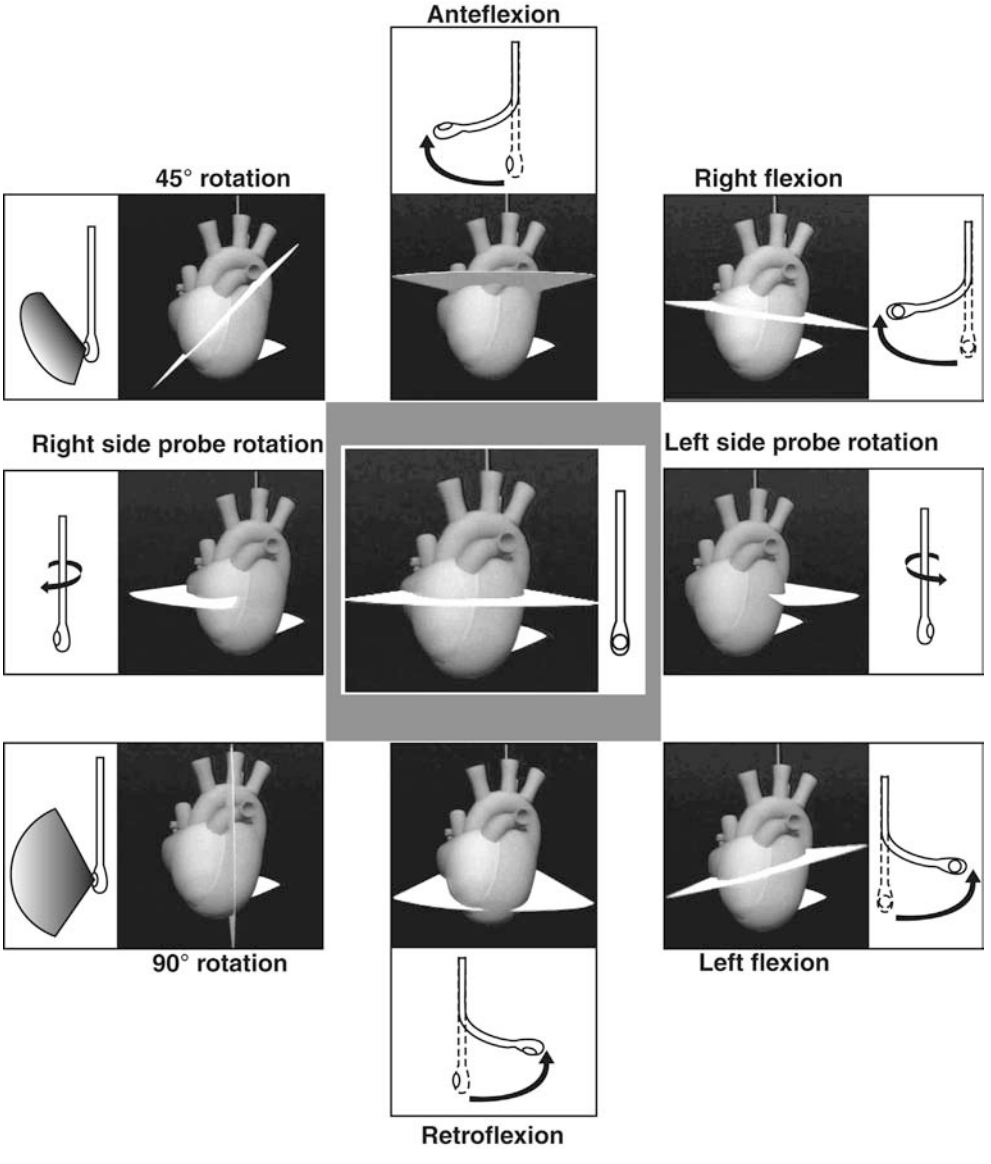

Figure 4.1 Graphical display of transesophageal probe manipulation and cardiac orientation.

- Anteflexion and retroflexion of the probe shaft (to view structures towards the heart base or towards the apex)
- Leftward and rightward flexion of the probe shaft (used infrequently, with the advent of multiplane probes)
- Electronic image plane rotation (0–180°, where 0° represents a transverse plane, perpendicular to the length of the probe).

Transesophageal echocardiography probe manipulation begins with the advancement or withdrawal of the transducer to specific levels within the upper gastrointestinal tract adjacent to the heart and vascular structures. Standard imaging plane levels (with their average distance from the incisors) include: upper or high esophageal (25–28 cm), mid-esophageal (29–33 cm), gastroesophageal junction (34–37 cm), transgastric (38–42 cm), and deep-transgastric (>42 cm). At each imaging level, a multiplane probe provides a continuous range of transverse and longitudinal images of the heart by electronic rotation of the transducer sector scan. Images can be rotated continuously through a 180° arc, producing an unlimited number of possible two-dimensional (2D) views of the heart, which can sometimes be complemented by additional probe lateral flexion. The electronic orientation of the ultrasound beam relative to the probe is usually indicated in degrees and with an icon on the ultrasound system's screen. Finally, additional rotation (clockwise = rightward and counterclockwise = leftward) and flexion (anteflexion, retroflexion, leftward and rightward flexion) of the probe shaft are used to optimize visualization of selected anatomic structures.

While there is considerable variation between patients, certain electronic imaging angles are useful as a starting point in most studies as they relate to specific transverse or longitudinal sections through the heart as listed in Table 4.1.

Table 4.1 Transesophageal Echocardiography Probe Orientation

Orientation	Description and features of view
0°	Transverse plane to the probe long axis Horizontal to the plane of the body Oblique to cardiac short axis
45°	Short-axis view of cardiac basal structures (e.g. aortic valve)
90°	Longitudinal plane (parallel to the probe long axis) Sagittal (vertical) to the plane of the body Oblique to the cardiac long axis Parallel to the ascending aorta
135°	Long-axis view of cardiac structures (LV and LVOT)
180°	Mirror image of the 0° transverse plane

2. Conventions of Image Display (Fig. 4.2)

Modern echo systems allow the acquired 2D images to be rotated electronically (up–down, left–right) before displaying them on screen. By convention, in TEE, the tip of the 2D sector is displayed on top of the screen and left-sided cardiac structures appear on the right side of the display. However, there are exceptions in certain circumstances, such as in pediatric echocardiograms where the tip of the 2D sector is displayed at the bottom of the screen for certain views.

Most centers retain the tip at the top format for TEE studies as well, but other centers (such as the Mayo Clinic) prefer flipping the TEE images sector tip down in order to reproduce the 2D cardiac views that are anatomically comparable to those obtained from transthoracic surface imaging. In this chapter, the more widespread sector tip on top image display orientation will be utilized for clarity and consistency. Furthermore, the American Society of Echocardiography (ASE) and the Society of Cardiovascular Anesthesiologists (SCA) recommend the tip of the 2D sector up with left cardiac structures on the right of the screen orientation as depicted in Fig. 4.2. They also recommend the acquisition of 20 cross-sectional views for a comprehensive TEE examination (Fig. 4.3) (3).

3. Views and Structures

A comprehensive multiplane TEE examination consists of acquiring 2D images and Doppler data by the systematic and skillful manipulation of the multiplane transducer through a series of positions in the patient's esophagus and stomach (3). The operator should proceed systematically, progressing from views obtained with the transducer tip in the mid to gradually more distal esophagus, fundus of the stomach after gentle advancement across the cardia, and finally slow withdrawal of the probe while a complete scan of the thoracic aorta is obtained from high esophageal views. A systematic approach avoids excessive to and fro movement of the probe and reduces patient discomfort while ensuring that all cardiovascular structures are appropriately and consistently evaluated. A complete TEE exam usually takes 15–20 min in a nonteaching environment. An abbreviated, or problem-focused, TEE study may occasionally be appropriate in unstable or uncooperative patients where the operator feels that there might not be sufficient time to obtain all possible views.

- Mid-esophageal level
- Basal heart multiplane views (0°, 45°, 90°, 135°, and 180°) [Figs. 4.3(a–c) and (g–i)].

The TEE exam usually begins with the insertion of the transducer tip into the mid-esophageal position and

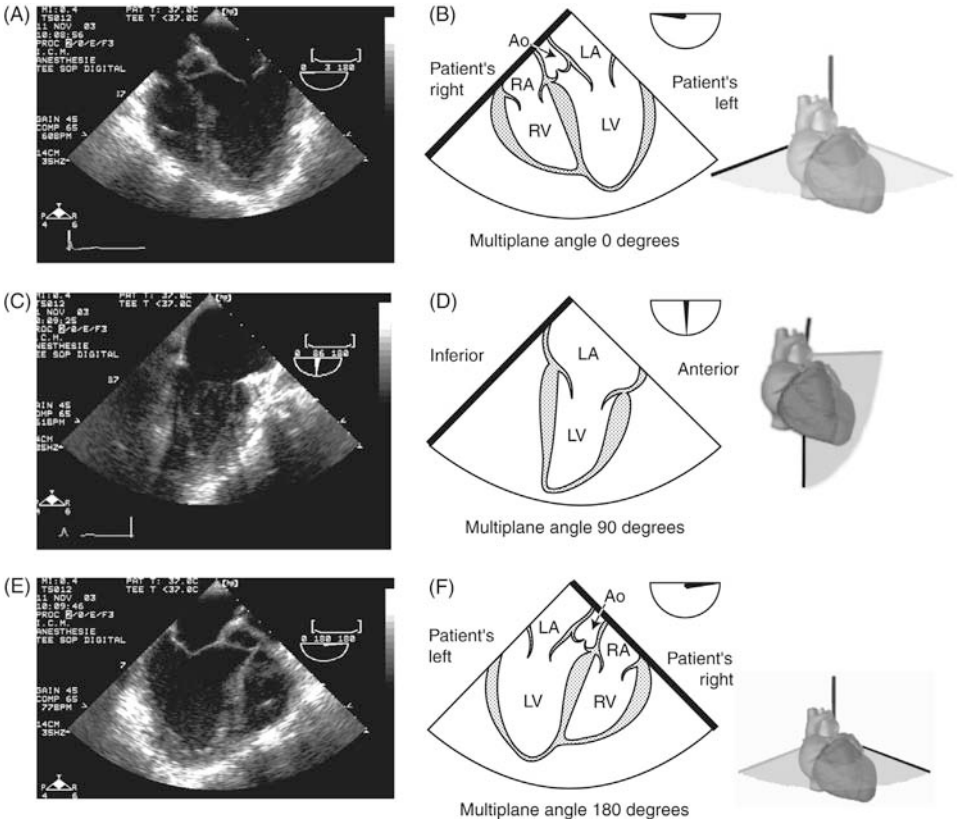

Figure 4.2 Display convention of transesophageal echocardiographic images. Mid-esophageal 0° (A, B), 90° (C, D), and 180° view (E, F) (Ao, aorta; LA, left atrium; LV, left ventricle; RA, right atrium; RV, right ventricle).

oriented anteriorly. From this position, at 0° orientation, multiple basal cardiac structures are visualized.

Tip 1: The operator should make fine adjustments in probe tip insertion, rotation, and anteflexion to position the probe in the middle of the left atrium, where optimal esophageal mucosal apposition with minimal interfering tissues will usually provide the best image quality. This is easier as the left atrium is large, and is inversely more difficult to do in young normal patients because of a small left atrial window. This is a good time for the operator to adjust the image depth as well as gain settings on the echo system. These are likely to remain the same until imaging of the descending aorta is performed at a shallower depth just prior to study completion.

The study then proceeds with examination of the mitral valve apparatus [0–135° sweep in 2D to assess structure and mobility of leaflets, then 135° back sweep to 0° with color flow Doppler to detect and characterize mitral regurgitation (MR)]. Digital clips are acquired repeatedly throughout this process. The objective is to evaluate both the severity and mechanism of MR, providing, for example, the information needed to determine if the valve is surgically repairable (see Chapter 17 for further details).

Tip 2: The operator should keep in mind certain key points during the mitral valve sweep where specific scallops or parts of the mitral leaflets are best seen (see following text). Clips should be taken at these points in order to enable precise assessment of the mechanism of a significant MR and help predict the success of repair.

The left atrial appendage (LAA) is imaged next with an initial orientation of 0–45° and slight leftward (counter clockwise) rotation (Fig. 4.4). The best orientation is the one that is aligned with the LAA long axis with clear visualization of the LAA inlet from the left atrium (LA). This varies from patient to patient and to optimize requires some fine probe adjustments.

Tip 3: Bilobed and multilobed cauliflower-like LAA are common, together with prominent pectinate muscle trabeculae, and these may reduce the accuracy of TEE for detecting or excluding a thrombus, unless the operator takes additional orthogonal views of the LAA at 90° up to 135° (Fig. 4.5) (4). Also, spontaneous echo contrast within the LAA may be associated with an increased risk of embolic phenomena. This can be more or less prominent depending on gain settings and the imaging frequency used. Considerable operator experience is,

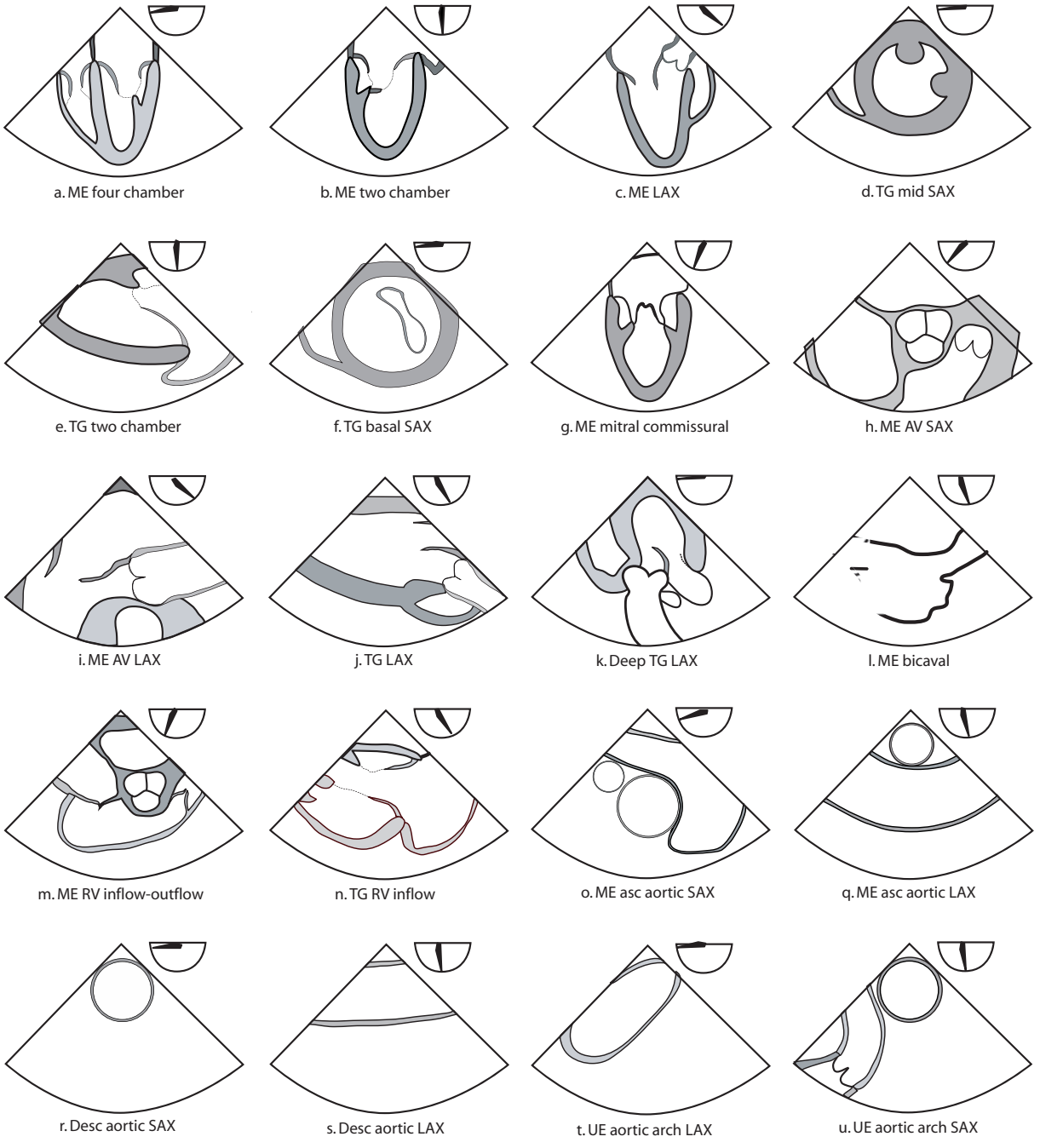

Figure 4.3 Recommended views for performing a comprehensive transesophageal echocardiographic exam (Asc, ascending; AV, aortic valve; Desc, descending; LAX, long axis; ME, mid-esophageal; RV, right ventricle; SAX, short axis; TG, transgastric; UE, upper esophageal). [With permission of Shanewise et al. (3).]

therefore, required in order to ensure a reliable assessment of the LAA.

Next, attention focuses on the aortic valve (AoV) along with the left ventricular outflow tract (LVOT) and proximal ascending aorta. At 0° with either slight probe withdrawal or anteflexion, a long axis view of the LVOT and AoV is obtained (Fig. 4.6). This can also be obtained from a four-chamber view at 0° while withdrawing the probe to a higher esophageal position (as the AoV is a superior structure in the heart anatomy), but care must then be taken to avoid leaving the optimal left transatrial imaging window. The orientation is gradually changed

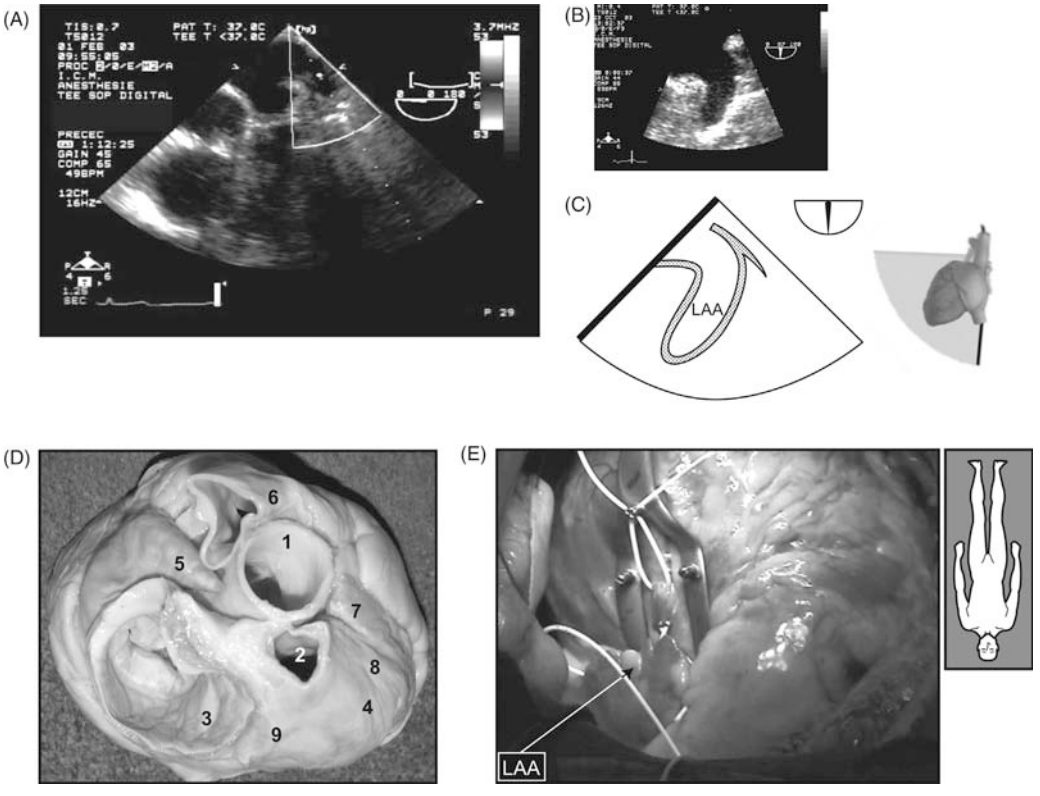

Figure 4.4 (A–C) Mid-esophageal view of the left atrial appendage (LAA). (D) Anatomically the LAA is anterolateral to the left atrium and close to the left upper pulmonary vein. (E) Intraoperative view of the LAA during off-pump bypass (1, aorta; 2, superior vena cava; 3, left atrium; 4, right atrium; 5, left atrial appendage; 6, pulmonary trunk; 7, right atrial appendage; 8, sulcus terminalis; 9, Waterston's groove). (Photo E courtesy of Dr. Raymond Cartier.)

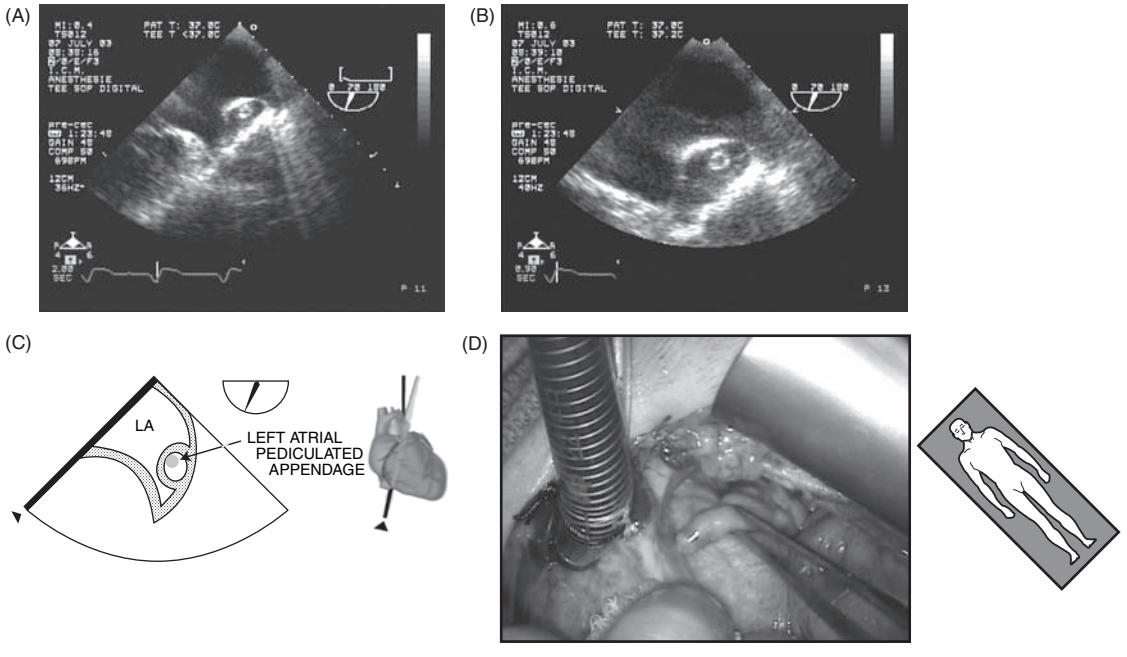

Figure 4.5 (A–C) Mid-esophageal two-chamber view of the left atrium (LA) in a 71-year-old woman scheduled for coronary revascularisation, aortic and mitral valve replacement. A mobile mass is seen close to the atrial appendage. (D) This mass represents the tip of a multilobe atrial appendage. (Photo D courtesy of Dr. Michel Pellerin.)

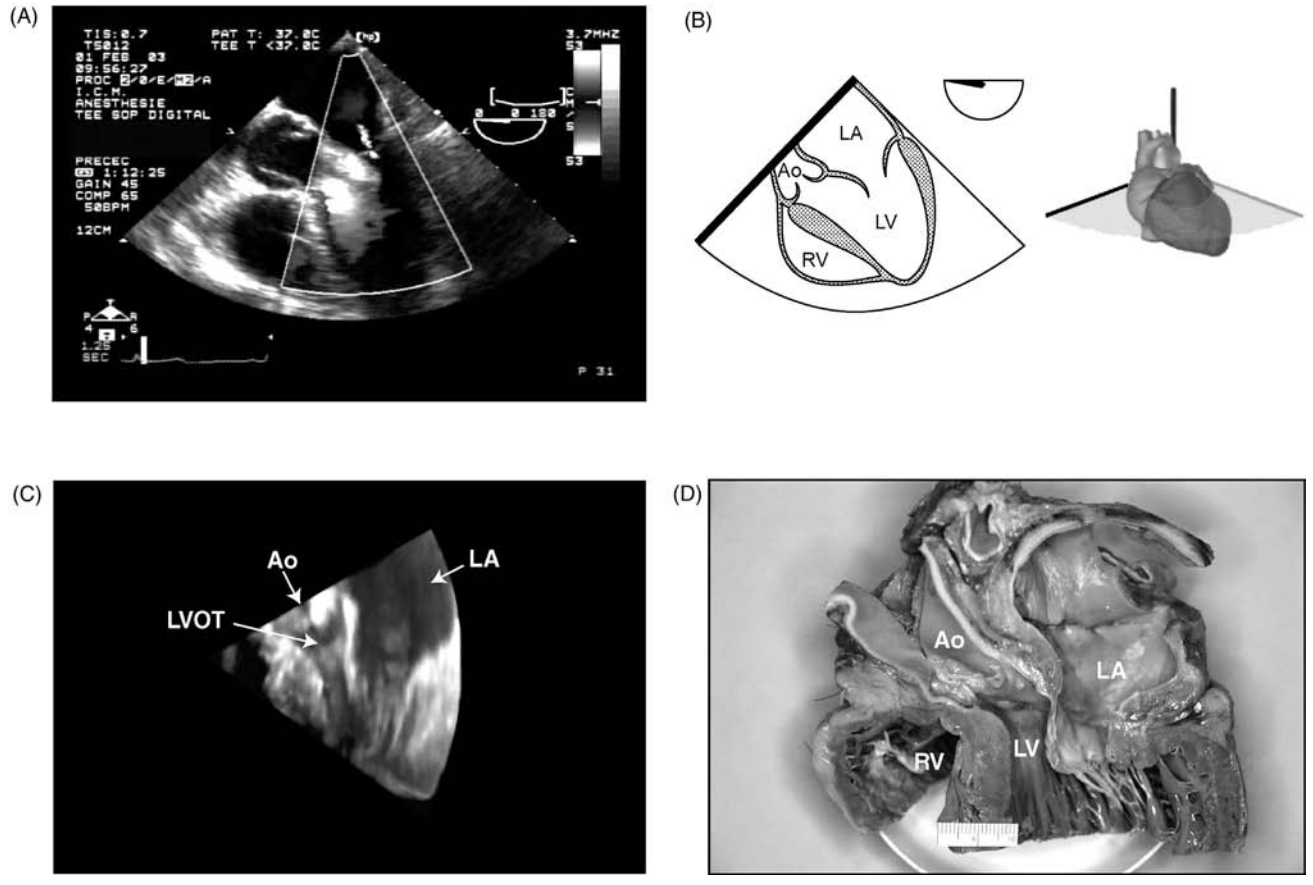

Figure 4.6 (A, B) Mid-esophageal long-axis view of the left ventricle (LV). (C) Three-dimensional echocardiogram. (D) Anatomical correlation (Ao, aorta; LA, left atrium; LVOT, left ventricular outflow tract; RV, right ventricle).

from 0° to 135° to obtain a comprehensive assessment of the AoV cusps and exclude aortic regurgitation (AR). An important orientation plane is at about 45° (±15°) when the imaging sector is most parallel to the AoV ring and there is optimal visualization of all three AoV cusps (Fig. 4.3h). Another is at 90° when, with slight leftward rotation, the imaging plane is parallel to the ascending aorta. It is this view which is most useful in excluding ascending aortic aneurysm as well as type A dissection (Fig. 4.3q). However, it is important to remember that a small portion of the distal ascending aorta is never well visualized by TEE due to interposition of the air-containing trachea and left mainstem bronchus. Finally, the view at approximatively 135°, which corresponds to the transthoracic left parasternal long-axis view, is important to get the best measurements of the LVOT diameter (Fig. 4.3i).

Tip 4: The aortic cusp facing the interatrial septum is always the noncoronary cusp, and the one that is anterior is always the right coronary cusp in the absence of major congenital heart disease. This principle assists with aortic cusp identification independent of the imaging modality [transthoracic echocardiography (TTE) or TEE] being used.

4. Four-Chamber View (0–20°, Retroflexion)

This view depicts the left and right ventricles, left and right atria, atrial septum and mitral and tricuspid valves (Figs. 4.3a and 4.7). However, the true apex of the left ventricle (LV) is often not optimally seen due to foreshortening. This can be corrected by more retroflexion, but loss of esophageal mucosal contact and image degradation is usually the limiting factor.

5. Transgastric Views (0°, 90°, and 135°)

The probe is advanced from the mid-esophageal position through the lower esophageal sphincter into the stomach. At 0° with anteflexion of the probe tip and gentle advancement or withdrawal, a short-axis view of the LV at papillary muscle level can be obtained (Figs. 4.3d and 4.8). From this position, withdrawal or anteflexion of the probe tip often allows a short-axis view of the mitral valve (Fig. 4.3f), while

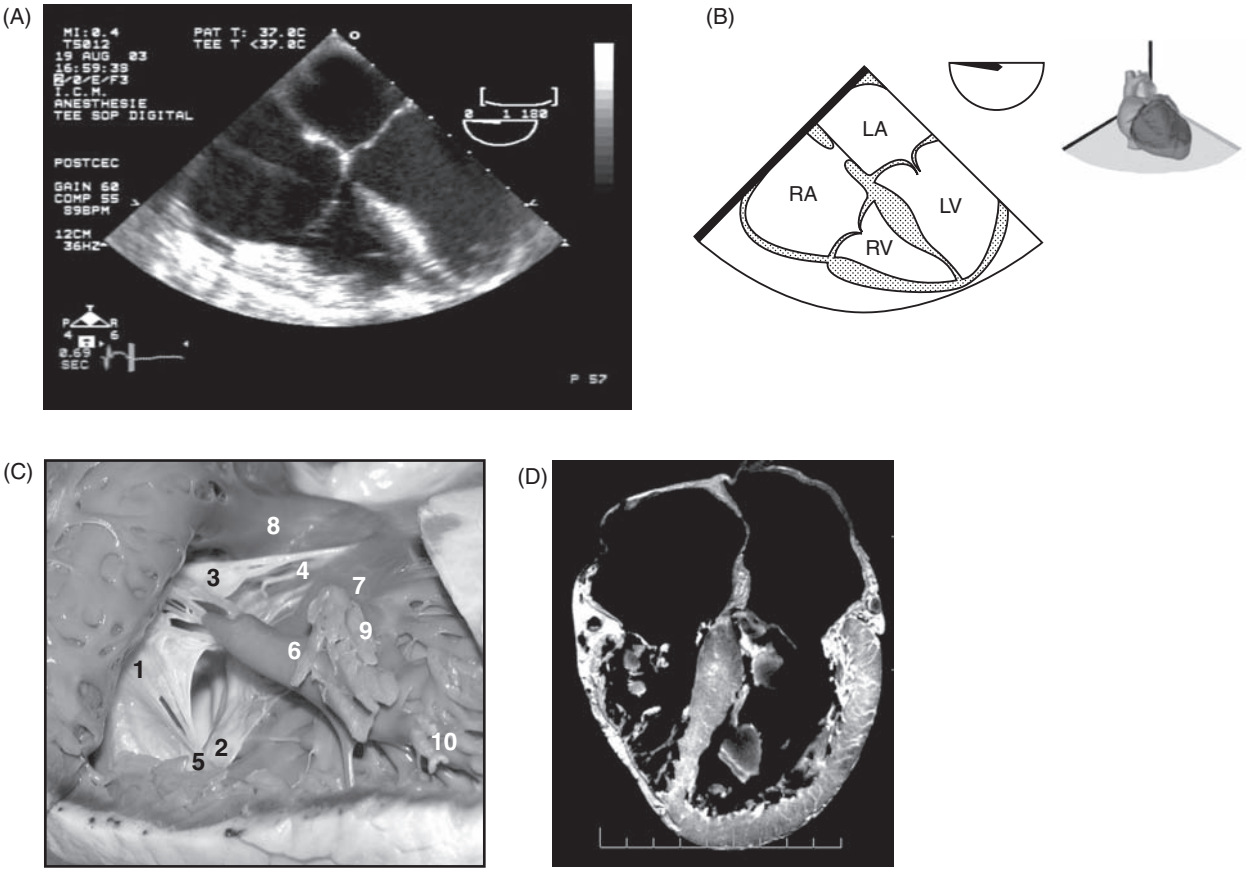

Figure 4.7 (A, B) Mid-esophageal four-chamber view of the right ventricle (RV). (C) Anatomical correlation. (D) Magnetic resonance imaging (LA, left atrium; LV, left ventricle; RA, right atrium) (1, anterior leaflet of tricuspid valve; 2, posterior leaflet of tricuspid valve; 3, septal leaflet of tricuspid valve; 4, medial papillary muscle; 5, inferior papillary muscle; 6, anterior papillary muscle; 7, trabecula septomarginalis; 8, crista supraventricularis; 9, moderator band; 10, trabecular zone).

further insertion or retroflexion of the probe tip will allow evaluation of the LV apex.

From the 0° short-axis view of the LV, rotation of the electronic plane to 90° provides a longitudinal two-chamber view of the LV (Figs. 4.3e and 4.9). Rightward (clockwise) rotation from this position results in a two-chamber view of the RA and ventricle together with the tricuspid valve (TV) (Figs. 4.3n and 4.10).

From the two-chamber view of the LA and LV at 90°, further transducer rotation to 100–135° may yield a long-axis view of the LV and LVOT (Fig. 4.3j). From this position, parallel cursor alignment with the AoV outflow allows for CW Doppler measurement of maximal flow velocity across the AoV and PW Doppler measurement of LVOT time–velocity integral (TVI) for the assessment of cardiac output by volumetric Doppler method.

6. *Thoracic Aorta Views (0°, 90°)*

Gradual withdrawal of the TEE probe from the transgastric position allows for visualization of the descending thoracic aorta and aortic arch. With the transducer at 0°, the operator begins by probe withdrawal to the level of the cardia, and rotation of the probe tip counterclockwise about 180° visualizes the descending thoracic aorta in a transverse view as a circular dark (blood filled) structure in the near field. The entire length of the descending thoracic aorta is then imaged with gradual pullback and slight clockwise rotation, keeping the aorta centered on the screen. The operator may switch between transverse (0°) (Fig. 4.3r) and longitudinal (90°) (Fig. 4.3s) views at different depths to better visualize any pathology identified. The position of identified abnormalities is recorded in centimeters from the patient's incisors by reading the distance off the scale on the probe. During pullback, color flow Doppler imaging can assist in differentiating artifactual from true anatomical echo densities in the aortic lumen as well as depicting the site of (re)entry and true and false lumens of a dissected aorta.

When the probe tip withdrawal reaches the level of the aortic arch, pullback is stopped while simultaneous clockwise rotation provides a longitudinal view of the arch and

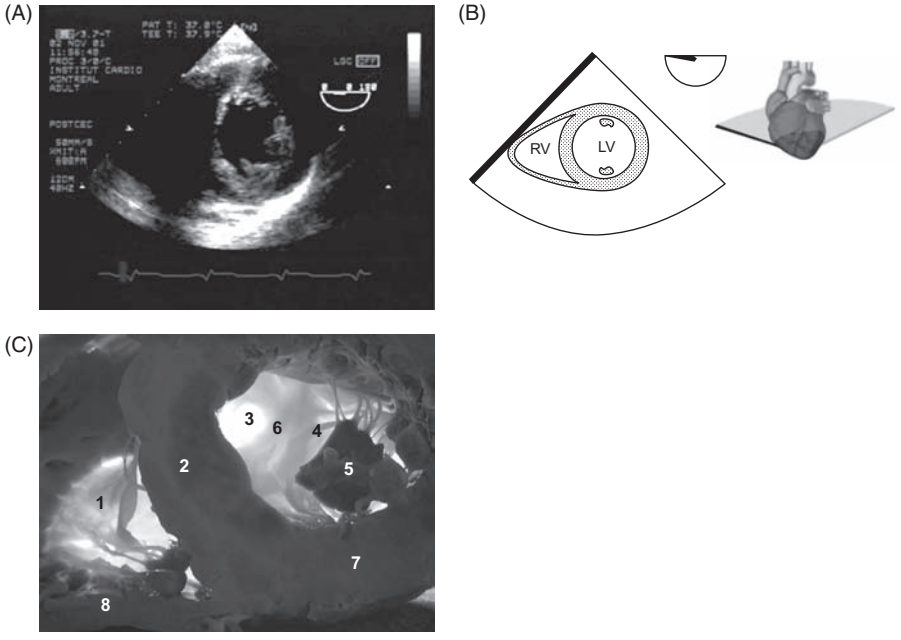

Figure 4.8 (A, B) Transgastric mid-papillary echocardiographic view of the left ventricle (LV). (C) Anatomical view (RV, right ventricle) (1, tricuspid valve; 2, ventricular septum; 3, aortic valve; 4, mitral valve; 5, papillary muscles; 6, mitral aortic continuity; 7, left ventricular wall; 8, right ventricular wall).

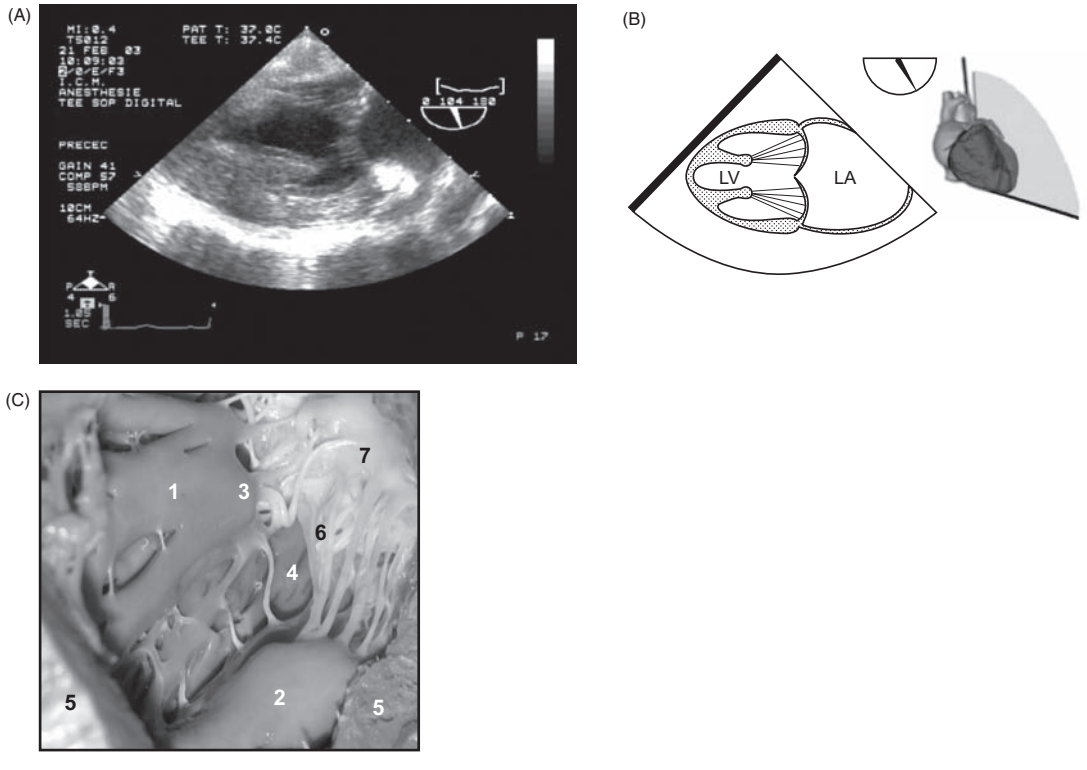

Figure 4.9 (A, B) Transgastric view at 90° of the left ventricle (LV). (C) Anatomical correlation (LA, left atrium) (1, posteromedial papillary muscle; 2, anterolateral papillary muscle; 3, chordae; 4, subvalvular apparatus; 5, left ventricular wall; 6, posterior leaflet; 7, anterior leaflet).

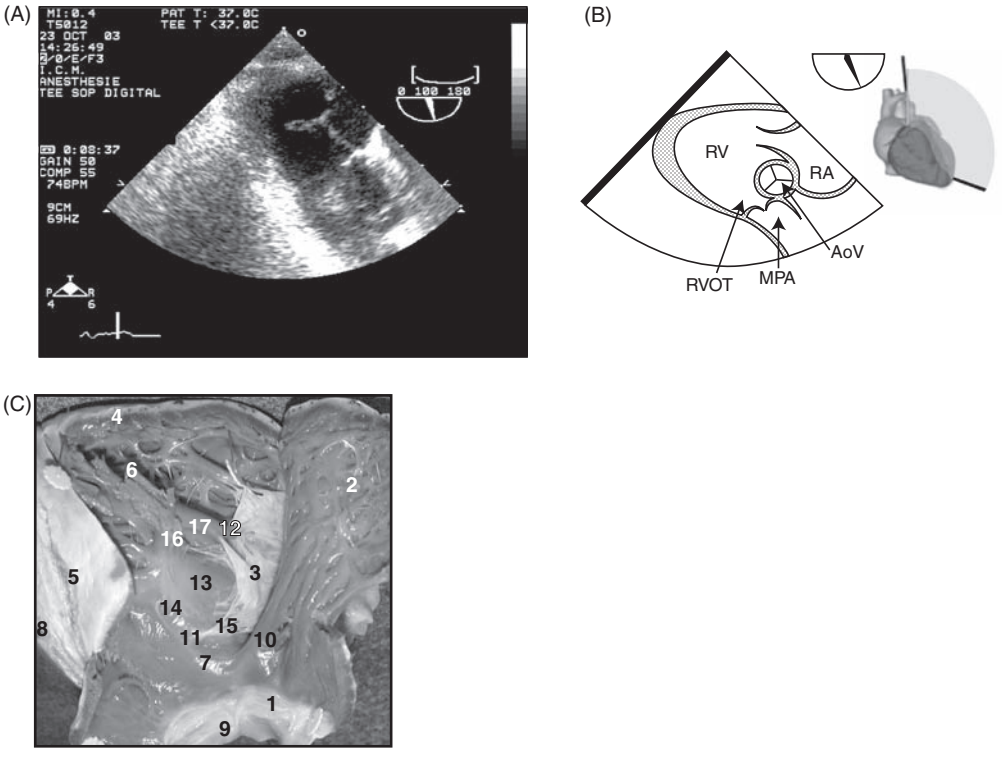

Figure 4.10 (A, B) Transgastric view at 110° of the right ventricle (RV). (C) Anatomical correlation (AoV, aortic valve; MPA, main pulmonary artery; RA, right atrium; RVOT, right ventricular outflow tract) (1, pulmonary annulus; 2, right ventricular anterior wall; 3, tricuspid valve; 4, epicardial fat with vessels; 5, interventricular sulcus or anterior interventricular groove; 6, trabecular zone; 7, anterior limb of trabecula septomarginalis (TSM); 8, left ventricle; 9, pulmonic valve; 10, crista supraventricularis; 11, outlet component or infundibulum; 12, inlet component; 13, posterior limb of TSM; 14, body of TSM; 15, medial papillary muscle;16, moderator band; 17, anterior papillary muscle).

(Fig. 4.3t) further rotation reveals the distal ascending aorta.

Tip: During imaging of the aorta, the operator should optimize depth and gain settings to allow the aorta to fill about two-thirds of the imaging sector. Sometimes, all the walls of the aorta may not be viewed at the same time on the sector scan, and therefore some left and right rotation may be necessary during the pullback to completely assess all the walls of the aorta.

B. Anatomy and Physiology

1. Cardiac Chambers

Left Ventricle

It is important to describe size, wall thickness, global and segmental systolic function. The maximal normal internal diameter is <60 mm in all views although no standardized measurements are used (unlike for TTE).

Transesophageal echocardiography allows analysis of contractility of all 16 segments of the LV in five views: three views from the mid-esophageal probe position (four-chamber, two-chamber, and long-axis views) and two views from the transgastric position (mid and basal short-axis views) (see Chapter 8). It is also important to keep in mind that the apical segments are frequently difficult to evaluate because of the foreshortening of the LV.

A visual assessment of global systolic function and ejection fraction should be possible from the different views of the LV used for segmental wall motion assessment.

Diastolic left ventricular function can be assessed from Doppler mitral inflow, mitral annulus tissue Doppler, left ventricular inflow color M-mode and pulmonary venous flow patterns (see Chapter 9).

Left Ventricular Outflow Tract

The LVOT is imaged from mid-esophageal position at 0° (Fig. 4.2[A]) and at 135° (Figs. 4.3i and 4.11), as well as from the deep transgastric view at 110° (Fig. 4.3j) that also allows the optimal ultrasound beam alignment for Doppler flow velocity measurement.

Right Ventricle (Inflow Chamber, Outflow Tract)

The RV has an inflow chamber and a right ventricular outflow tract (RVOT). The RVOT inflow chamber is

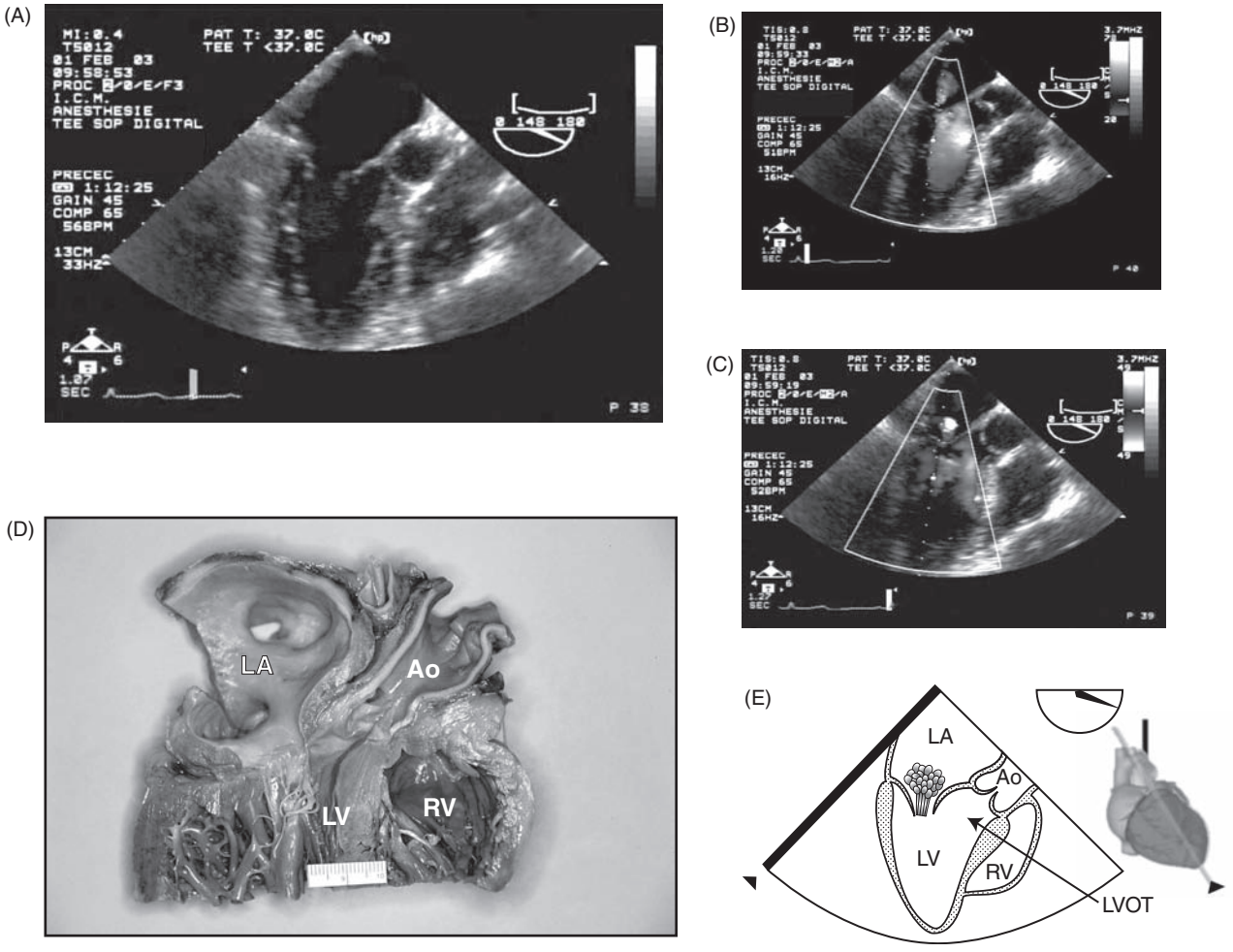

Figure 4.11 (A–E) Mid-esophageal long-axis view at 146°. (B, C) Color Doppler in the left ventricular outflow tract (LVOT). (D) Anatomical correlation (Ao, aorta; LA, left atrium; LV, left ventricle; RV, right ventricle).

imaged from the mid-esophageal position at 0° with slight retroflexion (four-chamber view) (Figs. 4.3a and 4.12) as well as from the transgastric position at 90° with rightward rotation (Fig. 4.10). Both inflow chamber and RVOT are seen simultaneously from the mid-esophageal position at 60–90° with slight rightward rotation (Figs. 4.3m and 4.13), or from a transgastric position at 60–90°. The RVOT, pulmonary valve, trunk and proximal right and left pulmonary arteries are viewed from the upper mid-esophageal position with anteflexion (Figs. 4.3o and 4.14).

Left Atrium

The LA, located anterior to the esophagus, can be easily imaged from all mid-esophageal views, including the four-chamber, the three-chamber, the two-chamber, the long-axis as well as the 0° short-axis and the 90° bicaval positions (Figs. 4.3–4.7).

Right Atrium

The RA is best visualized by TEE in the mid-esophageal four-chamber view at 0° with slight retroflexion (Figs. 4.3a and 4.12) and also in the 90° bicaval view (Figs. 4.3l and 4.15), and the RV inflow–outflow view at 45° (Figs. 4.3m and 4.13).

2. *Cardiac Septae*

Ventricular Septum

The ventricular septum is composed of a large muscular and a smaller membranous portion (Figs. 4.16 and 4.17). The trabecular muscular portion is easily assessed in the mid-esophageal four-chamber 0° (Fig. 4.16[A, B]) or long-axis 135° (three-chamber) views (Fig. 4.3c) and the transgastric long-axis view at 110° (Fig. 4.3j). The posteroapical muscular septum, where most of the postinfarct ventricular septal rupture occurs with sometimes a serpiginous course,

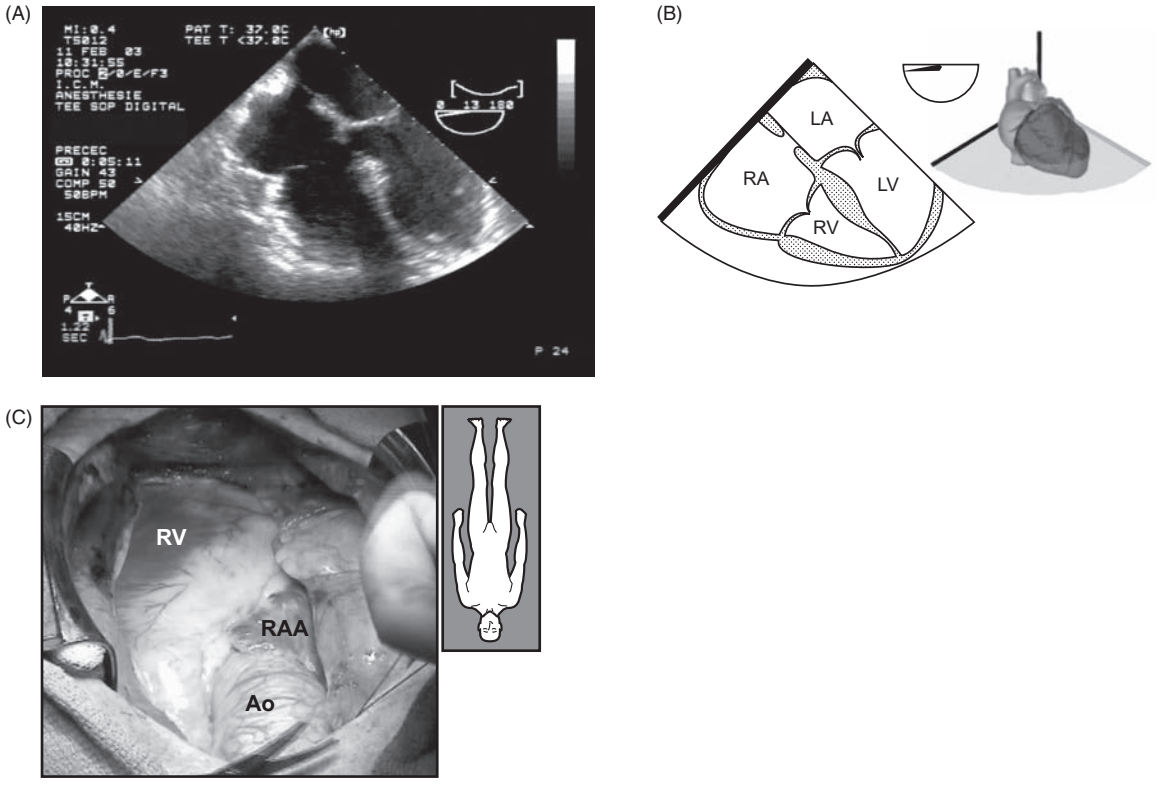

Figure 4.12 (A, B) Mid-esophageal echocardiographic view of the right ventricle (RV). (C) Intraoperative view (Ao, aorta; LA, left atrium; LV, left ventricle; RA, right atrium; RAA, right atrial appendage). (Photo C courtesy of Dr. Michel Pellerin.)

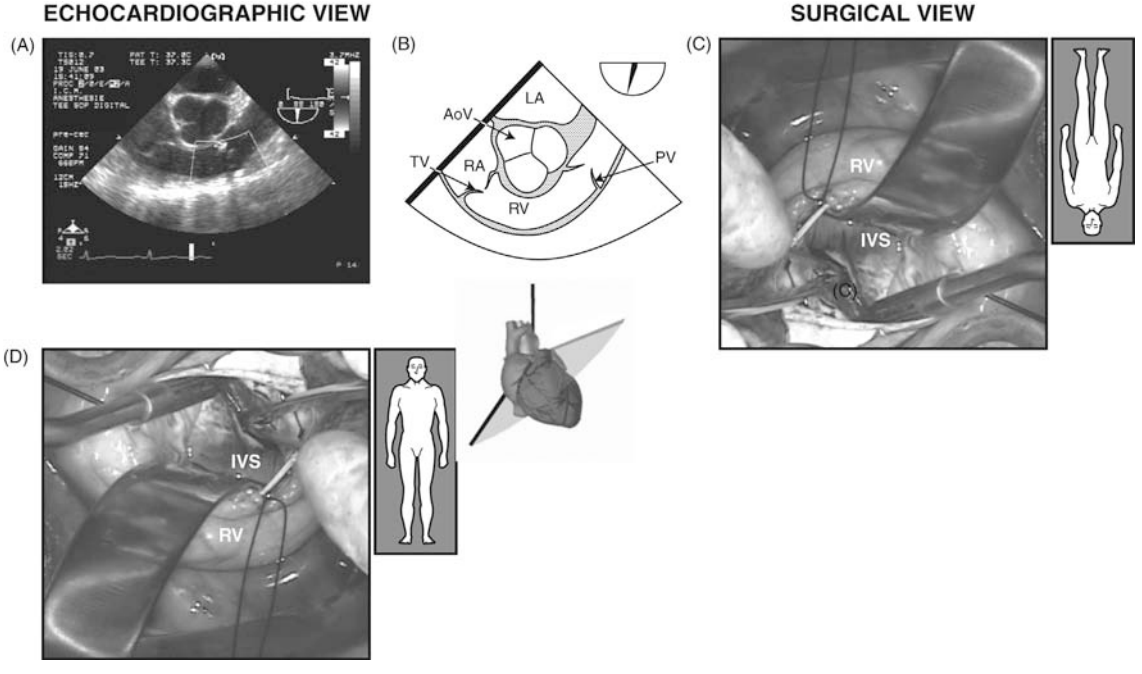

Figure 4.13 (A, B) Mid-esophageal short-axis view of the right ventricle (RV) and the right ventricular inflow and outflow tract. (C, D) The surgical view is repositioned to correlate better with the echocardiographic window in (D) (AoV, aortic valve; IVS, interventricular septum; LA, left atrium; PV, pulmonic valve; RA, right atrium; RV, right ventricle; TV, tricuspid valve). (Photo C courtesy of Dr. Nancy Poirier.)

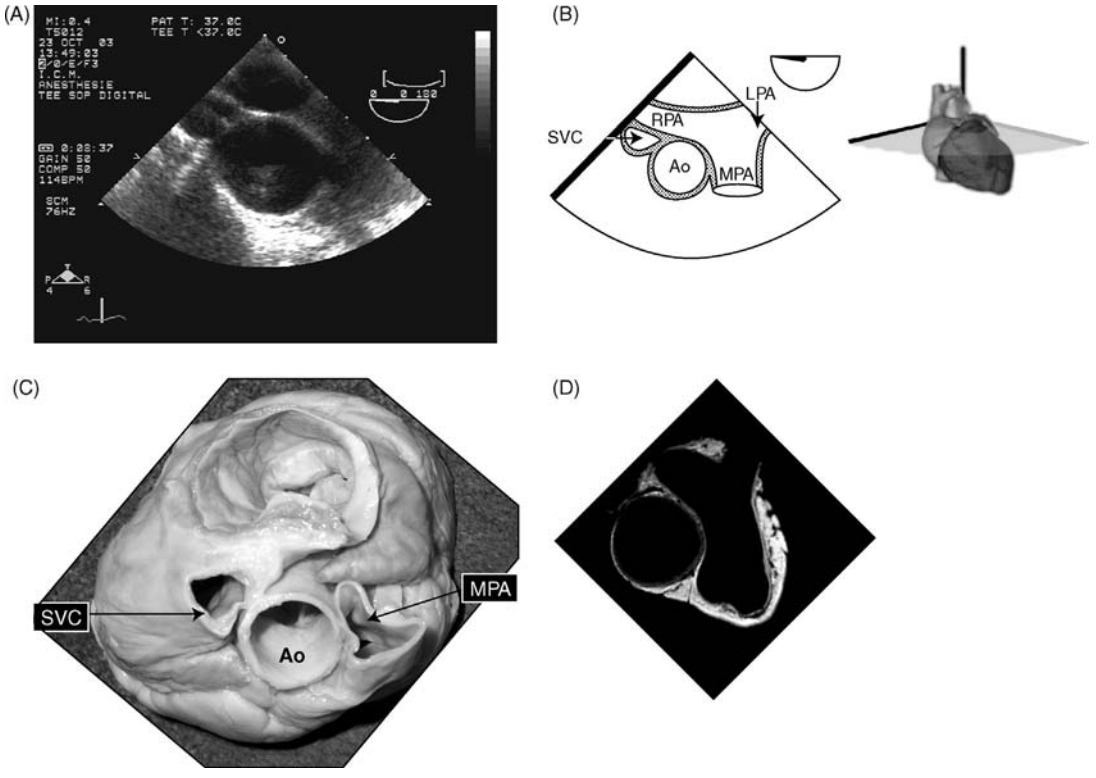

Figure 4.14 (A, B) Upper esophageal view at 0° of the great vessels. (C) Anatomical view. (D) Magnetic resonance imaging (Ao, aorta; LPA, left pulmonary artery; MPA, main pulmonary artery; RPA, right pulmonary artery; SVC, superior vena cava).

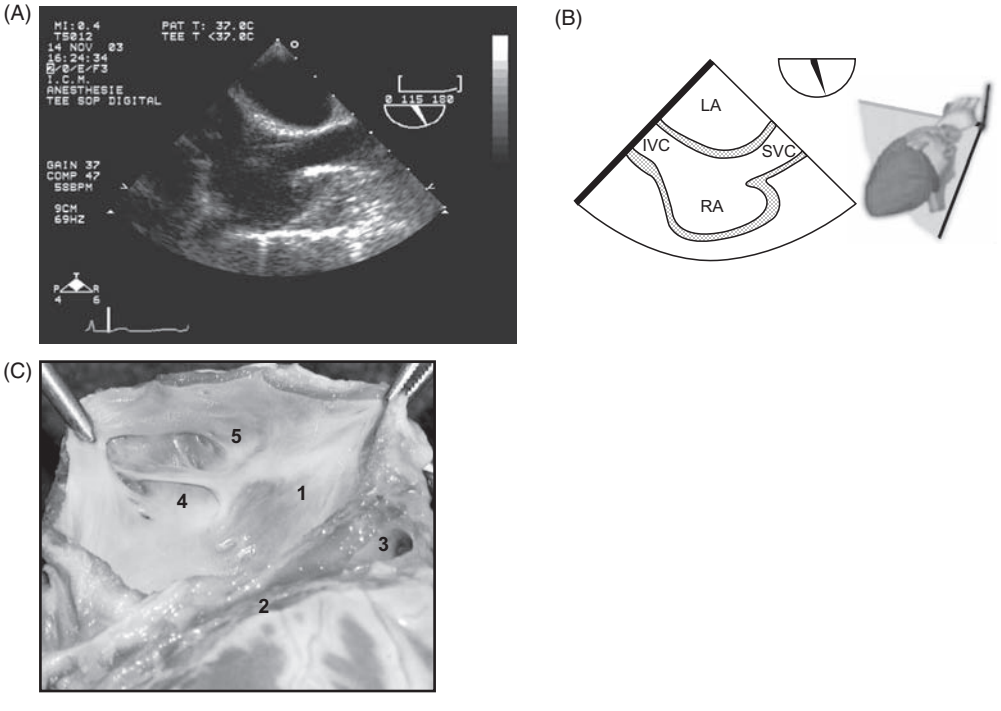

Figure 4.15 (A, B) Mid-esophageal bi-caval view in a 64-year-old man. (C) Anatomical aspect of the atrial septum viewed from the left atrium (LA) (IVC, inferior vena cava; LA, left atrium; RAA, right atrial appendage; SVC, superior vena cava) (1, left atrium; 2, atrioventricular groove; 3, coronary sinus; 4, foramen ovale; 5, rugose septum).

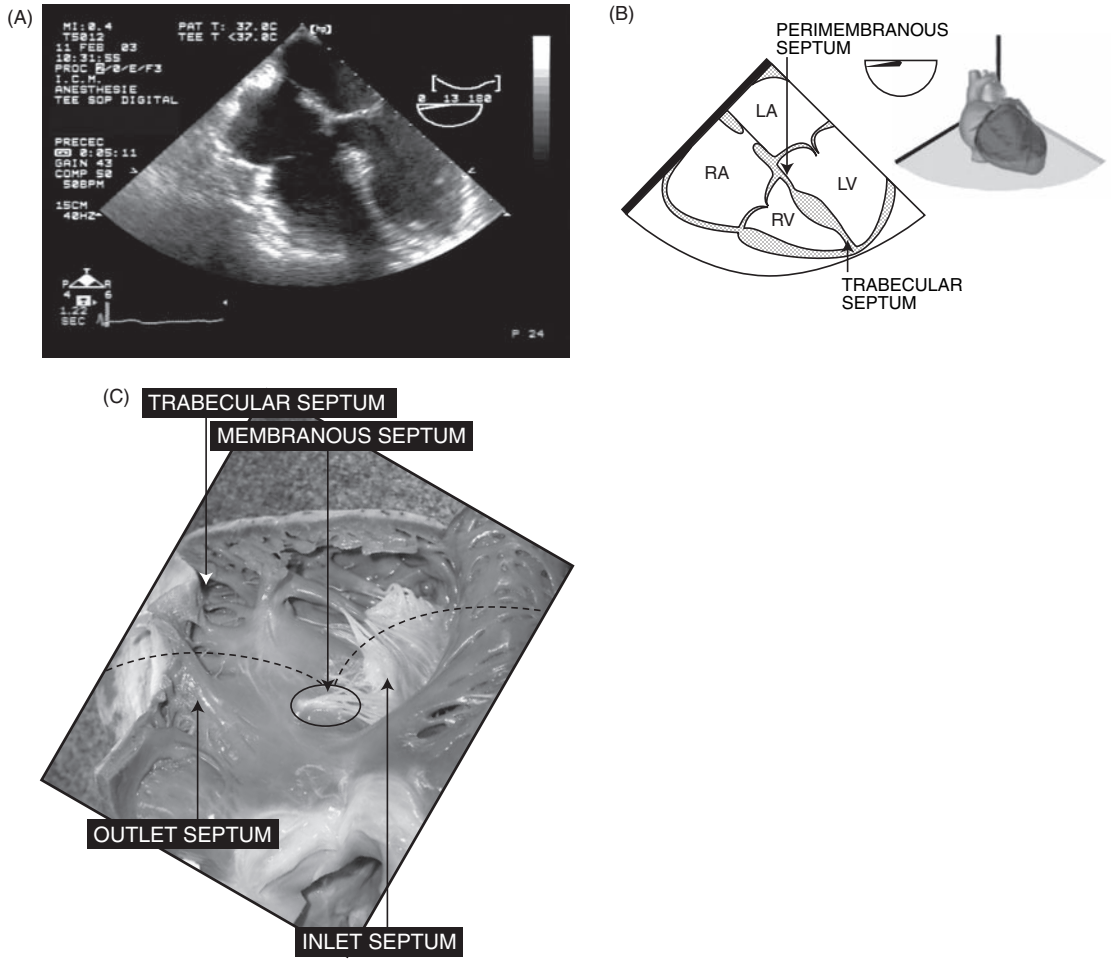

Figure 4.16 (A, B) Mid-esophageal four-chamber view at 130° of the ventricular septum. (C) Anatomical classification: the ventricular septum is divided into a membranous, trabecular, inlet and outlet portion (LA, left atrium; LV, left ventricle; RA, right atrium; RV, right ventricle).

can also be assessed through the deep transgastric short-axis views at 0° below the papillary muscle level.

The membranous septum is divided into an interventricular and an atrioventricular portion by the insertion of the tricuspid septal leaflet. The inlet portion beneath the TV is visualized in the mid-esophageal four-chamber view (Fig. 4.16[A, B]), as well as the transgastric short-axis view of the basal septum, both at 0°. The perimembranous

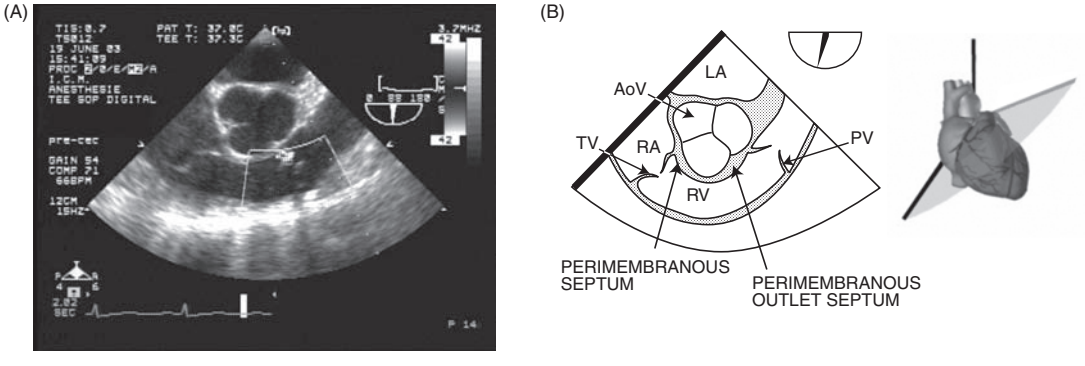

Figure 4.17 Examination of the ventricular septum through a mid-esophageal short-axis view at 88° (AoV, aortic valve; LA, left atrium; PV, pulmonic valve; RA, right atrium; RV, right ventricle; TV, tricuspid valve).

atrioventricular portion is evaluated through the upper mid-esophageal five-chamber view at 0° near the left ventricular outflow. It can also be assessed in the AoV short axis view at 45° near the base of the tricuspid septal leaflet (Fig. 4.17). The perimembranous outlet beneath the AoV is best evaluated through the mid-esophageal long-axis view at 135° or sometimes through the transgastric long-axis view at 110°.

Atrial Septum

The atrial septum consists of a thin central fossa ovalis with thicker limbus regions anteriorly and posteriorly, and is best viewed from the mid-esophageal probe position (Figs. 4.7 and 4.15).

The septum primum and the fossa ovalis are best seen in the four-chamber view at 0° (Fig. 4.7) with slight retroflexion. They can also be assessed in the vertical bicaval view at 90–100° with rightward (clockwise) rotation (Fig. 4.15). The latter view is also best for visualizing the superior portion of the atrial septum (Fig. 4.18) and excluding a sinus venosus atrial septal defect with the occasionally associated right anomalous pulmonary venous return (Fig. 4.18).

3. Cardiac Appendages

Left Atrial Appendage

See preceding text (Fig. 4.4).

Right Atrial Appendage

The right atrial appendage (RAA) is a broad-based outpouching of the RA (Fig. 4.19) seen in the far field by TEE in the 90–100° bicaval view of the atrial septum and RA as described earlier (Fig. 4.15).

4. Veins

Pulmonary Veins

The determination of normal pulmonary venous drainage is important in the assessment of congenital heart disease and two methods can be used to establish their normal connections to the LA consistently. The first method starts in the mid-esophageal AoV short-axis view at 45°—a central point in the heart. To image the left pulmonary veins, the probe will be rotated counterclockwise towards the left. Alternatively, to assess the right pulmonary veins, the probe will be rotated clockwise towards the right. To facilitate the visualization of both upper and lower pulmonary veins, the rotation plane usually needs to be increased to 60–80°.

With a slight rotation towards the left, the left upper pulmonary vein (LUPV) in its long axis can be found right next to the LAA from which it is separated by a linear echodensity terminated by a fold resembling a cotton tip, the limbus of the left upper pulmonary vein or "coumadin ridge" (Fig. 4.21).

Near the opening of the LUPV into the LA the orifice of the left lower pulmonary vein (LLPV) which will most often be viewed in its short axis and therefore not as easy to visualize as the LUPV. The LLPV is usually best viewed by advancing the TEE probe tip 1–2 cm from the plane in which the LUPV is best seen (Figs. 4.20 and 4.21). Occasionally, the LUPV and LLPV join each other prior to entering the LA as a single vessel in a "Y" shaped configuration on TEE (Fig. 4.20).

With a rotation towards the right from the AoV view, the right upper pulmonary vein (RUPV), like the LUPV, can be seen in its long axis entering the LA (Fig. 4.22).

The right lower pulmonary vein (RLPV), like the LLPV, enters the LA in a horizontal plane inferiorly to the RUPV and is often viewed in its short axis. It is best

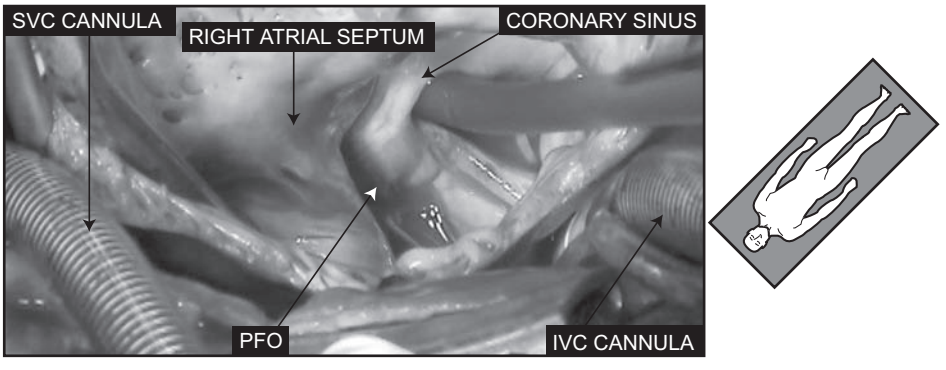

Figure 4.18 Right atrial surgical view of a 48-year-old man with sinus venosus and a patent foramen ovale (PFO). The inferior vena cava (IVC) and superior vena cava (SVC) cannulae are shown. Note the proximity of the PFO and the coronary sinus with its retrograde cannula. (Photo courtesy of Dr. Nancy Poirier.)

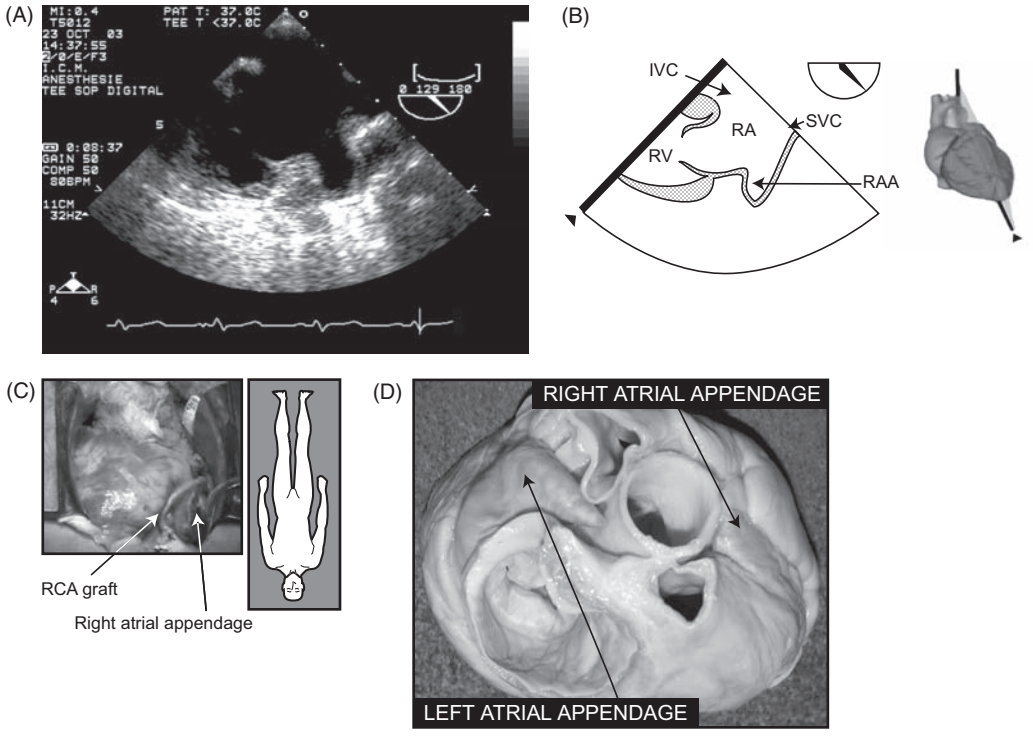

Figure 4.19 (A, B) Mid-esophageal long-axis view at 129° of the right atrium (RA) and right atrial appendage (RAA). (C) Intraoperative view of the RAA in a patient undergoing coronary revascularisation. (D) Anatomical location of both right and left atrial appendage (IVC, inferior vena cava; RCA, right coronary artery; RV, right ventricle; SVC, superior vena cava). (Photo C courtesy of Dr. Philippe Demers.)

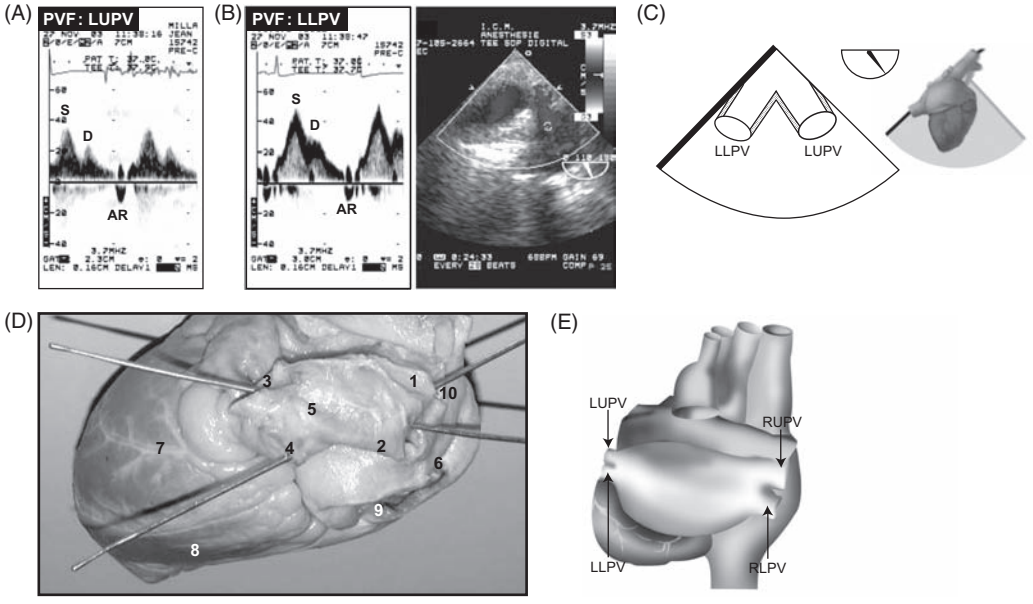

Figure 4.20 (A, B) Pulsed-wave Doppler interrogation of the left upper pulmonary vein (LUPV) in (A) and the left lower pulmonary vein (LLPV) in (B) from a mid-esophageal 110° view. The systolic (or S), diastolic (or D), and atrial reversal (AR) waves are shown. (D) Anatomical specimen. (E) Schematic representation of all four pulmonary veins (PVF, pulmonary venous flow; RUPV, right upper pulmonary vein; RLPV, right lower pulmonary vein) (1, right upper pulmonary vein; 2, right lower pulmonary vein; 3, left upper pulmonary vein; 4, left lower pulmonary vein; 5, left atrium; 6, right atrium; 7, left ventricle; 8, right ventricle; 9, inferior vena cava; 10, superior vena cava).

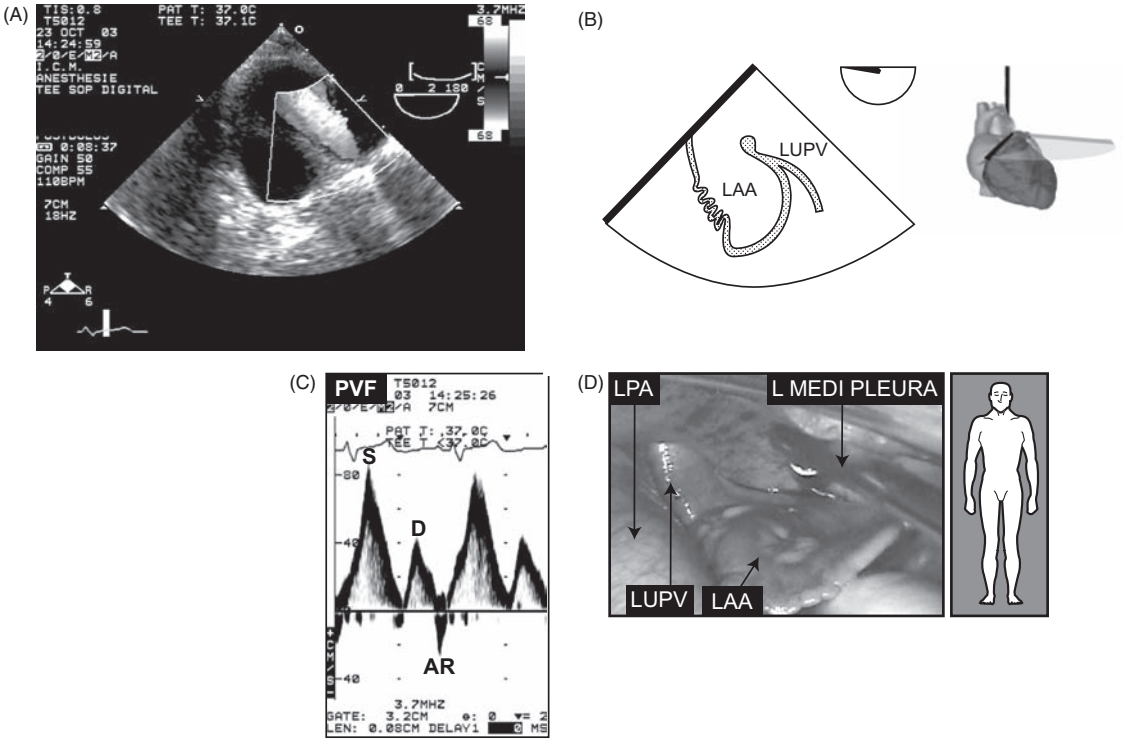

Figure 4.21 (A, B) Mid-esophageal view of the left upper pulmonary vein (LUPV) close to the left atrial appendage (LAA). (C) Pulsed-wave Doppler interrogation. The systolic (or S), diastolic (or D), and atrial reversal (AR) waves are shown. (D) Anatomical correlation (L MEDI, left medial; LPA, left pulmonary artery; PVF, pulmonary venous flow). (Photo D courtesy of Dr. Michel Pellerin.)

seen following optimal imaging of the RUPV by advancing the probe 1–2 cm and further rightward rotation (Fig. 4.23).

Occasionally, a right middle lobe pulmonary vein can be viewed entering the LA between the orifices of the RUPV and the RLPV.

The second method images the pulmonary veins at 0° in the transverse plane. All pulmonary veins should then be viewed in their longitudinal axis, which makes the recognition of the lower pulmonary veins easier than with the first method. Again, to image the left pulmonary veins, the probe will be rotated counterclockwise towards the left. Alternatively, to assess the right pulmonary veins, the probe will be rotated clockwise towards the right.

From a high esophageal position at the level of the short-axis view showing the superior vena cava (SVC), the aorta and the longitudinal view of the right pulmonary artery (RPA) (Fig. 4.14), the probe is rotated towards the right and slowly advanced. Near the junction of the SVC with the RA, the RUPV will be seen entering the LA. In the advent of an anomalous right upper venous connection, the RUPV would be seen entering the SVC instead, causing turbulent flow in the usually laminar SVC flow.

The RLPV can then be similarly visualized below the RUPV by advancing the probe at the same angulation. In this view, it may be easier to visualize than at 60–80° where it is seen in its short axis and therefore it is harder to track its course.

The LUPV is obtained starting from a high esophageal position at the level of the short-axis view SVC, the aorta and the longitudinal view of the RPA, but with the probe now rotated towards the left and slowly advanced. Again, the proximity of the LAA will help localize it (Fig. 4.21).

The LLPV is then visualized in its long axis by advancing the probe at the same angulation.

Superior and Inferior Vena Cavae

As mentioned, the SVC is visualized in its transverse view from the high esophageal position towards the right, posterior and to the right of the aorta (Fig. 4.14). This view is particularly helpful to see the intraluminal catheter or thrombus. The SVC (particularly its distal portion with its junction to the RA) can then be seen in its longitudinal axis in the mid-esophageal bicaval view at 90° (Fig. 4.15). A deep transgastric view can also be used to perform Doppler interrogation of the SVC (Fig. 4.24).

The distal inferior vena cava (IVC) is seen from the mid-esophageal bicaval view at 90° (Fig. 4.15). The rest

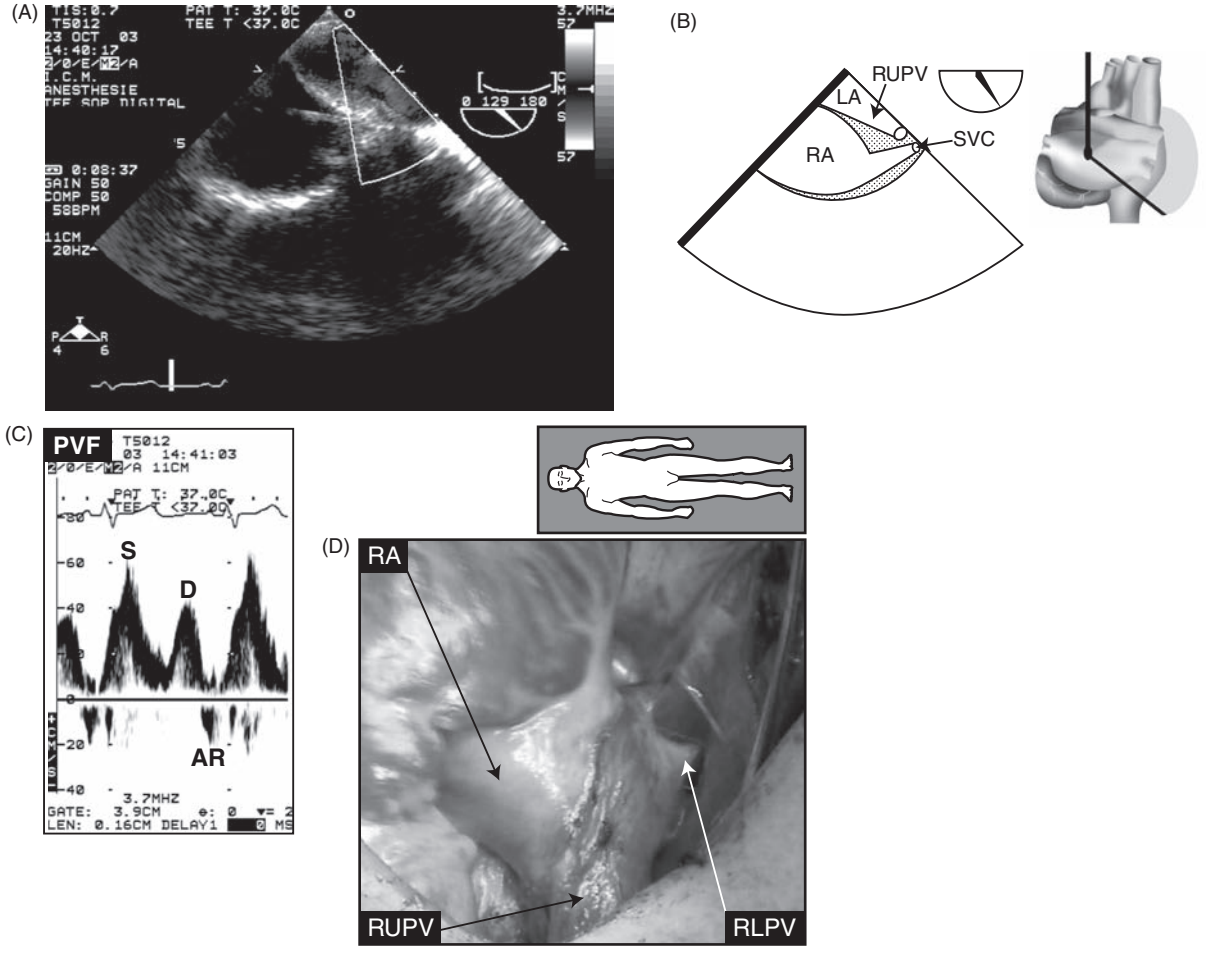

Figure 4.22 (A, B) Mid-esophageal view of the right upper pulmonary vein (RUPV) positioned behind the right atrium (RA) and close to the superior vena cava (SVC). (C) Pulsed-wave Doppler interrogation. The systolic (or S), diastolic (or D), and atrial reversal (AR) waves are shown. (D) Intraoperative view (LA, left atrium; PVF, pulmonary venous flow; RLPV, right lower pulmonary vein). (Photo D courtesy of Dr. Nancy Poirier.)

of the IVC can be assessed by advancing the probe to transgastric views, where its diameter can be assessed in response to respiratory variations. This view also provides an excellent Doppler interrogation angle of the hepatic veins as they merge with the IVC (Figs. 4.25 and 5.18).

Coronary Sinus

The coronary sinus runs in the posterior atrioventricular groove and empties into the RA at the inferoposterior aspect of the interatrial septum (IAS) near the attachment of the tricuspid septal leaflet (Fig. 4.18). The longitudinal image of the coronary sinus running lateral to medial behind the inferior aspect of the LA is obtained from the mid-esophageal four-chamber view with slight retroflexion of the probe tip (Fig. 4.26). A cross-sectional view of the coronary sinus appears in the lateral atrioventricular groove in the mid-esophageal two-chamber view at 90° (Fig. 4.26).

5. Arteries

Coronary Arteries

The coronary ostia and proximal coronary arteries can be seen from the mid-esophageal short-axis 45° view of the aortic annulus and aortic root. The left main coronary artery originates from the aortic root above the left coronary cusp and runs laterally toward the right side of the image sector (Fig. 4.27). Slight adjustment of probe tip depth and flexion together with color flow Doppler imaging is often needed to optimize its visualization. The left main bifurcation and proximal portions of the circumflex and left anterior descending (LAD) coronary artery can be seen in many patients. The left circumflex can sometimes be followed in the left atrioventricular groove with the coronary sinus. The right coronary artery (RCA) is more difficult to image with TEE. The RCA originates from the right coronary sinus and runs

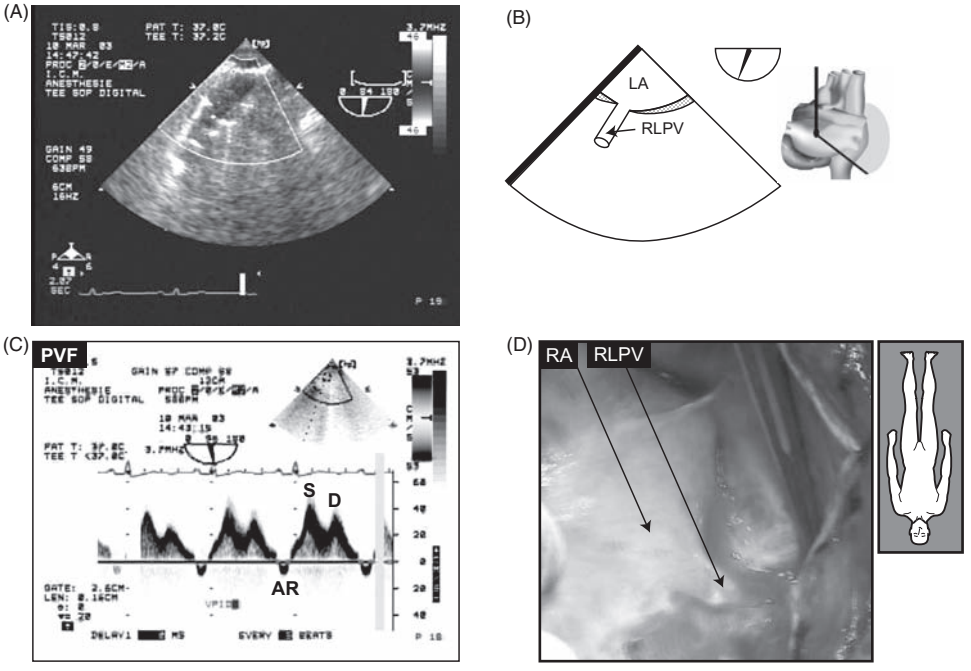

Figure 4.23 (A, B) Mid-esophageal view of the right lower pulmonary vein (RLPV). (C) Pulsed-wave Doppler interrogation. The systolic (or S), diastolic (or D), and atrial reversal (AR) waves are shown. (D) Intraoperative view (LA, left atrium; PVF, pulmonary venous flow; RA, right atrium). (Photo D courtesy of Dr. Nancy Poirier.)

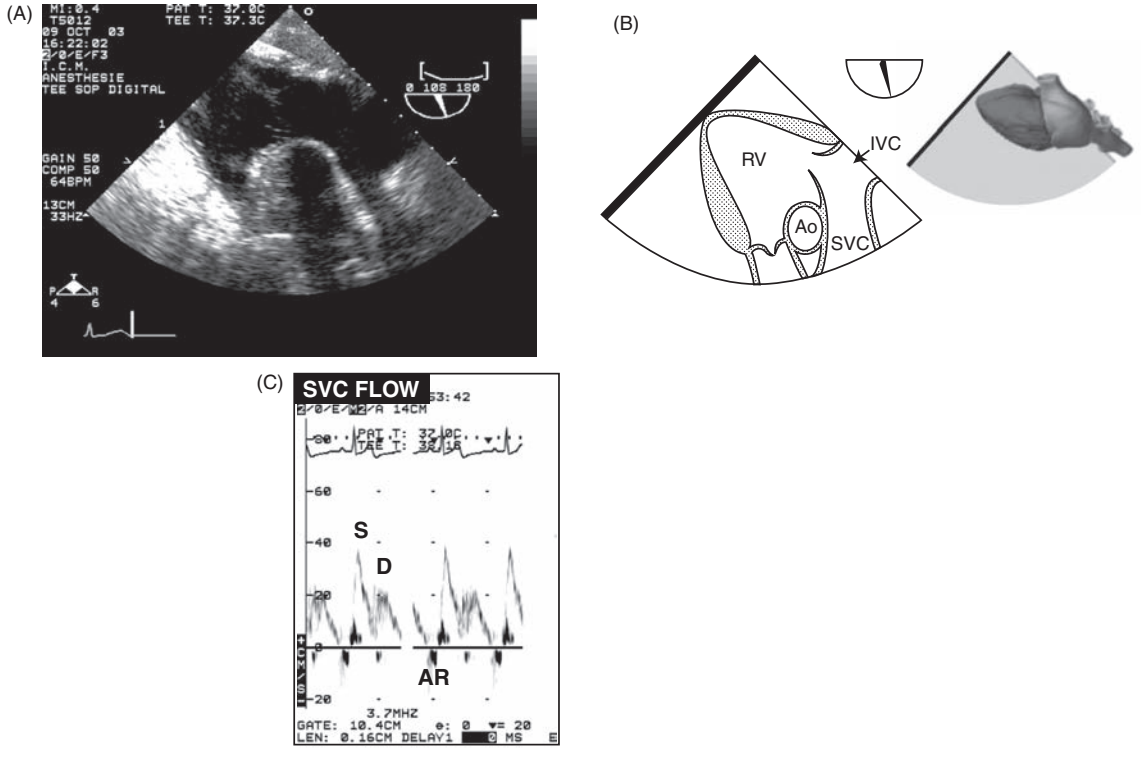

Figure 4.24 (A, B) Deep transgastric view of the superior vena cava (SVC). (C) Pulsed-wave Doppler interrogation. The systolic (S), diastolic (D), and atrial reversal (AR) waves are shown (Ao, aorta; IVC, inferior vena cava; RV, right ventricle).

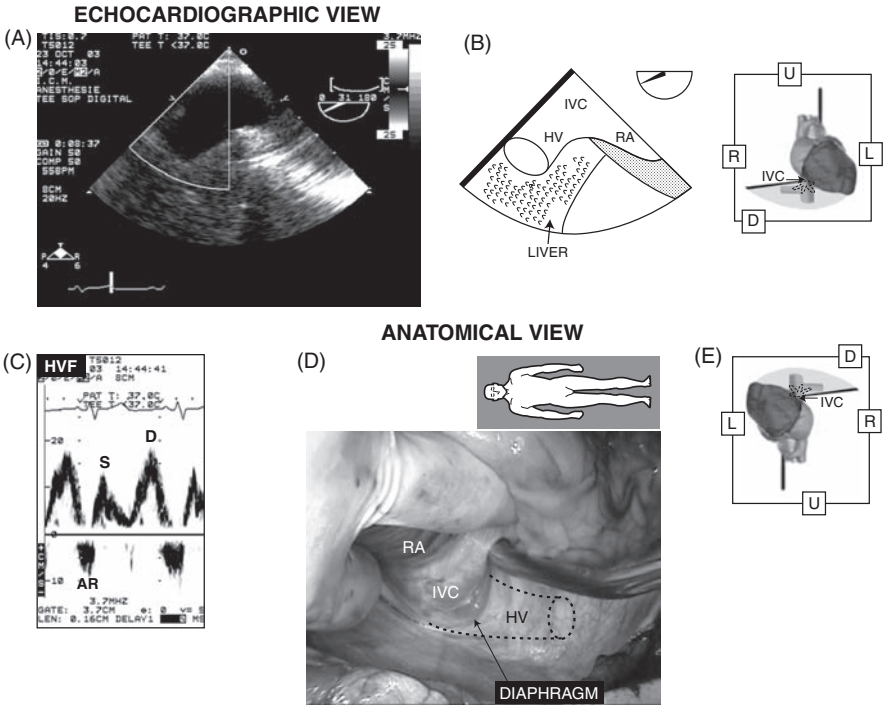

Figure 4.25 (A, B) Lower esophageal view of the inferior vena cava (IVC) and hepatic vein (HV). (C) Pulsed-wave Doppler interrogation of the HV. The systolic (or S), diastolic (or D), and atrial reversal (AR) waves are shown. Abnormal S/D ratio is present (<1). (D,E) Anatomical correlation and corresponding surgical positioning (D, down; HVF, hepatic venous flow; L, left; R, right; RA, right atrium; U, up). (Photo D courtesy of Dr. Michel Pellerin.)

anteriorly in the far field towards the bottom of the ultrasound sector away from the ultrasound probe tip. It is, therefore, rare to be able to see more than the first centimeter or two of the RCA by TEE (Fig. 4.28).

Tip: The noncoronary AoV cusp is always adjacent to the atrial septum and the right coronary cusp is always anterior in any ultrasound imaging view. The LAD coronary artery always runs anteriorly in any echo imaging view.

Aorta (Root, Sinotubular Junction, Ascending Aorta, Arch, Thoracic Descending Aorta)

Multiplane TEE allows a near complete visualization of the aorta from the aortic root to the upper abdominal aorta. Occasionally, the distal ascending aorta and proximal aortic arch may be masked by the interposition of the air-filled trachea and left mainstem bronchus between the esophagus and the aorta.

A short-axis view of the aortic root is seen from the mid-esophageal 45° (0–60°) short-axis position at about 30 cm from the incisors (Fig. 4.14). The rotation angle should be adjusted to optimize a circular view of the aortic ring and three AoV cusps (see AoV in the text that follows). Gentle probe withdrawal from this position and at 0° allows a short-axis view of the proximal ascending aorta.

The long axis view of the aortic root, sinuses of Valsalva, sinotubular junction, and proximal aorta (Fig. 4.29) are imaged by rotating the angle to 135° (100–150°) while the mid-ascending aorta (Fig. 4.30) is imaged often at a lower angle (100°) while withdrawing the probe. In this view, the anterior and posterior walls of the aorta are parallel to each other and perpendicular to the ultrasound beam allowing for precise measurement of aortic dimensions.

The distal aortic arch initially lies anterior to the esophagus and continues to the left to become the descending thoracic aorta. The latter then winds around from the left side to the posterior aspect of the esophagus at the level of the diaphragm (see Fig. 12.4). It is customary to image the descending and abdominal aorta from distal to proximal. From the lower-to-mid-esophageal four-chamber view at 0°, a slight quarter-turn towards the left will bring the lower descending thoracic aorta in view on its short axis (Fig. 4.31). While keeping the aorta in view, the probe tip is advanced gradually through the lower esophageal sphincter into the stomach until the abdominal aorta moves away from the stomach and is no longer clearly visible. The upper abdominal and descending thoracic aorta is imaged by slowly withdrawing the TEE probe from this most distal point to the level of the distal

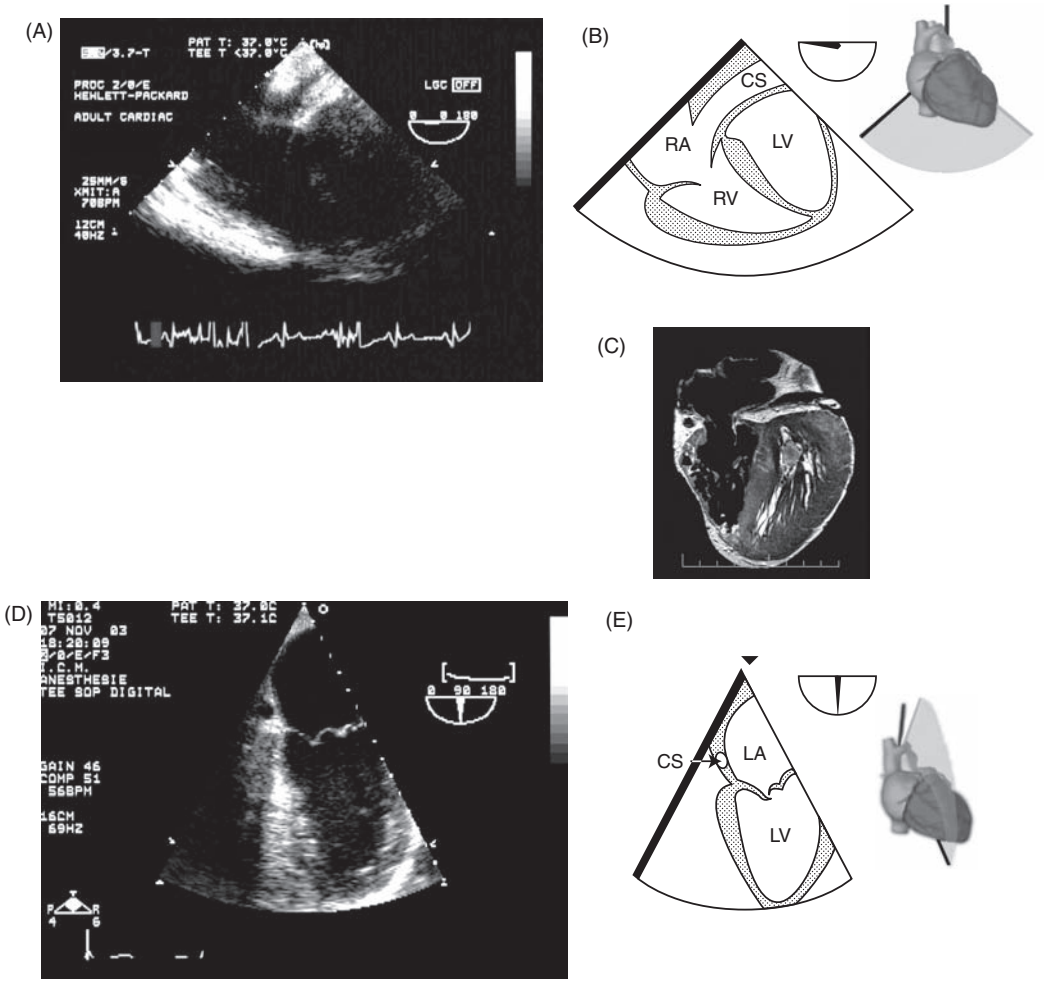

Figure 4.26 (A, B) Lower esophageal view of the right atrium (RA), right ventricle (RV), coronary sinus (CS), and left ventricle (LV). (C) Magnetic resonance correlation. (D, E) Mid-esophageal two-chamber view with the CS (LA, left atrium).

aortic arch (about 10–15 cm). The ultrasound sector is centered on the short-axis view of the aorta by gentle rightward (clockwise) rotation of the probe as it is withdrawn. A longitudinal view of the aorta can be obtained at any point if desired by changing the angle from 0° to 90° temporarily (Fig. 4.31).

Tip: The descending thoracic aorta lies immediately adjacent to the probe tip in the distal esophagus and

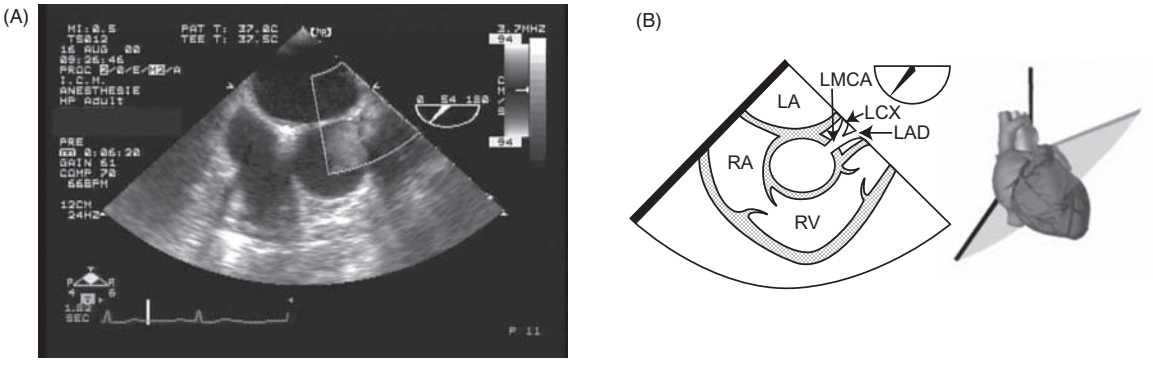

Figure 4.27 Upper esophageal short-axis view at 54° of the aorta and left main coronary artery (LMCA) (LA, left atrium; LAD, left anterior descending; LCX, left circumflex; RA, right atrium; RV, right ventricle).

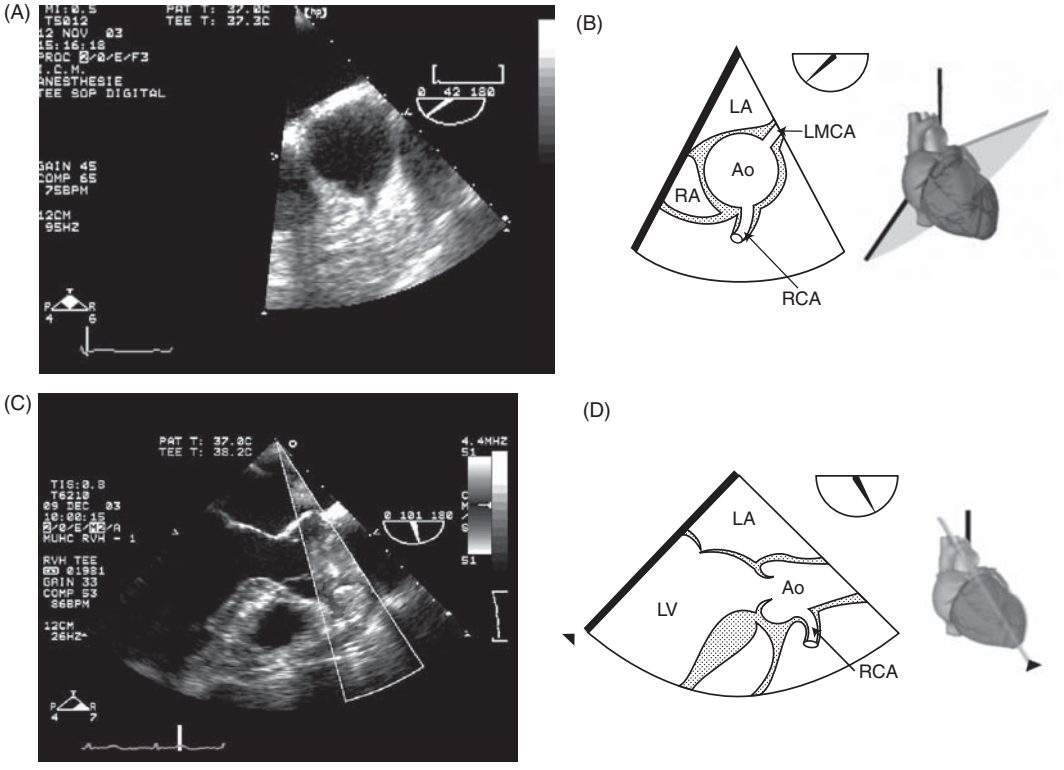

Figure 4.28 (A, B) Upper esophageal short-axis view of the aorta (Ao) and right coronary artery (RCA). (C, D) Long-axis view (LA, left atrium; LMCA, left main coronary artery; LV, left ventricle; RA, right atrium; RV, right ventricle).

appears in the near field of the ultrasound sector requiring several ultrasound system image adjustments for optimal visualization. Sector depth should be reduced to 6–8 cm, gain should be reduced and focus should be adjusted to the near field. Finally, air within the esophagus can reduce image quality if the ultrasound probe tip is not apposed to the wall of the esophagus. Proper probe tip apposition can be ensured through the maintenance of slight probe tip flexion. However, because the descending aorta can be tortuous, some alternance between slight anteflexion and retroflexion may occasionally be needed to ensure optimal image quality.

It is difficult to localize abnormalities anatomically within the descending thoracic aorta. The level of any abnormality is typically described in centimetres from the incisors (or sometimes from the left subclavian artery origin when seen). The location is further described relative to the probe tip in the esophagus (e.g. near-field, far-field, left side, or right side of the aorta at 30 cm).

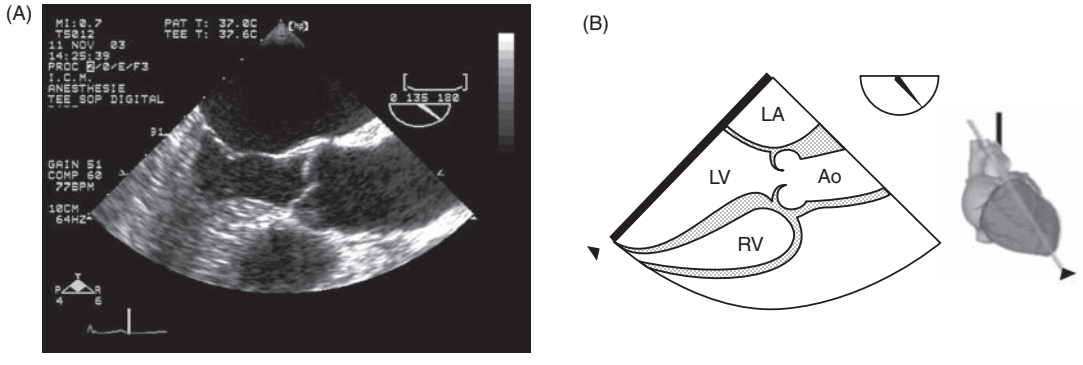

Figure 4.29 Mid-esophageal long-axis view at 135° of the ascending aorta (Ao) (LA, left atrium; LV, left ventricle; RV, right ventricle).

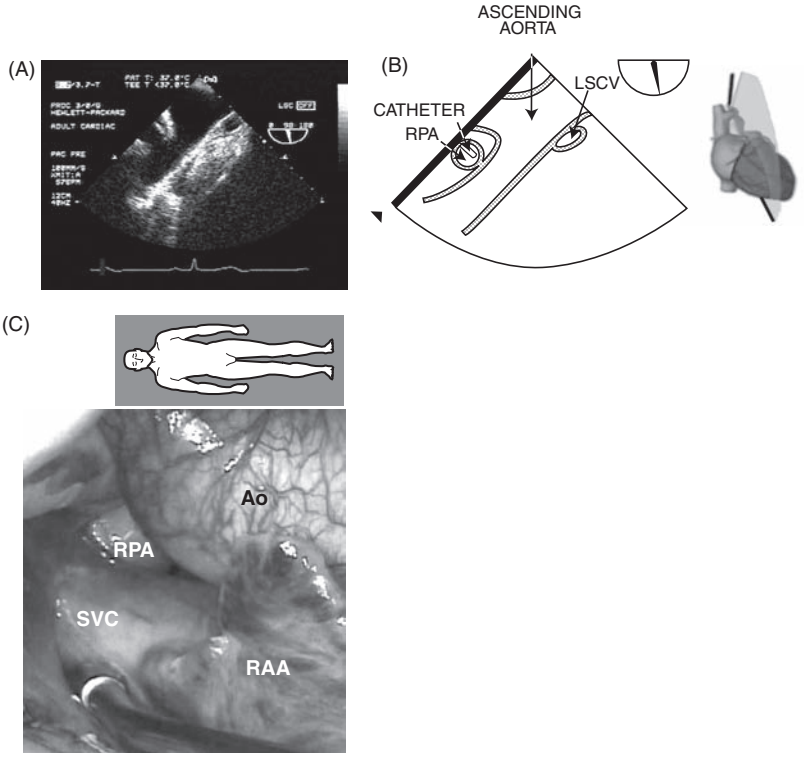

Figure 4.30 (A, B) Upper esophageal view of the proximal ascending aorta (Ao). (C) Intraoperative view (LSCV, left subclavian vein; RAA, right atrial appendage; RPA, right pulmonary artery; SVC, superior vena cava). (Photo C courtesy of Dr. Michel Pellerin.)

The aortic arch is viewed longitudinally at 0° on probe withdrawal from the descending aorta (Fig. 4.32). Its anterior course requires the combination of gentle withdrawal and simultaneous rightward rotation for optimal visualization. A short-axis view of the arch can then be obtained by plane rotation to 90° (Fig. 4.33): this is particularly useful to assess the whole anterior wall and the floor of the aorta. While rotating the probe towards the right, the origin of the left subclavian, left common carotid and right brachiocephalic arteries may be seen at 90° (Fig. 4.33).

Tip: This view is obtained from high esophageal position where the probe tip, applied against the posterior surface of the trachea, may cause discomfort and induce paroxysmal cough in lightly sedated patients. It is, therefore, best left until the end of examination and obtained just prior to probe withdrawal unless the patient is under deeper sedation or anesthesia.

6. Valves

Mitral Valve

The mitral valve (MV) apparatus consists of the annulus, the anterior and posterior leaflets, the chordae tendinae and the papillary muscles (Fig. 4.9). Each of these structures can be visualized with multiplane TEE (See also Chapter 17—Section I.1).

LEAFLETS. The anterior mitral leaflet (AML) has the larger surface of the two but has a smaller perimeter of attachment to the mitral valve annulus. For descriptive purposes, the AML surface is divided into three segments: the anterolateral (A1), the middle (A2) and the posteromedial segment (A3). The posterior mitral valve leaflet (PML) consists of three distinct scallops labeled anterolateral (P1), middle (P2), and posteromedial (P3). All aspects of the mitral valve leaflets can be viewed during a TEE exam from the mid-esophageal probe position. Beginning at 0° (A2–P2) (Fig. 17.4), the 2D echo structure of the leaflets is assessed as the angle is progressively changed through 30° (A3–P1), 60° (P3–A2–P1) (Fig. 17.6), then 90° (P3–A1), and finally 135° (P2–A2) (Fig. 4.34). Any degree of MR is assessed and semiquantified by color flow Doppler as the angle is returned from 135° back to 0° keeping any MR jet into the LA centered in the display. This comprehensive back and forth sweep of the mitral valve leaflets in the mitral annular plane from the mid-esophageal level should be an integral part of all TEE exams (see Chapter 17).

In addition to the mid-esophageal views, the mitral valve leaflets can also be visualized from the transgastric probe position with anteflexion of the probe tip towards the base and slight withdrawal from the papillary muscle short-axis plane (Figs. 4.3f and 4.35). In this view, the posteromedial mitral valve commissure is the

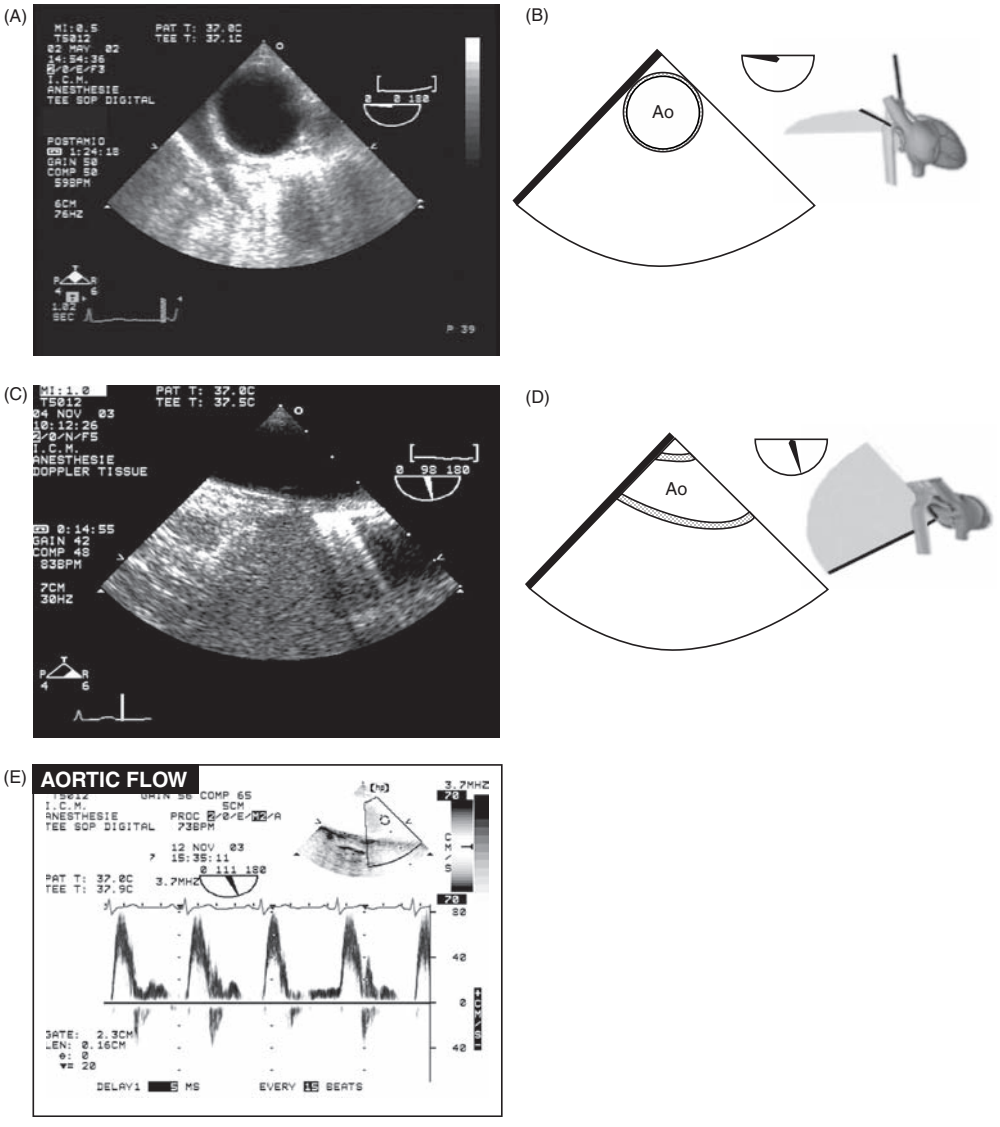

Figure 4.31 (A, B) Short-axis view of the thoracic aorta (Ao). (C, D) Longitudinal view. (E) Corresponding pulsed-wave Doppler signal.

closest to the transducer while the anterolateral commissure is the furthest, opposite to the septum. This transgastric short-axis view of the mitral valve is excellent for localizing precisely MV leaflet abnormalities or the extent of MV annular calcifications. Rotating the angle to 90° from this position yields a two-chamber view with the posterior leaflet closest to the transducer at the top of the display and the anterior leaflet towards the bottom of the display (Figs. 4.3e and 4.9).

CHORDAE TENDINAE. The chordae tendinae are best seen in the transgastric long-axis view at 90° where they are perpendicular to the ultrasound beam. In this two-chamber view, the anterior chordae can be tracked from the anterolateral papillary muscle at the bottom of the screen while the posterior chordae originate from the posteromedial papillary muscle closer to the transducer (Fig. 4.9).

ANNULUS. The mitral valve annulus is evaluated throughout the midesophageal sweep from 0° to 135° described above for assessment of the mitral valve leaflets.

PAPILLARY MUSCLES. The papillary muscles are best seen in the transgastric short-axis view at 0° while evaluating the contractility of the LV mid-level segments (Figs. 4.3d and 4.8).

Aortic Valve and Aortic Root

The aortic root comprises the AoV annulus, AoV cusps, the sinuses of Valsalva and coronary ostia, the sinotubular

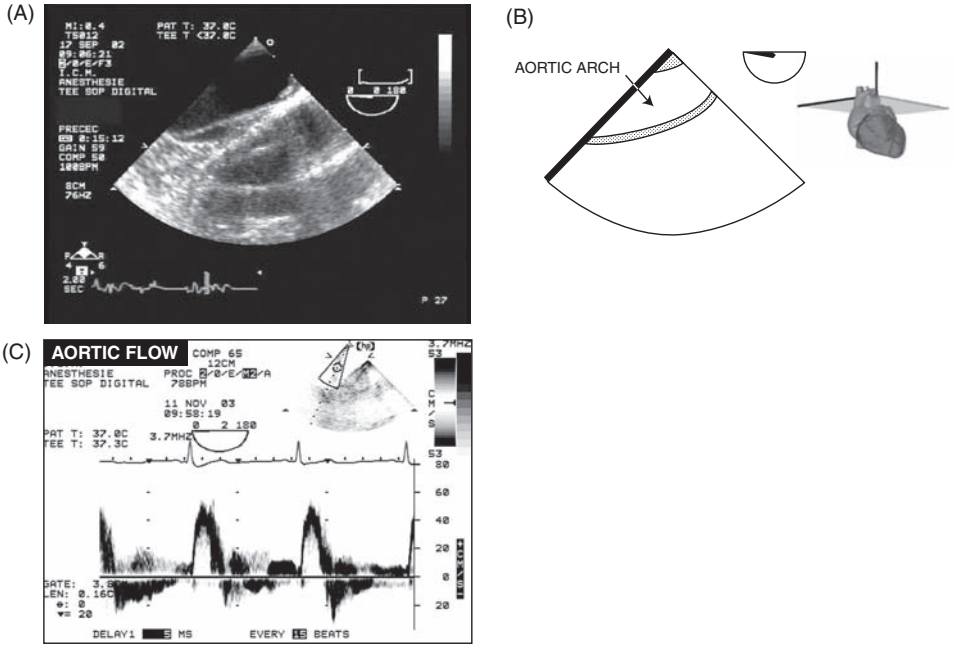

Figure 4.32 (A,B) Upper esophageal view of the aortic arch. (C) Corresponding pulsed-wave Doppler signal.

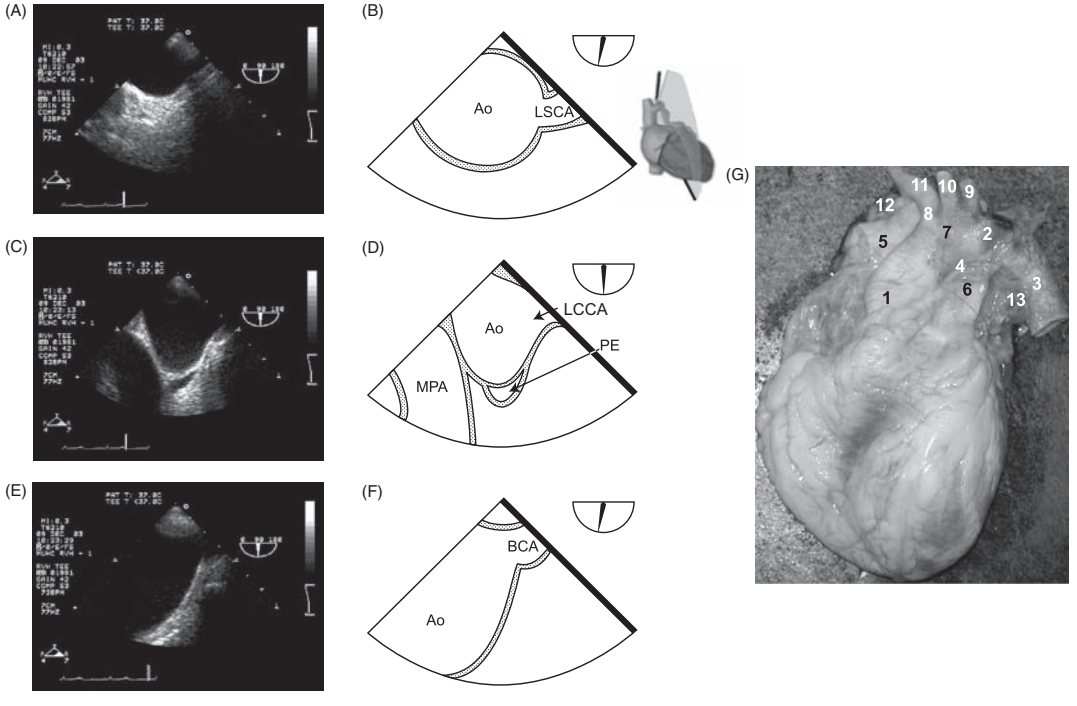

Figure 4.33 (A–F) Upper esophageal view of the transverse aorta (Ao) and proximal arch vessels. (G) Anatomical correlation. The proximal vessels are obtained with a left to right rotation of the transesophageal echocardiographic probe from a long-axis view. (BCA, brachiocephalic artery; LCCA, left common carotid artery; LSCA, left subclavian artery; MPA, main pulmonary artery; PE, pericardial effusion) (1, ascending aorta; 2, transverse aorta; 3, descending aorta; 4, ligamentum arteriosum; 5, superior vena cava; 6, pulmonary trunk; 7, arch of aorta; 8, brachiocephalic artery; 9, left subclavian artery; 10, left common carotid artery; 11, right common carotid artery; 12, right subclavian artery; 13, left pulmonary veins).

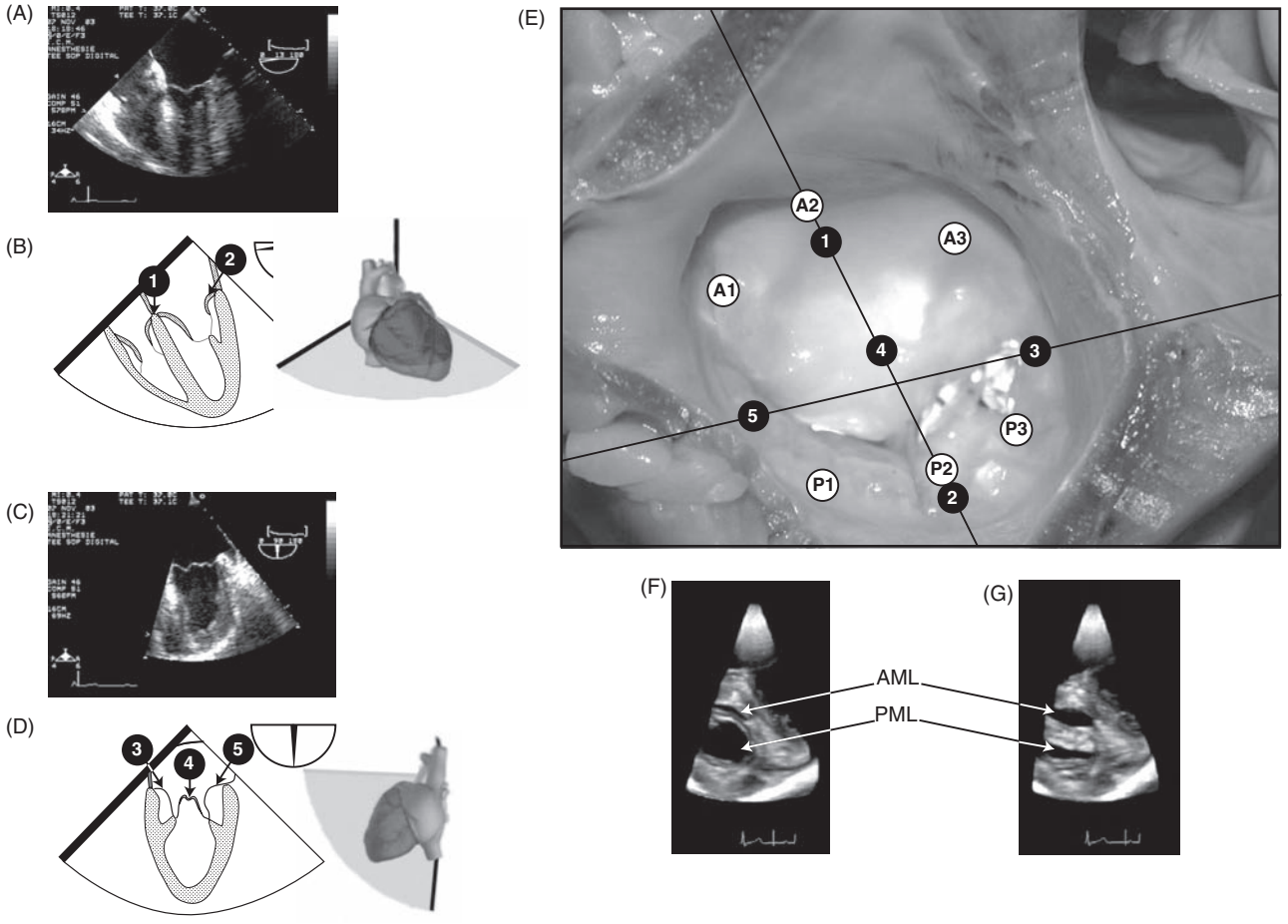

Figure 4.34 (A, B) Mid-esophageal four-chamber view of the mitral valve. (C, D) Mid-esophageal two-chamber view. (E) Anatomical view with corresponding planes. (F, G) Three-dimensional imaging of the mitral valve (A, anterior; AML, anterior mitral leaflet; P, posterior; PML, posterior mitral leaflet).

junction and the proximal ascending aorta. Complete visualization of all these structures can be achieved from the mid-esophageal position. The presence and degree of aortic regurgitation with color flow Doppler can also be assessed from the mid-esophageal probe position. While planimetry of the AoV orifice area is often feasible from this position as well, Doppler assessment of transaortic flow requires visualization of the LVOT, the AoV and the proximal ascending aorta from the transgastric probe position where transaortic flow is parallel to the ultrasound beam (Fig. 4.36).

The aortic root is imaged from the mid-esophageal short-axis position with an angle rotation of about 45–90° with slight anteflexion and sector depth of 10–12 cm. In this view, the ultrasound beam is perfectly parallel to the AoV annulus and the three aortic cups are visualized symmetrically, with the noncoronary cusp adjacent to the atrial septum and the right coronary cusp seen anteriorly at the bottom of the display (Fig. 4.37). Planimetry of the aortic orifice area is frequently possible in this view and has been found to correlate well with that obtained by Doppler with the continuity equation (see following text). Slight withdrawal and/or slight clockwise (rightward) rotation of the shaft brings the probe above the AoV to obtain the short-axis view of the sinuses of Valsalva, the left and right coronary ostia (see preceding text), and proximal ascending aorta respectively. Alternatively, further insertion and/or slight counterclockwise (leftward) of the shaft below the AoV yields the LVOT in cross section.

The mid-esophageal longitudinal view of the AoV may be obtained at 0° with some probe withdrawal (Fig. 4.6), but is better imaged at 135° where the LVOT, the AoV and the proximal aorta are viewed in the same plane (Fig. 4.29). Both positions allow for diagnosis and semi quantification of aortic regurgitation with color flow imaging. The 135° view is, however, best for making precise measurements of the aortic annulus, sinus of Valsalva, sinotubular junction and proximal ascending aorta diameters as

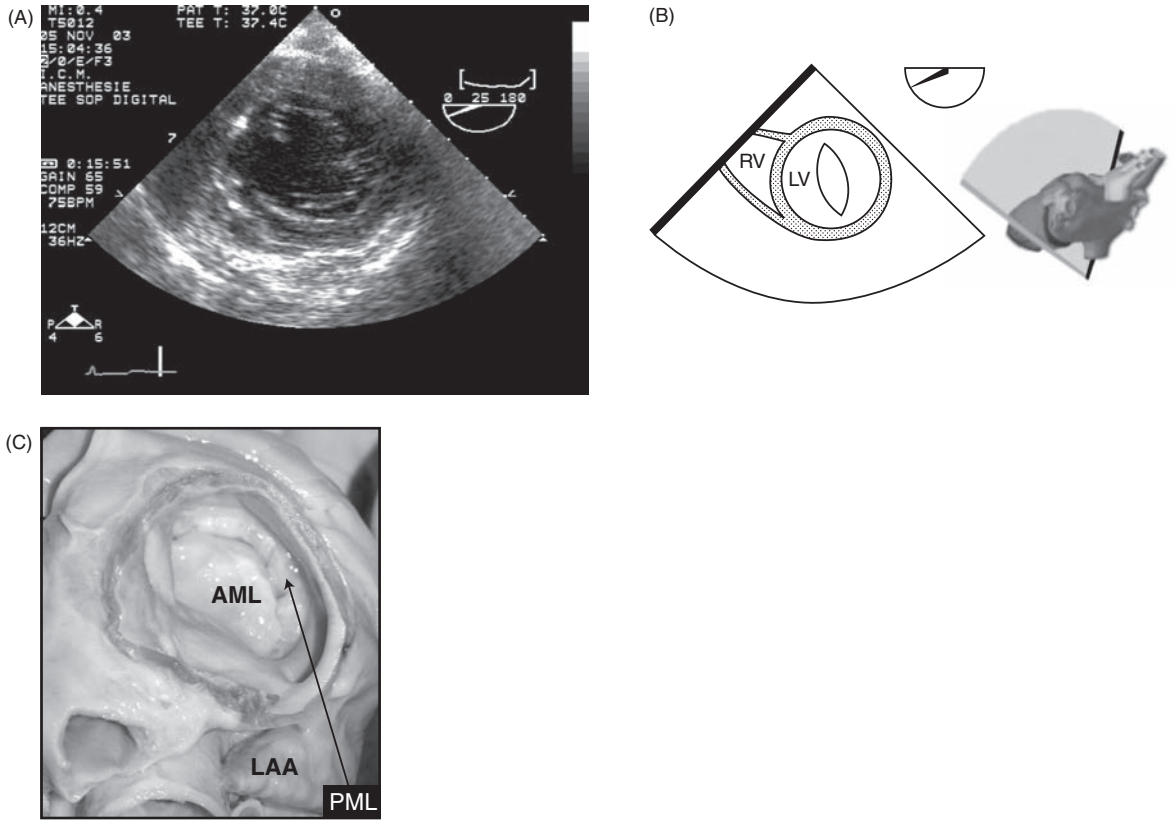

Figure 4.35 (A, B) Basal transgastric view of the mitral valve. (C) Anatomical correlation (AML, anterior mitral leaflet; LAA, left atrial appendage; LV, left ventricle; PML, posterior mitral leaflet; RV, right ventricle).

the ultrasound beam intersects these structures perpendicularly (see Fig. 12.1).

Parallel views of the aortic root in the far field of the display may sometimes be obtained from the transgastric probe position. Two options include further angle rotation to 90–120° from the transgastric two-chamber view as previously described or a deeper transgastric view obtained with further probe tip advancement and maximal anteflexion at an angle of 0° (Fig. 4.36). Color flow imaging is frequently useful to optimize pulsed- and continuous-wave Doppler alignment with aortic outflow in these positions where the distal aortic root location does not generally allow optimal 2D structure visualization.

Tricuspid Valve and Pulmonic Valve

The TV and pulmonic valve (PV) are anterior structures that are more difficult to visualize with TEE. Both valves are seen in the far field in the mid-esophageal short-axis 45° view (Fig. 4.13). In this position, the TV, RV, PV, and pulmonary trunk appear to wrap around the aortic root from left to right across the bottom of the display.

A similar view from a different imaging point can be obtained from a transgastric probe position at 90° with rightward rotation from the two-chamber view (Fig. 4.10). Sometimes, slight readjustment of the angle from 60° to 90° may be required to display at once the RA, TV, RV, and PV.

The PV, main pulmonary artery, and bifurcation in the proximal right and left pulmonary arteries are best visualized at 0° in the proximal esophageal probe position with more anteflexion (Fig. 4.14). While rightward rotation of the probe often enables visualization of the right pulmonary artery (RPA) up to its first bifurcation in the near field of the display, only the first 1–2 cm of the left PA can be visualized most of the time.

II. DOPPLER FLOW PROFILES FOR NORMAL AND ABNORMAL PHYSIOLOGY

A. Phases of the Cardiac Cycle (Systole vs Diastole/Four Phases)

The cardiac cycle consists of two phases: systole and diastole. Systole is defined as the period between MV closure and aortic valve closure. It consists of an isovolumic

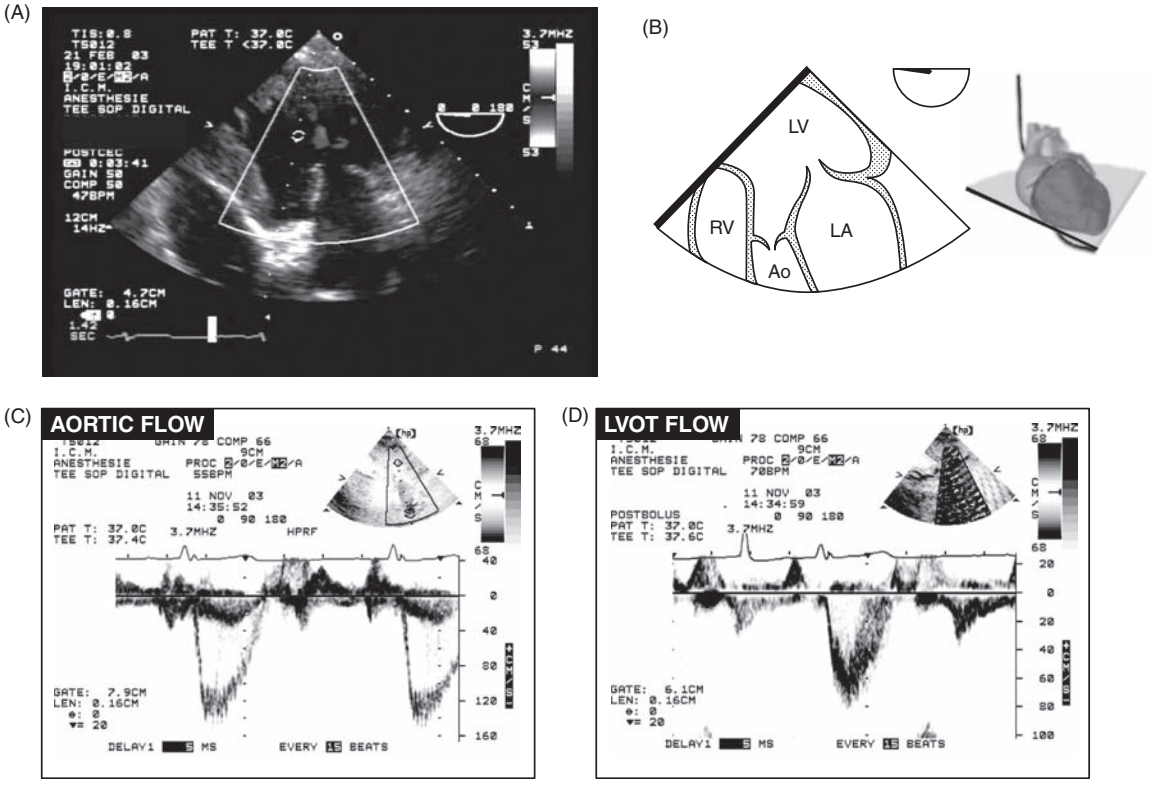

Figure 4.36 (A, B) Deep transgastric view of the left ventricular outflow tract (LVOT). (C) Corresponding aortic pulsed-wave Doppler interrogation. (D) LVOT pulsed-wave Doppler interrogation (Ao, aorta; LA, left atrium; LV, left ventricle; RV, right ventricle).

contraction period (both atrioventricular and semilunar valves closed) followed by the ejection time (ET) during which blood is expelled from the ventricles into the great arteries. The amount of blood ejected per cardiac cycle, or stroke volume (SV), multiplied by the number of cardiac cycles per minute, or heart rate (HR), yields the cardiac output (CO) (see Chapter 5, equation 5.10).

Diastole is more complex and is divided into four phases: isovolumic relaxation, rapid filling, diastasis, and atrial contraction. It begins with AoV closure and ends with mitral valve closure. The period between AoV closure and mitral valve opening is defined as the isovolumic relaxation time (IVRT) and is a period of active (energy-requiring) and rapid ventricular relaxation. On opening of the mitral valve, rapid initial filling of the ventricle from the atria occurs driven by the pressure gradient between the two chambers. Normally 70–80% of ventricular filling occurs during this rapid filling phase. A

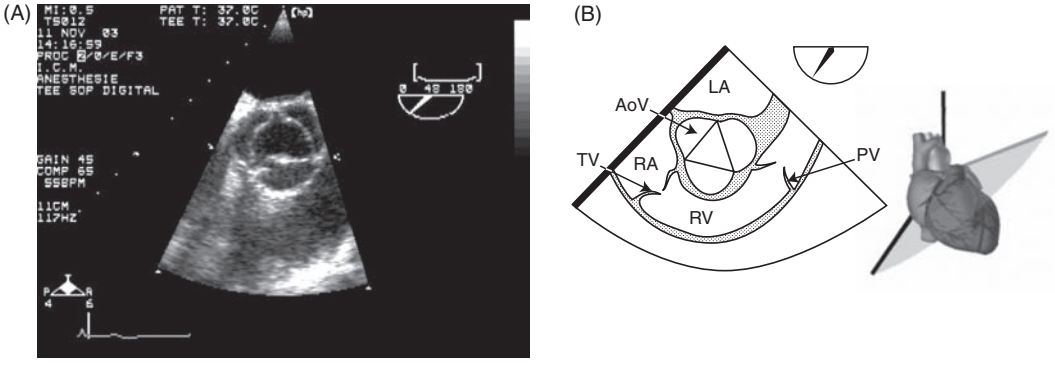

Figure 4.37 Basal short-axis view of the aortic valve (AoV) (LA, left atrium; PV, pulmonic valve; RA, right atrium; RV, right ventricle; TV, tricuspid valve).

period of near-pressure equalization between the atrium and ventricle follows (diastasis) when little forward flow occurs. Finally, atrial contraction follows with an additional 10–20% in ventricular filling (see Chapter 9).

While the systolic ejection time changes little with increasing heart rate, the diastolic phase of the cardiac cycle shortens substantially with exercise. Therefore, any degree of diastolic dysfunction is more likely to become symptomatic with exercise as the ventricle is unable to fill adequately at normal pressures.

B. Normal Pressures in Cardiac Chambers and Great Vessels

It is important to be aware of the normal pressures in the cardiac chambers and great arteries during the systolic and diastolic phases of the cardiac cycle (all in mmHg) (Table 4.2).

C. Mitral Valve

1. Mitral Regurgitation

From a mid-esophageal TEE probe position, regurgitant flow across the mitral valve is directed towards the probe, unless it is extremely eccentric. Transesophageal examination constitutes an excellent modality to assess MR, especially with prosthetic valves. Color flow imaging is used to detect and semiquantify MR on a scale of 1+ (trivial MR) to 4+ (severe MR). The width of the narrowest regurgitant color jet as it crosses the regurgitant orifice, or vena contracta, as well as the velocity of forward flow in early diastole, are also useful in the primary assessment of MR severity, while more quantitative methods can be implemented (see Chapter 17, Table 17.3). Care must be taken to differentiate mitral regurgitant signals from obstructive outflow tract jets. As jets can be identified by the company they keep, systolic mitral regurgitant jets will be associated with mitral inflow (with E and A velocities) in diastole, while systolic obstructive outflow tract signals may be accompanied by aortic regurgitant signals. Also the aortic regurgitant signal will be separated from the mitral diastolic signals by the isovolumic contraction time (IVCT) and IVRT intervals (see Chapter 15). Because of the usual LV–LA pressure gradient in systole, most mitral regurgitant jets velocities are >4 m/s, unless there is severe left ventricular systolic dysfunction.

Table 4.2 Normal Pressure in Cardiac Chambers and Great Vessels

	Pressure (mmHg)		
	Systolic	Diastolic	Mean
RA			1–8
RV	15–30	1–8	
PA	15–30	4–12	9–18
LA			2–12
LV	100–140	3–12	
Aorta	100–140	60–90	70–105

Note: LA, left atrial; LV, left ventricular; PA, pulmonary artery; RA, right atrial; RV, right ventricular.

2. Mitral Stenosis

Optimal ultrasound beam alignment with the mitral valve forward flow during TEE is also ideal for spectral (pulsed- or continuous-wave) Doppler assessment of mitral valve stenosis. Peak and mean transvalvular gradients, as well as mitral valve area (MVA), can be measured from the mitral valve diastolic inflow velocity spectra using the modified Bernoulli equation and pressure half-time methods, respectively (see Chapter 17).

D. Left Ventricular Inflow

1. Abnormal Relaxation

Abnormal left ventricular relaxation can be evaluated by pulsed-wave Doppler interrogation of the mitral valve inflow pattern. The pulsed-wave Doppler sample volume must be carefully positioned between the mitral valve leaflet tips while maintaining strict alignment with the direction of the mitral flow, often laterally directed because of the large anterior leaflet (Fig. 4.11c). From the spectral display obtained, a number of parameters can be evaluated, including the IVRT, the mitral deceleration time of the E velocity (mDT) and the E/A velocity ratio. With delayed LV relaxation, the IVRT and mDT are prolonged while the E/A velocity ratio is typically <1.0 as relatively more filling occurs in late diastole. However, these values may be affected by a number of additional factors, including left atrial and ventricular filling pressures, left ventricular passive compliance, heart rate, and age. Reliable Doppler assessment of diastolic function therefore, requires an integrated approach together with a thorough understanding of diastolic physiology (see Chapter 9).

2. Restrictive Filling

At this stage, the reduced passive operating compliance properties of the chamber lead to rapidly equalizing pressures: filling occurs mostly in early diastole and ends abruptly prior to diastasis and atrial contraction where little additional flow into the LV occurs. Therefore, in restriction, the pulsed-wave Doppler spectral display of mitral inflow usually shows prominent E and decreased A velocities (resulting in elevated E/A ratio), with shortened IVRT and deceleration time (DT) (see Chapter 9 for further details).

E. Tricuspid Valve

Tricuspid regurgitation (TR) can generally be assessed by TEE with color flow imaging from the TV views described above. The extent of the color regurgitant jet in the RA and the width of the TR vena contracta are used for semi-quantification in a manner similar to the evaluation of MR (see Chapter 19).

Tricuspid stenosis is rare in adults but may be seen with associated left-sided valve rheumatic involvement and with carcinoid syndrome and fenfluramine-phentermine (fen-phen) toxicity. Abnormal pressure gradients can also be found after valve repair and annuloplasty or replacement. Assessment of TV gradients is more challenging with TEE as parallel alignment of the ultrasound beam with TV inflow is generally not ideal from any of the conventional views. Visualization of the TV inflow jet by color flow imaging is key in minimizing errors in Doppler measurement. The best opportunity for acceptable alignment might be with the mid-esophageal four-chamber view where fine adjustments of angle and probe tip flexion may reduce the ultrasound beam to TV flow angle to $<20^{\circ}$ (Fig. 4.38). Sometimes, the mid-esophageal position in the short-axis view at $60-90^{\circ}$ can be tried with slightly further probe tip insertion.

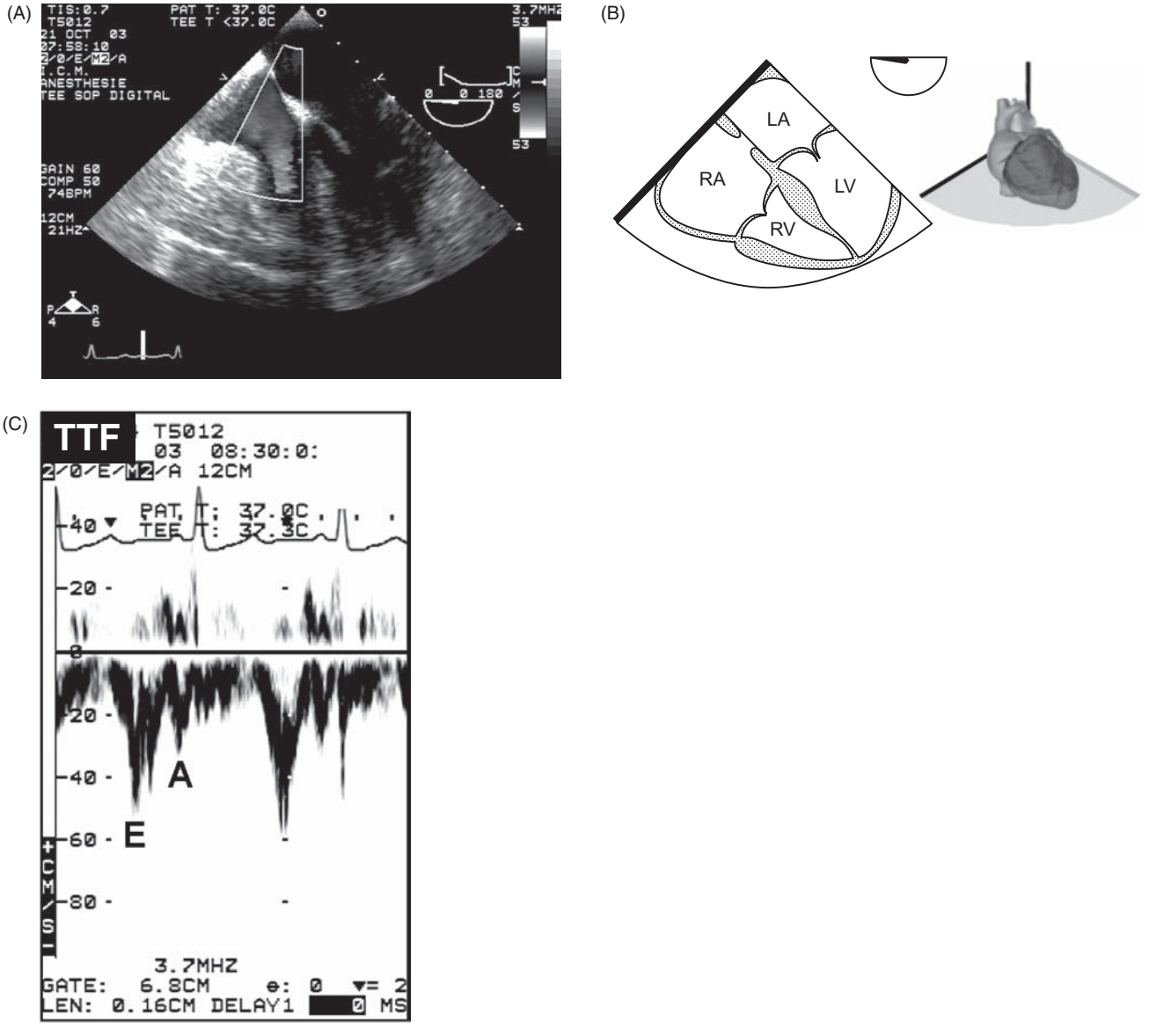

Figure 4.38 (A, B) Mid-esophageal view of the tricuspid valve. (C) Pulsed-wave Doppler interrogation. The early filling (E) and atrial contraction (A) waves are seen (LA, left atrium; LV, left ventricle; RA, right atrium; RV, right ventricle; TTF, transtricuspid flow).

F. Aortic Valve (See Chapter 15)

1. Aortic Regurgitation

Aortic regurgitant jets can be visualized in mid-esophageal short- and long-axis views of the AoV at 45° and 135°, respectively. However, for quantitative assessment, best alignment of the ultrasound beam with aortic regurgitant jets are usually obtained from long-axis transgastric views at 100–110° for measurement of regurgitant flow pressure half-time, as well as for measurements of regurgitant volume by the continuity equation.

2. Aortic Stenosis

Assessment of aortic stenosis (AS) severity requires measurement of valvular peak and mean pressure gradients as well as additional measurement of LVOT diameter, velocity, and time–velocity integral for the estimation of valve area by the continuity equation. Again, mid- or deep-transgastric views at either 100–110° or 0° are traditionally used to obtain these values, but to ensure that the aortic maximal gradient is obtained, continuous-wave Doppler interrogation through a high esophageal position looking down the distal ascending aorta should also be tried when windows are available (Figs. 4.30 and 4.33[E, F]).

G. Pulmonic Valve (Fig. 4.39) (See Chapter 19)

1. Pulmonic Regurgitation

Pulmonic regurgitant jets can be visualized in a mid-esophageal short-axis view of the AoV at 45° and 110°. However, for quantitative assessment of pulmonary diastolic pressures, the best alignment of the ultrasound beam with pulmonic regurgitant jets is usually obtained from an upper esophageal view at 0° of the main pulmonary trunk (Figs. 4.14 and 5.16) or, alternatively, from the transgastric view at 60–90° rotated towards the right looking up towards the RVOT (Figs. 4.10 and 4.24).

2. Pulmonic Stenosis

Assessment of pulmonic stenosis (PS) severity requires measurement of valvular peak and mean pressure gradients as well as additional measurement of RVOT diameter, velocity, and time–velocity integral for the

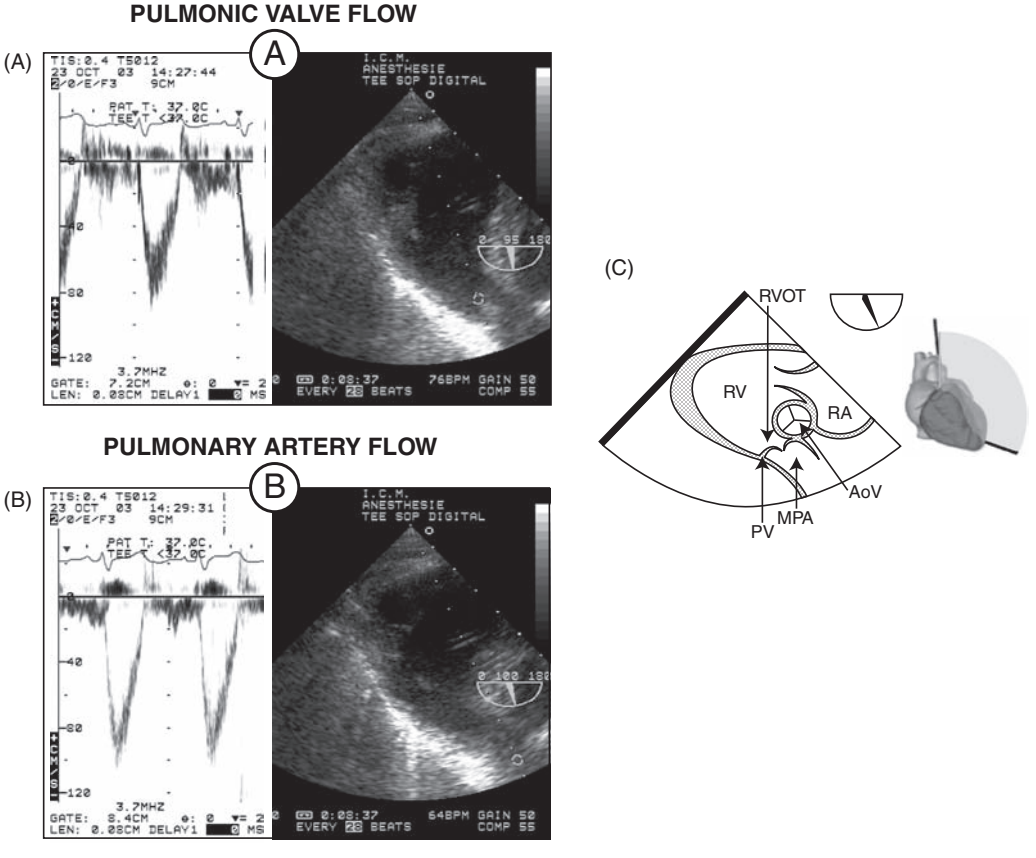

Figure 4.39 (A) Pulsed-wave Doppler interrogation of the pulmonic valve (PV) from a right ventricular inflow–outflow deep transgastric view. (B) Pulsed-wave Doppler interrogation of the main pulmonary artery (PA) (Ao, aorta; RA, right atrium; RV, right ventricle).

estimation of valve area by the continuity equation. Again, transgastric views at 60–90° can be used to obtain these values (Figs. 4.10 and 4.24). The pulmonic maximal gradient can also be measured from above the valve by continuous-wave Doppler interrogation through the upper esophageal position looking down the main pulmonary trunk at 0° (Figs. 4.14 and 5.16) or 90° (Fig. 19.5).

H. Left Ventricular Outflow Tract

See Section I.B.1, Figs. 4.36 and 5.29[A].

I. Pulmonary Vein

The right and left upper pulmonary veins usually present the best alignment for pulsed-wave Doppler interrogation, with the sample volume positioned approximately 1 cm inside the vein from the ostium (Figs. 4.21–4.23). Normal pulmonary venous flow is multiphasic, with two peaks in systole (S_1 and S_2), one peak in diastole (D) and one retrograde peak during atrial contraction, called atrial reversal (AR). The S_1 is related to atrial relaxation and may be proportional to the magnitude of atrial systole and therefore the AR wave. The S_2 velocity is influenced by the suction of blood from the pulmonary veins with LA expansion secondary to the mitral valve annulus descent during ventricular systole and to RV contraction. The diastolic velocity (D) depends on the LA pressure drop after the MV opening, and also on the LA–LV pressure gradient.

With normal LV filling pressures, there is more pulmonary venous flow in systole than in diastole, with the S/D ratio >1. In the case of a young adult with excellent ventricular relaxation, a S/D ratio <1 may be observed. The AR wave duration may also exceed the duration of the mitral A wave, but never by >30 ms with normal left-sided filling pressures. In the case of abnormally decreased LV compliance or elevated LA or LV filling pressures, such as in moderate-to-severe MR or significant LV systolic or diastolic dysfunction, there will be diastolic flow prominence ($S/D < 1$). Severe MR can even cause systolic flow reversal.

Elevated LV end-diastolic pressures during atrial contraction cause preferential blood backflow in the pulmonary veins rather than downstream through the mitral valve. This leads not only to increased AR velocity but also AR duration exceeding that of the mitral A wave by >30 ms (see Chapter 9).

J. Hepatic Vein

The hepatic veins are the equivalent of the pulmonary veins for the right heart (Fig. 4.25). Similarly, the hepatic venous Doppler flow is multiphasic, with systolic, diastolic, and atrial reversal waves. However, with operating pressures on the right heart lower than on the left, there is often some mild systolic flow reversal before diastolic flow. The S/D ratio is usually >1 with normal right-sided filling pressures (see Chapter 9).

When the right-sided filling pressures are elevated, normal systolic flow prominence may be lost with, occasionally, even an absence of forward flow during systole. In such cases, the S/D ratio will be inverted (<1) (see Chapter 9). Tamponade physiology can also be accompanied by abnormal expiratory diastolic flow reversal (see Chapter 11).

K. Ascending Aorta

As stated earlier in the evaluation of AS, maximal aortic velocity and pressure gradient should be sought from a high esophageal window looking down the distal ascending aorta even if this is not always achievable because of interference from the air-filled trachea (Fig. 4.32).

L. Descending Aorta-Flow Reversal and Aortic Regurgitation

Although the descending thoracic aorta easily lends itself to 2D examination because of its very close proximity to the esophagus, the direction of aortic flow is however often perpendicular to the direction of the ultrasound beam of the TEE probe. Therefore, precise measurements of the descending thoracic aorta pressure gradient (for coarctation evaluation, for instance) are usually precluded. Likewise, assessment of AR severity with measurement of the duration, velocity, and time–velocity integral of the diastolic flow reversal may be harder to achieve than by TTE (see Chapter 15).

M. Coronary Sinus

Coronary sinus Doppler examination is best conducted from the lower esophageal sphincter position while withdrawing the probe from the transgastric to the esophageal position in the longitudinal plane at 90°. As the coronary sinus in its short axis is centered over the display, the probe shaft is then rotated rightward towards the orifice of the coronary sinus in the RA. Most often the coronary sinus will then be imaged in its long axis, with the coronary sinus flow going away from the probe (Fig. 4.26). Coronary sinus flow is similar to multiphasic right-sided venous flow.

N. Pulmonary Artery

As stated previously in the evaluation of pulmonic stenosis, maximal pulmonic velocity, and pressure gradient can be assessed from upper esophageal transverse plane at 0° looking down the pulmonic valve. Alternatively, this can be achieved from below the valve through a modified transgastric view at 60–90° with the probe shaft rotated rightward. The aspect of the velocity is useful in the diagnosis of pulmonary hypertension (see Chapter 9).

III. CONCLUSION

Multiplane TEE enables a complete assessment of cardiac structure and function in most patients. Optimal use of TEE requires a thorough understanding of cardiac anatomy and pathophysiology together with considerable experience in TEE probe and ultrasound system manipulation. Adequate knowledge of ultrasound physics and TTE is an important prerequisite for the performance and interpretation of TEE studies. While a TEE study targeted at a specific clinical question is justified in certain circumstances, a comprehensive evaluation is encouraged in most patients. Finally, as with any imaging study in medicine, TEE should, preferably, only be performed if the results of the examination will have an impact on subsequent patient management as for type I indications of the ASA. Routine monitoring during coronary revascularization and valve surgery with TEE (type II indications) are more controversial (see Chapter 25).

REFERENCES

1. Frazin L, Talano JV, Stephanides L et al. Esophageal echocardiography. Circulation 1976; 54:102–108.
2. Khandheria BK, Tajik AJ, Seward JB. Multiplane transesophageal echocardiography: examination technique, anatomic correlations, and image orientation. Crit Care Clin 1996; 12:203–233.
3. Shanewise JS, Cheung AT, Aronson S et al. ASE/SCA guidelines for performing a comprehensive intraoperative multiplane transesophageal echocardiography examination: recommendations of the American Society of Echocardiography Council for Intraoperative Echocardiography and the Society of Cardiovascular Anesthesiologists Task Force for Certification in Perioperative Transesophageal Echocardiography. Anesth Analg 1999; 89:870–884.
4. Khandheria BK, Seward JB, Tajik AJ. Critical appraisal of transesophageal echocardiography: limitations and pitfalls. Crit Care Clin 1996; 12:235–251.

5

Quantitative Echocardiography

JEAN BUITHIEU
McGill University, Montreal, Canada

ANDRÉ Y. DENAULT
University of Montreal, Montreal, Canada

I. M-Mode and Two-Dimensional Imaging 90
A. Edge Recognition 90
B. Timing 90
C. Referencing Centroids 91
D. Centerline Method 92
E. Measurements and Calculations 93
1. M-Mode 93
2. Two-Dimensional Measurements 94
F. Chamber Dimensions, Volume Calculations, Ejection Fraction 101
1. The Modified Simpson's Biplane Method 103
2. The Single Plane Area–Length Method 103
3. Ejection Fraction 103
G. Global Function 104
1. Fractional Shortening 104
2. Ejection Fraction 104
3. Stroke Volume, Cardiac Output, and Cardiac Index 105
4. Systolic Time Intervals 105
H. Fractional Area Change 105
I. Circumferential Fiber Shortening 106
J. Wall Thickness, Mass, Stress 106
1. The ASE–Devereux Method 107
2. Wall Stress 107
II. Doppler 108
A. Blood Flow 108
B. Conservation of Energy Principle and Pressure Difference (Gradient) 108
C. Estimation of Intracardiac Pressures 110
1. Right Ventricular Systolic Pressure 110
2. Pulmonary Artery Systolic Pressure 110
3. Mean Pulmonary Artery Pressure 111
4. Pulmonary Artery and Right Ventricular (End)-Diastolic Pressure 112
5. Right Atrial Pressure 112
6. Left Ventricular End-Diastolic Pressure 112
7. Left Atrial Pressure 113
D. Volumetric Flow Calculations 113
1. Hydraulic Principle 113
2. Stroke Volume and Cardiac Output 115
3. The Principle of Conservation of Mass and the Continuity Equation 116
E. Valvular Areas 116
1. Valvular Areas by the Continuity Equation Method 116
2. Valvular Areas by the Pressure Halftime Method 116
F. Proximal Flow Convergence (Proximal Isovelocity Surface Area) 117
G. Regurgitant Volumes and Fractions 118
H. Shunt Fractions 118
III. Conclusion 119
References 119

I. M-MODE AND TWO-DIMENSIONAL IMAGING

A. Edge Recognition

The edge between the left ventricular cavity and the myocardium is represented by the endocardial border which reflects echoes with a certain thickness because of the presence of trabeculations, and ultrasound equipment quality and resolution. Since the introduction of echocardiography, over 50 years ago, several conventions have been proposed to measure the size of the cardiac structures. These have differed in the manner of whether or not they included the thickness of these echoes in the measurement. The leading edge of a structure is defined as the portion of the border closest to the transducer, while the trailing edge is the portion farthest from the transducer. In two-dimensional (2D) echocardiography, the inner edge is defined as the portion of the border closest to the center of the structure while the outer edge is the farthest from it (Fig. 5.1).

The *Standard Convention* was originally published in 1968 as guidelines for the only modality then available, M-mode echocardiography (1). This convention includes the edge thickness in the measurement of the wall thickness: the septum was defined as the area from leading to trailing edge; the posterior wall was defined as the area from the leading edge of the endocardium to the leading edge of the posterior pericardium. Good correlation of the posterior wall thickness measurement by this method was found compared with pathological specimens. Measuring the left ventricular internal dimension by this method correlated also with measurements obtained by contrast ventriculography. This method was, however, to evolve into 2D echocardiography.

The *Penn Convention* was developed to provide a better correlation between echocardiographically-derived mass and left ventricular mass calculations measured in pathology as a gold standard. Published in 1977 (2), this convention excluded the edge thickness in the measurement of the wall thickness: the septum was defined as the area from trailing edge to leading edge and the posterior wall, from trailing edge to inner edge. The left ventricular internal dimension therefore included the thickness of the endocardial borders.

Weyman and colleagues suggest measuring cardiac structures using the Wyatt convention from inner edge to inner edge, providing better consistency and reproducibility of measures obtained by either M-mode or 2D echocardiography (3).

In an attempt to improve the consistency and the interobserver variability of echocardiographic measurements, the American Society of Echocardiography (ASE) published a convention in 1978 (4) based on a consensus of questionnaire surveys returned from various echocardiographic laboratories rather than on validated correlative data in accuracy or reproducibility. They recommended using a leading edge to leading edge method to measure all cardiac structures in both M-mode and 2D techniques, based on the observation that this would be least affected by various equipment signal processing or gain settings from different laboratories.

B. Timing

The ASE recommends that end-diastolic and end-systolic measurements be made in reference to the mitral valve (5). The end of diastole can be timed at the frame where the mitral valve leaflets initially coapt, marking the mitral valve closure. Alternatively, if the mitral valve is not visualized, the end of the diastole can be determined with the electrocardiogram (ECG). Since the quality of the electrocardiographic monitoring lead tracing may vary and consequently result in a variable R wave of the QRS, the ASE believes that the end of diastole is best timed at the onset of the QRS complex.

The end of systole can be timed at the frame preceding the opening of the mitral valve leaflets. Alternatively, it should be set at the time when the left ventricular cavity

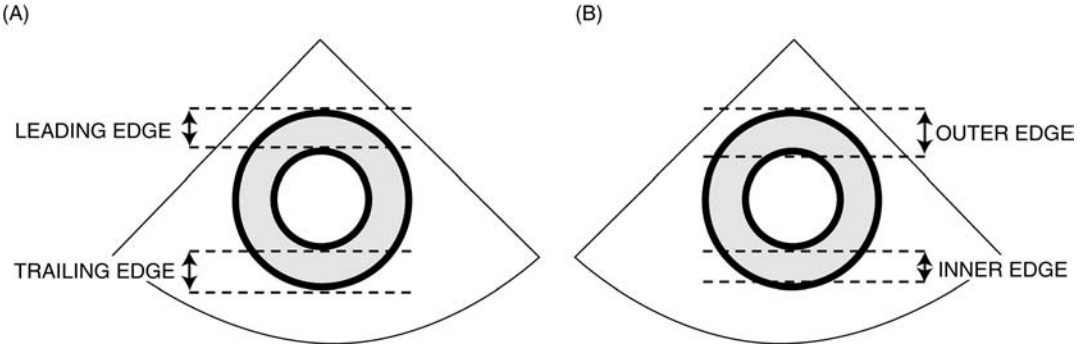

Figure 5.1 (A) The leading and trailing edge. (B) The inner and outer edge.

dimensions are at their minimum. However, on a M-mode echocardiogram of the left ventricle (LV), the peak downward motion of the interventricular septum often slightly precedes the peak upward motion of the left ventricular posterior wall. The apparent asynchrony of the inward motion of the two opposite walls may be accentuated with abnormal septal wall motion associated with decreased regional wall contractility, bundle branch conduction delays, pacing or cardiac surgery (Fig. 5.2). When timing the end of systole with the aortic valve (AoV) closure, determined by the second heart sound or more precisely with the dicrotic notch on a simultaneous carotid pulse contour tracing, the peak downward motion of the interventricular septum is more likely to correspond to the end of systole. Therefore, the ASE suggests making end-systolic measurements using the peak septal downward displacement. However, one may resort to using the peak upward motion of the posterior wall if there is abnormal septal motion.

C. Referencing Centroids

The decrease in myocardial perfusion has immediate consequences on the myocardial fibers relaxation and contractility, later resulting in anomalies of left ventricular regional wall systolic thickening and motion. However, evaluating the regional contractility of a three-dimensional (3D) spatial object against time by a tomographic technique, such as 2D echocardiography, is bound by certain limitations. The heart contracts in systole using at least five identified movements: (1) myocardial wall thickening in a radial fashion, towards the long axis, (2) base-to-apex long axis shortening towards the apex, (3) rotational motion around the long axis, (4) some degree of tilting, that is, rotational motion around the minor axis, and (5) translation of the entire ventricle in space (Fig. 5.3). This has an impact on the appearance of the image obtained by a tomographic plane fixed in the thorax, but is not relative to the heart in motion which is not often appreciated.

In the quantitative assessment of regional wall function, once epicardial and endocardial surfaces have been defined, a reference system is necessary to define the parameters of normal and abnormal function. While the pixel coordinate system of the video image frame appears easy to use for the comparison of the endocardial and epicardial contour traced at end-diastole and end-systole, it does not allow any correction for the 3D translational and rotational heart motions. Even in the absence of these motions, true assessment of wall thickening should be made perpendicular to the defined contours rather than in reference to an extracardiac point from a video-frame. Therefore, a polar coordinate system, revolving around a reference center of mass point (centroid) within the left ventricular internal

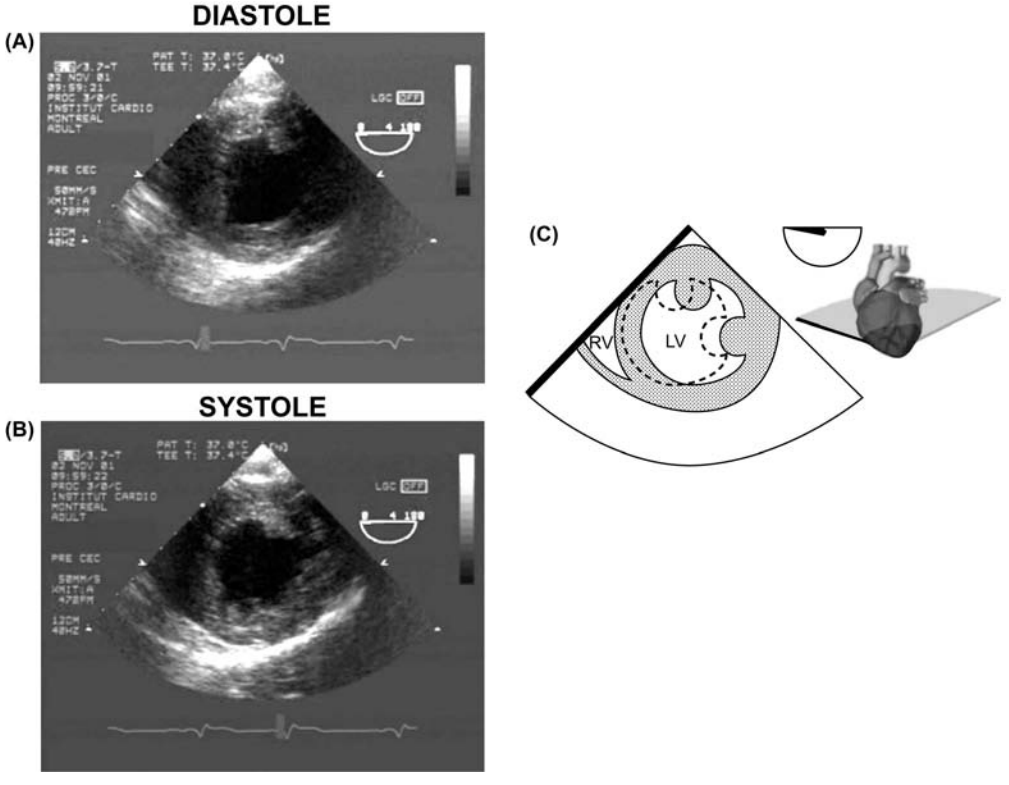

Figure 5.2 (A–C) Transgastric mid-papillary view of a patient with a left bundle branch block with abnormal septal motion (LV, left ventricle; RV, right ventricle).

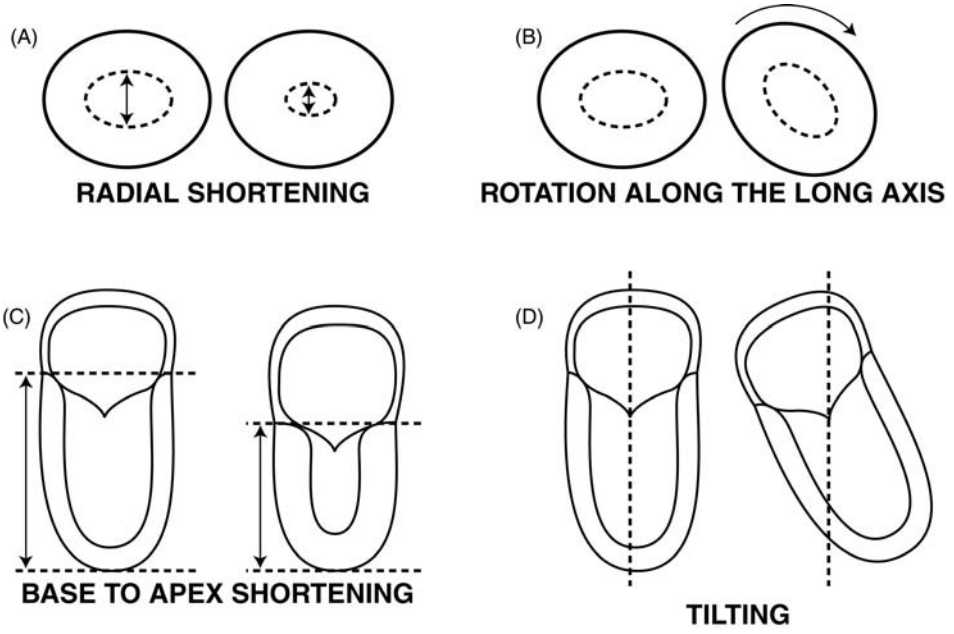

Figure 5.3 Schematic representation of heart movements. (A) Radial shortening. (B) Rotation along the long-axis contraction. (C) Base to apex shortening. (D) Tilting.

cavity, would be preferable. If defined from internal cardiac landmarks, this reference-based coordinate system would have the advantage of moving with the heart and allowing corrections for translational and rotational motions.

Different methods have been proposed to define the central reference point (centroid) for a given video-frame in time. The bisector of a line traced between an accepted landmark in the ventricular wall and the furthest point on the opposing wall may divide the cavity in half, but it may also be easily skewed by the presence of asymmetrical distortion of the left ventricular shape, such as in aneurysms or in dyskinetic ventricles. Other methods consist of computing the centroid from either the whole endocardial or epicardial contour using various algorithms.

As the heart moves during the cardiac cycle, the centroid determined for each video-frame during the contraction sequence will not be in the same position throughout this period. Therefore, it is necessary also to define the spatial centroid in the time coordinate. In the fixed axis reference method, all wall motion is referenced to a fixed centroid in time, which may be the centroid of a chosen particular frame (e.g. the end-diastolic point) or the average (or integration) of all the centroids found throughout the cardiac sequence. In the floating axis reference method, each video-frame keeps its own-derived centroid and the centroid position is allowed to change (float) during the contraction sequence (Fig. 5.4).

As the length of all the radii traced from the reference centroid to the myocardial border is influenced by the type of centroid chosen, each method has its own advantages and disadvantages. A floating centroid will better correct for the heart translation but will, for the same reason underestimate the amount and location of dyskinetic wall. Conversely, a fixed axis reference system will portray normal heart translation as abnormal wall motion, but may adequately detect nontranslating hypokinetic walls (Fig. 5.4). While none of the centroid methods are ideal for all situations, the comparison of results between data obtained with each method may shed some light on understanding the type and degree of heart motion contaminating the analysis of wall thickening. For instance, if there is no difference in short axis endocardial symmetrical motion between the fixed and the floating axis method, we can infer that no significant translation is present.

D. Centerline Method

Once the most appropriate reference system has been chosen, different approaches are proposed to measure the extent and severity of regional contractility. In short-axis views of the LV, radial chords can be traced between the centroid and the endocardial contour and followed throughout the cardiac cycle to endocardial excursion. Alternatively, the difference in the radial chord length between the centroid and the endocardial and epicardial contour can be tracked to measure myocardial wall thickening. For two- and four-chamber views, the major left ventricular long axis can be used to trace a series of parallel chords perpendicularly between the myocardial

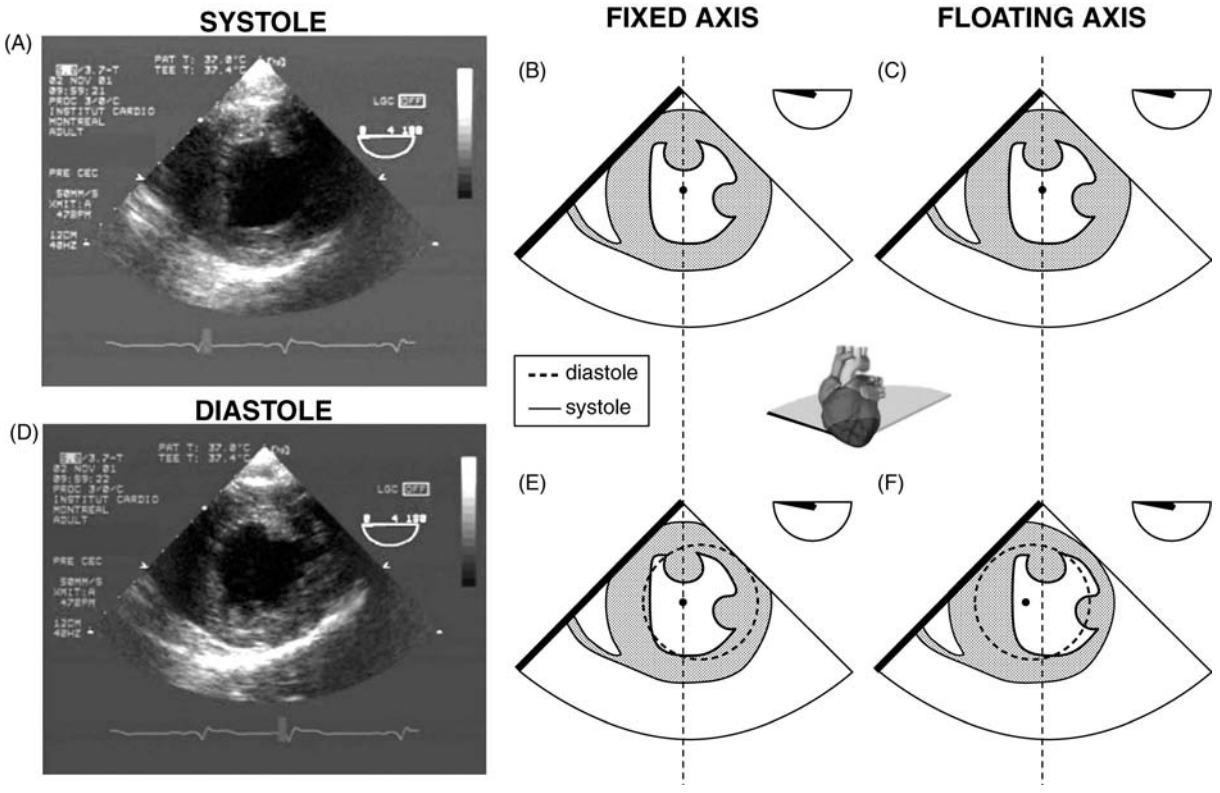

Figure 5.4 Transgastric mid-papillary view of a patient with a left bundle branch block with abnormal septal motion. (A–C) Systole. (D–F) Diastole. Using a fixed axis, the abnormal septal motion is identified without the rotational artefact. With a floating axis, the center of the image is displaced to the left but the normal segment appears hypokinetic.

contour and the major axis. A variation combining parallel chords for the base and the mid-ventricle and radial chords for the apical region may imperfectly help to reduce the shortcomings of apical thickening assessment with the parallel chords method.

The centerline method consists of finding and connecting all the mid-points between the endocardial contour in diastole and systole. A special recurring smoothing algorithm ensures that each perpendicular chord drawn along the centerline contour is perpendicular to both the diastolic and systolic endocardial contours. Endocardial excursion, starting from the end-diastolic contour, can then be measured along 100 perpendicular chords to the centerline, resulting in systematic assessment of regional wall motion. If a similar analysis is carried out conjointly with the epicardial contour in diastole and in systole, systematic assessment of regional wall thickening can also be performed.

E. Measurements and Calculations

1. M-Mode

Due to its superior temporal and axial resolution, M-mode echocardiography has generally been the method of choice for measuring cardiac chamber size dimensions. However, the validity of these measurements is based on a perpendicular alignment of the structures of interest with the line of examination represented by the M-mode cursor. It is, therefore, important to verify the correct spatial alignment of M-mode interrogation on 2D imaging (Fig. 5.5).

As the width of the M-mode echoes may be influenced by instrumentation and gain settings, the ASE recommends that all M-mode measurements of cardiac structures be made from leading edge to leading edge of the lines representing the structures' interface (4).

Measurements of Aorta and Left Atrium

From a short-axis 2D view of the AoV and the left atrium (LA), the M-mode cursor is positioned through the center of the AoV. The aortic root (Ao) is measured at end-diastole (onset of QRS complex on the ECG) from the leading edge of the anterior aortic wall to the leading edge of the posterior aortic wall. The normal value is 1.0–1.8 cm/m^2 in normal young adults (6). The LA is measured at end-systole (at the peak of the anterior motion of the posterior wall of the aorta) from the leading

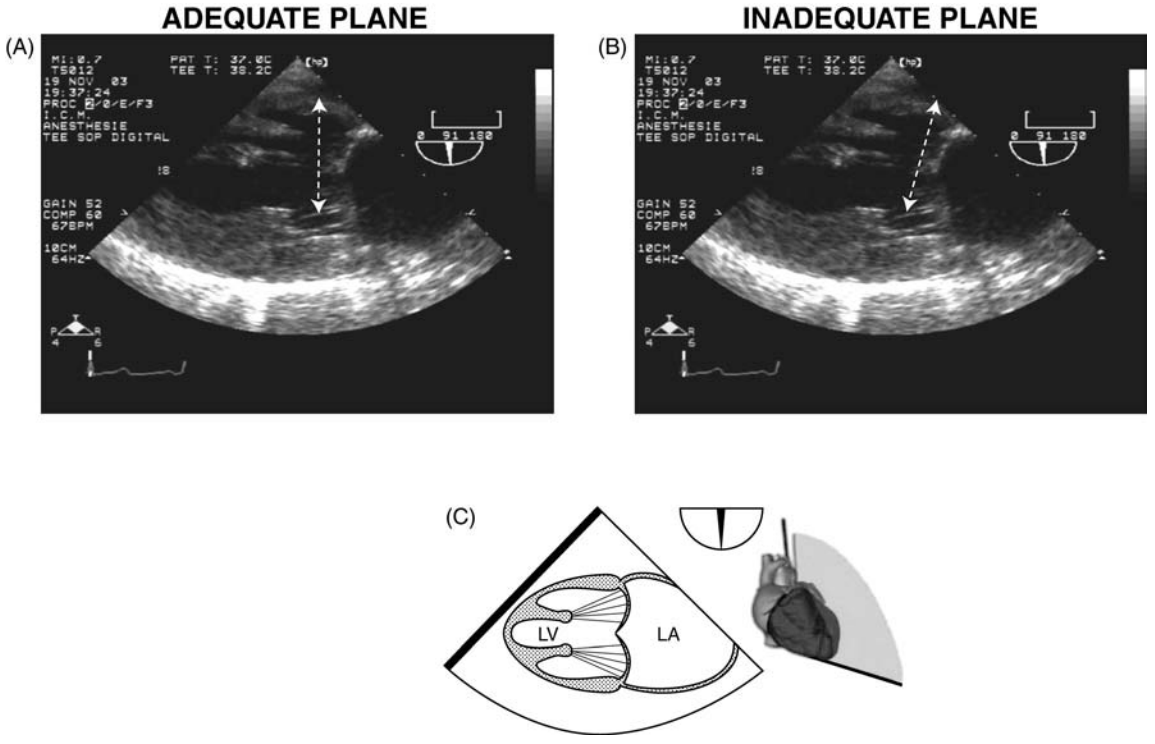

Figure 5.5 Importance of spatial orientation in the measurement of the diameter of the left ventricle (LV). The measurements obtained on (B) will overestimate ventricular diameters because they were obtained in an oblique plane (LA, left atrium).

edge of the posterior wall of the aorta to the leading edge of the posterior wall of the LA. The normal value is 3.8 ± 0.98 cm for the LA (7).

Measurements of the Left Ventricle

From a short-axis 2D view of the LV just beneath the mitral valve leaflets, the M-mode cursor is positioned through the center of the left ventricular cavity. End-diastolic measurements are first made at the onset of the QRS complex on the ECG (Fig. 5.6).

The interventricular septal thickness (IVST) is measured from the leading edge of the interventricular septum to the leading edge of the endocardial border of the interventricular septal wall.

The left ventricular end-diastolic dimension (LVEDD) is measured from the leading edge of the endocardial border of the interventricular septal wall to the leading edge of the endocardial border of the posterior wall.

The posterior wall thickness (PWT) is measured from the leading edge of the endocardial border of the posterior wall to the leading edge of the epicardial surface of the posterior wall.

End-systolic measurements are performed at the peak posterior displacement of the ventricular septum.

The left ventricular end-systolic dimension (LVESD) is measured from the leading edge of the endocardial border of the interventricular septal wall to the leading edge of the endocardial border of the posterior wall.

Measurements of the Right Ventricle

From the same view used earlier for the left ventricular dimension, the right ventricular end-diastolic dimension (RVEDD) is measured from the leading edge of the endocardial border of the right ventricular anterior wall to the leading edge of the right endocardial border of the interventricular septum.

Note that the normal values usually reported for these measurements are obtained by transthoracic M-mode echocardiography.

2. Two-Dimensional Measurements

When the cardiac structures of interest cannot be positioned so that they are perpendicular to the line of M-mode interrogation, 2D echocardiographic measurements are preferred. It is of note that the ASE recommended method for measuring cardiac structures by 2D echocardiography differs as it is done from inner edge to inner edge (as opposed to the leading edge to leading edge method in M-mode echocardiography) (8). Normal values have been reported for transesophageal echocardiography (TEE) (9,10) (Fig. 5.7).

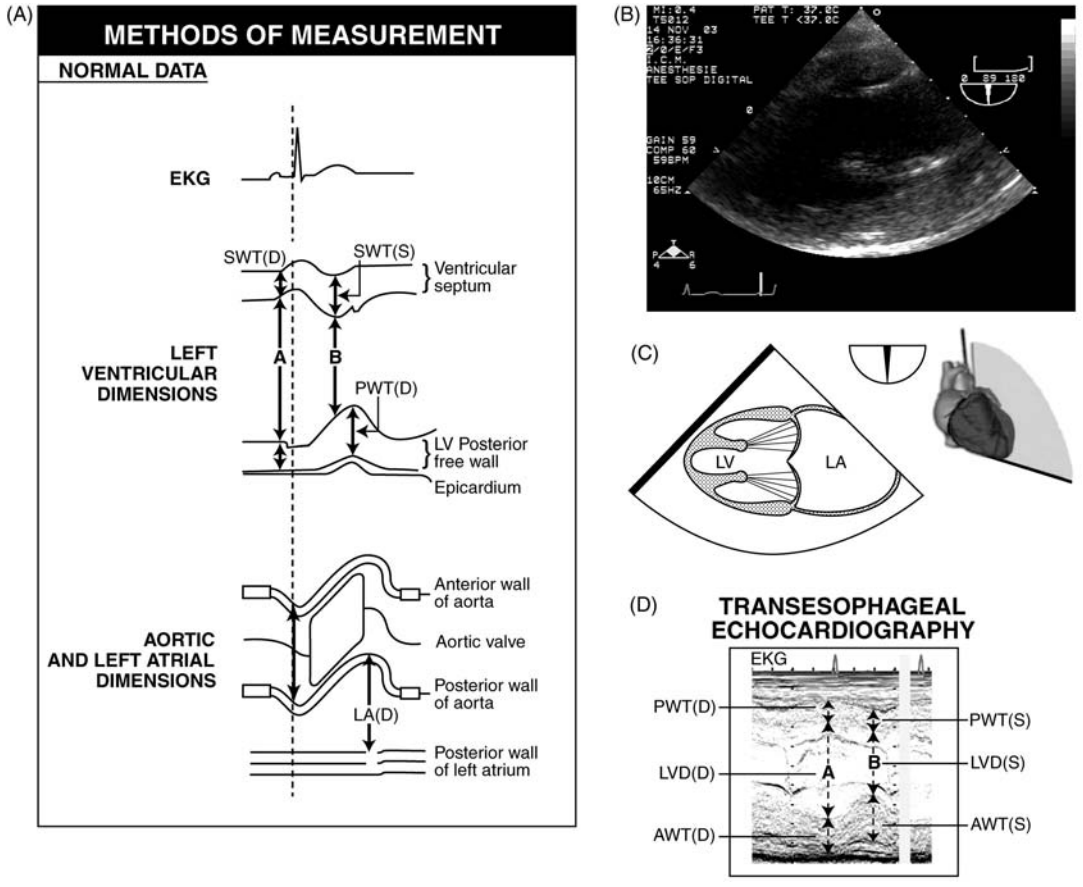

Figure 5.6 (A) Transthoracic echocardiography recommended M-mode measurement of ventricular, aortic and atrial dimensions. (B–D) Equivalent transesophageal echocardiographic measurements from a long-axis transgastric view (AWT, anterior wall thickness in diastole = A and in systole = B; D, diastole; EKG, electrocardiogram; LA, left atrium; LV, left ventricle; LVD, left ventricular diameter in diastole = A and in systole = B; PWT, posterior wall thickness in diastole = A and in systole = B; S, systole; SWT, septal wall thickness in diastole = A and in systole = B).

Measurement of the Left Ventricle

The major, or long, axis of the LV can be measured from a four-chamber view in the mid-esophageal position at 0°, from inner edge of the true apical endocardium to the middle of the mitral valve annulus as determined from the base of the two mitral valve leaflets.

The minor, or short, axis of the LV is measured in the lateral to septal plane perpendicular to the hypothetical long axis at a point located at the junction between the basal and the middle third of the LV (Fig. 5.8). Alternatively, the minor axis has been obtained from the long axis-aortic view in the mid-esophageal position at ~135° perpendicular to the hypothetical long axis at the level of chordal—leaflet junction or at the tips of the mitral valve leaflets. This different anatomical, rather than geometrical, landmark results in different reference values. Finally, the minor axis can also be measured in the anteroseptal–inferolateral plane from a left ventricular short axis transgastric view at 0° at the level of the chordae tendinae or at the papillary muscles (Fig. 5.9).

Measurement of the Right Ventricle

The major, or long, axis of the right ventricle (RV) can be measured from a four-chamber view in the mid-esophageal position at 0°, from inner edge of the true apical endocardium to the middle of the tricuspid valve (TV) annulus as determined from the base of the TV leaflets (Fig. 5.10).

The minor, or short, axis of the right ventricle (RV) is measured in the lateral to septal plane perpendicular to the hypothetical long axis at a point located at the junction between the basal and the middle third of the RV. Alternatively, the minor axis has been obtained from the long axis-aortic view in the mid-esophageal position at ~135° perpendicular to the hypothetical long axis, at the same level as for the minor axis of the LV, i.e. at the

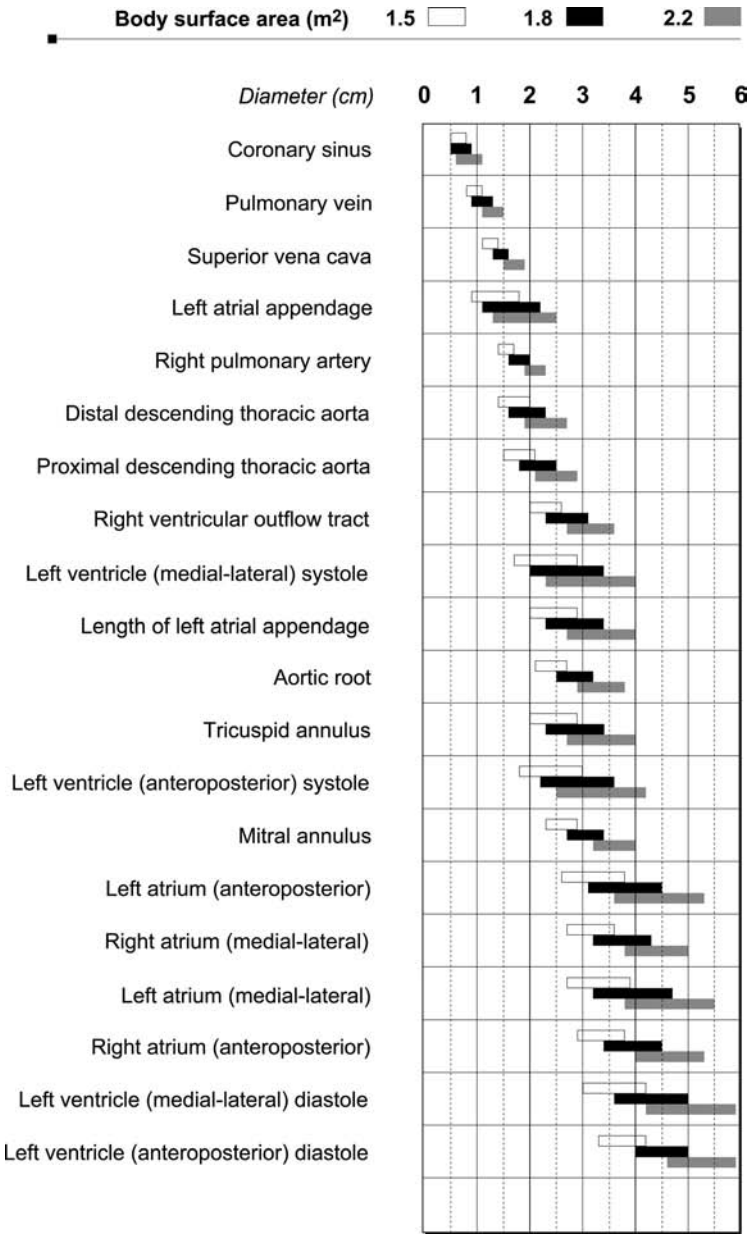

Figure 5.7 Diameters of 2D cardiac structures according to body surface area. [Adapted from Cohen (11)]

chordal–leaflet junction or at the tips of the mitral valve leaflets. However, this measurement may be quite variable.

Measurement of the Left and Right Atria

The major, or long, axis of the left and right atria can be measured in the superior–inferior plane from a four-chamber view in the mid-esophageal position at 0°, from inner edge of the dome of the atria to the middle of the atrioventricular valve annulus (Fig. 5.11). The minor, or short, axis of the left and right atria is measured in the lateral to septal plane perpendicular to the hypothetical long axis at a point located halfway (Fig. 5.12).

Measurement of the Left Ventricular Outflow Tract (LVOT) and Aorta Diameters

The diameter of the aorta is measured at various locations. From the long axis-aortic view in the mid-esophageal position at ∼100–135°, measurements are taken at the LVOT at the base of the aortic cusps, the aortic sinuses, the sinotubular junction and the proximal, middle, and distal ascending aorta (Fig. 5.13).

From the high esophageal position at 90°, the transverse arch can be measured before the origin of the brachiocephalic trunk and between the brachiocephalic trunk

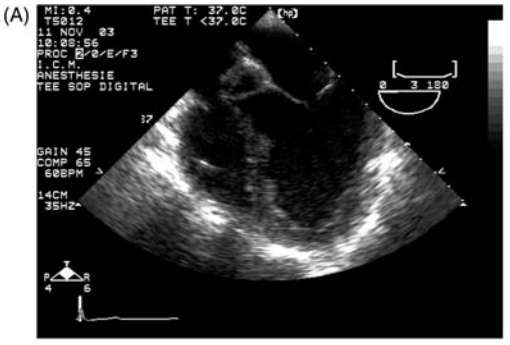

LV diastolic short axis [A] : 4.7 ± 0.7 cm (limits 3.8-5.6 cm)
LV systolic short axis [A] : 3.2 ± 0.7 cm (limits 2.3-4.1 cm)
LV diastolic long axis [B] : 6.1 ± 1.1 cm (limits 4.9-7.4 cm)
LV systolic long axis [B] : 4.9 ± 0.9 cm (limits 3.8-5.9 cm)

Figure 5.8 The left ventricular diameter can be obtained from a mid-esophageal five-chamber view. The normal values are those of a 25-year-old male with a body surface area of 1.8 m^2 [(A), short-axis; Ao, aorta; (B), long-axis; LA, left atrium; LV, left ventricle; RA, right atrium; RV, right ventricle] (6).

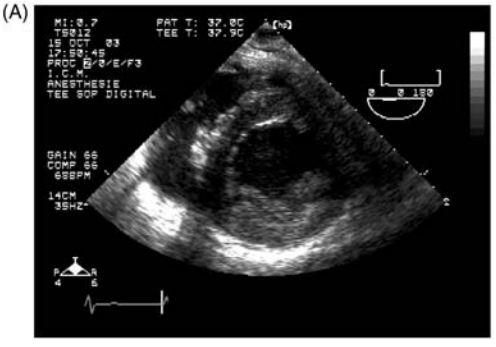

LV diastolic ML [A] : 4.7 ± 0.7 cm (limits 3.8-5.6 cm)
LV systolic ML [A] : 3.1 ± 0.5 cm (limits 2.3-3.8 cm)
LV diastolic AP [B] : 4.5 ± 0.5 cm (limits 3.8-5.2 cm)
LV systolic AP [B] : 3.1 ± 0.5 cm (limits 2.3-3.8 cm)

Figure 5.9 The left ventricular short-axes diameters can be obtained from a transgastric mid-papillary view. Measurements are made from inner edge to inner edge. The normal values are those of a 25-year-old male with a body surface area of 1.8 m^2 [(A), short-axis; AP, anteroposterior; (B), long-axis; LV, left ventricle; ML, medio-lateral; RV, right ventricle] (6).

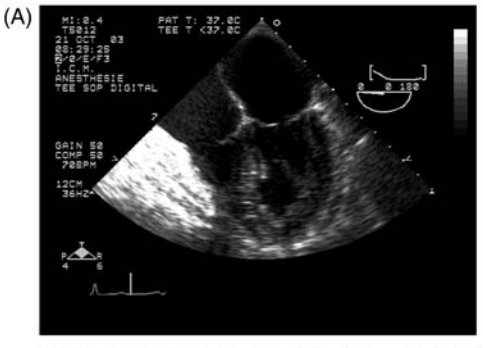

RV diastolic short axis [A] : 2.9 ± 0.5 cm (limits 2.2-3.6 cm)
RV systolic short axis [A] : 1.8 ± 0.4 cm (limits 1.4-2.2 cm)
RV diastolic long axis [B] : 5.0 ± 0.7 cm (limits 4.1-5.9 cm)
RV systolic long axis [B] : 4.1 ± 0.7 cm (limits 3.2-5.0 cm)

Figure 5.10 Mid-esophageal four-chamber view of the right ventricle (RV). The normal values are those of a 63-year-old male with a body surface area of 1.8 m^2 [(A), short-axis; (B), long-axis; LA, left atrium; LV, left ventricle; RA, right atrium] (6).

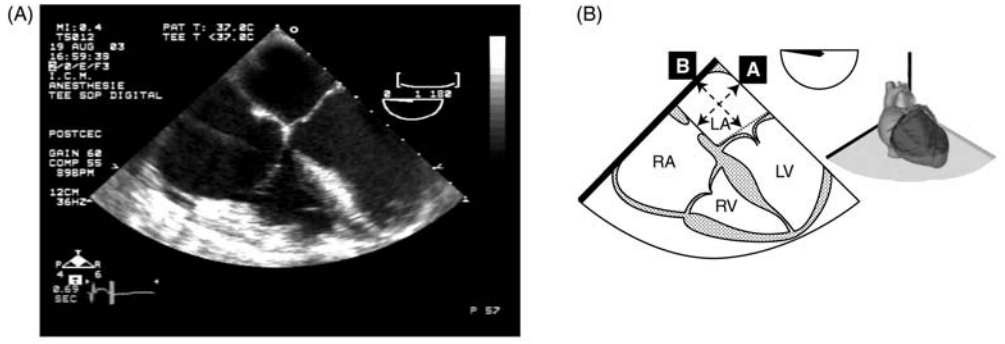

Figure 5.11 Mid-esophageal four-chamber view and measurements of the left atrium (LA). The normal values are those of a 25-year-old male with a body surface area of 1.8 m^2 [(A), short-axis; AP, antero-posterior; (B), long-axis; LV, left ventricle; ML, medio-lateral; RA, right atrium; RV, right ventricle] (6).

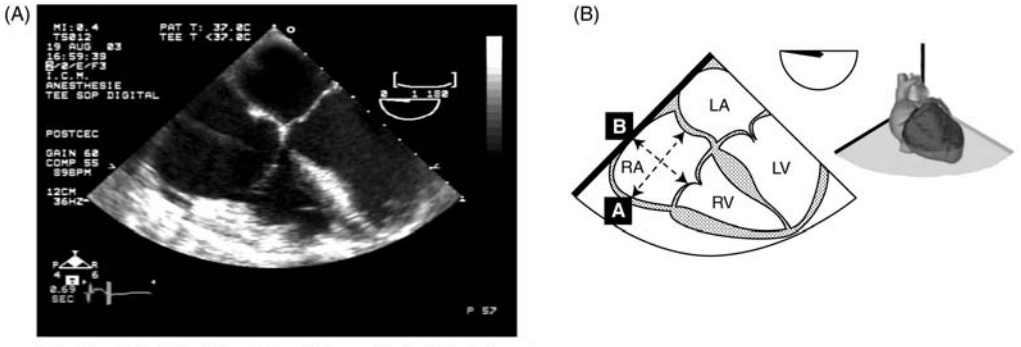

Figure 5.12 Mid-esophageal four-chamber view and measurements of the right atrium (RA). The normal values are those of a 25-year-old male with a body surface area of 1.8 m^2 [(A), short-axis; AP, antero-posterior; (B), long-axis; LA, left atrium; LV, left ventricle; ML, medio-lateral; RV, right ventricle] (6).

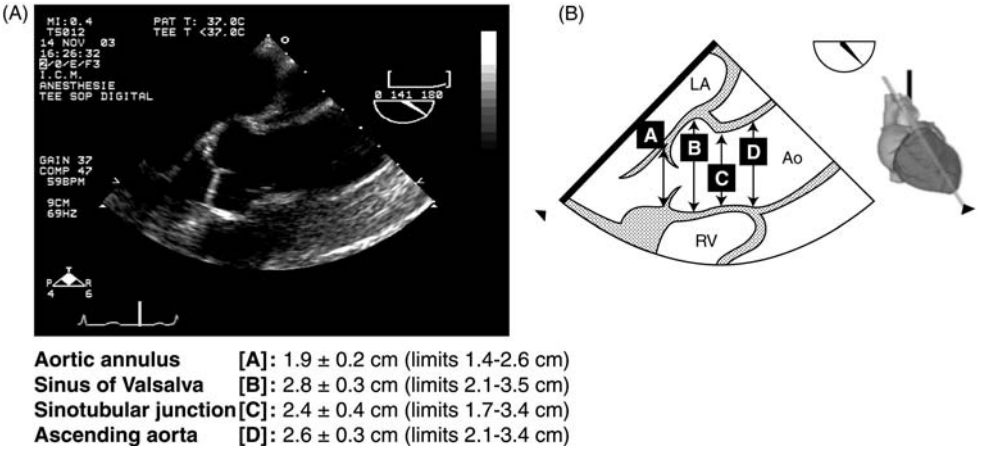

Figure 5.13 Mid-esophageal long-axis view of the left ventricular outflow tract (LVOT) and various parts of the ascending aorta (Ao). The LVOT diameter is measured at the aortic annulus (LA, left atrium; RV, right ventricle) (12).

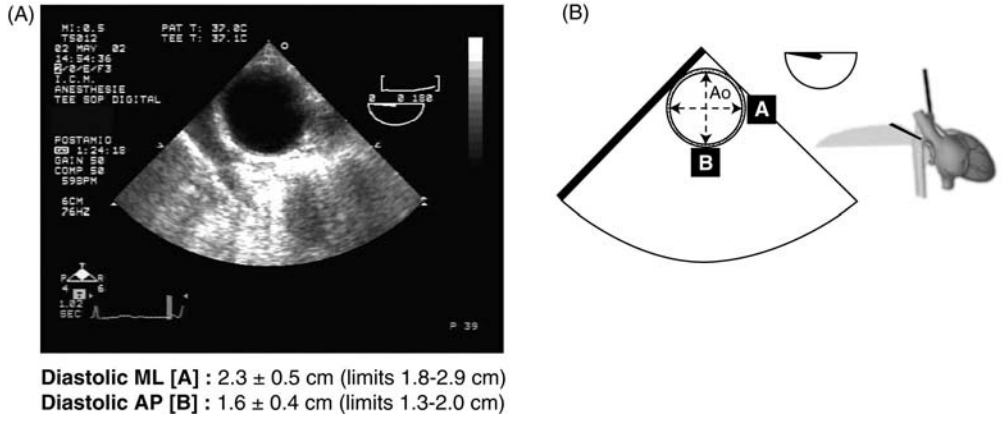

Figure 5.14 Deep esophageal view of the descending aorta (Ao) and two-dimensional measurements. The normal values are those in a 25-year-old male with a body surface area of 1.8 m^2 [(A), short-axis; AP, antero-posterior; (B), long-axis; ML, medio-lateral] (6).

and the left common carotid artery (see Fig. 4.33). At 0° from the high esophageal position to the transgastric position, the diameter of the descending thoracic and upper abdominal aorta can also be measured (Fig. 5.14).

Measurement of the Right Ventricular Outflow Tract and Pulmonary Artery Diameters

The diameter of the right venricular outflow tract (RVOT) can be measured at the base of the pulmonic valve cusps in the short-axis view of the AoV in the mid-esophageal position at ~45°, and that of the main pulmonary trunk is also obtained in this view (Fig. 5.15). However, the diameter of the origin of the right and left pulmonary arteries is more easily obtained in a slightly more superior esophageal position at 0° (Fig. 5.16).

Measurement of the Inferior Vena Cava and Hepatic Veins

The inferior vena cava and the hepatic veins can be measured from a transgastric view directed towards the liver on the right side at ~90° (Figs. 5.17 and 5.18).

Measurement of the Atrioventricular Valve Annular Diameters

The TV annulus diameter is obtained from the four-chamber view in the mid-esophageal position at 0°. The two diameters of the saddle-shaped mitral valve annulus may be obtained from the four-chamber view in the mid-esophageal position at 0° and from the two-chamber view at 90°. Measurements should be taken from the base of the leaflets (Fig. 5.19).

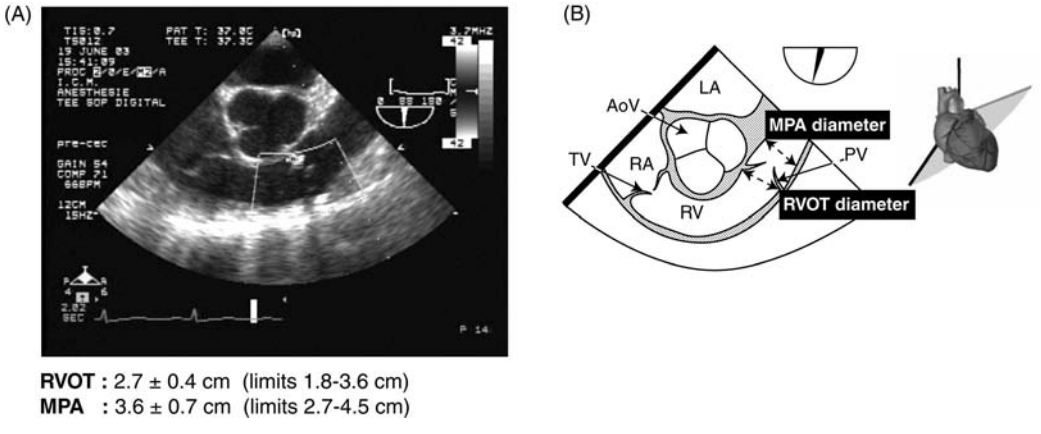

Figure 5.15 Mid-esophageal short-axis view of the right ventricle (RV) and the right ventricular inflow and outflow tract. Measurements for the right ventricular outflow tract (RVOT) and main pulmonary artery (MPA) are shown. The normal values are those of a 25-year-old male with a body surface area of 1.8 m^2 (AoV, aortic valve; LA, left atrium; PV, pulmonic valve; RA, right atrium; TV, tricuspid valve) (6,11).

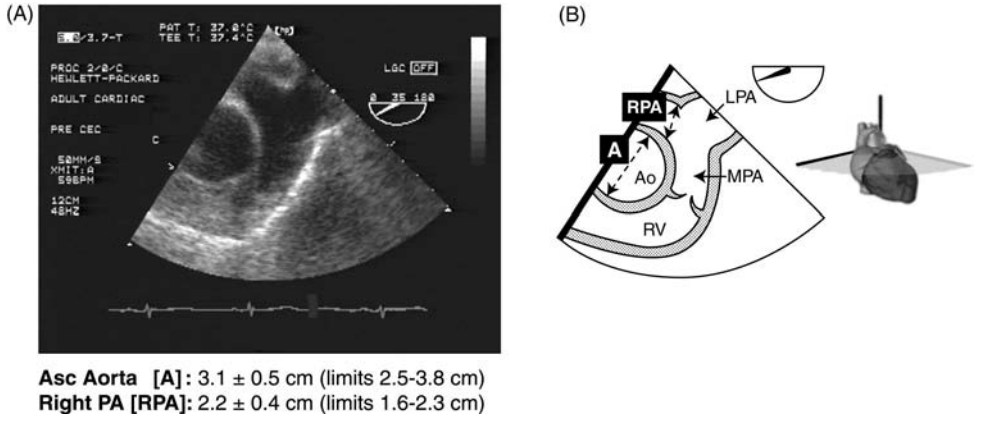

Figure 5.16 Upper esophageal short-axis view of the ascending aorta (Asc Ao) and pulmonary artery. Measurements of the origin of the right pulmonary artery (RPA) are made using this view. The normal values are those of a 25-year-old male with a body surface area of 1.8 m^2 [(A), short-axis; LPA, left pulmonary artery; MPA, main pulmonary artery; PA, pulmonary artery; RV, right ventricle] (6).

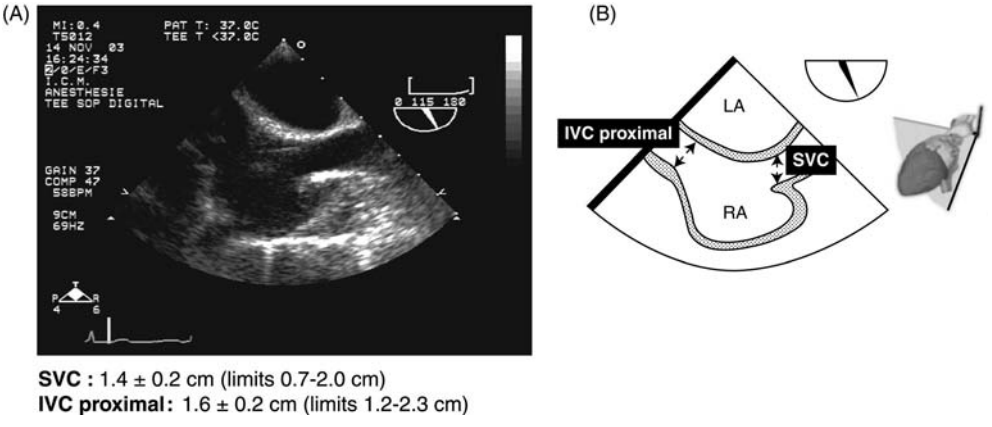

Figure 5.17 Mid-esophageal bicaval view for the measurements of the vena cavae (IVC, inferior vena cava; LA, left atrium; RA, right atrium; SVC, superior vena cava) (11,12).

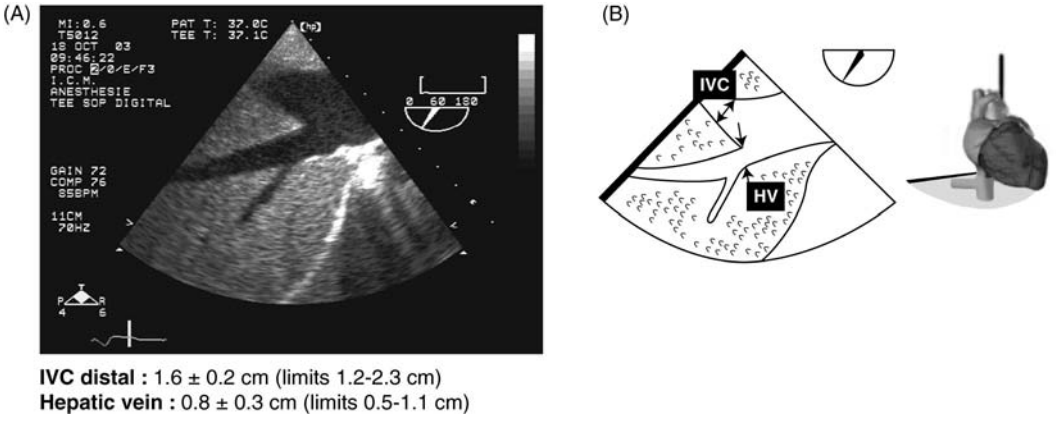

Figure 5.18 Lower esophageal view of the inferior vena cava (IVC) and hepatic vein (HV) (13).

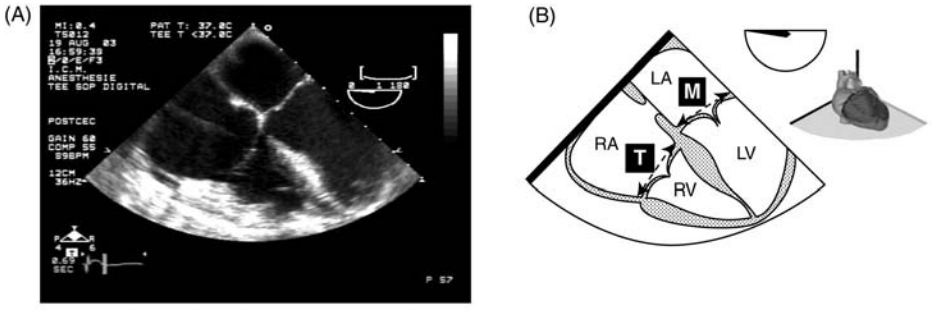

Figure 5.19 Both mitral (M) and tricuspid (T) annular diameters are obtained through a mid-esophageal four-chamber view. (LA, left atrium; LV, left ventricle; RA, right atrium; RV, right ventricle) (11).

Measurement of the Pulmonary Vein, Left Atrial Appendage and Coronary Sinus

The left upper pulmonary vein is easily located through a mid-esophageal view close to the left atrial appendage (LAA) where measurement of both structures can be performed (Figs. 5.20 and 5.21). The right-sided pulmonary veins are easier to identify using a bicaval view with right-side rotation (Fig. 5.22). Finally the coronary sinus diameter is measured with a mid-esophageal four-chamber view using retroflexion (Fig. 5.23).

F. Chamber Dimensions, Volume Calculations, Ejection Fraction

Various methods have been described to estimate left ventricular volumes from cardiac chamber dimensions measured in M-mode and 2D echocardiography. However, they are based on the assumption that the ventricle has a symmetrical geometric form. This assumption is correct if the heart is normal but may not hold true if the heart is deformed by an aneurysm, or becomes asymmetrical in systole due to regional wall motion abnormalities.

Earlier correlation with left ventricular volumes assessed by angiographic data (14) seemed to suggest a reasonable relationship with estimations derived from cubing the cavity dimensions. The cubic method assumes that the LV shape can be approximated by a prolate symmetrical ellipse with a major axis (L) and two minor axes (d_1 and d_2). Mathematically, the volume of a prolate ellipse is given by the following equation:

$$\text{Volume} = \pi \frac{4}{3} \times \frac{d_1}{2} \times \frac{d_2}{2} \times \frac{L}{2} \tag{5.1}$$

Assuming that the LV has two identical minor axes ($d_1 = d_2$) and a major axis twice the size of the minor axis ($L = 2d$), the volume can thus be estimated by the following simplified equation:

$$\text{Volume} = d^3 \tag{5.2}$$

where d represents the left ventricular dimension in diastole (LVEDD) or in systole (LVESD). This estimate is relatively close in diastole but less so in systole or with left ventricular dilatation. Other investigators have introduced correction factors for change in ventricular

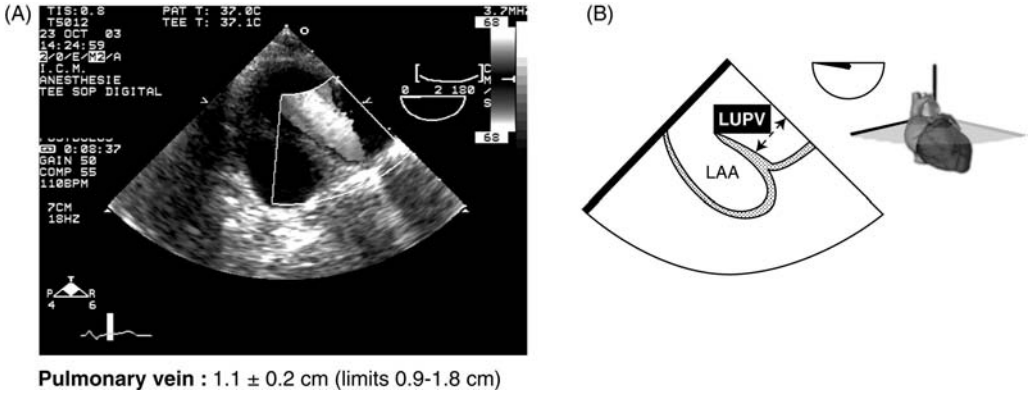

Figure 5.20 Mid-esophageal view of the left upper pulmonary vein (LUPV) close to the left atrial appendage (LAA). The measurement of the pulmonary vein diameter is made at 1 cm from where the pulmonary vein enters the left atrium (11).

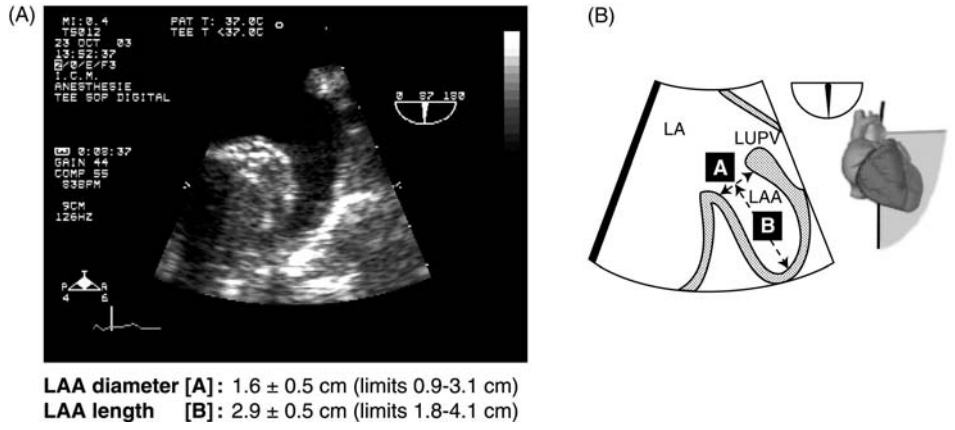

Figure 5.21 Mid-esophageal view of the left atrial appendage (LAA). The LAA diameter is taken at the ostium near the tip of the pulmonary vein limbus ("coumadin ridge" or "Q-tip" sign) representing the separation between the left upper pulmonary vein (LUPV) from the LAA. The length of the LAA extends from the tip to the line used for measuring the diameter [(A), short-axis; (B), long-axis or length; LA, left atrium] (11).

assumed shape and the Teichholz's method (15) seems to have the least imprecisions (16) and has been incorporated in most commercialized echocardiography system on-line analysis software as given by the following equation:

$$\text{Volume} = d^3 \times \frac{7.0}{2.4 + d} \tag{5.3}$$

To minimize the error caused by too many geometric assumptions, investigators have developed different methods utilizing more measurements available from 2D echocardiography. The ASE now recommends two methods to estimate left ventricular volumes from left ventricular cavity area, and long axis measurements from the four- and two-chamber orthogonal views: the modified

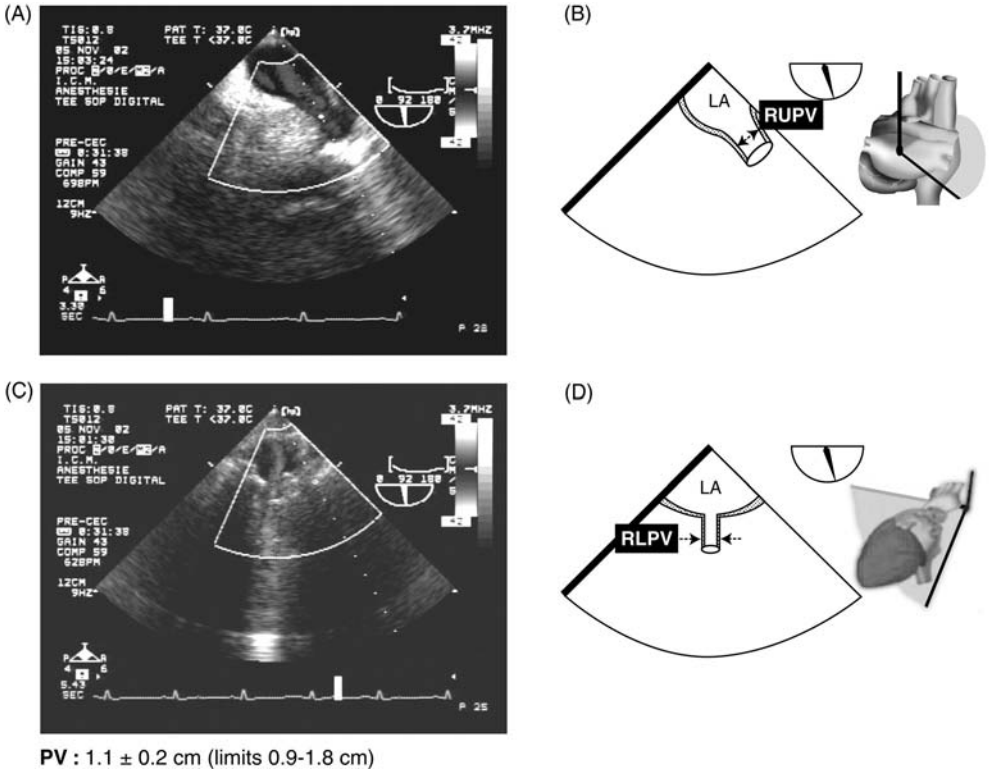

Figure 5.22 Mid-esophageal views of the right upper (A, B) and lower (C, D) pulmonary veins (PV). The measurement is made at 1 cm from where the PV enters the left atrium (LA) (RLPV, right lower pulmonary vein; RUPV, right upper pulmonary vein) (11).

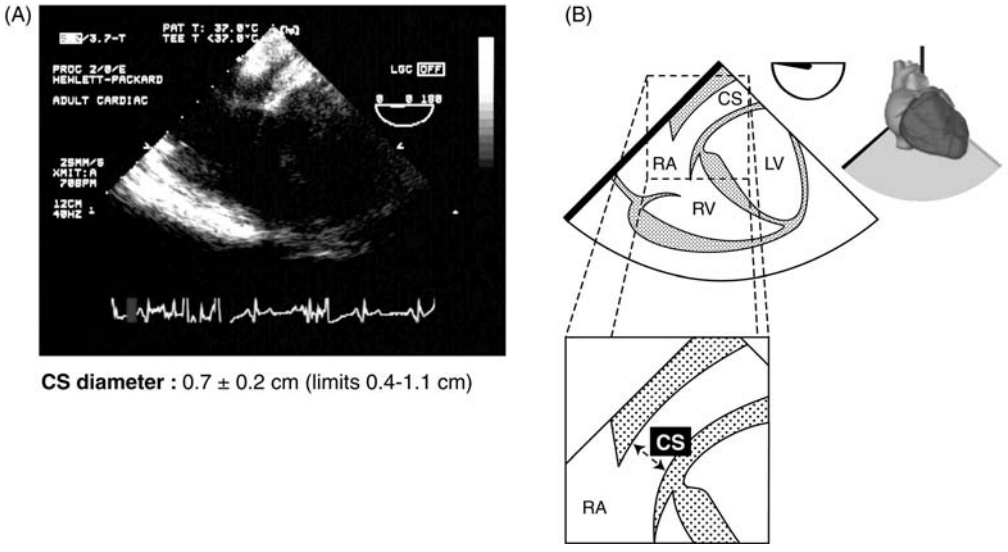

Figure 5.23 Low-esophageal four-chamber view of the coronary sinus (CS). The diameter is measured 1 cm proximal to where it enters the right atrium (RA) (LV, left ventricle; RV, right ventricle) (11).

Simpson's biplane method and the single plane area–length method.

1. *The Modified Simpson's Biplane Method*

The Simpson's rule states that the volume of a cavity is equal to the sum of the volumes of a series of smaller slices (disc summation method): the volume of each slice (disc) is obtained by knowing its surface area and thickness. The modified Simpson's biplane method applies this algorithm in the determination of left ventricular volume from two orthogonal views, the four- and the two-chamber views (Fig. 5.24). The thickness of each disc is calculated by dividing the length (L) of the left ventricular major axis into 20 equal segments ($L/20$). The surface area of each disc is obtained from measuring, on each of these 20 discs, the two orthogonal minor axes (a and b). Once the left ventricular endocardial border has been manually traced in the four- and the two-chamber views, most of the state-of-the-art cardiac ultrasound systems will nowadays derive those two orthogonal diameters (a and b) by taking the distance between the opposite endocardial intercepts of lines drawn perpendicular to the long axis at each disc. Thus, the left ventricular volume is automatically calculated with the following formula:

$$\text{Volume} = \frac{\pi}{4}\sum_{i=1}^{20} a_i b_i \frac{L}{20} \tag{5.4}$$

where a is the diameter (cm) of the disk in the four-chamber view; b is the diameter (cm) of the disk in the two-chamber view; and L is the length (cm) of the long axis of the LV.

However, as this method assumes that the length of the LV is similar in the two orthogonal views, its accuracy decreases if the measurements of the major axis of the LV in the four- and the two-chamber views differs by $>20\%$.

2. *The Single Plane Area–Length Method*

As its name implies it, this method uses the left ventricular area from one single view and assumes that the two orthogonal views of the LV are symmetrical. The formula for calculating the left ventricular volumes by this method is expressed by the following equation:

$$\text{Volume} = 0.85\frac{A^2}{L} \tag{5.5}$$

where A is the area (cm^2) of the LV in either the four- or two-chamber view and L is the length (cm) of the long axis of the LV.

3. *Ejection Fraction*

The left ventricular ejection fraction (LVEF) is defined as the percentage (or the fraction) of the left ventricular end-diastolic volume which is ejected with each systole, that is, the ratio of the stroke volume to the end-diastolic volume (Fig. 5.24). The LVEF (in %) can be expressed by the following equation:

$$\text{LVEF} = \frac{\text{SV}}{\text{LVEDV}} \times 100 = \frac{\text{LVEDV} - \text{LVESV}}{\text{LVEDV}} \times 100 \tag{5.6}$$

where LVEF is the left ventricular ejection fraction (in %); SV is the stroke volume (in mL); LVEDV is the left

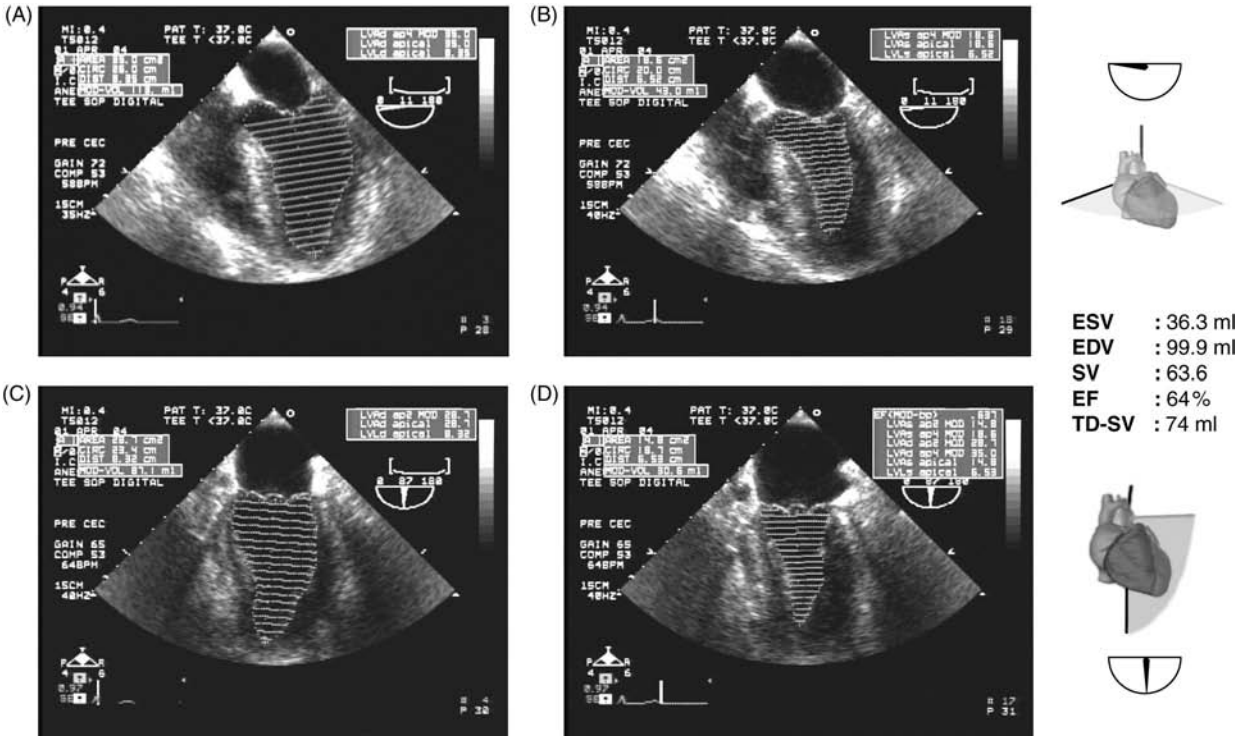

Figure 5.24 Measurement of left ventricular volumes by the modified Simpson's biplane method using a mid-esophageal four- (A, B) and two-chamber (C, D) views. The calculated echocardiographic stroke volume (SV) was slightly different from the SV measured with thermodilution (TD). (EDV, end-diastolic volume; EF, ejection fraction; ESV, end-systolic volume).

ventricular end-diastolic volume (in mL); and LVESV is the left ventricular end-systolic volume (in mL). The normal LVEF is 55–75%.

One must remember that the LVEF does not only constitute a measure of myocardial contractility. It represents the efficiency of the global cardiac pump to eject part of its end-diastolic volume, which may be affected by the preload, the afterload, and the myocardial contractility (see Chapter 9).

G. Global Function

Several indices of left ventricular global systolic function can be derived from the measurement of the LVEDD and LVESD. As these indices are based on measurements of a single dimension of the basal LV from the anteroseptal and the inferolateral walls, they are less accurate in the presence of regional wall motion abnormalities involving the other left ventricular segments.

1. Fractional Shortening

Left ventricular fractional shortening (FS) is defined as the percentage of change (shortening) of the left ventricular cavity dimension with each systole (Fig. 5.25). The FS (in %) can be expressed by the following equation:

$$\mathrm{FS} = \frac{\mathrm{LVEDD} - \mathrm{LVESD}}{\mathrm{LVEDD}} \times 100 \qquad (5.7)$$

where FS is the fractional shortening (in %); LVEDD is the left ventricular end-diastolic dimension (in cm); and LVESD is the left ventricular end-systolic dimension (in cm). The normal FS is 28–45% (17).

2. Ejection Fraction

The left ventricular ejection fraction can be determined from estimation of the end-diastolic and end-systolic volumes derived from standard M-mode measurements of the left ventricular cavity dimension (Fig. 5.25). The uncorrected LVEF (in %) is calculated from the following equation:

$$\mathrm{LVEF} = \frac{\mathrm{LVEDD}^2 - \mathrm{LVESD}^2}{\mathrm{LVEDD}^2} \times 100 \qquad (5.8)$$

where LVEF is the left ventricular ejection fraction (in %); LVEDD is the left ventricular end-diastolic dimension (in cm); and LVESD is the left ventricular end-systolic dimension (in cm).

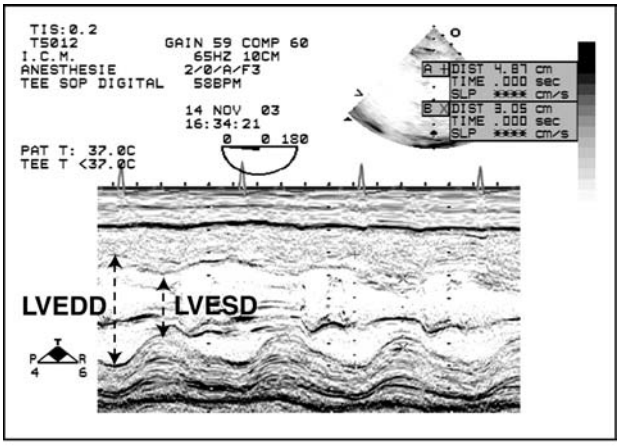

$$\text{FS}: \frac{\text{LVEDD} - \text{LVESD}}{\text{LVEDD}} \quad (\text{normal} = 28\text{-}45\%)$$

$$: \frac{4.8 - 3.0}{4.8} = 37.5\%$$

$$\text{EF}: \frac{\text{LVEDD}^2 - \text{LVESD}^2}{\text{LVEDD}^2} \quad (\text{normal} = 50\text{-}75\%)$$

$$: 60\%$$

Figure 5.25 Calculation of fractional shortening (FS) and ejection fraction (EF) using the left ventricular end-diastolic diameter (LVEDD) and left ventricular end-systolic diameter (LVESD) seen in a 64-year-old man before coronary revascularization.

As this method bases its estimate of the LVEF only on the change of the left ventricular minor axis, an alternate estimation of the EF described by Quinones and colleagues (18) accounts for the change in both minor and major axis during systole.

3. *Stroke Volume, Cardiac Output, and Cardiac Index*

The stroke volume (SV) is the blood volume ejected from the LV during each systole and can be calculated from the difference between the LVEDV and LVESV obtained by the previously described M-mode or 2D echocardiographic methods (Fig. 5.24).

Note that the SV can alternatively be calculated by Doppler volumetric method (*vide infra*). The cardiac output (CO) is the amount of blood pumped by the heart per minute. It is most commonly reported in liters per minute:

$$\text{SV} = \text{LVEDV} - \text{LVESV} \tag{5.9}$$

$$\text{CO} = \text{SV} \times \text{HR} \times 0.001 \tag{5.10}$$

where CO is the cardiac output (in L/min); SV is the stroke volume (in mL); and HR is the heart rate (in bpm).

The CO is often indexed to the patient's body size to facilitate comparison with reference values. The cardiac index (CI) is obtained by the following equation:

$$\text{CI} = \frac{\text{CO}}{\text{BSA}} \tag{5.11}$$

where CI is the cardiac index (in L/min per m^2) and BSA is the body surface area (m^2).

4. *Systolic Time Intervals*

Left ventricular systolic performance can be also evaluated by systolic time intervals, measured on the M-mode echocardiogram of the AoV. The left ventricular preejection period (LVPEP) is measured from the onset of the QRS to the opening of the AoV. The left ventricular ejection time (LVET), or period, encompasses the time between the AoV opening and closure. Both parameters decrease with increasing heart rate (HR). The ratio of LVPEP/LVET is less affected by HR. Furthermore, with worsening systolic function, the ratio changes to a greater extent than its component as the LVPEP increases while the LVET decreases. The LVET can be measured using TEE (19) (Fig. 5.26). The LVPEP/LVET ratio is normally inferior to 0.35 and has shown good correlation with LVEF measured by contrast left ventriculography in a small study (20).

The right and left ventricular myocardial performance index (MPI) incorporates both systolic and diastolic time intervals, and as these are more easily obtained on Doppler tracings, they will be covered further in Chapter 9.

H. Fractional Area Change

The fractional area change (FAC) can be used for the estimation of left ventricular systolic performance. The FAC (in %) can be expressed by the following equation:

$$\text{FAC} = \frac{\text{EDA} - \text{ESA}}{\text{EDA}} \times 100 \tag{5.12}$$

where FAC is the fractional area change (in %); EDA is the end-diastolic area (in cm^2); and ESA is the end-systolic area (in cm^2).

The left ventricular areas are obtained by tracing the inner edge of the endocardium in the transgastric short axis views. The normal values range from 36 to 64%, depending on the level where it is measured (40% for the base, 50% at the mid-papillary muscle, and 60% at the apical levels) (Fig. 5.27). Studies have shown good correlation between the FAC and the LVEF measured by both radionuclide and contrast biplane ventriculography (22). By tracking the endocardial border automatically using integrated backscatter, attempts were made to obtain real-time end-diastolic and end-systolic areas, and hence on-line real-time FAC measurements. However, compared with manual tracing by experienced operators,

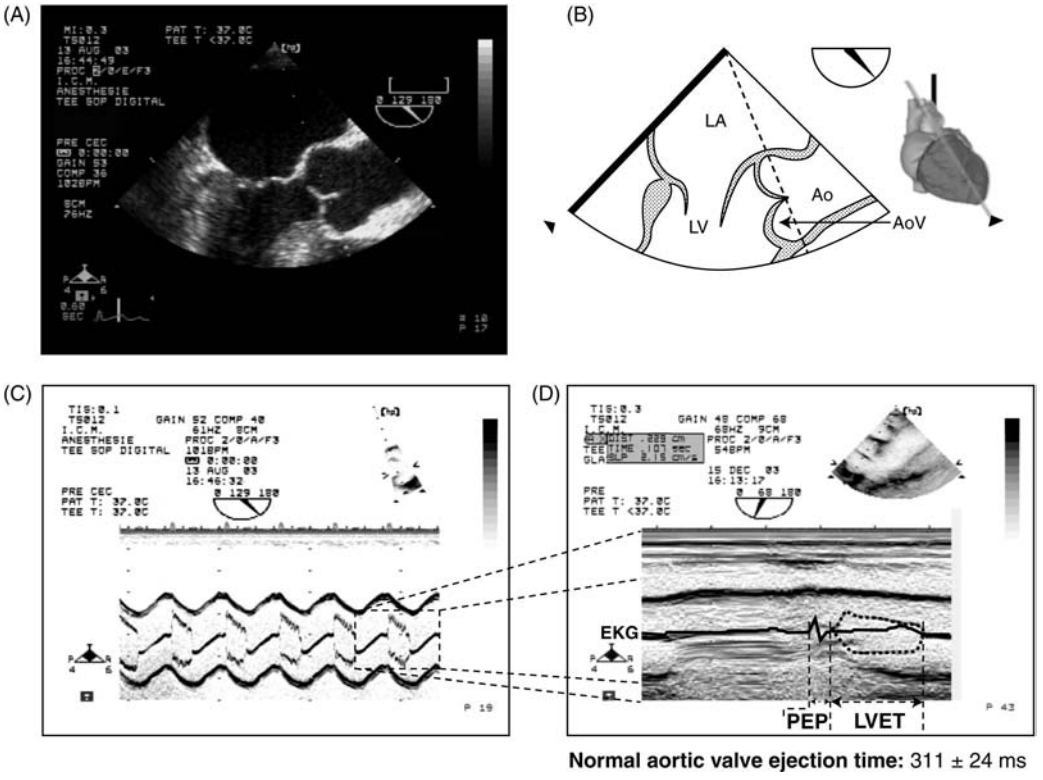

Figure 5.26 Measurement of the left ventricular time indices. (A, B) Mid-esophageal long-axis view. (C) M-mode at a sweep speed of 25 mm/s. (D) M-mode at a sweep speed of 100 mm/s with electrocardiographic tracing positionned in the M-mode. The left ventricular pre-ejection period (PEP) is measured from the onset of the QRS to the opening of the aortic valve (AoV). The left ventricular ejection time (LVET) corresponds to the duration of the AoV opening. Normal values are those obtained from healthy adult (21) (Ao, aorta; EKG, electrocardiogram; LA, left atrium; LV, left ventricle).

the automated border detection system tended to overestimate the ESA and underestimate the EDA, resulting in an unacceptably low FAC estimate (23). These errors were, in part, due to inadequate tracking influenced by critical time-gain compensation settings, myocardial dropout (anisotropy), and moving of the region of interest.

I. Circumferential Fiber Shortening

Circumferential fiber shortening is a different index of systolic function. As the circumference and the diameter are directly related by π, circumference change can be converted from diameter reduction. Furthermore, by dividing the extent of shortening over the LVET, this index reflects the mean velocity of ventricular circumferential shortening of the minor axis of the LV (mean Vcf), as illustrated by the following equation:

$$\text{Mean Vcf} = \frac{\text{FS}}{\text{LVET}} = \frac{\text{LVEDD} - \text{LVESD}}{\text{LVEDD} \times \text{LVET}} \qquad (5.13)$$

where Mean Vcf is the mean rate of circumferential fiber shortening (in units of circumferences per second); LVEDD is the left ventricular end-diastolic dimension (in cm); LVESD is the left ventricular end-systolic dimension (in cm); LVET is the left ventricular ejection time or period (in s); and FS is the left ventricular fractional shortening (in fraction, not in %). The normal Vcf is 1.09 ± 0.3 (24).

J. Wall Thickness, Mass, Stress

In 1935, Tennants and Wiggers (25) first described the immediate cessation of myocardial wall thickening after the ligation of a coronary artery in a canine model. Analysis has subsequently shown wall thickening to be an early sensitive marker of myocardial ischemia. This was initially reported by M-mode echocardiography which could detect thickening of the myocardium directly, but only on a 1D ice-pick view of the anteroseptal and inferolateral walls. With the advent of 2D echocardiography, this limitation was overcome by the ability to examine the entire myocardium utilizing multiple tomographic planes (26), and also by ensuring more accurate wall thickness measurements in a direction truly perpendicular to the wall. The

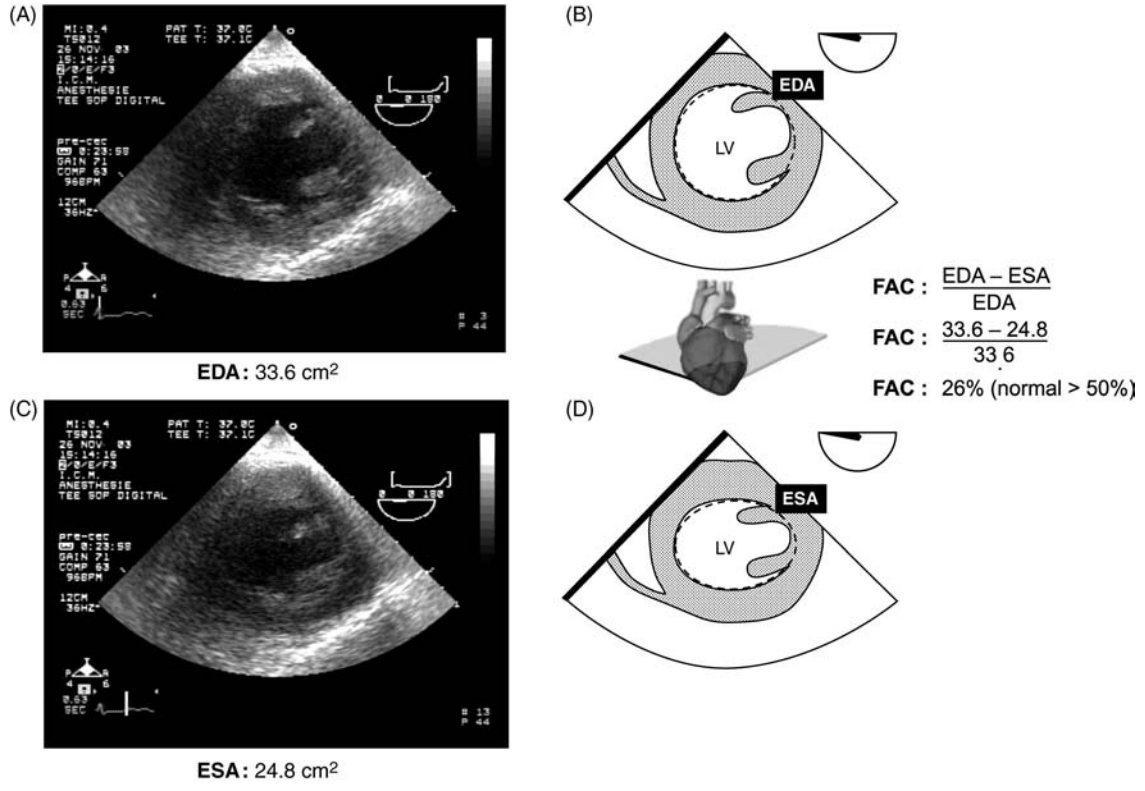

Figure 5.27 Measurement of fractional area change (FAC) in a 75-year-old man with unstable angina undergoing emergency revascularisation. A transgastric mid-papillary view of the left ventricle (LV) in diastole (A, B) and in systole (C, D) provides the measurements to calculate the FAC which was 26% (EDA, end-diastolic area; ESA, end-systolic area).

percentage of left ventricular wall thickening is helpful to compare the contractility of different myocardial segments. It is calculated according to the following equation:

$$\mathrm{WT} = \frac{\mathrm{EST} - \mathrm{EDT}}{\mathrm{EST}} \times 100 \tag{5.14}$$

where WT is the wall thickening (in %); EST is the end-systolic thickness; and EDT is the end-diastolic thickness.

Although an increase in left ventricular wall thickness could reflect an increase in left ventricular mass, redistribution of a normal left ventricular mass over a smaller cavity may cause an apparent increase in wall thickness without constituting left ventricular hypertrophy. Therefore, left ventricular mass as determined by pathologists is better assessed by determining the left ventricular muscle volume and converting the volume to a mass using the specific gravity of myocardium (1.040 g/mL). This is done by subtracting the left ventricular endocardial or chamber volume from the epicardial or total volume.

Left ventricular mass can be determined from the M-mode end-diastolic measurement of the interventricular septum wall thickness (IVST), the LVEDD, and the PWT using the ASE cube formula [see Eq. (5.15a)].

1. The ASE–Devereux Method

The ASE cube method [Eq. (5.15a)] uses a leading edge to leading edge technique for the M-mode measurements but this results in a 25% overestimation of the true left ventricular mass (27). Devereux and colleagues proposed the following corrected formula [Eq. (5.15)] to derive the left ventricular mass:

$$\mathrm{LV\ Mass_{ASE}} = 1.04[(\mathrm{IVST} + \mathrm{LVEDD} + \mathrm{PWT})^3 - (\mathrm{LVEDD})^3] \tag{5.15a}$$

$$\mathrm{LV\ Mass_{ASE\text{-}Devereux}} = 1.04[(\mathrm{IVST} + \mathrm{LVEDD} + \mathrm{PWT})^3 - (\mathrm{LVEDD})^3] \times 0.8 + 0.6 \tag{5.15b}$$

Left ventricular mass can also be measured by 2D methods estimating total ventricular volume contained within the epicardial borders less the left ventricular cavity volume delineated by the endocardial borders.

2. Wall Stress

Finally, evaluation of left ventricular wall stress provides an index of systolic function believed to be less dependent

on loading conditions. Usually measured in systole, it requires measurement of the left ventricular cavity dimension, the wall thickness (measured in the posterior wall), and the systolic blood pressure (SBP).

The left ventricular meridian wall stress is calculated according to the following equation:

$$\mathrm{LVWS_{meridian}} = 0.334\frac{\mathrm{sBP} \times \mathrm{LVESD}}{\mathrm{PWT}[1 + (\mathrm{PWT}/\mathrm{LVESD})]} \tag{5.16}$$

where LVWS is the left ventricular wall stress (in dynes/cm^2); sBP is the systolic blood pressure (in mmHg); LVESD is the left ventricular end-systolic diameter (in cm); and PWT is the posterior wall thickness (in cm).

As peak wall stress occurs during the isovolumetric contraction, the left ventricular dimension can be obtained at end-diastole. Therefore, left ventricular meridian wall stress can be obtained from the following simplified equation:

$$\mathrm{LVWS_{meridian}} = \frac{\mathrm{sBP} \times \mathrm{LVEDD}}{\mathrm{PWT}} \tag{5.17}$$

II. DOPPLER

The principles of Doppler are discussed in Chapter 2. Velocities obtained through the spectral analysis of the Doppler echo signals can be plotted on the *y* axis against time to give a spectral (Doppler) display (Fig. 5.28). The direction of flow is indicated by positive (above the zero baseline) values for flow directed towards the probe. The flow velocity is indicated over the *y* axis. The timing and the duration of the flow are measured on the *x* axis. The intensity of the signal gives an indication of the number of echoes from red blood cells measured at the indicated time and velocity variables: it serves not only to indicate how many red blood cells were found to move at that velocity at that particular time, but help to characterize if a flow is uniform, laminar, or turbulent by looking at the whole time and velocity display.

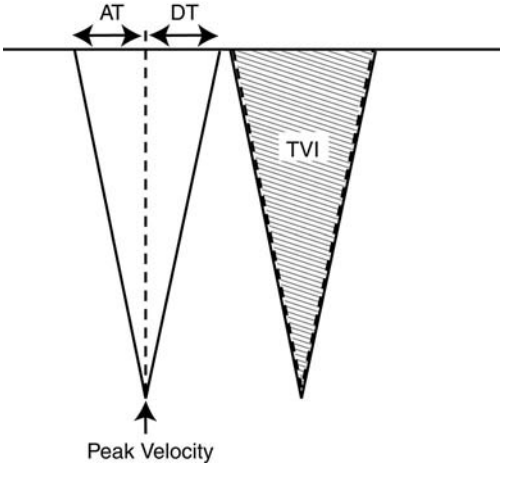

Figure 5.28 Schematic Doppler spectral display (AT, acceleration time; DT, deceleration time; TVI, time velocity integral).

The maximum velocity (either positive or negative) recorded during a flow period is called the peak velocity. All the measured velocities may be averaged over a flow period to give the mean velocity. Most of the modern echocardiography systems can easily display these two values by tracing the outline of the whole flow velocity signal. Integrating the area under the flow velocity values (in cm/sec) against time (in s) results in the time–velocity integral or TVI, which gives the *stroke distance*, the distance reached by the blood column with each heartbeat. These parameters are mostly measured on semilunar valve outflow signals or regurgitant jets (Fig. 5.29).

If, however, you trace the flow velocity signal where it is the brightest, that is, where most of the red blood cells are found, the value obtained represents the modal velocity which reflects the dominant flow velocity at any given time. These parameters are characteristically measured on atrioventricular valve inflow signals.

The estimation of blood flow velocities determined by the Doppler principle forms the basis of several hemodynamic measurements in quantitative echocardiography.

A. Blood Flow

The blood flow through a vessel is not only determined by the pressure difference between two points (the driving pressure), but also by the resistance to flow which is influenced by the radius and the length of the vessel, and the viscosity of the blood. This can be described by the following equation (Poiseuille's law):

$$Q = \frac{\Delta P}{R} = \frac{\Delta P \pi r^4}{8Lv} \tag{5.18}$$

where Q is the blood flow rate (in mL/sec); ΔP is the pressure gradient (in dynes/cm^2); R is the resistance to flow (in g/cm^4 per second); r is the radius of the blood vessel (in cm); L is the length of the blood vessel (in cm) over which the pressure drop occurs; and v is the viscosity of blood (in poise).

B. Conservation of Energy Principle and Pressure Difference (Gradient)

The driving pressure responsible for the movement of blood through the cardiovascular system can be derived from the application of the conservation of energy principle. This principle states that the total energy within a system is constant unless superimposed external forces are applied. This can be expressed by the

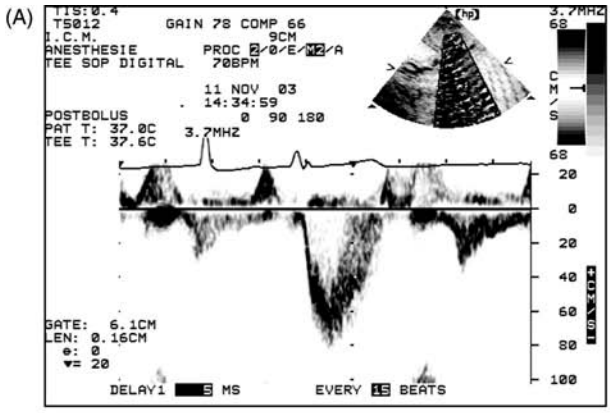

LVOT VELOCITY

Maximal velocity:	89 ± 14 cm/sec
Acceleration time:	98 ± 20 ms
Ejection time:	311 ± 24 ms
Mean acceleration:	8.45 ± 2.43 m/s^2
Time velocity integral:	17 ± 3 cm

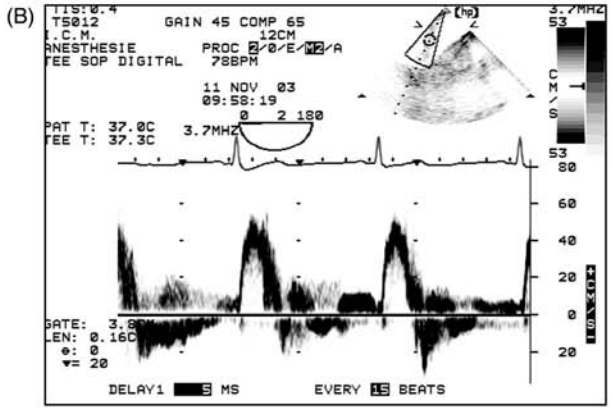

ASCENDING AORTIC VELOCITY

Maximal velocity:	66 ± 11 cm/sec
Acceleration time:	61 ± 3 ms
Ejection time:	239 ± 43 ms
Mean acceleration:	7.23 ± 2.12 m/s^2
Time velocity integral:	10.5 ± 2.7 cm

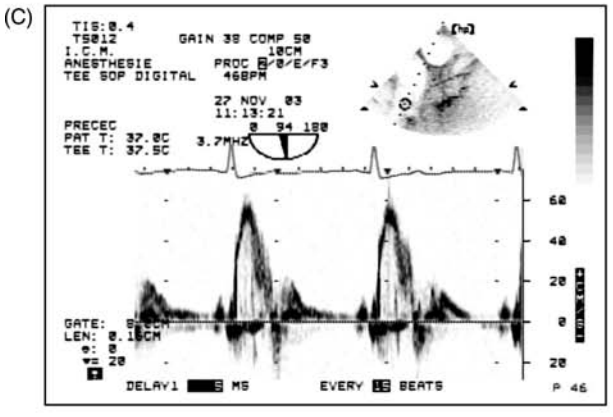

RVOT VELOCITY

Maximal velocity:	58 ± 1 cm/sec
Acceleration time:	93 ± 6 ms
Ejection time:	277 ± 23 ms
Mean acceleration:	3.82 ± 0.76 m/s^2
Time velocity integral:	11.1 ± 1.7 cm

Figure 5.29 Normal values of Doppler velocities in a healthy young adult recorded from the left ventricular outflow tract (LVOT) (21), the ascending aorta (28), and the right ventricular outflow tract (RVOT) (1 cm below the pulmonic valve) (29).

Bernoulli equation:

$$\begin{aligned}\text{Pressure difference} &= \text{convective acceleration} \\ &\quad + \text{flow acceleration} \\ &\quad + \text{viscous friction}\end{aligned}$$

$$\Delta P = \frac{1}{2}\rho(V_2^2 - V_1^2) + \int_1^2 \frac{\mathrm{d}v}{\mathrm{d}t}\mathrm{d}s + R(v) \qquad (5.19)$$

where ΔP is the pressure gradient (in dynes/cm^2); ρ is the density of the fluid (in g/cm^3); V_2 is the blood velocity at distal site (in m/s); V_1 is the blood velocity at proximal site (in m/s); dv is the change in velocity (in cm/sec) over the time period dt (in s); ds is the distance over which the pressure decreases (in cm); and R is the viscous resistance in the vessel (g/cm^4 per second).

The convective acceleration is particularly significant wherever there is a decrease in the cross-sectional area of the vessel. The flow acceleration is related to the pressure decrease necessary to overcome inertial forces. The viscous friction describes the loss of blood flow velocity due to friction between blood cellular elements and the vessel wall endoluminal surface.

For most clinical settings, if one assumes that:

1. the flow acceleration portion is negligible because acceleration is near zero at peak flow velocities;
2. the viscous friction portion is also negligible for flat flow profile within the center of the vessel lumen;

and after substituting known values for the mass density of normal blood ($\rho = 1.06 \times 10^3\ \mathrm{kg/m^3}$) and conversion factors where velocity in m/s yields pressure drop in mmHg, the Bernoulli equation can be simplified as follows:

$$\Delta P = 4(V_2^2 - V_1^2) \tag{5.20}$$

When flow velocity V_1 proximal to a reduced orifice is low, and particularly small relative to the peak velocity V_2 across the reduced orifice, V_1 can be ignored and the simplified Bernoulli equation be even reduced to Eq. (5.21):

$$\Delta P = 4V^2 \tag{5.21}$$

Several clinical situations do not meet the assumptions involved in the use of the simplified Bernoulli equation. In the hyperdynamic heart, or in the presence of subaortic dynamic obstruction, a $V_1 > 1.2\ \mathrm{m/s}$ is no longer negligible and calculation of the pressure gradient, ignoring a high V_1, overestimates the true gradient. When there is significant anemia (decreased viscosity) or polycythemia (increased viscosity), $(1/2)\rho$ can no longer be estimated by four. In the case of long, tubular obstructions seen, for example in long coarctations, tunnel subaortic, or supravalvular aortic stenosis (AS), the viscous friction element of the equation is no longer negligible and cannot be ignored. Also, inertial forces may no longer be negligible in dysfunctional prosthetic valves.

In the case of AoV stenosis evaluation, there is a pressure gradient across the AoV between the left ventricular and the aortic pressure. As the peak blood flow velocity measured by continuous-wave Doppler echocardiography is an instantaneous event, the pressure gradient derived from this measure is, therefore, maximum instantaneous pressure gradient. On the invasively obtained pressure tracings from the catheterization lab, this corresponds to the greatest instantaneous difference between the two pressure tracings measured simultaneously (see Fig. 15.20).

Integrating all the instantaneous pressure gradients throughout a flow period results in the mean pressure gradient. These two gradients must be differentiated from the peak-to-peak gradient, a measurement in the catheterization laboratory consisting of measuring the difference between the peak left ventricular pressure value and the peak aortic pressure value. As these two events are not synchronous, this constitutes a nonphysiological measurement. Several studies have documented the excellent correlation between echo-Doppler-derived and catheter-measured pressure gradients across AS (30), mitral stenosis (MS) (31), prosthetic valves (32), and TV (33).

C. Estimation of Intracardiac Pressures

1. *Right Ventricular Systolic Pressure*

The peak tricuspid regurgitant (TR) velocity reflects the peak pressure gradient between the RV and the right atrium (RA) (Fig. 5.30). Therefore, the right ventricular systolic pressure (RVSP) can be estimated with the continuous-wave Doppler by the following equation:

$$\mathrm{RVSP} = 4(V_{\mathrm{TR}})^2 + \mathrm{RAP} \tag{5.22}$$

where RVSP is the right ventricular systolic pressure (in mmHg); V_{TR} is the peak tricuspid regurgitant velocity, (in m/s); and RAP is the measured or estimated right atrial pressure (see Subsection 5 below) (in mmHg).

The peak systolic velocity obtained across a ventricular septal defect reflects the peak pressure gradient between the LV and RV. In the absence of left ventricular outflow obstruction (i.e. subvalvular, valvular, or supravalvular aortic stenosis), the peak left ventricular systolic pressure can be approximated by the systolic aortic pressure, and secondarily by the arm systolic blood pressure (34). Therefore, in the following equation:

$$\mathrm{RVSP} = \mathrm{sBP} - 4(V_{\mathrm{VSD}})^2 \tag{5.23}$$

where RVSP is the right ventricular systolic pressure (in mmHg); V_{VSD} is the peak VSD velocity, (in m/s); and sBP is the systolic arm blood pressure (in mmHg).

2. *Pulmonary Artery Systolic Pressure*

Unless there is a right ventricular outflow obstruction (such as pulmonic stenosis), the PASP should be equal to the RSVP (see Fig. 5.31). In this setting, we can, therefore rewrite the two preceding equations as follows (35):

$$\begin{aligned} \mathrm{PASP} &= 4(V_{\mathrm{TR}})^2 + \mathrm{RAP} \\ \mathrm{PASP} &= \mathrm{sBP} - 4(V_{\mathrm{VSD}})^2 \end{aligned} \tag{5.24}$$

where PASP is the pulmonary artery systolic pressure (in mmHg); V_{TR} is the peak tricuspid regurgitant velocity, (in m/s); and RAP is the measured or estimated right atrial pressure (see Subsection 5 below) (in mmHg). V_{VSD} is the peak VSD velocity, (in m/s); and sBP is the systolic arm blood pressure (in mmHg).

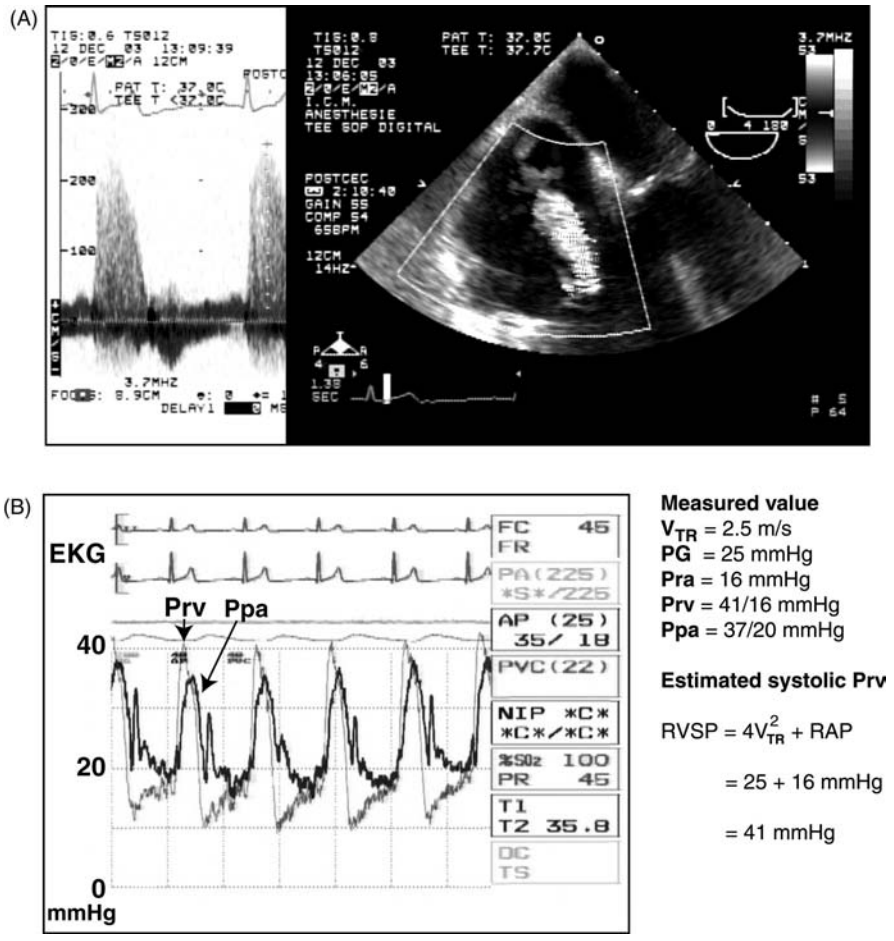

Figure 5.30 (A) Estimation of right ventricular systolic pressure (systolic Prv or RVSP) using the pressure gradient (PG) obtained from tricuspid regurgitation (TR) and right atrial pressure (Pra or RAP). (B) Note that the RVSP is higher than the systolic pulmonary artery pressure (Ppa) due to a small gradient across the pulmonic valve (EKG, electrocardiogram; V, velocity).

In the presence of a patent ductus arteriosus (PDA) (between the thoracic aorta and the pulmonary artery), the peak velocity reflects the peak pressure gradient between the aortic and pulmonary artery pressure (36) as given in the following equation:

$$\text{PASP} = \text{sBP} - 4(V_{\text{PDA}})^2 \tag{5.25}$$

where PASP is the pulmonary artery systolic pressure (in mmHg); V_{PDA} is the peak PDA velocity (in m/s); and sBP is the systolic arm blood pressure (in mmHg).

3. *Mean Pulmonary Artery Pressure*

The pulmonary regurgitant velocity represents the instantaneous pressure gradient between the main pulmonary artery and the RV during diastole. The mean pulmonary artery pressure was shown to be correlated to the peak pulmonary regurgitant velocity in protodiastole (37):

$$\text{MPAP} = 4(V_{\text{E-PR}})^2 \tag{5.26}$$

where MPAP is the mean pulmonary artery pressure (in mmHg) and $V_{\text{E-PR}}$ is the early peak pulmonary regurgitant velocity (in m/s).

The mean pulmonary artery pressure has also been estimated by several authors (38–40) using the right ventricular acceleration time, from the onset of the ejection to the peak pulmonic velocity. The Mahan (38) and Kitabake (40) equations are:

$$\begin{aligned} &\text{Mahan} && \text{MPAP} = 79 - (0.45 \times \text{RV}_{\text{accel}}\text{Time}) \\ &\text{Kitabake} && \text{MPAP} = 90 - (0.62 \times \text{RV}_{\text{accel}}\text{Time}) \end{aligned} \tag{5.27}$$

where MPAP is the mean pulmonary artery pressure (in mmHg) and RV_{accel}Time is the right ventricular acceleration time (in ms).

The MPAP estimated by the Mahan equation was studied in patients with a heart rate of 60–100 bpm. Also, the right ventricular acceleration time may not be

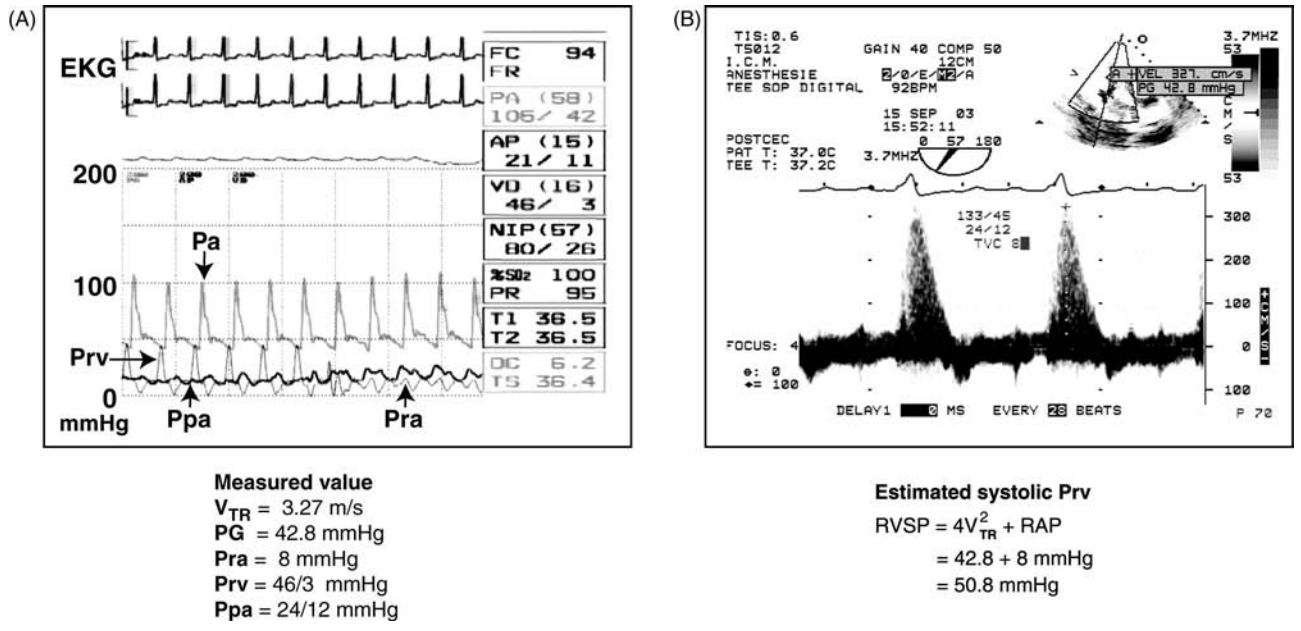

Figure 5.31 Estimation of right ventricular systolic pressure (systolic Prv or RVSP) using the pressure gradient (PG) obtained from tricuspid regurgitation (TR) and right atrial pressure (Pra or RAP) in a 46-year-old woman with aortic valve endocarditis. (A) Hemodynamic pressure tracing: after cardiopulmonary bypass, a difference between the systolic Prv and pulmonary artery pressure (Ppa) was observed. (B) Continuous wave Doppler: a PG of 42.8 mmHg would yield a RVSP of 50.8 mmHg. However, the Ppa is measured at 24/12 mmHg. The suspected right ventricular outflow tract obstruction is confirmed by direct measurement of a systolic Prv (or RVSP) of 46 mmHg using the right ventricular paceport of the Ppa catheter (EKG, electrocardiogram; Pa, arterial pressure; V, velocity).

shortened as much, despite high pulmonary pressures, when the right ventricular cardiac output is increased with left-to-right shunt.

4. *Pulmonary Artery and Right Ventricular (End)-Diastolic Pressure*

At the end of diastole, the right atrial pressure and the right ventricular pressure should have equalized, assuming there is no evidence of tricuspid valve stenosis (Fig. 5.32). Therefore, the following equation can be rewritten as (37):

$$\begin{aligned} \text{PAEDP} &= 4(V_{\text{PR-ED}})^2 + \text{RVEDP} \\ \text{PAEDP} &= 4(V_{\text{PR-ED}})^2 + \text{RAP} \end{aligned} \tag{5.28}$$

where PAEDP is the pulmonary artery end-diastolic pressure (in mmHg); $V_{\text{PR-ED}}$ is the end-diastolic pulmonary regurgitant velocity (in m/s); RVEDP is the right ventricular end-diastolic pressure (in mmHg); and RAP is the measured or estimated right atrial pressure (see below) (in mmHg).

5. *Right Atrial Pressure*

Several methods have been proposed to estimate the right atrial pressure used in the preceding equations to measure right-sided intracardiac pressures. The jugular venous pressure estimated by physical examination or an empirical value of 10 was evaluated and compared with other regression equations (33).

A normal-sized inferior vena cava (IVC) collapses with a rapid negative intrathoracic pressure during a sudden inspiration ("sniffing" maneuver). When the right atrial pressure increases, there is decreased venous return and compensatory increase in the IVC diameter which serves as a capacitance reservoir for the RA.

Moreover, during sniffing, the decrease in IVC diameter is either blunted or absent with high right atrial (RA) pressure (41). Table 5.1 has been proposed to estimate mean RAP.

Correlation studies with catheterization have also shown that combined information from the IVC diameter and the hepatic venous Doppler profile can be used to assess RAP (42) (Table 5.2).

The preceding estimate of RAP was however not prospectively validated in patients on positive pressure mechanical ventilation.

6. *Left Ventricular End-Diastolic Pressure*

The aortic regurgitant velocity reflects the instantaneous pressure gradient between the aorta and the LV during diastole (Fig. 5.33). As the arm diastolic blood pressure

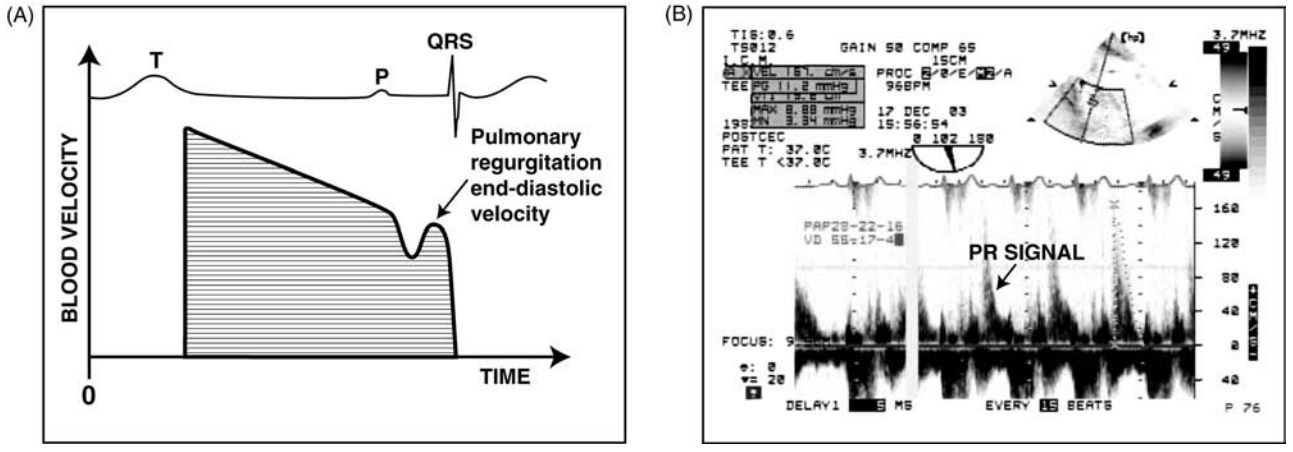

Figure 5.32 Estimation of pulmonary artery end-diastolic pressure (PAEDP) using the pulmonary regurgitation (PR) Doppler signal in a 58-year-old man after complex valvular surgery. (A) Schematic of ideal PR velocity signal with site of measurement of end-diastolic velocity. (B) Continuous wave Doppler of the pulmonic valve: the quality of the PR signal is often insufficient to allow measurement of the end-diastolic velocity due to improper angulation.

Table 5.1 Echocardiographic Estimation of Right Atrial Pressure (RAP) Using IVC Diameter

Size of IVC (cm)	Collapse with *sniffing*	Suggested mRAP (mmHg)
<1.5	$\geq 50\%$	0–5
1.5–2.5	$\geq 50\%$	5–10
1.5–2.5	$<50\%$	10–15
>2.5	$<50\%$	15–20
>2.5	Fixed diameter	>20

Table 5.2 Echocardiographic Estimation of Right Atrial Pressure (RAP) Using IVC Diameter and Hepatic Venous Doppler Profile

Size of IVC (cm)	Collapse with *sniffing*	Hepatic vein Doppler profile	Suggested mRAP (mmHg)
<1.5	$\geq 50\%$	$S + AR > 0$	5
<1.5	$<50\%$	$S + AR > 0$	10–14
>2.0	$\geq 50\%$	$S + AR < 0$	15–20
>2.0	$<50\%$	$S + AR < 0$	>20

approximates the end-diastolic pressure (EDP) in the aorta we can, therefore, obtain the left ventricular end-diastolic pressure (LVEDP) by the following equation:

$$\text{LVEDP} = \text{dBP} - 4(V_{\text{AR-ED}})^2 \tag{5.29}$$

where LVEDP is the left ventricular end-diastolic pressure (in mmHg); dBP is the diastolic blood pressure (in mmHg); and $V_{\text{AR-ED}}$ is the end-diastolic aortic regurgitant velocity (in m/s).

7. Left Atrial Pressure

The mitral regurgitant velocity reflects the instantaneous pressure gradient between the LV and the LA during systole. If there is no LVOT obstruction (such as subvalvular, valvular, or supravalvular aortic stenosis), the peak left ventricular systolic pressure can be approximated by the aortic systolic blood pressure. Therefore, left atrial pressure (LAP) can be estimated by the following equation:

$$\text{LAP} = \text{sBP} - 4(V_{\text{MR}})^2 \tag{5.30}$$

where LAP is the left atrial pressure (in mmHg); sBP is the systolic aortic blood pressure (in mmHg); and V_{MR} is the peak mitral regurgitant velocity (in m/s) (Fig. 5.33).

Several methods using other parameters obtained by pulsed-wave (PW) Doppler, color M-mode, and tissue-Doppler echocardiography have also been proposed to estimate LAP.

Using the velocity of the propagation of the E-wave velocity by color M-mode, the LAP can be estimated by (43) using the following equation:

$$\text{LAP} = 5.27(E/V_{\text{p}}) + 4.6\,\text{mmHg} \tag{5.31}$$

where LAP is the left atrial pressure (in mmHg); E is the peak early diastolic velocity of the mitral valve inflow (in cm/sec); and V_{p} is the velocity of propagation of the E-wave (in cm/sec).

D. Volumetric Flow Calculations

1. Hydraulic Principle

Assuming a constant mean flow velocity through a rigid circular tube of constant diameter and, therefore, fixed

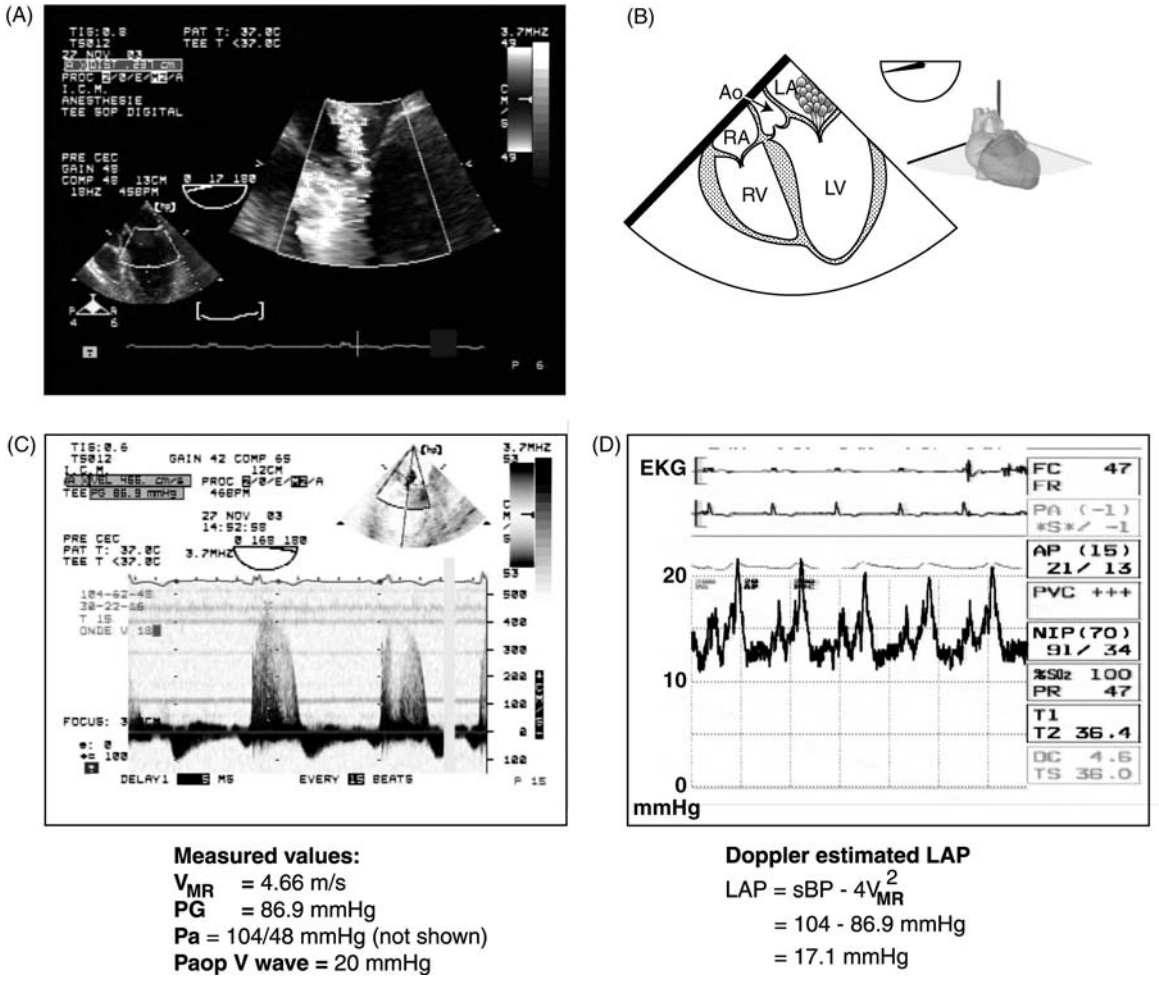

Figure 5.33 Estimation of left atrial pressure (LAP) using the mitral regurgitation (MR) Doppler signal in a 70-year-old man scheduled for off-pump bypass surgery with an arterial systolic blood pressure (sBP or Pa) of 104 mmHg. (A, B) Mid-esophageal four-chamber view with mitral regurgitation. (C) Continuous wave Doppler: peak pressure gradient (PG) of 86.9 mmHg between the left atrium (LA) and left ventricle (LV). This would yield a Doppler estimated LAP of 17.1 mmHg. (D) Hemodynamic pressure tracing: the pulmonary artery occlusion pressure (Paop) waveform is shown with a "v" wave of 20 mmHg. (Ao, aorta; EKG, electrocardiogram; RA, right atrium; RV, right ventricle; V, velocity).

cross-sectional area (CSA), volumetric flow rate can be expressed by the following hydraulic equation:

$$Q = V \times \text{CSA} \tag{5.32}$$

where Q is the volumetric flow rate (in L/s); V is the mean velocity (in cm/sec); and CSA is the cross-sectional area of the orifice (in cm/sec).

During pulsatile flow periods, volumetric flow is calculated by the TVI, the stroke distance reached by the column of blood during the flow period, and calculation of volumetric flows is equivalent to determine the volume of a cylinder, where

$$\text{Volume} = \text{CSA} \times \text{length} = \text{CSA} \times \text{TVI} \tag{5.33}$$

If we assume a symmetrical circular orifice, the CSA can be obtained from the following equation:

$$\text{CSA} = \pi r^2 = 0.785 d^2 \tag{5.34}$$

where CSA is the cross-sectional area (in cm^2); r is the radius of the circular orifice (in cm); and d is the diameter of the circular orifice (in cm).

Therefore, volumetric flow can be calculated from the following simplified equation:

$$\text{Vol} = 0.785 d^2 \times \text{TVI} \tag{5.35}$$

where Vol is the volume (in mL); d is the diameter of orifice (in cm); and TVI is the time–velocity integral (in cm).

One must remember all the above assumptions made by the hydraulic equation, and moreover the assumptions that the cross-sectional area remains constant through the flow period and that the sample volume remains at the same position throughout the flow period: this is not the case when assessing flow through an elastic blood vessel or a mobile, deformable and not always circular valvular annulus. Volumetric flow rates are particularly sensitive to inaccuracies in the orifice diameter measurement, as the error is magnified to the second power.

The measurement and comparison of volumetric flow rates at different locations within the cardiac pump form the basis of hemodynamic calculations essential to the assessment of SV and CO, valvular stenotic or prosthetic orifice areas, regurgitant volumes and fractions as well as shunt fractions and ratios.

2. Stroke Volume and Cardiac Output

Volumetric flow can be obtained by measuring the TVI across valves either during systole or diastole. When using semilunar (aortic and pulmonary) valves, the TVI is obtained during systole, enabling calculation of the SV:

$$\mathrm{SV} = 0.785d^2 \times \mathrm{TVI} \tag{5.36}$$

where SV is the stroke volume (in mL); d is the diameter of orifice (in cm); and TVI is the time–velocity integral (in cm), obtained by tracing the outer edge of the flow-velocity signal (Fig 5.34).

When using the atrioventricular (mitral and tricuspid) valves, the flow is evaluated during diastole and the TVI is measured by tracing the modal velocity, the most dense part of the flow velocity signal. Compared with the SV measured by 2D echocardiography, the Doppler-obtained volumetric flow does not make any geometric assumptions about the left ventricular cavity. Therefore, in the asymmetrical LV, secondary to the presence of an aneurysm or even regional wall motion abnormalities from coronary artery disease where geometric assumptions introduce errors more so during systole than diastole, SV measurement by the Doppler volumetric method may present a theoretical advantage. The calculation of left ventricular ejection fraction using the method of Dumesnil et al. (44) combines the measurement of SV by Doppler volumetric method and the end-diastolic volume by Teichholz's formula (44). To increase accuracy, it is suggested that you trace and average the TVI of at least three to five beats in normal sinus rhythm and up to 8–10 beats in atrial fibrillation.

By measuring the time interval between two consecutive beats, either on the ECG or on the Doppler tracing, one can deduce the heart rate by the following:

$$\mathrm{HR} = 60{,}000/\mathrm{time} \tag{5.37}$$

where HR is the heart rate (in bpm) and time is the time between two consecutive beats (in ms).

Therefore, CO and CI can be deduced by the equations:

$$\mathrm{CO} = 0.785d^2 \times \mathrm{TVI} \times \mathrm{HR} \tag{5.38}$$

$$\mathrm{CI} = \mathrm{CO}/\mathrm{BSA} \tag{5.39}$$

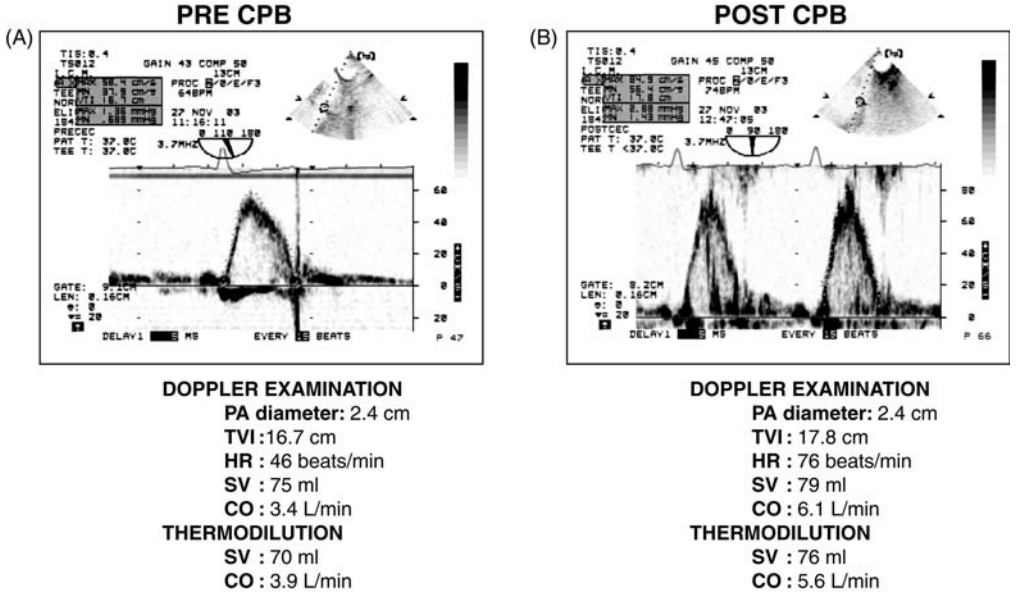

Figure 5.34 Mean pulmonary outflow tract velocities before and after cardiopulmonary bypass (CPB) in a 61-year-old man undergoing coronary revascularisation. Both increases in the time velocity integral (TVI) and heart rate (HR) contribute to a higher cardiac output (CO) after CPB (PA, pulmonary artery; SV, stroke volume).

where CO is the cardiac output (in mL/min); d is the diameter of orifice (in cm); TVI is the time–velocity integral (in cm); HR is the heart rate (in bpm); CI is the cardiac index (in mL/min/m^2); and BSA is the body surface area (in m^2).

This equation assumes that the R–R interval is constant over a minute and consequently, the CO obtained by this method is sensitive to the violations of this caveat in the case of irregular rhythm such as atrial fibrillation and multifocal atrial tachycardias.

3. *The Principle of Conservation of Mass and the Continuity Equation*

The principle of conservation of mass states that as long as there is no loss of fluid from the system between two points of interest, any mass or volume entering the system must flow out of it. The continuity equation is the mathematical expression of this principle:

$$Q_{\text{in}} = Q_{\text{out}}$$

where Q is the volumetric flow rate.

This equation can be clinically applied to the calculation of: (1) native or prosthetic valvular areas and (2) regurgitant orifices, volumes, and fractions.

E. Valvular Areas

1. *Valvular Areas by the Continuity Equation Method*

As the CSA of an orifice decreases, the mean velocity of the blood column must increase to maintain a constant flow rate to obey the principle of conservation of mass (volume). The CSA of a stenotic orifice can, therefore, be calculated from the maximal peak velocity across the orifice and the calculated volumetric flow proximal to the stenosis.

If

$$Q_{\text{in}} = \text{CSA}_{\text{proximal}} \times V_{\text{proximal}}$$

and

$$Q_{\text{out}} = \text{CSA}_{\text{stenosis}} \times V_{\text{stenosis}}$$

and

$$\text{CSA}_{\text{stenosis}} \times V_{\text{stenosis}} = \text{CSA}_{\text{proximal}} \times V_{\text{proximal}}$$

then

$$\text{CSA}_{\text{stenosis}} = \text{CSA}_{\text{proximal}} \frac{V_{\text{proximal}}}{V_{\text{stenosis}}}$$

Alternatively, the time–velocity integral can be substituted for the velocity:

$$\text{CSA}_{\text{stenosis}} = \text{CSA}_{\text{proximal}} \frac{\text{TVI}_{\text{proximal}}}{\text{TVI}_{\text{stenosis}}}$$

The aortic valve area (AVA) calculated by the continuity equation is obtained by the following equation:

$$\text{AVA} = 0.785\ d^2_{\text{LVOT}} \frac{V_{\text{LVOT}}}{V_{\text{maximal}}}$$

or

$$\text{AVA} = 0.785\ d^2_{\text{LVOT}} \frac{\text{TVI}_{\text{LVOT}}}{\text{TVI}_{\text{maximal}}} \tag{5.40}$$

where AVA is the aortic valve area (in cm^2); d_{LVOT} is the diameter of the left ventricular outflow tract (in cm); V_{LVOT} is the velocity (in m/s) measured at the left ventricular outflow tract by PWD; V_{maximal} is the maximal velocity (in m/s) across the valve, reflecting the smallest orifice, obtained by CWD; TVI_{LVOT} is the time–velocity integral (in cm) measured at the left ventricular outflow tract by PWD; and $\text{TVI}_{\text{maximal}}$ is the maximal time–velocity integral (in cm) across the valve, reflecting the smallest orifice, obtained by CWD.

The mitral valve area (MVA) can similarly be obtained by applying the continuity equation $Q_{\text{mitral}} = Q_{\text{aortic}}$, providing there is no significant mitral or aortic valve regurgitation as given in the following equation:

$$\text{MVA} = 0.785\ d^2_{\text{LVOT}} \frac{\text{TVI}_{\text{LVOT}}}{\text{TVI}_{\text{mitral}}} \tag{5.41}$$

where $\text{TVI}_{\text{mitral}}$ (in cm) is measured by CWD across the mitral native or prosthetic valve during diastole.

Estimating valvular stenotic disease severity by the continuity equation is subject to limitations which include the accuracy of the LVOT diameter measurement, the absence of angulation between the maximal jet and the Doppler ultrasound beam, optimal positioning of the sample volume before jet acceleration in the LVOT, as well as the consequence of low CO on the significance of the areas calculated. These limitations are reviewed in detail in Chapters 15 and 17.

2. *Valvular Areas by the Pressure Halftime Method*

The presence of mitral valve stenosis prevents the usual rapid equalization of intracardiac pressure between the LA and the LV. There is a resulting persisting increased pressure gradient during diastole across the mitral valve and its rate of decline is prolonged proportionally to the severity of the stenosis. This can be assessed by the pressure half-time (PHT), defined as the time during which the pressure gradient decreases to one-half its initial value. (Using the simplified Bernoulli equation, this can also be defined as the time during which the mitral diastolic velocity decreases to 0.707 of its initial value). The PHT is related to the mitral deceleration time (Mdt), which is the time required for the peak early diastolic mitral velocity to fall to zero, extrapolated from its deceleration slope. The PHT is equal to 0.29× Mdt.

Hatle, Anelsen, and Tromsdal reported that PHT correlates with the MVA and is less influenced by flow across the valve. They reported a value of <60 ms in normal mitral valves, increasing to 100 ms with mild stenosis and becoming progressively longer with increasing severity. A PHT >220 ms was usually associated with a MVA <1.00 cm^2, and Eq. (5.42) was derived from these studies (45):

$$\text{MVA} = \frac{220}{\text{PHT}} = \frac{759}{\text{Mdt}} \tag{5.42}$$

where MVA is the mitral valve area (in cm^2); PHT is the pressure half-time (in ms); and Mdt is the mitral deceleration time (in ms).

Although the MVA obtained by the PHT method is independent of the volumetric flow across the valve as determined by the CO or the presence of coexistent significant mitral regurgitation (MR), it is affected by other conditions modifying the differential pressure between the LA and the LV. The applicability of this method is decreased by changes in chamber compliance following percutaneous balloon mitral valvuloplasty or cardiac surgery, as well as other conditions such as severe aortic valve regurgitation or delayed left ventricular relaxation abnormalities which modify the transmitral pressure gradient decay by changing the left ventricular diastolic pressure. These limitations are reviewed in detail in Chapter 17.

F. Proximal Flow Convergence (Proximal Isovelocity Surface Area)

The proximal flow convergence method is another application of the principle of conservation of mass (volume) using a different hydraulic equation than the circular orifice and the TVI. In the proximal isovelocity surface area (PISA) flow model, as the red blood cells approach and converge towards a narrowed orifice, their velocity increases in a linear fashion, forming before the orifice a series of concentric hemispheric shells of similar velocity (called isovelocity hemispheres). The closer the hemispheres are to the orifice and, therefore, the smaller the radius of the isovelocity hemisphere, the higher the corresponding velocity.

The flow rate at a given hemispheric shell velocity is shown by the following equation:

$$Q = 2\pi r^2 v_r \tag{5.43}$$

where Q is the flow rate (in mL/s); $2\pi r^2$ is the area of the hemispheric shell from its radius r (in cm); and v_r is the velocity (in cm/sec) at the radius r.

Since the flow at the narrowest orifice is given by the following equation:

$$Q = \text{CSA} \times V_{\max} \tag{5.44}$$

where Q is the flow rate (in mL/s); CSA is the cross-sectional area of the narrowest orifice (in cm^2); and $V_{\max}$ is the maximal velocity across the orifice, obtained by CWD (in cm/sec).

Using the continuity equation, we can obtain the CSA by computing the following equation:

$$\text{CSA} = 2\pi r^2 \frac{v_r}{V_{\max}} \tag{5.45}$$

In MR, where the surface surrounding the regurgitant orifice is relatively planar, the effective regurgitant orifice can be calculated by the PISA method:

$$\text{ERO} = 2\pi r^2 \frac{v_r}{V_{\text{MR max}}} \tag{5.46}$$

where ERO is the effective regurgitant orifice (in cm^2); r is the measured radius (in cm) of the hemispheric shell of the aliased velocity; v_r is the aliased velocity at the radius r, identified as the Nyquist limit (in cm/sec); and $V_{\text{MR max}}$ is the maximal systolic velocity across the orifice, obtained by CWD (in cm/sec).

In the case of MS or TR, rather than being planar, the surface surrounding the narrowed orifice is funnel-shaped and distorts the PISA so that correction factors must be applied.

In the case of MS (46):

$$\text{MVA} = 2\pi r^2 \frac{v_r}{V_{\text{MS max}}} \times \frac{\alpha}{180} \tag{5.47}$$

where MVA is the mitral valve area (in cm^2); r is the measured radius of the hemispheric shell of the aliased velocity; v_r is the aliased velocity at the radius r, identified as the Nyquist limit (in cm/sec); $V_{\text{MS max}}$ is the maximal diastolic velocity across the orifice, obtained by CWD (in cm/sec); and α is the angle measured between the two mitral leaflets.

In the case of tricuspid regurgitation, two correction factors are required (47) as mentioned in the following equation:

$$\text{ERO} = 2\pi r^2 \frac{v_r}{V_{\text{TR max}}} \times \frac{v_r}{V_{\text{TR max}} - v_r} \times \frac{\alpha}{180} \tag{5.48}$$

where ERO is the effective regurgitant orifice (in cm^2); r is the measured radius (in cm) of the hemispheric shell of the aliased velocity; v_r is the aliased velocity at the radius r, identified as the Nyquist limit (in cm/sec); $V_{\text{TR max}}$ is the maximal systolic velocity across the orifice, obtained by CWD (in cm/sec); and α is the angle measured between the two tricuspid leaflets.

G. Regurgitant Volumes and Fractions

According to the principle of conservation of mass (volume), the volumetric flow across all the cardiac valves is equal as long as there is no regurgitation or intracardiac shunt. When valvular regurgitation occurs, a regurgitant volume is added to the forward SV present through all the valves. Therefore, the SV measured across a regurgitant valve is higher compared with the other competent valves by a value equal to the regurgitant volume. The regurgitant volume can be calculated by the following equation:

$$\text{Regurgitant Volume} = \text{SV}_{\text{regurgitant valve}} - \text{SV}_{\text{competent valve}} \quad (5.49)$$

The stroke volume across the aortic valve (SV_{ao}) is given by the following equation:

$$\text{SV}_{\text{ao}} = 0.785 d_{\text{LVOT}}^2 \times \text{TVI}_{\text{LVOT}} \quad (5.50)$$

where d_{LVOT} is the diameter (in cm) of the left ventricular outflow tract measured at the base of the aortic cusps in the left parasternal long-axis view from inner edge to inner edge and TVI_{LVOT} is the time–velocity integral (in cm) measured by PWD with the sample volume in the center of the LVOT, tracing the peak (outer edge of the) velocity Doppler signal envelope.

The stroke volume across the mitral valve (SV_{MV}) is given by the following equation:

$$\text{SV}_{\text{MV}} = 0.785 d_1 \times d_2 \times \text{TVI}_{\text{MV}} \quad (5.51)$$

where d_1 is the diameter of the mitral valve annulus measured at the base of the leaflets from inner edge to inner edge in the apical four-chamber view; d_2 is the diameter of the mitral valve annulus measured at the base of the leaflets from inner edge to inner edge in the apical two-chamber view; and TVI_{MV} is the time–velocity integral (in cm) measured by PWD with the sample volume in the center of the mitral valve annulus, tracing the modal (most dense) velocity on the Doppler signal envelope.

In the case of isolated aortic valve regurgitation, the aortic regurgitant volume is given by the following equation:

$$\text{Aortic Regurgitant Volume} = \text{SV}_{\text{LVOT}} - \text{SV}_{\text{MV}} \quad (5.52)$$

In isolated mitral valve regurgitation, the mitral regurgitant volume is given by following equation:

$$\text{Mitral Regurgitant Volume} = \text{SV}_{\text{MV}} - \text{SV}_{\text{LVOT}} \quad (5.53)$$

Note that in both situations, the SV obtained by the difference between left ventricular end-diastolic and end-systolic volume measured by 2D echocardiography corresponds to the sum of the forward SV and the regurgitant volume, and can be substituted to the first SV of the equation.

In the case of combined significant aortic and mitral valve regurgitation, respective aortic and mitral regurgitant volumes cannot be determined by the preceding continuity equation applied to the mitral and aortic flow alone. In the absence of intracardiac shunt and pulmonary valve regurgitation, the forward SV can be obtained from the RVOT, considered as the competent valve. Mitral regurgitant volume can alternatively be obtained from the convergence (PISA) method, as it invokes the continuity equation at the mitral valve only and is not affected by the presence of aortic regurgitation. Once the mitral effective regurgitant orifice is calculated, the regurgitant volume is obtained by the following equation:

$$\text{Mitral Regurgitant Volume} = \text{ERO}_{\text{MV}} \times \text{TVI}_{\text{MR}} \quad (5.54)$$

where ERO is the effective regurgitant orifice (in cm^2) and TVI_{MR} is the time–velocity integral (in cm) of the mitral regurgitant signal obtained by CWD, tracing the peak (outer edge) of the Doppler signal envelope.

The regurgitant fraction is defined as the ratio of the total volume ejected being regurgitated through the incompetent valve. This is mathematically expressed as follows:

$$\text{RF} = \frac{\text{Reg Vol}}{\text{SV}_{\text{Total}}} \times 100 \quad (5.55)$$

where RF is the regurgitant fraction (in %); Reg Vol is the regurgitant volume (in mL); and SV_{Total} is the total stroke volume (in mL), given by the Doppler-stroke volume across the incompetent valve or the stroke volume obtained by 2D methods.

H. Shunt Fractions

According to the principle of conservation of mass (volume), the volumetric flow through the right heart should be equal to that through the left heart. However, in the presence of an intracardiac shunt, the SV will be greater on the side receiving the additional shunt volumetric flow. Because the left-sided intracardiac pressures are usually greater than on the right, intracardiac shunts are most often from left to right, and the pulmonary blood flow will be greater than the systemic blood flow. The magnitude of systemic-to-pulmonary intracardiac shunt can be quantitated by determining the ratio of pulmonary blood

flow (Q_p) to systemic blood flow (Q_s) (Eq. 5.56):

$$\frac{Q_p}{Q_s} = \frac{SV_{pulmonary}}{SV_{systemic}} \quad (5.56)$$

where Q_p is the pulmonary blood flow, including the added left-to-right shunt flow; Q_s is the systemic blood flow; and SV is the stroke volume by the hydraulic formula ($= 0.785d^2 \times$ TVI).

To reflect the magnitude of the shunt adequately, the pulmonary blood flow must be measured at a site distal to the shunt inflow while the systemic blood flow should be measured at a site distal to the shunt outflow. The location of the shunt will determine where respective Q_p and Q_s measurements will be made.

In the case of left-to-right shunts at the atrial level, the pulmonary volumetric flow can be obtained at the TV annulus, the RVOT or the main pulmonary artery trunk. The systemic volumetric flow can be measured at the mitral valve annulus, the LVOT or the ascending aorta.

For left-to-right shunts at the ventricular level, the pulmonary volumetric flow can be obtained at the RVOT, the main pulmonary artery trunk or the mitral valve annulus, while the systemic volumetric flow is measured at the LVOT, the ascending aorta or the TV annulus.

For left-to-right shunts from aorta to pulmonary artery, such as in patent ductus arteriosus, the pulmonary blood flow is obtained at the mitral valve annulus, the LVOT or the ascending aorta while the systemic blood flow is taken from the TV annulus, the RVOT or the main pulmonary artery trunk.

For technical reasons, the preferred site of SV measurements appears to be at the LVOT or RVOT where the cross-sectional area diameter is best seen at the base of the semilunar cusps and the TVI outer edge is easily traced (as opposed to modal velocity in atrioventricular valves).

III. CONCLUSION

Transesophageal echocardiography is a powerful tool in the evaluation of ventricular structure and function through Doppler interrogation. The appreciation of the normal values is, however, important to interpret pathological conditions correctly.

REFERENCES

1. Feigenbaum H, Popp RL, Chip JN, Haine CL. Left ventricular wall thickness measured by ultrasound. Arch Intern Med 1968; 121:391–395.
2. Devereux RB, Reichek N. Echocardiographic determination of left ventricular mass in man. Anatomic validation of the method. Circulation 1977; 55:613–618.
3. Wyatt HL, Heng MK, Meerbaum S et al. Cross-sectional echocardiography. I. Analysis of mathematical models for quantifying mass of the left ventricle in dogs. Circulation 1979; 60:1104–1113.
4. Sahn DJ, DeMaria A, Kisslo J, Weyman A. Recommendations regarding quantitation in M-mode echocardiography: results of a survey of echocardiographic measurements. Circulation 1978; 58:1072–1083.
5. Schiller NB, Shah PM, Crawford M et al. Recommendations for quantitation of the left ventricle by two-dimensional echocardiography. American Society of Echocardiography Committee on Standards, Subcommittee on Quantitation of Two-Dimensional Echocardiograms. J Am Soc Echocardiogr 1989; 2:358–367.
6. Drexler M, Erbel R, Muller U et al. Measurement of intracardiac dimensions and structures in normal young adult subjects by transesophageal echocardiography. Am J Cardiol 1990; 65:1491–1496.
7. Block M, Hourigan L, Bellows WH et al. Comparison of left atrial dimensions by transesophageal and transthoracic echocardiography. J Am Soc Echocardiogr 2002; 15:143–149.
8. Schnittger I, Gordon EP, Fitzgerald PJ, Popp RL. Standardized intracardiac measurements of two-dimensional echocardiography. J Am Coll Cardiol 1983; 2:934–938.
9. Drexler M, Erbel R, Muller U et al. Measurement of intracardiac dimensions and structures in normal young adult subjects by transesophageal echocardiography. Am J Cardiol 1990; 65:1491–1496.
10. Cohen GI, White M, Sochowski RA et al. Reference values for normal adult transesophageal echocardiographic measurements. J Am Soc Echocardiogr 1995; 8:221–230.
11. Cohen GI, White M, Sochowski RA et al. Reference values for normal adult transesophageal echocardiographic measurements. J Am Soc Echocardiogr 1995; 8:221–230.
12. Weyman AE. Principles and Practice of Echocardiography. Philadelphia: Lea & Febiger, 1994.
13. Weyman AE, Weyman AE. Principles and Practice of Echocardiography. 2nd ed. Philadelphia: Lea & Febiger, 1994.
14. Feigenbaum H, Popp RL, Wolfe SB et al. Ultrasound measurements of the left ventricle. A correlative study with angiocardiography. Arch Intern Med 1972; 129:461–467.
15. Teichholz LE, Kreulen T, Herman MV, Gorlin R. Problems in echocardiographic volume determinations: echocardiographic–angiographic correlations in the presence of absence of asynergy. Am J Cardiol 1976; 37:7–11.
16. Kronik G, Slany J, Mosslacher H. Comparative value of eight M-mode echocardiographic formulas for determining left ventricular stroke volume. A correlative study with thermodilution and left ventricular single-plane cineangiography. Circulation 1979; 60:1308–1316.
17. Colan SD, Parness IA, Spevak PJ, Sanders SP. Developmental modulation of myocardial mechanics: age- and growth-related alterations in afterload and contractility. J Am Coll Cardiol 1992; 19:619–629.
18. Quinones MA, Waggoner AD, Reduto LA et al. A new, simplified and accurate method for determining ejection

fraction with two-dimensional echocardiography. Circulation 1981; 64:744–753.
19. Swaminathan M, Phillips-Bute BG, Mathew JP. An assessment of two different methods of left ventricular ejection time measurement by transesophageal echocardiography. Anesth Analg 2003; 97:642–647.
20. Garrard CL Jr, Weissler AM, Dodge HT. The relationship of alterations in systolic time intervals to ejection fraction in patients with cardiac disease. Circulation 1970; 42:455–462.
21. Kupari M, Koskinen P. Systolic flow velocity profile in the left ventricular outflow tract in persons free of heart disease. Am J Cardiol 1993; 72:1172–1178.
22. Rich S, Sheikh A, Gallastegui J et al. Determination of left ventricular ejection fraction by visual estimation during real-time two-dimensional echocardiography. Am Heart J 1982; 104:603–606.
23. Cahalan MK, Ionescu P, Melton HE Jr et al. Automated real-time analysis of intraoperative transesophageal echocardiograms. Anesthesiology 1993; 78:477–485.
24. Colan SD, Borow KM, Neumann A. Left ventricular end-systolic wall stress-velocity of fiber shortening relation: a load-independent index of myocardial contractility. J Am Coll Cardiol 1984; 4:715–724.
25. Tennant R, Wiggers CJ. The effect of coronary occlusion on myocardial contraction. Am J Physiol 1935; 112:351–361.
26. Pandian NG, Kerber RE. Two-dimensional echocardiography in experimental coronary stenosis. I. Sensitivity and specificity in detecting transient myocardial dyskinesis: comparison with sonomicrometers. Circulation 1982; 66:597–602.
27. Devereux RB, Alonso DR, Lutas EM et al. Echocardiographic assessment of left ventricular hypertrophy: comparison to necropsy findings. Am J Cardiol 1986; 57:450–458.
28. Levy B, Targett RC, Bardou A, McIlroy MB. Quantitative ascending aortic Doppler blood velocity in normal human subjects. Cardiovasc Res 1985; 19:383–393.
29. Targett RC, Heldt GP, McIlroy MB. Doppler blood velocity in the pulmonary artery of infants, children, and adults. Cardiovasc Res 1986; 20:816–821.
30. Currie PJ, Seward JB, Reeder GS et al. Continuous-wave Doppler echocardiographic assessment of severity of calcific aortic stenosis: a simultaneous Doppler-catheter correlative study in 100 adult patients. Circulation 1985; 71:1162–1169.
31. Hatle L, Brubakk A, Tromsdal A, Angelsen B. Noninvasive assessment of pressure drop in mitral stenosis by Doppler ultrasound. Br Heart J 1978; 40:131–140.
32. Burstow DJ, Nishimura RA, Bailey KR et al. Continuous wave Doppler echocardiographic measurement of prosthetic valve gradients. A simultaneous Doppler-catheter correlative study. Circulation 1989; 80:504–514.
33. Currie PJ, Seward JB, Chan KL et al. Continuous wave Doppler determination of right ventricular pressure: a simultaneous Doppler-catheterization study in 127 patients. J Am Coll Cardiol 1985; 6:750–756.
34. Murphy DJ Jr, Ludomirsky A, Huhta JC. Continuous-wave Doppler in children with ventricular septal defect: noninvasive estimation of interventricular pressure gradient. Am J Cardiol 1986; 57:428–432.
35. Ge Z, Zhang Y, Kang W et al. Noninvasive evaluation of right ventricular and pulmonary artery systolic pressures in patients with ventricular septal defects: simultaneous study of Doppler and catheterization data. Am Heart J 1993; 125:1073–1081.
36. Ge Z, Zhang Y, Fan D et al. Simultaneous measurement of pulmonary artery diastolic pressure by Doppler echocardiography and catheterization in patients with patent ductus arteriosus. Am Heart J 1993; 125:263–266.
37. Masuyama T, Kodama K, Kitabatake A et al. Continuous-wave Doppler echocardiographic detection of pulmonary regurgitation and its application to noninvasive estimation of pulmonary artery pressure. Circulation 1986; 74:484–492.
38. Mahan G, Dabestani A, Gardin JM, Allfie A, Burn C, Henry WL. Estimation of pulmonary artery pressure by pulsed Doppler echocardiography. Circulation 1983; 68(suppl III):367.
39. Dabestani A, Mahan G, Gardin JM et al. Evaluation of pulmonary artery pressure and resistance by pulsed Doppler echocardiography. Am J Cardiol 1987; 59: 662–668.
40. Kitabatake A, Inoue M, Asao M et al. Noninvasive evaluation of pulmonary hypertension by a pulsed Doppler technique. Circulation 1983; 68:302–309.
41. Otto CM, Pearlman AS. Textbook of Clinical Echocardiography. Philadelphia: W.B. Saunders, 1995.
42. Ommen SR, Nishimura RA, Hurrell DG, Klarich KW. Assessment of right atrial pressure with 2-dimensional and Doppler echocardiography: a simultaneous catheterization and echocardiographic study. Mayo Clin Proc 2000; 75:24–29.
43. Garcia MJ, Ares MA, Asher C et al. An index of early left ventricular filling that combined with pulsed Doppler peak E velocity may estimate capillary wedge pressure. J Am Coll Cardiol 1997; 29:448–454.
44. Dumesnil JG, Dion D, Yvorchuk K et al. A new, simple and accurate method for determining ejection fraction by Doppler echocardiography. Can J Cardiol 1995; 11:1007–1014.
45. Hatle L, Angelsen B, Tromsdal A. Noninvasive assessment of atrioventricular pressure half-time by Doppler ultrasound. Circulation 1979; 60:1096–1104.
46. Rodriguez L, Thomas JD, Monterroso V et al. Validation of the proximal flow convergence method. Calculation of orifice area in patients with mitral stenosis. Circulation 1993; 88(3):1157–1165.
47. Rivera JM, Vandervoort PM, Mele D et al. Quantification of tricuspid regurgitation by means of the proximal flow convergence method: a clinical study. Am Heart J 1994; 127:1354–1362.

6

Imaging Artifacts and Pitfalls

ROBERT AMYOT, MARIA DI LORENZO, RÉAL LEBEAU, CLAUDE SAUVÉ
University of Montreal, Montreal, Canada

I. Introduction 121
II. Image Features and Artifacts 121
A. Reverberation 121
B. Aliasing 123
C. Ghosting 124
D. Mirror Images 124
E. Near-Field Clutter 125
F. Range Ambiguity 125
G. Refraction 126
H. Shadowing 127
I. Electrocautery 127
J. Side Lobes 127
III. Misinterpretation of Normal Structures 129
A. Trabeculations 129
B. False Tendons 129
C. Pectinate Muscles 130
D. Moderator Band 132
E. Lipomatous Hypertrophy of the Atrial Septum 132
F. Eustachian Valve 132
G. Chiari Network 133
IV. Echo-Free Spaces 133
A. Persistent Left Superior Vena Cava 133
B. Transverse Sinus of Pericardium 134
V. Color Flow Doppler 135
A. Physiologic Regurgitation of Native and Prosthetic Valves 135
B. Gain 136
C. Frequency 137
D. Velocity Scale and Baseline Shift 137
E. Sector Depth 138
VI. Summary 138
References 138

I. INTRODUCTION

Kremkau and Taylor (1) define imaging artifacts as display phenomena not properly representing the structures to be imaged. Imaging pitfalls include artifacts, but also relate to misinterpretation of a properly represented structure, whether normal or pathologic. These obstacles to accurate image analysis are commonly encountered during transesophageal echocardiography (TEE). They must be recognized in order to avoid potentially serious errors. In inexperienced hands, this powerful diagnostic instrument may result in blunders. Understanding the types and mechanisms of echocardiographic artifacts depends on expertise and familiarity with this imaging modality, as well as maintenance of competency. This chapter focuses on the most prevalent artifacts and pitfalls encountered during TEE.

II. IMAGE FEATURES AND ARTIFACTS

A. Reverberation

Reverberations result from multiple reflections of the ultrasound beam before returning to the transducer. As the imaging system assumes that the backscattered echo signal strokes an object located within the ultrasound

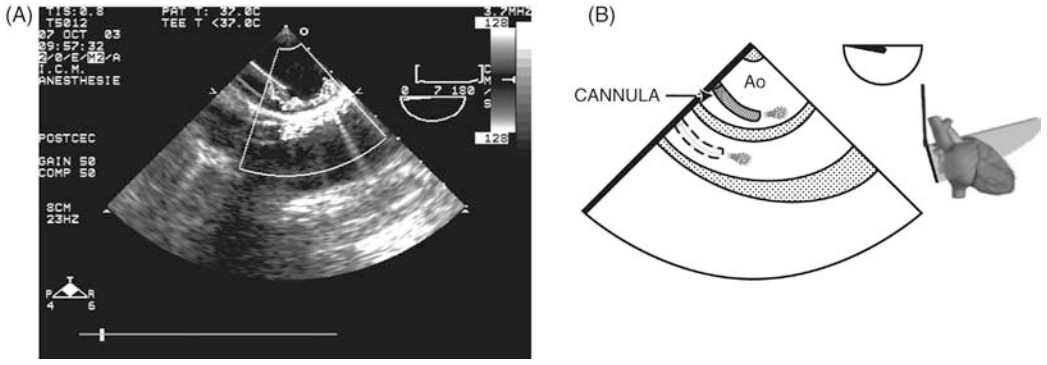

Figure 6.1 Reverberation. Upper-esophageal view of the ascending aorta (Ao). Reverberation in both 2D and color Doppler signal of the Ao and the cannula is displayed.

path and completes the round trip directly and unswervingly, the delay before the echo comes back to the transducer is interpreted as proportional to a straight-line distance between the object and the probe (1). The artifact, therefore, is displayed at a greater depth than the actual object location. The surface of the ultrasound transducer itself may act as a reflector and throw back part of the incoming signal that resumes its initial course and is backscattered a second time by the same target and returns again to the transducer (2) (see Fig. 2.18). Such a reverberation is displayed at twice (and sometimes multiples of) the depth of the real object. Moreover, if the structure is moving, the velocity and movement amplitude of the artifact will be double (and sometimes multiple) that of the object. In addition, color Doppler flow display in the vicinity of the actual target may also be reflected in conjunction with the bidimensional (2D) artifact. Reverberations also arise from other reflectors in the ultrasound field that may act in combination and create multiple reflection paths (Fig. 6.1).

Strongly reflective tissue–air and tissue–fluid interfaces with large impedance discontinuity, such as the aorta–lung interface and the anterior wall of the left atrium (LA) are often involved in these artifacts (3). The pericardium is another highly reflective surface with strong echogenicity that may reverberate the ultrasound beam. A typical example of reverberation is a linear artifact in the ascending aorta lumen that must be differentiated from an aortic dissection flap (Fig. 6.2).

Confirmation of the artifactual nature of an image requires a high index of suspicion and relies on several criteria that may, or may not, coexist: (a) indistinct boundaries, (b) nonplausible anatomy, (c) extension across normal surrounding structures, (d) disappearance with changes in sector depth setting, imaging planes and transducer position (Fig. 6.3), (e) absence of independent motion, but rather movement paralleling that of the reverberated object (when identifiable), and (f) absence of influence on blood flow as assessed by color Doppler showing flow crossing the artifact without turbulence or changes in direction or velocity (4). Foreign material, most often catheters and prosthetic valves, typically contains metal, plastic, and/or pyrolytic carbon that strongly reverberate the ultrasound beam (5). Multiple reflections of the ultrasound signal between different prosthetic components result in a dense succession of separate linear echoes

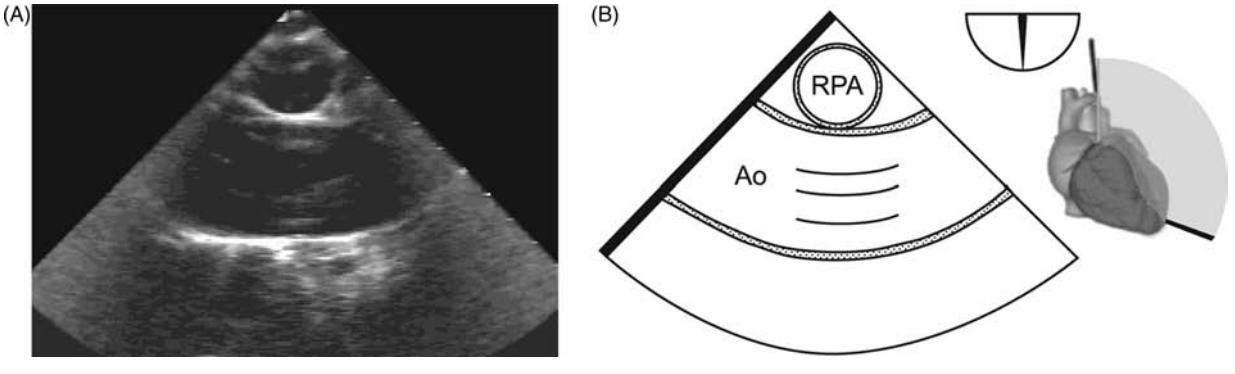

Figure 6.2 Linear artifacts in the ascending aorta (Ao) generated by reverberation of the ultrasound on the strongly reflective aortic–lung interface (RPA, right pulmonary artery).

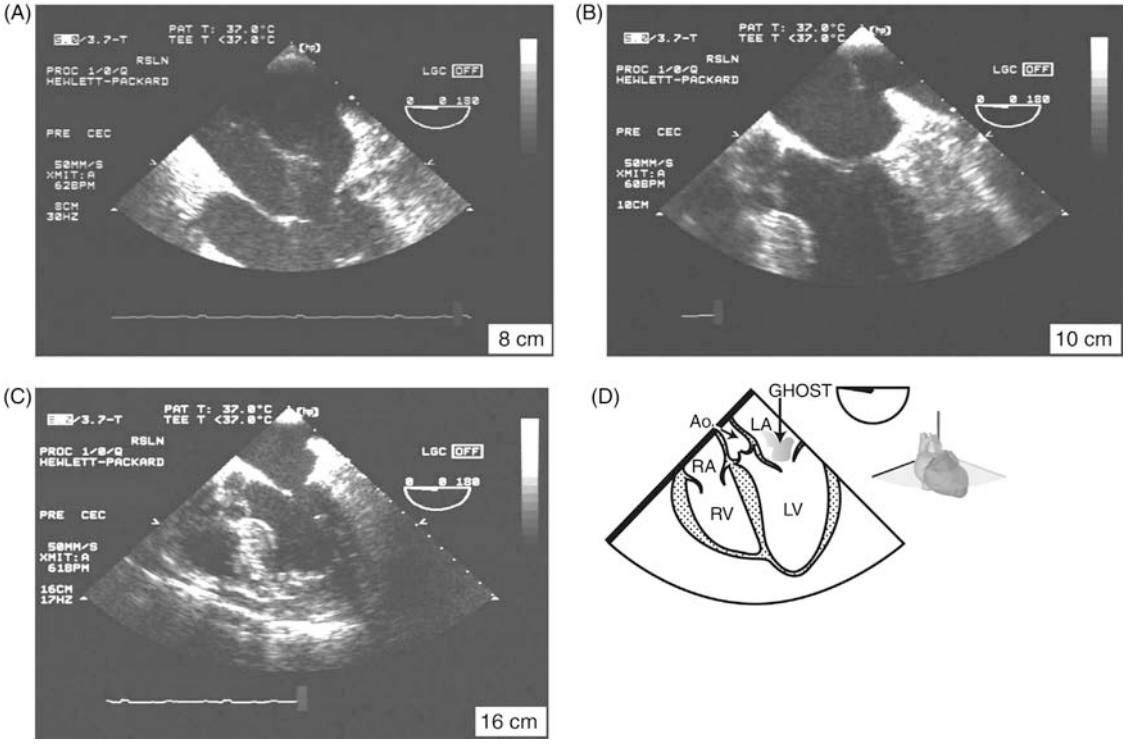

Figure 6.3 Ghosting phenomenon. (A–D) Mid-esophageal five-chamber view of an ill-defined artifact or ghost located in the left atrium (LA) of a 57-year-old man undergoing coronary revascularization. The progressive disappearance of the image as the sector depth is increased from 8 cm (A) to 10 cm (B) to 16 cm (C) confirms the artifactual nature (Ao, aorta; LV, left ventricle; RA, right atrium; RV, right ventricle).

extending from the prosthesis to the distal field (1,5) (Fig. 6.4).

B. Aliasing

Aliasing occurs in Doppler devices that operate in a pulsed mode: pulsed-wave (PW) and color Dopplers. These modalities have the ability to interrogate specific regions of interest within the ultrasound field. This sampling ability is achieved by transmitting ultrasound in intermittent short bursts rather than continuously [as in continuous-wave (CW) Doppler]. The transducer alternately acts as a transmitter and a receiver. Assuming the speed of sound remains constant in the thorax, the delay between pulse transmission and reception of the backscattered signal is proportional to the depth of the target. Therefore, the sampling depth determines the rate of ultrasound burst transmission, or *pulse repetition frequency* (PRF) (see Chapter 1). Accordingly, Doppler shift can be measured only intermittently—when the system functions as an echo signal receiver—over a limited range of frequencies. Aliasing occurs when the frequency of the Doppler shift of the incoming echo exceeds the maximal frequency that the ultrasound system can properly assess. This frequency limit is known as the Nyquist limit and is equal to one-half of the PRF. The direction of the aliasing signal is displayed as opposite to the actual flow direction on either spectral display or on color-coded flow imaging display (2,6,7).

In PW Doppler mode, high velocities exceeding the Nyquist limit are depicted as a signal displayed on both sides of the baseline of the spectral display: a truncated part, which peak velocity exceeds the upper limit of the velocity scale, displayed on the appropriate side of the baseline and, therefore, correctly reflecting the direction of the actual flow; and a second part, the aliasing signal, appearing and wrapping around on the opposite side of the baseline (Fig. 6.5). Therefore, aliasing prevents assessment of the peak velocity of the interrogated flow and may introduce confusion concerning its direction (2,6).

Shifting the baseline in order to obtain a complete PW Doppler signal and decreasing sampling depth may eliminate signal aliasing. Another approach to overcome aliasing is the utilization of high PRF Doppler mode where multiple sampling gates are aligned on an axis. Although this modality allows the increase of the Nyquist limit, it

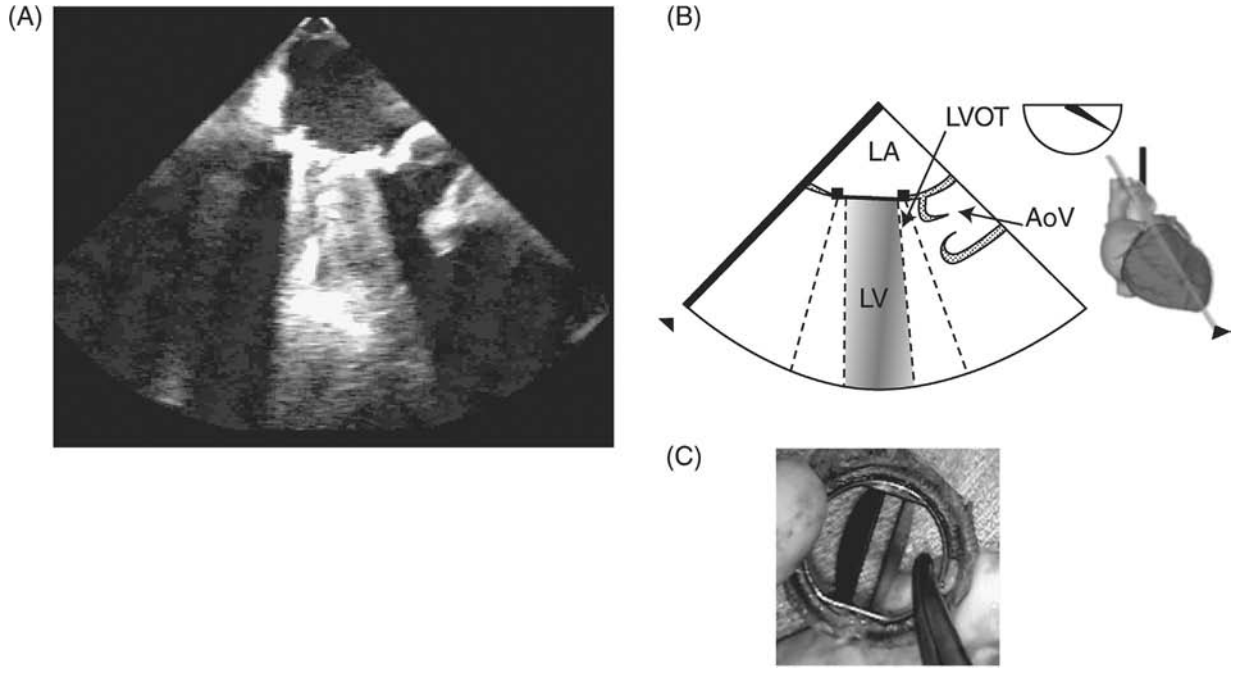

Figure 6.4 Multiple reflections and acoustic shadowing. (A, B) Dense succession of linear echoes extending from a bileaflet mechanical valve in mitral position to the far field. The prosthetic ring acts as an acoustic obstacle and the reverberation artifact is bordered by blind regions (shadowing) preventing visualization of the ventricular cavity and part of the basal ventricular septum. (C) Bileaflet mechanical prosthesis after surgical removal (AoV, aortic valve; LA, left atrium; LV, left ventricle; LVOT, left ventricular outflow tract). (Photo C courtesy of Dr. Michel Pellerin.)

introduces range ambiguity as it may become impossible to know which sampling gate recorded the highest displayed velocity.

In color-flow imaging Doppler mode, flow velocity exceeding the maximal value of the color scale is displayed by an abrupt change in color to the opposite end of the color-coded spectral scale (wrap-around phenomenon), wrongly suggesting a change in flow direction (Fig. 6.6) (2,6). The color-flow signal may, therefore, display a mosaic of colors from both sides of the color-coded scale.

C. Ghosting

The terms "ghost artifact" and "ghosting" can lead to confusion as they are utilized by different authors to identify distinct phenomena. For example, "ghost artifact" has been attributed to image duplication caused by refraction of the ultrasound beam (8). Reverberation artifacts have also been referred to as "ghosts" (Fig. 6.3) (6,9). Finally, "ghosting" has been used to describe at least two types of artifacts in color Doppler imaging. One phenomenon is produced by the rapid motion of a target, such as cardiac valve leaflets, in conjunction with the reduced frame rate of color Doppler imaging causing color flashes (2). A second phenomenon, also termed "ghosting" and identified during color Doppler imaging, refers to artifactual, low-amplitude color echoes within the cardiac chambers in the presence of tachycardia (7). In the view of the authors, these terms should be avoided in favor of more specific terminology.

D. Mirror Images

The mirror images artifact consists in the secondary representation of a target on the opposite side of a strongly reflective interface, due to a significant difference in acoustic impedance between two adjacent structures. It has been described most commonly around the diaphragm and pleura as the air-filled lungs act as total reflectors of the acoustic beam (1,9). Accordingly, the straight and regular interface between the thoracic aorta and the left lung behaves as a powerful ultrasound mirror (Fig. 6.1). Proximity of the reflector to the transducer allows for a high-energy echo reflection appearing in the usual depth range of the imaging sector (3). It is important to note that pulsed, CW, and color Doppler information of the actual target is also reflected and will be displayed in the artifactual image. In the presence of a curved or irregular reflective surface, the mirror image may be distorted, rendering its recognition more challenging.

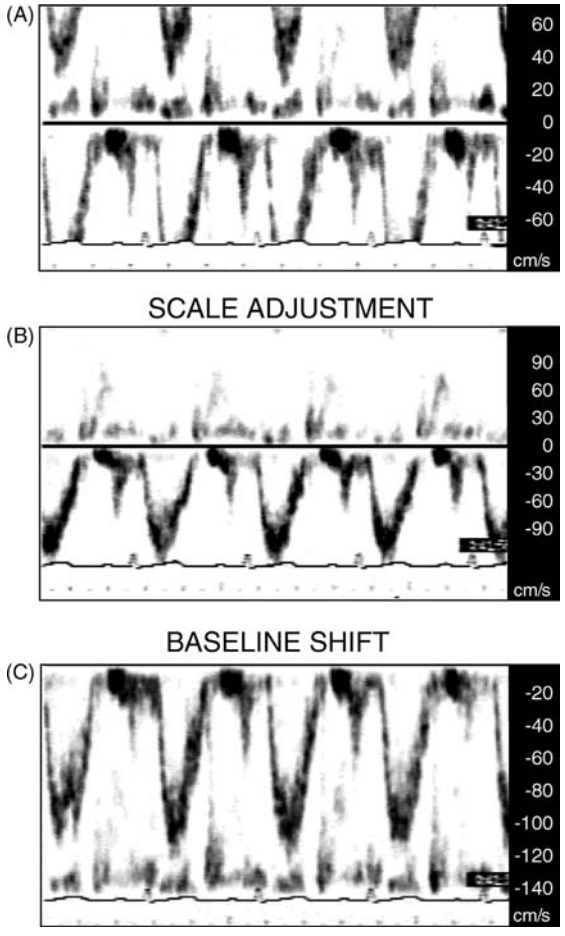

Figure 6.5 Aliasing. Pulsed-wave Doppler signal in the left ventricular outflow tract. (A) The peak negative velocity (<0 cm/sec or baseline) exceeds the upper limit of the velocity scale and a simultaneous aliasing signal appears on the opposite side of the baseline at the top of the display. Altering the scale peak velocity from -60 to -90 cm/sec (B) or shifting the baseline up with a maximum velocity of -140 cm/sec (C) eliminates the aliasing artifact.

E. Near-Field Clutter

Echocardiographic transducers are designed to generate an ultrasound beam providing optimal imaging in the center of the display sector. Near-field clutter arises from the complex and nonuniform energy distribution in the portion of the sector adjacent to the transducer. Reverberation between near-field structures has also been involved in producing such interference and wave cancellation during transthoracic echocardiography (TTE) (10). Also contributing to limited visualization in the vicinity of the ultrasound probe are high-intensity echoes from reflectors in the proximal zone of the ultrasound beam where the intensity of the signal is maximal (6,11). Adjusting gain controls, use of the focal point and introduction of

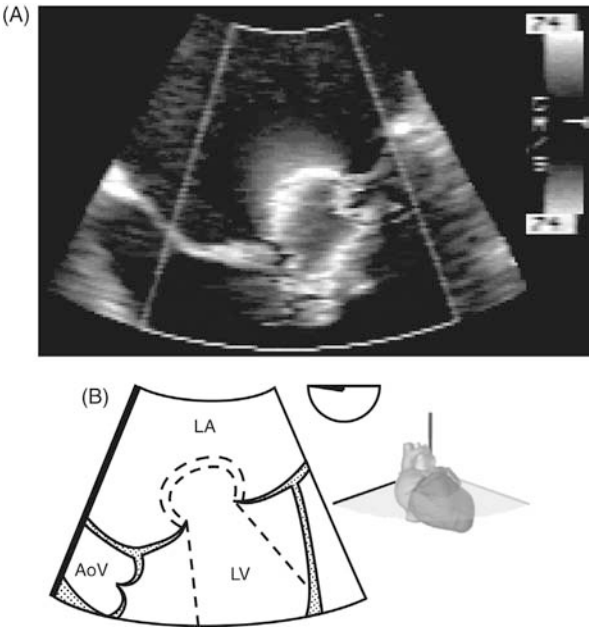

Figure 6.6 Color Doppler aliasing in mitral stenosis. In color Doppler mode, acceleration of the blood flow through a stenotic mitral valve reaches velocities beyond the upper limit of the velocity scale. Aliasing appears as an abrupt change of color from light blue to yellow on the display, which could suggest a flow going in the opposite direction (AoV, aortic valve; LA, left atrium; LV, left ventricle).

multifrequency probes, with the highest frequencies dedicated to the near field, improve visualization close to the transducer and decrease near-field noise (Fig. 6.7).

F. Range Ambiguity

As discussed in the section on aliasing, range ambiguity is an expected limitation of high PRF Doppler. This phenomenon may, however, occur during conventional PW Doppler recording and must be recognized to avoid inappropriate diagnosis. As previously explained, the PW transducer acts as an echo receiver for a limited time delay between each transmission of ultrasound burst. The system assumes that the incoming echoes represent the backscattered signal of the most recently transmitted ultrasound pulse. This may not be the case and rather represent the sum of returning echoes that include backscattering of pulses sent in previous cycles and having traveled to and from a target in the far field. These distal signals may display higher energy and represent higher velocities than the signal from the chosen sample volume. This situation is misleading as the displayed PW Doppler signal mostly represents echoes from blood flow farther in the acoustic field while the sampling gate is in a more proximal location (Fig. 6.8) (6,12). When range ambiguity is suspected, the

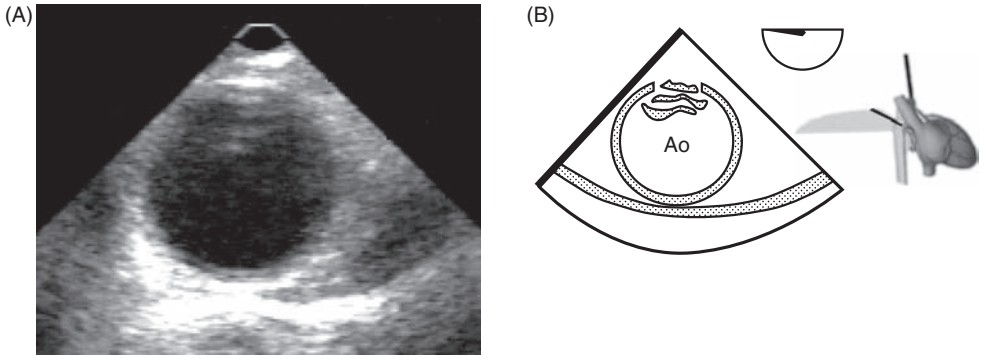

Figure 6.7 Near-field clutter. Linear echoes and poor image definition in the near field prevent optimal visualization of the descending aortic wall close to the transducer (Ao, aorta).

dominant source of the recorded signal may seem obvious; however, it may sometimes require a thorough examination for its identification.

G. Refraction

An ultrasound beam is transmitted in a straight line through a homogeneous medium. However, at the interface between two media of different acoustic impedance, both reflection and refraction of the ultrasound beam usually occur (Fig. 6.9). On one hand, a proportion of the ultrasonic energy does not enter the second medium and bounces on the interface (reflection) and on the other hand, part of the ultrasonic energy propagates through the second medium deviated with respect to the axis of the incident beam in the first medium (refraction). The amplitude of this deviation of the refracted signal is a function of the difference between the speed of sound in both media.

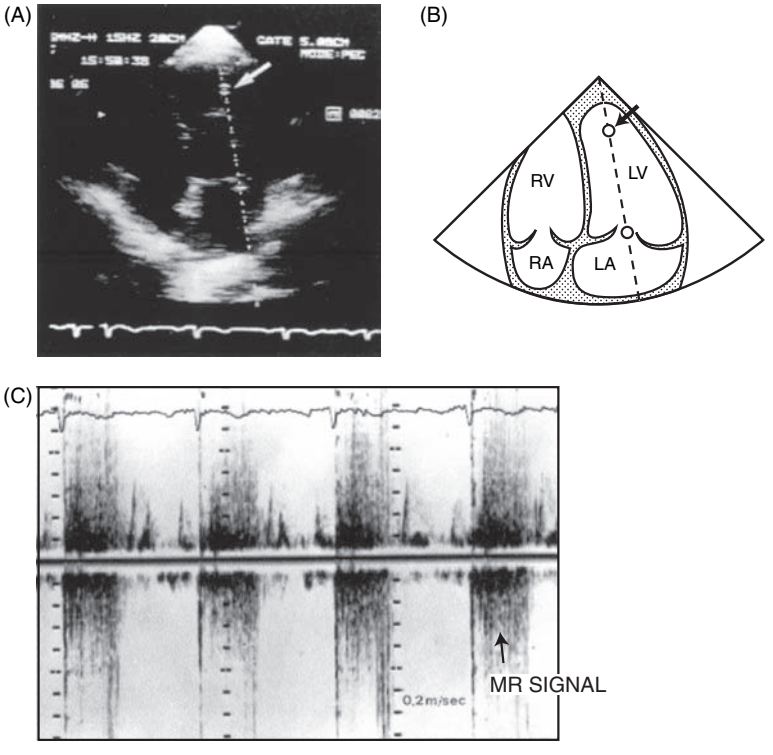

Figure 6.8 Range ambiguity. Transthoracic 4-chamber view. (A, B) The sample volume is located at the left ventricular apex (arrow). (C) However, the pulsed-wave Doppler signal also displays the mitral regurgitation (MR) flow from the far field (LA, left atrium; LV, left ventricle; RA, right atrium; RV, right ventricle). [Reproduced with permission from Weyman (6).]

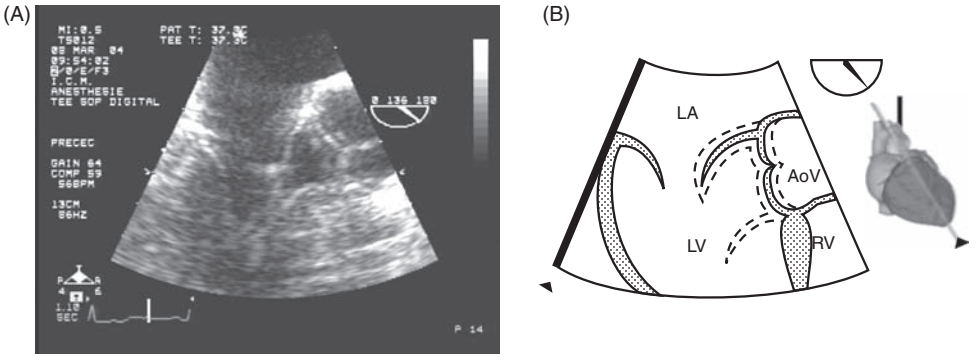

Figure 6.9 Refraction. Mid-esophageal long-axis view of the aortic valve (AoV) showing distortion and duplication through refraction of a part of the ultrasound beam (LA, left atrium; LV, left ventricle; RV, right ventricle).

As seen in Fig. 6.9, refraction may introduce image distortion by laterally displacing structures on the display. When part of the ultrasound beam is refracted, duplication, enlargement or even contraction of imaged structures may occur (13). This phenomenon is encountered most often during TTE where the ultrasound signal travels through media with various acoustic impedances, for example, costal cartilages, the chest wall, and the rectus abdominis muscle (subcostal window). Although less frequent, refraction may also cause significant image distortion during TEE.

H. Shadowing

Acoustic shadowing describes a partial or total loss of echoes distal to a structure with high attenuation, typically containing metal or calcium. These structures usually produce strong ultrasound scattering and most commonly display high echogenicity (1,2,5,6). While shadowing often confirms the high density of a target, it prevents proper imaging behind this interposed acoustic obstacle (Figs. 6.10 and 6.11). The blind region can usually be visualized from a different angle by positioning the transducer in order to avoid intervening of the shadowing object in the central axis of the ultrasound beam.

I. Electrocautery

Electrocautery utilization produces a characteristic, fan-shaped interference pattern artifact precluding proper 2D and color Doppler imaging (Fig. 6.12). It is easily identified as this artifact appears only during electrocautery use. The screen is then covered by a geometric, regular display bearing no relation or resemblance to any anatomic structure. The artifact vanishes instantly when the electrocautery ceases functioning.

J. Side Lobes

The geometry of the ultrasound field is determined by characteristics of the transducer and of the emitted signal. In the near field, there is minimal divergence of ultrasound energy from the main, central beam. Conversely, at a distance from the transducer, the ultrasonic

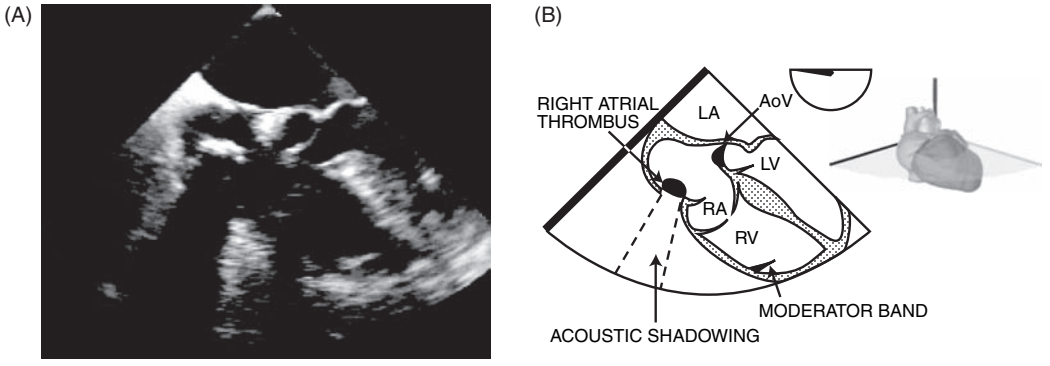

Figure 6.10 Acoustic shadowing. Mid-esophageal five-chamber view displaying a calcified thrombus (proven at surgery) in the right atrium (RA). A blind region extends from the thrombus surface to the far field (AoV, aortic valve; LA, left atrium; LV, left ventricle; RV, right ventricle).

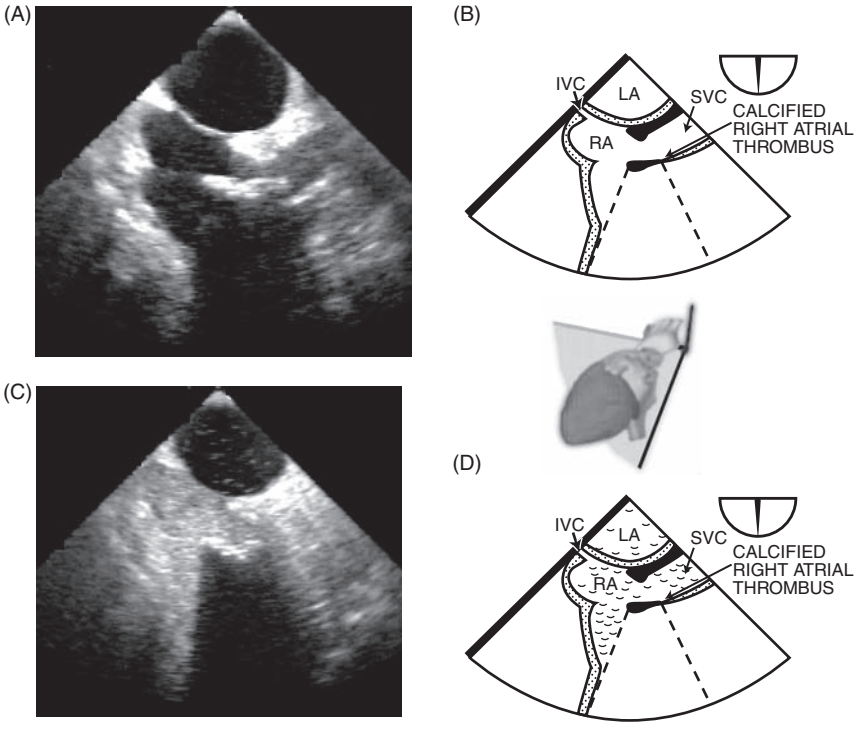

Figure 6.11 Acoustic shadowing. (A, B) Same patient as in Fig. 6.10 using a mid-esophageal bicaval view. The calcified thrombus is located high in the right atrium (RA) at the junction with the superior vena cava (SVC) and obscures the far field. (C, D) Acoustic shadowing is clearly delineated after opacification of the RA by intravenous injection of agitated saline. Note the passage of a few microbubbles to the left atrium (LA) via a patent foramen ovale (IVC, inferior vena cava).

field progressively widens as part of the ultrasound energy deviates from the main ultrasonic beam (Fig. 6.13) (6,10). These regions of ultrasonic energy lateral to the main beam in the far field are termed side lobes. Ultrasound systems are designed to suppress side lobes as they contribute to artifact generation. Side lobes display less energy than the main, primary beam and usually do not yield significant echoes. However, a strong reflector

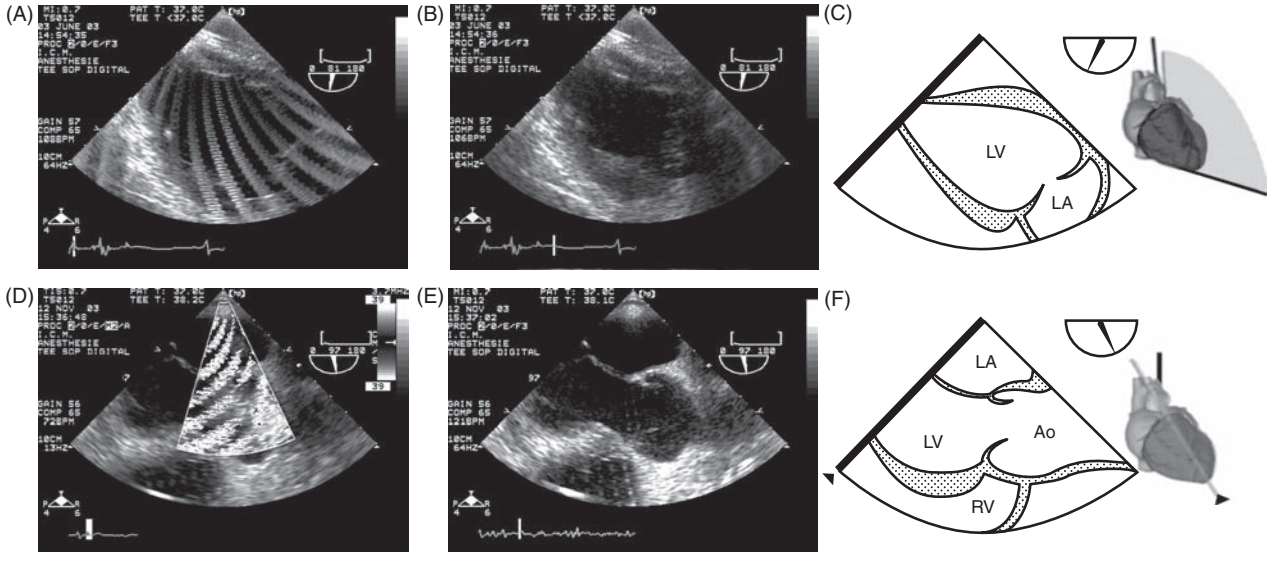

Figure 6.12 Electrocauter artefact. (A–C) Characteristic, fan-shaped electrocautery artifact from a transgastric two-chamber view. (D–F) Mid-esophageal long-axis view with color Doppler artifact (Ao, aorta; LA, left atrium; LV, left ventricle; RV, right ventricle).

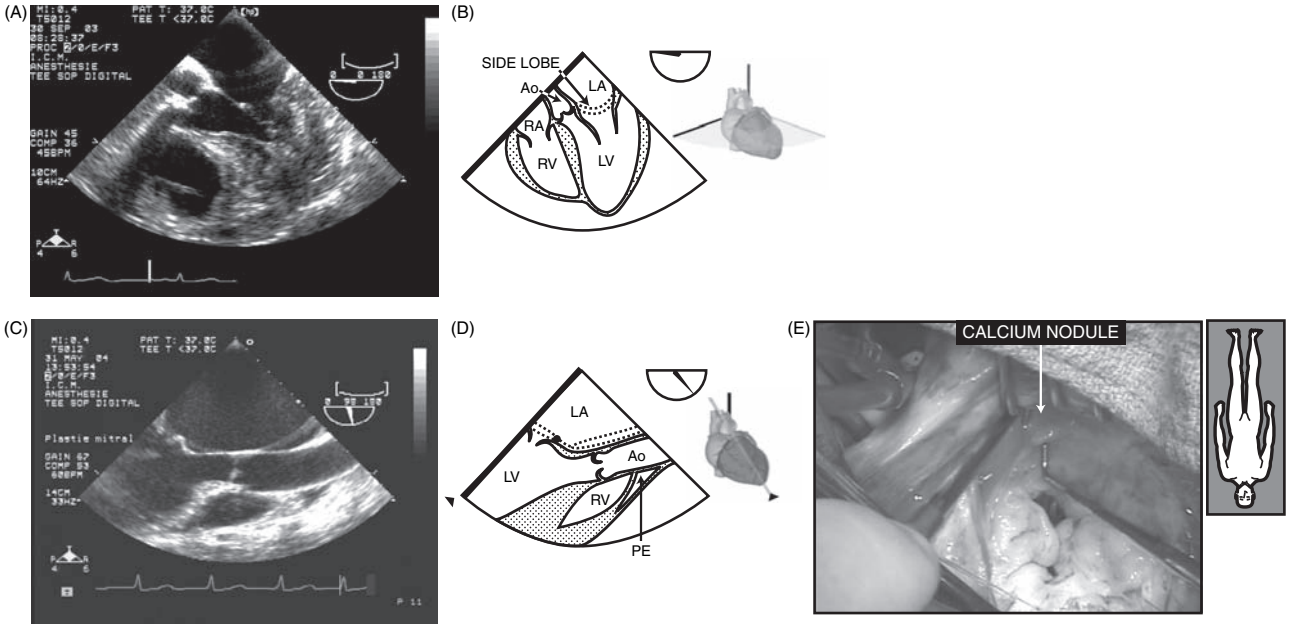

Figure 6.13 Side lobe. (A, B) Mid-esophageal five-chamber view of a 77-year-old woman before aortic valve replacement. A side lobe artifact is seen beside the aortic valve and extends to the left atrial lateral wall. (C, D) Mid-esophageal long-axis view of a 53-year-old woman before mitral valve repair with a side lobe artifact extending along the posterior aspect of the aorta (Ao). (E) Intraoperative view of the calcium nodule responsible for the side lobe artifact (LA, left atrium; LV, left ventricle; PE, pericardial effusion; RA, right atrium; RV, right ventricle). (Photo E courtesy of Dr. Michel Pellerin.)

located in a side lobe may produce a backscattered signal with enough intensity to be imaged. As all incoming echoes are considered backscattered signals generated in the main beam, a signal produced in a side lobe will be interpreted and imaged as if it were coming from a target located in the primary, central ultrasonic beam. Many such artifactual side lobe echoes are not detected because they are superimposed on properly imaged structures with high echogenicity (14). Side lobe artifacts become obvious when imaged over a relatively echo-free region (Fig. 6.13). Decreasing the gain and use of second harmonic tissue imaging contributes in reducing side lobe artifacts (see Chapter 3).

III. MISINTERPRETATION OF NORMAL STRUCTURES

A. Trabeculations

Trabeculations are muscle bundles lining the inner surface of the heart (6). They are coarser in the right-sided chambers, conferring a more irregular texture to the endocardium of the right atrium (RA) and ventricle (2). Nevertheless, prominent left ventricular trabeculations are a common finding, occurring in 68% of normal hearts at autopsy (12). These prominent muscle bundles are multiple in 53% of the cases, although more than four prominent trabeculations are rarely observed in a single left ventricle (LV) (Fig. 6.14). The majority is located, at least in part, in the apical region and may be misinterpreted as apical thrombi. Normal contractility of the adjacent myocardium and similar echo density and texture to the surrounding ventricular wall militate in favor of a prominent trabeculation rather than a thrombus.

B. False Tendons

False tendons, also termed false chordae tendineae or aberrant ventricular bands, have been defined as "stringlike structures with free intracavitary courses, unrelated to the atrioventricular valves, and connected to papillary muscles, ventricular walls, or both" (15). Their free intracavitary course differentiates them from ventricular trabeculations (Fig. 6.15). False tendons may be multiple and are a common finding with a prevalence of 28% in the right ventricle (RV) and 37% in the LV at pathologic examination (15). These linear, echodense fibromuscular structures are not associated with anatomic or physiologic cardiac anomalies, although they have been associated with innocent murmurs. Identification of false tendons is critical as they may simulate a subaortic membrane, the edge of a thrombus or mass, a flail aortic leaflet, asymmetric hypertrophic cardiomyopathy when parallel and close to the interventricular septum, etc.

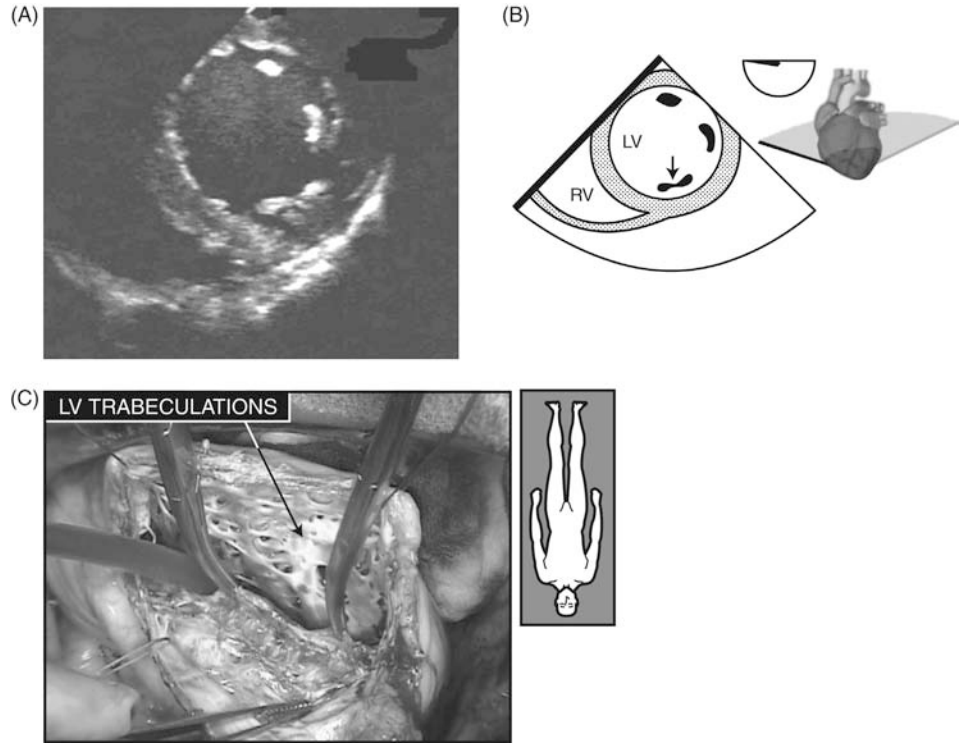

Figure 6.14 Ventricular trabeculations. (A, B) Numerous trabeculations cover the endocardial surface of the left ventricle (LV). A very prominent muscle bundle is observed on the anterior wall in this transgastric mid-papillary short-axis view of the LV (arrow). (C) Intraoperative view of LV trabeculations in a 56-year-old woman during LV remodeling surgery (RV, right ventricle). (Photo C courtesy of Dr. Pierre Pagé.)

The presence of an echo-free space on both sides of the false tendon and demonstration of blood flow around the band using color Doppler may prove helpful in its distinction from pathologic structures.

C. Pectinate Muscles

Pectinate muscles are parallel muscular ridges typically observed on the inner surface of both atrial appendages (Figs. 6.16 and 6.17). These trabeculations confer a characteristic crenelated appearance to the walls of both atrial appendages. They must be distinguished from thrombus or other pathologic cardiac masses. This is especially important when imaging the left atrial appendage (LAA), a recognized site of thrombus formation, with potential for systemic embolization. The vast majority of normal adult subjects have multiple pectinate muscles of 1 mm in width in the LAA (16). Pectinate muscles and

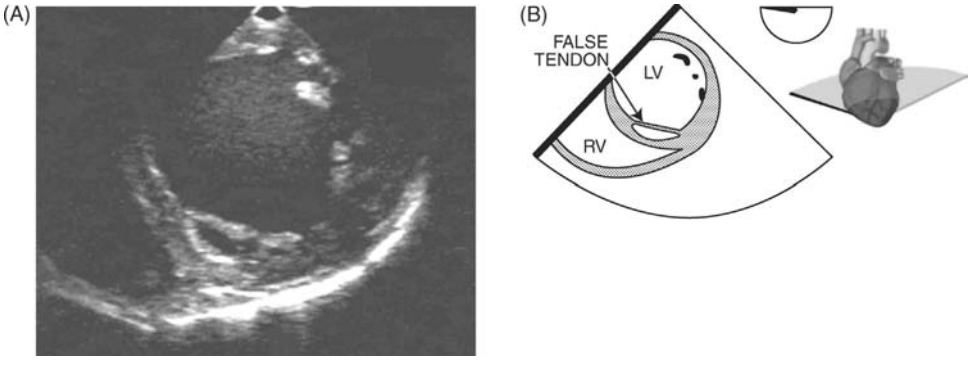

Figure 6.15 False tendon. Transgastric mid-papillary short-axis view of the left ventricle (LV) showing a false tendon extending from the ventricular septum to the anterior wall (RV, right ventricle).

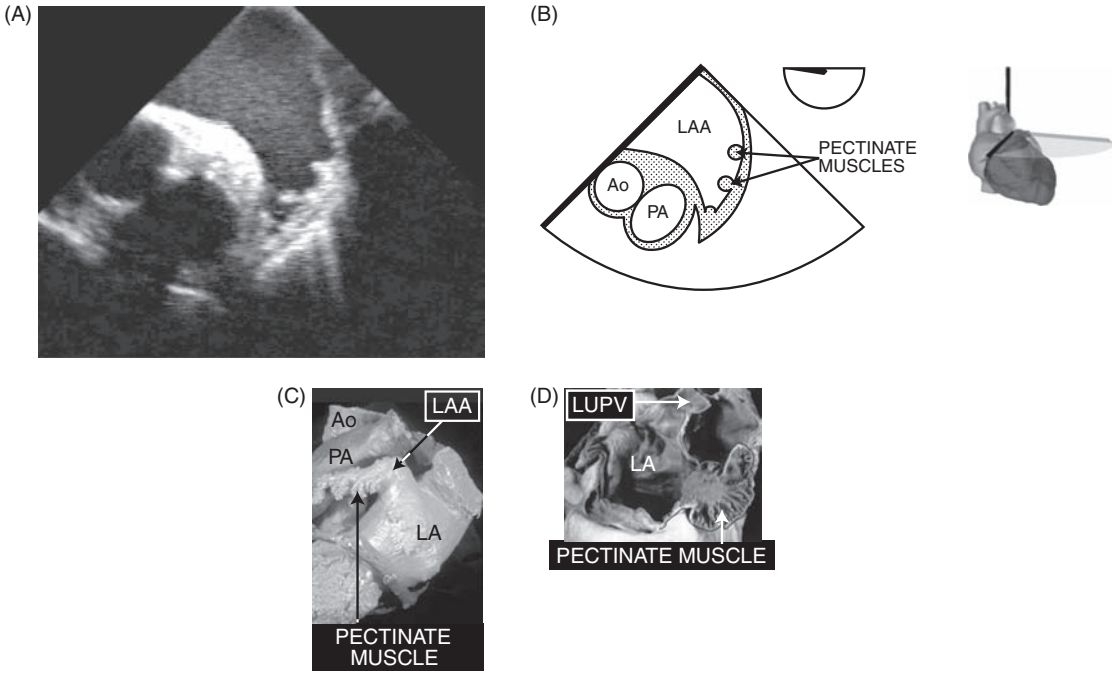

Figure 6.16 (A, B) Pectinate muscles in the left atrial appendage (LAA). (C, D) Anatomical luminal cast and view of a LAA (Ao, aorta; LA, left atrium; LUPV, left upper pulmonary vein; PA, pulmonary artery). [Photo C with permission from Anderson and Levy (17); photo D modified with permission from Veinot et al. (16).]

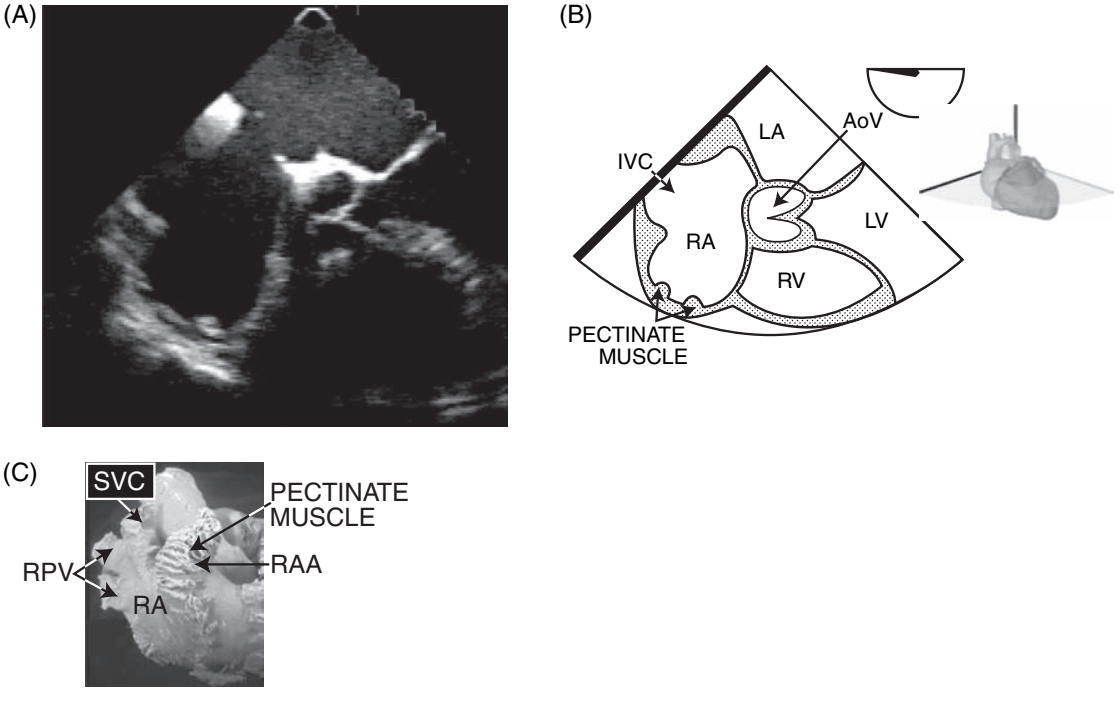

Figure 6.17 (A, B) Pectinate muscles in the right atrium (RA) in this mid-esophageal five-chamber view of the heart. (C) Anatomical luminal cast and view of a right atrial appendage (RAA) (AoV, aortic valve; IVC, inferior vena cava; LA, left atrium; LV, left ventricle; RPV, right pulmonary veins; RV, right ventricle; SVC, superior vena cava). [Photo C with permission from Anderson and Levy (17).]

the underlying atrial wall share the same texture and echogenicity and display the same motion. Conversely, thrombi exhibit a different acoustic density from the atrial walls and may be pedunculated. Moreover, thrombi are usually found in conjunction with reduced Doppler velocities at the level of the LAA and blood stasis in the LA in the context of arrhythmia, valvular disease, or reduced cardiac output (Fig. 6.18) (2,9,16).

D. Moderator Band

Usually classified as "anatomical or normal variant," the moderator band is a muscular structure located in the apical third of the RV. In the four-chamber view, it presents as a prominent band stretching from the inferior interventricular septum to the lateral free wall of the RV (Fig. 6.19). Other muscular bands and large trabeculations are commonly visualized in the apical portion of the RV and must be distinguished from pathologic entities (2,6).

E. Lipomatous Hypertrophy of the Atrial Septum

Fatty deposits in the atrial septum may lead to high echogenicity and severe thickening of its muscular region. Characteristic sparing of the central, fossa ovalis membrane results in the typical bilobed, dumbbell appearance of the atrial septum (Fig. 6.20). Severe adipose infiltration is rarely limited to the atrial septum and may involve the atrial wall, the atrioventricular groove and the entire subepicardium (18). In some cases, it may even interfere with proper visualization of the RA and tricuspid valve (TV). Criteria for the diagnosis of this entity have been suggested: 1—characteristic bilobed appearance of the atrial septum; 2—atrial septum thickness reaching $\geq$15 mm and 3—absence of any other process more likely to cause septal infiltration (metastatic malignancy, amyloidosis) (6). Lipomatous hypertrophy of the atrial septum must be distinguished from metastases, mural thrombi, primary tumors of the heart, and other infiltrative processes.

F. Eustachian Valve

The eustachian valve is an embryologic remnant commonly encountered in adult subjects. This rudimentary, incomplete valve is located at the junction between the inferior vena cava (IVC) and the RA (2,6). It consists of a crescent-shaped ridge on the anterior aspect of the orifice of the IVC. It may be redundant and appear as a thin, mobile membrane undulating in the RA. Unusually large eustachian valves causing obstruction to blood flow

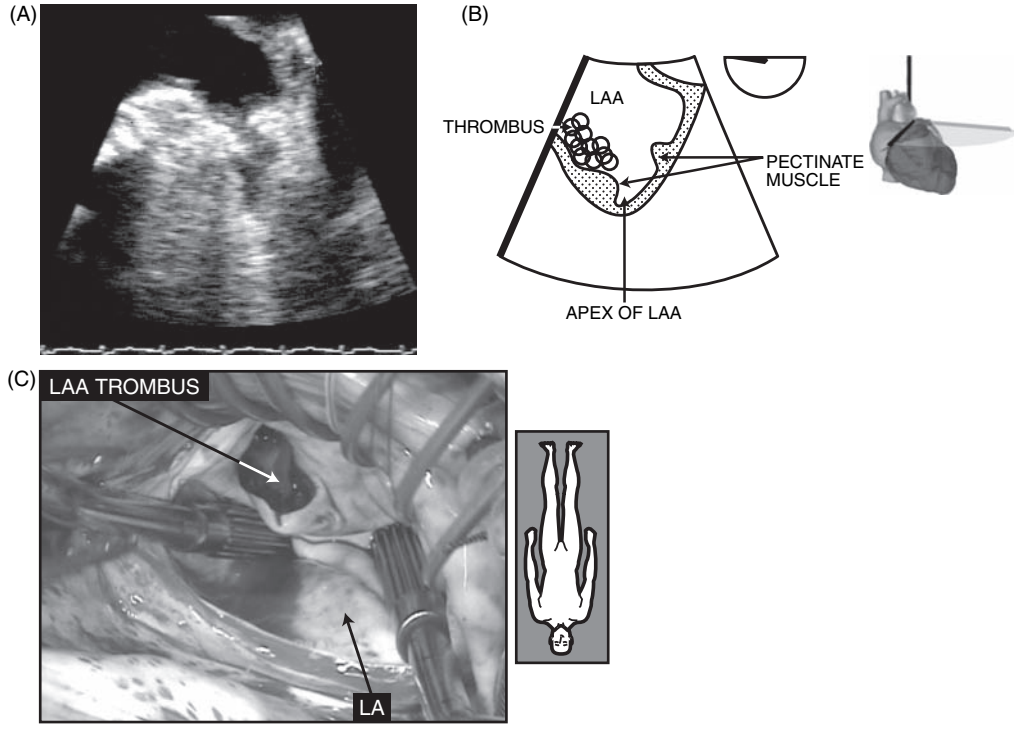

Figure 6.18 Atrial thrombus. (A, B) A thrombus fills the left atrial appendage (LAA) at the level of two prominent pectinate muscles. (C) Intraoperative view of a LAA thrombus (LA, left atrium). (Photo C courtesy of Dr. Michel Pellerin.)

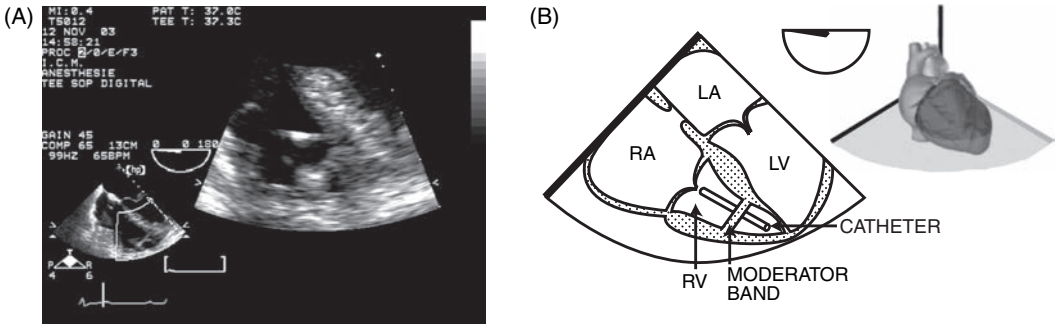

Figure 6.19 Moderator band. Mid-esophageal four-chamber view in a 62-year-old man before coronary revascularization. Dilation of the right ventricle (RV) facilitates visualization of the moderator band. Note the densely trabeculated aspect of the RV apex. (LA, left atrium; LV, left ventricle; RA, right atrium).

from the IVC have been described (2). The eustachian valve is best visualized when imaging both the superior and inferior venae cavae in longitudinal section (9). This imaging plane allows identification of its attachment, anteriorly at the orifice of the IVC (Fig. 6.21). It must not be confused with thrombi, central catheters, vegetations, tumors, or other pathologic processes.

G. Chiari Network

The Chiari network is an embryologic remnant found in 2–3% of normal hearts (6). This filamentous, fenestrated membrane is attached along the orifice of the coronary sinus (Fig. 6.22). It appears as a highly mobile structure within the RA, typically displaying random motion (2,6) between two insertion points on the anterior aspect of the orifice of the IVC (like the eustachian valve) and the superior aspect of the atrial septum. As mentioned for the eustachian valve, the Chiari network must not be mistaken for a pathologic finding such as fibrinous thrombus, or vegetations.

IV. ECHO-FREE SPACES

A. Persistent Left Superior Vena Cava

Persistent left superior vena cava (SVC) occurs in 0.5% of otherwise normal subjects as an isolated finding. It is more frequent in patients with congenital heart disease with a prevalence of 3–10% in that population (6). It most commonly drains into the coronary sinus which appears markedly dilated (2,6,9). Persistent left SVC presents as an echo-free space between the LAA and the left upper pulmonary vein (LUPV). When imaged in longitudinal section, it appears as a vascular structure anterior to the LA and connecting to the coronary sinus (Fig. 6.23) (9). Color Doppler confirms the presence of blood flow in its lumen, differentiating it from an abscess, a cystic cavity

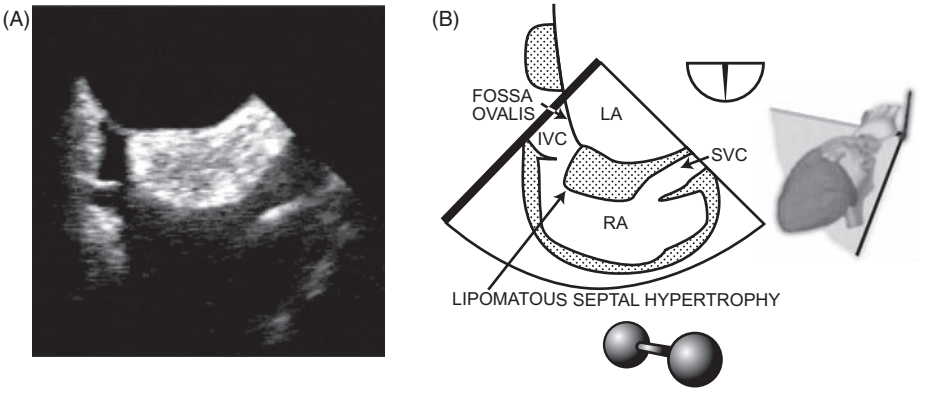

Figure 6.20 Lipomatous hypertrophy. Mid-esophageal bicaval view showing lipomatous hypertrophy of the atrial septum in a 74-year-old woman. The atrial septum reaches 25 mm in thickness. Sparing of the fossa ovalis results in a typical dumbbell appearance (IVC, inferior vena cava; LA, left atrium; RA, right atrium; SVC, superior vena cava).

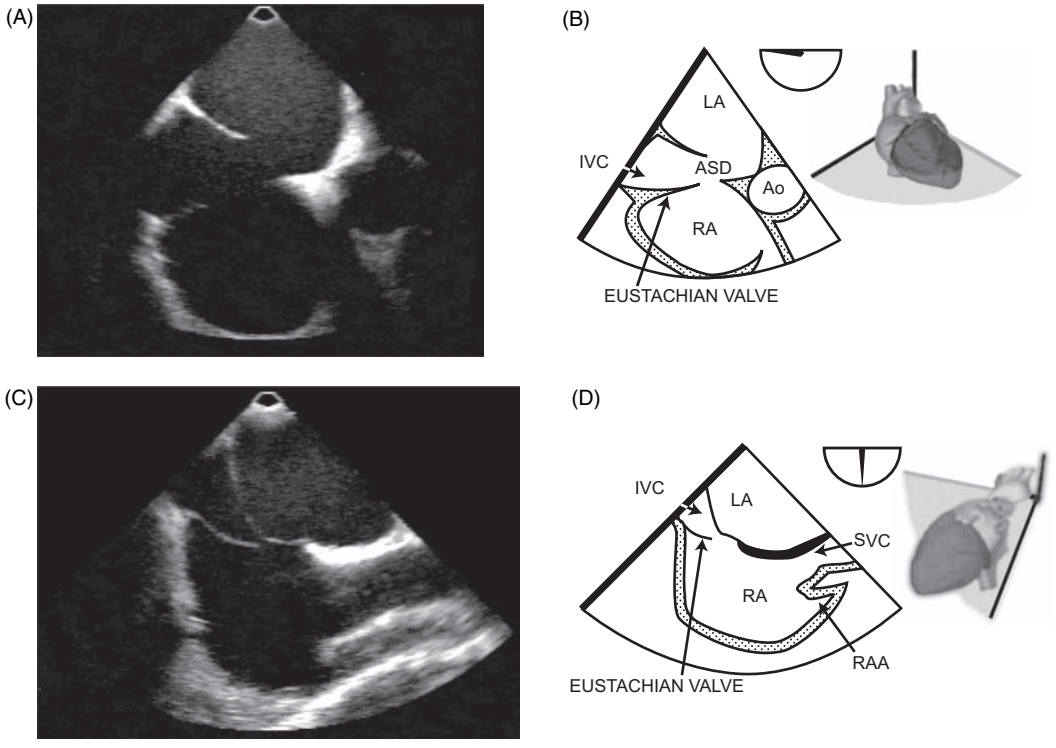

Figure 6.21 Eustachian valve. (A, B) Mid-esophageal view of an Eustachian valve. This embryologic remnant inserted on the anterior aspect of the orifice of the inferior vena cava (IVC) used to direct the flow in fetal life from the IVC towards the foramen ovale. Note the atrial septal defect (ASD). (C, D) The Eustachian valve is also seen in this mid-esophageal bicaval 90° view (Ao, aorta; LA, left atrium; RA, right atrium; RAA, right atrial appendage; SVC, superior vena cava).

or a fluid accumulation in a pericardial sinus. Another way to confirm the diagnosis is by injecting ultrasound contrast (such as agitated saline) in a left upper extremity vein, resulting in opacification of the persistent left SVC followed by the coronary sinus and the RA (Fig. 6.23). Identifying this abnormality in cardiac surgery is important, as cardioplegia administered through the coronary sinus in this situation could be inadequate.

B. Transverse Sinus of Pericardium

The transverse sinus consists of a pericardial reflection at the base of the heart. This blind segment, roughly triangular in cross-section, is located superiorly to the oblique pericardial sinus (Fig. 6.24). Echocardiographically, it appears as a small, echo-free space between the pulmonary artery, the ascending aorta, and the LA (Fig. 6.25). It must

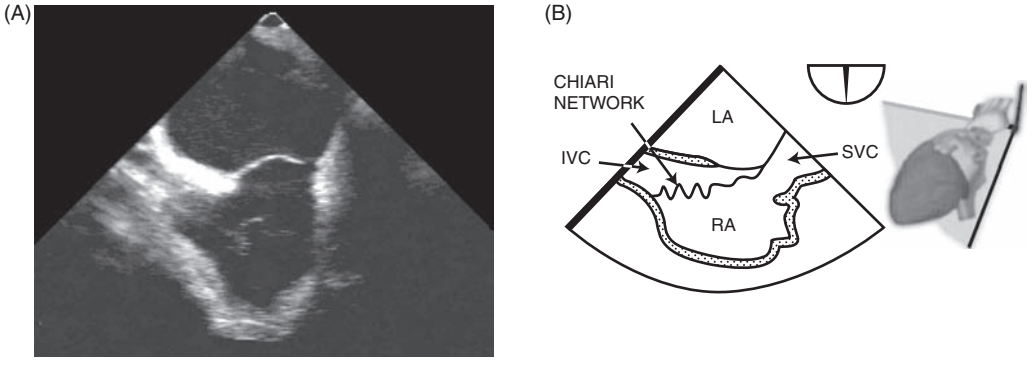

Figure 6.22 Chiari network. Mid-esophageal bicaval view showing a Chiari network undulating in the right atrium (RA) (IVC, inferior vena cava; LA, left atrium; SVC, superior vena cava).

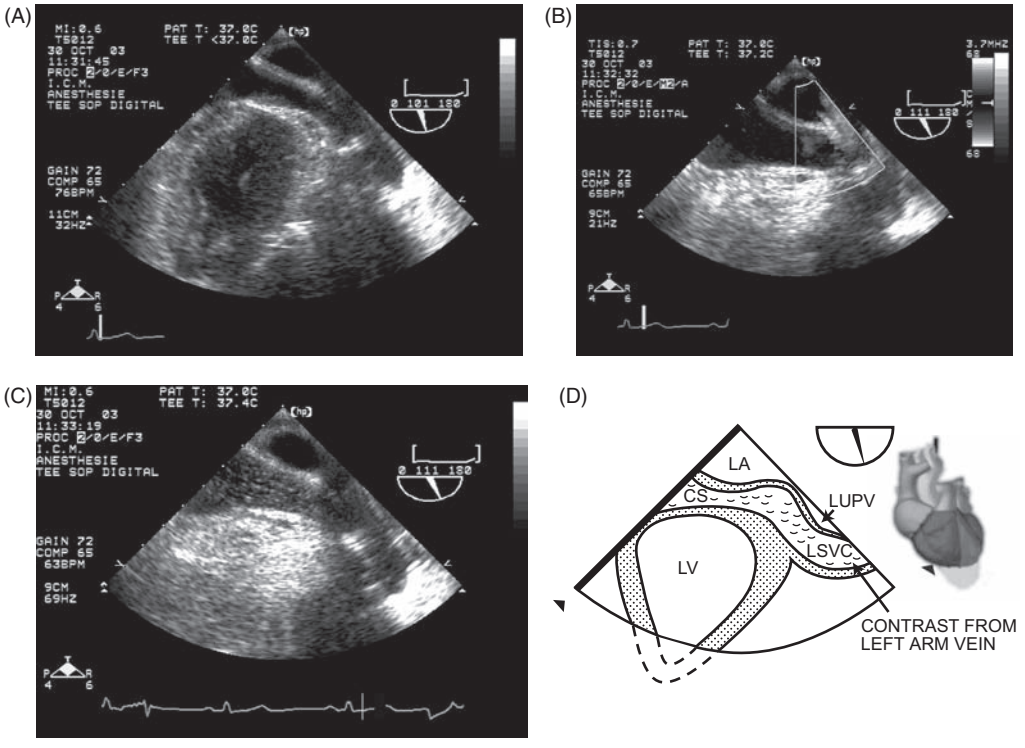

Figure 6.23 Left superior vena cava (LSVC). (A, B) Mid-esophageal deep longitudinal view from a 48-year-old man with a persistent LSVC draining in a dilated coronary sinus (CS). (C, D) Abnormal flow is also demonstrated using agitated saline injection into the left arm from the left subclavian vein with contrast material rapidly appearing into the CS (LA, left atrium; LUPV, left upper pulmonary vein; LV, left ventricle).

be distinguished from a cyst, an abscess, or an aortic dissection. In the presence of a pericardial effusion, the transverse sinus widens and epicardial fat lining the LAA, or the LAA itself, may manifest as irregular, high echogenicity indentations within the transverse sinus (Fig. 6.26). This pseudomass must be recognized to avoid misinterpreting it as a pathologic mass (6,9).

V. COLOR FLOW DOPPLER

A. Physiologic Regurgitation of Native and Prosthetic Valves

The heightened image quality of TEE confers a high sensitivity for even physiologic and trivial valvular regurgitation of native and prosthetic valves. Moreover, color

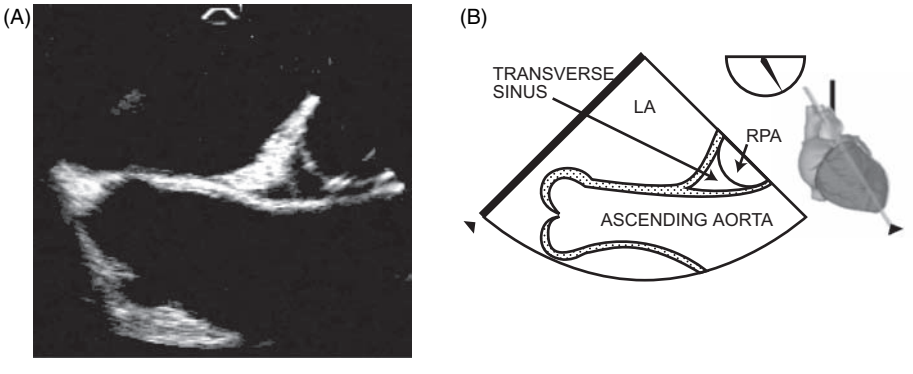

Figure 6.24 Transverse sinus. Mid-esophageal 120° view of the transverse sinus which appears as a small, triangular echo-free space between the ascending aorta and the right pulmonary artery (RPA) (LA, left atrium).

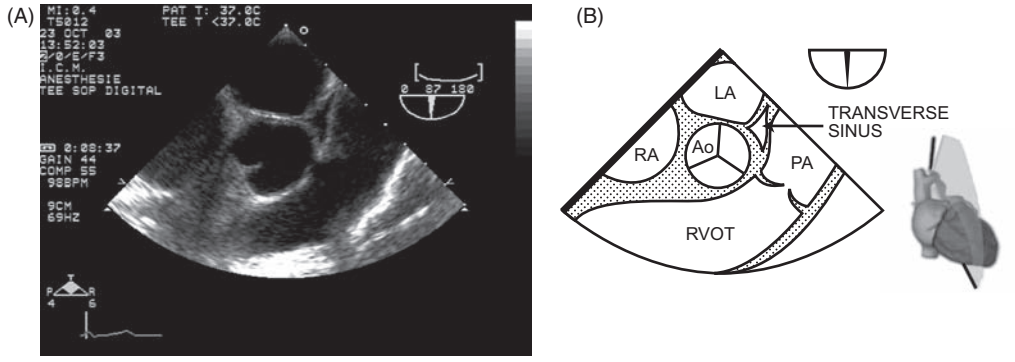

Figure 6.25 Transverse sinus. Mid-esophageal 90° view demonstrating the transverse sinus just beside the aorta (Ao) (LA, left atrium; PA, pulmonary artery; RA, right atrium; RVOT, right ventricular outflow tract).

Doppler imaging often detects an extremely short-lived, low velocity backward movement of blood near the leaflets at valve closure. This phenomenon must be distinguished from valvular regurgitation. A small amount of regurgitation from morphologically normal native valves, especially from atrioventricular valves, is commonly detected on color Doppler imaging. Such physiologic regurgitation is characterized by a brief, short and thin color jet. It is clinically inaudible and should be considered a normal variant (6,9).

Mere closure of mechanical prosthetic valves, and of some bioprosthetic valves, forces a small amount of blood backwards: the closing volume or closing backflow. In addition, in order to avoid thrombus formation, bileaflet and tilting disk mechanical prosthesis are designed to generate a small degree of transprosthetic regurgitation after closure of the valve is completed: the leakage volume or leakage backflow (5,6,9). The pattern of this physiologic regurgitation varies according to the prosthesis model and manufacturer. Typically, tilting disk mechanical prosthetic valves display small peripheral regurgitation jets around the periphery of the disk and a more prominent central jet through the central disk orifice on color Doppler recording. However, bileaflet mechanical prosthetic valves produce more prominent peripheral regurgitation jets. These more prominent jets originate at the periphery of the central closure line and some are centrally oriented, yielding a typical regurgitation pattern on color Doppler imaging (Fig. 6.27) (6). The closing and leakage volumes of mechanical prosthetic valves are considered physiologic regurgitation jets without clinical significance.

B. Gain

Color flow Doppler is widely used for blood flow detection and characterization. Moreover, various quantitative and semiquantitative approaches for estimating the severity of valvular regurgitation and shunt lesions involve color Doppler mapping. Numerous factors may interfere with the proper assessment of such cardiac conditions by color Doppler, including the hemodynamic status at the time of the evaluation and instrument settings. Gain setting represents one of the most influential of these factors (2,6). Augmenting the color Doppler gain from

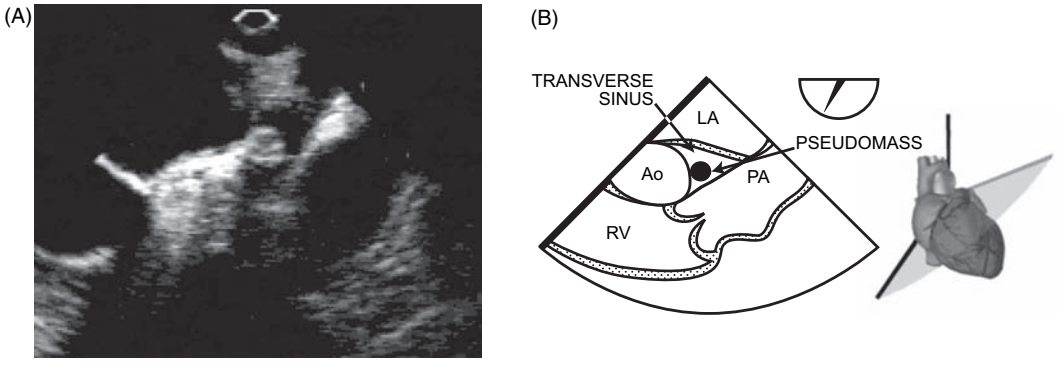

Figure 6.26 Transverse sinus. Mid-esophageal 60° view of the right ventricular outflow tract. A pseudomass in a dilated transverse sinus is present (Ao, ascending aorta; LA, left atrium; PA, pulmonary artery; RV, right ventricle).

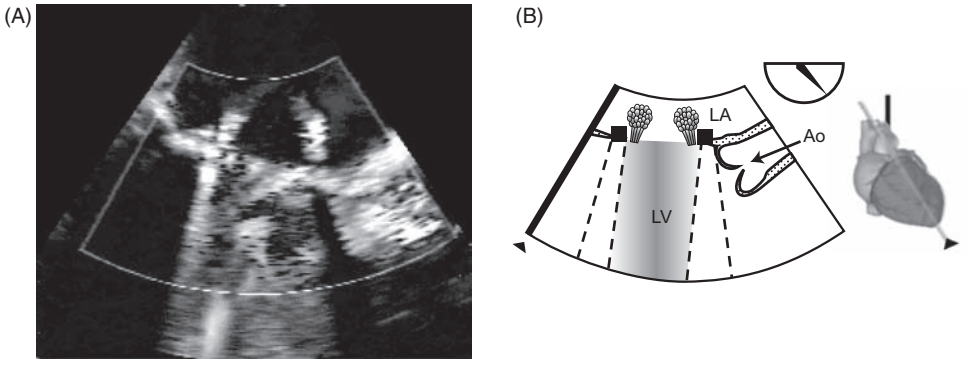

Figure 6.27 Normal prosthetic color Doppler flow. Mid-esophageal long-axis view demonstrating two small, transvalvular regurgitation jets in a normally functioning bileaflet St. Jude mechanical prosthetic valve in mitral position. The shadowing and reverberation extending from the prosthetic valve to the far field are also demonstrated (Ao, aorta; LA, left atrium; LV, left ventricle).

low to high level has been shown to increase the color jet area by >100% (19).

In order to achieve sensitive, specific and reproducible color Doppler evaluations, the gain setting must be optimized. Although no definitive standard criteria exist to ensure uniform color Doppler gain settings, a general principle is suggested. Starting from a low level, the color Doppler gain is progressively increased until background color noise artifacts appear. The gain is then slightly decreased to the highest level devoid of such color artifacts (see Fig. 2.15) (6,18). Perfect standardization, however, remains elusive because of individual differences in acoustic characteristics of the chest and because of the lack of uniform ultrasound system specifications from one manufacturer to another (20).

C. Frequency

Color jet area is determined by various technical factors in addition to color Doppler gain. These parameters may be overlooked because of a common tendency to focus exclusively on gain setting during an echocardiographic study. PRF and, to a lesser extent, transducer frequency are among these variables that need to be optimized. The size of the color jet area varies inversely with PRF and directly with transducer frequency (6).

At lower transducer frequency, lateral resolution is decreased. This reduced capability of precisely distinguishing velocities in two separate points explains the larger pixels on the color Doppler display. It also contributes, especially in conjunction with low color Doppler gain, to underestimate the turbulent flow component at the periphery of color jet areas. Therefore, the size of color flow areas appears smaller on the display with a lower frequency transducer (6,19). However, with more recent technology this factor is minimized as transesophageal probes transmit and receive ultrasounds over a broad range of frequencies simultaneously.

As previously explained in the section on *aliasing*, PRF represents a parameter inherent to color and PW Dopplers. It describes the capability of these modalities of alternately transmitting ultrasound bursts and functioning as echo receiver. The most decisive factor limiting PRF is the depth of the region of interest. When interrogating structures in the far field, the interval before the backscattered signal reaches the transducer is obviously longer than for closer targets. The system must then act as an ultrasound receiver for a longer period before it sends another ultrasound burst. The depth of field limits the number of transmitted pulses per time unit and, therefore, the maximal PRF is lower (2,6).

The PRF has been demonstrated to be inversely related to color flow area for both laminar and turbulent flows. In an animal model, increasing the PRF from 4 to 8 kHz caused a 36% decrease in color jet size (19). However, predicting absolute and relative changes in color flow area with PRF adjustments is much more complex as other system factors (gain, velocity scale, sector angle, instrument manufacturer, color algorithm, filter settings, etc.) may modulate the response to PRF changes. Moreover, the highest velocity that can be displayed without color aliasing varies inversely with transducer frequency and directly with PRF. A PRF corresponding to an aliasing velocity of 40–70 cm/sec on the color Doppler scale is recommended (20).

D. Velocity Scale and Baseline Shift

The common default setting of the color Doppler places the baseline in the center of the velocity scale display. This baseline represents zero velocity and is depicted in black. By convention, the superior-half of the velocity color bar shows a scale in shades of red used by the

system for mapping blood flowing towards the transducer. The velocity scale is surmounted by a positive number corresponding to the maximal velocity the system can display without signal aliasing. The lower half of the color bar is a scale in shades of blue utilized to depict blood moving away from the transducer. The number at the lower end of the velocity scale is equal to the number topping the scale, yet it is preceded by a negative sign implying opposite direction. That number corresponds to the maximal velocity of blood moving away from the probe that can be detected without signal aliasing (6). As stated in the previous section, the recommended aliasing velocity for color Doppler is between 40 and 70 cm/sec (20).

Lowering the velocity scale (and therefore both positive and negative aliasing velocities) below this range may result in color flow mapping that proves difficult to interpret because of excessive signal aliasing and mosaic flow. Moreover, by lowering the maximal velocity of the scale, every tint of red and blue represents a lower velocity interval. Consequently, lower velocity blood flows are allocated brighter colors and become more obvious on the display (6). Conversely, increasing the aliasing velocity above the recommended range may result in color jet areas appearing smaller: as the color scale is stretched over a wider velocity range, the darker shades of red or blue are assigned higher velocities that consequently become more difficult to see on the display.

Shifting the baseline results in an asymmetrical velocity scale display. The maximal velocities at each end of the scale change, aliasing occurring at different velocities according to blood flow direction (6). For example, shifting the baseline upward results in a lower positive velocity at the top of the color Doppler scale and a more negative velocity at the bottom of the scale display. Accordingly, color Doppler aliasing occurs at a lower velocity for blood flow directed towards the transducer and, on the contrary, at a higher velocity in the case of blood flow moving away from the transducer. Therefore, shifting the baseline may prove helpful to eliminate signal aliasing in color flow and PW Dopplers. It is also helpful in the quantitation of color flow jet (most often regurgitant jets) where the baseline of the color scale will be moved in the direction of the flow to enable flow rate measurement by the proximal isovelocity surface area (PISA) method (see Chapter 5).

E. Sector Depth

Color jet size widens with increasing depth. Various factors contribute to this phenomenon. As previously discussed, the main determinant of the PRF is depth of field. Increasing the distance between the transducer and the region of interest reduces the PRF and consequently generates a larger color flow area. Another postulated mechanism is the widening of the ultrasound beam in the far field involving color Doppler mapping. These factors contribute to produce a color jet that may artifactually be larger than the actual, anatomical far field structure confining the flow (6,20).

VI. SUMMARY

Sophisticated and accurate, TEE appears to grant the operator, a direct vision of a beating heart. One must remember however, that this is not the case. The images are merely a complex graphic reconstruction of the heart through mathematical formulas and assumptions. Artifacts must be distinguished from properly displayed structures, and normal variants must not be confused with pathology. In order to avoid misinterpretations, appropriate instrument settings are of paramount importance. Comprehension of the mechanisms involved in artifact formation and familiarity with the technique are prerequisites before performing and interpreting transesophageal echoes. Finally, the operator must stay alert and take the time to explore unusual findings using all the necessary imaging planes and modalities. Only then, will TEE achieve its full potential.

REFERENCES

1. Kremkau FW, Taylor KJ. Artifacts in ultrasound imaging. J Ultrasound Med 1986; 5(4):227–237.
2. Feigenbaum Harvey. Echocardiography. Philadelphia: Lea & Febiger, 1994.
3. Appelbe AF, Walker PG, Yeoh JK, Bonitatibus A, Yoganathan AP, Martin RP. Clinical significance and origin of artifacts in transesophageal echocardiography of the thoracic aorta. J Am Coll Cardiol 1993; 21(3):754–760.
4. Vignon P, Spencer KT, Rambaud G, Preux PM, Krauss D, Balasia B et al. Differential transesophageal echocardiographic diagnosis between linear artifacts and intraluminal flap of aortic dissection or disruption. Chest 2001; 119(6):1778–1790.
5. Bach DS. Transesophageal echocardiographic (TEE) evaluation of prosthetic valves. Cardiol Clin 2000; 18(4):751–771.
6. Weyman AE. Principles and Practice of Echocardiography. 2nd ed. Philadelphia: Lea & Febiger, 1994.
7. Rao SR, Richardson SG, Simonetti J, Katz SE, Caldeira M, Pandian NG. Problems and pitfalls in the performance and interpretation of color Doppler flow imaging: observations based on the influences of technical and physiological factors on the color Doppler examination of mitral regurgitation. Echocardiography 1990; 7(6):747–762.
8. Buttery B, Davison G. The ghost artifact. J Ultrasound Med 1984; 3(2):49–52.
9. Freeman WK, Seward JB, Khandheria BK, Tajik AJ. Transesophageal Echocardiography. Boston, MA: Little Brown and Company, 1994.

10. Schmailzl JG, Ormerod O. Ultrasound in Cardiology. Cambridge: Blackwell Science, 1994.
11. Hozumi T, Yoshida K, Abe Y, Kanda R, Akasaka T, Takagi T et al. Visualization of clear echocardiographic images with near field noise reduction technique: experimental study and clinical experience. J Am Soc Echocardiogr 1998; 11(6):660–667.
12. Boyd MT, Seward JB, Tajik AJ, Edwards WD. Frequency and location of prominent left ventricular trabeculations at autopsy in 474 normal human hearts: implications for evaluation of mural thrombi by two-dimensional echocardiography. J Am Coll Cardiol 1987; 9(2):323–326.
13. Sauerbrei EE. Duplication of the aortic ring. An artifact in echocardiography. J Ultrasound Med 1989; 8(9):477–480.
14. Kremkau FW. Artifacts. In: Kremkau FW, ed. Diagnostic Ultrasound: Principles and Instruments. Philadelphia: WB Saunders, 1993:221–239.
15. Keren A, Billingham ME, Popp RL. Echocardiographic recognition and implications of ventricular hypertrophic trabeculations and aberrant bands. Circulation 1984; 70(5):836–842.
16. Veinot JP, Harrity PJ, Gentile F, Khandheria BK, Bailey KR, Eickholt JT et al. Anatomy of the normal left atrial appendage: a quantitative study of age-related changes in 500 autopsy hearts: implications for echocardiographic examination. Circulation 1997; 96(9):3112–3115.
17. Anderson RH, Levy J. Electrical Anatomy of the Atrial Chambers. Medtronic, 2000.
18. Shirani J, Roberts WC. Clinical, electrocardiographic and morphologic features of massive fatty deposits ("lipomatous hypertrophy") in the atrial septum. J Am Coll Cardiol 1993; 22(1):226–238.
19. Stewart WJ, Cohen GI, Salcedo EE. Doppler color flow image size: dependence on instrument settings. Echocardiography 1991; 8(3):319–327.
20. Hoit BD, Jones M, Eidbo EE, Elias W, Sahn DJ. Sources of variability for Doppler color flow mapping of regurgitant jets in an animal model of mitral regurgitation. J Am Coll Cardiol 1989; 13(7):1631–1636.

7

Equipment, Complications, Infection Control, and Safety

GENEVIÈVE CÔTÉ, ANDRÉ Y. DENAULT
University of Montreal, Montreal, Canada

I. Introduction 141
II. Biological Effects 141
A. Thermal Bioeffect 142
B. Thermal Safety 143
C. Cavitation 143
D. Intensity Measurement and Quantification 144
E. Electrical Safety 144
III. Personnel and Equipment 144
IV. Patient Evaluation Before the Procedure 144
A. Indications 144
B. Evaluation 145
C. Contraindications 146
V. Prophylaxis Planification 146
VI. Monitoring and Patient Position During TEE Examination 147
VII. TEE Probe Inspection 147
VIII. Esophageal Intubation 149
IX. Complications of TEE 151
X. Probe Maintenance and Infection Control 154
XI. Concerns of Health Personnel 155
XII. Conclusion 155
References 156

I. INTRODUCTION

Transesophageal echocardiography (TEE) is now widely used as a diagnostic and monitoring instrument. The proximity of the probe location in the esophagus, immediately posterior to the heart, facilitates higher quality image acquisition in comparison with the transthoracic technique where bones and lungs interfere. European and American groups have published recommendations describing the minimal requirements for complete TEE examination (1). This chapter will discuss the biological effects of diagnostic ultrasound. The method, anatomy, preparation, and safety of the TEE examination will also be reviewed together with various complications.

II. BIOLOGICAL EFFECTS

Diagnostic ultrasound is a valuable modality. To date, there is no contraindication when medical benefit is expected. No confirmed biological effects have been reported resulting from exposure to the present diagnostic ultrasound instruments in humans, including its use in diagnostic cardiac imagery. Ultrasound operators have to understand potential bioeffects, assess the benefits vs the risks of a procedure for a patient, possess and maintain high levels of technical skill and apply the ALARA principle (ALARA principle "as low as reasonably achievable"). The bioeffects of ultrasound include thermal cavitation and other minor and experimentally observed

bioeffects such as microstreaming and torque force. These are observed at a higher exposition level rather than ultrasound level used for diagnostic echocardiography. Our discussion will focus on thermal and cavitation effects.

A. Thermal Bioeffect

The thermal effect is the most important bioeffect attributed to diagnostic ultrasound. This phenomenon is related to ultrasonic energy absorption and its conversion to heat. Increase in temperature during tissue exposure to diagnostic ultrasound fields depends on characteristics of the acoustic source, tissue properties, and exposure time (Table 7.1). Temperature elevation is offset by heat loss due to blood flow through tissue and heat diffusion. Until now, epidemiological studies have shown no health related problems associated with diagnostic ultrasound in humans.

The critical duration represents the duration of exposure for a given thermal elevation. The allowed time–temperature combination can be calculated for a given temperature T, between 39°C and 43°C (Table 7.2). According to the following equation, the duration varies from 1 to ~250 min:

$$t_c = 4^{(43-T)} \tag{7.1}$$

where t_c is the duration of exposure (min) and T is the thermal elevation.

No thermal effects are expected at temperatures <38°C, without regard to exposure length. In animal studies where exposure was sustained for >50 h, no significant biological effects were observed due to temperature elevation of less or equal to 2°C above normal. For example, the critical time for $T = 41$°C, an elevation of 4°C above normal, is 16 min. Exposure time becomes rapidly shorter with a further increase to 43°C, which brings the critical time to 1 min. The probe and the patient's temperature are indicated on the display screen of the TEE ultrasound equipment (Fig. 7.1).

Table 7.1 Acoustic Source and Tissue Properties Implicated in Temperature Increase

Acoustic source properties	Tissue properties
Frequency	Attenuation
Source dimensions	Absorption
Scan rate	Speed of sound
Power	Acoustic impedance
Pulse repetition frequency	Perfusion
Pulse duration	Thermal conductivity
Transducer self-heating	Anatomical structure
Wave shape	Nonlinearity parameters
	Cellular proliferation
	Potential for regeneration

Table 7.2 Maximum Exposure Time Allowed for Various Temperature Elevations Before Tissue Injury According to Eq. (7.1)

Temperature (°C)	Exposure time (min)
39	256
40	64
41	16
42	4
43	1

Calculation of the maximum temperature increase resulting from ultrasound exposure *in vivo* should not be assumed to be exact because of the uncertainties and approximations associated with thermal, acoustic, and structural characteristics of the tissue involved. Different tissues are generally heated by ultrasound in a similar manner, except for bone. Bone is so highly absorptive that it essentially stops the beam. Heating rate can be up to 50 times faster in bone than in typical soft tissue. Calculations can be used as a safety guide for clinical exposure where temperature measurements are not feasible. The rate of increase in temperature can be found by using the following equation:

$$dT/dt = 2\alpha I/C_v \tag{7.2}$$

where dT/dt is the rate of increase in temperature, α is the absorption coefficient of the tissue for a given frequency, I is the intensity of ultrasound exposure, and C_v is the specific heat capacity of the tissue.

Of all ultrasound operating modes, Doppler presents the highest risk for inducing biological effects that are thermally mediated. With Doppler utilization, significant temperature increases occur at bone/soft tissue interfaces. Effects of elevated temperature may be minimized by keeping dwell time as short as possible. The intensity released by an ultrasound transducer varies between 0.001 and 200 mW/cm^2 and it depends on transmission level, compression, captor surface, and emission time. With pulsed-wave (PW) Doppler, this energy can get as high as 1900 mW/cm^2. No biologic effect is observed with power between 100 and 200 mW/cm^2. As for current diagnostic systems, output ranges from 10 mW/cm^2 spatial peak/temporal average (SPTA) intensity for two-dimensional (2D) imaging to as high as 430 mW/cm^2 (SPTA) for PW Doppler. It is advisable to use the lowest level of energy, for a short duration and to turn off the Doppler mode between examinations.

Risks of injury from heating depend on the temperature elevation and the dwell time. Thermal gradient has been theoretically proposed potentially to increase the risk of

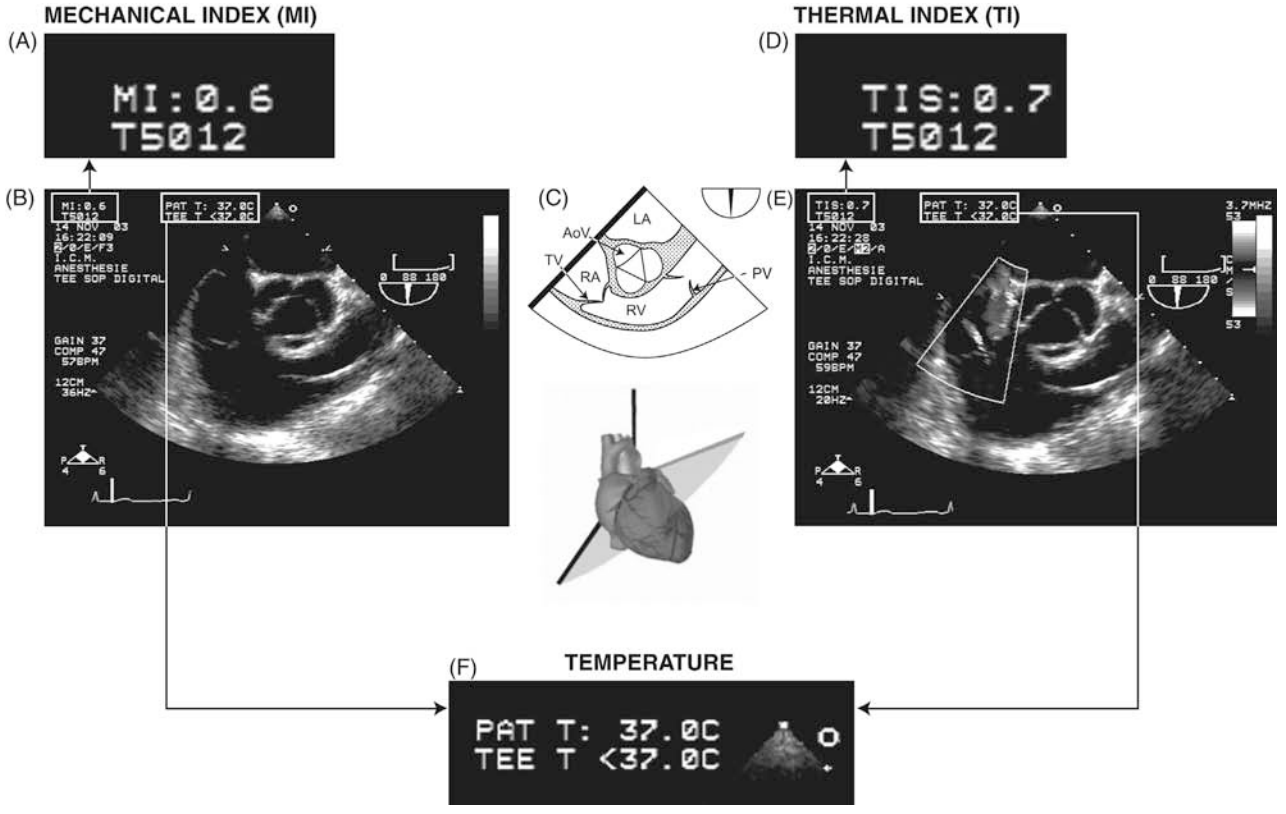

Figure 7.1 (A–F) Mid-esophageal short-axis view of the right ventricular outflow tract in a 64-year-old man scheduled for revascularization. The mechanical index (MI) (A, B), thermal index (TI) (D, E) and temperature (T) (F) are indicated on the top of the display screen of the echocardiographic system (AoV, aortic valve; LA, left atrium; PV, pulmonic valve; RA, right atrium; RV, right ventricle; TV, tricuspid valve).

injury. Therefore it is advisable to shut down the ultrasound transducer when not in use during the bypass period in heart surgery. Concerns were raised about the hypothermic, hypoperfused, and hypoxemic patient exposed for a prolonged duration. In general, adult tissues are more tolerant to temperature increase than fetal and neonatal tissues. Therefore, higher temperature and/or longer exposure would be required for thermal damage. Until now, reported lesions of the esophageal mucosa have been associated with local mechanical trauma attributed to difficult and extreme manipulation of the TEE probe, poor tolerance, and anatomic particularities of the patient, such as diverticula, oesophageal stenosis, or vertebral osteophytes.

B. Thermal Safety

The TEE probe contains a safety device that will shut down automatically in the event of the probe overheating. It is recommended that the temperature of the transducer be checked before insertion in febrile critically ill patients or when TEE monitoring is expected to last for prolonged periods and to modify the superior temperature limit otherwise the probe could turn itself off during the examination.

C. Cavitation

Gas–body activation and cavitation nuclei are subtypes of the general phenomenon of ultrasound cavitation. Cavitation corresponds to the oscillation or the vibration of gas-filled bodies when exposed to ultrasound beam, making them potentially biologically active. Depending on their relationship with the ultrasound field, microbubbles resonate. This phenomenon induces expansion and reduction in microbubble size. Bubbles contained in ultrasound contrast agents might be activated under some conditions. The cavitation level appears to be relatively high in mammals. The resonance frequency is defined by the radius of the microbubble by the following equation:

$$F_0 = \frac{3260}{R_0} \tag{7.3}$$

where F_0 is the resonance frequency (in Hz) and R_0 is the radius of the microbubble (in micrometers).

Until now, with the actual diagnostic system, cavitation has not been shown to occur in the human adult. Acoustic cavitation can alter mammalian tissues. Lung lesions are produced when animals are exposed to diagnostic pulsed ultrasound (1 MPa at 2 MHz). There have been no reports of lung hemorrhage with TEE use in humans. Direct mechanical action of cavitation yields pinpoint regions of destruction, such as petechial hemorrhage. Concerns about the cavitation phenomenon arise especially with the foetus. The World Federation of Ultrasound Medicine and Biology 1998, recommendations state that the operator should minimize ultrasound exposure of human postnatal lungs.

D. Intensity Measurement and Quantification

The intensity (I) of ultrasound exposure can be expressed in several ways, with its unit in W/cm^2. The SPTA corresponds to the highest exposure within the beam averaged over the period of exposure. Another common measure is spatial peak pulse average (SPPA), defined as the average pulse intensity at the spatial location where the pulse intensity is maximum.

The thermal index (TI) and mechanical index (MI) define exposure level with diagnostic ultrasound (see Chapter 1) (2). The TI assesses the potential for ultrasonic heating and is related to the average intensity and its value is indicated during Doppler examination (Fig. 7.1). The MI corresponds to cavitation effect which is related to peak pressure. This value is indicated during 2D exam (Fig. 7.1). These indices have incorporated factors such as tissue exposure to transmission period, the time the ultrasound beam dwells at a specific point (both being considerably shorter than the total examination time).

E. Electrical Safety

The risk of electrical harm with current ultrasound systems is very low. Erosion or perforation of its protective sheath can cause the loss of the system grounding. Loss of system electrical integrity increases the risk of thermal injury. Nowadays, operating room electrical systems are built in such a way that it takes two faults to induce an electrical shock. Also, when defibrillation is necessary, the echocardiography system does not have to be unplugged (<50 J). There have been reports of esophageal burns, perforation (3) and atrioesophageal fistula with intraoperative radiofrequency ablation of atrial fibrillation (4,5). It is, therefore, recommended to avoid using TEE in patients undergoing radiofrequency ablation. At the Montreal Heart Institute, we pull back the TEE probe above the left atrium (LA) during the procedure (Fig. 7.2). In addition, isolating scrub in the oblique sinus behind the left atrial wall could be used to prevent passage of electrical and thermal energy through the left atrial wall toward the esophagus (4).

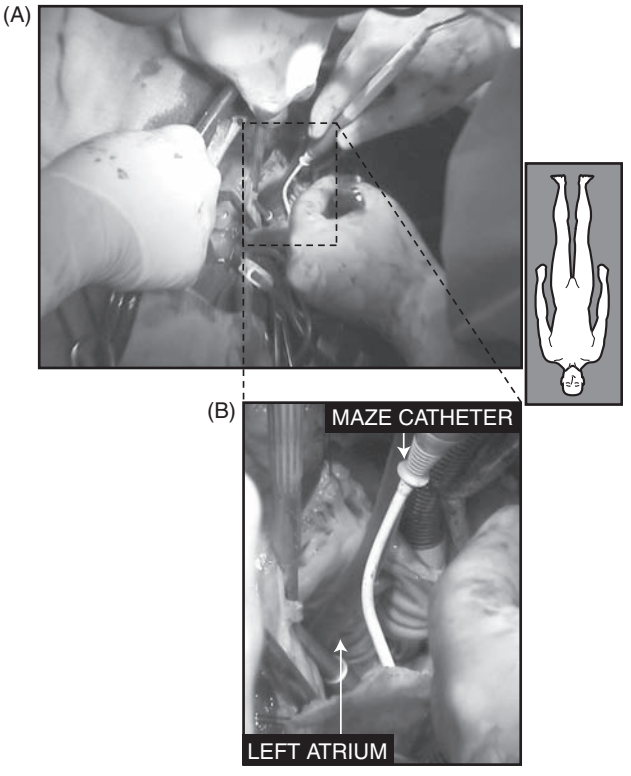

Figure 7.2 Closure of an atrial septal defect in a 48-year-old man. A Maze procedure is also performed for chronic atrial fibrillation. At that time the TEE probe is pulled back above the left atrium to avoid esophageal damage.

III. PERSONNEL AND EQUIPMENT

Various professional associations have published requirements for training, performance and maintenance of TEE examination skills (6). The TEE examination is performed in various settings, in clinics with outpatients, in operating rooms, and in intensive care units. Quality personnel, training, and monitoring can greatly reduce complications. Vigilance should be prime. Standard equipment should include all the proper material required for monitoring and patient resuscitation (Table 7.3).

IV. PATIENT EVALUATION BEFORE THE PROCEDURE

A. Indications

The indications for TEE have increased over the years. In several situations, valuable information can be rapidly

Table 7.3 Equipment Required for TEE Examination

Crash cart
Instruments and accessories for intubation
Suction
Oxygen
Pulse oxymetry
Blood pressure monitor
EKG monitor
Bite block
Gloves, mask, protective glasses, gown
Medication: atropine, epinephrine, lidocaine spray, midazolam, propofol, flumazenil, naloxone, sodium citrate

obtained, such as in the case of aortic dissection, native and prosthetic valvular dysfunctions, endocarditis and source of emboli (7), as well as a monitoring device in perioperative and emergency care. TEE is indicated whenever transthoracic echocardiography (TTE) is inconclusive and when further information could significantly alter the therapeutic management. The general approach to TEE is summarized in Fig. 7.3 and the indications for use are reviewed in Chapter 25 (see also Table 7.4).

B. Evaluation

Before proceeding to the TEE examination it is important that the patient be informed of the aims, technique, and risks of the procedure. The patient's informed consent should be documented in his/her medical record. The pre-procedure evaluation should include a review of the indications, present and past medical history, allergies, current medication, and pertinent physical examination findings. Potential contraindications to the examination should be anticipated (Table 7.5). Significant dysphagia should be regarded as indirect evidence of narrowing of the upper gastrointestinal tract and constitutes a relative contraindication to immediate insertion of the TEE probe. The diagnosis should be clarified by a barium swallow or a gastroenterology consultation. Adequate airway, mouth opening (sometimes reduced in diabetic patients with stiff joint syndrome), neck mobility and stability should be confirmed, particularly when cervical lesions are suspected such as with trauma or severe rheumatoid arthritis. Older patients are prone to occult esophageal lesion, arthritis, and diabetic gastroparesis. Adult congenital heart patients may present specific problems for sedation and airway management (8): for example, patients with Down's syndrome may have atlantoaxial

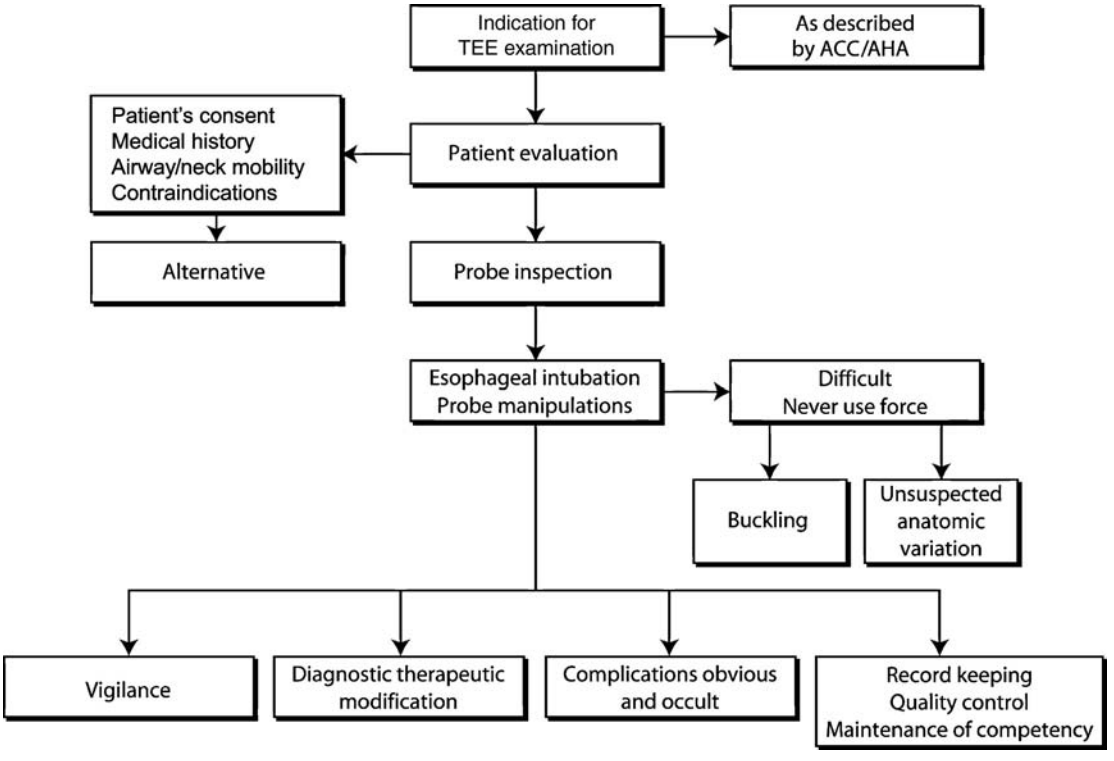

Figure 7.3 General approach to the use of TEE (ACC, American College of Cardiology; AHA, American Heart Association).

Table 7.4 Patient Evaluation and Preparation for TEE Examination

Informed consent from patient
Careful medical history:
Absolute and relative contraindications (see Table 7.5)
Medication use
Drug allergy
Examination
Teeth, oral/dental hygiene, throat neck deviation and mobility
Airway evaluation as for endotracheal intubation
Endocarditis prophylaxis for certain high-risk patient
Fasting status
Absence of recent food ingestion within 6 h and no clear fluid ingestion within 2 h
Availability of adequate patient's safety monitoring
Blood pressure, EKG and saturometry monitoring devices
Emergency resuscitation and suctioning equipment

Table 7.5 Contraindications to Transesophageal Echocardiography

Absolute contraindications
Lack of informed consent
Unwilling and uncooperative patient
Lack of expertise in intubation of TEE
Oesophageal obstruction (cancer, stricture)
Gastric volvulus
Active UGI bleeding
Perforated viscus (known or suspected)
Full stomach
Suspected neck injury
Relative contraindications
Known esophageal pathology
Esophageal varices without bleeding
Esophageal diverticulum
Esophageal fistula
Esophagitis/inflammatory process
Gastric herniation
Sclerodermia
Carcinoma
Penetrating or blunt thoracic esophageal trauma
History of previous esophageal surgery
Esophagectomy
Fundoplication gastric surgery
Cervical abnormalities
Severe cervical osteoarthritis/osteophytes/spondylosis
Neck surgery
Radiation therapy to the cervical area
Severe oropharyngeal distortion
Previous radiation therapy to the mediastinum
Bleeding diathesis

instability, large tongue, subglottic stenosis, and pulmonary hypertension. Finally, full anticoagulation at therapeutic level warrants caution during TEE. In the operating room, it is preferable to insert the TEE probe in patients requiring cardiopulmonary bypass before systemic anticoagulation (9).

C. Contraindications

Absolute contraindications include esophageal obstruction or interruption, gastric volvulus, active upper gastrointestinal bleeding and perforated viscus (Table 7.5). A nonfasting patient with a full stomach presents a major risk even in the case of an acute emergency such as aortic dissection. Prophylactic endotracheal intubation for airway protection against aspiration should be considered. In the presence of a history of significant trauma, cervical injury must be excluded before TEE examination. If cervical instability is present and TEE must be performed because information cannot be obtained otherwise, esophageal intubation under direct visualisation with continuous cervical stabilization during the entire examination must be performed.

Relative contraindications are numerous (Table 7.5). They include various esophageal pathologies, previous gastroesophageal surgeries, bleeding diathesis, cervical abnormalities or anatomical distortion from arthritis, previous surgeries, or radiation therapy. Relative contraindications may not preclude TEE examination but warrant careful evaluation of the risk–benefit ratio of the procedure and the possibility of using alternate diagnostic tests to obtain the relevant information sought. For instance, despite the fact that patients with liver failure present several relative contraindications such as esophageal varices, esophagitis, and acquired coagulopathy, TEE has nevertheless been cautiously used during liver transplantation (see Chapter 22).

V. PROPHYLAXIS PLANIFICATION

In preparation for TEE examination, the patient should be fasting for at least 6 h. In patients with gastroesophageal reflux and gastroparesis (common in the obese and diabetics), prophylaxis for aspiration should be considered, with H_2-blocker, substances neutralizing gastric pH (sodium citrate), and drugs that enhance gastric motility and emptying (metoclopramide). Endotracheal intubation should be further considered to protect the airways against potential aspiration in patients with severe symptoms or who still have a full stomach despite adequate preparation.

As with other diagnostic techniques, TEE is not exempt from possible bacteremia. There is no consensus against endocarditis prophylaxis during TEE examination.

Table 7.6 Antibioprophylaxis for TEE

Standard regimen
Ampicilline 2.0 g IV or IM and gentamycin 1.5 mg/kg IV or IM (not to exceed 80 mg) within 30 min before procedure
Amoxicillin 1.5 g PO 6 h after the initial dose
Alternatively, the parenteral regimen may be repeated once 8 h after the initial dose
Regimen for penicillin-allergic patients
Vancomycin 1.0 g IV over 1 h and gentamycin 1.5 mg/kg IV or IM (not to exceed 80 mg) within 30 min of starting the procedure
May be repeated once 8 h after the initial dose

Prophylaxis is *optional* for the high-risk patient when undergoing TEE as recommended by the American Heart Association (AHA) (Table 7.6) (10). High-risk categories include: prosthetic valves, previous endocarditis, complex cyanotic congenital heart disease, and surgically constructed systemic pulmonary shunts or conduits. High-risk patients with poor oral and dental hygiene or preexisting esophageal disease, may also benefit from antibiotic prophylaxis (10).

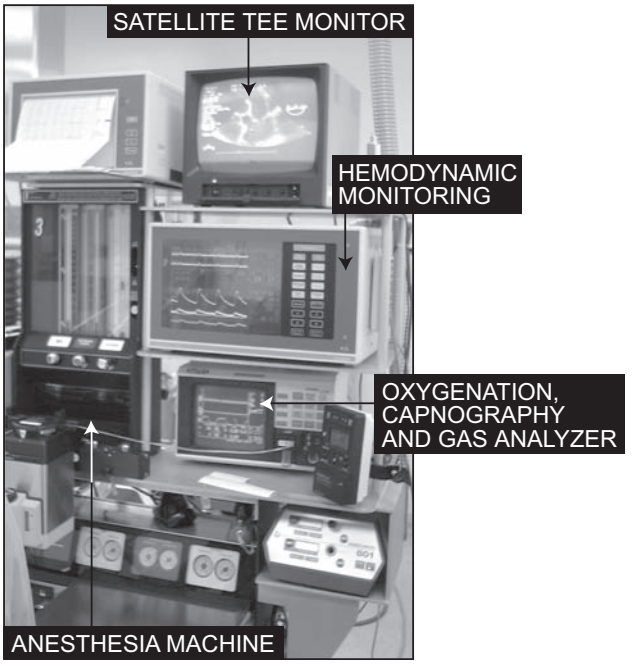

Figure 7.4 Intraoperative monitoring during TEE examination. The use of a satellite TEE monitor helps to maintain vigilance with both hemodynamic and echocardiographic monitoring.

VI. MONITORING AND PATIENT POSITION DURING TEE EXAMINATION

When performing a TEE examination, basic monitoring of the patient is essential. In the operating room at our institution, a satellite TEE display is positioned close to the hemodynamic monitor so that both are in the same visual field (Fig. 7.4). Pulse oxymetry, blood pressure, and electrocardiogram (EKG) must be monitored. Baseline vital signs should be recorded before the beginning of the procedure. A reliable intravenous access must be secured for administration of sedation, anesthesia, or resuscitation drugs. Suctioning devices, supplementary oxygen, and resuscitation equipment should be readily available, as well as trained personnel to assist the procedure and help to monitor the patient.

The performance of TEE under conscious sedation requires adequate knowledge of the pharmacodynamic and pharmacokinetic properties of sedative and narcotic agents. Guidelines on their utilization should be reviewed, particularly if given by non-anesthesiologists unfamiliar with them. Their dosage, utilization, and combination are beyond the scope of this chapter but there have been several reviews on this subject (11–13). It has to be kept in mind that dosage should be adjusted in the elderly or debilitated patient with reduced renal or liver function, and adverse reactions should be anticipated. The dosage of sedation is a delicate balance and both reduced and excessive sedation can be associated with undesirable side effects (Fig. 7.5). Reversal agents for benzodiazepine and narcotic overdose such as flumazenil and naloxone respectively should be readily available.

Oropharyngeal anesthesia with local anesthetic alone, or combined with sedation, improves patient tolerance to the procedure. It reduces the hemodynamic effects associated with esophageal intubation and probe manipulation. Additional superior laryngeal block can be performed if adequate local anesthesia and suppression of the gag reflex cannot be obtained. However, local anesthetic agents also have specific toxic dosages. Careful management of local anesthetic administration is important and many intoxication cases have been reported in the literature with TEE and upper gastrointestinal endoscopy due to inadequate administration of local anesthesia (14).

VII. TEE PROBE INSPECTION

The TEE probe consists of an ultrasound transducer installed at the distal extremity of a flexible endoscope. The maximal adult probe diameter is 0.9–1.6 cm and for the pediatric patient 0.5–0.6 cm. The probe total length varies between 70 and 120 cm. Two proximal control knobs permit anteroposterior and lateral motion of the head of the probe, of about 90° and 70° respectively.

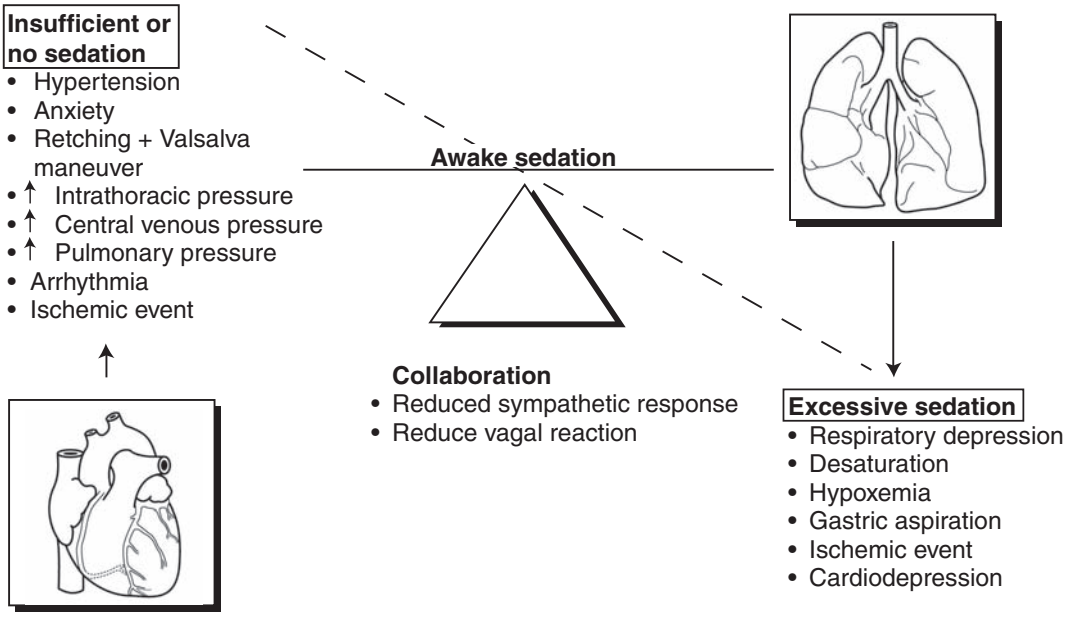

Figure 7.5 The sedative agents have to be titrated for adequate performance of TEE and this titration is a delicate balance between no sedation and excessive sedation. Insufficient or absent sedation will lead primarily to cardiac symptoms such as tachycardia and hypertension. On the other hand, excessive sedation can lead to pulmonary symptoms such as respiratory depression and hypoxia.

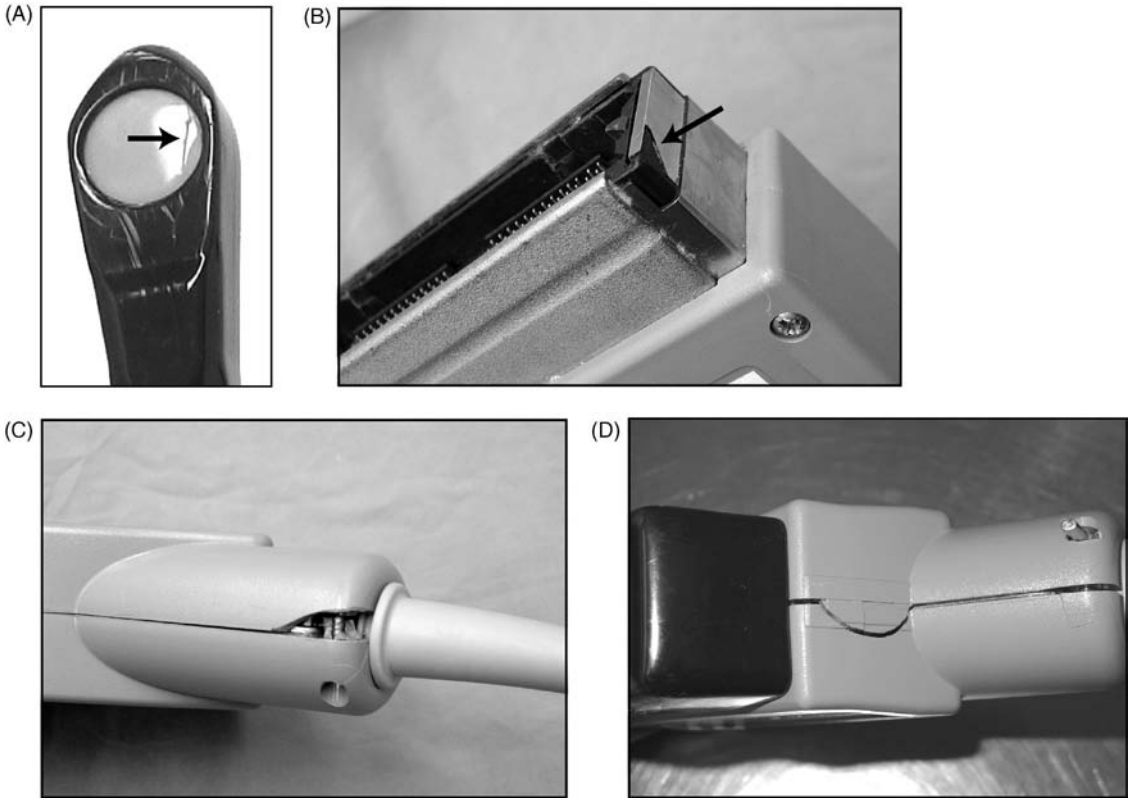

Figure 7.6 (A) Linear fissure in the distal tip of the TEE probe (arrow). (B) Broken connector plate (arrow). (C, D) Broken casing.

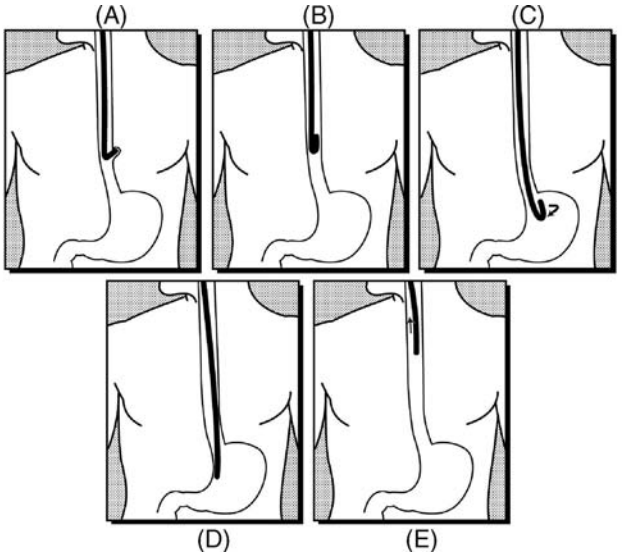

Figure 7.7 (A–C) Buckling of the TEE probe can result in the inability to pull it back from the esophagus. (D, E) If this condition is suspected, pushing the probe down with retroflexing back to a straight position will lead to successful removal. [Adapted from Oriashi (21).]

The ultrasound probe uses an imaging frequency of 3–7.5 MHz.

Between each use inspection of the outer sheath integrity for breaks, fissure or extruding wire should be systematically performed (Fig. 7.6). The plastic and rubber casing of the probe must be intact, and the electrical safety checked regularly. Electrical and mechanical dysfunction, such as excessive or restricted probe motion upon manipulation of the control knobs must be corrected before further use. Excessive motion range could result in buckling on TEE probe introduction (Fig. 7.7). It is useful to have a maintenance log book for each TEE probe to keep track of usage, cleaning, and periodic inspection.

VIII. ESOPHAGEAL INTUBATION

Insertion of the probe is attempted with control knobs in the neutral and unlocked position (Fig. 7.8). The distal end of the probe is lubricated with jelly and inserted through a mouth piece to protect the susceptible TEE shaft from teeth biting or jaw crushing (Fig. 7.9). The TEE examination can be performed under general

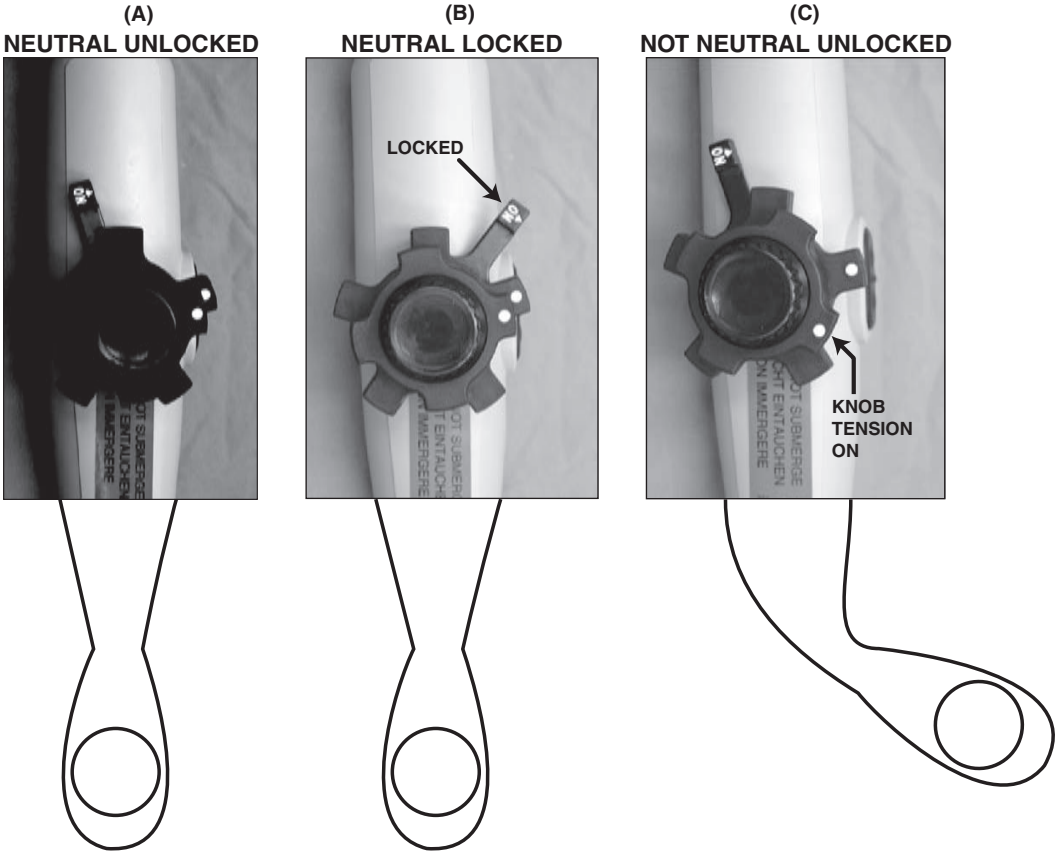

Figure 7.8 Control knobs of the TEE probe have to be in the neutral and unlocked position during insertion.

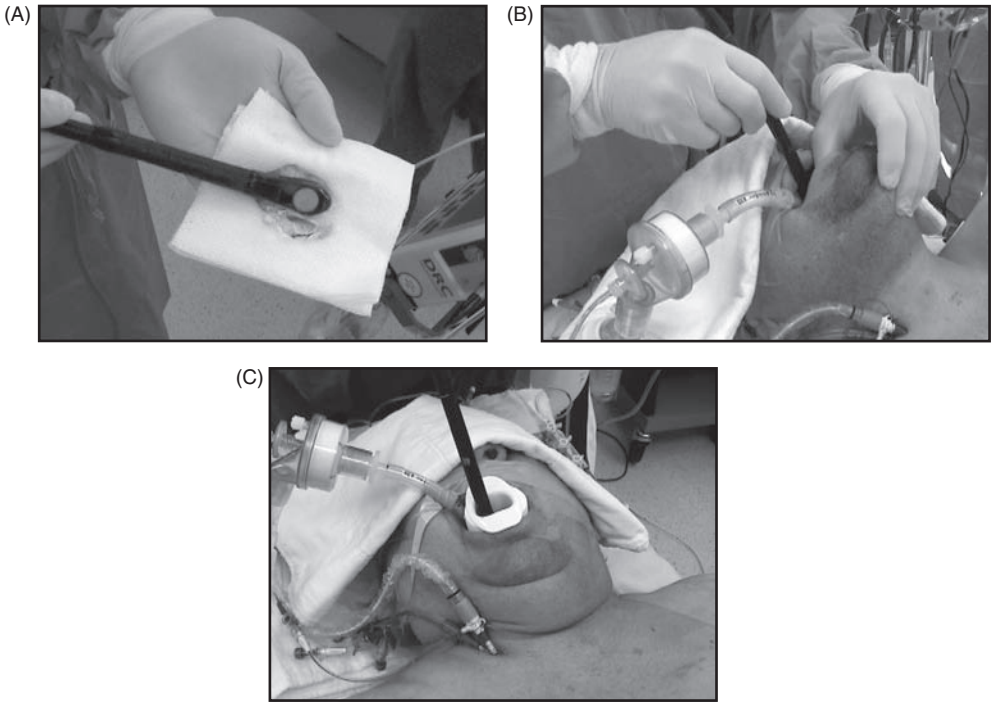

Figure 7.9 (A, B) Lubricant used prior to insertion of the TEE probe. (C) In non-edentulous patients, a bite block is then fixed at the front of the mouth in the anesthetised patient to protect the probe from teeth damage and to avoid displacement.

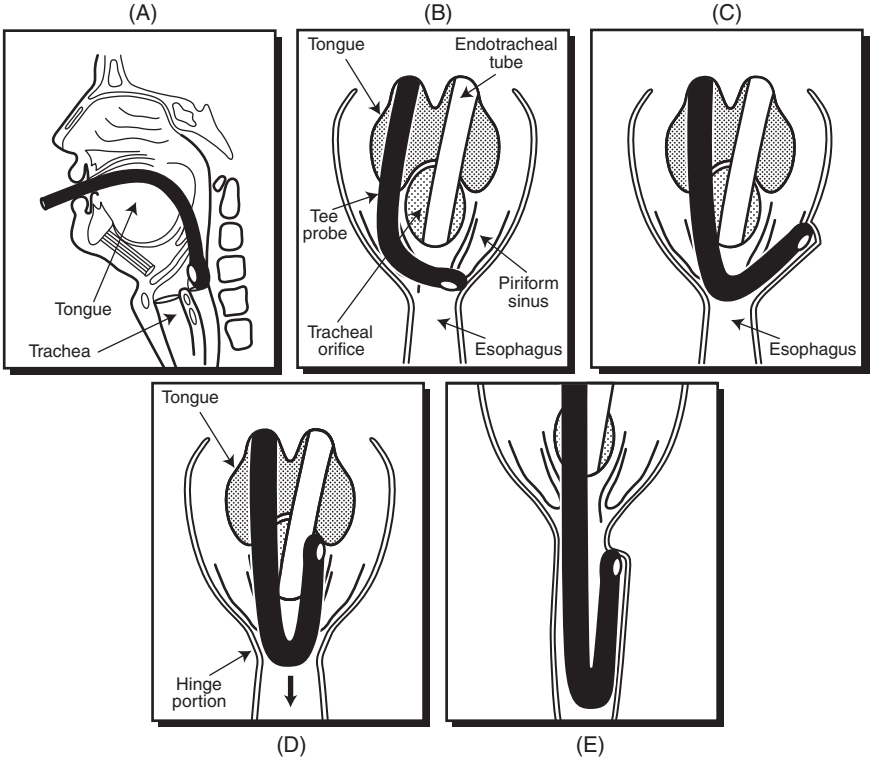

Figure 7.10 Difficult insertion of the TEE probe often results from a lateral insertion as opposed to one from the midline (B, C). If excessive pushing occurs (D), the probe could be inserted in a flexed position resulting in buckling (E). [Adapted from Oriashi (21).]

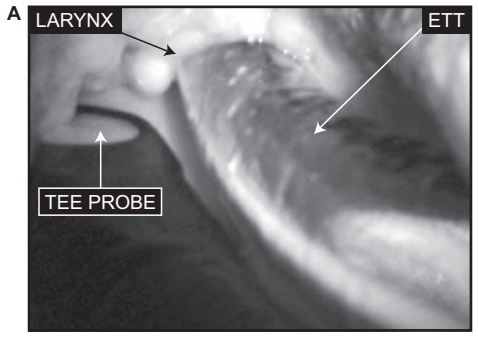

Figure 7.11 TEE probe insertion using the fiberoptic laryngoscope. Resistance will be encountered when the probe is not directed in the midline position (ETT, endotracheal tube).

anesthesia or conscious sedation in a cooperative patient. Under general anesthesia, blind intubation is commonly done using the second and third fingers as a guide or to pull up the mandible to assist TEE insertion while the probe is kept central to the tongue (Fig. 7.9). Unexpected difficult esophageal intubation may occur (Fig. 7.10) and benefit from placement under direct laryngoscopy to reduce the risk of lesion associated with numerous blind attempts (Fig. 7.11). Occasionally, the endotracheal tube cuff may have to be deflated to facilitate insertion.

Under conscious sedation, adequate local anesthesia combined with light sedation and reassurance can be sufficient for the patient to tolerate probe insertion and TEE examination. Placed in the left lateral decubitus or sitting position, the patient is asked to try to swallow the probe. The deglutition maneuver closes the vocal cords and the larynx moves forward to the posterior aspect of the tongue while the cricoid muscle relaxes. Local or systemic analgesia greatly contributes to patient tolerance by reducing retching and suppressing the gag reflex.

The probe insertion should be smooth and not meet undue resistance. Forced insertion can cause vocal cord trauma or esophageal wall laceration. Mobilization of the probe should never be performed with the probe in a locked and flexed position (Fig. 7.8). During insertion, the ultrasound system display can be monitored to confirm the correct insertion of the TEE probe and to detect rapidly inadvertant tracheal intubation with associated image loss or appearance of tracheal rings (Fig. 7.12) (15,16). Under general anesthesia, this could be missed unless ventilation pressure modification is recognized. In the awake and sedated patient, tracheal intubation may be suspected in the event of stridor, coughing, wheezing, and desaturation while the ultrasound system display reveals tracheal rings or poor images due to interference from air in the trachea. In heavily sedated patients, tracheal placement can sometimes only be suspected by the presence of desaturation. The insertion and removal of the TEE probe can also be associated with displacement of the endotracheal tube.

IX. COMPLICATIONS OF TEE

According to numerous studies, total complications, including minor and major events, vary between 0.6% and 3.5% (17–19). These results compare favorably with those encountered for gastrointestinal (GI) endoscopy. The TEE examination carried out in emergency settings has a higher complication rate of up to 12.6%. Several factors contribute to this situation, including the emergent nature of the TEE need, the hemodynamic status of the patient, the alteration of consciousness and the risk of aspiration from a full stomach. The TEE related complications are illustrated in Fig. 7.13.

Failure to introduce the probe correctly into the oesophagus occurs in an estimated 1–2% of attempted procedures. Most of the time, it is attributed to the lack of patient collaboration or tolerance, and to the operator's inexperience. In the setting of multiple unsuccessful attempts, it is sometimes beneficial to reschedule the exam and plan it under general anesthesia and direct laryngoscopic visualization.

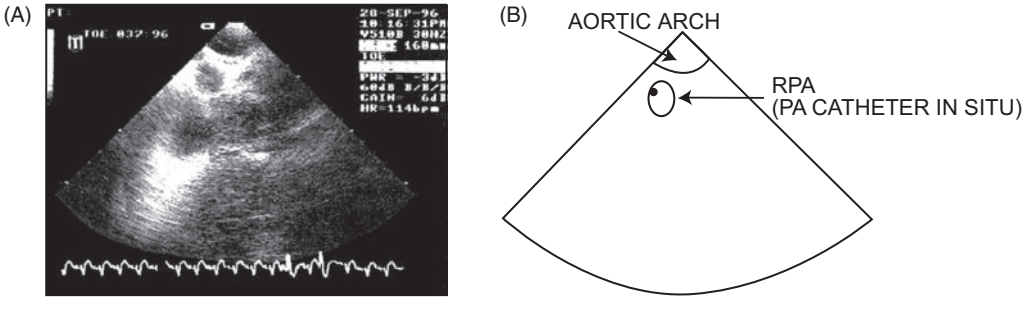

Figure 7.12 Transverse plane transtracheal image and diagram of aortic arch and right pulmonary artery. Distal structures were not clearly visualised (RPA, right pulmonary artery). [With permission from Sutton (16).]

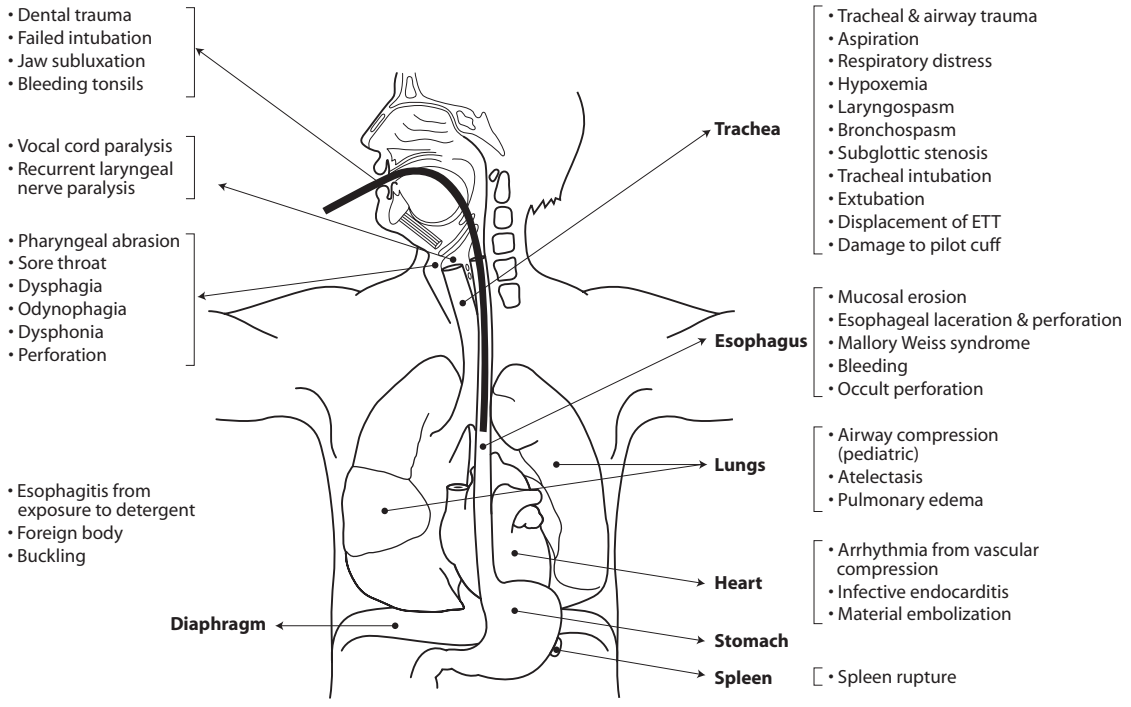

Figure 7.13 Summary of TEE-related complications (ETT, endotracheal tube).

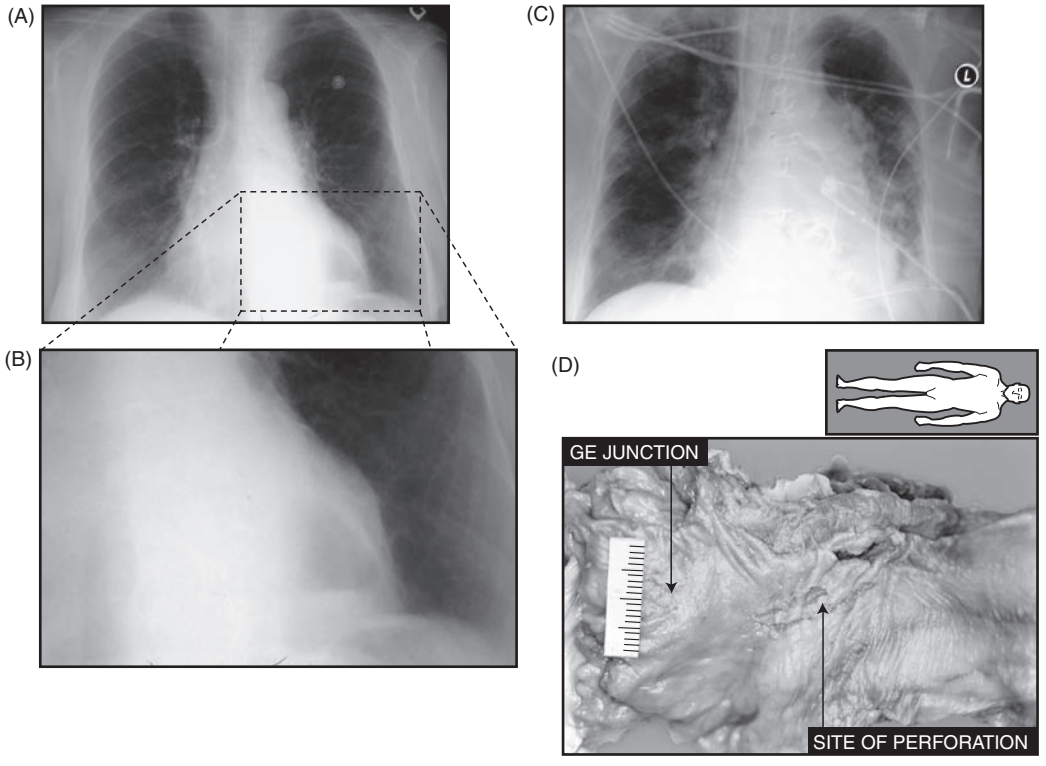

Figure 7.14 A 71-year-old woman is scheduled for aortic and mitral valve replacement with TEE monitoring. (A, B) On the preoperative chest X-ray a hiatal hernia was seen. (C) In the postoperative period she developed a left-sided pneumothorax and pleural effusion requiring a chest tube. She then went into multiple-organ failure and died. (D) The autopsy showed distal esophageal perforation and a posterior mediastinal abcess (GE, gastroesophageal). (Photo D courtesy of Dr. Tack Ki Leung.)

Excessive blind probe manipulation may result in buckling of the probe on itself when inserted into the esophagus (Figs. 7.7 and 7.10) (20,21). Forced withdrawal of a buckled probe may result in esophageal injury. The TEE probe must be delicately pushed into the stomach where it can unfold in a neutral straight position. Further assistance with fluoroscopy and the presence of an anesthesiologist and a gastroentorologist endoscopist may at times be necessary. At no time should forceful manipulation or mobilization in a locked control knob position be attempted because of the risk of mucosal tear.

Secondary oropharyngeal or upper gastro-intestinal significant bleeding is rarely reported. However, unrecognized esophageal laceration and perforation (0.02–0.03%) leading to mediastinitis and sepsis can be disastrous and sometimes discovered only at autopsy (Fig. 7.14).

Transient hypoxemia can occur during TEE examination, with or without sedation and analgesia, and can be problematic for patients suffering from significant cardiac and/or pulmonary diseases. Hypoxemia correlates with the additive effects of narcotics and benzodiazepines, the presence of chronic obstructive pulmonary disease and the size of the TEE probe. Alteration of the mental status after administration of sedation and analgesia also increases the risk of aspiration as the airway protective reflexes are blunted. Methemoglobinia can be induced by excessive administration of local anesthetic agent or in patients presenting certain enzymatic defect (cytochrome b5 reductase deficiency). The treatment is supportive and includes administration of methylene blue. An algorithm of hypoxia management during TEE insertion is presented in Fig. 7.15.

Hemodynamic effects associated with TEE probe insertion and mobilization can be dramatic in awake and sedated patients. Tachycardia and hypertension can result in an ischemic event in susceptible subjects. Prominent gag reflexes and retching have been described to

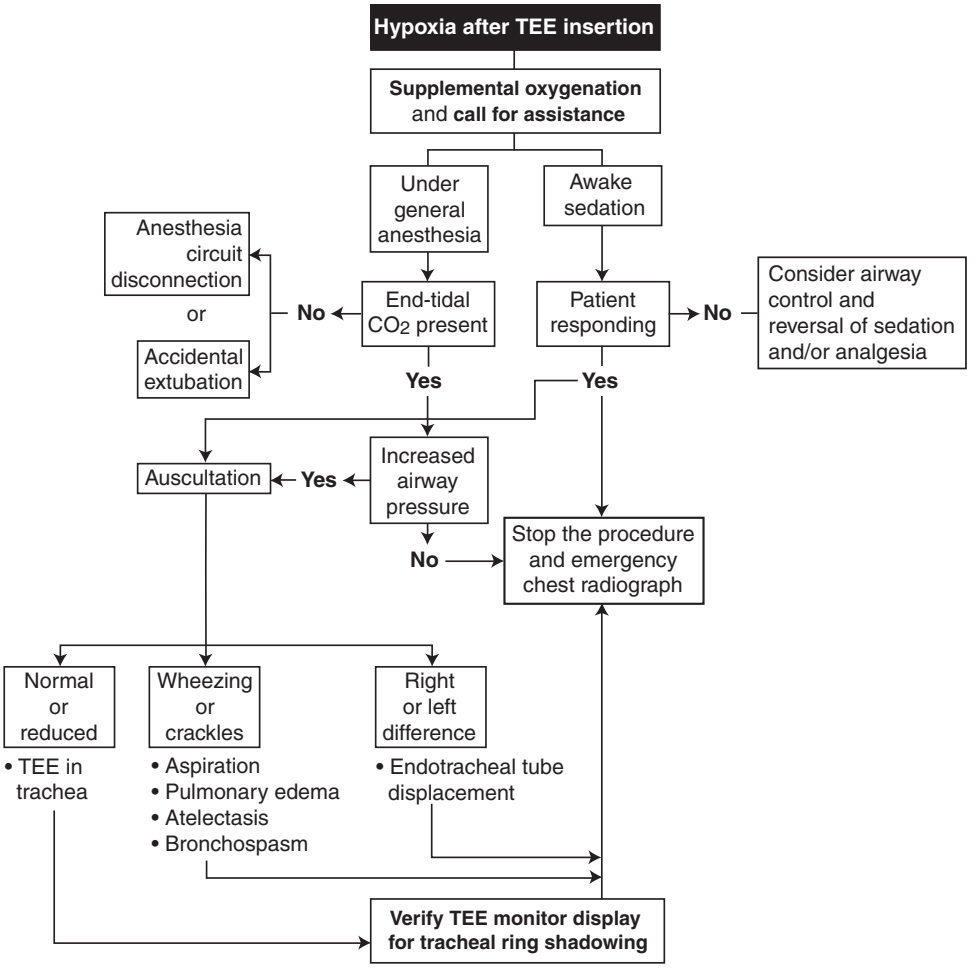

Figure 7.15 Hypoxia management algorithm during TEE probe insertion (CO_2, carbon dioxide; TEE, transesophageal echocardiography).

cause embolization of intracardiac mass and sudden death. Tachyarythmiae have also been reported during probe insertion and manipulation even under general anesthesia. Patients can also experience pain and vomiting. The TEE examination can exacerbate medical conditions such as cardiac and respiratory insufficiency, severe and uncontrolled high blood pressure, aortic dissection, pulmonary hypertension, and critical aortic stenosis.

X. PROBE MAINTENANCE AND INFECTION CONTROL

The TEE probe cleaning is necessary to prevent transmission of pathogens from one patient to the next. The emergence of multidrug-resistant bacteria, tuberculosis, prions and various viruses emphasizes a methodical work flow pattern and the importance of adequate disinfection. The cleaning process must clearly define the clean and soiled areas and eliminate the possibility of recontamination (Fig. 7.16).

Immediately after use and removal from the patient, the TEE probe shaft is separated from the ultrasound system and brought to the sink where it is washed with soap and running water. Gentle but thorough mechanical cleaning removes organic and inorganic debris and reduces the microbial contamination by 99%. Care must be taken not to immerse the probe control knobs and electrical proximal connector. The probe is then soaked in a bath of 2% glutaraldehyde solution for 20–30 min. This solution is effective against infection propagation and serves as a second line antibacterial and antiviral disinfectant (Tables 7.7 and

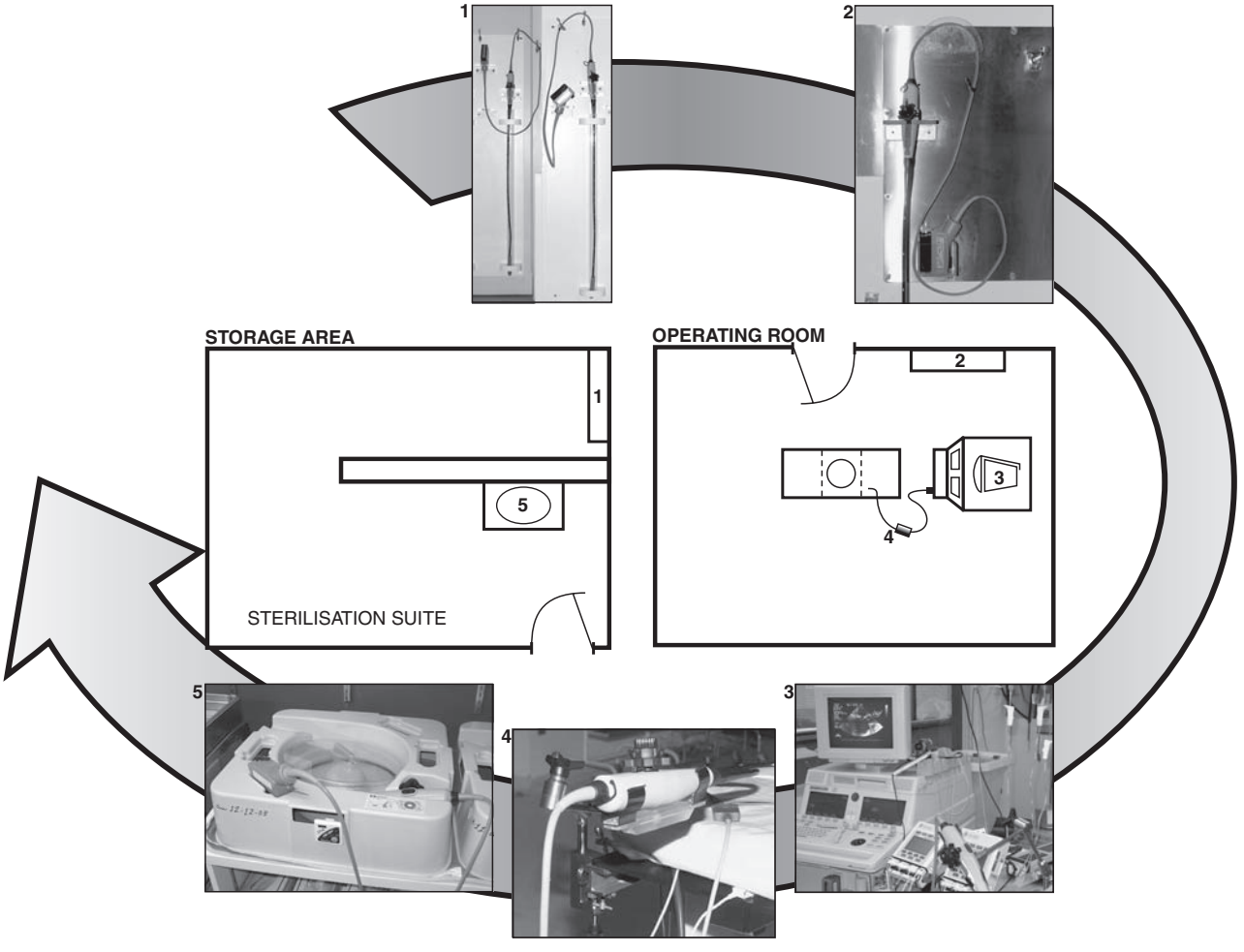

Figure 7.16 Operating room (OR) maintenance and cleaning system for the TEE probe at the Montreal Heart Institute. (1) The TEE probes are stored in a rack system in the clean area outside the cardiac OR. (2) Before the surgery, a TEE probe is brought to the cardiac OR where it is temporarily left on a supporting rack. (3) For use, the TEE probe is connected to the echocardiographic system. (4) During monitoring, the TEE handle is supported by a custom-made stabilizer. (5) Once the exam is completed, the TEE probe is transferred back to the cleaning and sterilization suite.

Table 7.7 Cleaning and Disinfection of the TEE Probe

1. Always follow universal precautions (protective clothing etc.)
2. All TEE and endoscopic equipment must be cleaned between each patient
3. Cleaning should be done by properly trained staff
4. Thorough but gentle mechanical cleaning under running water with soap or detergent to remove all gross organic material (secretions, saliva, etc.) from the probe
5. Probe soaking in a bath of 2% glutaraldehyde for 20–30 min, up to 45 min in case of HIV patients. Excessive soaking times may result in premature wear of the TEE probe protective coating
6. Probe rinsing to wash off all trace of glutaraldehyde
7. Inspection of the TEE probe for potential tear/break and break in electrical integrity

7.8). Finally, because of its potential for toxicity, the glutaraldehyde is rinsed off under running water and the probe is left to hang until dry. The distal end of the probe should be covered with a plastic cap to protect the ultrasound transducer during storage and installed in a protective supporting system (Fig. 7.17).

As an integral part of the reprocessing of the probe, the outer sheath, control knobs, and range of motion must routinely be inspected. With repeated abrasion from use, cleaning and damage from teeth bites or jaw crushing, the outer sheath can develop fissure and false lumen. This may result in sequestration of soiled liquid or glutaraldehyde disinfectant which can later be remobilized during use in a different patient, causing either contamination or chemical burn. A break in the sheath integrity caused by the steel wire of the inner probe control is rarely encountered (22). Exaggerated flexion of the probe tip should be repaired as they can contribute to buckling (Figs. 7.7 and 7.10).

Finally, with repeated plugging and unplugging of the TEE probe main electrical connector with the ultrasound platform electrical receptacle, defective probe function most commonly occurs secondary to worn-out and broken metal contacts, cracked shell, and accumulation of interfering dirt (Fig. 7.6).

Table 7.8 Duration of Glutaraldehyde Exposition and Pathogen Destruction

Glutaraldehyde exposition (min)	Pathogens
1	Bacteria
2	100% sterile solution
2	Inactivates HIV and enteroviruses
2.5–5	Inactivates HBV
5–10	Low titer of mycobacterium tuberculosis

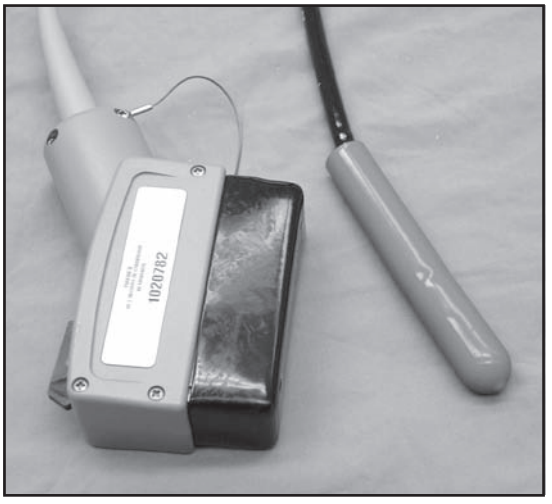

Figure 7.17 Protective covers for the TEE probe.

XI. CONCERNS OF HEALTH PERSONNEL

At all times, medical and paramedical staff should follow the rules for universal protection against transmittable diseases. Gloves, gowns, protective eyewear, and masks are worn to protect against splashing, spray, droplets, and other infectious materials that may be generated during coughing, retching, and vomiting by a patient during the procedure. Hepatitis vaccination is strongly recommended, as the infectious status of a patient is often unknown. Herpetic infection of a finger contaminated by oral secretions and herpetic conjunctivitis acquired during endoscopy by salivary spray occurs frequently enough to deserve the sobriquet "endoscopist's eye." The utilization of a bite block protects the operator and the probe from being bitten by teeth or crushed by an edentulous jaw.

The glutaraldehyde solution has a toxic potential which should be made known to the personnel dedicated to probe manipulation and disinfection. Indeed, this product causes lung and mucosal toxicity, with dermatitis, conjunctivitis, nasal irritation, and asthma. Thus, the disinfection area should be well ventilated and a lid should cover the glutaraldehyde container at all times to prevent propagation of toxic fumes to the whole room (Fig. 7.16).

XII. CONCLUSION

Since its inception as a diagnostic test, TEE examination has been clearly shown to yield important diagnostic information capable of altering cardiovascular disease management while being relatively easy to perform and it has an excellent safety record even in critically ill patients. However, this examination is, nevertheless, semi-invasive

and has a definite potential for significant complications particularly in ill-prepared procedures. It is, therefore, important for the clinician, who wishes to maximize the risk–benefit ratio of this test, to understand its indications, its limitations, to master the details of proper equipment usage and be alert to its potential complications by following a methodical and rigorous procedural technique meant to maximize patient safety.

REFERENCES

1. Quinones MA, Otto CM, Stoddard M et al. Recommendations for quantification of Doppler echocardiography: a report from the Doppler Quantification Task Force of the Nomenclature and Standards Committee of the American Society of Echocardiography. J Am Soc Echocardiogr 2002; 15:167–184.
2. Meltzer RS. Food and Drug Administration ultrasound device regulation: the output display standard, the "mechanical index," and ultrasound safety. J Am Soc Echocardiogr 1996; 9:216–220.
3. Doll N, Borger MA, Fabricius A et al. Esophageal perforation during left atrial radiofrequency ablation: is the risk too high? J Thorac Cardiovasc Surg 2003; 125:836–842.
4. Mohr FW, Fabricius AM, Falk V et al. Curative treatment of atrial fibrillation with intraoperative radiofrequency ablation: short-term and midterm results. J Thorac Cardiovasc Surg 2002; 123:919–927.
5. Sonmez B, Demirsoy E, Yagan N et al. A fatal complication due to radiofrequency ablation for atrial fibrillation: atrio-esophageal fistula. Ann Thorac Surg 2003; 76:281–283.
6. Quinones MA, Douglas PS, Foster E et al. American College of Cardiology/American Heart Association clinical competence statement on echocardiography: a report of the American College of Cardiology/American Heart Association/American College of Physicians—American Society of Internal Medicine Task Force on Clinical Competence. Circulation 2003; 107:1068–1089.
7. Flachskampf FA, Decoodt P, Fraser AG et al. Guidelines from the Working Group. Recommendations for performing transesophageal echocardiography. Eur J Echocardiogr 2001; 2:8–21.
8. Muhiudeen RI, Miller-Hance WC, Silverman NH. Intraoperative transesophageal echocardiography for pediatric patients with congenital heart disease. Anesth Analg 1998; 87:1058–1076.
9. St-Pierre J, Fortier LP, Couture P, Hebert Y. Massive gastrointestinal hemorrhage after transoesophageal echocardiography probe insertion. Can J Anaesth 1998; 45:1196–1199.
10. Dajani AS, Taubert KA, Wilson W et al. Prevention of bacterial endocarditis. Recommendations by the American Heart Association. J Am Med Assoc 1997; 277:1794–1801.
11. Recommended practices for managing the patient receiving moderate sedation/analgesia. AORN J 2002; 75:642–652.
12. Practice guidelines for sedation and analgesia by non-anesthesiologists. Anesthesiology 2002; 96:1004–1017.
13. Waring JP, Baron TH, Hirota WK et al. Guidelines for conscious sedation and monitoring during gastrointestinal endoscopy. Gastrointest Endosc 2003; 58:317–322.
14. Sharma SC, Rama PR, Miller GL et al. Systemic absorption and toxicity from topically administered lidocaine during transesophageal echocardiography. J Am Soc Echocardiogr 1996; 9:710–711.
15. Fagan LF Jr, Weiss R, Castello R, Labovita AJ. Transtracheal placement and imaging with a transesophageal echocardiographic probe. Am J Cardiol 1991; 67:909–910.
16. Sutton DC. Accidental transtracheal imaging with a transesophageal echocardiography probe. Anesth Analg 1997; 85:760–762.
17. Daniel WG, Erbel R, Kasper W et al. Safety of transesophageal echocardiography. A multicenter survey of 10,419 examinations. Circulation 1991; 83:817–821.
18. Stevenson JG. Incidence of complications in pediatric transesophageal echocardiography: experience in 1650 cases. J Am Soc Echocardiogr 1999; 12:527–532.
19. Kallmeyer IJ, Collard CD, Fox JA et al. The safety of intraoperative transesophageal echocardiography: a case series of 7200 cardiac surgical patients. Anesth Analg 2001; 92:1126–1130.
20. Kronzon I, Cziner DG, Katz ES et al. Buckling of the tip of the transesophageal echocardiography probe: a potentially dangerous technical malfunction. J Am Soc Echocardiogr 1992; 5:176–177.
21. Orihashi K, Sueda T, Matsuura Y et al. Buckling of transesophageal echocardiography probe: a pitfall at insertion in an anesthetized patient. Hiroshima J Med Sci 1993; 42:155–157.
22. Chan KL, Burwash I. Unusual structural abnormality in a biplane transesophageal transducer with normal imaging function. J Am Soc Echocardiogr 1998; 11:310–312.

8

Segmental Ventricular Function and Ischemia

ADY BUTNARU, ANIQUE DUCHARME, JEAN-CLAUDE TARDIF
University of Montreal, Montreal, Canada

I. Introduction 157
II. Anatomy and Function 157
A. Coronary Artery Distribution and Flow 157
B. Myocardial Segmental Identification 158
C. Normal Segmental Function 159
III. Global Systolic Function Changes 162
IV. Other Indices of Global Systolic Ventricular Function 165
V. Segmental Systolic Function Changes 167
VI. Diastolic Function Changes 169
VII. Complications and Associated Findings 171
A. Ventricular Septal Defect 172
B. Papillary Muscle Dysfunction or Injury and Evaluation of Mitral Regurgitation 173
C. Left Ventricular Thrombus 176
D. Right Ventricular Infarction 177
E. Ventricular Dilatation 177
F. Left Ventricular Aneurysm 178
G. Myocardial Rupture 179
VIII. Coronary Artery Imaging and Assessment of Coronary Vasodilator Reserve 181
IX. Conclusion 182
References 182

I. INTRODUCTION

During the last decade, the indications for transesophageal echocardiography (TEE) have expanded significantly with the advent of multiplane imaging (1). The close proximity of the transducer to the heart, the absence of intervening lung or bone tissue and an improved signal-to-noise ratio have promoted good image quality. Transesophageal echocardiography is an invaluable tool in the perioperative setting in patients with inadequate transthoracic images and in critically ill patients. Among its multiple intraoperative applications, TEE can be used to monitor global and regional ventricular function as well as the patient's volume status. This chapter focuses on the perioperative TEE evaluation of ventricular function and the detection of complications after myocardial infarction.

II. ANATOMY AND FUNCTION

A. Coronary Artery Distribution and Flow

Coronary anatomy can vary but an overall pattern of coronary artery distribution can be described. The left main coronary artery rises from the superior aspect of the left sinus of Valsalva and divides into the left anterior descending (LAD) coronary and circumflex coronary arteries (Fig. 8.1). The LAD artery descends into the anterior interventricular groove down to the left ventricular apex giving diagonal and septal branches. The circumflex artery continues laterally down the left atrioventricular groove giving rise to obtuse marginal branches (Fig. 8.2). The right coronary artery (RCA) rises from the superior

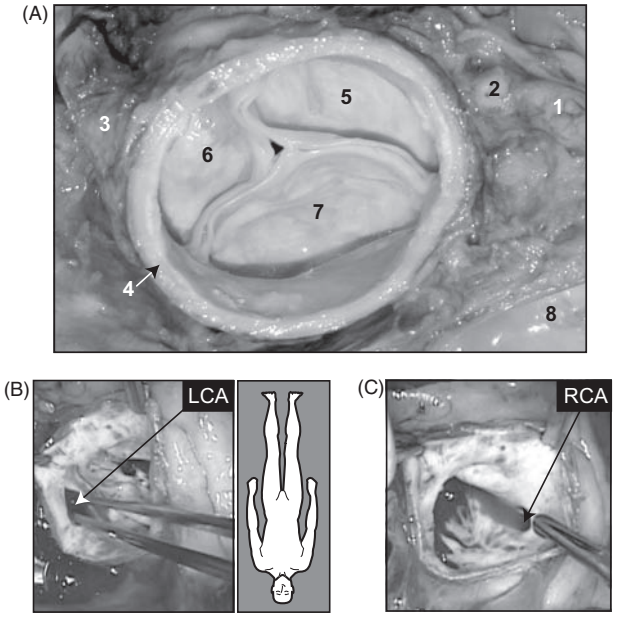

Figure 8.1 (A) Surgical anatomical view of the aortic valve and the origin of the coronary artery. (B, C) Intraoperative view of the left coronary artery (LCA) and right coronary artery (RCA) (1, right coronary artery; 2, infundibular artery; 3, left coronary artery; 4, aortic valve; 5, right coronary cusp; 6, left coronary cusp; 7, noncoronary cusp; 8, right atrium).

aspect of the right sinus of Valsalva and extends inferomedially along the right atrioventricular groove (Fig. 8.3). The system dominance is defined by the artery giving rise to the posterior descending artery which supplies the inferior aspect of the ventricular septum and the inferior free wall. The posterior descending artery arises from the RCA in 80% of patients and from the circumflex artery in 20%. On the basis of studies correlating coronary angiography with echocardiography, a scheme was developed describing the specific coronary artery perfusing each left ventricular segment (2) (Figs. 8.4 and 8.5). The LAD coronary artery supplies the anterior portion of the interventricular septum through septal branches (Fig. 8.6), the anterior left ventricular free wall through diagonal branches, and the septal and anterior portion of the apex. Because the basal portion of the anterior interventricular septum is perfused by the first septal perforator, a wall motion abnormality in this region is consistent with stenosis of the proximal LAD artery. The circumflex artery perfuses the inferolateral (posterior) and anterolateral walls and the lateral apex. The RCA supplies the right ventricle (RV) through proximal and mid-ventricular branches, the inferior free wall, the inferior-half of the septum and the inferior apex from the posterior descending artery. In the transgastric short-axis view, the LAD coronary artery supplies the anterior wall and the anterior septum, the circumflex artery supplies the anterolateral and inferolateral walls, and the RCA supplies the inferior septum and inferior wall (Fig. 8.5). In the mid-esophageal four-chamber view, the mid-septum and septal apex are perfused by the LAD coronary artery, the basal septum is supplied by the RCA artery and the basal and mid lateral walls are part of the circumflex artery territory (Fig. 8.7). In the two-chamber view, the anterior wall is perfused by the LAD artery, the inferior wall is supplied by the RCA, and the apex often has a dual coronary artery support (Fig. 8.7). Although there is a clear relationship between the epicardial coronary circulation and segmental function, the echocardiographer must also remember that in the presence of coronary artery stenosis, wall motion abnormalities are more likely to occur at a fast, rather than slow, heart rate (resulting in shorter diastolic duration).

B. Myocardial Segmental Identification

Different methods are available for reporting the location of wall motion abnormalities during the echocardiographic examination. They differ mainly by the number of segments in which the left ventricle (LV) is divided (between 15 and 20) but are similar with regard to the general nomenclature of the segment. From base to apex, the LV is divided into basal, mid, and apical thirds corresponding to the proximal, middle, and apical segments of the coronary arteries. The most current scheme, approved by the American Society of Echocardiography (ASE) (2), divides the ventricle into 17 segments, six segments both in the basal and mid portions (anteroseptal, inferoseptal, anterior, anterolateral, inferolateral, and inferior walls) and five at the apex (septal, anterior, lateral, inferior, and apical). As these segments can be recorded from three short-axis and several longitudinal views, it is possible (and useful) to evaluate a segment from more than one view (Figs. 8.7 and 8.8).

The mid-esophageal four-chamber view [transducer at 0°, posterior to the left atrium (LA)] allows simultaneous visualisation of the LV and RV (Fig. 8.7). Because foreshortening of the left and right ventricular cavities occurs in this view, it is useful to use probe retroflexion to attenuate the problem, although this may result in degradation of image quality. In this view, the segmental function of the septal, lateral walls, and apex can be assessed. Rotation of the transducer to $\sim 45^\circ$ depicts the inferior septum to the left of the screen and the anterolateral wall to the right. With the transducer at 90°, the mid-esophageal two-chamber view allows visualisation of the inferior and anterior walls and adjacent portions of the apex. Further transducer rotation up to $120-150^\circ$ will result in a long-axis view, with the anterior septum and inferolateral wall on the right and left respectively. Using the

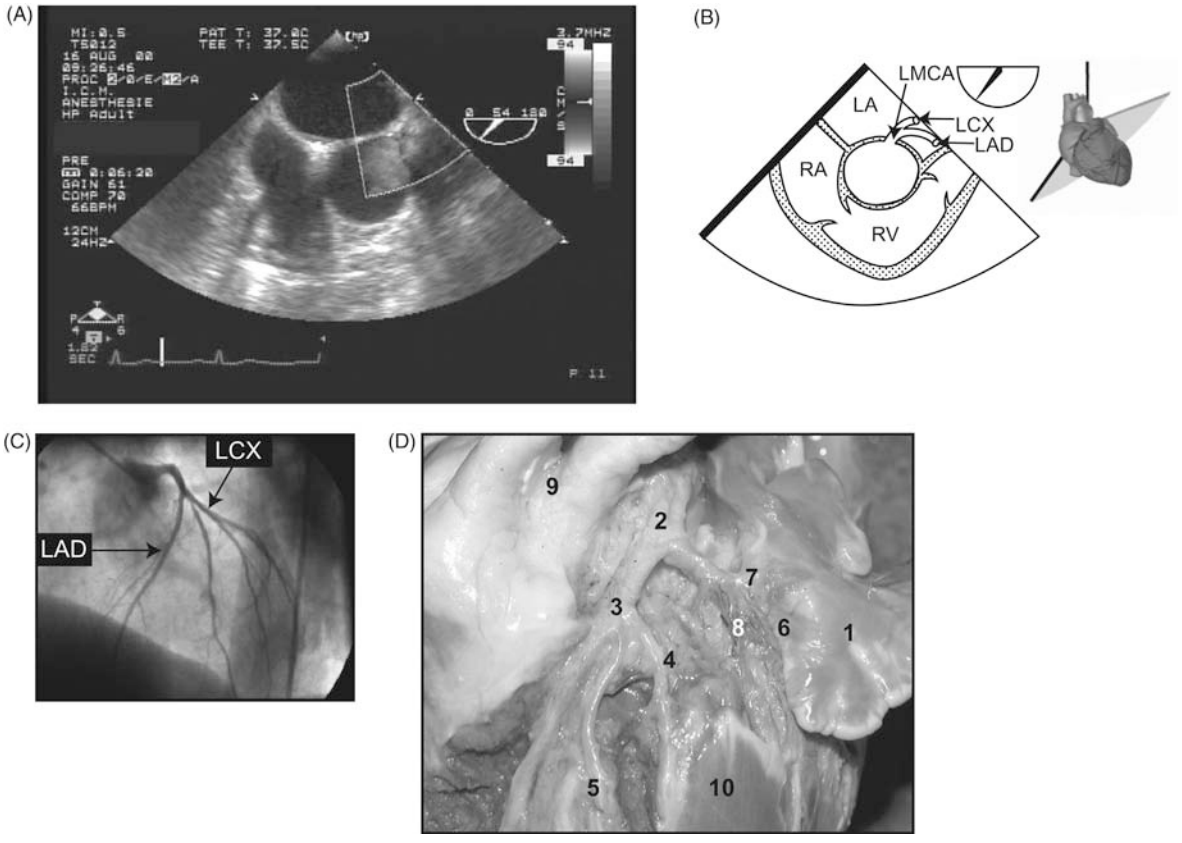

Figure 8.2 Echocardiographic (A, B), angiographic (C) and anatomical (D) views of the left main coronary artery (LMCA) (LA, left atrium; LAD, left anterior descending; LCX, left circumflex; RA, right atrium; RV, right ventricle; 1, left atrial appendage; 2, left coronary artery; 3, left anterior descending; 4, first diagonal branch; 5, second diagonal branch; 6, left circumflex; 7, branch of left atrial appendage; 8, marginal branches; 9, pulmonary trunk; 10, left ventricle). (Photos C and D courtesy of Drs. Philippe L. L'Allier and Nicolas Dürrleman.)

transgastric approach (Fig. 8.8), a series of short-axis views can be obtained at 0–20° by modifying probe depth and anteflexion. For example, maximal anteflexion will generally allow visualization of the basal ventricular segments and the mitral valve. A lesser degree of anteflexion or slight probe advancement will result in short-axis views at the high and low papillary muscle levels. In these short-axis views, the inferior wall is seen at the top of the screen, the anterior wall at the bottom, the inferolateral and anterolateral walls to the right, and the anterior and inferior septums to the lower left and upper left of the screen. Further probe advancement will often result in a short-axis view of the left ventricular apical segments. Because ventricular segments perfused by each of the three major coronary arteries are represented in the short-axis view at the mid-papillary muscle level, it is commonly used in the intraoperative setting to evaluate global and segmental function (3). Transducer rotation to 90° yields a two-chamber view, with the inferior and anterior walls at the top and bottom of the screen, respectively. It is usually possible to visualize the nontruncated, true left ventricular apex in this view on the left of the screen and to identify a wall motion abnormality, aneurysm, or thrombus. Further rotation to 120–150° will result in a long-axis view, with the inferolateral wall on top and the anterior septum at the bottom of the screen.

C. Normal Segmental Function

With ventricular contraction, a target point chosen along the endocardial border interface will move inward, towards the centre of the ventricle (endocardial excursion), resulting in reduced cavity area and increased distance between the endocardial and epicardial interfaces (wall thickening). During systole, a normally contracting myocardium is characterized by a radial shortening of >30% and myocardial thickening of 30–50% (3) (Table 8.1). It is important to take into account the heterogeneity of normal segmental function when assessing myocardial contractility. For example, the normally contracting basal inferior wall and basal interventricular septum often appear to have reduced wall motion compared with

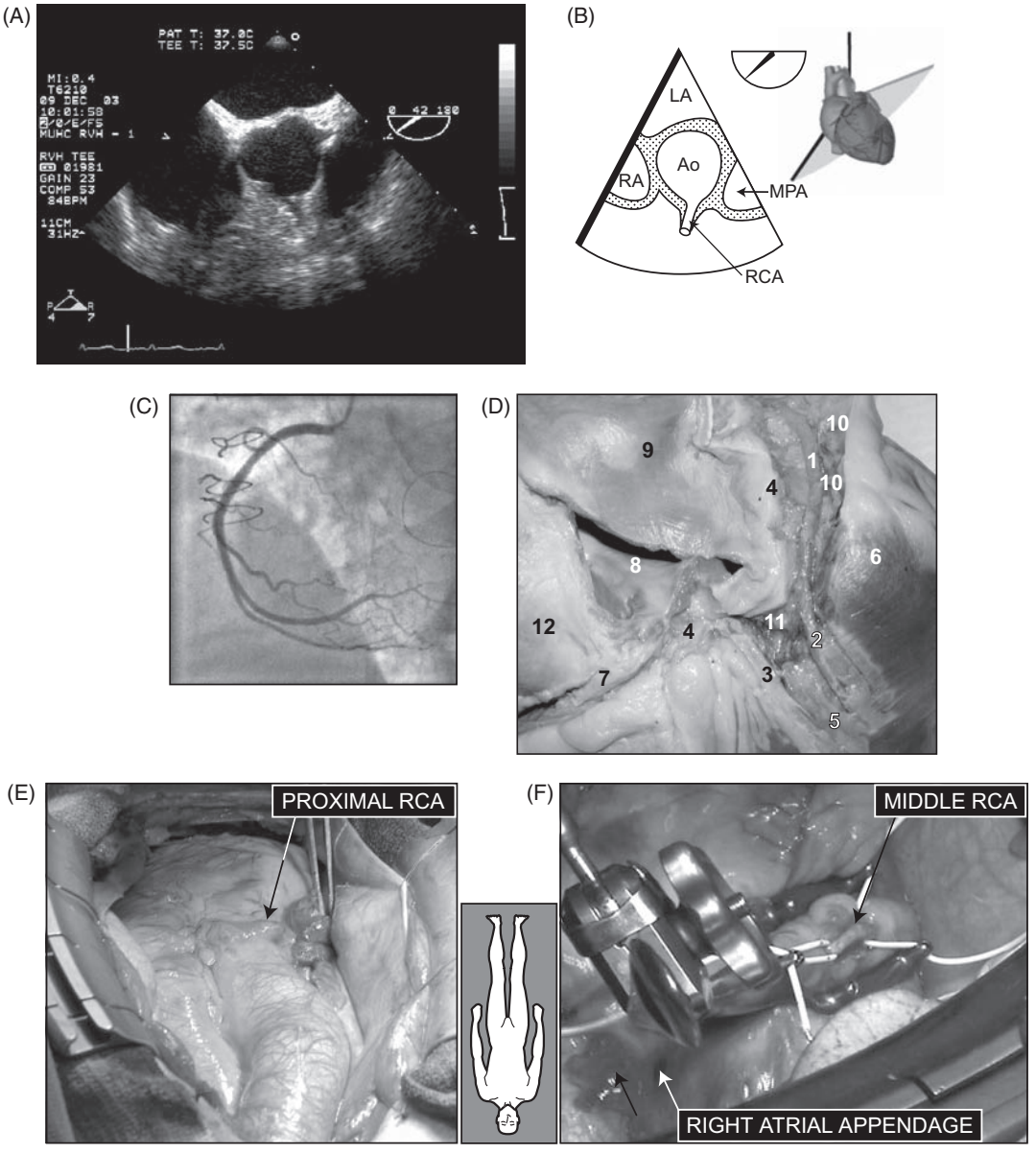

Figure 8.3 Echocardiographic (A, B), angiographic (C), anatomical (D), and intraoperative (E, F) views of the right coronary artery (RCA) (Ao, aorta; LA, left atrium; MPA, main pulmonary artery; RA, right atrium). (1, right coronary artery; 2, posterior descending artery; 3, middle cardiac vein; 4, atrioventricular groove; 5, posterior interventricular groove; 6, right ventricle; 7, coronary sinus; 8, inferior vena cava; 9, right atrium; 10, right marginal branches; 11, crux cordis; 12, left atrium). (Photos C–E courtesy of Drs. Philippe L.L'Allier, Nicolas Dürrleman, and Raymond Cartier.)

the other ventricular segments. In addition, the presence of a left bundle branch block, right volume overload, constrictive pericarditis, or the postoperative state after cardiac surgery often complicates the assessment of interventricular septal wall motion (Fig. 8.9). Using an abnormality in wall motion as the sole criterion for the presence of ischemia has its limitations as the movement of a given ventricular segment is affected by the rotation and the translation of the heart, and can be also be influenced by the adjacent muscle to which it is attached (tethering), resulting in overestimation of the extent of ischemia. Decreased myocardial thickening is more specific for ischemia (4) and, in extreme cases, systolic thinning can occur. Indeed, the assessment of myocardial thickening is not affected by cardiac rotation and translation. Although the mid-papillary short-axis view is the plane most commonly used to detect ischemia, one-third of regional wall motion abnormalities may not be detected

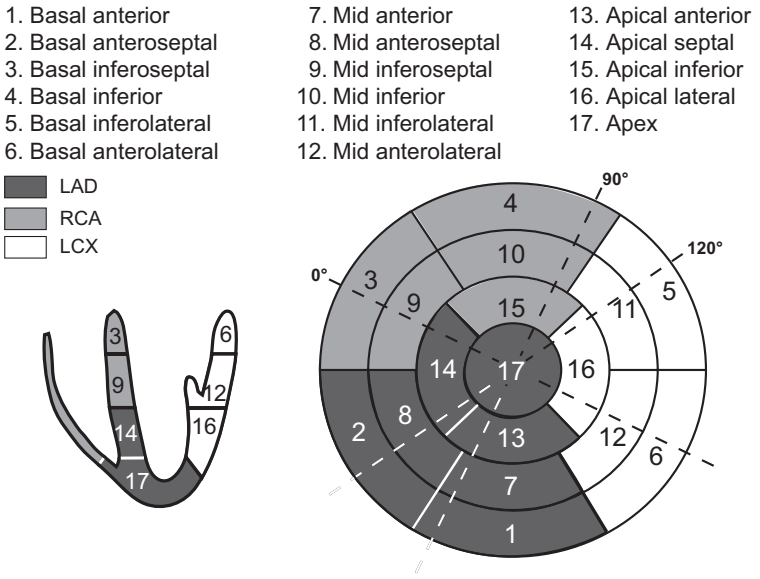

Figure 8.4 Coronary distribution from a transesophageal echocardiographic point of view (LAD, left anterior descending; LCX, left circumflex artery; RCA, right coronary artery). [Adapted from Cerqueira et al. (2).]

in this view (5,6). A complete analysis of all 17 ventricular segments, as described earlier, should be carried out.

Both animal and clinical studies have documented that wall motion is rapidly altered after coronary artery occlusion. The first detectable abnormalities are cellular biochemical changes and a perfusion defect (detected by radionuclide techniques), followed by delayed myocardial relaxation and/or decreased compliance, and within minutes, reduced systolic wall thickening and endocardial motion. The electrocardiographic ST–T changes and

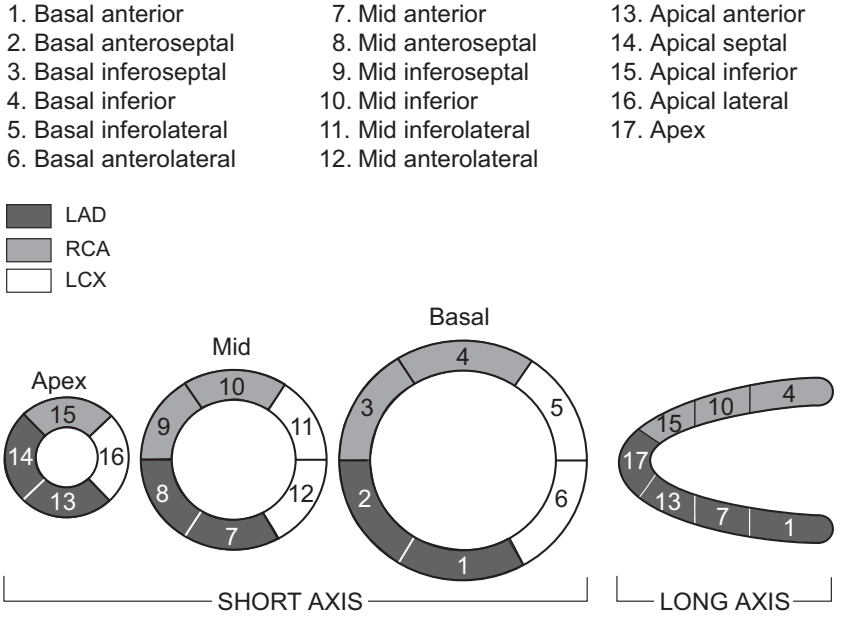

Figure 8.5 Coronary distribution from a transgastric echocardiographic point of view (LAD, left anterior descending; LCX, left circumflex artery; RCA, right coronary artery). [Adapted from Cerqueira et al. (2).]

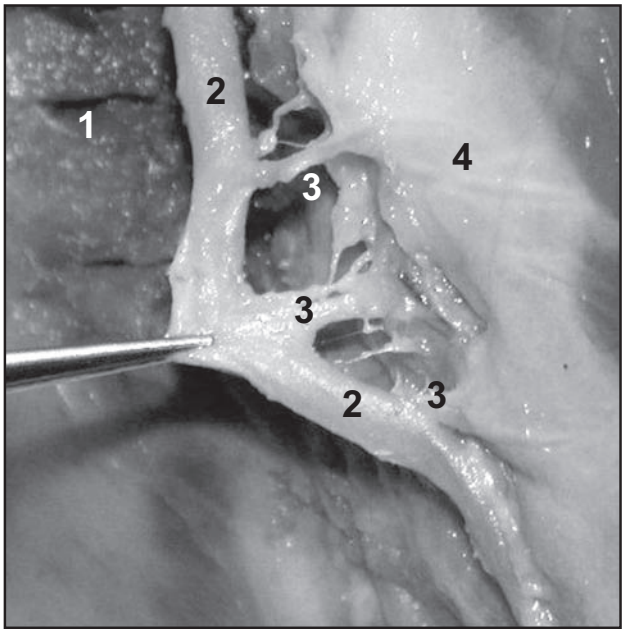

Figure 8.6 Septal branches of the left anterior descending artery (1, myocardium; 2, left anterior descending; 3, septal branches; 4, epicardial fat). (Courtesy of Nicolas Dürrleman.)

clinical symptoms of angina, if they appear, are late manifestations of ischemia.

III. GLOBAL SYSTOLIC FUNCTION CHANGES

When transthoracic images are suboptimal (e.g. patients who are obese, have chronic obstructive lung disease, or are in a postoperative state), in critically ill patient settings or when assessing patients undergoing cardiac or non-cardiac surgery, it is often useful to evaluate global and regional ventricular function from the transesophageal approach. This technique provides immediate data regarding segmental wall motion abnormalities, global ventricular function, volume status, and the presence of tamponade. In particular, TEE provides very important data on ventricular function in the hypotensive patient and allows the detection of ventricular or atrial compression from severe tamponade. The severely hypovolemic patient will most often have a normal or hyperkinetic ventricular function and obliteration of the left ventricular cavity in systole (7). Although acute ischemia is usually manifested echocardiographically as a regional wall motion abnormality, global ventricular dysfunction may result from high-grade obstruction of one or more arteries perfusing a large area, the acute obstruction of one artery in the setting of previous infarction in other areas or the presence of an ischemic mechanical complications such as papillary muscle rupture.

Global left ventricular systolic function can be evaluated either qualitatively or quantitatively. Global systolic function can be qualitatively classified as normal, mildly, moderately or severely reduced, but this information is considered incomplete by most clinicians. In contrast, determination of the left ventricular ejection fraction has major prognostic significance in patients with coronary artery disease (CAD). In the clinical setting, visual estimation of the left ventricular ejection fraction has become common practice. The correlation between the visual echocardiographic estimation (eye balling) and the radionuclide determination is surprisingly good, especially in patients with impaired ejection fraction. This method, however, requires experience and clinicians should validate their own performance with quantitative methods. All echocardiographic approaches for the assessment of regional and global ventricular function need to take into account the quality of endocardial border definition, the asynchronous contraction patterns observed with ventricular pacing or in the presence of conduction defects, the heterogeneity of normal ventricular function and the observed abnormality in septal wall motion frequent in the postoperative period.

The motion of the mitral annulus towards the apex can also be used as an indirect measure of left ventricular systolic function. It is usually measured in the apical four-chamber view, where the movement of the mitral annulus is parallel to the ultrasound beam and is normally 12 ± 2 mm. A motion of <8 mm has been reported to have a sensitivity of 98% and a specificity of 82% in the identification of an ejection fraction less than 50% (8). Pai et al. (9) examined the mitral annular systolic excursion in 57 patients with a wide range of LV ejection fraction (13–84%) and found a good correlation ($r = 0.95$, $p < 0.001$) between the mitral annulus motion and the ejection fraction as measured by the radionuclide approach (Fig. 8.10).

The quantitative assessment of global systolic function requires the determination of the left ventricular cavity dimensions on high-quality images. Volume estimations are based on geometric assumptions about ventricular shape which range from a simple ellipsoid to a complex hemicylindrical hemiellipsoid shape. A description of each geometric shape, the corresponding formula and requirements is beyond the scope of this chapter (Chapter 5). Nevertheless, the biplane modified Simpson's formula, which divides the ventricular cavity into multiple cylindrical slices of known volume with the sum representing left ventricular volume, is the most commonly used approach in clinical practice to assess left ventricular volume and global function. This involves tracing of the endocardial borders at end-systole and end-diastole in the mid-esophageal four- and two-chamber views (transducer at 0° and 90°, respectively). The left ventricular

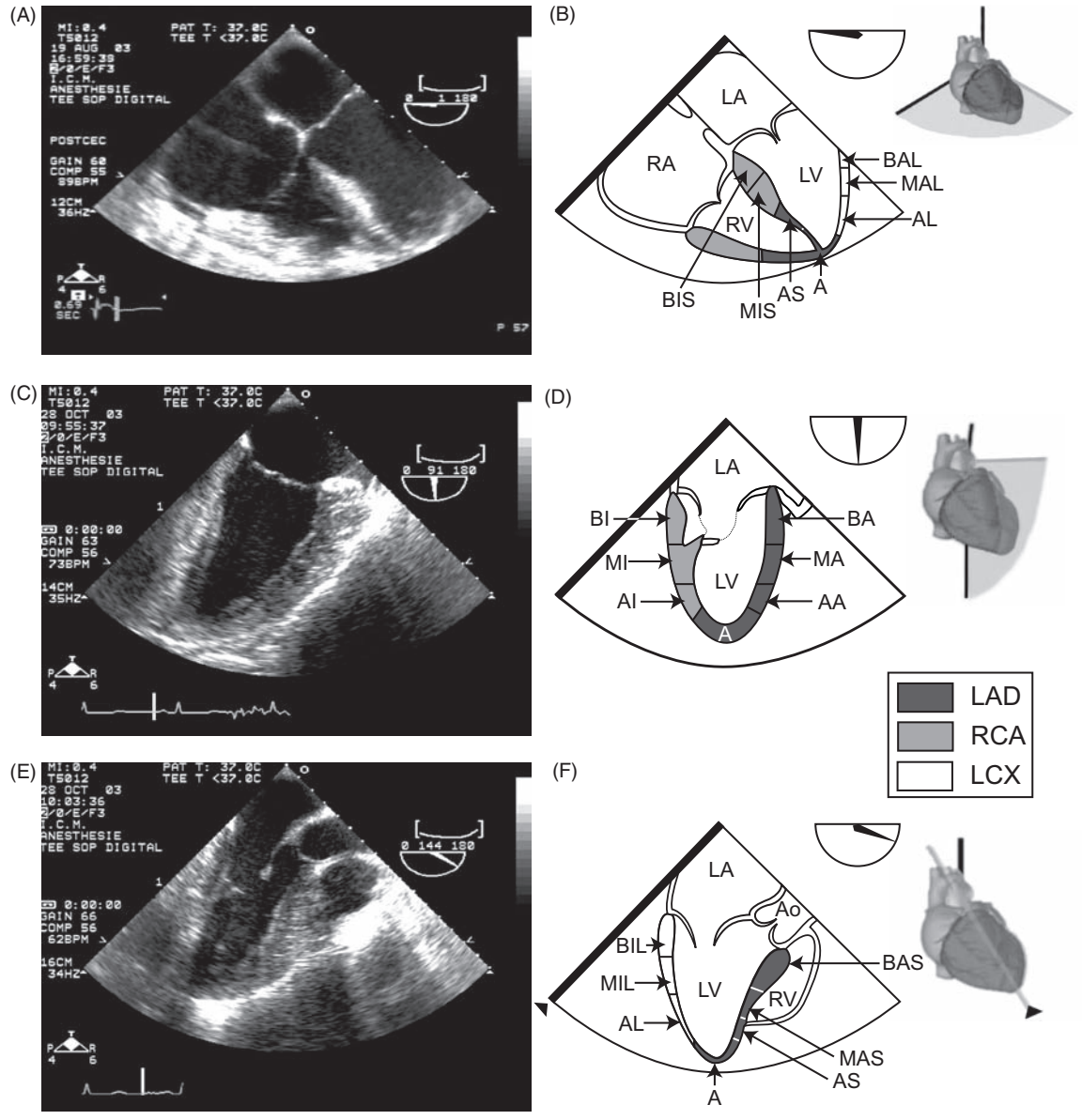

Figure 8.7 Mid-esophageal views to evaluate right and left ventricular function: four-chamber (A, B), two-chamber (C, D) and long axis (E, F) views (A, apex; AA, apical anterior; AI, apical inferior; AL, apical lateral; Ao, aorta; AS, apical septal; BA, basal anterior; BAL, basal anterolateral; BAS, basal anteroseptal; BI, basal inferior; BIL, basal inferolateral; BIS, basal inferoseptal; LA, left atrium; LAD, left anterior descending; LCX, left circumflex artery; LV, left ventricle; MA, mid-anterior; MAL, mid-anterolateral; MAS, mid-anteroseptal; MI, mid-inferior; MIL, mid-inferolateral; MIS, mid-inferoseptal; RA, right atrium; RCA, right coronary artery; RV, right ventricle).

ejection fraction is equal to the difference between the end-diastolic and end-systolic volumes divided by the end-diastolic volume, multiplied by 100. The area–length method to calculate volume uses the short-axis area of the LV from the transgastric mid-papillary short-axis view and the length of the LV measured in the mid-esophageal four-chamber view. One limitation of these volumetric methods is that the ventricular cavity is often foreshortened with TEE resulting in an underestimation of left ventricular volume. The multiple diameter method is a nonvolumetric approach to the determination of ejection fraction which is particularly suitable for TEE as it does not require tracing of the endocardial contour or volume determinations. This method, previously described and validated with transthoracic echocardiography (TTE), allows determination of the

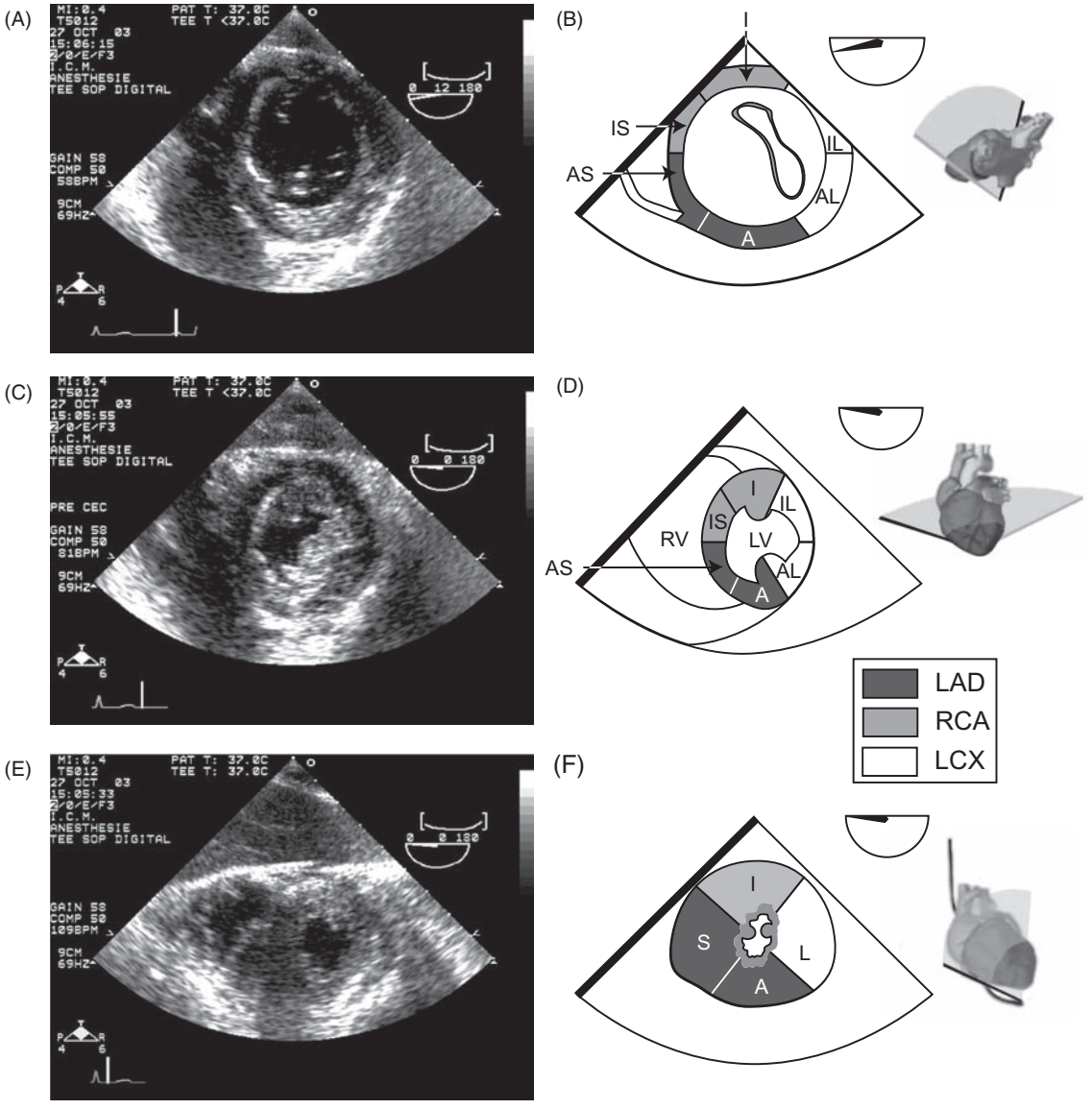

Figure 8.8 Basal (A, B), mid (C, D), and apical (E, F) short-axis transgastric views in a 49-year-old female (A, anterior; AL, anterolateral; AS, anteroseptal; I, inferior; IL, inferolateral; IS, inferoseptal; L, lateral; LAD, left anterior descending; LCX, left circumflex artery; LV, left ventricle; RCA, right coronary artery; RV, right ventricle; S, septal).

ejection fraction using the average of several left ventricular diameters from multiple views (measured at the base, mid-, and distal third of the LV) combined with the left ventricular long-axis fractional shortening (estimated from the descent of the mitral annulus towards the apex) (10). Doerr et al. (10) found a good correlation between the ejection fraction measured with this method and the ejection fraction measured with TTE ($r = 0.83$).

Table 8.1 Wall Motion Scoring System

Movement	Radial displacement	Thickening
Normal = 1	>30%	++
Hypokinesia = 2	0–30%	+
Akinesia = 3	0%	None
Dyskinesia = 4	Systolic lengthening	Systolic thinning

The left ventricular end-systolic diameter is a reliable indicator of global left ventricular contractile function, hemodynamic, and volume status. Leung et al. (7) have shown that left ventricular cavity obliteration is a highly sensitive indicator of hypovolemia. A good correlation has also been observed between left ventricular area as measured on the mid-papillary short-axis view and that obtained by the radionuclide approach. A very good

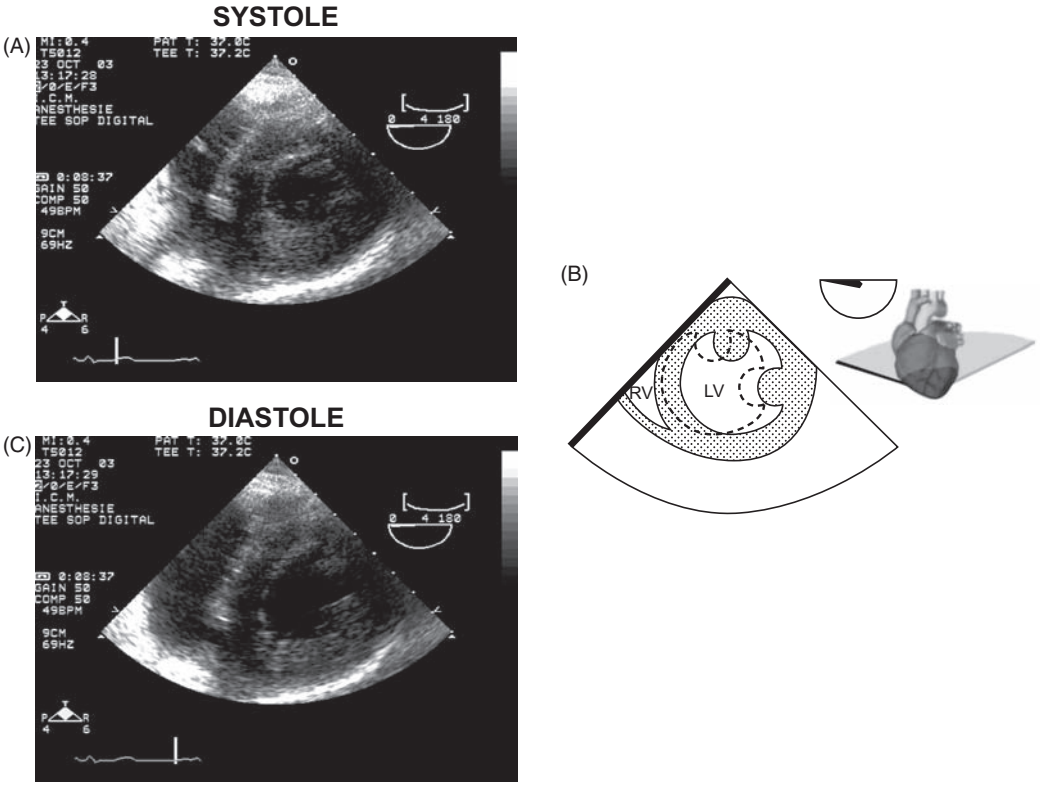

Figure 8.9 A 57-year-old woman scheduled for coronary revascularization. She has left bundle-branch block. Abnormal septal motion (dotted line) is present (LV, left ventricle; RV, right ventricle).

correlation was also found between radionuclide ejection fraction and fractional area change by TEE (11). The fractional area change is calculated as the difference between left ventricular areas measured at end-diastole and end-systole (measured in a transgastric short-axis view) divided by the end-diastolic area (Chapter 5). In contrast, the correlation between ventricular volume or area measurements and pulmonary capillary wedge pressure or pulmonary artery diastolic pressure is often poor (12). The weak correlation between ventricular volumes and filling pressures reflects independent variations in chamber compliance.

IV. OTHER INDICES OF GLOBAL SYSTOLIC VENTRICULAR FUNCTION

The echocardiographic determination of cardiac output (CO), although less commonly used than the ejection fraction, is an important hemodynamic index. The volumetric flow equation states that the stroke volume (SV) (cm^3) is equal to the product of the velocity time integral (in cm) across any nonregurgitant orifice [left ventricular outflow tract (LVOT), mitral valve, pulmonary main trunk] and the corresponding cross-sectional area (cm^2). Cardiac output is obtained by multiplying SV and heart rate (HR). The LVOT is the site most frequently used for this measurement. The LVOT diameter (D) is measured in the mid-esophageal long-axis view obtained at 120–150° and the LVOT cross-sectional area is obtained by the following formula: $\pi(D/2)^2$. The velocity–time integral (VTI) of the left ventricular outflow is measured with pulsed Doppler by placing the sample volume 5–10 mm below the aortic valve (AoV) in the transgastric long-axis view (120–150°) or in the deep transgastric five-chamber view (Chapter 5). Studies have found a good correlation between CO obtained by the Doppler approach at the level of the LVOT and by thermodilution (13). Gorcsan et al. (14) compared the CO measured with continuous- or pulsed-wave Doppler in the main pulmonary artery with that obtained by the thermodilution method. They found a better correlation when the CO was derived by continuous-wave (CW) Doppler ($r = 0.91$, $p < 0.0001$) than by pulsed-wave (PW) Doppler ($r = 0.83$, $p < 0.0001$). Pu et al. (15) compared CO calculated at the mitral annulus with that obtained by thermodilution in patients without mitral regurgitation (MR). Using an average of the minor and

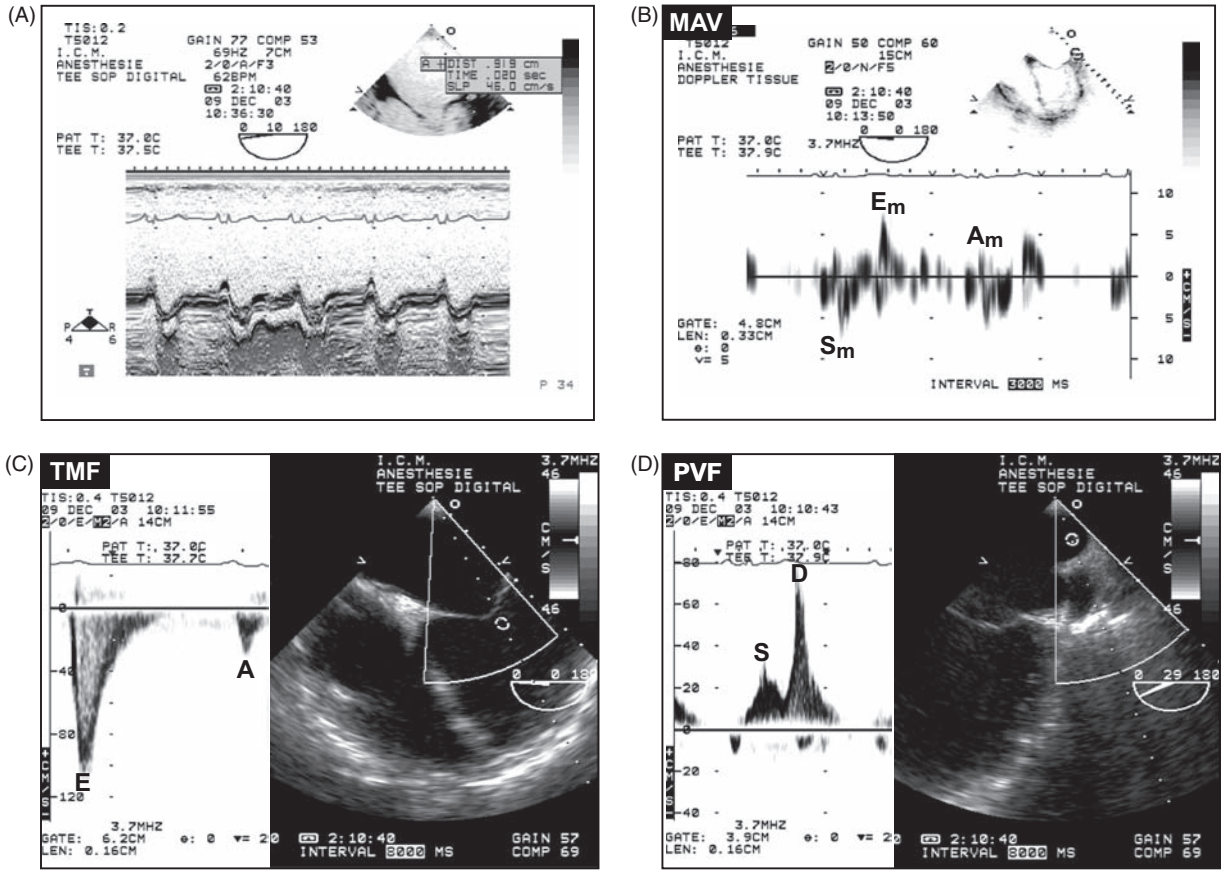

Figure 8.10 A 56-year-old woman has ischemic dilated cardiomyopathy and an ejection fraction of 20% before left ventricular remodeling procedure. (A) M-mode of the lateral mitral annulus: displacement is 9 mm. (B) Tissue Doppler of mitral annular velocities (MAV) were reduced. (C) Pulsed-wave Doppler of transmitral flow (TMF) with high E/A ratio. (D) Pulsed-wave Doppler of pulmonary venous flow (PVF) with decreased systolic or S fraction. These features are consistent with restrictive left ventricular filling.

major diameters for mitral annulus area calculation, a good correlation was observed between Doppler and thermodilution methods ($r = 0.92$) (15). In the presence of MR, the rate of change of the regurgitant jet velocity in early systole allows calculation of dP/dt, the maximum slope of pressure rise in the LV. The time required for the MR velocity to rise from 1 m/s to 3 m/s is determined. According to the modified Bernouilli equation, and assuming a normal left atrial pressure, the left ventricular pressure will have increased by 32 mmHg (from 4 to 36 mmHg) in that time. The normal rate of pressure change is >1200 mmHg/s. In contrast, it will be decreased below 1000 mmHg/s in the presence of poor left ventricular systolic function (see Fig. 9.14). A good correlation has been reported between invasively measured dP/dt and that measured by Doppler echocardiography (16). When MR is mild, a left-sided contrast agent may be used to enhance the regurgitant Doppler signal.

Methods of determining global systolic function which are relatively load independent have also been described in echocardiography. The mean velocity of fiber shortening is equal to the fractional area shortening divided by the left ventricular ejection time (17). The left ventricular ejection time is determined by M-mode evaluation of the duration of AoV opening or the duration of aortic flow using Doppler. Creation of pressure–volume or pressure–area loops with TEE requires simultaneous pressure measurements but allows determination of pressure–dimensions relationship at end-systole, one of the best load-independent indexes of left ventricular contractility. Circumferential wall stress and meridional wall stress are measures of systolic wall tension which require echocardiographic and blood pressure measurements. The circumferential wall stress changes as a function of left ventricular length and the meridional wall stress is independent of this dimension and reflects tension at the left ventricular equatorial plane (17) (Chapter 5).

V. SEGMENTAL SYSTOLIC FUNCTION CHANGES

Studies and clinical experience have shown that segmental wall motion abnormalities occur in the area supplied by the obstructed artery within seconds after the interruption of myocardial blood flow, well before (minutes) the development of ischemic electrocardiographic changes and chest pain (if they appear). Most quantitative methods are based on the evaluation of wall motion. A segmental wall motion abnormality is defined as hypokinesis when contraction is normally directed but reduced in magnitude, akinesis when it is absent, or dyskinesis when there is systolic bulging (Table 8.1).

A semiquantitative assessment of regional left ventricular contraction is provided by the wall motion score index (WMSI). The LV is divided into 17 segments (2) as suggested by the American Society of Echocardiography (ASE) and a score is assigned to each segment, according to its contractility (18). A score of 1 is given to a normally contracting or hyperkinetic segment, 2 for an hypokinetic segment, 3 for akinesis, and 4 in the presence of a dyskinetic segment (Table 8.1). Of note, there is no specific score for compensatory hyperkinesis. The WMSI is equal to the sum of the regional scores divided by the number of evaluable segments and can vary between 1.0 (for normal ventricular contraction) and 3.9 (for severe systolic dysfunction). Because CAD causes segmental dysfunction, which can be accompanied by compensatory hyperkinesis of nonischemic segments, regional assessment of systolic function is more sensitive for the detection of ischemia than global approaches. Furthermore, the prognostic value of the motion score has been shown in clinical studies. Among a group of patients admitted with acute myocardial infarction, those with favorable indices (best quintile) had an incidence of cardiovascular death of 8% at 1 year. In contrast, patients with motion indexes in the worst quintile had a mortality of 51% at 1 year (19). Kan et al. (20) also examined the value of WMSI in patients with acute myocardial infarction and found a significantly higher mortality rate in the group with the most abnormal score indexes compared with those with more favorable ones (61% vs 3%, respectively). Quantitative evaluation of regional left ventricular systolic function requires high-quality images with good endocardial resolution. The centerline method is a quantitative approach for assessing regional ventricular function, which first involves the construction of a line halfway between the end-diastolic and end-systolic endocardial perimeters (21). The endocardial excursion is determined along 100 equally spaced chords perpendicular to this centerline. Motion is then normalized for heart size by dividing by the length of the end-diastolic perimeter. The normalized length of each line is then converted into units of standard deviation from the mean excursion along a given chord, which allows the regional heterogeneity of ventricular contraction to be taken into account. By convention, negative and positive values indicate hypokinetic and hyperkinetic chords, respectively. The extent of abnormal wall motion is calculated as the number of chords with hypokinesis equal to or more severe than 2 standard deviations (SD). The severity of wall motion abnormalities is calculated as the area under the curve below the 0 SD line.

Compared with multilead electrocardiographic monitoring and invasive hemodynamic monitoring, transesophageal echocardiography has proved to be superior at detecting acute ischemia as reflected by new regional wall motion abnormalities (3,22). In a group of patients at high risk for intraoperative ischemia undergoing coronary artery bypass or major vascular surgery, Smith et al. (3) found that 24 (48%) of the 50 patients demonstrated new segmental wall motion abnormalities while only six (12%) patients presented new ischemic ST changes. Furthermore, Leung et al. (23) demonstrated that wall motion abnormalities occurred in the absence of hemodynamic changes and were predictive of adverse outcomes after cardiac surgery. In contrast, van Daele et al. (22) have shown the lack of sensitivity of hemodynamic measurements in predicting ischemia or postoperative cardiac complications. A few limitations and pitfalls of TEE for the assessment of regional systolic function should be mentioned. The segmental wall motion analysis system must first compensate for global motion of the heart, usually by a floating frame. When viable and nonischemic, the interventricular septum thickens during systole but its asynchronous motion can begin slightly before or after the inward motion of the other walls. Experimental and clinical studies have also defined important regional differences in normal myocardial contraction (24). As mentioned previously, it is important to realize that contraction of the inferobasal wall is often slightly more limited than that of the other ventricular segments and that not all systolic wall motion abnormalities are indicative of ischemia. Patients with myocarditis, septic shock, ventricular pacing, and bundle branch block can present segmental wall motion abnormalities (Fig. 8.9). Tethering of nonischemic myocardium adjacent to an ischemic or infarcted myocardium is a frequent cause of overestimation of the infarct size with echocardiography compared with postmortem examination (25). Force et al. (25) found that although tethering does lead to an unavoidable overestimation of the infarct size within 1 cm of the ischemic area, the amount of myocardium involved is small and relatively predictable. Altered loading conditions may also result in segment wall motion abnormalities or may unmask areas of scarring. For example, an acute elevation of the blood pressure may retard the contraction of an already damaged myocardial segment more than that of a normal one.

Identification of a persistent wall motion abnormality does not distinguish a stunned or hibernating region from infarcted myocardium. Stunning, defined as prolonged postischemic contractile dysfunction of the myocardium, has been observed in several clinical situations including stress-induced angina, unstable angina, thrombolysis, percutaneous transluminal angioplasty, and coronary artery bypass surgery. Complete recovery of myocardial function may require from three days to several weeks in the presence of stunning. Hibernation is a state of persistently impaired myocardial and left ventricular function at rest due to reduced coronary blood flow that can be partially or completely restored to normal if the myocardial oxygen supply/demand relationship is favorably altered, either by improving blood flow (surgery, percutaneous coronary angioplasty) and/or by reducing demand. Perioperatively it is extremely difficult to determine whether new segmental wall motion abnormality represents inadequate revascularization, ongoing ischemia, or stunned myocardium, but the distinction is of therapeutic significance and a dobutamine stress echocardiogram may be useful. Dobutamine has a positive inotropic effect at low doses (5–10 μg/kg per min), with additional inotropic and chronotropic effects at higher doses. The increase in systolic blood pressure during the infusion of dobutamine can be more pronounced in hypertensive than in normotensive patients. A paradoxical hypotension can be occasionally observed, and is either due to the vasodilating effect of dobutamine or transient outflow tract obstruction, but is rarely caused by ischemia (26). Demonstration of increased contractility in an hypokinetic or akinetic region suggests that the regional systolic function will improve either after revascularization in the case of hibernating myocardium (27) or spontaneously after recovery from stunning (28). A biphasic response to increasing dobutamine doses characterized by enhanced thickening at low doses (5–10 μg/kg per min) followed by deterioration of thickening at higher doses (>10 μg/kg per min) is the most accurate echocardiographic criterion to detect viable but hypoperfused myocardium. Arnese et al. (29) found that the specificity of low-dose dobutamine echocardiography in predicting recovery of function after surgical revascularization was 95% compared with only 48% for 201-thallium single photon emission computed tomography (SPECT) (29). The greater is the number of viable myocardial segments, the greater is the probability of improvement in regional and global left ventricular function after revascularization. The value of low-dose dobutamine stress echocardiography for the assessment of myocardial viability has been compared with that of positron emission tomography (PET) and nuclear perfusion imaging (30). Cumulative

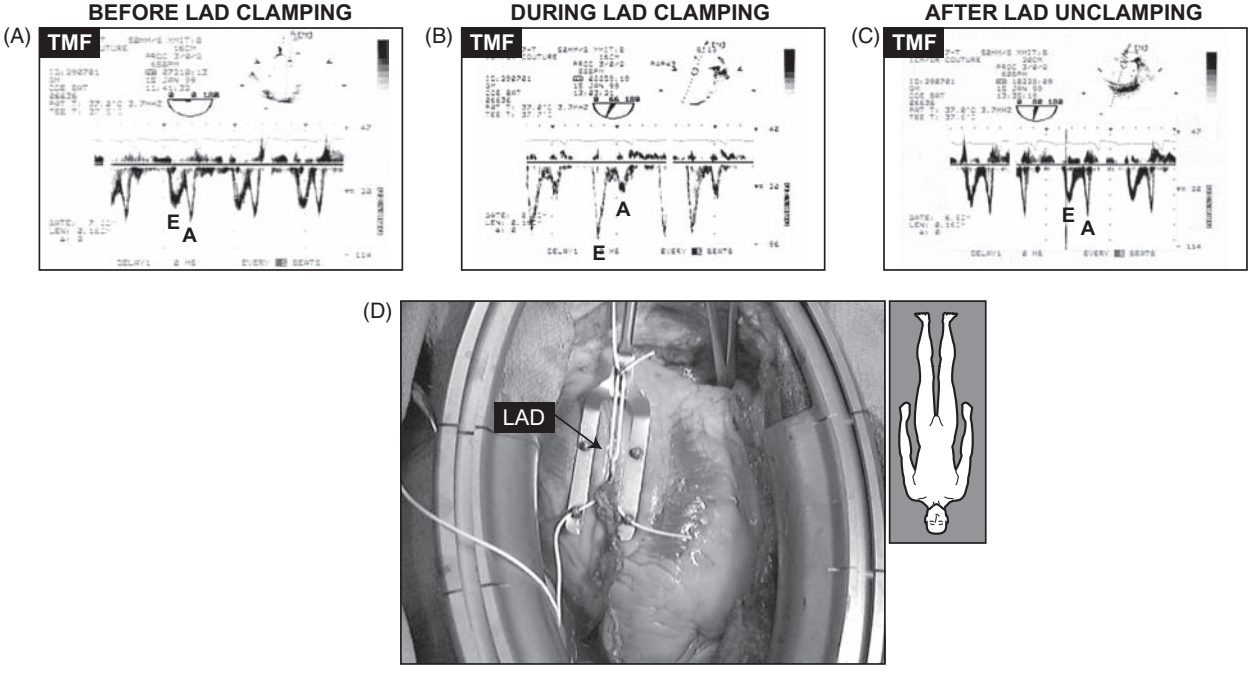

Figure 8.11 Pulsed-wave Doppler of transmitral flow (TMF) velocities in a 66-year-old man during off-pump bypass surgery. During the clamping of the left anterior descending (LAD), the transmitral pattern changed from a predominant A wave (A), to predominant *E* velocity (B) with short deceleration time suggesting a restrictive pattern. This reverted back to baseline after completion of revascularization (C). Intraoperative aspect of the LAD anastomosis (D). (Photo D courtesy of Dr. Raymond Cartier.)

data from multiple studies suggest that thallium SPECT images provide better sensitivity compared with dobutamine echocardiography for this indication (89% vs 81%), but low-dose dobutamine stress echocardiography has a higher specificity (83% vs 69%). In comparison, PET scanning has a positive predictive value of 82% and a negative predictive value of 83% for predicting recovery after revascularization, with an excellent agreement with dobutamine stress echocardiography (31).

VI. DIASTOLIC FUNCTION CHANGES

In patients with CAD, induction of ischemia rapidly results in diastolic dysfunction, even before the development of systolic dysfunction (Fig. 8.11). Doppler assessment of flow velocity patterns across the mitral valve and in the pulmonary veins is the most commonly used approach to assess ventricular filling and diastolic dysfunction. Two distinct patterns of abnormalities can be recognized and are associated with either impaired relaxation or impaired compliance. A left ventricular relaxation abnormality results in an increased delay between AoV closure and mitral valve opening, reflected by a prolonged isovolumic relaxation time (IVRT), reduced rapid ventricular filling (reduced *E*-wave velocity) due to a reduced pressure gradient between the atrium and the ventricle after mitral valve opening, slower decay of the atrioventricular gradient in early diastole (prolonged deceleration time) and a greater contribution of left atrial contraction to ventricular filling (increased *A*-wave velocity). Therefore, the isolated abnormal relaxation pattern results in an E/A ratio <1, a prolonged IVRT (≥ 100 ms) and a prolonged deceleration time (≥ 270 ms) (Fig. 8.12). A mild relaxation abnormality will usually be associated with a prominent systolic component of the pulmonary venous inflow. A more severe relaxation abnormality, which is associated with an elevation of the left ventricular end diastolic pressure, is manifested in the pulmonary veins by an increase in the maximal velocity (peak velocity ≥ 35 cm/sec) and duration (at least 30 ms more than the mitral A-wave duration) of the A reversal wave during atrial contraction.

Restriction to left ventricular filling due to abnormal compliance leads to a different Doppler pattern. The elevated atrial pressure and increased atrioventricular gradient is manifested by an increased peak *E*-wave velocity and a short deceleration time, as the ventricle has poor compliance and the LV and LA pressures equilibrate rapidly. This brief rapid filling phase is followed by a prolonged period of plateau during which little flow occurs between

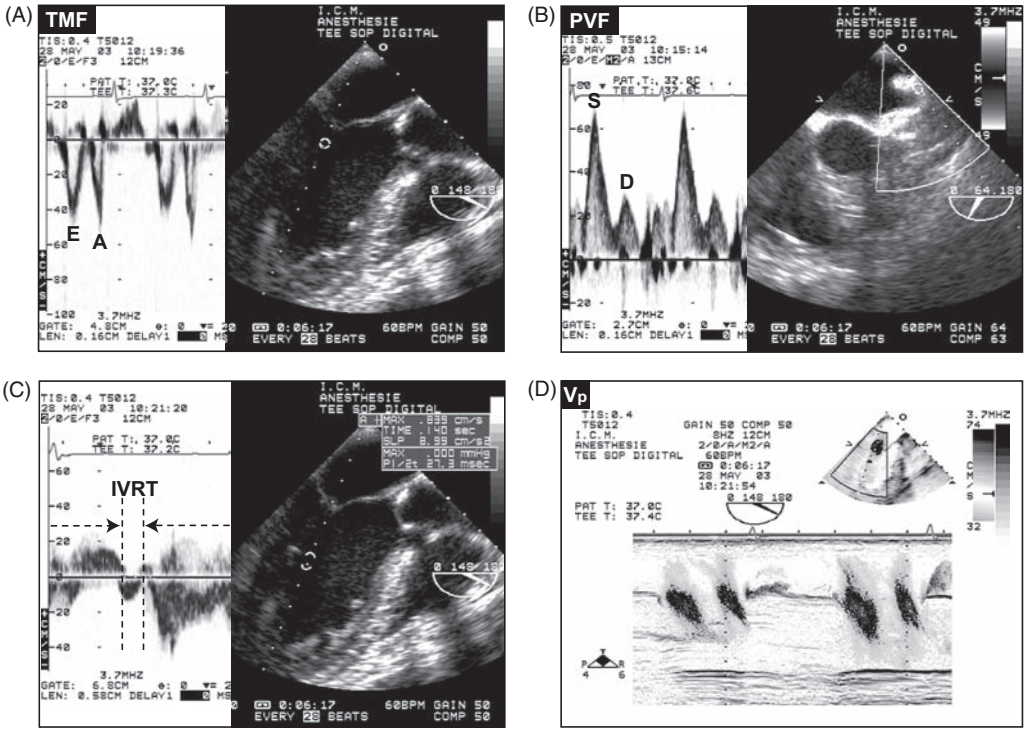

Figure 8.12 Impaired left ventricular relaxation in a 66-year-old man scheduled for coronary revascularization and aortic valve replacement. The predominant A wave on the pulsed-wave Doppler transmitral flow (TMF) (A), increased S-wave pulmonary venous flow (PVF) (B), prolonged isovolumic relaxation time (IVRT) of 140 ms (C) and reduced velocity of propagation (Vp) on color M-mode (D) are consistent with this mild degree of diastolic dysfunction.

the chambers. The A-wave is decreased at the time of atrial contraction due to elevated left ventricular diastolic pressure. In this restrictive type of diastolic dysfunction the E/A ratio is increased (>2), and the deceleration time is shortened (<150 ms) as is the IVRT (<70 ms) (Fig. 8.10). Between these two opposite abnormalities a pseudonormal pattern characterized by a normal E/A ratio and normal deceleration time exists, due to an increase in the left atrial pressure. A few methods can be used to distinguish a pseudonormal pattern from a truly normal one. First, analysis of the pulmonary venous flow can show, with the pseudonormal pattern, a prominent and prolonged pulmonary venous A-wave during atrial contraction (see preceeding text). In addition, the systolic fraction of total pulmonary venous flow (systolic flow VTI/systolic flow VTI + early diastolic flow VTI) has been correlated with left atrial pressure measurements. Kuecherer et al. (32) have demonstrated a strong negative correlation between the systolic fraction and the left atrial pressure. A systolic fraction of $<55\%$ was a sensitive and specific indicator of a left atrial pressure >15 mmHg. Therefore, a prominent systolic (S) wave suggests that the left atrial pressure is low whereas a predominant diastolic (D) peak wave with a reduced S-wave suggests that the left atrial pressure is elevated. Secondly, manoeuvres to decrease preload (Valsalva, nitroglycerin) can also be used to unmask a relaxation abnormality. Finally, tissue Doppler imaging at the mitral annulus can also be used to differentiate the two patterns, as described in the following text.

In recent years, color Doppler M-mode and tissue Doppler imaging have provided new tools for the study of diastolic function. Color Doppler M-mode of ventricular inflow generates a spectral display of mitral E- and A-waves. This flow occurs at a finite velocity called the propagation velocity (V_p), which is measured from the leading edge of the blood wave on color Doppler M-mode echocardiography. In contrast to standard Doppler filling indices, preliminary experience suggests that V_p is relatively independent of preload and may detect delayed apical filling in heart failure and help distinguish pseudonormal from normal patterns (33) (Fig. 8.13). Tissue Doppler imaging is a relatively new echocardiographic

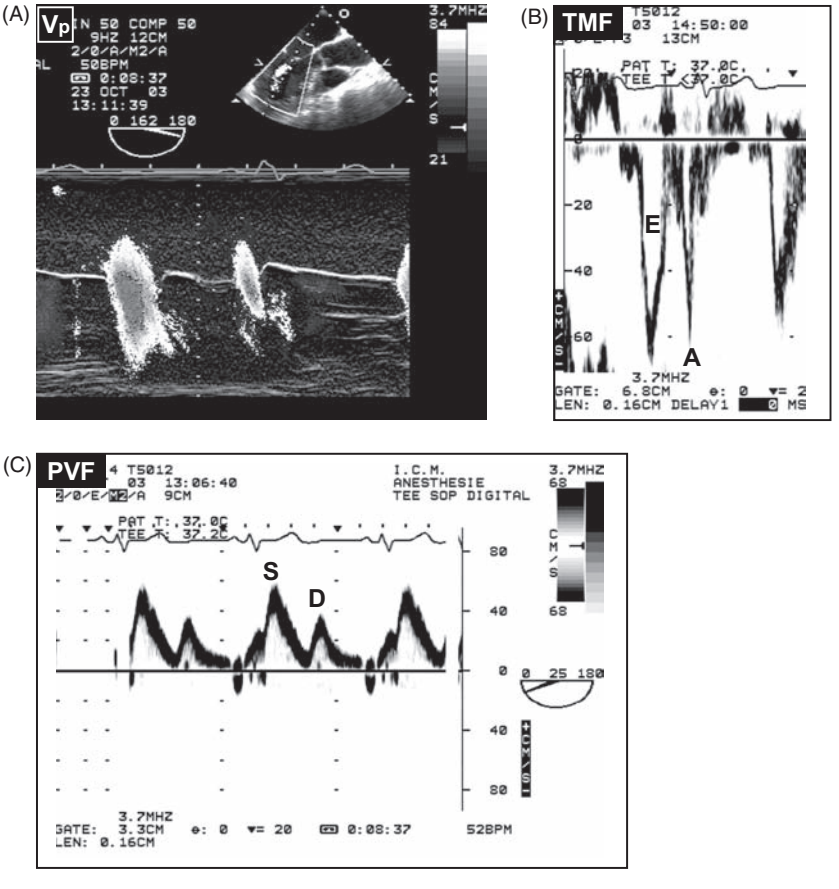

Figure 8.13 Normal diastolic function in a 57-year-old woman before revascularization. (A) Normal color M-mode propagation velocity (Vp) of 56 cm/sec associated with normal Doppler transmitral flow (TMF) profile (B) and pulmonary venous flow (PVF) velocities (C).

method that can be used to quantify myocardial velocities. When the pulsed Doppler cursor is positioned on the myocardium at the annulus level, early and late diastolic motion is detected and a E_m/A_m (or E'/A', e/a) ratio can be generated. This ratio, similar to the mitral inflow velocity (E/A) ratio decreases with aging and ischemic heart disease (Fig. 8.10). Studies in patients with ischemic heart disease have demonstrated that E_m is often reduced, the E_m/A_m ratio is <1, and IVRT is prolonged in patients when left ventricular segmental dysfunction is present (34) (Fig. 8.14). In patients with acute myocardial infarction, Alam et al. (35) determined the systolic and diastolic velocities at four different sites on the mitral annulus (septal, anterior, lateral, and inferior sites). Interestingly, the early diastolic velocities were particularly affected above the site of infarction (E-wave 0.67 m/s at the anterior site compared with 0.82 m/s at the inferior site in anterior myocardial infarction, and 0.64 m/s at the inferior site compared with 0.95 m/s at the anterior site in inferior myocardial infarction ($p < 0.001$). Garcia-Fernandez et al. (36) also observed a reduced E_m and E_m/A_m ratio in patients with significant CAD, but normal segmental left ventricular function.

VII. COMPLICATIONS AND ASSOCIATED FINDINGS

In a cardiac emergency, the cause of abnormalities such as a new murmur on physical examination, electrocardiogram (ECG) changes, a rise in myocardial enzymes, pulmonary edema, and hemodynamic instability must be rapidly established. Transthoracic echocardiography is frequently of limited value in these critically ill patients as they are often on mechanical respiratory and/or hemodynamic support such as an intra-aortic balloon pump and may have surgical dressings restricting the transthoracic imaging windows. In the cardiac operating room, of course, TTE is usually impossible as the chest wall is inaccessible. In this context, TEE is well tolerated, rapid, and provides answers. It is particularly useful in excluding cardiac tamponade and aortic dissection (Chapters 11 and 12) and in diagnosing the complications of acute myocardial infarction such as papillary muscle rupture or dysfunction, ventricular septal defect, ventricular aneurysm and/or pseudoaneurysm, severe left ventricular dysfunction, right ventricular infarction, and ventricular free wall rupture. Assessment of MR is another indication for

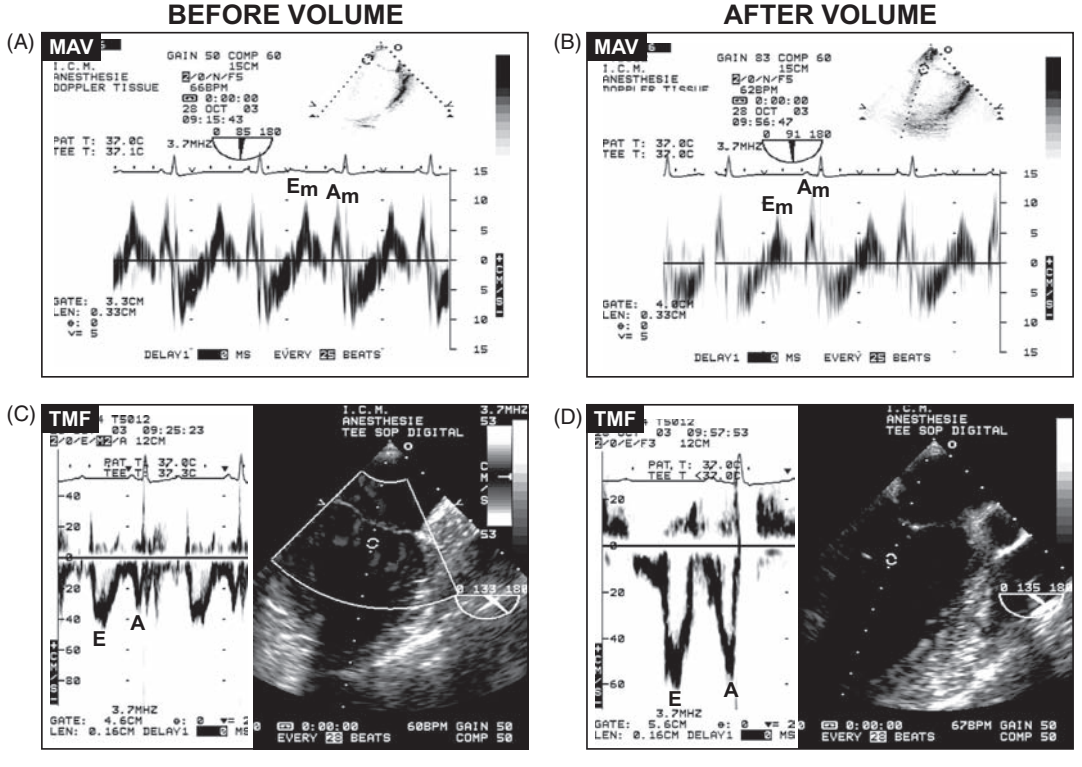

Figure 8.14 Mitral annular velocities (MAV) obtained with tissue Doppler and transmitral flow (TMF) velocities before and after volume challenge in a 59-year-old man undergoing coronary revascularization. (A) The predominant Am wave on the tissue Doppler signal is more evident after the fluid challenge (B). (C) Note that the TMF E and A velocities were normal before the fluid challenge but the E and A velocities increased after fluid loading (D). This demonstrates the influence of loading condition on these Doppler signals.

TEE, as the transesophageal approach allows better visualization of the mitral apparatus and provides important information about both the severity and the mechanism of the regurgitation before valvular surgery.

A. Ventricular Septal Defect

A ventricular septal defect (VSD) is a well-recognized complication of either anterior or inferior wall infarction, occurring in 1–2% of patients. Rupture of the septum typically occurs at the junction of the necrotic and noninfarcted myocardium, within the first week after infarction, and the rupture site and adjacent infarct are thinned and aneurysmal. The combination of a first transmural infarction in a territory supplied by a single diseased coronary vessel and the absence of collaterals is frequently present (37). Clinically, between two and seven days postinfarction, the patient presents with a new holosystolic murmur (which may be absent in extreme shock) and worsening heart failure. Prompt diagnosis is essential because deterioration may be rapid and the presence of shock is associated with an increased risk of a fatal outcome. Surgery is warranted in almost all cases as conservatively treated patients with an acute VSD do poorly. The timing of surgery is crucial, and an approach combining early percutaneous closure with delayed surgery has now been implemented in many centers. The VSD usually appears on echocardiography as a single perforation that varies between one to several centimeters in diameter. It is often described as a "through and through" hole but the VSD are irregularly shaped and serpiginous. The appearance of the defect may be preceded by formation of a septal aneurysm with thinning, which may be seen to bulge in the RV during systole. Defects with a serpentine course are more difficult to visualize. When complicating an anterior infarction, the septal defect is usually located near the apex in association with anterior akinesis (Figs. 8.15–8.19). When a VSD occurs with an inferior infarction, the apex is generally spared and the defect is in the basal septum, generally associated with an extensive area of inferior wall dyskinesis. Systolic flow acceleration can be identified by PW Doppler, but color flow Doppler imaging allows demonstration of the defect site, with a left-to-right mosaic signal indicating turbulence and is best seen in the RV (Fig. 8.16). The right ventricular systolic pressure can be estimated from the difference between the systolic arterial pressure obtained by the cuff method or the arterial line and the peak transventricular systolic gradient obtained by CW Doppler.

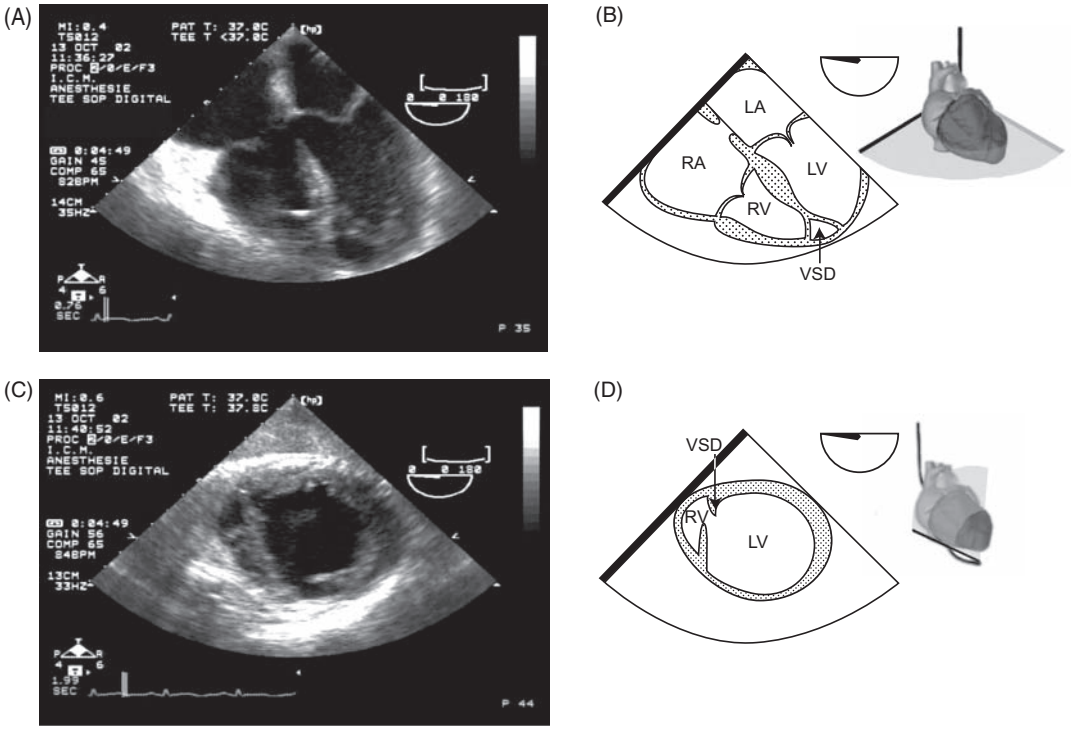

Figure 8.15 A 56-year-old man with acquired ventricular septal defect (VSD) following an anterior myocardial infarction. The VSD is located at the apex (A, B) and could also be seen in the apical transgastric view using color Doppler (C, D) (LA, left atrium; LV, left ventricle; RA, right atrium; RV, right ventricle).

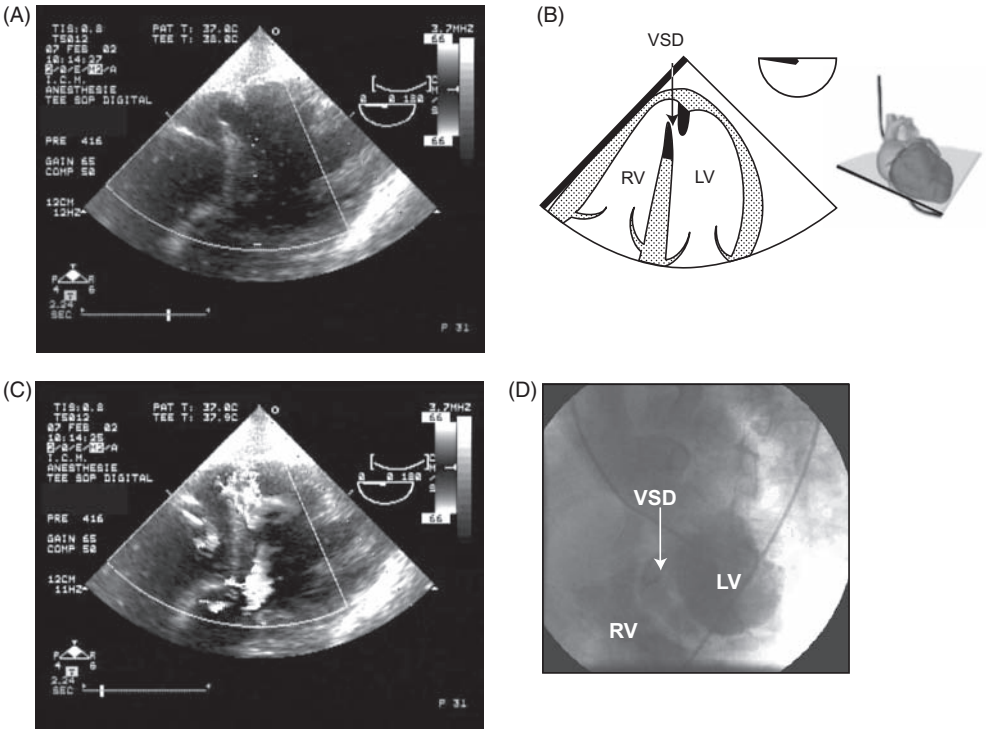

Figure 8.16 (A, B) Deep transgastric view from a 60-year-old man with an apical ventricular septal defect (VSD) after myocardial infarction. (C) The color Doppler localizes the VSD at the apex. (D) Left ventriculography showing passage of radiocontrast media from the left ventricle (LV) to the right ventricle (RV) through the serpiginous VSD. (Photo D courtesy of Dr. Philippe L. L'Allier.)

B. Papillary Muscle Dysfunction or Injury and Evaluation of Mitral Regurgitation

Dysfunction of the mitral valve and support apparatus can occur in patients with myocardial infarction and can lead to severe heart failure (Fig. 8.20). With acute partial rupture of a papillary muscle (1% of myocardial infarctions), severe MR may occur suddenly and require prompt surgical correction. More commonly, the papillary muscle dysfunction will be less severe as a result of ischemia and segmental wall dysfunction. The diagnosis requires a high index of suspicion as the systolic murmur heard in patients with acute severe MR may not be impressive because of near equalization of left ventricular and atrial pressures, and systemic hypotension. Because of its single blood supply from the RCA, the posteromedial muscle is the most often affected, usually in the setting of an acute inferior wall infarction (Fig. 8.21). In contrast, the anterolateral papillary muscle is rarely affected as it has a dual blood supply from the diagonal branches of

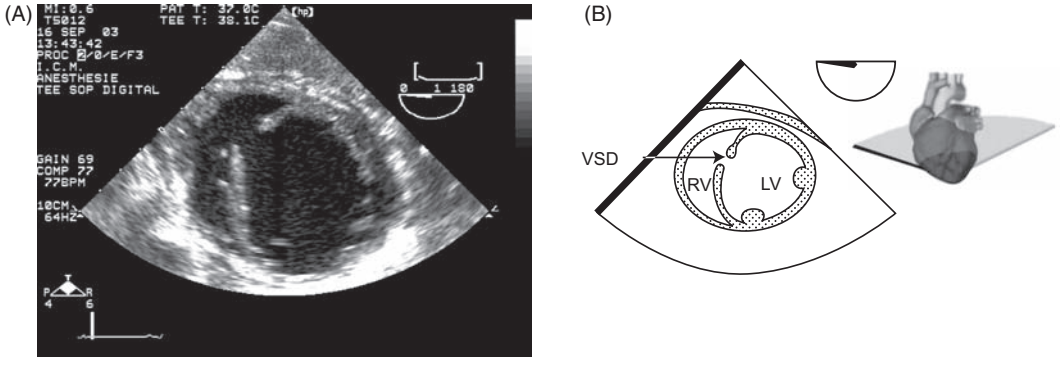

Figure 8.17 (A, B) Transgastric mid-papillary view of a ventricular septal defect (VSD) located in the mid-portion of the ventricular septum in a 62-year-old man after myocardial infarction (LV, left ventricle; RV, right ventricle).

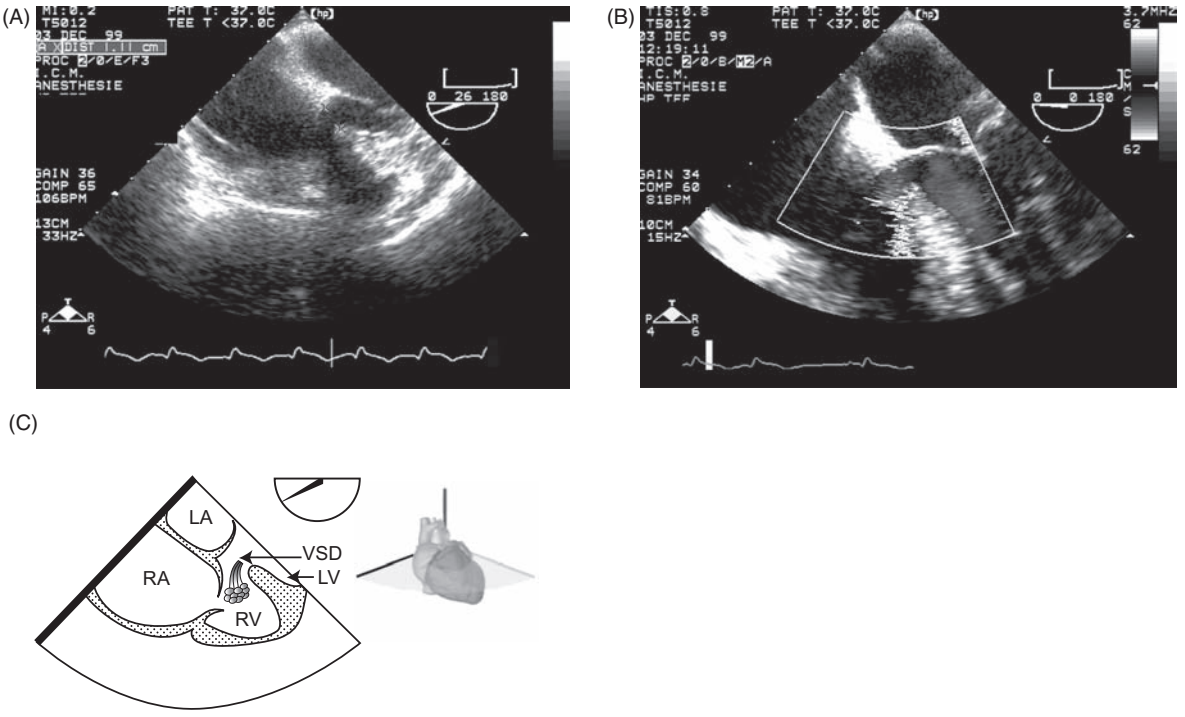

Figure 8.18 Mid-esophageal four-chamber view of an acquired basal ventricular septal defect (VSD) in a 71-year-old man after myocardial infarction (LA, left atrium; LV, left ventricle; RA, right atrium; RV, right ventricle).

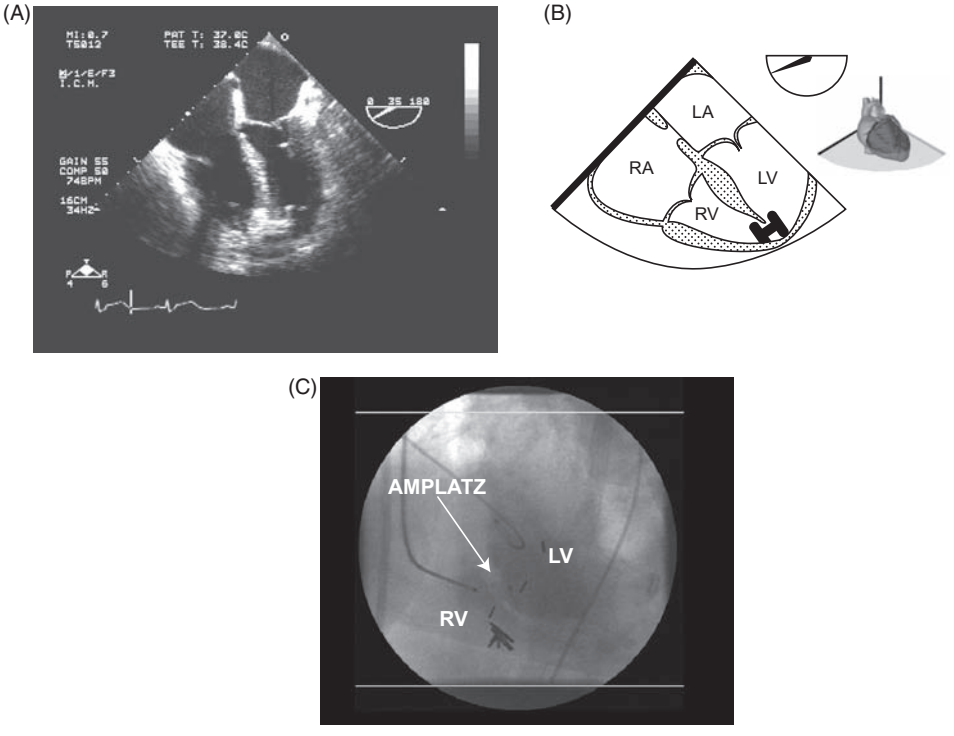

Figure 8.19 (A, B) Mid-esophageal four-chamber view in a 71-year-old woman with an 8 mm apical ventricular septal defect (VSD) in cardiogenic shock after acute myocardial infarct with a shunt or pulmonary to systemic flow (Q_P:Q_S) ratio of 3.1:1. The Amplatzer septal occluder device is seen at the ventricular apex. (C) She underwent percutaneous transcatheter closure device with an Amplatzer septal occluder. The angiogram shows a small residual flow through the prosthesis at the level of the ventricular septum (LA, left atrium; LV, left ventricle; RA, right atrium; RV, right ventricle). (Courtesy of Drs. Tomas Cieza and Reda Ibrahim.)

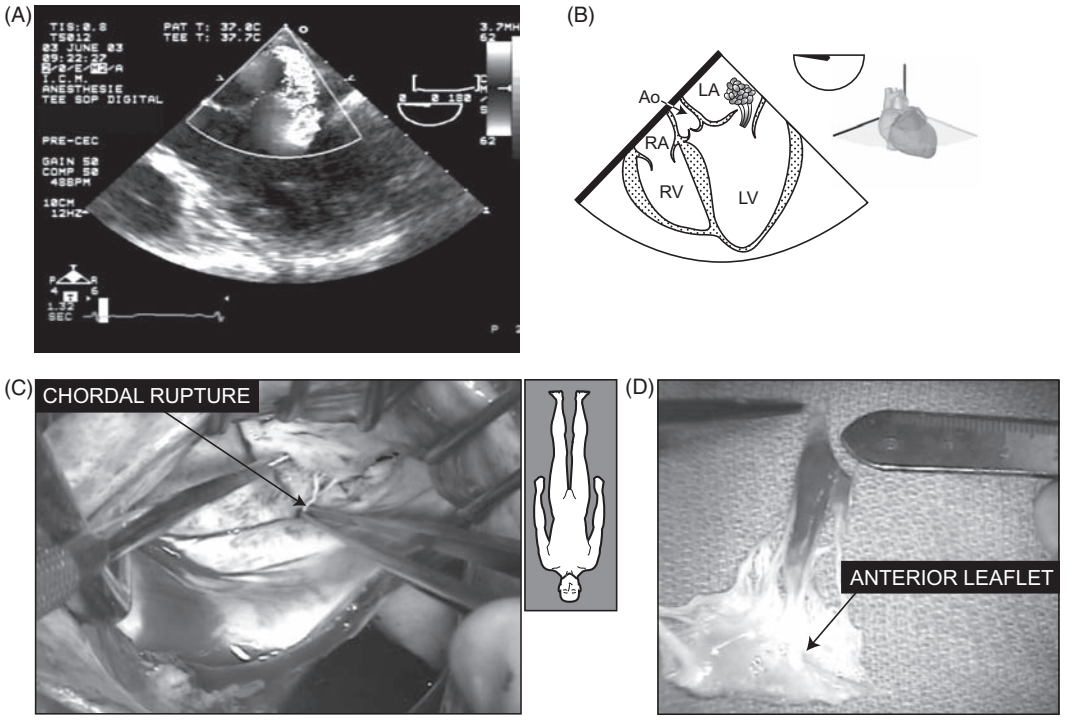

Figure 8.20 (A, B) Anterior (A3) chordal rupture in a 61-year-old man with myocardial infarction associated with severe mitral regurgitation. The ruptured chordae (C) and the ischemic papillary muscle (D) are shown (Ao, aorta; LA, left atrium; LV, left ventricle; RA, right atrium; RV, right ventricle). (Photos C and D courtesy of Dr. Michel Pellerin.)

the LAD artery and the circumflex artery (Fig. 8.20). Because TTE has a high specificity but a low sensitivity in detecting papillary-muscle rupture, TEE is helpful when the transthoracic approach is non-diagnostic. Papillary muscle rupture is obvious when the head of the papillary muscle prolapses into the left atrium (LA) during systole (Fig. 8.21). A discrete mass can be seen attached to the prolapsing anterior or posterior leaflet. The longitudinal views may show the ruptured head of the papillary muscle moving back and forth between the LV and LA. A flail mitral leaflet, defined as an upturning of the leaflet towards the LA in systole, is often noted. Mitral leaflet morphology will otherwise be normal in the setting of ischemic MR. When severe flail of one leaflet is present, the regurgitant orifice will be large and the mitral regurgitant flow will be less turbulent. As color Doppler techniques can be less reliable in such cases, PW Doppler interrogation of the pulmonary veins,

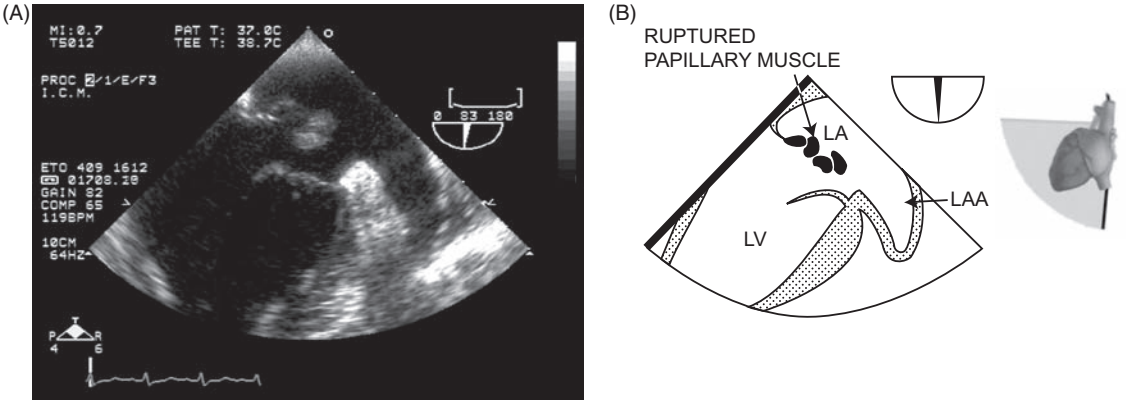

Figure 8.21 Mid-esophageal two-chamber view of a flail mitral leaflet caused by acute postero-medial papillary muscle rupture following an inferior myocardial infarction (LA, left atrium; LAA, left atrial appendage; LV, left ventricle).

which are better visualized with TEE, is an important aspect of the evaluation of the severity of MR (Chapter 17 section on ischemic mitral valve). A systolic reversal of pulmonary venous flow indicates severe MR. Because the characteristics of MR may change as a consequence of alterations in loading conditions, it is preferable to perform the TEE examination before the induction of general anesthesia.

C. Left Ventricular Thrombus

Left ventricular thrombus formation was a relatively frequent complication of acute myocardial infarction before the era of thrombolytic therapy. Thrombus is most often found after large anterior wall infarcts particularly when a ventricular aneurysm is present (Fig. 8.22). Although the superiority of TEE over TTE for the detection of atrial thrombi is undisputed, the situation is not as clear for the detection of ventricular thrombi. This has been attributed to difficulty in visualizing the left ventricular apex from the esophagus because of limited resolution at increased depths. With the help of TEE, Chen et al. (38) examined the nature of equivocal echodense structures found with TTE in the left ventricular apical region. Left ventricular thrombus was identified with certainty by TEE in 53% of their patients, and the investigators concluded that TTE and TEE can be complementary for this indication (38). Particular attention should be paid to the detection of a left ventricular thrombus in the presence of a recent or old anterior infarct, when there is a wall motion abnormality in the apical region, or when a cardiac source of embolus is suspected. Although the

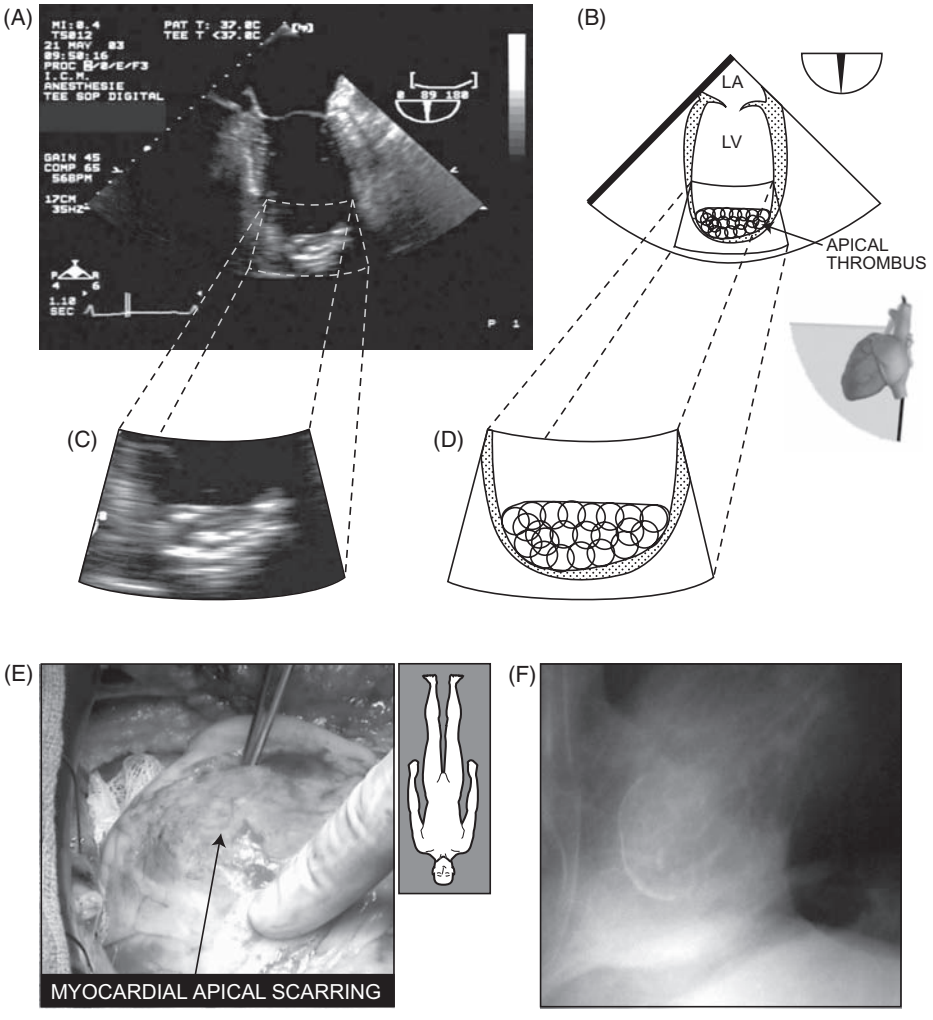

Figure 8.22 Apical calcified thrombus in a 79-year-old man following an anterior myocardial infarction. (A, B) A mid-esophageal two-chamber view with a close-up (C, D) is shown. (E) In the operating room, the thrombus was felt under the calcified scar. (F) Lateral chest X-ray showing the calcified aneurysm (LA, left atrium; LV, left ventricle). (Photo E courtesy of Dr. Raymond Cartier.)

appearance of a left ventricular thrombus is described in a separate chapter (Chapter 23), the echocardiographer should remember that either a deep transgastric on a two-chamber transgastric views are the most useful for its detection. It may occasionally be helpful to acquire a series of intermediate planes at the same level when doubts remain about a possible mass in the apical region (Fig. 8.23).

D. Right Ventricular Infarction

Occasionally, an inferior myocardial infarction may extend into the right ventricular free wall and compromise right ventricular function. Because its management differs substantially from that of left ventricular infarction, early and accurate diagnosis of right ventricular infarction is imperative (39). Echocardiography can be very helpful in the diagnosis of right ventricular infarction (Fig. 8.24). Findings include right ventricular regional hypokinesis or akinesis or global right ventricular dysfunction. Left ventricular inferior wall involvement is usually present. Because infarction of the RV may sometimes be revealed only by dysfunction of its inferior wall, attention should be paid to this region in optimized transgastric short-axis views. The short-axis view has been shown to have the highest sensitivity (82%), with a specificity ranging from 62% to 93% for hemodynamically significant right ventricular infarction (40). Right ventricular dilatation, abnormal interventricular septal motion, tricuspid regurgitation (TR), reduced systolic excursion of the tricuspid annulus, and dilatation of the inferior vena cavae can also be found and point towards the correct diagnosis. Interatrial septal bowing towards the LA, indicating an increased right to left atrial pressure gradient, is a prognostic marker in right ventricular infarction as patients with this finding have a higher incidence of hypotension and heart block resulting in a higher mortality (41).

E. Ventricular Dilatation

Infarct expansion, defined as a disproportionate dilation of the infarct segment with stretching and thinning of the infarct zone, contributes to global cardiac enlargement with marked augmentation of end-diastolic left ventricular volume within 48 h. This in turn may be a harbinger of myocardial wall rupture and eventual left ventricular aneurysm formation.

Two-dimensional echocardiography is ideally suited for assessing dynamic changes in LV shape and allows detection of infarct expansion. Echocardiographic features in left ventricular dilatation include abrupt angulation in

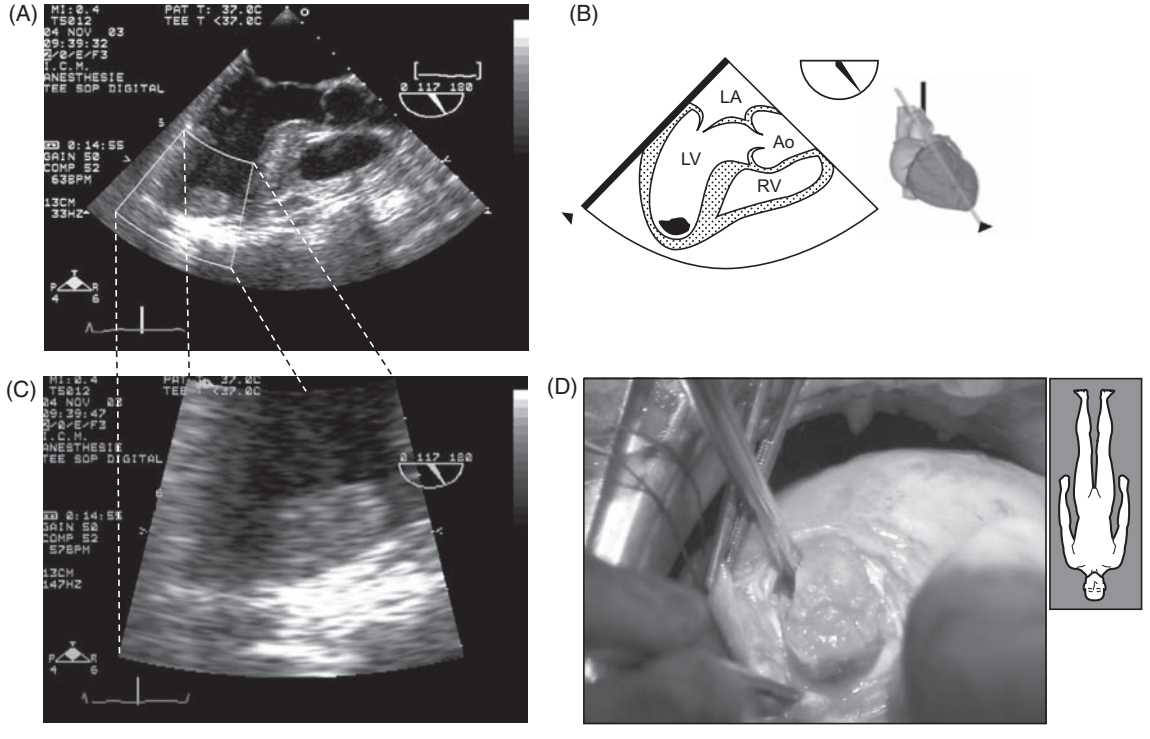

Figure 8.23 Apical ball thrombus in a 68-year-old woman before thrombectomy. (A, B) The thrombus is seen in a mid-esophageal long axis view. (C) Zooming is useful to confirm the observation. (D) Intraoperative findings (Ao, aorta; LA, left atrium; LV, left ventricle; RV, right ventricle). (Photo D courtesy of Dr. Michel Carrier.)

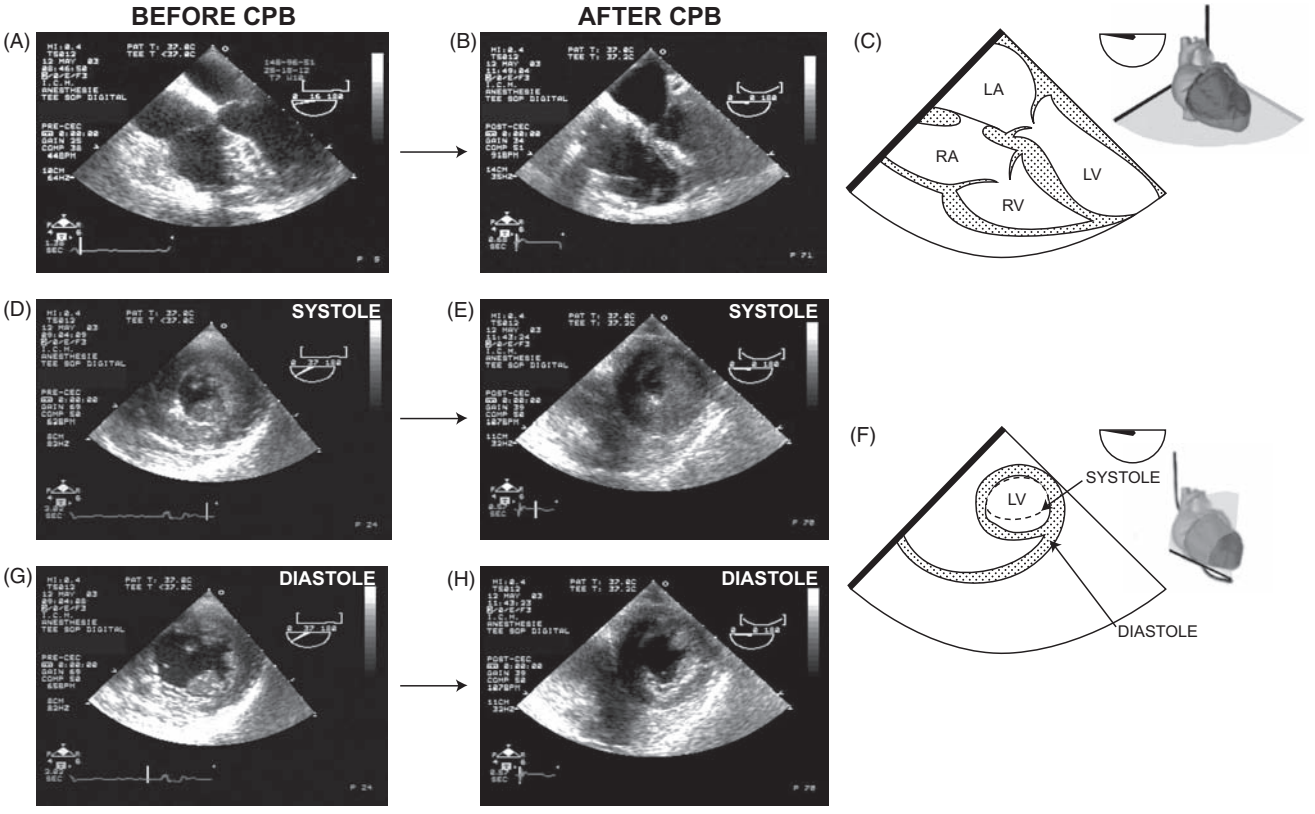

Figure 8.24 Severe acute right ventricular ischemic dysfunction in a 71-year-old woman after cardiopulmonary bypass (CPB). The four-chamber view demonstrates the new appearance of acute right ventricular dilatation (A–C) and inferior wall akinesis on the transgastric mid-papillary view indicated with the dotted line (D–H) (LA, left atrium; LV, left ventricle; RA, right atrium; RV, right ventricle).

the contour of the proximal anteroseptal wall in the long-axis view and a segmental dilation in the transgastric short-axis view. At this level, direct measurement of the segment length is possible, the papillary muscles serving as internal landmark to divide the ventricle into anterior and posterior segments. While in the first few days after a transmural infarction, ventricular dilatation mostly involves the infarcted segment, remodeling of the entire left ventricular cavity involving adjacent and nonischemic regions will be observed later.

F. Left Ventricular Aneurysm

A left ventricular aneurysm is a common complication among survivors of nonreperfused transmural myocardial infarction. Aneurysms occur four times more often at the apex and at the anterior wall than at the inferobasal wall (Fig. 8.25). True aneurysm results from expansion of the infarcted area and thinning of the myocardium. All three layers of the ventricular wall are preserved. Echocardiographically, the aneurysmal segments are dyskinetic or akinetic, and the distortion of the left ventricular shape consists of an outpouching of ventricular myocardium with well defined borders (Figs. 8.26 and 8.27). A wide neck persists in diastole. However, differentiating a true aneurysm from a pseudoaneurysm may sometimes be difficult.

A pseudoaneurysm, or false aneurysm, is a relatively rare complication of myocardial infarction. It is the result of a perforation of the ventricular free wall resulting in a localized hemopericardium which is contained by the parietal pericardium (Fig. 8.28). Echocardiographically, there is a pouchlike configuration of the LV with an abrupt discontinuity of myocardial echoes at the neck of the false aneurysm which is typically narrow. Pseudoaneurysms are commonly filled with thrombus but flow to and from the pseudoaneurysm may be documented by Doppler. Bulging also can be observed in the false aneurysm during systole. As a ventricular pseudoaneurysm is a contained rupture, mortality is high and immediate surgery is warranted as soon as the diagnosis is made. Figure 8.29 summarizes the difference between a pseudo and a true aneurysm.

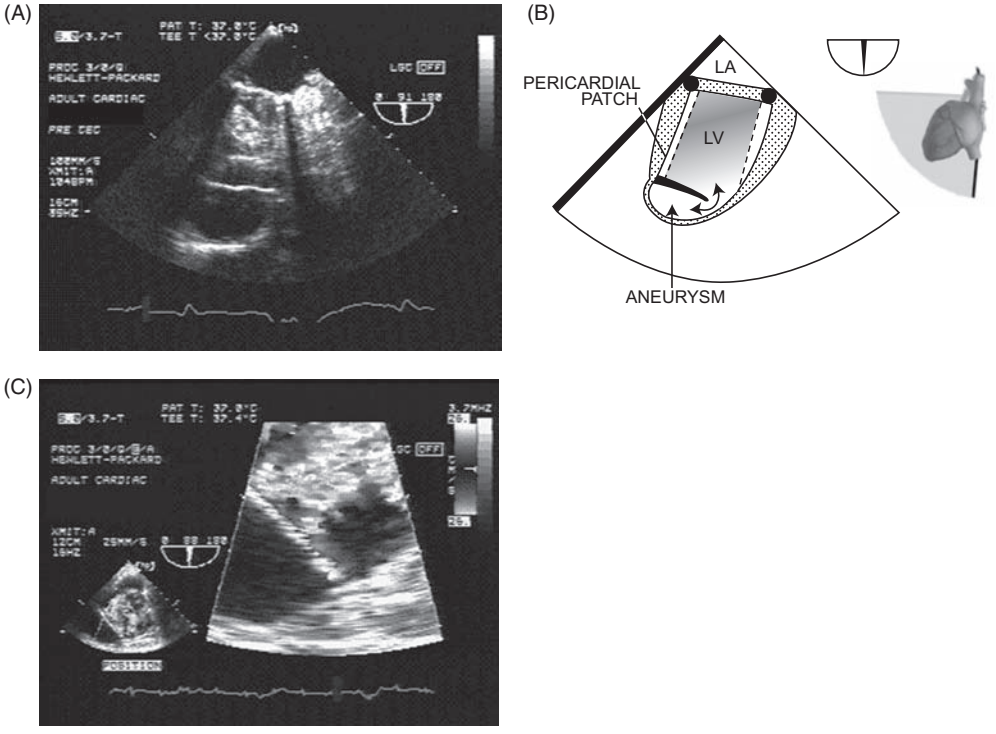

Figure 8.25 A patient with prosthetic mitral valve replacement and left ventricular aneurysm repaired with a pericardial patch. (A, B) Mid-esophageal two-chamber view of the dysfunctional pericardial patch above the apical aneurysm. (C) In the close-up view, flow between the left ventricle (LV) and the aneurysm is seen (LA, left atrium.)

G. Myocardial Rupture

Rupture of the LV free wall is usually a sudden event which accounts for 8–17% of all in-hospital deaths in the postinfarction period. It generally occurs in old hypertensive patients with Q-wave infarcts. The sites of myocardial rupture are equally distributed between the anterior, posterior, and lateral walls. Usually, there is an acute clinical deterioration with recurrent chest pain, massive hemopericardium, hemodynamic deterioration, electromechanical dissociation, and sudden death within minutes. A subacute form has been recognized with ongoing chest pain, hemodynamic deterioration, and signs of pericardial tamponade. In this form, a very high index of suspicion, together with urgent echocardiographic examination, is crucial. Two-dimensional echocardiography, the most sensitive and expeditious diagnostic modality for detecting subacute free wall rupture shows a pericardial

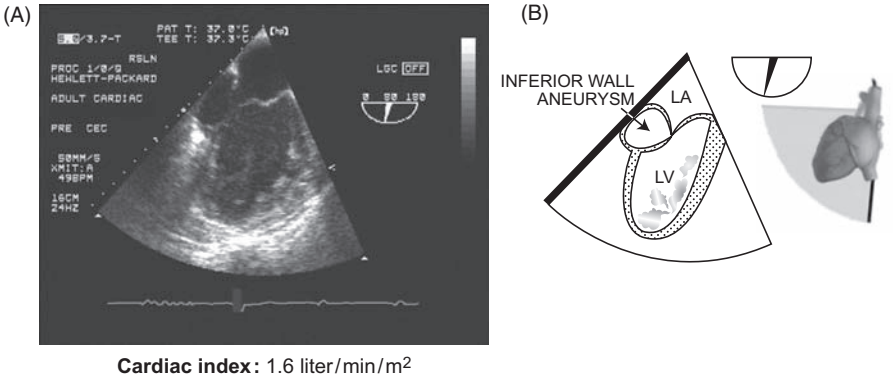

Figure 8.26 Mid-esophageal two-chamber view in a 57-year-old man with a basal inferior ventricular aneurysm. Spontaneous contrast was present in the left ventricle (LV) and the cardiac index was 1.6 L/min per m^2 (LA, left atrium).

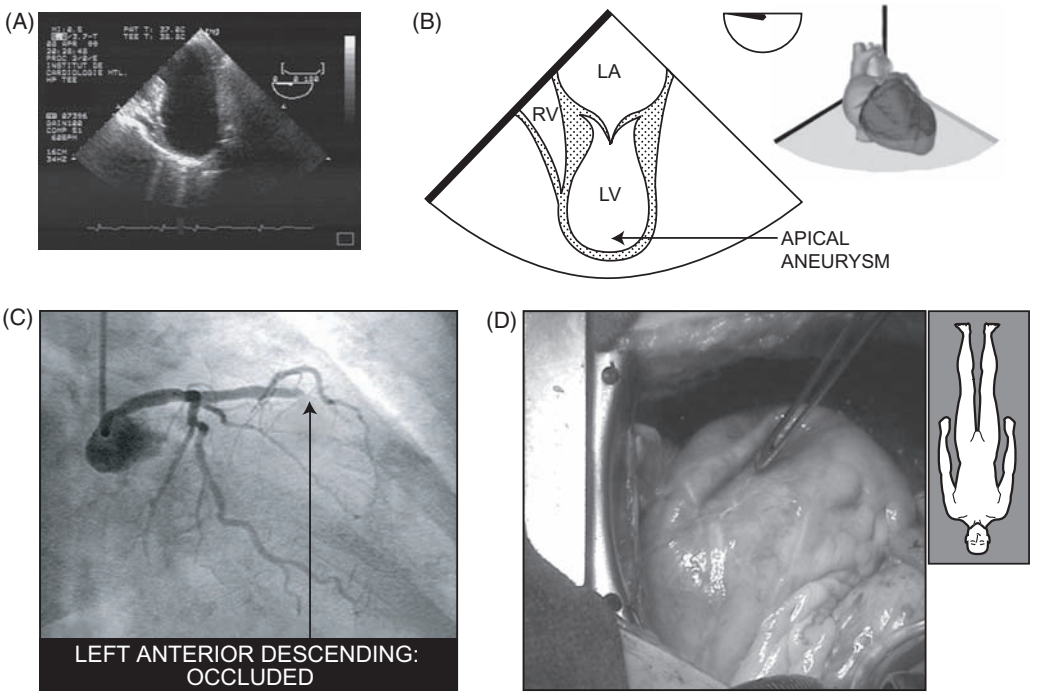

Figure 8.27 (A, B) Mid-esophageal four-chamber view in a 71-year-old man with an apical aneurysm. (C) The coronary angiogram showed complete obstruction of the left anterior descending artery. (D) Intraoperative findings. Note left ventricular wall thinning (LA, left atrium; LV, left ventricle; RV, right ventricle). (Photo D courtesy of Drs. Nicolas Noiseux and Michel Carrier.)

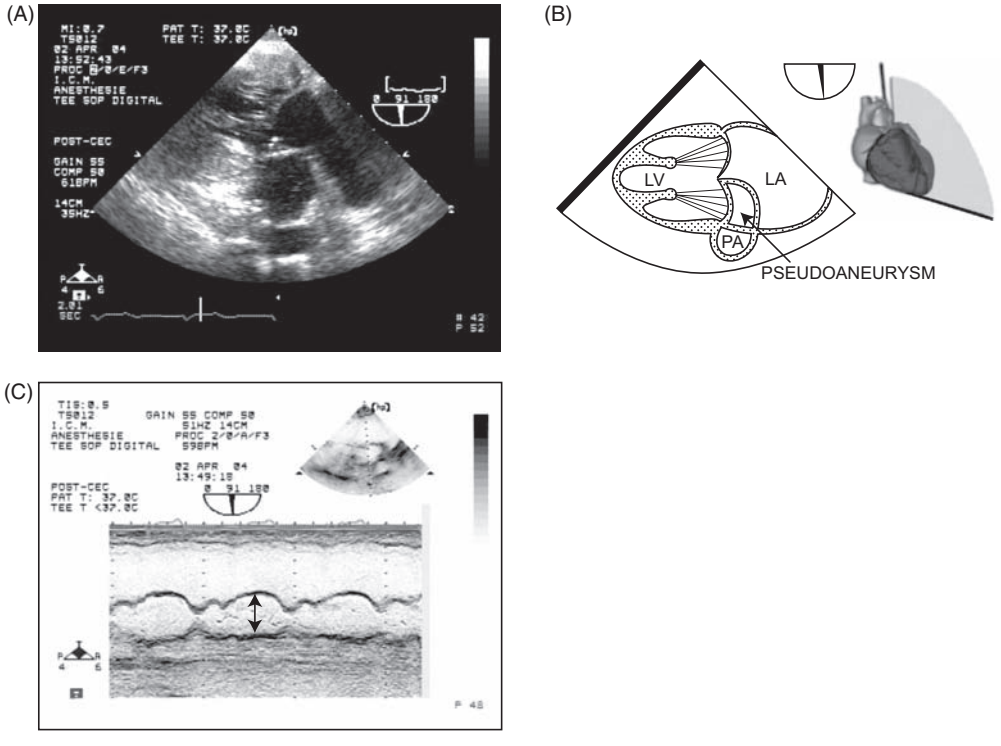

Figure 8.28 (A, B) Transgastric 90° view of a 71-year-old man with an unsuspected antero-basal left ventricular pseudoaneurysm located near the left atrium (LA). He had sustained a thoracic trauma 10 years ago. (C) The systolic expansion (arrow) and diastolic emptying is shown on M-mode (LV, left ventricle; PA, pulmonary artery).

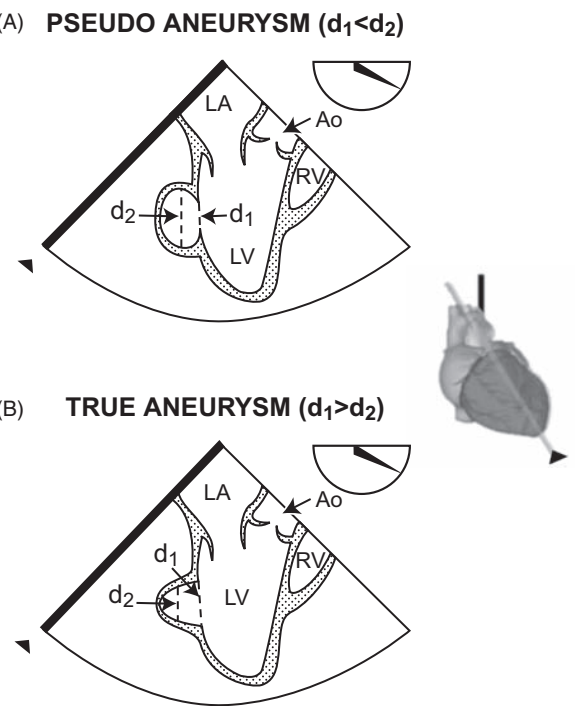

Figure 8.29 Difference between a pseudo and a true aneurysm. (A) In a pseudoaneurysm, the diameter of the orifice (d_1) is smaller than the diameter of the aneurysm (d_2). (B) The opposite is found in a true aneurysm (Ao, aorta; LA, left atrium; LV, left ventricle; RV, right ventricle).

effusion and the presence of echogenic pericardial thrombus (42). The associated findings of regional dilatation and decreased wall thickness may increase the specificity of echocardiography for rupture. The sensitivity and specificity of echocardiographic criteria for the diagnosis of rupture were investigated prospectively by Lopez-Sendon et al. (43). The presence of cardiac tamponade, a pericardial effusion >5 mm and high density intrapericardial echoes suggestive of thrombus have a diagnostic sensitivity of $\geq 70\%$ and specificity $>90\%$ for the diagnosis of myocardial rupture. Direct identification of the myocardial tear with TTE is difficult and TEE may be useful in these unstable patients.

VIII. CORONARY ARTERY IMAGING AND ASSESSMENT OF CORONARY VASODILATOR RESERVE

Although visualization rates of 58–90% have been described for the left main coronary artery with TTE, the right coronary and circumflex arteries are visualised only in 40% and 30% of cases, respectively. The superior resolution offered by the high frequency transducers (5–7 MHz) and the proximity of the coronary arteries to the esophagus account for improved coronary imaging with TEE. A stenosis is defined as an area of apparent luminal narrowing with high-intensity echoes followed by normal lumen. Color flow imaging helps to identify and follow the course of each coronary artery, a mosaic flow pattern often being present in the areas of suspected stenosis. Coronary artery imaging begins in the basal short-axis view at the esophageal level, just above the AoV leaflets. Anteflexion and leftward tilt of the probe tip usually reveals the ostium of the left main coronary artery and minor adjustments permit visualization of the whole artery. Transducer retroflexion reveals the LAD artery whereas the circumflex artery is seen as it passes leftward (on the right of the screen) and posteriorly along the left atrioventricular groove. The ostium of the RCA is usually visualized between 6 and 7 o'clock with the probe tip tilted rightward and retroflexed, whereas its proximal portion is seen extending towards the bottom of the screen. Although visualization of the coronary arteries is possible with single-plane and biplane TEE, evaluation is limited mainly to the left main coronary artery and the very proximal epicardial vessels (44) (Figs. 8.2 and 8.3). The numerous imaging planes provided by multiplane TEE allow enhanced visualization of extended lengths of the coronary arteries and provide a more reliable appraisal of any given abnormality. Tardif et al. (45) reported a sensitivity and specificity of 100% for detection of left main coronary artery narrowing when compared with angiography. In addition, the proximal segments of the LAD, circumflex, and right coronary arteries were visualized in 84%, 80%, and 62% of patients, respectively. The sensitivity and specificity for detection of proximal stenosis were, respectively, 80% and 100% for the LAD artery, 89% and 100% for the circumflex artery, and 82% and 100% for the RCA. It is also possible to evaluate the coronary flow vasodilator reserve with TEE, in order to determine the functional significance of a coronary stenosis (46). The coronary vasodilator reserve is defined as the ratio between the maximal (hyperemic) and baseline flow and its assessment requires the use of a physiologic stimulus (coronary occlusion) or vasorelaxant drugs (adenosine, dipyridamole, papaverine). The coronary hyperemic response is impaired not only in patients with a significant epicardial coronary stenosis, but also in those with systemic hypertension, diabetes mellitus, hypertrophic cardiomyopathy, or syndrome X who can have microvascular disease. Using color Doppler flow and adjusting the PW Doppler sample window as parallel as possible to the coronary flow, baseline velocities are measured. A vasodilator drug is then administered and coronary blood flow velocity is measured again. Iliceto et al. (47) studied LAD coronary artery velocities in 15 patients and observed that the flow reserve was 2.94 in normal patients and 1.46 in those with significant

stenoses. A good correlation was found between coronary flow reserve as measured by TEE and directly by an intracoronary Doppler catheter (48). Redberg et al. (49) reported that a coronary flow reserve value greater than 2.1 as determined by TEE had a sensitivity of 86%, a specificity of 79%, and positive and negative predictive value of 46 and 96%, respectively, in predicting the absence of a critical coronary artery narrowing, compared with quantitative coronary angiography.

IX. CONCLUSION

Transesophageal echocardiography is a sensitive tool in the perioperative setting for detecting segmental myocardial ischemia and for assessing its impact on regional and global systolic function and on diastolic function. In addition, mechanical complications of an acute myocardial infarction can be detected and evaluated thoroughly using the transesophageal approach.

REFERENCES

1. Daniel WG, Mugge A. Transesophageal echocardiography. N Engl J Med 1995; 332:1268–1279.
2. Cerqueira MD, Weissman NJ, Dilsizian V et al. Standardized myocardial segmentation and nomenclature for tomographic imaging of the heart: a statement for healthcare professionals from the Cardiac Imaging Committee of the Council on Clinical Cardiology of the American Heart Association. Circulation 2002; 105:539–542.
3. Smith JS, Cahalan MK, Benefiel DJ et al. Intraoperative detection of myocardial ischemia in high-risk patients: electrocardiography versus two-dimensional transesophageal echocardiography. Circulation 1985; 72:1015–1021.
4. Gallagher KP, Kumada T, Koziol JA et al. Significance of regional wall thickening abnormalities relative to transmural myocardial perfusion in anesthetized dogs. Circulation 1980; 62:1266–1274.
5. Shah PM, Kyo S, Matsumura M, Omoto R. Utility of biplane transesophageal echocardiography in left ventricular wall motion analysis. J Cardiothorac Vasc Anesth 1991; 5:316–319.
6. Rouine-Rapp K, Ionescu P, Balea M et al. Detection of intraoperative segmental wall-motion abnormalities by transesophageal echocardiography: the incremental value of additional cross sections in the transverse and longitudinal planes. Anesth Analg 1996; 83:1141–1148.
7. Leung JM, Levine EH. Left ventricular end-systolic cavity obliteration as an estimate of intraoperative hypovolemia. Anesthesiology 1994; 81:1102–1109.
8. Simonson JS, Schiller NB. Descent of the base of the left ventricle: an echocardiographic index of left ventricular function. J Am Soc Echocardiogr 1989; 2:25–35.
9. Pai RG, Bodenheimer MM, Pai SM et al. Usefulness of systolic excursion of the mitral anulus as an index of left ventricular systolic function. Am J Cardiol 1991; 67:222–224.
10. Doerr HK, Quinones MA, Zoghbi WA. Accurate determination of left ventricular ejection fraction by transesophageal echocardiography with a nonvolumetric method. J Am Soc Echocardiogr 1993; 6:476–481.
11. Urbanowicz JH, Shaaban MJ, Cohen NH et al. Comparison of transesophageal echocardiographic and scintigraphic estimates of left ventricular end-diastolic volume index and ejection fraction in patients following coronary artery bypass grafting. Anesthesiology 1990; 72:607–612.
12. Thys DM, Hillel Z, Goldman ME et al. A comparison of hemodynamic indices derived by invasive monitoring and two-dimensional echocardiography. Anesthesiology 1987; 67:630–634.
13. Estagnasie P, Djedaini K, Mier L et al. Measurement of cardiac output by transesophageal echocardiography in mechanically ventilated patients. Comparison with thermodilution. Intensive Care Med 1997; 23:753–759.
14. Gorcsan J III, Diana P, Ball BA, Hattler BG. Intraoperative determination of cardiac output by transesophageal continuous wave Doppler. Am Heart J 1992; 123:171–176.
15. Pu M, Griffin BP, Vandervoort PM et al. Intraoperative validation of mitral inflow determination by transesophageal echocardiography: comparison of single-plane, biplane and thermodilution techniques. J Am Coll Cardiol 1995; 26:1047–1053.
16. Chen C, Rodriguez L, Lethor JP et al. Continuous wave Doppler echocardiography for noninvasive assessment of left ventricular dP/dt and relaxation time constant from mitral regurgitant spectra in patients. J Am Coll Cardiol 1994; 23:970–976.
17. Kuecherer HF, Foster E. Hemodynamics by transesophageal echocardiography. Cardiol Clin 1993; 11:475–487.
18. Schiller NB, Shah PM, Crawford M et al. Recommendations for quantitation of the left ventricle by two-dimensional echocardiography. American Society of Echocardiography Committee on Standards, Subcommittee on Quantitation of Two-Dimensional Echocardiograms. J Am Soc Echocardiogr 1989; 2:358–367.
19. Berning J, Steensgaard-Hansen F. Early estimation of risk by echocardiographic determination of wall motion index in an unselected population with acute myocardial infarction. Am J Cardiol 1990; 65:567–576.
20. Kan G, Visser CA, Koolen JJ, Dunning AJ. Short and long term predictive value of admission wall motion score in acute myocardial infarction. A cross sectional echocardiographic study of 345 patients. Br Heart J 1986; 56:422–427.
21. Sheehan FH, Bolson EL, Dodge HT et al. Advantages and applications of the centerline method for characterizing regional ventricular function. Circulation 1986; 74:293–305.
22. van Daele ME, Sutherland GR, Mitchell MM et al. Do changes in pulmonary capillary wedge pressure adequately reflect myocardial ischemia during anesthesia? A correlative preoperative hemodynamic, electrocardiographic, and transesophageal echocardiographic study. Circulation 1990; 81:865–871.

23. Leung JM, O'Kelly B, Browner WS et al. Prognostic importance of postbypass regional wall-motion abnormalities in patients undergoing coronary artery bypass graft surgery. SPI Research Group. Anesthesiology 1989; 71:16–25.
24. Shapiro E, Marier DL, John Sutton MG, Gibson DG. Regional non-uniformity of wall dynamics in normal left ventricle. Br Heart J 1981; 45:264–270.
25. Force T, Kemper A, Perkins L et al. Overestimation of infarct size by quantitative two-dimensional echocardiography: the role of tethering and of analytic procedures. Circulation 1986; 73:1360–1368.
26. Marcovitz PA, Bach DS, Mathias W et al. Paradoxic hypotension during dobutamine stress echocardiography: clinical and diagnostic implications. J Am Coll Cardiol 1993; 21:1080–1086.
27. Cigarroa CG, deFilippi CR, Brickner ME et al. Dobutamine stress echocardiography identifies hibernating myocardium and predicts recovery of left ventricular function after coronary revascularization. Circulation 1993; 88:430–436.
28. Smart SC, Sawada S, Ryan T et al. Low-dose dobutamine echocardiography detects reversible dysfunction after thrombolytic therapy of acute myocardial infarction. Circulation 1993; 88:405–415.
29. Arnese M, Cornel JH, Salustri A et al. Prediction of improvement of regional left ventricular function after surgical revascularization. A comparison of low-dose dobutamine echocardiography with 201Tl single-photon emission computed tomography. Circulation 1995; 91:2748–2752.
30. Perrone-Filardi P, Pace L, Prastaro M et al. Assessment of myocardial viability in patients with chronic coronary artery disease. Rest–4-hour–24-hour 201Tl tomography versus dobutamine echocardiography. Circulation 1996; 94:2712–2719.
31. Bonow RO. Identification of viable myocardium. Circulation 1996; 94:2674–2680.
32. Kuecherer HF, Muhiudeen IA, Kusumoto FM et al. Estimation of mean left atrial pressure from transesophageal pulsed doppler echocardiography of pulmonary venous flow. Circulation 1990; 82:1127–1139.
33. Takatsuji H, Mikami T, Urasawa K et al. A new approach for evaluation of left ventricular diastolic function: spatial and temporal analysis of left ventricular filling flow propagation by color M-mode Doppler echocardiography. J Am Coll Cardiol 1996; 27:365–371.
34. Derumeaux G, Ovize M, Loufoua J et al. Doppler tissue imaging quantitates regional wall motion during myocardial ischemia and reperfusion. Circulation 1998; 97:1970–1977.
35. Alam M, Wardell J, Andersson E et al. Effects of first myocardial infarction on left ventricular systolic and diastolic function with the use of mitral annular velocity determined by pulsed wave doppler tissue imaging. J Am Soc Echocardiogr 2000; 13:343–352.
36. Garcia-Fernandez MA, Azevedo J, Moreno M et al. Regional diastolic function in ischaemic heart disease using pulsed wave Doppler tissue imaging. Eur Heart J 1999; 20:496–505.
37. Hill JD, Stiles QR. Acute ischemic ventricular septal defect. Circulation 1989; 79:I112–I115.
38. Chen C, Koschyk D, Hamm C et al. Usefulness of transesophageal echocardiography in identifying small left ventricular apical thrombus. J Am Coll Cardiol 1993; 21:208–215.
39. Kinch JW, Ryan TJ. Right ventricular infarction. N Engl J Med 1994; 330:1211–1217.
40. Lopez-Sendon J, Garcia-Fernandez MA, Coma-Canella I et al. Segmental right ventricular function after acute myocardial infarction: two-dimensional echocardiographic study in 63 patients. Am J Cardiol 1983; 51:390–396.
41. Lopez-Sendon J, Lopez DS, Roldan I et al. Inversion of the normal interatrial septum convexity in acute myocardial infarction: incidence, clinical relevance and prognostic significance. J Am Coll Cardiol 1990; 15:801–805.
42. Hermoni Y, Engel PJ. Two-dimensional echocardiography in cardiac rupture. Am J Cardiol 1986; 57:180–181.
43. Lopez-Sendon J, Gonzalez A, Lopez DS et al. Diagnosis of subacute ventricular wall rupture after acute myocardial infarction: sensitivity and specificity of clinical, hemodynamic and echocardiographic criteria. J Am Coll Cardiol 1992; 19:1145–1153.
44. Yoshida K, Yoshikawa J, Hozumi T et al. Detection of left main coronary artery stenosis by transesophageal color Doppler and two-dimensional echocardiography. Circulation 1990; 81:1271–1276.
45. Tardif JC, Vannan MA, Taylor K et al. Delineation of extended lengths of coronary arteries by multiplane transesophageal echocardiography. J Am Coll Cardiol 1994; 24:909–919.
46. Wilson RF, Marcus ML, White CW. Prediction of the physiologic significance of coronary arterial lesions by quantitative lesion geometry in patients with limited coronary artery disease. Circulation 1987; 75:723–732.
47. Iliceto S, Marangelli V, Memmola C, Rizzon P. Transesophageal Doppler echocardiography evaluation of coronary blood flow velocity in baseline conditions and during dipyridamole-induced coronary vasodilation. Circulation 1991; 83:61–69.
48. Zehetgruber M, Porenta G, Mundigler G et al. Transesophageal versus intracoronary Doppler measurements for calculation of coronary flow reserve. Cardiovasc Res 1997; 36:21–27.
49. Redberg RF, Sobol Y, Chou TM et al. Adenosine-induced coronary vasodilation during transesophageal Doppler echocardiography. Rapid and safe measurement of coronary flow reserve ratio can predict significant left anterior descending coronary stenosis. Circulation 1995; 92:190–196.

9

Global Ventricular Function and Hemodynamics

ANDRÉ Y. DENAULT, PIERRE COUTURE
University of Montreal, Montreal, Canada

JEAN BUITHIEU
McGill University, Montreal, Canada

I. Normal Right and Left Ventricular Morphology 186
II. Normal Right and Left Ventricular Function 186
A. Descent of the Base, Segmental Contraction, and Septal Curvature 186
B. Pressure–Volume Relationship 186
1. Preload 187
2. Afterload 190
3. Contractility and Ventricular Performance 191
III. Abnormal Left Ventricular Function 192
A. Acute vs Chronic Etiology 192
B. Problems Confounding Diagnosis 193
C. Transesophageal Echocardiographic Evaluation 193
IV. Abnormal Right Ventricular Function 193
A. Importance 193
B. Transesophageal Echocardiography Findings 194
V. Abnormal Diastolic Function 198
A. Left Ventricular Diastolic Dysfunction 198
B. Right Ventricular Diastolic Dysfunction 200
VI. Causes of Severe Hypotension and Specific Hemodynamic Derangements 201
A. Myocardial Ischemia 204
B. Left Ventricular Outflow Tract Obstruction 204
C. Right Ventricular Outflow Tract Obstruction 206
D. Mitral Valve Fluttering from Aortic Regurgitation 206
E. Midsystolic Pulmonary Valve Closure in Pulmonary Hypertension 206
VII. Pulmonary Thromboembolism 209
VIII. Conclusion 211
References 212

Important roles of perioperative transesophageal echocardiography (TEE) include the determination of baseline ventricular function before a surgical procedure and the identification of changes in ventricular function during cardiac and noncardiac procedures which in some cases may lead to severe hemodynamic instability which, when unresponsive to therapy, is considered a category 1 indication for the use of TEE (1). In such cases TEE allows precise determination of the mechanism of hemodynamic instability through evaluation of both left and right systolic and diastolic function.

I. NORMAL RIGHT AND LEFT VENTRICULAR MORPHOLOGY

The normal ventricular morphology and quantitative evaluation of ventricular size and function are described in Chapters 4 and 5 and in the American Society of Echocardiography (ASE) guidelines (2).

II. NORMAL RIGHT AND LEFT VENTRICULAR FUNCTION

A. Descent of the Base, Segmental Contraction, and Septal Curvature

There are several points which should be emphasized in the evaluation of normal ventricular function. Normal left ventricular function is associated with radial shortening but also longitudinal displacement of the base towards the apex by 15–20 mm which can be quantified using M-mode (3) or tissue Doppler imaging (4) and which correlates with ejection fraction (Fig. 9.1). There are normal regional variations in the thickening of ventricular segments with increasing contractility from the base to the apex. There is also rightward ventricular septal curvature because normal left ventricular pressure is generally superior to right ventricular pressure.

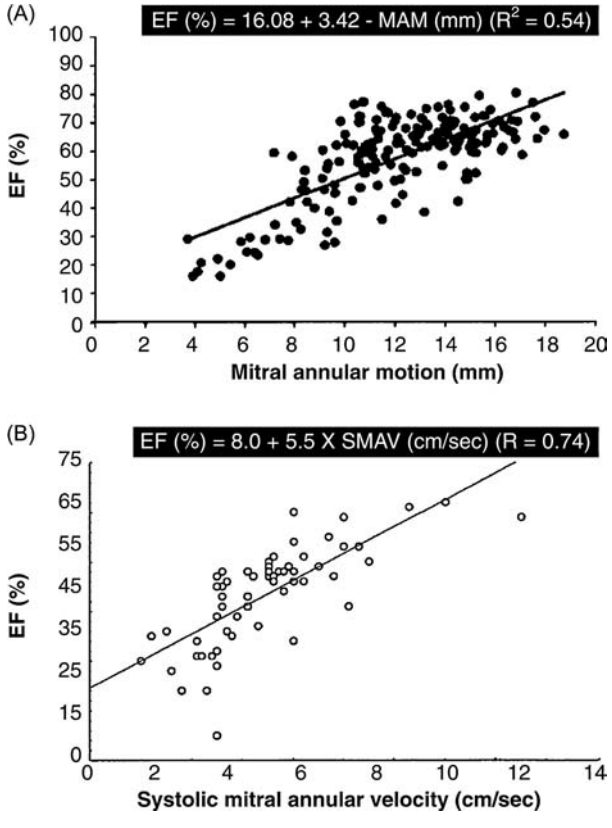

Figure 9.1 Relationship between ejection fraction (EF) and mitral annular motion (MAM) in 182 patients (A) and systolic mitral annular velocity (SMAV) by tissue Doppler in 60 patients (B). [Adapted with permission from Emilson et al. (3) and Alam et al. (4).]

B. Pressure–Volume Relationship

The determination of the relationship between ventricular function and hemodynamics is best described using the pressure–volume curves which allow graphical description of ventricular function by displaying a single cardiac cycle volume against pressure–time relationship (Fig. 9.2). This includes seven time-related events. Diastole starts with isovolemic relaxation (phase 4), continues with the opening of the mitral valve (MV) and early left ventricular filling, diastasis and atrial systole (phases 5–7) and ends with MV closure prior to isovolumic contraction (phase 1). Systole begins with the isovolumic contraction (phase 1), proceeds with the opening of the aortic valve (AoV) and ejection of the stroke volume (SV) (phases 2 and 3). The pressure–volume diagram can be obtained through continuous pressure and volume measurement but is rarely done in clinical practice.

Many determinants of the pressure–volume relationship may be obtained using TEE, a pulmonary artery catheter and a systemic arterial pressure catheter. Transesophageal echocardiography allows estimation of the volume component (or abscissa). Pressure components of the ordinate axis may be estimated from the pulmonary artery catheter and from systemic arterial pressure (Fig. 9.3). The left ventricular end-diastolic pressure (LVEDP) will be estimated by the pulmonary artery occlusion pressure (Paop) or wedge pressure at end-diastole, in the absence of any obstruction between the pulmonary capillary bed and the left ventricle (LV) such as mitral stenosis (MS). The left ventricular end-systolic pressure (LVESP) can be estimated by the systolic arterial pressure (SAP) if aortic valvular obstruction is absent (5,6). The left ventricular end-systolic volume (LVESV) and left ventricular end-diastolic volume (LVEDV) can be approximated by the left ventricular end-systolic area (LVESA) and left ventricular end-diastolic area (LVEDA) obtained from TEE short-axis transgastric views. The SV is calculated from the ratio of the thermodilution-derived cardiac output (CO) to the heart rate or through Doppler measurement (see Chapter 5). The area within the left ventricular pressure–volume curve is the left ventricular stroke work [LVSW = SV × (mean arterial pressure or MAP − Paop) × 0.0136] and this value is obtained through automated calculation of the cardiopulmonary profile.

Determinants of cardiac function, preload, afterload and contractility are easily plotted on the left ventricular pressure–volume relationships (Fig. 9.4). Each change in

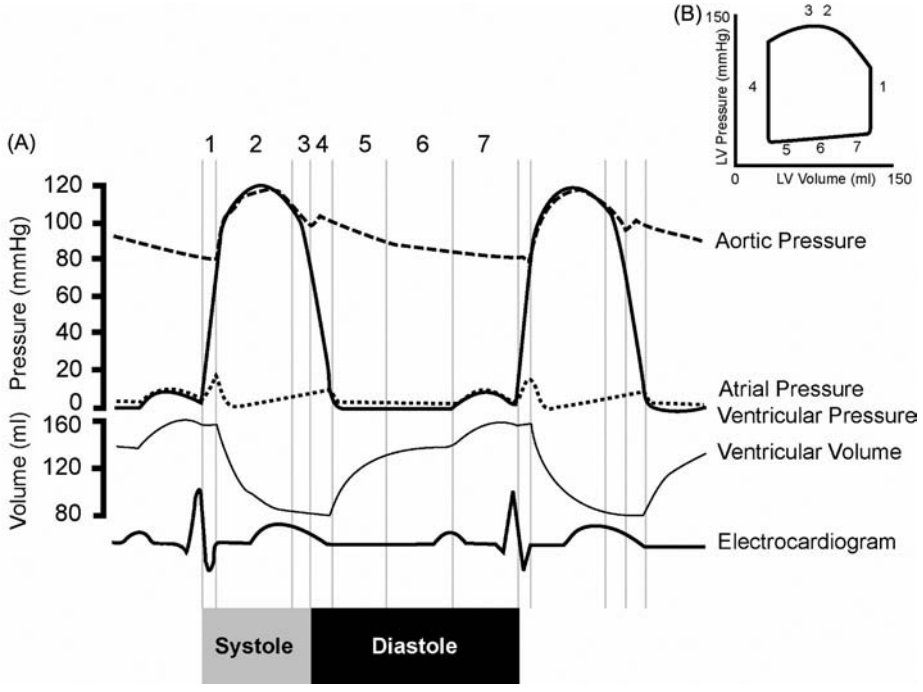

Figure 9.2 (A) Changes in aortic, atrial, ventricular pressure, and ventricular volume in relation to the electrocardiogram. Left ventricular (LV) pressure and volume over time during a cardiac cycle is characterized by seven time-related events. Isovolumic contraction [1] is followed by early [2] and late [3] ejection. Diastole starts with isovolumic relaxation [4] followed by the early filling phase after the opening of the mitral valve [5], diastasis [6], and atrial contraction [7]. (B) Corresponding LV pressure–volume relationship during one cardiac cycle.

these determinants will affect the pressure–volume relationship differently. In the following discussion, when possible, the effects of changes in cardiac function and their determinants will be explained by using the pressure–volume relationship.

1. Preload

A decrease in preload will be associated with a fall in LVEDV and LVEDP [Fig. 9.4(A)]. It is difficult clinically to differentiate between hypovolemia from reduced

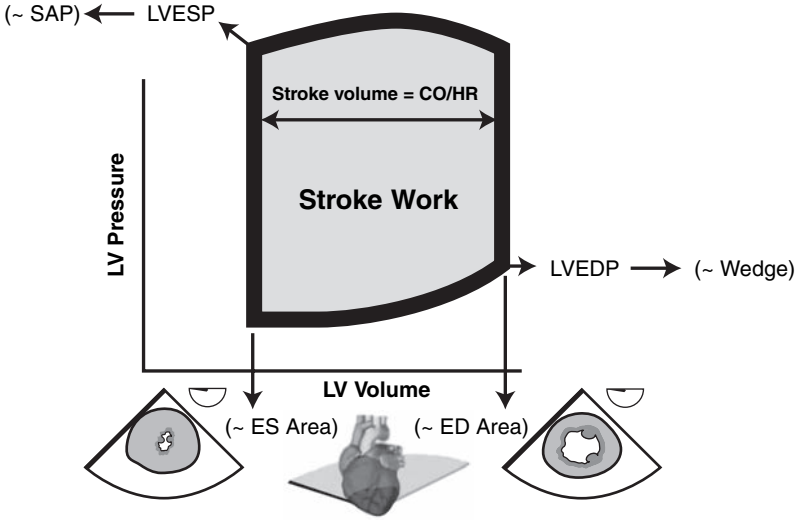

Figure 9.3 Left ventricular (LV) pressure–volume relationship during one cardiac cycle. The LV end-systolic pressure (LVESP) can be estimated using systolic arterial pressure (SAP) and the LV end-diastolic pressure (LVEDP) can be estimated with the pulmonary artery-derived "wedge" pressure at end-diastole. Using echocardiography, the LV end-systolic (ES) volume can be estimated with the ES area and the LV end-diastolic (ED) volume can be estimated with the ED area. The stroke volume, which is the difference between the ED volume and the ES volume, can be calculated from the ratio of the cardiac output (CO) obtained by Doppler or thermodilution divided by heart rate (HR). The LV stroke work corresponds to the area under the LV pressure–volume diagram (gray area). Changes in compliance of the left ventricle can explain why filling pressure does not always correlate with ventricular size.

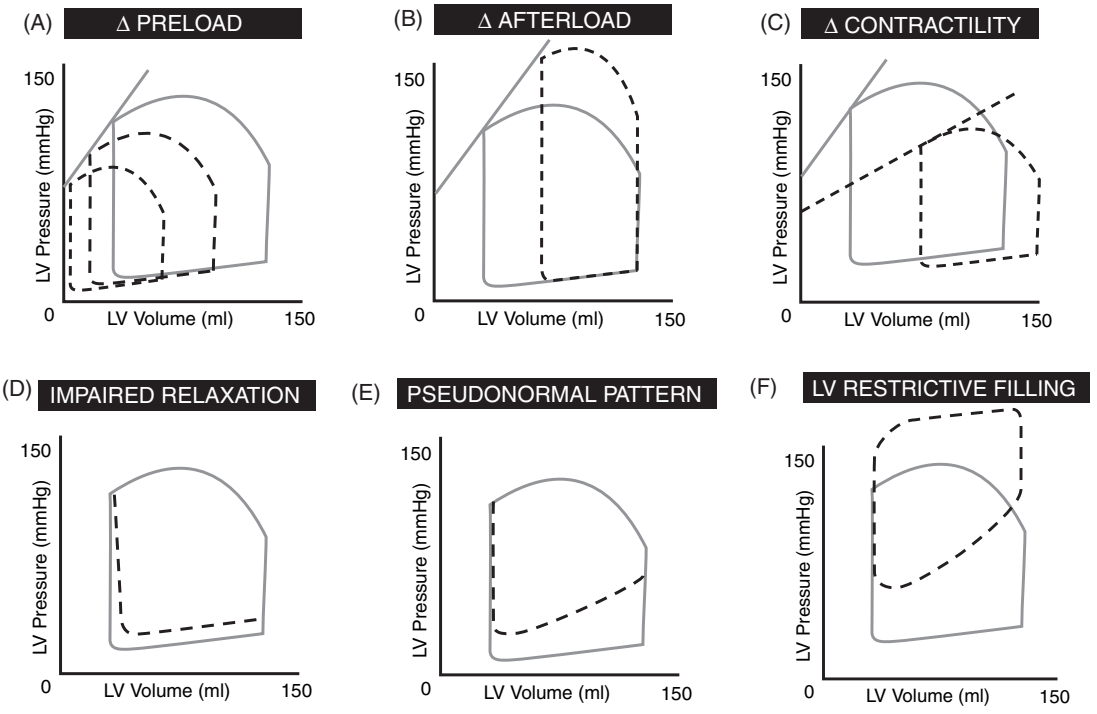

Figure 9.4 Left ventricular (LV) pressure–volume relationship showing changes in preload, afterload, contractility, and diastolic function. (A–C) Changes (Δ) in systolic function. (A) Decrease in preload: leftward and downward shift of the LV pressure–volume relationship with a reduction in end-diastolic pressure (EDP) and in end-diastolic volume (EDV). The elastance (left upper line) connects all the end-systolic points through which the pressure–volume diagram moves. (B) Increase in afterload: rightward and upward shift of the pressure–volume relationship with an increase in end-systolic pressure and in end-systolic volume. (C) Reduction in contractility: downward shift of the elastance with rightward displacement of the pressure–volume diagram. (D–F) Changes in diastolic function: with increasing severity, higher EDP is observed for the same EDV. (D) Stage I diastolic dysfunction: delayed LV relaxation. (E) Stage II diastolic dysfunction: pseudonormal filling pattern. (F) Stage III diastolic dysfunction: restrictive filling.

systemic vascular resistance (SVR) using TEE because both conditions will lead to reduction in preload. Both two-dimensional (2D) and Doppler indices have been used and validated to estimate left ventricular filling pressure and volume. Clinically useful echocardiographic 2D images for the diagnosis of hypovolemia or reduced SVR are the progressive reduction in LVEDA, left ventricular end-systolic cavity obliteration (Fig. 9.5), atrial septal displacement (Fig. 9.6) and both inferior and superior vena cava collapsibility (Fig. 9.7) (7), which will be discussed in the following text.

Left ventricular end-systolic cavity obliteration and its relationship to hypovolemia was studied by Leung et al. (8) in 139 patients undergoing cardiac surgery who were monitored continuously with TEE in the mid-papillary view. Hypovolemia, defined as a 10% reduction in LVEDA, was present in 80% of the observations of left ventricular end-systolic cavity obliteration. Consequently, this sign can occur in patients with increased ventricular performance, where a reduction in LVESV may be observed, without necessarily a reduction in LVEDV. Furthermore, the use of LVEDA as a predictor of responsiveness to increased preload has been shown to be limited (9–11). Kusumoto et al. (12) studied the atrial septal displacement as an index of reduced preload. As left atrial pressure is normally superior to right atrial pressure, the atrial septum should normally bulge towards the right atrium (RA) (convexity toward the RA) during most of the cardiac cycle (Fig. 9.6). In patients with mechanical ventilation, the authors observed that mid-systolic reversal of the atrial septal normal convexity occurred during expiration in 64 of 72 episodes when the wedge pressure was <15 mmHg and only two of 40 episodes when it was >15 mmHg. If the mid-systolic reversal of the atrial septum occurred during both inspiration and expiration, the wedge would usually be, <10 mmHg.

Another sign of preload responsiveness was described by Vieillard-Baron et al. (7). They observed that the presence of superior vena caval diameter collapse during

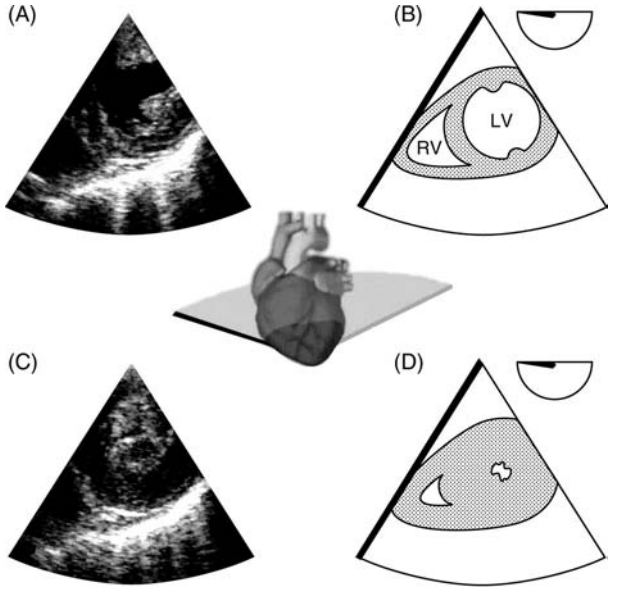

Figure 9.5 Left ventricular end-systolic cavity obliteration. Two-dimensional echocardiographic images of the left ventricle (LV) taken from a mid-papillary transgastric view during diastole (A, B) and systole (C, D). Example taken from an hypovolemic patient (RV, right ventricle).

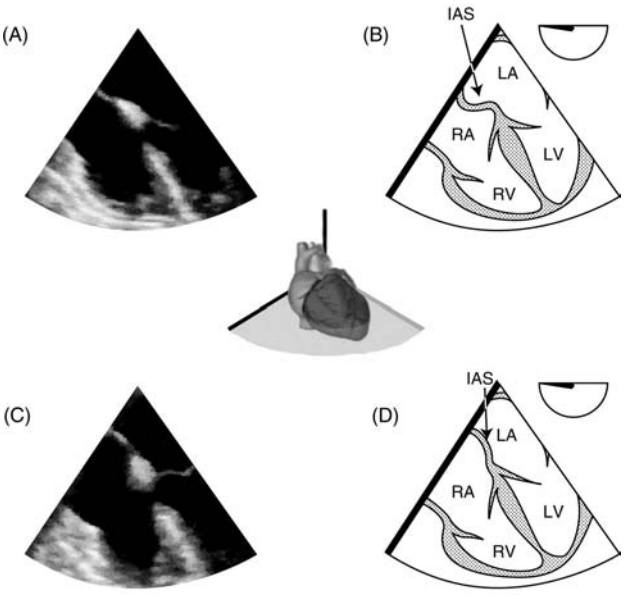

Figure 9.6 Using interatrial septal (IAS) displacement in the assessment of filling pressure. Mid-esophageal four-chamber view of the left ventricle (LV) in a patient following cardiopulmonary bypass. (A, B) The IAS deviated to the right: this implies that atrial pressure is higher on the left than on the right. The pulmonary artery occlusion pressure or "wedge" was 17 mmHg. (C, D) Following vasodilator therapy, the "wedge" pressure dropped to 7 mmHg. Now the IAS is displaced toward the left. This is consistent with the left atrial pressure being lower than the right (LA, left atrium; RA, right atrium; RV, right ventricle).

positive-pressure ventilation correlated with significant reduction in preload measured using Doppler velocities in the pulmonary artery. Using a collapsibility index, defined as the maximal expiratory diameter minus the minimal inspiratory diameter divided by the maximal diameter on expiration, patients with an index $>60\%$ had an inspiratory decrease in right ventricular outflow velocity close to 70%, as opposed to patients with a collapsibility index of $<30\%$, who had a decrease in right ventricular outflow velocities only to 30%. Fluid challenge reduced the variation in superior vena caval diameter through a change in caval zone condition in a similar fashion to the West zones conditions (Fig. 9.7).

Several Doppler indices have been studied to estimate left ventricular filling pressure. These are provided through pulsed-wave (PW) Doppler interrogation of the MV inflow, the pulmonary venous flow (PVF) (Fig. 9.8) and more recently, the use of tissue Doppler interrogation of the MV annulus. Acute preload reduction is associated with a reduction of the E/A ratio on the MV inflow signal: this pattern has been shown to correlate with left ventricular filling pressure in several studies (13,14). Not only is the E/A ratio related to pulmonary capillary wedge pressure (PCWP) (15), but the difference between the duration of the atrial reversal wave in the pulmonary veins and that of the mitral A-wave is a useful variable for the estimation of LVEDP (16). As downstream left ventricular filling pressure is increased, the duration of the atrial reversal in the pulmonary veins increases and exceeds the duration of the mitral A-wave. The PVF flow pattern has also been studied as an index of preload. Kuecherer et al. (17) reported the inverse relationship between the PVF ratio of the systolic to diastolic (S/D) velocity–time integral and the left atrial filling pressure (17). Girard et al. (18) demonstrated a greater respiratory variation of the systolic component (S) with PCWP <18 mmHg (18). Lattik et al. (19) observed that patients with normal or mildly abnormal diastolic function and a low to normal E/A ratio respond to a fluid bolus by increasing their CO and SV as opposed to patients with elevated E/A ratio (Fig. 9.9). The MV E/A ratio was superior to left ventricular filling pressure and 2D echocardiographic area measurements in predicting the response to volume infusion (19).

More recently, the velocity of propagation (V_p) of the E-wave assessed by color M-mode and tissue Doppler imaging of the MV annulus have been used in the estimation of LV filling pressure. The E/e ratio of the MV

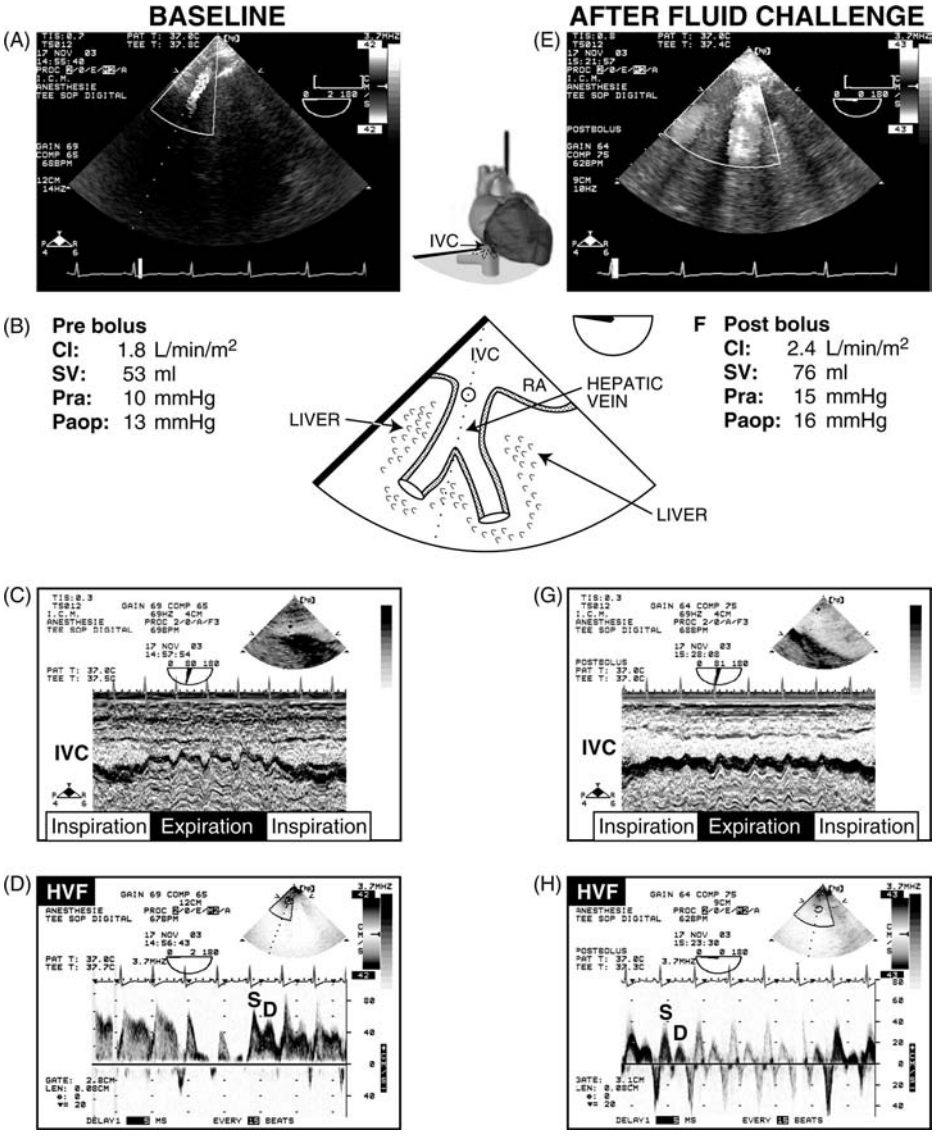

Figure 9.7 Effect of fluid loading on hemodynamic and echocardiographic parameters in a 62-year-old man on mechanical ventilation. (A–D) Baseline: the diameter of the inferior vena cava (IVC) and hepatic veins is small. (C) The IVC collapse during the lowest intrathoracic pressure period: here with the expiration phase of positive-pressure ventilation. (D) Hepatic venous flow (HVF) Doppler interrogation: systolic velocities are elevated up to 80 cm/sec because of the small hepatic vein caliber. (E–H) After fluid challenge, the diameter of the IVC and hepatic veins has enlarged. (F) The cardiac index (CI) and filling pressure increased. (G) Significant IVC collapse is absent. (H) The larger diameter of the hepatic vein results in lower velocities (Paop, pulmonary artery occlusion pressure; Pra, right atrial pressure; RA, right atrium; SV, stroke volume).

inflow E velocity to the MV annulus e (also labeled E_m) ≥ 9 best identifies patient with LVEDP >12 mmHg (20,21). Likewise, the E/V_p ratio of the MV inflow E velocity to the color M-mode V_p with a value >1.5 best identified patients with PCWP >12 mmHg (22,23). Both E/e and E/V_p ratios have been shown to correlate well with left ventricular filling pressure independently of ventricular function. Table 9.1 summarizes the effect of a reduction or an increase in preload on these Doppler parameters.

2. *Afterload*

An increase in afterload will be associated with an increase in the LVESP necessary to open the AoV and consequently the LVESV will increase [Fig. 9.4(B)], while the slope of the relationship or the elastance remains unchanged. In the preoperative clinical setting, we do not routinely measure echocardiographic indices of afterload. It can however be estimated using the arterial

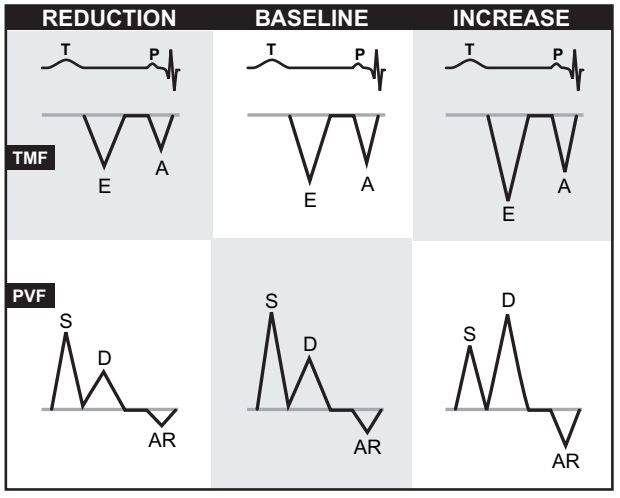

Figure 9.8 Effect of changes in preload on the pulsed-wave Doppler interrogation of the transmitral valve flow (TMF) and the pulmonary venous flow (PVF). With reduction in volume, both the early diastolic mitral valve inflow E-wave and the diastolic D-wave of the PVF are reduced. With increase in preload, the TMF E-wave and PVF D-wave are increased (AR, atrial reversal).

elastance, that is, the ratio of LVESP over the LVESV (24) or by estimating the LVES wall stress which combines M-mode or 2D measurements with pressure data (see Chapter 5). An often unrecognized important clinical scenario leading to an increase in afterload is seen with the systolic anterior motion (SAM) of the MV and its associated left ventricular outflow tract (LVOT) obstruction which results in mosaic flow due to aliasing on color imaging of the LVOT (Fig. 9.10). Systolic anterior motion of the MV can occur during MV repair and several other extreme physiologic situations during which left ventricular filling is significantly reduced.

3. Contractility and Ventricular Performance

Changes in preload and afterload will displace the pressure–volume loops along a line called maximal elastance. Decreasing or increasing contractility will be associated with a downward or upward shift of the elastance and a displacement of the pressure volume relationship towards the right. In Fig. 9.4(C), for instance, the decrease in contractility (dotted loop) results in a greater LVESV for the same LVESP. The concept of elastance is important to understand because this measure is considered relatively independent of changes in preload and afterload. Measurements such as ejection fraction and CO are not pure indices of contractility but rather markers of ventricular performance. Consequently, changes in preload or afterload may affect the ejection fraction but no changes in elastance will be observed. A study with

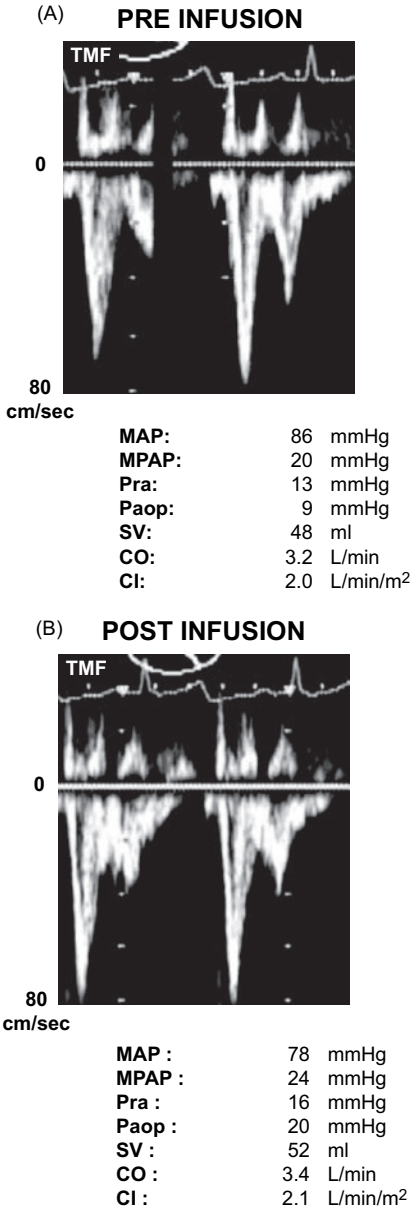

Figure 9.9 Echocardiographic and hemodynamic effect of volume loading: a high baseline E/A ratio predicts limited response to fluid infusion. (A) The transmitral flow (TMF) early diastolic E-wave is predominant compared with the atrial A-wave. (B) Following a bolus of 500 mL of a colloid solution, the E/A ratio increased. This was associated with an increase in mean pulmonary artery pressure (MPAP), right atrial pressure (Pra), pulmonary artery occlusion (Paop) or "wedge" pressure but no significant change in mean arterial pressure (MAP), stroke volume (SV), cardiac output (CO), and cardiac index (CI).

patients undergoing coronary artery bypass also documented the fact that despite the absence of significant postoperative change in SV, fractional area change (FAC) and CO, the elastance index suggested a reduction in

Table 9.1 Summary of the Doppler Indices in the Evaluation of Hypovolemia

	Decrease in filling pressure	Increase in filling pressure
MV inflow PW Doppler		
E velocity	↓	↑
A velocity	↑	↓
E/*A* ratio	↓	↑
Deceleration time	↑	↓
Pulmonary veins PW Doppler		
S velocity	↑	↓
D velocity	↓	↑
AR velocity	↓	↑
AR duration	↓	↑
S/*D* TVI ratio	↑	↓
Respiratory variations	↑	↓
MV annulus tissue Doppler		
e velocity	↑	↓
Color M-mode		
Velocity of propagation (V_p) of the E-wave	↑	↓
Derived indices		
Difference A wave duration (MV–PV)	↓	↑
E/*e*	↓	↑
E/V_p	↓	↑

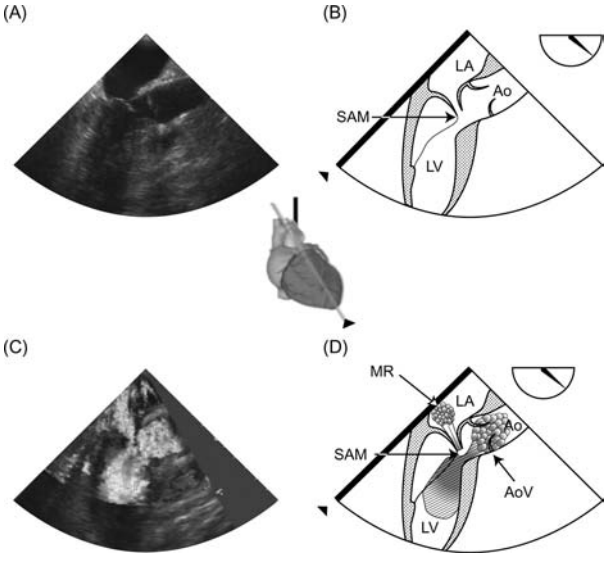

Figure 9.10 Dynamic left ventricular outflow tract obstruction: mid-esophageal long-axis view in a 38-year-old man with septic shock and hemodynamic instability. (A, B) Part of the anterior mitral valve is obstructing the left ventricular outflow tract. (C, D) This was associated with mitral regurgitation (MR). His hemodynamic condition improved with fluid and β-blockade (Ao, aorta; AoV, aortic valve; LA, left atrium; LV, left ventricle; SAM, systolic anterior motion).

contractility after the surgical procedure (Fig. 9.11) (25). In clinical practice, elastance is rarely obtained because artificial preload alteration is required to calculate the slope of the pressure–volume relationship.

The most commonly used echocardiographic evaluation of ventricular performance includes measurements of FAC, ejection fraction and CO. Fractional area change provides an estimation of ejection fraction and is commonly obtained from a transgastric view (Fig. 9.5). Ejection fraction calculation can be obtained through the measurement of ventricular volumes from the four- and two-chamber views using one of several formulas available for volume measurements (see Chapter 5) (2). Stroke volume and secondly CO can be calculated from either 2D volume end-diastolic and end-systolic measurements, or from volumetric Doppler-derived results (see Chapter 5). Other indirect echocardiographic signs useful in the identification of reduced left ventricular systolic function include the presence of intracavitary spontaneous echo contrast, increased anterior MV leaflet septal distance (see Fig. 10.22) reduced mitral annular displacement (26) and an abnormal myocardial performance index (27). The latter (see Fig. 9.12) is altered by abnormalities in either systolic and/or diastolic function and it can be used in the evaluation of both left and right ventricular function (28,29).

III. ABNORMAL LEFT VENTRICULAR FUNCTION

A. Acute vs Chronic Etiology

Acute left ventricular dysfunction can be either systolic or diastolic in origin. It is typically associated with both increased wall motion score index (see Chapter 8) and moderate to severe diastolic dysfunction. Severe left ventricular systolic dysfunction will sometimes be accompanied by pulsus alternans, where the left ventricular stroke volume and systolic blood pressure will be decreased on every alternate beat (Fig. 9.13). Left ventricular diastolic dysfunction is commonly seen in unstable patients after cardiac surgery, even in patients with normal systolic function (30). Chronic left ventricular systolic dysfunction will be associated with ventricular dilatation and diastolic dysfunction which severity can range from mild delayed relaxation to restrictive filling pattern (see following text). Atrial dilatation is more common in chronic condition but can be observed also in the acute setting and often correlates with the degree of diastolic dysfunction. This can be associated with mitral annular dilatation, mitral regurgitation (MR), and atrial fibrillation.

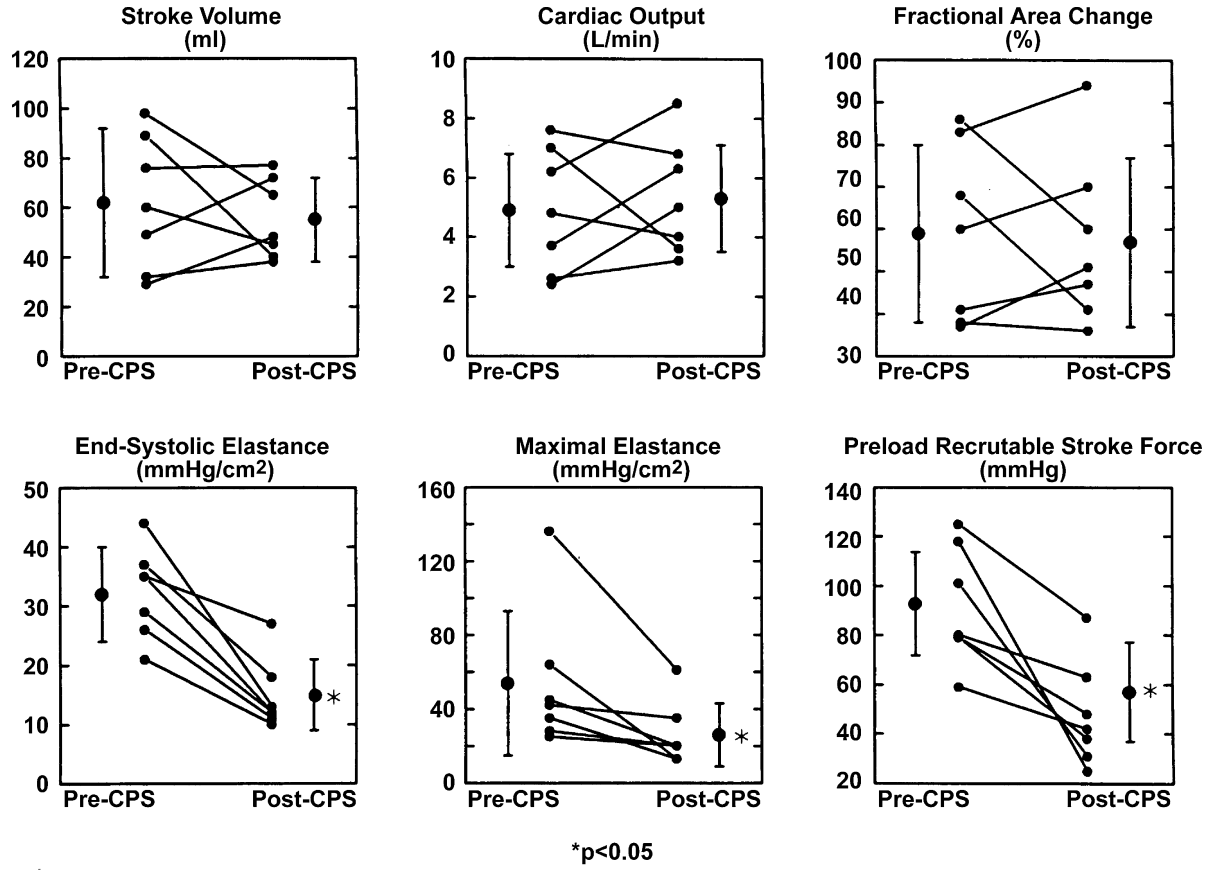

Figure 9.11 Changes in stroke volume, cardiac output, fractional area change, end-systolic elastance, maximal elastance, and preload recruitable stroke force in seven patients before and after cardiopulmonary bypass surgery (CPS). No significant changes were observed in stroke volume, cardiac output and fractional area change. However the indices based on the pressure–volume relationship were lower after CPS. [With permission of Gorcsan et al. (25).]

B. Problems Confounding Diagnosis

In the evaluation of left ventricular function, several errors can be made in the measurement of left ventricular dimensions. In the mid-esophageal four-chamber view, the apex of the LV can be foreshortened leading to underestimation of ventricular volume. Further retroflexion of the probe tip may reduce the impact of this problem. A transgastric short-axis view with an oblique cross section leads not only to faulty measurements of left ventricular dimensions, but also to misinterpretation of regional wall motion. Moderate to severe MR or ventricular septal defect may result in a left ventricular ejection fraction which overestimates intrinsic myocardial contractility. The presence of MR allows the measurement of left ventricular dP/dt, a different index of left ventricular contractility and function (Fig. 9.14) which can be used to estimate ejection fraction postoperatively (31). Finally, the estimation of left ventricular ejection fraction may vary according to the site of measurement as one moves from the ventricular apex (75%) to the short axis (65%) to the base of the heart (50%). Longitudinal contraction (shortening of the left ventricle long axis) contributes 10–15% of the ejection fraction.

C. Transesophageal Echocardiographic Evaluation

Figures 9.15–9.18 summarize our approach to the evaluation of ventricular function using four specific views that allow the evaluation of both left and right ventricular systolic and diastolic dysfunction and also mitral, aortic, and tricuspid valvular function.

IV. ABNORMAL RIGHT VENTRICULAR FUNCTION

A. Importance

Right ventricular systolic dysfunction is associated with high morbidity after cardiac surgery (32,33), chest trauma (34) and with sepsis (35) and can be difficult to diagnose

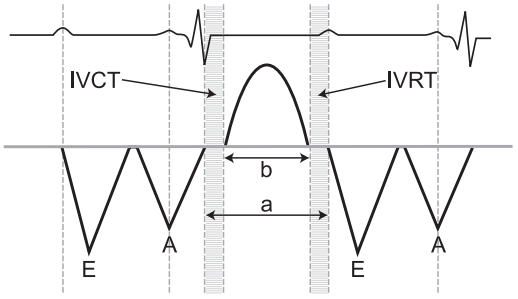

$a = IVRT + IVCT + ET$

$b = ET$

$$MPI = \frac{a - b}{b} = \frac{IVRT + IVCT}{ET}$$

Normal value: LV = 0.39 ± 0.05
RV = 0.28 ± 0.04

Figure 9.12 Measurement of myocardial performance index (MPI) or Tei index. (1) For the MPI of the left ventricle (LV), the transmitral inflow is used for measurement of the duration "a" from the end of atrial contraction (A-wave) to the beginning of LV filling (E-wave). (2) The ejection time (ET) or "b" is measured from a deep transgastric long-axis view Doppler interrogation of the left ventricular outflow tract. The MPI of the right ventricle (RV) is similarly obtained using the transtricuspid flow and the mid-esophageal ascending aorta short-axis view for the right ventricular outflow tract (IVCT, isovolumic contraction time; IVRT, isovolumic relaxation time) (28).

with conventional hemodynamic criteria after cardiac surgery (30). Davila-Roman et al. (36) observed that right ventricular dysfunction cannot be differentiated from left ventricular dysfunction using pulmonary artery catheter-derived variables in the postbypass period. This stresses the importance of the echocardiographic assessment of right ventricular function. The RV is anterior to the LV and has a crescentic configuration. Because of this complex shape, which is more difficult to describe by a mathematical geometric model, right ventricular volume has been more difficult to estimate from 2D parameters compared with the left-sided volume.

B. Transesophageal Echocardiography Findings

Echocardiographic evaluation of right ventricular function includes measurements of chamber size, evaluation of regional wall motion, ventricular septal motion, tricuspid annular displacement, and vena cava size. Evaluation can be complemented with PW Doppler interrogation of the pulmonary outflow tract, tricuspid inflow and hepatic venous flow and tissue Doppler interrogation of the tricuspid annulus. These measurements can be obtained using the four-chamber view (Fig. 9.15), the transgastric short- (Fig. 9.17) and long-axis view (Fig. 9.18) of the RV. Echocardiographic manifestations of right ventricular failure

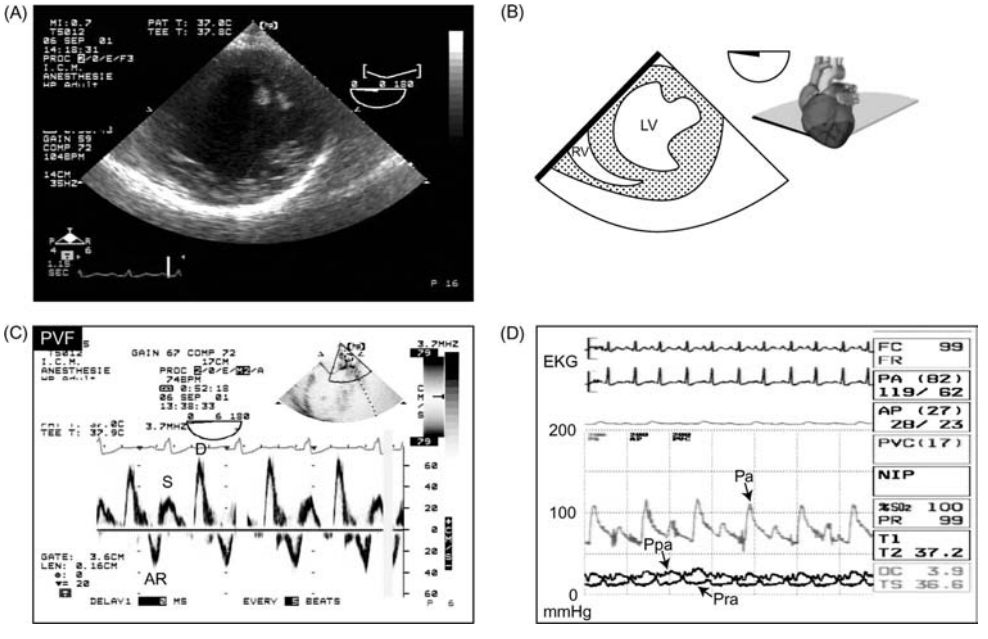

Figure 9.13 Left ventricular severe systolic and diastolic dysfunction in a 71-year-old woman before revascularisation. (A, B) The mid-papillary transgastric short-axis view demonstrates dilated left ventricle (LV) with severe systolic dysfunction. (C) Pulmonary venous flow (PVF) showing diastolic predominance ($S < D$) consistent with moderate diastolic dysfunction. (D) Pulsus alternans on the arterial pressure (Pa) tracing was present (AR, atrial reversal; EKG, electrocardiogram; Ppa, pulmonary artery pressure; Pra, right atrial pressure; RV, right ventricle).

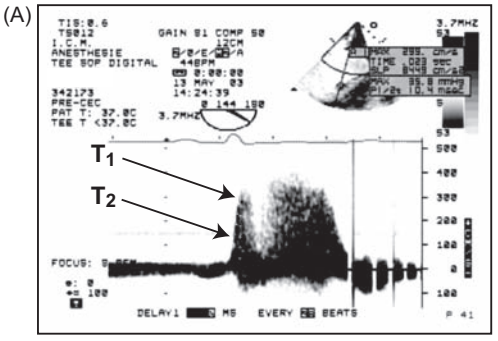

Figure 9.14 Measurement of left ventricular change in pressure over time (dP/dt) using continuous-wave Doppler of mitral regurgitation in a 58-year-old man. Before surgery the left ventricular dP/dt was 32 mmHg per 0.023 s = 1391 mmHg/s.

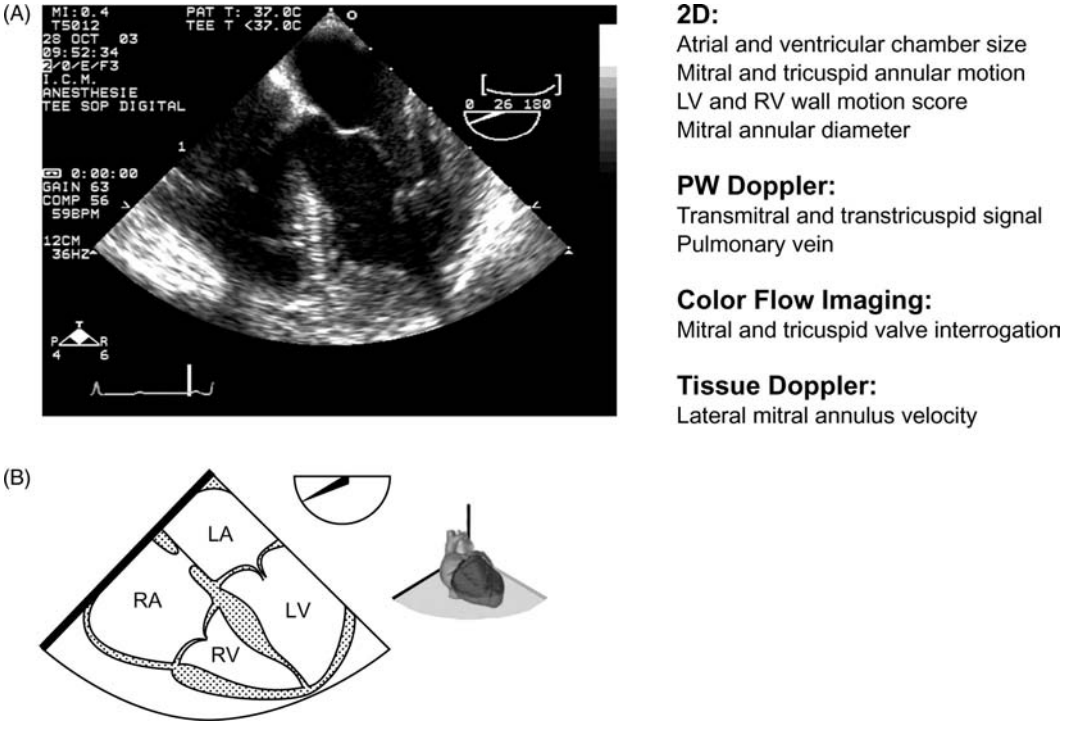

Figure 9.15 Biventricular function evaluation. Using a mid-esophageal four-chamber view, right and left atrial and ventricular dimensions are evaluated as well as regional contractility and mitral annular motion. Volumetric stroke volume through the mitral valve is measured with the mitral annulus diameter and modal time-velocity integral of pulsed-wave Doppler of mitral inflow at the annulus level. Both the transmitral and transtricuspid pulsed-wave Doppler inflow signal correct alignment for Doppler measurement should be verified by color flow imaging. The lateral mitral annular plane is evaluated with tissue Doppler and with left-sided rotation and pull-back. The left upper pulmonary vein can also be interrogated (LA, left atrium; LV, left ventricle; RA, right atrium; RV, right ventricle).

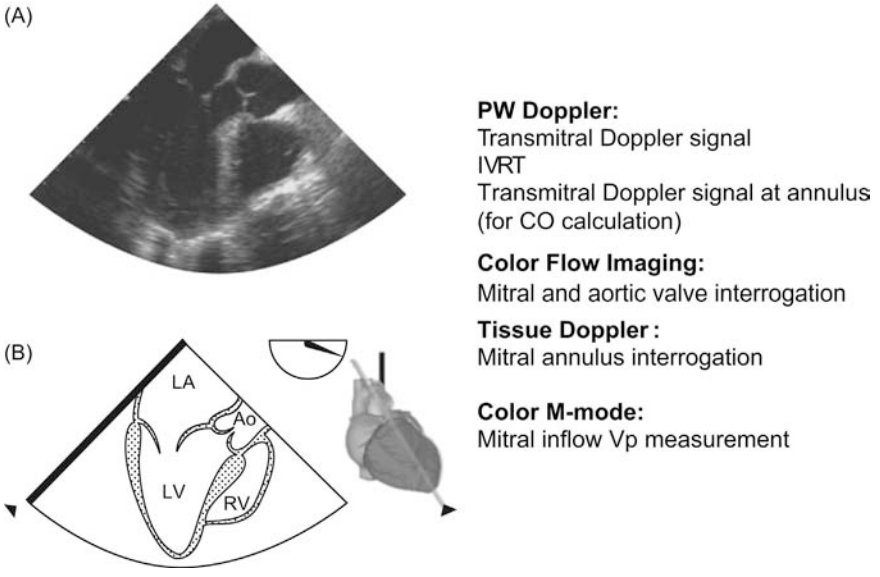

Figure 9.16 Mid-esophageal view at 130° is ideal to quickly screen for both mitral and aortic regurgitation with color Doppler. The transmitral pulsed-wave Doppler signal is often of higher quality than at 0°. Isovolumic relaxation time (IVRT), tissue Doppler interrogation of the mitral annulus and color M-mode velocity of propagation (*Vp*) are easily obtained. Cardiac output (CO) of the left ventricle (LV) can be obtained using mitral annulus diameter and pulsed-wave (PW) Doppler interrogation of the mitral valve at the same level (Ao, aorta; LA, left atrium; RV, right ventricle).

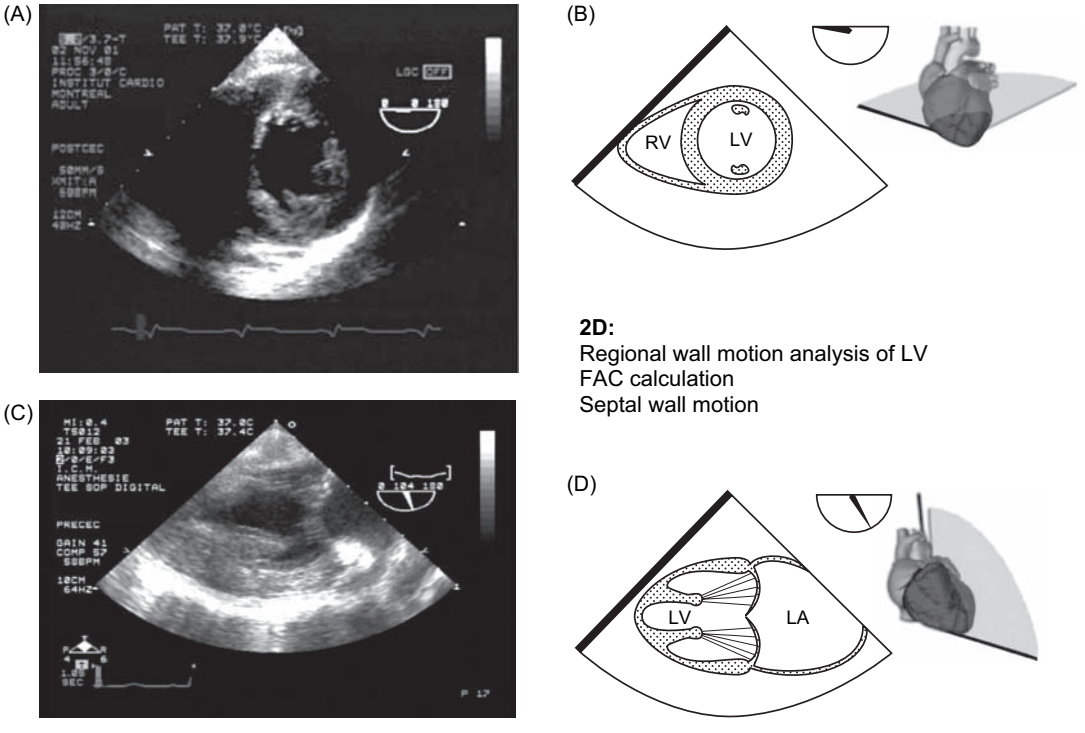

Figure 9.17 Evaluation of systolic function of the left ventricle (LV). (A, B) The mid-papillary short-axis view is obtained for the fractional area change (FAC) calculation and wall motion score of the LV. Attention is paid to septal wall motion which can be altered with right ventricular dysfunction. (C, D) A 90° view is obtained to ensure that the mid-papillary view is perpendicular to the ventricular axis and to complete the basal and apical wall motion score evaluation of the four-chamber (LA, left atrium; RV, right ventricle).

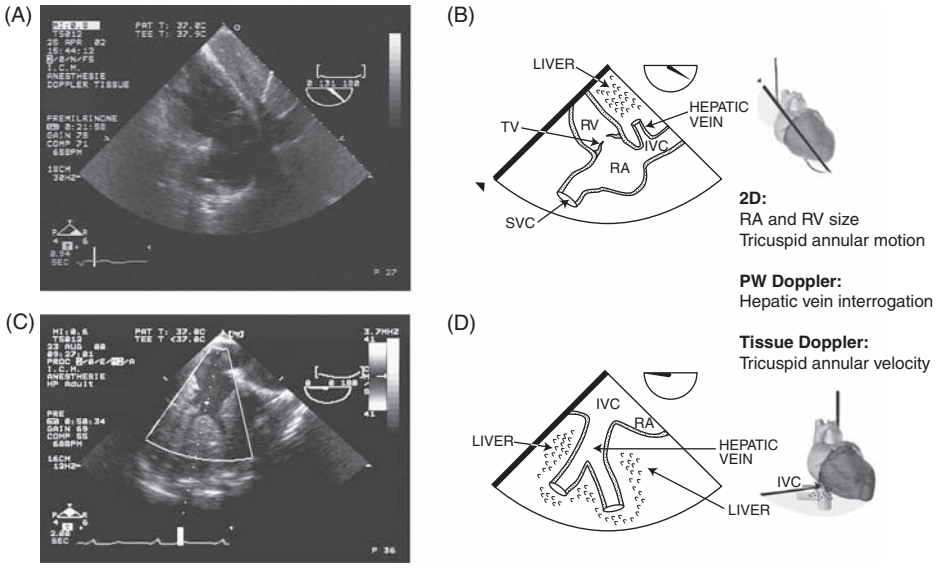

Figure 9.18 Evaluation of systolic and diastolic function of the right ventricle (RV). (A, B) Transgastric right ventricular long axis. Right chamber size is evaluated. Pulsed-wave (PW) Doppler interrogation of the hepatic vein and tissue Doppler evaluation of the tricuspid annulus. (C, D) Alternative deep esophageal 0° position with rightward rotation to perform PW Doppler interrogation of the hepatic vein (IVC, inferior vena cava; RA, right atrium; SVC, superior vena cava; TV, tricuspid valve).

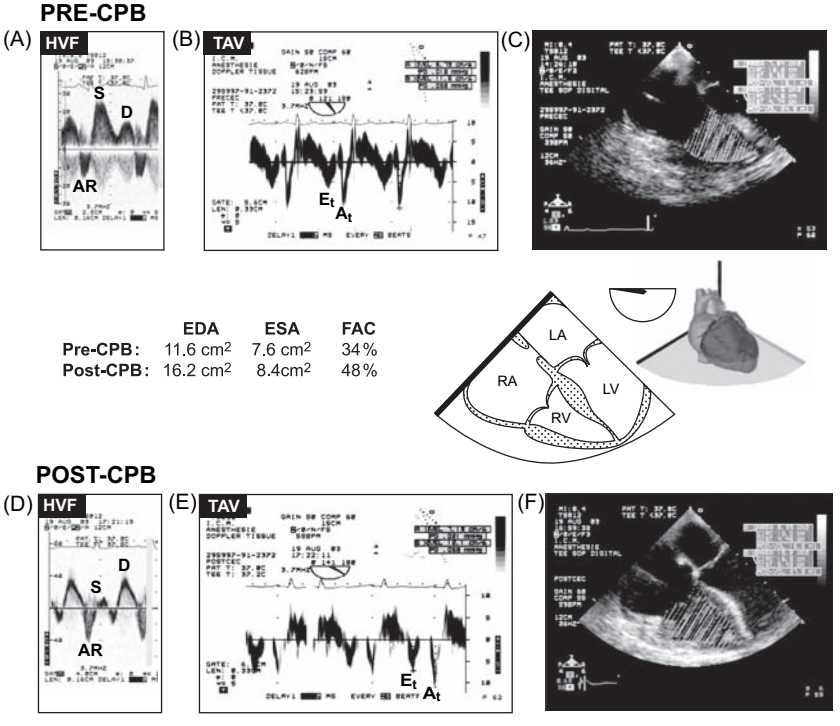

Figure 9.19 Systolic and diastolic function of the right ventricle (RV) in a 65-year-old man with previous inferior myocardial infarction scheduled for coronary revascularization. (A–C) Before cardiopulmonary bypass (CPB): the ejection fraction of the left ventricle (LV) is 20% with a low cardiac index of 1.5 L/min per m^2. (A) Pulsed-wave Doppler hepatic venous flow (HVF) shows systolic flow S predominance. (B) Tissue Doppler of tricuspid annular velocities (TAV) shows a E_t/A_t ratio <1 ($E_t = 5.7$ and $A_t = 11.5$ cm/sec). Both suggest mild diastolic dysfunction of the RV. (C) The fractional area change (FAC) of the RV is 34%. (D–F) Post-CPB. (D) The HVF showed new blunting of the systolic flow S. (E) The TAV are increased with a similar ratio ($E_t = 7.1$ and $A_t = 12.1$ cm/sec). This suggests decreased RV compliance. (F) Right ventricular FAC increased to 48% consistent with the surgeon's visual appreciation of improved right ventricular function. Upon arrival to the intensive care unit, the cardiac index was 3.0 L/min per m^2 (AR, atrial reversal; EDA, end-diastolic area; ESA, end-systolic area; LA, left atrium; RA, right atrium).

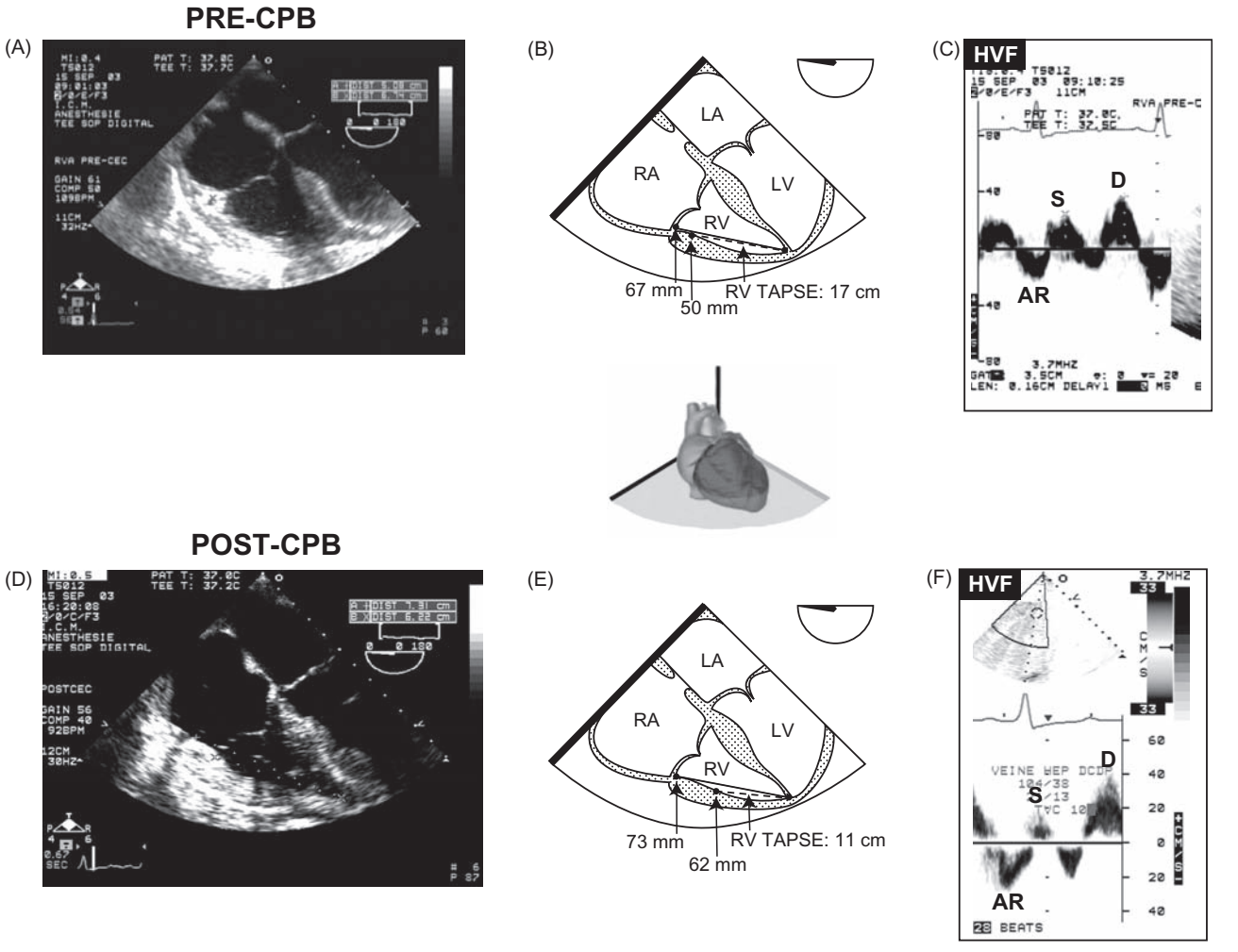

Figure 9.20 Evaluation of right ventricular systolic function. (A, B) Tricuspid annular plane systolic excursion (TAPSE) was 17 mm/67 mm (25%) before cardiopulmonary bypass (CPB). (C) Hepatic venous flow (HVF) was abnormal before CPB with systolic attenuation. (D, E) After CPB, TAPSE was 11 mm/73 mm (15%). (F) Systolic attenuation was more pronounced post-CPB (AR, atrial reversal; LA, left atrium; LV, left ventricle; RA, right atrium; RV, right ventricle; TV, tricuspid valve).

are RV and RA dilatation, reverse convexity of the atrial septum towards the LA, right to left shunting through a patent foramen ovale, reduction in annular tricuspid displacement (37), and abnormal Doppler profile of the hepatic veins (38,39). Right ventricular dilatation is considered mild, moderate, or severe when the RVEDA measured from a four-chamber view is smaller, equal or greater than LVEDA. The right ventricular area, calculation of right ventricular FAC (Fig. 9.19) and tricuspid annular motion (Fig. 9.20) (40) can be obtained using a four-chamber view (33). With right ventricular volume overload, the RV will be dilated and the ventricular septum, normally convex towards the RV, will be flattened or even convex towards the LV during diastole only (Fig. 9.21), with associated paradoxical motion during systole. With right ventricular pressure overload, flattening of the ventricular septum occurs during both systole and diastole.

V. ABNORMAL DIASTOLIC FUNCTION

A. Left Ventricular Diastolic Dysfunction

Diastolic function should be an integral part of the evaluation of cardiac function. Indeed, left ventricular diastolic dysfunction is a predictor of difficult weaning from bypass as good as systolic dysfunction (41). Diastolic dysfunction can be isolated or associated with systolic dysfunction or pericardial disease. Echocardiographically, left ventricular diastolic dysfunction has been classified as mild (impaired left ventricular relaxation), moderate (pseudonormal pattern) and severe (left ventricular restrictive filling) with increasing left ventricular filling pressures. We use a combination of Doppler-derived variables in the diagnosis of left ventricular diastolic dysfunction (Fig. 9.22) and a diagnostic algorithm (Fig. 9.23) (42).

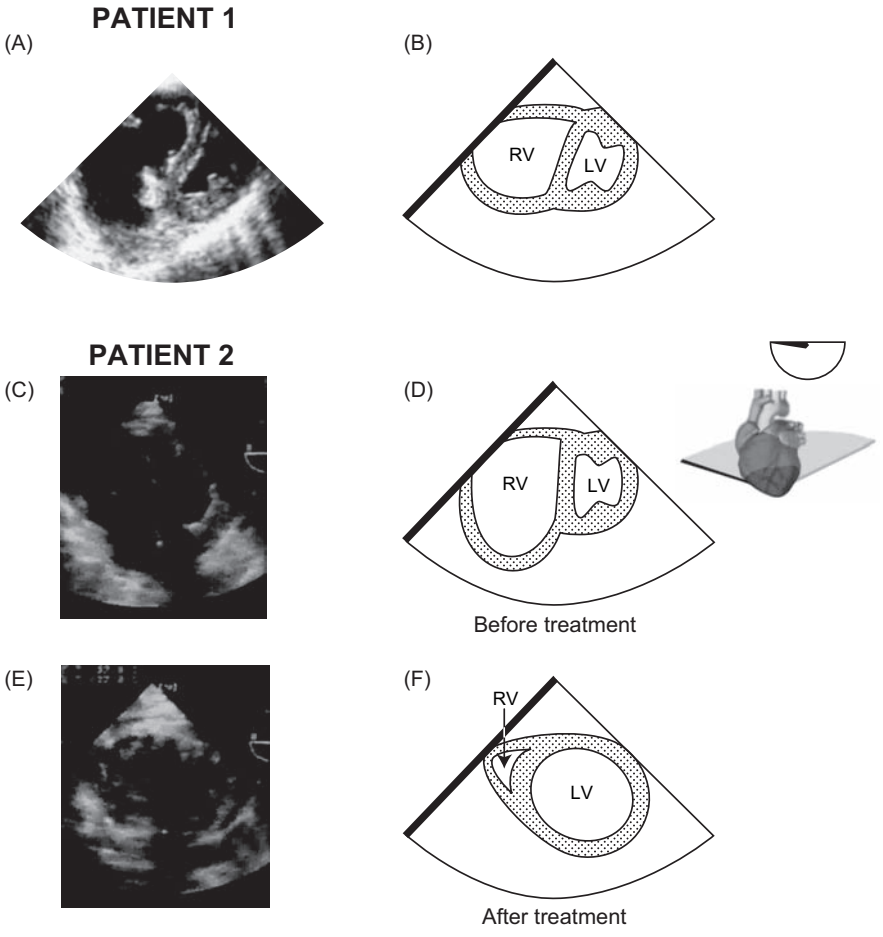

Figure 9.21 Systolic dysfunction of the right ventricle (RV) in two different patients. (A, B) Transgastric view of a 50-year-old woman with severe pulmonary hypertension associated with scleroderma. The RV is dilated with a D-shaped left ventricle (LV) and systolic septal flattening. (C–F) Right ventricular dysfunction from fluid overload in another patient before (C, D) and after (E, F) vasodilator therapy. Note the reduction in right ventricular size and change in septal curvature after treatment.

Diastolic dysfunction alters the pressure volume relationship [Figs. 9.4(D–F)] and could explain some of the observed changes in this relationship between filling pressure and ventricular volume observed after cardiopulmonary bypass (CPB) (Fig. 9.3). Impaired or delayed relaxation (mild diastolic dysfunction) results in decreased left ventricular pressure decay during diastole and prolonged isovolumic relaxation time (IVRT). This will be reflected with higher diastolic filling pressure for the same left ventricular volume [Fig. 9.4(D)]. Echocardiographic evaluation of abnormal relaxation using PW Doppler interrogation of the MV will demonstrate prolonged IVRT, prolonged E-wave deceleration time, and a reduction of the E/A ratio. The pulmonary vein PW Doppler signal will show an increased S/D ratio. Tissue Doppler of the mitral annulus will demonstrate an E_m/A_m ratio <1 while on color M-mode, V_p will be decreased (Fig. 9.24). The delayed relaxation abnormality is the most common form of diastolic dysfunction (70% in our practice) and is the most sensitive manifestation of myocardial ischemia. It is commonly associated with left ventricular hypertrophy either due to hypertension or aortic stenosis (AS).

Left ventricular restrictive filling abnormality represents a more severe degree of diastolic dysfunction. This is associated with an upward shift of the diastolic pressure–volume curve [Fig. 9.4(F)]. In these patients the following echocardiographic findings are observed: PW Doppler of the mitral inflow reveals shortened IVRT and E-wave deceleration time, a high E/A ratio >2; PW Doppler interrogation of the pulmonary vein shows predominant diastolic flow while tissue Doppler imaging of the mitral annulus demonstrates reduced E_m velocity, and color M-mode propagation velocity will be decreased. This type of abnormality is commonly seen in hemodynamically unstable patients before or after cardiac surgery (Fig. 9.25).

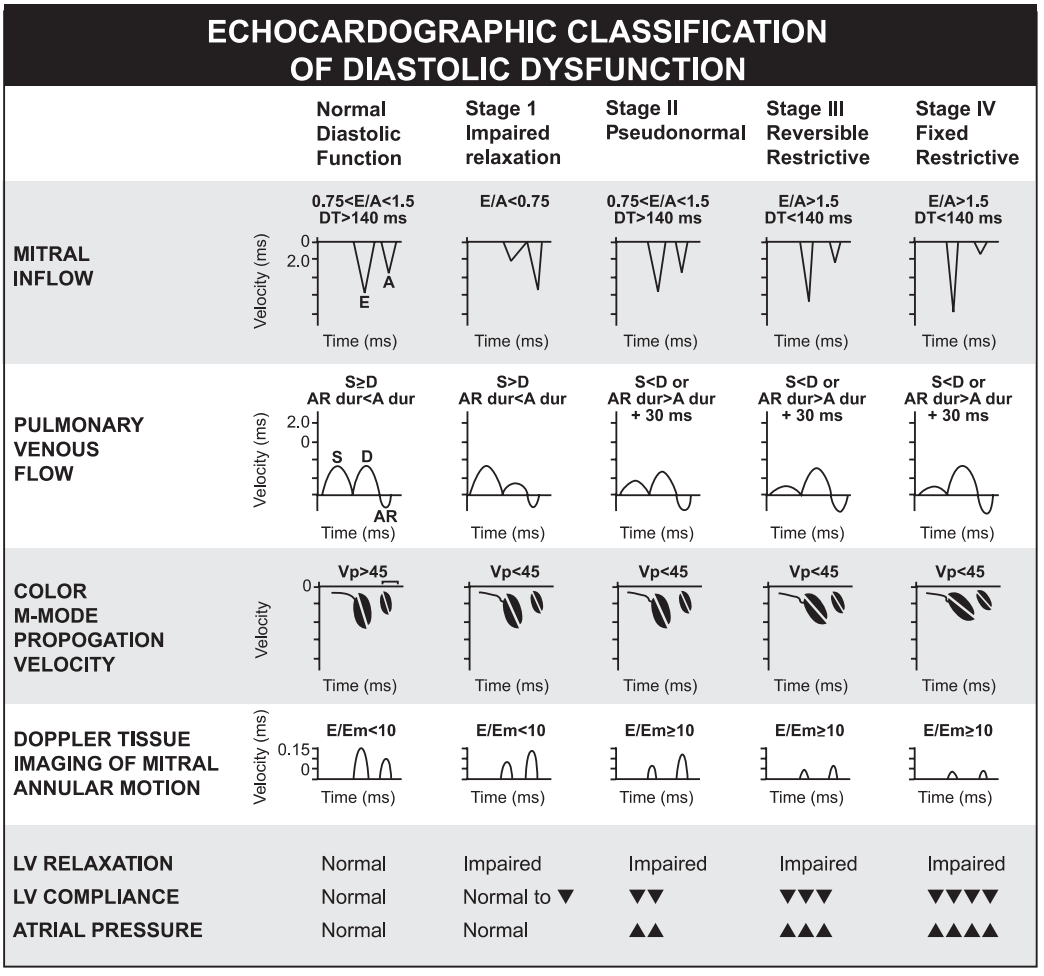

Figure 9.22 Echocardiographic classification of diastolic dysfunction adapted for transesophageal echocardiography (A, peak late diastolic transmitral flow velocity; A dur, duration of mitral inflow A-wave; AR dur, peak pulmonary venous atrial reversal flow velocity duration; D, peak diastolic pulmonary venous flow velocity; DT, deceleration time; E, peak early diastolic transmitral flow velocity; Em, peak early diastolic myocardial velocity; LV, left ventricular; S, peak systolic pulmonary venous flow velocity; V_p, flow propagation velocity). Adapted for TEE. [With permission of Khouri et al. (42).]

Finally, in patients with relaxation abnormalities and increased filling pressure, a moderate or intermediate form of diastolic dysfunction called the pseudonormal pattern is seen. The expression pseudonormal is a consequence of the normal looking PW Doppler mitral inflow signal while the PVF pattern is clearly abnormal ($S/D < 1$). With a pseudonormal pattern, the pressure–volume diagram will demonstrate moderate upward elevation of the diastolic waveform [Fig. 9.4(E)]. Echocardiographically, it is characterized by reduced IVRT, a "pseudo" normal E/A ratio and deceleration time, PVF with inverted S/D ratio <1 and atrial reversal wave velocity exceeding 40 cm/sec, abnormal tissue Doppler of the mitral annulus with a reduced E_m/A_m ratio and abnormally low color M-mode propagation velocity (Fig. 9.26) (42).

These abnormalities represent a spectrum of disease severity ranging from the milder form of diastolic dysfunction, shown by impaired relaxation abnormalities, to the more severe form such as the restrictive filling pattern. In the perioperative monitoring of cardiac function, particularly in the post-bypass setting, we commonly observe changes in diastolic function irrespective of those in systolic function. Worsening of diastolic function tends to correlate with subsequent deterioration of the hemodynamic function (Fig. 9.26). Diastolic dysfunction can occur in conditions other than those previously described such as the brain–heart syndrome secondary to high-grade subarachnoid hemorrhage (Fig. 9.27).

B. Right Ventricular Diastolic Dysfunction

Right ventricular dysfunction in patients undergoing cardiac surgery is also associated with difficult weaning from CPB bypass and hemodynamic instability (30).

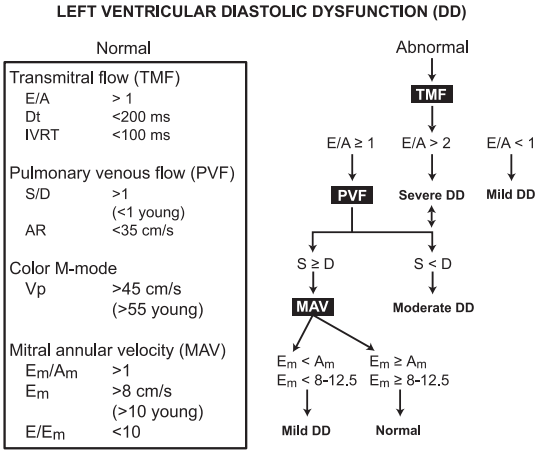

Figure 9.23 Suggested algorithm used in the diagnosis and classification of left ventricular diastolic dysfunction (DD). Diastolic function is classified using pulsed-wave Doppler of transmitral flow (TMF), pulmonary venous flow (PVF) and tissue Doppler examination of mitral annular velocity (MAV). Mild, moderate, and severe DD corresponds to stages I, II, and III. Stage IV corresponds to a fixed restrictive filling pattern. Patients with pacemaker, atrial fibrillation, non-sinus rhythm, moderate to severe mitral regurgitation, those undergoing mitral valve surgery, or with aortic insufficiency are excluded from analysis (AR, atrial reversal; Dt, deceleration time; IVRT, isovolumic relaxation time; V_p, velocity of propagation).

Pulsed-wave Doppler interrogation of the tricuspid valve (TV) inflow (43), hepatic veins (38), and tissue Doppler of the tricuspid annulus (44) (Figs. 9.15 and 9.18) allow assessment of right ventricular diastolic function. An algorithm in the diagnosis of right ventricular diastolic dysfunction is used in our practice (Fig. 9.28). When invasive hemodynamic tracings are available through a pulmonary artery catheter, we have also observed a correlation between the right ventricular diastolic pressure tracing and right ventricular diastolic dysfunction (Figs. 9.29 and 9.30). Examples of right ventricular diastolic dysfunction are shown in Figs. 9.31–9.33. The measurements needed for the evaluation of right ventricular diastolic dysfunction are shown in Figs. 9.15 and 9.18. Using Doppler to evaluate right-sided velocities, it is important to consider the fact that they are associated with a normal 20% respiratory change (see Chapter 13).

VI. CAUSES OF SEVERE HYPOTENSION AND SPECIFIC HEMODYNAMIC DERANGEMENTS

In the hemodynamically unstable patient, Costachescu et al. (30) observed that hypotension may be secondary to several simultaneous factors, all related to problems

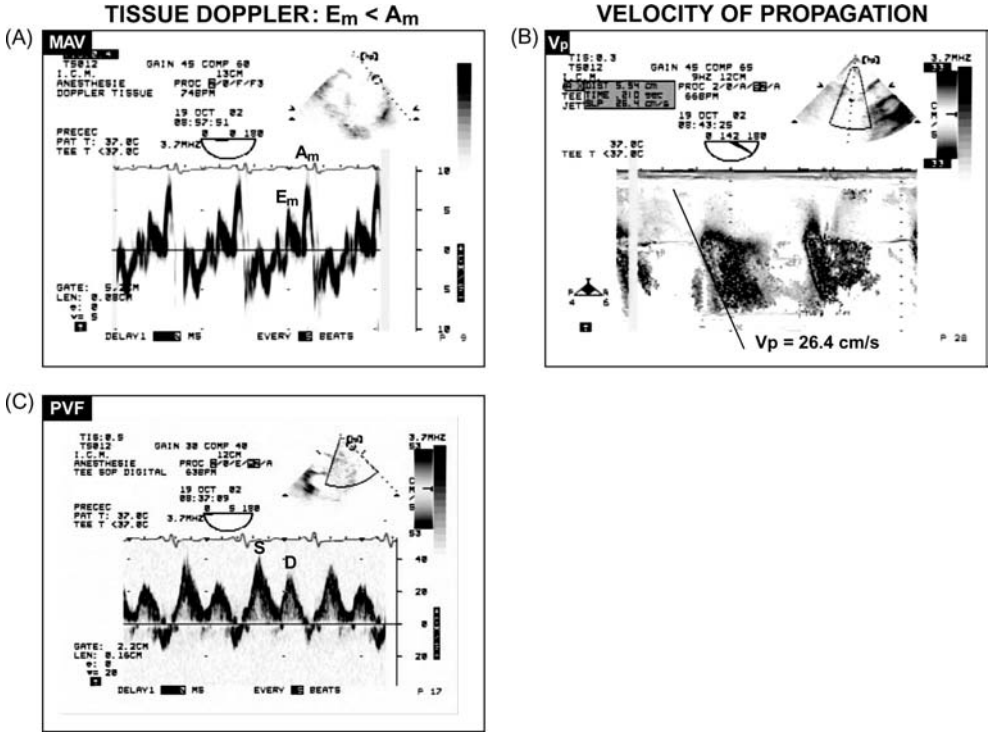

Figure 9.24 Stage 1 diastolic dysfunction (impaired relaxation) in a 72-year-old woman undergoing coronary revascularisation before cardiopulmonary bypass. (A) Tissue Doppler of the lateral mitral annular velocity (MAV): the E_m/A_m ratio is <1. (B) On color M-mode, the propagation velocity (Vp) of the E-wave is 26.4 cm/sec. (C) The pulmonary venous flow (PVF) reveals normal S > D waves.

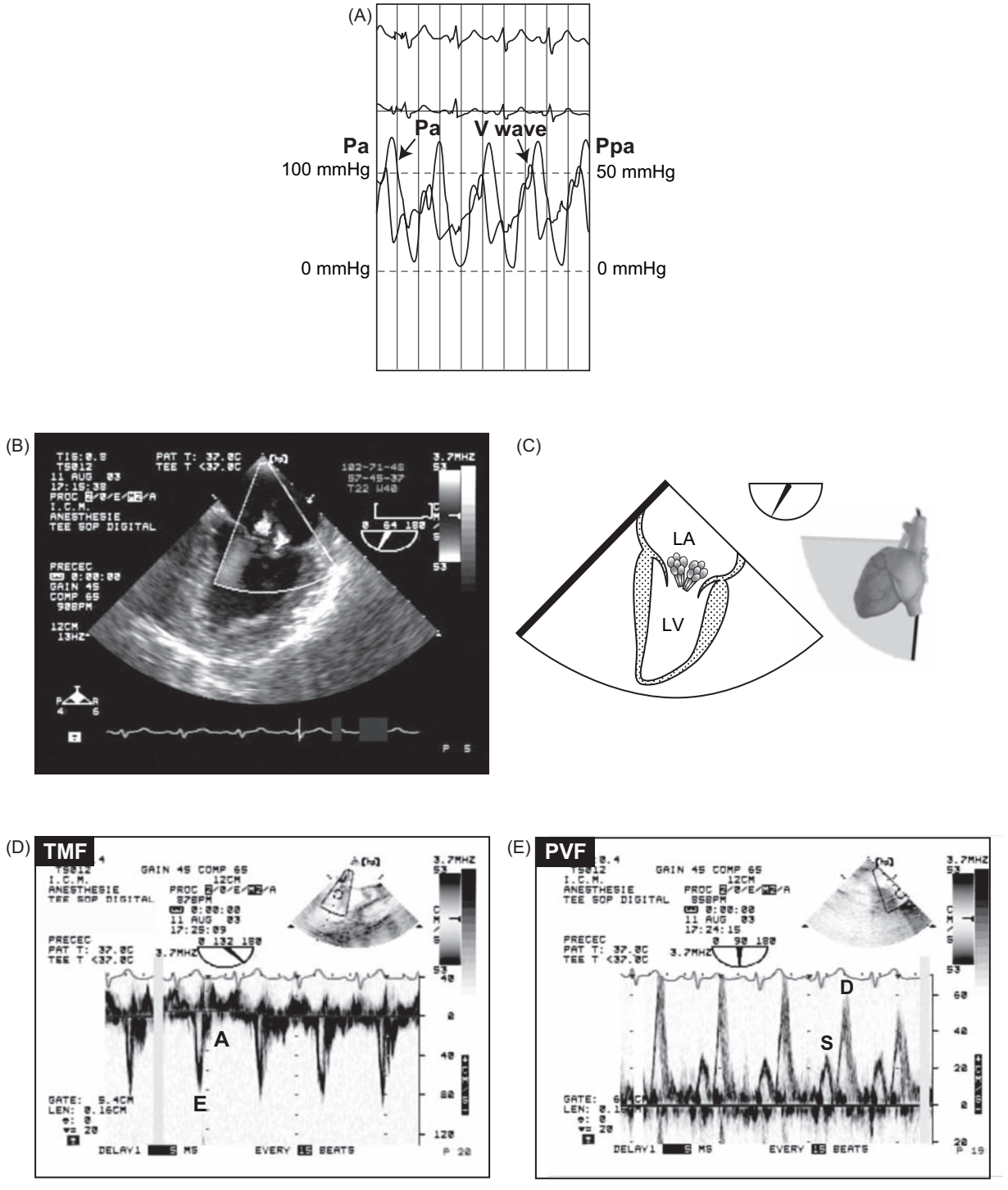

Figure 9.25 Stage III left ventricular diastolic dysfunction (restrictive filling) in a 61-year-old woman with cardiogenic shock brought to the Operating Room for emergency coronary revascularisation. (A) She was hemodynamically unstable on an intra-aortic balloon pump and vasoactive support. A 50 mmHg "V" wave on the wedged pulmonary artery catheter tracing was seen without any significant mitral regurgitation on color flow imaging (B, C). (D) The transmitral flow (TMF) showed an E/A ratio >2 with a deceleration time <60 ms and isovolumic relaxation time of 40 ms. (E) The left upper pulmonary venous flow (PVF) showed an abnormal S/D ratio with S wave blunting (LA, left atrium; LV, left ventricle; Pa, arterial pressure on the 0–100 mmHg left-sided scale, Ppa, pulmonary arterial pressure on the 0–50 mmHg right-sided scale).

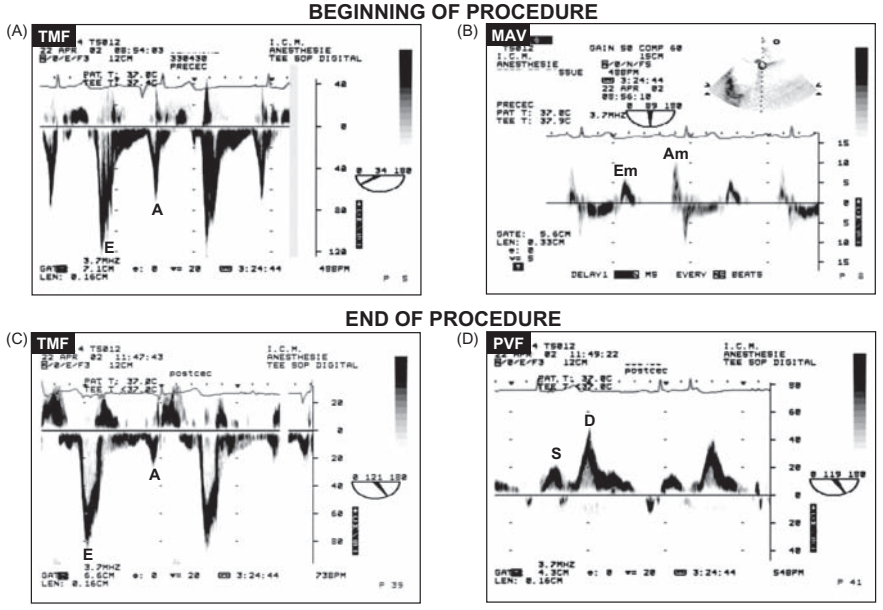

Figure 9.26 Left ventricular diastolic dysfunction in a 73-year-old woman during off-pump bypass surgery. (A, B) At the beginning of the procedure, the transmitral flow (TMF) demonstrates a E/A ratio >1 with a tissue Doppler E_m/A_m ratio <1 (B) consistent with at least moderate diastolic dysfunction (pseudonormal pattern). (C, D) Following revascularization, a higher E/A ratio with left upper pulmonary venous flow (PVF) blunted S-wave suggests worsening diastolic function and higher operating filling pressures. This was associated with significant hemodynamic instability requiring vasoactive support (MAV, mitral annular velocity).

with preload, afterload, contractility and diastolic function rarely acting alone and often in different combinations. Etiologies of hypotension can be grouped according to their mechanism (45). Reduced left ventricular preload can result from hypovolemia, reduced systemic vascular resistance or venous tone, tamponade (see Chapter 11) and decreased right ventricular CO. Increases in left and right ventricular afterload leading to hypotension include left and right ventricular outflow tract obstruction. Reduced contractility and diastolic dysfunction can be

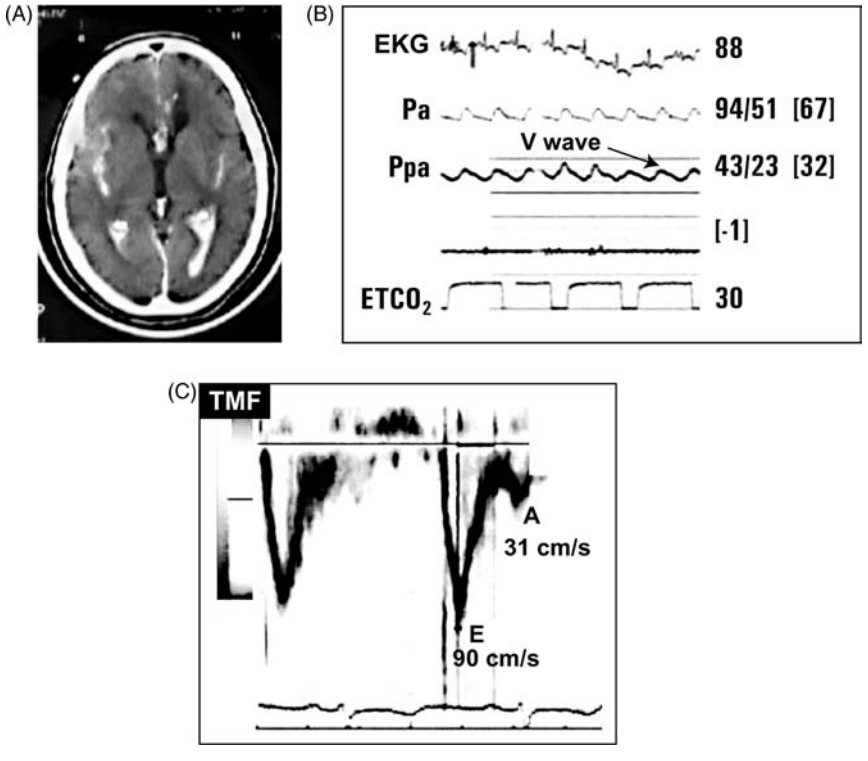

Figure 9.27 Left ventricular diastolic dysfunction in a 37-year-old woman with subarachnoid haemorrhage and brain–heart syndrome associated with hemodynamic instability. (A) The patient's head computed tomography scan showed intraventricular bleeding. (B) The hemodynamic tracing shows a heart rate of 88 beats/min, systolic, and diastolic arterial pressure (Pa) of 94 and 51 mmHg, systolic, and diastolic pulmonary artery pressure (Ppa) of 43 and 23 mmHg with a prominent "V" wave appearing on the wedged tracing without significant mitral regurgitation on color Doppler (not shown). (C) Transmitral flow (TMF) reveals a high E/A ratio (EKG, electrocardiogram; $ETCO_2$, end-tidal carbon dioxide) (Courtesy of Dr. Nancy McLaughlin).

secondary to ischemia. Finally valvular abnormalities (see Chapters 15 and 17) and acquired septal defects (see Chapter 8) are other causes of hypotension. The role of TEE is to assess all potential causes of hypotension and to determine which mechanisms are involved. Some of these conditions will be discussed.

A. Myocardial Ischemia

Myocardial ischemia is the most common cause of hemodynamic instability and is discussed in Chapter 8.

B. Left Ventricular Outflow Tract Obstruction

Left ventricular outflow tract obstruction is a well-known complication of MV repair (46) with or without asymmetric left ventricular hypertrophy (Chapter 10) (47), but is also increasingly recognized in conditions associated with severe preload reduction without significant cardiac disease (Fig. 9.10). The presence of LVOT obstruction has been reported in 5–10% of hemodynamically unstable patients in the intensive care unit (ICU) (48–50). The pressure–volume relationship associated with LVOT obstruction shows the effect of an increased afterload [Fig. 9.4(B)]. In patients with LVOT obstruction, the anterior MV leaflet is displaced into the outflow tract and is associated with MV regurgitation. Distinguishing LVOT obstruction from pure MR as a cause of hemodynamic instability associated with a "v" wave is critical as the treatment of those two conditions is quite different: afterload reduction, inotropic support, and increase in heart rate are recommended for MR but would be deleterious for LVOT obstruction. This abnormality has been observed not only after MV repair but also following AoV replacement (Fig. 9.34). In the operating room (OR) and in the ICU, LVOT obstruction in patients with left ventricular hypertrophy and hypovolemia can also

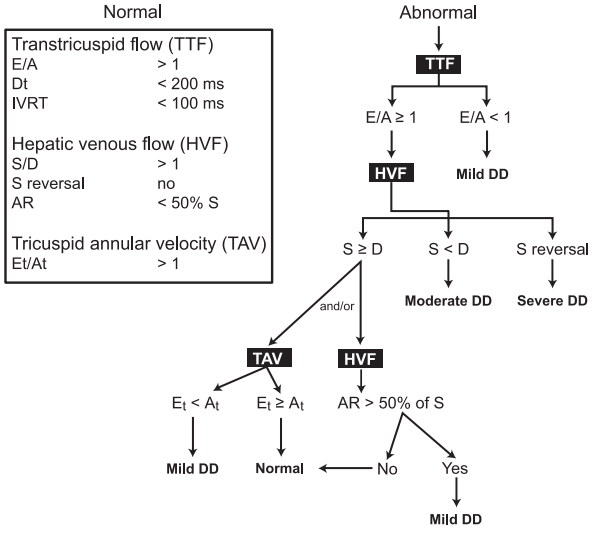

Figure 9.28 Suggested algorithm used in the diagnosis and classification of right ventricular diastolic dysfunction (DD). Diastolic function is classified using pulsed-wave Doppler of transtricuspid flow (TTF), hepatic venous flow (HVF) and tissue Doppler imaging of the tricuspid annulus or tricuspid annular velocity (TAV). Patients with pacemaker, atrial fibrillation, non-sinus rhythm, moderate to severe tricuspid regurgitation, and following tricuspid annuloplasty are excluded from analysis (AR, atrial reversal; Dt, deceleration time; IVRT, isovolumic relaxation time).

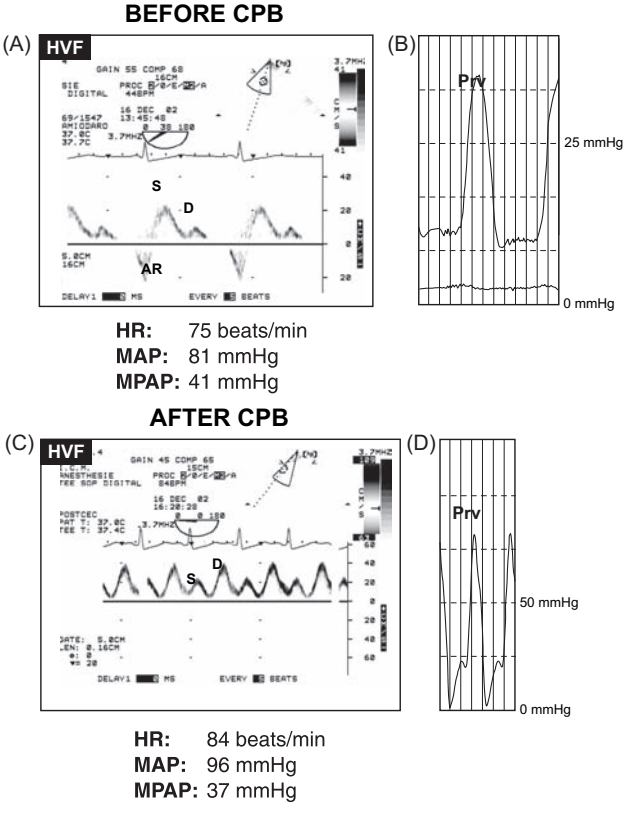

Figure 9.29 Right ventricular diastolic dysfunction in a 56-year-old man who is scheduled for aortic valve replacement. (A) The Doppler hepatic venous flow (HVF) before cardiopulmonary bypass (CPB) showed a normal S/D ratio > 1 but with an increased atrial reversal (AR) wave. (B) He had a normal right ventricular pressure (Prv) waveform despite preoperative pulmonary hypertension with a mean pulmonary artery pressure (MPAP) of 41 mmHg. (C) After CPB, the S/D ratio is <1 with predominant D-wave. (D) This was associated with a change in the slope of the Prv in diastole from a flat to a steep diastolic waveform. Weaning from CPB was difficult requiring 17.5 μg/min of noradrenaline and 0.4 μg/kg per min of nitroglycerine. The abnormal right ventricular filling can be appreciated visually (HR, heart rate; MAP, mean arterial pressure).

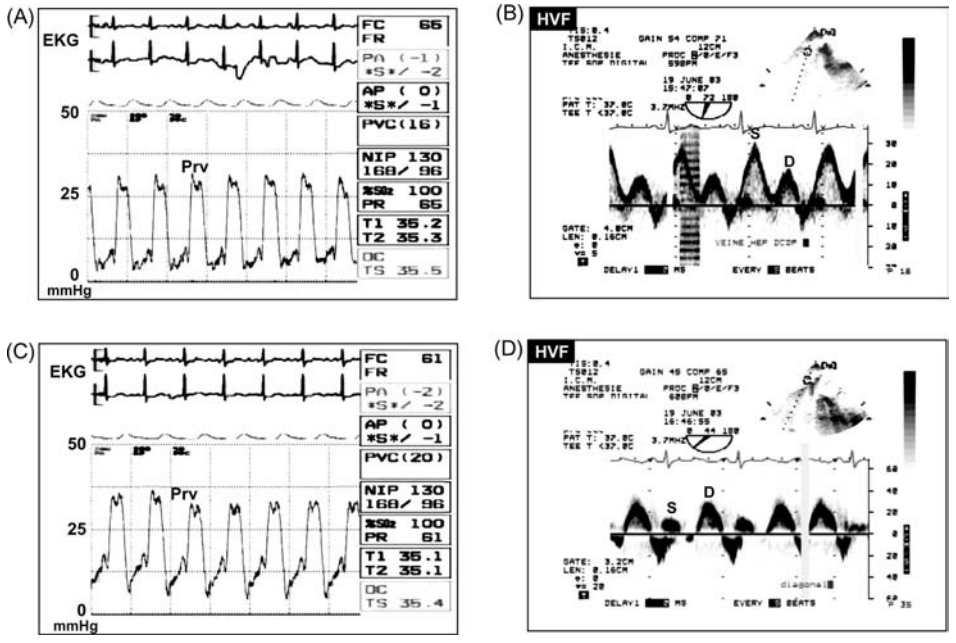

Figure 9.30 Right ventricular diastolic dysfunction during off-pump bypass surgery in a 67-year-old man. (A, B) Baseline: right ventricular pressure (Prv) tracing and hepatic venous flow (HVF) profile. The S/D ratio is >1. (C, D) Hemodynamic instability during clamping of the left diagonal coronary artery. The Prv becomes increasingly steeper in diastole. The S/D ratio is inverted. (EKG, electrocardiogram).

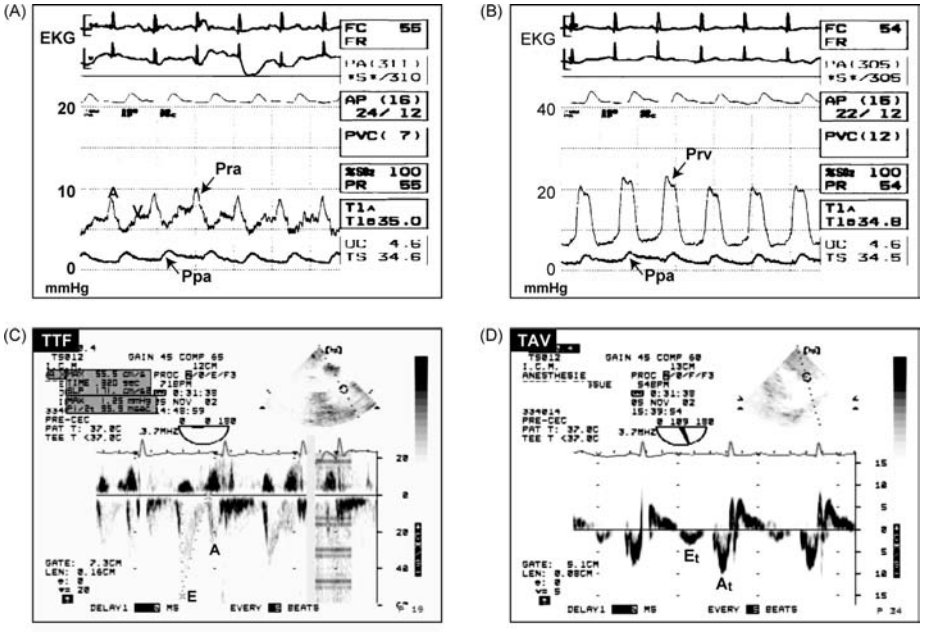

Figure 9.31 Mild right ventricular diastolic dysfunction in a 70-year-old man before cardiac revascularization. (A) On the pressure tracing, the right atrial pressure (Pra) waveform shows a predominant "A" wave. (B) The right ventricular pressure (Prv) tracing shows a normal relatively flat diastolic waveform. (C) The pulsed-wave Doppler transtricuspid flow (TTF) tracing shows a predominant E-wave with a prolonged deceleration time (320 ms). (D) The tricuspid annular velocities (TAV) present an E_t/A_t ratio consistent with mild right ventricular diastolic dysfunction. The hepatic venous flow was normal (not shown). The atrial kick can be seen on the beating heart. The Pra, Prv, and pulmonary artery pressure (Ppa) are on a 0–20, 0–40, and 0–200 mmHg scale respectively (EKG, electrocardiogram).

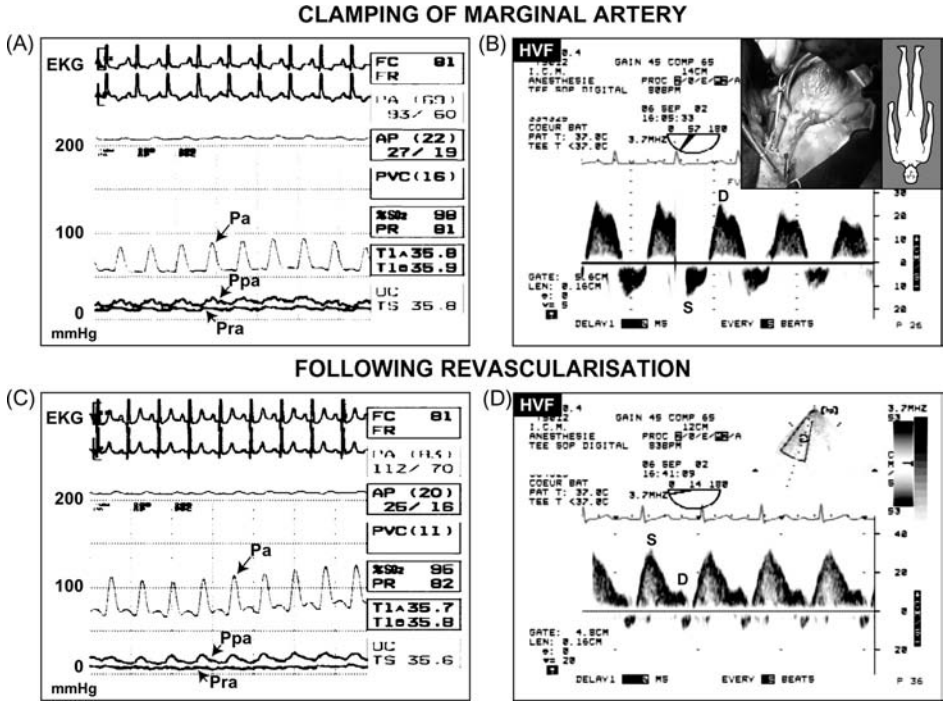

Figure 9.32 Transient severe right ventricular diastolic dysfunction in a 72-year-old patient undergoing off-pump bypass surgery. During clamping of the left obtuse marginal artery, the patient became hemodynamically unstable. (A) This was associated with a reduction in systolic and diastolic systemic arterial blood pressure (Pa) down to 93/60 mmHg, a slight increase in systolic and diastolic pulmonary artery pressure (Ppa) of 27/19 mm Hg and an increase in right atrial pressure (Pra) of 16 mmHg. (B) Systolic flow reversal in the hepatic venous flow (HVF) was present. (C, D) These abnormalities normalized after revascularization was completed. (Photo in B courtesy of Dr. Raymond Cartier).

occur (Fig. 9.10). Left ventricular outflow tract obstruction has also been reported with apical myocardial infarction (51), with the use of intra-aortic balloon counterpulsation (52), with MV prolapse and during lung transplantation (53).

C. Right Ventricular Outflow Tract Obstruction

Right ventricular outflow tract (RVOT) obstruction can be extrinsic or intrinsic. Extrinsic compression can occur for instance from an aortic (54) or pulmonary artery aneurysm (55), mediastinal hematoma (56), or from direct surgical compression during off-pump surgery. Intrinsic compression can be seen in congenital heart disease (57), congenital surgery (58), septal patch repair (59), and lung transplantation. It is typically classified as subvalvular, valvular, or supravalvular. The dynamic form of RVOT obstruction occurs in a setting of reduced preload and hypertrophied RV, exacerbated by inotropic drugs (60). It has been observed in biventricular hypertrophic cardiomyopathy (61) and after lung transplantation (62). The diagnosis can be established by right ventricular catheterization and by TEE (62) (Figs. 9.35–9.37).

D. Mitral Valve Fluttering from Aortic Regurgitation

During diastole, the presence of a significant aortic regurgitant jet may interfere with the full opening of the MV anterior leaflet and cause diastolic high-frequency fluttering best demonstrated by M-mode. This may be secondary to a severe jet of aortic regurgitation (AR), or with milder jets eccentrically directed towards the base of the anterior mitral leaflet. In the presence of severe AR, it will be associated with premature closure of the MV. It will not be observed if the leaflet is sclerotic and rigid or if the regurgitant jet is directed towards the ventricular septum (63) (Fig. 9.38) (see Chapter 15).

E. Midsystolic Pulmonary Valve Closure in Pulmonary Hypertension

The presence of a mid-systolic decrease or a notch in Doppler flow or using M-mode through the pulmonary valve is a useful sign indicative of severe pulmonary hypertension (Fig. 9.39). It is thought to be secondary to the reflected wave due to elevated distal pulmonary artery pressure and vascular resistance (64). However, it

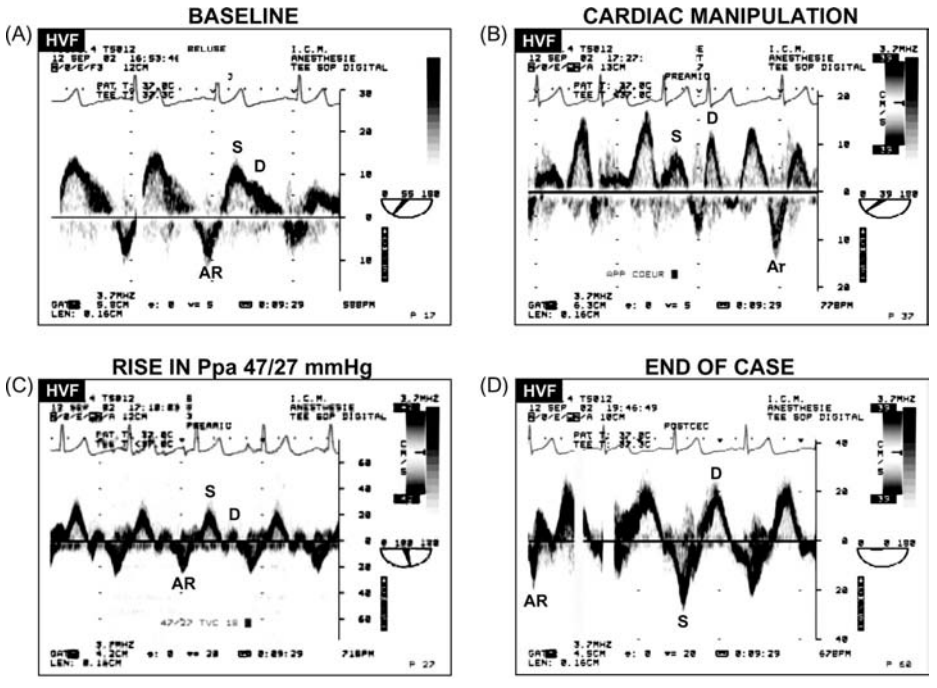

Figure 9.33 Worsening right ventricular diastolic function during mitral valve repair in a 69-year-old man. (A) The hepatic venous flow (HVF) S/D ratio is normal with increased atrial reversal (AR) velocities. (B) During manual cardiac manipulations of the heart, the S velocity is reduced. (C) With further elevation of the pulmonary pressure (Ppa) to 47/27, the AR velocity increases in relation to the S-wave. (D) Finally at the end of the procedure, systolic flow reversal is observed.

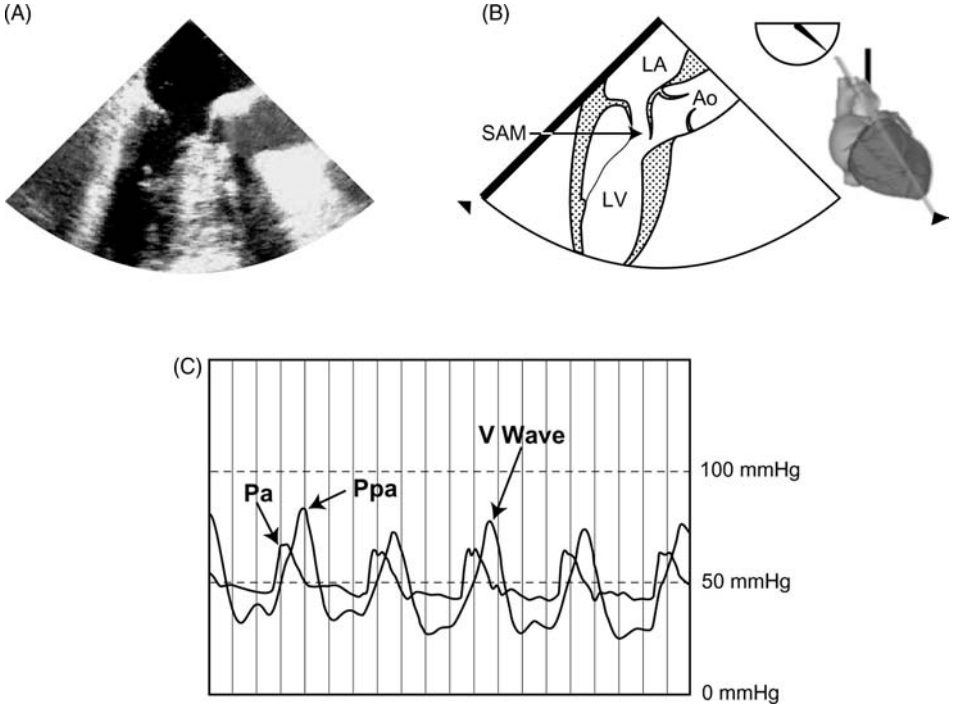

Figure 9.34 Left ventricular outflow tract obstruction in a 53-year-old man after aortic valve replacement. (A, B) The mid-esophageal long-axis view showed the LVOT obstruction secondary to left ventricular septal hypertrophy. (C) Systemic hypotension was associated with the appearance of a giant "V" wave on the wedged pulmonary artery pressure (Ppa) tracing occurred as the patient was weaned from cardiopulmonary bypass. The "V" wave was secondary to mitral valve regurgitation from abnormal systolic anterior motion (SAM). This patient did not respond to medical therapy and underwent mitral valve replacement (Ao, aorta; LA, left atrium; LV, left ventricle; Pa, arterial pressure).

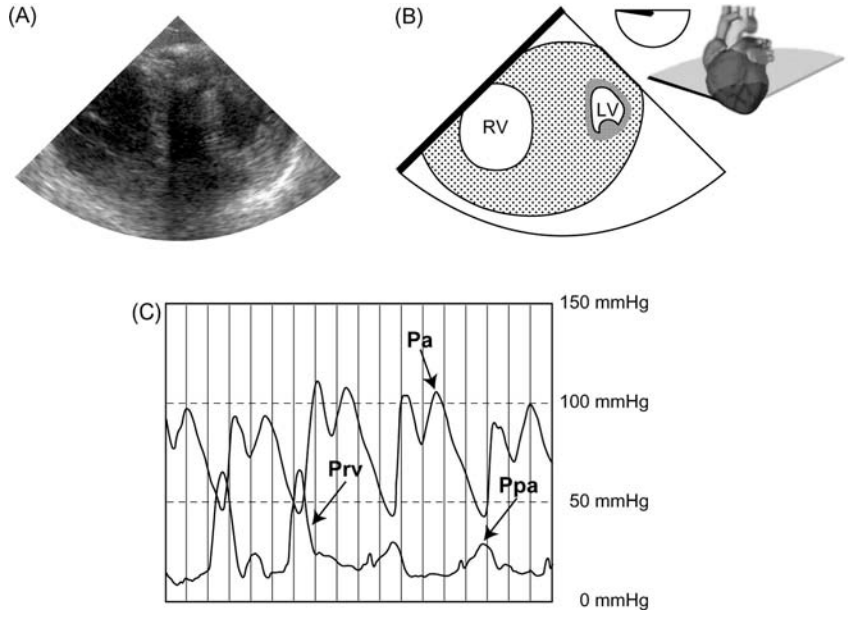

Figure 9.35 Right ventricular outflow tract obstruction in a 75-year-old man after coronary revascularization and aortic valve replacement. The procedure was complicated by two failed attempt of weaning from cardiopulmonary bypass requiring intra-aortic balloon counterpulsation. (A, B) Transgastric mid-papillary short-axis view revealed a dilated and hypertrophied right ventricle (RV). Unexplained acute right heart failure was present without pulmonary hypertension. (C) Pulmonary artery pressure (Ppa) was 34/22 mmHg and right atrial pressure 20 mmHg. However, a significant systolic pressure gradient between the right ventricular pressure (Prv) and the pulmonary artery was present (LV, left ventricle; Pa, arterial pressure).

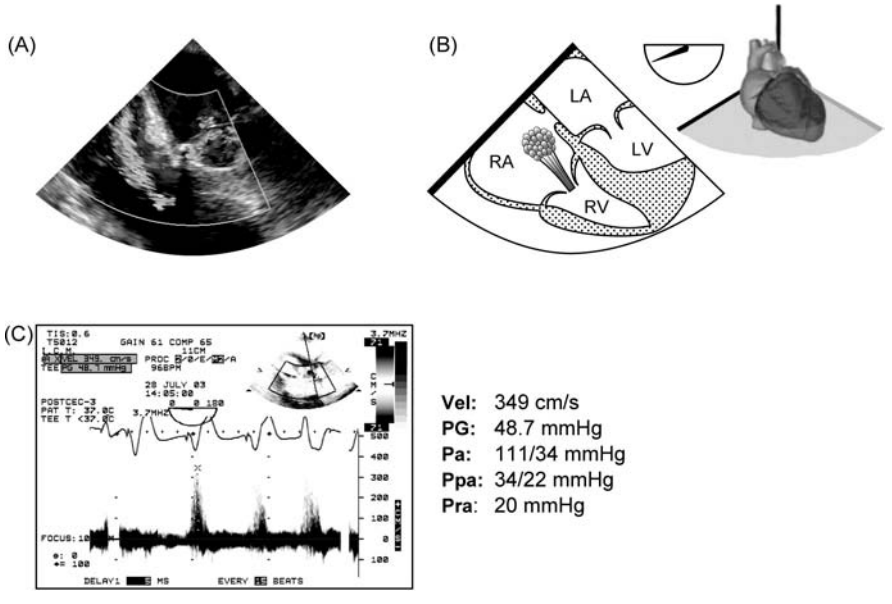

Figure 9.36 Right ventricular outflow tract obstruction. Same patient as in Fig. 9.35. (A, B) The right ventricular systolic pressure is estimated at 68.7 mmHg based on a right atrial pressure (Pra) of 20 mmHg and a right ventricle (RV) to right atrium (RA) pressure gradient (PG) of 48.7 mmHg from a tricuspid regurgitant velocity (Vel) of 349 cm/sec. The pulmonary artery pressure (Ppa) was directly measured at 34/22 mmHg. This would yield an outflow tract dynamic obstruction PG of 34.7 mmHg confirmed by directed right ventricular pressure tracing (see previous figure). The obstruction was exacerbated by intravenous milrinone and dopamine which were promptly discontinued. Weaning from cardiopulmonary bypass was then successful. The next day, all vasoactive medications were stopped and no residual right ventricular to pulmonary artery pressure gradient was present (LA, left atrium; LV, left ventricle; Pa, arterial pressure).

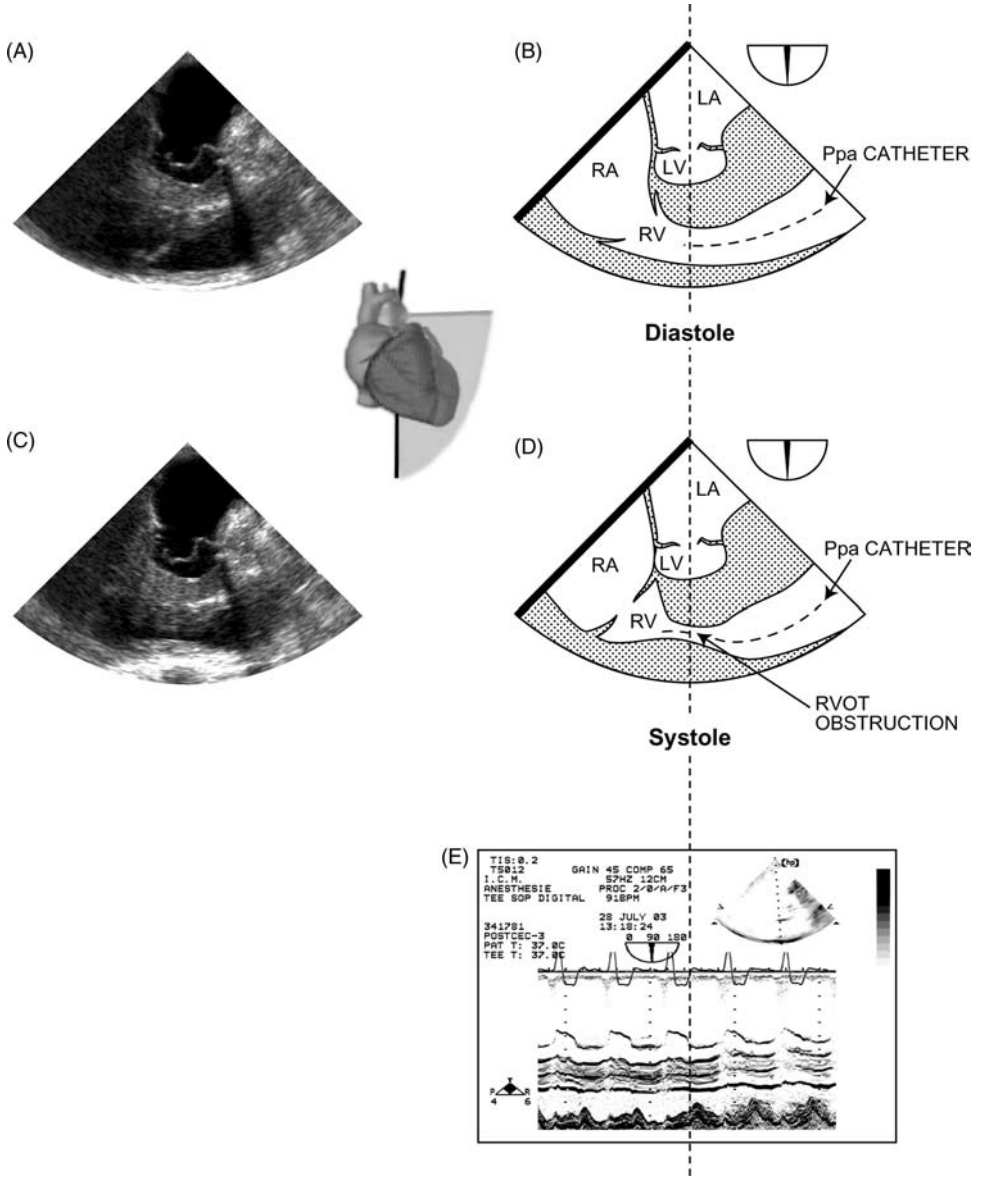

Figure 9.37 Right ventricular outflow tract obstruction. Same patient as in Fig. 9.35. The mid-esophageal right ventricular inflow–outflow view exam showed dynamic right ventricular outflow tract (RVOT) obstruction using 2D (A–D) and M-mode echocardiography (E) (LA, left atrium; LV, left ventricle; Ppa, pulmonary artery pressure; RA, right atrium; RV, right ventricle).

has also been reported in patients with pulmonary artery dilatation without pulmonary hypertension (65).

VII. PULMONARY THROMBOEMBOLISM

Pulmonary thromboembolism can be associated with severe right ventricular systolic and diastolic dysfunction. It can be due to *in situ* thrombus or thromboembolic material from deep venous thrombosis (Fig. 9.40) (66) or nonthrombotic from CO_2 (Fig. 9.41) (67), air (Fig. 9.42), or fat emboli as it may occur during orthopedic procedures (68). Echocardiography is considered pivotal in the evaluation of hemodynamically unstable patients suspected of pulmonary embolism (69) because it helps stratify those with evidence of right ventricular involvement. Such patients with right ventricular dysfunction or enlargement are at increased risk of hemodynamic instability and death. In the presence of hemodynamic instability, thrombolytic therapy, or surgical embolectomy may be lifesaving. Echocardiographic observations in pulmonary embolism include thrombus in transit in the RA, RV, or pulmonary artery, a dilated main

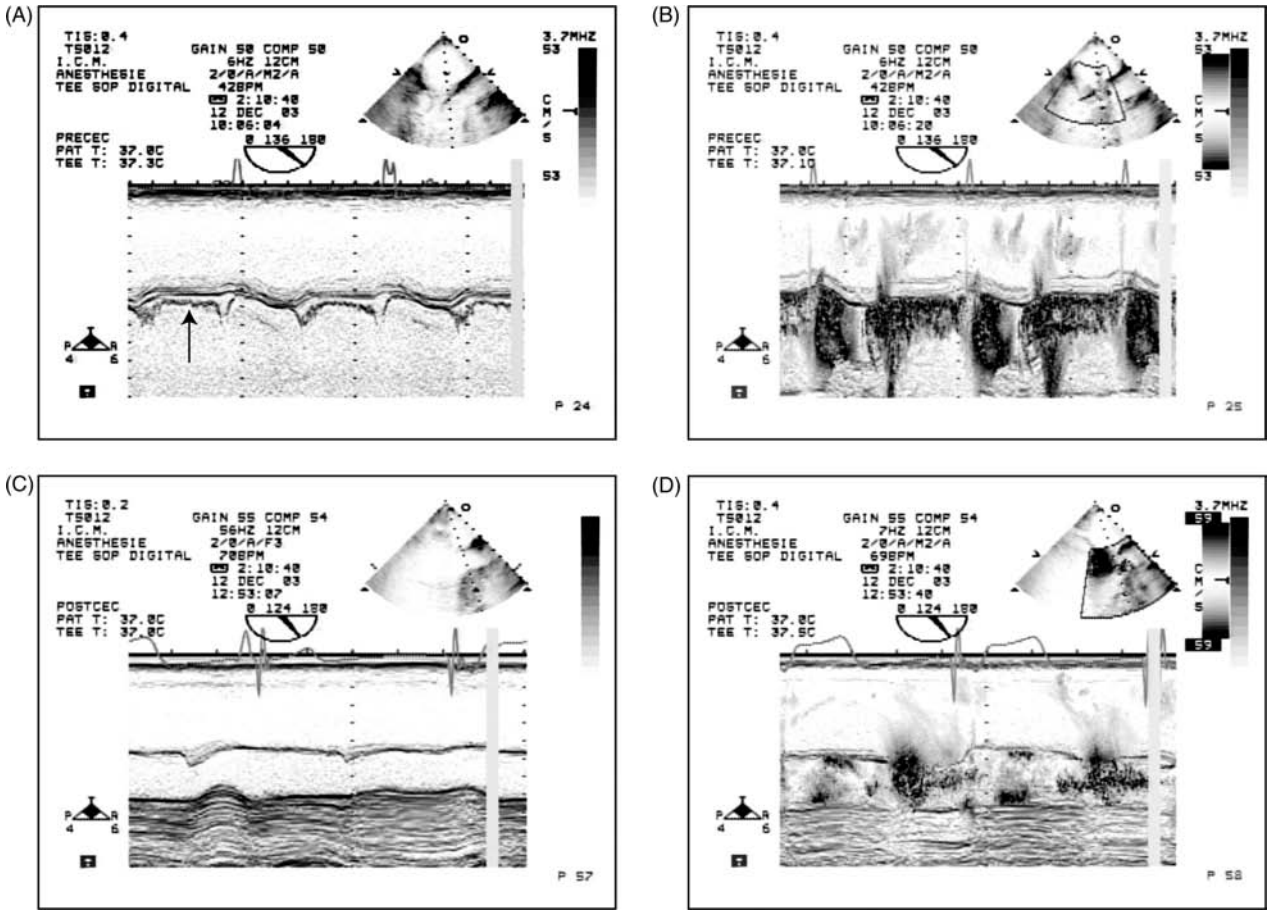

Figure 9.38 Mitral valve fluttering in a 56-year-old man being operated on for severe aortic regurgitation. (A) Fluttering of the anterior mitral leaflet (arrow) is seen using M-mode. (B) Aortic regurgitation on color M-mode. (C) After aortic valve replacement, the fluttering of the anterior mitral leaflet has disappeared. (D) The aortic regurgitation is now trivial.

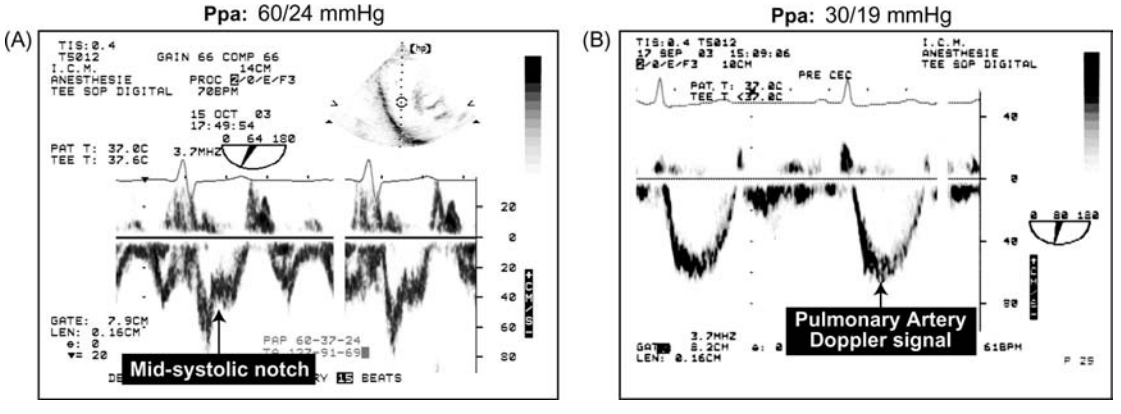

Figure 9.39 (A) Pulmonary hypertension in a 70-year-old man hemodynamically unstable with a pulmonary artery pressure (Ppa) of 60/24 mmHg. The pulmonary artery signal has a mid-systolic notch. (B) For comparison, a normal laminar pulmonary artery Doppler signal is shown from a 64-year-old woman before coronary revascularisation with a Ppa of 30/19 mmHg.

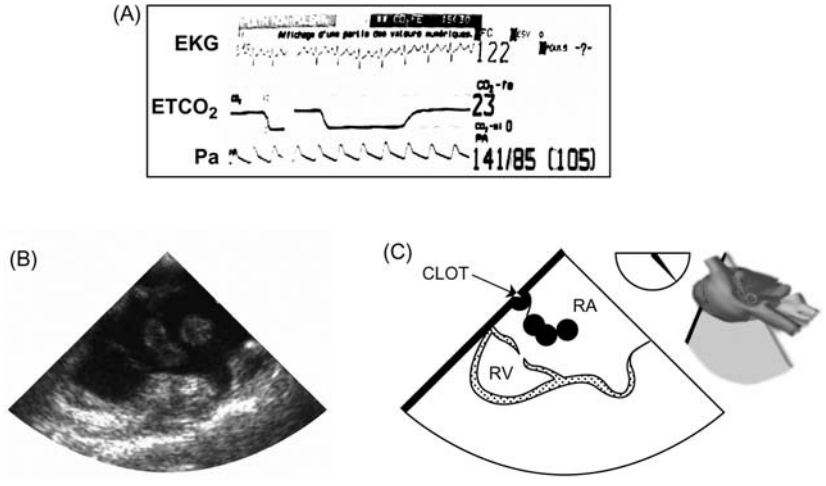

Figure 9.40 Thrombotic pulmonary emboli in a 68-year-old woman with hypotension and shortness of breath 4 weeks after a brain meningioma removal. (A) Hemodynamic data: heart rate of 122 beats/min, arterial pressure (Pa) of 141/85 mmHg on noradrenaline at 10 μgmin with end-tidal CO_2 ($ETCO_2$) of 22 mmHg. Note the peaked P-waves on the electrocardiogram (EKG) waveform suggesting right atrial dilatation. (B, C) Highly mobile clots floating in the right atrium (RA) are seen on a mid-esophageal 120° view (RV, right ventricle). (Photo B courtesy of Dr. Guy Cousineau.)

pulmonary artery, RV, RA, and inferior vena cava, in conjunction with reduced LV size, tricuspid regurgitation (TR), and abnormal flattening of the ventricular septum. In patients with gaseous embolism, air bubbles will tend to localize to the most vertically superior part of the heart which is the pulmonic valve and the atrial septum in a supine patient (Fig. 9.42).

VIII. CONCLUSION

In summary, TEE is an important tool for evaluation of global left and right ventricular systolic and diastolic function. It provides a unique and rapid diagnostic tool that has been, so far, unsurpassed in the setting of hemodynamic instability.

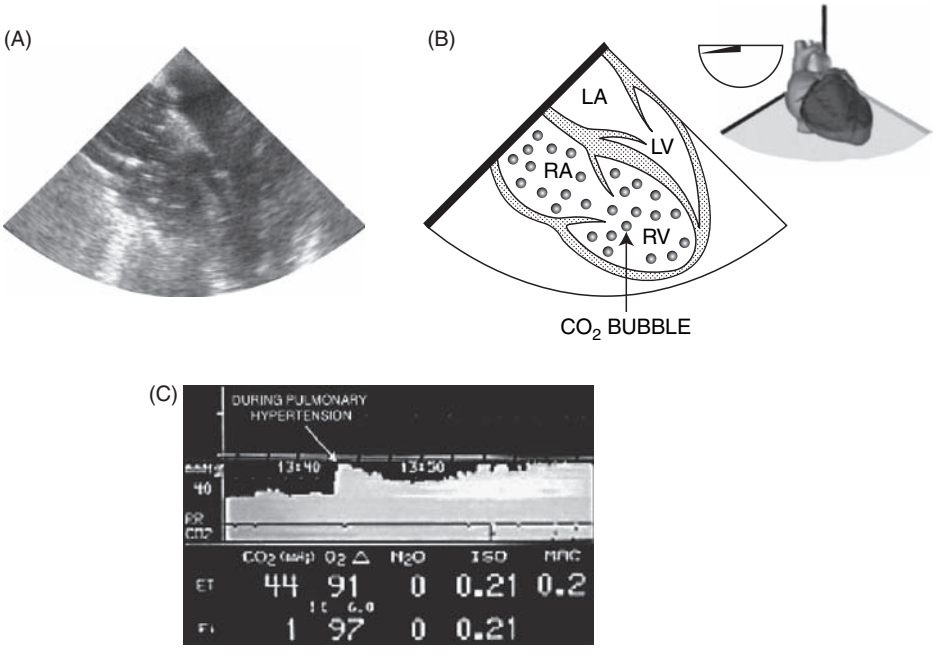

Figure 9.41 Carbon dioxide (CO_2) embolism in a 69-year-old man undergoing laparoscopic saphenectomy who suddenly became hemodynamically unstable. (A, B) A mid-esophageal four-chamber view showed the appearance of bubbles in the right atrium (RA) and right ventricle (RV) originating from the inferior vena cava. This was associated with right cardiac chamber dilatation. (C) The hemodynamic instability coincide with an abrupt rise in end-tidal CO_2 (LA, left atrium; LV, left ventricle). [Adapted from Martineau et al. (67).]

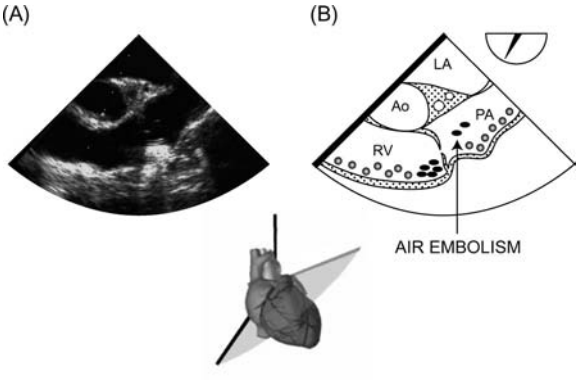

Figure 9.42 Air embolism in a 46-year-old woman hemodynamically unstable during spinal surgery in a ventral position. (A, B) She was turned back to a supine position and a mid-esophageal right ventricular outflow view revealed the residual presence of air bubbles on the most anterior aspect of the right ventricle (RV), pulmonary artery (PA) and on both sides of the anterior pulmonic valve (Ao, aorta; LA, left atrium).

REFERENCES

1. Practice guidelines for perioperative transesophageal echocardiography. A report by the American Society of Anesthesiologists and the Society of Cardiovascular Anesthesiologists Task Force on Transesophageal Echocardiography. Anesthesiology 1996; 84:986–1006.
2. Schiller NB, Shah PM, Crawford M et al. Recommendations for quantitation of the left ventricle by two-dimensional echocardiography. American Society of Echocardiography Committee on Standards, Subcommittee on Quantitation of Two-Dimensional Echocardiograms. J Am Soc Echocardiogr 1989; 2:358–367.
3. Emilsson K, Alam M, Wandt B. The relation between mitral annulus motion and ejection fraction: a nonlinear function. J Am Soc Echocardiogr 2000; 13:896–901.
4. Alam M, Wardell J, Andersson E et al. Effects of first myocardial infarction on left ventricular systolic and diastolic function with the use of mitral annular velocity determined by pulsed wave doppler tissue imaging. J Am Soc Echocardiogr 2000; 13:343–352.
5. Gorcsan J III, Denault A, Gasior TA et al. Rapid estimation of left ventricular contractility from end-systolic relations by echocardiographic automated border detection and femoral arterial pressure. Anesthesiology 1994; 81:553–562.
6. Denault AY, Gorcsan J III, Mandarino WA et al. Left ventricular performance assessed by echocardiographic automated border detection and arterial pressure. Am J Physiol 1997; 272:H138–H147.
7. Vieillard-Baron A, Augarde R, Prin S et al. Influence of superior vena caval zone condition on cyclic changes in right ventricular outflow during respiratory support. Anesthesiology 2001; 95:1083–1088.
8. Leung JM, Levine EH. Left ventricular end-systolic cavity obliteration as an estimate of intraoperative hypovolemia. Anesthesiology 1994; 81:1102–1109.
9. Tavernier B, Makhotine O, Lebuffe G et al. Systolic pressure variation as a guide to fluid therapy in patients with sepsis-induced hypotension. Anesthesiology 1998; 89:1313–1321.
10. Tousignant CP, Walsh F, Mazer CD. The use of transesophageal echocardiography for preload assessment in critically ill patients. Anesth Analg 2000; 90(2):351–355.
11. Feissel M, Michard F, Mangin I et al. Respiratory changes in aortic blood velocity as an indicator of fluid responsiveness in ventilated patients with septic shock. Chest 2001; 119:867–873.
12. Kusumoto FM, Muhiudeen IA, Kuecherer HF et al. Response of the interatrial septum to transatrial pressure gradients and its potential for predicting pulmonary capillary wedge pressure: an intraoperative study using transesophageal echocardiography in patients during mechanical ventilation. J Am Coll Cardiol 1993; 21:721–728.
13. Mulvagh S, Quinones MA, Kleiman NS et al. Estimation of left ventricular end-diastolic pressure from Doppler transmitral flow velocity in cardiac patients independent of systolic performance. J Am Coll Cardiol 1992; 20:112–119.
14. Nomura M, Hillel Z, Shih H et al. The association between Doppler transmitral flow variables measured by transesophageal echocardiography and pulmonary capillary wedge pressure. Anesth Analg 1997; 84:491–496.
15. Appleton CP, Galloway JM, Gonzalez MS et al. Estimation of left ventricular filling pressures using two-dimensional and Doppler echocardiography in adult patients with cardiac disease. Additional value of analyzing left atrial size, left atrial ejection fraction and the difference in duration of pulmonary venous and mitral flow velocity at atrial contraction. J Am Coll Cardiol 1993; 22:1972–1982.
16. Kimura K, Murata K, Tanaka N et al. The importance of pulmonary venous flow measurement for evaluating left ventricular end-diastolic pressure in patients with coronary artery disease in the early stage of diastolic dysfunction. J Am Soc Echocardiogr 2001; 14:987–993.
17. Kuecherer HF, Muhiudeen IA, Kusumoto FM et al. Estimation of mean left atrial pressure from transesophageal pulsed doppler echocardiography of pulmonary venous flow. Circulation 1990; 82:1127–1139.
18. Girard F, Couture P, Boudreault D et al. Estimation of the pulmonary capillary wedge pressure from transesophageal pulsed Doppler echocardiography of pulmonary venous flow: influence of the respiratory cycle during mechanical ventilation. J Cardiothorac Vasc Anesth 1998; 12:16–21.
19. Lattik R, Couture P, Denault AY et al. Mitral Doppler indices are superior to two-dimensional and conventional hemodynamic indices to predict fluid responsiveness. Anesth Analg 2002; 94:1092–1099.
20. Nagueh SF, Middleton KJ, Kopelen HA et al. Doppler tissue imaging: a noninvasive technique for evaluation of left ventricular relaxation and estimation of filling pressures. J Am Coll Cardiol 1997; 30:1527–1533.
21. Kim YJ, Sohn DW. Mitral annulus velocity in the estimation of left ventricular filling pressure: prospective study in 200 patients. J Am Soc Echocardiogr 2000; 13:980–985.
22. Firstenberg MS, Levine BD, Garcia MJ et al. Relationship of echocardiographic indices to pulmonary capillary wedge

pressures in healthy volunteers. J Am Coll Cardiol 2000; 36:1664–1669.
23. Garcia MJ, Ares MA, Asher C et al. An index of early left ventricular filling that combined with pulsed Doppler peak E velocity may estimate capillary wedge pressure. J Am Coll Cardiol 1997; 29:448–454.
24. Sunagawa K, Maughan WL, Sagawa K. Optimal arterial resistance for the maximal stroke work studied in isolated canine left ventricle. Circ Res 1985; 56:586–595.
25. Gorcsan J, Gasior TA, Mandarino WA et al. Assessment of the immediate effects of cardiopulmonary bypass on left ventricular performance by on-line pressure–area relations. Circulation 1994; 89:180–190.
26. Simonson JS, Schiller NB. Descent of the base of the left ventricle: an echocardiographic index of left ventricular function. J Am Soc Echocardiogr 1989; 2:25–35.
27. Tei C, Dujardin KS, Hodge DO et al. Doppler index combining systolic and diastolic myocardial performance: clinical value in cardiac amyloidosis. J Am Coll Cardiol 1996; 28:658–664.
28. Eidem BW, O'Leary PW, Tei C, Seward JB. Usefulness of the myocardial performance index for assessing right ventricular function in congenital heart disease. Am J Cardiol 2000; 86:654–658.
29. Moller JE, Sondergaard E, Poulsen SH et al. Serial Doppler echocardiographic assessment of left and right ventricular performance after a first myocardial infarction. J Am Soc Echocardiogr 2001; 14:249–255.
30. Costachescu T, Denault AY, Guimond JG et al. The hemodynamically unstable patient in the intensive care unit: hemodynamic vs. transesophageal echocardiographic monitoring. Crit Care Med 2002; 30:1214–1223.
31. Pai RG, Bansal RC, Shah PM. Doppler-derived rate of left ventricular pressure rise. Its correlation with the postoperative left ventricular function in mitral regurgitation. Circulation 1990; 82:514–520.
32. Reichert CL, Visser CA, van den Brink RB et al. Prognostic value of biventricular function in hypotensive patients after cardiac surgery as assessed by transesophageal echocardiography. J Cardiothorac Vasc Anesth 1992; 6:429–432.
33. Maslow AD, Regan MM, Panzica P et al. Precardiopulmonary bypass right ventricular function is associated with poor outcome after coronary artery bypass grafting in patients with severe left ventricular systolic dysfunction. Anesth Analg 2002; 95:1507–1518.
34. Eddy AC, Rice CL, Anardi DM. Right ventricular dysfunction in multiple trauma victims. Am J Surg 1988; 155:712–715.
35. Mitsuo T, Shimazaki S, Matsuda H. Right ventricular dysfunction in septic patients. Crit Care Med 1992; 20:630–634.
36. Davila-Roman VG, Waggoner AD, Hopkins WE, Barzilai B. Right ventricular dysfunction in low output syndrome after cardiac operations: assessment by transesophageal echocardiography. Ann Thorac Surg 1995; 60:1081–1086.
37. Wranne B, Pinto FJ, Hammarstrom E et al. Abnormal right heart filling after cardiac surgery: time course and mechanisms. Br Heart J 1991; 66:435–442.
38. Appleton CP, Hatle LK, Popp RL. Superior vena cava and hepatic vein Doppler echocardiography in healthy adults. J Am Coll Cardiol 1987; 10:1032–1039.
39. Pinto FJ, Wranne B, St Goar FG et al. Hepatic venous flow assessed by transesophageal echocardiography. J Am Coll Cardiol 1991; 17:1493–1498.
40. Pinto FJ, Wranne B, St Goar FG et al. Systemic venous flow during cardiac surgery examined by intraoperative transesophageal echocardiography. Am J Cardiol 1992; 69:387–393.
41. Bernard F, Denault A, Babin D et al. Diastolic dysfunction is predictive of difficult weaning from cardiopulmonary bypass. Anesth Analg 2001; 92:291–298.
42. Khouri SJ, Maly GT, Suh DD, Walsh TE. A practical approach to the echocardiographic evaluation of diastolic function. J Am Soc Echocardiogr 2004; 17:290–297.
43. Ozer N, Tokgozoglu L, Coplu L, Kes S. Echocardiographic evaluation of left and right ventricular diastolic function in patients with chronic obstructive pulmonary disease. J Am Soc Echocardiogr 2001; 14:557–561.
44. Caso P, Galderisi M, Cicala S et al. Association between myocardial right ventricular relaxation time and pulmonary arterial pressure in chronic obstructive lung disease: analysis by pulsed Doppler tissue imaging. J Am Soc Echocardiogr 2001; 14:970–977.
45. Denault A, Couture P, Perrault LP, Tardif JC. Diagnosis, predictors, mechanisms, and treatment of hemodynamic instability in cardiac surgery: research perspective at the Montreal Heart Institute. In: Pandalai SG, ed. Recent Research Developments in Anesthesia and Analgesia. Kerala: Transworld Research Network, 2003:25–43.
46. Freeman WK, Schaff HV, Khandheria BK et al. Intraoperative evaluation of mitral valve regurgitation and repair by transesophageal echocardiography: incidence and significance of systolic anterior motion. J Am Coll Cardiol 1992; 20:599–609.
47. Pollick C, Morgan CD, Gilbert BW et al. Muscular subaortic stenosis: the temporal relationship between systolic anterior motion of the anterior mitral leaflet and the pressure gradient. Circulation 1982; 66:1087–1094.
48. Heidenreich PA, Stainback RF, Redberg RF et al. Transesophageal echocardiography predicts mortality in critically ill patients with unexplained hypotension. J Am Coll Cardiol 1995; 26:152–158.
49. Gouello JP, Bouachour G, Vincent JF et al. Detection of left cardiopathy using echocardiography during acute respiratory failure in chronic respiratory insufficiency. Rev Mal Respir 1995; 12:145–150.
50. Murtha W, Guenther C. Dynamic left ventricular outflow tract obstruction complicating bilateral lung transplantation. Anesth Analg 2002; 94:558–559.
51. Di Chiara A, Plewka M, Fioretti PM. Systolic anterior movement of mitral valve during acute apical myocardial infarction: an unusual mechanism of acute mitral regurgitation. J Am Soc Echocardiogr 1999; 12:1117–1121.
52. Morewood GH, Weiss SJ. Intra-aortic balloon pump associated with dynamic left ventricular outflow tract obstruction

after valve replacement for aortic stenosis. J Am Soc Echocardiogr 2000; 13:229–231.
53. Murtha W, Guenther C. Dynamic left ventricular outflow tract obstruction complicating bilateral lung transplantation. Anesth Analg 2002; 94:558–559.
54. Doshi SN, Kim MC, Sharma SK, Fuster V. Images in cardiovascular medicine. Right and left ventricular outflow tract obstruction in hypertrophic cardiomyopathy. Circulation 2002; 106:e3–e4.
55. Agarwal S, Choudhary S, Saxena A et al. Giant pulmonary artery aneurysm with right ventricular outflow tract obstruction. Indian Heart J 2002; 54:77–79.
56. Tardif JC, Taylor K, Pandian NG et al. Right ventricular outflow tract and pulmonary artery obstruction by postoperative mediastinal hematoma: delineation by multiplane transesophageal echocardiography. J Am Soc Echocardiogr 1994; 7:400–404.
57. Dall'Agata A, Cromme-Dijkhuis AH, Meijboom FJ et al. Use of three-dimensional echocardiography for analysis of outflow obstruction in congenital heart disease. Am J Cardiol 1999; 83:921–925.
58. Bennink GB, Hitchcock FJ, Molenschot M et al. Aneurysmal pericardial patch producing right ventricular inflow obstruction. Ann Thorac Surg 2001; 71:1346–1347.
59. Basaria S, Denktas AE, Ghani M, Thandroyen F. Ventricular septal defect patch causing right ventricular inflow tract obstruction. Circulation 1999; 100:e12–e13.
60. Kirshbom PM, Tapson VF, Harrison JK et al. Delayed right heart failure following lung transplantation. Chest 1996; 109:575–577.
61. Stierle U, Sheikhzadeh A, Shakibi JG et al. Right ventricular obstruction in various types of hypertrophic cardiomyopathy. Jpn Heart J 1987; 28:115–125.
62. Gorcsan J, Reddy SC, Armitage JM, Griffith BP. Acquired right ventricular outflow tract obstruction after lung transplantation: diagnosis by transesophageal echocardiography. J Am Soc Echocardiogr 1993; 6:324–326.
63. Winsberg F, Gabor GE, Hernberg JG, Weiss B. Fluttering of the mitral valve in aortic insufficiency. Circulation 1970; 41:225–229.
64. Weyman AE, Dillon JC, Feigenbaum H, Chang S. Pulmonary valve echo motion in pulmonary regurgitation. Br Heart J 1975; 37:1184–1190.
65. Bauman W, Wann LS, Childress R et al. Mid systolic notching of the pulmonary valve in the absence of pulmonary hypertension. Am J Cardiol 1979; 43:1049–1052.
66. Leibowitz D. Role of echocardiography in the diagnosis and treatment of acute pulmonary thromboembolism. J Am Soc Echocardiogr 2001; 14:921–926.
67. Martineau A, Arcand G, Couture P et al. Transesophageal echocardiographic diagnosis of carbon dioxide embolism during minimally invasive saphenous vein harvesting and treatment with inhaled epoprostenol. Anesth Analg 2003; 96:962–964.
68. Parmet JL, Horrow JC, Pharo G et al. The incidence of venous emboli during extramedullary guided total knee arthroplasty. Anesth Analg 1995; 81:757–762.
69. Wood KE. Major pulmonary embolism: review of a pathophysiologic approach to the golden hour of hemodynamically significant pulmonary embolism. Chest 2002; 121:877–905.

10

Cardiomyopathy

VICKY SOULIÈRE, PHILIPPE L.-L'ALLIER, ANIQUE DUCHARME
University of Montreal, Montreal, Canada

I. Hypertrophic Cardiomyopathy 215
A. Epidemiology 215
B. Clinical Features 216
C. Anatomical Features 216
D. Pathophysiology of Outflow Tract Obstruction 216
E. Echocardiographic Features 218
1. M-mode and Two-Dimensional Imaging 218
2. Doppler and Color Flow Imaging 221
3. Diastolic Function 222
F. Condition Simulating Hypertrophic Cardiomyopathy 223
1. Hypertrophy 223
2. SAM and LVOT Obstruction 223
G. Monitoring Therapy 223
1. Intensive Care Unit and Noncardiac Surgery 223
2. Nonsurgical Septal Ablation 224
3. Surgical Septal Myectomy 225
II. Dilated Cardiomyopathy 227
A. Epidemiology 227
B. Clinical Features 228
C. Echocardiographic Features 228
1. Chambers Dilatation 228
2. Ventricular Systolic Dysfunction 229
3. Diastolic Dysfunction 230
4. Secondary Findings 230
D. Noncompacted LV 233
1. Epidemiology 233
2. Clinical Features 233
3. Anatomical Features (Pathoanatomic Findings) 233
4. Echocardiographic Features 234
5. Conclusion 234
E. Nontransplant Surgery 234
III. Restrictive and Infiltrative Cardiomyopathy 234
A. Definition 234
B. Clinical Findings 234
C. Echocardiographic Features 235
D. Difference Between Restrictive Cardiomyopathy and Constrictive Pericarditis 236
E. Amyloidosis 237
F. Sarcoidosis 237
G. Hemochromatosis 238
IV. Conclusion 238
References 238

I. HYPERTROPHIC CARDIOMYOPATHY

A. Epidemiology

Hypertrophic cardiomyopathy (HCM) is defined as a nondilated heart with right, left (or both) ventricular hypertrophy without an obvious cause such as aortic stenosis (AS) or systemic hypertension (1). This disorder is transmitted as an autosomal dominant trait in about half of the patients and more than 200 mutations on 10 different genes have been identified. Most of these

encode for sarcomeric proteins (such as myosin heavy chain and tropomyosin), resulting in myofibrillar disarray and dysfunctional myocytes, which in turn trigger reactional hypertrophy. The vast array of genetic defects and their variable penetrance accounts for the heterogeneity of this disease, even within the same family. The cause of HCM in the remainder of the patients is unknown.

This disorder has an estimated prevalence of 1/500 individual in the general population (2), but can be found in 0.5% of the patients referred for an echocardiogram.

B. Clinical Features

The clinical manifestations are quite diverse. Patients with HCM can be completely asymptomatic or present with heart failure, exertional dyspnea, angina, postexertional syncope or serious arrhythmias. Sudden death could be the first manifestation in as many as 10% and the estimated annual mortality rate is 1–2%. It is of clinical importance to distinguish between the obstructive and nonobstructive forms of HCM as management strategies are usually tailored to the hemodynamic status. A common characteristic feature of HCM (obstructive and nonobstructive) is diastolic dysfunction (3). Abnormal relaxation of the left ventricle (LV) results from excessive wall thickness and causes impaired ventricular filling, increased left ventricular end-diastolic pressure (LVEDP), and consequently, pulmonary congestion and dyspnea which can be potentiated by outflow tract obtruction. Angina can occur without epicardial coronary stenosis and is thought to result from multiple mechanisms: inadequate capillary density, impaired coronary flow (secondary to the high left ventricular diastolic pressure or by myocardial bridging), or small vessel disease with further increase in O_2 demand when left ventricular outflow tract (LVOT) obstruction occurs. Exertional syncope may be due to hypotension, caused by the inability to increase cardiac output (CO) because of the obstruction, together with inappropriate vasodilatation or arrhythmia. Sudden death usually results from malignant arrhythmia; patients with HCM have an arrhythmogenic substrate that predisposes them to ventricular arrhythmias, with a variable role from triggers such as hypotension, ischemia or supraventricular arrhythmias (4).

C. Anatomical Features

The anatomic hallmark of HCM is ventricular hypertrophy with increased myocardial mass, small left ventricular cavity size, and dilated left atrium (LA) secondary to high LVEDP (3). The increased wall thickness varies in severity and distribution; the "classic" asymmetric hypertrophy of the septal wall represents 70–75% of cases (Fig. 10.1), followed by basal septal location (10–15%), concentric symmetrical (5%), apical (5%) and isolated hypertrophy of the lateral wall (1–7%). The mitral valve may be intrinsically abnormal: the papillary muscles can be displaced anteriorly and the leaflets can be elongated. These abnormalities, associated with a hypertrophied and bulging basal septum, will maximize the reduction in LVOT width, providing a substrate for dynamic subaortic obstruction. Obstruction may also occur at the mid-cavitary level involving anomalous papillary muscle insertion, preferential mid-ventricular, or papillary muscle hypertrophy, and malalignment.

The left ventricular function is usually hyperdynamic. However, long-standing HCM might evolve, and the hypertrophic segments could be replaced by thinner, dysfunctional fibrotic walls with increased left ventricular systolic and diastolic dimensions. This end-stage HCM could be indistinguishable from dilated cardiomyopathy (DCM), and occurs in ~20% of patients.

D. Pathophysiology of Outflow Tract Obstruction

Almost a quarter of the patients with septal hypertrophy will have significant resting outflow tract obstruction. In the others, the obstruction may be absent at rest but can be revealed by provocative maneuvers or changes in hemodynamic conditions. There is a general consensus that a true mechanical impediment to the left ventricular ejection exists and results from the mitral valve (MV) and its apparatus moving anteriorly, the systolic anterior motion (SAM).

Rapid left ventricular ejection from the hypertrophied LV will increase the velocity of blood flow across the narrowed LVOT, producing a *Venturi effect*. These forces will drag the abnormal mitral leaflets and support apparatus towards the septum (5), creating a defect in the closure of the MV; the point of coaptation will then occur in the body of the elongated leaflets instead of at their tips as in normal. The portion of the anterior leaflet distal from the coaptation point is then free to move with the subaortic flow (anteriorly and superiorly), leading to mitral leaflet-septum contact. This contact causes further narrowing of the LVOT, resulting in a SAM (Fig. 10.2). The severity and duration of the SAM is highly related to the extent of the subaortic obstruction (5). The SAM also creates a gap between the mitral leaflets, in which mitral regurgitation (MR) can develop; this occurs predominantly in mid-to-late systole, reflecting the dynamic nature of this insufficiency. The jet of MR is usually directed posteriorly (59%), but central (38%) and anterior jets (3%) can also be found, owing to concurrent prolapse of the posterior leaflet (6,7). This sequence of events follows the "eject–obstruct–leak" pattern described in earlier angiographic

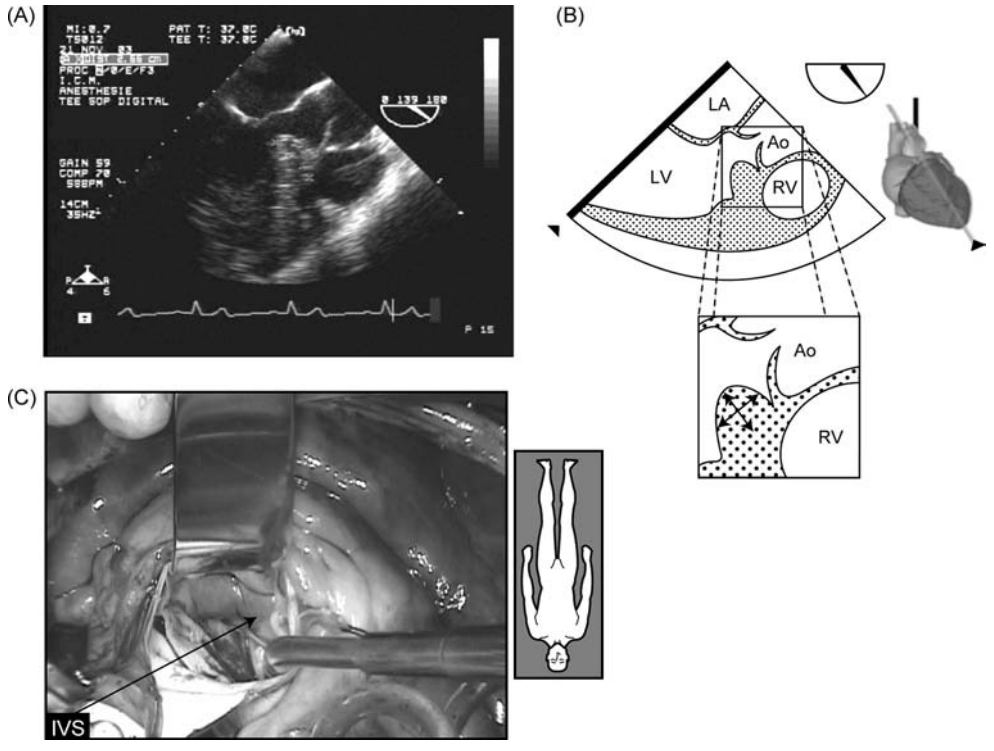

Figure 10.1 (A, B) Mid-esophageal long-axis view of a 26-year-old man with hypertrophic septal cardiomyopathy. The septal thickness was 26.6 mm. The septal measurements that the surgeon required for septal myectomy are shown in the zoomed box. (C) Intraoperative view of the interventricular septum (IVS) before septal myectomy (Ao, aorta; LA, left atrium; LV, left ventricle; RV, right ventricle). (Photo C courtesy of Dr. Nancy Poirier.)

studies. The amount of MR is related to the degree of LVOT obstruction, and is usually moderate in severity. Other factors might influence the severity of MR, including MV prolapse, annular calcification, and leaflet damage from repeated trauma.

Latent obstruction is associated with localized subaortic hypertrophy (in 53% of cases) or with hypertrophy involving the basal two-thirds of the septum (in 35%). Right ventricular outflow tract obstruction may also be present, owing to right ventricular hypertrophy with dynamic reduction in right ventricular outflow tract size. Left ventricular outflow tract obstruction does not develop in patients with isolated apical, lateral, or free wall hypertrophy. In the nonobstructive forms of the disease, no significant pressure gradient is present either at rest or with provocative maneuvers.

An important characteristic of the subaortic obstruction is its dynamic nature; any hemodynamic conditions reducing ventricular volume will accentuate apposition of the MV leaflets against the septum, thus increasing the outflow gradient: the elongated leaflets and chordae of the MV will become even longer relative to the (smaller) cavity and encroach more easily on the LVOT. This phenomenon can also occur with enhanced contractility, which will also increase the flow velocity, and therefore the dragging force on the mitral apparatus. Thus, any maneuvers that decrease the preload, afterload or increase the inotropic state would exacerbate or even provoke a LVOT obstruction. A physiological example of this phenomenon is the post-extrasystolic potentiation. Normally, the compensatory pause following a ventricular extrasystole leads to: (1) an increase in the left ventricular diastolic volume, stretching the ventricular fibers; (2) increased calcium reuptake; and (3) reduced afterload, due to lower aortic end-diastolic pressure. All these phenomena promote increased contractility of the next beat, resulting in a higher aortic pulse pressure. In HOCM, this phenomenon increases the gradient between the left ventricular and the aortic pressure and leads to a paradoxically smaller aortic systolic pressure than on the previous beats: this constitutes the Braunwald–Brockenbrough sign (Fig. 10.3).

Many drugs can have deleterious hemodynamic effects in patients with HOCM. Those with vasodilatory or positive inotropic properties are known to increase the LVOT gradient. In contrast, negative inotropic (β-blockers and calcium antagonists) or pure vasopressive drugs can have beneficial effects. Knowledge of all the

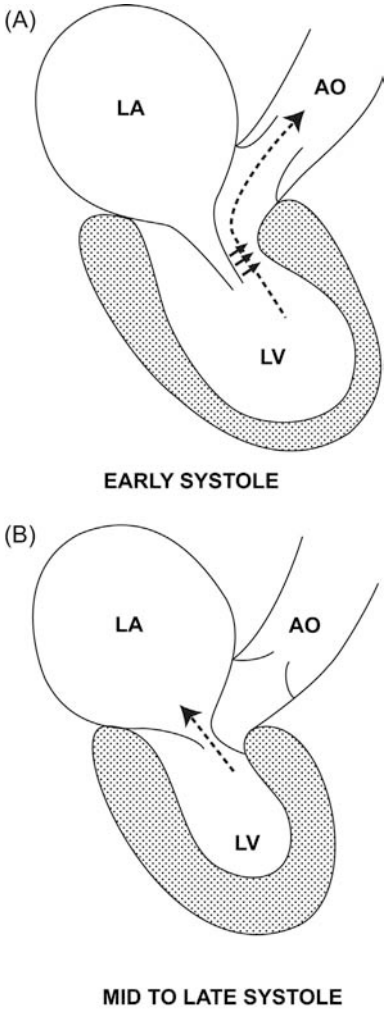

Figure 10.2 Proposed mechanism of systolic anterior motion or SAM. (A) In early systole, septal hypertrophy causes the narrowed outflow tract to be closer to the mitral valve. (B) The resulting Venturi forces drag the anterior mitral valve leaflet and apparatus toward the septum, causing leaflet-septal contact in mid-systole, left ventricular outflow tract obstruction and mitral regurgitation (Ao, aorta; LA, left atrium; LV, left ventricle). [Adapted from Braunwald (8).]

conditions that modulate this dynamic process is essential when caring for patients with HOCM. The Valsalva maneuver is a useful tool at the bedside to unmask or increase an LVOT gradient. By lowering the preload, this maneuver increases the dynamic obstruction and the intensity of the cardiac systolic murmur, a useful sign to differentiate it from that of fixed aortic valvular stenosis.

E. Echocardiographic Features

Echocardiography is an indispensable tool in the diagnosis of HCM as well as to follow patients with known HCM.

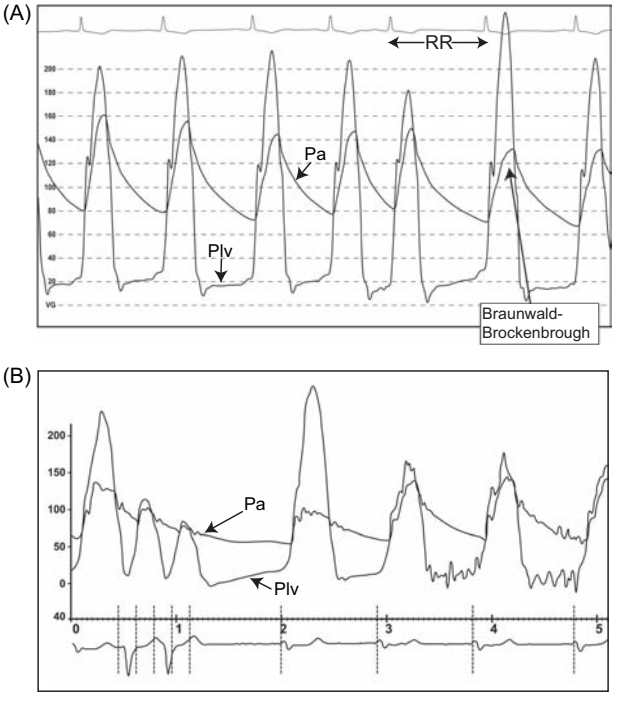

Figure 10.3 Two examples of Brockenbrough-Braunwald phenomenon on left ventricular pressure (Plv) and arterial pressure (Pa) hemodynamic tracings. (A, B) In hypertrophic obstructive cardiomyopathy, postextrasystolic potentiation of left ventricular contraction results in a higher gradient between the left ventricle and the aorta and a decreased aortic pulse pressure than on the previous beats. See text for details.

It permits the evaluation of the extent and severity of the hypertrophy, the associated LVOT obstruction and the degree of MR.

1. M-mode and Two-Dimensional Imaging

Hypertrophy and Systolic Function

The most striking feature is LV hypertrophy, which is often asymmetrical (Fig. 10.1). Hypertrophy is defined as an increased LV mass, indexed to the body surface area (BSA). Methods to calculate left ventricular mass have been validated mainly with transthoracic echocardiography (TTE), by measuring the left ventricular cavity dimension and the ventricular septal and posterior wall thickness at the mid-ventricular level at end-diastole (Chapter 5). The upper limit of normal for wall thickness in diastole is 12 mm (2). The hypertrophy is considered asymmetrical if the ratio of septal wall thickness to posterior wall exceeds 1.3 (9) (Fig. 10.4). With transesophageal echocardiography (TEE), it is recommended to measure the wall thickness by M-mode in the transgastric short axis view at 0° with anteflexion at the mid-papillary level, paying particular attention to avoid oblique measurements and ensuring correct

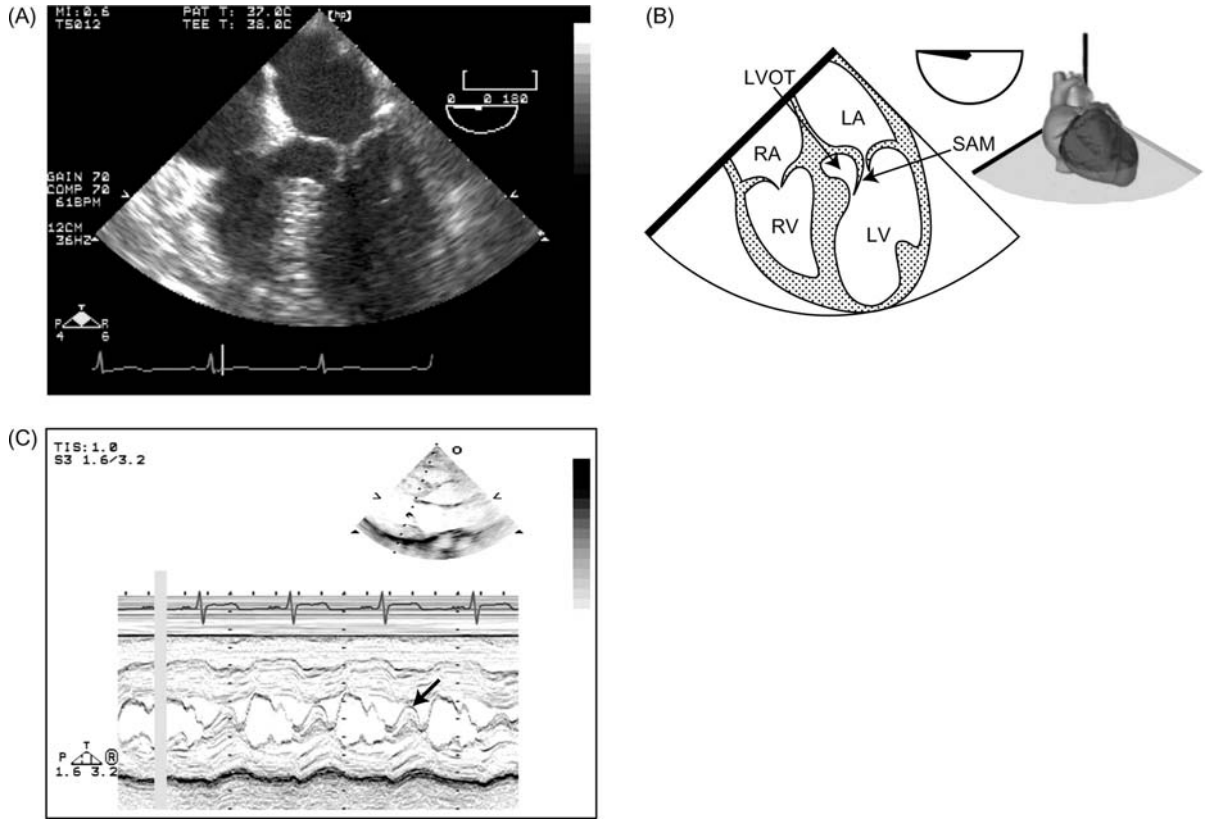

Figure 10.4 Systolic anterior motion (SAM) of the mitral valve. (A, B) Mid-esophageal four-chamber view in a patient with asymmetrical septal hypertrophy with SAM and dynamic obstruction of the left ventricular outflow tract (LVOT). (C) Transthoracic M-mode echocardiography of the mitral valve through a long-axis view, demonstrating SAM of the mitral leaflets toward the septum wall (arrow) (LA, left atrium; LV, left ventricle; RA, right atrium; RV, right ventricle).

alignment by obtaining a circular left ventricular cavity; precise measurements are essential as the severity of the hypertrophy carries an important prognostic value, being highly correlated with the risk of sudden death, independent of the LVOT obstruction (10). A wall thickness of >30 mm triples the risk of sudden death and has become a growing indication for implantable cardiac defibrillator. Hence, given the asymmetrical nature of the disease, one must be cautious and use multiple views when evaluating the extent and severity of HCM. The long-axis (120°) and four-chamber (0°) mid-esophageal views are useful to visualize the entire septum, particularly the basal part that is more frequently involved. The unusual form of apical hypertrophy can be missed if a meticulous examination is not performed, because left ventricular wall thickness is usually not increased at the basal and mid levels. The apex can be imaged at the mid-esophageal level by retroflexing the probe or in transgastric view by pushing the probe further than the short-axis mid-papillary level. However, as a general rule, the apex is often foreshortened in TEE. Furthermore, differentiation between apical hypertrophy and apical thrombus may be difficult, but looking at the apical wall motion can help, as it is usually abnormal in the latter.

Earlier studies have described changes in the acoustic texture of the affected myocardium, with a ground-glass appearance of the hypertrophied muscle. This was thought to represent abnormal cell architecture and myocardial fibrosis. This finding is neither sensitive nor specific for the diagnosis of HCM and can be present in other conditions (amyloidosis, hypertensive disease with renal insufficiency, and glycogen storage disease), or be absent in affected individuals. Nevertheless, hyperechogenic (fibrotic) lesions are often seen in the septum at the level of the mitral–septal contact.

The systolic function is usually well preserved in some patients with HCM, until late in the course of the disease. The ejection fraction is usually supra-normal because the presence of a small ventricular cavity size and increased wall thickness results in reduced wall stress, according to Laplace's law, where wall stress = (pressure × radius)/(2× wall thickness). Consequently, the hypertrophied ventricle will contract forcefully in the face of a reduced afterload.

Mitral Valve Apparatus

In addition to the abnormally large and elongated mitral leaflets, other MV abnormalities can be found. Ruptured chordae, anomalous papillary muscles insertion, leaflet(s) prolapse, or degenerative changes from repeated septal contact have all been described in association with HOCM and can result in severe MR. Special attention should be given when identifying these abnormalities preoperatively, as they will need to be addressed separately to ensure complete correction of the MR.

Systolic Anterior Motion of the Mitral Valve

The SAM of the MV and its contact with the septum is best evaluated in the mid-esophageal four-chamber (0°) or long-axis views (120°) (Fig. 10.5). The extent and duration of the mitral–septal contact can also be appreciated using M-mode of the LV in the same views (Fig. 10.4).

A septal contact lasting at least 30% of the systole duration is thought to be necessary to produce significant obstruction. The transgastric long-axis view at 120° and the deep transgastric view at 0° both display the LVOT but the latter is the optimal view to assess the LVOT gradient by TEE.

Other Findings

First, the LA is often dilated because of associated MR, chronically increased left ventricular diastolic pressure and the presence of atrial fibrillation, which is a frequent complication of HCM. Second, as the LVOT obstruction begins in mid- or late systole, the aortic cusps may close prematurely as a result of the reduced flow in the latter half of the ejection period. This mid-systolic closure is best appreciated using M-mode of the aortic valve (AoV) at the mid-esophageal long- (120°) or short-axis (30°) views. Finally, the right ventricle (RV) and the

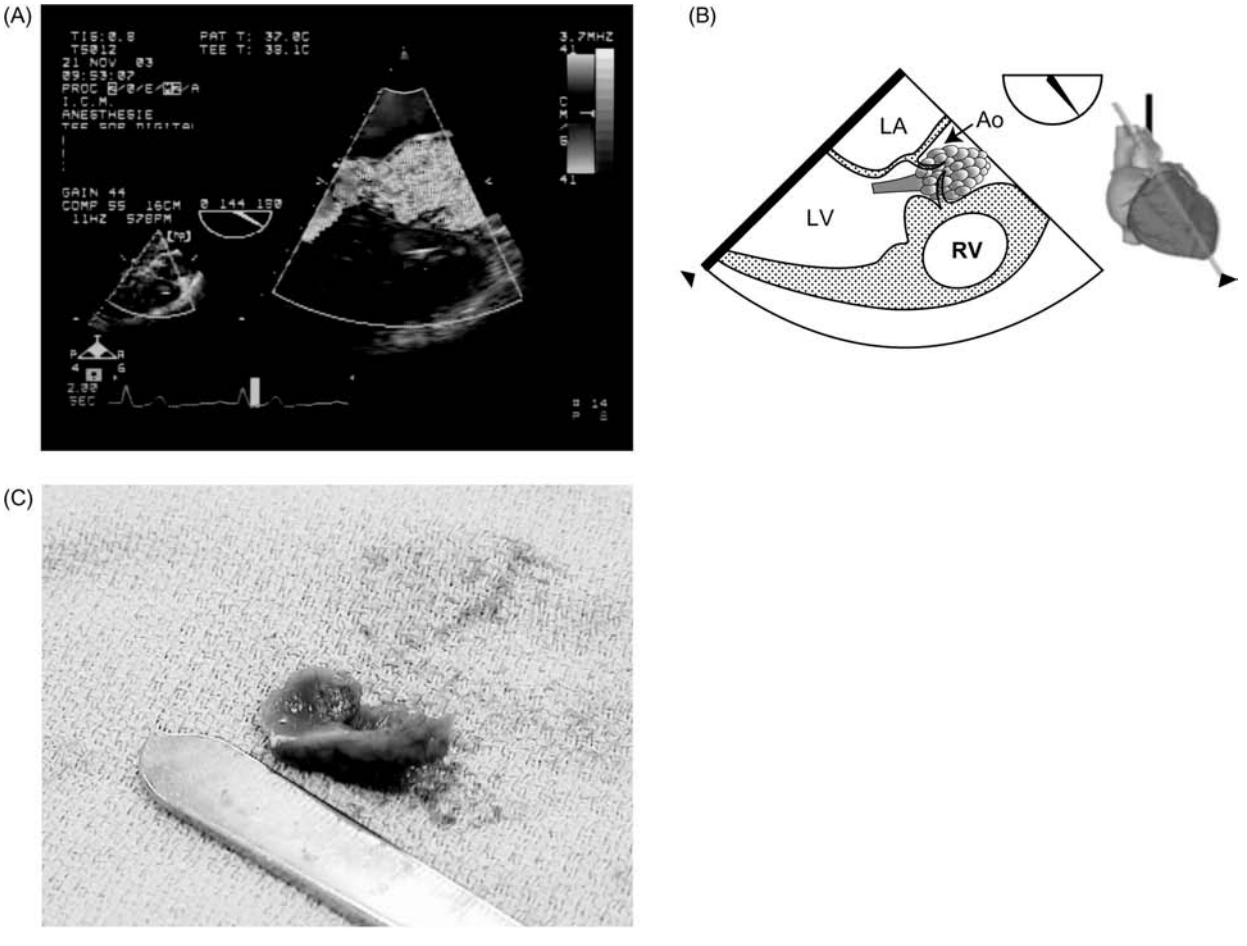

Figure 10.5 Preoperative transesophageal echocardiographic exam of a 26-year-old man with hypertrophic cardiomyopathy and refractory symptoms despite optimal medical therapy. (A–B) Mid-esophageal long-axis view with color flow imaging: flow acceleration is already present in the subaortic region. (C) The resected basal septum is shown. (Ao, aorta; LA, left atrium; LV, left ventricle; RV, right ventricle) (Courtesy of Dr. Nancy Poirier).

RVOT must also be carefully inspected, as occasionally they too can be involved.

2. *Doppler and Color Flow Imaging*

Color Flow Doppler

Color flow imaging is essential to localize the obstruction at the LVOT level; the turbulent color flow acceleration is seen below the AoV which differentiates it from true valvular AS. This can be demonstrated using the mid-esophageal long-axis view at 135° (Fig. 10.1). Alternatively, transgastric long-axis or deep transgastric views (Fig. 10.6) with color flow Doppler can also display the flow acceleration, although less precisely because of the farther position of the LVOT in the scan field. Color flow imaging is also essential in the evaluation of concomitant MR. The SAM of the MV distorts the coaptation point of the leaflets, resulting in a jet of MR directed posteriorly (Fig. 10.5). Therefore, variable degrees of MR almost always accompany the obstructive form of HCM. The severity of MR should be quantified as usual, but can greatly fluctuate over time given the dynamic nature of the SAM; this phenomenon may be particularly important in the operating room (OR) where under general anesthesia, the LVOT obstruction may partially or completely disappear.

Pulsed-Wave Doppler

The pulsed-wave (PW) Doppler is useful for precisely identifying the level of the obstruction. The PW Doppler sample volume is advanced progressively from the apex to the LVOT in a long-axis view (ideally through the deep transgastric views) until a rapid increase in flow velocity is encountered, locating the obstruction. This is particularly useful if a mid-ventricular obstruction is suspected. However, the PW Doppler is of limited value to evaluate severe obstruction or gradients in series (valvular and subvalvular, e.g.), as the V_1 velocity proximal to the stenosis exceeds the Nyquist limit and is therefore already aliasing. Modifying machine settings with high pulse repetition frequency (PRF) may alleviate this problem. By definition, continuous-wave (CW) Doppler will yield the sum of all gradients, as it measures the highest velocity in the LV–aorta axis (Fig. 10.7). Planimetry of the AoV in a short-axis view can help sort out the severity of concomitant valvular stenosis.

Continuous-Wave Doppler

The severity of LVOT obstruction is assessed with CW Doppler. Increased flow velocity can be detected by positioning the Doppler beam through the LVOT, parallel to the flow acceleration, guided by color flow Doppler as needed. This is best achieved using the deep transgastric views; the transgastric long-axis view at 110–120° can be used if the deep transgastric views are not satisfactory. The LVOT obstructive dynamic gradient is late peaking and rises significantly in mid- to late systole. The CW Doppler velocity profile takes a characteristic *dagger* shape, in contrast to the more symmetrical shape of a fixed valvular stenosis or a regurgitant jet of MR (Fig. 10.7). The peak velocity obtained is then transformed to a maximal pressure gradient using the simplified Bernoulli equation: $PG_{max} = 4\,V^2_{max}$. Maneuvers to modify the loading condition should be done to unmask latent LVOT or mid-ventricular obstructions. However, performing a Valsalva maneuver is often impractical in sedated patients as is inhalation of amyl nitrate; also waiting for an extrasystolic beat is not time-effective; intravenous or sublingual nitroglycerin administration can be used as an alternate method to decrease preload, and to a lesser extent, afterload in order to provoke or

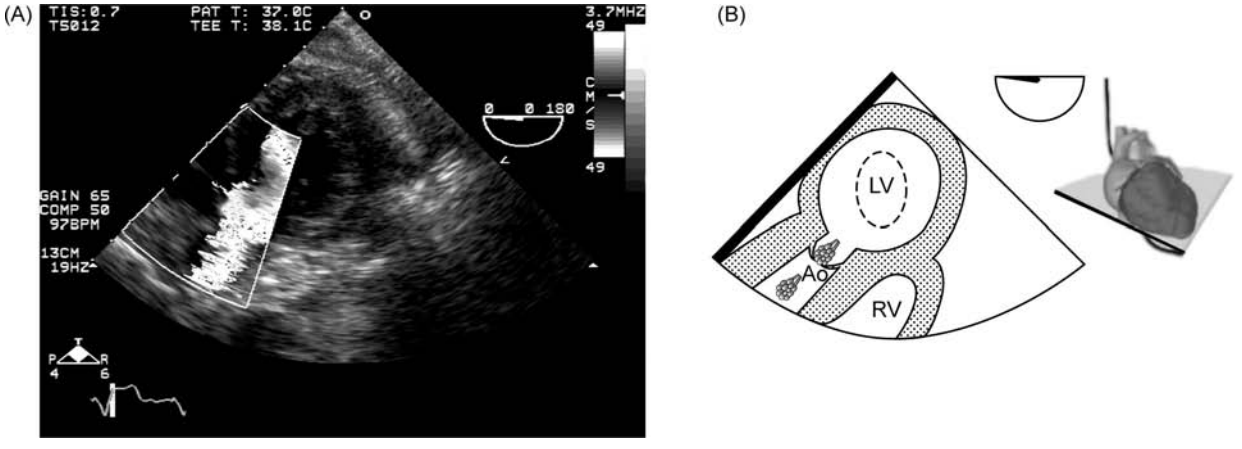

Figure 10.6 Color flow Doppler in a deep transgastric view showing the color flow acceleration in the left ventricular outflow tract. There is a good interrogation angle for pulsed- or continuous-wave Doppler (Ao, aorta; LV, left ventricle; RV, right ventricle).

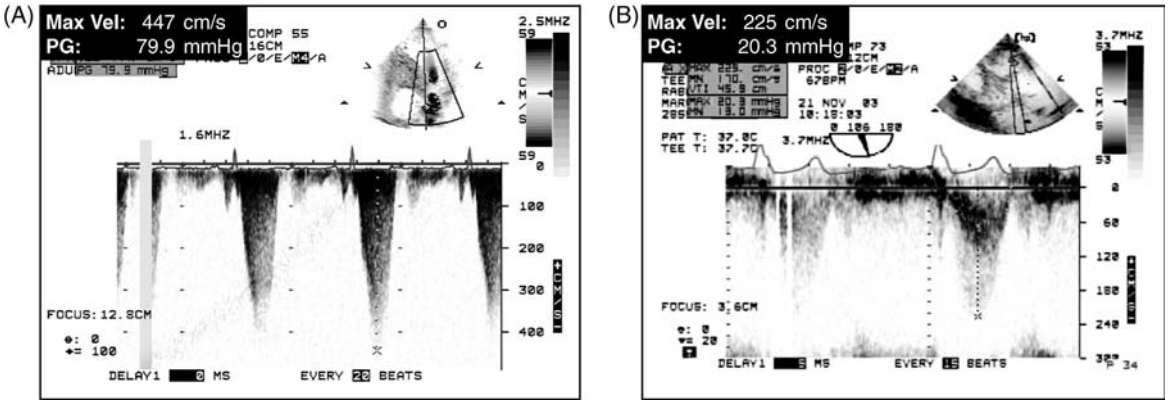

Figure 10.7 Measurement of a left ventricular outflow tract gradient in two patients with hypertrophic obstructive cardiomyopathy (HOCM). (A) In the first patient, a maximal instantaneous systolic pressure gradient (PG) of 79.9 mmHg is obtained from a transthoracic exam. (B) In the second patient, a 26-year-old man with asymmetrical septal HOCM, the peak systolic PG obtained through a deep transgastric long-axis view is measured at 20.3 mmHg after induction of general anesthesia. The gradient was however much higher (56 mmHg) in the awake state (Max Vel, maximum velocity).

enhance the obstruction. Because of its short half-life, nitroglycerin is relatively safe. Nevertheless, there is no additional diagnostic benefit to enhance an already severe dynamic obstruction in a given patient.

The Doppler signal of the LVOT obstruction is occasionally confused with the signal of MR, particularly when the jet is directed anteriorly towards the subaortic wall. The timing and duration of the velocity profile might help differentiate between the two. The typical MR Doppler signal is usually of a longer duration and begins sooner, as it includes the isovolumetric contraction and relaxation times. However, when MR is entirely due to SAM of the MV, it begins after the onset of the LVOT obstruction and hence, the velocity profile starts later in systole, and usually terminates with MV opening, as opposed to the LVOT dynamic obstruction signal which ends with AoV closure. Pulsed-wave Doppler with the sample volume located in the LVOT also helps to identify the true origin of the velocity signal obtained. The MR peak velocity should be higher than the obstruction velocity and can even be used to estimate the LVOT gradient. For example, a MR peak velocity of 6 m/s corresponds to an instantaneous left atrial–left ventricular systolic gradient of 144 mmHg from the simplified Bernoulli equation. The ventricular systolic pressure can then be calculated by adding the left atrial pressure (estimated by the wedge pressure from a pulmonary artery catheter); if the left atrial pressure is 20 mmHg, the left ventricular peak systolic pressure is estimated at 164 mmHg. The peak LVOT gradient can be easily estimated by subtracting the systemic systolic blood pressure from the estimated systolic left ventricular pressure, hence, $164 - 120 = 44$ mmHg. This way of approximating the LVOT gradient can be useful when the Doppler tracing quality is unsatisfactory. However, care must be taken to ensure that the MR Doppler signal is complete and taken parallel to the regurgitant jet. In addition, because of the dynamic nature of the LVOT obstruction, clinical situations affecting loading conditions or inotropy such as general anesthesia can change the severity of the dynamic obstruction (Fig. 10.7).

3. *Diastolic Function*

Systolic function is usually normal, but abnormalities in diastolic function can be found in ~80% of patients, whether or not a subaortic gradient is present. Ventricular hypertrophy and fibrosis lead to abnormal chamber stiffness and delayed relaxation. Interestingly, there seems to be little correlation between the severity of diastolic dysfunction and the extent of hypertrophy (4). The state of the diastolic function is assessed with PW Doppler examination of the mitral inflow: the sample volume is positioned at the tip of the mitral leaflets in the mid-esophageal four-chamber view. The most frequent pattern encountered is delayed left ventricular relaxation. The early filling "*E*" wave velocity is diminished because the delayed left ventricular relaxation reduces the rate of pressure drop in the LV, decreasing the left atrial–left ventricular gradient. This yields a smaller "*E*" wave velocity with prolonged deceleration time and isovolumetric relaxation time (*T*). Consequently, the contribution of the late part of the diastole to ventricular filling is more important, producing a prominent "*A*" wave and an "E/A" ratio <1. This increased role of the atrial contraction in left ventricular filling helps to understand the dramatic clinical deterioration of HCM patients when they develop atrial fibrillation. More severe patterns of diastolic function also occur. As the left atrial pressure increases,

either by reduced left ventricular compliance or by MR, the driving pressure for the early filling increases and makes the "*E*" wave taller and shorter. Hence, the diastolic pattern can progress to a restrictive filling pattern. The pseudonormal profile (normal deceleration time and "*E*/*A*" ratio) constitutes an intermediate level of diastolic dysfunction between the abnormal relaxation and the restrictive patterns. It is differentiated from a true normal pattern by PW Doppler of the pulmonary veins, where the systolic flow velocity will be lower than its diastolic counterpart.

F. Condition Simulating Hypertrophic Cardiomyopathy

1. Hypertrophy

There are a number of conditions producing either left ventricular hypertrophy (either symmetrical or asymmetrical) or SAM with LVOT obstruction; they must be considered in the differential diagnosis of HCM. Aortic stenosis, systemic hypertension, metabolic disorders, and amyloidosis can all lead to increased wall thickness, usually symmetrical. Asymmetrical distribution of hypertrophy is less frequently associated with other diagnoses than with HCM. However, it has been described in a variety of conditions, the most frequent being isolated right ventricular hypertrophy caused by pressure overload, which affects the septal wall and produces a disproportional increase in septal wall thickness relative to the normal left ventricular posterior wall (11). Also a patient with left ventricular concentric hypertrophy that has sustained a posterior myocardial infarction (MI) can exhibit asymmetrical hypertrophy once thinning of the infarcted region and fibrosis has occurred. Amyloidosis, Freidriech's ataxia, myxedema, and D-transposition have all been associated with a disproportionate increase in septal wall thickness. Older people are sometimes found to have sigmoid-shape LV with a prominent basal septum which seems to bulge in the LVOT: this finding is probably due to a more acute angle between the septal bulge and the aortic root and is not considered a pathological state.

2. SAM and LVOT Obstruction

The SAM of the MV and subsequent LVOT obstruction can theoretically happen whenever predisposing conditions are reunited. Most of the conditions causing asymmetrical hypertrophy can also be associated with SAM and its consequences. The highest incidence of spontaneously occurring SAM outside HCM is D-transposition of the great vessels where it has been seen to occur after an atrial switch operation or in patients without corrective surgery (12). The SAM and LVOT obstruction have also been described in hypertensive older individuals with secondary left ventricular hypertrophy (LVH). This phenomenon is usually transient and occurs with hypovolemia secondary to gastrointestinal (GI) bleeding or excessive diuresis and resolves with volume repletion (see Fig. 9.10).

Two postoperative conditions may be complicated by SAM and hence, deserve special attention. Aortic valve replacement for AS in a patient with preexisting LVH can develop significant SAM in the postoperative period. This results from the acute reduction in afterload, which allows increased left ventricular ejection in a small LVOT, thereby producing subvalvular stenosis (see Fig. 9.34) or mid-ventricular obstruction. This is usually transient and responds well to volume loading and cessation of inotropic drugs, but in certain cases, surgical correction may be required (see Fig. 9.34) (13). Systolic anterior motion can also occur after MV repair for prolapse. This complication must be specifically looked for while in the OR after surgery. The incidence of LVOT obstruction after MV repair varies from 2% to 14% (14) and is more frequent with myxomatous changes involving both leaflets. The underlying mechanisms include anterior displacement of the coaptation point, a longer and redundant posterior leaflet (with or without a more acute mitroaortic angle), causing the MV apparatus to be displaced toward the LVOT and be dragged by the outflow, provoking typical SAM and subsequent subvalvular obstruction. Preoperatively, a longer posterior leaflet relative to the anterior (anterior/posterior length ratio ≤ 1.3) and a shorter distance (≤ 2.5 cm) between the coaptation point and the septum are predictors of SAM development postrepair (Fig. 10.8) (15). For some patients the problem can be alleviated by increasing left ventricular filling or by reducing inotropic support. However, other patients require MV replacement or subsequent repair. The sliding technique has been developed to decrease the incidence of this complication by reducing the posterior leaflet redundancy (Fig. 10.9) (16).

G. Monitoring Therapy

1. Intensive Care Unit and Noncardiac Surgery

In recent years, TEE has had an increasing role in hemodynamic monitoring. The HOCM patient can benefit from this tool, particularly in clinical situations with rapidly changing loading conditions in the intensive care unit (ICU) or the OR.

Noncardiac surgery is a stressful event for a patient with HOCM and may be associated with significant cardiac adverse events in as many as 40% of patients (17). Surgery is often associated with rapid shift of blood and volume, and anesthetic drugs frequently reduce vascular systemic resistance. All these conditions together promote the increase of LVOT obstruction. To

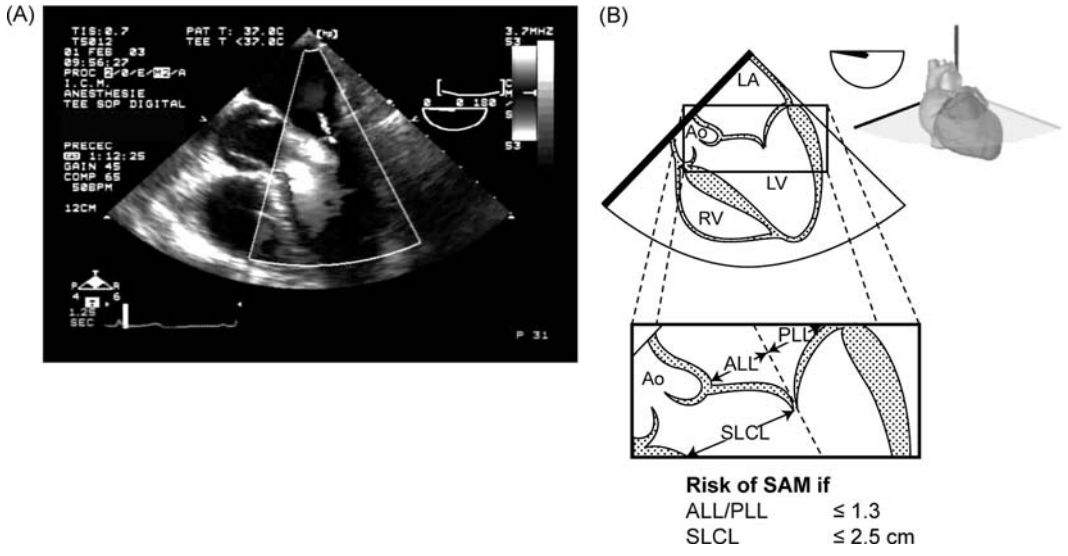

Figure 10.8 Assessing the risk for postoperative systolic anterior motion (SAM) after mitral valve repair. (A, B) Mid-esophageal four-chamber view measurements before septal resection (ALL, anterior leaflet length; Ao, aorta; LA, left atrium; LV, left ventricle; PLL, posterior leaflet length; RA, right atrium; RV, right ventricle; SAM, systolic anterior motion; SLCL, septal to leaflet coaptation length).

that effect, TEE can help carefully titrating fluid and drug administration. This method has been used with success in different surgical settings and will probably have an increasing role in the future (18).

Caring for a patient with HOCM in the Critical Care Unit can be difficult: while inotropes as well as vasodilators can paradoxically decrease the cardiac output by increasing the LVOT obstruction, invasive hemodynamic monitoring with Swan–Ganz catheter provides values of filling pressure usually increased and difficult to integrate in the presence of significant diastolic dysfunction. Transesophageal echocardiography is particularly useful in providing direct evaluation of LVOT obstruction, SAM, and degree of MR. Some authors have suggested that the volemic state be gauged serially by measuring the end-diastolic and end-systolic areas in transgastric short-axis views at the mid-papillary level (18). By integrating hemodynamic and echocardiographic monitoring data, it is easier to administer the ideal amount of fluid properly or to introduce and titrate drugs that reduces the inotropic state (calcium channel blockers, β-blockers) (Fig. 10.10) or selectively increase systemic vascular resistance (pure α-agonists as vasopressors) in order to minimize the LVOT obstruction (18).

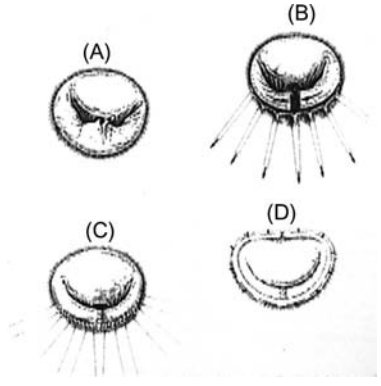

Figure 10.9 Illustration of the Carpentier sliding leaflet technique for preventing systolic anterior motion of the mitral leaflets. (A) In case of excess tissue of the mural leaflet, the quadrangular resection is completed by two triangular resections of the posterior leaflet remnants to correct excess tissue. (B) Remnants are translated medially to close the gap. (C, D) Repair is completed and an annuloplasty ring is implanted to reinforce the repair. [With permission of Jebara et al. (16).]

2. Nonsurgical Septal Ablation

Patients with HOCM typically suffer from exertional dyspnea, syncope or angina. Initial management typically involves negative inotropic drugs. Rarely, a dual chamber pacemaker can be implanted to improve symptoms, presumably by reducing the LVOT gradient. However, for those who remain symptomatic despite maximal medical therapy, mechanical relief of the obstruction should be considered. To that effect, surgical myomectomy has been, so far, the traditional treatment of choice (Fig. 10.1), but catheter-based septal ablation has evolved into an acceptable alternative in selected patients with isolated subaortic obstruction (19). Both techniques reduce LVOT obstruction and symptoms, possibly to a lesser extent with the percutaneous approach (19). Echocardiography is an essential tool to assist the operators for both interventions.

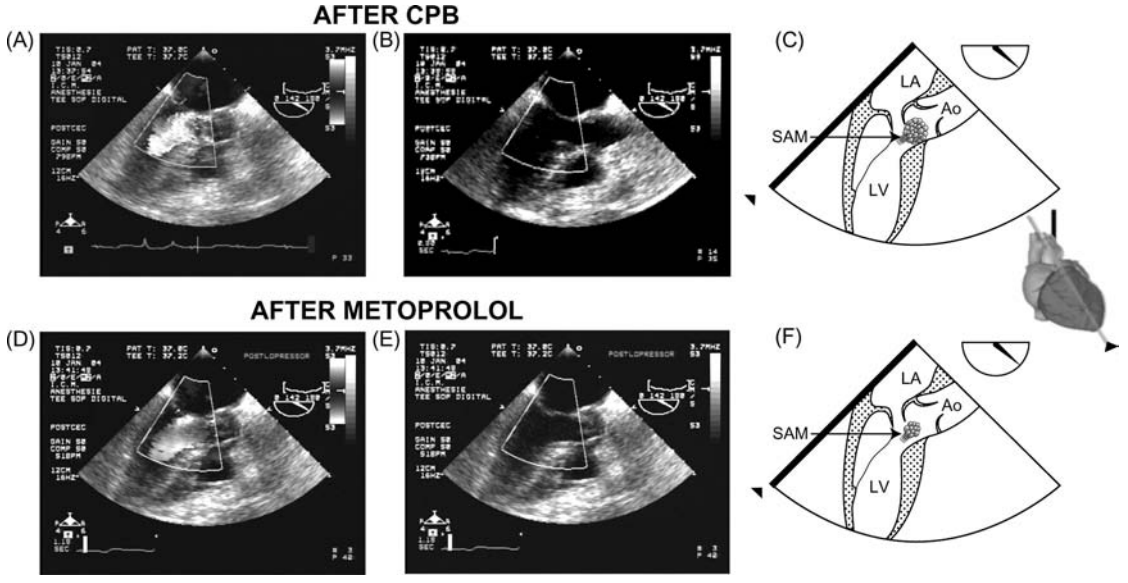

Figure 10.10 Flow acceleration in the left ventricular outflow tract in a 63-year-old hemodynamically unstable woman after coronary revascularisation. (A–C) Immediately after cardiopulmonary bypass (CPB). (D–F) Clinical improvement after administration of an intravenous bolus of metoprolol (Ao, aorta; AoV, aortic valve; LA, left atrium; LV, left ventricle; SAM, systolic anterior motion).

The first case of septal ablation with coronary ethanol injection was described in 1995. Selective injection of alcohol in one or two septal branches of the left anterior descending artery is performed to induce a localized septal myocardial infarction at the site of the SAM-septal contact. The proximal septal branch is selectively cannulated and an angioplasty balloon is initially positioned and inflated; angiographic contrast media is then injected through the distal lumen to identify unwanted potential of spillage back into the left anterior descending (LAD) or in another coronary bed by way of collaterals, before the definitive ethanol injection. At our institution, myocardial contrast echocardiography is routinely used before definitive alcohol injection to define the distribution of each potential septal branch and appropriately select the one(s) supplying the target myocardium (Fig. 10.11). This method minimizes the risk of major complications, such as papillary muscle, anterior or inferior wall extension of the infarct zone, and maximizes the success rate. Echocardiography together with continuous hemodynamic monitoring (aortic and apical left ventricular catheters) is used to monitor the acute changes in LVOT gradient. An immediate drop in the LVOT systolic pressure gradient is typically obtained (Fig. 10.12). Procedural success is usually defined as a 50% reduction in resting LVOT gradient or abolition of provocable gradient (Fig. 10.12) (19). When patients are carefully selected (LVOT obstruction with SAM in the absence of mitral valve structural anomaly), the procedure is successful in $>90\%$ of cases. Further improvement in LVOT gradient is expected during six- to twelve-month follow-up, as septal thinning and fibrosis supervenes. The most frequent complication of alcohol septal ablation is complete atrioventricular block, which occurs in 5–15% of cases. Ventricular septal defect is another potential risk, but has not been reported when the dimension of the treated septal wall exceeds 18 mm at baseline. Echocardiographic monitoring is done with TTE, but TEE can be used in poorly echogenic patients, to improve delineation of the mechanism of obstruction.

3. Surgical Septal Myectomy

The surgical septal myectomy was first described by Brock in 1957 and is still in use today. The procedure involves the removal of a rectangular portion of the hypertrophied septum by a transaortic approach. The surgery is very effective in relieving the obstruction and reducing the symptoms (19), with a mortality rate $<2\%$ in experienced centers (4). Although nonsurgical septal reduction has recently gained popularity, surgical septal myectomy remains the procedure of choice for patients with severe symptoms despite optimal medical therapy, or in patients who have concomitant surgical valvular or coronary artery disease warranting surgical correction.

The success of the procedure depends on excising the appropriate amount of septum in order to enlarge significantly the LVOT. This is believed to reduce the flow acceleration in the LVOT, alleviate the concomitant SAM and by doing so, relieve the obstruction and possibly the MR (4).

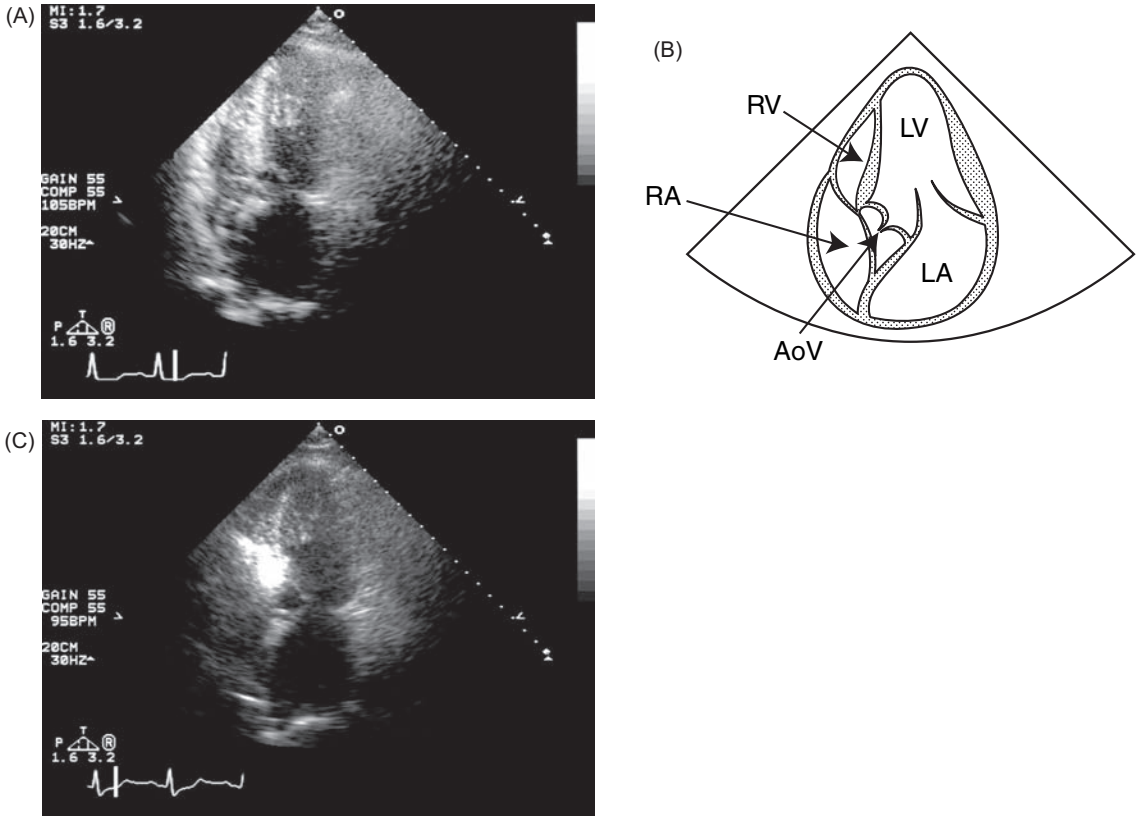

Figure 10.11 Percutaneous alcohol septal ablation. (A, B) Transthoracic apical five-chamber view before the procedure. (C) Myocardial contrast enhancement: the brightened septal area confirms that the septal branch to be injected is indeed the one providing the vascular supply to the systolic anterior motion (SAM) septal contact region (LA, left atrium; LV, left ventricle; RA, right atrium; RV, right ventricle).

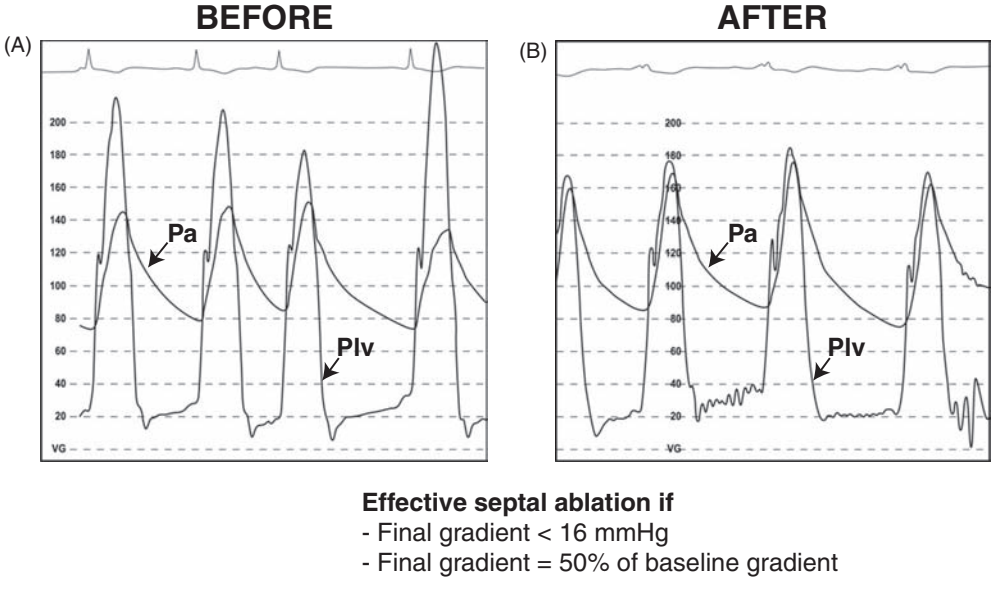

Figure 10.12 Left ventricular (Plv) and aortic pressure (Pa) hemodynamic tracings before (A) and immediately after (B) percutaneous septal ablation with alcohol. The resting systolic pressure gradient is greatly improved after ablation.

On the other hand, an excessive muscle resection can create a ventricular septal defect, either acutely or during the healing period (Fig. 10.13). In addition, complete AV block can occur in up to 7% of cases (19). Unfortunately, the surgeon has limited exposure to the LVOT and, in the past, the extent of the resection was frequently incomplete, the results being mainly gauged by simple palpation. Transesophageal echocardiography is now an invaluable tool to assist the surgeon in this task: the septum can be measured precisely (Fig. 10.1), and the extent and level of obstruction (usually the region of the septal–mitral contact, but not always) can be identified in order to guide the septal myectomy procedure (6). It is also helpful in evaluating the immediate postoperative results, and as many as 20% of the patients may need reinstitution of the cardiopulmonary bypass in order to correct a sub-optimal surgical result such as moderate residual MR.

As stated previously, a meticulous examination of the mitral apparatus is warranted to define the amount and mechanism of the MR. In a recent study (20), all patients free of anatomic MV abnormality exhibit significant reduction of the MR by septal myectomy alone, and none needed MV surgery. In contrast, half of the patients with superimposed mitral pathology needed valve surgery in addition to their septal myectomy procedure. Interestingly, 97% of the "pure" HOCM-related MR is directed posteriorly compared with 0% in those with additional causes of MR. Thus, a MR jet directed posteriorly seems to predict a good response to surgery. Intraoperative isoproterenol is used in our institution to evaluate not only to confirm the severity of the preoperative obstruction hypertrophy but also to assess the surgical result of the procedure (Fig. 10.14).

II. DILATED CARDIOMYOPATHY

A. Epidemiology

Dilated cardiomyopathy (DCM) is characterized by dilatation and impaired systolic function of the left or both ventricles (1). The prevalence in the USA is 36 cases per 100,000 of population, where it is the most common indication for

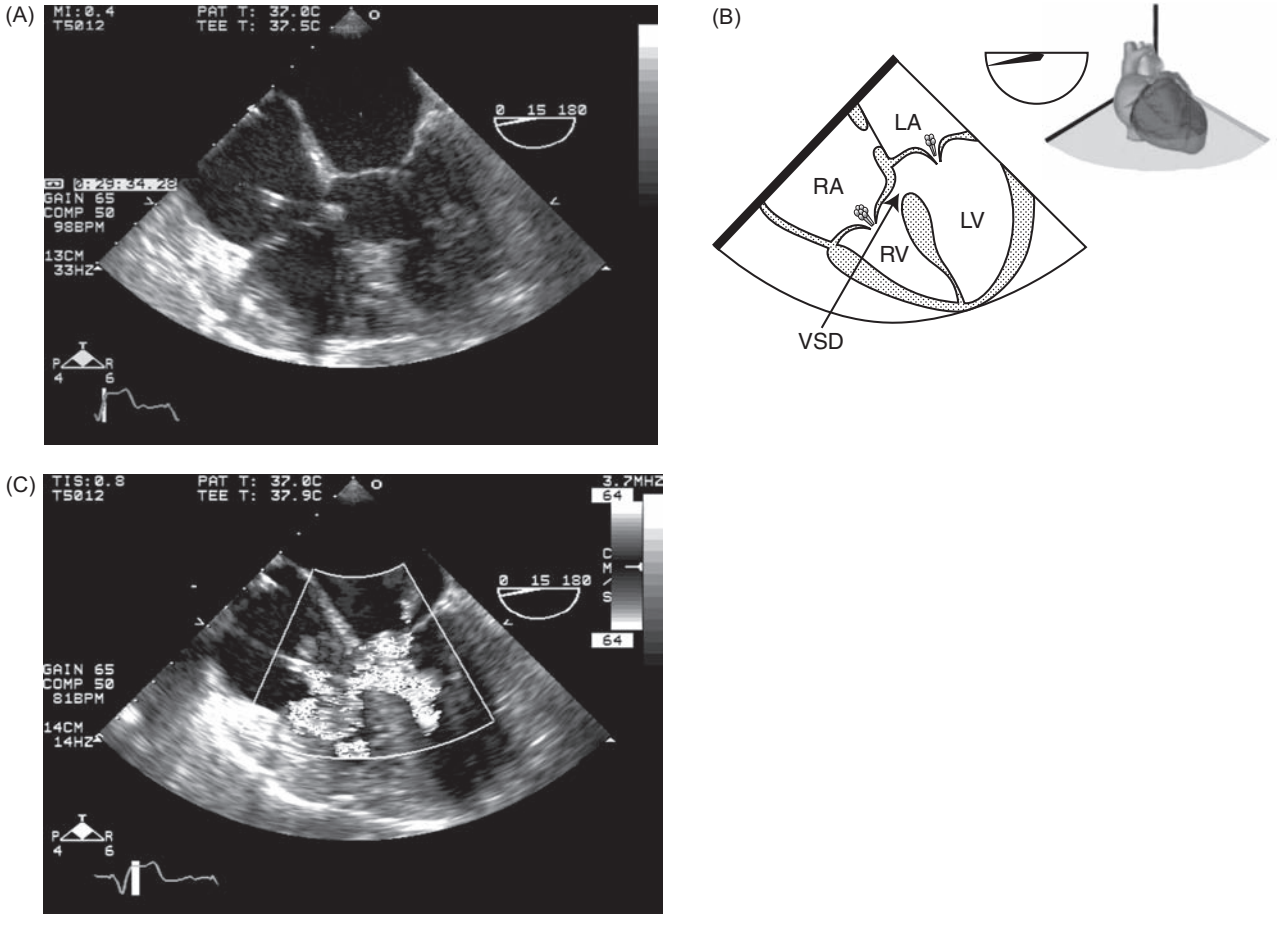

Figure 10.13 Ventricular septal defect (VSD) occurring 2 weeks after surgical septal myectomy. (A, B) The mid-esophageal four-chamber view demonstrates the VSD at the site of the myectomy. (C) Color Doppler depicts flow going across the interventricular septum with an important left-to-right shunt through the VSD (LA, left atrium; LV, left ventricle; RA, right atrium; RV, right ventricle).

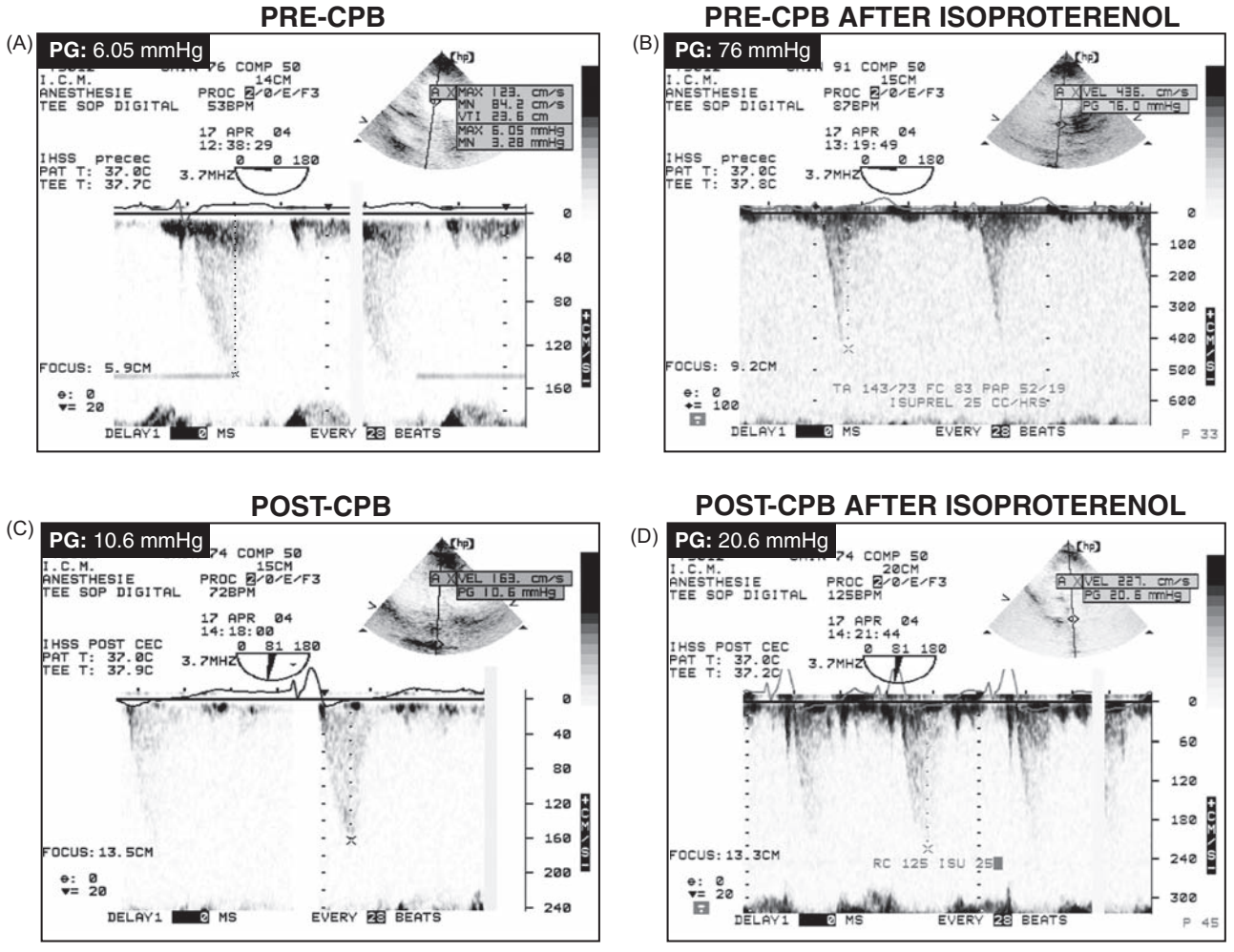

Figure 10.14 Maximum pressure gradient (PG) before (A) and after isoproterenol (B) at 1.6 μg/min in a 46-year-old man with hypertrophic cardiomyopathy before cardiopulmonary bypass (CPB). (C, D) Following septal myectomy the increase in the PG was less pronounced after the use of isoproterenol.

cardiac transplantation. The possible etiology is extensive and includes causes of ischemic, valvular, hypertensive, toxic (alcohol, adriamycin), metabolic, peri-partum, inflammatory, infectious, and neuromuscular origins. Familial cause constitutes 20–30% of cases, usually transmitted in an autosomal dominant fashion. The diagnosis of *idiopathic* DCM should be reserved for patients in whom no other etiologic factor can be found after a thorough evaluation. Unfortunately, the echocardiographic features provide little insight into the underlying cause and DCM usually represents a final common pathway for different disorders.

B. Clinical Features

Dyspnea, fatigue and edema are the most frequent symptoms of DCM, with 95% of the patients having symptomatic manifestations of heart failure during the course of their illness. Some will complain of exertional chest pain indistinguishable from angina, even in the absence of epicardial coronary stenosis. This is believed to be secondary to increased wall stress with reduced coronary flow reserve. Ventricular or supraventricular arrhythmias are frequent in DCM, but sudden death is unusual at initial presentation, although it can occur in 12% of these patients during the course of their disease (21). Thromboembolic events can occur with an incidence at 1–3% patient/year (22), originating either from ventricular or atrial chambers, the latter usually being associated with atrial fibrillation.

C. Echocardiographic Features

1. *Chambers Dilatation*

The hallmark of DCM is left, and to a variable degree, right ventricular dilatation. Systolic and diastolic dimensions and

volumes are both increased. They are typically >50 mm in systole and >70 mm in diastole. As stated previously, it is recommended that the dimension of the LV be measured using M-mode in the transgastric short-axis view at the level of the papillary muscles (Fig. 10.15). The ventricular volumes can be estimated with the Simpson's method of disks, but this technique applied to TEE often underestimates the true volume because of foreshortening of the apex. Ventricular mass is also increased, principally because of enlarged LV, with variable increase in wall thickness, developing in order to reduce wall stress. This finding seems to identify patients with a better prognosis (23).

Right ventricular involvement is variable and usually parallels left ventricular dilatation. Its involvement secondary to pulmonary hypertension or tricuspid regurgitation (TR) can also be found. Occasionally, the RV is spared by disease, in which case an ischemic etiology should be suspected. Right and left atrial dilatation is common as a result of chronically elevated filling pressure and/or atrial fibrillation.

2. Ventricular Systolic Dysfunction

Reduced contractility is the hallmark of DCM. Evaluation of global and segmental wall motion should be done using multiple windows; the transgastric short-axis views at 0° are particularly useful for this purpose (Fig. 10.15). The decrease in systolic function is typically diffuse, but regional wall motion abnormalities can be present, suggesting an underlying ischemic etiology. However, this finding is neither sensitive nor specific for coronary artery disease (CAD), as regional wall motion abnormalities have been described in DCM in the absence of coronary lesion.

Many techniques have been described to quantify systolic function (Chapter 5): "E" point–septal separation (Fig. 10.16), volumetric-based measurements, Doppler-derived stroke volume quantification, dP/dt evaluation, myocardial performance index calculation, or simple global visual estimation. All these methods reflect, to a variable extent, the depressed systolic function. The

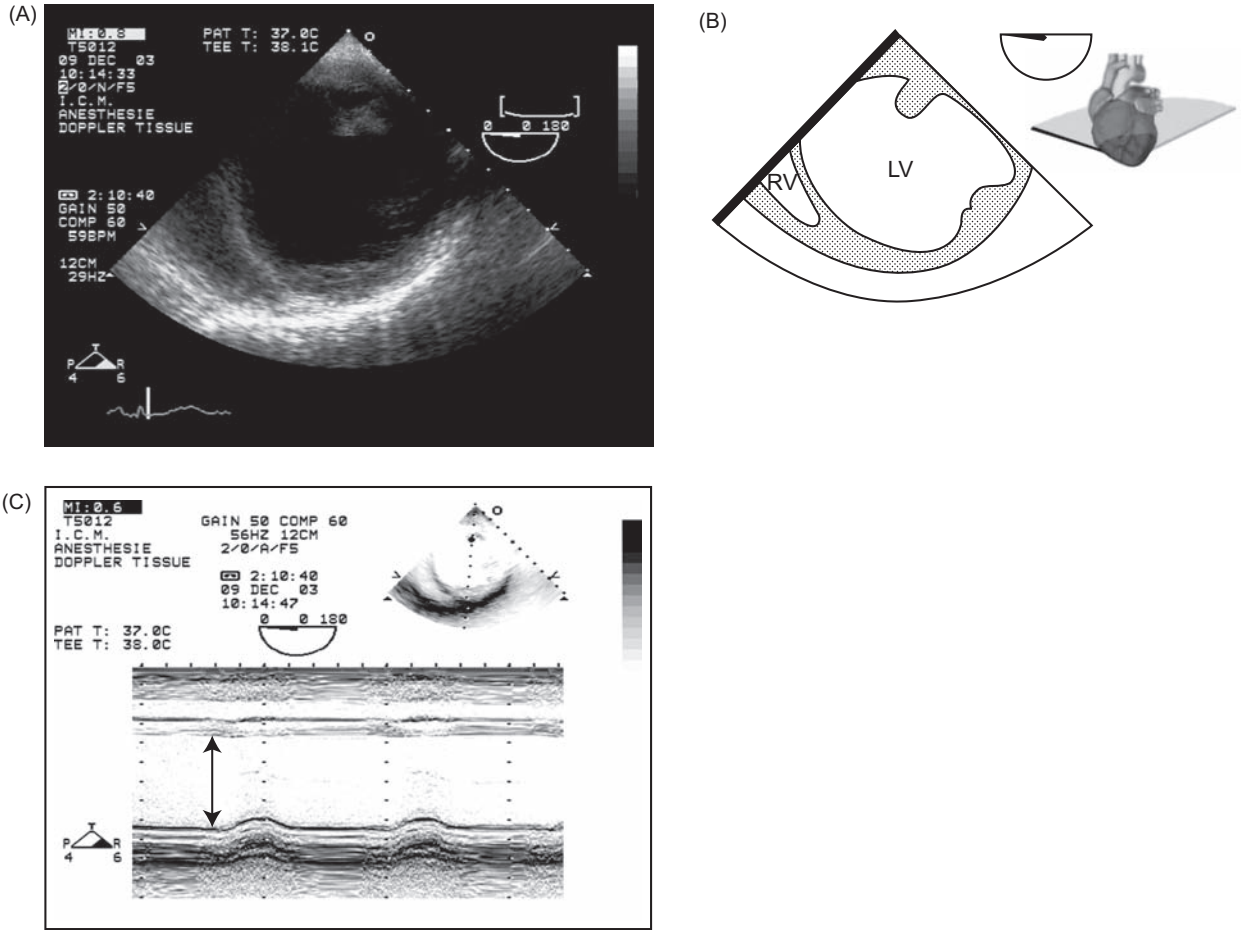

Figure 10.15 (A, B) Transgastric mid-papillary view in a 56-year-old woman with dilated ischemic cardiomyopathy. (C) M-mode measurements show akinesis of the inferior wall and hypokinesis of the anterior wall. The left ventricular end-diastolic diameter (arrow) is 7.1 cm (Normal <5.5 cm) (LV, left ventricle; RV, right ventricle).

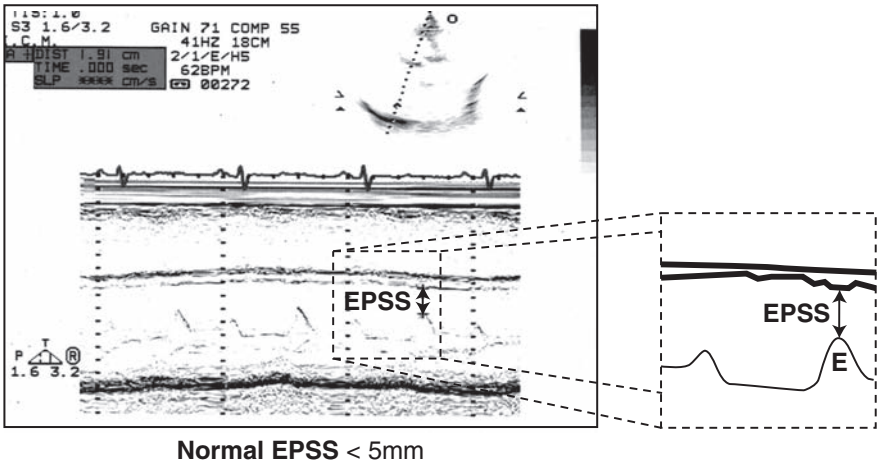

Figure 10.16 Transthoracic parasternal long-axis view showing an increased E point septal separation (EPSS) on an M-mode tracing of a patient with dilated cardiomyopathy.

ejection fraction correlates inversely, although roughly, to the prognosis.

3. Diastolic Dysfunction

Patients with DCM can exhibit all the different patterns of diastolic dysfunction. Pulsed-wave Doppler of the mitral inflow is used to characterize the degree of dysfunction, from abnormal relaxation (with "E/A" < 1 and prolonged deceleration time (DT > 250 ms) to a restrictive filling pattern (with short DT < 150 ms and "E/A" > 2), or the intermediate pseudonormal profile. Interestingly, the severity of diastolic dysfunction carries independent prognostic implication in addition to left ventricular ejection fraction (LVEF) and clinical status (NYHA class): patients with severe diastolic dysfunction and restrictive filling pattern (shorter DT, "E/A" > 2) have a worse prognosis in terms of need for transplantation, or death (24). Moreover, patients who revert to a milder degree of diastolic dysfunction with medical treatment have a better prognosis than those who persistently exhibit a restrictive filling pattern despite optimal therapy (25). Furthermore, attenuation of the systolic flow in the pulmonary vein reflects increased left-sided filling pressures and has also been shown to be an independent predictor of adverse events (Fig. 10.17) (26).

4. Secondary Findings

Mitral regurgitation is frequently present with DCM. It results from incomplete coaptation of the leaflets, with two underlying mechanisms: (1) alteration in the geometry of the subvalvular and valvular apparatus and/or (2) dilatation of the annulus. Because of the ventricular dilatation, apical displacement of the papillary muscles occurs, creating traction on the leaflets and displacing their coaptation point apically. This impairs the ability of the leaflets to coapt normally, their closing point occurring only at their tips, and therefore incompletely. Annular dilatation can exacerbate this already incomplete coaptation by modifying the geometry of the MV annulus (from a saddle-shape to a more circular shape), thus increasing the valve area that needs to be sealed. The resulting central regurgitant jet could be semiquantified by color flow Doppler. Other adjunct methods (PISA, Doppler quantification, pulmonary venous flow patterns) are also helpful in grading the severity of MR and estimating left atrial pressure (Fig. 10.18). Of note, severe MR with secondary left ventricular dilatation and dysfunction can sometimes be confused with a primary cardiomyopathic process with secondary MR. Careful examination of the mitral apparatus and the regurgitant jet will usually determine the initial underlying mechanism.

Tricuspid regurgitation can be secondary to right ventricular dilatation (and annular dilatation) or from postcapillary pulmonary hypertension. In the absence of RVOT obstruction, the maximum TR velocity can be used to estimate the pulmonary artery systolic pressure, although the angle of Doppler interrogation may not be ideal in TEE (Fig. 10.19).

Ventricular thrombi are also associated with DCM, usually found at the apex of the LV; they are believed to result from blood stasis caused by the low flow velocity (Fig. 10.20). The adjacent left ventricular wall is usually akinetic or even aneurysmal. The thrombus' echogenicity is usually different from the underlying myocardium, helping to differentiate between the two. Multiple views should confirm their presence and help to differentiate a thrombus from prominent left ventricular trabeculations or false tendon and aberrant chords. Round and protruding thrombi are easy to demonstrate; in contrast, laminated thrombi (Fig. 10.20) may be more difficult to diagnose

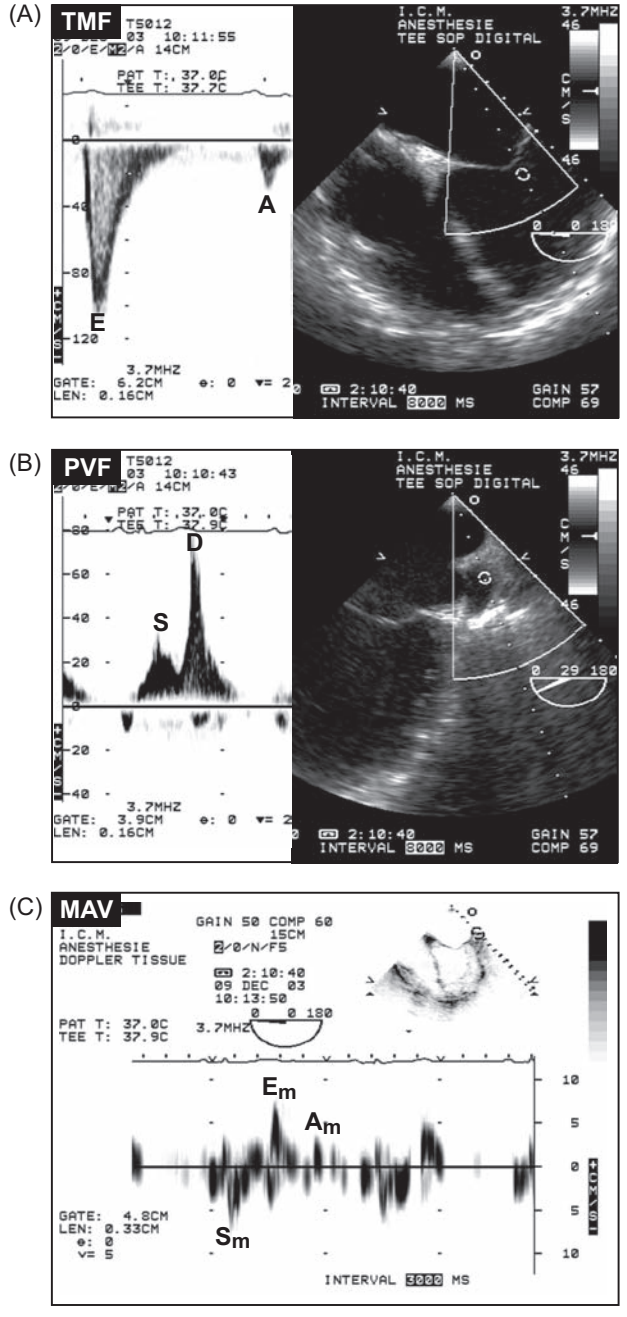

Figure 10.17 Stage III diastolic dysfunction (restrictive left ventricular filling) in a 56-year-old woman with dilated ischemic cardiomyopathy. Pulsed-wave Doppler interrogation of the transmitral flow (TMF) (A), pulmonary venous flow (PVF) (B), and tissue Doppler examination of the lateral mitral annulus (C) (MAV, mitral annular velocity).

and must be suspected whenever the apical cavity has an unusually round appearance, or if akinetic apical walls exhibit normal or even increased thickness. The sensitivity of the TTE is good (>90%), and even better than TEE because of the inherent foreshortening of the apex in the

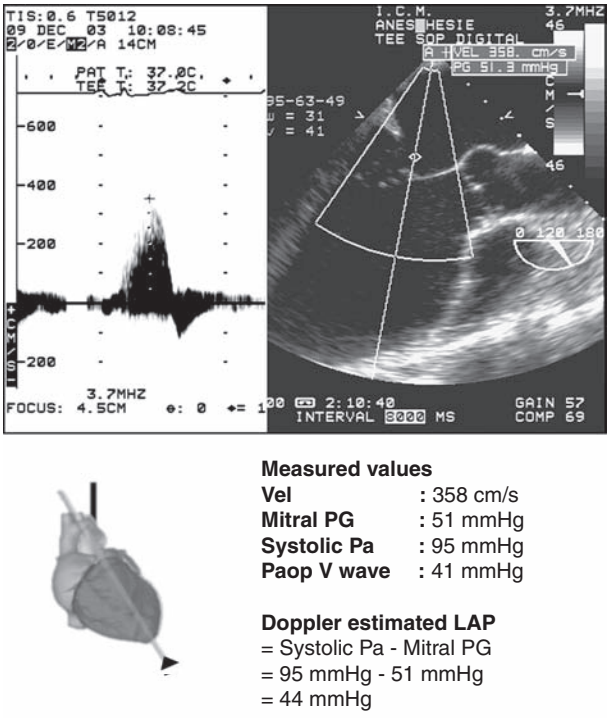

Figure 10.18 Estimation of left atrial pressure using the mitral regurgitation signal in a 56-year-old woman with dilated ischemic cardiomyopathy prior to coronary revascularization, surgical ventricular remodeling and mitral valve repair. The maximal pressure gradient (PG) between the left ventricle and left atrium was 51 mmHg. If we assume that the systolic arterial pressure (Pa = 95 mmHg) is equal to the left ventricular systolic pressure, the estimated maximal left atrial pressure (LAP) is (95 mmHg − PG) equal to 44 mmHg. The pulmonary artery occlusion pressure (Paop) showed a "V" wave of 41 mmHg (Vel, velocity).

transesophageal views. Nevertheless, it is possible to image the apex and identify a thrombus even with TEE, using mid-esophageal views with retroflexion of the probe and some additional lateral tilting as needed. The propensity of such thrombus to cause embolic event is variable. It is probably higher in the month following a MI, or with mobile or protruding thrombus in the LV cavity. Anticoagulation is clinically recommended whenever a left ventricular thrombus is found. As mentioned in Chapter 14, ruling out apical thrombus is of paramount importance before proceeding to the insertion of a left-ventricular assist device.

Left atrial thrombus, usually located in the left atrial appendage, is also found in patients with DCM and can be a source of embolism (Fig. 10.21). This finding is usually encountered in the presence of atrial fibrillation. Spontaneous swirling echo contrast can also be demonstrated and has been associated with an increased incidence of thromboembolic events.

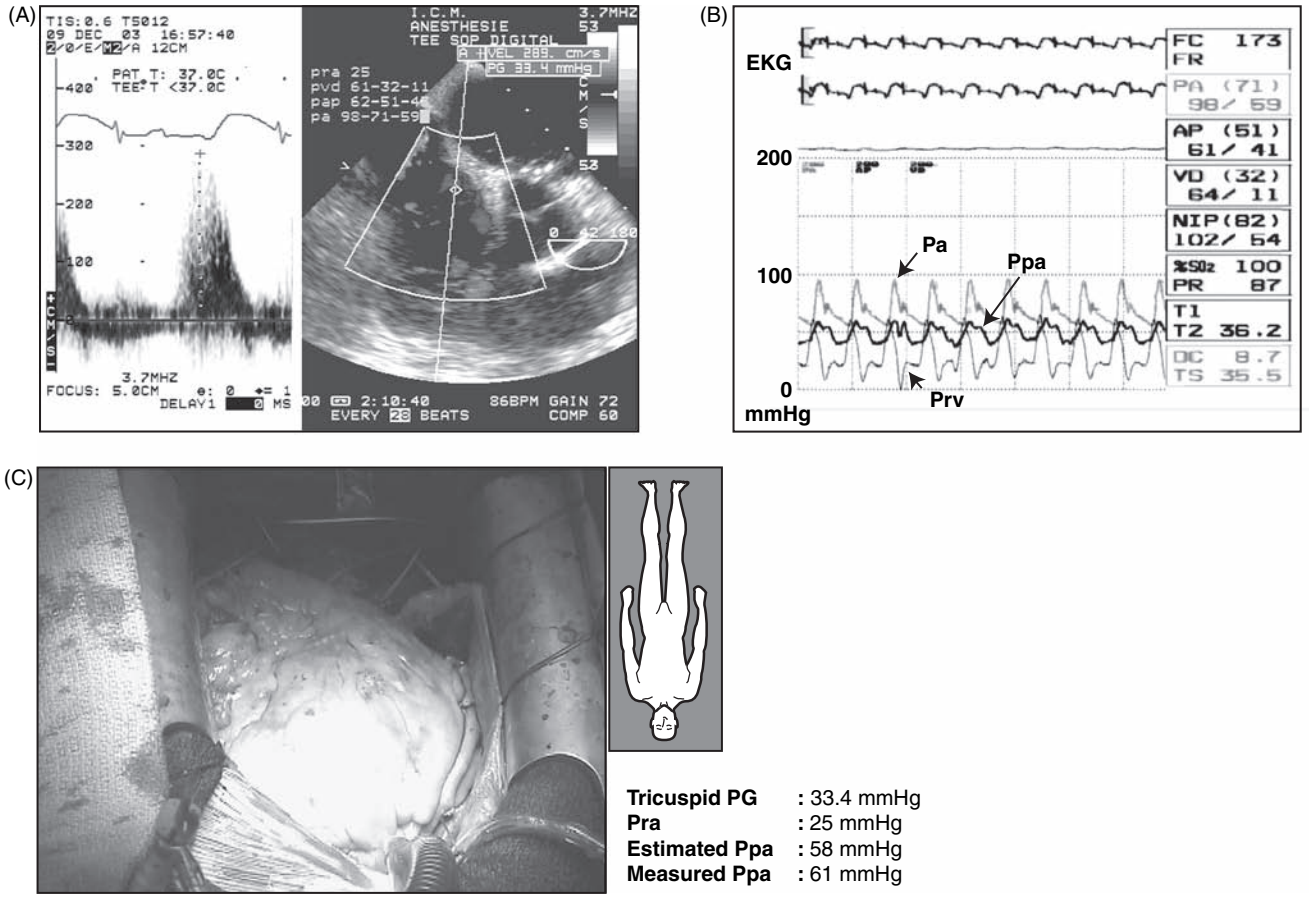

Figure 10.19 Acute tricuspid regurgitation associated with right ventricular dysfunction in a 56-year-old woman with dilated ischemic cardiomyopathy after revascularization, surgical ventricular remodeling and mitral annuloplasty. (A) The tricuspid regurgitation maximum pressure gradient (PG) was 33.4 mmHg and the estimated systolic pulmonary artery pressure (Ppa) was 58 mmHg. (B) This estimation was close to the measured Ppa value of 61 mmHg. Note the square root appearance of the right ventricular pressure (Prv) waveform associated with right ventricular dysfunction. (C) Intraoperative aspect of the dilated right ventricle after the procedure (EKG, electrocardiogram; Pa, arterial pressure; Pra, right atrial pressure). (Photo C courtesy of Dr. Pierre Pagé.)

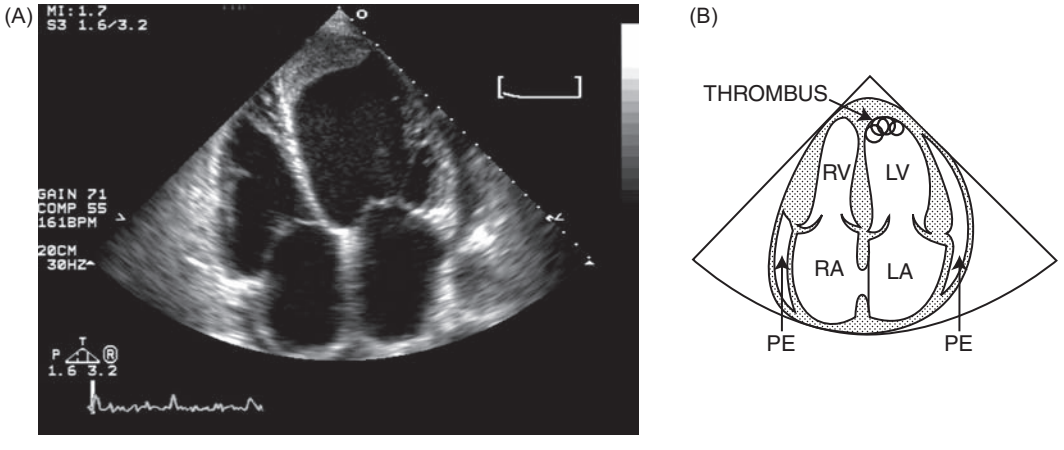

Figure 10.20 Transthoracic apical four-chamber view in a patient with dilated cardiomyopathy, showing a laminated left ventricular apical thrombus (LA, left atrium; LV, left ventricle; PE, pericardial effusion; RA, right atrium; RV, right ventricle).

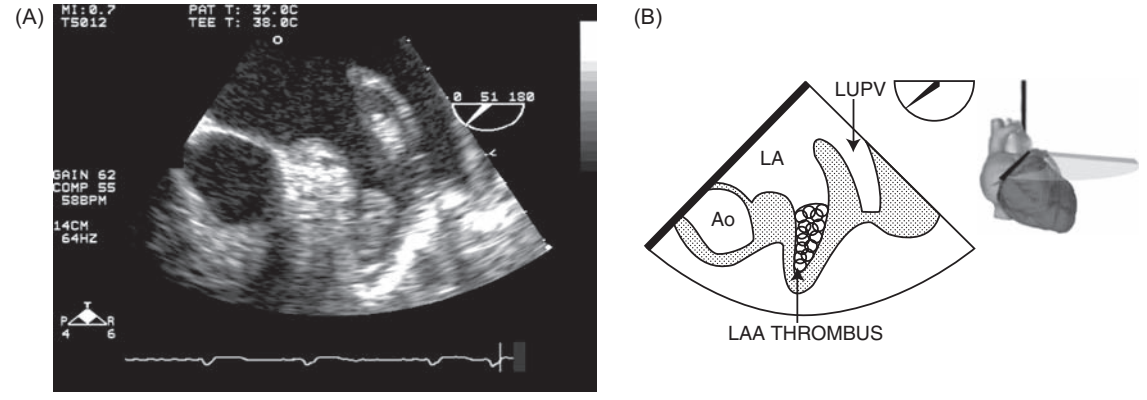

Figure 10.21 Upper-esophageal 51° view of a patient with atrial fibrillation and dilated cardiomyopathy. A thrombus is seen in the left atrial appendage (LAA) (Ao, aorta; LA, left atrium; LUPV, left upper pulmonary vein).

D. Noncompacted LV

In humans, the LV is less trabeculated than the RV, but rarely more than three prominent trabeculations in the LV can be found; many names have been given to this abnormality, including spongy myocardium, persistant myocardial sinusoids, left ventricular hypertrabeculation or more frequently left ventricular noncompaction (LVNC). Many cases with LVNC have been primarily misdiagnosed as hypertrophic cardiomyopathy (27), dilated cardiomyopathy (28), restrictive cardiomyopathy (29), endocardial fibroelastosis (30), or endomyocardial fibrosis (31). Recent developments in echocardiography with second harmonics imagings permit a better visualization of the left ventricular apical regions, including detection of trabeculations and recesses and suggest that LVNC has a higher prevalence than previously thought.

1. Epidemiology

The prevalence of LVNC varies from 0.05% to 0.24% per year in echocardiographic studies, probably reflecting both ethnic differences and increasing awareness of this abnormality in certain centers. Men represented two-thirds of cases, due to possible X-linked recessive inheritance (32) with heterogeneity. Several genetic mutations have been described including genes encoding for dystrophin or α-dystrobrevin, and also for transcription factors limited to the heart and mitochondrial mutations (33).

2. Clinical Features

Heart failure symptoms are predominant, being present in 52% of the patients, usually associated with left ventricular systolic dysfunction, followed by palpitations or syncope (16%) (34). Prognosis is poor with premature death by either end-stage heart failure or sudden death (50% of the fatality) (35). The electrocardiogram is abnormal in 94% of the patients, with signs of LV hypertrophy and ST-T changes. Wolff–Parkinson–White syndrome, ventricular tachycardia (41%, primarily nonsustained), abnormalities in cardiac conduction system and atrial fibrillation have also been reported (34). The pathophysiologic mechanisms of heart failure, systolic dysfunction, and arrhythmia in LVNC are unknown, but myocardial ischemia may play a role. In addition, LVNC is believed to be associated with embolic events, but the majority of reported cases also presented other risk factors for increased embolic risk, such as atrial fibrillation, left ventricular systolic dysfunction or malignancy (36). Nevertheless, 24% of patients presented with embolic symptoms (35). Thus, it is currently uncertain whether LVNC with its intramyocardial recesses is a source of cardiac embolism or whether associated abnormalities are responsible for the embolic events.

3. Anatomical Features (Pathoanatomic Findings)

The intramyocardial recesses are usually located at the left ventricular apex and its adjacent parts of the lateral and inferior walls, probably due to regional nonuniformity, in which the thickest part of the LV wall is basal and the myocardium becomes thinner toward the apex. Three different morphology of LVNC has been described: (1) extensive spongy transformation of the myocardium, similar to an hemangioma, and frequently associated with other cardiac morphologic abnormalities (30); (2) prominent coarse trabeculations of the ventricular wall and deep recesses of the ventricular cavity, covered with endocardium, not communicating with the coronary arteries and usually not associated with other cardiac morphologic abnormalities (28); and (3) a dysplastic appearance of the myocardium with thinned myocardium and excessive trabeculations, not associated with other cardiac morphologic abnormalities (37). Currently, it is uncertain whether these

different morphologies represent different diseases or diverse stages of the same disease process.

At least five *pathogenetic concepts* have been suggested to explain the occurrence of LVNC. Complete description is beyond the scope of this chapter and can be found elsewhere (34).The term isolated ventricular noncompaction is used to describe an idiopathic cardiomyopathy characterized by an altered structure of the myocardial wall, but the World Health Organisation has not yet classified it as a distinct pathology.

4. *Echocardiographic Features*

The typical echocardiographic image of noncompacted myocardium is characterized by an altered structure of the left ventricular myocardium with extremely thickened, hypokinetic ventricular segments consisting of two layers. There is a thin epicardial compacted zone and a thicker noncompacted endocardial zone, with deep recesses filled with blood from the left ventricular cavity (34). Since there are no established clinical diagnostic criteria, different echocardiographic criteria for LVNC have been suggested. One classification relies on an anatomical definition, with more than three trabeculations within one imaging plane, located apically from the insertion of the papillary muscles, and diagnosed by echocardiography, magnetic resonance imaging (MRI), or computed tomography (CT) (36). Others have suggested methods for quantification of LVNC, by (1) the depth of the intertrabecular recesses in relation to the thickness of the myocardium or (2) the ratio of noncompacted to compacted layers of the myocardium at end-systole ($N/C \geq 2$). These methods are not precise, being dependent of the location of the measurements and volume status of the patient. In addition, suboptimal images quality may preclude adequate assessment of the depths of the recesses. Additional echocardiographic findings include usually variable degrees of left ventricular diastolic dysfunction, enlarged left ventricular end-diastolic dimensions (67%) and reduced systolic function (82%). In a series of 34 patients, left ventricular thrombi were documented in 10% of cases (35).

5. *Conclusion*

Left ventricular noncompaction seems to be more often recognized due to improvement of cardiac imaging technique. As for any rare entity, clinical awareness is the key to diagnosis, even though controversies still persist about diagnostic criteria, nomenclature, pathogenesis, and the necessity to classify LVNC as a distinct cardiomyopathy.

E. Nontransplant Surgery

With the increasing prevalence of heart failure and the limited organ supply for transplant, new surgical therapies have emerged in order to help patients with end-stage heart failure. Partial left ventriculotomy (Batista procedure), dynamic cardiomyoplasty, patch ventriculoplasty or isolated MV repair are procedures designed to unload the LV, reduce the wall stress in order to increase heart performance and alleviate symptoms (Fig. 10.22). The role of TEE in these settings is yet to be defined.

III. RESTRICTIVE AND INFILTRATIVE CARDIOMYOPATHY

A. Definition

Restrictive cardiomyopathy (RCM) is characterized by a myocardial process that restricts ventricular filling, resulting in elevated ventricular diastolic pressures, typically with normal or slightly decreased systolic function and usually with normal ventricular size; it can affect the LV or both ventricles. Etiologies are numerous and include storage diseases, infiltrative disorders, myocardial noninfiltrative process and endomyocardial diseases (Fig. 10.23). Idiopathic forms have been described, usually from a familial cluster, with or without associated peripheral myopathy. Taken together, RCM is much less frequently encountered than its dilated or hypertrophic counterpart. In contrast to DCM with their common final findings, the unique features of the different restrictive conditions warrant separate considerations. We will briefly review the typical findings of RCM and then discuss more specifically the features of amyloidosis, sarcoidosis and hemochromatosis.

B. Clinical Findings

Restrictive left ventricular filling with elevated diastolic pressures is the hallmark of the disease. Increased filling pressures from left ventricular involvement lead to dyspnea, exercise intolerance, and orthopnea. Congestive peripheral manifestations such as elevated jugular venous pressure, peripheral edema and ascite can be prominent features, as the RV is also frequently involved in the process. These clinical findings in a patient without cardiomegaly should raise the suspicion of either RCM or constrictive pericarditis. The differentiation between the two is important as surgical resection of the pericardium could cure the latter. Arrhythmias, mainly atrial fibrillation, and conduction system disease are often associated with RCM.

A search for involvement of other organs is essential in the diagnosis, as it can help identify an underlying systemic disease responsible for the cardiac manifestations which could, although rarely, respond to a specific treatment.

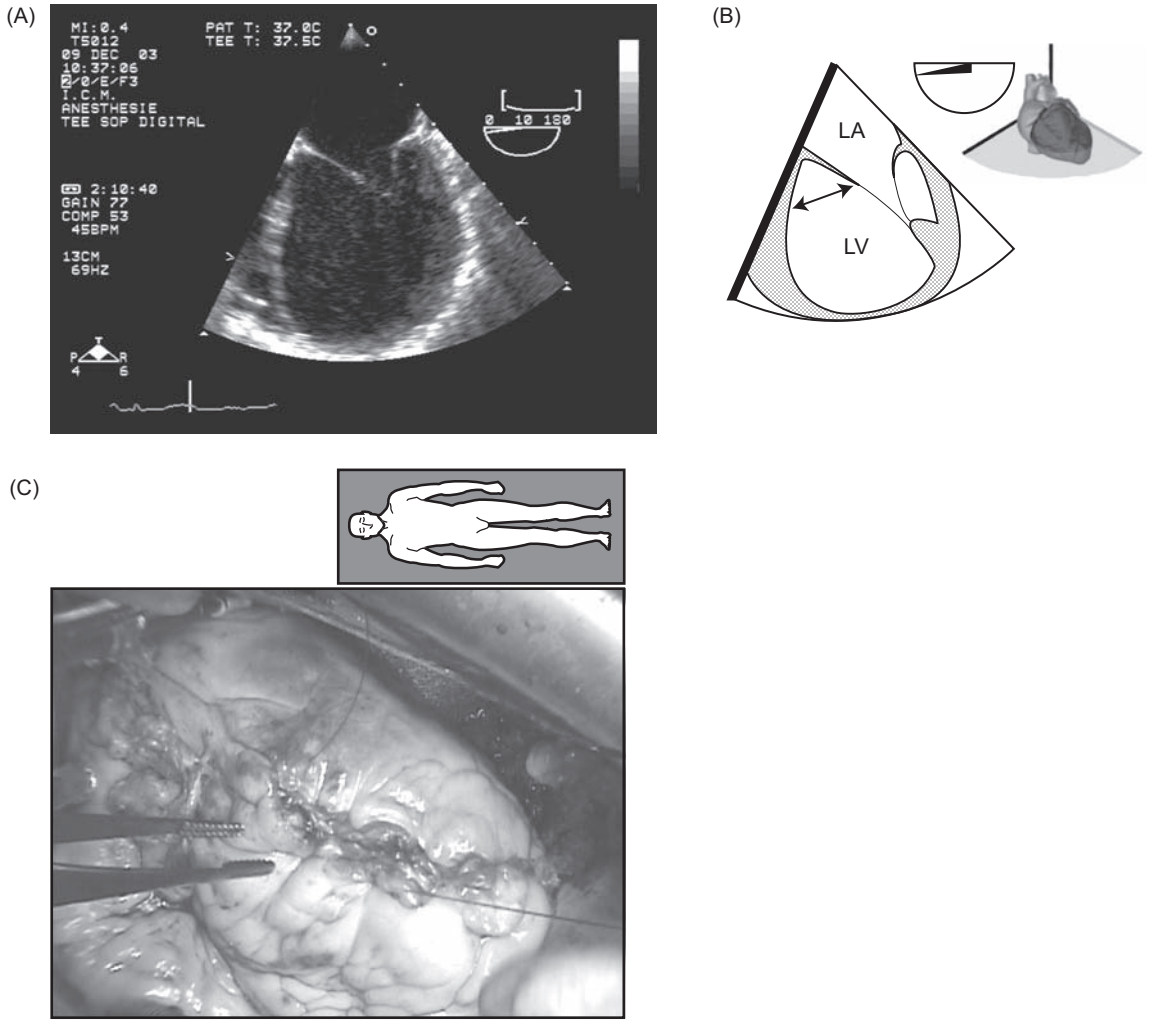

Figure 10.22 (A, B) Mid-esophageal four-chamber view in a 56-year-old woman with dilated ischemic cardiomyopathy before coronary revascularization, surgical ventricular remodeling and mitral valve repair. Note the increased septal to anterior mitral leaflet separation (arrow). (C) Surgical aspect of the heart after remodeling (LA, left atrium; LV, left ventricle). (Photo C courtesy of Dr. Pierre Pagé.)

C. Echocardiographic Features

Ventricular dimensions and systolic function are usually normal in RCM. Wall thickness, although typically normal in idiopathic form, can be increased in infiltrative disorders like amyloidosis. In contrast, the left and right atria are markedly enlarged because of chronically elevated filling pressures. In one study, the presence of an LA size >60 mm was an independent predictor of mortality in patients with idiopathic RCM (38).

The demonstration of abnormal filling patterns of both ventricles is necessary for a diagnosis of RCM. PW Doppler interrogation of mitral and tricuspid inflow, pulmonary and hepatic venous flow (when feasible) should be done. Typically, a restrictive filling pattern is encountered, with elevated early "*E*" wave velocity, short mitral deceleration time and increased "E/A" ratio (>2). Because of the elevated left atrial pressure, the MV opening occurs earlier, shortening the isovolumic relaxation time (IVRT) and producing an increased early diastolic "*E*" wave velocity; because of increased ventricular stiffness, the left ventricular diastolic pressure rises rapidly during atrial emptying and LV filling, leading to an abrupt ending of the early diastolic filling with a short DT: this is the equivalent of the square root sign seen on the pressure curves of the LV or RV. Giving the already elevated diastolic pressure, the atrial contribution to ventricular filling is reduced with a smaller "*A*" wave velocity in the mitral inflow patterns and an increased atrial reversal flow velocity and duration (a) in the pulmonary and hepatic venous flows. The increased pressure is also reflected by a reduced systolic forward component of the

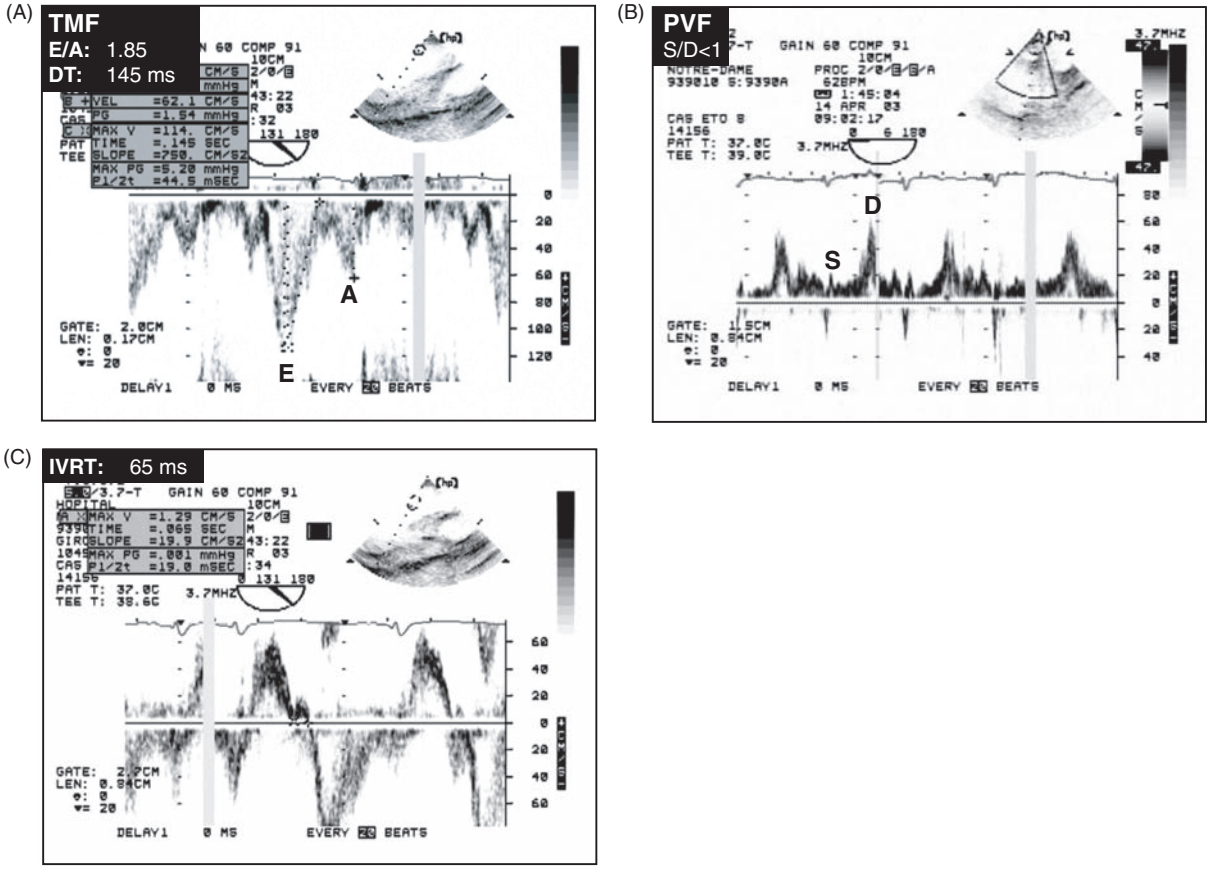

Figure 10.23 Stage III diastolic dysfunction in a 36-year-old ventilator-dependent patient with Duchenne dystrophy. A restrictive diastolic filling pattern was confirmed using pulsed-wave Doppler interrogation of the transmitral flow (TMF) (A), pulmonary venous flow (PVF) (B), and measurement of the isovolumic relaxation time (IVRT) which was shortened at 65 ms (C). The patient died shortly after hospitalization (DT, deceleration time).

venous flow, producing diastolic flow velocity predominance with a S/D ratio <1.

The restrictive filling pattern is the classic diastolic profile encountered in RCM, particularly when symptoms are overt. Interestingly enough, less severe forms can be found earlier in the course of the disease or after aggressive treatment of reversible etiologies. Alternatively, restrictive filling pattern can also be demonstrated in the absence of RCM in severe DCM, severe aortic regurgitation (AR) or significant hypertrophy.

D. Difference Between Restrictive Cardiomyopathy and Constrictive Pericarditis

It is critical to distinguish RCM from constrictive pericarditis, as the latter can manifest with the same clinical findings, but can be cured with surgical removal of the diseased pericardium. Some echocardiographic characteristics help to differentiate the two conditions. One of the key elements is the demonstration of ventricular interdependence. In constrictive pericarditis, because of the fixed volume caused by the rigid pericardium, ventricular volume respiratory variation in one cavity is associated with reciprocal change in the opposite one, which is best appreciated using the respiratory profile provided by a respirometer. With inspiration, the RV enlarges from increased venous return and, in presence of pericardial constriction, the LV will become smaller. This can be demonstrated by two-dimensional or sometimes even better by M-mode examination through short-axis transgastric views. Doppler respiratory variations will exhibit reciprocal and exaggerated changes ($>25\%$) of the mitral and tricuspid inflow velocities as well as diastolic pulmonary venous flow blunting or reversal, which resolves after pericardiectomy. Newer techniques like Doppler tissue imaging of the mitral annular motion or color M-mode seem promising in discriminating the two pathologies (see Fig. 11.22). Some other but less specific findings such as elevated pulmonary pressures, more

than moderate MR (or TR) or increased wall thickness may all suggest the presence of RCM. In contrast, finding a thickened or calcified pericardium rather suggests constrictive pericarditis.

Besides echo, other diagnostic tools are available to help identify the correct diagnosis: hemodynamic pressure tracings from left and right heart catheterization, clinical clues, thoracic imaging (MRI, CT), and endomyocardial biopsy. An integrated approach is needed to find the correct diagnosis in the majority of the cases.

E. Amyloidosis

Cardiac amyloidosis is the most frequent RCM. It is caused by amyloid fibrils deposition in the myocardium, valve tissue, atrial septum, pericardium, and conduction system. Cardiac involvement is usually associated with the primary and senile forms of amyloidosis.

Echocardiographic features include a progressive increase in right and left ventricular wall thickness [discordant with the presence of low QRS voltage on electrocardiography (ECG)], typically symmetrical with a characteristic "speckled" appearance and normal-sized or even small ventricular cavities (Fig. 10.24). The severity of the wall thickening is a prognostic marker. In addition, the systolic function is preserved until late in the course of the disease. Small to moderate pericardial effusion is also commonly encountered (Fig. 10.24). Of note, SAM and LVOT obstruction can sometimes coexist and be confused with HCM (39). A thickened atrial septum with multivalvular involvement (multiple regurgitation, usually mild), again with low QRS voltage on ECG are useful clues to the diagnosis of amyloidosis.

Although a restrictive filling pattern is typically encountered in advanced disease, observational studies have shown that in some patients the degree of diastolic dysfunction, which parallels disease progression may evolve in time. The patients initially exhibit a delayed relaxation pattern ("E/A" <1, prolonged DT), progressing to a pseudonormal and finally to the typical restrictive filling profile. The severity of diastolic dysfunction encountered is highly correlated to the prognosis: the shorter the DT, the worse the survival (40).

F. Sarcoidosis

Sarcoidosis is a granulomatous disorder involving multiple systems of unknown etiology. The lungs and mediastinal lymph nodes are the most commonly involved, although virtually any organ can be infiltrated by these noncaseating granulomas. Heart involvement is clinically present in $\sim$5–10% of patients, but reaches 25% in autopsy series, suggesting that a high degree of suspicion is necessary in these patients. Cardiac sarcoidosis may affect the ventricular septum with secondary conduction abnomalities, the papillary muscle with associated MR or the pericardium. Even more troublesome is the fact that sudden death can be the first cardiac manifestation of the disease (41).

Echocardiography is a useful tool for the assessment of cardiac involvement and its severity. Myocardial sarcoidosis leads to fibrosis, resulting in increased stiffness, like RCM, but with earlier decrease in systolic function and ventricular dilatation as a rule. Regional wall motion abnormalities are frequent even in the absence of coronary artery disease, and tend to involve the basal and midventricular segments. This finding is believed to result from the patchy involvement by granulomas. Ventricular aneurysm can also be found. Severe pulmonary sarcoidosis can also lead to pulmonary hypertension and secondary right ventricular hypertrophy with variable degree of dysfunction, without myocardial involvement *per se*.

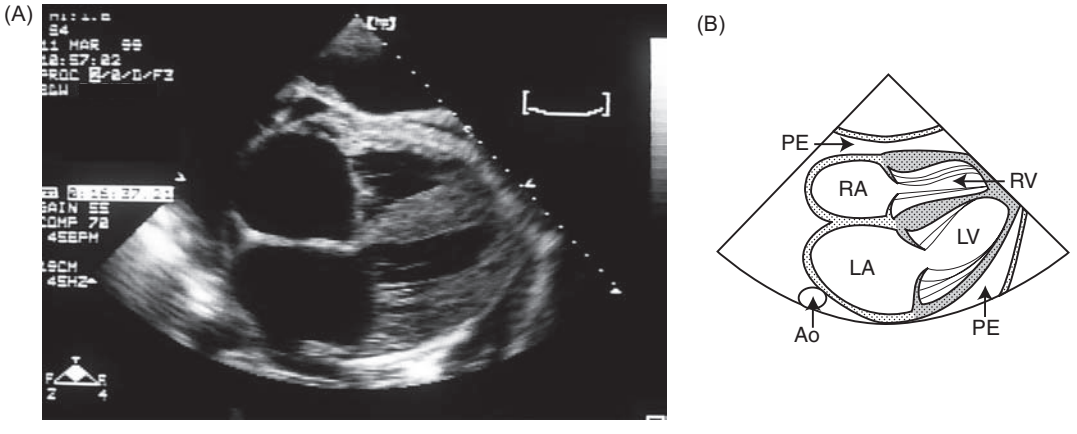

Figure 10.24 Transthoracic subcostal view of a patient with amyloidosis. Note the biatrial dilatation, the increased ventricular wall thickness with the characteristic sparkling appearance and the small circumferential pericardial effusion (PE) (Ao, aorta; LA, left atrium; LV, left ventricle; RA, right atrium; RV, right ventricle).

G. Hemochromatosis

Hemochromatosis is one of the most frequent autosomal recessive diseases and causes iron deposition in tissues, resulting in heart failure, hepatic cirrhosis and diabetes, as well as pituitary, skin, and gonadal involvement. A clinical picture indistinguishable from the primary form can be seen with iron overload secondary to multiple transfusions for the treatment of severe anemia. Cardiac involvement is the first manifestation of the presence of the disease in 15% of patients and is the cause of death in 30% of untreated patients. Early diagnosis is important, as the heart disease can be reversed with phlebotomy, at least initially.

The echocardiographic features of symptomatic cardiac hemochromatosis are dilatation of the LV or both ventricles with reduced systolic function, which can be mimicked (42). Wall thickness can be slightly increased, particularly in the earlier stage of the disease when the LV diameters and function are still normal. The valves appear to be spared by the process. Echocardiography is also a useful tool in the evaluation of response to treatment.

IV. CONCLUSION

Echocardiography is an essential tool for the diagnosis of different categories of cardiomyopathy; it also helps in the identification of the associated abnormalities that can be encountered in specific diseases and can markedly influence the treatment of a given patient. Moreover, it can also be useful in the evaluation of the response of an individual to a specific treatment. Finally, TEE is an invaluable tool in the monitoring of these patients when undergoing noncardiac surgery or when they suffer from superimposed acute illnesses.

REFERENCES

1. Richardson P, McKenna W, Bristow M et al. Report of the 1995 World Health Organization/International Society and Federation of Cardiology Task Force on the Definition and Classification of cardiomyopathies. Circulation 1996; 93:841–842.
2. Maron BJ, Gardin JM, Flack JM et al. Prevalence of hypertrophic cardiomyopathy in a general population of young adults. Echocardiographic analysis of 4111 subjects in the CARDIA Study. Coronary Artery Risk Development in (Young) Adults. Circulation 1995; 92:785–789.
3. Braunwald E. Hypertrophic cardiomyopathy—continued progress. N Engl J Med 1989; 320:800–802.
4. Spirito P, Seidman CE, McKenna WJ, Maron BJ. The management of hypertrophic cardiomyopathy. N Engl J Med 1997; 336:775–785.
5. Pollick C, Morgan CD, Gilbert BW et al. Muscular subaortic stenosis: the temporal relationship between systolic anterior motion of the anterior mitral leaflet and the pressure gradient. Circulation 1982; 66:1087–1094.
6. Grigg LE, Wigle ED, Williams WG et al. Transesophageal Doppler echocardiography in obstructive hypertrophic cardiomyopathy: clarification of pathophysiology and importance in intraoperative decision making. J Am Coll Cardiol 1992; 20:42–52.
7. Schwammenthal E, Nakatani S, He S et al. Mechanism of mitral regurgitation in hypertrophic cardiomyopathy: mismatch of posterior to anterior leaflet length and mobility. Circulation 1998; 98:856–865.
8. Braunwald E. Heart Disease: A Textbook of Cardiovascular Medicine. 5th ed. Philadelphia: W.B. Saunders, 1997.
9. Henry WL, Clark CE, Epstein SE. Asymmetric septal hypertrophy. Echocardiographic identification of the pathognomonic anatomic abnormality of IHSS. Circulation 1973; 47:225–233.
10. Spirito P, Maron BJ. Relation between extent of left ventricular hypertrophy and diastolic filling abnormalities in hypertrophic cardiomyopathy. J Am Coll Cardiol 1990; 15:808–813.
11. Maron BJ, Clark CE, Henry WL et al. Prevalence and characteristics of disproportionate ventricular septal thickening in patients with acquired or congenital heart diseases: echocardiographic and morphologic findings. Circulation 1977; 55:489–496.
12. Maron BJ, Gottdiener JS, Perry LW. Specificity of systolic anterior motion of anterior mitral leaflet for hypertrophic cardiomyopathy. Prevalence in large population of patients with other cardiac diseases. Br Heart J 1981; 45:206–212.
13. Schwinger ME, O'Brien F, Freedberg RS, Kronzon I. Dynamic left ventricular outflow obstruction after aortic valve replacement: a Doppler echocardiographic study. J Am Soc Echocardiogr 1990; 3:205–208.
14. Lee KS, Stewart WJ, Lever HM et al. Mechanism of outflow tract obstruction causing failed mitral valve repair. Anterior displacement of leaflet coaptation. Circulation 1993; 88:II24–II29.
15. Maslow AD, Regan MM, Haering JM et al. Echocardiographic predictors of left ventricular outflow tract obstruction and systolic anterior motion of the mitral valve after mitral valve reconstruction for myxomatous valve disease. J Am Coll Cardiol 1999; 34:2096–2104.
16. Jebara VA, Mihaileanu S, Acar C et al. Left ventricular outflow tract obstruction after mitral valve repair. Results of the sliding leaflet technique. Circulation 1993; 88:II30–II34.
17. Haering JM, Comunale ME, Parker RA et al. Cardiac risk of noncardiac surgery in patients with asymmetric septal hypertrophy. Anesthesiology 1996; 85:254–259.
18. Nam E, Toque Y, Quintard JM et al. Use of transesophageal echocardiography to guide the anesthetic management of cesarean section in a patient with hypertrophic cardiomyopathy. J Cardiothorac Vasc Anesth 1999; 13:72–74.
19. Qin JX, Shiota T, Lever HM et al. Outcome of patients with hypertrophic obstructive cardiomyopathy after percutaneous transluminal septal myocardial ablation and septal myectomy surgery. J Am Coll Cardiol 2001; 38:1994–2000.

20. Yu EH, Omran AS, Wigle ED et al. Mitral regurgitation in hypertrophic obstructive cardiomyopathy: relationship to obstruction and relief with myectomy. J Am Coll Cardiol 2000; 36:2219–2225.
21. Dec GW, Fuster V. Idiopathic dilated cardiomyopathy. N Engl J Med 1994; 331:1564–1575.
22. Hunt SA, Baker DW, Chin MH et al. ACC/AHA Guidelines for the Evaluation and Management of Chronic Heart Failure in the Adult: Executive Summary A Report of the American College of Cardiology/American Heart Association Task Force on Practice Guidelines (Committee to Revise the 1995 Guidelines for the Evaluation and Management of Heart Failure): Developed in Collaboration with the International Society for Heart and Lung Transplantation; Endorsed by the Heart Failure Society of America. Circulation 2001; 104:2996–3007.
23. Feild BJ, Baxley WA, Russell RO Jr. et al. Left ventricular function and hypertrophy in cardiomyopathy with depressed ejection fraction. Circulation 1973; 47:1022–1031.
24. Xie GY, Berk MR, Smith MD et al. Prognostic value of Doppler transmitral flow patterns in patients with congestive heart failure. J Am Coll Cardiol 1994; 24:132–139.
25. Pinamonti B, Zecchin M, Di Lenarda A et al. Persistence of restrictive left ventricular filling pattern in dilated cardiomyopathy: an ominous prognostic sign. J Am Coll Cardiol 1997; 29:604–612.
26. Dini FL, Dell'Anna R, Micheli A et al. Impact of blunted pulmonary venous flow on the outcome of patients with left ventricular systolic dysfunction secondary to either ischemic or idiopathic dilated cardiomyopathy. Am J Cardiol 2000; 85:1455–1460.
27. Sakamoto T. Apical hypertrophic cardiomyopathy (apical hypertrophy): an overview. J Cardiol 2001; 37(suppl 1): 161–178.
28. Angelini A, Melacini P, Barbero F, Thiene G. Evolutionary persistence of spongy myocardium in humans. Circulation 1999; 99:2475.
29. Hamamichi Y, Ichida F, Hashimoto I et al. Isolated noncompaction of the ventricular myocardium: ultrafast computed tomography and magnetic resonance imaging. Int J Cardiovasc Imaging 2001; 17:305–314.
30. Allenby PA, Gould NS, Schwartz MF, Chiemmongkoltip P. Dysplastic cardiac development presenting as cardiomyopathy. Arch Pathol Lab Med 1988; 112:1255–1258.
31. Mousseaux E, Hernigou A, Azencot M et al. Endomyocardial fibrosis: electron-beam CT features. Radiology 1996; 198:755–760.
32. Bleyl SB, Mumford BR, Brown-Harrison MC et al. Xq28-linked noncompaction of the left ventricular myocardium: prenatal diagnosis and pathologic analysis of affected individuals. Am J Med Genet 1997; 72:257–265.
33. Stollberger C, Finsterer J, Valentin A et al. Isolated left ventricular abnormal trabeculation in adults is associated with neuromuscular disorders. Clin Cardiol 1999; 22:119–123.
34. Stollberger C, Finsterer J. Left ventricular hypertrabeculation/noncompaction. J Am Soc Echocardiogr 2004; 17:91–100.
35. Oechslin EN, Attenhofer Jost CH, Rojas JR et al. Long-term follow-up of 34 adults with isolated left ventricular noncompaction: a distinct cardiomyopathy with poor prognosis. J Am Coll Cardiol 2000; 36:493–500.
36. Stollberger C, Finsterer J, Blazek G. Left ventricular hypertrabeculation/noncompaction and association with additional cardiac abnormalities and neuromuscular disorders. Am J Cardiol 2002; 90:899–902.
37. Duru F, Candinas R. Noncompaction of ventricular myocardium and arrhythmias. J Cardiovasc Electrophysiol 2000; 11:493.
38. Ammash NM, Seward JB, Bailey KR et al. Clinical profile and outcome of idiopathic restrictive cardiomyopathy. Circulation 2000; 101:2490–2496.
39. Oh JK, Tajik AJ, Edwards WD et al. Dynamic left ventricular outflow tract obstruction in cardiac amyloidosis detected by continuous-wave Doppler echocardiography. Am J Cardiol 1987; 59:1008–1010.
40. Klein AL, Hatle LK, Taliercio CP et al. Serial Doppler echocardiographic follow-up of left ventricular diastolic function in cardiac amyloidosis. J Am Coll Cardiol 1990; 16:1135–1141.
41. Newman LS, Rose CS, Maier LA. Sarcoidosis. N Engl J Med 1997; 336:1224–1234.
42. Olson LJ, Baldus WP, Tajik AJ. Echocardiographic features of idiopathic hemochromatosis. Am J Cardiol 1987; 60:885–889.

11

Pericardium

YAN-FEN SHI, ANDRÉ Y. DENAULT, JEAN-CLAUDE TARDIF
University of Montreal, Montreal, Canada

I. Normal Pericardium 241
II. Pericardial Effusion and Cardiac Tamponade 242
A. Pericardial Effusion 243
1. Location, Volume, and Nature of Pericardial Effusion 243
2. Differentiating Pericardial Effusion from Epicardial Fat, Pleural Fluid 243
B. Cardiac Tamponade 244
1. Two-Dimensional Echocardiographic Features of Cardiac Tamponade 248
2. Doppler Features in Cardiac Tamponade 250
3. Localized Chamber Compression from Hematoma 250
4. Pericardiocentesis and Surgical Drainage Assessment 251
III. Constrictive Pericarditis 252
A. Echocardiographic Findings in Constrictive Pericarditis 252
B. Differentiating Constrictive Pericarditis from Restrictive Cardiomyopathy 253
IV. Pericardial Cyst 258
V. Congenital Absence of the Pericardium 259
References 259

Echocardiography is widely used to assess the pericardium and extracardiac anatomical structures for evaluation of conditions such as pericardial effusion (PE). Doppler evaluation in relation to respiratory changes has given useful insights into the physiological consequences of these abnormalities and helped to confirm the presence of cardiac tamponade or differentiate pericardial constriction from restrictive cardiomyopathy. Finally, echocardiography has become extremely useful in aiding diagnostic pericardiocentesis and catheter drainage as well as in evaluating the results of surgical drainage and pericardiectomy.

I. NORMAL PERICARDIUM

The pericardium prevents unrestrained wide displacement of this organ in the thoracic cavity during body motion. The outer pericardial layer is fibrous and lined with a serous surface (the parietal pericardium) which is reflected over the epicardium (as the visceral pericardium) (Fig. 11.1). Those two layers delineate a virtual space, the pericardial cavity, which completely surrounds the heart with the exception of areas located posteriorly near the origin of the great vessels. These areas, where the parietal and visceral pericardium meet, constitute pericardial reflections. As a result of these, the pericardial sac behind the heart forms two blind pockets: the transverse sinus is small, horizontal and located under the ascending aorta and pulmonary trunk (Figs. 11.2 and 11.3); the oblique sinus is relatively larger, vertically oriented and interposed between the pulmonary veins (Fig. 11.3). The pericardial space normally contains a small amount of serous liquid (20–50 mL), lubricating the normal heart movements (rotation and translation) during the cardiac cycle.

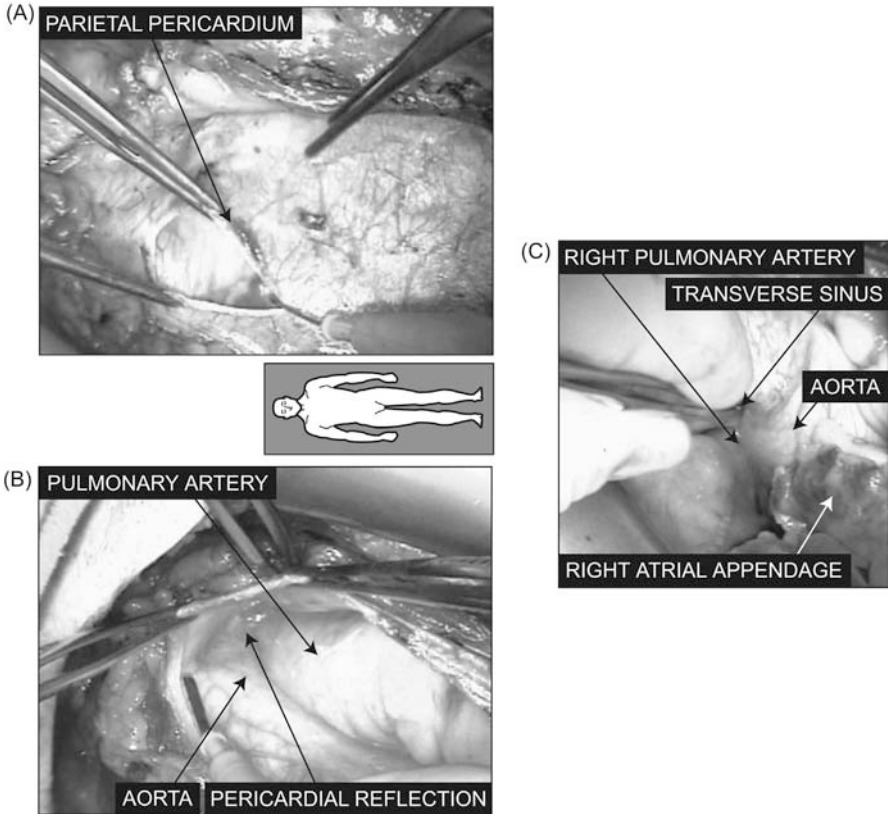

Figure 11.1 Intraoperative view of the pericardium. (A) The fibrous pericardium is opened. (B) A pericardial reflection is seen close to the ascending aorta and pulmonary artery. (C) The transverse sinus is shown under the ascending aorta in front of the right pulmonary artery. (Courtesy of Dr. Michel Pellerin.)

II. PERICARDIAL EFFUSION AND CARDIAC TAMPONADE

The amount of serous liquid in the pericardial sac can increase due to inflammation, myocardial infarction, bacterial or viral infection, neoplasia or intracardiac–pericardial communication. The resulting larger collection of pericardial fluid separates the visceral pericardium from the parietal layer. When pericardial pressure exceeds intracardiac pressure, the PE causes cardiac tamponade. Even with the recent advances in medical imaging, echocardiography remains an extremely valuable tool in the diagnosis of PE and cardiac tamponade.

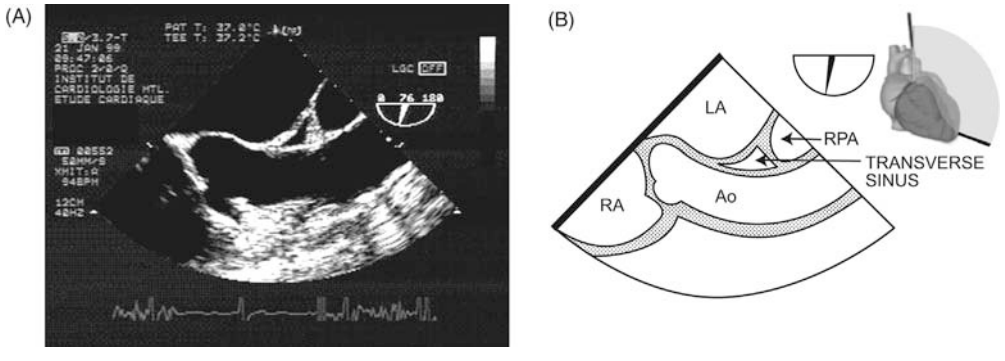

Figure 11.2 Mid-esophageal long-axis view of the ascending aorta. Pericardial fluid is present in the transverse sinus (Ao, aorta; LA, left atrium; RA, right atrium; RPA, right pulmonary artery).

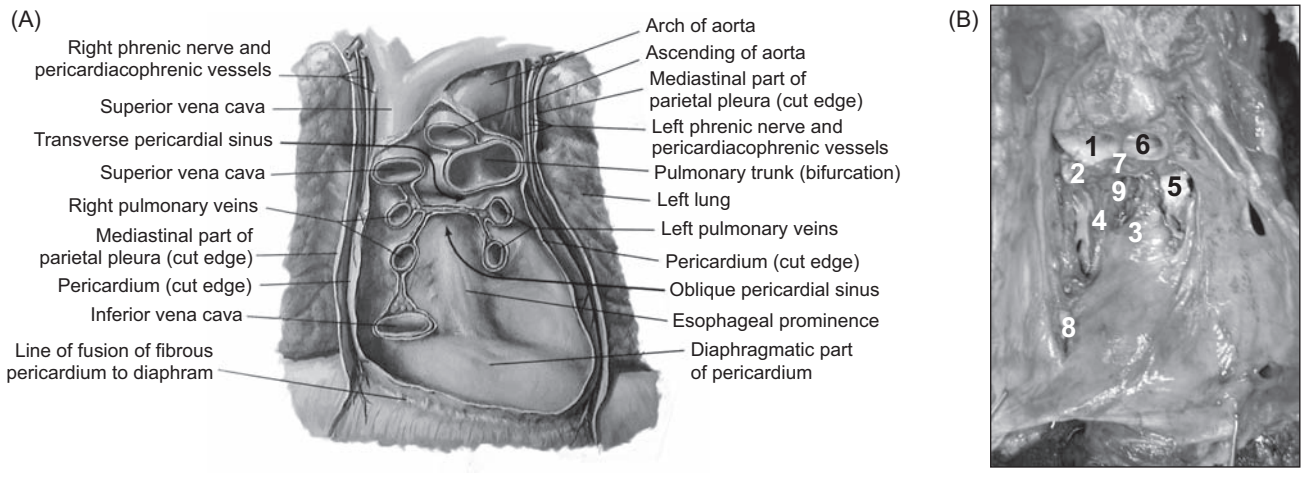

Figure 11.3 Pericardial sac with the heart removed. (A) Anatomical drawing. (B) Autopsy specimen (1, ascending aorta; 2, superior vena cava; 3, oblique sinus; 4, right pulmonary veins (superior and inferior); 5, left pulmonary veins (superior and inferior); 6, pulmonary artery; 7, ligamentum arteriosum; 8, inferior vena cava; 9, transverse sinus). [Reproduced with permission from Netter and Yonkman (1). Photo (B) courtesy of Dr. Nicolas Dürrleman.]

A. Pericardial Effusion

1. Location, Volume, and Nature of Pericardial Effusion

A PE is recognized on echocardiography as a clear space adjacent to the cardiac structures, enclosed in the pericardial sac by the parietal pericardium. Two types of effusion may be observed: free effusions, where the pericardial fluid is able to move within the pericardial sac without limitations, and loculated effusions, where the pericardial fluid is enclosed within a compartment in the pericardial sac (Figs. 11.4 and 11.5). With the patient recumbent or in left lateral decubitus, excess pericardial fluid tends to move posteriorly and laterally. With increased PE, it extends laterally and apically, being characteristically less prominent at the apex than at the base of the heart. With greater fluid collection, the echo-free space extends up to the posterior atrioventricular groove, and behind the left atrium (LA), in the oblique sinus, with decreasing amount of fluid from the left ventricle (LV) to the LA. The transthoracic echocardiographic subcostal view can demonstrate fluid between the diaphragm and the right ventricle (RV). On transesophageal echocardiography (TEE), pericardial fluid will be noticeable in the transverse sinus (Figs. 11.2, 11.4, and 11.5) between the ascending aorta and the right pulmonary artery. Moreover, it can accumulate in front of the left atrial appendage (LAA) next to the LV (Fig. 11.4).

In long-standing inflammatory PEs, adherences between the visceral and parietal pericardium may stretch as the gradually accumulating fluid separates the two layers: a web of adherences between the two layers then becomes apparent. If fibrous bridges rupture, echogenic fibrous strands may become visible in the effusion and on the epicardial surface (Fig. 11.4). Pericardial effusions sometimes become loculated between adherences, depending on their distribution.

Assessment of the volume of free PEs is, at best, semiquantitative and is based on the size of the heart and the distribution of fluid around it. The following estimations of PEs may be used: a PE <50 mL may not be reliably detected. Small effusions (<200 mL) are usually only detectable posteriorly. Moderate effusions (200–500 mL) are generally present both posteriorly and anteriorly and can have a thickness of up to ~ 1.5 cm. Although large (>500 mL) PEs are most often circumferential, regional, or loculated accumulations can occur in the postoperative setting that can even lead to tamponade (2). Other authors suggest that the size of a PE should be considered small when the separation between parietal and visceral pericardium is <0.5 cm, moderate when it is between 0.5 and 2 cm, and large when it is >2 cm.

Assessment of the echotexture of the PE is also important. A highly echogenic effusion suggests the presence of blood while fibrin strands are often associated with chronicity. The presence of an echogenic pericardial mass raises the possibility of neoplasia.

2. Differentiating Pericardial Effusion from Epicardial Fat, Pleural Fluid

Epicardial fat can be mistaken for pericardial fluid. The characteristics of epicardial fat are that it is seen anterior to the heart but is absent posteriorly, and it is mildly echogenic (Fig. 11.6). A retrocardiac left pleural effusion is the most common posterior finding mistaken for a PE. The differentiating points between a pleural effusion and

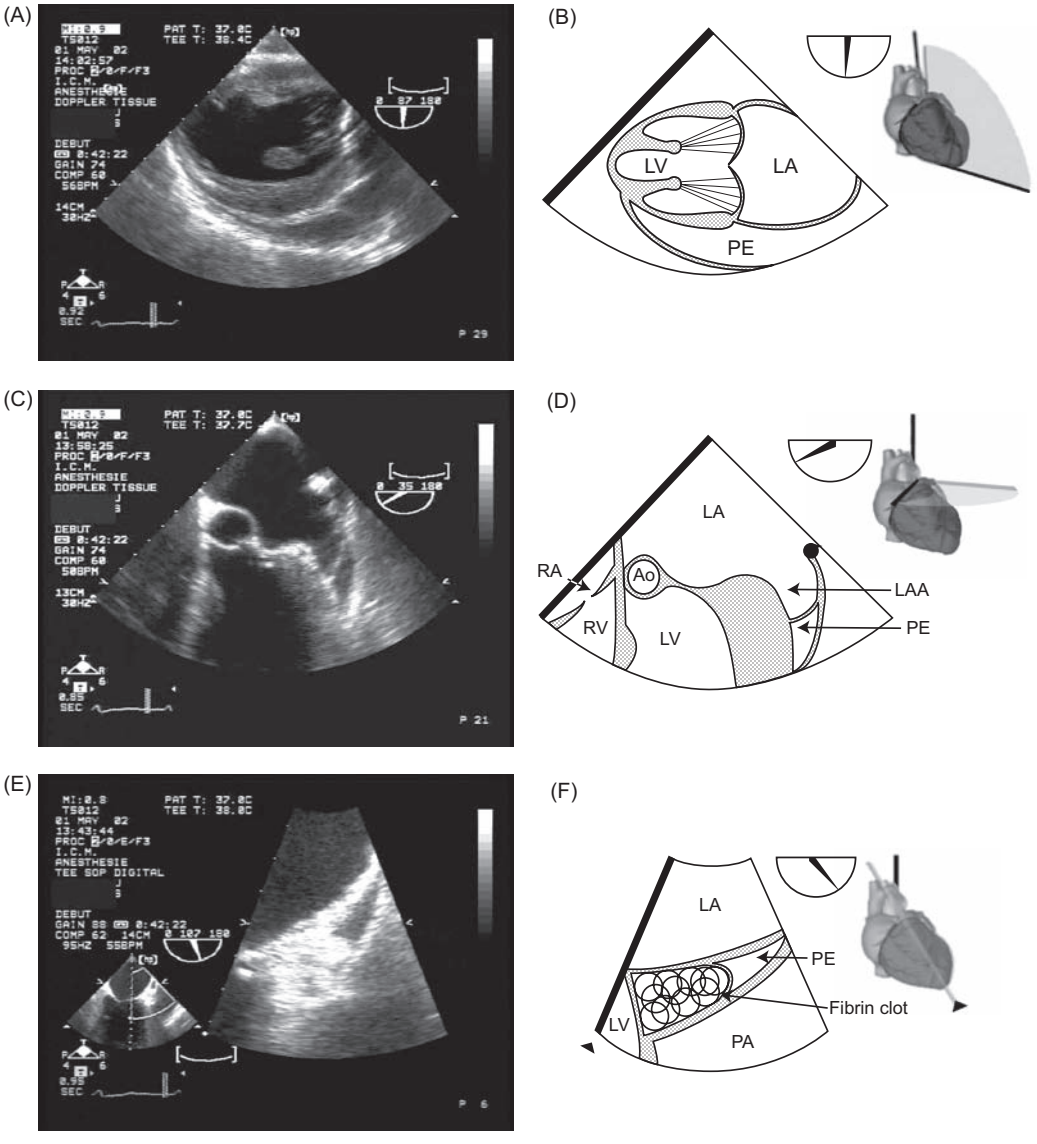

Figure 11.4 Pericardial effusion in a 67-year-old man with renal transplant scheduled for coronary revascularization. Pericardial effusion (PE) was seen in front of the left ventricle (LV) (A, B), anterior to the left atrial appendage (LAA) (C, D) and in the transverse sinus where fibrin clot can be seen (E, F). The PE was seen upon chest opening (Ao, aorta; LA, left atrium; PA, pulmonary artery; RA, right atrium; RV, right ventricle). (Intraoperative video clip courtesy of Dr. Raymond Cartier.)

a PE include: (1) a retrocardiac left pleural effusion presents as a large posterior effusion in the absence of any anterior effusion; (2) a pleural effusion lacks the characteristic decrease in echo-free space width from LV to LA seen with a PE; and (3) the echo-free space is posterior to the descending thoracic aorta in the case of a pleural effusion but anterior to the descending aorta (i.e. between the descending aorta and the posterior LV wall) with a PE (Fig. 11.7). In the four-chamber view, an isolated echo-free space superior to the right atrium most likely represents pleural fluid.

Pericardial and pleural effusions may coexist in the same patient. They can be recognized by locating the position of the descending thoracic aorta, and by identifying the pericardium as the membrane separating the two echo-free spaces. Indeed the presence of a small PE often aids in the accurate identification of a pleural effusion.

B. Cardiac Tamponade

Cardiac tamponade occurs when a PE causes the pericardial pressure to exceed the intracardiac pressure, resulting in impaired cardiac filling. The amount of fluid alone is of less importance than the rapidity of fluid accumulation for the occurrence of tamponade. A slowly expanding PE can

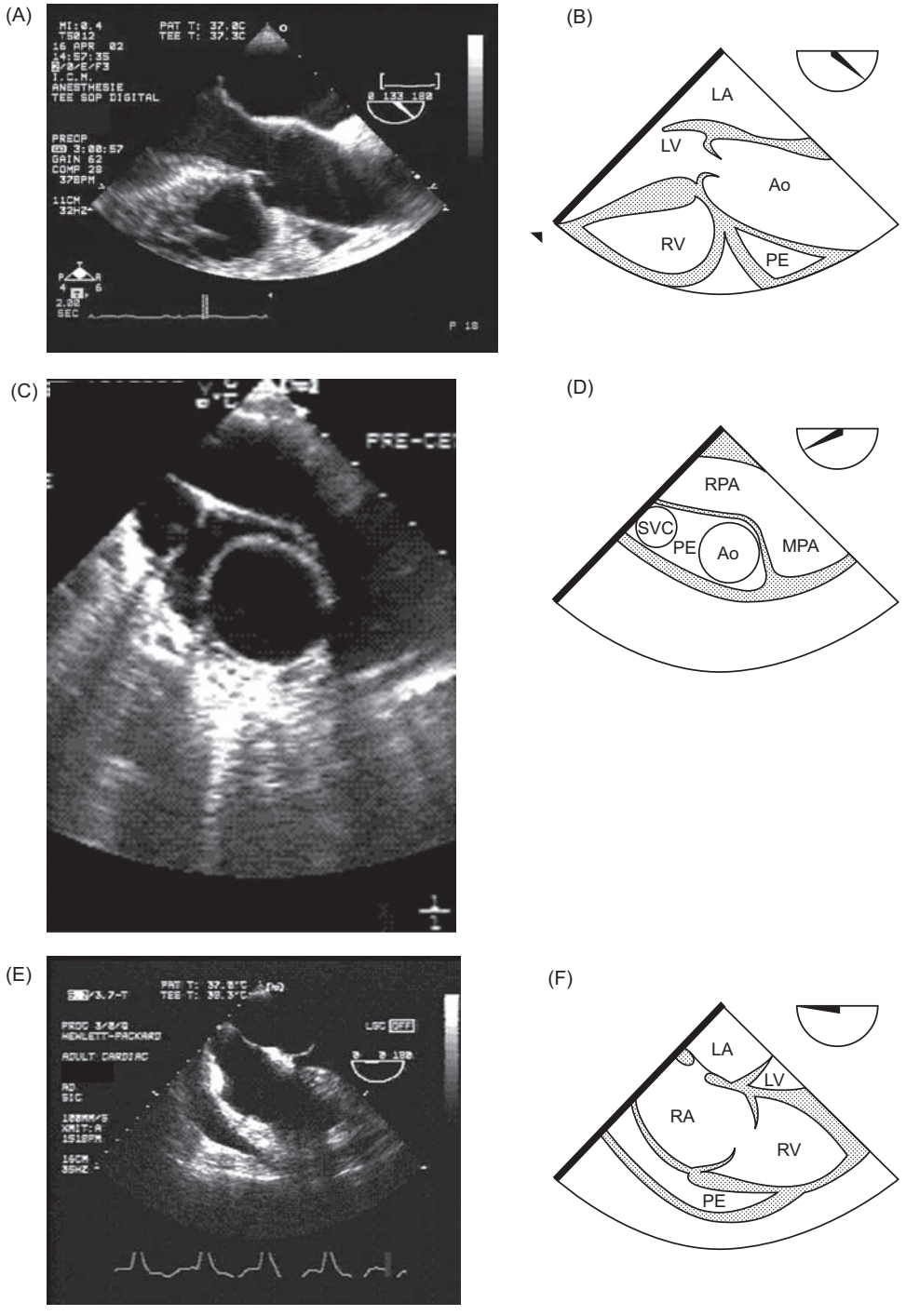

Figure 11.5 Localizations of pericardial effusion (PE): anterior to the ascending aorta (Ao) from which it communicates with the transverse sinus (A, B), between the aorta and the superior vena cava (SVC) (C, D) and anterior to the right ventricle (RV) and right atrium (RA) (E, F) (LA, left atrium; LV, left ventricle; MPA, main pulmonary artery; RPA, right pulmonary artery).

become quite large (up to 1000 mL) with little increase in pericardial pressure, while rapid accumulation of fluid with a volume as small as 100 mL may be sufficient to increase the pericardial pressure markedly and cause cardiac tamponade. It is important to remember that tamponade after cardiac surgery will often be due to a localized PE (Figs. 11.8–11.10). In contemporary practice, echocardiography combined with clinical features has

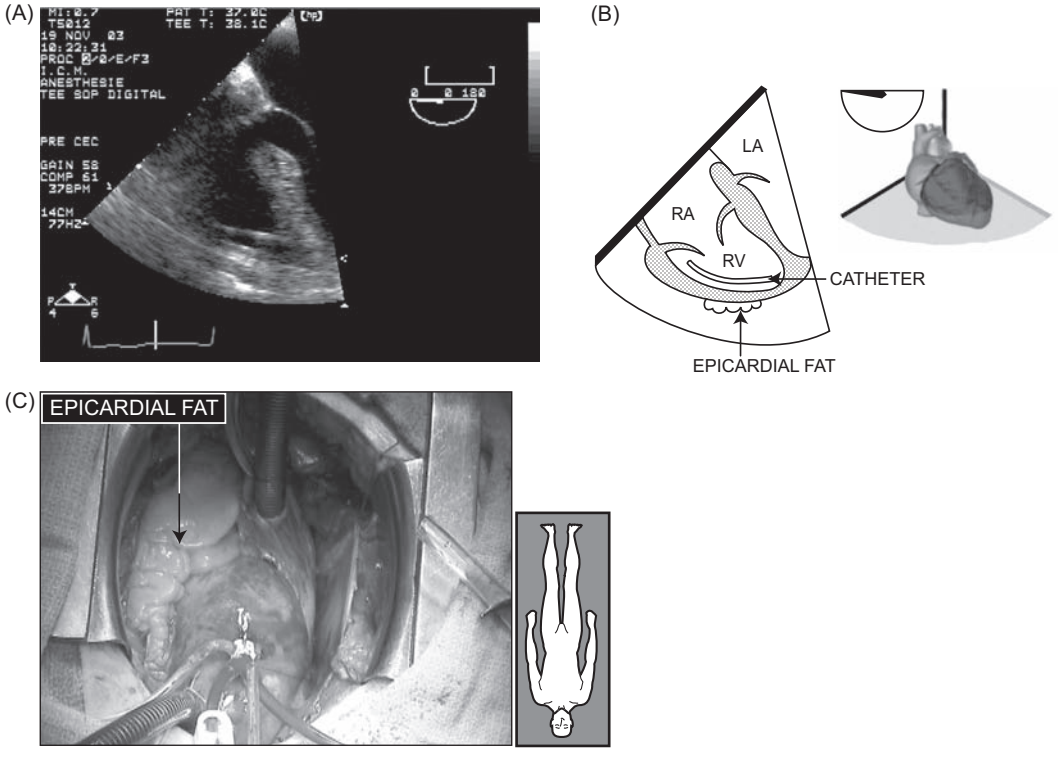

Figure 11.6 Epicardial fat in a 67-year-old man before aortic surgery. (A, B) Mid-esophageal four-chamber view. (C) Intraoperative view (LA, left atrium; RA, right atrium; RV, right ventricle). (Photo C courtesy of Dr. Michel Pellerin.)

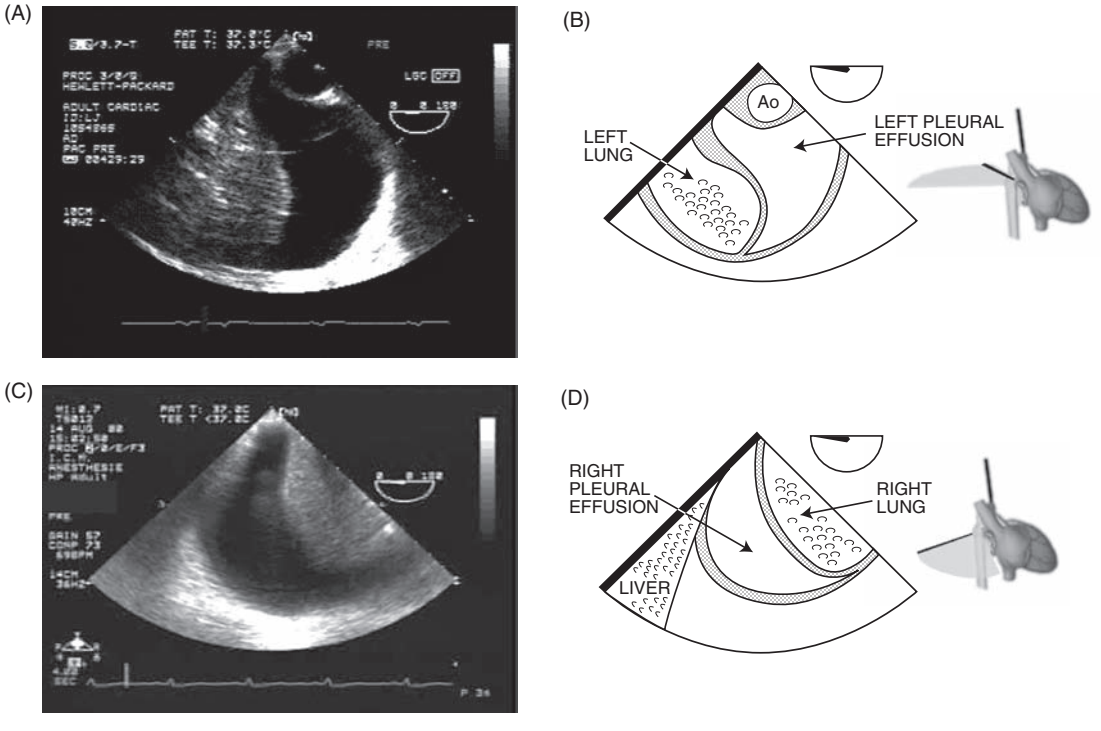

Figure 11.7 Bilateral pleural effusion. (A, B) The left pleural effusion is typically posterior to the descending aorta (Ao) and on the right side of the screen. (C, D) The right pleural effusion is on the left side of the screen where part of the liver can be seen. A combined total of 2300 mL of pleural fluid was removed from the left and right pleural cavities: 900 and 1400 mL, respectively.

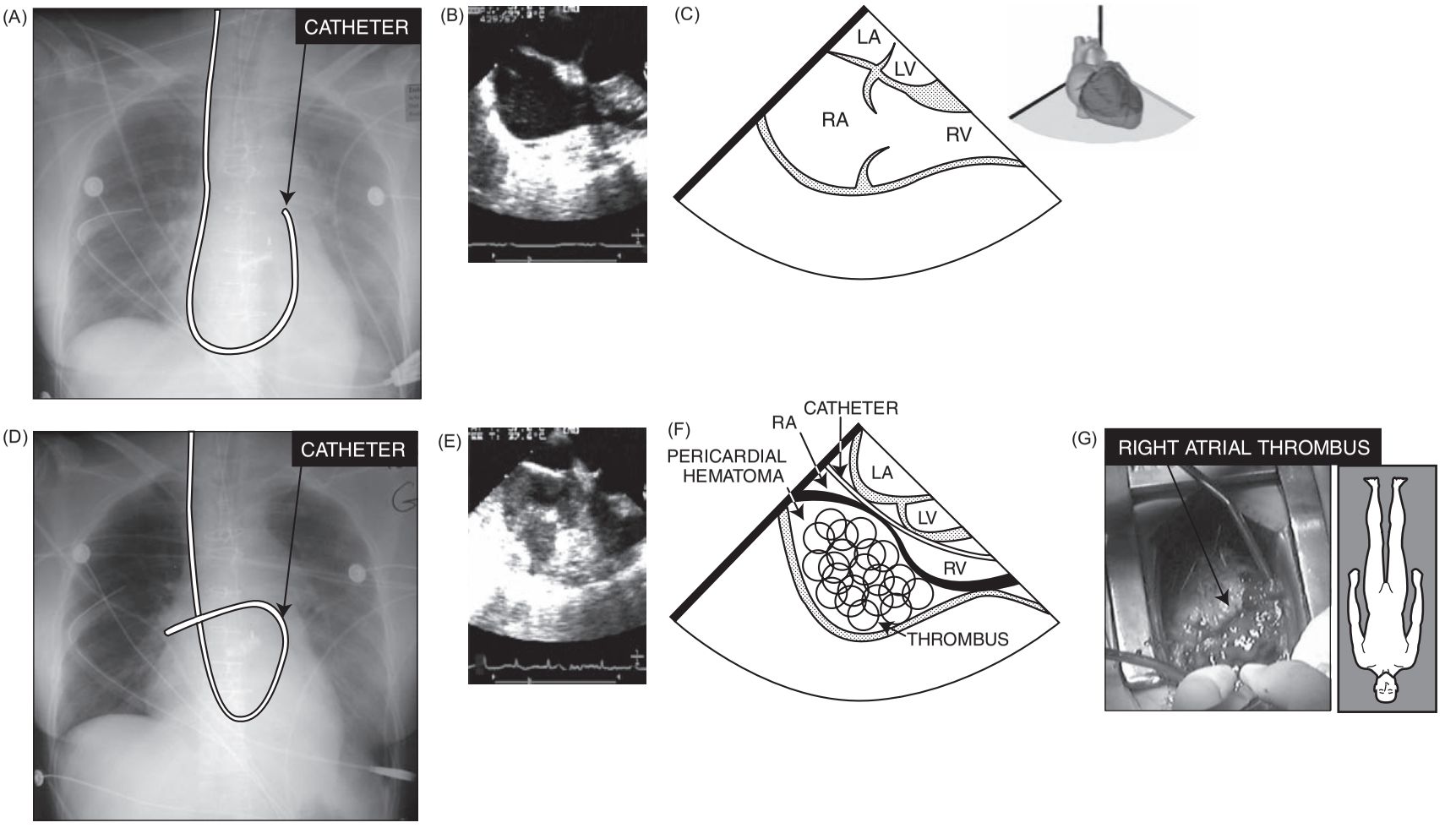

Figure 11.8 Cardiac tamponade in a hemodynamically unstable 29-year-old woman, 1 day after aortic valve surgery. (A) The diagnosis was initially suspected from serial chest X-rays. (B, C) Immediate postoperative mid-esophageal four-chamber view. (D) The next day, the pulmonary artery catheter moved from a lateral position initially after surgery (A) to a medial and more distal position secondary to displacement of the right-sided cardiac chambers by the thrombus. (E, F) The diagnosis is confirmed by TEE. (G) Intraoperatively, a localized hematoma was found compressing the right atrium (RA) (LA, left atrium; LV, left ventricle; RV, right ventricle).

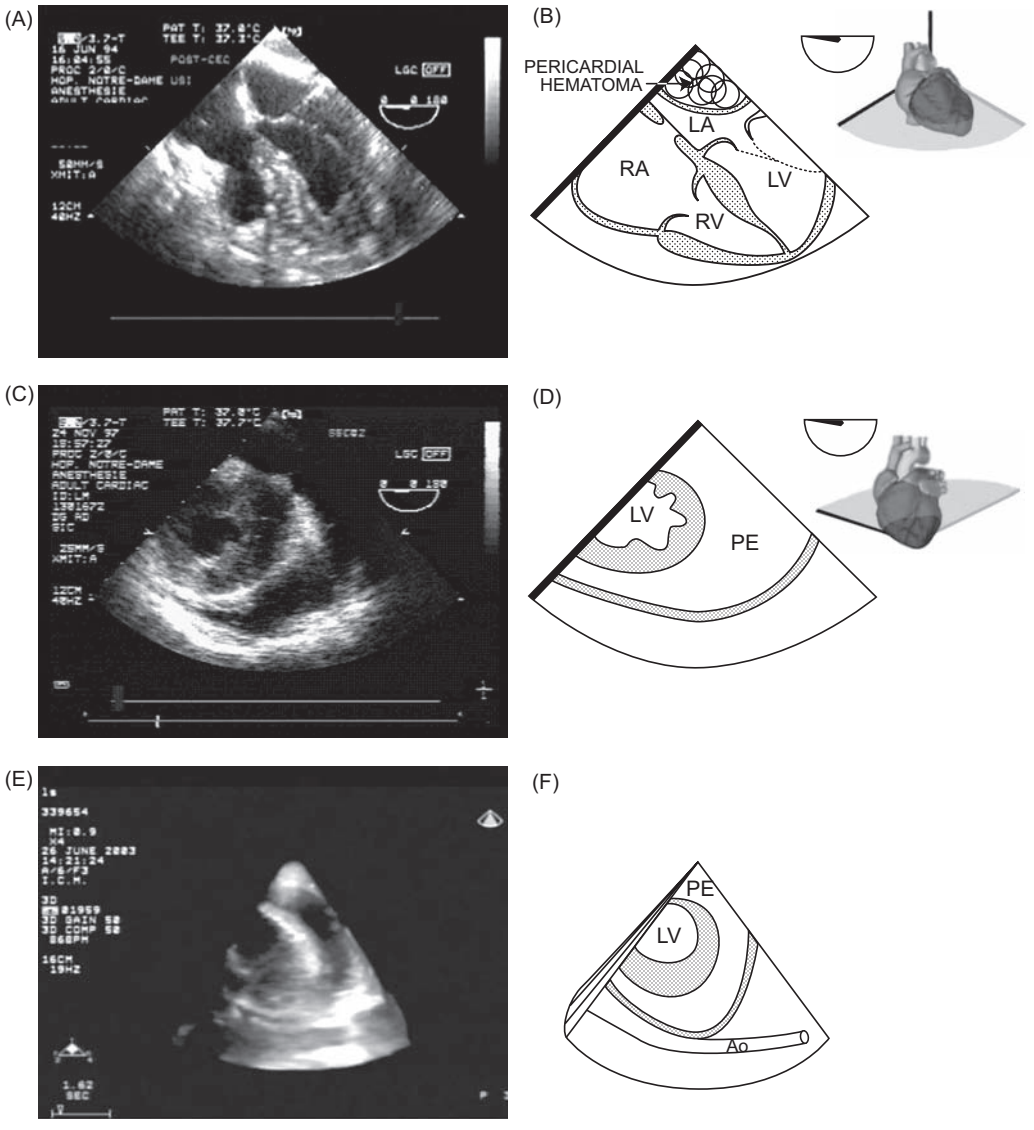

Figure 11.9 Left atrial (A, B) and left ventricular tamponade (C, D) in two hemodynamically unstable patients after cardiac surgery. The tamponade on the left atrium (LA) was missed by TTE. (E, F) A three-dimensional view of a pericardial effusion (PE) is shown (Ao, aorta; LV, left ventricle; RA, right atrium; RV, right ventricle).

become a gold standard for diagnosing cardiac tamponade and has proven useful for directing the treatment.

1. *Two-Dimensional Echocardiographic Features of Cardiac Tamponade*

Although cardiac tamponade is generally suspected clinically (hypotension, tachycardia, pulsus paradoxus, and distended jugular veins), two-dimensional echocardiography can be helpful in confirming the diagnosis when the following signs are present: (1) moderate to large PE; (2) right atrial systolic collapse that lasts for more than one-third of systole; (3) right ventricular diastolic collapse; (4) reciprocal changes in right and left ventricular volumes during respiration; and (5) inferior vena cava plethora.

Right Atrial Systolic Collapse

Right atrial systolic collapse is believed to be an early sign of diffuse cardiac tamponade because this chamber has the lowest intracavitary pressure. When intrapericardial pressure exceeds right atrial systolic pressure, inversion or collapse of the right atrial free wall occurs. The longer the duration of right atrial free wall inversion in relation to the cardiac cycle, the higher the intrapericardial pressure is in relation to the right atrial pressure and the greater is the likelihood of cardiac tamponade. Right atrial systolic inversion longer than one-third of the duration of systole has been considered a sensitive indicator for the diagnosis of tamponade. Right atrial systolic collapse is best sought in the mid-esophageal four-chamber

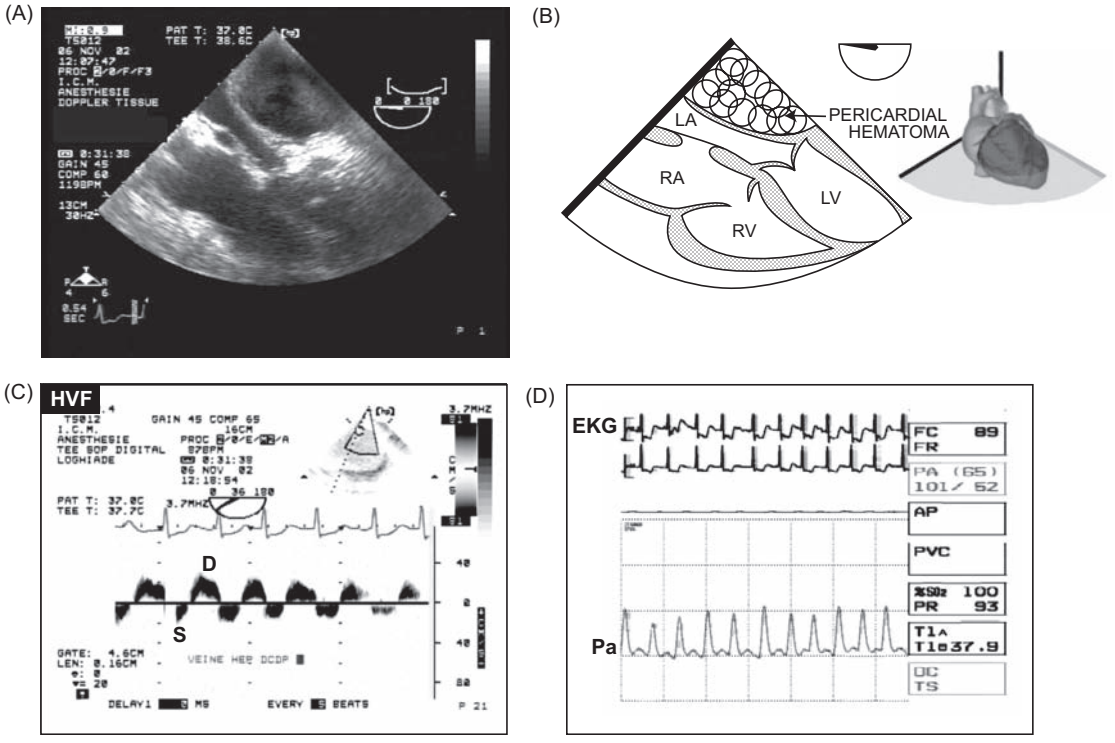

Figure 11.10 Localized tamponade in a 74-year-old woman after mitral valve repair. (A, B) A pericardial hematoma is localized in the oblique sinus compressing the left atrium (LA). The clot is seen in the mid-esophageal four-chamber view. (C) The Doppler signal from the hepatic venous flow (HVF) showed inverted S wave, which persisted after drainage suggesting persistent right ventricular diastolic dysfunction. (D) No significant pulsus paradoxus was seen (EKG, electrocardiogram; LV, left ventricle; Pa, arterial pressure; RA, right atrium; RV, right ventricle).

view but may be seen wherever the RA can be well visualized (Fig. 11.11). It is to be noted that if the pericardial reflection in the oblique sinus behind the LA is sufficiently high to allow fluid accumulation; the LA may also demonstrate systolic collapse.

Right Ventricular Diastolic Collapse

Right ventricular diastolic collapse is a more specific but less sensitive sign than right atrial collapse for the diagnosis of cardiac tamponade. This sign occurs when intrapericardial pressure exceeds right ventricular diastolic pressure. Right ventricular diastolic collapse can be seen in the mid-esophageal four-chamber view or in the right ventricular inflow–outflow view at the level of the aortic valve.

Right and Left Ventricular Dimension Changes with Respiration

Right ventricular dimension and volume normally increase with spontaneous inspiration and decrease during expiration; opposite changes are observed with positive-pressure ventilation. These respiratory variations are exaggerated in the presence of cardiac tamponade and are accompanied by exaggerated reciprocal changes in left ventricular dimension and volume (3). Exaggerated reciprocal respiratory variations in right and left ventricular dimensions and volumes are best demonstrated with simultaneous recording of the breathing cycle (Fig. 11.11). On two-dimensional imaging the reciprocal variation in ventricular volumes is also recognized by the abnormal ventricular septal motion towards the LV in diastole during spontaneous inspiration that normalizes during spontaneous expiration (Fig. 11.12).

Inferior Vena Cava Plethora

The inferior vena cava (IVC) can be visualized from both the esophageal and transgastric views (Fig. 11.13). Normally, its dimension significantly decreases with deep inspiration. The decrease in IVC diameter (measured near its junction with the RA) during inspiration should normally be $>50\%$ and this is negatively correlated with central venous pressure. The IVC plethora is defined as a dilated IVC with $<50\%$ reduction in diameter with spontaneous inspiration (4). As elevated right-sided pressures are part of tamponade physiology, the absence of IVC plethora strongly argues against global cardiac tamponade. Although

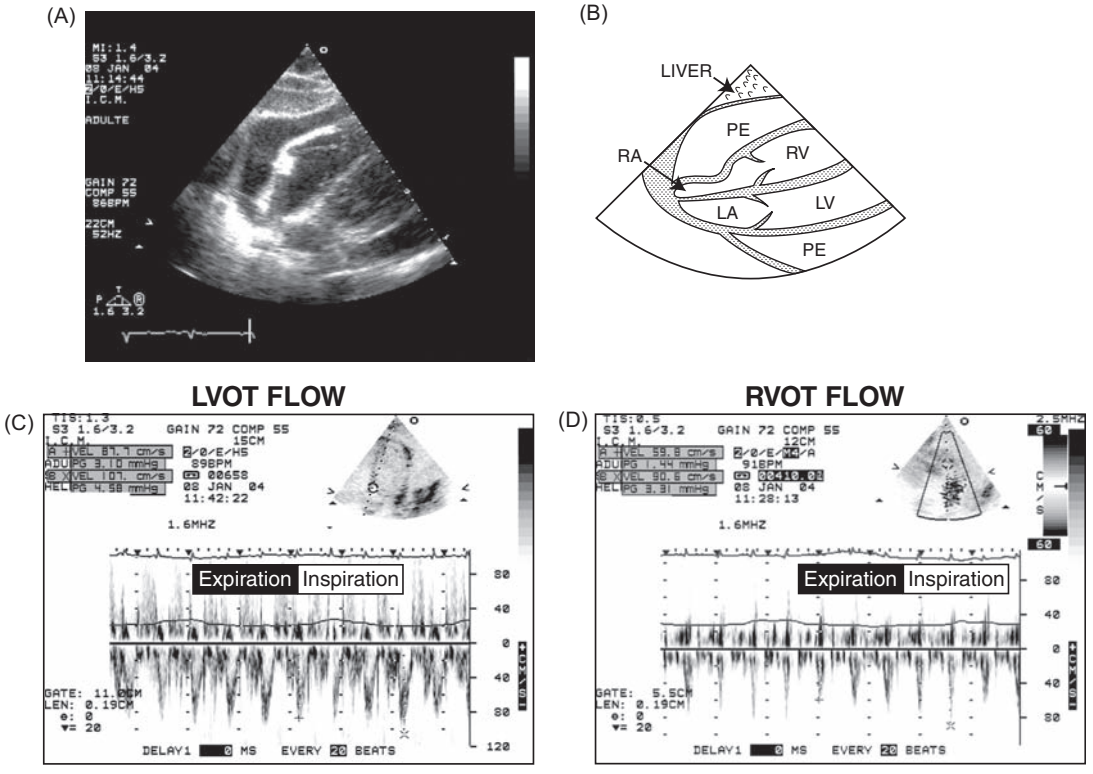

Figure 11.11 (A, B) Right atrial collapse in tamponade seen on TTE in a 53-year-old woman treated for a pericarditis. (C, D) Note that the right ventricular outflow tract (RVOT) Doppler velocities increase with inspiration as opposed to the left ventricular outflow tract (LVOT) velocities that decrease with spontaneous inspiration (LA, left atrium; LV, left ventricle; PE, pericardial effusion; RA, right atrium; RV, right ventricle). (Courtesy of Drs. François Haddad and François Marcotte.)

sensitive, IVC plethora is not a specific indicator of tamponade as it only reflects elevated right atrial pressure.

2. *Doppler Features in Cardiac Tamponade*

With normal physiology, small increases ($<15\%$) in tricuspid and pulmonic peak flow velocities and right ventricular stroke volume and corresponding decreases ($<10\%$) in left-sided parameters are seen during inspiration (Fig. 11.14). These respiratory variations are markedly increased in tamponade: both tricuspid and pulmonic valve peak velocities nearly double with spontaneous inspiration, while both mitral and aortic valve velocities are decreased by $>25\%$ (5) (Fig. 11.14). The largest increase in right-sided velocities and the largest fall in left-sided velocities are observed on the first beat after the beginning of inspiration when cardiac tamponade occurs. Similar changes may be observed in patients with significant chronic obstructive pulmonary disease (COPD) due to wide intrathoracic pressure changes, but in contradistinction, the changes in velocities are more gradual and the largest variation does not fall on the first beats of inspiration. Thus, a fall of $>25\%$ in the first inspiratory mitral inflow *E* velocity compared with the first expiration *E* velocity in conjunction with a reciprocal expiratory decrease of $>25\%$ in the late diastolic hepatic venous flow velocity (or even diastolic flow reversal) [Fig. 11.15(A)] strongly suggests the presence of cardiac tamponade. Tricuspid inflow signals show a reciprocal increase in early *E* velocities from spontaneous expiration to inspiration.

The diagnostic criteria of cardiac tamponade in patients under positive-pressure mechanical ventilation are reversed as the inspiratory changes described during spontaneous breathing will be observed during the positive-pressure expiratory phase.

In our experience, drainage of pericardial effusion in patients under positive-pressure ventilation can be associated with deterioration of ventricular diastolic function (Fig. 11.15).

3. *Localized Chamber Compression from Hematoma*

Localized PEs commonly occur after cardiac surgery, frequently due to localized bleeding and thrombus. Most

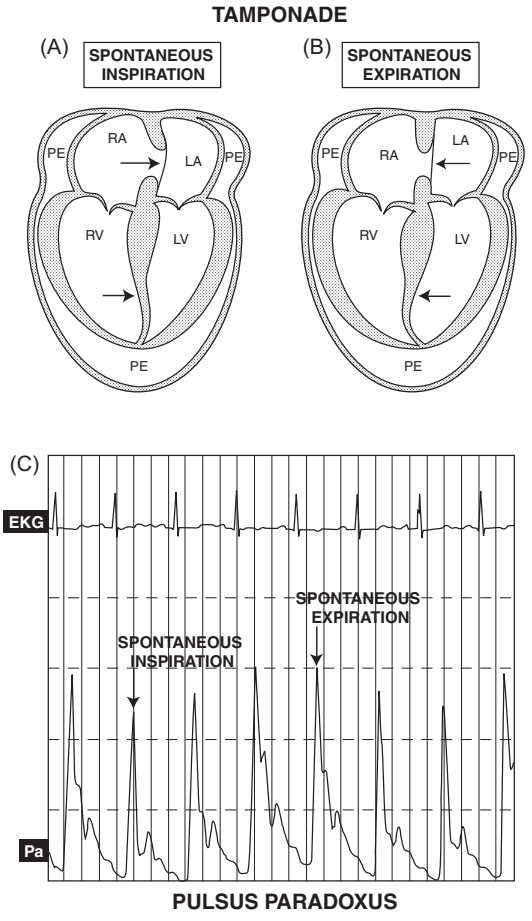

Figure 11.12 Ventricular changes with respiration in patients with tamponade. (A) During spontaneous inspiration, the increase in venous return with resulting higher right-sided pressures caused a leftward shift in the interatrial and interventricular septum. (B) The opposite changes will occur in expiration. (C) This explains why the arterial pressure (Pa) is reduced upon inspiration and increases with expiration (EKG, electrocardiogram; LA, left atrium; LV, left ventricle; PE, pericardial effusion; RA, right atrium; RV, right ventricle).

importantly, regional postoperative PEs may cause tamponade when they compress the lower pressure RA and LA (6). A mid-esophageal four-chamber view can show a pericardial hematoma compressing the right atrial free wall potentially resulting in a slit-like appearance of the right atrial cavity (Fig. 11.8). The RV, LA, and LV can also be compressed (Fig. 11.9). In the postoperative cardiac patient, TEE is superior to transthoracic echocardiography (TTE) in diagnosing localized tamponade and differentiating it from other causes of hemodynamic instability. The classical respiratory changes in the Doppler signals and hemodynamic parameters are less evident with localized effusions (7) (Fig. 11.10). However, abnormal right-sided diastolic patterns suggestive of restrictive ventricular filling are commonly seen (Fig. 11.10).

4. *Pericardiocentesis and Surgical Drainage Assessment*

Two-dimensional echocardiography is extremely valuable in assisting pericardiocentesis. Echocardiography not only confirms the presence of pericardial fluid and whether it is loculated or not, but can also identify the optimal approach for pericardiocentesis by defining the area of largest fluid accumulation most easily reached percutaneously while avoiding vital organs and abnormal structures. Injection of an ultrasound contrast agent through the pericardiocentesis needle may help ensure that it is located in the pericardial cavity. Similarly, ultrasound contrast injection through an intravenous line may help localize the origin of pericardial fluid by demonstrating its escape from one of the cardiac chambers.

In adult patients, pericardiocentesis is most often assisted using transthoracic imaging guidance. However, TEE monitoring during pericardiocentesis has the advantages of allowing better imaging of the PE without interfering with the sterile procedure field and helping to monitor fluid disappearance during pericardiocentesis drainage. However, it may not be easy to localize the tip

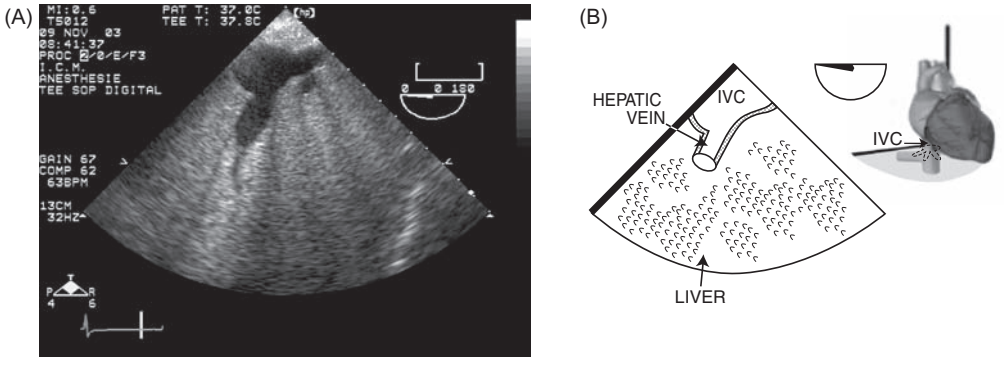

Figure 11.13 Tamponade in a 49-year-old woman under mechanical ventilation. Dilatation of both inferior vena cava (IVC) and hepatic vein.

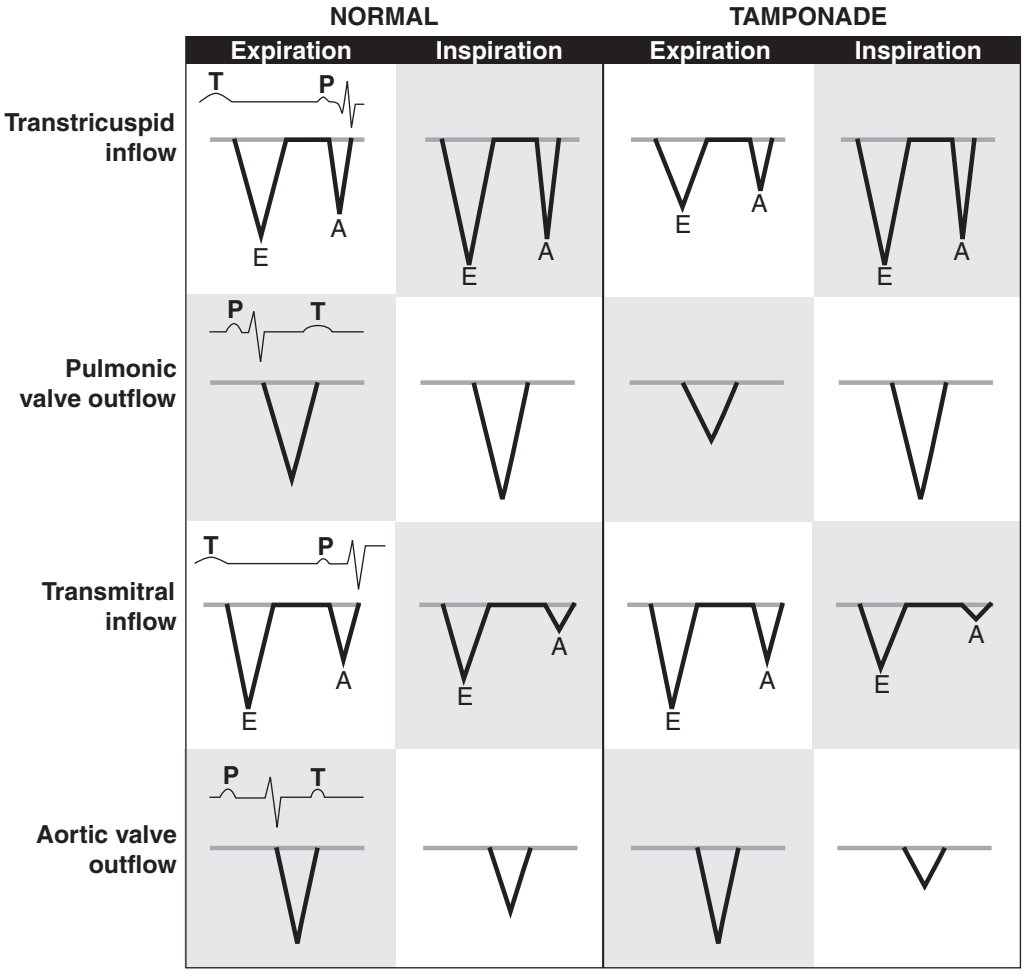

Figure 11.14 Normal spontaneous respiratory changes and those observed with tamponade in Doppler transtricuspid inflow, pulmonic valve outflow, transmitral inflow, and aortic valve outflow.

of the needle precisely using TEE, in contrast to the guidewire which generally can be easily detected (Fig. 11.16).

III. CONSTRICTIVE PERICARDITIS

A. Echocardiographic Findings in Constrictive Pericarditis

Constrictive pericarditis (CP) is characterized by impaired diastolic cardiac filling due to the abnormal pericardium constraining the cardiac structures like a rigid shell, separating the intrathoracic pressure changes from the intracardiac pressure (Fig. 11.17). Echocardiographic findings in CP include: 1—Thickened pericardium (>3 mm): this anatomical finding may be difficult to demonstrate (8). 2—Abnormal septal motion (Fig. 11.18): exaggerated ventricular interdependence in a constrained pericardial shell results in exaggerated inspiratory leftward movement of both the atrial and ventricular septa and abnormal bouncing of the interventricular septum. 3—Restrictive filling pattern (Fig. 11.19): pulsed-wave Doppler examination of atrioventricular inflow typically shows high E and small A velocities with the E/A ratio usually >1.5, in conjunction with short E wave deceleration time (<160 ms) and isovolumetric relaxation time (IVRT <70 ms). This is consistent with increased left and right ventricular filling pressures. However, a restrictive filling pattern indicative of increased filling pressures is also found in patients with restrictive cardiomyopathy. 4—Respiratory variation of the mitral inflow and pulmonary venous flow velocities: Doppler echocardiography performed simultaneously with respirometry is a useful method to diagnose CP, as marked respiratory changes in ventricular filling and central venous flow velocities result from a thickened pericardial shell which shields the heart from the variation in intrathoracic pressure (9) (Fig. 11.20). As the change in intrathoracic pressure is not transmitted to the cardiac chambers because of the rigid pericardium,

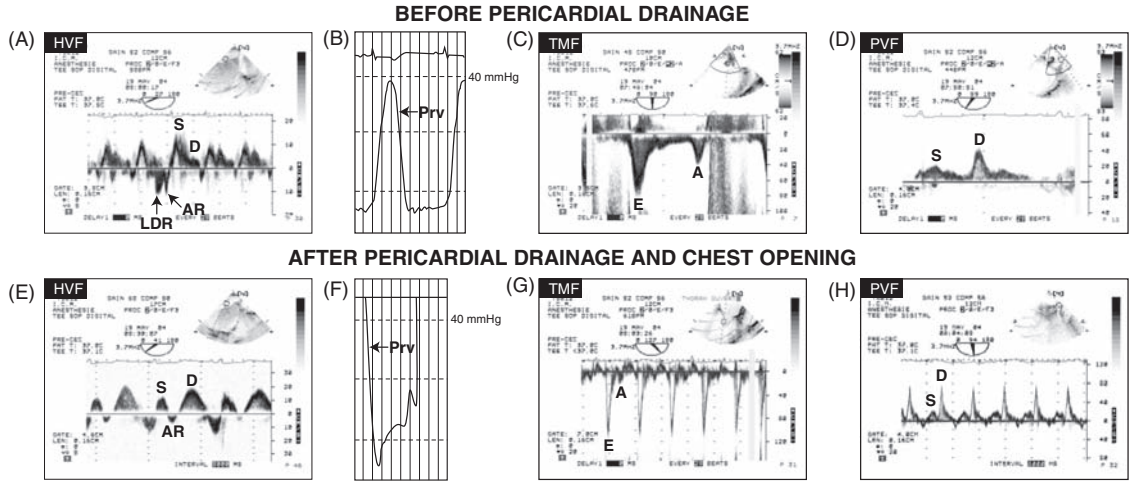

Figure 11.15 Pericardial effusion (200 mL) in a 50-year-old woman scheduled for coronary revascularization. (A) The hepatic venous flow (HVF) showed intermittent late diastolic reversal (LDR) with normal S/D ratio >1. (B) Note the flat diastolic portion of the right ventricular pressure (Prv) curve. (C) The E/A ratio was >1 on the transmitral flow (TMF) and S/D ratio <1 on the pulmonary venous flow (PVF). (D) Following pericardial drainage of 200 mL upon chest opening, the HVF S/D ratio became <1 with disappearance of the LDR (E), the diastolic slope of the Prv increased (F) and both the E/A ratio of the TMF (G) and the S/D ratio of the PVF (H) became more pronounced: these observations are consistent with a deterioration of both right and left ventricular diastolic functions (AR, atrial reversal; Pra, right atrial pressure).

the pulmonary venous pressure therefore decreases to a greater degree than the left atrial and left ventricular pressures. The pressure gradient responsible for left ventricular filling is, therefore, decreased, resulting in decreased left ventricular output with inspiration. In the right-sided cavities during spontaneous inspiration, the intrathoracic pressure drop leads to increased venous return to the RA and increased right ventricular filling. The total cardiac volume being fixed by the constraining pericardium, a decrease in left ventricular volume is consequently accompanied by reciprocal increase in right ventricular volume, characteristic of ventricular interdependence. This is reflected by a leftward shift or bulging of the septum, which further contributes to decreased LV compliance.

On pulsed-wave Doppler examination, the aforementioned event will, during spontaneous inspiration, cause a characteristic decrease $>25\%$ of the mitral inflow E velocity and pulmonary venous flow D wave velocity with a concomitant increase $>40-50\%$ in tricuspid inflow E velocity, while hepatic venous flow diastolic velocity will typically decrease and in some patients reverse during the opposite expiratory phase (Fig. 11.20).

Positive-pressure inspiration decreases systemic venous return which is later followed by reduced left ventricular output. In the early phase however, left ventricular stroke volume increases because the increased intrathoracic pressure compresses the LV and increases the pressure gradient between intra- and extrathoracic vascular beds. Hence, positive-pressure mechanical ventilation will display an inverted pattern of respiratory variations in the Doppler mitral inflow and pulmonary venous flow tracing in patients with constrictive pericarditis. Thus, positive-pressure inspiration causes an increase (instead of the usual decrease) in the mitral inflow and pulmonary venous flow Doppler velocities with reciprocal changes in the tricuspid inflow and hepatic venous flow. The percentage of change in the peak velocities induced by positive-pressure ventilation is in the same range as reported during spontaneous breathing (Fig. 11.20). 5—Tissue Doppler imaging: the early diastolic right and left ventricular wall motion velocity patterns along the short and long axes as measured by pulsed-wave tissue Doppler imaging provide very useful information for the diagnosis of constrictive pericarditis: normal or elevated mitral annular early E_m velocity will be observed as opposed to the reduced E_m velocity in restrictive cardiomyopathy (10). 6—Extracardiac abnormalities: these will include dilated IVC and hepatic veins, with peritoneal fluid in patients with chronic right-sided failure. Pericardial calcifications are more easily seen on the chest X-ray, computed tomography (CT), or magnetic resonance imaging (MRI) (Fig. 11.21).

B. Differentiating Constrictive Pericarditis from Restrictive Cardiomyopathy

Restrictive cardiomyopathy (RCMP) is an uncommon disease characterized by normal-sized ventricles with diastolic dysfunction (see Chapter 10). The differential

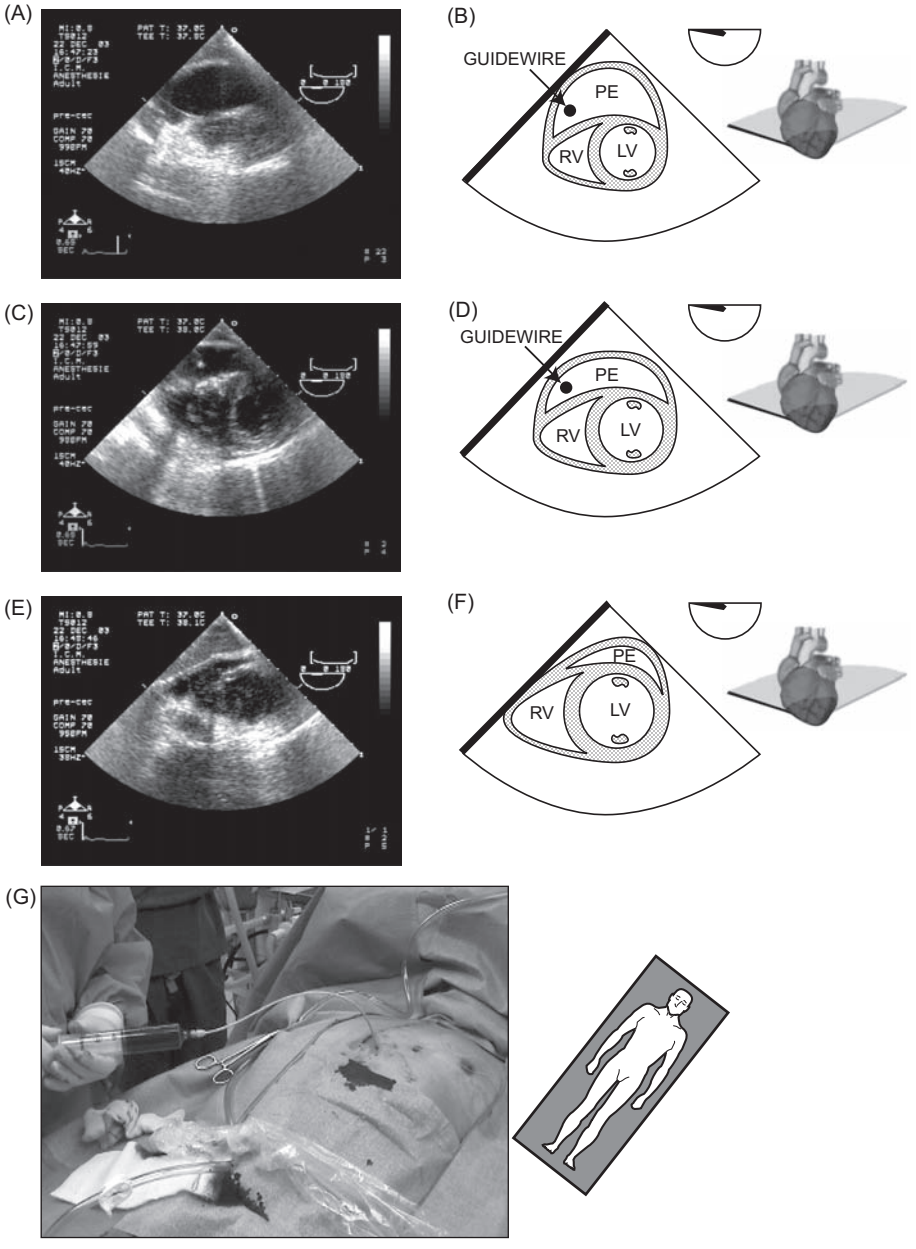

Figure 11.16 (A–F) Percutaneous drainage of pericardial fluid assisted with TEE. The guidewire is seen behind the ventricles. A total of 900 mL of fluid was removed. (G) Intraoperative setting (LV, left ventricle; PE, pericardial effusion; RV, right ventricle). (Photo G courtesy of Dr. Raymond Cartier.)

diagnosis between RCMP and constrictive pericarditis is challenging, because the two entities share many hemodynamic features. The main differences between RCMP and CP are: 1—Atrial enlargement: Bi-atrial enlargement is generally more marked in RCMP than CP. 2—Pulmonary artery pressure: patients with RCMP typically have moderate to severe pulmonary hypertension while those with CP have only mild elevations in pulmonary arterial pressure. Estimation of pulmonary pressure can be performed from tricuspid and pulmonary regurgitation jet velocity. 3—Doppler respiratory variations: in CP, the mitral inflow E velocity will typically vary by $>25\%$ between expiration and inspiration. The same degree of respiratory variation in the pulmonary venous peak diastolic (D) velocity is also observed in CP. In contradistinction, the respiration variation of the mitral inflow E velocity will be $<10\%$ with RCMP. 4—Tissue Doppler imaging: tissue Doppler interrogation of the lateral mitral valve annulus in RCMP will typically reveal decreased early peak E_m velocity of longitudinal expansion to <8.0 cm/sec while it

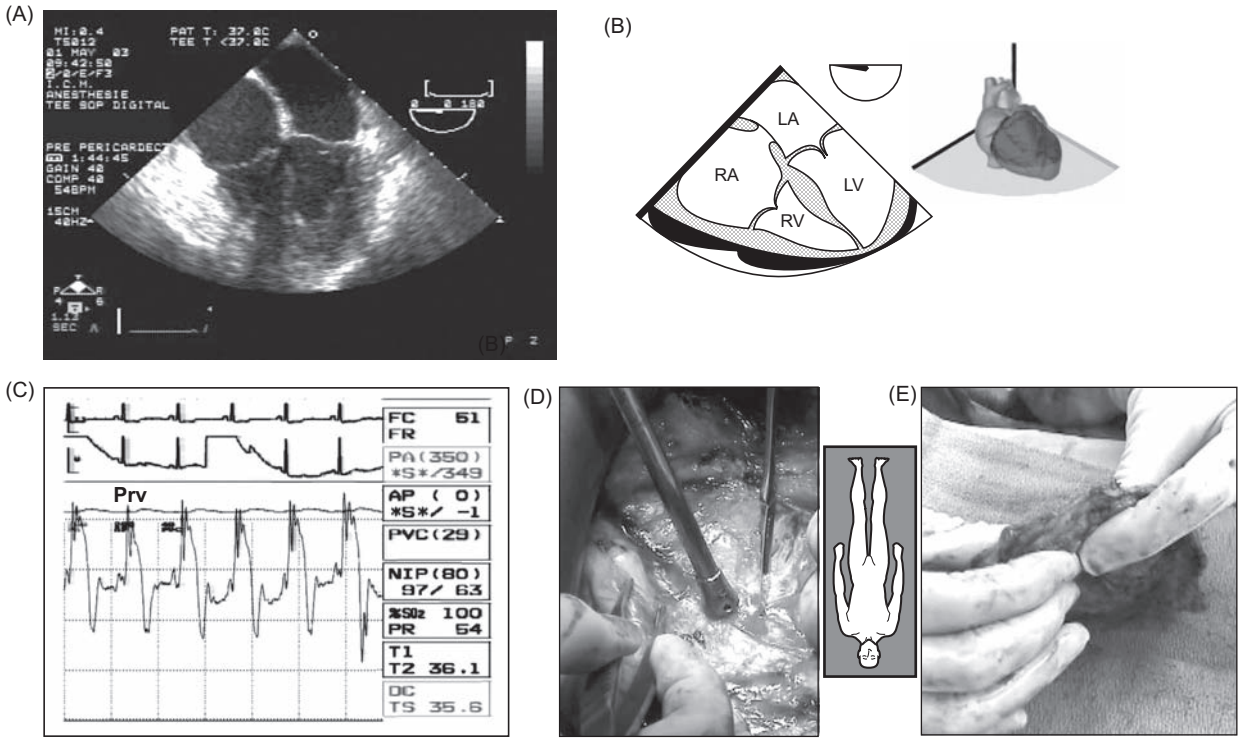

Figure 11.17 A 68-year-old man is scheduled for pericardectomy. (A, B) A mid-esophageal four-chamber view shows dilated right atrium (RA) and left atrium (LA) with deviation of the atrial and ventricular septa towards the left, suggesting significantly increased right-sided pressure. (C) Right ventricular pressure (Prv) tracing shows typical diastolic square root sign consistent with restrictive filling. (D, E) Upon opening of the chest cavity, the fibrous pericardium is seen with abnormal thickness (LV, left ventricle; RV, right ventricle). (Photos D and E courtesy of Dr. Raymond Cartier.)

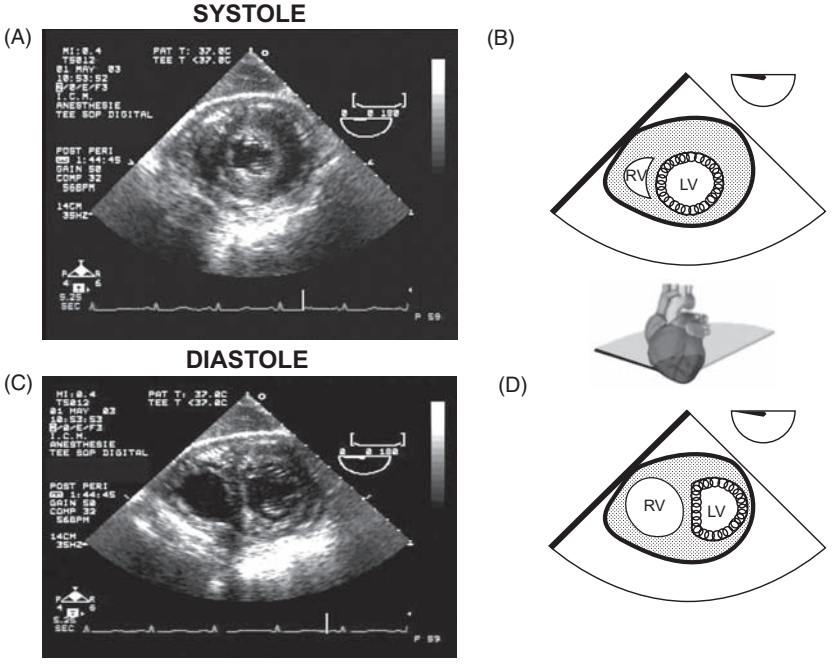

Figure 11.18 A 68-year-old man with constrictive pericarditis is scheduled for pericardectomy. The transgastric view in systole (A, B) and diastole (C, D) is shown. Note the abnormal ventricular septal flattening and shift towards the left during diastole (LV, left ventricle; RV, right ventricle).

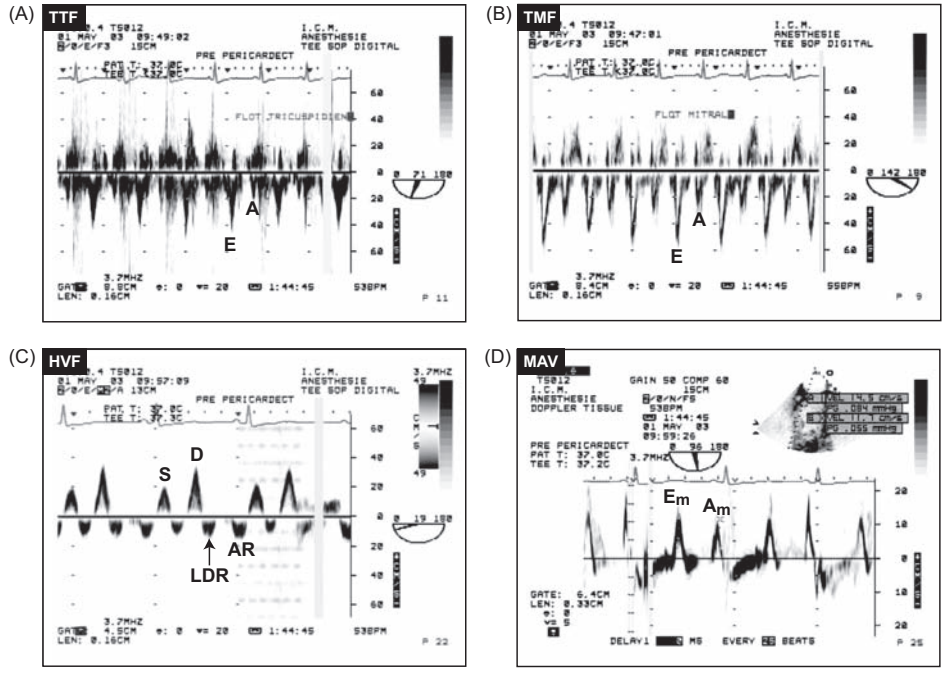

Figure 11.19 A 68-year-old man with constrictive pericarditis is scheduled for pericardectomy. He is on mechanical ventilation. (A) The transtricuspid flow (TTF) velocity tracing displays respiratory variation. On both the Doppler TTF and transmitral flow (TMF) (B), there is predominance of the early *E* diastolic velocities. (C) On the hepatic venous flow (HVF) Doppler tracing, there is abnormal systolic or S flow blunting with diastolic or D flow predominance and even late diastolic reversal (LDR) flow. (D) Mitral annular velocity (MAV) shows normal E_m velocities, which argues against the presence of restrictive cardiomyopathy (AR, atrial reversal).

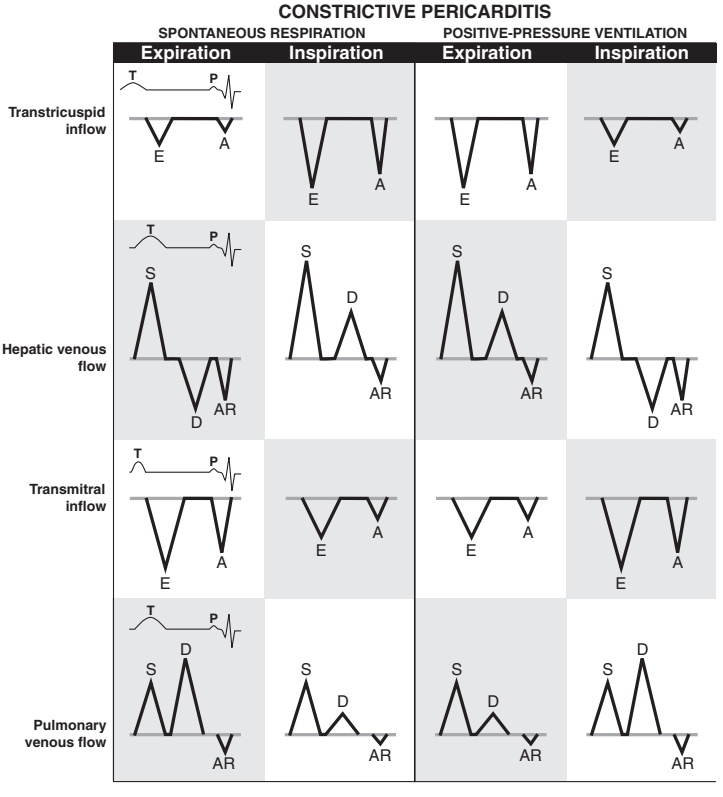

Figure 11.20 Doppler changes in transtricuspid inflow, hepatic venous flow, transmitral inflow, and pulmonary venous flow during spontaneous respiration and positive-pressure ventilation in constrictive pericarditis (AR, atrial reversal). [Adapted from Klein and Cohen (9).]

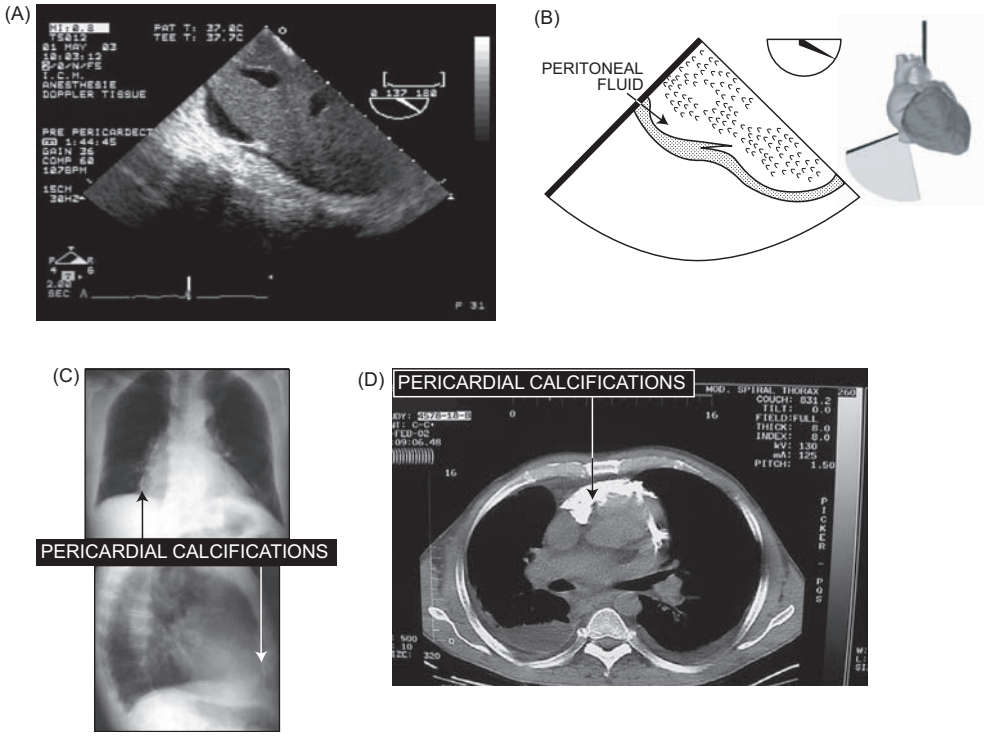

Figure 11.21 Associated findings in constrictive pericarditis. (A, B) Peritoneal fluid from right-sided failure in a 68-year-old man scheduled for pericardectomy. Pericardial calcifications are seen on the chest X-ray (C) and computed tomography (D).

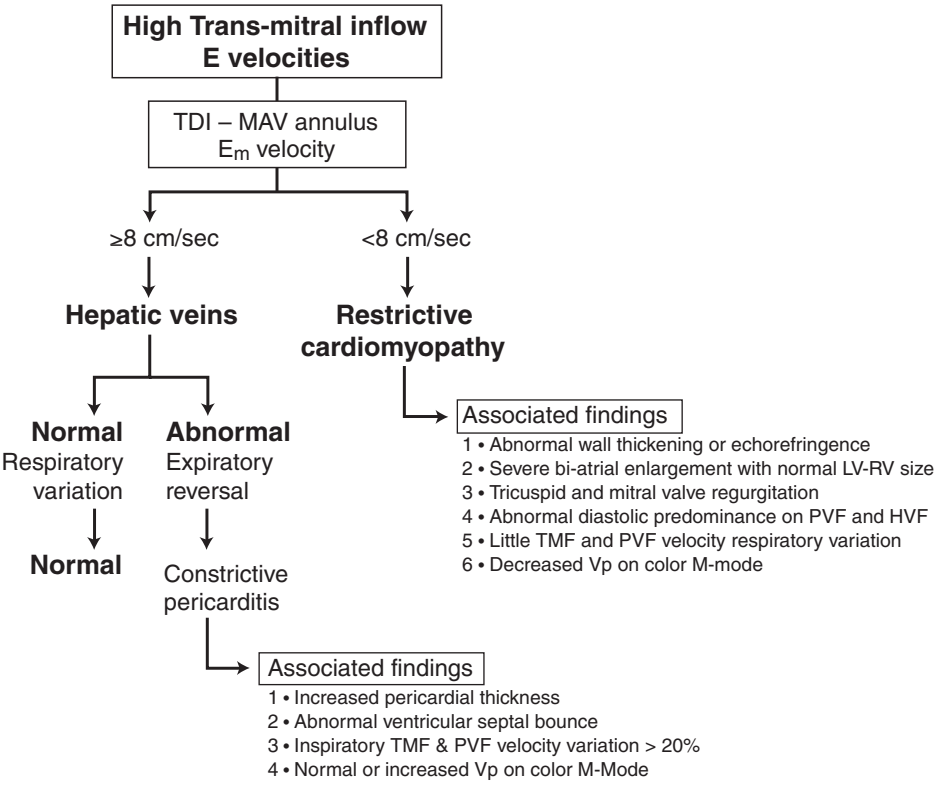

Figure 11.22 Algorithm to differentiate constrictive pericarditis from restrictive cardiomyopathy (HVF, hepatic venous flow; LV, left ventricle; MAV, mitral annular velocity; PVF, pulmonary venous flow; TDI, tissue Doppler imaging; TMF, transmitral flow; RV, right ventricle; Vp, velocity of propagation). [Adapted from Ha et al. (13).]

Table 11.1 Doppler Criteria for Constrictive Pericarditis

Method	Variable	Criteria for CP	Specificity (%)	Sensitivity (%)
Mitral Doppler	Resp. variation in peak E	$\geq$10%	84	91
Pulmonary vein Doppler	Resp. variation in peak D	$\geq$18%	79	91
Tissue Doppler	Peak E_m	$\geq$8 cm/sec	89	100
Color M-mode	Slope of first alias	$\geq$100 cm/sec	74	91

Note: CP, constrictive pericarditis; Resp., respiratory.
Source: Adapted from Rajagopalan et al. (12).

will be preserved ($>$8.0 cm/sec) in constrictive pericarditis (Fig. 11.19). The Doppler myocardial velocity gradient (MVG) measured from the LV posterior wall also helps to discriminate RCMP from CP. Indeed, the MVG is decreased in RCM patients compared with both normal and CP patients during ventricular ejection and rapid ventricular filling (11). During isovolumic relaxation, the MVG is positive in RCMP and negative in both normal and CP patients. 5—Color M-mode flow propagation of left ventricular filling: a slope $\geq$100 cm/sec for the first aliasing contour in color M-mode flow propagation of left ventricular filling can predict patients with CP, while it is typically reduced $<$45 cm/sec in RCMP (12).

An algorithm that incorporates mitral inflow Doppler signal and tissue Doppler has been proposed to differentiate constriction from restrictive cardiomyopathy and normal physiology (13) (Fig. 11.22). The sensitivity and specificity of the different Doppler criteria for CP are shown in Table 11.1 (12).

IV. PERICARDIAL CYST

Pericardial cysts are uncommon intrathoracic lesions and are typically located in the right cardiophrenic angles on chest X-ray. Transthoracic echocardiography will reveal a spherical cystic echo-free space contiguous to the heart. Usually, they are associated with an excellent long-term prognosis and are often detected incidentally, but complicated clinical courses, including sudden death,

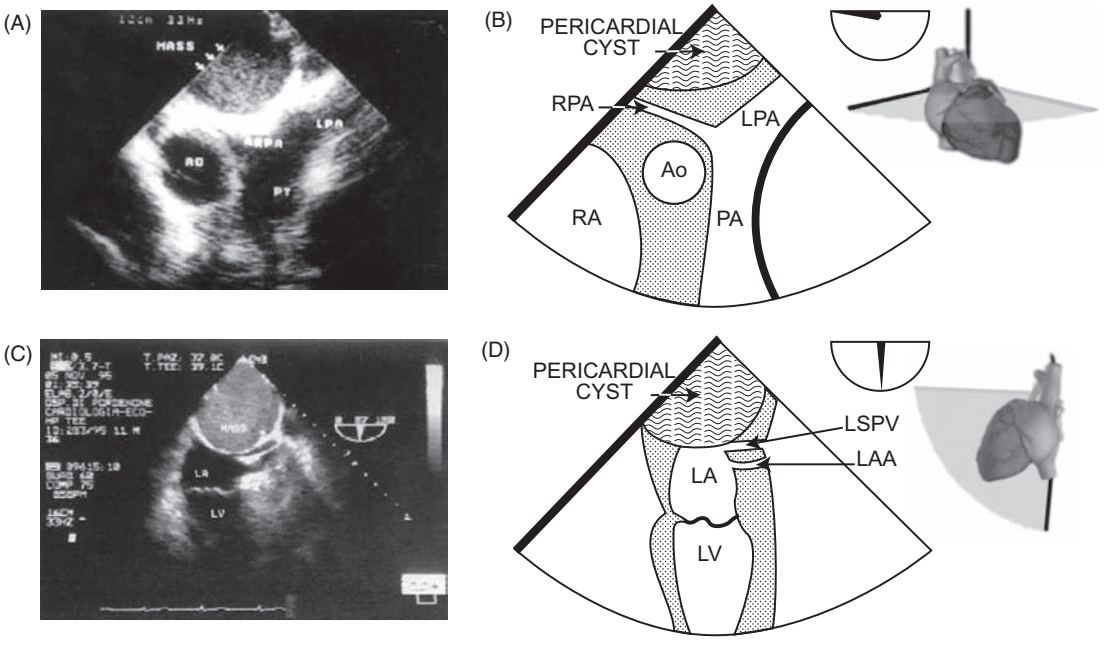

Figure 11.23 (A, B) Upper esophageal view at 0° showing a round hypodense mass consisting of a pericardial cyst compressing the posterior wall of the right pulmonary artery (RPA) in a 29-year-old man with retrosternal chest pain. (C, D) In a 36-year-old-man consulting for dyspnea, a mid-esophageal two-chamber view reveals a pericardial cyst compressing the left atrium (Ao, aorta; LA, left atrium; LAA, left atrial appendage; LPA, left pulmonary artery; LSPV, left superior pulmonary vein; LV, left ventricle; PA, pulmonary artery; PT, pulmonary trunk; RA, right atrium). [Adapted from Antonini-Canterin et al. (15).]

have been reported (14), especially when pericardial cysts are causing compression of cardiac structures and hemodynamic changes. Transesophageal echocardiography can help to recognize malignant cardiac-compressing pericardial cysts in life-threatening conditions (15) (Fig. 11.23).

V. CONGENITAL ABSENCE OF THE PERICARDIUM

Congenital absence of the pericardium (CAP) is a rare clinical entity. Chest X-ray findings combined with MRI usually establish the diagnosis. Although absence of a pericardial echo has been associated with excessive cardiac motion, right ventricular enlargement, and paradoxical septal motion, differentiation from right ventricular volume overload may be difficult by echocardiography alone (16). Transesophageal echocardiography examination may however help to exclude other conditions that may lead to right ventricular enlargement and volume overload (17).

REFERENCES

1. Netter FH, Yonkman FF, Ciba Pharmaceutical Company. Heart: a compilation of paintings on the normal and pathologic anatomy and physiology, embryology, and diseases. Summit, N. J: CIBA Pharmaceutical Company, 1978.
2. Chuttani K, Pandian NG, Mohanty PK, Rosenfield K, Schwartz SL, Udelson JE et al. Left ventricular diastolic collapse. An echocardiographic sign of regional cardiac tamponade. Circulation 1991; 83:1999–2006.
3. Gerber TC, Safford RE. Intrapericardial Doppler flow signals in cardiac tamponade. Clin Cardiol 1999; 22(3):231–232.
4. Himelman RB, Kircher B, Rockey DC, Schiller NB. Inferior vena cava plethora with blunted respiratory response: a sensitive echocardiographic sign of cardiac tamponade. J Am Coll Cardiol 1988; 12(6):1470–1477.
5. Merce J, Sagrista-Sauleda J, Permanyer-Miralda G, Evangelista A, Soler-Soler J. Correlation between clinical and Doppler echocardiographic findings in patients with moderate and large pericardial effusion: implications for the diagnosis of cardiac tamponade. Am Heart J 1999; 138(4 Pt 1):759–764.
6. Pepi M, Muratori M, Barbier P, Doria E, Arena V, Berti M et al. Pericardial effusion after cardiac surgery: incidence, site, size, and haemodynamic consequences. Br Heart J 1994; 72(4):327–331.
7. Larose E, Ducharme A, Mercier LA, Pelletier G, Harel F, Tardif JC. Prolonged distress and clinical deterioration before pericardial drainage in patients with cardiac tamponade. Can J Cardiol 2000; 16(3):331–336.
8. Ling LH, Oh JK, Tei C, Click RL, Breen JF, Seward JB et al. Pericardial thickness measured with transesophageal echocardiography: feasibility and potential clinical usefulness. J Am Coll Cardiol 1997; 29(6):1317–1323.
9. Klein AL, Cohen GI. Doppler echocardiographic assessment of constrictive pericarditis, cardiac amyloidosis, and cardiac tamponade. Cleve Clin J Med 1992; 59(3):278–290.
10. Oki T, Tabata T, Yamada H, Abe M, Onose Y, Wakatsuki T et al. Right and left ventricular wall motion velocities as diagnostic indicators of constrictive pericarditis. Am J Cardiol 1998; 81(4):465–470.
11. Palka P, Lange A, Donnelly JE, Nihoyannopoulos P. Differentiation between restrictive cardiomyopathy and constrictive pericarditis by early diastolic doppler myocardial velocity gradient at the posterior wall. Circulation 2000; 102(6):655–662.
12. Rajagopalan N, Garcia MJ, Rodriguez L, Murray RD, Apperson-Hansen C, Stugaard M et al. Comparison of new Doppler echocardiographic methods to differentiate constrictive pericardial heart disease and restrictive cardiomyopathy. Am J Cardiol 2001; 87(1):86–94.
13. Ha JW, Oh JK, Ommen SR, Ling LH, Tajik AJ. Diagnostic value of mitral annular velocity for constrictive pericardits in the absence of respiratory variation in mitral inflow velocity. J Am Soc Echocardiogr 2002; 15(12):1468–1471.
14. Fredman CS, Parsons SR, Aquino TI, Hamilton WP. Sudden death after a stress test in a patient with a large pericardial cyst. Am Heart J 1994; 127(4 Pt 1):946–950.
15. Antonini-Canterin F, Piazza R, Ascione L, Pavan D, Nicolosi GL. Value of transesophageal echocardiography in the diagnosis of compressive, atypically located pericardial cysts. J Am Soc Echocardiogr 2002; 15(2):192–194.
16. Gatzoulis MA, Munk MD, Merchant N, Van Arsdell GS, McCrindle BW, Webb GD. Isolated congenital absence of the pericardium: clinical presentation, diagnosis, and management. Ann Thorac Surg 2000; 69(4):1209–1215.
17. Fukuda N, Oki T, Iuchi A, Tabata T, Manabe K, Kageji Y et al. Pulmonary and systemic venous flow patterns assessed by transesophageal Doppler echocardiography in congenital absence of the pericardium. Am J Cardiol 1995; 75(17):1286–1288.

12

Aorta

IVAN IGLESIAS, DANIEL BAINBRIDGE, JOHN MURKIN
University of Western Ontario, London, Ontario, Canada

ALAN H. MENKIS
University of Manitoba, Manitoba, Canada

I. Anatomical Considerations 261
II. Transesophageal Echocardiography as a Diagnostic Tool 262
III. TEE Imaging of the Thoracic Aorta and Aortic Arch Vessels 263
A. Ascending Aorta 263
B. Descending Aorta 263
C. Aortic Arch 264
IV. Epiaortic Scanning 265
V. Aortic Atherosclerosis 266
A. Aortic Atherosclerosis and Outcomes After Cardiac Surgery 266
B. Sensitivity and Specificity of Intraoperative Techniques for Assessment of Aortic Atheromatosis: TEE, Epiaortic Scan, Clinical Palpation 270
C. Related Echocardiographic Findings with Aortic Atherosclerosis 270
VI. Aortic Dilatation and Aneurysms 270
A. TEE as a Diagnostic Tool for Thoracic Aortic Aneurysms 271
B. Sinus of Valsalva Aneurysms 271
VII. Aortic Dissection 272
A. Clinical Background 272
B. Classification of Aortic Dissection 274
C. Imaging Modalities and Diagnostic Accuracy in Aortic Dissection 276
D. Associated Complications 277
E. Aortic Intramural Hematoma 278
VIII. Traumatic Rupture of Aorta 279
IX. Surgical Strategy in the Management of the Atherosclerotic Ascending Aorta 280
References 282

I. ANATOMICAL CONSIDERATIONS

The aortic wall is composed of three layers: the intima, the media, and the adventitia. The intima is a delicate endothelial layer. The media is a layer composed mainly of elastic fibers arranged in a spiral manner; it contains relatively little smooth muscle and collagen between the elastic fibers. The adventitia, the outer layer of the aortic wall, is composed predominantly of elastic tissue, collagen, and the vasa vasorum. The elastic tissue is responsible for the distensibility (elastic recoil) of the aorta (Ao) while the collagen is the main determinant of the tensile strength. The vasa vasorum provides blood flow to the outer half of the aortic wall including much of the media.

The Ao is divided anatomically into thoracic and abdominal components. The thoracic Ao is further subdivided into ascending, transverse (arch) and descending segments. The ascending Ao is $\sim$5 cm in length. It is divided into the proximal aortic root and a more distal tubular portion which joins the aortic arch. The aortic root extends from the aortic valve (AoV) to the sinotubular junction and contains the sinuses of Valsalva which bulge

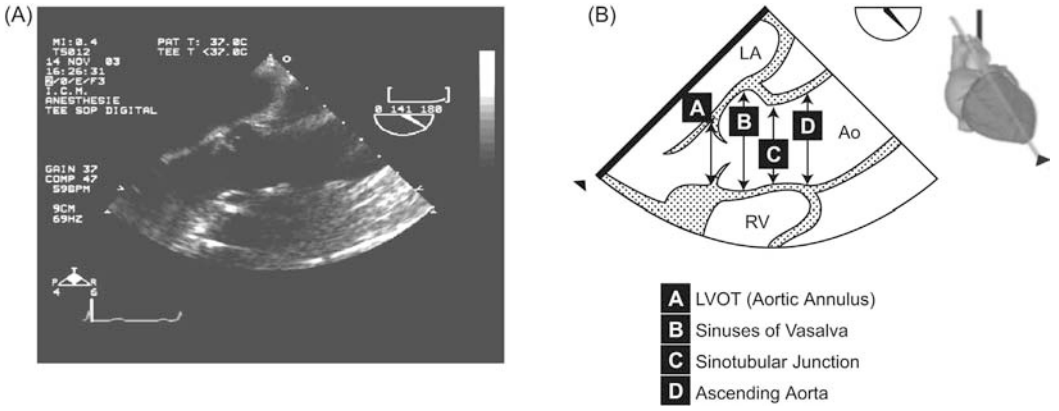

Figure 12.1 Mid-esophageal long-axis view of the ascending aorta (Ao). The sites of measurement of the left ventricular outflow tract (LVOT), aortic annulus, sinus of Valsalva, sinotubular junction, and proximal ascending Ao are indicated (LA, left atrium; RV, right ventricle).

outward from the aortic root allowing full excursion of the aortic leaflets during systole. This segment represents the widest portion of the Ao and measures ~3.3 cm (Fig. 12.1). The aortic annulus supports the aortic leaflets and is crown-shaped with three points extending to the sinotubular junction (see Chapter 15). The right and left main coronary arteries arise from the right and the left sinuses of Valsalva, respectively.

The ascending Ao sits just to the right of the midline and its proximal portion lies within the pericardial cavity. The aortic arch lies superior to the pulmonary artery bifurcation and to the right pulmonary artery. It courses slightly leftward in front of the trachea and then proceeds posteriorly. From the transverse Ao arise the arch vessels, that is, the right brachiocephalic, the left common carotid, and the left subclavian arteries. The aortic isthmus is the point at which the transverse Ao joins the descending Ao (Fig. 12.2). The Ao is relatively vulnerable to acceleration and deceleration injury at this point because it is anchored by the ligamentum arteriosum (see following text) (1,2) (Fig. 12.2).

II. TRANSESOPHAGEAL ECHOCARDIOGRAPHY AS A DIAGNOSTIC TOOL

Echocardiography is considered a good noninvasive tool for the assessment of aortic pathology. Transesophageal echocardiography (TEE) improves resolution of the Ao due to the proximity of the esophagus to the thoracic Ao and the use of high-frequency transducers. It is considered highly accurate, time-saving, and provides assessment of other involved structures such as valves. Moreover, contrary to computed tomography (CT) or magnetic resonance imaging (MRI) scanning, TEE can be easily brought to the patient's bedside and can also be used intraoperatively. Using a multiplane probe, both short- and long-axis views of the ascending Ao are possible with visualization up to 10 cm. The most cephalad portion of the ascending Ao and the proximal segment

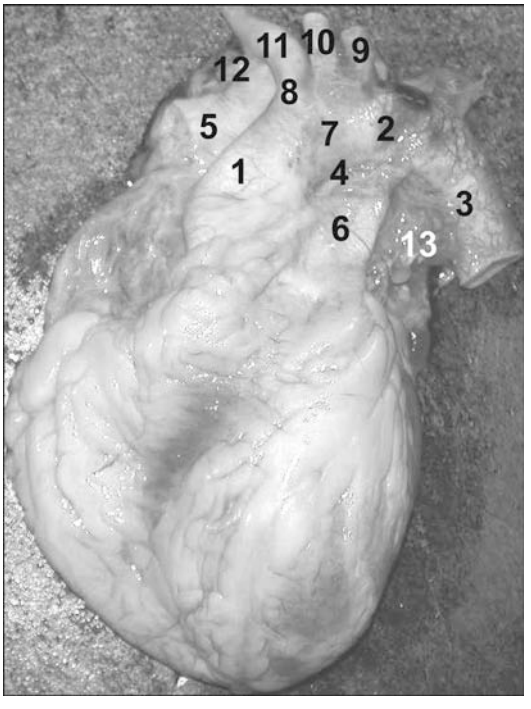

Figure 12.2 Anatomical description of the large vessels (1, ascending aorta; 2, transverse aorta; 3, descending aorta; 4, ligamentum arteriosum; 5, superior vena cava; 6, pulmonary trunk; 7, arch of aorta; 8, brachiocephalic artery; 9, left subclavian artery; 10, left common carotid artery; 11, right common carotid artery; 12, right subclavian artery; 13, left pulmonary veins). (Courtesy of Nicolas Dürrleman.)

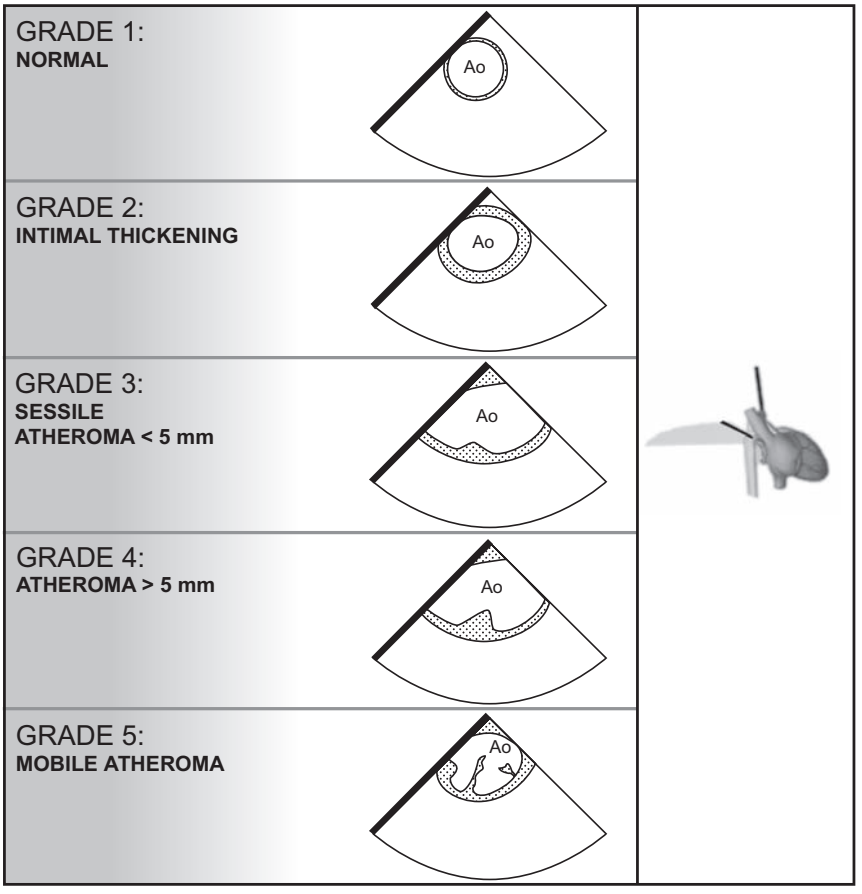

Figure 12.3 Classification of aortic atheromatosis (Ao, aorta). [Adapted from Katz et al. (5).]

of the arch may not always be satisfactorily visualized due to interposition of the right mainstem bronchus and/or the trachea. The descending Ao can usually be scanned entirely and the quality of the images is comparable to CT scan imaging (3,4). The echocardiographic grading of atherosclerotic disease is shown in Fig. 12.3 (5).

By TEE, the normal aortic wall is usually <3 mm thick while the overall diameter of the aortic root is <3.3 cm at the level of the sinuses of Valsalva and <3 cm at the tubular portion of the ascending Ao (Fig. 12.1). The descending Ao is usually <2.8 cm in diameter (4). The echocardiographic examination of the thoracic Ao is shown in Figs. 12.4–12.10.

III. TEE IMAGING OF THE THORACIC AORTA AND AORTIC ARCH VESSELS (SEE ALSO CHAPTER 4)

A. Ascending Aorta

The TEE multiplane probe is positioned at the mid-esophageal (ME) level at 30–40 cm from the incisors in the long-axis (LAX) view at an angle of 135°. From that view, the aortic root and the initial 1–3 cm of the proximal ascending Ao are visible longitudinally (Fig. 12.5); the mid-portion of the ascending Ao will be visualized by withdrawing the probe and lowering the angle to approximately 100° (Fig. 12.8) until the distal ascending Ao is eventually obscured by the acoustical shadowing from the air in the right mainstem bronchus or trachea. The ME short-axis (SAX) view, at an angle of 45°, gives a transverse view of the AoV (Fig. 12.6). As the TEE probe is withdrawn, to an angle of 0–30°, the aortic root, as well as the adjacent superior vena cava (SVC), main pulmonary artery (MPA), and its right and left branches are visualized (Fig. 12.7).

B. Descending Aorta

From the ME view at 0°, the multiplane probe is rotated posteriorly a quarter turn towards the left to reveal a transverse view of the descending Ao (Fig. 12.9). The corresponding longitudinal view of the descending Ao is readily obtained by rotating to an angle of 90°. The probe

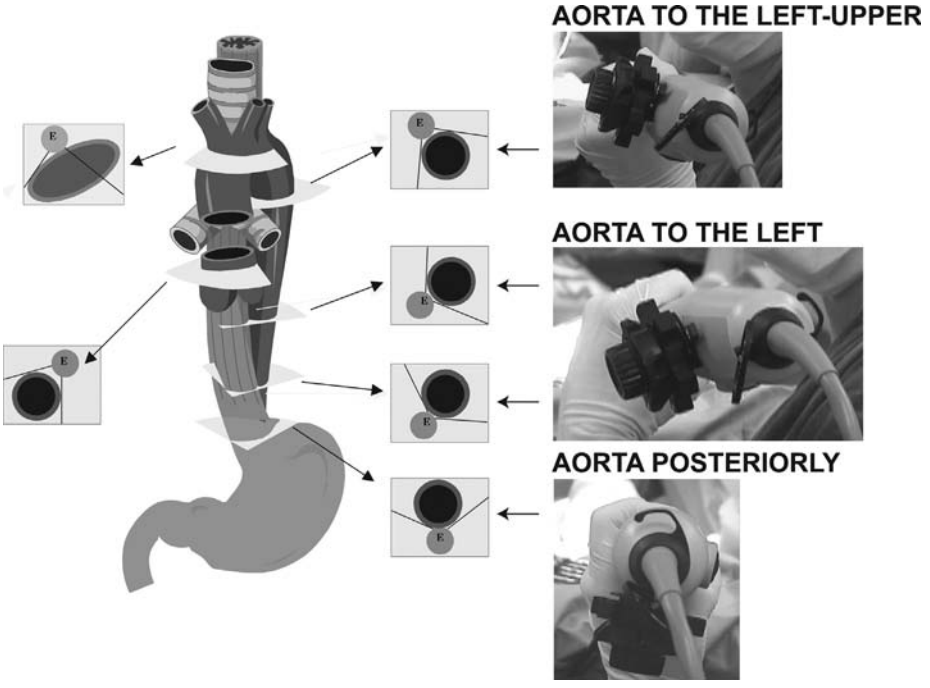

Figure 12.4 Echocardiographic examination of the aorta. Right-sided structures are represented on the left side of the image display. The descending aorta is initially anterior, left and then becomes posterior in the distal portion. Consequently the anatomical orientation of the descending aorta varies according to the position of the transesophageal echocardiographic probe and the aorta (E, esophagus). [Adapted from Freeman et al. (6).]

is advanced into a deep gastric view to follow the descending Ao down to the upper abdominal Ao. Likewise, the proximal descending Ao is assessed by withdrawing the probe to the upper esophageal (UE) level, up to the junction with the distal transverse Ao at 20–25 cm from the incisors.

C. Aortic Arch

In a transverse view at 0°, once in the UE level, the distal transverse arch is revealed at the left of the image (Fig. 12.10) as the probe is rotated anteriorly towards the right. As the imaging plane is rotated to 90°, a vertical SAX view of the mid-portion of the arch is obtained. As the probe shaft is gradually rotated towards the right, the origins of the arch vessels are successively visualized (left subclavian, left common carotid, and right brachiocephalic arteries). More rotation of the probe shaft towards the right will bring into view the distal ascending Ao and the adjacent main pulmonary artery trunk.

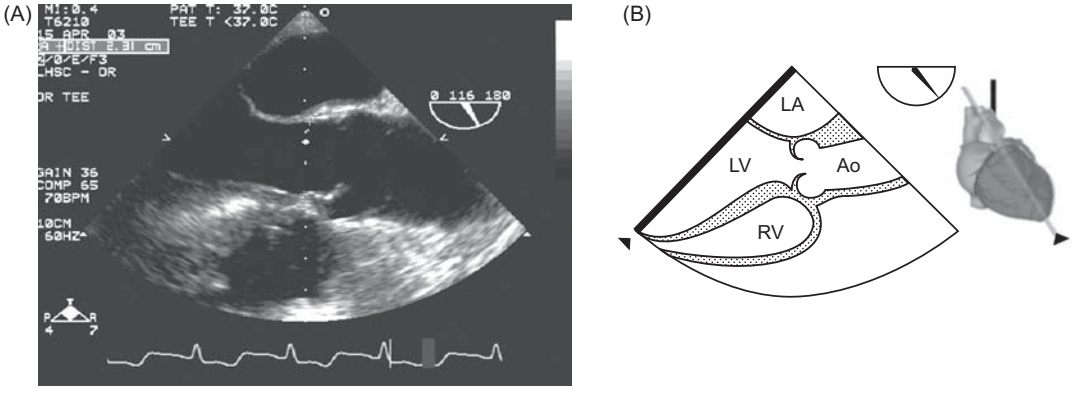

Figure 12.5 Mid-esophageal long-axis view of the ascending aorta (Ao) (LA, left atrium; LV, left ventricle; RV, right ventricle).

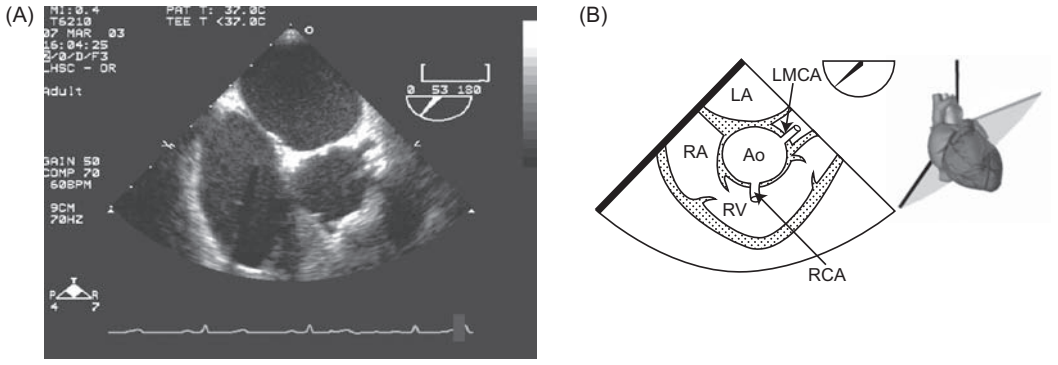

Figure 12.6 Mid-esophageal short-axis view of the aorta (Ao). The two coronary ostia can be visualized (LA, left atrium; LMCA, left main coronary artery; RA, right atrium; RCA, right coronary artery; RV, right ventricle).

IV. EPIAORTIC SCANNING

Ultrasound epiaortic scanning (EAS) using a 5–15 MHz probe directly applied to the ascending Ao by the surgeon has been found to be more reliable than TEE to identify plaque in the mid- and distal ascending Ao, as this segment is obscured by the overlying trachea and right main stem bronchus (5). Epiaortic scanning imaging may be limited by the difficulty with direct application of ultrasound gel within the surgical field, near-field artifacts, and air/tissue interference. This may be minimized by using the epiaortic ultrasound probe with a sterile saline-filled glove acting as a stand off, allowing improved resolution of the anterior wall of the Ao (Figs. 12.11 and 12.12).

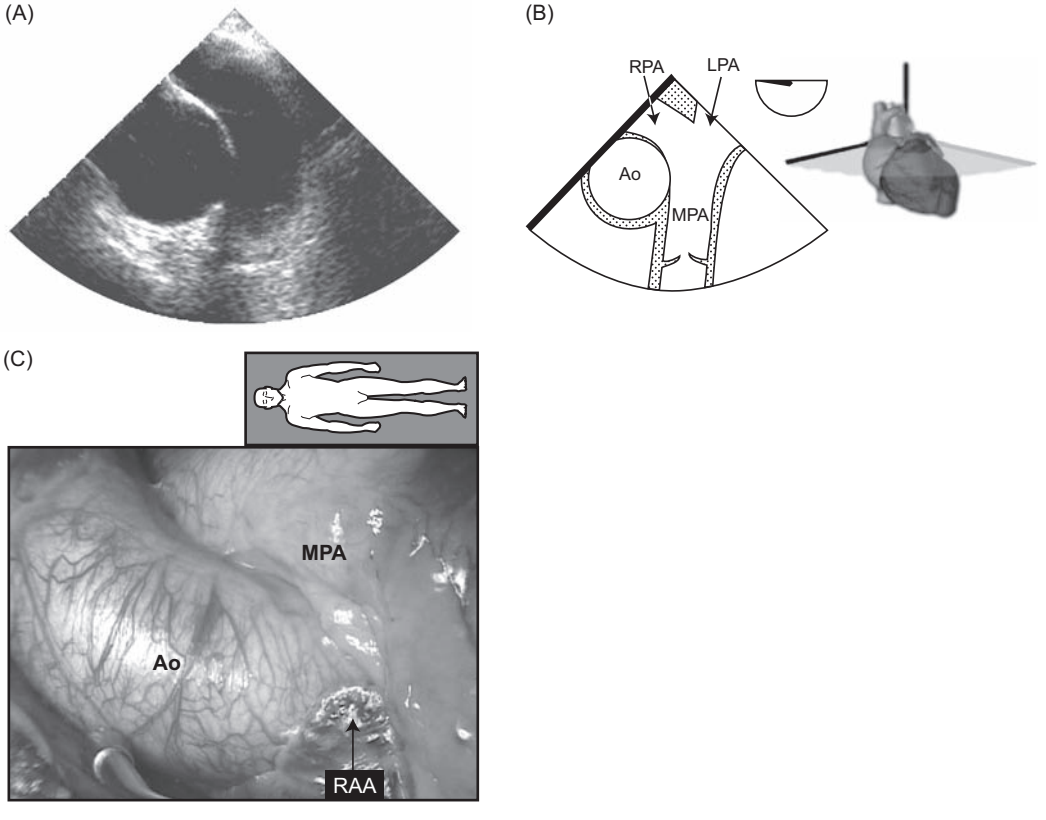

Figure 12.7 (A, B) Upper esophageal view of the aorta (Ao) where the main pulmonary artery (MPA), the right pulmonary artery (RPA), and the origin of the left pulmonary artery (LPA) can be seen. (C) Intraoperative view of the ascending aorta (RAA, right atrial appendage). (Photo C courtesy of Dr. Michel Pellerin.)

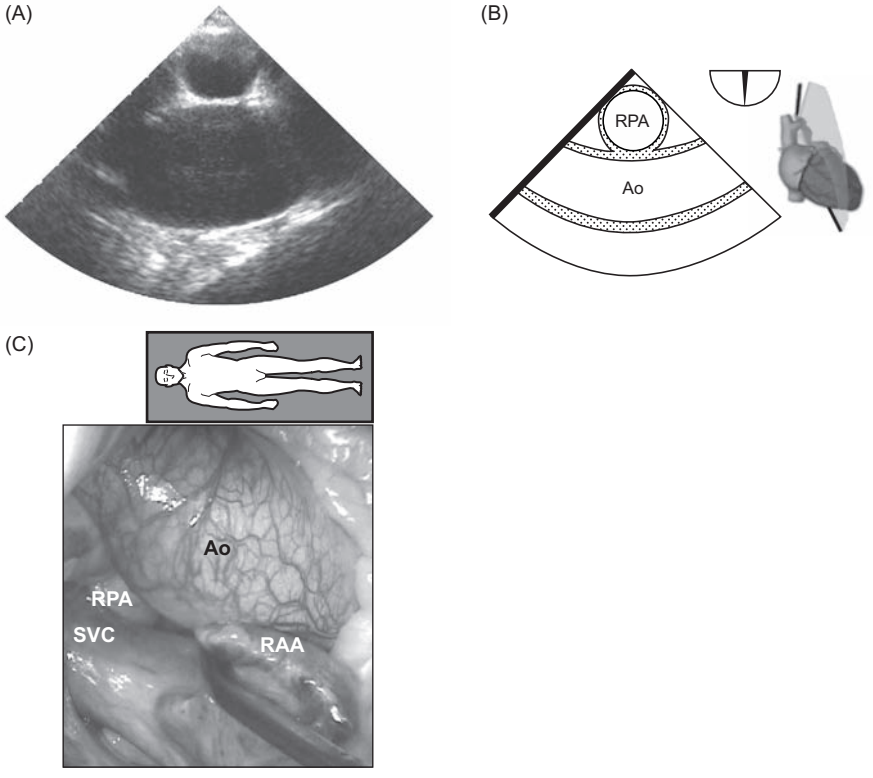

Figure 12.8 (A, B) A more distal view of a dilated ascending aorta (Ao) is obtained by pulling back the probe at 90°. The right pulmonary artery (RPA) is behind the ascending Ao. (C) Operating Room view of the ascending Ao and the RPA (RAA, right atrial appendage; SVC, superior vena cava). (Photo C courtesy of Dr. Michel Pellerin.)

Alternatively, air/tissue interference may be decreased by flooding the mediastinum with warmed saline while keeping the EAS probe tip immersed.

V. AORTIC ATHEROSCLEROSIS

A. Aortic Atherosclerosis and Outcomes After Cardiac Surgery

Aortic atheromatosis is recognized as a significant cause of stroke independent of cardiac surgery, with noncalcific plaque representing the greatest risk (7). It is apparent that atheroemboli, due to disruption of aortic atherosclerotic plaque within the ascending Ao and aortic arch, account for a large portion of the central nervous system (CNS) injury during cardiac surgery (5,8). The risk is higher when mobile plaques are seen in the aortic lumen (Fig. 12.13) compared with aortic wall thickening (Fig. 12.14).

In a series of 1200 patients aged $\geq$50 years in whom intraoperative ultrasound EAS was employed, moderate (3–5 mm thick) or severe (>5 mm, ulcerated plaque, mobile atheroma, or circumferential aortic involvement) ascending aortic atherosclerotic disease was found in 231 patients (19.3%) (9). In 27 patients with severe atherosclerotic disease, the ascending Ao was replaced, with no strokes occurring in this group. Epiaortic Scanning of the ascending Ao was performed in 500 patients aged $\geq$50 years (mean 68 years) who underwent a variety of cardiac operations (10) (89% required bypass grafting). Sixty-eight patients (13.6%) with a mean age of 72 years (range 55–85 years) had significant atheromatous disease in the ascending Ao and were considered to be at increased risk for embolization. Of note, palpation identified atheromatous disease in only 26 patients (38%) and underestimated its severity. A total of 168 modifications to the standard techniques for cannulation and clamping of the Ao were implemented in those 68 patients (mean 2.5 per patient) and included alterations in the sites of aortic cannulation (50 patients), aortic clamping (54 patients), attachment of the vein grafts (35 patients), and cannulation for infusion of cardioplegic solution (29 patients). Ten patients with severe diffuse atheromatous disease underwent graft replacement of the ascending aorta with hypothermic circulatory arrest without aortic clamping. Permanent neurologic deficits occurred in only five patients (1%) in the entire group but in none of the 68 patients with significant atheromatous disease in whom technical modifications were used.

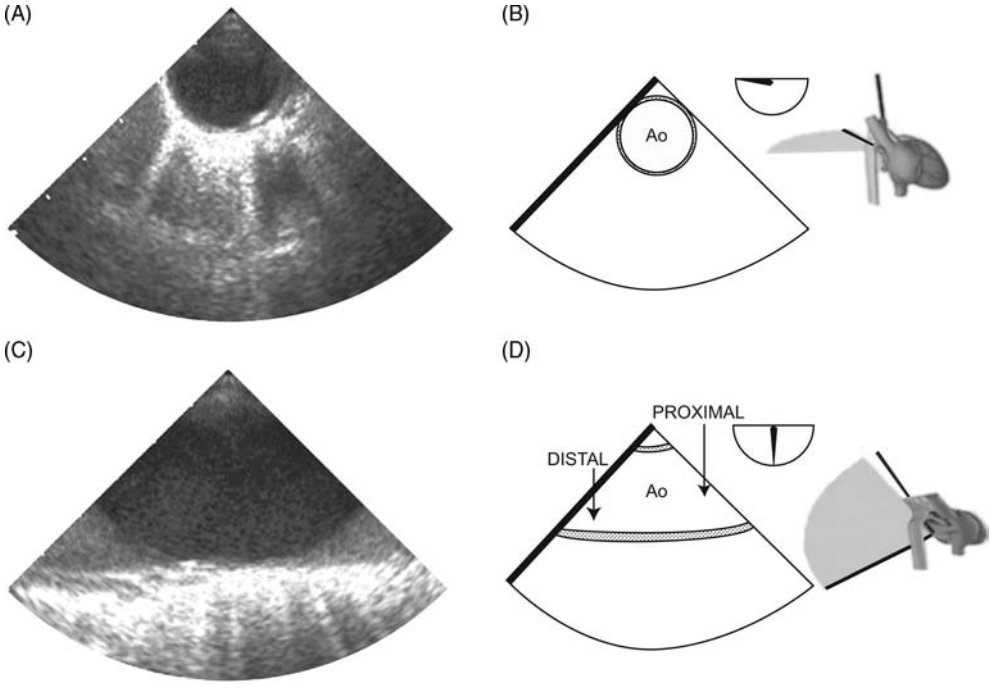

Figure 12.9 Short- (A, B) and long-axis (C, D) views of the aorta (Ao).

The presence of aortic atheromatosis significantly increases the risk of plaque fracture and intimal flap formation after aortic cannulation and clamping as demonstrated by EAS (11). Thus, the potential for subsequent embolization of either plaque or thrombus is high and probably accounts for many of the otherwise unexplained strokes seen on the second or third postoperative day. Whether identification of such lesions warrants the

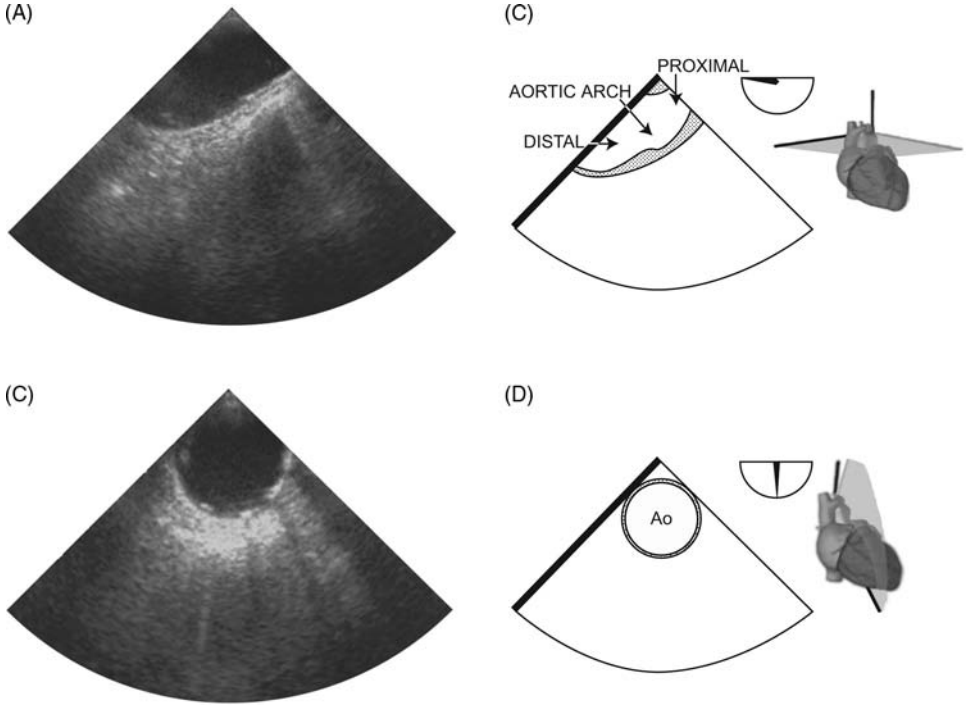

Figure 12.10 Upper esophageal 0° (A, B) and 90° (C, D) views of the aortic arch (Ao, aorta).

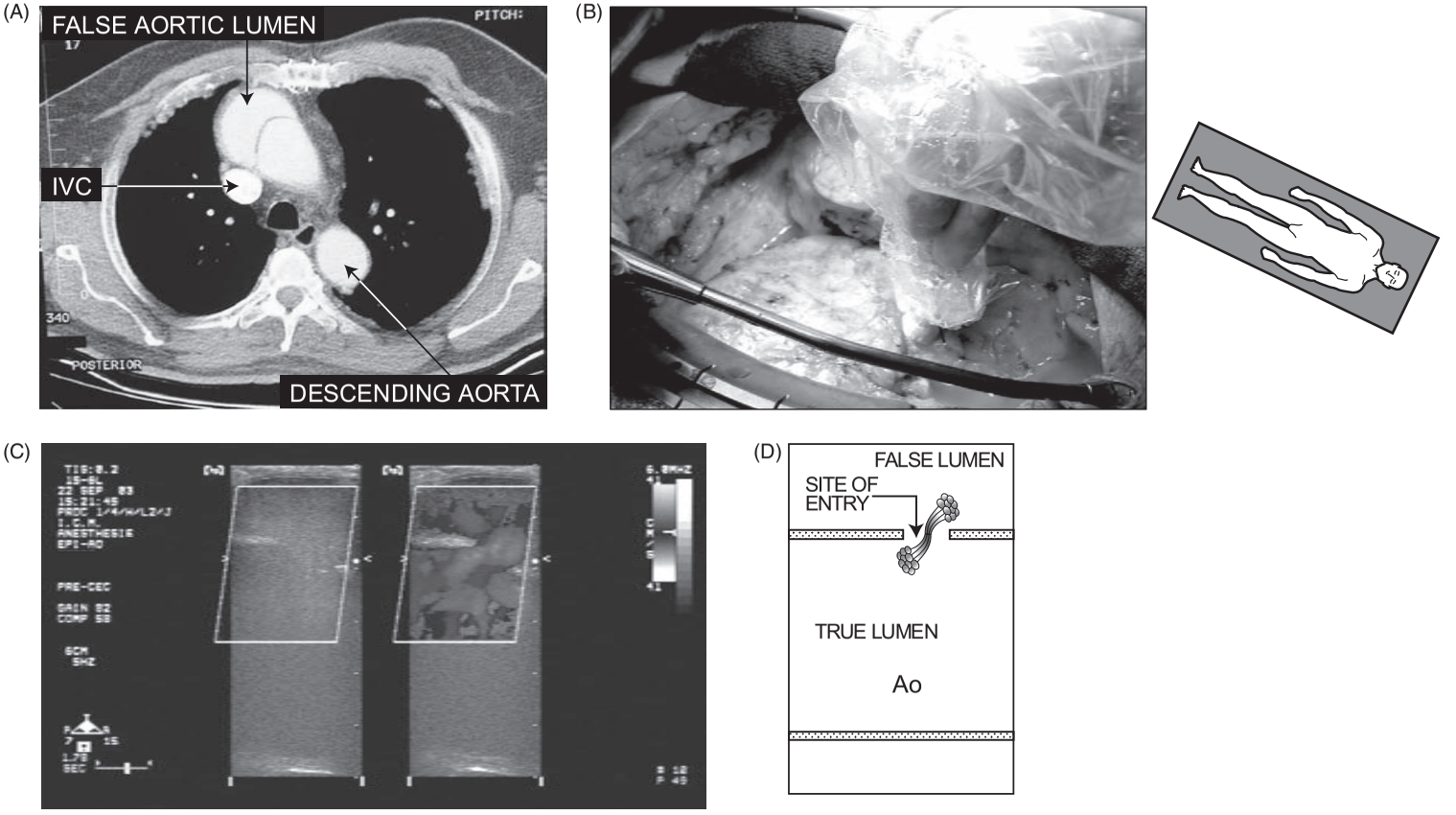

Figure 12.11 Traumatic aortic dissection in a 69-year-old man reoperated on after coronary artery revascularisation. (A) Computed tomography scan. (B) Epiaortic probe imaging is used to localise the site of the aortic rupture (C, D) (Ao, aorta; IVC, inferior vena cava). (Photo B courtesy of Dr. Raymond Cartier.)

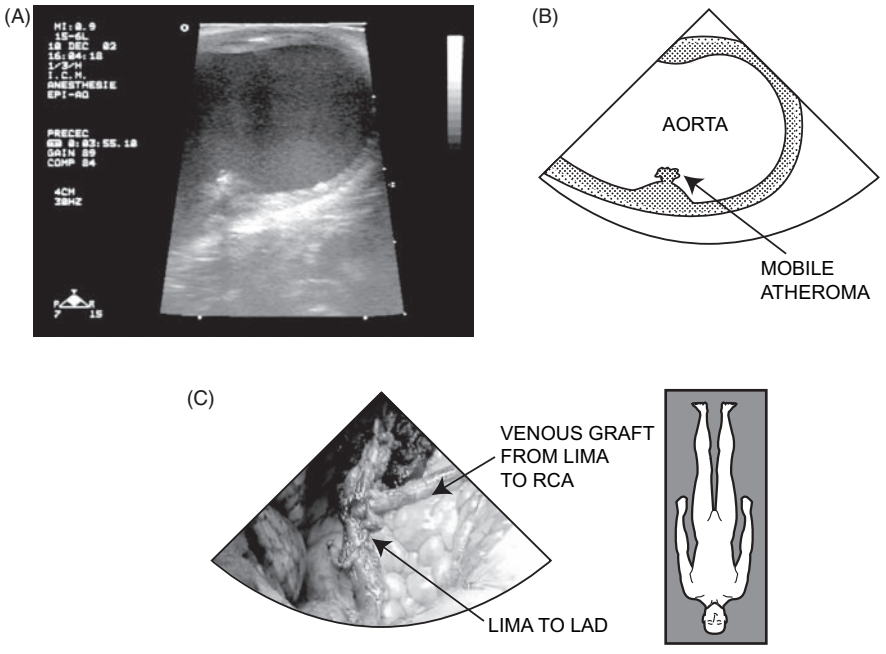

Figure 12.12 (A, B) Epiaortic probe imaging of the aortic arch revealing a mobile atheroma (grade 5) in a 74-year-old woman before cardiopulmonary bypass. (C) To avoid aortic clamping during off-pump coronary artery bypass grafting, the saphenous vein graft to the right coronary artery (RCA) was anastomosed to the left internal mammary (LIMA) graft rather than on the aorta as is usually the case (LAD, left anterior descending coronary artery). (Photo C courtesy of Dr. Louis P. Perrault.)

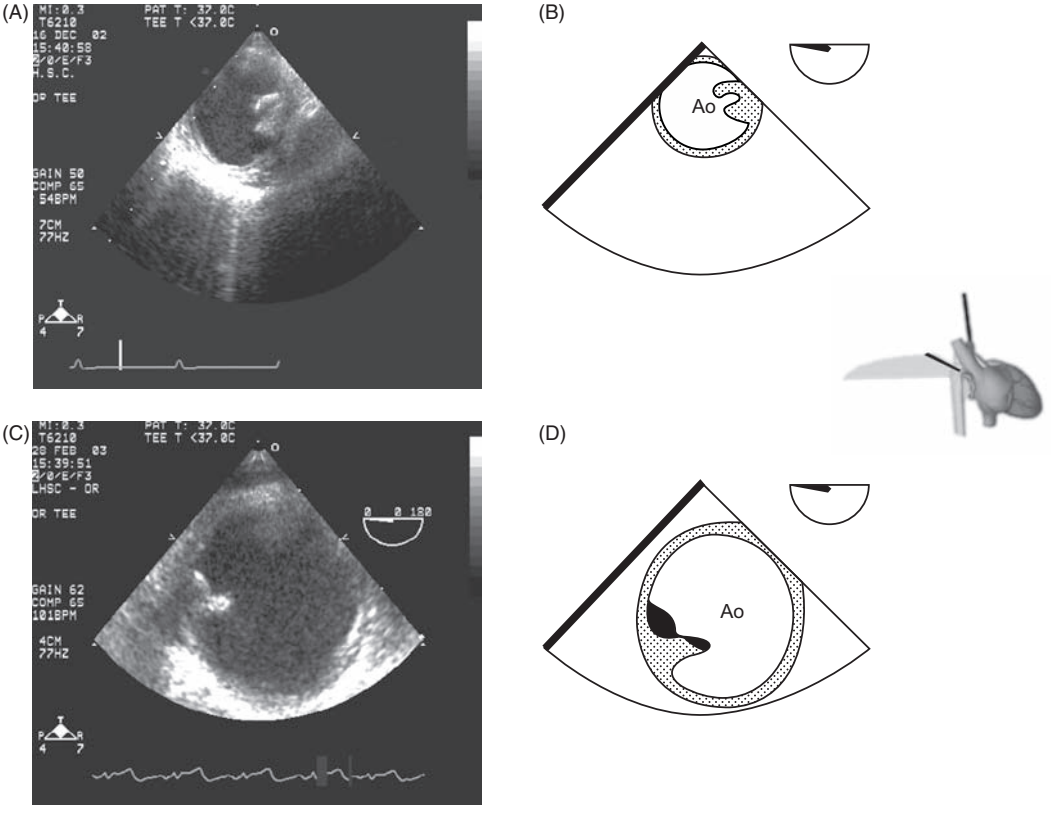

Figure 12.13 (A–D) Short-axis view of mobile plaques (grade 5) in the descending aorta (Ao).

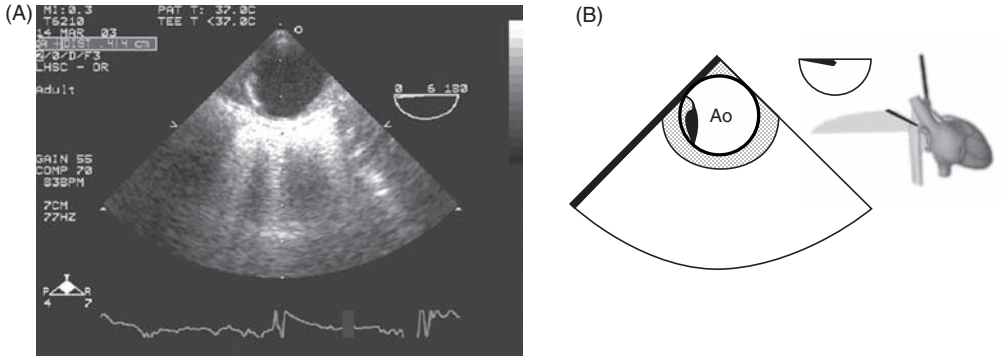

Figure 12.14 Short-axis view of a 4.1 mm thick plaque (grade 3) in the aorta (Ao) before cardiopulmonary bypass.

administration of postoperative antithrombotic therapy to decrease the risk of stroke is unclear.

B. Sensitivity and Specificity of Intraoperative Techniques for Assessment of Aortic Atheromatosis: TEE, Epiaortic Scan, Clinical Palpation

Several authors (12,13) have demonstrated the lower reliability of both palpation and TEE examination for assessing atheromatosis in the mid- and distal ascending Ao.

Transesophageal echocardiography detection of significant atheromatosis in the descending Ao has been felt to indicate a high likelihood of coexisting involvement of the ascending Ao. However, in one study (14), the positive predictive value for ascending aortic atheroma or the presence of atheroma in the descending Ao was only 39%. However, of the 32 patients with only mild or no atheroma in the descending Ao, only one had moderate to severe atheromatous disease in the ascending Ao (negative predictive value 94%).

The presence of atherosclerosis in the aortic arch can be predicted in $<50\%$ of patients preoperatively by age, chest X-ray (CXR), and aortogram. Transesophageal echocardiography detects atheromatous disease in 55% of patients with a normal CXR (8). Furthermore, 50–80% of significant atherosclerotic lesions present in the ascending Ao are missed by intraoperative palpation when compared with TEE (8,9,15–17). Katz et al. (5), in a prospective study involving 130 patients, found on TEE that 19 of 23 patients (83%) initially considered to have no or mild atheroma by manual palpation had in fact severe disease. While calcific plaque can be reasonably well detected, atheroma it is more difficult to detect by palpation (18).

Direct manual palpation of the Ao was shown to have a sensitivity of only 46% for detecting aortic atherosclerosis when compared with intraoperative EAS in 89 cardiac surgical patients (19). In 11.2% of patients, the operative approach was modified to avoid the plaques detected by EAS. This diagnostic tool appears to be the most sensitive method to assess the ascending Ao intraoperatively. As the presence of significant atherosclerosis in the descending Ao on TEE would predict a 40% probability of concomitant involvement of the ascending Ao, the authors suggested the use of more sensitive EAS in such patients.

C. Related Echocardiographic Findings with Aortic Atherosclerosis

Further indication of the presence of atherosclerosis in the Ao may be inferred from the presence of cardiac valvular calcification. A significant association between the presence of aortic valvular and mitral annular calcification and the presence and severity of ascending aortic atheroma has been demonstrated (20). Thus, aortic valve calcification may serve as a marker for atherosclerosis of the Ao (20). When preoperative TEE discloses AoV or mitral annulus calcification, plaque in the ascending or descending Ao, some authors have recommended proceeding directly to EAS of the ascending Ao prior to cannulation and instrumentation (20,21).

Other indications for EAS include age (>60 years old), calcified aortic knob on CXR or palpable calcifications in the ascending Ao, severe peripheral vascular disease (PVD) and previous history of transient ischemic attack (TIA) or cerebrovascular accident (CVA).

VI. AORTIC DILATATION AND ANEURYSMS

An aortic aneurysm is defined as a localized dilatation or enlargement of the Ao. As the Ao dilates, its wall tensile strength becomes progressively weakened and may lead to dissection and/or rupture (2,22). Aneurysms can result from a variety of congenital and acquired pathologies and involve any segment of the Ao. Aortic aneurysms are considered significant when their diameter exceeds two standard deviations above the normal

diameter (22). Aneurysms of the thoracic Ao are reported to occur with an incidence of 5.9 per 100,000 patients and are more commonly observed in the older age groups. Aortic aneurysms can be classified based on four characteristics: shape, location, etiology, and histology (Table 12.1). Ascending aortic aneurysms are located proximal to the origin of the brachiocephalic trunk (innominate artery); aortic arch aneurysms are located between the brachiocephalic trunk and the left subclavian artery; descending aortic aneurysms are located between the left subclavian artery and the diaphragm (Fig. 12.15). Aneurysms may have either a fusiform or saccular shape. Histologically, they may be classified into three categories: (1) true aneurysms, where all three normal layers (intima, media, and adventitia) are present in the aneurysm wall; (2) dissecting aneurysms, where the normal aortic wall layers are divided with the formation of a false lumen; and (3) false aneurysms, due to aortic wall rupture that is contained only by the adventitia (1,22,24) (Table 12.1).

Aortic aneurysms involve the ascending Ao in approximatively 50% of cases, the descending portion in 40% and the arch in 10%. The most common etiologies of aortic aneurysms are atherosclerosis and/or cystic medial degeneration. Descending Ao aneurysms are caused most often by atherosclerosis while ascending and transverse aortic aneurysms are commonly due to cystic medial degeneration (1–3,25) (Fig. 12.15). Aortic aneurysms are frequently associated with hypertension and their incidence is higher in the seventh decade of life.

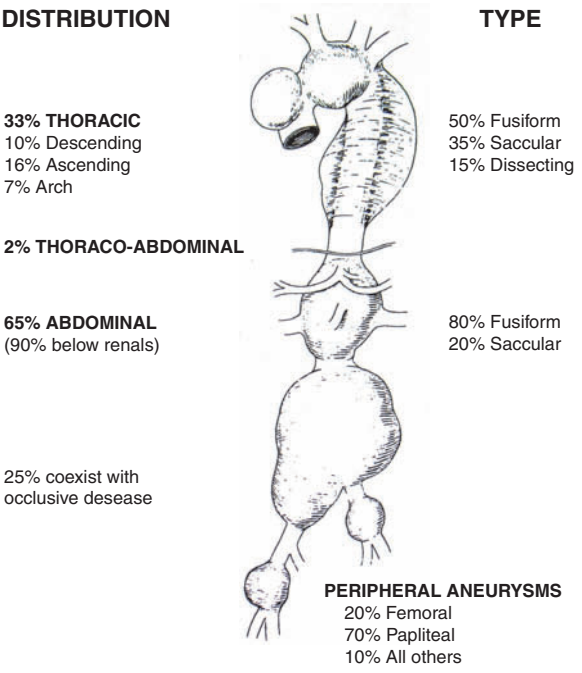

Figure 12.15 Frequency and distribution of aortic aneurysms. [With permission from Jackson (23).]

A. TEE as a Diagnostic Tool for Thoracic Aortic Aneurysms

Characteristic findings on two-dimensional (2D) echocardiography include dilatation of the Ao (Fig. 12.16), increased echogenicity of the aortic wall and presence of intraluminal spontaneous echo contrast reflecting decreased blood flow locally and mural thrombus formation (Fig. 12.17). In the presence of a mural thrombus, differentiation of an aortic aneurysm from aortic dissection may become difficult (Fig. 12.17) (4,24,26).

Table 12.1 Classification of Aortic Aneurysms (See Text for Details)

Shape	Saccular
	Fusiform
Histology	True
	Dissecting
	False aneurysm
Location	Ascending
	Arch
	Descending
Etiology	Cystic medial degeneration/necrosis
	Atherosclerosis
	Congenital
	Inflammatory
	Other

B. Sinus of Valsalva Aneurysms

Aneurysms of the sinus of Valsalva are considered to be a congenital defect resulting from the discontinuity between the aortic media and the annulus fibrosus. The frequent association of aneurysms of the sinus of Valsalva with ventricular septal defects also supports a congenital etiology. These aneurysms arise from the right coronary sinus in 65–85% (Fig. 12.18), from the noncoronary sinus in 10–30% but rarely (<5%) from the left coronary sinus (Fig. 12.19). Associated lesions include ventricular septal defects in 30–60% of cases, aortic regurgitation (AR) in 20–30% and less commonly, bicuspid AoV, atrial septal defect and pulmonic valve stenosis. Such congenital aneurysms show a male to female ratio of 4:1 and a racial predominance of Asian patients.

Aneurysms of the sinus of Valsalva commonly cause symptoms from the compression of neighboring coronary arteries, obstruction of the right ventricular outflow tract (RVOT) or rupture into an adjacent chamber. The latter may be spontaneous or may occur after intense physical

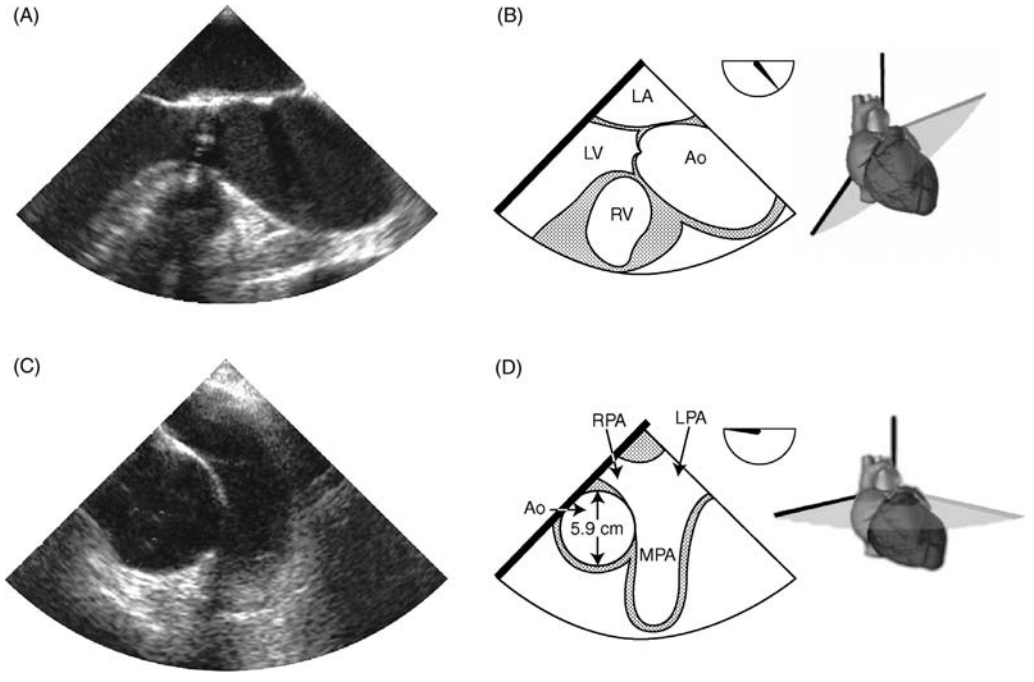

Figure 12.16 Mid-esophageal long-axis (A, B) and upper esophageal short-axis (C, D) views of an ascending aortic aneurysm. The ascending aorta (Ao) diameter is 5.9 cm, which is almost twice the upper limit of normal (LA, left atrium; LPA, left pulmonary artery; LV, left ventricle; MPA, main pulmonary artery; RPA, right pulmonary artery; RV, right ventricle).

exercise or trauma, or result from complicated acute bacterial endocarditis. Aneurysms of the right coronary sinus tend to extend to the right atrium (RA) and right ventricle (RV) while those of the noncoronary sinus usually extend to the RA. Rarely, these aneurysms may rupture into the pericardium and cause a lethal tamponade.

On TEE imaging, these aneurysms present as a finger-like "wind sock" cavity extending from the affected sinus (Fig. 12.18). Potential involvement of the AoV and both coronary arteries as well as extension or communication of the aneurysm with any of the heart chambers must be ruled out using color flow Doppler (4,22,26,27).

VII. AORTIC DISSECTION

A. Clinical Background

The incidence of aortic dissection in the general population is around five per million. However, several necropsy series have reported evidence of aortic dissection in ~0.2% of cases. Hypertension is the most commonly reported risk factor. Males have a higher incidence than females, with ratios varying from 2:1 to 5:1. Patients with Marfan or Turner syndrome, as well as those with Ehlers–Danlos or coarctation, have an increased risk of

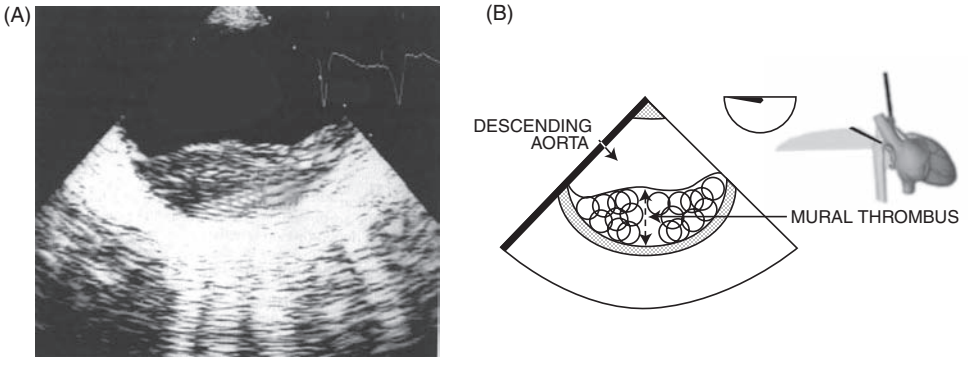

Figure 12.17 Mid-esophageal posterior view showing ectasia of the descending aorta and mural thrombus formation. [With permission from Erbel and Zamorano (24).]

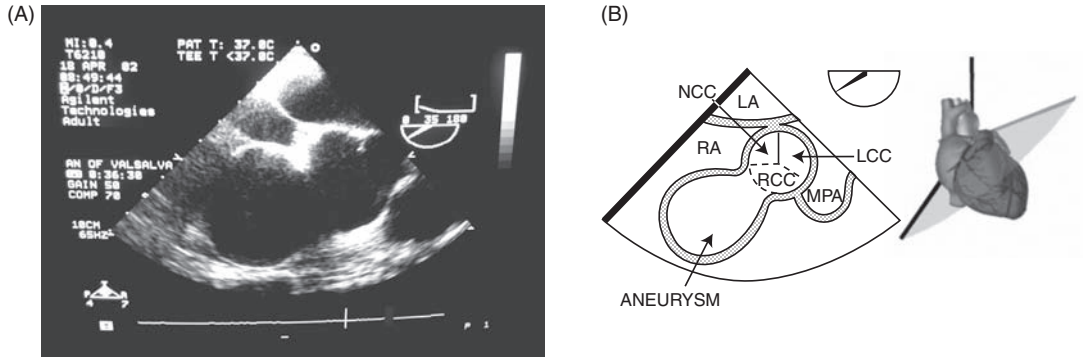

Figure 12.18 Mid-esophageal short-axis view of an aneurysm of the right sinus of Valsalva (LA, left atrium; LCC, left coronary cusp; NCC, noncoronary cusp; MPA, main pulmonary artery; RA, right atrium; RCC, right coronary cusp).

aortic dissection. Patients with unicuspid or bicuspid AoVs are also at increased risk of aortic dissection. Interestingly, atherosclerosis is not considered an independent risk factor for aortic dissection but does increase the risk of free rupture following dissection (28).

Patients with acute aortic dissection typically describe sudden severe chest and/or back pain. At the onset, the pain is most severe, sometimes excruciating, with little or no change in the intensity but sometimes with migrating location or in association with syncope. Sixty percent of

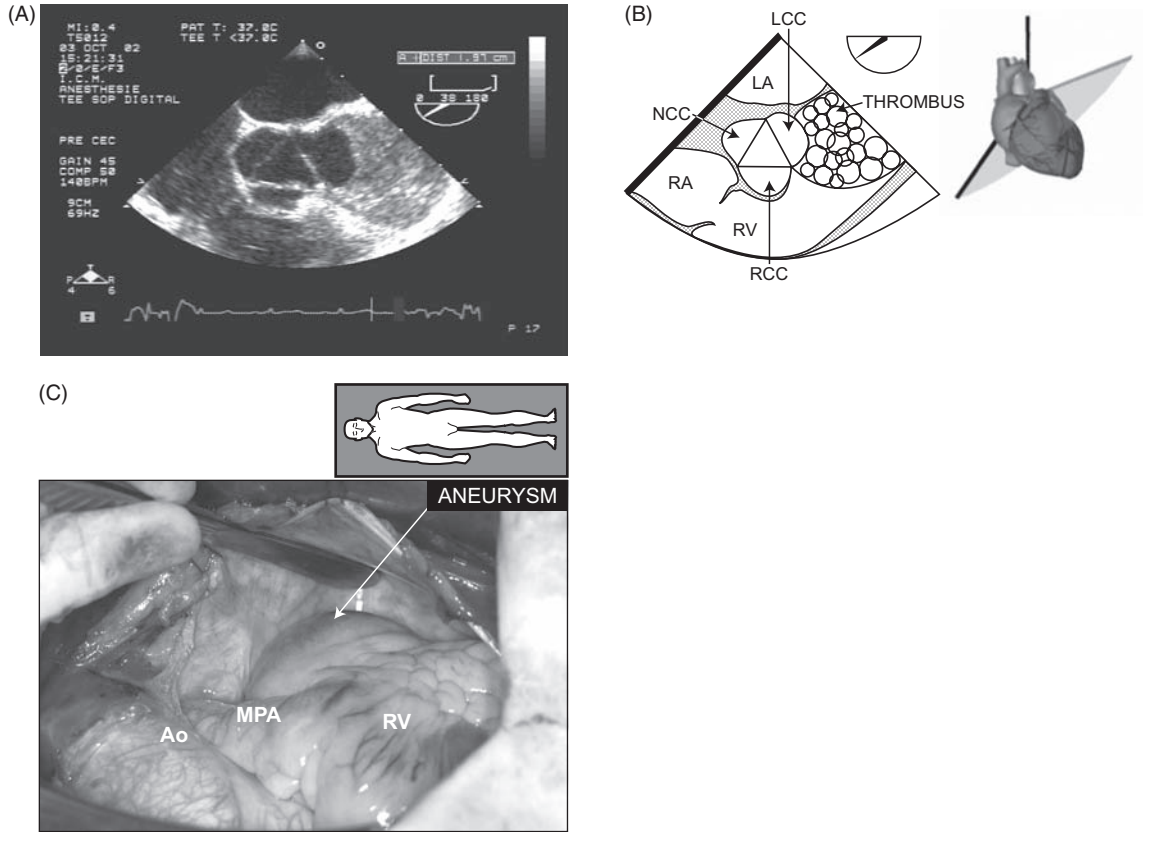

Figure 12.19 A 64-year-old woman was scheduled for repair of a left sinus of Valsalva aneurysm. (A, B) A mid-esophageal short-axis view showed the aneurysm of the sinus of Valsalva originating from the left coronary cusp (LCC). Thrombus is present in the aneurysmal sac. (C) Intraoperative view (LA, left atrium; NCC, noncoronary cusp; MPA, main pulmonary artery; RA, right atrium; RCC, right coronary cusp; RV, right ventricle). (Photo C courtesy of Dr. Denis Bouchard.)

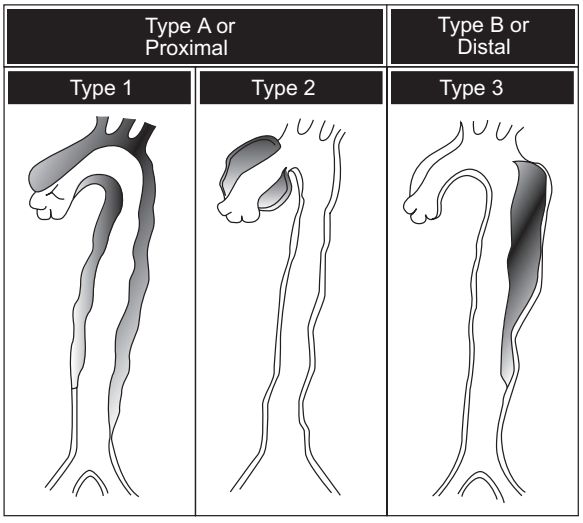

Figure 12.20 Classifications of aortic dissection: Stanford type A or B, DeBakey types I–III.

patients will demonstrate a pulse deficit or asymmetry in arterial blood pressure in at least one limb due to the occlusion of one or more aortic branches caused by aortic dissection. Hypertension or hypotension may be present. Hypertension may be related to several factors including pain, anxiety, and preexisting elevated blood pressure. Hypotension may result from severe AR, dissection and occlusion of a coronary ostium, cardiac tamponade or right ventricular failure from right pulmonary artery compression. Patients may also present with neurologic symptoms including stroke, Horner's syndrome, or paraplegia. These result from compromised perfusion or direct compression by expanding anatomical structures.

B. Classification of Aortic Dissection

Two classifications are currently used for aortic dissection and both are based on the anatomical location of the tear (Fig. 12.20). In the *Stanford* classification, any involvement of the ascending Ao is categorized as type A (Fig. 12.21) and all other tears are categorized as type B. The *DeBakey* system categorizes dissection limited to the ascending Ao as type I; tears which propagate past this area are classified as type II; finally, tears limited to the descending Ao are labeled as type III with the IIIa designation denoting a tear limited to the supradiaphragmatic region and a IIIb indicating extension below the diaphragm.

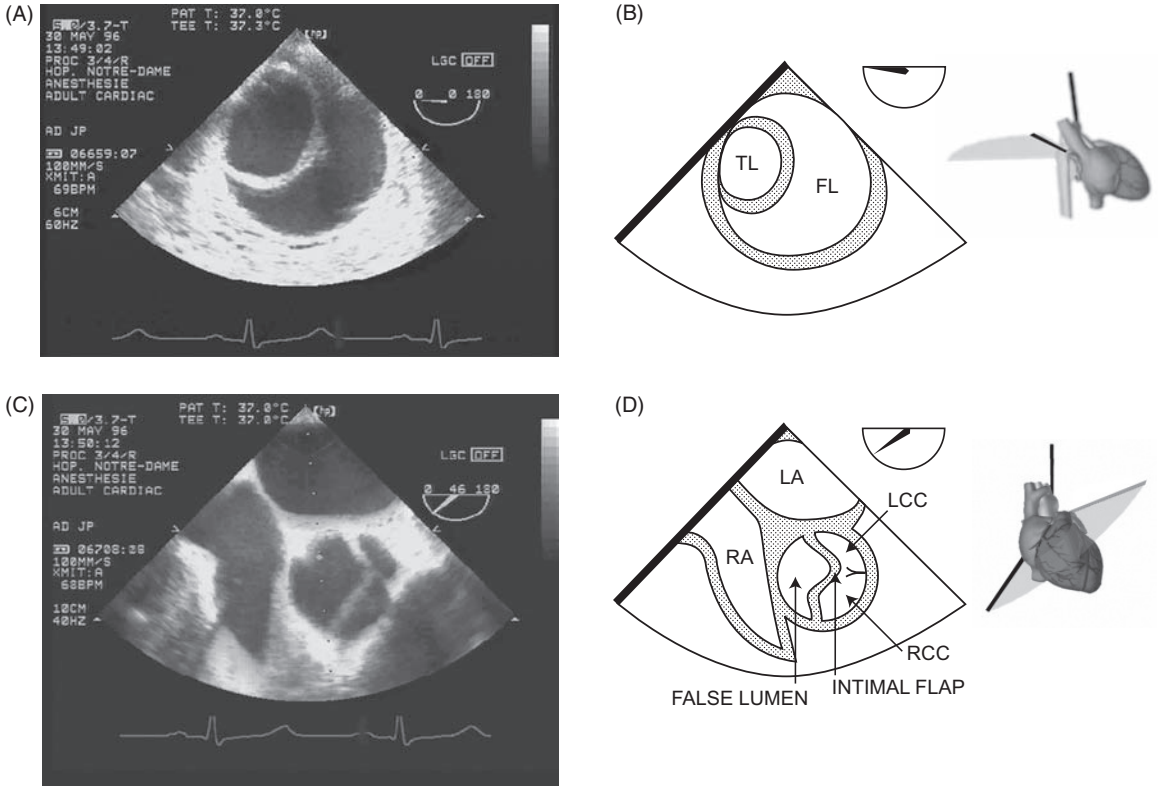

Figure 12.21 Acute aortic dissection Stanford type A (A, B) with extension up to the aortic valve (C, D). The true lumen (TL) has a smaller diameter and is more pulsatile compared with the false lumen (FL) (LA, left atrium; LCC, left coronary cusp; RA, right atrium; RCC, right coronary cusp).

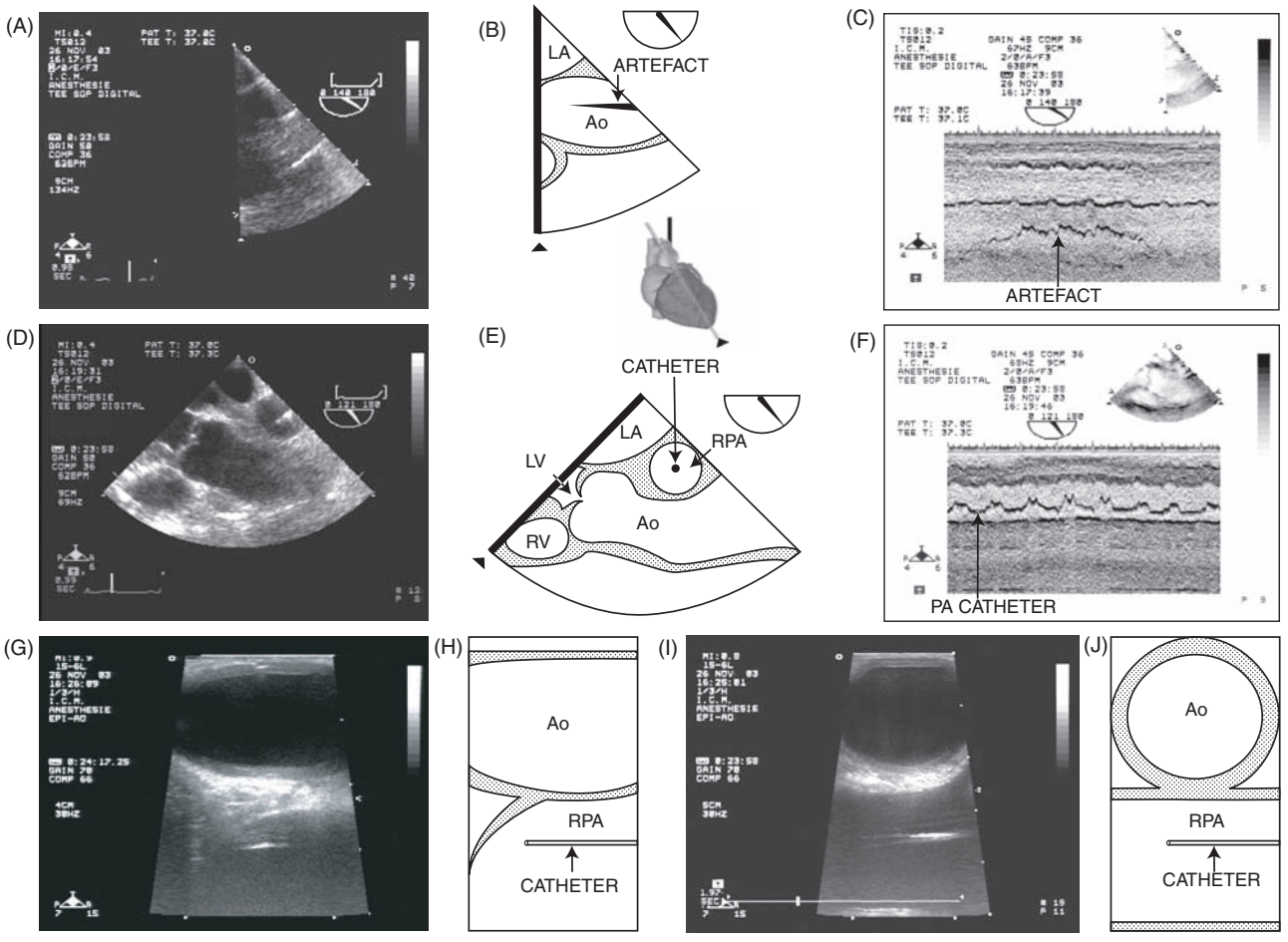

Figure 12.22 A 57-year-old man is scheduled for coronary revascularization. Insertion of the canula in the aorta (Ao) was problematic and suggested aortic dissection to the surgeon. A mobile linear shadow was seen in a long-axis mid-esophageal view of the ascending Ao (A, B) and the linear shadow was seen below the aortic wall on M-mode (arrow on C). A pulmonary artery (PA) catheter was present in the right pulmonary artery (RPA) (D, E) and its excursion on M-mode was similar to the movement of the suspected aortic flap (arrow on F). An epiaortic examination of the ascending aortic root was performed which ruled out aortic dissection (G, H). The PA catheter was also seen in the epiaortic view (G–J). The suspected flap was an artefact originating from the PA catheter in the RPA (LA, left atrium; LV, left ventricle; RV, right ventricle).

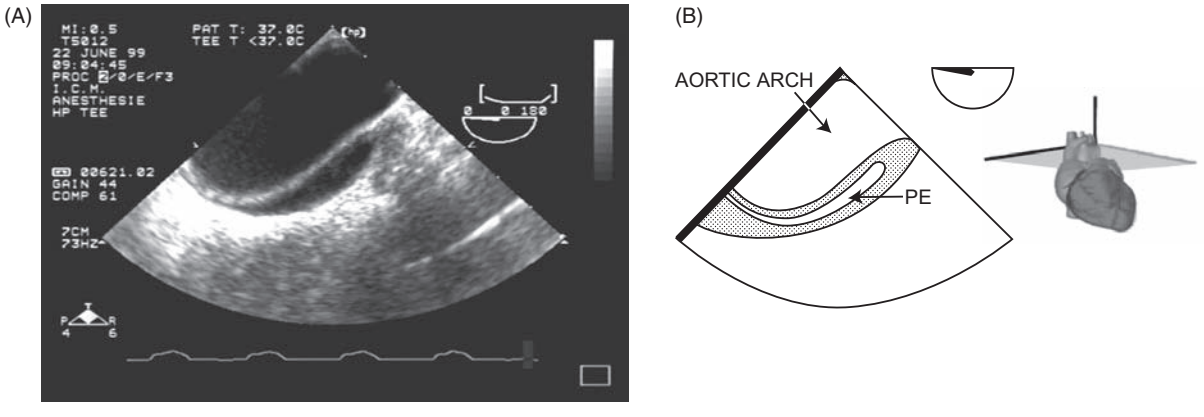

Figure 12.23 A 25-year-old woman was scheduled for aortic valve replacement. A pericardial effusion (PE) along the distal ascending aorta was present and mimicked an aortic dissection.

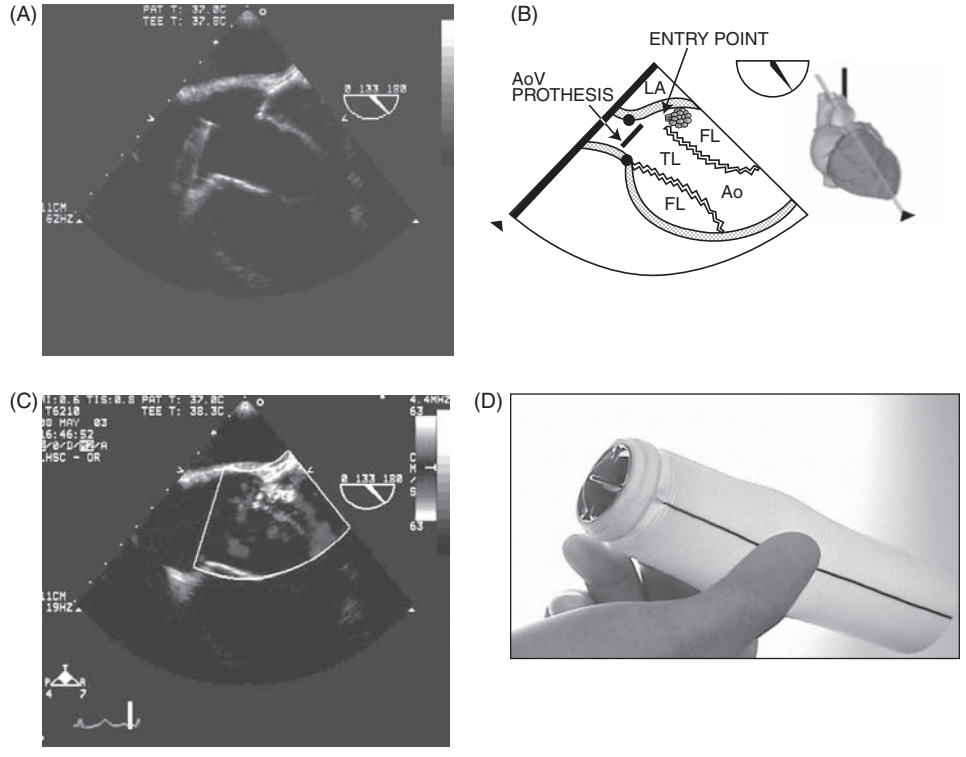

Figure 12.24 Mid-esophageal long-axis view of an ascending aortic dissection in a patient with a previously placed ascending aortic graft. (A, B) The true lumen (TL) is contiguous with the aortic valve (AoV) and is easily identified in this 133° view. The false lumen is also identified (FL). (C) Color Doppler imaging allowed identification of the entry point. Blood flow was confined by the graft and forced the blood to exit eventually via an aortoatrial fistula. (D) Ascending aortic graft with a single-disk valve (Ao, aorta; LA, left atrium).

C. Imaging Modalities and Diagnostic Accuracy in Aortic Dissection

The diagnosis of aortic dissection has evolved as new diagnostic techniques have become available. In the past, conventional contrast angiography was the gold standard used to establish the diagnosis. However, this technique was invasive, required time and expertise in planar image acquisition and interpretation to demonstrate intimal flap. New techniques such as digital subtraction angiography, tomographic CT, and MRI scanning as well as TEE imaging have broadened the diagnostic armamentarium available to clinicians.

Many studies have examined the accuracy of diagnosis of these different diagnostic modalities. Erbel et al. (29) showed TEE to be 99% sensitive and 98% specific for

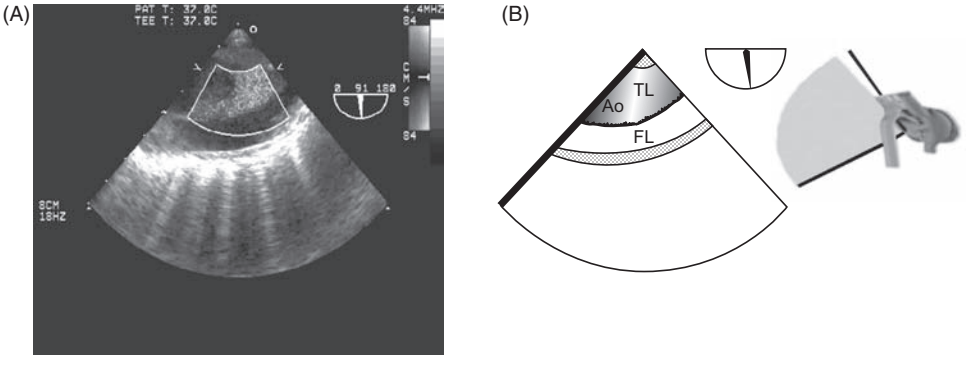

Figure 12.25 Low esophageal long-axis view of an aortic dissection occurring after cardiopulmonary bypass. The true lumen (TL) is demonstrated by the presence of blood flow as seen with color Doppler. The false lumen (FL) lacks blood flow and has formed a blind sac (Ao, aorta).

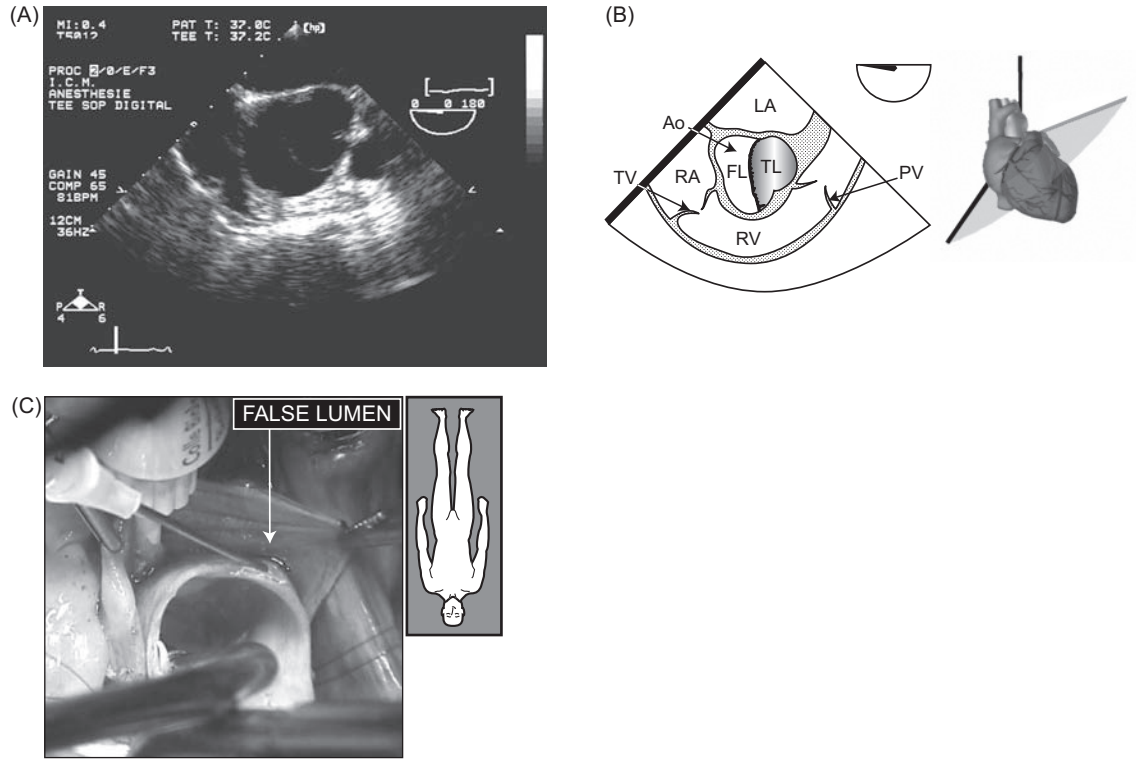

Figure 12.26 A 59-year-old woman with sudden onset of severe chest pain while swimming was admitted after the diagnosis of aortic dissection was made with computed tomography scan and confirmed intraoperatively. (A, B) The aortic dissection involved the proximal ascending aorta and all the rest of the aorta down to the iliac arteries. (C) Intraoperative view. Note the false lumen (FL) (Ao, aorta; LA, left atrium; PV, pulmonic valve; RA, right atrium; RV, right ventricle; TL, true lumen; TV, tricuspid valve). (Photo C courtesy of Drs. Nicolas Noiseux and Raymond Cartier.)

the diagnosis of dissection. In a report by Adler et al. (20), the sensitivity, specificity, positive, and negative predictive values for CT scanning were 83%, 100%, 100%, and 86% respectively. Corresponding values for aortography were reported to be at 88%, 94%, 96%, and 84%. While Nienaber et al. (30) reported a sensitivity of 100% for both TEE and MRI, the specificity of TEE was lower (68%) than that of MRI (100%). Nevertheless, TEE has the advantage of being more easily accessible at the bedside for hemodynamically unstable patients and may also be performed intraoperatively. This allows unstable patients to be monitored and treated in a safe environment. As mentioned previously, a complete evaluation of the entire ascending Ao with TEE may sometimes be impossible due to the trachea and/or the right mainstem bronchus interfering with the visualization of the mid and distal ascending aortic segments. Dissections discretely limited to these blind areas could therefore be missed despite careful TEE examination (31). An erroneous diagnosis can also occur when there is increased aortic diameter (>5 cm), which is associated with a higher incidence of linear artifacts (32). Other linear artifacts may also originate from pulmonary artery catheters (Fig. 12.22) and pericardial effusions (Fig. 12.23).

The diagnosis of aortic dissection is based on the identification of an intimal flap dividing the Ao into two separate channels, the true and the false lumen (Figs. 12.24–12.27). Determining which lumen is the false one may sometimes be difficult. Nevertheless, blood should not flow freely through the false lumen if it is a blind pouch. On 2D imaging, the pulsatile lumen could represent the true lumen, while smoke-like or twirling spontaneous echo contrast suggests sluggish or absent flow in the false lumen (Fig. 12.21). Color flow imaging and pulsed-wave (PW) Doppler may also confirm decreased flow in the blind false lumen (Fig. 12.25). However, these criteria may also be misleading in certain settings: indeed if the false lumen has a proximal entry and a distal exit site, blood may flow freely both in the false and true lumen. Epiaortic scanning can be helpful to localize the site of intimal rupture.

D. Associated Complications

In addition to identifying the location and extent of dissection, evidence of associated complications must also be sought. Aortic regurgitation may result from both annular dilation of the aortic root and direct geometric disruption of the support by the false lumen. The extent and

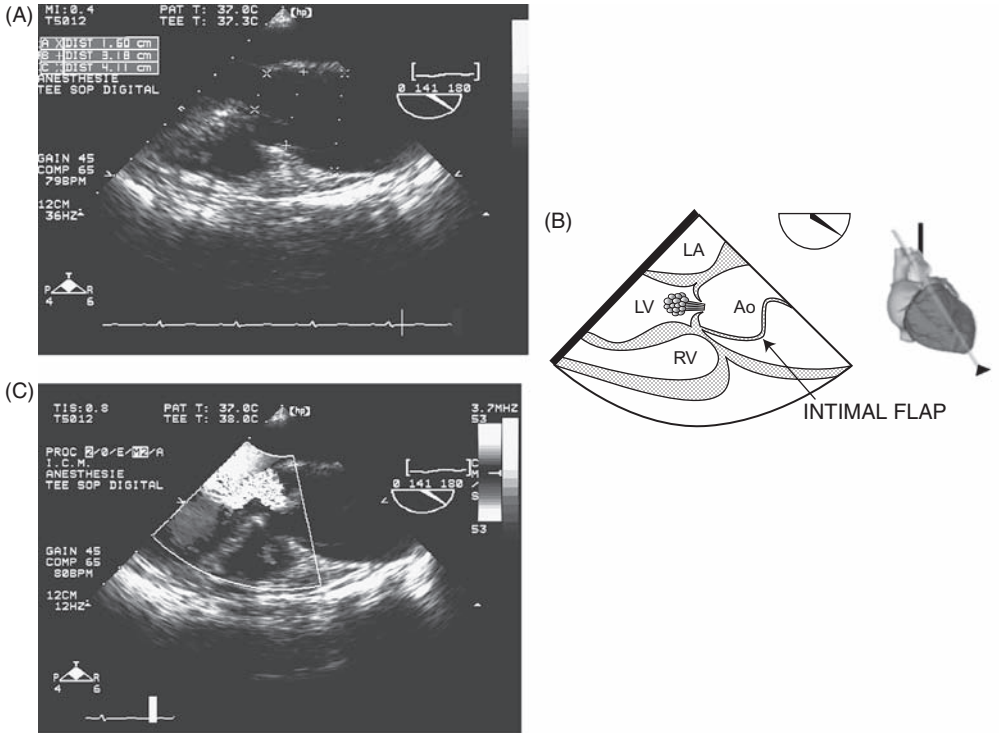

Figure 12.27 A 59-year-old man with acute aortic dissection. The ascending aorta (Ao) diameter was 41 mm (A, B) and aortic regurgitation was present (C) (LA, left atrium; LV, left ventricle; RV, right ventricle).

mechanism of AR should be evaluated and the potential for valve repair or the need for valve replacement assessed (Fig. 12.27). Free aortic rupture into the pericardial sac may be evident, but contained localized rupture should also be actively looked for. Although compression of the coronary arteries may be difficult to detect with TEE, attempts should be made to assess the patency of coronary ostia. Flow in the right and left main coronary arteries can be assessed by color flow imaging and PW Doppler interrogation. Finally, the presence of regional wall motion abnormalities may suggest impaired coronary perfusion.

E. Aortic Intramural Hematoma

Aortic intramural hematomas are presented as a possible early variant of aortic dissection (33) (Fig. 12.28). The aortic hematomas can be localized in the ascending Ao (type A) or in the descending Ao (type B). Hypertension and trauma are predisposing factors. The clinical presentation resembles that of aortic dissection, apart from less commonly associated AR, myocardial infarction and extracardiac complications. On 2D imaging, intramural aortic hematomas appear as localized, often homogeneous, thickenings of the aortic wall (>7 mm) (Fig. 12.29), that are either crescent-shaped (Fig. 12.30) or circumferential. The intramural accumulation of blood is evident, in the absence of an intimal flap (34). Surgical therapy in type A lesions is associated with a reduction in mortality (35).

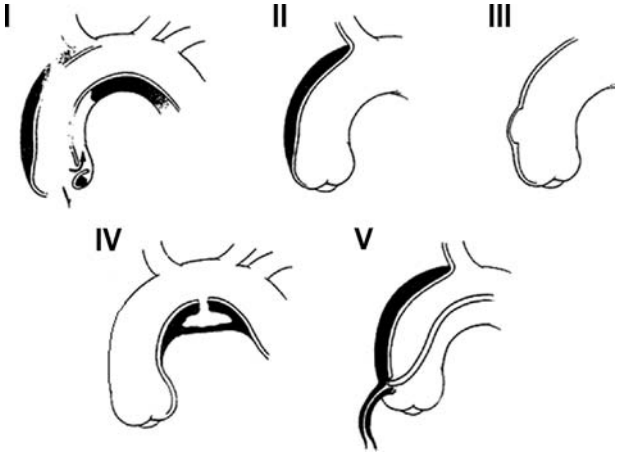

Figure 12.28 Classification of variants of aortic dissection. Type I is a classic dissection with lumen separation and a flap. Type II is an intramural hematoma. Type III is a localized intimal tear. Type IV is an atherosclerotic penetrating ulcer. Type V is iatrogenic or traumatic dissection. [Reprinted with permission from Svensson et al. (33).]

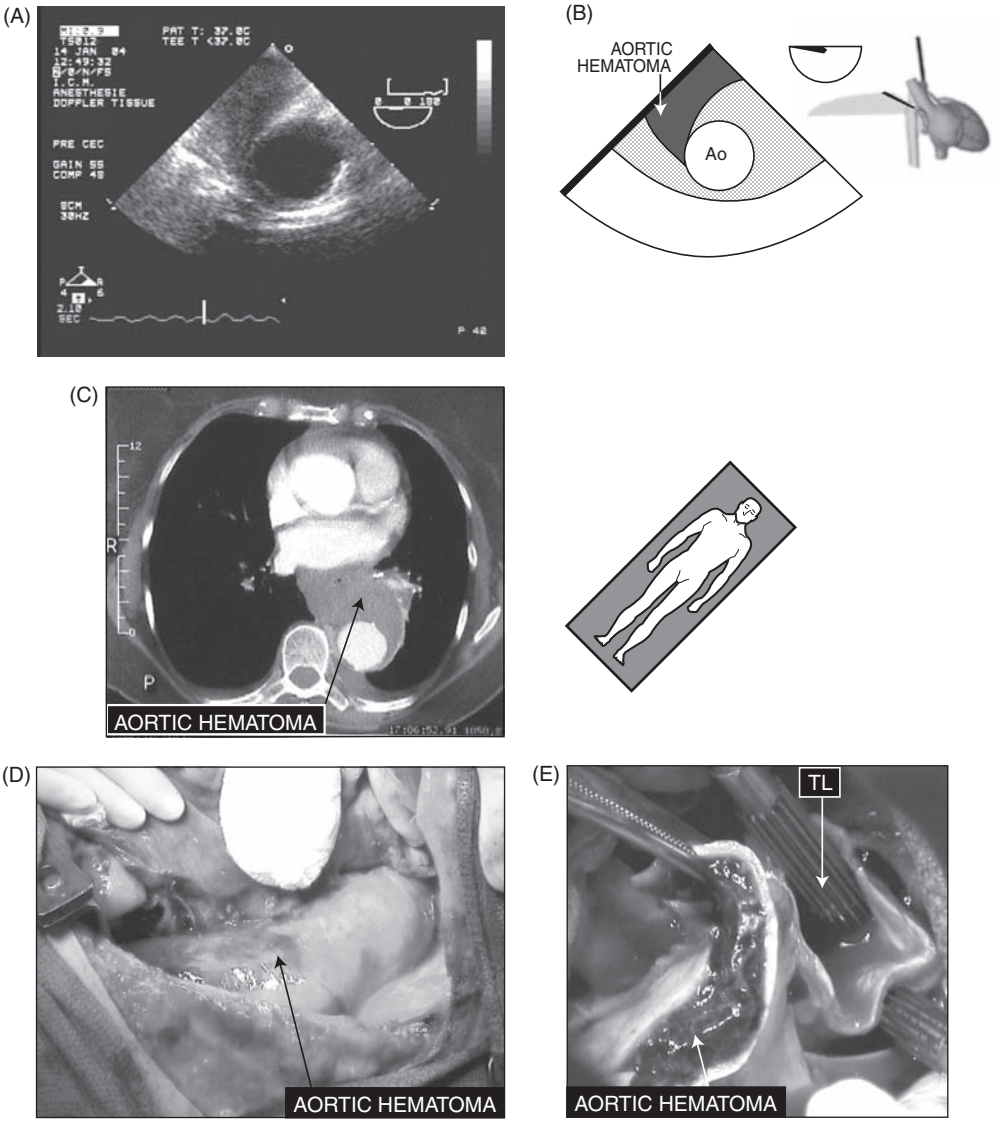

Figure 12.29 (A, B) Hematoma in the descending aorta in a 76-year-old patient. (C) The hematoma is seen on the computed tomography scan. (D) Intraoperatively, a distended and edematous descending aorta (Ao) was seen. (E) Upon opening the aorta, the intramural hematoma is seen (TL, true lumen). (Photos D and E courtesy of Dr. Philippe Demers.)

VIII. TRAUMATIC RUPTURE OF AORTA

Traumatic rupture of the Ao is believed to account for up to 30% of motor vehicle accidental deaths. Mortality and morbidity are still significant in patients who survive to hospital admission (36). The lesion commonly occurs at the aortic isthmus where the ligamentum arteriosum and left subclavian artery firmly affix the Ao to the thoracic cage (Fig. 12.2). Goarin et al. (37) recently published their experience in 28 patients diagnosed with traumatic disruption of the Ao: 19 showed thick stripes at the site of disruption, 15 presented an intimal flap, and 13 had fusiform aneurysms (>1.5 times normal) (Fig. 12.31). Vignon and Lang (38) examined 115 trauma patients and diagnosed 14 with aortic disruption (3 intimal and 11 subadventitial) yielding a sensitivity of 91% and a specificity of 100% compared with intraoperative pathology. Medial flaps are caused by subadventitial tears and are thicker than intimal flaps as they contain both intimal and medial layers. In all cases, the medial flap runs perpendicular to the wall of the Ao unlike in dissections where it is most often parallel (Fig. 12.31). Medial flaps are mobile and influenced by the flow of blood within the Ao. Intimal tears appeared as thin flaps within the aortic lumen itself.

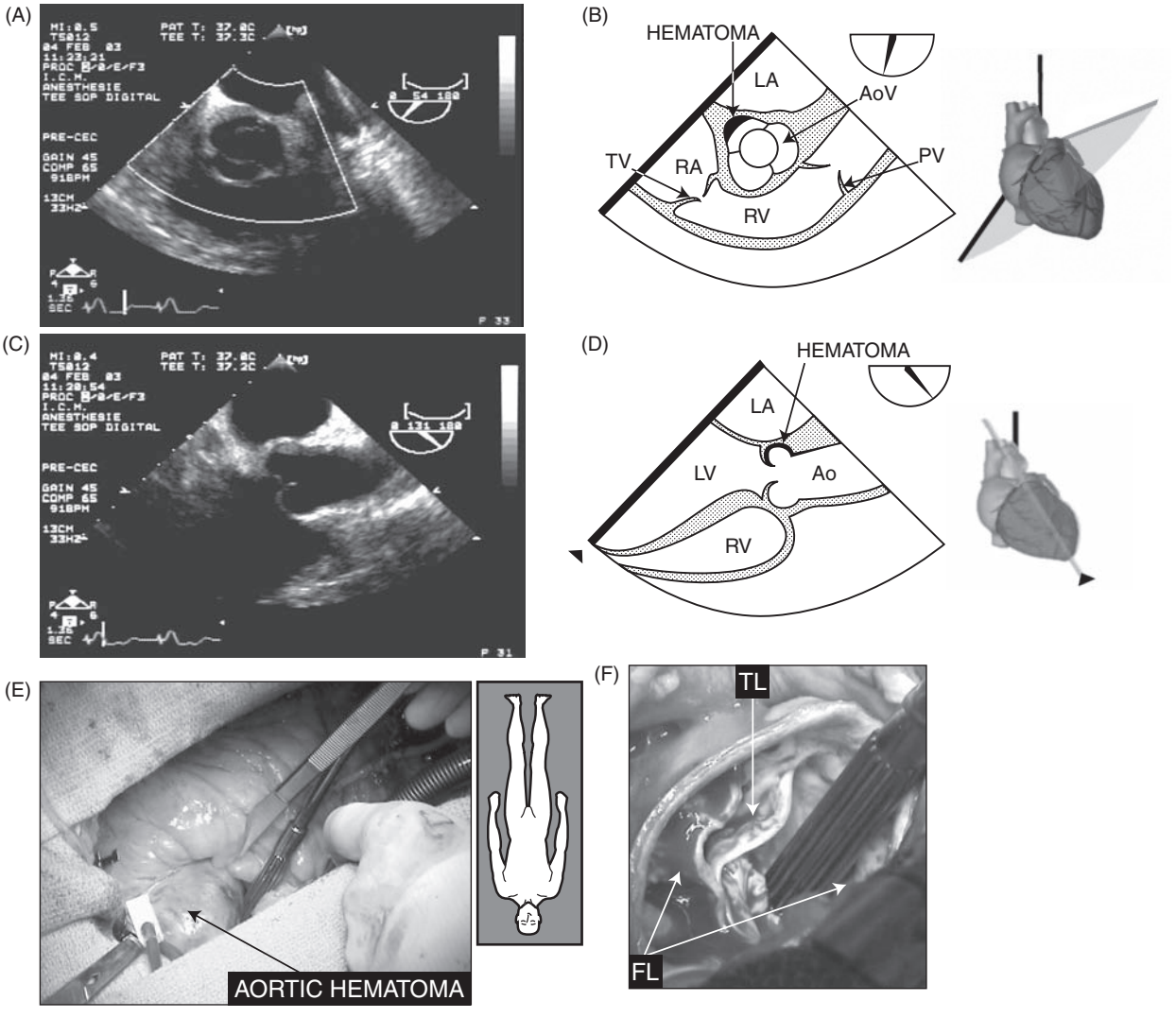

Figure 12.30 (A, B) Mid-esophageal short-axis view in a 66-year-old man operated on for an aortic hematoma localised in the ascending aorta (Ao) behind the noncoronary cusp. (C, D) The hematoma is located in the posterior aspect of the aortic root as seen also in the mid-esophageal long-axis view. No aortic regurgitation was present. (E) The hematoma could be seen on the proximal Ao in the operating room. (F) A false lumen (FL) and a true lumen (TL) were seen upon opening of the Ao (AoV, aortic valve; LA, left atrium; LV, left ventricle; PV, pulmonic valve; RA, right atrium; RV, right ventricle; TV, tricuspid valve). (Photos E and F courtesy of Dr. Michel Pellerin.)

IX. SURGICAL STRATEGY IN THE MANAGEMENT OF THE ATHEROSCLEROTIC ASCENDING AORTA

There are many tools and techniques available to the surgeon for evaluation, investigation and management of the atherosclerotic ascending Ao around the time of cardiac surgery. The history and physical examination should be carefully performed to identify risks factors for atherosclerotic disease. These include age, diabetes, and peripheral vascular disease. These factors increase the incidence of atherosclerotic involvement of the ascending Ao. Intraoperative transesophageal echocardiogram has become standard care for cardiac surgical procedures. Echocardiography and an EAS probe should be available in each cardiac operating room.

The data collected from these studies must be properly interpreted and acted upon appropriately. Epiaortic scanning is becoming the gold standard for intraoperative assessment of the ascending Ao. Based on the information collected, the surgical approach for individual patients is then determined in response to objective findings of the patient's diagnosis, comorbid condition, epiaortic scan, and the nature of the surgery comtemplated. An algorithm on the evaluation and surgical management of the atherosclerotic ascending Ao is shown (Fig. 12.32).

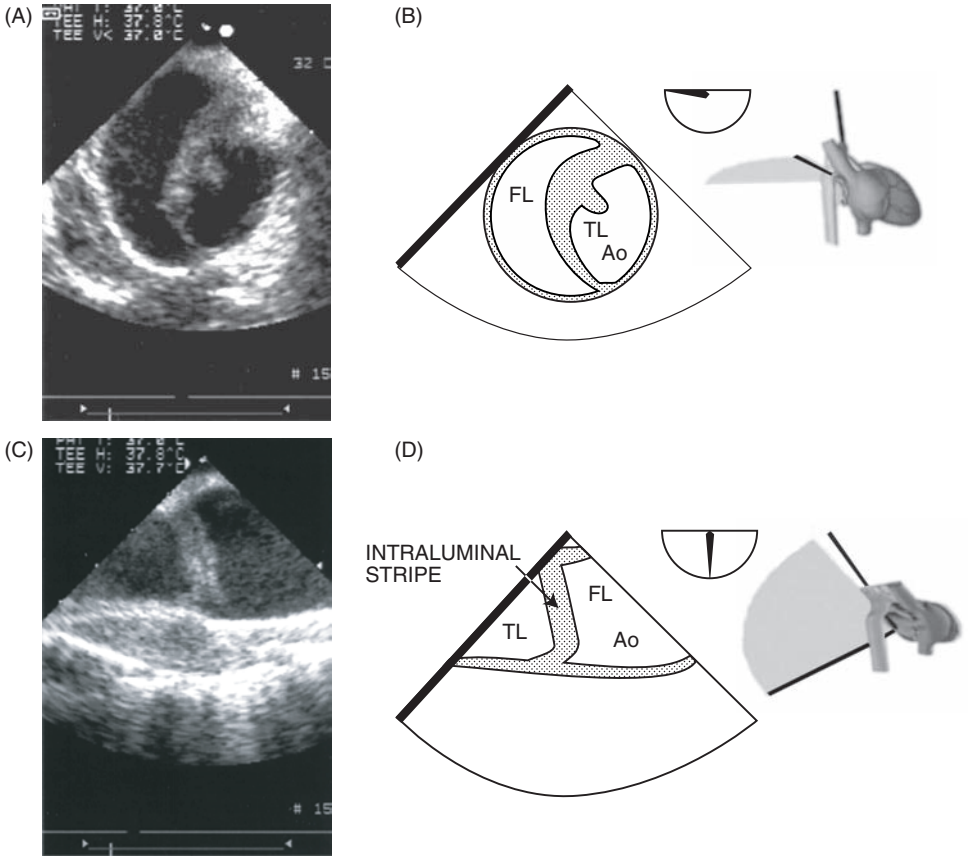

Figure 12.31 Intraluminal stripe due to intimal and medial laceration seen in short-axis (A, B) and long-axis (C, D) views in a 32-year-old man with traumatic aortic injury (Ao, aorta; FL, false lumen; TL, true lumen). [With permission from Goarin et al. (37).]

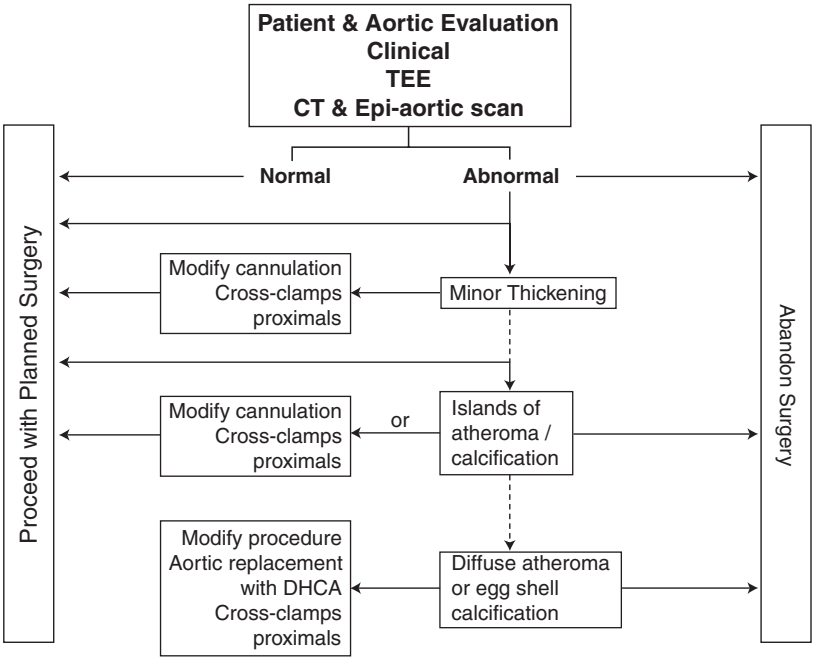

Figure 12.32 Algorithm for the management of the ascending aorta using transesophageal echocardiography (TEE), computed tomography (CT), and epiaortic scanning (DHCA, deep hypothermic cardiac arrest). [Adapted from Ref. (15).]

In conclusion, TEE is a powerful tool in the evaluation of the Ao. It can alter patient management at the bedside but it is important to bear its limitations in mind. Examination with EAS or other diagnostic modalities should be considered if a clear diagnosis cannot be obtained.

REFERENCES

1. Oliver WC, Nuttall G, Murray M. Thoracic aortic disease. In: Kaplan JA, ed. Cardiac Anesthesia. Orlando: W.B. Saunders, 1999.
2. Braunwald E. Heart Disease: A Textbook of Cardiovascular Medicine. 5th ed. Philadelphia: W.B. Saunders, 1997.
3. Urban BA, Bluemke DA, Johnson KM, Fishman EK. Imaging of thoracic aortic disease. Cardiol Clin 1999; 17:659–682.
4. Feigenbaum H. Diseases of the aorta. In: Feigenbaum H, ed. Echocardiography. Philadelphia: Lea & Febiger, 1994:630–657.
5. Katz ES, Tunick PA, Rusinek H et al. Protruding aortic atheromas predict stroke in elderly patients undergoing cardiopulmonary bypass: experience with intraoperative transesophageal echocardiography. J Am Coll Cardiol 1992; 20:70–77.
6. Freeman WK, Seward JB, Khandheria BK, Tajik AJ. Transesophageal Echocardiography. Boston: Little, Brown and Company, 1994.
7. Cohen A, Tzourio C, Bertrand B et al. Aortic plaque morphology and vascular events: a follow-up study in patients with ischemic stroke. FAPS Investigators. French Study of Aortic Plaques in Stroke. Circulation 1997; 96:3838–3841.
8. Hosoda Y, Watanabe M, Hirooka Y et al. Significance of atherosclerotic changes of the ascending aorta during coronary bypass surgery with intraoperative detection by echography. J Cardiovasc Surg (Torino) 1991; 32:301–306.
9. Wareing TH, Davila-Roman VG, Daily BB et al. Strategy for the reduction of stroke incidence in cardiac surgical patients. Ann Thorac Surg 1993; 55:1400–1407.
10. Wareing TH, Davila-Roman VG, Barzilai B et al. Management of the severely atherosclerotic ascending aorta during cardiac operations. A strategy for detection and treatment. J Thorac Cardiovasc Surg 1992; 103:453–462.
11. Ura M, Sakata R, Nakayama Y, Goto T. Ultrasonographic demonstration of manipulation-related aortic injuries after cardiac surgery. J Am Coll Cardiol 2000; 35:1303–1310.
12. Konstadt SN, Reich DL, Quintana C, Levy M. The ascending aorta: how much does transesophageal echocardiography see? Anesth Analg 1994; 78:240–244.
13. Sylivris S, Calafiore P, Matalanis G et al. The intraoperative assessment of ascending aortic atheroma: epiaortic imaging is superior to both transesophageal echocardiography and direct palpation. J Cardiothorac Vasc Anesth 1997; 11:704–707.
14. Royse C, Royse A, Blake D, Grigg L. Screening the thoracic aorta for atheroma: a comparison of manual palpation, transesophageal and epiaortic ultrasonography. Ann Thorac Cardiovasc Surg 1998; 4:347–350.
15. Bainbridge D, Murkin J, Calaritis C, Menkin A. Aortic dissection in a patient with a previous ascending aortic dissection and repair: the role of new monitoring devices in the high-risk patient. Semin Cardiothorac Vasc Anesth 2004; 8(1):3–7.
16. Barzilai B, Marshall WG Jr, Saffitz JE, Kouchoukos N. Avoidance of embolic complications by ultrasonic characterization of the ascending aorta. Circulation 1989; 80:I275–I279.
17. Landymore R, Kinley CE. Classification and management of the diseased ascending aorta during cardiopulmonary bypass. J Thorac Cardiovasc Surg 1983; 85:639–640.
18. Boyd MT, Seward JB, Tajik AJ, Edwards WD. Frequency and location of prominent left ventricular trabeculations at autopsy in 474 normal human hearts: implications for evaluation of mural thrombi by two-dimensional echocardiography. J Am Coll Cardiol 1987; 9:323–326.
19. Nicolosi AC, Aggarwal A, Almassi GH, Olinger GN. Intraoperative epiaortic ultrasound during cardiac surgery. J Card Surg 1996; 11:49–55.
20. Adler Y, Vaturi M, Wiser I et al. Nonobstructive aortic valve calcium as a window to atherosclerosis of the aorta. Am J Cardiol 2000; 86:68–71.
21. Adler Y, Shohat-Zabarski R, Vaturi M et al. Association between mitral annular calcium and aortic atheroma as detected by transesophageal echocardiographic study. Am J Cardiol 1998; 81:784–786.
22. Ring WS. Congenital Heart Surgery Nomenclature and Database Project: aortic aneurysm, sinus of Valsalva aneurysm, and aortic dissection. Ann Thorac Surg 2000; 69:S147–S163.
23. Jackson B. Surgery of Acquired Vascular Disorders: Aneurysms. Springfield: Charles C Thomas, 1969.
24. Erbel R, Zamorano J. The aorta. Aortic aneurysm, trauma, and dissection. Crit Care Clin 1996; 12:733–766.
25. Coady MA, Rizzo JA, Goldstein LJ, Elefteriades JA. Natural history, pathogenesis, and etiology of thoracic aortic aneurysms and dissections. Cardiol Clin 1999; 17:615–635.
26. King ME. Echocardiographic evaluation of the adult with unoperated congenital heart disease. In: Otto CM, ed. The Practice of Clinical Echocardiography. Philadelphia: W.B. Sanders, 1997:697–728.
27. Snider RA. General echocardiographic approach to the adult with suspected congenital heart disease. In: Otto CM, ed. The Practice of Clinical Echocardiography. Philadelphia: W.B. Sanders, 1997:665–695.
28. Larson EW, Edwards WD. Risk factors for aortic dissection: a necropsy study of 161 cases. Am J Cardiol 1984; 53:849–855.
29. Erbel R, Engberding R, Daniel W et al. Echocardiography in diagnosis of aortic dissection. Lancet 1989; 1:457–461.
30. Nienaber CA, Spielmann RP, von Kodolitsch Y et al. Diagnosis of thoracic aortic dissection. Magnetic resonance imaging versus transesophageal echocardiography. Circulation 1992; 85:434–447.

31. Bansal RC, Chandrasekaran K, Ayala K, Smith DC. Frequency and explanation of false negative diagnosis of aortic dissection by aortography and transesophageal echocardiography. J Am Coll Cardiol 1995; 25:1393–1401.
32. Losi MA, Betocchi S, Briguori C et al. Determinants of aortic artifacts during transesophageal echocardiography of the ascending aorta. Am Heart J 1999; 137:967–972.
33. Svensson LG, Labib SB, Eisenhauer AC, Butterly JR. Intimal tear without hematoma: an important variant of aortic dissection that can elude current imaging techniques. Circulation 1999; 99:1331–1336.
34. Vilacosta I, San Roman JA, Ferreiros J et al. Natural history and serial morphology of aortic intramural hematoma: a novel variant of aortic dissection. Am Heart J 1997; 134:495–507.
35. von Kodolitsch Y, Csosz SK, Koschyk DH et al. Intramural hematoma of the aorta: predictors of progression to dissection and rupture. Circulation 2003; 107:1158–1163.
36. Schmidt CA, Jacobson JG. Thoracic aortic injury. A ten-year experience. Arch Surg 1984; 119:1244–1246.
37. Goarin JP, Catoire P, Jacquens Y et al. Use of transesophageal echocardiography for diagnosis of traumatic aortic injury. Chest 1997; 112:71–80.
38. Vignon P, Lang RM. Use of transesophageal echocardiography for the assessment of traumatic aortic injuries. Echocardiography 1999; 16:207–219.

13

Echocardiography During Cardiac Surgery

PIERRE COUTURE, ANDRÉ Y. DENAULT, RAYMOND CARTIER
University of Montreal, Montreal, Canada

I. Introduction 285
II. Devices Used During Cardiopulmonary Bypass 286
A. Central Venous and Intracardiac Catheters 286
B. Mediastinal Catheter for Pleural Fluid Drainage 287
C. Vascular Clamp Placement and Aortic Canulation 287
D. Coronary Sinus Catheter 289
E. Vents and Venous Canulation 291
III. Cardiac Physiology and Procedures Before Cardiopulmonary Bypass 291
A. Controlled Ventilation 291
B. Anesthestic Drugs 295
1. Inhalation Agents 296
2. Intravenous Anesthetic Agents on Systolic Function 299
3. Effect of Intravenous Anesthetic Agents on Diastolic Function 300
C. Nonanesthetic Drugs Commonly Used During Cardiac Surgery 300
1. Positive Inotropic Drugs 300
2. Synthetic Catecholamines 301
3. Phosphodiesterase Inhibitors 302
D. Internal Mammary Dissection 302
E. Arterial Cannulation 302
IV. Cardiac Physiology and Procedures During Cardiopulmonary Bypass 304
A. Hypothermia, Hemodilution, and Nonpulsatile Flow 304
B. Myocardial Perfusion and Cardioplegia 304
C. Spontaneous Echo Contrast 305
V. Changes in Cardiac Physiology During Weaning from Cardiopulmonary Bypass 306
A. Assessment of Regional Left Ventricular Function 306
B. Assessment of Global Left Ventricular Function 306
C. Preload Assessment 306
D. Assessment of Right Ventricular Function 308
E. Assessment of Diastolic Function 308
F. Air Detection 308
VI. Changes in Cardiac Physiology After Cardiopulmonary Bypass 309
A. Protamine 309
B. Right and Left Ventricular Contractile Function and Valve Function 309
References 310

I. INTRODUCTION

Several indications for perioperative transesophageal echocardiography (TEE) have become well established in cardiac surgery and include evaluation of mitral valve repairs, congenital heart repairs requiring cardiopulmonary bypass (CPB), and evaluation of life threatening conditions (1). These indications are considered Category 1

(supported by strong evidence/expert opinion), as published in the American Society of Anesthesiologists (ASA) practice guidelines for perioperative TEE. However, many other indications for the use of TEE remain controversial. For example, routine use in patients at risk for myocardial ischemia or infarction is considered a Category II indication (supported by fair/good evidence) while monitoring during cardioplegia administration or intra-aortic balloon pump insertion is considered a Category III indication (no good supporting evidence). As more experience is acquired with the use of perioperative TEE, we have documented, as other authors have done, the favorable impact of routine use of TEE in cardiac surgery (2). The goal of the present chapter is to review some of the general applications of TEE during cardiac surgery. Monitoring of segmental and global myocardial function, assessment of valvular function and aortic pathology will also be discussed although briefly, as they have been reviewed in more detail in other chapters.

II. DEVICES USED DURING CARDIOPULMONARY BYPASS

Many devices are used during CPB. Although it is considered a Category III indication by the ASA guidelines (1), TEE can be used to assist their insertion and to ensure the proper functioning and location of the various catheters.

A. Central Venous and Intracardiac Catheters

The use of surface ultrasound techniques to assist the insertion of central venous catheters has been described (3). Although TEE is not helpful for this purpose, it has been used to guide central venous catheter placement in children with congenital heart disease and also in adults. Correct placement of a catheter in the superior vena cava (SVC) [at 10 mm from the junction of the SVC with the right atrium (RA)] was achieved in 100% of cases guided by TEE compared with 86% in the control group of patients with congenital heart disease (4). This may be particularly useful in this population as external topographical landmarks and withdrawn blood color are less reliable to confirm proper vessel cannulation. Transesophageal echocardiography may also be helpful to confirm proper guidewire position prior to introduction of the introducer sheath into the jugular vein, especially when difficulty in passing the guidewire is encountered (5). This can be accomplished in the standard bicaval view at mid-esophageal level at $\sim 90-130^{\circ}$ (Fig. 13.1). Improper intra-arterial insertion of a central venous catheter can be detected by TEE, particularly when the subclavian vein approach is used (6). Other authors have suggested using TEE during pulmonary artery catheter insertion after tricuspid valve (TV) surgery to avoid damage to the tricuspid annuloplasty ring (7). Finally, in the course of difficult catheter insertion, TEE may disclose a persistent left SVC known to be present in 0.5% of adults and 1% of children. This is usually connected to the RA via a dilated coronary sinus, but may sometimes open into the left atrium (LA), resulting in a right-to-left shunt. The presence of a persistent left SVC is suspected when a central catheter inserted through a left-sided access vein is seen lying vertically in the left pulmonary field on the chest X-ray (CXR). Catheter placement in the persistent left SVC was reported potentially to lead to arrhythmiae or angina if the tip of the catheter is in the coronary sinus (8). Its presence in the coronary sinus may also preclude the insertion of a retrograde cardioplegia catheter. The diagnosis of persistent left SVC is confirmed when ultrasound contrast injection through a left-sided access vein appears in the (usually dilated) coronary sinus before the RA: this is easily visualized in a mid-esophageal four-chamber view (Fig. 13.2).

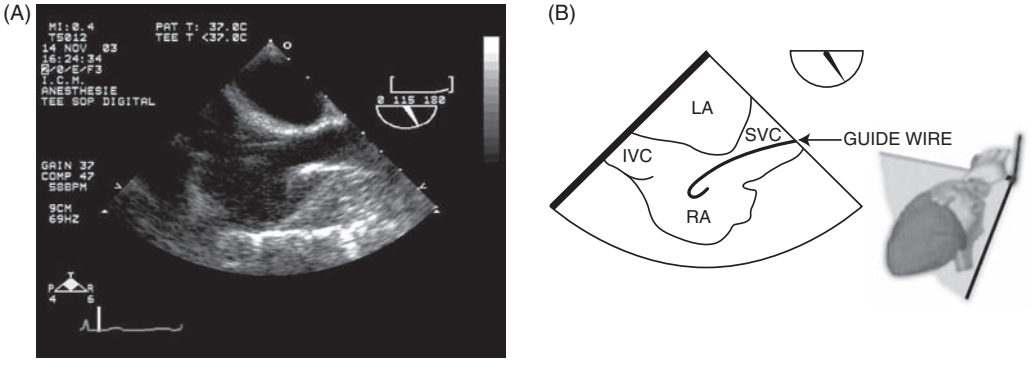

Figure 13.1 Mid-esophageal bicaval view at 115°. The J-shaped guidewire is seen originating from the superior vena cava (SVC) (IVC, inferior vena cava; LA, left atrium; RA, right atrium).

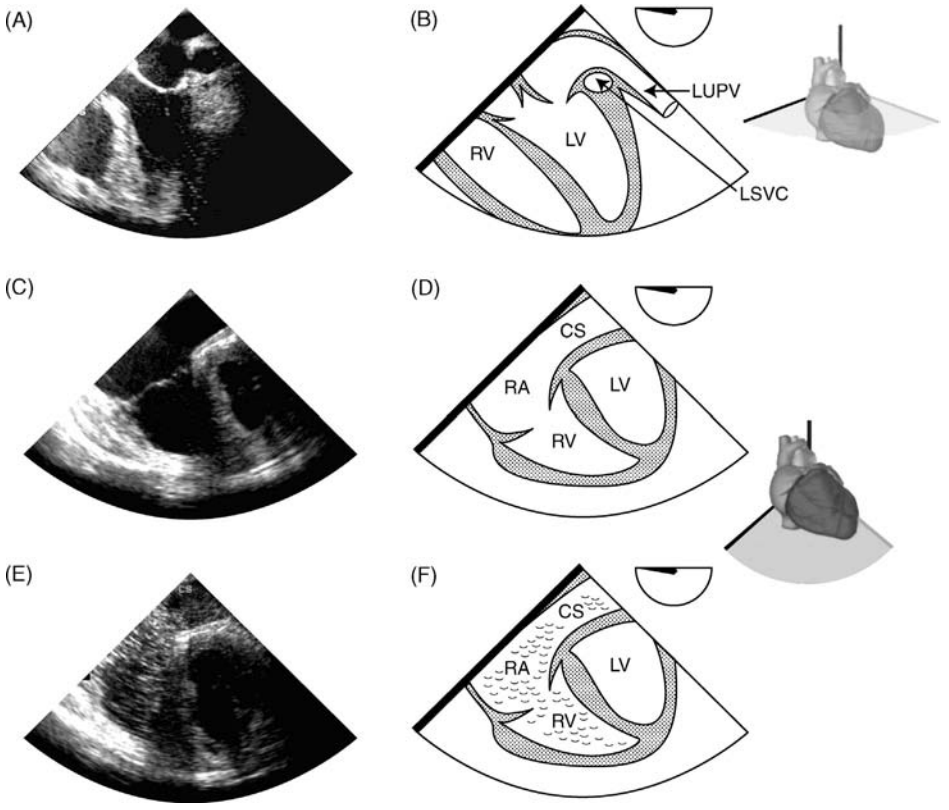

Figure 13.2 Persistent left superior vena cava (LSVC). (A, B) Mid-esophageal four-chamber view at 0°: the atrioventricular groove reveals a dilated coronary sinus (CS) connected to the LSVC. (C, D) Lower esophageal view showing the dilated CS coursing into the right atrium (RA). (E, F) Intravenous agitated saline contrast injection in the left upper extremity vein reveals the presence of microbubbles in the CS before its appearance in the RA, suggesting a connection between the left upper extremity vein and the CS, that is, a persistent LSVC (LUPV, left upper pulmonary vein; LV, left ventricle; RV, right ventricle).

B. Mediastinal Catheter for Pleural Fluid Drainage

The detection of pleural effusions using TEE has been reported (9). Pleural effusions are visualized as crescent-shape, echo-free areas and are seen by rotating the transducer shaft clockwise from the standard four-chamber view to image the right pleural space and counterclockwise from the LA towards the left pleural space (see Fig. 11.7). The fluid on the dorsal side of the pleural space, with the patient in supine position, is observed between the lung and the aorta (Ao) on the left side, and the lung and esophagus on the right side. The lung parenchyma adjacent to the pleural effusion is commonly atelectatic and appears echogenic, consistent with minimal attenuation of ultrasound echoes due to the absence of normal air. Transesophageal echocardiography cannot only localize the presence of pleural fluid but can also help monitor its removal: suction catheters appear as an echogenic structure with acoustic shadowing in the clear echo-free space while larger chest tubes appear as double parallel linear echodensities. It may detect intraoperatively malposition of the chest tubes or confirm adequate mediastinal drainage after chest closure: removal of pleural fluid should result in the shrinking and ultimate disappearance of the echo-free space. The volume of pleural fluid can be estimated by measuring cross-sectional area and axial dimension (10).

C. Vascular Clamp Placement and Aortic Canulation

Perioperative cerebrovascular events may occur in up to 6% of patients undergoing coronary revascularization. Complications include stroke, prolonged encephalopathy, stupor or seizures, and these adverse neurologic events are associated with a 10-fold increase in mortality rate from 2% to 21% and prolonged hospitalization from 10 to 25 days (11). The presence of severe atherosclerosis in the ascending and transverse Ao increases exponentially with age and has been associated with the risk of embolic complications and stroke: patients with documented aortic arch atheroma

had a significantly higher incidence of intraoperative stroke than those without (15% vs 2%) (12). Multiple classification systems are currently used to grade the severity of atherosclerotic disease and are detailed in Chapter 12. Grades IV and V atheromas, found frequently to represent superimposed thrombi on ulcerated atherosclerotic plaques, have the highest potential for embolization. Noncalcified, hypoechoic plaques, believed to be rich in lipidic material and thus less stable, are also believed at risk of embolization, irrespective of their morphology (13).

Disruption of atherosclerotic plaques or thrombi and dissection may occur during aortic manipulation with cannulation, cross-clamping, side-clamping, and clamp removal (Fig. 13.3). Studies using TEE and methods of detection of cerebral embolization with transcranial Doppler have shown that approximately 50% of the emboli occur during instrumentation of the heart and great vessels and 50% randomly while on the cardiopulmonary bypass pump (14). In order to identify atherosclerotic lesions, thorough TEE examination of the thoracic Ao should be routinely performed (15). The technical aspects of thoracic Ao imaging with TEE can be found in Chapters 4 and 12 (15).

Unfortunately, complete visualization of the ascending thoracic Ao with TEE is not always possible. A study comparing TEE with epiaortic scanning (EAS) found that as much as 42% (or a length of 4.5 cm) of the ascending Ao was not visualized with TEE. In addition, the aortic cannula was not seen by TEE in 26 of 27 patients studied: the mid- and distal ascending and transverse Ao where cannulation and clamping are performed may frequently be obscured by shadowing from the air in the trachea and the right mainstem bronchus. Severe atherosclerosis was identified with EAS in five of these patients (16). As mentioned in Chapter 12, manual palpation may also be attempted to detect significant atheromas but this misses severe disease in 50–70% of patients, as only large calcified plaques are identified by this approach (15).

Epiaortic scanning has, therefore, become the gold standard in the intraoperative assessement of the thoracic Ao, but more experience and data are needed before guidelines on its routine use after, or with, TEE can be clearly formulated. Indeed, moderate to severe atheromas in the descending thoracic Ao detected by TEE has a 34% positive predictive value but a 100% negative predictive value for concomitant lesions in the ascending Ao, when compared with EAS (17). This would suggest that EAS need not be performed if TEE screening of the descending Ao is negative but this has not yet been tested prospectively. Other authors have advocated performing EAS

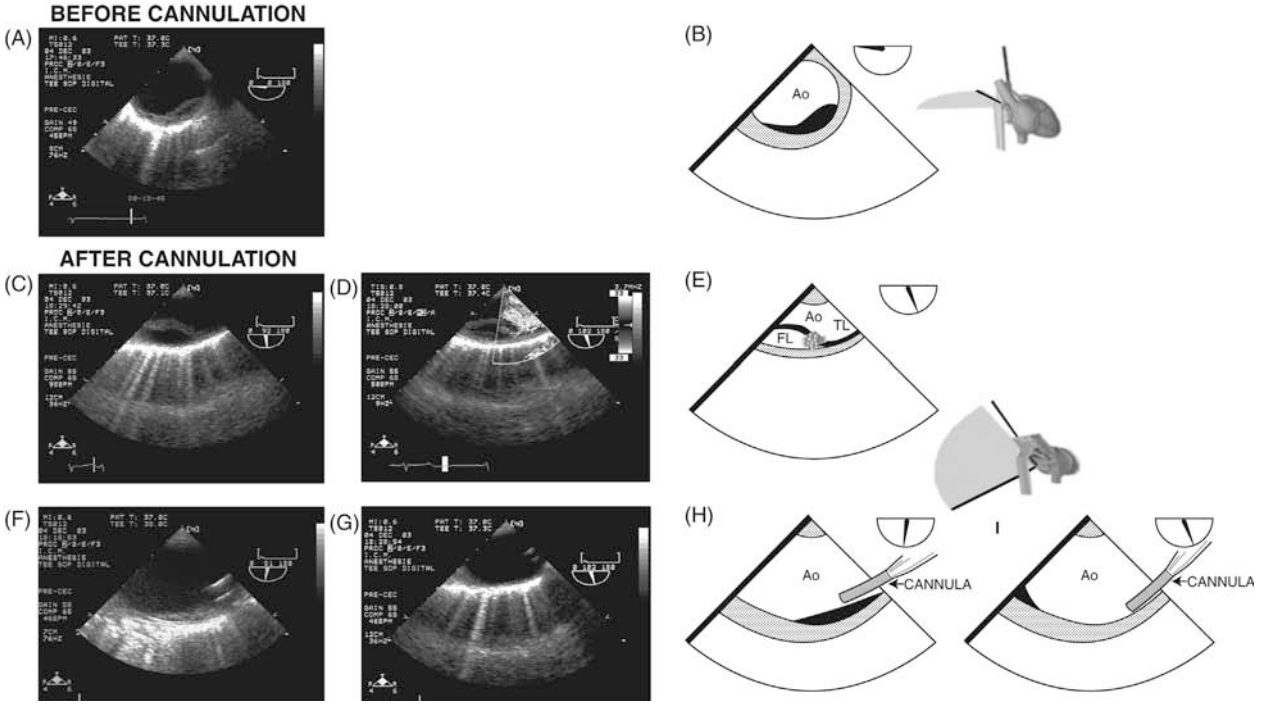

Figure 13.3 A 60-year-old man with thoracic aortic aneurysm is scheduled for a Bentall procedure. (A, B) Examination of the descending aorta (Ao) before cannulation revealed the presence of thickened intima compatible with an intramural hematoma. (C–E) Shortly after the onset of flow in the aortic cannula, a new dissecting flap associated with false lumen (FL) was seen. (F–I) The canula which was positionned close to the hematoma was then pulled back (TL, true lumen).

in patients with a history of transient ischemic attacks, stroke, severe peripheral vascular disease, palpable calcifications in the ascending Ao, calcified aortic knob on CXR, and those older than 60 years (15).

Focal areas of moderate to severe atheromas with thickness >3 mm located in the surgical field warrant change in operative technique to avoid manipulation and disruption of these lesions (see Figs. 12.13 and 12.14). More aggressive management of severe extensive disease, especially protuding plaques, is more controversial because the changes in technique often involve deep hypothermic circulatory arrest and atherectomy or aortic replacement (15).

D. Coronary Sinus Catheter

The technique for inserting the retrograde cardioplegia catheter from the internal jugular vein has been described using the Port-access system (Heartport Inc., Redwood City, CA). Transesophageal echocardiography has been used to visualize the catheter entering the coronary sinus orifice. Fluoroscopy is then used to advance the wire and catheter to the correct depth. The coronary sinus can be visualized from a four-chamber view at a lower esophageal level at 0° in which it appears longitudinally (Fig. 13.4). However, catheter guidance is best performed using the bicaval view at 100° (Fig. 13.5 A, B) while locating the orifice of the sinus from this plane: as the inferior vena cava (IVC) is visualized, the probe shaft is rotated towards the patient's left; the coronary sinus can be identified following its course in the left atrioventricular groove where it appears in cross-section as a circular structure. A transgastric right ventricular longitudinal view at 90° may also be used to visualize the coronary sinus (Fig. 13.5 C, D). Simultaneous visualization of both SVC and coronary sinus is often facilitated by changing the viewing angle to 110° or more. The coronary sinus must be distinguished from the IVC, which is twice as broad in diameter, located to the right of the coronary sinus and leads to the liver (18).

Insertion of a coronary sinus catheter from the RA is most often uncomplicated and its position, easily confirmed by palpation and pressure tracing measurements. However, difficult insertion may be anticipated when

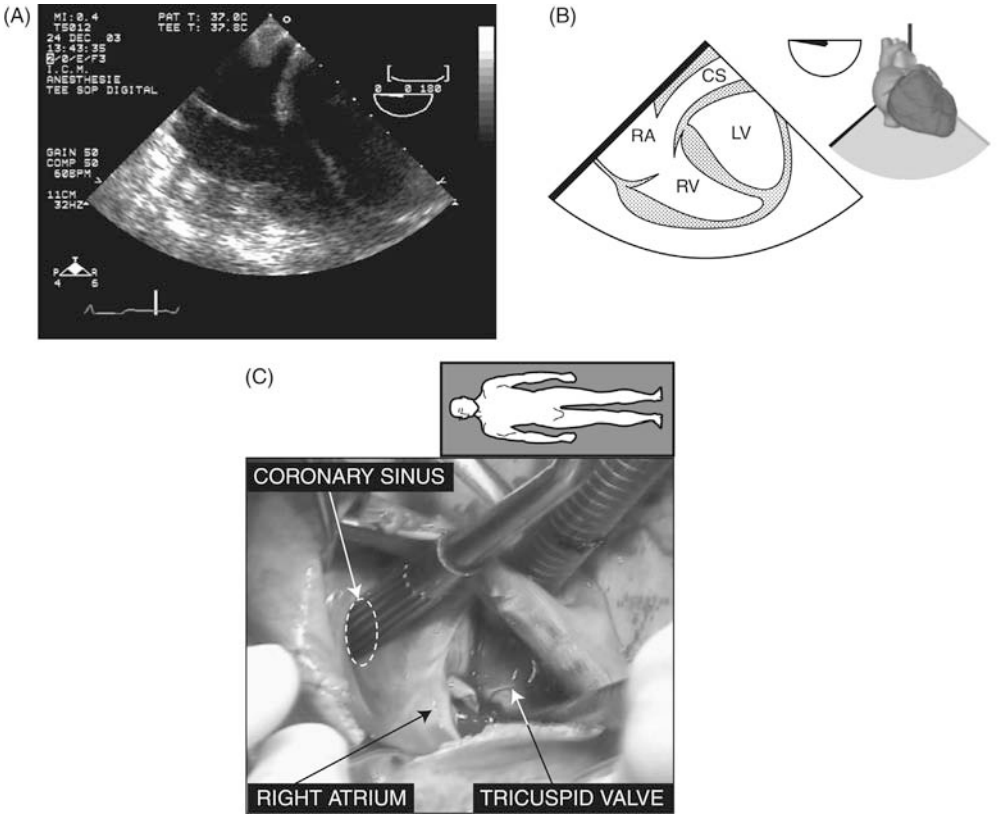

Figure 13.4 Coronary sinus (CS) visualization. (A, B) Lower esophageal view at 0°: longitudinal view of the CS in the left posterior atrioventricular groove near the gastroesophageal junction. (C) Intraoperative view of the CS in a 56-year-old woman before tricuspid annuloplasty through right atriotomy. The suctionning device is in the CS (LV, left ventricle; RA, right atrium; RV, right ventricle). (Photo C courtesy of Dr. Louis P. Perrault.)

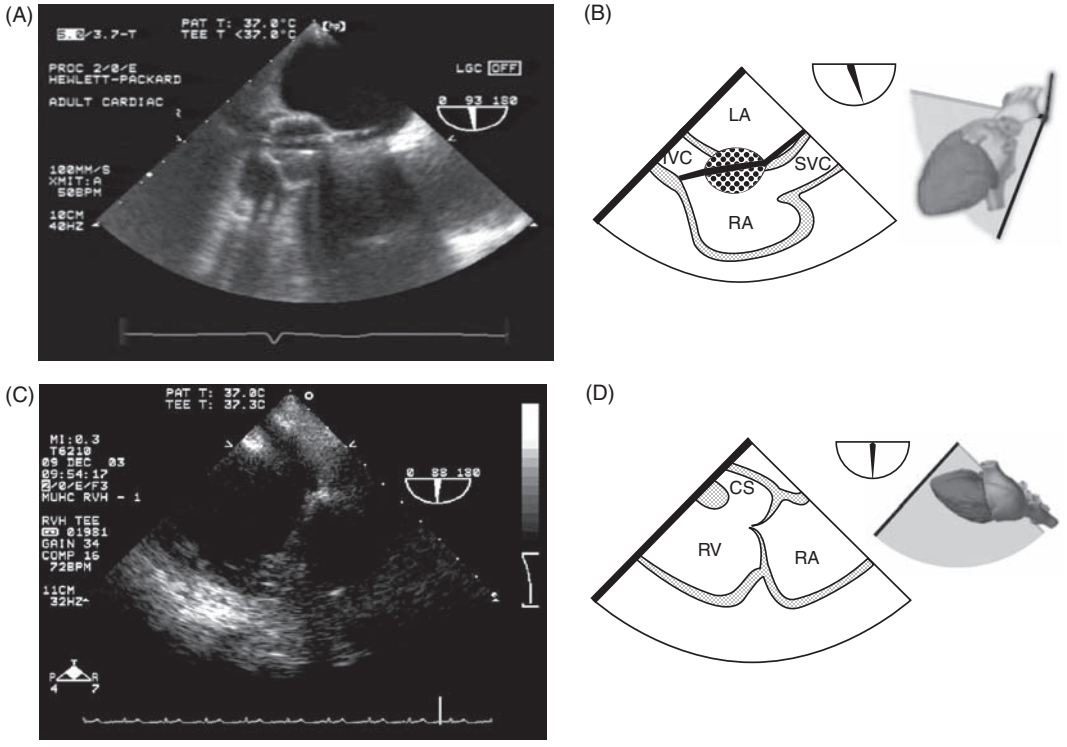

Figure 13.5 (A, B) Bicaval view showing the retrograde cardioplegia cannula positioned toward the atrial septum through the patent foramen ovale. (C, D) Transgastric 88° view of the right ventricle (RV) and coronary sinus (CS) (IVC, inferior vena cava; LA, left atrium; RA, right atrium; SVC, superior vena cava). (Photo A courtesy of Dr. Baqir Qizilbash.)

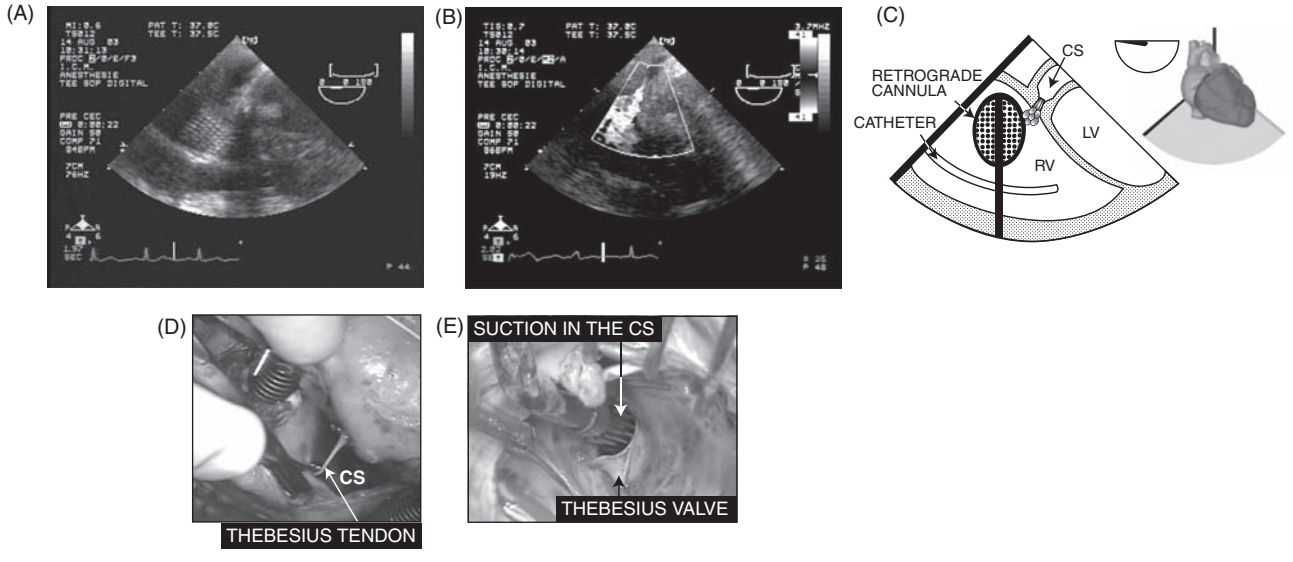

Figure 13.6 A re-operation on the mitral valve is planned on this 23-year-old man. (A–C) The retrograde cannula cannot be inserted in the coronary sinus (CS). This was secondary to ostial stenosis of the CS, maybe from a previous cannulation or from a large Thebesius valve. A secondary CS flow acceleration is demontrated with color Doppler. (D, E) Intraoperative aspect of two types of Thebesius valve at the ostium of the CS: the first is a rudimentary small ligament (D) and the second (E) a more developed valve (LV, left ventricle; RV, right ventricle). (Photos D and E courtesy of Dr. Michel Pellerin.)

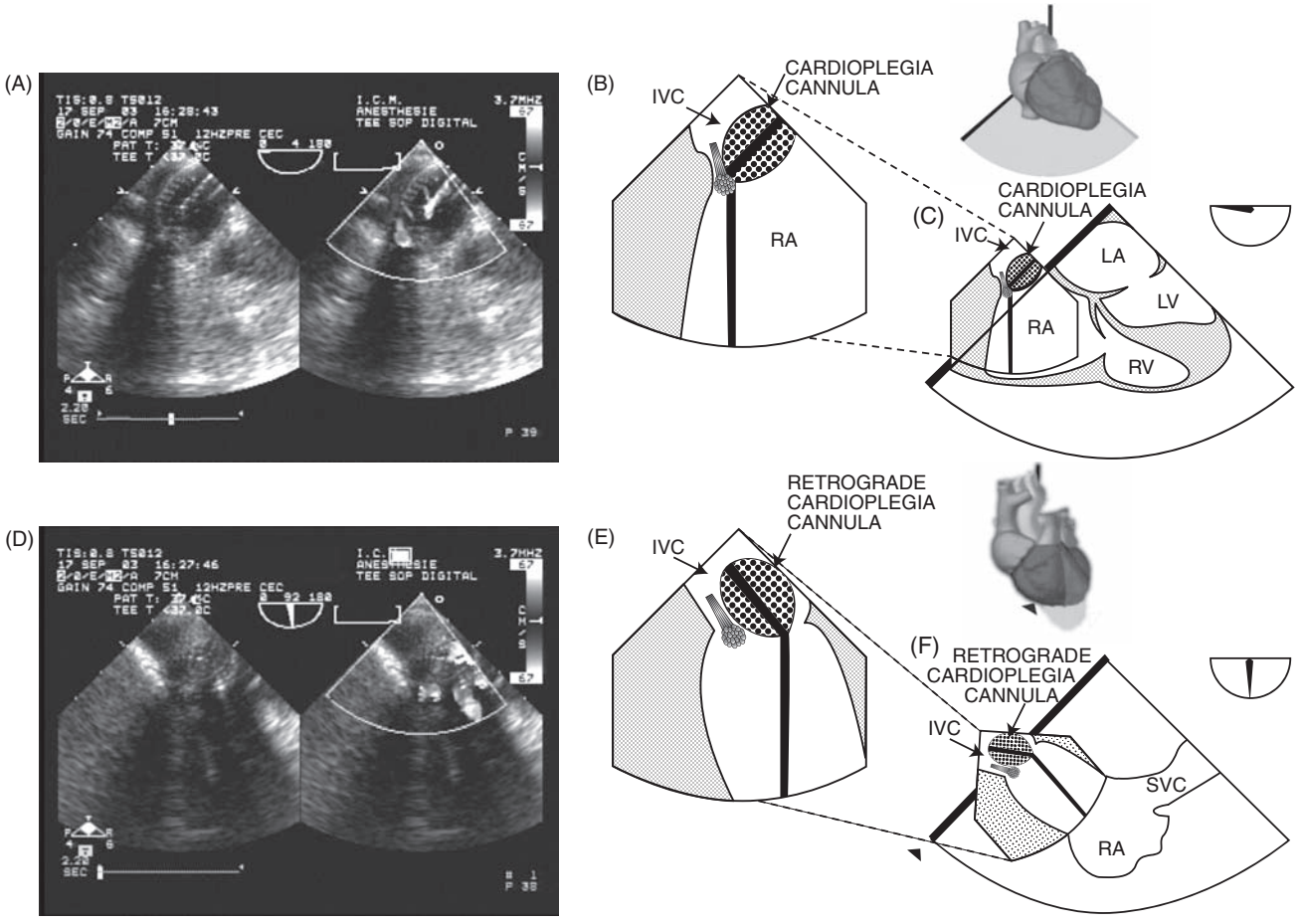

Figure 13.7 Retrograde cardioplegia cannula malpositioned in the outlet of the inferior vena cava (IVC) during cardiopulmonary bypass in a 64-year-old woman undergoing revascularisation. Low-esophageal 0° (A–C) and 90° (D–F) view (LA, left atrium; LV, left ventricle; RA, right atrium; RV, right ventricle; SVC, superior vena cava).

ostial abnormalities, The Thebesian valve, small or stenotic sinus from previous procedures are present (Fig. 13.6). In these circumstances, TEE can assist cannulation, confirm and monitor adequate catheter placement (Fig. 13.7) (19). Transesophageal echocardiography may also identify coronary sinus injury, leading to atrioventricular groove hematoma. This usually results from high perfusion pressure, traumatic stylet-guided catheter insertion and perforation of the coronary sinus wall or laceration due to balloon overinflation or overpressurization during retrograde cardioplegia infusion (20).

E. Vents and Venous Canulation

Proper functioning of vents and the venous cannulation catheter during CPB is both confirmed by surgical palpation and on TEE by the observing emptied right and left ventricular cavities (Fig. 13.8). During double venous cannulation (Fig. 13.9), malposition of the IVC cannula in a suprahepatic vein leads to decreased venous return to the CBP reservoir and left ventricular drainage (Fig. 13.10): once recognized, this is easily corrected by repositioning under TEE. Repositioning of a venous cannula during femorofemoral CPB has also been described (9) as well as a long aortic cannula in the aortic arch (Fig. 13.11) or to confirm adequate guidewire positioning in the true lumen during aortic dissection (Figs. 13.12 and 13.13).

III. CARDIAC PHYSIOLOGY AND PROCEDURES BEFORE CARDIOPULMONARY BYPASS

A. Controlled Ventilation

The hemodynamic effects of mechanical ventilation on the right and left ventricular function are complex and interrelated. They depend on the tidal volume, the amount of positive-pressure and the underlying baseline right and left ventricular function. The effects of positive-pressure

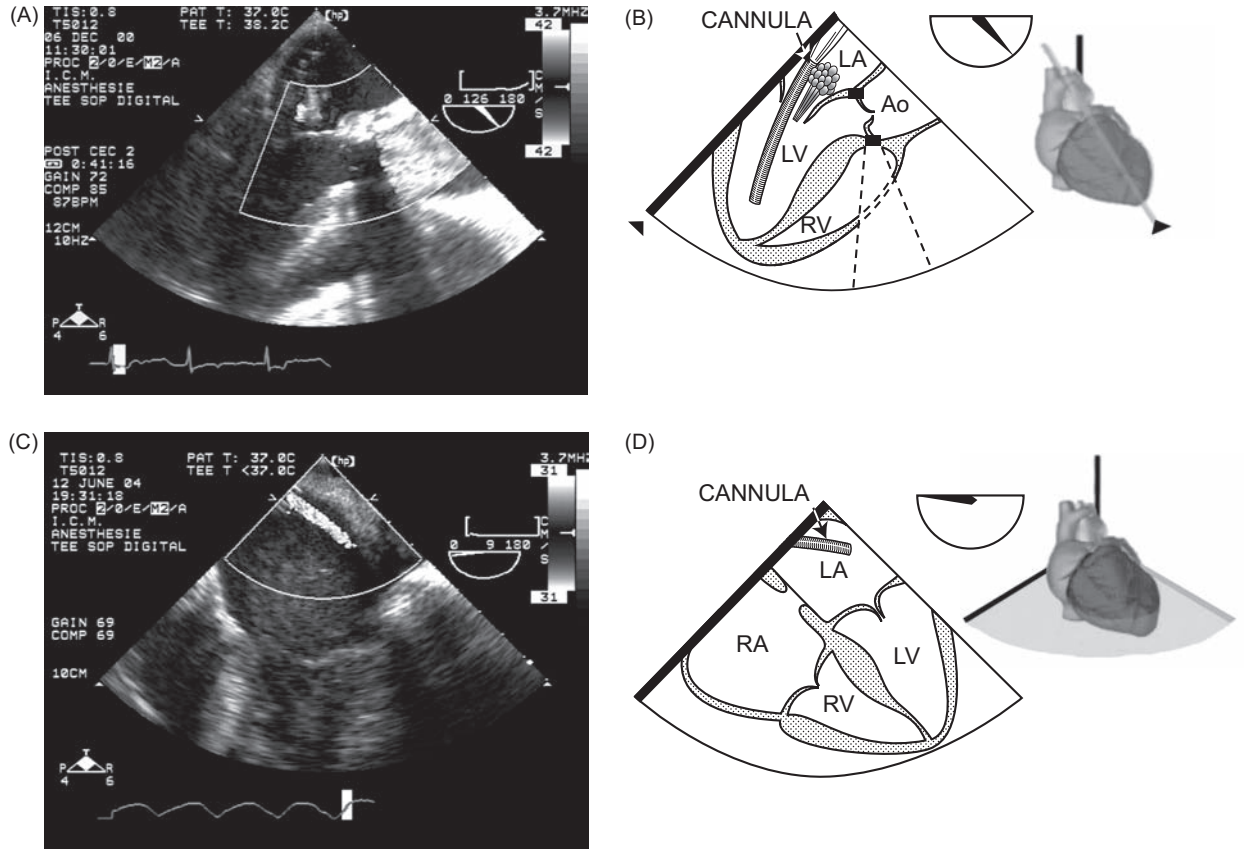

Figure 13.8 A 60-year-old man is undergoing aortic valve replacement. (A, B) A left ventricular decompression cannula is present through the mitral valve and left atrium (LA) from the right upper pulmonary vein. Mitral regurgitation occurred because of incomplete closure of the valve due to the cannula. This can help to confirm that the decompression canula is in an adequate position. (C, D) A 51-year-old man operated on for aortic regurgitation secondary to aortic dissection. The decompression cannula is malpositionned in the LA only and no mitral regurgitation is present (Ao, aorta; LV, left ventricle; RA, right atrium; RV, right ventricle).

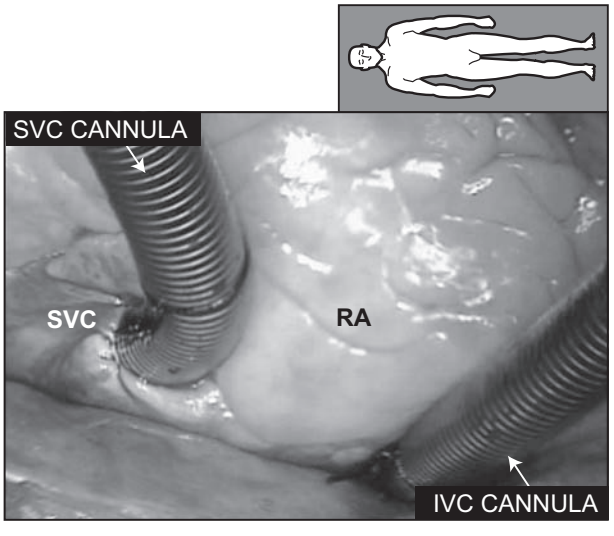

Figure 13.9 Position of both superior vena cava (SVC) cannula inserted through the right atrial appendage and inferior vena cava (IVC) canula (RA, right atrium). (Courtesy of Dr. Michel Pellerin.)

ventilation on the right ventricle (RV) include reduced preload and/or increased afterload and might be summarized as an increase in RV afterload relative to RV preload (22). The final result is a reduced RV stroke output resulting in decreased filling of the left ventricle (LV) (Fig. 13.14) (23).

The contribution of increased right ventricular outflow impedance to the adverse consequences of respiratory support has often been underestimated because it might be partly offset by increased preload. In adequately preloaded resuscitated patients under mechanical ventilation for acute respiratory distress syndrome (ARDS), Vieillard-Baron et al. (22) described the effect on right ventricular function of cyclic right ventricular afterloading produced by the inspiratory phase of intermittent positive pressure ventilation (IPPV) at a tidal volume (V_t) of 8 mL/kg. Using TEE, lung inflation was shown to decrease pulmonary arterial flow velocity–time integral (VTI) from 14.2 ± 2.6 cm at end-expiration to 11.3 ± 2.1 cm at end-inspiration during positive-pressure ventilation. This was not preceded but rather followed by a decrease

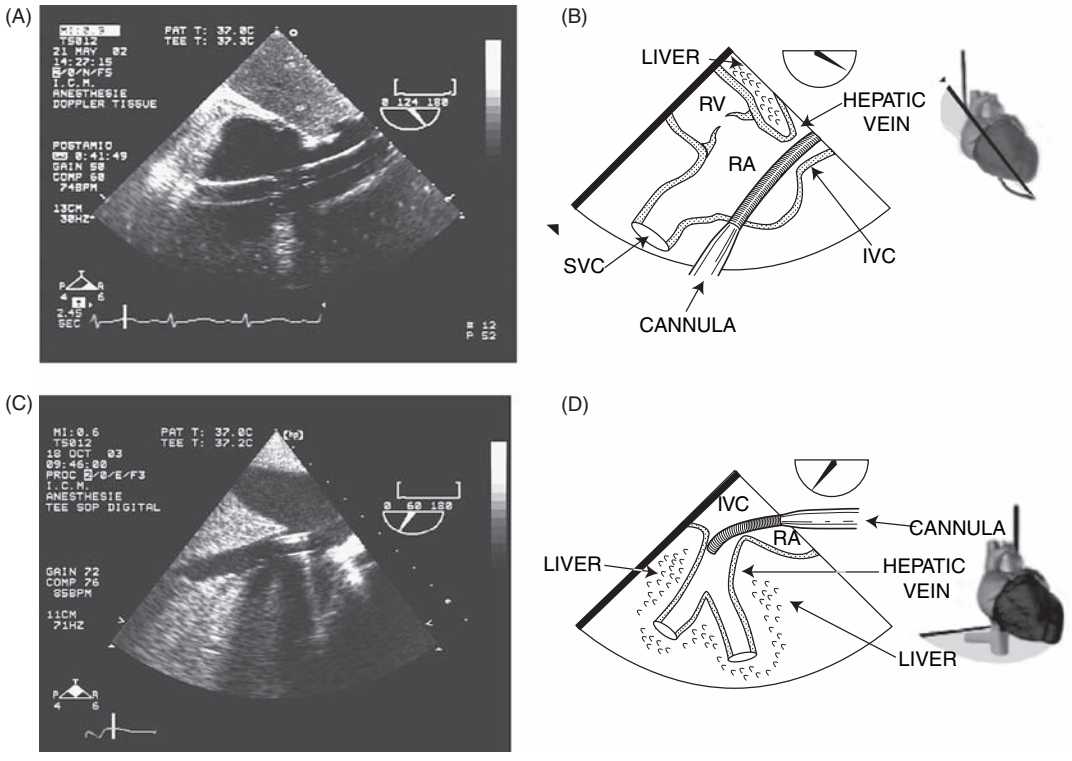

Figure 13.10 (A, B) Deep transgastric longitudinal view at 120° through the right ventricle (RV): the venous cannula appears correctly located in the inferior vena cava (IVC). (C, D) Deep transgastric transverse view at 0° where the venous cannula is incorrectly located in a hepatic vein. This explained the poor venous return to the cardiopulmonary bypass reservoir (RA, right atrium; SVC, superior vena cava).

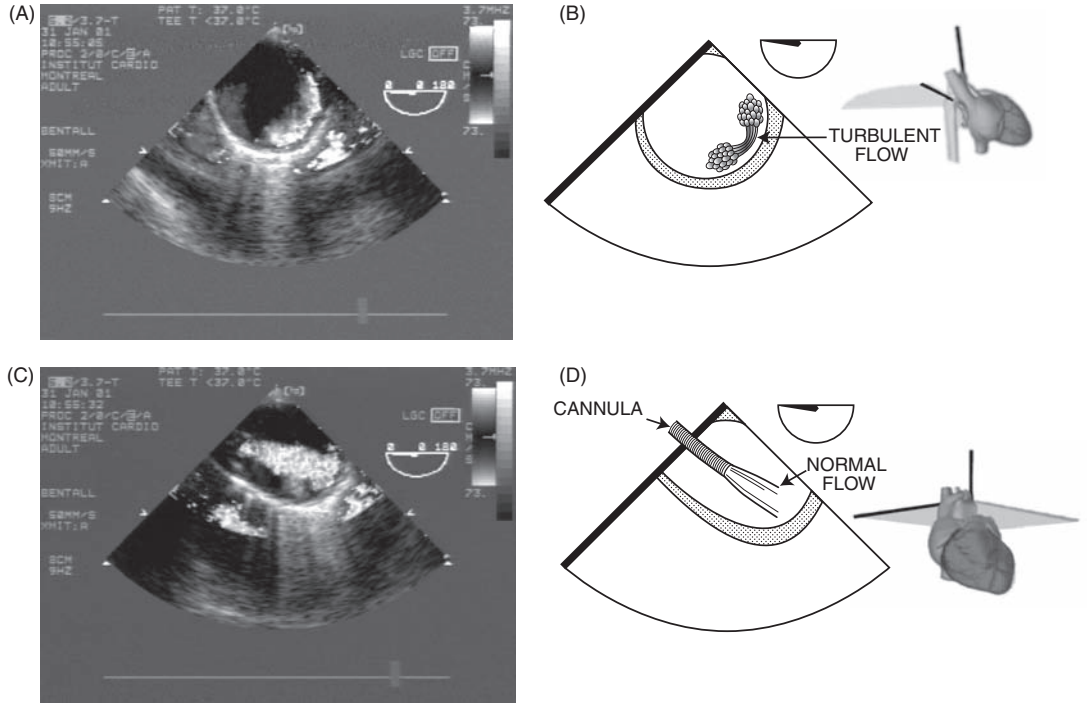

Figure 13.11 (A, B) Aortic mid-esophageal view showing malposition of an aortic cannula leading to turbulent flow and increased pressure in the arterial line. (C, D) Normal flow is restored and the arterial pressure reduced by pulling back the cannula. (Courtesy of Dr. Peter Sheridan.)

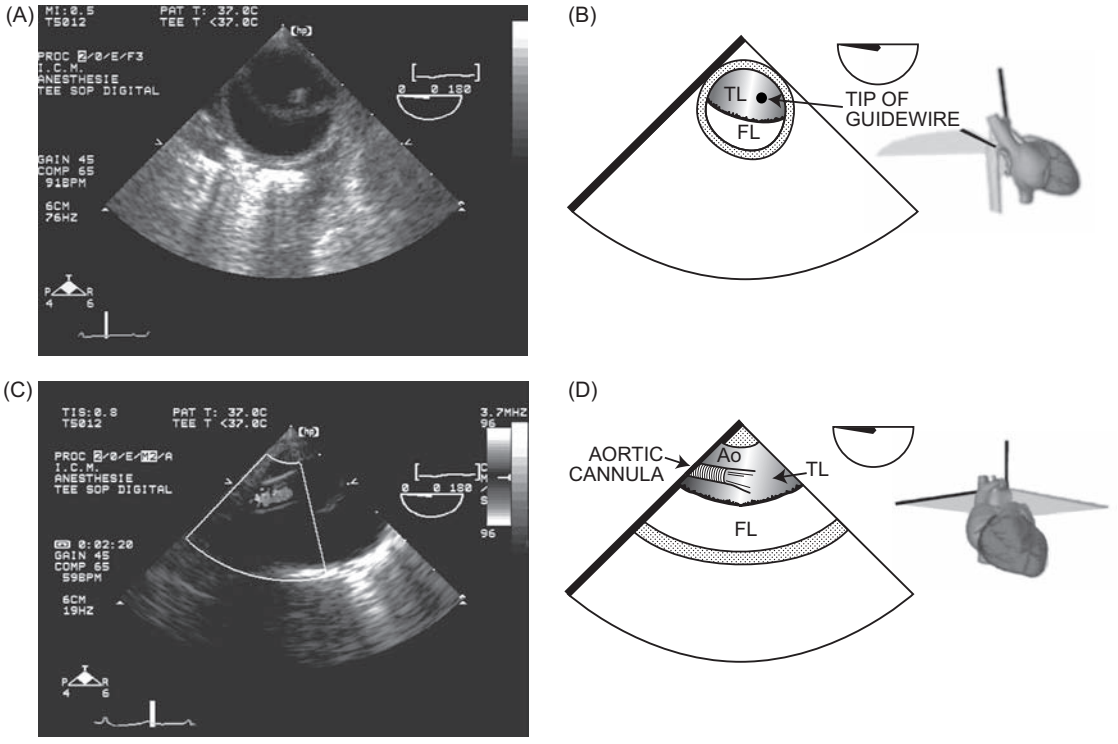

Figure 13.12 A 59-year-old woman with sudden onset of severe chest pain while swimming was transferred to the hospital after the diagnosis of aortic dissection was made by a computed tomography scan. The aortic dissection involved the proximal ascending aorta (Ao) and all the remaining distal Ao (A, B) down to the iliac arteries. (C, D) Cannulation of the proximal aortic arch for cardiopulmonary bypass was performed under transesophageal echocardiography guidance to secure true lumen (TL) perfusion (FL, false lumen). (Courtesy of Drs. Nicolas Noiseux and Raymond Cartier.) [Adapted from Noiseux et al. (21).]

in tricuspid inflow VTI, thus confirming an increase in right ventricular outflow impedance. This reduction in VTI occurred without concomitant decrease in right atrial or right ventricular diastolic dimensions and with increased right ventricular systolic dimensions, causing a drop in inspiratory right ventricular ejection fraction consistent with right ventricular systolic function impairment. Tidal volume was the main determining factor of right ventricular afterloading during mechanical ventilation in that study. According to the authors, in normovolemic patients, left atrial filling improved with increased LA dimensions, which indicates that blood might be squeezed from the capillary bed, as suggested by other authors (24). Moreover, Vieillard-Baron et al. (23) also reported that cyclic changes in right ventricular outflow were greater in patients with partial collapse of the SVC during IPPV (at a tidal volume of $6-8\,mL/kg$) and positive end expiratory pressure (PEEP) of 5 cmH_2O.

Patients with a SVC caval collapsibility index (defined as the difference of SVC maximal expiratory diameter and minimal inspiratory diameter over the maximal diameter) $>60\%$ had greater inspiratory decrease in right ventricular outflow velocity ($\sim 70\%$) compared with patients with an index $<30\%$ ($\sim 30\%$) (23). Partial collapse of SVC occurred when the transmural pressure was ≤ 9 mmHg. Thus, a specific preload limitation is added to the increase in outflow impedance in these patients and results in suboptimal filling of the LV (see Fig. 9.7). The effect of positive-pressure ventilation on right ventricular afterload can also be demonstrated using a four-chamber view and measuring caval diameter changes (Fig. 13.15). Jet ventilation which uses small tidal volume and can improve oxygenation in certain patients can also reduce the effect of IPPV on right ventricular function (Fig. 13.16).

The negative impact of mechanical ventilation on the loading condition of both the RV and LV is worsened by the application of PEEP which reduces preload through a decrease in systemic venous return and an increase in right ventricular afterload (Fig. 13.17) (25). Lower levels of PEEP (<8 cmH_2O) have minimal hemodynamic effects (26) while higher levels (≥ 16 cmH_2O) have been reported to cause concomitant reduction in right and left ventricular dimensions with displacement of the interventricular septum (IVS) towards the right (26). In contrast, following uncomplicated coronary artery bypass graft (CABG) surgery, Poelaert et al. (27) observed that

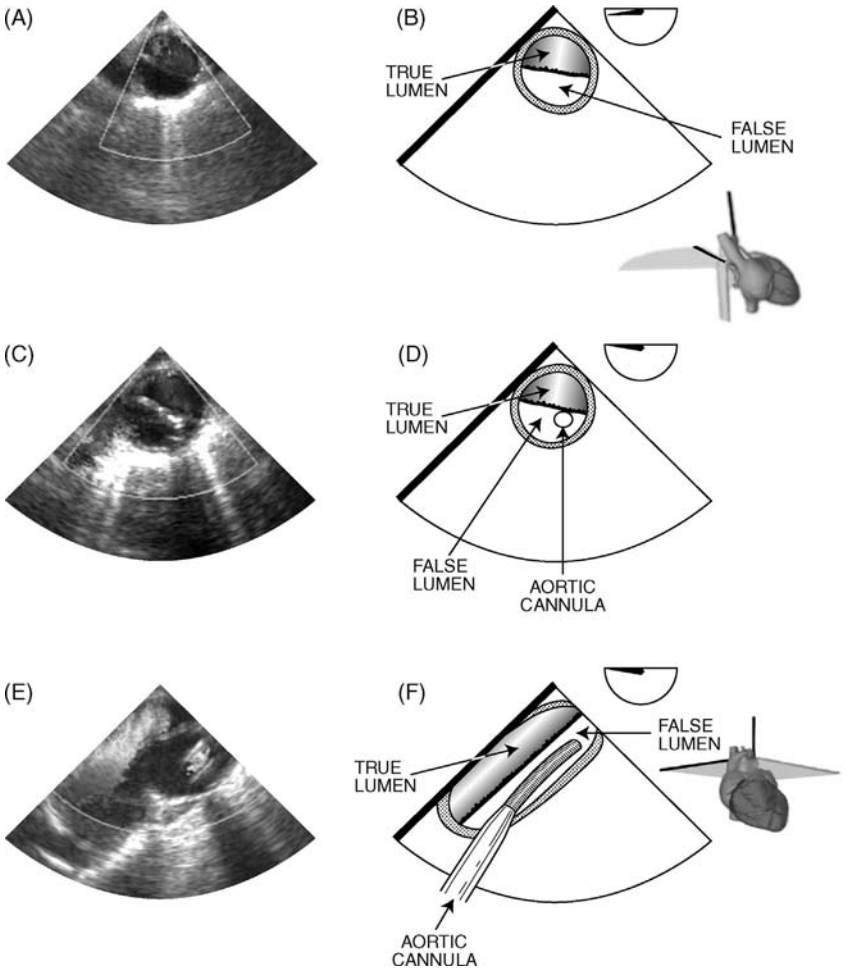

Figure 13.13 Aortic dissection involving the transverse and descending thoracic aorta. (A, B) Transverse view at 0° of the proximal descending thoracic aorta. The flow in the true lumen is visualized by color flow imaging. The aortic cannula appears incorrectly positioned in the false aortic lumen as observed in the descending (C, D) and distal transverse aorta (E, F).

application of 20 cmH_2O of PEEP for 10 min resulted in increased right ventricular diastolic area (27%) that coincided with a reduction of early mitral inflow *E* velocity of 25% and pulmonary artery flow velocity of 27% at end-expiration and 42% at end-inspiration. The increase in RV dimension is apparently the result of a greater impedance increase than the reduction of systemic venous return. The left and right ventricular function, as assessed by fractional area change (FAC) on TEE, was not affected by the application of PEEP.

The effect of PEEP on left atrial inflow has also been evaluated by Meijburg et al. (28). Application of 20 cmH_2O of PEEP decreased the systolic component of the pulmonary venous flow (PVF) while the early diastolic component did not change. Consequently, baseline systolic predominance was changed to a slight diastolic predominance at a higher level of PEEP, perhaps reflecting diminished left atrial compliance secondary to high intrathoracic pressures. Thus, the left atrial pressure rises during systole when the mitral valve is closed and the decreased pulmonary vein to left atrial gradient results in reduced left atrial inflow. The left ventricle with thicker walls is less influenced by high intrathoracic pressure. Variations in pulmonary venous flow have also been described with IPP and are more important in patients with pulmonary capillary wedge pressure (PCWP) <18 mmHg (29).

B. Anesthestic Drugs

A complete review of the hemodynamic effects of anesthetic agents is beyond the scope of this chapter, but we will briefly describe the hemodynamic effects of inhalation

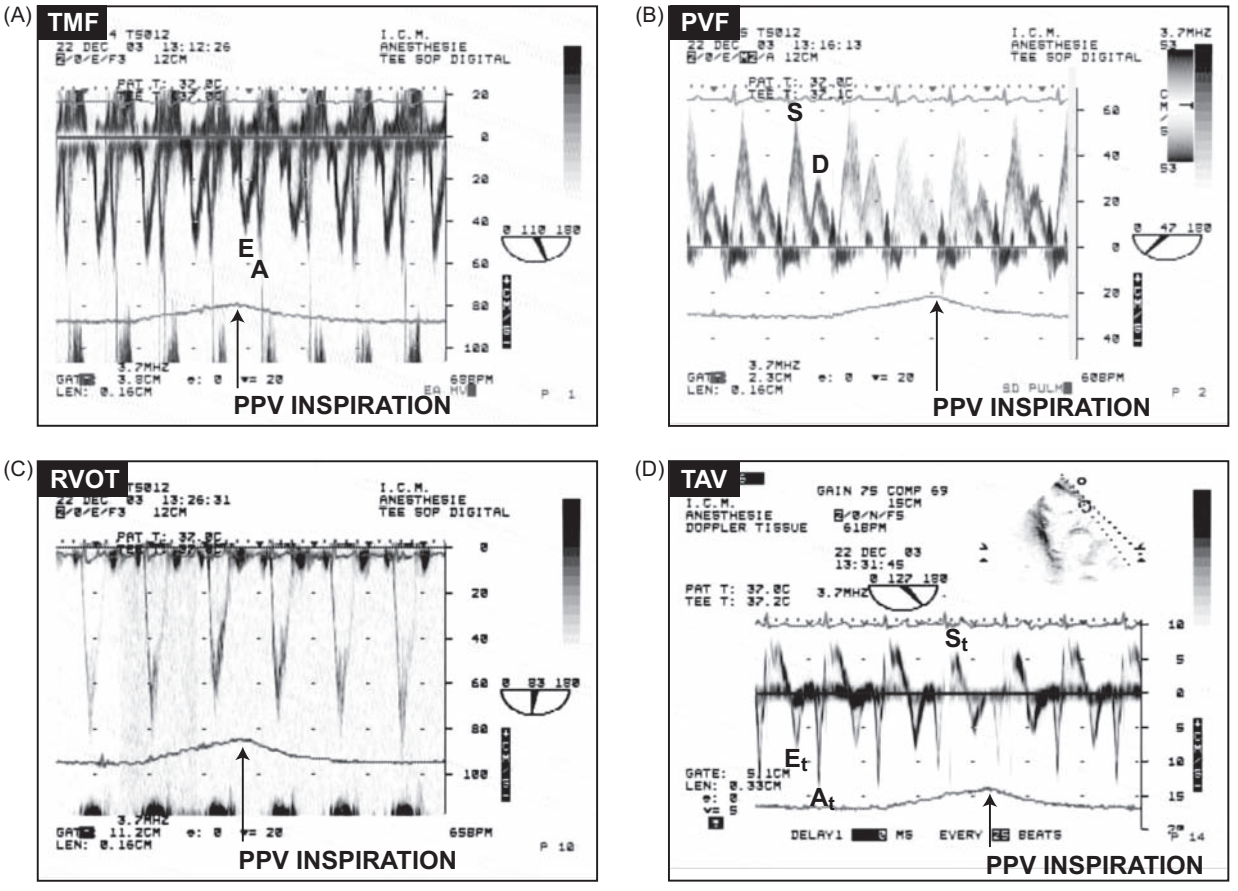

Figure 13.14 Effect of positive-pressure ventilation (PPV) on the Doppler transmitral flow (TMF) (A), pulmonary venous flow (PVF) (B), right ventricular outflow tract (RVOT) velocity obtained from a deep transgastric view (C) and tricuspid annular velocities (TAV) (D) in a 58-year-old man. Note the reduction in systolic velocities in all four Doppler signals with positive-pressure inspiration displayed from simultaneous respirograms.

agents and intravenous anesthetics, as they may influence cardiac function and echocardiographic measurements.

Reduction in myocardial contractility induced by the administration of volatile anesthetic agents may not be detected with the conventional ventricular performance indices such as FAC and circumferential fiber shortening (Vcf). The use of pressure–dimension indices such as the end-systolic elastance (Ees) and preload recruitable stroke force (PRSF) are more sensitive to reductions in myocardial contractility, but their measurements are considerably more complex than the traditional indices of myocardial performance (30).

1. Inhalation Agents

All the inhalation anesthetics produce dose-related negative inotropic effects. Enflurane and halothane depress myocardial contractility to a similar extent but more severely than isoflurane, desflurane and sevoflurane. A rapid increase in desflurane concentration may however stimulate the sympathetic nervous system and temporarily mask its negative inotropic effect, inducing an increase in heart rate. Moreover, enflurane and halothane also induce an increase in left ventricular filling pressure. (Effects of inhalational anesthetics on systemic hemodynamics and the coronary circulation. In: Kaplan JA, ed. Cardiac Anesthesia. 4th ed. Chapter 16. WB Saunders Company, 1999.) In abnormal hearts, indices of contractility appear more sensitive to a given concentration of a volatile anesthetic than in normal hearts. Nitrous oxide has a weak direct myocardial depressant action that may be counterbalanced by sympathetic activation.

There is a lack of noninvasive-derived data regarding the effects of potent volatile anesthetic agents on diastolic function. Using invasive measurements of diastolic function, halothane and enflurane seem to prolong the isovolumic relaxation period and increase chamber stiffness while isoflurane, sevoflurane and desflurane prolong the

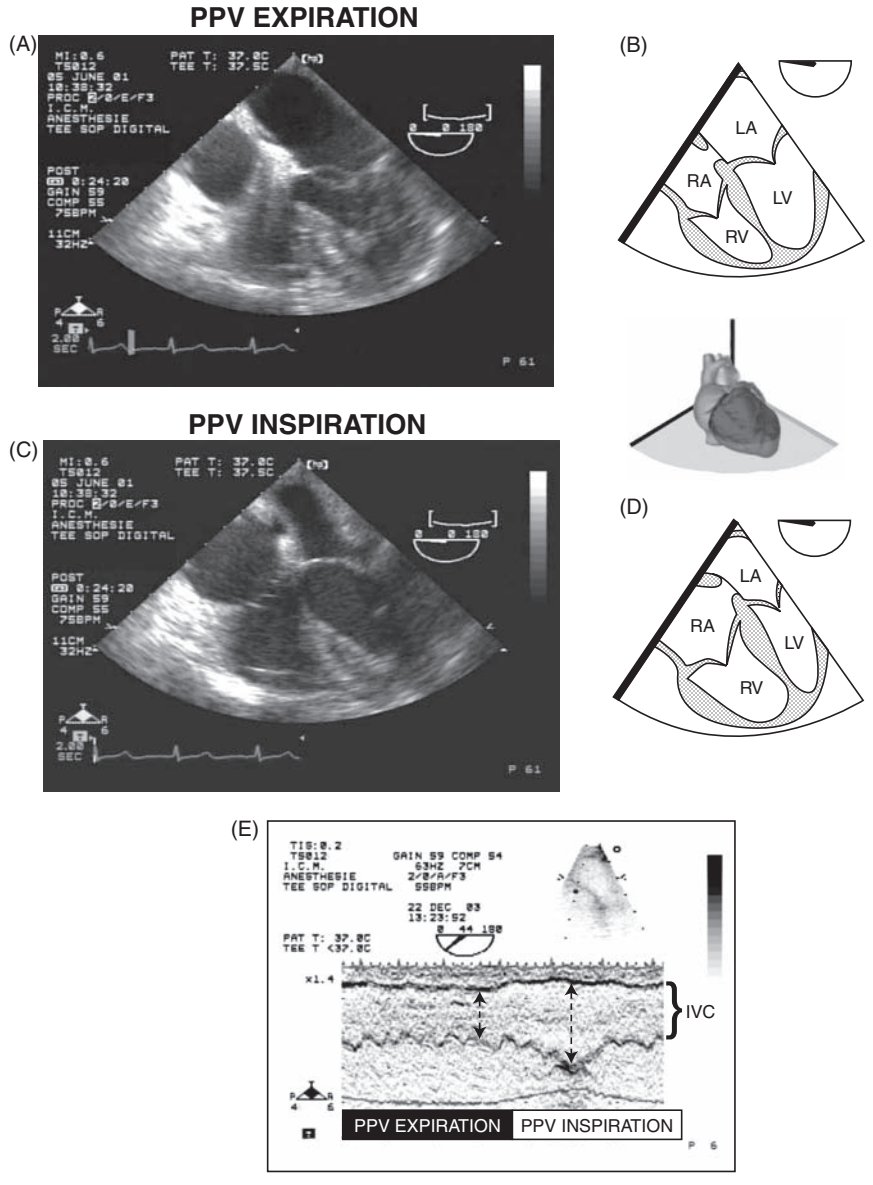

Figure 13.15 Aortic valve replacement is scheduled in this 59-year-old woman with previous mild right ventricular dysfunction. (A–D) Positive-pressure ventilation (PPV) was associated with significant reduction on the diameter of the right atrium (RA) in expiration compared with inspiration. (E) Changes in diameter of the inferior vena cava (IVC) taken at the junction of the RA. Again note that during PPV-inspiration, the diameter of the IVC increases (LA, left atrium; LV, left ventricle; RV, right ventricle).

isovolumic relaxation period but without altering invasively measured myocardial chamber stiffness. There is little available in the literature regarding the effect of nitrous oxide on diastolic function.

Studies in intact animals and humans have shown a decrease in sytemic vascular resistance (SVR) in a dose-dependant fashion by isoflurane, enflurane, sevoflurane and desflurane, while halothane has minimal direct effect. Potent inhalation anesthetics can also reduce preload through direct (vascular smooth muscle dilatation) and indirect (sympathetic nervous system) mechanisms. Nitrous oxide raises central venous pressure by increasing both venous tone and peripheral vascular resistance and by possibly decreasing left ventricular contractility. (Cardiovascular pharmacology of anesthetics. In: Estafanous FG, ed. Cardiac Anesthesia: Principles and Clinical Practice. 2nd ed. Chapter 10. Lippincott Williams & Wilkins, 2001.)

Finally, volatile anesthetics have been found to be cardioprotective in many studies of myocardial ischemia and reperfusion. In contrast, nitrous oxide appears to be

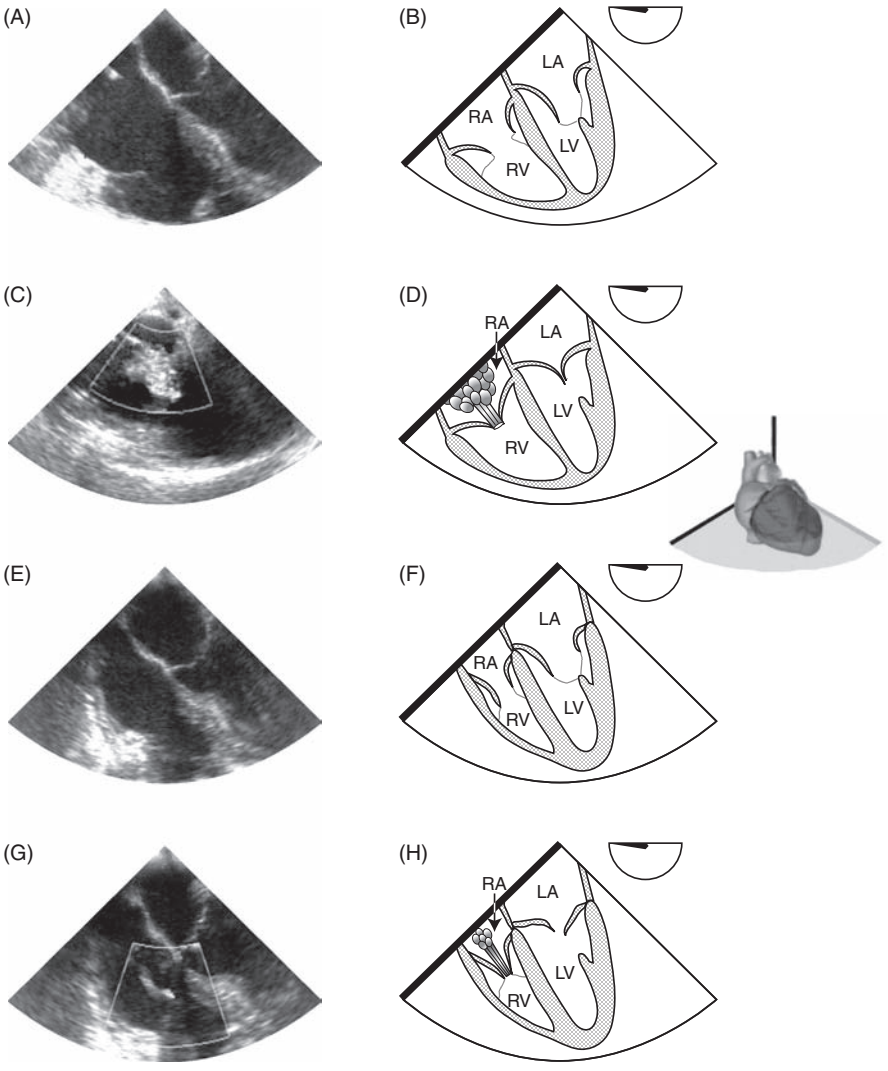

	PPV	Jet
MAP (mmHg):	80	100
MPAP (mmHg):	26	34
Pra (mmHg):	15	22
Paop (mmHg):	21	21
CI (L/m/m2):	2.1	4.8
PaO2 (mmHg):	66	524

Figure 13.16 Signs of right ventricular dysfunction in a 69-year-old man following cardiopulmonary bypass. With positive-pressure ventilation (PPV), right ventricular dilatation (A, B) with moderate tricuspid valve regurgitation (C, D) was present. The use of jet ventilation has a favorable effect on right ventricular function, with a reduction of right-sided cardiac chamber size (E, F) and tricuspid regurgitation (G, H) with associated increase in cardiac index (CI) and oxygen partial pressure (PaO_2) at an inspired oxygen of 100%. The reduction in pulmonary vascular resistance could be secondary to both the reduced tidal volume with jet ventilation and improved oxygenation (LA, left atrium; LV, left ventricle; MAP, mean arterial pressure; MPAP, mean pulmonary artery pressure; Paop, pulmonary artery occlusion pressure; Pra, right atrial pressure; RA, right atrium; RV, right ventricle).

detrimental. The mechanisms of cardioprotection are largely unknown, although potential mechanisms include favorable alteration of the determinants of myocardial oxygen supply and demand, preservation of high energy phosphates, modification of intracellular calcium handling and activation of adenosine triphosphate-regulated potassium channels. (Effects of inhalational anesthetics on systemic hemodynamics and the coronary circulation. In: Kaplan JA, ed. Cardiac Anesthesia. 4th ed. Chapter 16. WB Saunders Company, 1999.)

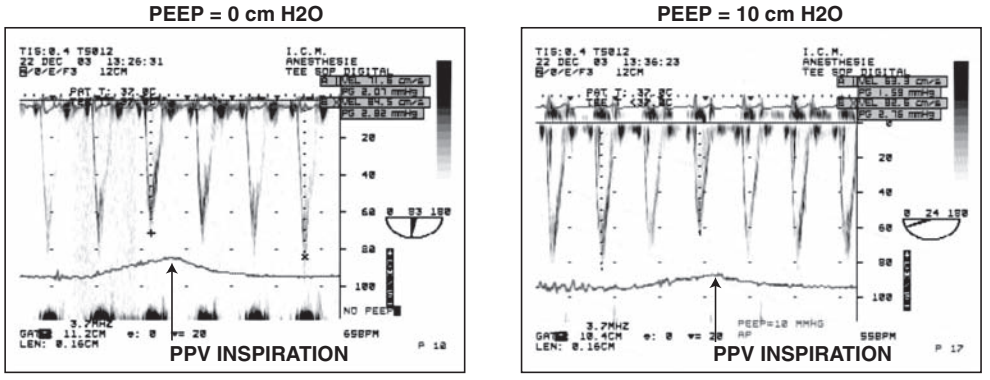

Figure 13.17 Effect of 10 cmH_2O of positive-end expiratory pressure (PEEP) on the right ventricular outflow tract velocities obtained from a deep transgastric view. Note that the absolute velocities values were reduced and the inspiratory to expiratory gradient increased (PPV, positive-pressure ventilation).

2. Intravenous Anesthetic Agents on Systolic Function

Opioids

Most evidence indicates that fentanyl produces little or no direct change in myocardial contractility and that opioids have depression-sparing actions when combined with a potent inhaled agent. Maintaining preload is essential to promote hemodynamic stability and preserve adequate cardiac function. Opioids can decrease preload through direct sympatholytic and vagotonic actions. (Cardiovascular pharmacology of anesthetics. In: Estafanous FG, ed. Cardiac Anesthesia: Principles and Clinical Practice. 2nd ed. Lippincott Williams & Wilkins, 2001.)

Benzodiazepines

Benzodiazepines by themselves produce only a mild decrease in myocardial contractility. Nevertheless, ventricular filling pressures can decrease after the induction of anesthesia with benzodiazepines, particularly during hypovolemia. The SVR may also decrease, resulting in lowering of systemic blood pressure by up to 20%. (Cardiovascular pharmacology of anesthetics. In: Estafanous FG, ed. Cardiac Anesthesia: Principles and Clinical Practice. 2nd ed. Chapter 10. Lippincott Williams & Wilkins, 2001.)

Propofol

More often than not, propofol has been shown to be a direct myocardial depressant in animals and humans. Using arterial systolic blood pressure and TEE short-axis left ventricular measurements to evaluate the end-systolic pressure–volume relationship in humans, Mulier et al. (31) demonstrated that propofol has dose-dependent, negative inotropic properties. Furthermore, the negative inotropic properties of propofol are greater than those of equipotent doses of thiopenthal in both intensity and duration (Fig. 13.18). More recently, Schmidt et al. (32) suggested that milder sedative concentrations of propofol (0.65–2.6 $\mu g/mL$) produce significant vasodilatation but no direct negative inotropic effects. Venodilatation and reduction in preload as well as dose-related arterial vasodilatation and afterload reduction have been demonstrated to be important effects of propofol administration. These phenomena affect the systemic circulation to a greater degree than the pulmonary circulation. (Cardiovascular pharmacology of anesthetics. In: Estafanous FG, ed. Cardiac Anesthesia: Principles and Clinical Practice. 2nd ed. Chapter 10. Lippincott Williams & Wilkins, 2001.)

Barbiturates

Myocardial contractility is decreased with barbiturates, through mechanisms involving calcium transport and its interaction with myofibrils. Its negative inotropic action is greater than that produced by benzodiazepines, etomidate, or ketamine, but probably not as large as the one produced by potent inhaled anesthetics. (Cardiovascular pharmacology of anesthetics. In: Estafanous FG, ed. Cardiac Anesthesia: Principles and Clinical Practice. 2nd ed. Chapter 10. Lippincott Williams & Wilkins, 2001).

Ketamine

Induction doses of ketamine increase heart rate (HR), cardiac output (CO), pulmonary and systemic blood pressure, as well as pulmonary and systemic vascular

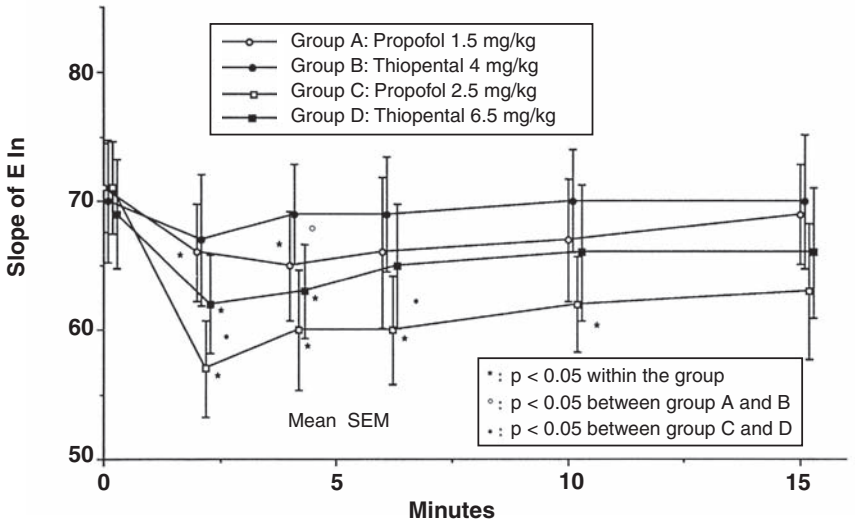

Figure 13.18 Changes in left ventricular elastance (Eln) (mmHg/mL) as a parameter of contractility after successive single-bolus intravenous injections of 4.0 and 6.5 mg/kg of thiopental and 1.5 and 2.5 mg/kg of propofol. [Reproduced with permission from Mulier et al. (31).]

resistance. Effects on pulmonary arterial pressure may be greater than on systemic arterial pressure. Higher doses can result in paradoxical effects, with predominant hemodynamic depression instead of stimulation. (Cardiovascular pharmacology of anesthetics. In: Estafanous FG, ed. Cardiac Anesthesia: Principles and Clinical Practice. 2nd ed. Chapter 10. Lippincott Williams & Wilkins, 2001.)

Etomidate

Etomidate produces the fewest hemodynamic changes among the sedative–hypnotic agents. The inotropic effects of etomidate are mild. Dose-dependent decreases in sympathetic tone, venous return, preload and cardiac contractility can occur with etomidate but are typically less obvious than with thiopenthal. Arterial blood pressure usually remains stable. (Cardiovascular pharmacology of anesthetics. In: Estafanous FG, ed. Cardiac Anesthesia: Principles and Clinical Practice. 2nd ed. Chapter 10. Lippincott Williams & Wilkins, 2001.)

3. *Effect of Intravenous Anesthetic Agents on Diastolic Function*

Little data is available on the effect of intravenous anesthetic agents on diastolic function. Recently, Gare et al. (33) studied the effects of sedative doses of midazolam and propofol in patients with normal and mild diastolic dysfunction (relaxation abnormalities), using transthoracic mitral inflow pulsed-wave (PW) Doppler and annular tissue Doppler imaging. Their results suggest that sedation with midazolam or propofol does not affect the indices of left ventricular diastolic performance in the two groups.

C. Nonanesthetic Drugs Commonly Used During Cardiac Surgery

1. *Positive Inotropic Drugs*

Endogenous Catecholamines

EPINEPHRINE. Epinephrine is a potent α- and β-adrenoreceptor agonist. In the heart, epinephrine is a potent stimulant of myocardial inotropy, has significant arrhythmogenic potential and increases stroke volume (SV), coronary blood flow and HR. Doses of 0.01–0.03 μg kg per min provide low-dose epinephrine in which β-agonist effects predominate. However, at a higher dose (maximum 0.1 μg kg per min), the α-agonist effect tends to predominate, inducing vasoconstriction.

NOREPINEPHRINE. Norepinephrine, predominantly, stimulates the α-adrenoreceptors although concurrent stimulation of the β_1-adrenoreceptors occurs to a lesser extent. Thus, blood pressure increases as a result of increased SVR; this in turn tends to decrease the HR due to vagal reflex pathways which overcome the direct stimulation of myocardial β_1-adrenergic receptors. β_1-mediated increase in myocardial contractility do occur, so norepinephrine is considered a positive inotropic agent particularly at low doses where the β_1 effects predominate over the peripheral α effects. The overall cardiac effects of norepinephrine include increased SV, coronary blood flow, and arrhythmogenic potential while there is minimal change in CO and a potential decrease in HR.

DOPAMINE. The cardiovascular effects of dopamine are dose-dependent. At low doses (1–3 μg kg per min), dopamine predominantly stimulates dopaminergic receptors. At moderate doses (3–10 μg kg per min), dopamine directly stimulates β_1- and β_2-receptors, explaining its positive inotropic effects. At high intravenous doses (10–15 μg kg per min), α-stimulation predominates and causes vasoconstriction.

2. Synthetic Catecholamines

Dobutamine

Dobutamine is primarily a direct β-agonist, relatively selective for the β_1-receptor subtype. It is more effective in providing positive inotropic effects than increases in HR. In typical clinically used concentrations (2–15 μg kg per min), a modest increase in HR and minimal change in SVR are seen (despite partial α-receptor stimulation). Dobutamine administration in patients with right ventricular failure also has positive inotropic effects. The effects on hemodynamics and left ventricular performance after CPB in patients undergoing CABG have recently been revisited (34). After CPB, dobutamine improves left ventricular performance in a dose-dependent manner, as indicated by an increase in cardiac index and FAC (measured by TEE). Decreased end-diastolic (EDA) and end-systolic areas (ESA) (Fig. 13.19) are also observed as well as a reduction in PCWP and central venous pressure (CVP). After CPB, the dominant mechanism by which this agent improves ventricular performance is by a dose-dependent increase in HR, as stroke volume index (SVI) decreased with higher dobutamine doses (34).

A low dose of dobutamine has also been used intraoperatively to predict improvement in regional myocardial function after CABG. Indeed, using TEE to assess regional wall motion, Aronson et al. (35) found that positive response to low dose dobutamine (5 μg kg per min) before CPB could predict improved regional contractility with a positive predictive value of 0.88 early after weaning from CPB and a value of 0.94, 30 min after the administration of protamine. On the other side, the lack of improvement with dobutamine was less predictive (NPV = 0.70). The same group of investigators (36) later reported a positive predictive value of 0.81 at one year to predict improved regional contractility. Again, regional contractility evolution could not be predicted in the case of failure to improve with low-dose dobutamine before revascularization with a negative predictive value of 0.34.

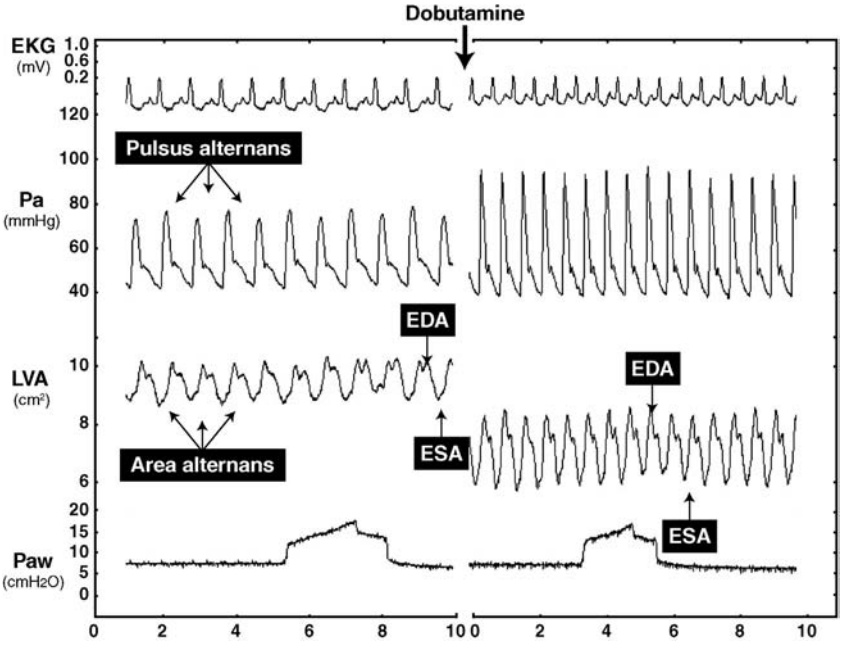

Figure 13.19 Effect of dobutamine on hemodynamic and echocardiographic parameters. The use of dobutamine is associated with an increased heart rate and arterial pressure (Pa), a decrease in end-diastolic area (EDA) and end-systolic area (ESA) with a significant increase in stroke area (SA) (SA = EDA − ESA) and in fractional area change (FAC) (FAC = EDA − ESA/EDA). Note that pulsus alternans and area alternans disappear after the use of dobutamine. The continuous ventricular area tracing was obtained by automated border detection through acoustic quantification (EKG, electrocardiogram; LVA, left ventricular area; Paw, airway pressure) [see also Fig. 9.4(C)]. (Courtesy of Dr. Michael R. Pinsky.)

3. Phosphodiesterase Inhibitors

Phosphodiesterases inhibitors prevent the breakdown of cyclic adenosine monophosphate (AMP), prolonging its effectiveness and augmenting its physiologic response. In addition to positive inotropic properties, phosphodiesterases inhibitors cause vasodilatation. The bypiridines inamrinone (formerly amrinone) and milrinone are two drugs of this class commonly used during cardiac surgery. In cardiac surgical patients, a milrinone loading dose of 50 μg/kg followed by a continuous infusion of 0.5 μg kg per min resulted in a plasma concentration in excess of 100 ng/mL, producing a substantial hemodynamic effect (the plasma concentration associated with a 50% increase in cardiac index was 167 ng/mL) (37). Using both standard hemodynamic measurements and echocardiography, Kikura et al. (38) studied the effects of milrinone in cardiac surgical patients immediately after separation from CPB: left ventricular function and hemodynamic parameters were improved in patients already treated with catecholamines and/or vasodilators under constant loading conditions ensured by constant reinfusion from CPB reservoir. A loading dose of 50 μg/kg and a loading dose plus three different continuous infusions (50–75 μg/kg + 0.5–0.75 μg kg per min) produced an increase in cardiac index and SVI with a decrease in peripheral vascular resistance. No significant changes in HR, main arterial pressure (MAP), PCWP, and CVP as well as the EDA measured by TEE were noted. However, velocity of circumferential shortening corrected for HR, an index of cardiac performance not affected by preload, significantly increased and was positively correlated with the milrinone serum concentration ($r = 0.43$). Amrinone and milrinone were found to have similar hemodynamic effects in patients undergoing elective cardiac surgery (39).

Milrinone also improves diastolic parameters in patients with heart failure, reducing diastolic pressure at any given volume while elevating the maximum rate of rise of left ventricular pressure (18%) and decreasing the mean aortic pressure. The peak left ventricular filling rate increased by 42% and the PCWP decreased (40). Using TEE in cardiac surgery, Lobato et al. (41) observed that CPB was associated with a 20% decrease in left ventricular compliance as measured by change in left ventricular end diastolic area (LVEDA) in relation to the left atrial pressure (41). Administration of milrinone after CPB was associated with a partial return of left ventricular compliance to pre-CPB values.

Phosphodiesterase inhibitors can also improve right ventricular function and reduce right ventricular afterload after cardiac surgery. Using right ventricular pressure–area relationship obtained by TEE, Ochiai et al. (42) found that the administration of amrinone in the postoperative period results in improved right ventricular contractility, as reflected by an increase in end-systolic elastance.

Despite the favorable effects on left and right ventricular function, administration of phosphodiesterase inhibitors may cause a decrease in preload and afterload which could require substantial volume loading (which can be guided by TEE) and administration of vasoactive agents like phenylephrine, norepinephrine and dopamine.

Phenylephrine

Phenylephrine, an α_1-adrenergic agonist, is frequently administered to increase arterial pressure during anesthesia. In patients with coronary artery disease, an intravenous bolus may cause a transient increase in the left ventricular wall stress with an impairment of left ventricular global function, as suggested by the observed decrease in FAC (Fig. 13.20) and $mVcf_c$. As these indices of left ventricular global function are afterload-dependent, the impairment of left ventricular function with phenylephrine most likely reflects the increase in left ventricular wall stress rather than altered intrinsic myocardial contractility.

Phenylephrine given to patients with valvular aortic stenosis (AS) did not exhibit any negative effect on their ventricular performance: ventricular afterload in this group of patients is mainly dependent on the pressure gradient across the aortic valve (AoV) rather than on the SVR (43).

D. Internal Mammary Dissection

During this period, TEE may be used to monitor the global and segmental ventricular function (Chapters 8 and 9), and to detect the occurrence of pneumothorax and hemothorax.

E. Arterial Cannulation

The role of TEE and EAS imaging to position the aortic and femoral cannula has been discussed above. While the frequency of intraoperative aortic dissection during cardiac surgery is infrequent at 0.16%, its mortality amounts to 20% if discovered intraoperatively vs 50% for dissections diagnosed postoperatively. After CPB, TEE can detect aortic dissection involving the proximal aortic arch at the aortic cannulation site, which can extend distally (Fig. 13.21). Although the site of the initial intimal tear is most often located at the site of arterial cannulation, dissection can also originate distally from the trauma induced by the jet of blood from the aortic cannula to a fragile atherosclerotic Ao (44). The incidence of retrograde ilioaortic dissection may be as high as 3% with common femoral artery cannulation for standard CPB. However, falsely positive TEE diagnosis of

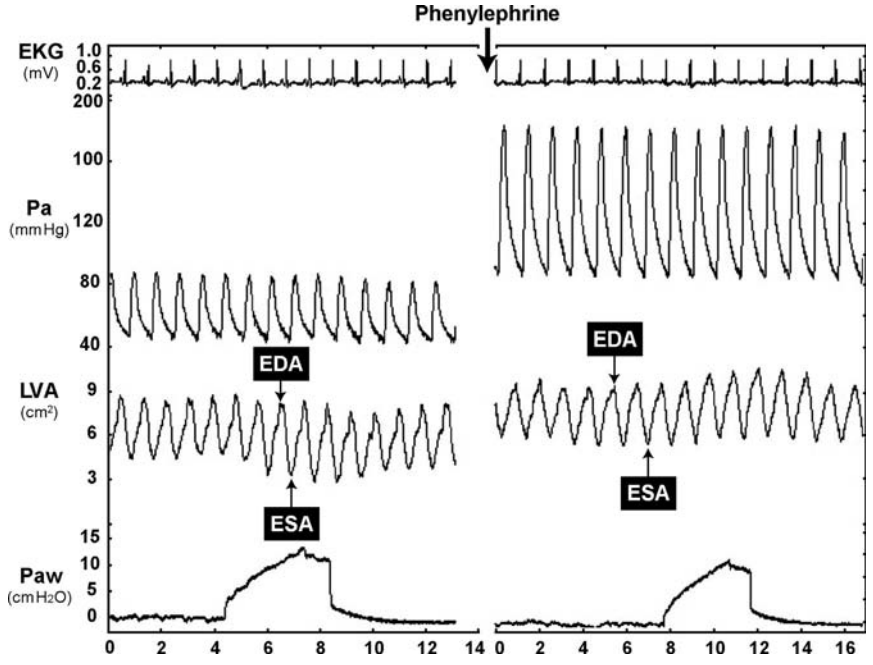

Figure 13.20 Effect of phenylephrine on hemodynamic and echocardiographic parameters. The use of phenylephrine is associated with no change in heart rate, an increase in arterial pressure (Pa), an increase in end-diastolic area (EDA) and end-systolic area (ESA) with no significant change in stroke area (SA) (SA = EDA − ESA) and in fractional area change (FAC) (FAC = EDA − ESA/EDA). The continuous ventricular area tracing was obtained by automated border detection through acoustic quantification [see also Fig. 9.4(B)] (EKG, electrocardiogram; LVA, left ventricular area; Paw, airway pressure). (Courtesy of Dr. Michael R. Pinsky.)

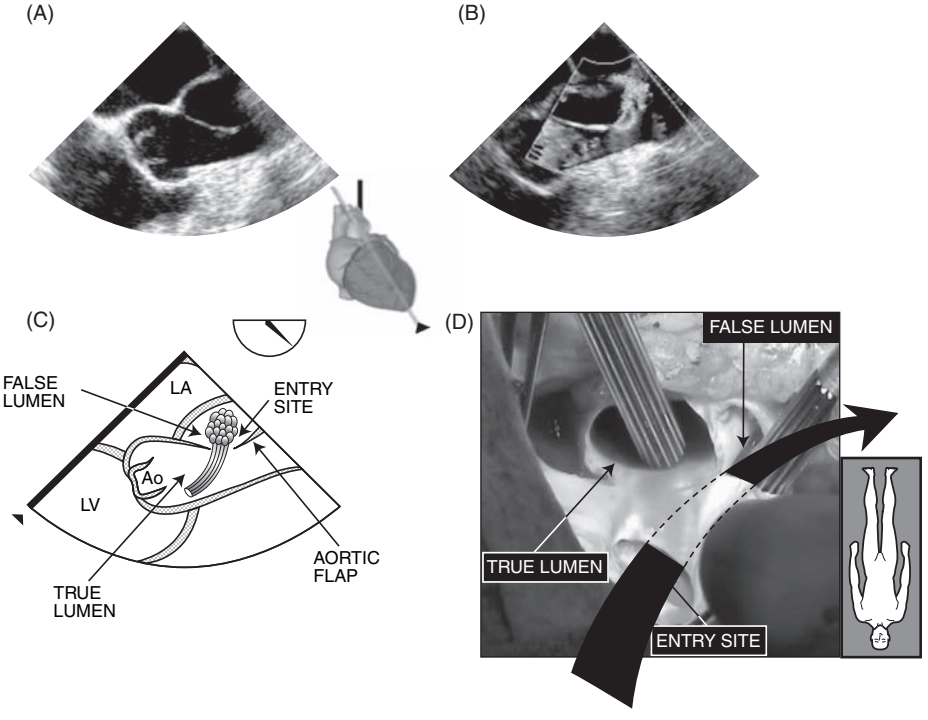

Figure 13.21 Aortic dissection involving the ascending aorta (Ao) most likely from a tear in the posterior Ao at the site of aortic cannula insertion. (A–C) Mid- and higher esophageal long-axis views demonstrate an intimal flap extending to the sinotubular junction as well as flow from the true to the false lumen through an entry site. (D) Surgical findings showing the true lumen and the entry site (LA, left atrium; LV, left ventricle). (Photo D courtesy of Dr. Michel Carrier.)

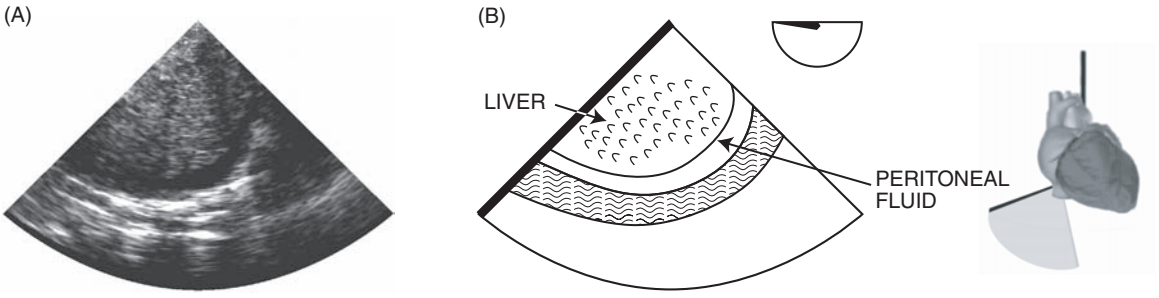

Figure 13.22 Presence of a new echo-free space (blood) around the liver consistent with peritoneal bleeding from arterial dissection during the insertion of a femoral arterial cannula.

dissection have been described with femoral CPB (see Chapter 12) (45): layering of blood with crystalloid pump-prime produces a fluid interface simulating an intimal flap, with the stasis of aortic blood flow mimicking slow flow in a false lumen. This phenomenon may be present in up to 50% of femoral bypass cases and occurs as soon as 30–40 s after initiation of the CPB. Retrograde arterial dissection may also result in retroperitoneal surgical dissection. This presents as an echo-free space under the liver and around the kidneys (46) (Fig. 13.22).

IV. CARDIAC PHYSIOLOGY AND PROCEDURES DURING CARDIOPULMONARY BYPASS

A. Hypothermia, Hemodilution, and Nonpulsatile Flow

The period on CPB can indirectly affect cardiac physiology through general effects including hypothermia, hemodilution, and nonpulsatile flow.

The adverse effects of hypothermia on myocardial performance are illustrated by studies demonstrating a decreased incidence of low-output syndrome and lower cardiac isoenzyme fractions elevation in the group kept warm. (Pathophysiology and management of cardiopulmonary bypass. In: Estafanous FG, ed. Cardiac Anesthesia: Principles and Clinical Practice. 2nd ed. Chapter 14. Lippincott Williams & Wilkins, 2001.)

To decrease viscosity and increase tissue perfusion, hemodilution is used during CPB, particularly during those using hypothermia. In patients with a normal heart, Bak et al. (47) found that acute normovolemic hemodilution (ANH) down to 80 g/L of hemoglobin caused a decrease in SVR and an increase in CO proportional to the hemodilution, whereas systemic pressure and HR remained unchanged. Using TEE, they also observed that the FAC increased from 44 $\pm$ 7% to 60 $\pm$ 9% as a result of increased LVEDA and reduced left ventricular end systolic area (LVESA) while diastolic function was unchanged.

Finally, although organ perfusion seems better maintained with pulsatile than nonpulsatile perfusion, in fact little is known about its real effect on cardiac function.

B. Myocardial Perfusion and Cardioplegia

For a detailed review of myocardial intraoperative perfusion echocardiography, the reader is referred to a comprehensive review by Aronson and Wiencek (48). One application of contrast echocardiography is the evaluation of the cardioplegia delivery. Homogenous delivery of cardioplegia is an important component of myocardial protection. Poorly protected myocardial segments may have decreased contractility following ischemia. Cardioplegic solutions can be delivered via the aortic root (antegrade) or through the coronary sinus (CS) (retrograde). Although coronary stenosis may impede the uniform distribution of cardioplegic solutions, myocardial protection may also be impaired by noncoronary causes. For instance, antegrade cardioplegia administered through the aortic root may be incompletely delivered to the coronary arteries during transient aortic regurgitation (AR) inadvertently induced by aortic cross-clamping (Fig. 13.23). Using intraoperative contrast TEE, Voci et al. (49) observed in patients with normal AoV, that antegrade administration of cardioplegia was associated with AR in 25% of the cases. Significant aortic regurgitation during antegrade cardioplegia is easily identified by the surgeon. In this situation the heart will distend. Gentle cardiac compression can be performed to avoid ventricular overdistension and myocardial ischemia. The delivery of cardioplegia as assessed by myocardial opacification with concomitant contrast injection was decreased in patients with severe AR compared with patients without regurgitation (49). Regurgitation of cardioplegic solution into the LV may also lead to left ventricular dilatation and mitral regurgitation (MR) easily diagnosed with TEE and the pulmonary artery catheter (Fig. 13.23). Because antegrade delivery of cardioplegia

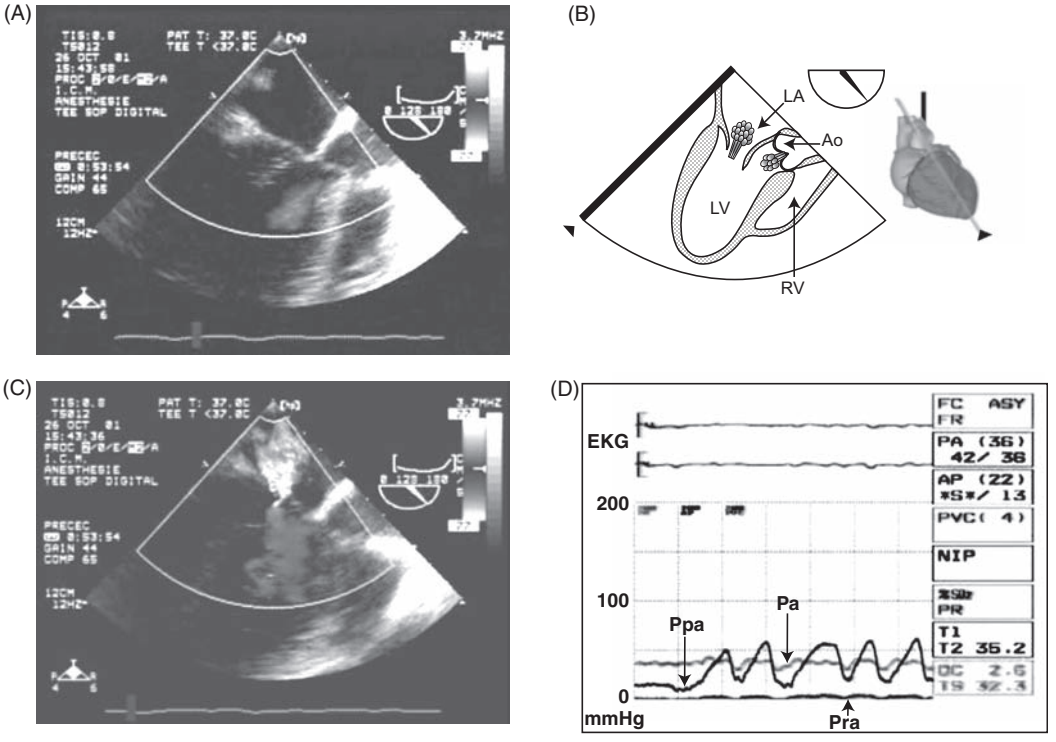

Figure 13.23 Aortic (A, B) and mitral valve regurgitation (C) during cardioplegia infusion in a 75-year-old woman undergoing revascularisation. (D) New waves were seen on the pulmonary artery pressure (Ppa) tracing secondary to mitral regurgitation (Ao, aorta; EKG, electrocardiogram; LA, left atrium; LV, left ventricle; Pa, arterial pressure; Pra, right atrial pressure; RV, right ventricle).

may result in inhomogeneous perfusion of myocardium in patients with occluded or severely stenotic coronary arteries, retrograde cardioplegia via the CS has been proposed to provide better myocardial protection. Using myocardial contrast TEE in patients with significant coronary artery disease and good collateral circulation to the LV, Borger et al. (50) attempted to evaluate both left and right ventricular perfusion during warm antegrade and retrograde cardioplegia (50). Antegrade cardioplegia was found to provide better left ventricular myocardial perfusion than retrograde cardioplegia unless, for instance, severe triple vessel coronary disease is present. Several explanations are proposed: (1) retrograde perfusion may provide reduced perfusion because the cardioplegia catheter may be positioned too distally, causing the occlusion of veins which drain in the distal portion of the CS, especially the middle and small cardiac veins; (2) veins draining in the CS may have a uni- or bicuspid valve at their origin, impeding retrograde progression of the cardioplegic solution; (3) retrograde delivery may be limited by the presence of widespead venovenous anastomoses. Shunting of retrograde perfusion into both left and right ventricular cavities via the Thebesian channels could be visualized in all patients in the study by Borger et al. (50). Right ventricular perfusion was poor with both techniques before coronary revascularization (25% vs 7% of visualized segments for antegrade vs retrograde cardioplegia), a finding which was confirmed by other authors (51). Reduced right ventricular perfusion with antegrade delivery may be explained by the lack of collateral circulation in patients with occluded or severely stenotic right coronary artery (RCA). Cardioplegic perfusion of the right coronary bypass graft early after cardioplegic arrest may improve right ventricular protection. Evaluation of myocardial perfusion would allow surgeons to assess both the patency of bypass grafts and the regional distribution of myocardial flow subserved by each graft. Using TEE and sonicated Renografin-76 injected in the aortic root after the completion of CABG, Aronson et al. (52) found that areas with perfusion defects after revascularization but before separation from CPB correlated with regional wall motion abnormalities after separation from CPB.

C. Spontaneous Echo Contrast

At the beginning of the period on CPB, intracardiac blood flow decreases and spontaneous echo contrast may be observed, particularly in the LA, even in normal hearts.

The significance of spontaneous echo contrast in pathologic hearts has been discussed in previous chapters.

V. CHANGES IN CARDIAC PHYSIOLOGY DURING WEANING FROM CARDIOPULMONARY BYPASS

The termination of CPB presents a challenging task to the anesthesiologist. The myocardium is often compromised by acute dysfunction from the residual effects of cardioplegia, iatrogenic ischemia and hyperkaliemia superimposed on chronic abnormalities in ventricular performance. Although it is usually not critical to successful weaning from CPB, TEE monitoring has several advantages over conventional hemodynamic monitoring during this period.

A. Assessment of Regional Left Ventricular Function

The reader is referred to Chapter 8 for a more detailed discussion on the value and limitations of myocardial ischemia monitoring with TEE. Transesophageal echocardiography can detect myocardial ischemia more reliably than electrocardiography in cardiac surgery. Importantly, there is a correlation between ischemic episodes detected by TEE and adverse outcomes in cardiac surgery. In 50 patients having elective coronary revascularisation, Leung et al. (53) found an association between postbypass wall-motion abnormalities and postoperative myocardial infaction. Thirty-three percent of patients with postbypass ischemia had a myocardial infarction compared with none in patients without ischemia. More recently, Comunale et al. (54) showed that a myocardial infarction was five times more likely to happen in patients displaying ischemia on electrocardiogram (ECG) and TEE compared with patients without ischemia (54). During off-pump beating heart CABG, most of the new wall motion abnormalities resolve within a few minutes after revascularization (55). However, (56,57) the main interest of intraoperative TEE is focused on the period after reperfusion: detection of persistent systolic wall motion abnormalities is associated with postoperative cardiac systolic wall motion abnormalities, more myocardial necrosis as evidenced by higher elevation of cardiac enzyme levels, and more subsequent clinical events such as pulmonary edema and atrial fibrillation (55). Thus, persistent regional wall motion abnormalities in revascularized areas after reperfusion should lead the surgeon to reassess the adequacy of the coronary bypass graft.

B. Assessment of Global Left Ventricular Function

Transesophageal echocardiography is useful to determine the etiology of hemodynamic instability in patients difficult to wean from CPB, to monitor cardiac function while therapy is initiated and to assess global and regional left ventricular function after termination of CPB.

Intraoperatively, global left ventricular function is most frequently assessed by estimating the FAC of the LV (cf Chapter 5). This measurement is readily obtained by imaging the heart in the transgastric short-axis view at the mid-papillary level of the LV. The FAC overestimates left ventricular function if regional wall motion abnormalities exist at the base or apex of the LV, because they are not taken into account in the calculation. Moreover, the measurement of FAC is a load-dependent index of left ventricular performance (58) and loading conditions must be considered in its interpretation. The end-systolic pressure–volume relationship is a relatively load-independent measure of left ventricular contractility (termed elastance) which can be measured using both continuous TEE automated border detection and femoral arterial pressure measurements. This index has been shown to decrease after CPB (59) (Fig. 13.24). Even if the end-systolic pressure–volume relationship may appear to be a better parameter of left ventricular function, the FAC can still be used to guide clinical decision making. For example, in an unstable patient with hyperdynamic left ventricular function and a small LVEDA, hypovolemia is the most likely cause of hemodynamic compromise. On the other hand, if the FAC is decreased with increased LVEDA, the most likely cause of instability is decreased left ventricular contractility, suggesting that inotropic therapy would be helpful.

The circumferential Vcf is another index of contractility that incorporates a time-related element and seems to be less preload-dependent than the FAC (see Chapter 5). Its value in normal individuals is 1.09 ± 0.3 circumferences per second (60).

C. Preload Assessment

Preload is an important determinant of cardiac function, which is traditionally measured in clinical settings by the PCWP as an estimate of left ventricular end-diastolic pressure (LVEDP). The relationship between LVEDP and left ventricular diastolic volume can, however, be altered by several variables, including myocardial ischemia, afterload reduction, the use of vasopressors and ventricular interaction. Preload can also be estimated by TEE through direct measurement of cavity dimensions as an estimate of left ventricular end-diastolic volume (LVEDV). Left ventricular end-diastolic area has been

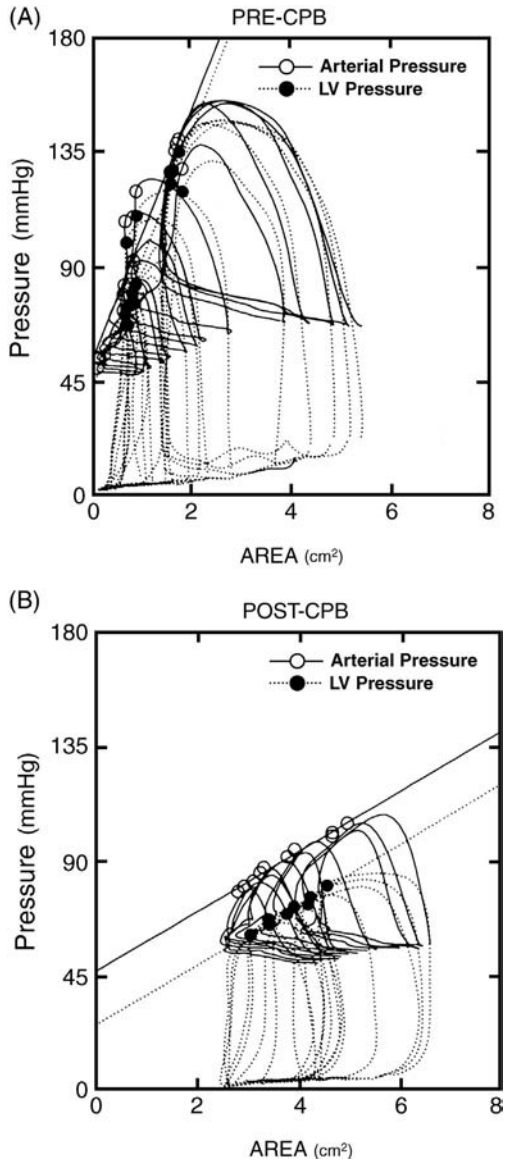

Figure 13.24 Simultaneous arterial pressure–area loops (solid lines) and left ventricular (LV) pressure–area loops (dashed lines) before (A) and after (B) cardiopulmonary bypass (CPB). The LV pressure end-systolic elastance (E'es) decreased from 49 to 12 mmHg/cm^2 with similar change in arterial E'es from 50 to 12 mmHg/cm^2. The LV area is used to estimate LV volume. [Reproduced with permission from Gorcsan et al. (59).]

shown to reflect more accurately left ventricular preload than PCWP (61). It is measured from the short axis transgastric view at the mid-papillary muscle. A LV EDA of 5.5 cm^2/m^2 or less reflects hypovolemia, but can also be present in hyperdynamic heart. In severe hypovolemia, near-obliteration of the left ventricular cavity in systole usually accompanies the decrease in LV EDA (see Chapter 9). Although measurement of LV EDA is considered the best method to determine left ventricular preload, it is not possible to establish a threshold of EDA below which a large proportion of patients increase their cardiac output after volume administration in a cardiac surgical group, with the responders being unfortunately distributed over a wide range of LV EDA (62). Lattik et al. (63) reported that the type of mitral inflow Doppler filling pattern may predict the improvement in CO after intravascular fluid challenge in patients undergoing CABG. The analysis of Doppler interrogation of the mitral inflow may indeed provide an idea of the patient's location on the diastolic pressure–volume relationship (see Fig. 9.9).

Left atrial pressure can also be inferred from the PVF pattern as measured by PW Doppler examination. In normal hearts, the PVF is a systolic and diastolic forward phase followed by an atrial reversal phase corresponding to the atrial contraction (see Fig. 4.20). When left atrial pressure is <15 mmHg, the PVF shows systolic flow predominance. Elevation of left atrial pressure >15 mmHg results in diastolic flow predominance. The ratio of systolic to total PVF VTI is negatively correlated with LA pressure (64). However, PVF pattern is also modified by other factors, including age, HR, CO, left ventricular systolic and diastolic function, and left atrial function. Other studies have found a correlation between the atrial reversal velocity (65) or the relative duration of the mitral inflow and the pulmonary venous A-wave and the left ventricular end-diastolic pressure (66).

Mitral inflow pattern is not only affected by preload, but also by the state of left ventricular relaxation, compliance and systolic function as well as left atrial compliance (67). Nomura et al. (68) found significant correlations between PCWP and the mitral deceleration time or slope in patients with decreased left ventricular systolic function (EF $<35\%$) undergoing CABG: the sensitivity, specificity, and positive predictive value of a deceleration time ≥ 150 ms were 93.3%, 100%, and 100%, respectively for the detection of a PCWP value <10 mmHg.

Finally, the PCWP can be estimated by observing the behavior of the atrial septal motion during positive pressure ventilation. At normal levels of preload, the increase in right-sided venous return relative to that on the left side with passive mechanical expiration will cause a mid-systolic reversal in the septal convexity towards the left. The presence of expiratory midsystolic reversal is associated with a PCWP <15 mmHg with a positive predictive value of 0.97. When mid-systolic reversal is present during all ventilatory phases, the PCWP is probably <10 mmHg (positive predictive value $= 0.85$) (69) (see Fig. 9.6). These findings should, however, be interpreted with caution in patients displaying severe mitral or tricuspid regurgitation (TR).

D. Assessment of Right Ventricular Function

Assessment of the right ventricular function is reviewed in Chapter 9. Right ventricular dysfunction may present the following features on TEE examination: right atrial and ventricular dilatation (Fig. 13.16), decreased tricuspid annular longitudinal motion (Fig. 13.15), regional wall motion abnormalities, shift of the atrial and the ventricular septum towards the left, TR (Fig. 13.16), and plethora of the IVC. In addition, on hepatic venous flow PW Doppler interrogation, increased atrial reversal velocity can be present in mild right ventricular dysfunction while systolic reversal will be observed in more severe cases (see Fig. 9.32).

Acute right ventricular failure may result from pulmonary embolism, right ventricular infarction, poor preservation of the RV by cardioplegia during CPB, air embolism to the right coronary artery, significant pulmonary hypertension or right ventricular dysfunction secondary to left ventricular dysfunction.

The diagnosis of right ventricular dysfunction before (70) or after (71) CPB has prognostic and therapeutic implications. Although not systematically assessed in cardiac surgical patients, right ventricular dysfunction is associated with higher mortality in patients with hypotension despite inotropic therapy: the hospital mortality was as high as 86% compared with 30–40% for patients with moderately impaired or normal right ventricular function with severe left ventricular systolic dysfunction and only 15% for those with normal RV and left ventricular systolic function (71). More recently, Maslow et al. (70) found that the presence of pre-CPB right ventricular dysfunction defined as a RV FAC $<35\%$ predicted a poor outcome after CABG in patients with severe left ventricular systolic dysfunction. Patients with poor RV FAC required a longer duration of mechanical ventilatory support (12 vs 1 day, $p < 0.01$), a longer stay in the Intensive Care Unit (ICU) (14 vs 2 days, $p < 0.01$) and in the hospital (14 vs 7 days, $p = 0.02$); left ventricular diastolic dysfunction was more frequent and severe in these patients while improvement in left ventricular ejection fraction immediately after CPB was decreased ($4.1 \pm 8.3\%$ vs $12.5 \pm 9.2\%$, $p = 0.03$). Finally, all patients with poor right ventricular function died within two years of surgery, while 94% of patients with preserved right ventricular function survived beyond that period.

E. Assessment of Diastolic Function

For a complete discussion of diastolic function, the reader is referred to Chapter 9. Bernard et al. (72) recently found that diastolic dysfunction is encountered in 30% of patients undergoing cardiac surgery and that its presence before CPB predicts difficult weaning and the need for inotropic support at the end of the procedure and up to 12 h postoperatively.

The clear effect of CPB, transient global ischemia, CABG, and cardioplegic solutions on the left ventricular diastolic function is controversial. Indeed, while myocardial revascularization improves left ventricular diastolic stiffness and Doppler indices of ventricular relaxation when evaluated weeks to months after surgery (73), only a few studies have documented the effects of CABG on left ventricular diastolic function in the early postoperative period. The potential improvement in diastolic function by revascularization could be offset by global ischemia during the cardioplegic arrest. If changes in the mitral inflow Doppler profile suggesting diastolic dysfunction are described post-CPB, no clear change in ventricular relaxation could be demonstrated after statistical correction for the effect of HR on the mitral indices (74). In fact, Humphrey et al. (75) have reported an improvement in diastolic relaxation after CABG and CPB using left ventricular intracavitary pressure and dimension measurements.

F. Air Detection

During valvular heart surgery, and occasionally during CABG, when veins are anastomosed to the ascending Ao, air is introduced into the heart cavities and may lead to coronary and cerebral embolism. Transesophageal echocardiography is useful to detect the presence of intracardiac air and to assess the efficacy of the measures to eliminate it. Two types of intracardiac air are encountered:

1. Air bubbles: these present as highly mobile, strongly echogenic dots, often accompanied by side lobe and reverberation artifacts with acoustic shadowing. Because of their buoyancy, bubbles will gather in the superior aspects of cardiac chambers (see Fig. 9.42). Dynamic tearing away of small air bubbles from the surface of an air pocket into the cardiac chambers can also be observed and is known as the popcorn sign.
2. Pooled air: this is depicted as a highly mobile, strongly echogenic line or area adjacent to the wall at the highest level in each chamber and also accompanied by side lobe and reverberation artifacts with acoustic shadowing.

Orihashi et al. (76) prospectively looked for the presence of intracardiac air with TEE in 13 consecutive patients undergoing left cardiotomy. The most frequent location of air retention was the right upper pulmonary vein (RUPV) (13/13), followed by the LV (9/13), the LA (8/13), and the right sinus of Valsalva (8/13). All patients undergoing right cardiotomy displayed air trapping in the main and the right pulmonary arteries. Air in

the pulmonary arteries is stopped by the lungs which act as a filter. Air in the RUPV is visualized near their junction to the LA. Pooled air is also found in the superior aspect of the LA near the atrial septum, as well as in the apex of the left atrial appendage (LAA). Intracardiac air may also accumulate along the anterior mitral leaflet and in the apex of the LV near the ventricular septum. Bubbles in the right sinus of Valsalva are easily mobilized and expelled within several beats of left ventricular contraction (Fig. 13.25).

When TEE still reveals the persistence of air in the cardiac chambers, other procedures to remove it are suggested:

1. Filling the cardiac chambers with blood during suturing with concomitant application of suction to the left ventricular or aortic root vent.
2. Venting through a balloon inserted into the LV in patients undergoing mitral valve replacement.
3. Allowing the air to flow out of the ascending Ao through a cardioplegic needle with the patient's head down.
4. Applying hyperinflation of the lungs.
5. Aspirating air through fine needles located in the LA or the left ventricular apex.
6. Expelling air out of the LV by agitation.
7. Administrating cardioplegia into the left ventricular vent.

VI. CHANGES IN CARDIAC PHYSIOLOGY AFTER CARDIOPULMONARY BYPASS

A. Protamine

After CPB, protamine sulfate administration may have an hypotensive effect partly by decreasing SVR. Additional human data also suggest that protamine sulfate may have cardiovascular depressant properties which become apparent in patients with impaired left ventricular function (78).

B. Right and Left Ventricular Contractile Function and Valve Function

Re-evaluation of right and left ventricular systolic and diastolic function can be performed as previously

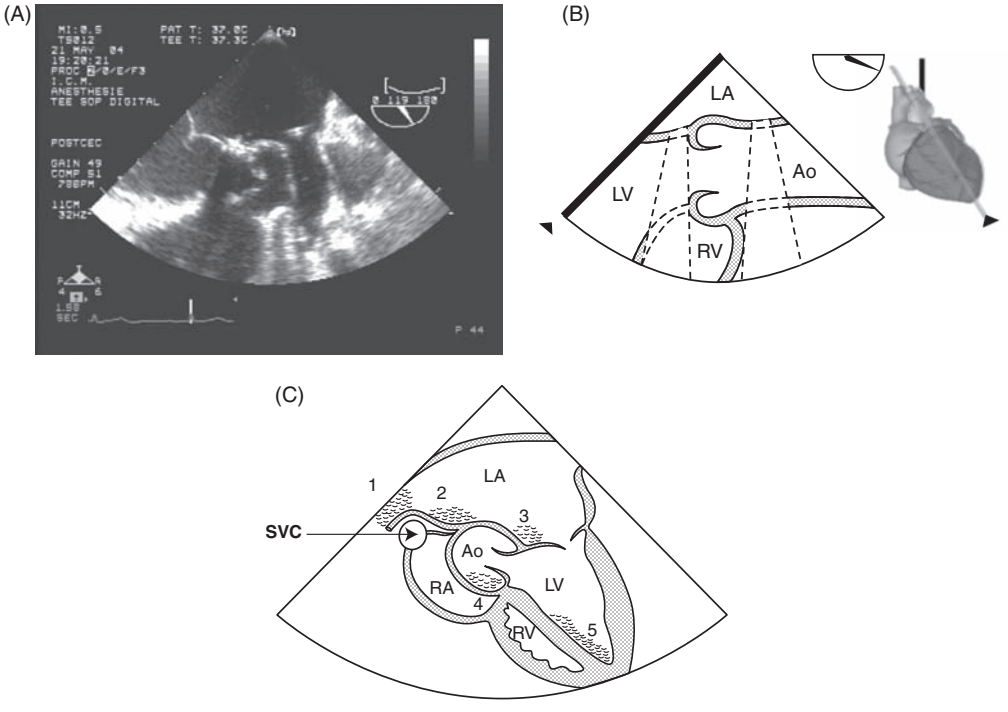

Figure 13.25 (A, B) Mid-esophageal long-axis view in a 78-year-old woman after mitral valve replacement. Residual air was localised in the left atrium (LA) with associated acoustic shadowing. (C) Most frequent sites of retained air after cardiopulmonary bypass: 1, right upper pulmonary vein; 2, superior aspect of the LA at the atrial septal level; 3, atrial side of the anterior mitral leaflet; 4, right sinus of Valsalva; 5, apex of the left ventricle (LV) near the ventricular septum (Ao, aorta; RA, right atrium; RV, right ventricle; SVC, superior vena cava). [Fig. C adapted with permission from Bettex and Chassot (77).]

Table 13.1 Summary of the Role of TEE in Patients Undergoing Cardiac Surgery

	Importance
Before the procedure	
Left and right ventricular function	Loading condition and need for postoperative inotropic and/or mechanical support
Aortic, mitral, tricuspid, and pulmonic valve competency	Detect unrecognized valvular disease
PFO	Risk of hypoxia by left-to-right shunt if right ventricular dysfunction
Aortic atheromatosis (epiaortic)	Grade 4 or 5 could complicate cannula insertion
Detection of pleural effusion	Optimization of oxygenation and ventilation
Monitor the insertion of devices: PA catheter, CPB and cardioplegias cannulas and intra-aortic balloon counterpulsation	Early detection and correction of devices misplacement
During CPB	
Monitor the position of CPB and cardioplegias canulas	Early detection and correction of canula displacement
De-airing process	Air removed before weaning from CPB
After CPB	
Re-evaluate left and right ventricular function	Loading condition and need for postoperative inotropic and/or mechanical support
Re-evaluate valvular function	New onset regurgitation, LVOT and RVOT dynamic obstruction could complicate weaning from CPB
Re-evaluate aorta	Rule out new iatrogenic aortic dissection
Rule out significant pleural effusion	Optimise chest tube drainage
In the intensive care unit	
Rule out specific complications if hemodynamically unstable	Tamponade, ventricular dysfunction, valvular insufficiency, LVOT and RVOT dynamic obstruction hypovolemia, shunting through a PFO, intracavitary thrombus

described, as well as valvular assessment as described in Chapters 15 to 19.

In conclusion, the role of TEE during cardiac surgery has shifted from a diagnostic tool to a complete monitoring and a diagnostic device. This allows the cardiac anesthesiologist to follow each step of the surgical procedure and to provide continuous feedback to the surgeon (Table 13.1). This requires both knowledge in TEE and in the surgical procedure and good communication skills.

REFERENCES

1. Practice guidelines for perioperative transesophageal echocardiography. A report by the American Society of Anesthesiologists and the Society of Cardiovascular Anesthesiologists Task Force on Transesophageal Echocardiography. Anesthesiology 1996; 84(4):986–1006.
2. Couture P, Denault AY, McKenty S, Boudreault D, Plante F, Perron R et al. Impact of routine use of intraoperative transesophageal echocardiography during cardiac surgery. Can J Anaesth 2000; 47(1):20–26.
3. Troianos CA, Savino JS. Internal jugular vein cannulation guided by echocardiography. Anesthesiology 1991; 74(4):787–789.
4. Andropoulos DB, Stayer SA, Bent ST, Campos CJ, Bezold LI, Alvarez M et al. A controlled study of transesophageal echocardiography to guide central venous catheter placement in congenital heart surgery patients. Anesth Analg 1999; 89(1):65–70.
5. Sawchuk C, Fayad A. Confirmation of internal jugular guide wire position utilizing transesophageal echocardiography. Can J Anaesth 2001; 48(7):688–690.
6. Nelson JE, Croft LB, Nahar T, Vorchheimer D. Evaluation of subclavian catheter position. J Cardiothorac Vasc Anesth 1999; 13(3):359–361.
7. Zimmermann P, Steinhubel B, Greim CA. Facilitation of pulmonary artery catheter placement by transesophageal echocardiography after tricuspid valve surgery. Anesth Analg 2001; 93(1):242–243.
8. Catoire P, Beydon L, Delaunay L, Liu N, Bonnet F. Persistent left superior vena cava diagnosed by transesophageal echocardiography. J Cardiothorac Vasc Anesth 1993; 7(3):375–379.
9. Orihashi K, Hong YW, Chung G, Sisto D, Goldiner PL, Oka Y. New applications of two-dimensional transesophageal echocardiography in cardiac surgery. J Cardiothorac Vasc Anesth 1991; 5(1):33–39.
10. Swenson JD, Bull DA. Intraoperative diagnosis and treatment of pleural effusion based on transesophageal echocardiographic findings. Anesth Analg 1999; 89(2):309–310.
11. Roach GW, Kanchuger M, Mangano CM, Newman M, Nussmeier N, Wolman R et al. Adverse cerebral outcomes after coronary bypass surgery. Multicenter Study of Perioperative Ischemia Research Group and the Ischemia Research and Education Foundation Investigators. N Engl J Med 1996; 335(25):1857–1863.

12. Katz ES, Tunick PA, Rusinek H, Ribakove G, Spencer FC, Kronzon I. Protruding aortic atheromas predict stroke in elderly patients undergoing cardiopulmonary bypass: experience with intraoperative transesophageal echocardiography. J Am Coll Cardiol 1992; 20(1):70–77.
13. Tunick PA, Kronzon I. Atheromas of the thoracic aorta: clinical and therapeutic update. J Am Coll Cardiol 2000; 35(3):545–554.
14. Murkin JM. Etiology and incidence of brain dysfunction after cardiac surgery. J Cardiothorac Vasc Anesth 1999; 13(4 suppl 1):12–17.
15. Beique FA, Joffe D, Tousignant G, Konstadt S. Echocardiography-based assessment and management of atherosclerotic disease of the thoracic aorta. J Cardiothorac Vasc Anesth 1998; 12(2):206–220.
16. Konstadt SN, Reich DL, Quintana C, Levy M. The ascending aorta: how much does transesophageal echocardiography see? Anesth Analg 1994; 78(2):240–244.
17. Konstadt SN, Reich DL, Kahn R, Viggiani RF. Transesophageal echocardiography can be used to screen for ascending aortic atherosclerosis. Anesth Analg 1995; 81(2):225–228.
18. Clements F, Wright SJ, de Bruijn N. Coronary sinus catheterization made easy for Port-access minimally invasive cardiac surgery. J Cardiothorac Vasc Anesth 1998; 12(1):96–101.
19. Akhtar S. Off-axis view using a multiplane transesophageal echocardiography probe facilitates cannulation of the coronary sinus. J Cardiothorac Vasc Anesth 1998; 12(3):374–375.
20. Poirier NC, Ugolini P, Pellerin M, Petitclerc R, Tardif JC. Transesophageal echocardiographic evaluation of perioperative coronary sinus trauma. Ann Thorac Surg 1998; 66(2):573–575.
21. Noiseux N, Cartier R, Couture P, Sheridan P. Aortic cannulation for type A dissection: guidance by transesophageal echocardiography. Int Cardiovasc Thorac Surg 2003; (2):178–180.
22. Vieillard-Baron A, Loubieres Y, Schmitt JM, Page B, Dubourg O, Jardin F. Cyclic changes in right ventricular output impedance during mechanical ventilation. J Appl Physiol 1999; 87(5):1644–1650.
23. Vieillard-Baron A, Augarde R, Prin S, Page B, Beauchet A, Jardin F. Influence of superior vena caval zone condition on cyclic changes in right ventricular outflow during respiratory support. Anesthesiology 2001; 95(5):1083–1088.
24. Brower R, Wise RA, Hassapoyannes C, Bromberger-Barnea B, Permutt S. Effect of lung inflation on lung blood volume and pulmonary venous flow. J Appl Physiol 1985; 58(3):954–963.
25. Fellahi JL, Valtier B, Beauchet A, Bourdarias JP, Jardin F. Does positive end-expiratory pressure ventilation improve left ventricular function? A comparative study by transesophageal echocardiography in cardiac and noncardiac patients. Chest 1998; 114(2):556–562.
26. Schuster S, Erbel R, Weilemann LS, Lu WY, Henkel B, Wellek S et al. Hemodynamics during PEEP ventilation in patients with severe left ventricular failure studied by transesophageal echocardiography. Chest 1990; 97(5): 1181–1189.
27. Poelaert JI, Reichert CL, Koolen JJ, Everaert JA, Visser CA. Transesophageal Echo-doppler evaluation of the hemodynamic effects of positive-pressure ventilation after coronary artery surgery. J Cardiothorac Vasc Anesth 1992; 6(4):438–443.
28. Meijburg HW, Visser CA, Wesenhagen H, Westerhof PW, Robles de Medina EO. Transesophageal pulsed-Doppler echocardiographic evaluation of transmitral and pulmonary venous flow during ventilation with positive end-expiratory pressure. J Cardiothorac Vasc Anesth 1994; 8(4):386–391.
29. Girard F, Couture P, Boudreault D, Normandin L, Denault A, Girard D. Estimation of the pulmonary capillary wedge pressure from transesophageal pulsed-Doppler echocardiography of pulmonary venous flow: influence of the respiratory cycle during mechanical ventilation. J Cardiothorac Vasc Anesth 1998; 12(1):16–21.
30. Declerck C, Hillel Z, Shih H, Kuroda M, Connery CP, Thys DM. A comparison of left ventricular performance indices measured by transesophageal echocardiography with automated border detection. Anesthesiology 1998; 89(2):341–349.
31. Mulier JP, Wouters PF, Van Aken H, Vermaut G, Vandermeersch E. Cardiodynamic effects of propofol in comparison with thiopental: assessment with a transesophageal echocardiographic approach. Anesth Analg 1991; 72(1):28–35.
32. Schmidt C, Roosens C, Struys M, Deryck YL, Van Nooten G, Colardyn F et al. Contractility in humans after coronary artery surgery. Anesthesiology 1999; 91(1):58–70.
33. Gare M, Parail A, Milosavljevic D, Kersten JR, Warltier DC, Pagel PS. Conscious sedation with midazolam or propofol does not alter left ventricular diastolic performance in patients with preexisting diastolic dysfunction: a transmitral and tissue Doppler transthoracic echocardiography study. Anesth Analg 2001; 93(4):865–871.
34. Romson JL, Leung JM, Bellows WH, Bronstein M, Keith F, Moores W et al. Effects of dobutamine on hemodynamics and left ventricular performance after cardiopulmonary bypass in cardiac surgical patients. Anesthesiology 1999; 91(5):1318–1328.
35. Aronson S, Dupont F, Savage R, Drum M, Gunnar W, Jeevanandam V. Changes in regional myocardial function after coronary artery bypass graft surgery are predicted by intraoperative low-dose dobutamine echocardiography. Anesthesiology 2000; 93(3):685–692.
36. Dupont FW, Lang RM, Drum ML, Aronson S. Is there a long-term predictive value of intraoperative low-dose dobutamine echocardiography in patients who have coronary artery bypass graft surgery with cardiopulmonary bypass? Anesth Analg 2002; 95(3):517–523.
37. Levy JH, Bailey JM, Deeb GM. Intravenous milrinone in cardiac surgery. Ann Thorac Surg 2002; 73(1):325–330.
38. Kikura M, Levy JH, Michelsen LG, Shanewise JS, Bailey JM, Sadel SM et al. The effect of milrinone on hemodynamics and left ventricular function after emergence from cardiopulmonary bypass. Anesth Analg 1997; 85(1):16–22.

39. Rathmell JP, Prielipp RC, Butterworth JF, Williams E, Villamaria F, Testa L et al. A multicenter, randomized, blind comparison of amrinone with milrinone after elective cardiac surgery. Anesth Analg 1998; 86(4):683–690.
40. Monrad ES, McKay RG, Baim DS, Colucci WS, Fifer MA, Heller GV et al. Improvement in indexes of diastolic performance in patients with congestive heart failure treated with milrinone. Circulation 1984; 70(6):1030–1037.
41. Lobato EB, Gravenstein N, Martin TD. Milrinone, no epinephrine, improves left ventricular compliance after cardiopulmonary bypass. J Cardiothorac Vasc Anesth 2000; 14(4):374–377.
42. Ochiai Y, Morita S, Tanoue Y, Kawachi Y, Tominaga R, Yasui H. Effects of amrinone, a phosphodiesterase inhibitor, on right ventricular/arterial coupling immediately after cardiac operations. J Thorac Cardiovasc Surg 1998; 116(1):139–147.
43. Goertz AW, Seeling W, Heinrich H, Lindner KH, Rockemann MG, Georgieff M. Effect of phenylephrine bolus administration on left ventricular function during high thoracic and lumbar epidural anesthesia combined with general anesthesia. Anesth Analg 1993; 76(3): 541–545.
44. Varghese D, Riedel BJ, Fletcher SN, Al Momatten MI, Khaghani A. Successful repair of intraoperative aortic dissection detected by transesophageal echocardiography. Ann Thorac Surg 2002; 73(3):953–955.
45. Watke CM, Clements F, Glower DD, Smith MS. False-positive diagnosis of aortic dissection associated with femoral cardiopulmonary bypass. Anesthesiology 1998; 88(4):1119–1121.
46. Yamaura K, Okamoto H, Maekawa T, Kanna T, Irita K, Takahashi S. Detection of retroperitoneal hemorrhage by transesophageal echocardiography during cardiac surgery. Can J Anaesth 1999; 46(2):169–172.
47. Bak Z, Abildgard L, Lisander B, Janerot-Sjoberg B. Transesophageal echocardiographic hemodynamic monitoring during preoperative acute normovolemic hemodilution. Anesthesiology 2000; 92(5):1250–1256.
48. Aronson S, Wiencek JG. Intraoperative perfusion echocardiography. J Cardiothorac Vasc Anesth 1994; 8(1):97–107.
49. Voci P, Bilotta F, Caretta Q, Chiarotti F, Mercanti C, Marino B. Mechanisms of incomplete cardioplegia distribution during coronary artery surgery. An intraoperative transesophageal contrast echocardiography study. Anesthesiology 1993; 79(5):904–912.
50. Borger MA, Wei KS, Weisel RD, Ikonomidis JS, Rao V, Cohen G et al. Myocardial perfusion during warm antegrade and retrograde cardioplegia: a contrast echo study. Ann Thorac Surg 1999; 68(3):955–961.
51. Aronson S, Jacobsohn E, Savage R, Albertucci M. The influence of collateral flow on the antegrade and retrograde distribution of cardioplegia in patients with an occluded right coronary artery. Anesthesiology 1998; 89(5): 1099–1107.
52. Aronson S, Lee BK, Wiencek JG, Feinstein SB, Roizen MF, Karp RB et al. Assessment of myocardial perfusion during CABG surgery with two-dimensional transesophageal contrast echocardiography. Anesthesiology 1991; 75(3):433–440.
53. Leung JM, O'Kelly B, Browner WS, Tubau J, Hollenberg M, Mangano DT. Prognostic importance of postbypass regional wall-motion abnormalities in patients undergoing coronary artery bypass graft surgery. SPI Research Group. Anesthesiology 1989; 71(1):16–25.
54. Comunale ME, Body SC, Ley C, Koch C, Roach G, Mathew JP et al. The concordance of intraoperative left ventricular wall–motion abnormalities and electrocardiographic S-T segment changes: association with outcome after coronary revascularization. Multicenter Study of Perioperative Ischemia (McSPI) Research Group. Anesthesiology 1998; 88(4):945–954.
55. Couture P, Denault A, Limoges P, Sheridan P, Babin D, Cartier R. Mechanisms of hemodynamic changes during off-pump coronary artery bypass surgery. Can J Anaesth 2002; 49(8):835–849.
56. Kotoh K, Watanabe G, Ueyama K, Uozaki M, Suzuki M, Misaki T et al. On-line assessment of regional ventricular wall motion by transesophageal echocardiography with color kinesis during minimally invasive coronary artery bypass grafting. J Thorac Cardiovasc Surg 1999; 117(5):912–917.
57. Malkowski MJ, Kramer CM, Parvizi ST, Dianzumba S, Marquez J, Reichek N et al. Transient ischemia does not limit subsequent ischemic regional dysfunction in humans: a transesophageal echocardiographic study during minimally invasive coronary artery bypass surgery. J Am Coll Cardiol 1998; 31(5):1035–1039.
58. Robotham JL, Takata M, Berman M, Harasawa Y. Ejection fraction revisited. Anesthesiology 1991; 74:172–183.
59. Gorcsan J, Denault A, Gasior TA, Mandarino WA, Kancel MJ, Deneault LG et al. Rapid estimation of left ventricular contractility from end-systolic relations by echocardiographic automated border detection and femoral arterial pressure. Anesthesiology 1994; 81(3):553–562.
60. Colan SD, Borow KM, Neumann A. Left ventricular end-systolic wall stress-velocity of fiber shortening relation: a load-independent index of myocardial contractility. J Am Coll Cardiol 1984; 4(4):715–724.
61. Thys DM, Hillel Z, Goldman ME, Mindich BP, Kaplan JA. A comparison of hemodynamic indices derived by invasive monitoring and two-dimensional echocardiography. Anesthesiology 1987; 67(5):630–634.
62. Tousignant CP, Walsh F, Mazer CD. The use of transesophageal echocardiography for preload assessment in critically ill patients. Anesth Analg 2000; 90(2):351–355.
63. Lattik R, Couture P, Denault AY, Tardif JC, Carrier M, Babin D et al. Mitral Doppler indices are superior to two-dimensional and conventional hemodynamic indices to predict fluid responsiveness. Anesth Analg 2002; 94(5):1092–1099.
64. Kuecherer HF, Muhiudeen IA, Kusumoto FM, Lee E, Moulinier LE, Cahalan MK et al. Estimation of mean left atrial pressure from transesophageal pulsed doppler

echocardiography of pulmonary venous flow. Circulation 1990; 82(4):1127–1139.
65. Nishimura RA, Abel MD, Hatle LK, Tajik AJ. Relation of pulmonary vein to mitral flow velocities by transesophageal Doppler echocardiography. Effect of different loading conditions. Circulation 1990; 81(5):1488–1497.
66. Appleton CP, Galloway JM, Gonzalez MS, Gaballa M, Basnight MA. Estimation of left ventricular filling pressures using two-dimensional and Doppler echocardiography in adult patients with cardiac disease. Additional value of analyzing left atrial size, left atrial ejection fraction and the difference in duration of pulmonary venous and mitral flow velocity at atrial contraction. J Am Coll Cardiol 1993; 22(7):1972–1982.
67. Yamamoto K, Nishimura RA, Chaliki HP, Appleton CP, Holmes DR Jr, Redfield MM. Determination of left ventricular filling pressure by Doppler echocardiography in patients with coronary artery disease: critical role of left ventricular systolic function. J Am Coll Cardiol 1997; 30(7):1819–1826.
68. Nomura M, Hillel Z, Shih H, Kuroda MM, Thys DM. The association between Doppler transmitral flow variables measured by transesophageal echocardiography and pulmonary capillary wedge pressure. Anesth Analg 1997; 84(3):491–496.
69. Kusumoto FM, Muhiudeen IA, Kuecherer HF, Cahalan MK, Schiller NB. Response of the interatrial septum to transatrial pressure gradients and its potential for predicting pulmonary capillary wedge pressure: an intraoperative study using transesophageal echocardiography in patients during mechanical ventilation. J Am Coll Cardiol 1993; 21(3):721–728.
70. Maslow AD, Regan MM, Panzica P, Heindel S, Mashikian J, Comunale ME. Precardiopulmonary bypass right ventricular function is associated with poor outcome after coronary artery bypass grafting in patients with severe left ventricular systolic dysfunction. Anesth Analg 2002; 95(6):1507–1518.
71. Reichert CL, Visser CA, van den Brink RB, Koolen JJ, van Wezel HB, Moulijn AC et al. Prognostic value of biventricular function in hypotensive patients after cardiac surgery as assessed by transesophageal echocardiography. J Cardiothorac Vasc Anesth 1992; 6(4):429–432.
72. Bernard F, Denault A, Babin D, Goyer C, Couture P, Couturier A et al. Diastolic dysfunction is predictive of difficult weaning from cardiopulmonary bypass. Anesth Analg 2001; 92(2):291–298.
73. Lawson WE, Seifert F, Anagnostopoulos C, Hills DJ, Swinford RD, Cohn PF. Effect of coronary artery bypass grafting on left ventricular diastolic function. Am J Cardiol 1988; 61(4):283–287.
74. Houltz E, Hellstrom A, Ricksten SE, Wikh R, Caidahl K. Early effects of coronary artery bypass surgery and cold cardioplegic ischemia on left ventricular diastolic function: evaluation by computer-assisted transesophageal echocardiography. J Cardiothorac Vasc Anesth 1996; 10(6):728–733.
75. Humphrey LS, Topol EJ, Rosenfeld GI. Immediate enhancement of left ventricular relaxation by coronary artery bypass grafting: intraoperative assessment. Circulation 1988; 77:886–896.
76. Orihashi K, Matsuura Y, Hamanaka Y, Sueda T, Shikata H, Hayashi S et al. Retained intracardiac air in open heart operations examined by transesophageal echocardiography. Ann Thorac Surg 1993; 55(6):1467–1471.
77. Bettex D, Chassot PG. Échographie transoesophagienne en anesthésie-réanimation. Édition Pradel, 2002:1–12.
78. Del Re MR, Ayd JD, Schultheis LW, Heitmiller ES. Protamine and left ventricular function: a transesophageal echocardiography study. Anesth Analg 1993; 77(6): 1098–1103.

14

Perioperative Role of TEE in Mechanical Circulatory Assistance

YANICK BEAULIEU, DENIS BOUCHARD
University of Montreal, Montreal, Canada

I. Introduction 315
II. Description of Assist Devices and Role of TEE 315
A. Intra-Aortic Balloon Counterpulsation 316
B. Ventricular Assist Devices 317
1. Centrifugal Pumps 317
2. Pulsatile Blood Pumps 319
III. Conclusion 326
References 327

I. INTRODUCTION

Over the last 20 years, considerable advances have been made in the field of mechanical circulatory support (1). The cardinal feature of the patient requiring implantation of a mechanical circulatory device is the presence of decompensated heart failure refractory to medical management. This population presents significant challenges to the medical team, specifically to the cardiac anesthesiologist in the perioperative setting. Several clinical features accompany the placement of ventricular assist device (VAD) compared with other cardiovascular procedures including the advanced degree of heart failure, the circulatory change induced by VAD therapy, complications specific to these devices and the higher incidence of associated right ventricular failure and bleeding (2). Since its early use in cardiac surgery, transesophageal echocardiography (TEE) has played an increasing role in the perioperative care of patients with severe heart failure and VAD placement, both as a diagnostic and a monitoring tool. In this chapter, the essential role of TEE for VAD placement and monitoring will be reviewed.

II. DESCRIPTION OF ASSIST DEVICES AND ROLE OF TEE

Two general subsets of patients may benefit from these devices and they are Food and Drug Administration (FDA) approved: first, patients with severe hemodynamic instability who need a device *as a bridge to transplant*, and secondly, patients in cardiogenic schock requiring a device *as a bridge to recovery* (3,4). Approximately 5% of the patients undergoing open heart surgery develop post-cardiotomy shock. Most of these patients will be able to be weaned from the cardiopulmonary bypass (CPB) with aggressive medical treatment and intra-aortic balloon pump (IABP) or counterpulsation system. However, 1% require temporary mechanical support until further recovery, or a more prolonged type of assist device for subsequent transplantation (1).

Destination therapy is an evolving third indication for mechanical circulatory support and designates its permanent use in patients with end-stage heart failure who are not candidates for a transplant (1,2). Research is in progress for this indication which is not yet FDA approved.

Circulatory assist devices are available in different configurations tailored to specific clinical situations, from simple IABP to implantation of a total artificial heart. The choice of the specific type of mechanical assistance must be based on the careful analysis of the factors underlying the cause of heart failure, the urgency of the situation, the patient's characteristics (body mass index, degree of organ dysfunction), the functional assistance needed (left ventricular, right ventricular, biventricular, implantable vs paracorporeal) and the indication (bridge to transplant or bridge to recovery).

Transesophageal echocardiography plays an important role in the perioperative management of these devices, especially those necessitating ventricular, atrial, and great vessel cannulation. In the practice guidelines for perioperative TEE published by the American Society of Anesthesiologists (ASA) and the Society of Cardiovascular Anesthesiologists (SCA) in 1996 (3), the use of TEE for the monitoring of placement of VADs is listed as a level 2 indication (supported by fair/good evidence). The different types of mechanical assist devices and the specific role of TEE are reviewed next.

A. Intra-Aortic Balloon Counterpulsation

The intra-aortic balloon (IAB) is an intravascular, catheter-mounted, counterpulsation device with a balloon volume between 30 and 50 mL. It is usually inserted percutaneously (rarely surgically) via the femoral artery using the Seldinger technique. The IAB is positioned in the descending thoracic aorta (Ao) (Figs. 14.1 and 14.2) and set to inflate at the dicrotic notch of the aortic arterial pressure waveform and deflate during the isovolumetric phase of left ventricular contraction.

The IABP creates a favorable shift in the myocardial oxygen supply/demand balance by decreasing myocardial

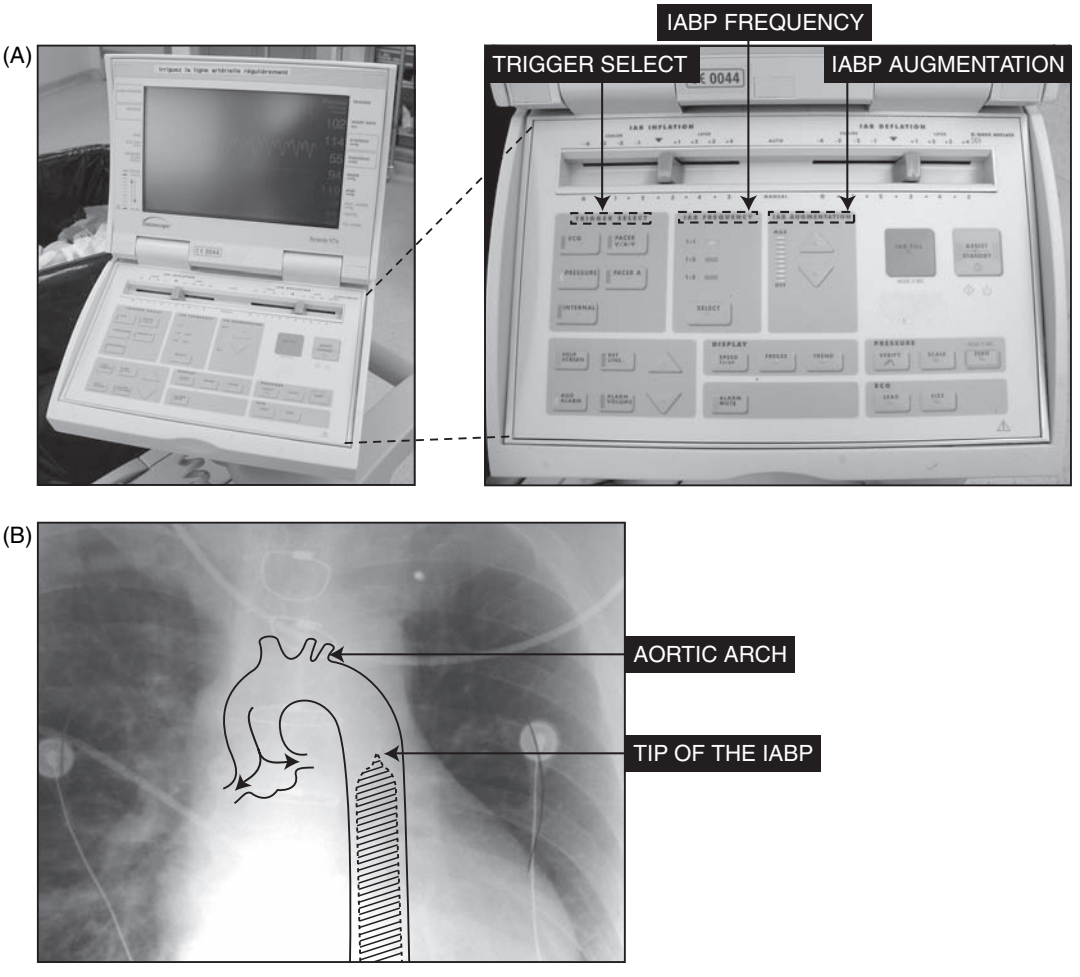

Figure 14.1 Intra-aortic balloon pump (IABP) or counterpulsation system. (A) Adjustable factors are the trigger (most commonly the electrocardiogram), the frequency (1:1, 1:2, and 1:3) and the degree of augmentation. (B) Correct insertion is confirmed by the chest X-ray or TEE when inserted intraoperatively.

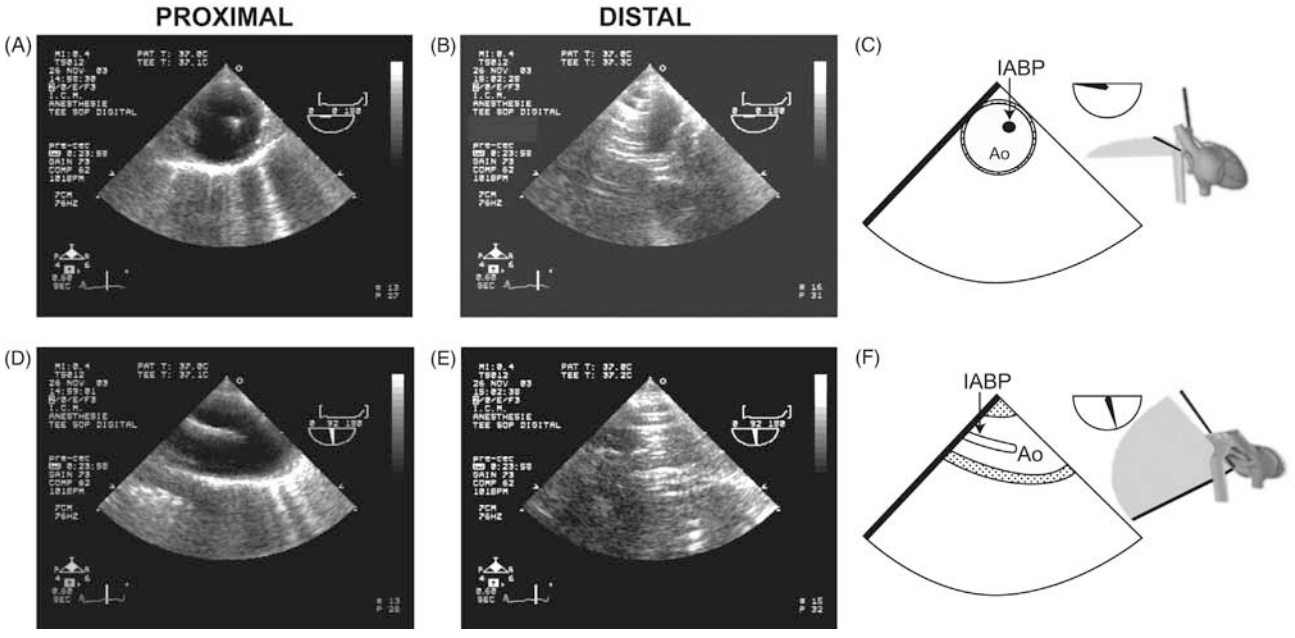

Figure 14.2 Intraaortic balloon pump (IABP) positioned in the aorta (Ao) of a 75-year-old man before coronary revascularization. The short-axis (A–C) and longitudinal views (D–F) are shown. The tip of the IABP should ideally be located 5–10 cm below the origin of the left subclavian artery. Note that as the probe is advanced more distally in the aorta, air in the IABP prevents visualization of the the aortic wall.

O_2 consumption by ~15–20% while increasing systemic and diastolic coronary perfusion (Fig. 14.3) and cardiac output (CO) (Fig. 14.4). While in that setting, TEE is currently limited and listed as a level 3 indication (no good supporting evidence) by the ASA and SCA task forces (3), it may sometimes prove useful in certain cases. For instance, the discovery by TEE of significant atherosclerotic debris in the descending Ao could contraindicate the use of IABP because of the high risk of fragmentation and embolization. Significant unsuspected aortic regurgitation (AR) disclosed by TEE would also be a contraindication to IABP use. TEE may also be helpful in confirming the correct location of the IAB in the descending thoracic Ao below the origin of the left subclavian artery. Also, the correct operation of the balloon can be confirmed by visualization of its inflation and deflation (Fig. 14.2). In case of malfunction, the presence of aortic dissection or balloon perforation can be ascertained. Lastly, TEE may be used postoperatively, for monitoring of ventricular function before finally removing the IABP device.

B. Ventricular Assist Devices

Unlike IABP, which is designed to improve the myocardial oxygen supply/demand balance while supporting systemic organ perfusion to a modest degree, VADs are designed to unload the right ventricle (RV) and/or left ventricle (LV) effectively while completely supporting the pulmonary and/or systemic circulation.

In a left ventricular assistance device (LVAD), blood flow is diverted from either the left atrium (LA) or the apex of the LV. The blood flow passes through the LVAD and is returned to the body through the ascending Ao (Figs. 14.5 and 14.6). As for IABP, unsuspected AR disclosed by TEE would be a contraindication to LVAD use (Fig. 14.7). In a right ventricular assistance device (RVAD), blood is taken from the right atrium (RA) or RV and returned to the main pulmonary artery (MPA).

Three types of mechanical blood pumps capable of replacing the function of one or both ventricles are known based on their flow design: centrifugal, pulsatile, and axial (1,3). The respective indications, contraindications, design features, and functional characteristics of these pumps will not be thoroughly reviewed in this chapter but the reader is referred to excellent reviews on the topic for further information (1–4).

1. Centrifugal Pumps

Centrifugal pumps are simple to use, relatively inexpensive, and readily available in most cardiovascular surgical centers. Standard CPB atrial and arterial cannulas are used and connected to a centrifugal head by polyvinyl chloride

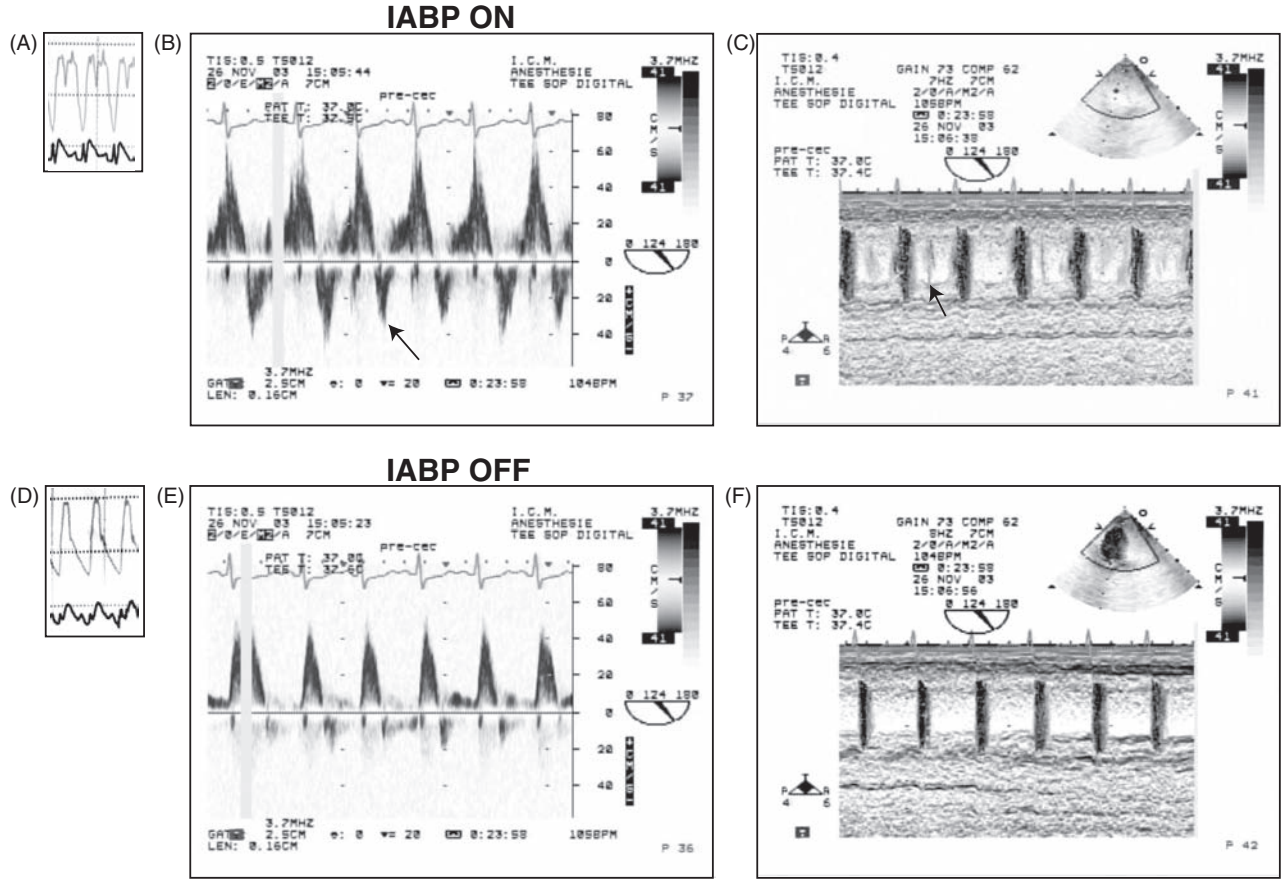

Figure 14.3 Hemodynamic and Doppler profile when the intra-aortic balloon pump (IABP) in the ascending aorta is on (A–C) and off (D–F). Note the diastolic velocities (arrow) on the the pulsed-wave Doppler (B) and on the color M-mode (C), which disappear when the IABP is turned off.

tubing. The centrifugal head imparts forward flow to blood by creating a vortex that provides nonpulsatile blood flow. Left, right, or biventricular assistance can be provided (3). Cannulation may be performed centrally using, most of the time, the RA for venous drainage and the great vessels for arterial return, as discussed in Chapter 13. Besides its availability this system has the advantage of enabling peripheral cannulation for full cardiopulmonary support. This can be performed either percutaneously or via open "cut-down" of the femoral artery and either the femoral or internal jugular vein (Fig. 14.8). This type of support is used as a bridge to recovery in postcardiotomy cardiogenic shock and can also be used as part of an extracorporeal membranous oxygenation (ECMO) circuit for cardiac or respiratory decompensation (2).

Intraoperative Assessment

Transesophageal echocardiography is helpful for several reasons (5). It will confirm the correct location of the cannulas. On the venous side, with either central or peripheral cannulation technique, this is achieved by visualization of the catheter tip in the RA. Also, correct positioning of the arterial catheter in the ascending (central cannulation) or descending thoracic Ao (peripheral cannulation) can be confirmed. Venous drainage must then be optimized and close echocardiographic monitoring is helpful in this regard. It can also be used to monitor the CO supplied by the centrifugal mechanical assistance. The management of fluid balance also benefits from the surveillance of the cardiac chamber size. Flow at a given centrifugal pump speed is preload and afterload dependent. With inadequate preload, the atrium will collapse about the inlet cannula, causing cessation of blood inflow and hemodynamic instability. Transesophageal echocardiography can, therefore, indirectly help to determine the current volume status of the patient.

Postoperative Assessment

Transthoracic echocardiography is useful to detect cardiovascular complications and to monitor regional

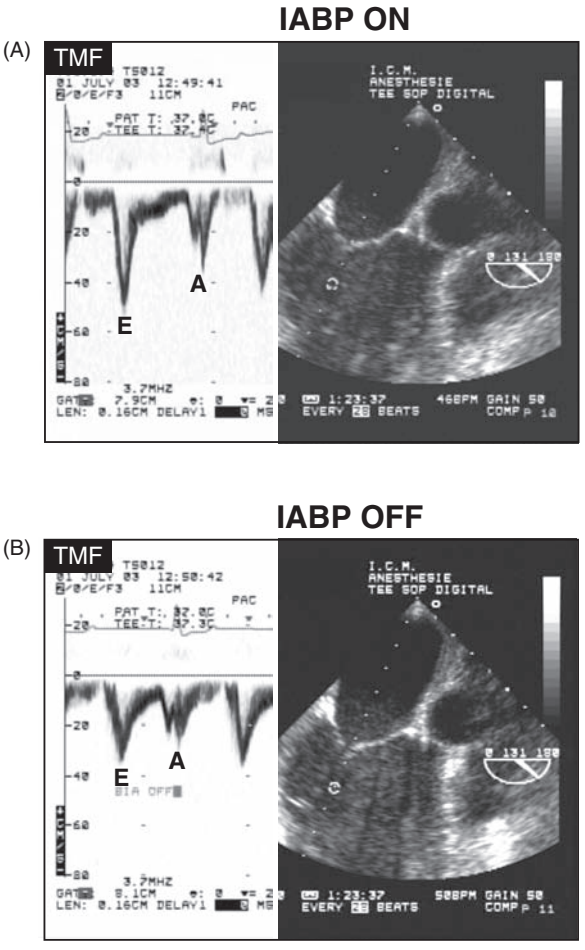

Figure 14.4 Effect of the intra-aortic balloon pump (IABP) on the Doppler transmitral flow (TMF) velocities. When the IABP is turned off, the TMF velocities are reduced with associated reduction in stroke volume.

and global left and right ventricular function, but is frequently technically difficult and limited in postoperative patients. The assessment of regional and global ventricular function as well as the diagnosis of complications benefits from the availability of TEE (6).

The degree and timing of myocardial recovery can be periodically evaluated in the intensive care unit (ICU) by frequent assessment of left and right ventricular function. Progressive withdrawal of circulatory support can be initiated when signs of hemodynamic improvement are present.

Ventricular assist devices should be removed as soon as hemodynamic competence and stability are restored, as morbidity significantly increases after 24–48 h of support. Weaning of *left* ventricular centrifugal mechanical assistance can be monitored by the gradual pulse pressure restoration at full flow as the left ventricular function recovers on TEE. Right ventricular output may also be evaluated with CO measurement by thermodilution. By subtracting the assisted flow from this measurement, the portion of CO contributed by the recovering LV can be serially measured and followed.

The weaning of a *biventricular* assist device is more difficult to assess: indeed, because venous mixing does not occur in the RV, CO determination by thermodilution is less accurate, while the relative contributions of RV and LV to forward flow cannot be precisely determined (2). For those reasons, TEE may provide useful additional data in assessing right and left CO (7).

In addition to its role in assessing cardiac function, TEE can also be used to detect complications in the postoperative setting of centrifugal circulatory assistance (8). Conditions susceptible to causing hemodynamic instability can be diagnosed such as the presence of intracardiac (or intracatheter) thrombus (Fig. 14.9), vegetations on the catheter tip, pericardial tamponade (Figs. 14.10 and 14.11), and the displacement or collapse of one of the cannulae.

2. *Pulsatile Blood Pumps*

Pulsatile VADs are considerably more expensive and complex than centrifugal pump systems, both in their insertion and operation, but they are capable of producing pulsatile flow with minimal or no trauma to blood cellular elements. Furthermore, their integrated sophisticated controls are largely self-regulating, and despite more operating modalities, they usually require minimal supervision beyond the first few days after device insertion. Different models of pulsatile VADs are available (Thoratec, Heartmate, Novacor, Abiomed) (Fig. 14.12). Each has their own set of indications, contraindications, advantages, and disadvantages. Some are pneumatically driven while others are electrically driven. These types of mechanical assistance can offer a complete circulatory support of right and/or left ventricular function. They are, in general, used in patients who need a high degree of circulatory support for a medium to long-term period, and are also used as a bridge to cardiac transplantation (2–4). These devices have similar cannulation system set-ups and are ideally suited to patients with unlikely ventricular recovery who receive mechanical circulatory support as a bridge to cardiac transplantation. For support of the systemic circulation (Fig. 14.3), the inflow cannula is usually inserted in the apex of the LV. In general, the left atrial inflow cannulation is technically easier to perform but is thought to provide incomplete ventricular decompression. The outflow cannula goes from the LVAD to the ascending Ao. For support of the pulmonary circulation, the inflow cannula is generally inserted in the

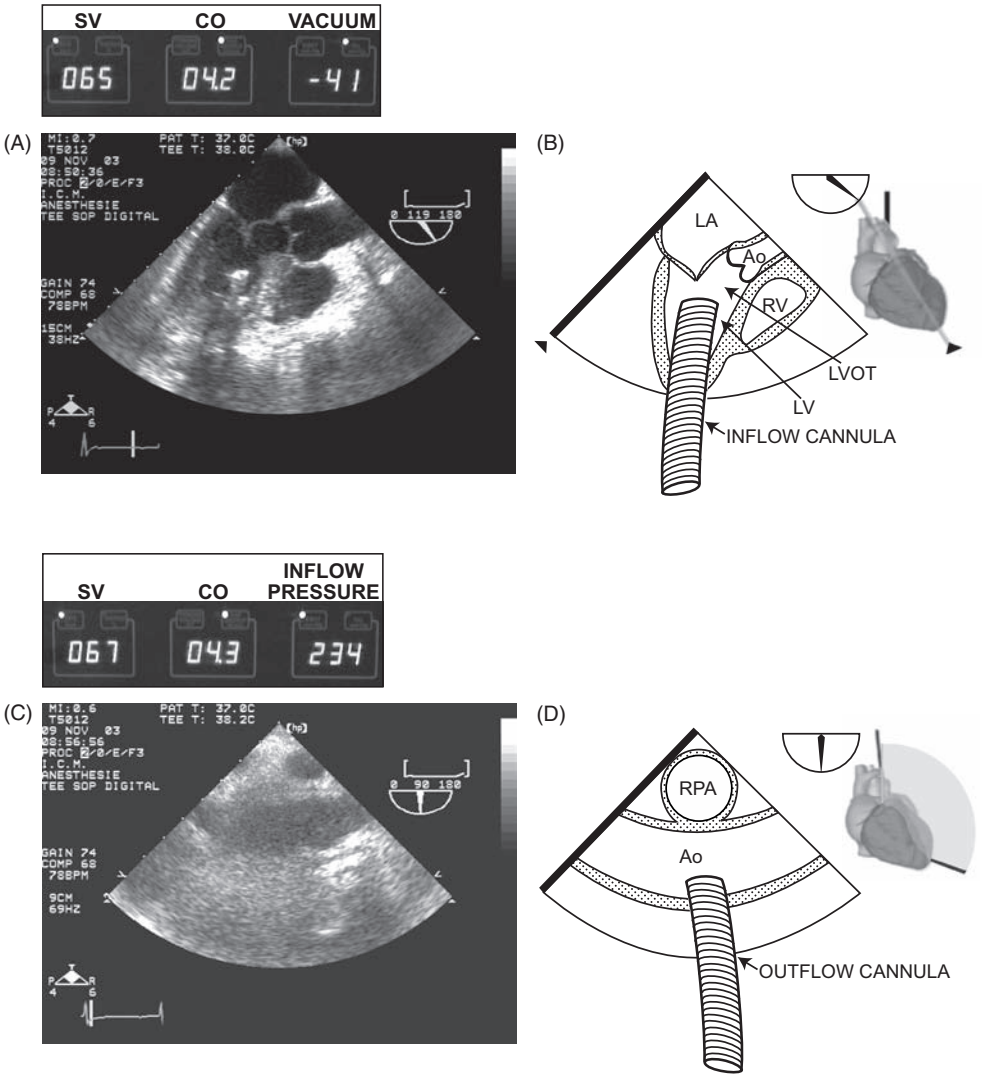

Figure 14.5 Left ventricular assist device (LVAD) (Thoratec system) in a 46-year-old woman in cardiogenic shock. (A, B) Blood flow is diverted from the left ventricle (LV) towards the LVAD through a cannula in the left ventricular apex with a vacuum pressure of −41 mmHg. (D, E) Blood is reinjected into the patient through the ascending aorta (Ao) with an inflow pressure of 234 mmHg (CO, cardiac output; LA, left atrium; LVOT, left ventricular outflow tract; RPA, right pulmonary artery; RV, right ventricle; SV, stroke volume).

RA or the apex of the RV while the outflow cannula goes from the RVAD to the pulmonary artery (1–3).

Again, TEE is useful for several aspects of the pre-, intra-, and postoperative management of patients undergoing pulsatile pump VAD implantation (Table 14.1). It allows selection of the best type of support needed (left, right, or biventricular support), assists insertion and determination of optimal pump settings, speeds up identification of VAD-related complications and may help weaning attempts (often unsuccessful) from the device (9).

Before Cardiopulmonary Bypass

Systematic evaluation of key anatomical structures must be performed in the prebypass period:

1. The aortic valve (AoV) must be shown to be competent (Fig. 14.7): this is a *sine qua non* condition as a significantly regurgitant valve would cause recirculation of the blood from the outflow aortic cannula retrogradely to the LV, ultimately back into the VAD via the inflow cannula (2). This would greatly impair the efficacy of LVAD

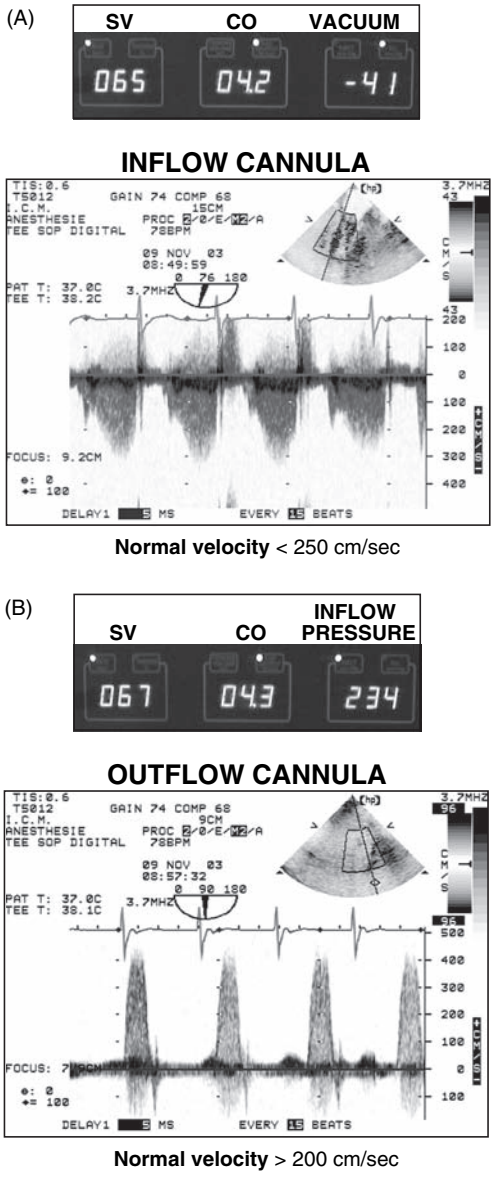

Figure 14.6 From the left ventricular apex, on continuous-wave Doppler, flow is seen directed away from the probe. Normal flow should be laminar with a peak velocity <250 cm/sec. (A) In this example, the peak velocity was at the upper limit due to restricted inflow in the canula secondary to left-sided ventricular septal shift from severe right ventricular dilatation. (B) Flow at the level of the ascending aorta is seen directed towards the transducer. The normal outflow velocity should be >200 cm/sec. (CO, cardiac output; SV, stroke volume) (5).

support. If the AoV is found regurgitant, it must be either replaced or oversewn. This permanent closure of the AoV does not usually have hemodynamic consequences as, during full LVAD support, the AoV normally does not open at all (Fig. 14.7).

2. The presence of intracardiac shunts such as *atrial septal defect* (ASD) or *patent foramen ovale* (PFO) must be methodically ruled out using two-dimensional (2D), color Doppler as well as ultrasound contrast imaging (2). Because these patients often have a left atrial pressure exceeding right atrial pressure during the entire cardiac cycle, a PFO, present in up to 20–30% of the general population (10) may not be readily obvious, even with intravenous injection of agitated saline ultrasound contrast. To elicit the presence of a potential right-to-left shunt, a manoeuver equivalent to a Valsalva must be performed by inducing a sudden release of a sustained positive airway pressure previously achieved by inflating the lungs manually. This maneuver will transiently reverse the atrial transseptal gradient and may help uncover a PFO that would not have been seen otherwise. When a PFO or an ASD is discovered, it must be repaired. Indeed, failure to recognize the presence of a right-to-left shunt, even small at baseline, can result in important arterial desaturation during LVAD support (11) from increased shunting due to the combination of frequently increased right atrial pressure and left atrial decompression by LVAD.
3. Baseline right ventricular function must also be carefully assessed (Fig. 14.11): poor right ventricular function warrants insertion of a RVAD. The level of preoperative right ventricular function also helps to predict the eventual level of pharmacologic support required to support the right ventricular at the end of LVAD implantation.
4. The degree of tricuspid regurgitation (TR) should also be quantified (see Chapter 19).
5. The apices of both ventricles (and atrium) should be carefully inspected to rule out the presence of thrombus: ventricular cannulation with thrombi could induce catastrophic embolic events. Cautious removal of thrombus may be attempted by the surgeon to minimize embolic complications.
6. The ascending, transverse, and descending thoracic Ao should also be scrutinized for the presence of mobile atherosclerotic debris. Incomplete TEE visualization should be supplemented by epiaortic scanning (EAS). A safe site for aortic cannulation (outflow) could thus be determined.

During Cardiopulmonary Bypass

Surgical positioning of the "inflow" cannulae in the atrium or the ventricle can be directly assisted by TEE.

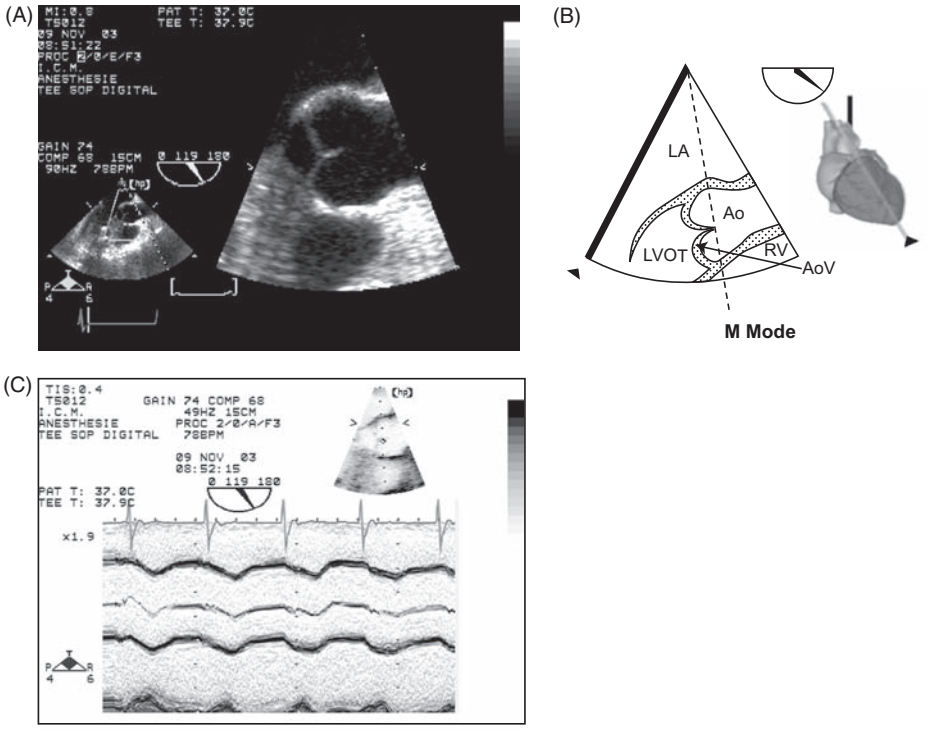

Figure 14.7 (A, B) Aortic valve (AoV) closure in a 46-year-old woman with cardiogenic shock on left ventricular assist device (Thoratec system). (C) The M-mode illustrates the continuous closure of the valve throughout the cardiac cycle. No aortic regurgitation was present (Ao, aorta; LA, left atrium; LVOT, left ventricular outflow tract; RV, right ventricle).

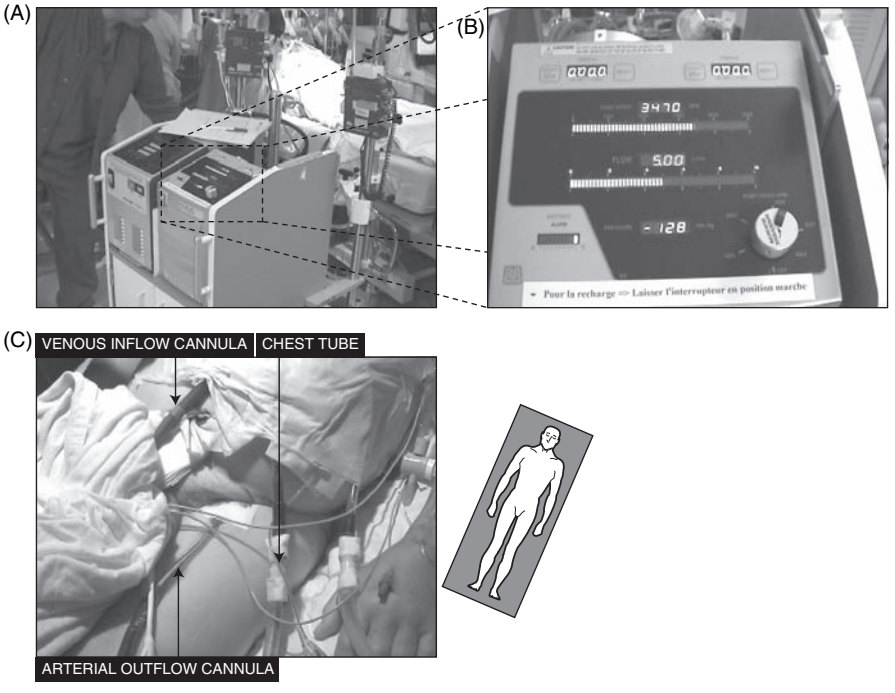

Figure 14.8 Centrifugal pump used as a venoarterial extracorporeal membrane oxygenator (ECMO) in a 64-year-old man after a complicated heart transplantation. (A, B) The top number on the ECMO device indicates the number of cycles per minute (3470); the middle number, the cardiac output (5 L/min); and −128 mmHg correspond to the vacuum pressure. (C) The inflow cannula is positioned in the femoral artery and the outflow is directly connected to the right atrium through the chest.

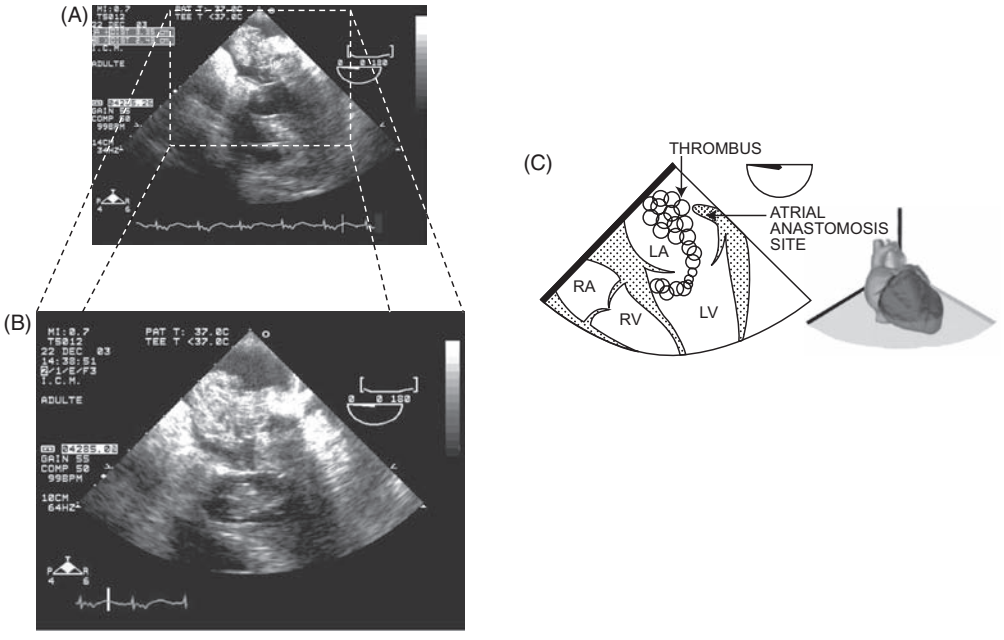

Figure 14.9 A 64-year-old man on a centrifugal pump for cardiogenic shock after cardiac transplantation. (A–C) An unexpected left atrial and ventricular thrombus was found attached to the atrial anastomosis site on the third day (LA, left atrium; LV, left ventricle; RA, right atrium; RV, right ventricle).

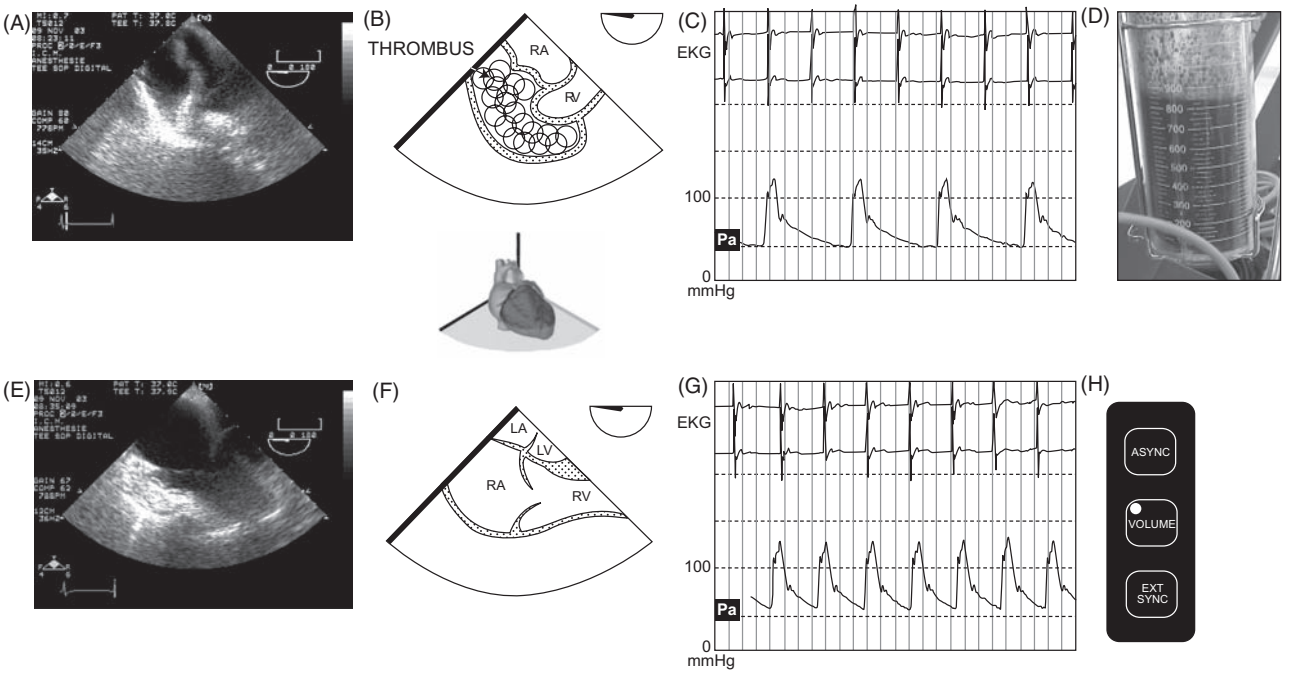

Figure 14.10 (A, B) Left ventricular assist device (LVAD) (Thoratec system) in a 46-year-old woman in cardiogenic shock complicated by tamponade and compression of the right atrium (RA). (C) The LVAD output was insufficient and the machine pumping rate was reduced as seen on the arterial pressure (Pa) tracing. (D) Following withdrawal of >600 mL of pericardial fluid and 200 mL of pleural fluid, the right atrial compression has disappeared (E, F) with concomitant improvement of the output of the LVAD. (G) The LVAD pumping rate increases on the Pa tracing. As the Thoratec LVAD is on a volume-mode (H) and the ejection is triggered when the pump chamber reaches the 90% fill level, the Pa is dissociated from the patient heart rate. It will be reduced with inadequate filling (ASYNC, asynchrone; EKG, electrocardiogram; EXT SYNC, external synchronization; LA, left atrium; LV, left ventricle; RV, right ventricle).

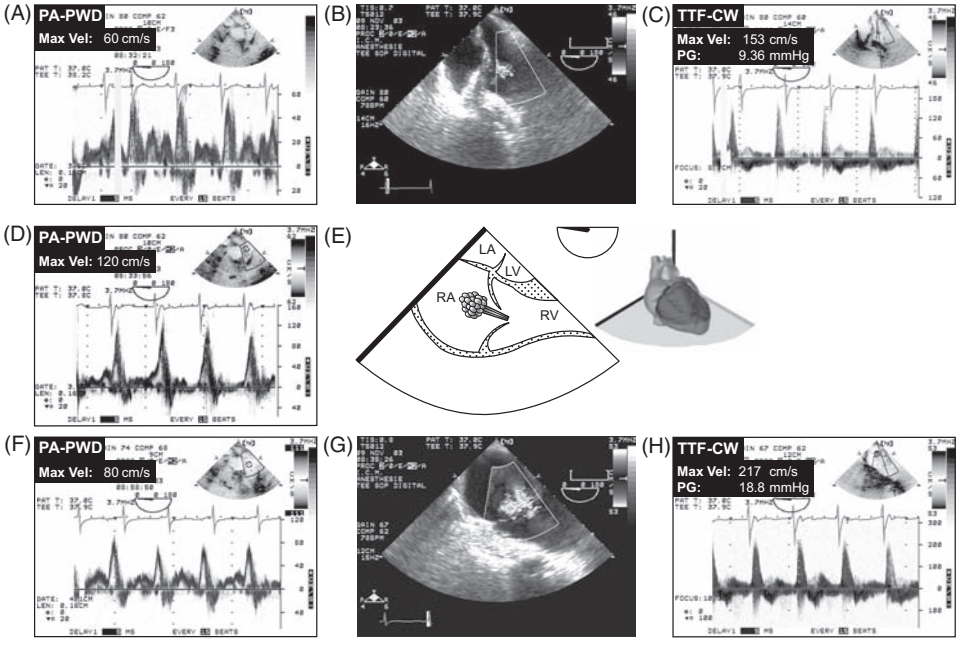

Figure 14.11 Evaluation of right ventricular performance during pericardiocenthesis in a 46-year-old woman with left ventricular assist device (LVAD) (Thoratec system). (A) The maximum systolic pulmonary artery pulsed-wave Doppler (PA-PWD) velocity was 60 cm/sec just before the pericardial drainage began. (B, C) Mild tricuspid regurgitation is present with a tricuspid systolic pressure gradient (PG) of 9.36 mmHg. (D, E) With pericardiocenthesis, the maximum systolic pulmonary Doppler velocity increased to 120 cm/sec but then stabilized down to 80 cm/sec (F). This could have been secondary to unmasked right ventricular dysfunction associated with increased tricuspid regurgitation (G, H). Of note, the cardiac output of the LVAD increased but the vasoactive support was unchanged (LA, left atrium; LV, left ventricle; Max, maximum; RA, right atrium; RV, right ventricle; TTF-CW, transtricuspid flow by continuous-wave Doppler; Vel, velocity).

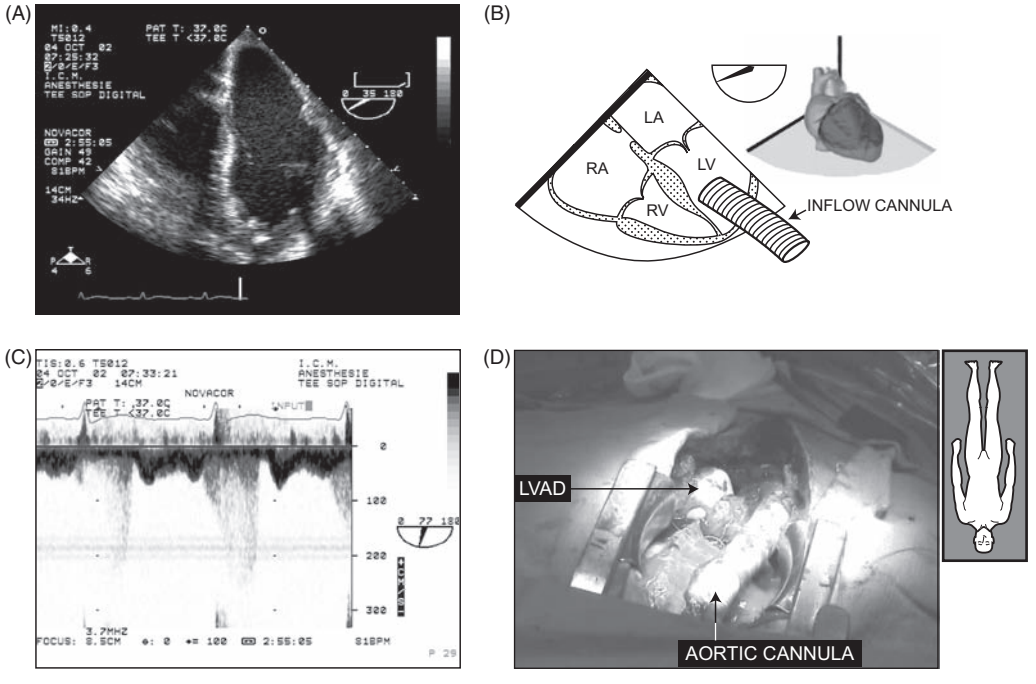

Figure 14.12 (A, B) Mid-esophageal four-chamber view in a 37-year-old man with a Novacor system. (C) Continuous-wave Doppler velocities from the inflow cannula. (D) Intraoperative view (LA, left atrium; LV, left ventricle; LVAD, left ventricular assist device; RA, right atrium; RV, right ventricle). (Photo D courtesy of Dr. Michel Carrier.)

Table 14.1 Summary of the Role of TEE in Patients with Ventricular Assist Device (VAD)

	Importance
Before insertion	
Right and left ventricular function	Selection the device: right, left, or both
Aortic valve competency	Regurgitation will have to be corrected
Patent foramen ovale	Risk of hypoxia from right to left shunting
Mitral and tricuspid valve evaluation	Usually will improve with VAD
Ventricular apex evaluation	An apical thrombus will complicate cannula insertion
Aortic atheromatosis (epiaortic)	Grade 4 or 5 could complicate cannula insertion
During insertion	
Assist the insertion	Inlet cannula well positioned in the LV and RV and outlet cannula in the ascending aorta or PA
Deairing process	Air removed before activating the VAD
After insertion	
Confirm ventricular decompression	The LVAD chamber should reduce its size
Re-evaluate aortic, mitral, and tricuspid valve	Regurgitation could complicate VAD function
Reconfirm the absence of PFO	
Evaluate right ventricular function (LVAD)	Specific agents if a dysfunction of the RV occur
Evaluate and measure inlet and outlet velocity	Normal inlet and outlet velocities should be <230 and >250 cm/sec with no regurgitant signal
In the intensive care unit	
Rule out specific complications if hemodynamically unstable	Tamponade, inlet, or outlet valve incompetency, or obstruction, device malposition, RV failure (with LVAD), hypovolemia, shunting through a PFO, intracavitary thrombus
Evaluation of right and left ventricular function during weaning	Estimation of ventricular recovery

Note: LV, left ventricle; LVAD, left ventricular assist device; PA, pulmonary artery; PFO, patent foramen ovale; RV, right ventricle; TEE, transesophageal echocardiography.

Effective decompression is best obtained when the inflow cannula is positioned in the apex of the ventricle (Fig. 14.13). Moreover, it is very important to ensure that the apical inflow cannula of the LVAD be appropriately directed away from the ventricular septum which can occlude the cannula: it should be directed towards the mitral valve for LVAD (Fig. 14.13) and towards the tricuspid valve (TV) for RVAD (2). Near the end of the implantation, before initiating LVAD support, it is crucial to check the adequacy of chamber deairing by TEE. Various deairing techniques have already been described in Chapter 13. The consequences of air emboli include migration in the coronary circulation with right ventricular myocardial infarction and arrhythmias, migration in the systemic circulation with peripheral, visceral, or cerebral emboli, and migration in the venous circulation with pulmonary emboli. The occurrence of ischemic right ventricular failure from air embolization could present a final insult to a already dysfunctional RV, requiring additional RVAD support.

After Cardiopulmonary Bypass

At the conclusion of the implantation procedure, right ventricular function and TV competence are best monitored by TEE during weaning from CPB (2,11). Indeed, assessment of right ventricular systolic function and loading conditions helps identify the nature (inotropes, nitric oxide, peripheral vasodilatators, fluid) and adjust the level of the therapeutic support needed (Fig. 14.1). Transesophageal echocardiography also helps to reconfirm the absence of significant AR and the adequacy of left-sided chamber decompression. Once fully weaned from CPB, the absence of a PFO must absolutely be reascertained before leaving the operating room for the ICU. Re-examination of the LVAD inlet must also reconfirm the correct positioning of the cannula away from the ventricular septum to prevent left ventricular collapse and/or LVAD inlet occlusion. Finally, an independent measure of LVAD flow can be derived by the Doppler volumetric method (see Chapter 5) using the diameter of the outflow aortic cannula and the time-velocity integral of the continuous-wave (CW) Doppler signal in the cannula. Normally the inlet velocity should be <230 cm/sec (Fig. 14.6) (5). Higher values can occur with cannula malpositioning.

Monitoring in the Intensive Care Unit

Different specific complications may occur after LVAD implantation such as important bleeding and hemodynamic instability. Maintenance of LVAD flow is a key indicator of the overall status. In the postoperative period, low LVAD flow is, in general, due to hypovolemia and/or right ventricular dysfunction, easily assessed by TEE examination. Right ventricular failure has been

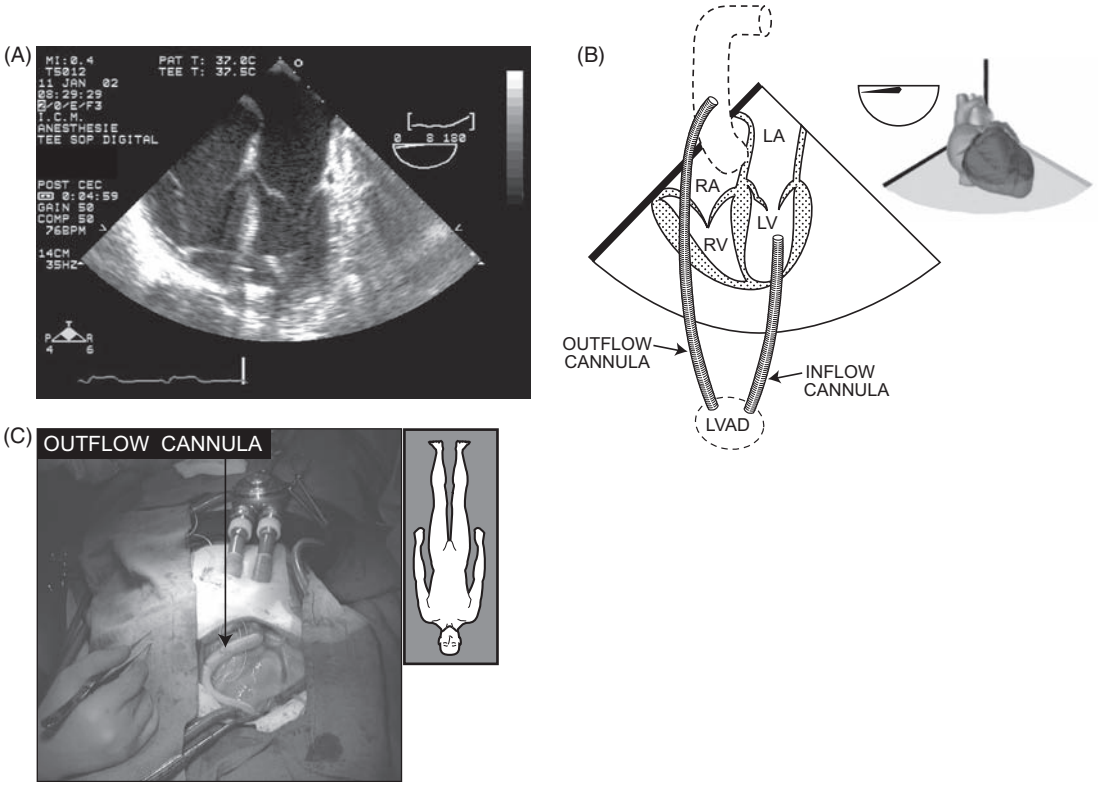

Figure 14.13 Adequate positioning of the outlet cannula in a 21-year-old man with a left ventricular assist device (LVAD). (A, B) Care must be taken so that the cannula is at the apex not too close to the ventricular septal wall and directed toward the mitral valve. Schematic (B) and intraoperative aspect (C) of the LVAD (Thoratec system) (LA, left atrium; LV, left ventricle; RA, right atrium; RV, right ventricle). (Photo C courtesy of Dr. Michel Carrier.)

reported in approximately 20–25% of patients supported by isolated LVADs (Fig. 14.14) (4).

Dramatic changes in respective ventricular volumes and hemodynamic conditions due to ventricular interactions may occur as a result of transient VAD dysfunction. Transesophageal echocardiography monitoring is invaluable in diagnosing these developments in the face of hemodynamic instability (12). Not only can the inadequacy of VAD flow be confirmed, but the etiology of the dysfunction may also be picked up by assessing the patency of both inflow and outflow cannulae, ruling out the presence of thrombi, air, collapse, or displacement of the cannulae. The early diagnosis of cardiac tamponade warrants immediate pericardial drainage (Fig. 14.11). Severe hypoxemia in the ICU period may be due to pulmonary problems, but it is also prudent to rule out the presence of a new right-to-left shunting through a reopened PFO. The occurrence of cerebrovascular events during VAD support also warrants TEE examination to rule out the presence of intracavitary thrombus.

Cases of successful weaning from LVAD support are infrequent (<5%) (2,4). As the patient's hemodynamic parameters improve and weaning from VAD is initiated, TEE monitoring of RV and LV dimensions and ejection fraction is helpful in assisting changes in the degree of circulatory assistance withdrawal. Experimental studies have shown that ventricular function and recovery could be monitored in the postoperative setting by obtaining pressure–area loops from transgastric transverse view using automated border detection and high-fidelity intraventricular pressure recording (13,14). Newer modalities such as Doppler tissue imaging have also been used to predict myocardial recovery during mechanical circulatory support (15).

III. CONCLUSION

Transesophageal echocardiography appears to be an extremely valuable tool in the management of patients on mechanical circulatory assistance. It is an important component to the different aspects of assisted circulation, from the selection of the most appropriate form of ventricular assistance to the fine-tuning of pre-, intra-, and postoperative care. When TEE is combined with comprehensive hemodynamic assessment, it contributes to optimal management of

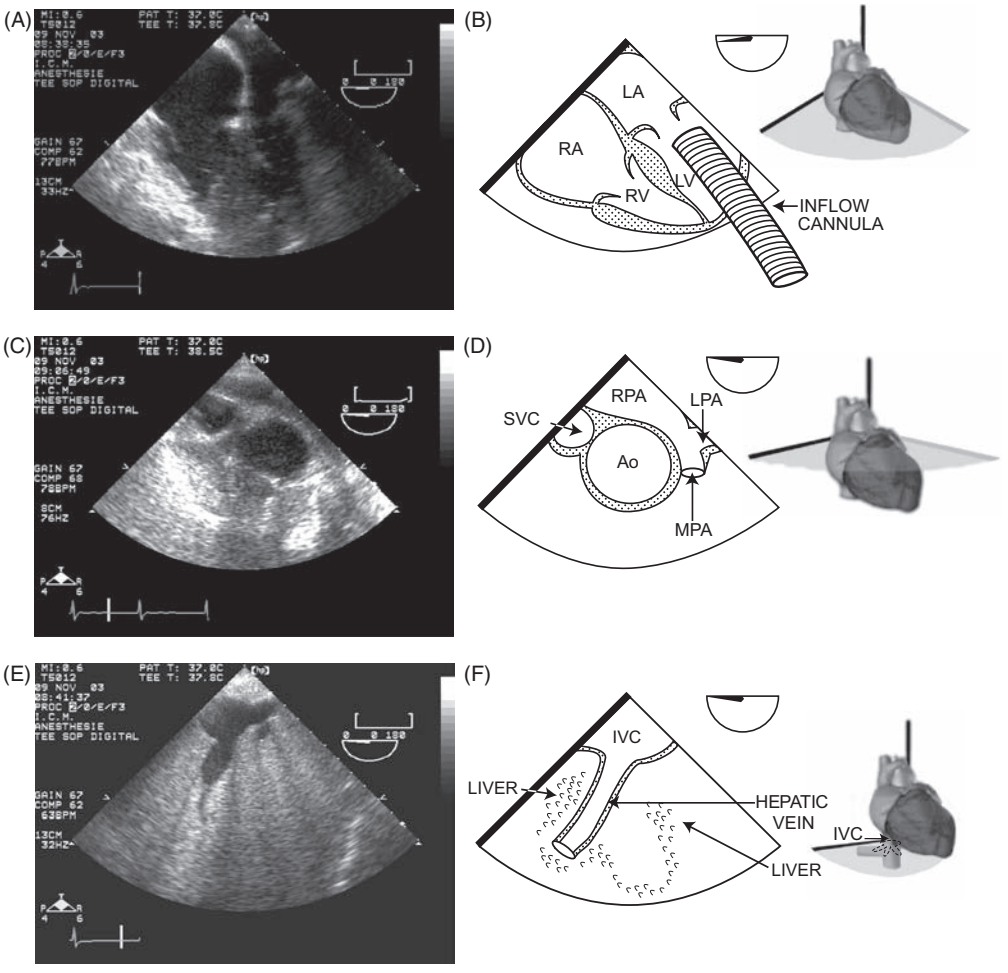

Figure 14.14 Right ventricular dysfunction in a 46-year-old woman with a left ventricular assist device (Thoratec system). (A, B) The right atrium (RA) is dilated with left atrial compression and right ventricular dysfunction. This is associated with dilated superior vena cava (SVC) (C, D) and inferior vena cava (IVC) (E, F) (Ao, aorta; LA, left atrium; LPA, left pulmonary artery; LV, left ventricle; MPA, main pulmonary artery; RPA, right pulmonary artery; RV, right ventricle).

this complex condition in patients with end-stage heart failure. As new modalities in TEE imaging evolve, further diagnostic applications and refinements of this technique in the management of mechanical circulatory support will likely emerge.

REFERENCES

1. Stevenson LW, Kormos RL. Mechanical Cardiac Support 2000: Current applications and future trial design. J Thorac Cardiovasc Surg 2001; 121(3):418–424.
2. Rose EA, Gelijns AC, Moskowitz AJ, Heitjan DF, Stevenson LW, Dembitsky W et al. Long-term mechanical left ventricular assistance for end-stage heart failure. N Engl J Med 2001; 345(20):1435–1443.
3. Practice guidelines for perioperative transesophageal echocardiography. A report by the American Society of Anesthesiologists and the Society of Cardiovascular Anesthesiologists Task Force on Transesophageal Echocardiography. Anesthesiology 1996; 84(4):986–1006.
4. Goldstein DJ, Oz MC, Rose EA. Implantable left ventricular assist devices. N Engl J Med 1998; 339(21): 1522–1533.
5. Scalia GM, McCarthy PM, Savage RM, Smedira NG, Thomas JD. Clinical utility of echocardiography in the management of implantable ventricular assist devices. J Am Soc Echocardiogr 2000; 13(8):754–763.
6. Brack M, Olson JD, Pedersen WR, Goldenberg IF, Gobel FL, Pritzker MR et al. Transesophageal echocardiography in patients with mechanical circulatory assistance. Ann Thorac Surg 1991; 52(6):1306–1309.
7. Barzilai B, Davila-Roman VG, Eaton MH, Rosenbloom M, Spray TL, Wareing TH et al. Transesophageal

echocardiography predicts successful withdrawal of ventricular assist devices. J Thorac Cardiovasc Surg 1992; 104(5):1410–1416.
8. Pollock SG, Dent JM, Kaul S, Lake C. Diagnosis of ventricular assist device malfunction by transesophageal echocardiography. Am Heart J 1992; 124(3):793–794.
9. Simon P, Owen AN, Moritz A, Rokitansky A, Laczkovics A, Wolner E et al. Transesophageal echocardiographic evaluation in mechanically assisted circulation. Eur J Cardiothorac Surg 1991; 5(9):492–497.
10. Sukernik MR, Mets B, Bennett-Guerrero E. Patent foramen ovale and its significance in the perioperative period. Anesth Analg 2001; 93(5):1137–1146.
11. Baldwin RT, Duncan JM, Frazier OH, Wilansky S. Patent foramen ovale: a cause of hypoxemia in patients on left ventricular support. Ann Thorac Surg 1991; 52(4):865–867.
12. Farrar DJ. Ventricular interactions during mechanical circulatory support. Semin Thorac Cardiovasc Surg 1994; 6(3):163–168.
13. Gorcsan J, Gasior TA, Mandarino WA, Deneault LG, Hattler BG, Pinsky MR. Assessment of the immediate effects of cardiopulmonary bypass on left ventricular performance by on-line pressure–area relations. Circulation 1994; 89:180–190.
14. Mandarino WA, Winowich S, Gorcsan J III, Gasior TA, Pham SM, Griffith BP et al. Right ventricular performance and left ventricular assist device filling. Ann Thorac Surg 1997; 63(4):1044–1049.
15. Vermes E, Houel R, Simon M, Le Besnerais P, Loisance D. Doppler tissue imaging to predict myocardial recovery during mechanical circulatory support. Ann Thorac Surg 2000; 70(6):2149–2151.

15

Native Aortic Valve

FRANÇOIS A. BÉÏQUE
McGill University, Montreal, Canada

I. Anatomy of the Aortic Valve 329
A. Normal Aortic Valve Anatomy 329
B. Congenital Anomalies of the Aortic Valve 331
C. Echocardiographic Imaging of the Aortic Valve 332
II. Aortic Stenosis 334
A. Etiology of Aortic Stenosis 334
1. Congenital and Acquired Aortic Valve Stenosis 334
2. Supra- and Subaortic Stenosis 336
B. Quantitative Assessment of Aortic Stenosis 338
1. Pressure Gradient 338
2. Flow Velocity Ratio 342
3. Aortic Valve Area 342
4. M-Mode 349
III. Aortic Regurgitation 349
A. Etiology of Aortic Regurgitation 349
B. Quantification of Aortic Regurgitation 350
1. Jet Height/LVOT Height 350
2. Short-Axis Jet Area/LVOT Area 352
3. Flow Reversal 352
4. Regurgitant Fraction 352
5. Effective Regurgitant Orifice 354
6. Vena Contracta 356
7. CW Doppler and Pressure Half-Time 357
IV. Conclusion 359
Acknowledgments 360
References 360

I. ANATOMY OF THE AORTIC VALVE

A. Normal Aortic Valve Anatomy

The ascending aorta (Ao) is ~5 cm long and has two distinct segments. The distal segment is the tubular ascending Ao which begins at the sinotubular junction. The proximal segment is the aortic root which extends from the aortic valve (AoV) to the sinotubular junction. The aortic root is comprised of the AoV, the aortic annulus, the sinotubular junction, the sinuses of Valsalva, and the coronary ostiae. The AoV has three distinct and symmetrical cusps: the right coronary, the left coronary, and the noncoronary (Figs. 15.1 and 15.2). Above the AoV, an outpouching of the aortic wall forms the sinuses of Valsalva which represent the widest portion of the aortic root and measure ~3.3 cm in diameter. The upper limit of the sinuses of Valsalva, called the sinotubular junction, marks the beginning of the tubular segment of the ascending Ao (Fig. 15.3). Each coronary cusp attaches to the aortic wall in a curvilinear fashion, forming a crown-shaped aortic annulus with three tips located at the level of the sinotubular junction (Fig. 15.3). Measurement of the aortic root at the level of the sinotubular junction is generally 10–15% larger than at the level of the left

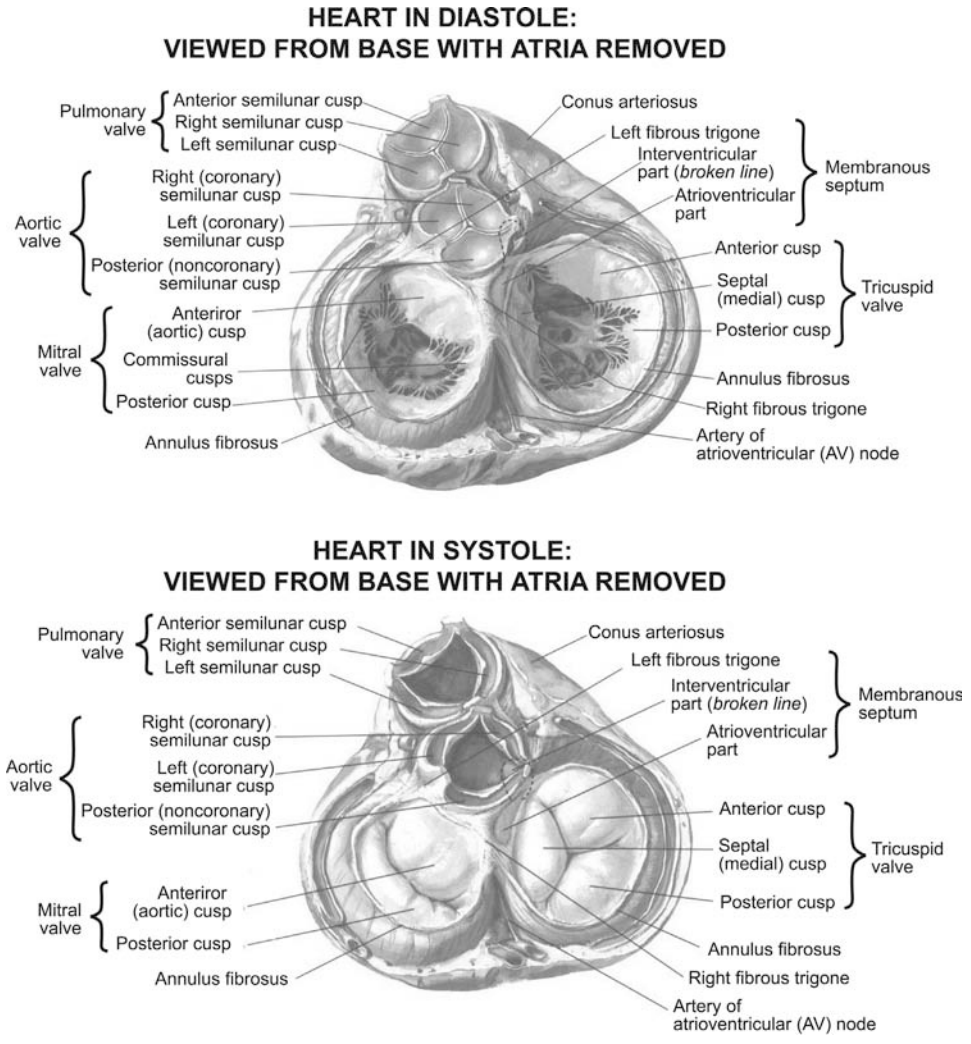

Figure 15.1 View of heart valves in systole and diastole with both atria removed. Note that the aortic valve in diastole resembles the logo of the Mercedes Benz company while in systole it has a triangular opening. The noncoronary cusp is positioned posteriorly, opposite to the atrial septum. The relationship of the right and left fibrous trigone to the aortic valve is indicated. Also note the relationship of the aortic valve to the membranous septum and the division of this structure into an interventricular and an atrioventricular component by the tricuspid valve leaflet insertion. [Anatomic drawings with permission of Netter and Yonkman (1).]

ventricular outflow tract (LVOT). Within the aortic root, the coronary ostiae are located in the sinuses of Valsalva (Fig. 15.3). The right and left coronary cusps are associated with the origin of the coronary artery which bears the same name. The noncoronary cusp located posteriorly, is not associated with a coronary ostium and is in close proximity to the atrial septum (Fig. 15.1). The height of the aortic cusps is slightly less than half the length of its free margin. The free edge of each cusp is concave and there is a large contact zone between the cusps which creates a visible zone of redundancy, the lunula, above the closure line (Fig. 15.4). On the ventricular surface of each aortic cusp the nodule of Arantius is located in the center of the free edge at the point of coaptation (Fig. 15.4). Lambl's excrescences are thin mobile filamentous strands that are commonly observed on the aortic valve in elderly patients. They are variable in number and usually appear near the closure line. Lambl's excrescences can measure 1 mm in thickness and up to 1 cm in length. They are thought to originate from small endothelial tears on the surface of the aortic valve. They contain a fibroelastic core and are covered by a thin layer of endothelial cells. These strands are not pathological, their incidence increases with age and they should not be mistaken for AoV pathology or endocarditis (see Chapter 23, Fig. 23.16).

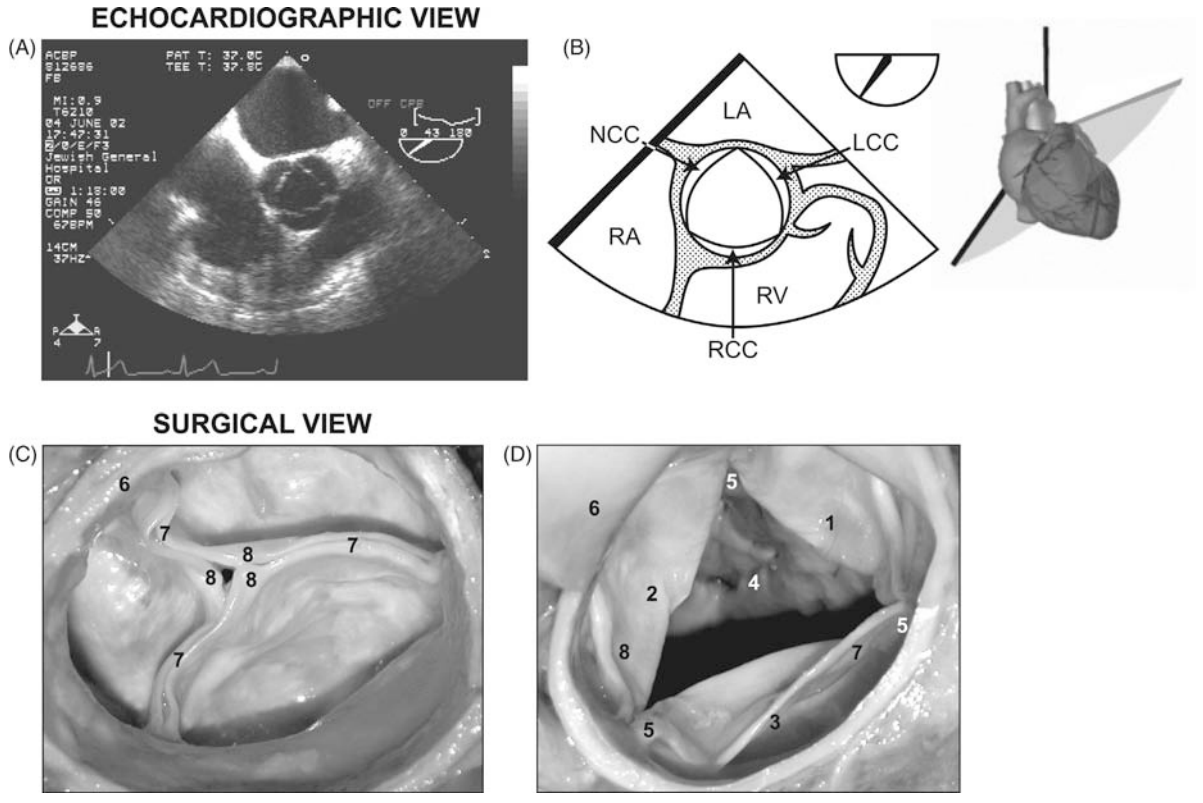

Figure 15.2 (A, B) Mid-esophageal short-axis view of the aortic valve. Anatomical aspect of the aortic valve in diastole (C) and in systole (D) (LA, left atrium; LCC, left coronary cusp; NCC, noncoronary cusp; RA, right atrium; RCC, right coronary cusp; RV, right ventricle) (1, RCC; 2, LCC; 3, NCC; 4, ventricular septum; 5, aortic commissure; 6, aorta; 7, lunula; 8, nodules of Arantius). (Photos C and D courtesy of Dr. Nicolas Dürrleman.)

The relationship of the AoV to structures within or near the base of the heart is important in understanding pathological echocardiographic findings. The AoV is part of the fibroskeleton at the base of the heart. The left and the noncoronary cusp are in fibrous continuity with the anterior leaflet of the mitral valve (MV) (Fig. 15.5). This fibrous continuity is the subaortic curtain, or mitral–aortic intervalvular fibrosa. It is located between the two fibrous trigones which are the strongest component of the cardiac fibroskeleton. The left trigone is in close proximity to the posterior aspect of the left coronary cusp (Fig. 15.3) while the right fibrous trigone is opposite the noncoronary cusp (Fig. 15.1). The conduction system is located near the posterior noncoronary cusp and may be injured during AoV surgery or involved by endocarditis. The membranous septum immediately below the AoV is divided by the attachment of the tricuspid valve (TV) into an interventricular and an atrioventricular component (Fig. 15.1). The AoV is also in close proximity to the other heart valves and to both the left and right atrium (RA).

B. Congenital Anomalies of the Aortic Valve

Congenital anomalies of the AoV include bicuspid, unicuspid, and quadricuspid valves. Pentacuspid AoVs have also been described (2). The most common congenital anomaly of the AoV is a bicuspid AoV with an occurrence of 1–2% in the general population. A bicuspid AoV may have two equal cusps with a commissural opening that may be oriented in either a vertical or a horizontal position (Fig. 15.6). A bicuspid valve may also have one small cusp and a larger one with a raphe resulting from the failure of separation of two cusps. Most commonly, the raphe will be observed between the right and the left coronary cusps (Fig. 15.7). This rudimentary raphe predisposes the larger leaflet to restricted leaflet motion and premature calcification. A bicuspid valve with a raphe between two cusps will have an eccentric opening in systole (nearer one of the aortic walls) while in diastole the valve may appear to have normal tricuspid morphology (Fig. 15.7). Therefore, echocardiographic evaluation of the AoV should be done in systole and in diastole. A bicuspid

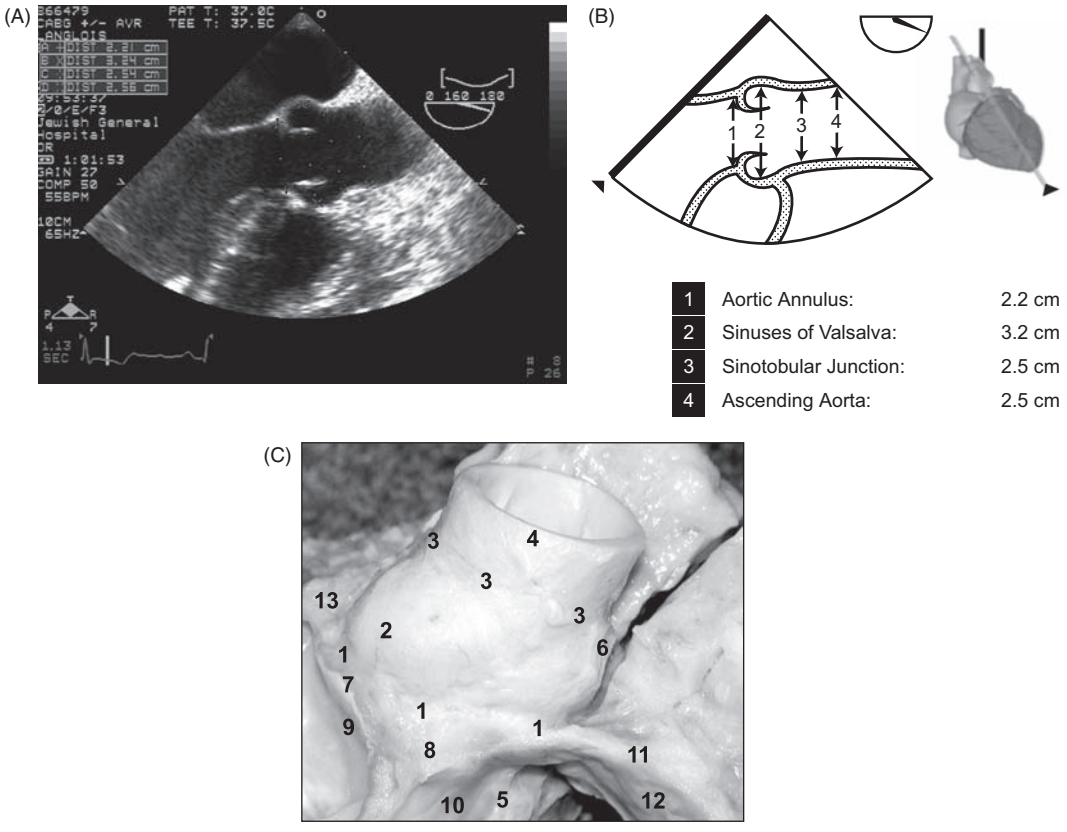

Figure 15.3 Mid-esophageal long-axis view of aortic root (A, B). The aortic root is shown (C) (1, aortic annulus; 2, sinus of Valsalva; 3, sinotubular junction; 4, ascending aorta; 5, septal leaflet of tricuspid valve; 6, right coronary artery; 7, mitral aortic continuity; 8, central fibrous body; 9, mitral annulus; 10, atrial septum; 11, tricuspid annulus; 12, anterior tricuspid leaflet; 13, left fibrous trigone). (Photo C courtesy of Dr. Nicolas Dürrleman.)

valve is bicommissural when the patient has three cusps and two of them are fused with a raphe. When two equal cusps are seen without a raphe, the bicuspid valve is also described as unicommissural (Fig. 15.6). A unicuspid valve may be acommissural or unicommissural: the latter has one commissure with only one attachment point next to the aortic wall. The orifice is eccentric and usually tear-drop shaped, and although a raphe may be observed, the opening does not extend to the opposite aortic wall (Fig. 15.8). Quadricuspid AoVs occur in approximately 0.01% of the population and usually have four equal cusps symmetrically separated by an X-shaped commissure in diastole, but may also include asymmetric leaflets (Fig. 15.9). Unlike bicuspid and unicuspid AoVs where stenosis is the predominant pathology, quadricuspid AoVs tend to be associated with aortic insufficiency.

C. Echocardiographic Imaging of the Aortic Valve

The AoV can be imaged by inserting the transesophageal echocardiography (TEE) probe to a depth of $\sim$35 cm from the upper incisors. With the transducer at 0°, a slightly off-axis longitudinal view of the AoV in a five-chamber view can be obtained at the mid-esophageal level (Fig. 15.10). Rotating the transducer angle to 45° ($\pm$15°) will image the AoV in its short axis (Fig. 15.10). With the angle at 135° ($\pm$15°), the long-axis view of the AoV will be obtained (Fig. 15.10). The five-chamber view at 0° is not included in the American Society of Echocardiography/Society of Cardiovascular Anesthesiologists (ASE/SCA) comprehensive perioperative TEE assessment guidelines, but may occasionally prove useful in assessing AoV pathology. At 0°, the right and the noncoronary cusps of the AoV are usually imaged but sometimes, part of the left coronary cusp may be seen off-axis, giving the appearance of a pseudo-mass in the LVOT (Fig. 15.11). In the long-axis view at 135°, the cusp furthest from the transducer is the right cusp, next to the right ventricle (RV), while the cusp closest to the transducer is either the left or the noncoronary cusp opposite the left atrium (LA). Leftward (counterclockwise) rotation of the probe shaft in the long-axis view will bring the transducer towards the left coronary cusp

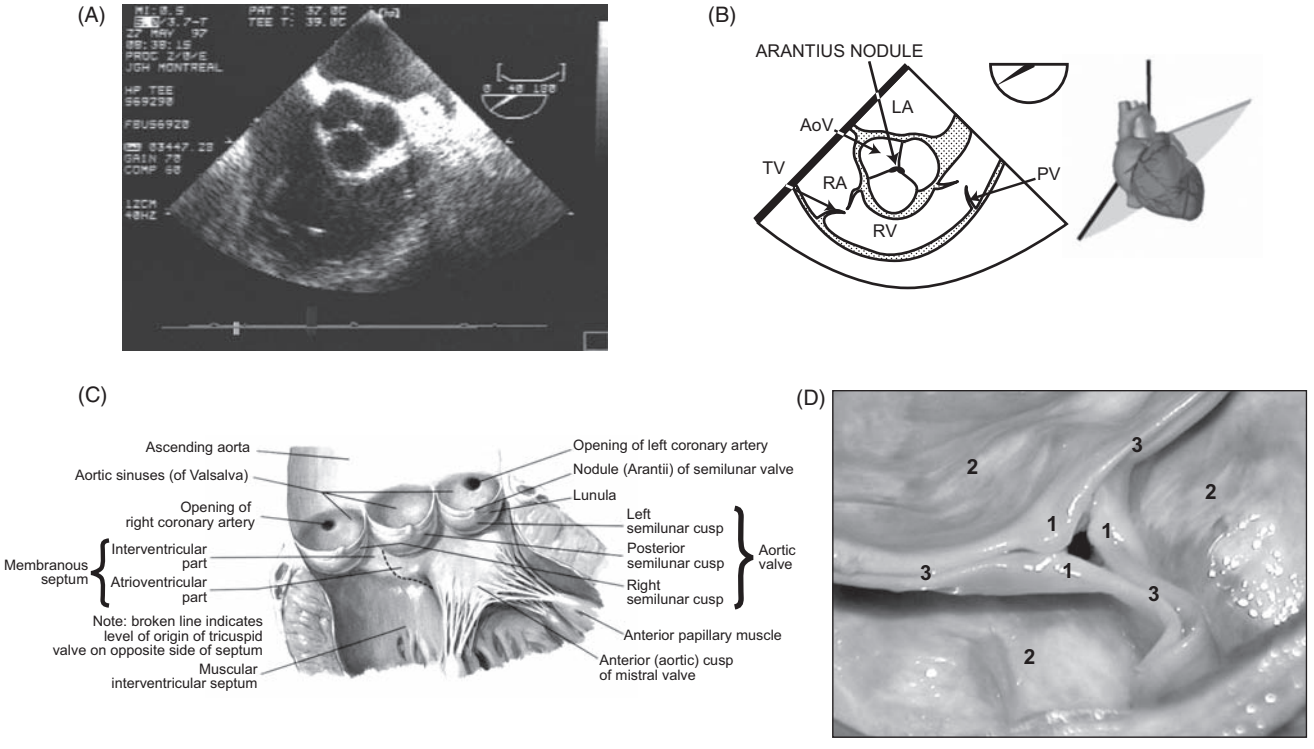

Figure 15.4 (A, B) Mid-esophageal short-axis view of the aortic cusps. (C) Open view of the aortic root. Note the aortic–mitral curtain which represents the fibrous continuity between the aortic root and the anterior mitral leaflet (intervalvular fibrosa). The aortic–mitral curtain is located between the right and the left fibrous trigone. (D) Anatomical aspect of the aortic valve (AoV). Note the curvilinear attachment of each aortic cusps (2), the lunula (3), and the location of the nodules of Arantius (1) near the middle portion of the edge of each leaflets (LA, left atrium; PV, pulmonic valve; RA, right atrium; RV, right ventricle; TV, tricuspid valve). (Anatomic drawings in C with permission of Netter and Yonkman (1) and photo D courtesy of Dr. Nicolas Dürrleman.)

while rightward (clockwise) rotation of the probe will bring the noncoronary cusp in view. The visualization of the left main coronary artery in this plane will help identify the left coronary cusp. Imaging of the right ventricular outflow tract (RVOT/PA) in the long axis view is associated with leftward rotation of the probe indicating that the left coronary cusp is most likely in view.

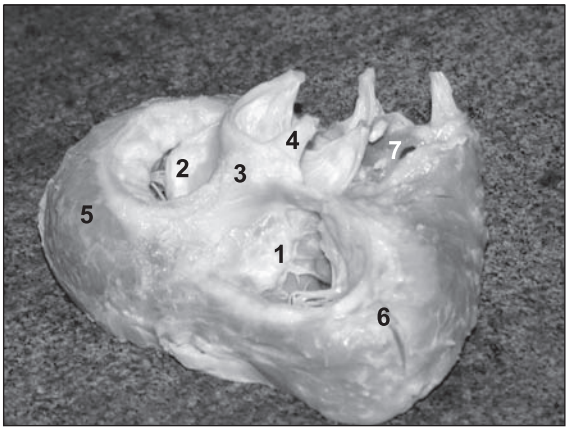

Figure 15.5 Fibrous skeleton of the heart [1, tricuspid valve; 2, mitral valve; 3, central fibrous body; 4, aortic valve (sinus of Valsalva resected); 5, left ventricle; 6, right ventricle; 7, pulmonic valve]. (Courtesy of Dr. Nicolas Dürrleman.)

These three transesophageal views can be used to assess the coaptation and the excursion of each cusp and to rule out the presence of either prolapse or decreased cusp mobility. The short-axis view of the AoV is most useful to assess AoV morphology and can also be used for measuring the aortic valve area (AVA) by planimetry. Mid-esophageal views are particularly important to assess valvular, subvalvular (dynamic LVOT obstruction, subvalvular membrane) or aortic root pathology (supravalvular obstruction, dilatation, aneurysm, or dissection) by two-dimensional (2D), M-Mode, and color flow imaging. However, these views are not ideally suited for spectral pulsed-wave (PW) or continuous-wave (CW) Doppler interrogation of the AoV, because the ultrasound beam is misaligned with the direction of aortic blood flow.

Transgastric imaging of the AoV provides complementary views to that effect. With the probe positioned at the left ventricular mid-papillary level, the transducer can be rotated from 0° to a long-axis view of the AoV at 120°

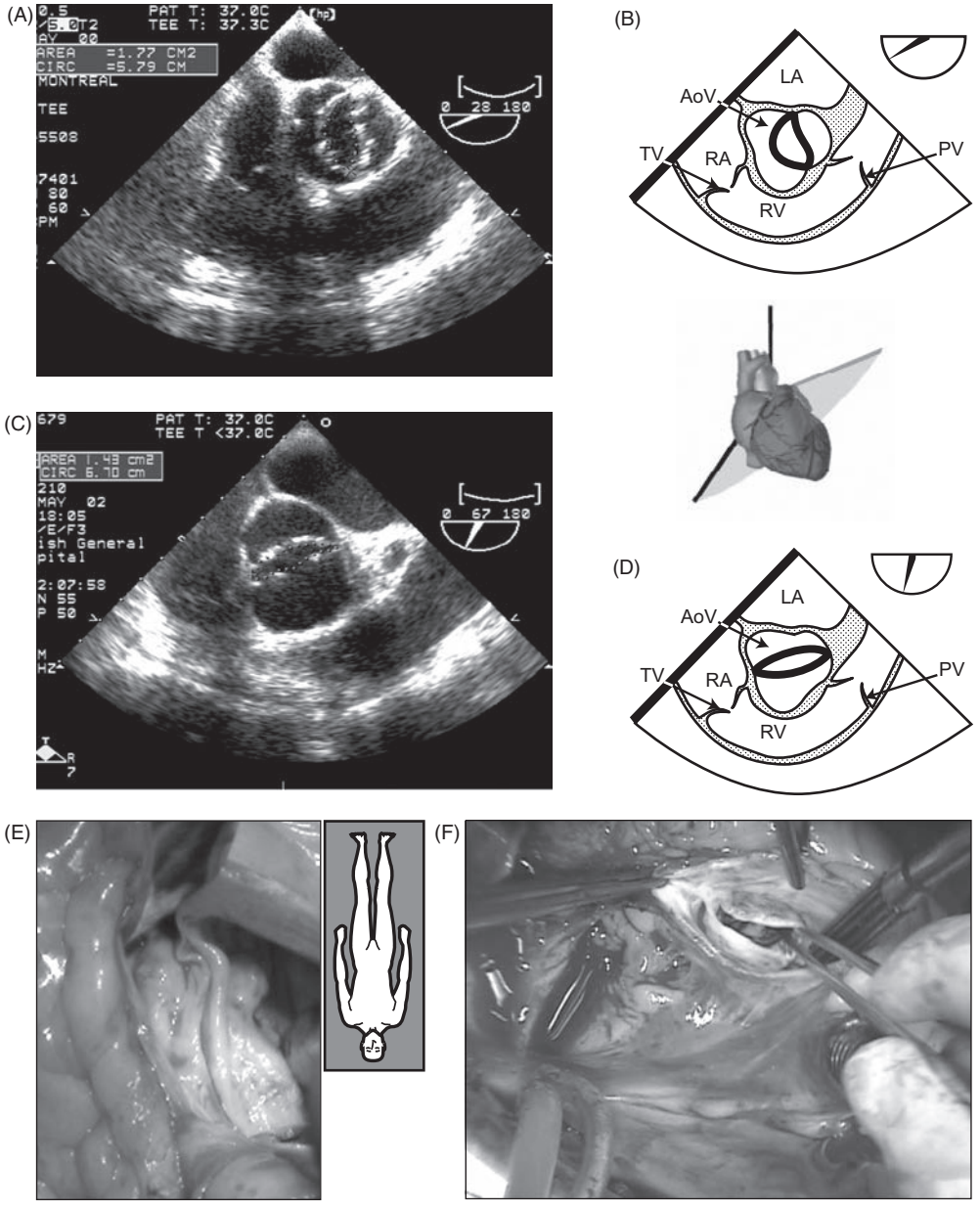

Figure 15.6 Bicuspid unicommissural aortic valves. Note that the oval-shaped orifice can be oriented either vertically (A, B) or horizontally (C, D). (E, F) Corresponding intraoperative findings (AoV, aortic valve; LA, left atrium; PV, pulmonic valve; RA, right atrium; RV, right ventricle; TV, tricuspid valve).

($\pm 15^{\circ}$). In this view the AoV is aligned for Doppler interrogation (Fig. 15.12). A deeper transgastric view at 0° with marked anteflexion of the TEE probe (Fig. 15.13) or light anteflexion from a more basal view at 0° (Fig. 15.14) may also allow optimal Doppler interrogation of the LVOT/AoV. The accuracy of Doppler flow velocity measurements will reach 94% when the interrogation angle does not exceed 20°.

II. AORTIC STENOSIS

A. Etiology of Aortic Stenosis

1. Congenital and Acquired Aortic Valve Stenosis

The etiology of aortic stenosis (AS) is either acquired or congenital. The most common etiology of congenital AS is a bicuspid valve. Unicuspid and quadricuspid valves

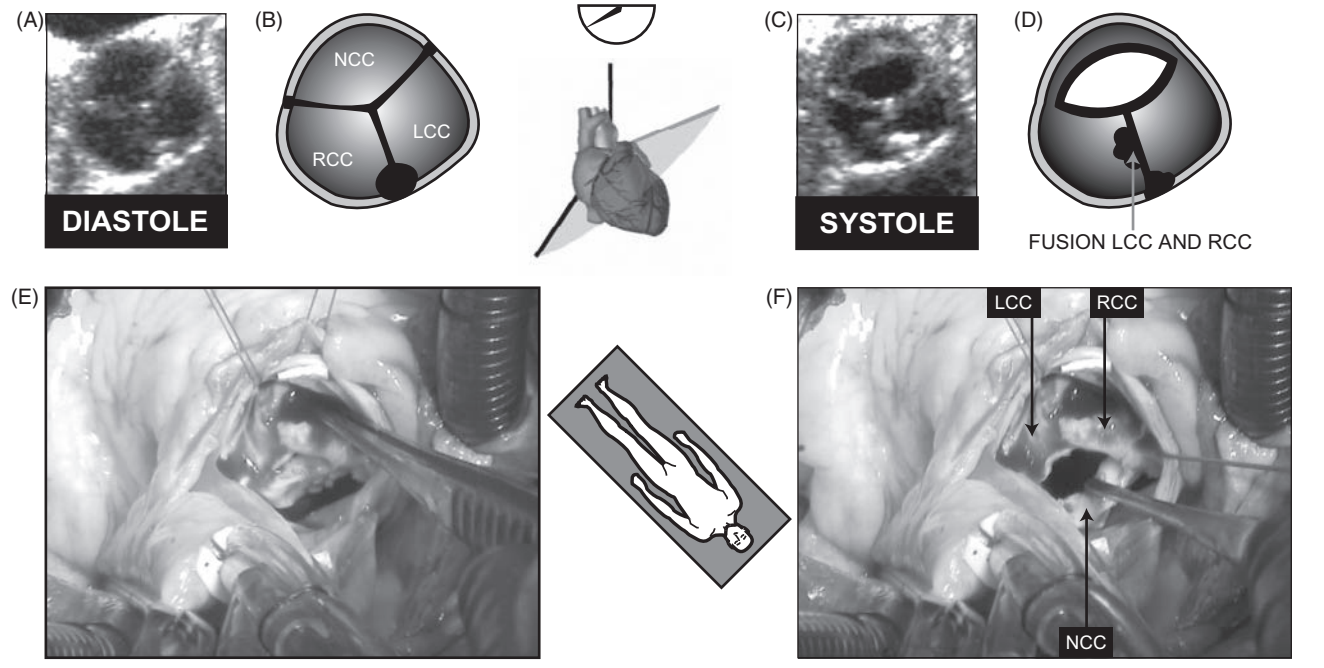

Figure 15.7 (A–D) Bicuspid bi-commissural aortic valve with a raphe between the left (LCC) and right coronary cusp (RCC). (E, F) Surgical view: the non-coronary cusp (NCC) is located posteriorly in the lower part, as opposed to the transesophageal echocardiographic view where it is seen on the upper part of the screen. Note that in diastole (A, B) the aortic valve appears to have three normal cusps. (Photos E and F courtesy of Dr. Denis Bouchard.)

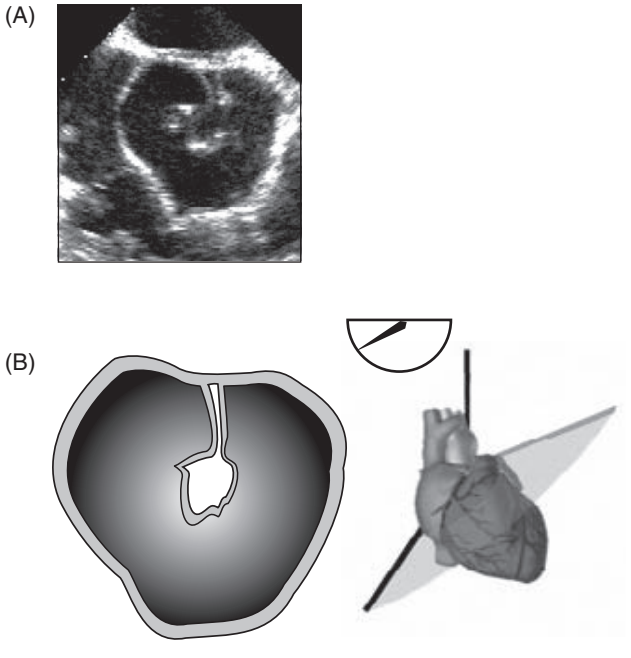

Figure 15.8 Mid-esophageal short-axis view of a patient with unicommissural unicuspid aortic valve. Unicuspid aortic valves have been described as having the appearance of a shirt collar, toilet seat, or tear drop.

can also lead to AS. Most patients born with a bicuspid AoV will have a normal life span without pathological valvular deterioration, but those who display symptomatic severe degenerative calcific stenosis will usually do so around 50 years of age.

Acquired etiology of AS includes rheumatic and calcific degenerescence. Rheumatic involvement is characterized by thickening or fibrocalcification of the cusp edges, restricted mobility and commissural fusion (Fig. 15.15). The MV is frequently involved in rheumatic heart disease such that isolated rheumatic AoV disease is rare. Nonrheumatic calcific degenerescence of the AoV is the most common cause of stenosis in older adults and its incidence increases with age. It is characterized by calcification, which usually starts from the annulus and extends into the body of the aortic leaflets. Leaflet mobility becomes reduced but there is usually no commissural fusion (Fig. 15.15). Patients with a three-cusped AoV will more often develop symptoms from severe AoV stenosis around 70 years of age. The average rate of decrease in the AVA per year is 0.12 ± 0.19 cm^2 (3,4). Increased age, the presence of coronary artery disease, hypercholesterolemia, and renal disease are associated with a more rapid progression of aortic valve stenosis. Although the progression of AS in

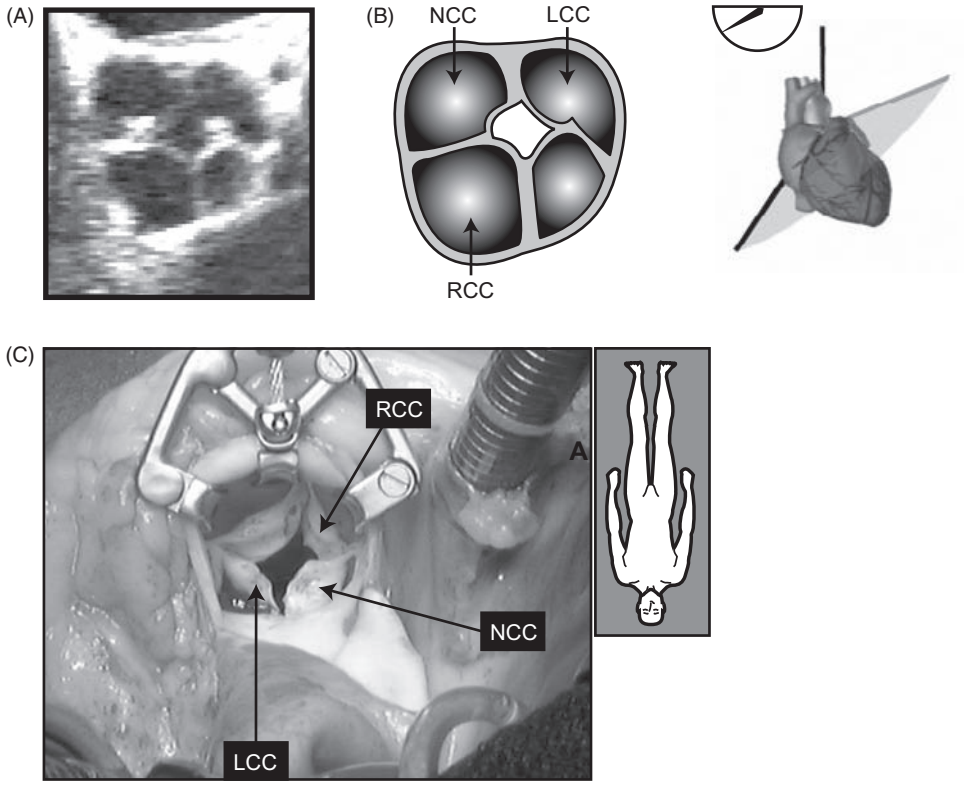

Figure 15.9 Quadricuspid aortic valve. (A, B) Note the lack of coaptation in the center of the valve which results in a diamond-shaped regurgitant orifice. (C) Corresponding intraoperative finding of a quadricuspid aortic valve of a different patient is shown below (LCC, left coronary cusp; NCC, non-coronary cusp; RCC, right coronary cusp). (Photo C courtesy of Dr. Raymond Cartier.)

patients with degenerative calcification tends to be faster than in rheumatic heart disease, it is difficult to predict the rate of progression in individual patients. Survival significantly decreases when left ventricular ejection fraction (LVEF) decreases to $<45-50\%$ or when the left ventricular end-systolic dimension (LVESD) exceeds 55 mm (3).

Two-dimensional echocardiographic evaluation should identify the number, morphology (thickening, calcification), and mobility (restriction) of the aortic cusps. Systolic doming occurs when the AoV does not fully open, and is most commonly associated with bicuspid AoVs but may also be observed with commissural fusion in rheumatic heart disease (Fig. 15.15). Senile calcification or AoV sclerosis may occur without stenosis. Indirect signs of significant AS include the presence of left ventricular hypertrophy (usually concentric) and poststenotic aortic root dilatation. The latter in some patients, particularly those with bicuspid valves, represents an inherent aortopathy rather than a consequence of the altered hemodynamics from the AS (Fig. 15.16) (5,6). An association between bicuspid AoV disease and coarctation of the descending thoracic Ao has also been reported.

2. Supra- and Subaortic Stenosis

Patients with a significant systolic gradient across the AoV should always be evaluated for evidence of supra- (Fig. 15.17) or subvalvular disease. While native supravalvular stenosis is uncommon, subvalvular stenosis (proximal to the AoV) may originate from dynamic obstruction or fixed structural abnormalities. Congenital causes of fixed obstruction include the presence of a subaortic membrane (Fig. 15.18) or diaphragm and, tunnel subvalvular stenosis. Dynamic LVOT obstruction can occur with hypertrophic obstructive cardiomyopathy (HOCM), basal septal hypertrophy, and following MV repair (Fig. 15.19). In these conditions, the systolic gradient across the LVOT will increase with tachycardia, increased contractility, and decreased ventricular filling. The dynamic LVOT obstruction is associated with systolic anterior motion (SAM) of the MV which is thought to result from either "venturi" effect and/or drag forces. Significant septal contact of the anterior mitral leaflet

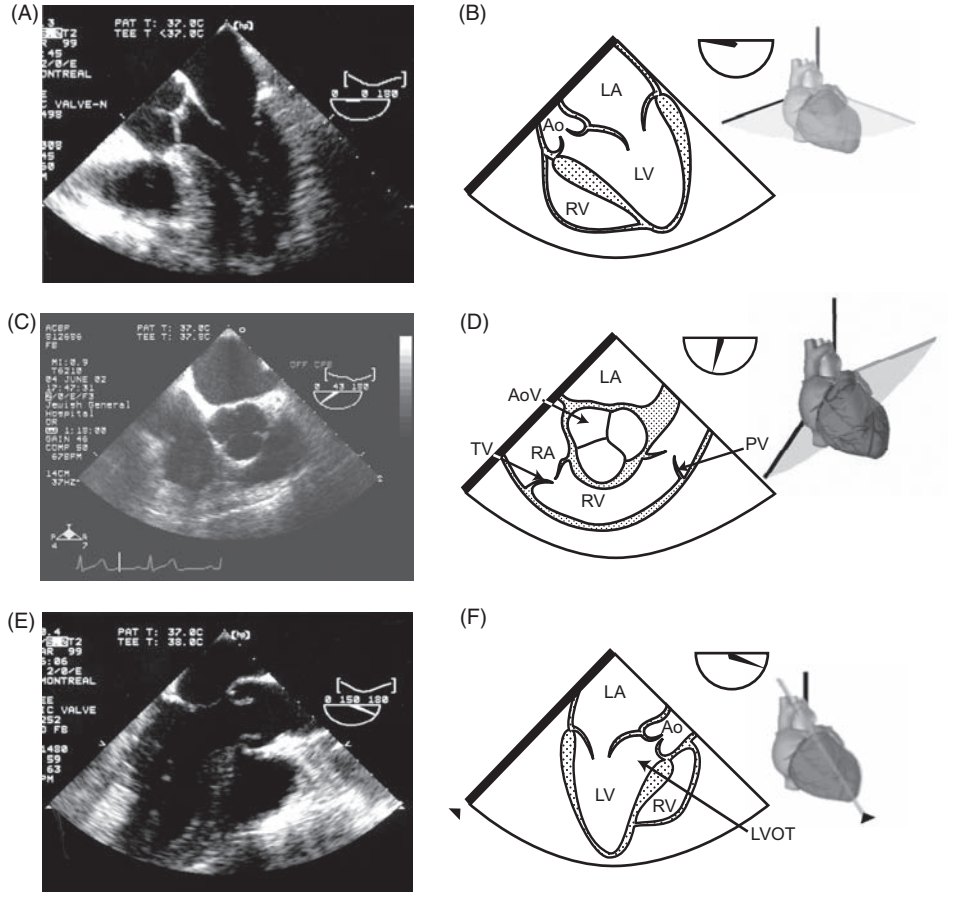

Figure 15.10 Mid-esophageal five-chamber view at 0° (A, B), short-axis view at 45° (C, D), and long-axis view at 135° (E, F) of the aortic valve (AoV) (Ao, aorta; LA, left atrium; LV, left ventricle; LVOT, left ventricular outflow tract; PV, pulmonic valve; RA, right atrium; RV, right ventricle; TV, tricuspid valve).

indicates severe SAM (Fig. 15.19) (see Chapter 10) and is usually associated with a posteriorly directed jet of mitral regurgitation (MR). Unlike fixed AS, the peak systolic gradient occurs in late systole, giving a typical dagger-shaped appearance to the Doppler signal envelope (Fig. 15.19). As the obstruction increases in late systole, flow across the AoV decreases and premature closure of the AoV may be observed on 2D and M-mode imaging.

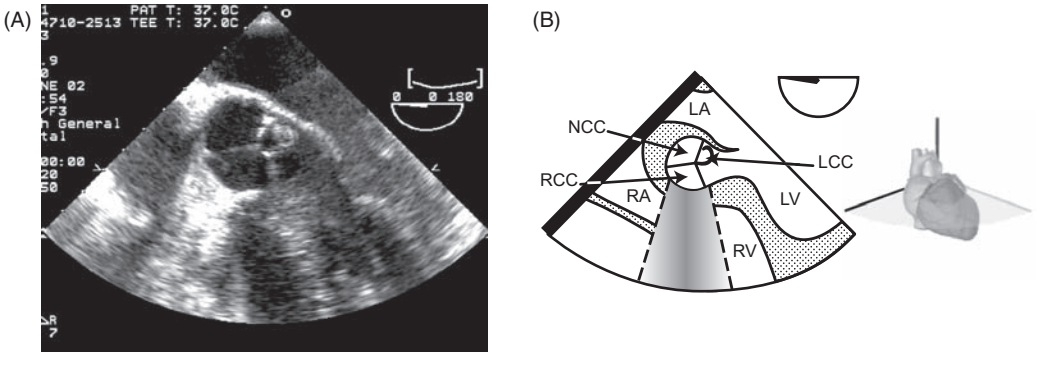

Figure 15.11 A five-chamber view at 0°. Off-axis view of the aortic valve which gives an oblique view of the left coronary cusp (LCC), giving the appearance of a pseudomass in the left ventricular outflow tract (LA, left atrium; LV, left ventricle; NCC, non-coronary cusp; RCC, right coronary cusp; RA, right atrium; RV, right ventricle).

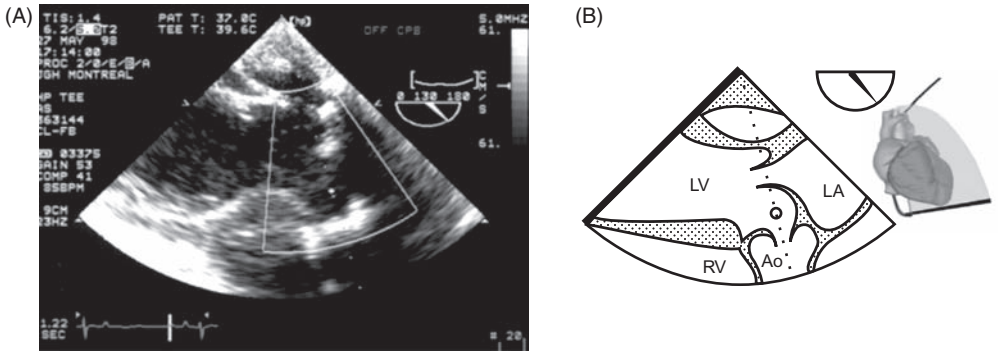

Figure 15.12 Transgastric long-axis view at 130°. In this view, the aortic flow is aligned with the Doppler ultrasound beam (Ao, aorta; LA, left atrium; LV, left ventricle; RV, right ventricle).

B. Quantitative Assessment of Aortic Stenosis

1. *Pressure Gradient*

The Bernoulli Equation

The measured blood flow velocity across cardiac valves can be converted to a pressure gradient according to the Bernoulli equation. This equation takes into account flow acceleration, viscous friction, and convective acceleration using a complex mathematical formula. Flow acceleration and viscous friction have little impact on the pressure gradient and can be ignored in the calculations. Therefore, the modified Bernoulli equation only accounts for convective acceleration. In the modified Bernoulli equation, the pressure gradient (ΔP) measured with spectral Doppler across the AoV equals four times the square of the measured peak velocity (V_{AoV}) minus the square of the LVOT velocity.

$$\Delta P = 4 \times (V_{\mathrm{AoV}}^2 - V_{\mathrm{LVOT}}^2) \tag{15.1}$$

In most cases, the square value of the LVOT velocity is insignificant compared with the maximal aortic velocity and the Bernoulli equation can be simplified to:

$$\Delta P = 4 \times V_{\mathrm{AoV}}^2 \tag{15.2}$$

The ASE task force on Doppler quantifications recommends that the simplified Bernoulli equation should not be used when the LVOT velocity exceeds 1.5 m/s (7).

Doppler Pressure Gradient vs Cardiac Catheterization

Doppler-derived measurements correspond to an instantaneous gradient while the pull back technique of the catheter from the Ao to the left ventricle (LV) during cardiac catheterization represents a peak-to-peak pressure difference. This explains in part why the measured peak-to-peak gradient in the catheterization laboratory is often lower than the instantaneous gradient obtained with Doppler echocardiography. However, the mean pressure gradient correctly measured by simultaneous pressure tracings from the LV and the aortic root during cardiac catheterization correlates well with the mean gradient obtained with Doppler echocardiography (Fig. 15.20).

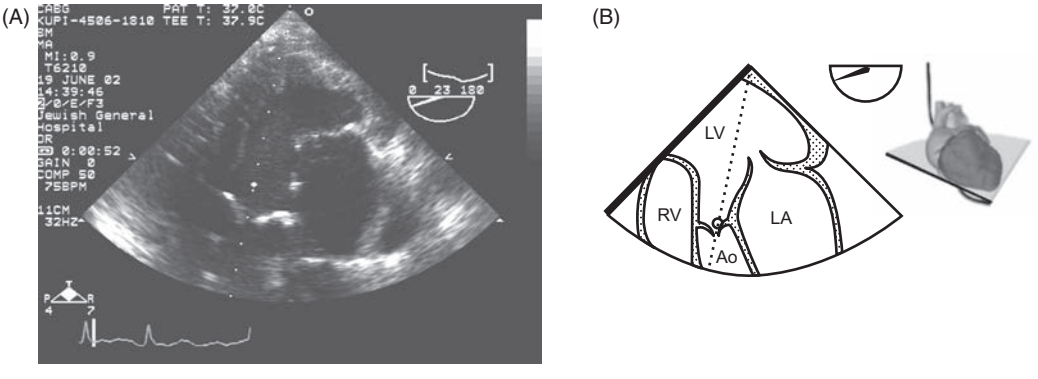

Figure 15.13 Deep transgastric view. Note the parallel alignment of the Doppler ultrasound beam with the aortic flow and the longitudinal imaging of the mitral valve (Ao, aorta; LA, left atrium; LV, left ventricle; RV, right ventricle).

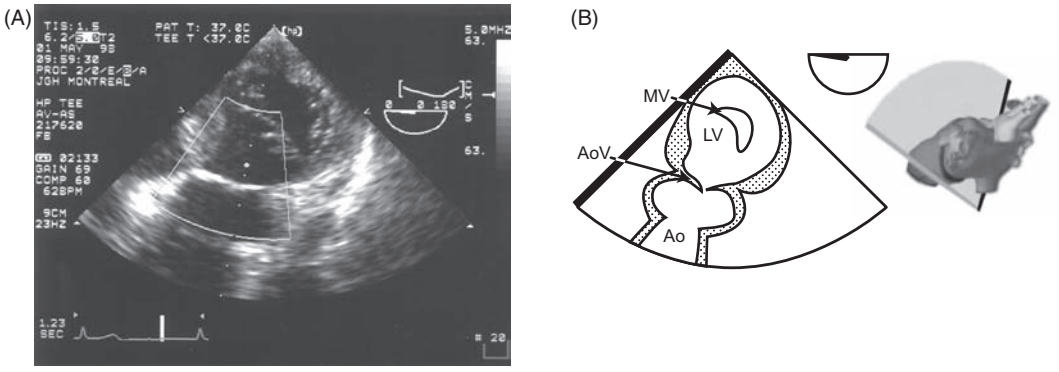

Figure 15.14 (A, B) Basal transgastric view of the aortic valve (AoV). Note the alignment of the Doppler signal with aortic blood flow. In this view, the mitral valve (MV) is imaged in a short-axis view (Ao, aorta; LV, left ventricle).

Pitfalls of Pressure Gradient

PRESSURE RECOVERY. Pressure recovery is the increase in pressure which occurs downstream from a stenosis due to reconversion of kinetic energy into potential energy. Pressure recovery is an important phenomenon which may result in a measured Doppler mean systolic gradient that is 3–54 mmHg higher than the measured catheter gradient. Indeed, the Doppler measurement reflects the highest pressure gradient across the stenosis, or the difference between the highest proximal pressure and the lowest distal pressure, which occurs immediately downstream from the AoV at the vena contracta. The Doppler measured gradient should correspond to the invasively measured gradient if the catheter is positioned at the level of the vena contracta. However, the catheter is frequently positioned in the ascending Ao rather than at the level of the vena contracta. This explains in part, the discrepancy observed between Doppler- and catheter-derived pressure gradients across the AoV. The measured pressure gradient will progressively decrease over several

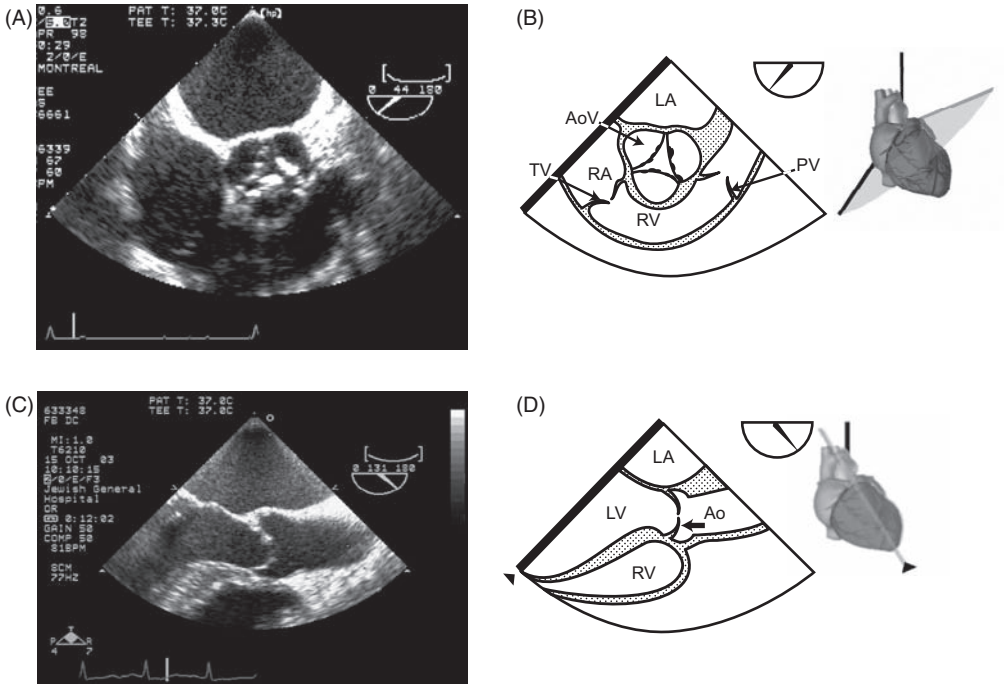

Figure 15.15 (A, B) Mid-esophageal short-axis view of the aortic valve (AoV) in a patient with severe calcific non-rheumatic aortic stenosis. Note the absence of commissural fusion in this patient. (C, D) Mid-esophageal long-axis view of the AoV in a patient with rheumatic heart disease. Note systolic doming (arrow) and commissural fusion characteristic of rheumatic heart disease (Ao, aorta; LA, left atrium; LV, left ventricle; PV, pulmonic valve; RA, right atrium; RV, right ventricle; TV, tricuspid valve).

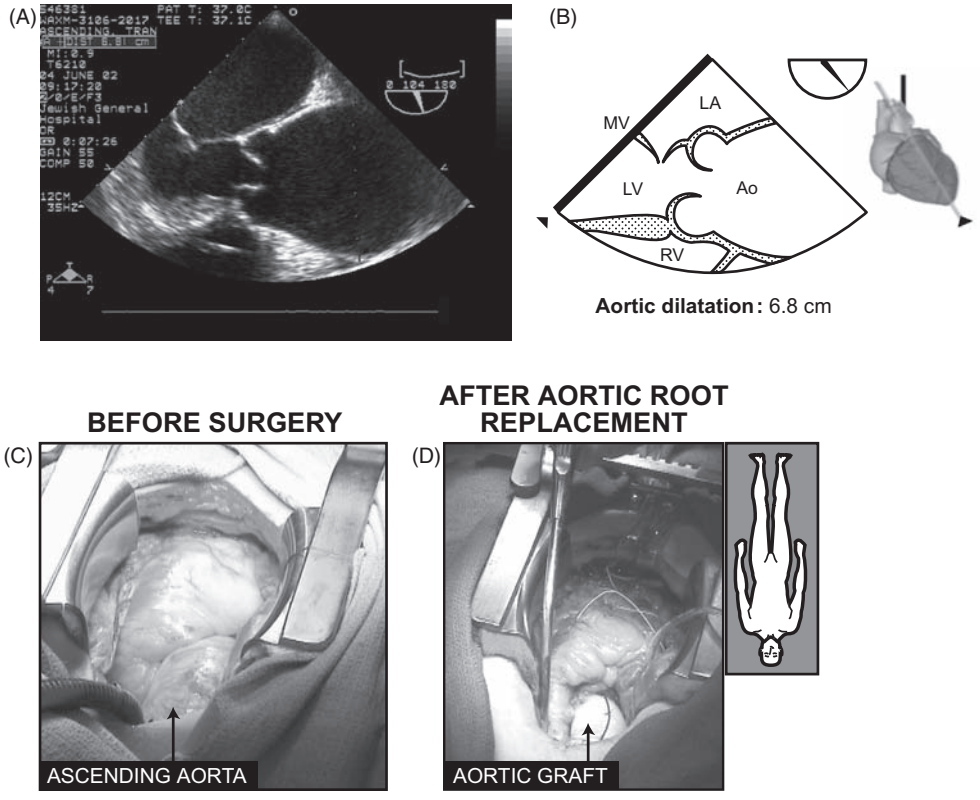

Figure 15.16 Aortic dilatation of 6.8 cm in a patient with mild bicuspid aortic stenosis. (A, B) Mid-esophageal long-axis view. (C, D) Intraoperative findings before and after aortic valve replacement and resection of the aortic aneurysm (Ao, aorta; LA, left atrium; LV, left ventricle; MV, mitral valve; RV, right ventricle). (Photos C and D courtesy of Dr. Michel Pellerin.)

centimeters as the catheter is withdrawn beyond the AoV and the pressure recovers in the ascending Ao. As most of the pressure recovery occurs in the first few centimeters, catheter gradient is unlikely to be affected by pressure recovery if the downstream measurement is made at least 5 cm away from the stenotic valve in the ascending Ao. In a patient with at least moderate AS, a small caliber ascending Ao (<3 cm) distal to the sinotubular junction may be the most important factor for the occurrence of clinically significant pressure recovery (8–11).

In patients with an eccentric jet across a stenotic AoV, VanAuker et al. (12) has demonstrated, using a computational model, that for a constant anatomic area, the effective valve area decreased, the maximal pressure gradient increased and, the distance to complete pressure recovery increased with the degree of jet eccentricity.

MITRAL REGURGITATION. Improper alignment of the Doppler signal may result in the inadvertent measurement of the MR pressure gradient instead of the AoV pressure gradient. This is more likely to occur when the jet of MR is directed anteriorly towards the wall of the LA beneath the Ao. It is, therefore, important to differentiate the characteristics of these two Doppler signals. The mitral regurgitant jet starts earlier with MV closure at the onset of the isovolumic contraction period compared with the AS signal which begins after the isovolumic contraction phase. The mitral regurgitant jet also ends later at the start of the isovolumic relaxation phase. Mitral regurgitant and AS signal may also be differentiated by the diastolic company they keep: the mitral regurgitant signal will be accompanied by a mitral inflow signal (with E- and A-waves) while the aortic signal may be associated with a typical aortic regurgitant signal (Fig. 15.21).

PRESSURE GRADIENT VARIES WITH FLOW. The measurement of aortic pressure gradient will overestimate the severity of AS in high output states while in low output states and cardiac decompensation, the ventricle may be unable to generate a significant gradient even if the AS is critical. Blood flow is proportional to the square of the pressure gradient so a small increase in blood flow will translate into a more significant change in the measured pressure gradient.

PITFALL OF THE SIMPLIFIED BERNOULLI EQUATION. Software from echocardiography systems uses the simplified Bernoulli equation to measure pressure

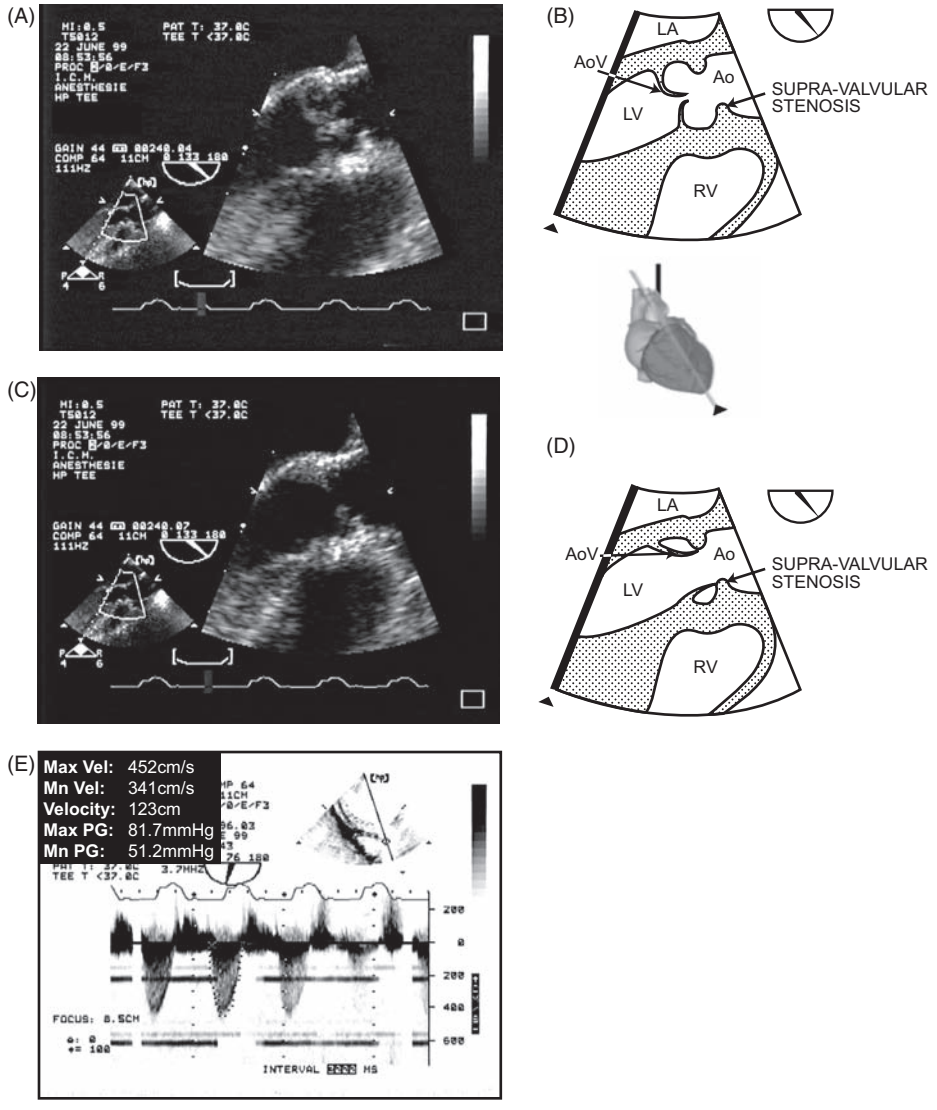

Figure 15.17 Mid-esophageal long-axis view in a 25-year-old woman operated on for supravalvular aortic stenosis. (A–D) Mid-esophageal long-axis view showing the normal opening of the aortic cusps but a stenosing membrane is present 9 mm above the level of the aortic valve (AoV). (E) A maximal (Max) and mean (Mn) pressure gradient (PG) of 81.7 and 51.2 mmHg, respectively, is measured across the stenosing membrane (Ao, aorta; LA, left atrium; LV, left ventricle; RV, right ventricle; Vel, velocity).

gradients and assumes V_1 (velocity in the LVOT) to be negligible in the calculation. However, when subaortic LVOT velocities are increased, this assumption is no longer valid. The ASE task force on Doppler quantifications recommends that a V_1 value >1.5 m/s must be included in the calculations for the Bernoulli equation (7). This will usually occur in patients with subaortic obstruction or narrowing as seen in HOCM or severe basal septal hypertrophy. Other instances where V_1 may be increased, and should be accounted for, include the pediatric patient and hyperdynamic states (e.g. sepsis, stress, severe anemia, hyperthyroidism, etc.). Finally, significant aortic regurgitation (AR) may also result in a large stroke volume (SV) and increased V_1. In those situations, software from most echocardiographic systems can be reprogrammed to include V_1 in the calculation of pressure gradients.

PRESSURE GRADIENT AND SERIAL STENOSIS. In patients with dynamic LVOT obstruction and SAM, it is difficult to determine the proportion of the pressure gradient that is attributable to the obstruction at the valvular *vs* the subvalvular level (e.g. HOCM). Planimetry of the AVA by 2D imaging may help identify the degree of stenosis at the valve level in this situation. Measurement of V_1 proximal to the AoV and distal to the subvalvular

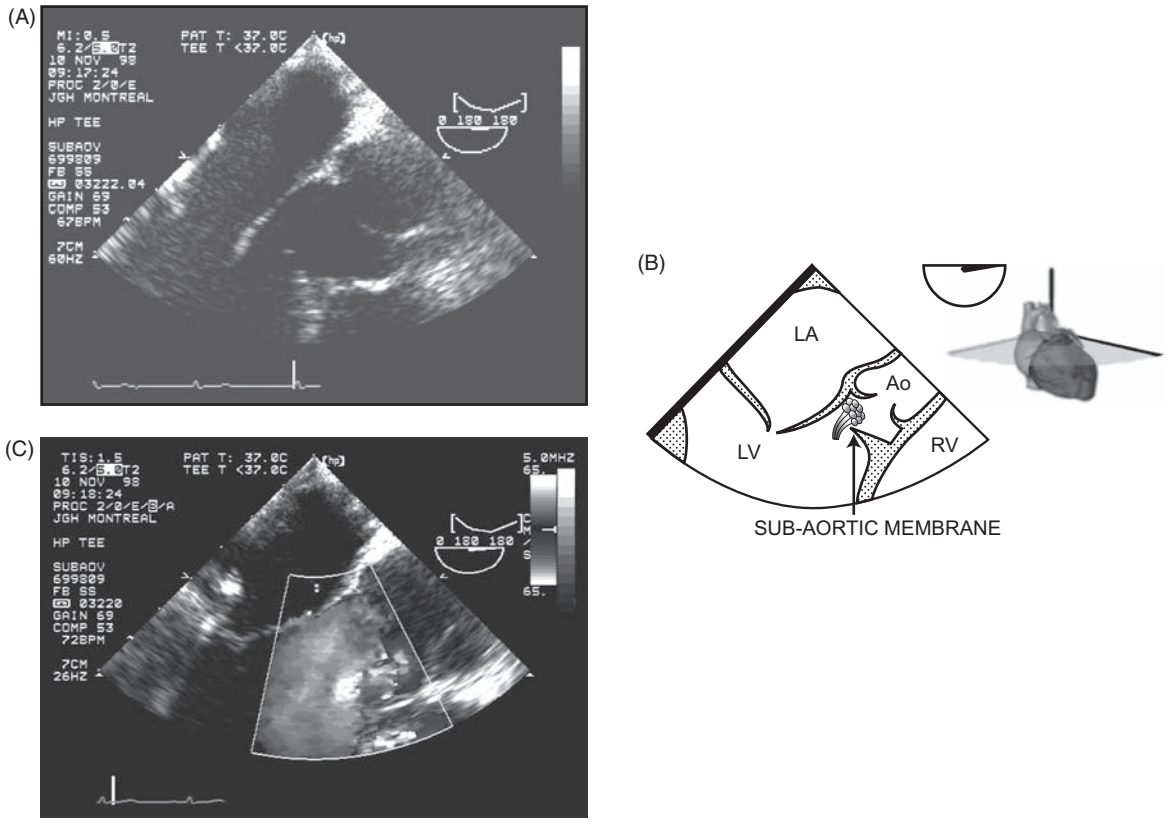

Figure 15.18 (A, B) Mid-esophageal long-axis view of a patient with a subaortic membrane. (C) Only mild acceleration is seen at the level of the membrane. This was an incidental finding in a patient scheduled for coronary revascularization and was not associated with any significant gradient (Ao, aorta; LA, left atrium; LV, left ventricle; RV, right ventricle).

obstruction may reflect turbulent flow distal to an obstruction and invalidate the Bernoulli equation.

2. Flow Velocity Ratio

Flow velocity ratio (also known as the dimensionless index) is defined as the ratio of the flow velocity proximal to the stenosis (in the LVOT) over the flow velocity distal to the obstruction in the vena contracta (the respective time–velocity integrals may alternatively be substituted for the peak velocities). This index will remain constant despite variations in hemodynamics. A flow velocity ratio (FVR) of ≤ 0.25 is consistent with severe AS. The use of FVR may prove useful in the setting of low gradient AS or AS in patients with a low ejection fraction.

$$\text{FVR} = \frac{V_{\text{LVOT}}}{V_{\text{AoV}}} \tag{15.3}$$

3. Aortic Valve Area

Two-dimensional Measurement of Aortic Valve Area

A normal AVA measures 2.5–4.0 cm^2. The AVA is commonly measured with planimetry tracing of the AoV orifice in the transesophageal short-axis view during systole (Fig. 15.22) (13). It is important to advance and withdraw the TEE probe to identify the level with the smallest aortic valve opening. Overestimation of AoV area can occur if planimetry tracing is performed with an oblique plane, above or below the most stenotic level of the aortic valve (Fig. 15.22). As stenotic valves open and close more slowly than normal valves and remain maximally opened for a shorter period of time, the maximal rather than the mean planimetered area should be used as it corresponds more closely to the mean Doppler-derived measurements (14). Overestimation of AVA can easily occur if the short-axis view of the AoV is off-axis (Fig. 15.23).

In the measurement of volumetric flow across a three-cusped nonstenotic AoV, the shape of an equilateral triangle can be used for the measurement of AVA. Although the orifice of the AoV varies throughout systole and resembles more a circle than a triangle when fully opened, the area of an isosceles triangle is considered to represent the average nonstenotic AVA during systole. The measurement of the average AVA can be used for volumetric flow calculation (Fig. 15.24). The area of an

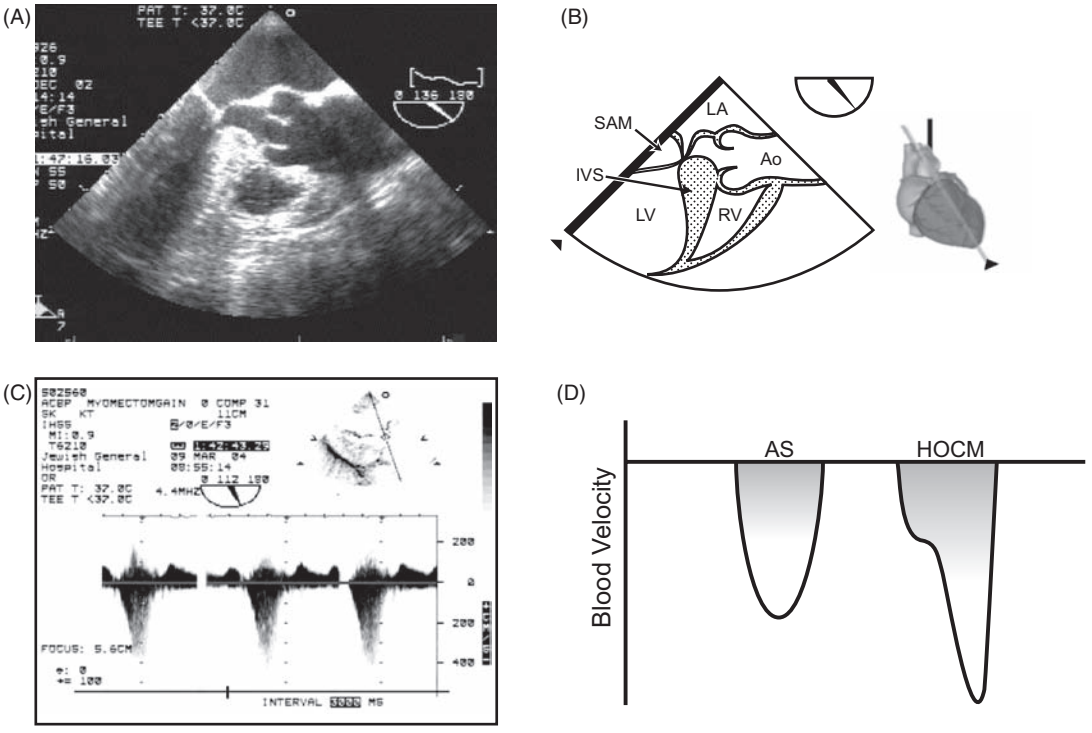

Figure 15.19 Hypertrophic obstructive cardiomyopathy (HOCM). (A, B) Mid-esophageal long-axis view. Note the systolic anterior motion (SAM) and the septal contact of the anterior mitral leaflet in a patient with severe basal septal hypertrophy. The SAM is often associated with a posteriorly directed jet of mitral regurgitation and may be associated with significant left ventricular outflow tract (LVOT) obstruction and flow acceleration. (C) Continuous-wave Doppler interrogation of a patient with HOCM. (D) Compared with aortic stenosis (AS), dynamic LVOT obstruction is characterized by late-peaking flow velocity and dagger-shaped velocity profile (Ao, aorta; IVS, interventricular septum; LA, left atrium; LV, left ventricle; RV, right ventricle).

isosceles triangle can easily be calculated by measuring the distance between two commissures (L) and applying the following formula:

$$\text{Area} = 0.433 \times L^2 \tag{15.4}$$

Doppler-derived Measurement of AoV Area: The Continuity Equation

Doppler-derived measurements of the AVA are usually performed using the continuity equation. The continuity equation is based on the principle that flow across the LVOT must equal flow across the AoV. The ASE task force on Doppler quantification recommends that the measurement of blood flow velocity in the LVOT should be performed with the PW Doppler sample volume positioned ~5 mm beneath the AoV (7). The peak velocity measured with CW Doppler represents the maximal blood flow velocity across the AoV.

Measurement of the AVA using the continuity equation and peak velocities is obtained through the following formula:

$$\text{Flow} = \text{area}(\text{cm}^2) \times \text{velocity}(\text{cm/sec}) = \text{cm}^3/\text{sec} \tag{15.5}$$

$$\text{Flow LVOT} = \text{Flow AoV} \tag{15.6}$$

$$\text{Area}_{\text{LVOT}} \times \text{Velocity}_{\text{LVOT}}(\text{PW}) = \text{AVA} \times \text{Velocity}_{\text{AoV}}(\text{CW})$$

$$\text{AVA} = \text{Area}_{\text{LVOT}} \times \frac{\text{Velocity}_{\text{LVOT}}}{\text{Velocity}_{\text{AoV}}}$$

$$= \frac{\pi R^2 \times \text{Velocity}_{\text{LVOT}}}{\text{Velocity}_{\text{AoV}}}$$

$$= \frac{\pi D^2/4 \times \text{Velocity}_{\text{LVOT}}}{\text{Velocity}_{\text{AoV}}}$$

$$\text{AVA} = \frac{0.785 D^2 \times \text{Velocity}_{\text{LVOT}}(\text{PW})}{V_{\max}(\text{CW})} \tag{15.7}$$

Measurement of the AVA can also be performed using the volumetric principle in the continuity equation by substituting the velocity measurement (cm/sec) with the

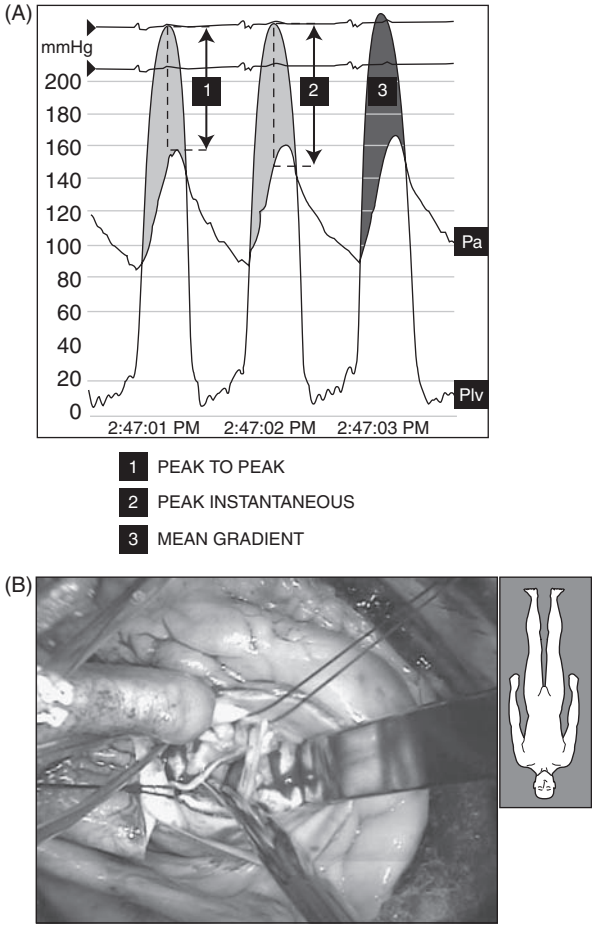

Figure 15.20 Invasive measurement of the pressure gradient between the left ventricle and the aorta in a 64-year-old woman with aortic stenosis before cardiac surgery. (A) The maximal instantaneous pressure gradient is higher than the traditional peak-to-peak pressure gradient reported during cardiac catheterization. Doppler measurements correspond to the instantaneous pressure gradient. Note the delayed upstroke of the arterial pressure (Pa) or pulsus tardus. (B) Intraoperative view of this patient's bicuspid aortic valve (Plv, left ventricular pressure). (Photos A and B courtesy of Drs. Philippe L.-L'Allier and Michel Pellerin.)

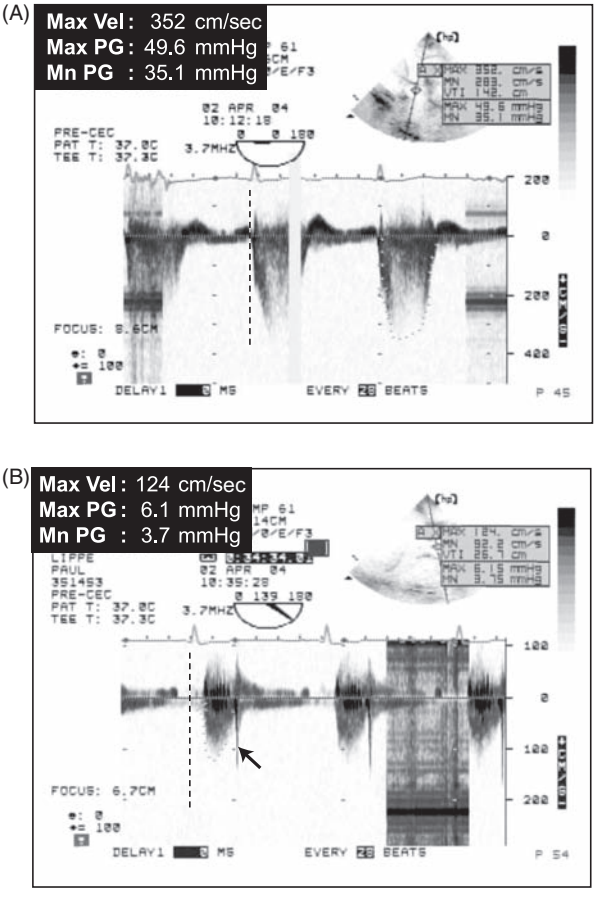

Figure 15.21 Difference between the continuous-wave Doppler of mitral regurgitation (MR) (A) and aortic sclerosis (B) in a 61-year-old man. The MR Doppler signal was obtained from a deep-transgastric view and yielded a mean pressure gradient (PG) of 35.1 mmHg. The MR signal begins within the QRS of the electrocardiogram as opposed to the aortic sclerosis which starts later after the isovolumic contraction period. Note also the closure click observed with aortic sclerosis (arrow) (Max, maximum; Mn, mean; Vel, velocity).

measurement of the velocity–time integral (VTI):

$$\text{Area}(\text{cm}^2) \times \text{VTI}(\text{cm}) = \text{cm}^3$$

$$\text{Area}_{\text{LVOT}} \times \text{VTI}_{\text{LVOT}}(\text{PW}) = \text{AVA} \times \text{VTI}_{\text{Vmax}}(\text{CW})$$

$$\text{AVA} = \frac{0.785D^2 \times \text{VTI}_{\text{LVOT}}(\text{PW})}{\text{VTI}_{\text{Vmax}}(\text{CW})} \quad (15.8)$$

A difference of 0.2 cm^2 in the measurement of the AVA using either technique is not uncommon. A rapid way to estimate the AVA in the operating room in a patient with a pulmonary catheter is to use the calculated thermodilution-derived SV instead of the LVOT-derived SV (Fig. 15.25). However, there are limitations in the use of thermodilution SV as a substitute for Doppler-derived SV in the continuity equation. The SV measured with a thermodilution pulmonary artery catheter uses a different algorithm than the Doppler-derived measurement of SV thereby introducing a potential source of error. In addition, the use of the thermodilution SV in the continuity equation is likely to overestimate AVA if the Doppler signal is misaligned for the measurement of V_{max}. Conversely, an angulation error with the Doppler-derived SV across the AoV and the LVOT is more likely to affect both of these measurements in a similar fashion, thus minimizing the impact of this error in the continuity equation.

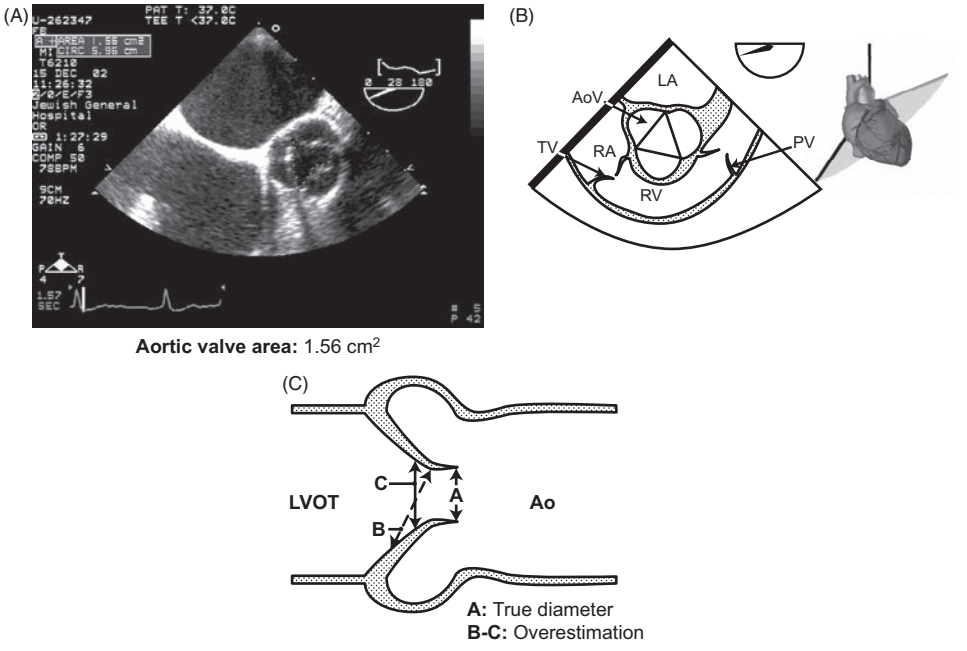

Figure 15.22 (A, B) Mid-esophageal short-axis view of the aortic valve (AoV) at 28°. The AoV area measured by planimetry was 1.56 cm^2. (C) In aortic stenosis, overestimation can occur if the measurement plane is below or oblique to the most stenotic area (Ao, aorta; LA, left atrium; LVOT, left ventricular outflow tract; PV, pulmonic valve; RA, right atrium; RV, right ventricle; TV, tricuspid valve).

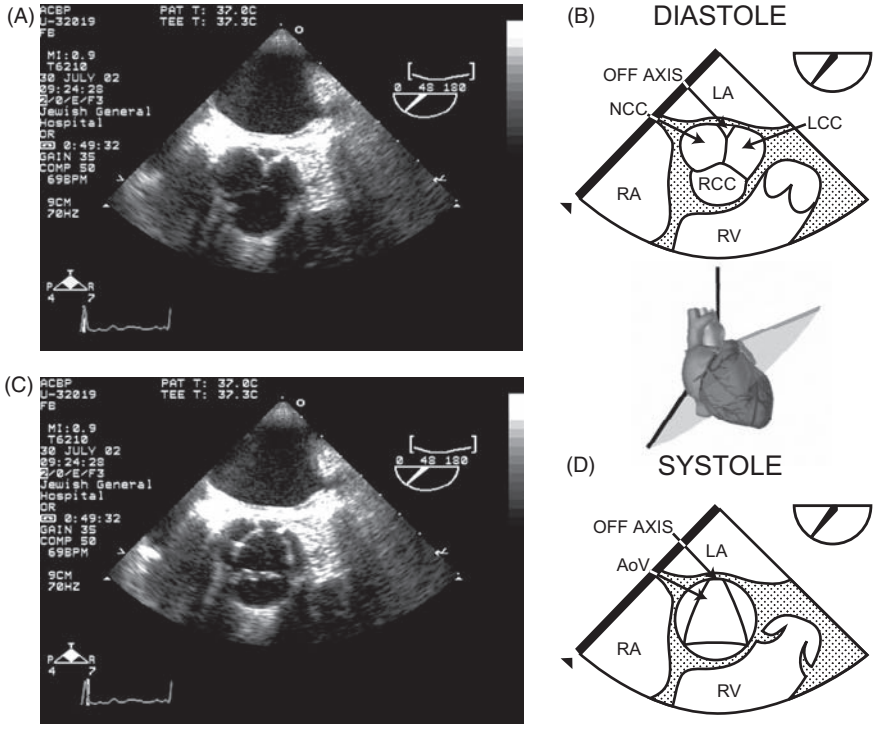

Figure 15.23 (A, B) Mid-esophageal short-axis view of the aortic valve (AoV) at 48° in diastole. Note at 12:00, the separation between the left coronary cusp (LCC) and the non-coronary cusp (NCC) at the base of the commissure, indicating that the imaging plane is suboptimally aligned with the true short axis of the valve. (C, D) In systole with improper alignment of the image with the true short axis of the AoV, planimetry of the orifice would overestimate the AoV area (LA, left atrium; RA, right atrium; RCC, right coronary cusp; RV, right ventricle).

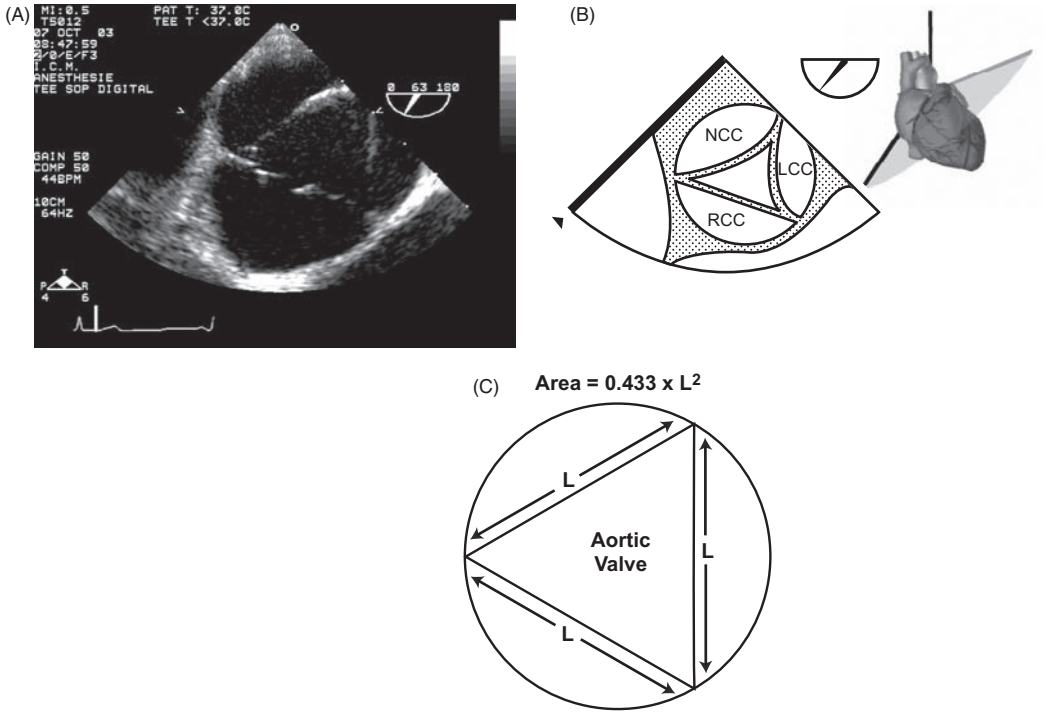

Figure 15.24 (A, B) Mid-esophageal short-axis view of an aortic valve in a 42-year-old man with Ehler–Danlos' disease. (C) The area of the equilateral triangle represents the average aortic valve area during systole (L, length; LCC, left coronary cusp; NCC, non-coronary cusp; RCC, right coronary cusp).

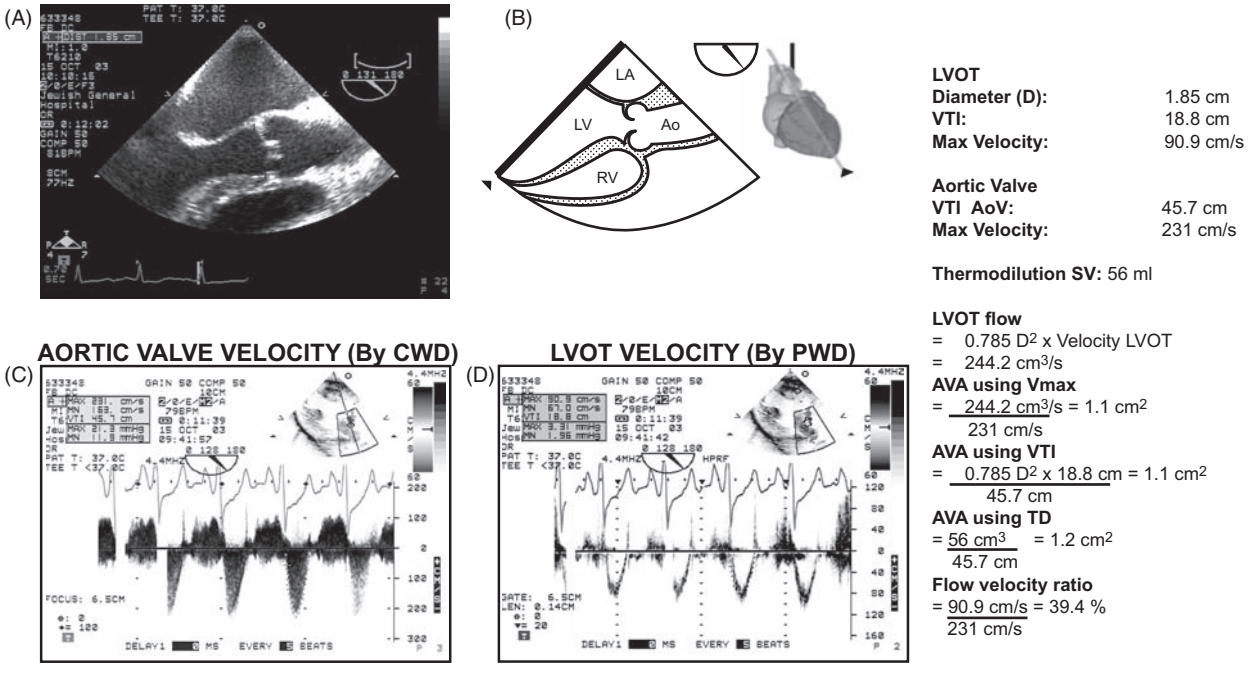

Figure 15.25 (A, B) Mid-esophageal long-axis view of the left ventricular outflow tract (LVOT) in a 71-year-old woman with aortic stenosis. (C, D) The aortic valve area (AVA) is calculated using the maximum (Max) velocity across the aortic valve and either the LVOT flow velocity or stroke volume derived from thermodilution (TD) (Ao, aorta; CWD, continuous-wave Doppler; D, diameter; LA, left atrium; LV, left ventricle; PWD, pulsed-wave Doppler; RV, right ventricle; SV, stroke volume; VTI, velocity–time integral).

Although there are limitations in the use of the thermodilution-derived SV in the continuity equation, this remains a useful tool to validate the Doppler-derived measurement of SV across the LVOT (15). A significant discrepancy between these two measurements may indicate an error in the measurement of SV by thermodilution CO or the 2D measurement of the LVOT and misalignment, or malposition of the Doppler signal in the LVOT. The presence of spectral broadening may indicate that the sample volume is positioned too close to the aortic valve in the area of proximal acceleration. In this scenario, measurement of V_1 will be overestimated. Conversely, V_1 will be underestimated if the Doppler sample volume is positioned too far from the AoV.

The measurement of the LVOT diameter (D) should be performed in a longitudinal view immediately below the AoV. The long-axis view is most commonly used for this purpose. Extreme care must, therefore, be taken to ensure that the measurement of the LVOT diameter is made from the base of the right cusp insertion to the base of the opposite cusp insertion. It is also important to ensure that the measurement of the LVOT is perpendicular and not oblique to the LVOT. Adequate visualization of symmetrical leaflet separation and symmetrical sinuses of Valsalva in a longitudinal view of the AoV should improve the accuracy of the LVOT measurement. As this measurement is squared, a small error will be magnified in the calculation of the AVA. In a study by Harpaz, the end-diastolic measurement of the LVOT was a more accurate predictor of AoV prosthetic size than the end-systolic measurement. However, the author believes that either the end-diastolic or the early systolic measurement (Fig. 15.26) correlates well with the intraoperative surgical measurement of the LVOT.

Aortic Valve Area and the Double Envelope Technique

Flow velocity in the LVOT and across the AoV can also be measured using the double envelope technique with CW Doppler (16,17). Flow velocity in the LVOT and flow velocity across the AoV are both represented with CW Doppler when the spectral Doppler tracing depicts simultaneously two distinct and superimposed Doppler signals (double envelope). The lower velocity envelope represents flow in the LVOT and the "lighter" high

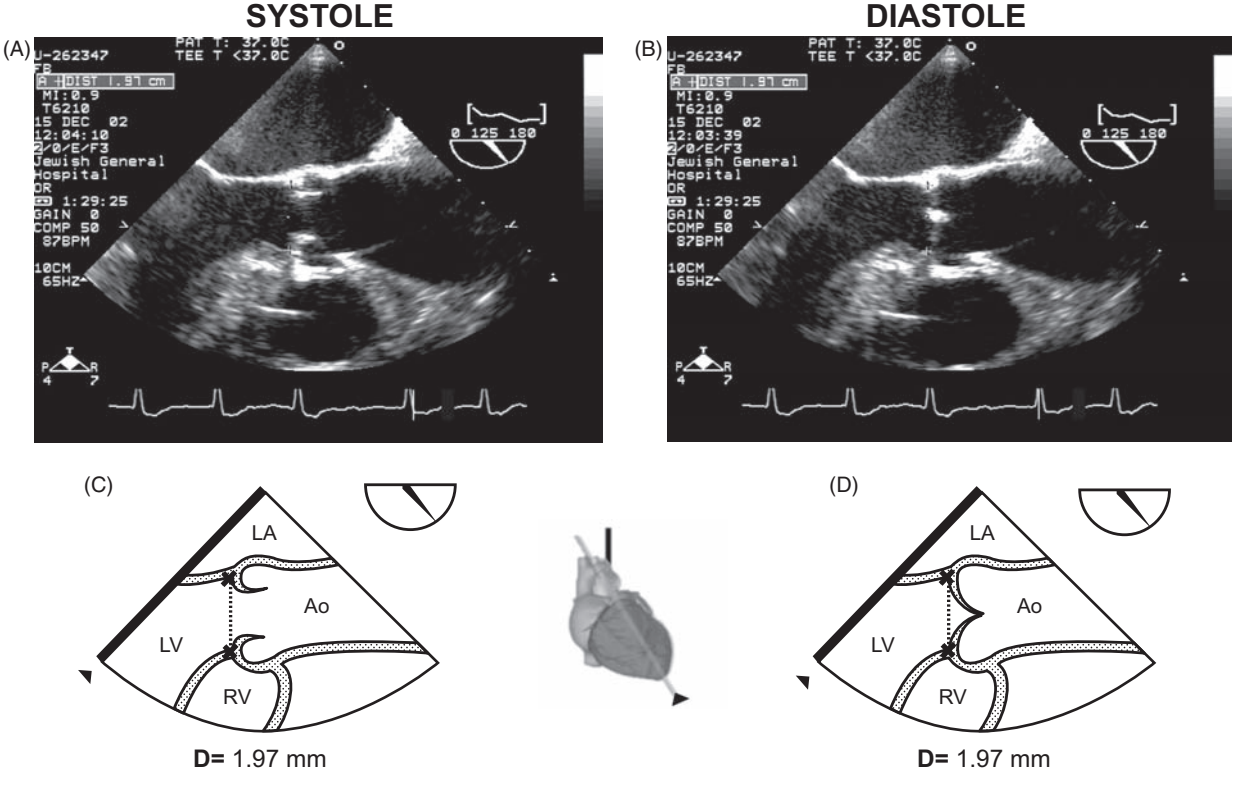

Figure 15.26 Mid-esophageal long-axis view of the aortic valve at 125°. Measurement of the LVOT diameter (D) at the aortic annulus in early systole (A, B) and end-diastole (C, D). No significant difference is noted. By convention, it is measured at end-diastole (Ao, aorta; LA, left atrium; LV, left ventricle; RV, right ventricle).

velocity envelope represents flow across the AoV. Either V_{max} or VTI can be used for each of the two envelopes in the calculation of AVA in the continuity equation. The double envelope is not always visible but when present it is an accurate and rapid method to measure flow in the LVOT and across a stenotic AoV. The double envelope technique is especially useful when the hemodynamic conditions fluctuate because of arrhythmias or during surgical manipulation of the heart as it ensures that the measurement of flow across the LVOT and AoV are obtained simultaneously with the same SV volume.

Aortic Valve Area: Planimetry vs The Continuity Equation

Measurement of the AVA using the Gorlin formula during cardiac catheterization correlates well with the measurements obtained with either TEE planimetry or the continuity equation by transthoracic echocardiography (TTE) (18). Although some authors have stated that these three methods may be used interchangeably, others have found that TEE planimetry overestimates the AVA measured by the other two methods (19). This apparent discrepancy may be explained by other studies where the correlation between TEE planimetry and Doppler measurement was dependent on the amount of valvular calcification (Table 15.1). In a study by Cormier et al. (13), the hemodynamic and echocardiographic correlation in the estimation of the AVA in patients with milder grade 1 or 2 AoV calcification was good as opposed to those with more abundant grade 3 or 4 calcifications where a poor correlation between these two measurement techniques was observed.

Aortic Valve Area and Blood Flow

Changes in flow may affect the measurement of the AVA. In a study by Tardif et al. (20) looking at patients with moderate or severe AS, acute changes in SV and cardiac output (CO) did not result in significant changes in TEE measurement of AVA by planimetry. In a subsequent study, Tardif et al. (21) compared simultaneous determination of the AVA by the Gorlin formula and by TEE under different transvalvular flow conditions. While the CO increased by 42% and the mean pressure gradient across a stenotic AoV increased by 54% during dobutamine infusion, the AVA by TEE planimetry did not change. However, using the Gorlin formula, there was a difference of 0.44 cm^2 between calculations made under minimal flow versus maximal flow (21). This study suggests that the Gorlin calculation of the AVA has disproportionate flow dependence and that the measured increase in area with this technique does not correlate with a true widening of the orifice.

Table 15.1 Aortic Valve Calcification

Grade 1	Single area of increased echo brightness
Grade 2	Scattered areas of moderate echo brightness
Grade 3	Extensive calcification (possible to determine commissural area)
Grade 4	Heavily calcified valve with acoustic shadowing into the aortic valve orifice

Pitfalls in the Measurement of Aortic Valve Area

PSEUDO AORTIC STENOSIS. In patients with low CO and pressure gradient across the AoV, blood flow may be insufficient to fully mobilize and open the AoV cusps. The measured effective orifice area (EOA) of the AoV may, therefore, appear falsely low in these patients. This dilemma can be resolved by performing repeat measurements during a dobutamine administration or other intervention which will increase CO. In patients with true AS, no significant change in the small measured EOA will be seen. On the other hand, patients with pseudoaortic stenosis will demonstrate an increase in the AoV EOA with the increase in blood flow.

AORTIC VALVE AREA AND PRESSURE RECOVERY. Pressure recovery is the increase in pressure seen downstream from a stenosis due to reconversion of kinetic energy into potential energy. The pressure recovery decreases the net loss of pressure across the AoV and therefore decreases the workload of the LV. Measurement of the Doppler-derived EOA is linked to the maximum velocity at the vena contracta and therefore, the Bernoulli equation does not take into account the pressure recovery downstream from the stenosis. The catheter measurement of the EOA using the Gorlin formula will more closely agree with the Doppler-derived measurement if the catheter is positioned at the level of the vena contracta. As the catheter is usually positioned in the ascending Ao and not at the level of the vena contracta, the Gorlin-derived EOA tends to exceed the Doppler-derived EOA. Discrepancies between catheter and Doppler-derived measurements of AoV EOA may be attributed to the pressure recovery phenomenon. Garcia et al. (10,11) defined a simple equation to reconcile this discrepancy and proposed an equation to correct the Doppler EOA for pressure recovery based on angiographic data. This equation was derived from an *in vitro* model measuring the effects of different flow rates and aortic diameters on two fixed stenosis and seven bioprosthesis. This equation was also validated in an animal model and in humans using the raw data of a study by Schöbel et al. (22).

The catheter-derived EOA with the Gorlin formula was determined using a constant of 50 instead of the 44.3 based on previous studies which demonstrated that this

substitution should provide a more accurate assessment of catheter-derived EOA.

$$\text{EOA Gorlin} = \frac{Q}{50\sqrt{\text{Pressure Gradient}_{\text{AoV}}}}, \quad Q = \text{cardiac output} \quad (15.9)$$

$$\text{EOA Gorlin} = \frac{\text{EOA Doppler} \times A_{\text{A}}}{A_{\text{A}} - \text{EOA}}, \quad A_{\text{A}} = \text{ascending aorta (cm}^2\text{)} \quad (15.10)$$

It is too early to know whether the use of this simple equation will be routinely adopted in the echocardiography laboratory but an understanding of pressure recovery and its effect on the measurement of Doppler-derived EOA is important in the assessment of patients with AS.

4. M-Mode

Aortic stenosis is characterized by decreased aortic leaflet excursion in systole. The M-mode can be used to measure aortic leaflet separation in the evaluation of AS. This measurement may, however, significantly overestimate or underestimate the severity of AS if the valve is bicuspid or when asymmetric leaflet separation occurs (Fig. 15.27). This is, therefore, not very useful in the quantification of AS.

Measurement of the transvalvular gradient and the AVA (by either planimetry and/or the continuity equation) are the most commonly used and validated methods to quantify the severity of AS with TEE. Table 15.2 summarizes the classification of AS.

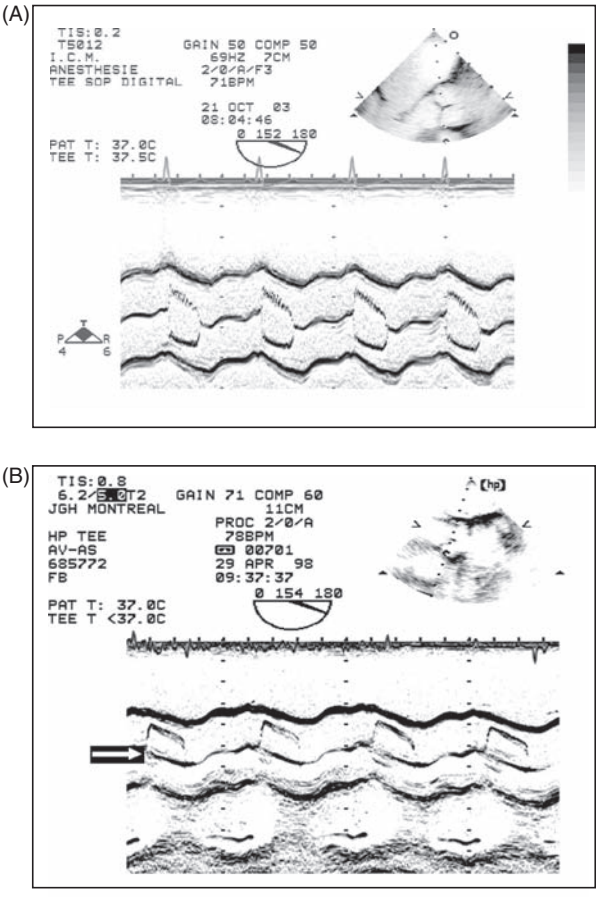

Figure 15.27 (A) Mid-esophageal M-mode view of a normal aortic valve. (B) Same view from a patient with an immobile right coronary cusp (arrow) and an opposing aortic leaflet with preserved mobility.

III. AORTIC REGURGITATION

A. Etiology of Aortic Regurgitation

Aortic regurgitation may be caused by aortic root dilatation, dissection or intrinsic cusp pathology. Patients with a dilated ascending Ao develop AR when enlargement of the sinotubular junction causes outward displacement of the commissures. When the aortic cusps are concomitantly stretched (annuloaortic ectasia) and the length of their free margin approximates that of their base, they are prone to develop small tears or fenestrations (Fig. 15.28) and are considered less desirable for preservation during aortic root surgery (25). Conversely, patients without annuloaortic ectasia constitute good candidates for preservation of aortic cusps and root remodeling (25). Aortic root disease leading to dilatation and AoV regurgitation includes Marfan's syndrome, Ehlers–Danlos' syndrome (Fig. 15.29), and aortitis. There is also evidence suggesting that patients with a bicuspid AoV have abnormal elastic properties in the Ao leading to dilatation of the aortic root, even if there is no AS and the AR is only mild or trivial.

The AR seen during aortic dissection may have been preexisting if previous annuloaortic ectasia and/or dilatation of the sinotubular junction was present (see Chapter 12). However, AR during aortic dissection most often results from disruption of the cusp geometry when the intimal flap itself prolapses across the AoV or when the cusp insertion between the sinotubular junction and the aortic annulus is involved by the dissection (26).

Intrinsic cusp pathology causing AR is either congenital or can be acquired with connective tissue disorders, rheumatic heart disease, degenerative calcification, or infective endocarditis. Poor coaptation may result from either decreased cusp mobility or increased mobility with prolapse (Fig. 15.30). Subacute bacterial endocarditis may cause leaflet destruction, perforation, or tear causing various degrees of AR. Periaortic abscess must be excluded in these patients (Fig. 15.31).

When the aortic regurgitant jet is eccentrically directed towards the base of the anterior mitral leaflet, diastolic

Table 15.2 Aortic Valve Stenosis

Aortic valve	Normal	Mild stenosis	Moderate stenosis	Severe stenosis
Aortic valve area (3) (cm^2)	2.5–4.0	>1.5	1.1–1.5	≤1.0
AVA index (23) (cm^2/m^2)		>0.9	0.6–0.9	<0.6
M-mode separation (24)	>15 mm			<8 mm
Leaflet separation (24) Ao root diameter	>75%	50–75%	30–50%	<30%
Mean gradient (3,23,24) (mmHg)		<30	30–50	>50
Peak gradient (3,23,24) (mmHg)		<50	50–75	>75

fluttering of the anterior mitral leaflet may be seen on 2D imaging or with M-mode (see Fig. 9.38). Significant AR can cause relative mitral stenosis (MS) in late diastole corresponding clinically to the Austin–Flint murmur. Other clues suggesting significant AR include increased aortic systolic expansion (Corrigan pulse), a restrictive mitral inflow pattern, a left ventricular end-systolic diameter >55 mm and reverse diastolic doming of the MV. In patients with severely elevated left ventricular end-diastolic pressure (LVEDP), diastolic MR, premature closure of the MV, and early AoV opening may be observed. Late diastolic MR is a better predictor of severe AR than either M-mode demonstration of premature MV closure or early AoV opening.

B. Quantification of Aortic Regurgitation

1. *Jet Height/LVOT Height*

Color flow imaging can be used to quantify the severity of AR. The ratio of jet height to LVOT diameter measured immediately below the cusps in the TEE long-axis view at 120–150° correlates well with the severity of AR and is a good predictor of the angiographic grade. In mild AR, the jet height is less than one-third of the LVOT diameter (Fig. 15.32) while this ratio exceeds two-thirds in severe AR (Fig. 15.32) (27,28). This measurement can also be performed in a five-chamber view at 0°. Occasionally, this method may overestimate the true severity of AR when the imaging plane happens to be aligned with a

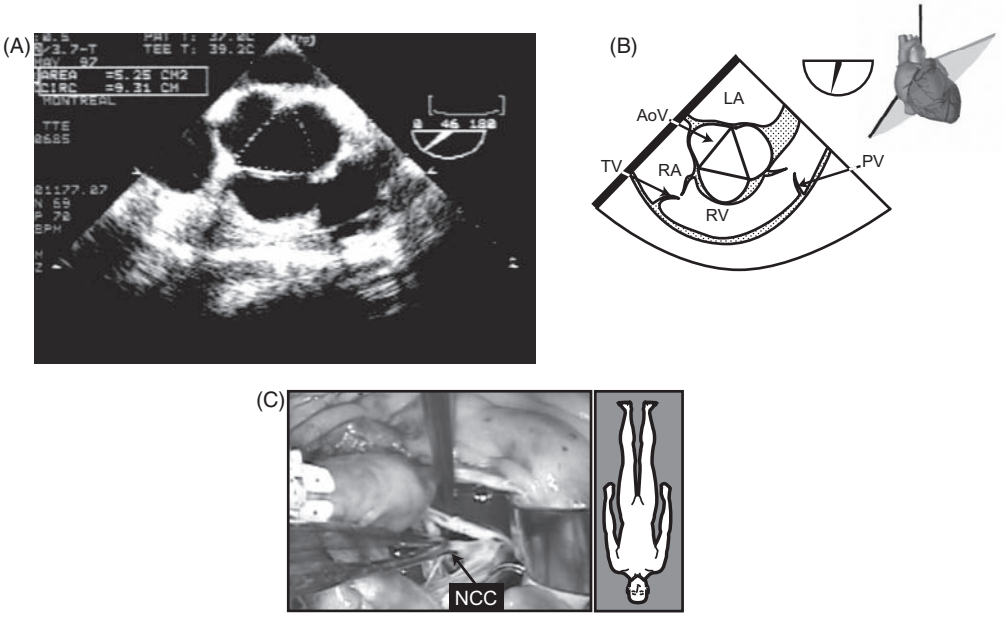

Figure 15.28 (A, B) Mid-esophageal short-axis view of the aortic valve (AoV) at 46° in a patient with dilated aortic root and enlarged sinuses of Valsalva. The aortic leaflets are stretched, with decreased central coaptation in diastole. Any further dilatation would result in increased aortic regurgitation. In systole, the free margin of the cusps is distant from the wall of the enlarged sinuses. (C) Corresponding intraoperative finding in a 70-year-old man with the same pathology. Note the non-coronary cusp (NCC) fenestration (LA, left atrium; PV, pulmonic valve; RA, right atrium; RV, right ventricle; TV, tricuspid valve). (Photo C courtesy of Dr. Michel Pellerin.)

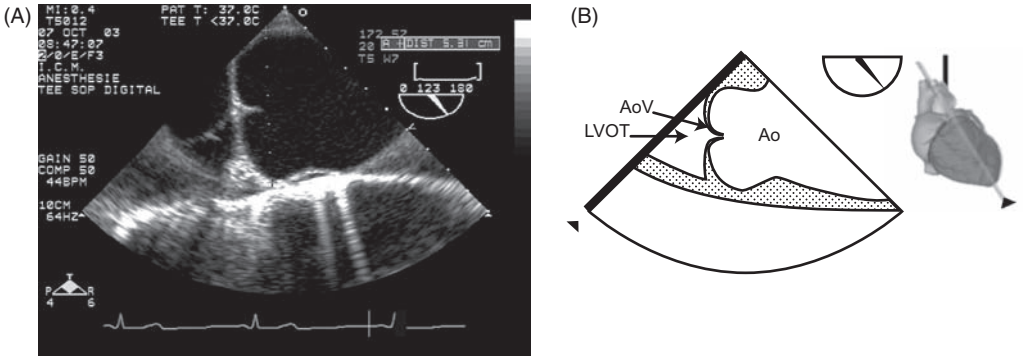

Figure 15.29 Long-axis view of the aortic valve at 123° in a 42-year-old man with Ehler–Danlos' disease. The aortic root measures 53 mm at the level of the aortic sinus (Ao, aorta; AoV, aortic valve; LVOT, left ventricular outflow tract).

narrow jet of AR spanning most of the commissural closure line, as may be observed in the bicuspid AoV with a vertical commissure. Likewise, the severity of AR could be underestimated if the imaging plane is tangential to a narrow regurgitant jet. In patients with an eccentric regurgitant jet, the measurement of jet height should be done perpendicular to the axis of the jet direction. In a TTE study by Evangelista et al. (29), jet eccentricity decreased correlation with angiographic grade by underestimating the severity of AR. The jet width (height) was defined as the smallest diameter of the jet at the junction of the LVOT and the aortic annulus in the parasternal long-axis view. In that study, the jet width corresponded better with the angiographic grade of AR than the ratio of jet height to LVOT height. However, in several echocardiography laboratories, the ratio of jet height to LVOT diameter remains one of the most commonly used measurements to assess the severity of AR in spite of its limitations.

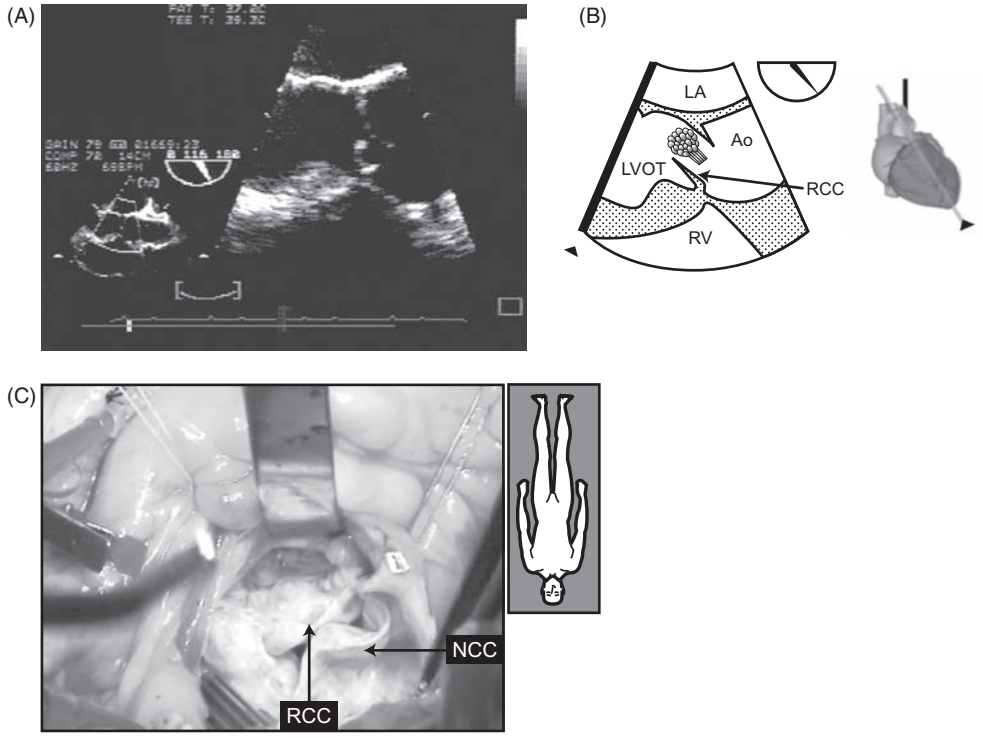

Figure 15.30 (A, B) Long-axis view of the aortic valve at 116° in a patient with a bicuspid aortic valve. A prolapsed right coronary cusp (RCC) is accompanied by an eccentric jet of aortic regurgitation directed towards the anterior mitral leaflet. (C) Intraoperative image of a RCC prolapse (Ao, aorta; LA, left atrium; LVOT, left ventricular outflow tract; NCC, non-coronary cusp; RV, right ventricle). (Photo C courtesy of Dr. Pierre Pagé.)

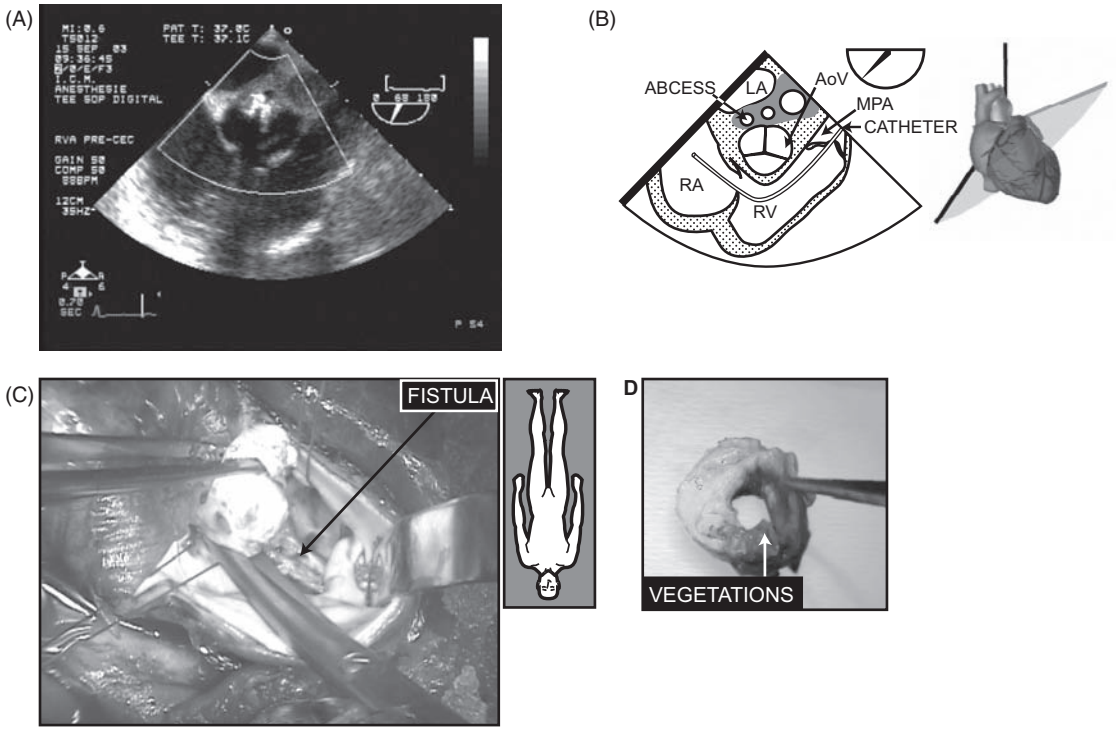

Figure 15.31 A 46-year-old woman with a bicuspid aortic valve (AoV) is diagnosed with endocarditis. (A, B) When the transesophageal echocardiographic exam was performed in the operating room, a posterior root abcess with a fistula was diagnosed from this mid-esophageal short-axis view. (C, D) The echocardiographic findings were confirmed intraoperatively (LA, left atrium; MPA, main pulmonary artery; RA, right atrium; RV, right ventricle). (Photos C and D courtesy of Dr. Michel Pellerin.)

2. Short-Axis Jet Area/LVOT Area

The ratio of the regurgitant jet area to the LVOT area in the short-axis view immediately below the AoV can be used to estimate the severity of AR with color flow imaging. It is essential that this measurement is made high in the LVOT, where part of the AoV is still visualized to ensure that the jet is truly measured at its origin. In the study by Perry et al. (29), this measurement was slightly more predictive of AR severity by angiography than jet height to LVOT height. It is, however, the opinion of the author that this measurement often underestimates the severity of AR.

3. Flow Reversal

On PW examination of the proximal descending thoracic Ao, mild early diastolic flow reversal is often observed in normal patients but this flow reversal usually has a low velocity and a short duration. However, the presence of holodiastolic flow reversal on PW examination of the descending thoracic Ao with an initial velocity ≥ 0.6 cm/sec and an end-diastolic velocity of ≥ 0.2 m/s is an index of severe AR (Fig. 15.33) (24). This finding proves particularly useful in assessing AR when the regurgitant jet is eccentric and more difficult to quantify at the valve level.

4. Regurgitant Fraction

The measured flow across a regurgitant cardiac valve is increased as it includes not only the effective forward SV, but also the regurgitant volume. Thus, the difference in measured SV across a competent valve (the effective forward flow) and the SV across the incompetent valve represents the regurgitant volume. The regurgitant fraction is the ratio of the regurgitant volume over the SV across the regurgitant valve. For AR, the forward flow across the AoV is compared with the diastolic volumetric flow across the MV, provided the MV is competent.

$$\begin{aligned}\text{Regurgitant volume} &= \text{Aortic stroke volume} \\ &\quad - \text{Mitral diastolic volume} \\ \text{Aortic regurgitant fraction} &= \frac{\text{Aortic stroke volume} - \text{Mitral diastolic volume}}{\text{Aortic stroke volume}}\end{aligned} \tag{15.11}$$

Volumetric flow across the MV is obtained by positioning the sample volume of the PW Doppler at the level of the mitral annulus and tracing the VTI of the mitral inflow signal. The mitral annular area is then obtained with 2D echocardiography by using the formula for an

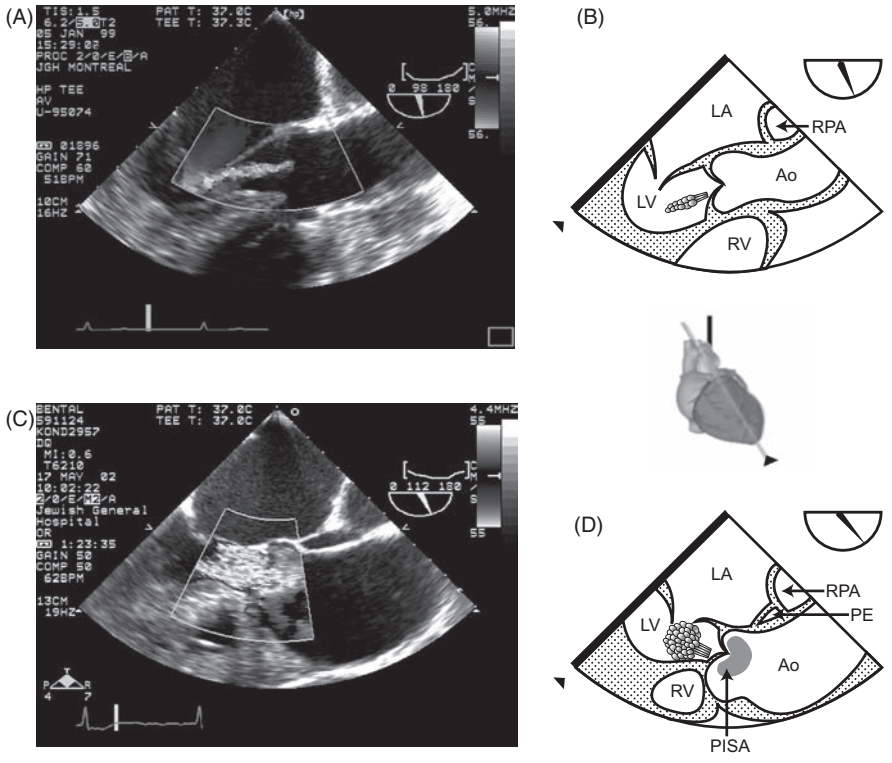

Figure 15.32 (A, B) Mid-esophageal long-axis view of the aortic valve at 98° in a patient with mild aortic regurgitation: the width of the regurgitant jet immediately below the aortic valve is less than one-third of the left ventricular outflow tract (LVOT) diameter indicating mild aortic regurgitation. (C, D) Same view at 112° in a different patient: the width of the regurgitant jet is as wide as the LVOT diameter, consistent with severe aortic regurgitation. Note also the hemisphere of proximal isovelocity surface area (PISA) on the aortic side of the anatomic regurgitant orifice and the dilated ascending aorta (Ao) (LA, left atrium; LV, left ventricle; PE, pericardial effusion; RPA, right pulmonary artery; RV, right ventricle).

ellipse and measuring the diameters of the mitral annulus in the four- and two-chamber midesophageal views (D_1 and D_2). The product of mitral inflow VTI (cm) and mitral annular area (cm^2) yields the mitral diastolic stroke volume (cm^3).

$$\text{Area of ellipse} = \frac{\pi(D_1 \times D_2)}{4} \qquad (15.12)$$

Alternatively, flow across any other competent valve could also be used, although it is more difficult to align the Doppler ultrasound beam properly with the direction of tricuspid or pulmonic flow by TEE.

Pitfalls of Regurgitant Fraction

The measurement of regurgitant fraction is not usually done by anesthesiologists in the operating room because it is time-consuming and may distract from patient care and monitoring. Moreover, the measurement of the SV across the mitral and the AoV should be done under the same hemodynamic conditions. Therefore, as these measurements are obtained sequentially rather than simultaneously, rapid transient changes occurring during anesthesia and/or surgery may affect the validity of the obtained regurgitant fraction.

Another important source of error originates from the measurement of the mitral annulus and LVOT diameter. A small error in the measurement of these diameters is magnified to its square value in the calculation of the cross sectional area for the measurement of the volumetric flow rate.

Measurement of the aortic regurgitant volume is also critically influenced by the position of the sample volume during PW Doppler examination. Doppler angulation exceeding 20° between the ultrasound beam and the direction of flow will yield a value lower than the true forward aortic SV, and consequently a lower aortic regurgitant volume. Overestimation of the effective forward SV at the MV will also result in a smaller aortic regurgitant volume. This may occur when the sample volume is located at the tip of the mitral leaflets rather than at the level of the mitral annulus. Sampling below the mitral annulus may also result in contamination of the mitral inflow signal with the AR jet which would further

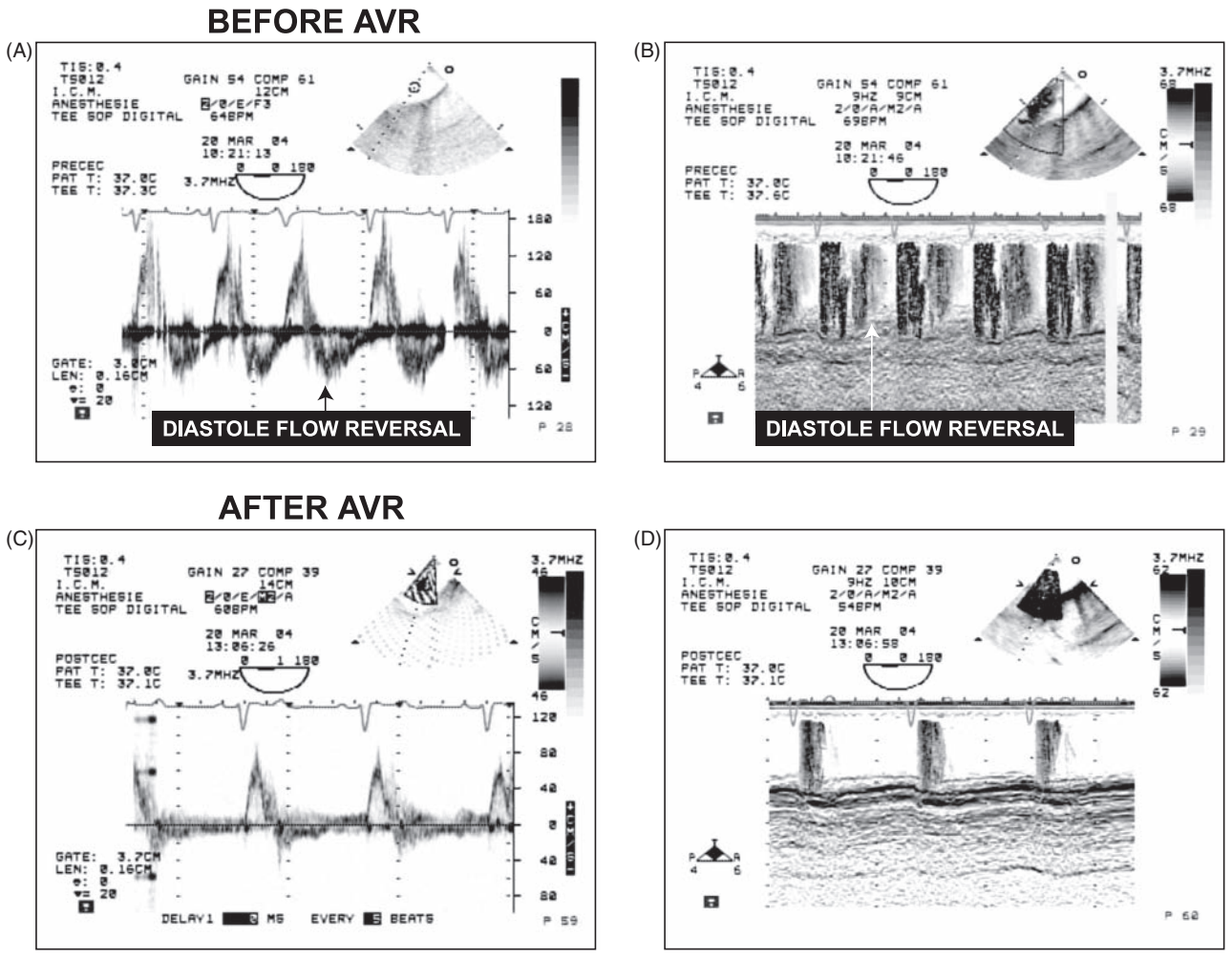

Figure 15.33 A 78-year-old man is scheduled for aortic valve replacement (AVR) for severe aortic regurgitation secondary to endocarditis. (A, B) Diastolic flow reversal is shown using pulsed-wave and color Doppler interrogation of the ascending aorta. (C, D) This abnormality disappeared after AVR.

underestimate the aortic regurgitant fraction (RF). Conversely, the aortic forward SV and corresponding aortic regurgitant volume will be overestimated if the sampling volume is positioned too close to the AoV in the flow acceleration zone. Even with careful attention to these pitfalls, a RF of 20% has been calculated in normal subjects making this measurement less reliable than it may appear to be (7,28).

5. *Effective Regurgitant Orifice*

The effective regurgitant orifice (ERO) area provides a quantitative assessment of the severity of AR. The following methods can be used to calculate the ERO.

ERO Measurement with 2D Planimetry

Transesophageal echocardiography planimetric measurement of the end-diastolic gap between the aortic cusps can be used to determine the severity of AR. This measurement of the anatomic regurgitant orifice area has been shown to correlate with measurements by TTE and by angiographic grading of AR (Fig. 15.34) (30).

ERO Measurement with the PISA Method

The proximal isovelocity surface area (PISA) method is based on the principle of conservation of mass (see Chapter 5). Although it is more commonly used in the quantification of MR, it has also been validated in the assessment of AR (31). As red blood cells converges towards the regurgitant orifice, their velocity increases creating multiple hemispheric shells of isovelocity. The principle of conservation of mass states that the flow rate at each hemispheric isovelocity shell should be equal to each other and to the regurgitant orifice flow rate. This is in fact a variant of the continuity equation, using two

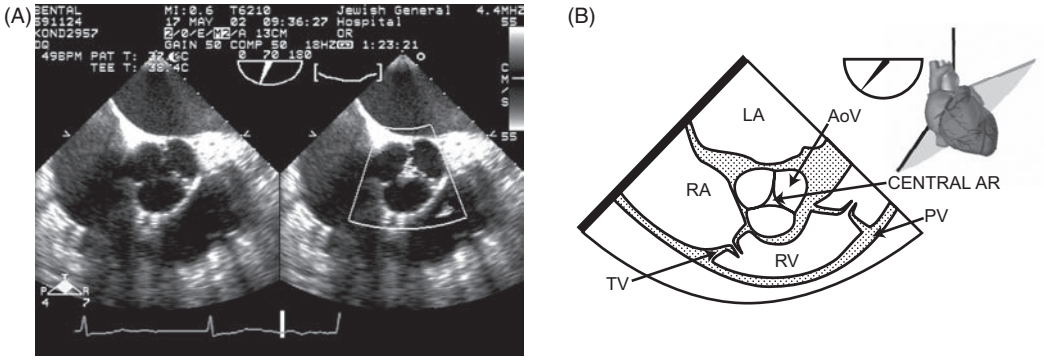

Figure 15.34 Mid-esophageal short-axis split screen view of the aortic valve (AoV) at 70° in a patient with central aortic regurgitation (AR). The anatomic effective regurgitant orifice area is seen on 2D imaging (left split screen) and with color flow imaging (right split screen) (LA, left atrium; PV, pulmonic valve; RA, right atrium; RV, right ventricle; TV, tricuspid valve).

measurements on a single (regurgitant) valve rather than separate measurements of flow on a regurgitant valve and on another competent valve. From the transgastric views, the regurgitant aortic jet is directed towards the transducer during diastole, forming hemispheric shells of isovelocity above the valve. As blood flow from the ascending Ao accelerates towards the regurgitant orifice it will be coded in progressively lighter shades of red until the velocity exceeds the Nyquist limit and changes to shades of blue. The velocity of the hemispheric shell where the color switches from red to blue is given by the Nyquist limit, indicated on the color scale (38 cm/sec in Fig. 15.35). The surface of the hemispheric shell is calculated from its radius with the formula $2\pi r^2$. The velocity of the hemispheric shell (Nyquist limit) and its surface area are used to calculate the flow rate of the regurgitant lesion. This is equal to the flow rate at the minimal regurgitant orifice, where the aortic regurgitant velocity reaches its maximum velocity (V_{max}) during early diastole and can be measured by CW Doppler across the AoV (Fig. 15.35). Thus, the continuity equation using PISA and ERO flow rate will give an estimate of the ERO area as follows:

$$\begin{aligned} &\text{Flow} = \text{area (cm}^2) \times \text{velocity (cm/sec)} = \text{cm}^3/\text{sec} \\ &\text{ERO flow rate} = \text{PISA flow rate} \qquad (15.13) \\ &\text{ERO area} \times V_{max} = \text{PISA} \times V_{Nyquist} \\ &\text{ERO area} = \frac{2\pi r^2 \times V_{Nyquist}}{V_{max}} \qquad (15.14) \end{aligned}$$

The radius of the hemisphere will be easier to measure if the zoom function is used. A lower Nyquist limit should also be used to obtain a larger hemisphere. In the measurement of the PISA radius, positioning of the caliper at the edge of the hemispheric PISA is easily done in the color flow Doppler mode. However, positioning of the caliper at the level of the regurgitant orifice of the AR jet is more easily achieved by using the color suppress mode on the echocardiography machine. The PISA method for measurement of the ERO has also been validated with TTE in patients with an eccentric jet of AR (32). Technical difficulties in imaging proximal flow acceleration at the level of the AoV with TEE may limit the applicability of this technique.

ERO Measurement with 2D Imaging and Quantitative Doppler

The total left ventricular stroke volume (LV-SV) can be calculated as the difference between the end-systolic (LVESV) and the end-diastolic volume (LVEDV), which can be measured from 2D images by several methods, including the Simpson's method of disks (see Chapter 5). The difference between the LV-SV obtained by 2D echocardiography and the SV measured by PW Doppler across a competent valve yields the aortic regurgitant volume. The MV is most often used as the competent valve for the measurement of SV with PW Doppler as shown in the following:

$$\begin{aligned} &\text{LV-SV(2D)} = \text{LVEDV} - \text{LVESV} \\ &\text{Mitral stroke volume (cm}^3) \\ &\qquad = \text{mitral annular area (cm}^2) \times \text{TVI annulus (cm)} \\ &\text{Regurgitant volume} = \text{LV total SV(2D measurement)} \\ &\qquad - \text{mitral SV(PW measurement)} \\ &\text{ERO(cm}^2) = \frac{\text{Regurgitant volume (cm}^3)}{\text{Aortic regurgitant TVI (cm)}} \\ &\qquad = \frac{\text{LV total SV} - \text{mitral SV (cm}^3)}{\text{Aortic regurgitant TVI (cm)}} \end{aligned} \qquad (15.15)$$

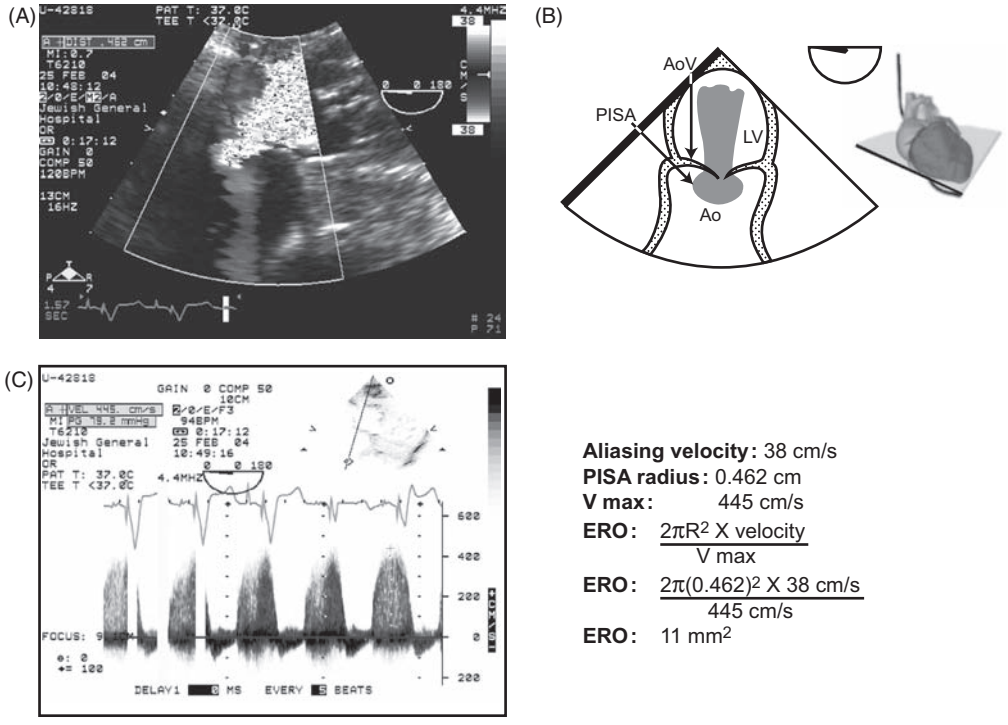

Figure 15.35 (A, B) Basal transgastric longitudinal view of the aortic valve (AoV). The Nyquist limit velocity is set at 38 cm/sec. Note the proximal isovelocity surface area (PISA) on the aortic side of the AoV with color flow Doppler. (C) The continuous-wave Doppler tracing of the aortic regurgitant jet is associated with a maximal velocity (V_{max}) of 445 cm/sec. This corresponds to a peak transvalvular gradient of 79 mmHg during diastole. The effective regurgitant orifice (ERO) can be calculated from these values (Ao, aorta; LV, left ventricle).

The aortic regurgitant VTI (cm) is obtained by tracing the AR Doppler envelope obtained with CW Doppler across the AoV during diastole.

ERO Measurement with Quantitative Doppler Echocardiography

The regurgitant volume can also be calculated by measuring the difference between the forward SV across the LVOT and the SV across the MV.

$$\text{Regurgitant volume} = \text{aortic SV} - \text{mitral SV}$$

$$\text{Aortic SV} = \text{LVOT area (cm}^2) \times \text{TVI}_{\text{LVOT}}\text{ (cm)} = \text{cm}^3$$

$$\text{Mitral SV} = \text{mitral annular area (cm}^2) \times \text{TVI}_{\text{MVannulus}}\text{ (cm)} = \text{cm}^3$$

$$\text{ERO} = \frac{\text{regurgitant volume (cm}^3)}{\text{Aortic regurgitant TVI (cm)}} = \frac{\text{Aortic SV} - \text{mitral SV (cm}^3)}{\text{Aortic regurgitant TVI (cm)}} \quad (15.16)$$

In a study by Kim et al. (33) in sheep, the ERO area did not change with loading conditions.

ERO Measurement with Color Doppler Imaging of the Vena Contracta

The vena contracta is the narrowest point of a regurgitant jet and occurs slightly downstream of the regurgitant orifice. In AR, the vena contracta will be imaged below the AoV within the LVOT (34). Assuming a spherical regurgitant orifice, the ERO area can be calculated using the maximal vena contracta width in early diastole using the following formula:

$$\text{ERO area} = \pi \times (\text{vena contracta width}/2)^2 \quad (15.17)$$

This technique has been validated in sheep studies. In patients, a vena contracta of >6 mm has been shown to correlate with severe AR (7,35–37) and using the equation above, corresponds to an ERO of ≥ 28 mm^2.

6. Vena Contracta

The vena contracta is the narrowest portion of the AR jet and occurs in the LVOT immediately below the AoV. This measurement does not appear to vary with afterload manipulation (35). As indicated previously, a vena contracta of >6 mm is indicative of severe AR. This criteria has also been validated in eccentric jets of AR (37).

In those patients, measurement of the vena contracta should be performed perpendicular to the long axis of the eccentric jet.

7. *CW Doppler and Pressure Half-Time*

The intensity of the CW Doppler signal is determined by the number of red blood cells reflecting the incident ultrasound beam. Therefore, a very dense regurgitant flow signal is suggestive of a large regurgitant volume. Severe AR also results in rapid equilibration of pressures between the Ao and the LV. Thus, a rapid decay of the Ao − LV pressure gradient in diastole is also seen in severe AR. This can be assessed by measurement of the aortic regurgitant flow velocity during diastole, which reflects the instantaneous pressure gradient between the Ao and the LV from the Bernoulli simplified equation. The decay of the Ao − LV pressure gradient is estimated from the slope of the aortic regurgitant velocity and the regurgitant pressure half-time (PHT), which is defined as the time needed for the pressure gradient to fall to half of its initial value during diastole (Fig. 15.36). From the manipulations shown below, the regurgitant PHT also corresponds to the time needed for the maximum velocity to decrease by 70% of its initial value:

Bernoulli equation:

$$P_{\max} = 4(V_{\max})^2$$

$$P_{T_{1/2}} = 4(V_{T_{1/2}})^2$$

Regurgitant PHT:

$$P_{T_{1/2}} = \frac{1}{2}(P_{\max})$$

Therefore:

$$4(V_{T_{1/2}})^2 = \frac{1}{2}4(V_{\max})^2$$

$$V_{T_{1/2}}^2 = \frac{1}{2}V_{\max}^2 \qquad V_{T_{1/2}} = \frac{V_{\max}}{\sqrt{2}}$$

$$V_{T_{1/2}} = 0.7V_{\max}$$

A deceleration slope $>3\ \mathrm{m/s^2}$ or a regurgitant PHT <200 ms suggests either a rapidly decreasing aortic pressure or rapidly increasing LV pressure, both suggesting the presence of severe AR (Fig. 15.36). The regurgitant PHT should ideally be measured on the slope of beats with longer duration. From a technical standpoint, the initial peak velocity represents the pressure gradient between the Ao and the LV during early diastole (Fig. 15.35). As this gradient should be at least 40 mmHg, an initial peak velocity <300 cm/sec usually indicates improper alignment of the ultrasound beam with the regurgitant jet.

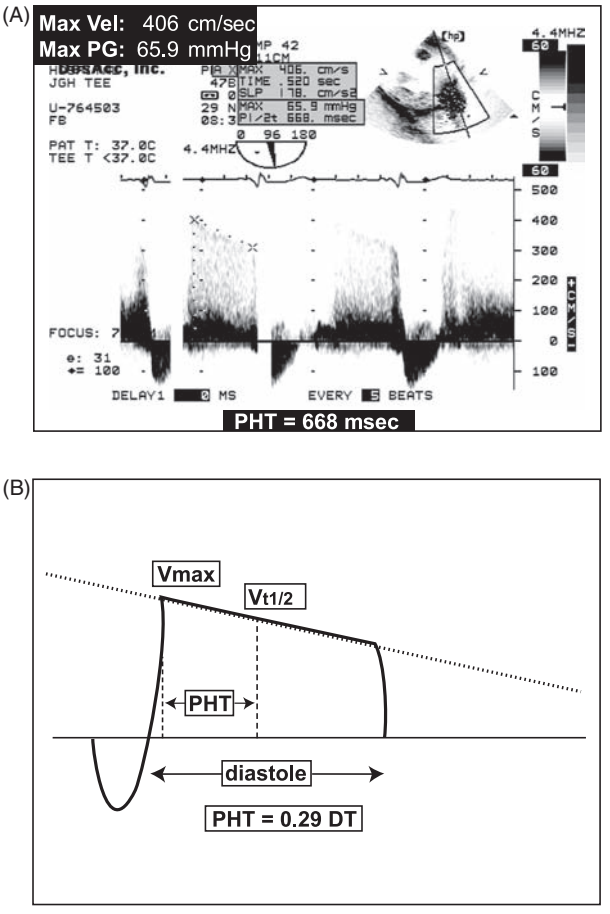

Figure 15.36 (A) Continuous-wave Doppler interrogation across the regurgitant aortic valve through a transgastric window. The regurgitant pressure half-time (PHT) is measured at 668 ms, consistent with mild regurgitation. (B) The relationship between pressure half-time and blood flow velocity across the aortic valve in diastole is illustrated (DT, deceleration time; Max, maximum; PG, pressure gradient; V_{max}, maximal velocity; $Vt_{1/2}$ = velocity at the PHT point).

Pitfalls of Pressure Half-Time

Several factors must be considered in the interpretation of this quantitative measurement of AR. In certain conditions, a short regurgitant PHT may not necessarily indicate severe AR: changes in left ventricular compliance will influence the rate of pressure equilibration between the Ao and the LV. A noncompliant LV is associated with a faster left ventricular pressure rise causing a steeper AR slope and shorter regurgitant PHT. Also, patients with chronic AR tend to have a more dilated and compliant LV which can accommodate a greater volume of regurgitant blood. Therefore, for the same regurgitant volume, acute AR will have a steeper AR slope and a shorter regurgitant PHT compared with chronic AR (Fig. 15.37). Other conditions leading to

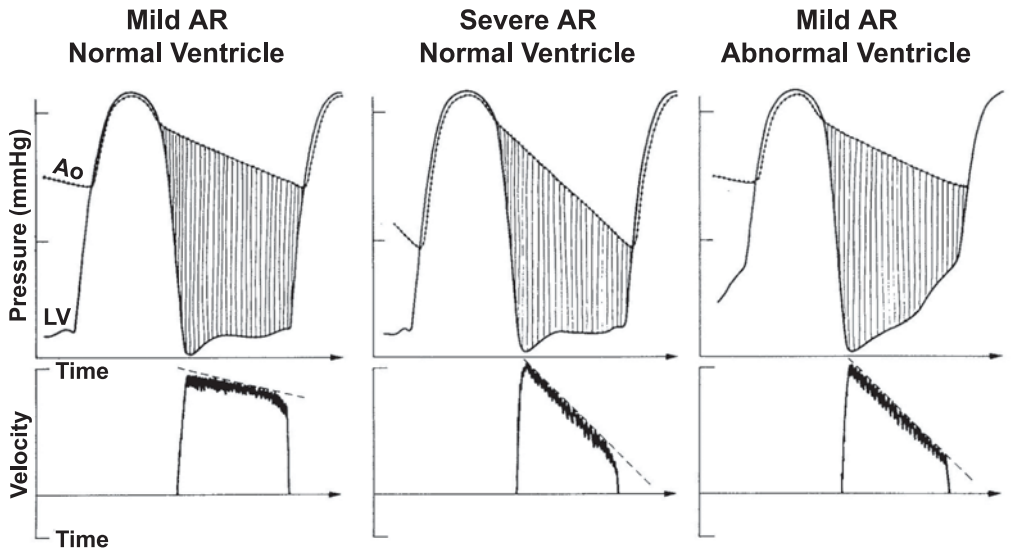

Figure 15.37 Determinants of regurgitant pressure half-time (PHT) in aortic regurgitation (AR). Upper panels: invasively obtained pressure tracings in the aorta (Ao) and in the left ventricle (LV). Lower panels: continuous-wave Doppler tracings across the aortic valve during diastole. The slope of the blood flow velocity corresponds to the fall in the measured pressure gradient between the aorta and the left ventricle. The calculation of PHT with Doppler echocardiography is derived from the rate of decrease in blood flow velocity across the aortic valve in patients with AR. [Reproduced with permission from Obeid (38).]

Table 15.3 Qualitative and Quantitative Parameters Useful in Grading Aortic Regurgitation Severity

	Mild	Moderate		Severe
Structural parameters				
LA size	Normal[a]	Normal or dilated		Usually dilated[b]
Aortic leaflets	Normal or abnormal	Normal or abnormal		Abnormal/flail, or wide coaptation defect
Doppler parameters				
Jet width in LVOT —color flow[c]	Small in central jets	Intermediate		Large in central jets; variable in eccentric jets
Jet density—CW	Incomplete or faint	Dense		Dense
Jet deceleration rate—CW (PHT, ms)[d]	Slow >500	Medium 500–200		Steep <200
Diastolic flow reversal in descending aorta—PW	Brief, early diastolic reversal	Intermediate		Prominent holodiastolic reversal
Quantitative parameters[e]				
VC width, cm[c]	<0.3	0.3–0.60		>0.6
Jet width/LVOT width, %[c]	<25	25–45	46–64	≥65
Jet CSA/LVOT CSA, %[c]	<5	5–20	21–59	≥60
R Vol, mL/beat	<30	30–44	45–59	≥60
RF, %	<30	30–39	40–49	≥50
EROA, cm^2	<0.10	0.10–0.19	0.20–0.29	≥0.30

[a]Unless there are other reasons for LV dilation. Normal 2D measurements: LV minor axis ≤2.8 cm/m^2, LV end-diastolic volume ≤82 mL/m^2 (2).
[b]Exception: would be acute AR, in which chambers have not had time to dilate.
[c]At a Nyquist limit of 50–60 cm/sec.
[d]PHT is shortened with increasing LV diastolic pressure and vasodilator therapy, and may be lengthened in chronic adaptation to severe AR.
[e]Quantitative parameters can subclassify the moderate regurgitation group into mild-to-moderate and moderate-to-severe regurgitation as shown.
Note: AR: aortic regurgitation; CSA, cross-sectional area; CW, continuous-wave Doppler; EROA, effective regurgitant orifice area; LV, left ventricle; LVOT, left ventricular outflow tract; PHT, pressure half-time; PW, pulsed-wave Doppler; R Vol, regurgitant volume; RF, regurgitant fraction; VC, vena contracta.

Table 15.4 Echocardiographic and Doppler Parameters Used in the Evaluation of Aortic Regurgitation Severity: Utility, Advantages, and Limitations

	Utility/Advantages	Limitations
Structural parameters		
LV size	Enlargement sensitive for chronic significant AR, important for outcomes. Normal size virtually excludes significant chronic AR	Enlargement seen in other conditions. May be normal in acute significant AR
Aortic cusp alterations	Simple, usually abnormal in severe AR; flail valve denotes severe AR	Poor accuracy, may grossly underestimate or overestimate the defect
Doppler parameters		
Jet width or jet cross-sectional area in LVOT—color flow	Simple, very sensitive, quick screen for AR	Expands unpredictably below the orifice. Inaccurate for eccentric jets
Vena contracta width	Simple, quantitative, good at identifying mild or severe AR	Not useful for multiple AR jets. Small values; thus small error leads to large % error
PISA method	Quantitative. Provides both lesion severity (EROA) and volume overload (R vol)	Feasibility is limited by aortic valve calcifications. Not valid for multiple jets, less accurate in eccentric jets. Provides peak flow and maximal EROA. Underestimation is possible with aortic aneurysms. Limited experience
Flow quantitation—PW	Quantitative, valid with multiple jets and eccentric jets. Provides both lesion severity (EROA, RF) and volume overload (R vol)	Not valid for combined MR and AR, unless pulmonic site is used
Jet density—CW	Simple. Faint or incomplete jet compatible with mild AR	Qualitative. Overlap between moderate and severe AR. Complementary data only
Jet deceleration rate (PHT)—CW	Simple	Qualitative; affected by changes in LV and aortic diastolic pressures
Diastolic flow reversal in descending aorta—PW	Simple	Depends on rigidity of aorta. Brief velocity reversal is normal

Note: AR, aortic regurgitation; CW, continuous-wave Doppler; EROA, effective regurgitant orifice area; LV, left ventricle; LVOT, left ventricular outflow tract; MR, mitral regurgitation; PHT, pressure half-time; PW, pulsed-wave Doppler; R vol, regurgitant volume; RF, regurgitant fraction; VC, vena contracta width. [With permission of Zoghbi WA et al. (39).]

rapidly rising left ventricular pressure during diastole will also shorten the regurgitant PHT, as in restrictive cardiomyopathy or severe MR.

Quantification of AR remains a diagnostic challenge in some patients. Although a recent study reported that the color jet width had a stronger correlation with angiography than the ratio of jet width to LVOT diameter, the latter index remains the most commonly used method in the echocardiographic evaluation of AR. In the quantification of AR, measurement of flow reversal in the descending thoracic Ao, regurgitant deceleration slope, and pressure half-time are also useful parameters. Conversely, in the operating room, the measurement of regurgitant fraction is less commonly performed because it is time-consuming, and flow through different valves must be measured under the same hemodynamic conditions. Newer approaches, including ERO measurement, vena contracta, and PISA, although promising, are not yet routinely used in clinical practice. A combination of techniques remains the most reasonable approach considering the limitations inherent in each method. The ASE has published guidelines on the evaluation of AR (39). They are summarized in Tables 15.3–15.5.

IV. CONCLUSION

In the assessment of valvular heart disease there are several different methods which are used to quantify and/or qualify the severity of a stenotic or regurgitant

Table 15.5 Application of Specific and Supportive Signs, and Quantitative Parameters in the Grading of Aortic Regurgitation Severity

	Mild	Moderate		Severe
Specific signs for AR severity	Central jet, width <25% of LVOT[a] Vena contracta <0.3 cm[a] No or brief early diastolic flow reversal in descending aorta	Signs of AR > mild present but no criteria for severe AR		Central jet, width ≥65% of LVOT[a] Vena contracta >0.6 cm[a]
Supportive signs	Pressure half-time >500 ms Normal LV size[b]	Intermediate values		Pressure half-time <200 ms Holodiastolic aortic flow reversal in descending aorta Moderate or greater LV enlargement[c]
Quantitative parameters[d]				
R vol, mL/beat	<30	30–44	45–59	≥60
RF, %	<30	30–39	40–49	≥50
EROA, cm^2	<0.10	0.10–0.19	0.20–0.29	≥0.30

[a]At a Nyquist limit of 50–60 cm/sec.
[b]LV size applied only to chronic lesions. Normal 2D measurements: LV minor axis ≤2.8 cm/m^2, LV end-diastolic volume ≤82 mL/m^2 (2).
[c]In the absence of other etiologies of LV dilatation.
[d]Quantitative parameters can help subclassify the moderate regurgitation group into mild-to-moderate and moderate-to-severe regurgitation as shown.
Note: AR, aortic regurgitation; EROA, effective regurgitant orifice area; LV, left ventricle; LVOT, left ventricular outflow tract; R vol, regurgitant volume; RF, regurgitant fraction. [With permission of Zoghbi WA et al. (39).]

valve. There is no single golden echocardiographic measurement in the evaluation of valvular heart disease. Multiple techniques and views should be used to obtain a composite assessment of severity. Accurate echocardiographic evaluation and quantification of AoV pathology are crucial in determining whether or not a patient will have to undergo a surgical intervention. Detailed knowledge of the aortic root anatomy not only allows the physician to understand pathological echocardiographic findings but also provides crucial information in the planning of the surgical procedure for the patient.

ACKNOWLEDGMENTS

Special thanks to Dr. Lawrence Rudski for reviewing this manuscript and his expert advice.

REFERENCES

1. Netter FH, Yonkman FF, Ciba Pharmaceutical Company. Heart a compilation of paintings on the normal and pathologic anatomy and physiology, embryology, and diseases. Summit, N. J: CIBA Pharmaceutical Company, 1978.
2. Cemri M, Cengel A, Timurkaynak T. Pentacuspid aortic valve diagnosed by transoesophageal echocardiography. Heart 2000; 84:E9.
3. Bonow RO, Carabello B, de LA Jr et al. Guidelines for the management of patients with valvular heart disease: executive summary. A report of the American College of Cardiology/American Heart Association Task Force on Practice Guidelines (Committee on Management of Patients with Valvular Heart Disease). Circulation 1998; 98:1949–1984.
4. Otto CM, Burwash IG, Legget ME et al. Prospective study of asymptomatic valvular aortic stenosis. Clinical, echocardiographic, and exercise predictors of outcome. Circulation 1997; 95:2262–2270.
5. Keane MG, Wiegers SE, Plappert T et al. Bicuspid aortic valves are associated with aortic dilatation out of proportion to coexistent valvular lesions. Circulation 2000; 102:III35–III39.
6. Nistri S, Sorbo MD, Basso C, Thiene G. Bicuspid aortic valve: abnormal aortic elastic properties. J Heart Valve Dis 2002; 11:369–373.
7. Quinones MA, Otto CM, Stoddard M et al. Recommendations for quantification of Doppler echocardiography: a report from the Doppler Quantification Task Force of the Nomenclature and Standards Committee of the American Society of Echocardiography. J Am Soc Echocardiogr 2002; 15:167–184.
8. Baumgartner H, Stefenelli T, Niederberger J et al. "Overestimation" of catheter gradients by Doppler ultrasound in patients with aortic stenosis: a predictable manifestation of pressure recovery. J Am Coll Cardiol 1999; 33:1655–1661.
9. Laskey WK, Kussmaul WG. Pressure recovery in aortic valve stenosis. Circulation 1994; 89:116–121.
10. Garcia D, Dumesnil JG, Durand LG et al. Discrepancies between catheter and Doppler estimates of valve effective orifice area can be predicted from the pressure recovery phenomenon: practical implications with regard to quantification of aortic stenosis severity. J Am Coll Cardiol 2003; 41:435–442.

11. Levine RA, Schwammenthal E. Stenosis is in the eye of the observer: impact of pressure recovery on assessing aortic valve area. J Am Coll Cardiol 2003; 41:443–445.
12. VanAuker MD, Chandra M, Shirani J, Strom JA. Jet eccentricity: a misleading source of agreement between Doppler/catheter pressure gradients in aortic stenosis. J Am Soc Echocardiogr 2001; 14:853–862.
13. Cormier B, Iung B, Porte JM et al. Value of multiplane transesophageal echocardiography in determining aortic valve area in aortic stenosis. Am J Cardiol 1996; 77:882–885.
14. Arsenault M, Masani N, Magni G et al. Variation of anatomic valve area during ejection in patients with valvular aortic stenosis evaluated by two-dimensional echocardiographic planimetry: comparison with traditional Doppler data. J Am Coll Cardiol 1998; 32:1931–1937.
15. Perrino AC Jr, Harris SN, Luther MA. Intraoperative determination of cardiac output using multiplane transesophageal echocardiography: a comparison to thermodilution. Anesthesiology 1998; 89:350–357.
16. Maslow AD, Haering JM, Heindel S et al. An evaluation of prosthetic aortic valves using transesophageal echocardiography: the double-envelope technique. Anesth Analg 2000; 91:509–516.
17. Maslow AD, Mashikian J, Haering JM et al. Transesophageal echocardiographic evaluation of native aortic valve area: utility of the double-envelope technique. J Cardiothorac Vasc Anesth 2001; 15:293–299.
18. Kim CJ, Berglund H, Nishioka T et al. Correspondence of aortic valve area determination from transesophageal echocardiography, transthoracic echocardiography, and cardiac catheterization. Am Heart J 1996; 132:1163–1172.
19. Bernard Y, Meneveau N, Vuillemenot A et al. Planimetry of aortic valve area using multiplane transoesophageal echocardiography is not a reliable method for assessing severity of aortic stenosis. Heart 1997; 78:68–73.
20. Tardif JC, Miller DS, Pandian NG et al. Effects of variations in flow on aortic valve area in aortic stenosis based on in vivo planimetry of aortic valve area by multiplane transesophageal echocardiography. Am J Cardiol 1995; 76:193–198.
21. Tardif JC, Rodrigues AG, Hardy JF et al. Simultaneous determination of aortic valve area by the Gorlin formula and by transesophageal echocardiography under different transvalvular flow conditions. Evidence that anatomic aortic valve area does not change with variations in flow in aortic stenosis. J Am Coll Cardiol 1997; 29:1296–1302.
22. Schöbel WA, Voelker W, Haase KK, Karsch KR. Extent, determinants and clinical importance of pressure recovery in patients with aortic valve stenosis. Eur Heart J 1999; 20:1355–1363.
23. Rahimtoola SH. "Prophylactic" valve replacement for mild aortic valve disease at time of surgery for other cardiovascular disease?... No. J Am Coll Cardiol 1999; 33:2009–2015.
24. Kerut EK, McIlwain EF, Plotnick GD. Handbook of Echo-Doppler Interpretation. Armonk, NY: Futura Pub, 1996.
25. Tirone ED. Remodeling the aortic root and preservation of the native aortic valve. Oper Tech Card Thorac Surg 1996; 1:44–56.
26. Movsowitz HD, Levine RA, Hilgenberg AD, Isselbacher EM. Transesophageal echocardiographic description of the mechanisms of aortic regurgitation in acute type A aortic dissection: implications for aortic valve repair. J Am Coll Cardiol 2000; 36:884–890.
27. Perry GJ, Helmcke F, Nanda NC et al. Evaluation of aortic insufficiency by Doppler color flow mapping. J Am Coll Cardiol 1987; 9:952–959.
28. Oh JK, Seward JB, Tajik AJ. The Echo Manual. 2nd ed. Philadelphia: Lippincott Williams & Wilkins, 1999.
29. Evangelista A, del Castillo HG, Calvo F et al. Strategy for optimal aortic regurgitation quantification by Doppler echocardiography: agreement among different methods. Am Heart J 2000; 139:773–781.
30. Ozkan M, Ozdemir N, Kaymaz C et al. Measurement of aortic valve anatomic regurgitant area using transesophageal echocardiography: implications for the quantitation of aortic regurgitation. J Am Soc Echocardiogr 2002; 15:1170–1174.
31. Tribouilloy CM, Enriquez-Sarano M, Fett SL et al. Application of the proximal flow convergence method to calculate the effective regurgitant orifice area in aortic regurgitation. J Am Coll Cardiol 1998; 32:1032–1039.
32. Sato Y, Kawazoe K, Nasu M, Hiramori K. Clinical usefulness of the proximal isovelocity surface area method using echocardiography in patients with eccentric aortic regurgitation. J Heart Valve Dis 1999; 8:104–111.
33. Kim YJ, Jones M, Shiota T et al. Effect of load alterations on the effective regurgitant orifice area in chronic aortic regurgitation. Heart 2002; 88:397–400.
34. Ishii M, Jones M, Shiota T et al. Quantifying aortic regurgitation by using the color Doppler-imaged vena contracta: a chronic animal model study. Circulation 1997; 96:2009–2015.
35. Willett DL, Hall SA, Jessen ME et al. Assessment of aortic regurgitation by transesophageal color Doppler imaging of the vena contracta: validation against an intraoperative aortic flow probe. J Am Coll Cardiol 2001; 37:1450–1455.
36. Eren M, Eksik A, Gorgulu S et al. Determination of vena contracta and its value in evaluating severity of aortic regurgitation. J Heart Valve Dis 2002; 11:567–575.
37. Tribouilloy CM, Enriquez-Sarano M, Bailey KR et al. Assessment of severity of aortic regurgitation using the width of the vena contracta: a clinical color Doppler imaging study. Circulation 2000; 102:558–564.
38. Obeid AI. Echocardiography in Clinical Practice. Philadelphia: JB Lippincott Company, 1992.
39. Zoghbi WA, Enriquez-Sarano M, Foster E et al. Recommendations for evaluation of the severity of native valvular regurgitation with two-dimensional and Doppler echocardiography. J Am Soc Echocardiogr 2003; 16:777–802.

16

Perioperative Evaluation of Aortic Valve Surgery

JEAN G. DUMESNIL, PHILIPPE PIBAROT
Laval University, Quebec City, Canada

I. Surgical Indications for Aortic Valve Replacement 363
A. Surgical Indications for Aortic Valve Stenosis 363
1. Asymptomatic Patients 363
2. Symptomatic Patients 364
3. Patients Undergoing Cardiac Surgery 364
B. Surgical Indications for Aortic Regurgitation 365
II. Type of Operation 365
III. Avoiding Patient–Prosthesis Mismatch 365
IV. Choice of Operation in Patients with Left Ventricular Dysfunction 368
V. Echocardiography in the Operating Room 369
A. Before Operation 369
B. During Cardiopulmonary Bypass 370
C. After Cardiopulmonary Bypass 370
VI. Echocardiographic Technique 376
VII. Echocardiography in the Immediate Postoperative Period 377
References 380

I. SURGICAL INDICATIONS FOR AORTIC VALVE REPLACEMENT

In 1998, the American College of Cardiology (ACC) and the American Heart Association (AHA) established guidelines for the management of patients with valvular heart disease (1). Three categories were established to indicate the weight of evidence supporting the current recommendations.

Class I: Conditions for which there is evidence and/or general agreement that a given procedure or treatment is useful and effective.
Class II: Conditions for which there is conflicting evidence and/or divergence of opinion about the usefulness/efficacy of a procedure or treatment.
Class IIa: Weight of evidence or expert opinion is in favor of usefulness/efficacy.
Class IIb: Usefulness/efficacy is less well established by evidence/opinion.
Class III: Conditions for which there is evidence and/or general agreement that the procedure is not useful and in some cases may be harmful.

A. Surgical Indications for Aortic Valve Stenosis (Table 16.1)

1. Asymptomatic Patients

Asymptomatic patients with severe aortic stenosis (AS) have a 2–3% per year incidence of serious complications while death related to aortic prosthesis occurs at a rate of ~1% per year. However, when the operative morbidity

Table 16.1 Surgical Indications for Patients with Aortic Stenosis (AS) (1)

Class 1	Symptomatic patients with severe AS Patients with severe AS undergoing coronary artery bypass surgery Patients with severe AS undergoing surgery on the aorta or other heart valves
Class 2a	Patients with moderate AS undergoing coronary artery bypass surgery or surgery on the aorta or other heart valves Asymptomatic patients with severe AS and: a. left ventricular systolic dysfunction b. abnormal response to exercise (e.g. hypotension)
Class 2b	Asymptomatic patients with severe AS and: a. ventricular tachycardia b. marked or excessive left ventricular hypertrophy (wall thickness >15 mm) c. valve area $<0.6\ cm^2$
Class 3	Prevention of sudden death in asymptomatic patients with none of the above findings

and mortality is combined with the late complication rate of prosthetic aortic valve replacement (AVR), there is no benefit in survival or outcome. The current recommendations are, therefore, to delay surgery in patients with severe asymptomatic AS until they develop left ventricular systolic dysfunction or an abnormal response to exercise (e.g. hypotension). The development of left ventricular hypertrophy (wall thickness ≥ 15 mm), ventricular tachycardia or an aortic valve area (AVA) $<0.6\ cm^2$ are weaker indications for proceeding with AVR (Table 16.1).

Recent data suggest that the rate of progression of AS might also become an important consideration in establishing the indications for surgery. Indeed, Rosenhek et al. (2) have shown that in asymptomatic patients with severe AS (defined as maximal aortic velocity $>4.0\ m/s$) and concomitant moderate calcifications of the valve and a $>0.3\ m/s$ increase in velocity per year, the chance of undergoing valve replacement or dying within four years was $>80\%$. Consideration should be given for early valve replacement in this subgroup of patients. Amongst the Doppler-echocardiographic criteria presently used to define severe AS (1–3) are a valve area $<1.0\ cm^2$, an indexed valve area $<0.6\ cm^2/m^2$, a mean gradient >40–50 mmHg and a maximal velocity >4.0–$4.5\ m/s$ (i.e. a maximal gradient >65–80 mmHg).

2. *Symptomatic Patients*

In the absence of serious comorbid disease, patients with severe AS and concomitant angina, syncope, congestive heart failure, or dyspnea should undergo AVR. Survival is improved by surgery even in patients with severe left ventricular dysfunction and low gradient severe AS, unless the left ventricular dysfunction is irreversible.

3. *Patients Undergoing Cardiac Surgery*

Patients with severe AS undergoing other cardiac surgery (revascularization) should have their aortic valve (AoV) replaced even if they are not symptomatic for AS and have no evidence of left ventricular dysfunction. The evidence also favors proceeding with AVR in patients with moderate AS who are scheduled to have cardiac surgery for other pathology. In the 1998 guidelines published by the ACC and the AHA, moderate AS is defined with an AVA of 1.1–$1.5\ cm^2$. However, a subsequent editorial by Rahimtoola (4), one of the committee members on the task force, recommended a slightly more conservative approach, suggesting AVR only if the AVA is more severe at 1.0–$1.3\ cm^2$ or 0.60–$0.75\ cm^2/m^2$. The AVA indexed to the body surface area may help the decision in borderline cases involving larger or smaller than average patients.

Table 16.2 Surgical Indications in Chronic Severe Aortic Regurgitation (AR) (1)

Class 1	1. Symptomatic patients with NYHA III–IV and preserved systolic function (LVEF $\geq 50\%$) 2. NYHA II and LVEF $>50\%$ but with either a. progressive LV dilatation b. declining ejection fraction at rest on serial echocardiogram c. declining effort tolerance on exercise testing 3. Asymptomatic patients with EF 25–49% at rest 4. Canadian Heart Association class II angina with or without CAD 5. Patients undergoing coronary artery bypass surgery or surgery on other heart valves
Class 2a	1. NYHA II and preserved systolic function (LVEF $\geq 50\%$) and stable LV size and exercise tolerance 2. Asymptomatic patients with LVEF $>50\%$ and severe LV dilatation (LVEDD >75 mm or LVESD >55 mm)
Class 2b	1. Severe LV dysfunction (LVEF $<25\%$) 2. Asymptomatic patients with LVEF $>50\%$ and LVEDD 70–75 mm or LVESD 50–55 mm 3. Asymptomatic patients with LVEF $>50\%$ but decline in LVEF during a. exercise radionuclide angiography b. stress echocardiography
Class 3	Asymptomatic patients and LVEF $>50\%$ and LVEDD <70 mm and/or LVESD <50 mm

Note: CAD, coronary artery disease; LVEDD, left ventricular end-diastolic diameter; LVEF, left ventricular ejection fraction; LVESD, left ventricular end-systolic diameter; NYHA, New York Heart Association.

B. Surgical Indications for Aortic Regurgitation (Table 16.2)

According to the ACC/AHA recommendations in the evaluation of patients with chronic isolated aortic regurgitation (AR), only those in whom it is severe should be considered for AVR (1). The following recommendations, therefore only apply to those patients with severe AR. More than 25% of patients with severe AR who develop left ventricular dysfunction or die have no warning symptoms, emphasizing the importance of close follow-up. Appropriate timing of AVR is difficult, but in patients with symptoms attributable to severe AR, the mortality rate approaches 10% per year and these patients should undergo AVR even in the absence of left ventricular dysfunction or significant left ventricular dilatation. In asymptomatic patients, the discovery of either left ventricular dysfunction or significant left ventricular dilatation [defined as a left ventricular end-diastolic dimension (LVEDD) >75 mm and/or a left ventricular end-systolic dimension (LVESD) >55 mm] is a class IIa indication for AVR (1). Fortunately, left ventricular systolic dysfunction is initially a reversible phenomenon, and full recovery of left ventricular function and left ventricle (LV) size following AVR is possible if surgery is performed within the first 12 months.

II. TYPE OF OPERATION

When AR is due to annuloaortic ectasia with preserved valve morphology, repair of the aorta (Ao) with valve sparing can be attempted. Otherwise, the operation consists of valve replacement and the choice of prosthesis is mostly decided on the basis of age and the expected freedom of structural failure of the prosthesis being implanted. However, other considerations such as level of physical activity (e.g. involvement in competitive sports) and underlying pathology (e.g. endocarditis) (Fig. 16.1) are also taken into account. Hence, characteristically in the 20–40 years age group, the choices are a pulmonary autograft (Ross operation), a homograft, or a mechanical prosthesis; in the 41–64 years old group, a pulmonary autograft, a stentless porcine bioprosthesis, a homograft, or a mechanical prosthesis and in the 65 years or older group, either a stented porcine or pericardial bioprosthesis, a stentless porcine bioprosthesis or a homograft. Nevertheless, these options must not be considered as hermetic and the final decision is made after discussion between the surgeon and the patient with regard to the risks and advantages of each type of prosthesis. Moreover, our knowledge regarding the performance and durability of this prosthesis is continually evolving. For instance, it has been well demonstrated that pulmonary autografts have an excellent performance rate and very long durability and up until recently, notwithstanding the availability of the pulmonary homograft necessary for the performance of this procedure, it was almost considered the ideal operation. However, initial enthusiasm has been somewhat dampened by the recent demonstration that the pulmonary autograft can rapidly degenerate and become stenotic in up to 20% of patients who underwent this operation (5). On the other hand, based on experimental results and a few valve explants, it is anticipated that the bioprosthesis submitted to newer antimineralisation treatments such as α-aminoleic acid will have a much better longevity and should thus become suitable for implantation in younger age groups (6).

III. AVOIDING PATIENT–PROSTHESIS MISMATCH

The anticipated hemodynamics of the prosthesis being implanted is another consideration when choosing the type of valve replacement to be performed in a given patient. Recent evidence has shown that suboptimal postoperative hemodynamics may occur in up to 70% of patients being operated on depending on the type of prosthesis being used and that this may have a direct impact on short- and long-term survival as well as on the improvement of functional class (7–11). Figure 16.2 is an example of a patient with severe patient–prosthesis mismatch with symptoms of severe AS. Notwithstanding the rare occurrence of intrinsic prosthesis dysfunction, a suboptimal postoperative course is usually due to patient–prosthesis mismatch, that is, that the effective orifice area of the prosthesis being implanted is less than that of the normal human valve and too small to ensure optimal hemodynamics. In this context, it should be emphasized that different types of prosthesis usually have different hemodynamic profiles depending largely on the proportion of the valvular area occupied by the supporting apparatus of the prosthesis rather than by flow, and to a lesser degree, by the opening dynamics of the prosthesis. Therefore, size for size, autografts and homografts have the best hemodynamic profile as evidenced by larger postoperative effective orifice areas and lower gradients (Fig. 16.3); they are followed in decreasing order by stentless bioprostheses, mechanical prostheses and stented bioprostheses. There is general agreement that the postoperative indexed effective orifice area (EOA) of the prosthesis being implanted should not be $<0.85–0.90\ cm^2/m^2$ and it has been suggested (7) that the algorithm described next should be followed in the operating room (OR) in order to achieve this goal (Fig. 16.4):

1. Calculate body surface area (BSA) from patient's body height and weight using the formula of

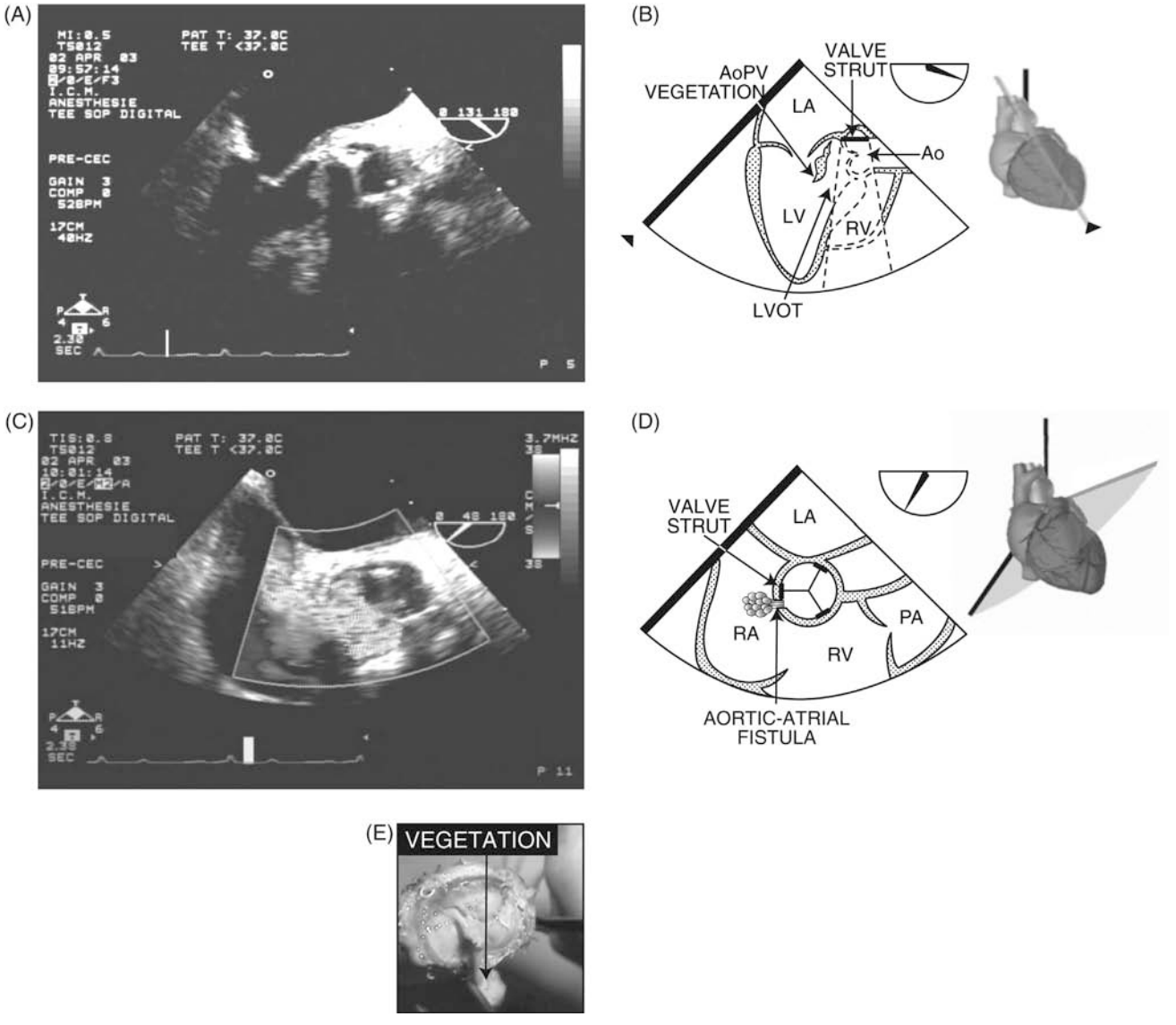

Figure 16.1 Aortic valve bioprosthesis endocarditis in an 83-year-old man. (A, B) A mobile mass was seen in the mid-esophageal long-axis view. (C, D) Furthermore, a fistula between the aorta (Ao) and the right atrium (RA) was present. (E) Intraoperative findings: the mobile mass was a vegetation attached to the inferior aspect of the aortic bioprosthetic valve (AoPV) (LA, left atrium; LV, left ventricle, LVOT: left ventricular outflow tract; PA, pulmonary artery; RA, right atrium; RV, right ventricle). (Photo E courtesy of Dr. Denis Bouchard.)

Dubois and Dubois {BSA = [(Weight kg)$^{0.425}$ × (Height cm)$^{0.725}$] × 0.007184} or the charts derived from that formula.

2. Determine the minimal EOA that the prosthesis being implanted must have in order to avoid mismatch; this is accomplished by multiplying the desired objective for the postoperative indexed EOA (e.g. 0.85 cm^2/m^2) by the patient's BSA. Therefore, if the patient's BSA is 1.53 m^2, the minimal EOA that the prosthesis being implanted should have in order to avoid mismatch is 1.53 m^2 multiplied by 0.85 cm^2/m^2, that is, 1.30 cm^2 (Fig. 16.5).
3. The prosthesis is then chosen using the published reference values of EOA for different types and sizes of prostheses (Table 16.3). To follow the aforementioned example, if one had chosen to insert a Carpentier–Edwards pericardial bioprosthesis, the minimal size that should be utilized to yield the desired objective of 1.30 cm^2 should be a #21 (Fig. 16.5).
4. The aortic annulus diameter is measured at the base of the aortic leaflet. Therefore, if the patient's annulus accepted only a size #19, as may be the case in patients with a small aortic annulus

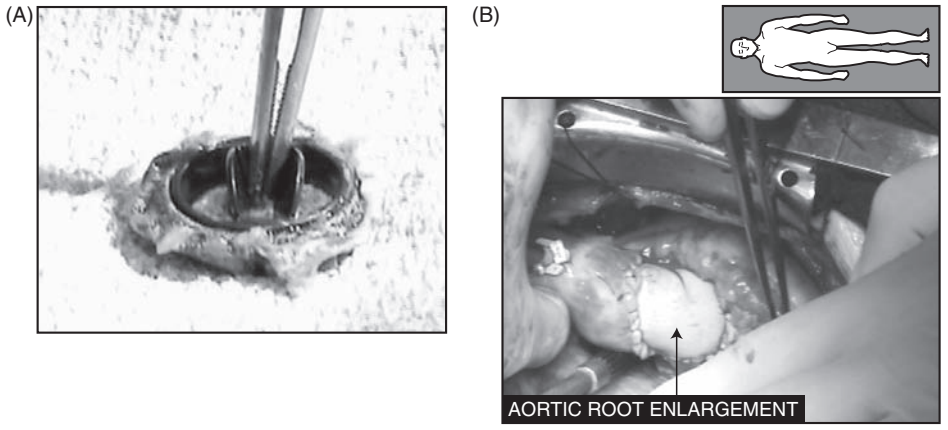

Figure 16.2 Patient–prosthesis mismatch. (A) A 71-year-old man with a body surface area of 1.89 m^2 was re-operated on for symptoms of severe aortic valve stenosis (severe dyspnea, New York Heart Association class IV and pulmonary hypertension of 60/15 mmHg). He had aortic valve replacement 4 years ago with a Carbomedics #19 mechanical bileaflet prosthesis [effective orifice area (EOA) = 1.06 cm^2]. The preoperative mean gradient was 41 mmHg. The intraoperative aspect of the valve was completely normal. (B) Example of an aortic root enlargement procedure in a 69-year-old patient with a reduced aortic diameter requiring aortic valve replacement. (Courtesy of Dr. Michel Carrier.)

associated with calcific AS, the available options to avoid mismatch would have been either to perform an additional aortic root enlargement procedure to accommodate the #21 prosthesis or to use another type of prosthesis with a better hemodynamic profile (e.g. a stentless bioprosthesis or a mechanical valve) (Table 16.3).

Castro et al. (21) prospectively used this strategy in 657 patients whereby an aortic root enlargement was performed whenever the indexed EOA, using steps 1 and 2 of the algorithm, was projected to be <0.85 cm^2/m^2. As a result, the overall incidence of mismatch in their population was only 2.5% instead of the 17% that would have occurred had this prospective strategy not been used. Moreover, operative mortality was not increased as a result of the additional aortic root enlargement procedure (overall mortality = 3.6%). It must be noted that aortic root enlargement was performed with a novel technique using the insertion of a patch made of Dacron. These results demonstrate that a prospective strategy to avoid mismatch can easily be applied with success. It should also be emphasized that the information necessary to do the calculation is readily available as it requires only patient's height, weight, and the EOA reference values for the different types and sizes of prosthesis being contemplated for the operation. The latter information should be provided by the manufacturers and can easily be found in the literature (Table 16.3). In this regard, there are however three caveats worth mentioning: (1) the values should be derived from *in vivo* rather than *in vitro* data as the latter are usually too optimistic,

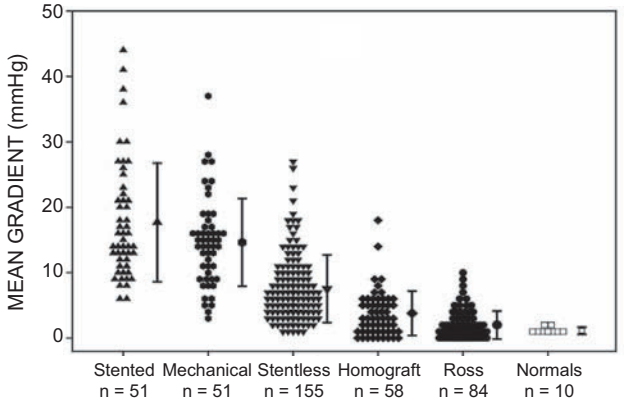

Figure 16.3 Comparison between mean gradients and type of valve prosthesis used for aortic valve replacement.

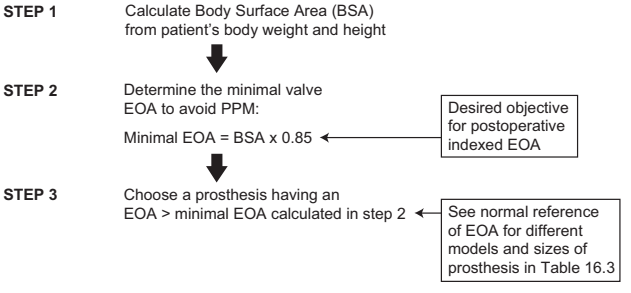

Figure 16.4 Three easy steps to avoid patient–prosthesis mismatch (PPM) (EOA, effective orifice area). [Reproduced with permission from Pibarot and Dumesnil (12).]

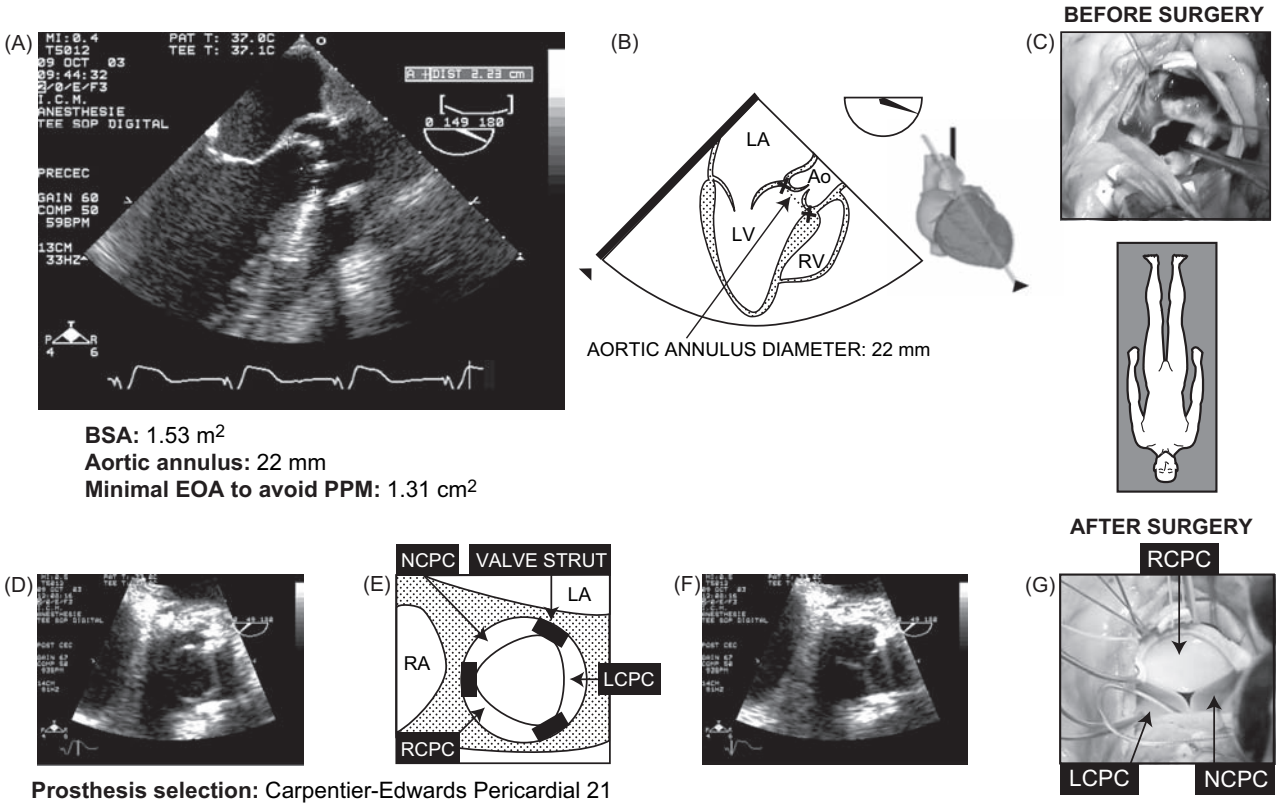

Figure 16.5 A 70-year-old man is scheduled for aortic valve replacement. His body surface area (BSA) is 1.53 m^2. (A, B) The aortic annulus measurement (22 mm) is performed in the long-axis mid-esophageal view. The minimal effective orifice area (EOA) required to avoid patient–prosthesis mismatch (PPM) should be higher than 1.53 $m^2 \times 0.85\ cm^2/m^2$ or 1.30 cm^2. (C) The intraoperative aspect of the valve is shown. (D–F) The selected prosthesis was a Carpentier–Edwards Pericardial 21 with an EOA of 1.30 cm^2. (G) Intraoperative (inverted view) aspect of the bioprosthesis. Note that the prosthetic valve cusps are positioned similarly to the native aortic valve (Ao, aorta; LA, left atrium; LCPC, left coronary prosthetic cusp; LV, left ventricle; NCPC, non-coronary prosthetic cusp; RCPC, right coronary prosthetic cusp; RA, right atrium; RV, right ventricle). (Photos C and G courtesy of Dr. Denis Bouchard.)

particularly in the case of stentless valves; (2) values derived from geometric measurements (e.g. internal diameters or geometric areas) are totally inadequate as they do not predict postoperative gradients (12); (3) caution should, nevertheless, be exercised when new data are published, a case in point being the recently reported values for the Carpentier–Edwards prosthesis (22), which appear much more optimistic and not consistent with values reported from other centers (22,23).

Notwithstanding these considerations, and as endorsed by the Canadian Consensus Conference on Heart Valve Surgery, the calculation of the projected indexed EOA should become an integral part of the decision process leading to the choice of a particular type and size of prosthesis and, in this context, it should ideally be performed in the OR as it is only at that time that the aortic annulus diameter can best be measured accurately. As stated, the ideal objective is that the prosthesis has an indexed EOA $>0.85\ cm^2/m^2$ after operation but lower values may be acceptable in a less active and/or older population.

IV. CHOICE OF OPERATION IN PATIENTS WITH LEFT VENTRICULAR DYSFUNCTION

Recent evidence suggests that prosthesis size and the avoidance of patient–prosthesis mismatch should be an even greater consideration in patients with left ventricular dysfunction as these may increase perioperative mortality. Indeed, Connolly et al. (24) have reported an operative mortality of 47% in patients with severe AS and low ejection fraction (<35%) receiving a small size prosthesis (≤21 mm) compared with 15% in the same category of patients receiving a larger size (>21 mm) prosthesis. Subsequent studies (8,25) also suggest that patients with more than moderate (EOA $<0.75\ cm^2/m^2$) or severe

Table 16.3 Normal Reference Values of Effective Orifice Areas for the Prosthetic Valves

	Prosthetic valve size (mm)						
	19	21	23	25	27	29	Reference
Stented bioprosthetic valves							
Medtronic Mosaic	1.20	1.22	1.38	1.65	1.80	2.00	(13)
Hancock II	–	1.18	1.33	1.46	1.55	1.60	(7)
Carpentier–Edwards Perimount	1.10	1.30	1.50	1.80	1.80	–	(7)
Stentless bioprosthetic valves							
Medtronic Freestyle	1.15	1.35	1.48	2.00	2.32	–	(7)
St. Jude Medical Toronto SPV	–	1.30	1.50	1.70	2.00	2.50	(7)
Prima Edwards	0.80	1.10	1.50	1.80	2.30	2.80	
Mechanical valves							(14)
Medtronic–Hall	1.19	1.34	–	–	–	–	(15)
St. Jude Medical Standard	1.04	1.38	1.52	2.08	2.65	3.23	(7)
St. Jude Medical HP	1.30	2.01	–	–	–	–	(16,17)
St. Jude Medical Regent	1.60	2.00	2.20	2.50	3.60	4.40	(18)
MCRI On-X	1.50	1.70	2.00	2.40	3.20	3.20	(19)
Carbomedics	1.00	1.54	1.63	1.98	2.41	2.63	(7)
Sorin Bicarbon	–	1.66	1.96	–	–	–	(20)

Note: Effective orifice area is expressed as mean values available in the literature.
Source: Reproduced and modified with permission from Cardiac Surgery Today (12).

(EOA $<0.65\ cm^2/m^2$) mismatch have a much greater risk of not surviving the perioperative period than patients without these characteristics. Recently reported data from the Quebec Heart Institute/Laval Hospital (10) in a series of 1266 consecutive patients undergoing AoV replacement also show a perioperative mortality of 67% in patients with the combined evidence of severe mismatch and an ejection fraction $<40\%$ compared with 3% in patients with no mismatch and ejection fraction $>40\%$, intermediate mortality rates being observed in the other subgroups (Fig. 16.6). These are indeed very compelling data suggesting that avoidance of potential mismatch should become a mandatory consideration in patients with left ventricular dysfunction. From the standpoint of physiopathology, it would also make sense to consider that these patients have a decreased ventricular reserve and are thus more vulnerable to the different degrees of mismatch, particularly in the critical perioperative period.

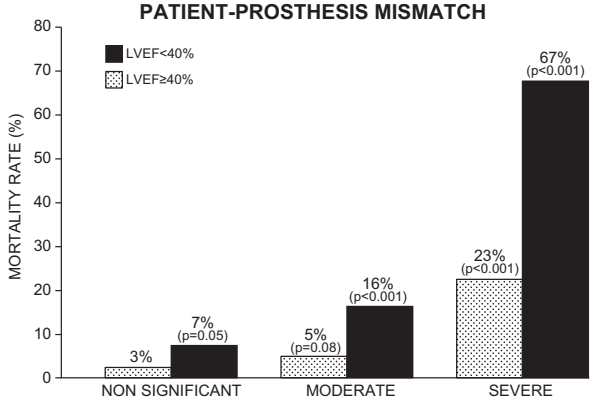

Figure 16.6 In-hospital mortality according to patient–prosthesis mismatch and preoperative left ventricular ejection fraction (LVEF). The *p* values above the bars correspond to the comparison with the group with nonsignificant mismatch and normal LVEF. [Adapted from Blais et al. (10).]

V. ECHOCARDIOGRAPHY IN THE OPERATING ROOM

A. Before Operation

Before cardiopulmonary bypass (CPB), intraoperative transesophageal echocardiography (TEE) can be used to confirm the diagnosis as well as establish the status of left ventricular function. It should not however be seen as a substitute for a good preoperative transthoracic or transesophageal echocardiogram (depending on the indication). A significant intraoperative decrease in ventricular function should be worrisome even if it was preoperatively evaluated as being adequate. Indeed, deterioration in the intervening period may be the first manifestation of a left ventricular myocardium with limited reserve. As stated previously, it will be even more important in such cases to implement a preventive strategy to avoid patient–prosthesis mismatch as it may have an important impact on perioperative mortality. Other preoperative information may also be relevant before the procedure.

This includes the evaluation of the presence of fistulas in patients with endocarditis (Fig. 16.1), the evaluation of diastolic function (26), right ventricular function in patients with pulmonary hypertension (27), and the exclusion of conditions such as mitral regurgitation (MR) (Fig. 16.7) and patent foramen ovale that could complicate the postoperative course.

B. During Cardiopulmonary Bypass

Details of echocardiography during cardiopulmonary bypass are given in Chapter 13.

C. After Cardiopulmonary Bypass

The first concern will be to monitor the ventricular function to ensure that the myocardium is recuperating properly and that a satisfactory cardiac output (CO) is generated. The next step will be to examine valve morphology. Mechanical and stented bioprostheses are very echogenic and it may be difficult to image occluders and leaflets in a short- or long-axis view. Indirect evidence of bileaflet motion can sometimes be inferred from the reverberation artefacts associated with leaflet opening and closing. Alternatively, when one of the two leaflets is immobile, color flow Doppler may reveal an asymmetric color flow signal. The presence of an unexpectedly high gradient across an aortic mechanical prosthesis should prompt further evaluation and may suggest a dysfunctional leaflet fixed in closed position. Dehiscence of the prosthesis may be suggested by abnormal rocking motion of the sewing ring and important perivalvular AR on color flow imaging. Bioprosthetic valves can usually be imaged in the short-axis view and are rarely associated with malfunction unless they are inadvertently damaged during implantation or are dysfunctional (Fig. 16.8). On the other hand, because of the absence of a rigid armature, there is wider variation in the morphology of stentless prostheses and homografts. These valvular substitutes may be implanted following a variety of techniques which, for our purposes, can be classified into two general categories:

1. The prosthesis is implanted as a root replacement in which case the native aortic root is replaced by the porcine aortic root, and requires the coronary arteries to be sectioned and reimplanted on the prosthetic root.
2. The porcine AoV and part of the porcine Ao are implanted within the patient's Ao using two suture lines one proximal to the valve and one distal to the valve. There are three variations of the latter technique: complete subcoronary

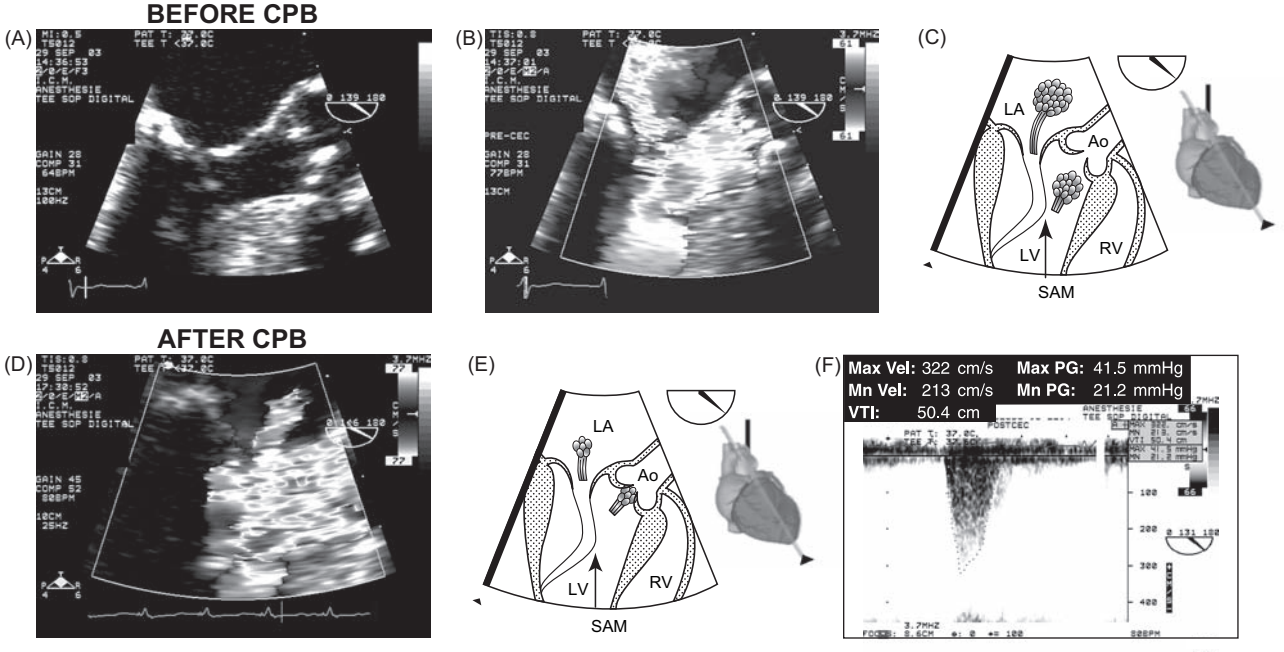

Figure 16.7 (A–C) Mid-esophageal long-axis view in an 82-year-old woman with preoperative systolic anterior motion (SAM) of the mitral valve and mitral regurgitation before aortic valve replacement. (D, E) After aortic valve replacement and septal myectomy, the SAM was still present but associated with less severe mitral regurgitation and a mean subvalvular gradient of 21 mmHg. (F) (Ao, aorta; CPB, cardiopulmonary bypass; LA, left atrium; LV, left ventricle; Max, maximum; Mn, mean; PG, pressure gradient; RV, right ventricle; Vel, velocity; VTI, velocity–time integral).

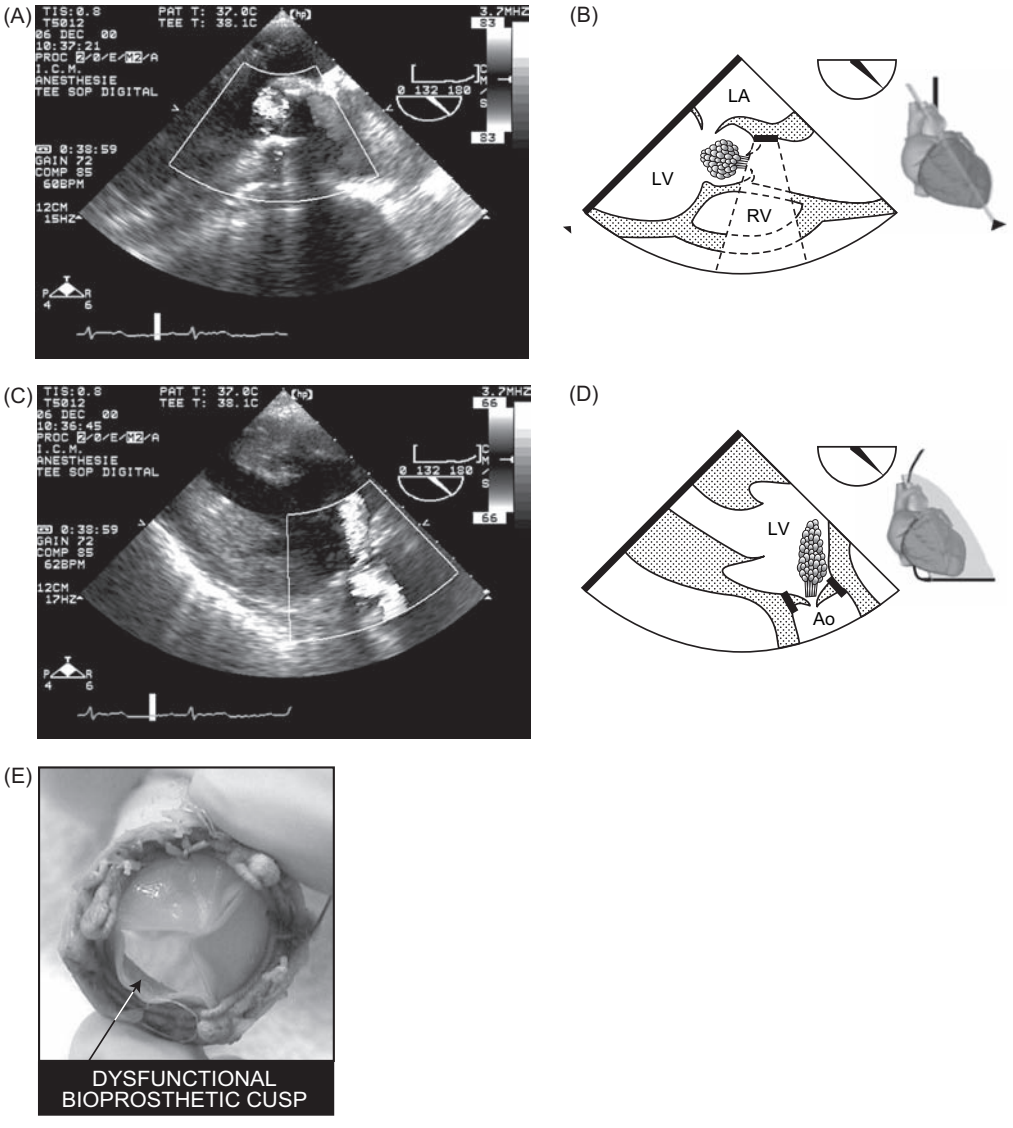

Figure 16.8 A 60-year-old man reoperated on for periprosthetic aortic regurgitation (AR). A bioprosthetic valve was inserted. (A–D) However, after the procedure, abnormal significant AR is still visible on the mid-esophageal long-axis and deep transgastric views. The bioprosthesis was replaced. (E) Upon examination of the defective prosthesis, abnormal motion of one of the leaflets was noted (Ao, aorta; LA, left atrium; LV, left ventricle; RV, right ventricle). (Photo E courtesy of Dr. Tack Ki Leung.)

insertion, root inclusion, or modified subcoronary insertion (Fig. 16.9). The inclusion techniques will usually result in the formation of a virtual space between the prosthesis and the patient's Ao in which blood and/or debris may accumulate: this may appear as an echo-free space encircling the valve (Fig. 16.10). Unless this echo-free space is very large or causes significant deformation of the valve geometry, the finding should be considered as normal and it invariably regresses within the first few months after the operation. The regression of this perivalvular space may also explain the improvement in valve EOA and gradients observed within the first few months after operation with this type of prosthesis (6). When interpreting these images, one must, nevertheless, be attentive to a possible deformation or "crimping" of the valve that may occur when the surgeon is overzealous in attempting to oversize the valve. If in doubt, measurement of the transvalvular velocity should be performed to ensure the absence of abnormal obstruction to flow. In evaluating the structural integrity of stentless prostheses, a flap corresponding to a partial dehiscence of one of the suture lines may be encountered but this is rare.

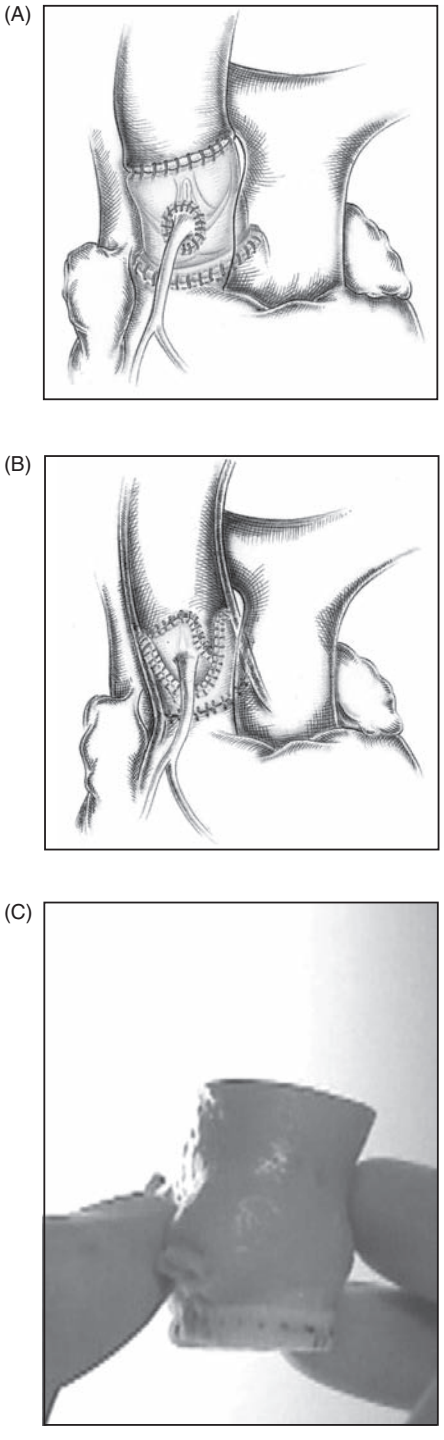

Figure 16.9 Aortic valve replacement with a stentless Freestyle™ bioprosthesis. (A) Full root technique. After excising the native valve and sinus walls, the coronary arteries are excised from the aorta and reattached to the buttonholes of the bioprosthesis. An end-to-end anastomosis attaches the bioprosthesis to the ascending aorta. (B) Modified subcoronary technique. The noncoronary sinus of the bioprosthesis is maintained, and right and left sinuses are scalloped. (C) Freestyle™ bioprosthesis. (A & B Courtesy of Medtronic Inc.)

The next priority, after having examined the morphology of the valve, is to determine the presence or absence of any valvular regurgitation and its severity. In the case of mechanical prostheses, small jets of transvalvular regurgitation within the prosthesis may be normally observed: two in the case of tilting disk prostheses (e.g. Medtronic-Hall) or three in bileaflet prostheses (e.g. St-Jude or On-X). These jets, also known as closing volumes, occur as the result of the normal necessary space between the occluder(s) and the sewing ring without which jamming of these parts would occur. The inexperienced observer should not be alarmed by these jets, which at times may even appear moderate (2+) particularly when the jets are superimposed. Small perivalvular jets of regurgitation may also be observed with all types of prosthesis. In this context, it should be emphasized that echocardiography is a very sensitive technique and will detect even minute amounts of regurgitation. Such small jets are a frequent occurrence. Some will significantly decrease after the injection of protamine before CPB weaning (28,29) and will often disappear in the days, weeks, or months after the operation as the healing process evolves (Fig. 16.11). More important regurgitation is rare and is most often due to a technical problem after insertion of a stentless prosthesis or an homograft. It may be either periprosthetic or centrovalvular and more than 1+ regurgitation usually requires returning to CPB for immediate correction (Fig. 16.12).

It is not always possible to obtain accurate measurements of intraoperative gradients and they are usually not necessary with mechanical prosthesis or stented bioprosthesis as there is no immediate reason for these prostheses to malfunction. However, such measurements may become more relevant in the case of stentless prostheses, homografts, or autografts especially if the two-dimensional (2D) images suggest some inherent technical problem (e.g. perivalvular hematoma and/or crimping of the valve).

If a high gradient is noticed in the operating room, one must first determine whether or not it is partially or principally related to a high flow velocity in the left ventricular outflow tract (LVOT). In particular, relief of the valvular obstruction in patients operated on for AS may result in some remodeling and temporary narrowing of the LVOT. The administration of inotropic agents upon coming off CPB may also contribute to this phenomenon. Notwithstanding these considerations, the most frequent cause of high postoperative gradients is patient–prosthesis mismatch as it may occur in up to 70% of cases (7), depending on the type of prosthesis being implanted. It is much less likely to occur if the aforementioned prospective strategy was followed (Fig. 16.4). If not, its presence may easily be confirmed by going through the same algorithm after the fact, that is, dividing the reference

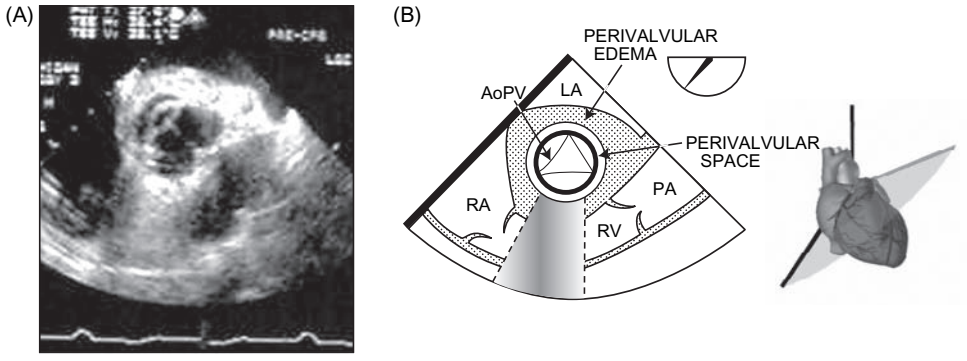

Figure 16.10 Intraoperative transesophageal echocardiogram of stentless prosthesis showing perivalvular echo-free space caused by accumulation of blood and/or debris. This space usually regresses within a few months after operation (AoPV, aortic prosthetic valve; LA, left atrium; PA, pulmonary artery; RA, right atrium; RV, right ventricle). (Courtesy of Dr. David Bach, University of Michigan.)

value of the EOA of the prosthesis having been implanted by the body surface area of the patient to yield the indexed EOA (Fig. 16.13). In patients with normal CO, postoperative gradients are directly related to the indexed EOA and become progressively higher as this value becomes lower. Therefore, an indexed EOA $<0.85\ cm^2/m^2$ is considered mild/moderate mismatch whereas a value $<0.65\ cm^2/m^2$ corresponds to severe mismatch. In patients with high gradients and an indexed EOA $<0.85\ cm^2/m^2$, consideration should be given to reintervening to implant a

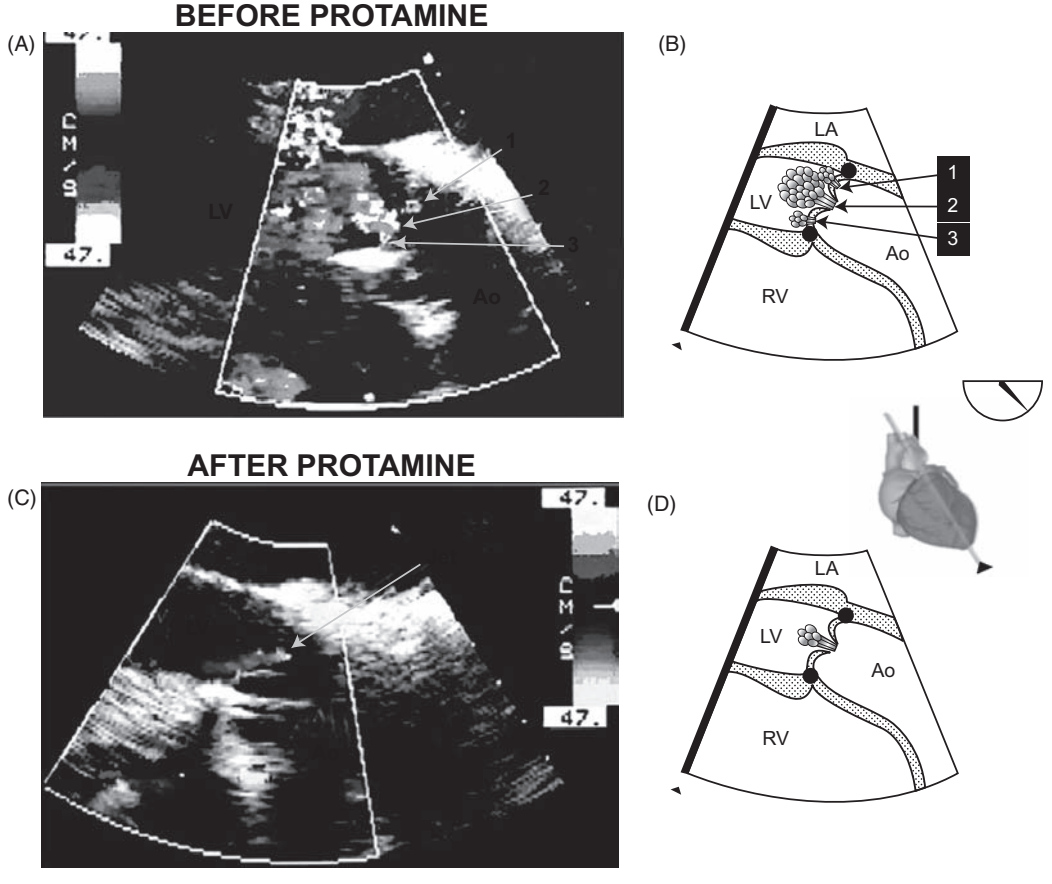

Figure 16.11 Intraoperative transesophageal echocardiographic exam of an aortic prosthesis imaged in the 130° plane demonstrating three regurgitant jets (A, B) before and one jet after protamine (C, D) (Ao, Aorta; LA, left atrium; LV, left ventricle; RV, right ventricle). [Adapted with permission from Morehead et al. (29).]

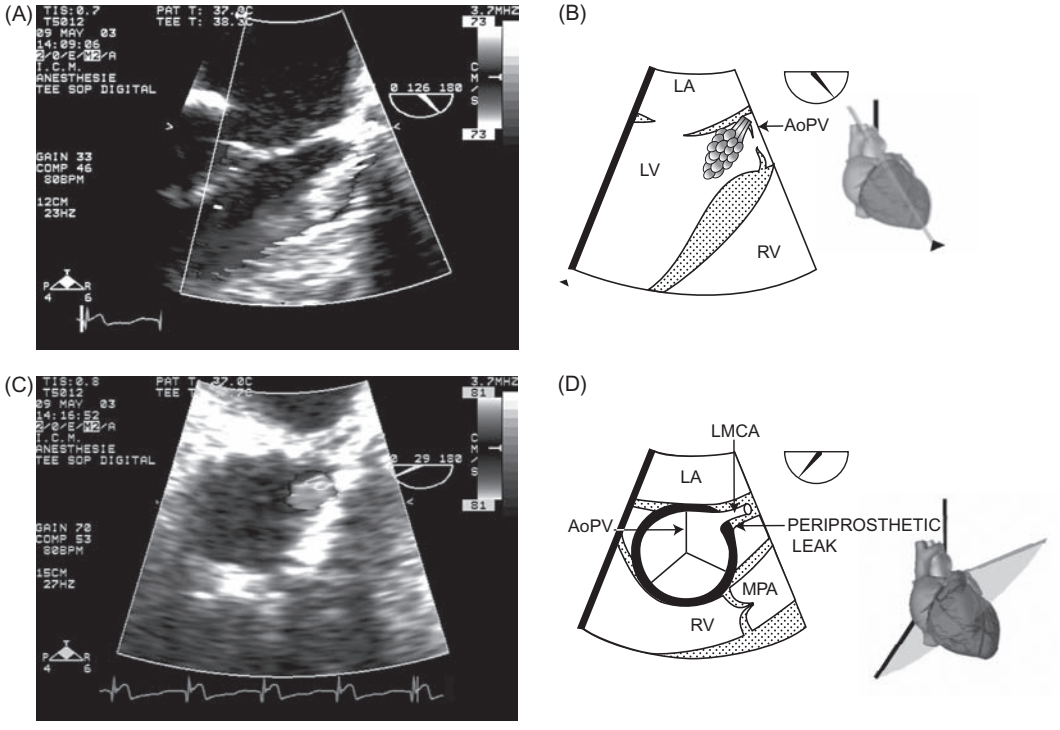

Figure 16.12 Periprosthetic aortic regurgitation in a 70-year-old woman. (A, B) Immediately after the aortic valve replacement, a small aortic regurgitant jet was seen in the mid-esophageal long-axis view. (C, D) In the short-axis view, it was located outside the origin of the left main coronary artery (LMCA) ostium. (AoPV, aortic prosthetic valve; LA, left atrium; LV, left ventricle; MPA, main pulmonary artery; RV, right ventricle).

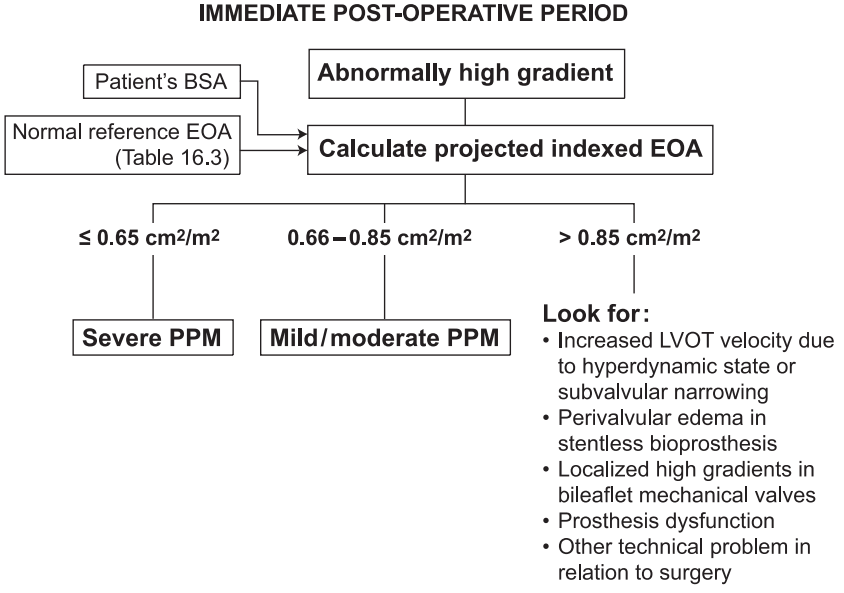

Figure 16.13 Algorithm used for evaluating abnormally high transvalvular pressure gradients during operation or in the immediate postoperative period. The projected indexed effective orifice area (EOA) is calculated from the normal reference value of EOA for the model and size of prosthesis implanted and patient's body surface area (BSA). If the projected indexed EOA is $\leq 0.85\ cm^2/m^2$, the abnormally high gradient is most likely due to patient–prosthesis mismatch (PPM). If the projected indexed EOA is $>0.85\ cm^2/m^2$, several possible conditions or technical pitfalls must be ruled out before concluding the presence of an intrinsic dysfunction of the prosthesis (LVOT, left ventricular outflow tract).

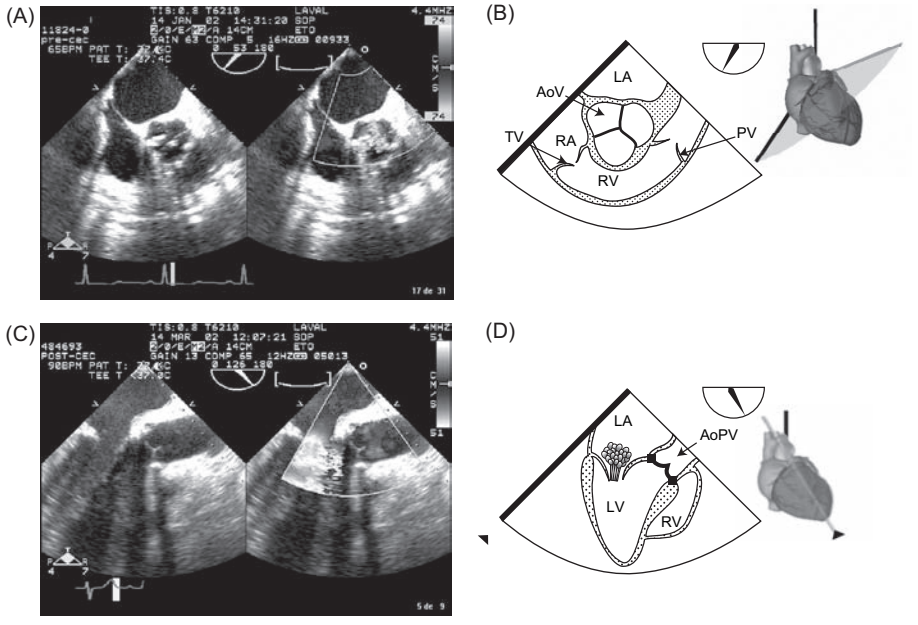

Figure 16.14 (A, B) Transesophageal echocardiographic evaluation in the mid-esophageal transverse plane before operation showing a three-cusped aortic valve (AoV) with severe stenosis. (C, D) Mid-esophageal longitudinal view of the recently implanted stented aortic bioprosthesis (AoPV) (Ao, aorta; LA, left atrium; LV, left ventricle; PV, pulmonic valve; RA, right atrium; RV, right ventricle; TV, tricuspid valve).

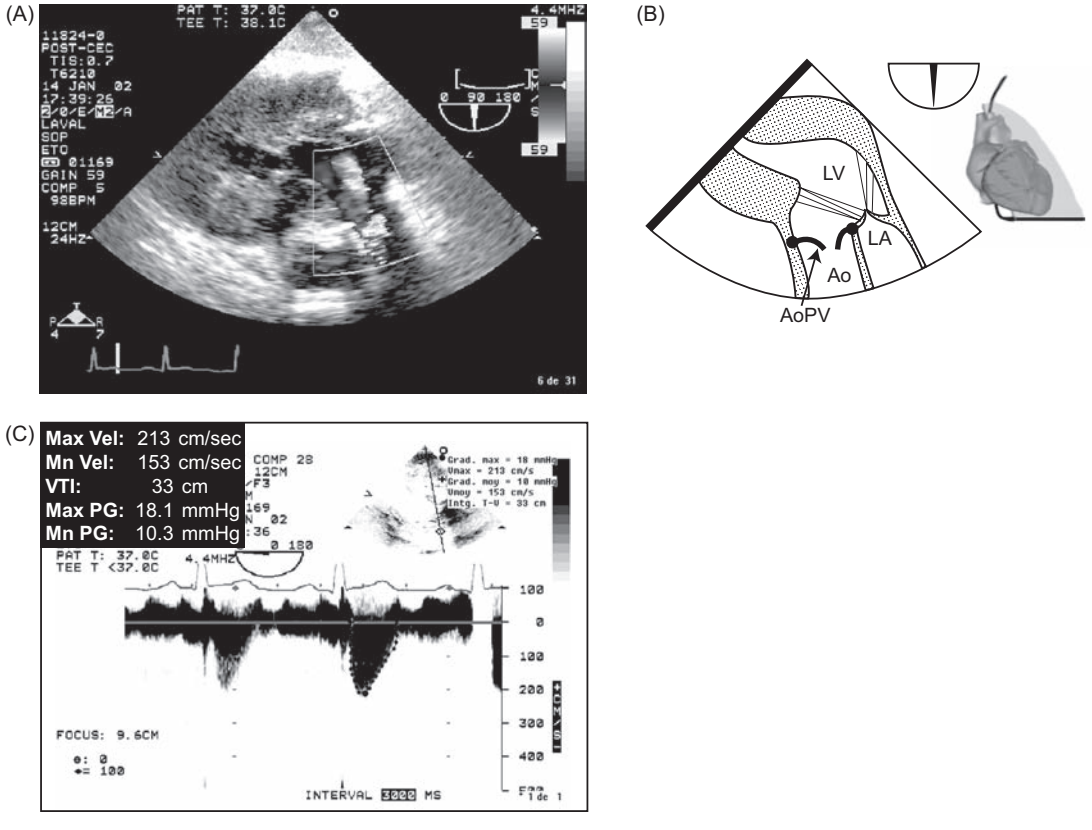

Figure 16.15 Transgastric longitudinal view (A, B) with intraoperative recording of transvalvular pressure gradient (PG) in recently implanted aortic prosthetic valve (AoPV) (C) (Ao, aorta; LA, left atrium; LV, left ventricle; Max, maximum; Mn, mean; Vel, velocity; VTI, velocity–time integral).

prosthesis with a larger EOA. This may be accomplished either by implanting another type of prosthesis with a better hemodynamic profile (e.g. stentless or mechanical) or by performing an additional aortic root enlargement procedure. An indexed EOA value $<0.65\,cm^2/m^2$ should be considered unacceptable whereas clinical judgment, based on patient's age, level of physical activity, and status of left ventricular function, should be used to determine optimal management in patients with an indexed EOA between 0.65 and $0.85\,cm^2/m^2$ (Fig. 16.13). For obvious reasons, it is clearly preferable to perform this evaluation before, rather than after, implanting the prosthesis. As a footnote, it should also be emphasized that a small indexed EOA with a low systolic gradient is the worst case scenario as it is indicative of a low CO.

VI. ECHOCARDIOGRAPHIC TECHNIQUE

Morphological evaluation of the AoV should be done in both the transverse and longitudinal planes (Fig. 16.14). For this purpose, the probe is placed behind the left atrium (LA) and transverse visualization of the AoV is usually obtained by rotation of the plane between 20° and 75° whereas longitudinal visualization is obtained by rotating the probe to between 90° and 150°. The same incidences are used to determine the degree of regurgitation with color flow imaging.

Transvalvular gradients are best evaluated using a transgastric approach. The deep transgastric and the transgastric long-axis view are most commonly used for this purpose (see Chapter 15). The deep transgastric view is obtained with the probe anteflexed and located more towards the apex of the left ventricle (LV). The transgastric long-axis view can also be used to measure Doppler flow velocities (Fig. 16.15). This view is obtained by rotating the transducer between 90° and 150°. The exact position of the probe and its angle of rotation can vary considerably for each view and it may often be difficult to obtain satisfactory views of the AoV in order to obtain accurate measurements of gradients, either because the valve simply cannot be visualised in this position or the angle between the ultrasound beam and the direction of blood flow exceeds 20°, thus rendering Doppler measurements of velocities inaccurate. If satisfactory images can be obtained, transvalvular gradients are estimated by continuous-wave (CW) Doppler interrogation across the valve whereas pulsed-wave (PW) Doppler is used to measure

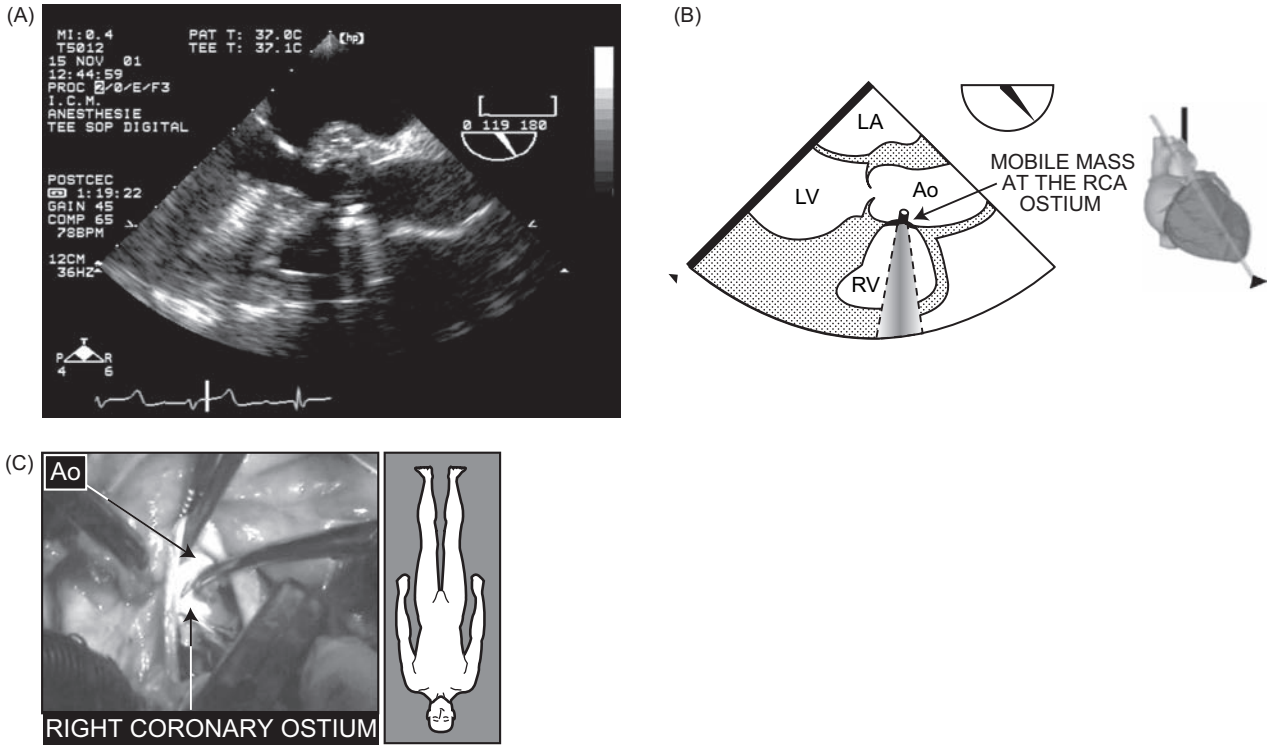

Figure 16.16 A 77-year-old woman with aortic stenosis who underwent aortic valve replacement. (A, B) During weaning from cardiopulmonary bypass (CPB) an abnormal moving calcified mass is seen anterior to the aorta (Ao). (C) The surgeon went back on CPB and found dislodged calcified plaques at the right coronary artery (RCA) ostium: coronary endarterectomy was performed with an uneventful subsequent postoperative course (LA, left atrium; LV, left ventricle; RV, right ventricle). (Photo C courtesy of Dr. Raymond Cartier.)

velocities in the LVOT. If the maximal velocity in the LVOT exceeds 1 m/s, the velocity profile should then be traced as if measuring a gradient and the results for peak and mean gradients subtracted from the results obtained with CW Doppler in order to obtain the true pressure gradients across the valve.

An alternate approach for measuring aortic gradients in the OR is to perform epicardial measurements. A transthoracic, epiaortic probe or the TEE probe may be used for this purpose. In either case, the probe is inserted with a fair amount of gel in a sterile bag to be directly placed over the Ao by the surgeon. This approach obviously requires echocardiography-trained surgeons, but beyond this initial hurdle, we have found the rate of success in obtaining accurate measurements of gradients to be close to 100%. The use of the TEE probe is particularly convenient because it is more easily manipulated over the heart and can easily be inserted between the heart and/or great vessels and the chest wall. Other aspects of the postoperative TEE evaluation include assessment of the other valves and ruling out unexpected complications of single or complex AoV surgery (Figs. 16.16–16.18).

VII. ECHOCARDIOGRAPHY IN THE IMMEDIATE POSTOPERATIVE PERIOD

Because of left ventricular remodeling, relative high output states and the frequent occurrence of tachycardia, hemodynamic assessment of the prosthetic valve done in the immediate postoperative period cannot be considered as definitive. Moreover, the echocardiograms are technically challenging because of the location of the various incisions and the quality of the images is often suboptimal.

The main objectives of a postoperative echocardiogram in a patient with AoV replacement are to obtain accurate measurements of peak and mean gradients as well as the nonindexed and indexed EOA. With regard to these measurements, the main pitfalls to be encountered when performing such an examination in the immediate postoperative period are given in the following list:

- Erroneous measurement of the true diameter of the LVOT: poor-quality images make this parameter prone to over- or underestimation. Moreover, one

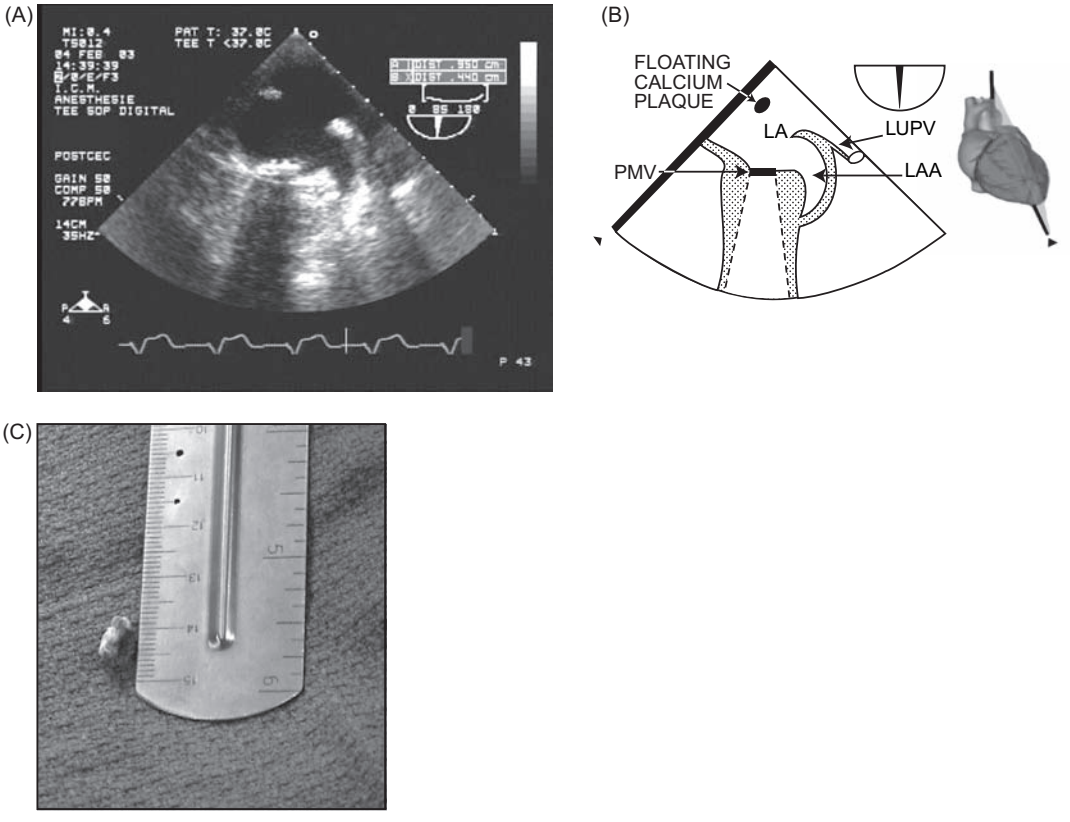

Figure 16.17 A 70-year-old man who underwent coronary revascularization and combined aortic and mitral valve replacement. (A, B) As weaning from cardiopulmonary bypass (CPB) proceeded, floating material was seen in the left atrium (LA). The attending surgeon went back immediately to full CPB. (C) This material was a 4 × 1 mm floating calcium plaque which was removed. He had no postoperative neurological complications (LAA, left atrial appendage; LUPV, left upper pulmonary vein; PMV, prosthetic mitral valve).

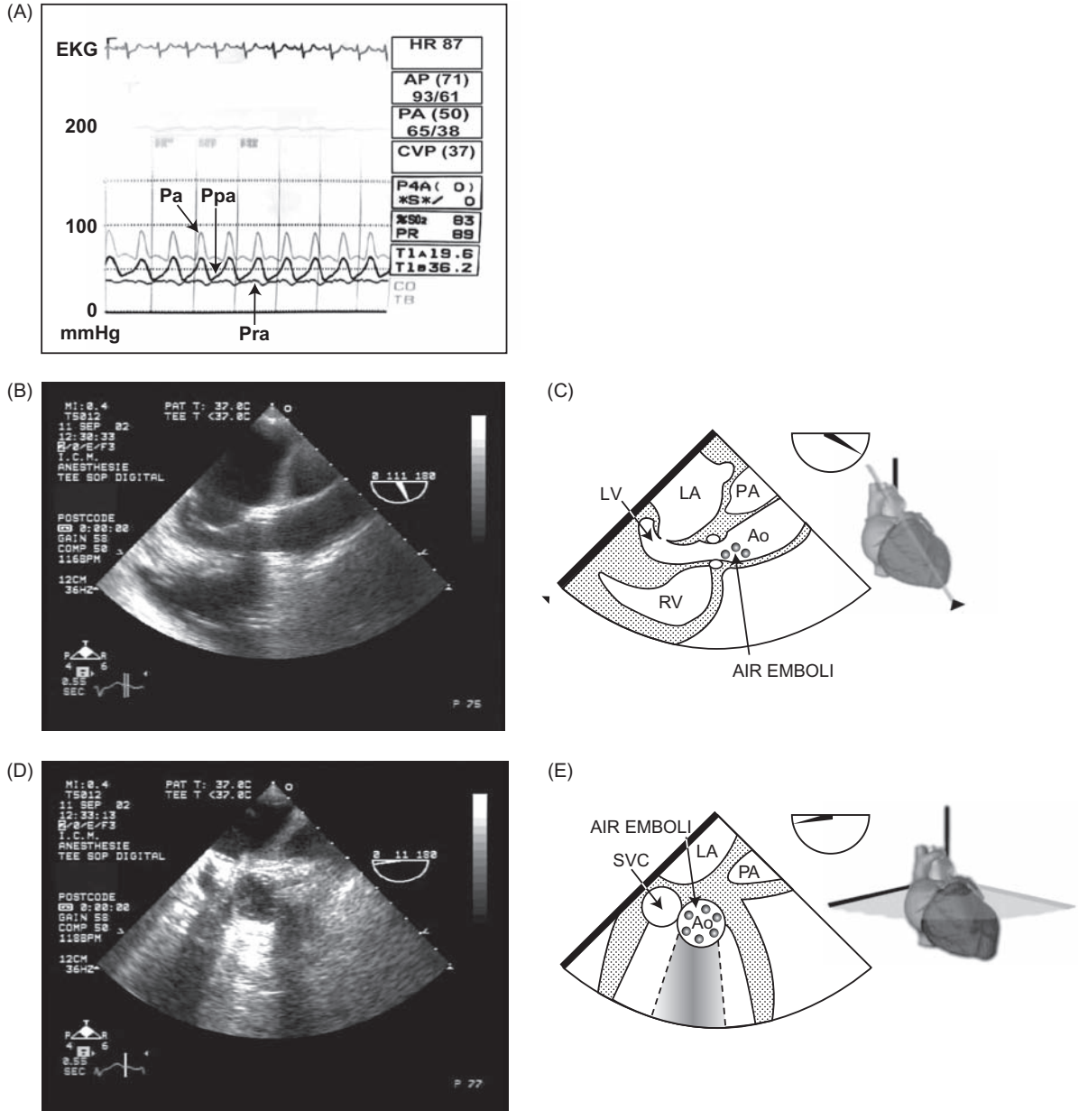

Figure 16.18 A 61-year-old woman underwent aortic valve replacement. She was easily weaned from cardiopulmonary bypass (CPB). As she was transferred onto the transportation bed, she developed acute pulmonary hypertension (A) followed by ventricular fibrillation. (B–E) She was resuscitated and transesophageal echocardiographic exam was performed, which revealed strong echogenic material close to the prosthetic valve consistent with air emboli dislodged during mobilization of the patient (Ao, aorta; EKG, electrocardiogram; LA, left atrium; LV, left ventricle; Pa, arterial pressure; PA, pulmonary artery; Ppa, pulmonary artery pressure; Pra, right atrial pressure; RV, right ventricle; SVC, superior vena cava).

could be tempted to take the labeled size of the prosthetic valve sewing ring, but LVOT tissue protrusion or a supra-annular implantation invalidates its use as a substitute of the LVOT diameter (30).

- High LVOT flow velocity: this parameter may be abnormally increased by high CO or dynamic obstruction from temporary remodeling of the LVOT, precluding or limiting the validity of the simplified Bernoulli equation for the estimation of transvalvular gradients or effective orifice areas; indeed, the simplified Bernoulli equation ignores the subvalvular gradient as it is most often negligible compared with the aortic velocity. When the subvalvular gradient is high (e.g. maximum gradient >10 mmHg), it is no longer negligible and must be subtracted from the transvalvular gradients

recorded by CW Doppler in order to obtain the true gradient across the valve.

- The presence of perivalvular edema or hematoma in stentless prosthesis during the immediate postoperative period may result in a lower than expected EOA during the first few months after operation.

For these reasons, the recording of relatively high gradients in the immediate postoperative period should not be viewed with undue concern. A simple algorithm may be used to assess abnormally high gradients in the immediate postoperative period (Fig. 16.13); this algorithm is identical to the one used during operation. Given that patient–prosthesis mismatch is the most frequent cause of high gradients, the first step of this algorithm is to determine if mismatch is present by calculating the projected indexed EOA. It should be noted that the Doppler-echocardiographic measurement of LVOT stroke volume (SV) and thus of valve EOA in the immediate postoperative period is often not feasible and/or reliable. It is, therefore, preferable to use the projected indexed EOA to assess the presence and severity of mismatch. This parameter is simply calculated by dividing the normal reference EOA for the model and size of prosthesis implanted (see Table 16.3) by the patient's BSA. If the projected indexed EOA is $\leq 0.85\ cm^2/m^2$, the abnormally high gradient is likely due to mismatch. If the projected indexed EOA is $> 0.85\ cm^2/m^2$, several aforementioned conditions and technical pitfalls must first be ruled out before concluding prosthesis dysfunction. Therefore, unless the transvalvular gradients are very high or are associated with significant symptoms or deterioration in left ventricular function, a conservative approach with observation and repeat assessment 3–6 months later is advocated.

Granted these considerations, a more comprehensive algorithm may be used for evaluating abnormally high gradients after AoV replacement (Fig. 16.19). However, this algorithm should be used only when the hemodynamic condition has settled down and there is, in particular, no high CO state or an abnormally high velocity in the LVOT. The diagnosis of patient–prosthesis mismatch is established by a nonindexed EOA of the prosthesis under study comparable to its normal reference value (Table 16.3). On the other hand, if the nonindexed EOA is much lower than the reference value for the prosthesis, the diagnosis of intrinsic dysfunction should be raised. Causes of such dysfunction include the presence of thrombosis, pannus, or endocarditis. Occasionally, an abnormally high velocity jet corresponding to a localized gradient may be recorded by CW Doppler interrogation through the smaller central slit-like orifice of bileaflet mechanical prosthesis. This is not reproduced when redirecting the ultrasound beam through either lateral major orifices. This is a limitation of the echocardiographic evaluation of bileaflet prostheses inherent in their design which should be kept in mind when encountering a relatively high gradient in an otherwise asymptomatic patient with this type of mechanical prosthesis.

In conclusion, perioperative echocardiography may be useful to detect clinically unsuspected abnormalities that may alter or add operative procedures during AoV surgery (Table 16.4). Patient–prosthesis mismatch is by

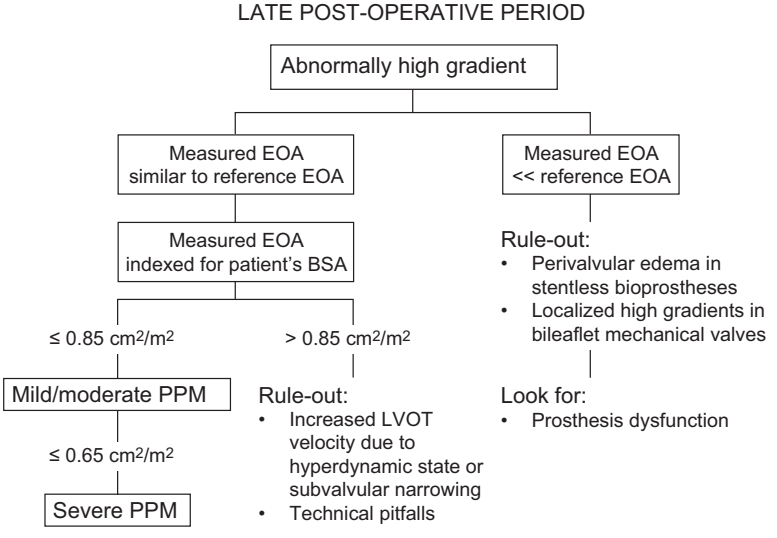

Figure 16.19 Algorithm used for evaluating abnormally high transvalvular pressure gradients in the late postoperative period after aortic valve replacement. This algorithm should be used only when the hemodynamic condition has stabilized and there is no high cardiac output state or abnormally high left ventricular outflow tract (LVOT) velocity (BSA, body surface area; EOA, effective orifice area; PPM, patient–prosthesis mismatch).

Table 16.4 Summary of the Role of TEE in Patients Undergoing Aortic Valve Surgery

Before the procedure	Importance
See Table 13.1 for the role of TEE in cardiac surgery	
Measurement of aortic annulus and ascending aortic dimensions	Calculation of the projected effective orifice area to prevent patient–prosthesis mismatch Need for concomitant aortic procedure (replacement or enlargement)
Evaluate the severity of left ventricular septal hypertrophy	Anticipate the occurrence of dynamic LVOT obstruction and the need for septal myectomy
Rule out coarctation if bicuspid aortic valve disease	Concomitant repair may be considered
During CPB	
See Table 13.1	
After CPB	
See Table 13.1	
Evaluate result of repair or replacement	Early detection and correction of prosthetic dysfunction or suboptimal repair
In the intensive care unit	
See Table 13.1	

Note: CPB, cardiopulmonary bypass; LVOT, left ventricular outflow tract; TEE, transesophageal echocardiography.

far the most frequent cause of high transvalvular gradients after AoV replacement. Nevertheless, this problem can largely be avoided with the use of a prospective strategy before prosthesis implantation.

REFERENCES

1. Bonow RO, Carabello B, de LA Jr et al. Guidelines for the management of patients with valvular heart disease: executive summary. A report of the American College of Cardiology/American Heart Association Task Force on Practice Guidelines (Committee on Management of Patients with Valvular Heart Disease). Circulation 1998; 98:1949–1984.
2. Rosenhek R, Binder T, Porenta G et al. Predictors of outcome in severe, asymptomatic aortic stenosis. N Engl J Med 2000; 343:611–617.
3. ACC/AHA guidelines for the management of patients with valvular heart disease. A report of the American College of Cardiology/American Heart Association. Task Force on Practice Guidelines (Committee on Management of Patients with Valvular Heart Disease). J Am Coll Cardiol 1998; 32:1486–1588.
4. Rahimtoola SH. "Prophylactic" valve replacement for mild aortic valve disease at time of surgery for other cardiovascular disease?...No. J Am Coll Cardiol 1999; 33:2009–2015.
5. Briand M, Pibarot P, Dumesnil JG, Cartier P. Midterm echocardiographic follow-up after Ross operation. Circulation 2000; 102:III10–III14.
6. Dumesnil JG, LeBlanc MH, Cartier PC et al. Hemodynamic features of the freestyle aortic bioprosthesis compared with stented bioprosthesis. Ann Thorac Surg 1998; 66:S130–S133.
7. Pibarot P, Dumesnil JG. Hemodynamic and clinical impact of prosthesis–patient mismatch in the aortic valve position and its prevention. J Am Coll Cardiol 2000; 36:1131–1141.
8. Rao V, Jamieson WR, Ivanov J et al. Prosthesis–patient mismatch affects survival after aortic valve replacement. Circulation 2000; 102:III5–III9.
9. Mecozzi G, Milano AD, De Carlo M et al. Intravascular hemolysis in patients with new-generation prosthetic heart valves: a prospective study. J Thorac Cardiovasc Surg 2002; 123:550–556.
10. Blais C, Dumesnil JG, Baillot R et al. Impact of valve prosthesis–patient mismatch on short-term mortality after aortic valve replacement. Circulation 2003; 108:983–988.
11. Ruel M, Rubens FD, Masters RG et al. Late incidence and predictors of persistent or recurrent heart failure in patients with aortic prosthetic valves. J Thorac Cardiovasc Surg 2004; 127:149–159.
12. Pibarot P, Dumesnil JG. Patient–prothesis mismatch and the predictive use of indexed effective orifice area: is it relevant? Card Surg Today 2003; 1:43–51.
13. Thomson DJ, Jamieson WR, Dumesnil JG et al. Medtronic Mosaic porcine bioprosthesis: midterm investigational trial results. Ann Thorac Surg 2001; 71:S269–S272.
14. Dossche K, Vanermen H, Daenen W et al. Hemodynamic performance of the PRIMA Edwards stentless aortic xenograft: early results of a multicenter clinical trial. Thorac Cardiovasc Surg 1996; 44:11–14.
15. Wiseth R, Hegrenaes L, Rossvoll O et al. Validity of an early postoperative baseline Doppler recording after aortic valve replacement. Am J Cardiol 1991; 67:869–872.
16. Zingg U, Aeschbacher B, Seiler C et al. Early experience with the new Masters series of St. Jude Medical heart valve: in vivo hemodynamic and clinical results in patients with narrowed aortic annulus. J Heart Valve Dis 1997; 6:535–541.
17. De Paulis R, Sommariva L, De Matteis GM et al. Hemodynamic performances of small diameter carbomedics and

St. Jude valves. J Heart Valve Dis 1996; 5 (suppl 3):S339–S343.
18. Bach DS, Sakwa MP, Goldbach M et al. Hemodynamics and early clinical performance of the St. Jude Medical Regent mechanical aortic valve. Ann Thorac Surg 2002; 74:2003–2009.
19. Chambers J, Ely JL. Early postoperative echocardiographic hemodynamic performance of the On-X prosthetic heart valve: a multicenter study. J Heart Valve Dis 1998; 7:569–573.
20. De Carlo M, Milano AD, Nardi C et al. Serial Doppler echocardiographic evaluation of small-sized sorin bicarbon prostheses. J Thorac Cardiovasc Surg 2003; 126:337–343.
21. Castro LJ, Arcidi JM Jr, Fisher AL, Gaudiani VA. Routine enlargement of the small aortic root: a preventive strategy to minimize mismatch. Ann Thorac Surg 2002; 74:31–36.
22. Cohen G, Christakis GT, Joyner CD et al. Are stentless valves hemodynamically superior to stented valves? A prospective randomized trial. Ann Thorac Surg 2002; 73:767–775.
23. Dellgren G, David TE, Raanani E et al. Late hemodynamic and clinical outcomes of aortic valve replacement with the Carpentier–Edwards Perimount pericardial bioprosthesis. J Thorac Cardiovasc Surg 2002; 124:146–154.
24. Connolly HM, Oh JK, Schaff HV et al. Severe aortic stenosis with low transvalvular gradient and severe left ventricular dysfunction: result of aortic valve replacement in 52 patients. Circulation 2000; 101:1940–1946.
25. Hanayama N, Christakis GT, Mallidi HR et al. Patient prosthesis mismatch is rare after aortic valve replacement: valve size may be irrelevant. Ann Thorac Surg 2002; 73:1822–1829.
26. Lund O, Flo C, Jensen FT et al. Left ventricular systolic and diastolic function in aortic stenosis. Prognostic value after valve replacement and underlying mechanisms. Eur Heart J 1997; 18:1977–1987.
27. Malouf JF, Enriquez-Sarano M, Pellikka PA et al. Severe pulmonary hypertension in patients with severe aortic valve stenosis: clinical profile and prognostic implications. J Am Coll Cardiol 2002; 40:789–795.
28. Lau WC, Carroll JR, Deeb GM et al. Intraoperative transesophageal echocardiographic assessment of the effect of protamine on paraprosthetic aortic insufficiency immediately after stentless tissue aortic valve replacement. J Am Soc Echocardiogr 2002; 15:1175–1180.
29. Morehead AJ, Firstenberg MS, Shiota T et al. Intraoperative echocardiographic detection of regurgitant jets after valve replacement. Ann Thorac Surg 2000; 69:135–139.
30. Pibarot P, Honos GN, Durand LG, Dumesnil JG. Substitution of left ventricular outflow tract diameter with prosthesis size is inadequate for calculation of the aortic prosthetic valve area by the continuity equation. J Am Soc Echocardiogr 1995; 8:511–517.

17

Mitral Valve

ANDRÉ SAINT-PIERRE
Laval University, Quebec City, Canada

STÉPHANE COUTU
University of Sherbrooke, Sherbrooke, Canada

PIERRE COUTURE, ANDRÉ Y. DENAULT
University of Montreal, Montreal, Canada

JEAN BUITHIEU
McGill University, Montreal, Canada

I. Anatomical Manifestations of Mitral Valvular Lesions 384
1. Mitral Valve Examination 384
2. Etiology of Mitral Regurgitation 388
A. Endocarditis 388
1. Vegetations 389
2. Abscesses 389
B. Rheumatic Valve Disease 390
C. Myxoid Degeneration 390
1. Complexity of Lesion and Relationship to Repair 392
D. Ischemic Mitral Valvular Disease 392
1. Chordal Rupture 394
E. Traumatic Mitral Valve Injury 394
II. Functional Manifestations of Valve Lesions 395
A. Mitral Valve Regurgitation—Mechanism and Quantification 395
1. Color Flow Doppler Jet Area Mapping 397
2. Jet Width (Vena Contracta) 398
3. Pulmonary Venous Flow 398
4. Continuous-Wave Doppler 401
5. Proximal Isovelocity Surface Area 401
6. Regurgitant Volume 403
7. Integrated Approach 404
8. Provocative Testing 405
B. Mitral Stenosis 405
1. Echocardiographic Findings 405
2. Associated Findings 406
3. Quantitative Echocardiographic Evaluation 409
C. Diastolic Pressure Gradient 409
D. Mitral Valve Area 409
1. Planimetry 409
2. Pressure Half-Time 409
3. Continuity Equation 410
4. Proximal Flow Convergence 411
Acknowledgment 413
References 413

Echocardiography is the method of choice for the noninvasive assessment of the severity and mechanisms of mitral regurgitation (MR). The following chapter includes the recent recommendations of the American Society of Echocardiography (ASE) for the evaluation and assessment of the severity of native valvular regurgitation (1) with emphasis on Transesophageal echocardiography (TEE) examination.

I. ANATOMICAL MANIFESTATIONS OF MITRAL VALVULAR LESIONS

1. Mitral Valve Examination

The mitral valve is a complex structure and its functional anatomy comprises not only the valve itself with the annulus, the leaflets, the chordae tendinae and the papillary muscles, but also the left atrium (LA) and ventricle (LV) (2). Dysfunction, or abnormalities, of any of these components can result in MR. The surgical anatomical and corresponding echocardiographic views are presented in Fig. 17.1.

In 1999, Lambert et al. (3) published a systematic approach for the evaluation of the mitral valve using the cardiac anatomy as a reference for the description of structures, each view being used in relation to each other. Their descriptions were drawn up following the classification of Carpentier et al. (4), but stated that they could be used with other classification systems. The description of these echocardiographic plans is depicted in Figs. 17.2–17.9.

The suggested anatomical two-dimensional (2D) examination is performed in a sequence of five steps. (Step 1) The mid-esophageal five-chamber view at 0° is used initially to evaluate the elements of the valve closer to the anterior wall, that is, the A1–A2 segments of the anterior leaflet and the P1–P2 scallops of the posterior leaflet (Fig. 17.3). (Step 2) The elements of the valve near the posterior wall, A2–A3 and P2–P3 (from left to right), are then assessed by moving to a mid-esophageal four-chamber view at 0° using gentle retroflexion and further insertion of the probe (Fig. 17.4). (Step 3) From

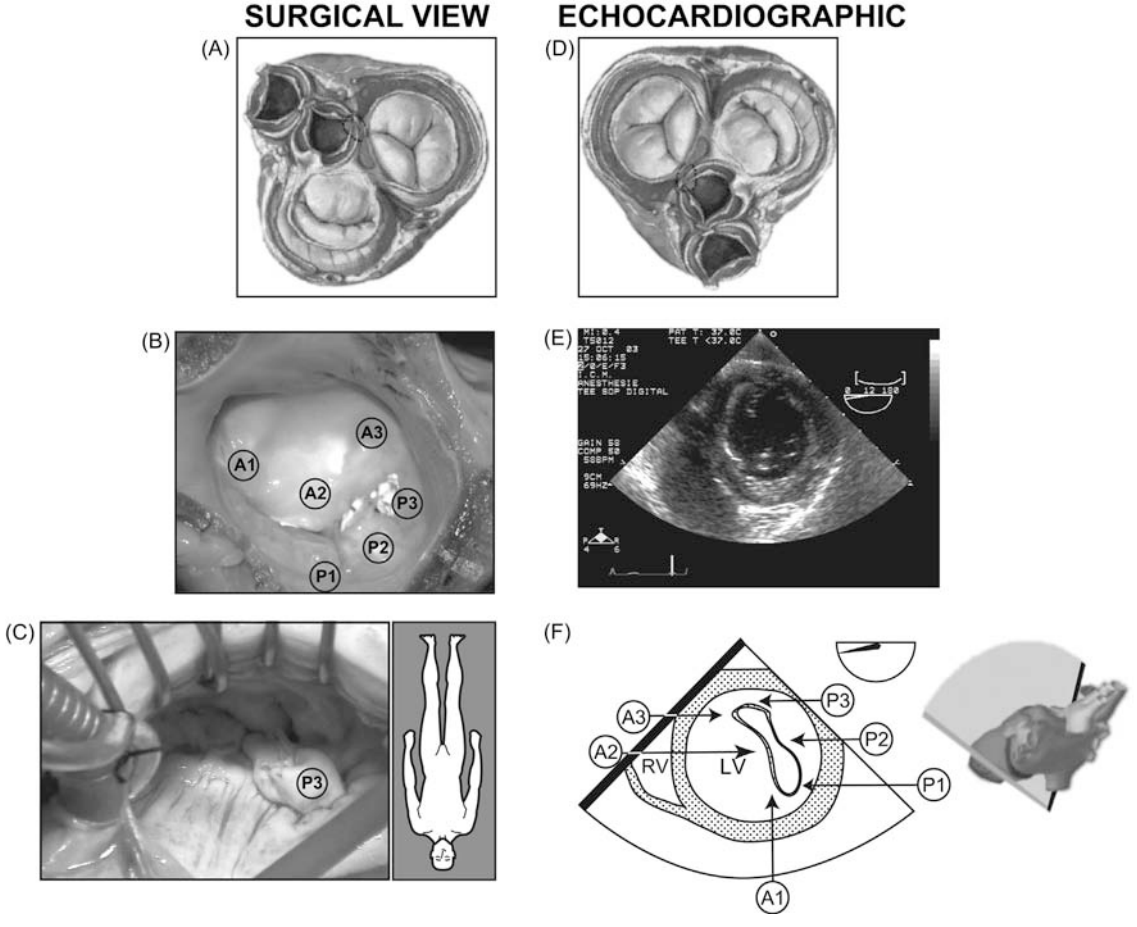

Figure 17.1 Traditional surgical (A) and intraoperative view (B) of the mitral valve. The Carpentier classification divides both the anterior and the posterior leaflets into three parts: the anterior leaflet is seen above while the posterior leaflet is visible inferiorly with the lateral part of the valve (A1 and P1) being oriented towards the left. (C) An example of a prolapse of the P3 segment is shown. (D–F) In transgastric echocardiographic view, the structures are visualized upside down. Indeed, in transgastric basal views of the mitral valve, the P3 segment appears at the top right of the screen, while the P1 segment is displayed to bottom (LV, left ventricle; RV, right ventricle). (Photo B courtesy of Dr. Nicolas Dürrleman, anatomical drawings with permission from Netter.)

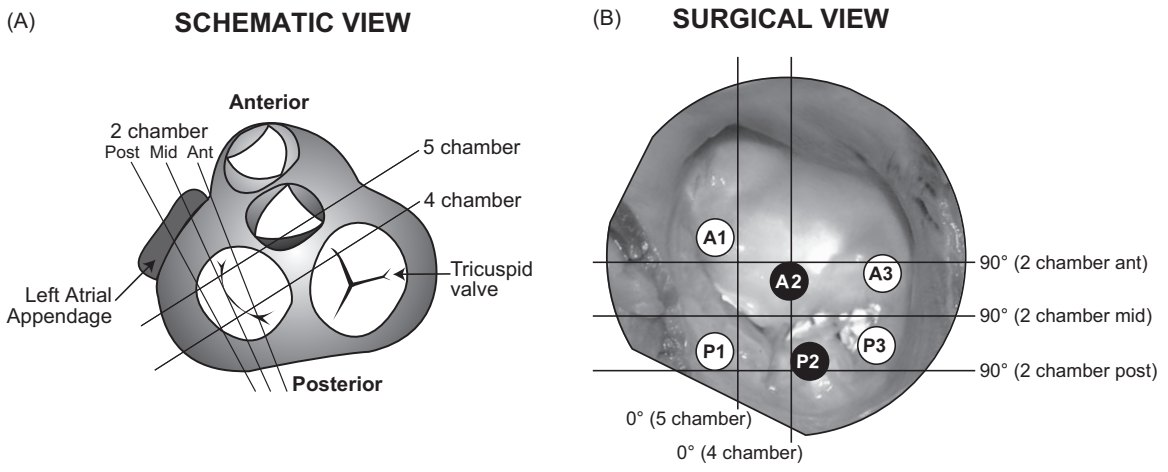

Figure 17.2 (A) Schematic drawing of the heart through the plane of the atrioventricular valves. This drawing depicts the planes of the different cross-sections used during systematic examination. The plane of the short axis is parallel to the page and cannot be demonstrated. The image must be rotated upside down to obtain the same orientation as the standard transesophageal echocardiography planes. (B) Surgical view (ant, anterior; mid, middle; post, posterior). [Adapted with permission from Lambert (3).] (Photo B courtesy of Dr. Nicolas Dürrleman.)

there, the mid-esophageal two-chamber view is obtained at 90° showing orthogonal cross sections of the mitral valve. (3a) Rotating the probe shaft clockwise completely towards the patient's right until the commissure is no longer visible reveals the base of the anterior mitral leaflet and the intervalvular fibrosa. (3b) Gradual counterclockwise rotation of the probe shaft back towards the patient's left first shows the anterior cross-section of the valve, with a small portion of the posterior leaflet (P1) and a large part of the anterior leaflet, A3–A2 (Fig. 17.5). (3c) Continuing progressive counterclockwise rotation of the probe shaft back towards the patient's left then reaches the mitral valve mid cross-section or mid-commissural view (70–90°), where two coaptation points are visualized between P3 and A2 and between A2 and P1 (Fig. 17.6). As the mitral valve orifice is C-shaped, this tomographic plane crossing the tip of the A2 segment should reveal coaptation points on either side of it. Thus, the apparent presence of two flow orifices should not be mistaken for a commissural point and a perforated anterior leaflet in the setting of endocarditis. (3d) Further counterclockwise rotation of the probe shaft back towards the patient's left leads to the most posterior aspect of the mitral valve where only the P3–P2–P1 scallops are visualized (Fig. 17.7). (Step 4) The probe shaft is then advanced in the stomach where the examination moves to the transgastric basal short-axis view at 0°. With variable anteflexion, the mitral valve may be shown almost "*en face*" with a complete view of the C-shaped orifice. The use of color flow imaging at this level is useful to demonstrate the exact origin of the regurgitation jet(s) (Fig. 17.8). With some retroflexion, or further insertion of the probe, the subvalvular apparatus including the anterolateral and posteromedial chordae and papillary muscles may be assessed in a transverse plane at the lower right and the top of the display respectively. (Step 5) Orthogonal views of the mitral valve in the longitudinal plane are obtained by changing the imaging plane to 90° in the transgastric two-chamber view: this is particularly helpful to evaluate the subvalvular apparatus, particularly the papillary muscles, the chordae tendinae and their insertions on the leaflets margins (Fig. 17.9): by rotating the probe shaft counterclockwise towards the left of the patient, the anterolateral papillary muscle will be seen in the far-field near the anterior left ventricular wall. Clockwise rotation of the probe shaft towards the patient's right will bring the posteromedial papillary muscle into view in the near-field near the inferior LV wall (5).

Close inspection of the anatomical integrity of the mitral valve by 2D examination should predict the presence of abnormal regurgitant flow, which can then be confirmed by color flow imaging in all the above views. The jet should be characterized by its origin (along the mitral commissure as medial, central or lateral or outside the commissure as eccentric) and by its direction (anterior, central, posterior, or multiple). Its description should be consistent with the mechanism hypothesized from the 2D findings, such as any hyperechogenic material evoking sclerosis of the coapting surface of the leaflets, calcification in the annulus or the mitral apparatus or hypermobile structures consistent with torn chordae tendinae or even part of the papillary muscles (6) (see Figure 8.21).

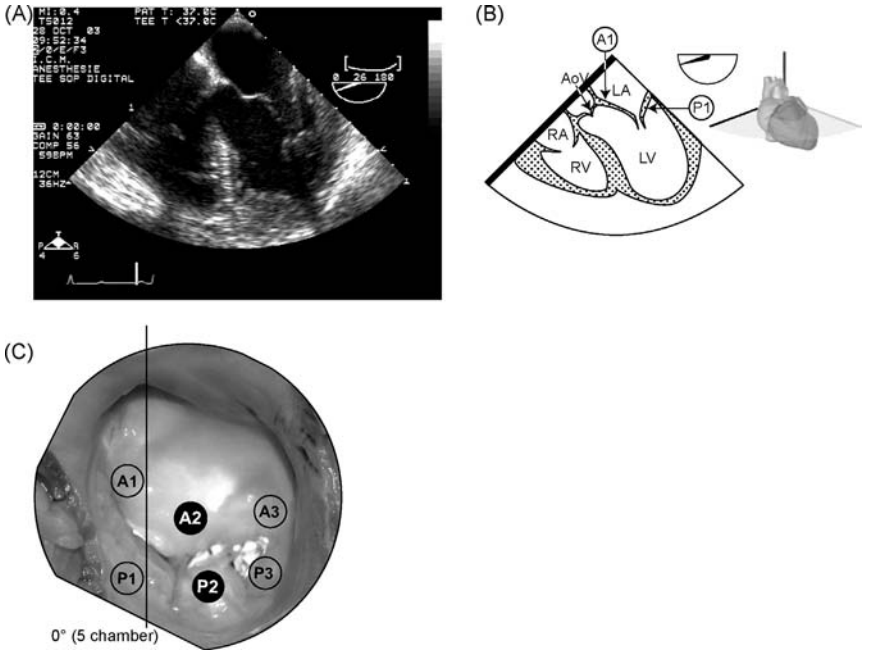

Figure 17.3 Echocardiographic (A, B) and anatomical (C) representation of the mitral valve in the mid-esophageal five-chamber view at $\sim 0^{\circ}$ with slight anteflexion (AoV, aortic valve; LA, left atrium; LV, left ventricle; RA, right atrium; RV, right ventricle). (Photo C courtesy of Dr. Nicolas Dürrleman.)

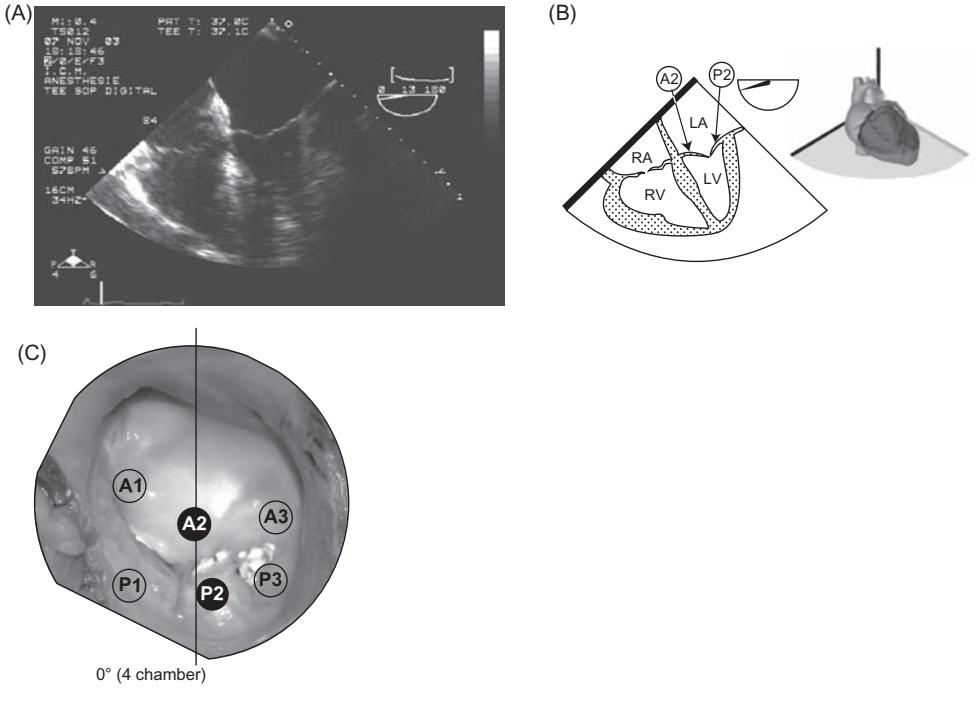

Figure 17.4 Echocardiographic (A, B) and anatomical (C) representation of the mitral valve in the mid-esophageal four-chamber view at $\sim 0^{\circ}$. This tomographic view is at a lower esophageal level than the five-chamber view, and is thus easily obtained by inserting the transesophageal echocardiographic probe slightly deeper than with figure 17.3 and releasing anteflexion (LA, left atrium; LV, left ventricle; RA, right atrium; RV, right ventricle). (Photo C courtesy of Dr. Nicolas Dürrleman.)

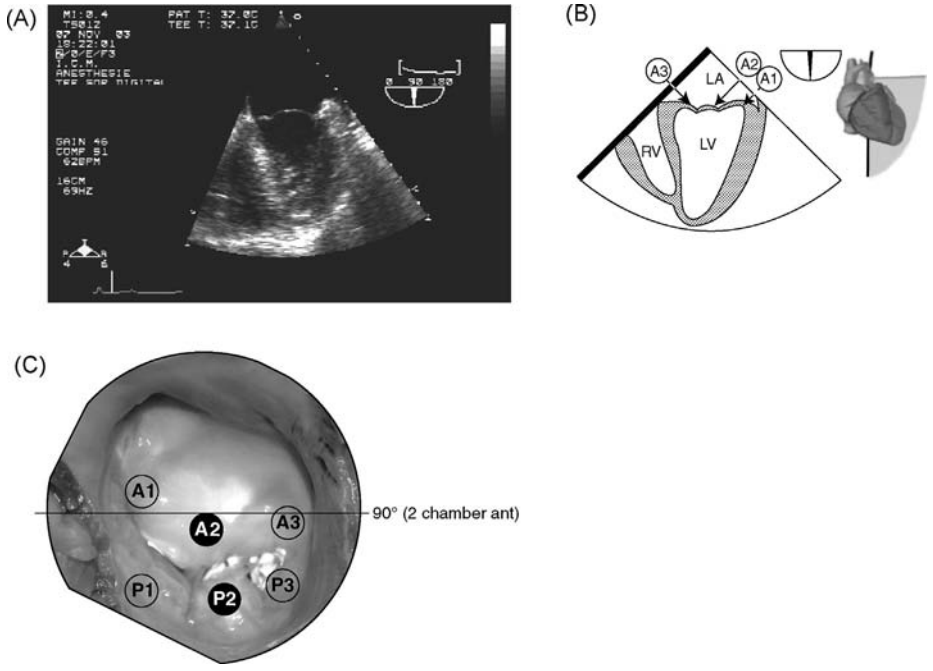

Figure 17.5 Echocardiographic (A, B) and anatomical (C) representation of the mitral valve in the mid-esophageal view at 90° with slight anterior clockwise rotation towards the right of the transesophageal echocardiographic shaft. Note that part of the right ventricle (RV) may become visible as the field of view is progressively aimed towards the right (LA, left atrium; LV, left ventricle). (Photo C courtesy of Dr. Nicolas Dürrleman.)

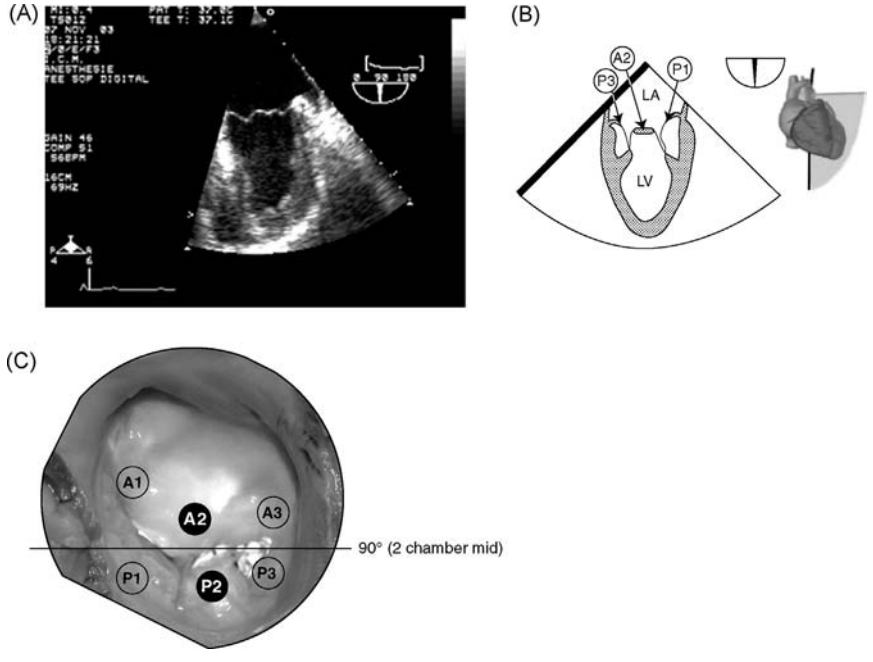

Figure 17.6 Echocardiographic (A, B) and anatomical (C) representation of the mitral valve in the mid-esophageal two-chamber view at 90°. In this view, the tip of the anterior leaflet (A2) is visible in the center of the mitral annulus, while the posteromedial (P3) and anterolateral (P1) scallops of the posterior leaflet appear attached to their respective left ventricular wall (LA, left atrium; LV, left ventricle). (Photo C courtesy of Dr. Nicolas Dürrleman.)

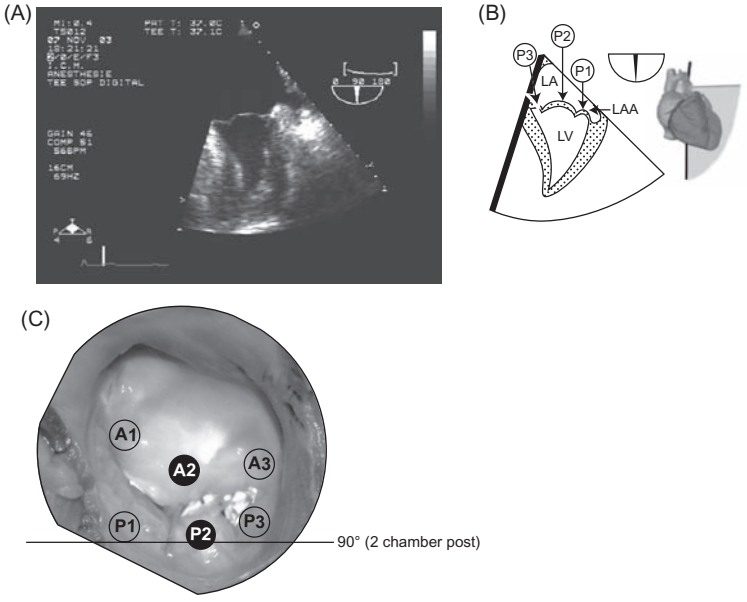

Figure 17.7 Echocardiographic (A, B) and anatomical (C) representation of the mitral valve in the mid-esophageal two-chamber view at 90° with slight counterclockwise posterior rotation of the transesophageal echocardiographic shaft towards the left (LA, left atrium; LAA, left atrial appendage; LV, left ventricle). (Photo C courtesy of Dr. Nicolas Dürrleman.)

2. Etiology of Mitral Regurgitation

In a recent review of 1000 patients undergoing mitral valve surgery for MR, 50% had valvular degenerescence, 20% rheumatic disease, 17% ischemic regurgitation while 8% of MR originated from infectious processes and the remaining 5% had miscellaneous causes. Identifying the causes of MR has prognostic implication for long-term survival, being at six years 85% for floppy valve disease, 64% for organic nonfloppy valve disease, and 46% for ischemic or functional MR (7).

In the following discussion, we will review the main etiologies of MR.

A. Endocarditis

Echocardiography is an integral part of the clinical assessment of a patient with suspected endocarditis. The echocardiographic findings have been included in the Duke criteria for evidence of cardiac involvement (8) (Table 17.1).

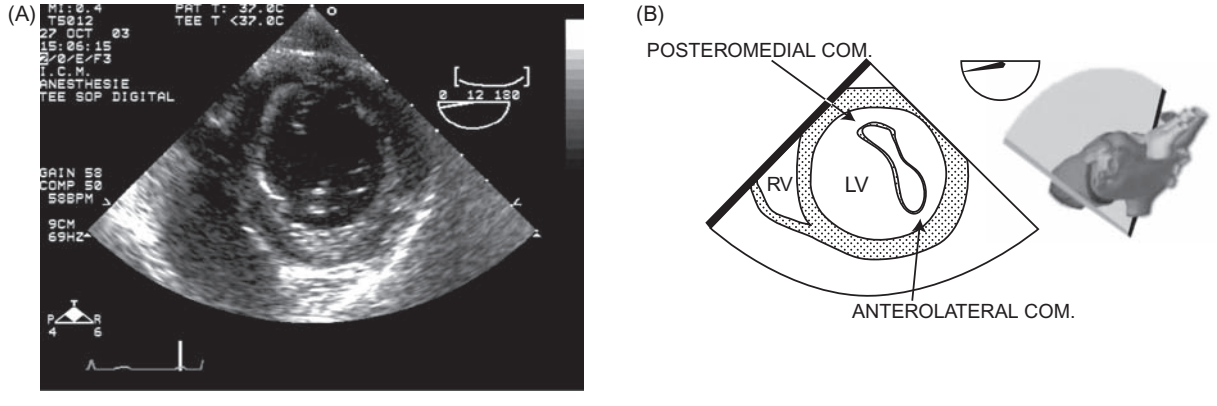

Figure 17.8 Echocardiographic representation of the mitral valve in the transgastric basal short-axis view at ~0° (COM, commissure; LV, left ventricle; RV, right ventricle).

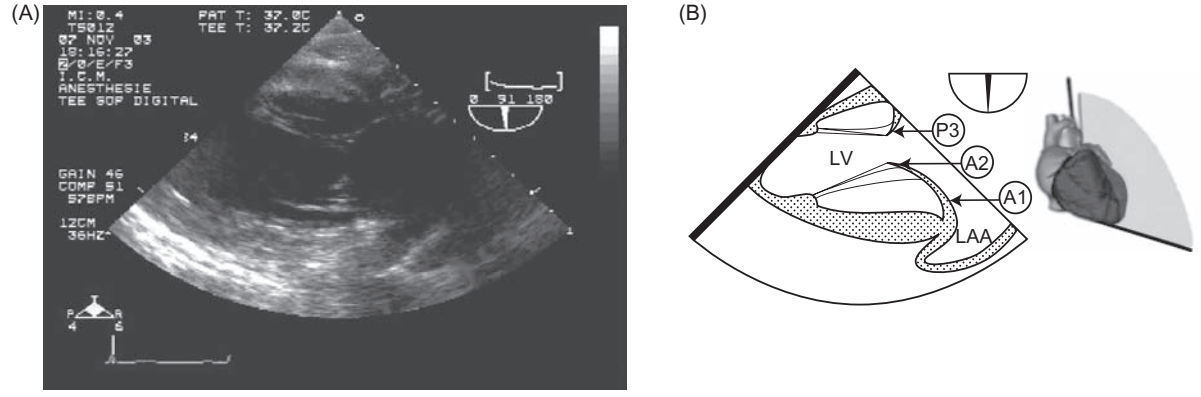

Figure 17.9 Echocardiographic representation of the mitral valve in the transgastric long-axis view at 90°. Note the left atrial appendage (LAA) in the far field (LV, left ventricle).

1. Vegetations

The presence of vegetations constitutes a major diagnostic criterion for endocarditis in the Duke classification. Five characteristics are described to help classify a mass as a vegetation: (1) a gray scale and a low level of reflectance similar to mid-myocardium; (2) localization to the upstream side of the valve: for instance, on the atrial side of the mitral valve, or on the ventricular side of the aortic valve (AoV); (3) localization at sites of endothelial injury from regurgitant or stenotic jet impinging on the valve or wall; (4) morphologic features: mass usually lobulated, amorphous, and mobile; and (5) mobility of the mass may be random or appear to orbit around the valve. Fine vibratory motion may be imparted to vegetation by the jet. Accompanying abnormalities include periannular abcess, fistulas and severe regurgitation from disruption of the leaflet function and/or perforation. Vegetations can also be described according to their size, density, extent and mobility (Figs. 17.10–17.12). Complications are more likely to be associated with higher grades of mobility and lesion extent, but less so with the presence of calcified elements. The size of the vegetation seems to be the most powerful predictor of complications. Indeed, the risk of septic emboli is increased threefold by the presence of a vegetation >10 mm (10).

When endocarditis is strongly suspected on clinical grounds and a transthoracic echocardiogram does not yield positive findings, TEE is recommended (12). It has a higher sensitivity for abscess and valve perforation (13,14) and a higher diagnostic accuracy for the detection of vegetations. Its mean sensitivity for the presence of vegetations is 92%, compared with 62% for transthoracic echocardiography (TTE).

Table 17.1 Duke Criteria for Endocarditis

Definite IE
Pathologic criteria
- Microorganism: demonstrated by culture or histology in a vegetation, or in a vegetation that has embolized, or in an intracardiac abscess OR
- Pathologic lesions: vegetation or intracardiac abscess, confirmed by histology showing active endocarditis.

Clinical criteria[a]
- 2 major criteria OR
- 1 major and 3 minor criteria OR
- 5 minor criteria.

Possible IE[a]
- 1 major and 1 minor criterion OR 3 minor criteria.

Rejected IE
- Firm alternate diagnosis for manifestations of endocarditis OR
- Resolution of manifestations of endocarditis, with antibiotic therapy for 4 days or less OR
- No pathologic evidence of infective endocarditis at surgery or autopsy after antibiotic therapy for 4 days or less.
- Does not meet criteria for possible infective endocarditis, as above.

[a]The category of possible IE represents a modification from the previous published Duke criteria. Major criteria include: positive blood cultures, evidence of endocardial involvement, positive echocardiogram showing a valvular vegetation or abscess, new valvular regurgitation. Minor criteria are predisposing heart condition, fever of 38°C or more, vascular or immunologic manifestations, microbiologic or serologic evidence of active infection.
Source: Adapted from Li et al. (9).

2. Abscesses

An abscess is defined echocardiographically as a finite area of reduced echo density within the valve annulus or an adjacent cardiac structure, in the setting of a valvular infection (15). Its wall may be lined by weakened necrotizing tissue, prone to rupture with fistulization into

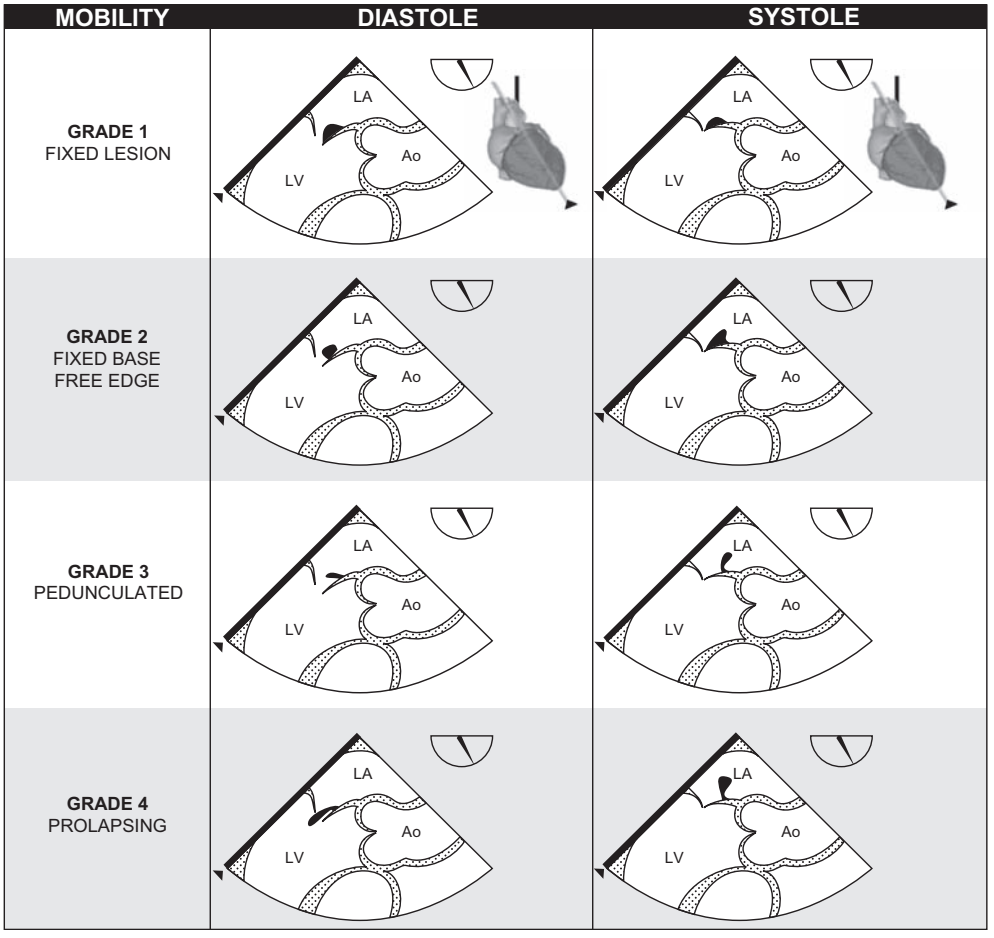

Figure 17.10 Vegetation mobility score in a mid-esophageal long-axis view (Ao, aorta; LA, left atrium; LV, left ventricle). [Adapted from Sanfilippo et al. (11).]

neighboring cardiac chambers or great vessels. Abscess complicating endocarditis is encountered in up to 37% of patients and is usually associated with a complicated clinical course. Transesophageal echocardiography was found to be more sensitive and specific than TTE for identifying the localization of the abscess (15). The differential diagnosis includes caseous infiltration in rheumatic disease which can mimic a mitral valve abscess (Fig. 17.13).

B. Rheumatic Valve Disease

Rheumatic involvement of the mitral valve is suggested by decreased mobility of the leaflets with doming into the LV in association with valve and subvalvular thickening, chordal shortening and calcification. Mitral regurgitation in this condition usually results from malcoaptation of the leaflets.

Most patients with rheumatic MR have some degree of concomitant stenosis, with variable involvement of the aortic and/or the tricuspid valve as well. Mitral valve repair is not as successful for correcting MR in rheumatic valves as for other etiologies such as myxoid degeneration (16). The severity of MR also has significant bearing on the eligibility of a rheumatic mitral stenosis for treatment with percutaneous balloon valvotomy and commissurotomy, in addition to its morphology score (17,18) (see following text).

C. Myxoid Degeneration

Myxomatous valve disease is characterized by thickened, redundant leaflets and chordae with sagging into the LA in systole. Leaflets are considered abnormally thickened when their thickness is >5 mm (19,20). In addition, the mitral valve annulus is deemed abnormally dilated when its maximal end-diastolic annular diameter in the longitudinal or transverse plane is >34 mm (21). Regurgitation in the setting of mitral valve myxoid degenerescence and prolapse is most often associated with annular dilatation (Fig. 17.14) (22).

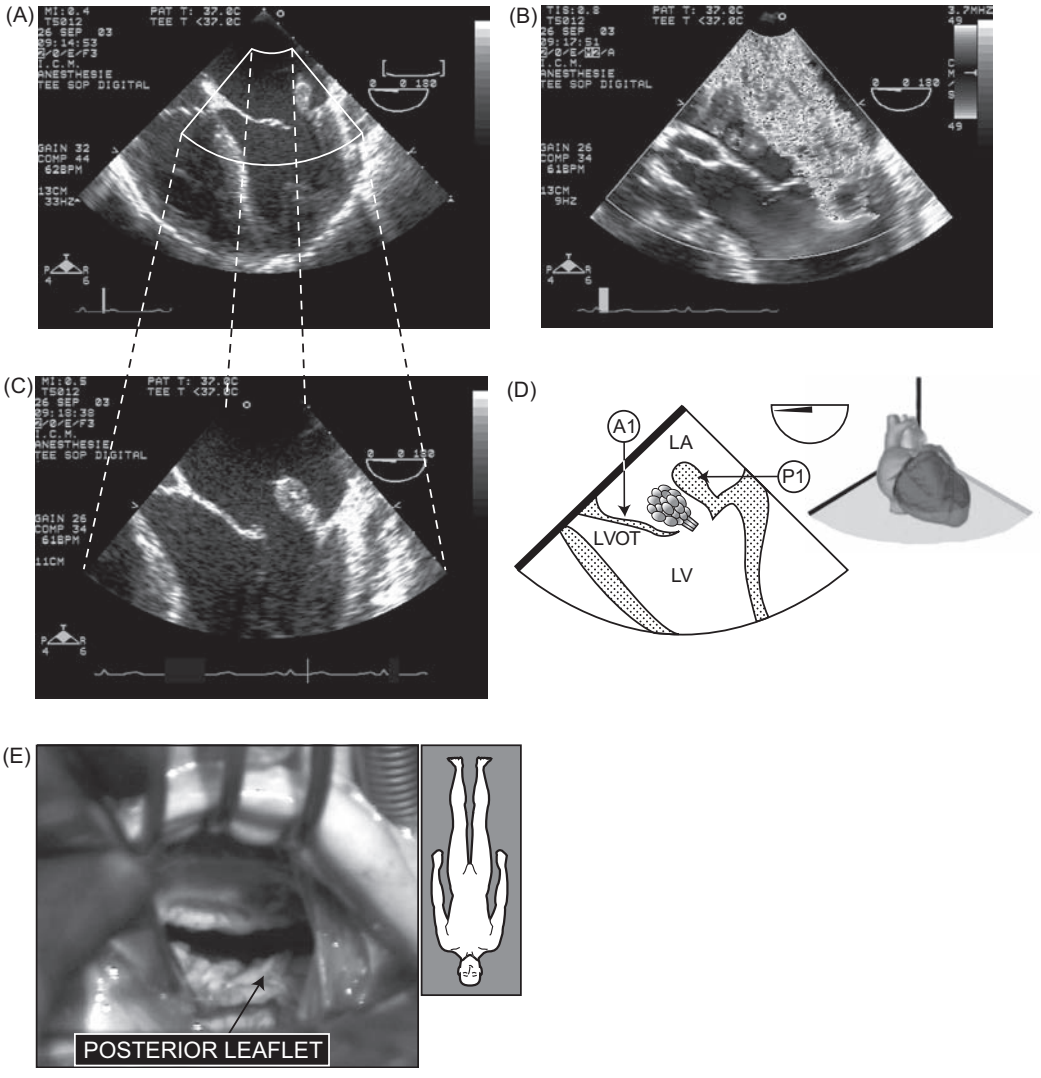

Figure 17.11 Mid-esophageal four-chamber (A) and five-chamber (B–D) views at 0° of a 57-year-old man with endocarditis and large flail of the posterior leaflet (P1 scallop shown here) associated with severe mitral regurgitation. (E) Intraoperative findings: flail of the entire posterior leaflet was present. The patient underwent mitral valve replacement (LA, left atrium; LV, left ventricle; LVOT, left ventricular outflow tract). (Photo E courtesy of Dr. Michel Carrier.)

Myxomatous degenerescence affects preferentially the tip of the leaflets which present a club-like deformity with a ground glass apprearance, extending sometimes onto the inserting chordae tendinae. The severity of the disease may vary from minor valve billowing to severe involvement of both leaflets with frankly prolapsed or flail segments and scallops (Fig. 17.15). On TTE, prolapse has traditionally been diagnosed on the basis of a posterior displacement of one or both leaflets of at least 2 mm beyond the plane of the annulus in the parasternal long-axis view. The same criteria have been applied to the transgastric longitudinal views although this has not been as extensively studied.

As for the diagnosis of flail mitral valve by transthoracic study, this was established when the presence of inverted leaflet in systole with loss of coaptation and an associated rapidly moving linear echodensity was seen in the LA, corresponding to the ruptured chordae tendinae (Figs. 17.16–17.19) (6,23).

The diagnosis of mitral valve prolapse by TEE may easily be missed unless one examines all anterior segments and posterior scallops in multiple incidences systematically, following the method proposed by Lambert et al. (3). Using a systematic approach, Agricola et al. (24) found a 97% overall diagnostic accuracy when TEE results were compared with surgical findings.

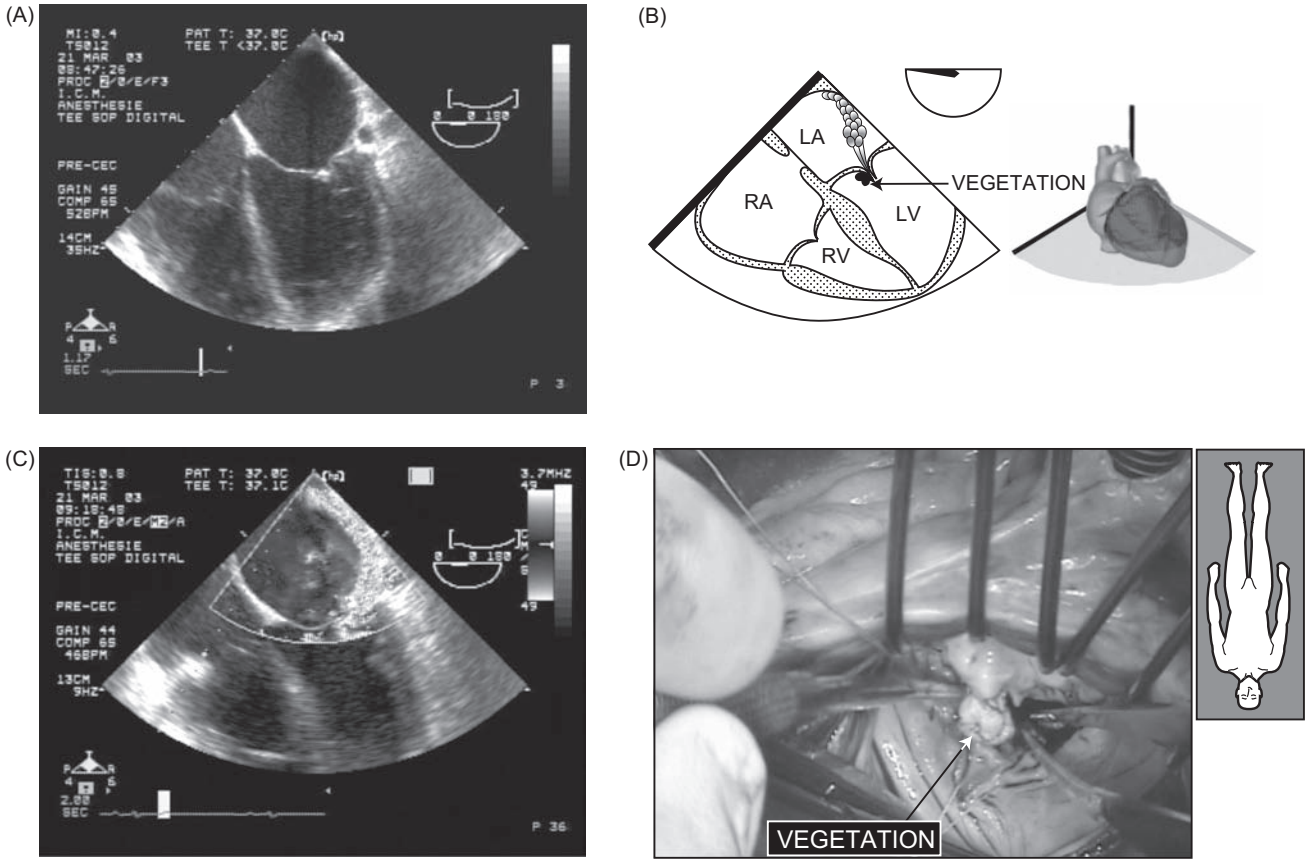

Figure 17.12 A 64-year-old man is scheduled for mitral valve replacement. (A–C) Eccentric mitral regurgitation is due to endocarditis shown in this mid-esophageal four-chamber view: a vegetation with a mobility score of 4 is present on the tip of A2 segment. (D) Intraoperative findings show a vegetation attached to the anterior leaflet at the junction of A1 and A2 (LA, left atrium; LV, left ventricle; RA, right atrium; RV, right ventricle). (Photo D courtesy of Dr. Michel Pellerin.)

Two diagnostic pitfalls were mentioned by these authors: first, when a large P2 scallop prolapse extends on most of the posteromedial commissural area, the adjacent P3 is also, erroneously, identified as prolapsing. As the mid-esophageal four- and two-chamber views often transsect the middle and lateral scallops close to P2, P2 may be mistaken for either P1 or P3. This could be avoided by using the commissural and the long-axis view instead. The other frequent misdiagnosis is failing to diagnose the prolapse of a scallop or a segment opposite to a more obviously prolapsing one.

1. Complexity of Lesion and Relationship to Repair

Nonrheumatic posterior leaflet prolapse due to degenerative mitral valve disease or ruptured chordae tendinae is most often amenable to surgical repair. However, this is more difficult with involvement of the anterior leaflet, presence of rheumatic or ischemic disease as well as calcifications of the leaflets or annulus. In a report of 286 patients with MR, the feasibility of repair was found to be dependent on the mechanism, being higher in the posterior leaflet disease or flail group (88%) than the anterior leaflet disease or flail group (59%) or the severe bileaflet chordal rupture group (29%) (25). Calcifications of the annulus significantly complicate mitral repair. They appear as echo-dense structures with acoustic shadowing, most commonly located in the posterior atrioventricular groove with a typical C-shape distribution between 10 and 2 o'clock in the transgastric short-axis view.

D. Ischemic Mitral Valvular Disease

Ischemic mitral regurgitation (IMR) can be simply defined as the occurrence of MR in a clinical context of myocardial ischemia. It accounts for 13–30% of MV surgery. Four clinical settings are generally recognized: papillary muscle rupture, regurgitation in the setting of acute myocardial infarction, regurgitation due to reversible ischemia with preserved overall left ventricular systolic function, and regurgitation associated with end-stage ischemic

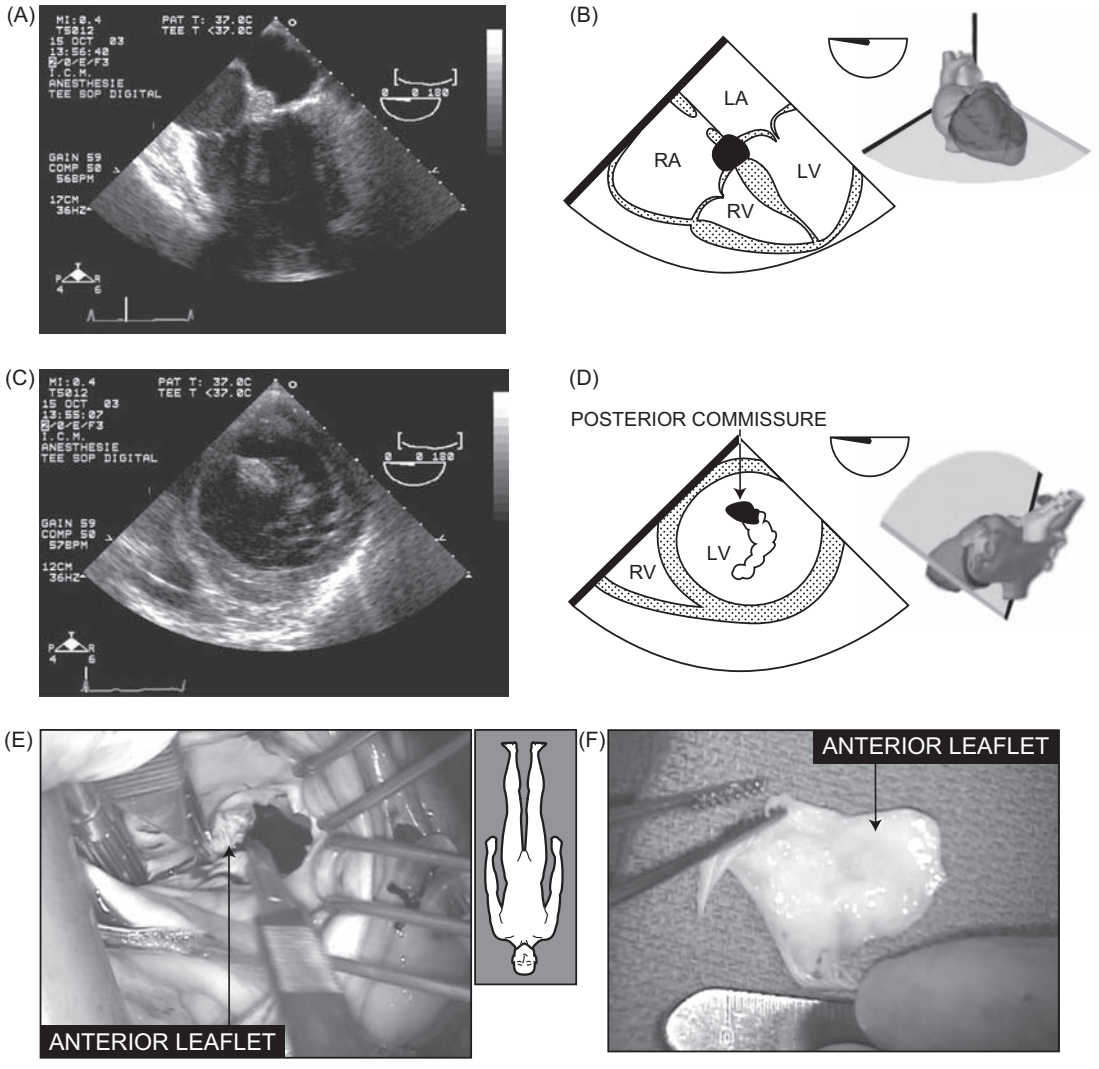

Figure 17.13 A 63-year-old man scheduled for aortic and mitral valve replacement. (A–D) Mitral annular and anterior leaflet thickening was seen in the mid-esophageal and basal transgastric views. (E, F) Surgical exploration of the mitral valve disclosed the presence of material suspicious for an abcess: pathologic examination later found it to be caseous infiltration of the mitral valve (LA, left atrium; LV, left ventricle; RA, right atrium; RV, right ventricle). (Photos E and F courtesy of Michel Pellerin.)

disease and severe left ventricular systolic dysfunction (see Figures 8.20 and 8.21).

Papillary muscle rupture usually happens in the setting of acute myocardial infarction. Because of its dual vascular supply, the anterolateral papillary muscle is less vulnerable to coronary occlusion than the posteromedial papillary muscle and this condition more commonly occurs with inferior wall infarcts. The diagnosis is suspected when a new systolic murmur is heard in a previously stable patient who develops cardiogenic shock during acute myocardial infarction (Fig. 17.20). Partial rupture may also occur.

Ischemic MR results from alterations in the left ventricular shape due to regional wall systolic dysfunction, with preserved leaflets and annular dimensions. It is also typically associated with inferior wall ischemia or infarction. These conditions could involve the posteromedial papillary muscle, leading to subsequent loss of support of the middle aspects of the anterior and posterior leaflets. On 2D imaging, the underlying mitral valve apparatus is shortened, and the leaflets do not reach the level of the mitral annulus, resulting in incomplete closure and regurgitation. The MR jet is usually directed towards the posterolateral atrial wall.

The MR associated with end-stage ischemic heart disease and severe ventricular systolic dysfunction may arise through several mechanisms: these include annular

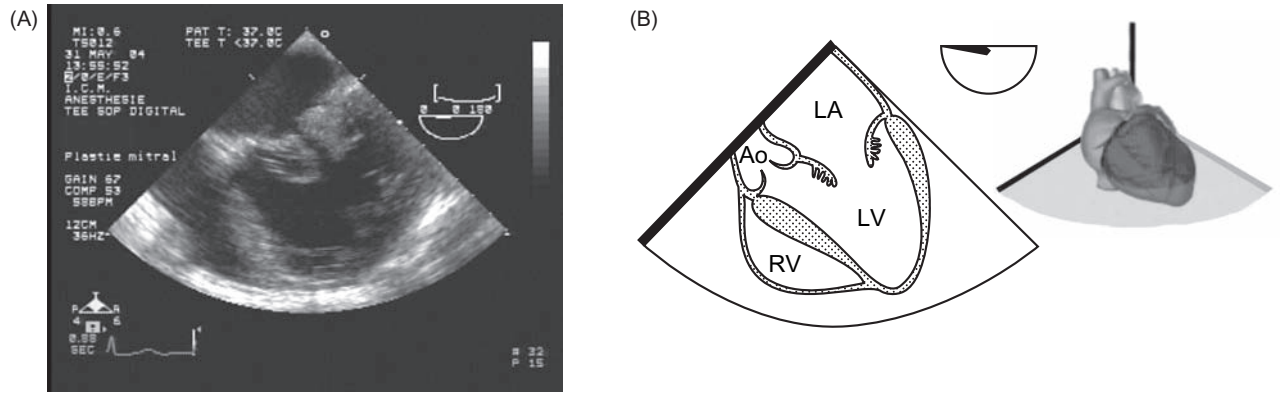

Figure 17.14 Mid-esophageal four-chamber view of a 53-year-old man with severe myxomatous thickening of both anterior and posterior mitral valve leaflets (Barlow's disease) before mitral valve repair (Ao, aorta; LA, left atrium; LV, left ventricle; RV, right ventricle).

dilatation, inadequate papillary muscle traction from myocardial ischemia, excessive obtuse angulation between the papillary muscle and the mitral annular plane, and significant alteration in left ventricular geometry in association with cavity dilatation. The MR is labeled functional, with a central jet where the leaflets are tethered by outward displacement of the left ventricular walls and papillary muscles, with or without concomitant annular dilatation. Similar MR mechanisms are also observed in advanced dilated cardiomyopathy of other etiologies (see Chapter 10).

The prognosis of patients with IMR is substantially worse than regurgitation from other causes.

1. Chordal Rupture

One of the most common causes of flail mitral valve is chordal rupture, often associated with mitral valve prolapse, endocarditis, trauma, or in the setting of acute myocardial infarction (Figs. 17.16–17.20).

E. Traumatic Mitral Valve Injury

The most common cardiac injury seen after blunt chest trauma is myocardial contusion. When cardiac valves are involved, the AoV is the most frequently damaged, followed by the mitral and tricuspid valves. The mitral

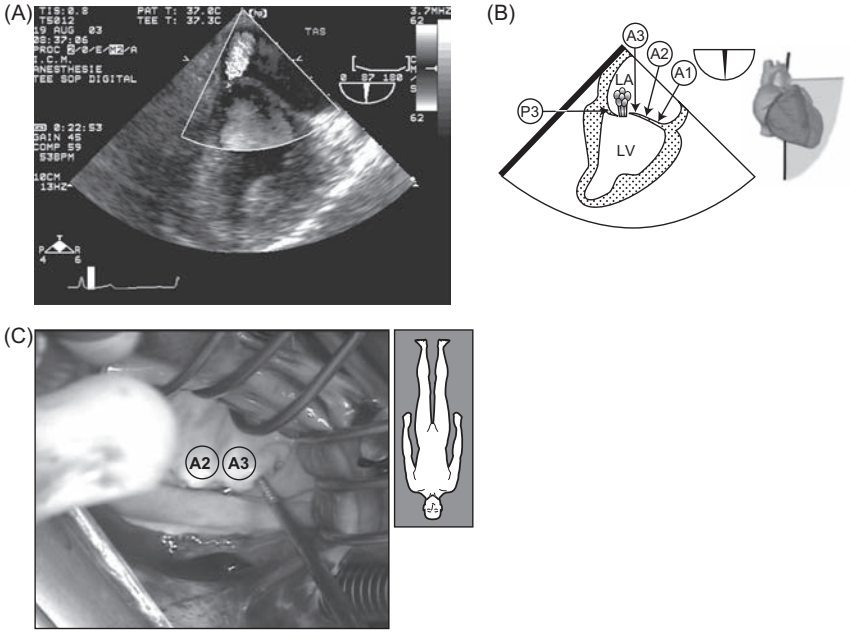

Figure 17.15 A 58-year-old woman scheduled for mitral valve repair. As shown with the mid-esophageal two-chamber view, mitral regurgitation is secondary to a prolapsed anterior mitral leaflet (A2 and A3). (C) Intraoperative findings (LA, left atrium; LV, left ventricle). (Photo C courtesy of Dr. Michel Pellerin.)

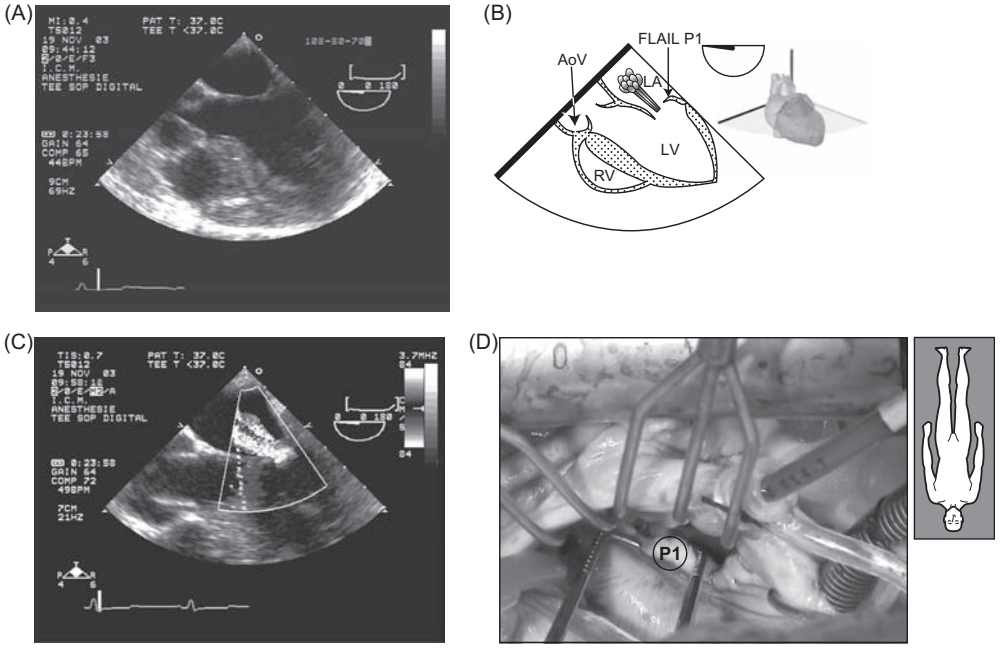

Figure 17.16 74-year-old woman operated on for acute mitral regurgitation. (A–C) Mid-esophageal five-chamber view with anteflexion showing a flail posterior leaflet (P1 scallop) with eccentric mitral regurgitant jet directed anteriorly. (D) Corresponding intraoperative findings (AoV, aortic valve; LA, left atrium; LV, left ventricle; RV, right ventricle). (Photo D courtesy of Dr. Denis Bouchard.)

valve lesions may include, in order of frequency, rupture of a papillary muscle, rupture of chordae tendinae, and laceration of a leaflet. Traumatic rupture of papillary muscles is a relatively rare cause of MR, with an occurrence of only 4% in a postmortem study of 546 patients seen for blunt chest trauma (26). The latter is frequently related to a motor vehicle accident, with injury occurring either through sudden deceleration, traumatic compression of the heart or abrupt increase in intrathoracic or intra-abdominal pressures.

A recent review by Simmers et al. (27) reported 25 cases of successful surgical repair of traumatic MR. The most frequent lesion observed was a tear of the anterolateral papillary muscle (32%), while other injuries included tears of the posterior leaflet (28%), the anterior leaflet (12%), and the posteromedial papillary muscle (8%). A motor vehicle accident was the origin of 60% of the cases and the delay between the initial trauma and the surgical repair varied from a fews days to 25 years.

Transesophageal echocardiography is an extremely valuable tool for excluding mitral valve injury in the hemodynamically unstable trauma patient with pulmonary edema.

II. FUNCTIONAL MANIFESTATIONS OF VALVE LESIONS

Two-dimensional imaging reflects the impact of volume overload from MR on the cardiac chambers. Thus, the evaluation of left atrial and LV size and function provides important information regarding the severity and/or chronicity of the MR which is necessary to assess the need for, and timing of surgery (28). By transthoracic left parasternal views, the end-diastolic minor axis dimension of the LV is normally inferior to 2.8 cm/m^2 while the end-diastolic left ventricular volume is <82 mL/m^2. The normal anteroposterior diameter of the LA does not exceed 2 cm/m^2 with a normal volume no greater than 36 mL/m^2.

A. Mitral Valve Regurgitation—Mechanism and Quantification

Mitral valve regurgitation may be caused by one or a combination of mechanisms related to the etiologies reviewed in the preceding text. Systematic examination by 2D imaging of the valve elements and its surrounding anatomical structures should be aimed at assessing the quality and degree of coaptation between opposite surfaces of the valve occluder and at predicting the location and severity of regurgitant jets by defining their mechanism. These findings are then confirmed by color flow imaging which should display regurgitant flow orientation and characteristics consistent with the presumed mechanism(s) (25). The specific locations of normal and abnormal function of leaflet segments must be sought, with particular attention to the leaflet motion in relation to the

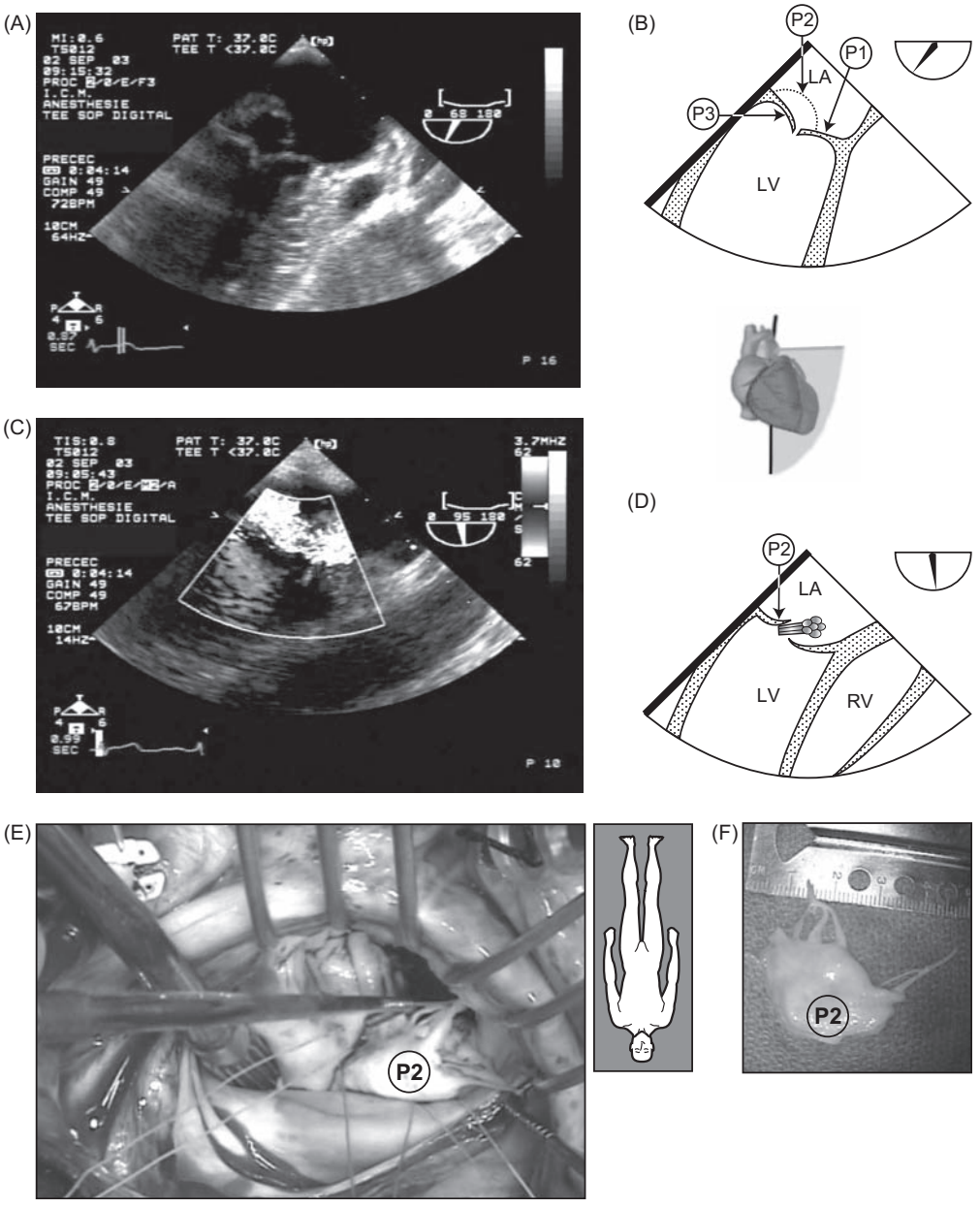

Figure 17.17 75-year-old man with a prolapsed P2 scallop secondary to chordal rupture. (A–D) Mid-esophageal views at ~90° with clockwise rotation. (E, F) Corresponding intraoperative findings with the excised P2 scallop (LA, left atrium; LV, left ventricle; RV, right ventricle). (Photos E and F courtesy of Dr. Michel Pellerin.)

mitral annulus. Leaflet motion should be described as being excessive, normal, or restricted if a portion of the leaflet moves during closure respectively beyond, at or under the annulus plane, using the classification of Carpentier (Table 17.2).

Excessive leaflet mobility is a frequent mechanism and the ensuing jet is typically directed toward the contralateral side of the pathologic leaflet. Myxomatous degenerescence and endocarditis are the usual culprit diseases. Regurgitation caused by papillary muscle infarction usually originates from its respective commissural area.

In contrast, restricted leaflet motion results in a jet directed towards the side ipsilateral to the affected leaflet. If both leaflets are equally limited, the jet is usually central. The most frequent cause of restricted leaflet motion is ischemia. Rheumatic valve disease can also cause restriction in leaflet motion (29).

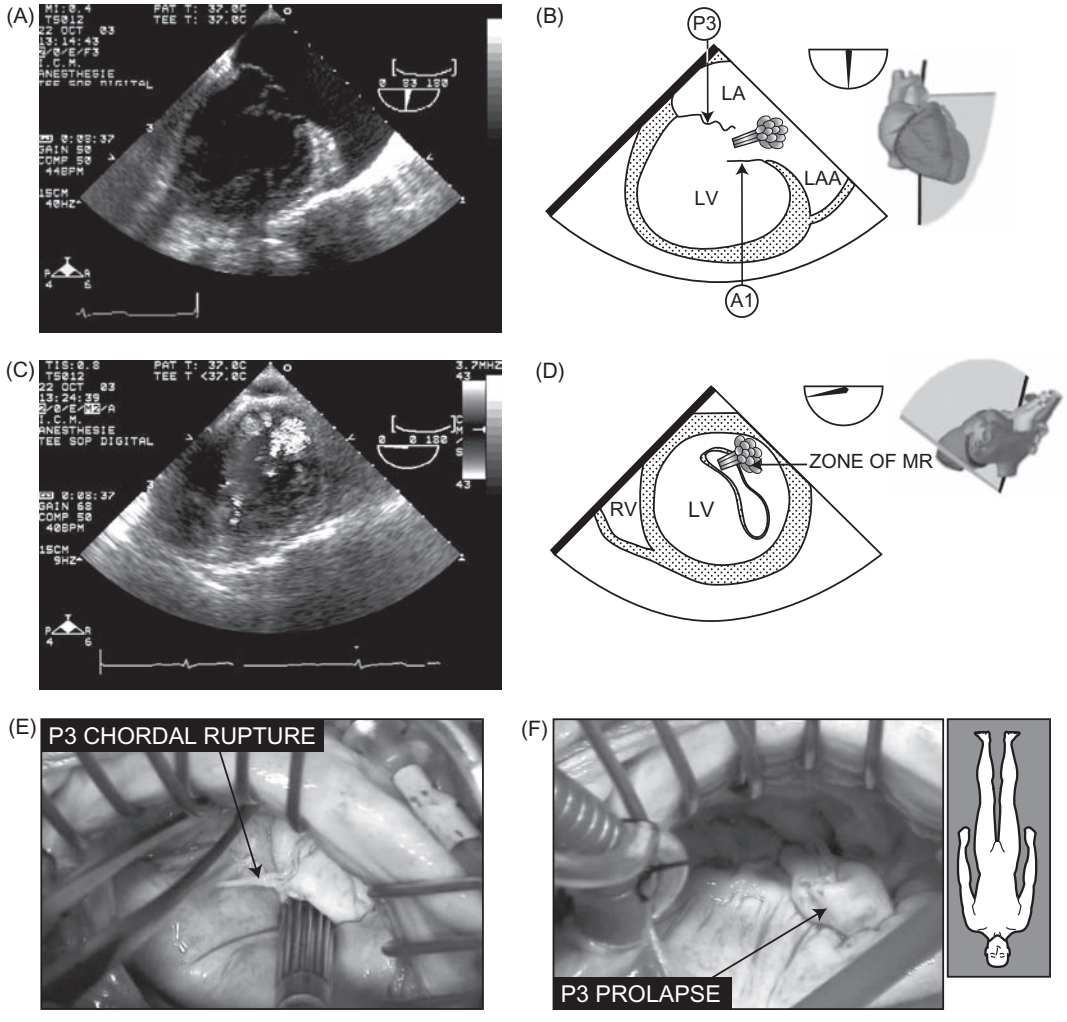

Figure 17.18 75-year-old man with acute mitral valve regurgitation. (A, B) Mid-esophageal view showing a prolapsed P3 scallop secondary to chordal rupture. (C, D) The transgastric basal view at 0° shows an eccentric mitral regurgitation (MR) jet originating from the P3 area. (E, F) Intraoperative findings (LA, left atrium; LAA, left atrial appendage; LV, left ventricle; RV, right ventricle). (Photos E and F courtesy of Dr. Denis Bouchard.)

Last, regurgitation with normal leaflet motion is associated with annular dilatation, leaflet perforation (Fig. 17.21) or a congenital cleft or perforation (Fig. 17.22). The origin of the jet in the latter two conditions is frequently described as eccentric to the commissural line (25).

The advantages and limitations of various quantification methods (Table 17.3) will be reviewed, but no single measure is foolproof.

1. Color Flow Doppler Jet Area Mapping

This is the planimetry of the maximal color flow imaging area occupied by the regurgitant jet during systole. The jet area is assumed to be proportional to the regurgitant volume (30–33). However, the correlation between jet area and MR severity is not consistently good due to a multitude of technical and hemodynamic limitations, including the compliance of the LA, the chronicity and the eccentricity of the regurgitation (1). This method is specifically not reliable with eccentric jets hugging LA walls because of the Coanda effect (which describe the tendency of a fluid to follow a curve surface immediately adjacent to its course). Nevertheless, small, noneccentric jets with an area $<4.0\,cm^2$ or $<20\%$ of the total left atrial area are usually consistent with a trivial or mild degree of MR. Of note, the ratio of the MR jet area over the left atrial area is less used with TEE as this is often not entirely visualized at a given time in 64% of patients (34) due to the close proximity of the transducer to the LA. In the operating room, general anesthesia can reduce the area of the regurgitant jet. The use of phenylephrine to increase blood pressure will however improve the correlation with the measurements obtained in the awake state (Fig. 17.23).

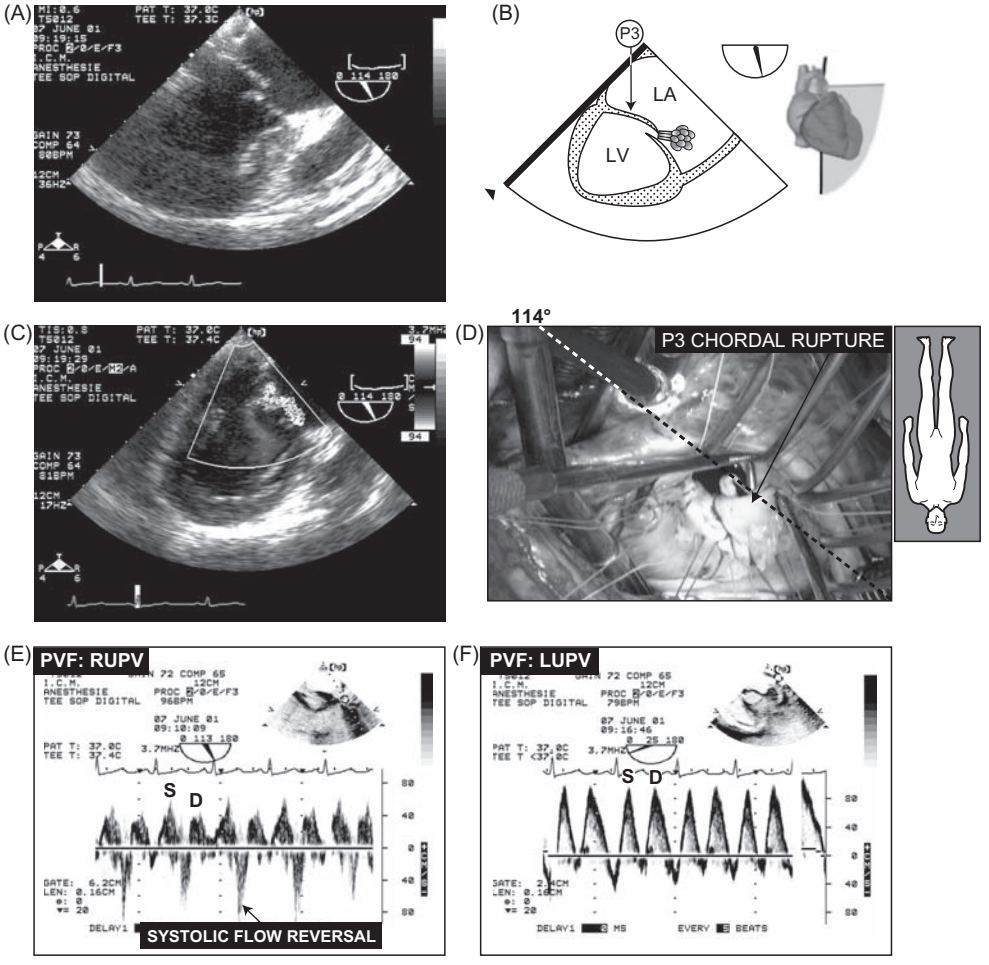

Figure 17.19 (A, B) A 64-year-old woman with acute mitral regurgitation due to P3 chordal rupture seen on a mid-esophageal two-chamber view and at 114°. (C) The prolapsing scallop is seen with an eccentric regurgitant jet directed anteriorly towards the atrial wall and the right upper pulmonary vein (RUPV). (D) Surgical findings. (E, F) Pulsed-wave Doppler examination reveals the presence of systolic flow reversal in the RUPV but not in the left upper pulmonary vein (LUPV) (LA, left atrium; LV, left ventricle; PVF, pulmonary venous flow). (Photo D courtesy of Dr. Michel Pellerin.)

2. Jet Width (Vena Contracta)

This method uses the width of the regurgitant jet at its narrowest portion (vena contracta) close to its origin to evaluate the severity of the lesion. This is best performed by obtaining high resolution, zoomed in views of the mitral valve with color flow imaging in either four-chamber or long-axis mid esophageal views (35). The two-chamber view is not ideally suited for this measurement as it invariably crosses through several parts of the line of leaflet coaptation and may show a wide vena contracta even in mild MR.

The correlation reported by Hall et al. (36) between the vena contracta and the regurgitant volume or the effective regurgitant orifice area (EROA) suggests that it is reliable and efficient in predicting mild and severe MR while being less accurate for discriminating moderate degrees of MR. A vena contracta <3.0 mm usually denotes mild MR whereas the cut-off value for severe MR has ranged between 6.0 and 8.0 mm (Fig. 17.24) (35). The size of the vena contracta is relatively independent of flow rate and driving pressure for a fixed orifice and is less sensitive to hemodynamic variations (Fig. 17.25), instrument settings, orifice geometry and interindividual interpretation (37). It works equally well for central and eccentric jets, but is less useful in quantifying MR with multiple jets (Table 17.3).

3. Pulmonary Venous Flow

In normal adults, pulmonary venous flow (PVF) is characterized by predominant flow during systole (Figures 4.20 and 4.21), except in younger healthy adults with low ventricular compliance (see Chapter 4–Section II.I).

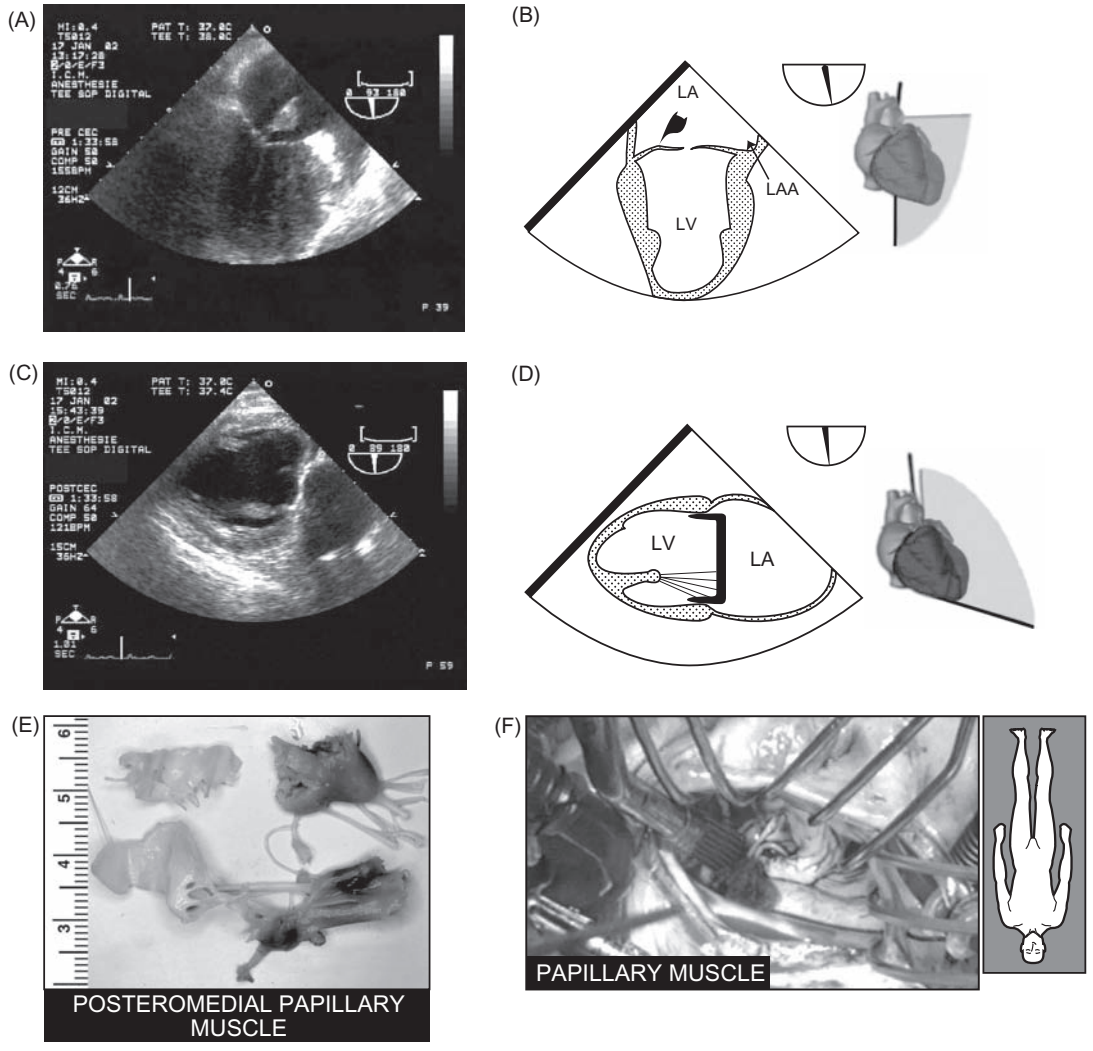

Figure 17.20 Posteromedial papillary muscle rupture with acute severe mitral regurgitation in a 58-year-old man with acute inferior myocardial infarction. (A, B) The torn posteromedial papillary muscle is seen prolapsing in the left atrium (LA) from this two-chamber mid-esophageal view. (C, D) After prosthetic mitral valve replacement (MVR), the subvalvular apparatus is seen from the transgastric view at 90°. (E, F) Intraoperative findings (LAA, left atrial appendage; LV, left ventricle). (Photos E and F courtesy of Drs. Nicolas Noiseux and Denis Bouchard.)

With increasing MR severity, there is systolic PVF blunting with progressive diminution of the systolic velocity. However, systolic flow blunting can also be seen in other situations such as elevated left atrial pressure from other etiologies and atrial fibrillation. Severe MR results in systolic flow reversal in the pulmonary veins (Fig. 17.26). Pulmonary venous flow systolic reversal is 98% specific but unfortunately 34% sensitive for severe MR when compared with calculation of the effective regurgitant orifice (38). The presence of PVF reversal is dependent on hemodynamic conditions (Fig. 17.27). Indeed, hypotension associated with general anesthesia may mask this reversal of systolic flow. Finally, interrogation of all pulmonary veins should be performed as an eccentric jet may be preferentially directed towards a single vein where systolic flow reversal will be found, while it may not be present in the other pulmonary veins (Fig. 17.19).

Table 17.2 Functional Classification of Carpentier

Type I:	Normal leaflet motion
Type II:	Excessive leaflet motion (prolapse)
Type III:	Restricted leaflet motion
	a. during diastole & systole (rheumatic)
	b. during systole (ischemic)

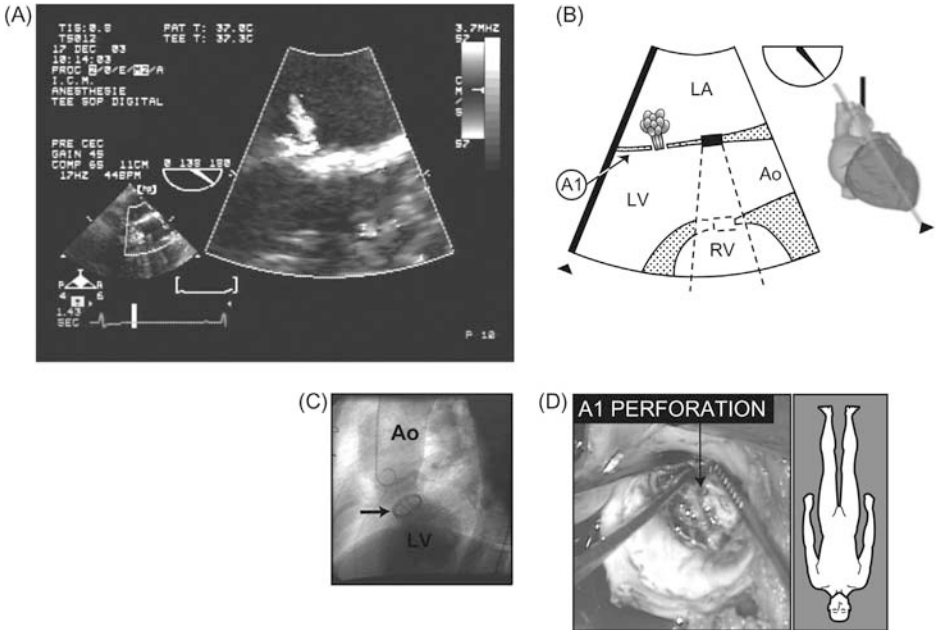

Figure 17.21 Perforated anterior leaflet in a 58-year-old man re-operated on for an aortic aneurysm and severe aortic regurgitation after aortic valve replacement. (A, B) Mid-esophageal long-axis view showing mitral regurgitation from a perforated A1 segment. (C) Aortogram showing the aneurysmal ascending aorta, the bi-leaflet aortic valve prosthesis (arrow) with severe aortic regurgitation opacifying the left ventricle (LV). Note also opacification of the coronary arteries. (D) Intraoperative findings: a small perforation of A1 was present just below the aortic valve prosthesis (Ao, aorta; LA, left atrium; RV, right ventricle). (Photo C courtesy of Dr. Michel Pellerin.)

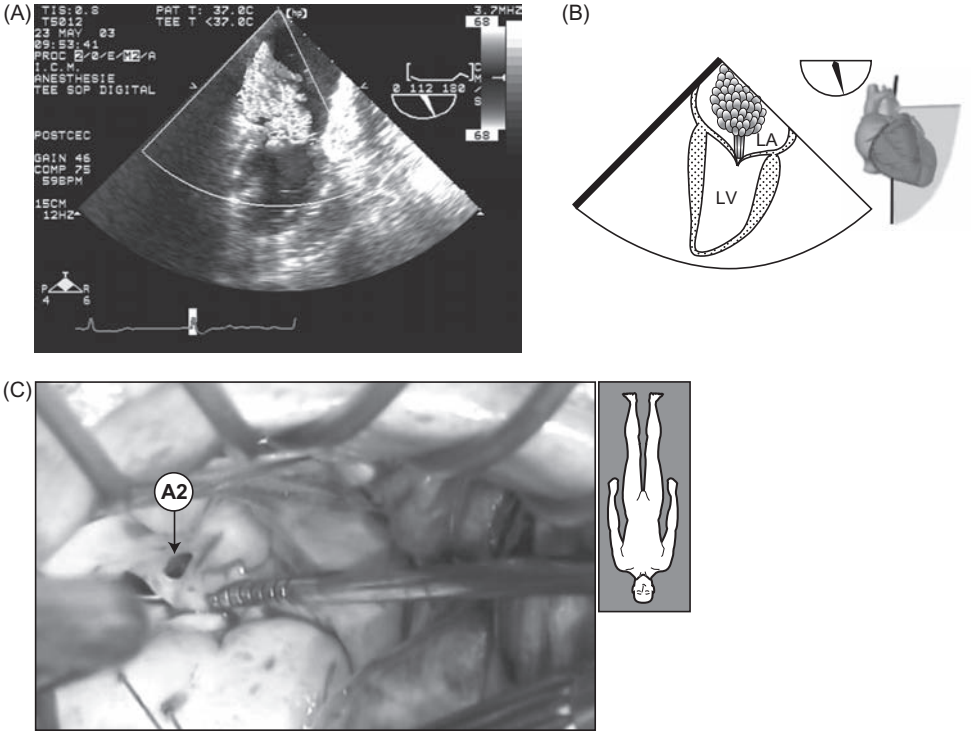

Figure 17.22 (A, B) New onset severe mitral regurgitation after closure of an atrial septal defect in a 56-year-old woman from a mid-esophageal two-chamber view. (C) A congenitally perforated anterior leaflet (A2) was found upon exploration of the mitral valve (LA, left atrium; LV, left ventricle). (Photo C courtesy of Dr. Louis P. Perrault.)

Table 17.3 Mitral Regurgitation Severity Score

	Mild	Moderate		Severe
Structural parameters				
LA size	Normal AP diameter $\leq$2 cm/m^2 LA vol $<$36 mL/m^2	Normal or dilated		Usually dilated (unless acute MR)
LV size	Normal LV diam $\leq$2.8 cm/m^2 LVEDV $\leq$82 mL/m^2	Normal or dilated		Usually dilated (unless acute MR)
MV leaflets or subvalvular apparatus	May be abnormal	May be abnormal		Dilated annulus Flail leaflet Ruptured papillary muscle
Doppler parameters				
MR jet area on CFI	$<$4 cm^2, $<$20% LA area	Variable		$>$10 cm^2, $>$40% LA area (unless wall-hugging jet)
MV inflow (PWD)	E/A $<$ 1	Variable		E $>$ 1.2 cm/sec
MR jet density (CWD)	Faint	Dense		Dense
MR jet contour (CWD)	Parabolic	Parabolic		Early-peaking triangular
Pulmonary veins (PWD)	Normal systolic flow predominance	Systolic flow blunting (may also occur with high LA pressure or A fib)		Systolic flow reversal
MR quantitation				
Vena contracta (cm)	$<$0.3	0.30–0.69		$\geq$0.70
PISA diameter (cm) at a Nyquist limit 40 cm/sec	$<$0.4	0.4–0.89		$>$0.9
Regurgitant volume (mL)	$<$30	30–44	45–59	$\geq$60
Regurgitant fraction (%)	$<$30	30–39	40–49	$\geq$50
EROA (cm^2)	$<$0.20	0.20–0.29	0.30–0.39	$\geq$0.40

Note: A fib, atrial fibrillation; AP, anteroposterior; CFI, color flow interrogation; CWD, continuous-wave Doppler; EROA, effective regurgitant orifice area; LA, left atrium; LV, left ventricle; LVEDV, left ventricular end-diastolic volume; MR, mitral regurgitation; MV, mitral valve; PISA, proximal isovelocity surface area; PWD, pulsed-wave Doppler; vol, volume.
Source: Adapted with permission from Zoghby et al. (1).

4. *Continuous-Wave Doppler*

The maximal velocity of the regurgitant jet itself does not provide useful information about the severity of MR. However, the density of the continuous-wave (CW) Doppler signal, which is proportional to the number of red blood cells (i.e. the regurgitant volume) reflecting the ultrasound beam, is a qualitative index of MR severity. The contour of the MR velocity profile may also provide information about MR severity: for example, a truncated, triangular jet contour with early peaking of the maximal velocity suggests elevated left atrial pressure or a prominent regurgitant wave in the LA.

5. *Proximal Isovelocity Surface Area*

The Proximal Isovelocity Surface Area (PISA) method is derived from the hydrodynamic principle describing flow through a narrowed orifice: as red blood cells approach the smaller orifice, their velocity increases gradually and red blood cells with similar velocity form concentric hemispheric shells which surface or diameter decrease as the isovelocity increases. From this principle, the following equations are derived (see Chapter 5–Section II.F).

$$\text{ERO} = 2\pi r^2 \frac{v_r}{V_{\text{MR max}}} \tag{17.1}$$

where ERO is the effective regurgitant orifice (in cm^2); r is the measured radius of the hemispheric shell of the aliased velocity; v_r is the aliased velocity at the radius r, identified as the Nyquist limit (in cm/sec); and $V_{\text{MR max}}$ is the maximal MR velocity across the orifice, obtained by CW Doppler (in cm/sec).

$$\text{Mitral Regurgitant Volume} = \text{ERO}_{\text{MV}} \times \text{TVI}_{\text{MR}} \tag{17.2}$$

where ERO is the effective regurgitant orifice (in cm^2); and TVI_{MR} is the time velocity integral (in cm) of the mitral regurgitant signal obtained by CWD doppler.

To obtain the ERO and the regurgitant volume, four parameters are required. The measured radius (r) of the hemispheric shell of the aliased velocity (v_r) is obtained

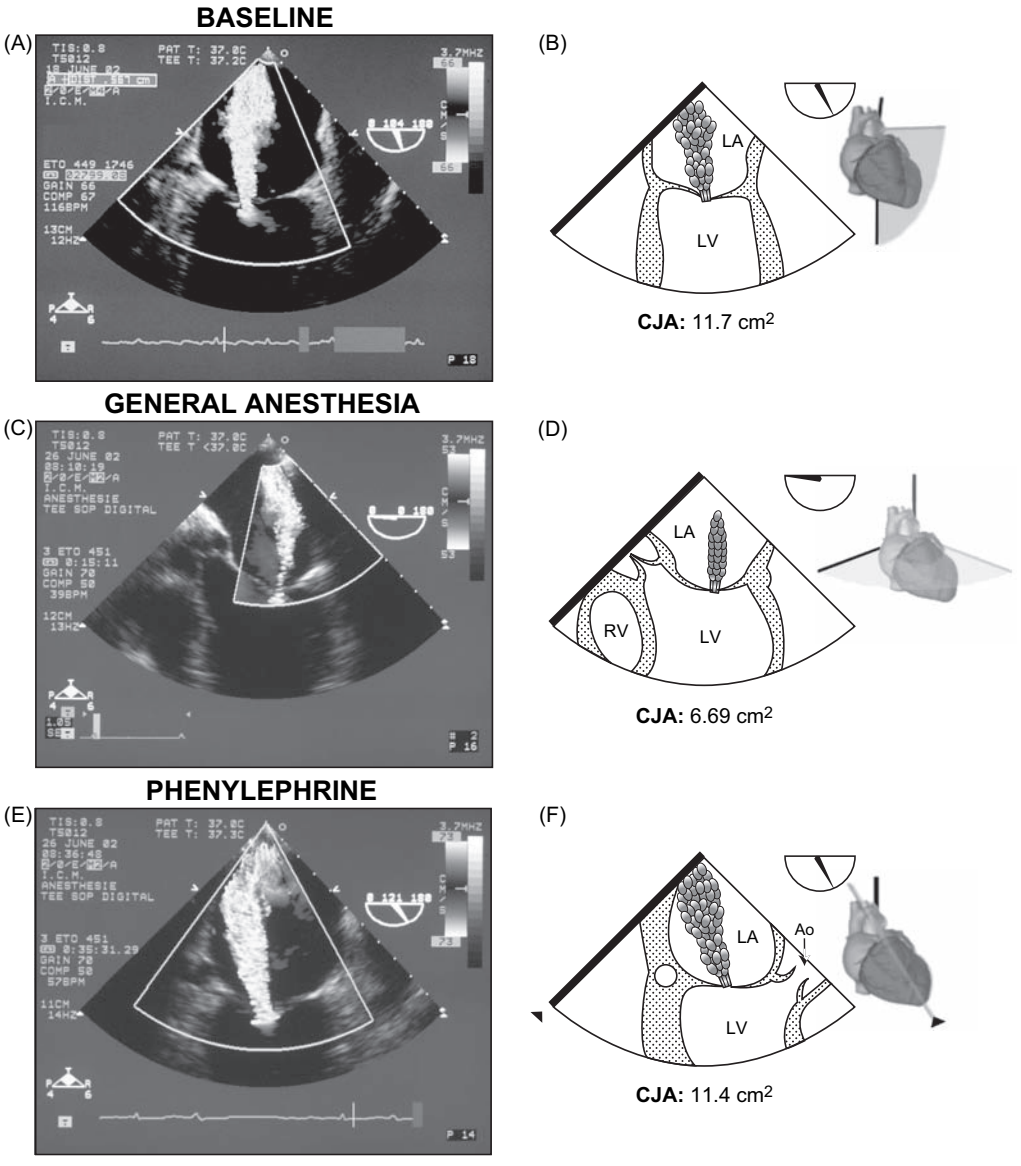

Figure 17.23 Color jet area (CJA) in the same patient with mitral regurgitation during awake baseline state (A, B), after induction of general anesthesia (C, D) and using phenylephrine to obtain the same systolic arterial pressure (150 mmHg) as during baseline (E, F). Note the reduction in the CJA after general anesthesia (Ao, aorta; LA, left atrium; LV, left ventricle; RV, right ventricle). (Courtesy of Drs. Alexandro Gisbert and Arsene Basmadjian.)

by obtaining high resolution, zoomed-in views of the mitral valve with color flow imaging, carefully positioned at the center of the regurgitant jet and aligned with the direction of the jet: this is confirmed by the uninterrupted visualization of the hemispheric shell with the vena contracta. Failure to obtain this position will result in significant underestimation of the true radius of the hemispheric shell. Next, the v_r of the color scale is adjusted down to generate a nice hemispheric shell. This is generally done by shifting the baseline of the color scale towards the direction of the regurgitant flow or, less frequently, by changing the Nyquist limit through lowering the maximal velocity of the color scale. The range of v_r for this measurement is usually between 25 and 40 cm/sec. Qualitatively, the presence of a PISA visible at a Nyquist limit of 50–60 cm/sec should alert to the presence of severe MR.

The r is measured from the edge of the hemispheric shell where the color scale changes (from one edge of the spectrum to the other) to the base of the shell at the plane of the

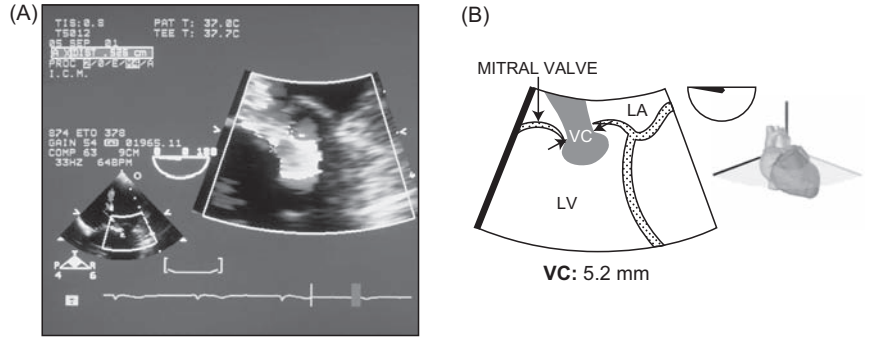

Figure 17.24 Moderate mitral regurgitation with a vena contracta (VC) measured at 5.2 mm on color-flow imaging at a mid-esophageal five-chamber view (LA, left atrium; LV, left ventricle). (Courtesy of Dr. Arsene Basmadjian.)

leaflets. The latter is best visualized by intermittently turning off the color flow overlay on the freeze frame.

To complete the calculation of the ERO and the regurgitant volume, the maximal velocity (V_{MR}) and the time velocity integral (TVI) of the regurgitant jet are measured on continuous-wave Doppler examination well aligned with the direction of the jet.

The PISA method is more accurate for central jets than for eccentric jets, and for regurgitation with a circular orifice. It is sometimes difficult to judge the precise location of the orifice and the flow convergence shape. The r is the critical measurement, as any error introduced on this parameter will be magnified to its squared value. Generally, an ERO $>0.40\ cm^2$ is consistent with severe MR, $0.20–0.39\ cm^2$ with moderate MR, and $<0.20\ cm^2$ with mild MR (Table 17.3). The ERO is a more robust parameter compared with color Doppler planimetry and is less altered with changing hemodynamic conditions (Fig. 17.25).

6. *Regurgitant Volume*

Determination of regurgitant volume by PISA method has been described earlier. The mitral regurgitant volume may equally be obtained by the continuity equation using volumetric flow calculation (see Chapter 5, Section II.G) (39):

$$\text{Mitral Regurgitant Volume} = SV_{MV} - SV_{LVOT} \tag{17.3}$$

The stroke volume across the aortic valve (SV_{LVOT}) is given by the following equation:

$$SV_{LVOT} = 0.785\ d^2_{LVOT} \times TVI_{LVOT} \tag{17.4}$$

where d_{LVOT} is the diameter (in cm) of the left ventricular outflow tract; and TVI_{LVOT} is the time velocity integral (in cm) by PWD.

The diameter of the left ventricular outflow tract (LVOT) is measured through a zoomed-in view of the AoV in the mid-esophageal window at 135°, from the base of the right coronary cusp to the base of the opposite cusp (from inner edge to inner edge). The TVI of the LVOT is best obtained by pulsed-wave Doppler interrogation through the transgastric view at approximatively 110°, tracing the peak (outer edge of the) velocity Doppler signal envelope (40).

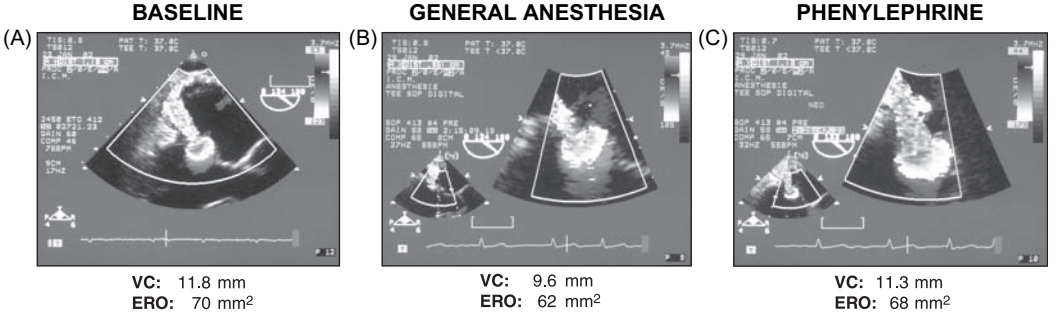

Figure 17.25 Effective regurgitant orifice (ERO) area and vena contracta (VC) in the same patient with mitral regurgitation during awake baseline state (A), after induction of general anesthesia (B) and using phenylephrine (C) to obtain the same arterial pressure (150 mmHg) as during baseline. Note the similarity between values in all three conditions. (Courtesy of Drs. Alexandro Gisbert and Arsene Basmadjian.)

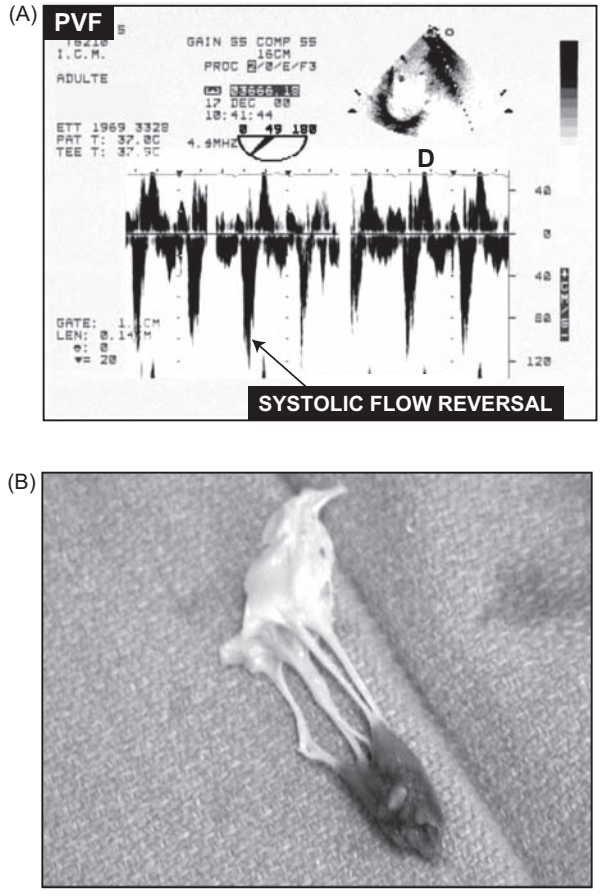

Figure 17.26 Acute mitral regurgitation in a 61-year-old man with rupture of the posteromedial papillary muscle. (A) Pulsed-wave examination of the pulmonary venous flow (PVF) showing significant systolic flow reversal (the equivalent of a "v" wave), consistent with severe regurgitation. (B) Excised pathology specimen. (Photo B courtesy of Dr. Yves Hébert.)

In the case of MR without associated significant aortic regurgitation (AR), the left ventricular total stroke volume (SV) is given by the SV across the mitral valve (SV_{mv}):

$$SV_{MV} = 0.785\ d_1 \times d_2 \times TVI_{MV} \tag{17.5}$$

where d_1 is the diameter of the mitral valve annulus in the four-chamber view; d_2 is the diameter of the mitral valve annulus in the two-chamber view or mid-commisural; and TVI_{MV} is the time velocity integral (in cm) measured by PWD with the sample volume in the center of the mitral valve annulus.

This equation assumes that the mitral valve annulus has an elliptical shape and requires the measurement of the two diameters d_1 and d_2 in orthogonal views (four- and two-chamber views), from inner edge to inner edge at the base of the mitral leaflets in diastole (41). The precise measurement of the TVI at the mitral annulus level requires an optimal alignment of the ultrasound beam with the direction of the flow. In contrast to the LVOT, the measurement of TVI is performed at the mitral annulus tracing the modal (most dense) velocity on the Doppler signal envelope, rather than the peak velocity (outer edge of the signal). Although the measurements of diameters for aortic and mitral valve measurements are the most common source of error in the calculation of volumetric flow, they were however found to be reproducible in an individual patient (42).

In the presence of significant AR, the systemic volumetric flow can alternatively be calculated at the pulmonary valve annulus or the pulmonary trunk.

While the PISA method measures the ERO first and secondly deducts the regurgitant volume, the continuity equation yields first the regurgitant volume and then the ERO using the following equation:

$$ERO_{MV} = \frac{MR\ Vol}{TVI_{MR}} \tag{17.6}$$

where ERO is the effective regurgitant orifice (in cm^2); and TVI_{MR} is the time–velocity integral (in cm) of the mitral regurgitant signal obtained by CWD, tracing the peak (outer edge) of the Doppler signal envelope.

The regurgitant fraction is given by the following equation:

$$RF = \frac{RegVol}{SV_{Total}} \times 100 \tag{17.7}$$

where RF is the regurgitant fraction (in %); RegVol is the regurgitant volume (in mL); and SV_{Total} is the total stroke volume (in mL) of the left ventricle.

The regurgitant volume is obtained either by the PISA method or through the continuity equation. The total SV of the LV is obtained by volumetric measurement at the level of the mitral valve annulus, but it can be equally measured from the difference between the 2D tracing of end-diastolic (EDV) and end-systolic volumes (ESV).

Determination of regurgitant volume and ERO through the continuity equation offers an advantage in the presence of very eccentric jets or multiples jets, where the PISA and vena contracta method may be more difficult to perform. On the other hand, these calculations are time-consuming and require careful execution which is sometimes difficult to perform in the operating room.

7. *Integrated Approach*

The task force suggests a scheme of specific signs, supportive and quantitative to help grade MR (Table 17.3). The approach to the evaluation of MR severity should ideally integrate multiple parameters rather than depend on a single measurement. If multiple qualitative signs of MR are present, no further measurements are required. If there

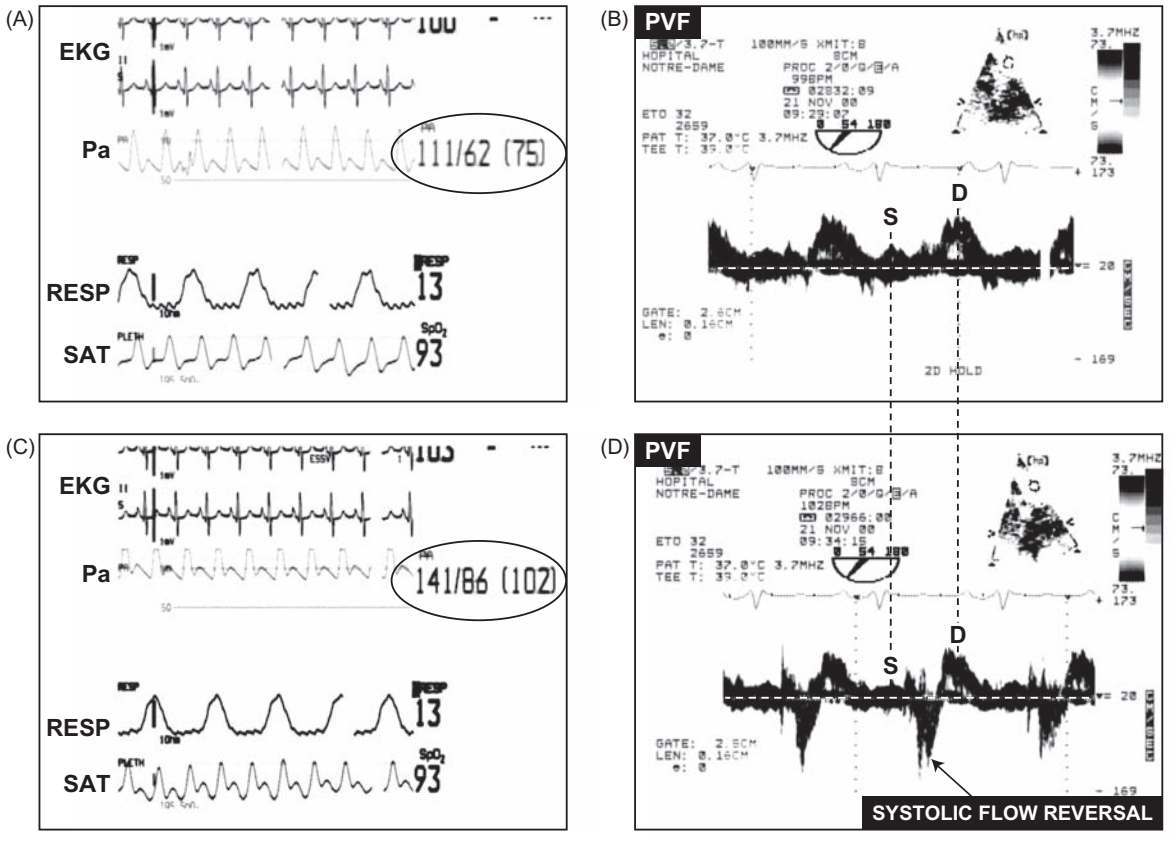

Figure 17.27 Changes in pulmonary venous flow (PVF) in a 54-year-old patient with mitral regurgitation in response to manipulation of loading conditions. With an arterial pressure (Pa) of 111/62 mmHg in (A), the pulsed-wave Doppler profile of the PVF shows systolic forward flow blunting, with diastolic flow predominance (B). With increased afterload by giving intravenous phenylephrine to raise the Pa up to 141/86 mmHg (C), frank pulmonary venous systolic flow reversal develops, consistent with severe mitral regurgitation (D) (EKG, electrocardiogram; RESP, respiration; SAT, saturation.)

is discordance between these signs, or if they suggest more severe degree of MR than mild, quantitative measurements of MR through several methods should be performed.

8. Provocative Testing

In the operating room, a change in the loading conditions is frequently observed after induction of anesthesia, resulting in an apparent decrease in the severity of MR (Figs. 17.23 and 17.25). To reflect the state of preoperative MR correctly, dynamic re-evaluation must be performed by carefully increasing systolic blood pressure using small boluses of phenylephrine (50 μg). In a study of patients with IMR, Basmadjian et al. (personal communication) reported that the severity of intraoperative MR evaluated with neosynephrine challenge was comparable to that observed by TEE in the awake patient.

B. Mitral Stenosis

The most common etiology of mitral stenosis (MS) is rheumatic heart disease. Other causes include nonrheumatic calcification or infiltration of the mitral annulus and leaflets (such as seen in chronic intoxication with ergot-derived substances), congenital lesions (parachute MV, supravalvular ring, mitral arcade) and several miscellaneous lesions (vegetation, tumor, cor triatriatum, thombi) as well as prosthetic valve dysfunction.

1. Echocardiographic Findings

The typical 2D echocardiographic features of the rheumatic mitral valve include (Fig. 17.28):

1. Thickening and calcification of the mitral leaflets with commissural fusion.
2. Calcification, fusion, fibrosis, and shortening of the subvalvular apparatus.
3. "Hockey-stick" deformation of the anterior mitral leaflet in diastole.
4. Decreased mobility of the posterior mitral leaflet.

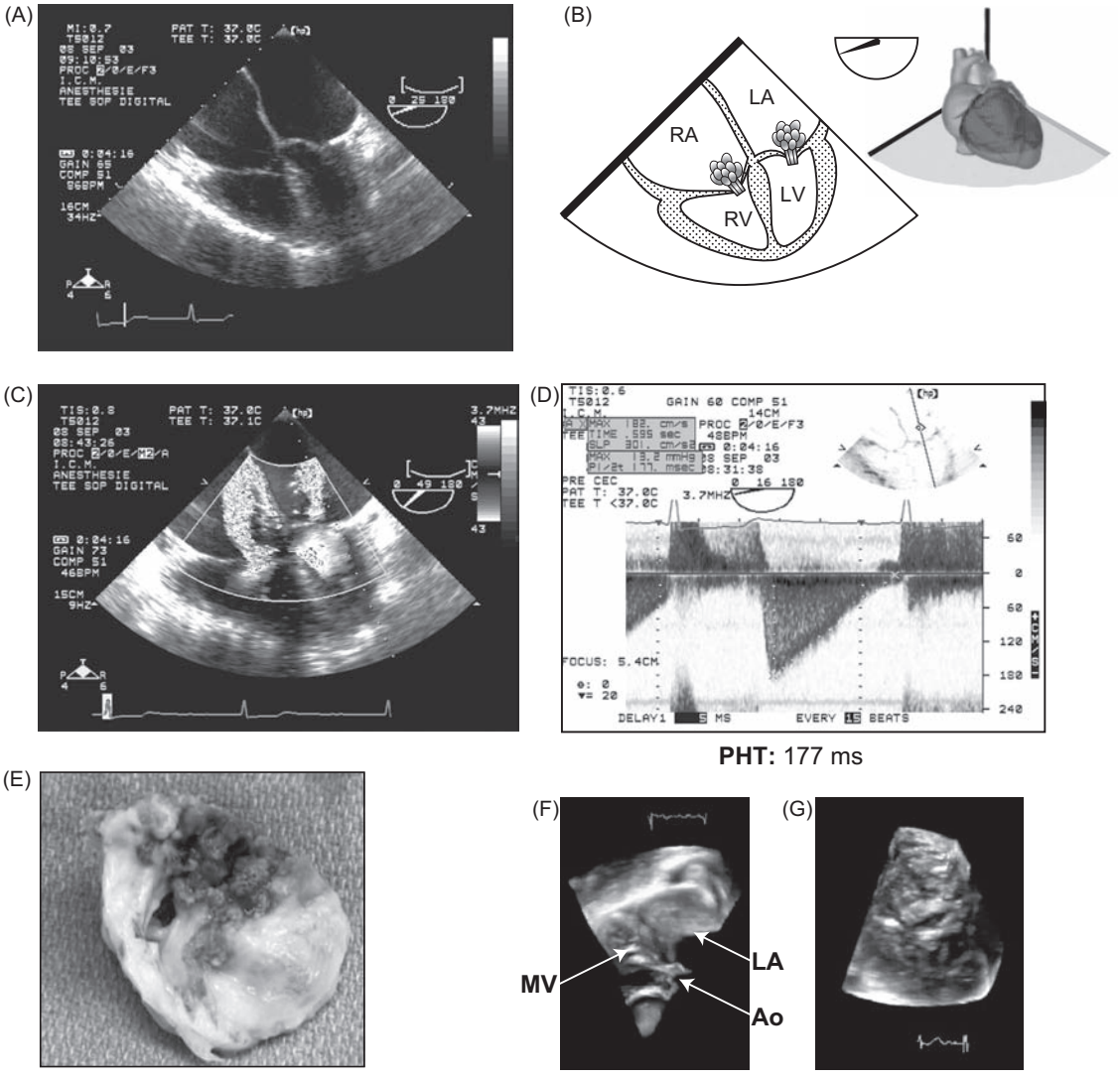

Figure 17.28 Moderate mitral stenosis and regurgitation in a 51-year-old woman. (A–C) Mitral and tricuspid regurgitation are evident on the mid-esophageal four-chamber view. (D) On continuous-wave Doppler, the mean mitral valvular diastolic gradient is measured at 4.9 mmHg with a pressure half-time (PHT) of 177 ms. (E) Intraoperative aspect of a stenotic mitral valve (MV). (F, G) Three-dimensional echocardiographic aspect of mitral stenosis (Ao, aorta; LA, left atrium; LV, left ventricle; RA, right atrium; RV, right ventricle). (Photo E courtesy of Michel Pellerin and F, G courtesy of Philips.)

Abascal et al. (43) have proposed an echocardiographic score (BVR score) for patients undergoing mitral balloon valvuloplasty based on the valve thickness, the extent of calcification, the mobility of the leaflets and the extent of the subvalvular apparatus involvement (Table 17.4). Patients with a score under eight (8/16) fare better with a 90% chance of achieving good results, defined as a valve area $>1.5\,cm^2$ or an increase of 25% of mitral valve area (MVA) above the baseline value, with a low incidence of restenosis at one year. The score is also useful in predicting the progression of the disease (44). Finally, moderate to severe MR is a contraindication to percutaneous mitral valvuloplasty.

2. Associated Findings

Patients with rheumatic mitral disease may present for valvular replacement with a history of percutaneous balloon valvuloplasty through a trans-septal approach. A variable size residual atrial septal defect may, therefore, be present (Fig. 17.29).

The typical picture of severe MS includes significant left atrial enlargement with a normal-sized or small LV (Fig. 17.29). Left atrial thrombus should always be ruled out, especially in the presence of atrial fibrillation (Fig. 17.30). The whole LA and particularly the left atrial appendage (LAA) should be carefully scanned and

Table 17.4 BVR Echocardiographic Score Used to Predict Outcome of Mitral Valve Valvuloplasty

Grade	Mobility	Subvalvular thickening	Thickening	Calcification
0	Normal mobility	No thickening	Normal leaflet thickness	No calcification
1	Highly mobile valve with only leaflets tips restricted	Minimal thickening just below the mitral leaflets	Leaflets near normal in thickness (4–5 mm)	A single area of increased echo brightness
2	Leaflet mid and base portions have normal mobility	Thickening of chordal structures extending up to one-third of the chordal length	Midleaflets normal, considerable thickening of margins (5–8 mm)	Scattered areas of brightness confined to leaflet margins
3	Valve continues to move forward in diastole, mainly from the base	Thickening extending to the distal third of the chords	Considerable thickening of all leaflet tissue (5–8 mm)	Extensive brightness extending to the mid-portion of the leaflet
4	No or minimal forward movement to the leaflets in diastole	Extensive thickening and shortening of all chordal structures extending down to the papillary muscles	Considerable thickening of all leaflet tissues (>8–10 mm)	Extensive brightness throughout much of the leaflet tissue

Note: Each of the four characteristics is given a score from 0 to 4, and the BVR score is calculated as the sum of the four individual scores, with results thus ranging from 0 to 16.

examined. Spontaneous echo contrast (smoke) may be seen in the LA, particulary if the MVA is $<1.4\,cm^2$. Its presence signals a very high risk for atrial thrombus (up to 60%) (45) and systemic embolism (46). The contractility of the left atrial appendage may also be assessed by pulsed-wave (PW) Doppler interrogation (Fig. 17.31) (47): when velocities are <25 cm/sec, the risk of thrombosis is high.

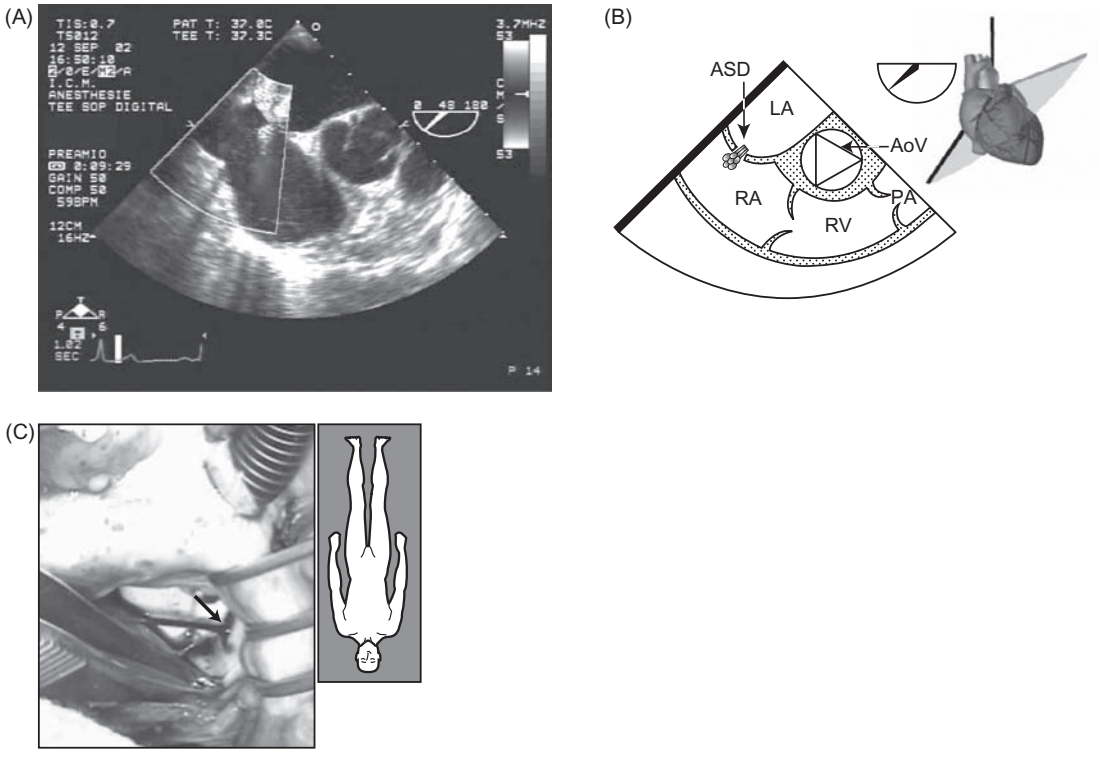

Figure 17.29 (A, B) Mid-esophageal 48° view of an iatrogenic atrial septal defect (ASD) with a left-to-right shunt in a 69-year-old man following transseptal catheterisation. (C) Intraoperative findings showing jet through the ASD (arrow) from a left atrial view (AoV, aortic valve; LA, left atrium; PA, pulmonary artery; RA, right atrium; RV, right ventricle). (Photo C courtesy of Dr. Michel Pellerin.)

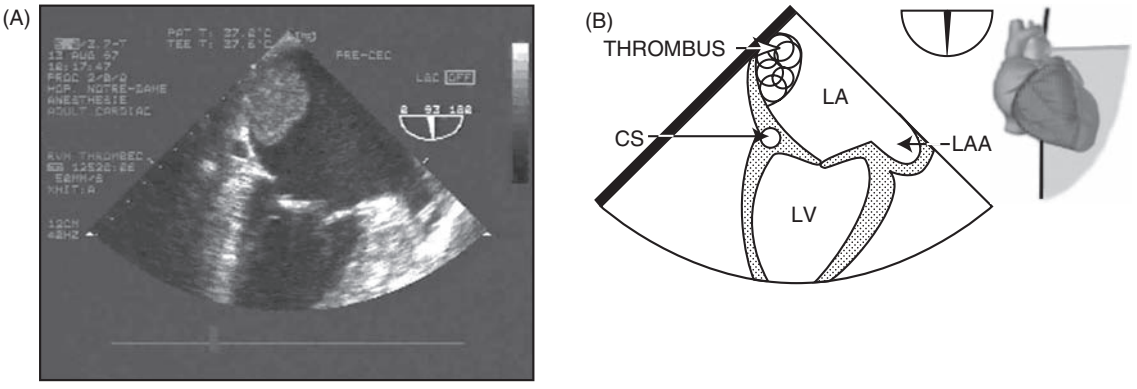

Figure 17.30 An elderly woman with known mitral valve stenosis undergoing emergency surgery for acute bilateral iliac artery thrombosis. (A, B) The mid-esophageal two-chamber view revealed a large thrombus attached to the posterior wall of the left atrium (LA) (CS, coronary sinus; LAA, left atrial appendage; LV, left ventricle).

Upstream hemodynamic repercussions of MS should also be assessed. Pulmonary veins enlarge proportionately to the severity of MS. Tabata et al. (48) reported decreased peak diastolic velocities on PW Doppler examination of the PVF. More importantly, significant postcapillary pulmonary hypertension results in right ventricular hypertrophy, dilatation and tricuspid regurgitation (Fig. 17.28). In the transgastric short-axis view, flattening of the normal ventricular septal curvature is suggestive of right ventricular pressure or volume overload (see Chapter 9, Section II.A). The severity of the tricuspid regurgitation must be carefully evaluated to assess the potential indication of repairing the tricuspid valve at the same time of mitral valve surgery (Fig. 17.28).

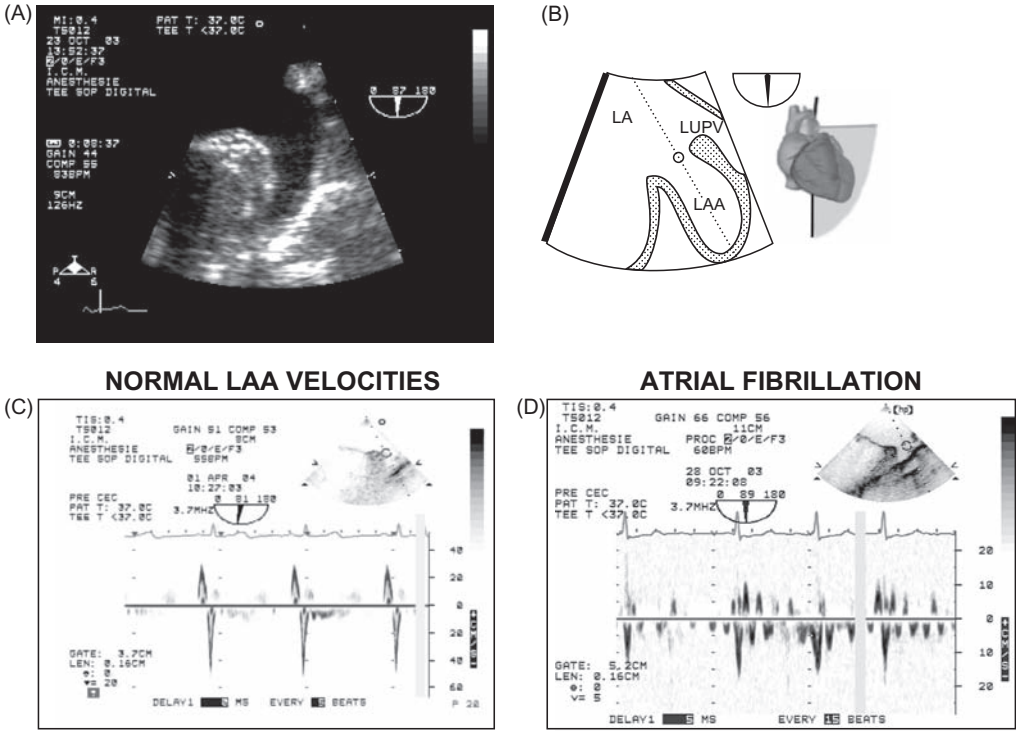

Figure 17.31 (A, B) Left atrial appendage (LAA) pulsed-wave Doppler examination. (C) Normal velocities showing atrial contraction (positive) and relaxation (negative) waves in a 71-year-old man before aortic valve replacement. (D) Atrial fibrillation showing multiple chaotic waves with reduced velocities (<50 cm/sec) in a 52-year-old woman with mitral stenosis (LA, left atrium; LUPV, left upper pulmonary vein).

Left ventricular systolic performance is subnormal in one-fourth of patients with MS as a result of rheumatic myocarditis. Diastolic dysfunction may also be present and be secondary to a reduction in LV compliance related to functional restriction resulting from chordal tethering and the rigid valve apparatus.

3. *Quantitative Echocardiographic Evaluation*

The severity of MS is graded on the basis of the MVA and the magnitude of the transvalvular diastolic pressure gradient (Table 17.5). As the MVA is independent of transvalvular flow, it is a more reliable measurement. The MVA can be measured by direct planimetry of the orifice in short-axis view or calculated by the pressure half-time, the continuity equation or the proximal flow convergence methods. As patients with MS often have concomitant atrial fibrillation, measurements of Doppler signals should be averaged over at least 8–10 cycles. Mitral inflow velocities are best obtained from the mid-esophageal four-chamber and long-axis views. CW Doppler should always be used for these measurements.

C. Diastolic Pressure Gradient

The diastolic maximal and mean pressure gradient across the mitral valve is measured from the velocities of the mitral inflow according to the modified Bernoulli equation (Fig. 17.28). The gradient should be obtained by CW Doppler. The ultrasound beam should be optimally aligned ($<20^{\circ}$) with the direction of the mitral valve inflow in either the mid-esophageal four-chamber or long-axis views. The measurement of the pressure gradient will be influenced by two factors: the MVA and the flow through the orifice. The gradient increases with the severity of MS and the magnitude of the flow across the valve (Table 17.6). Thus, with concomitant moderate to severe mitral valve regurgitation, forward flow through the mitral orifice increases. Therefore, an elevated diastolic pressure gradient may be present despite a mild degree of MS. Other conditions known to modify the pressure gradient independently of the MVA are listed in Table 17.6.

Table 17.6 Conditions Affecting the MV Diastolic Pressure Gradient

Conditions	Pressure gradient
Low cardiac output	↓
High cardiac output	↑
Severe mitral regurgitation	↑
Diastolic dysfunction (increased LV pressure)	↓

D. Mitral Valve Area

1. *Planimetry*

Direct planimetry of the mitral valve orifice by TTE has been well validated for determining the MVA (51). In TEE, the transgastric short-axis view similarly allows direct planimetry of the MVA. As the geometry of the mitral valve inflow resembles a funnel with the smallest cross-sectional area at the tip of the leaflets, it is important to begin scanning in 2D from the apex, slowly moving the image plane towards the base of the mitral valve in order to identify the location of the smallest orifice correctly. This may be difficult to achieve, as there is a tendency with this method to overestimate the true MVA.

An alternate method using color flow imaging was originally described for TTE (52). The smallest diameter of the stenotic mitral flow is measured in two orthogonal planes, the mid-esophageal four- and two-chamber views for TEE. Using the equation for an ellipse, the MVA equals $\pi/4 \times D_{4ch} \times D_{2ch}$. This method may underestimate the true MVA.

2. *Pressure Half-Time*

The pressure half-time (PHT) is defined as the time interval between the maximum early diastolic transmitral pressure gradient and the time point where the pressure gradient has decreased to half its maximal initial value (Fig. 17.28).

As the mitral valve becomes more stenotic, the left ventricular pressure takes more time to equalize with the left atrial pressure and the diastolic pressure gradient decreases more slowly. The relationship between the PHT and the MVA was determined empirically by the

Table 17.5 Grading of Mitral Stenosis Severity

	Normal	Mild	Moderate	Severe
Mitral valve area	4.0–6.0 cm^2	1.6–2.0 cm^2	1.1–1.5 cm^2	<1.0 cm^2
Mean diastolic gradient		<5 mmHg	5–10 mmHg	>10 mmHg
Pressure half-time	60 ms	90–150 ms	150–220 ms	>220 ms

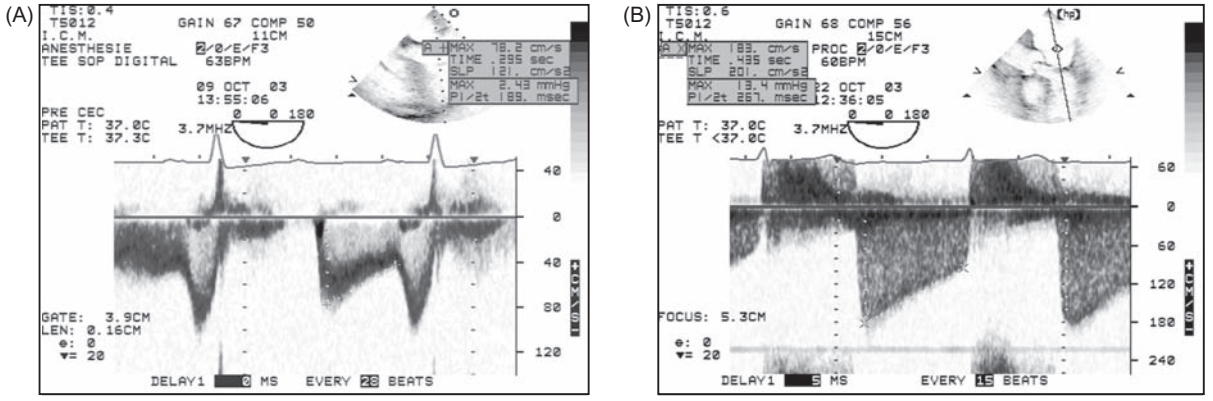

Figure 17.32 Pressure half-time (PHT) and mitral stenosis severity. (A) A 79-year-old patient with moderate disease: the PHT is 189 ms. (B) A 52-year-old woman with severe mitral stenosis: the PHT is 267 ms.

following equation (see Chapter 5, Section II.E.2) [Hatle et al. (53)]:

$$\text{MVA} = \frac{220}{\text{PHT}} = \frac{759}{\text{Mdt}} \tag{17.8}$$

where MVA is the mitral valve area (in cm^2); PHT is the pressure half-time (in ms); and Mdt is the mitral deceleration time (in ms).

The severity of MS can then be estimated using the PHT measured on the same CW Doppler signal previously obtained for the maximal and mean diastolic pressure gradient (Fig. 17.32).

The rate of equalization of left ventricular and atrial pressures and, therefore, the PHT may be affected by several hemodynamic factors (Table 17.7). The rate of rise of the left ventricle diastolic pressure may be abnormally increased with significant aortic regurgitation or diastolic dysfunction. This results in decreased PHT, independent of the mitral valve status, and leads to underestimation of the severity of stenosis. Concomitant AR may also complicate MS assessment when an eccentric aortic regurgitant jet causes a functional stenosis (the Austin–Flint phenomenon) when it keeps the anterior mitral leaflet from its full diastolic excursion and holds it in a relatively closed position (Fig. 17.33).

The left atrial and ventricular compliance may change after valvuloplasty and CPB. For this reason, the use of PHT to determine MVA in this context may not be accurate. Moreover, the PHT equation, originally reported by Hatle et al. (53) for native mitral valve, has not been validated for the determination of the valve area in the prosthesis. Nevertheless, a decrease in prosthetic valve area will be reflected by progressive lengthening of the PHT, such that serial measurements of PHT are useful to follow these patients even if it cannot be used to yield the effective valve area (see Chapter 18, Section III).

Mitral valve area determination by the PHT method is also affected by declines in left atrial pressure due to hypovolemia or increased compliance with enlarged left atrial size. The decreased decay of the diastolic pressure gradient results in overestimation of the true severity of the MS.

3. *Continuity Equation*

The continuity equation states that in the absence of valvular regurgitation and atrial or ventricular septal defect, the

Table 17.7 Factors Affecting Pressure Half-time

Factors	Effect on pressure half-time	Effect on estimation of mitral stenosis severity
↓ ventricular compliance, aging	↓	Underestimate
Moderate to severe aortic regurgitation (49)	↓	Underestimate
Large left atrium	↑	Overestimate
Eccentric aortic regurgitant jet directed towards the mitral valve	↑	Overestimate
Hypovolemia (50)	↑	Overestimate
↑ Cardiac output (50)	↓	Underestimate

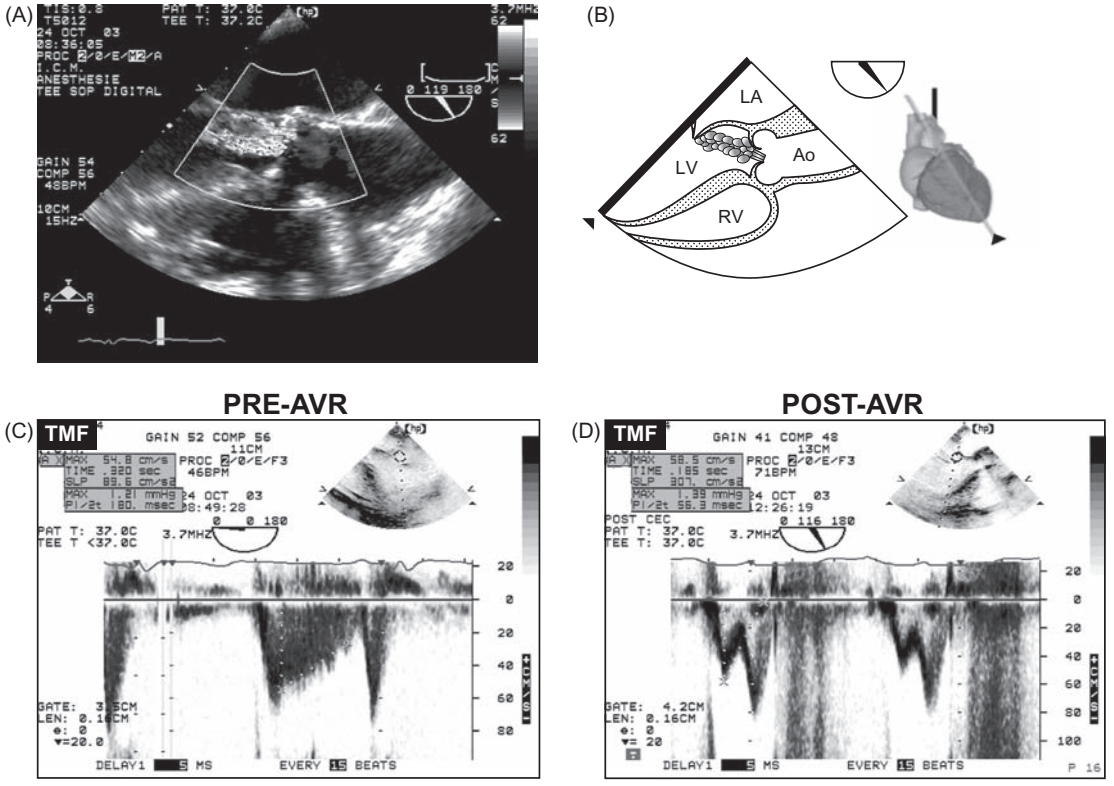

Figure 17.33 (A, B) Mid-esophageal long-axis view of a 78-year-old woman scheduled for aortic valve replacement (AVR). (C) She had aortic regurgitation associated with a pseudomitral stenosis Doppler pattern secondary to either restricted opening of the anterior leaflet or contamination from the aortic regurgitant signal. The pressure half-time obtained from the Doppler transmitral flow (TMF) was 180 ms. (D) The Doppler TMF pressure half-time after aortic surgery was 56 ms (Ao, aorta; LA, left atrium; LV, left ventricle; RV, right ventricle).

stroke volume across the mitral valve must equal that of other valves such as LVOT, the aortic or pulmonic valve at the same time and during hemodynamic stability.

The MVA can be obtained by applying the continuity equation:

$Q_{\text{mitral}} = Q_{\text{aortic}}$, providing there is no significant mitral or aortic valve regurgitation:

$$\text{MVA} = 0.785\ d^2_{\text{LVOT}} \frac{\text{TVI}_{\text{LVOT}}}{\text{TVI}_{\text{mitral}}} \tag{17.9}$$

The TVI_{LVOT} is measured using PW Doppler examination through the transgastric long-axis view at 110° close to the aortic annulus at the same position where the diameter of the LVOT is measured (Fig. 17.34). The $\text{TVI}_{\text{mitral}}$ is measured by continuous-wave Doppler across the mitral native or prosthetic valve through mid-esophageal four-chamber or long-axis views.

4. Proximal Flow Convergence

The basis of the PISA or proximal flow convergence method has been described earlier for mitral regurgitant lesions.

In the case of MS, the surface surrounding the stenosed orifice is funnel-shaped rather than planar and distorts the PISA such that a correction factor must be added in contradistinction to MR:

$$\text{MVA} = 2\pi r^2 \frac{V_r}{V_{\text{MS max}}} \frac{\alpha}{180} \tag{17.10}$$

where MVA is the mitral valve area (in cm^2); r is the measured radius of the hemispheric shell of the aliased velocity; v_r is the aliased velocity at the radius r is the Nyquist limit (in cm/sec); $V_{\text{MS max}}$ is the maximal velocity across the orifice, obtained by CWD (in cm/sec); and α is the angle measured between the two mitral leaflets.

The PISA radius is best obtained from the mid-esophageal four-chamber or long-axis view, with high resolution zoomed-in views. The color flow scale baseline is shifted in the direction of the flow measured, which is in the case of MS away from the transducer. In contrast to MR, Deng et al. (54) reported that an aliasing velocity of 21 cm/sec is optimal for the PISA method in MS. Indeed, higher aliasing velocities may underestimate the

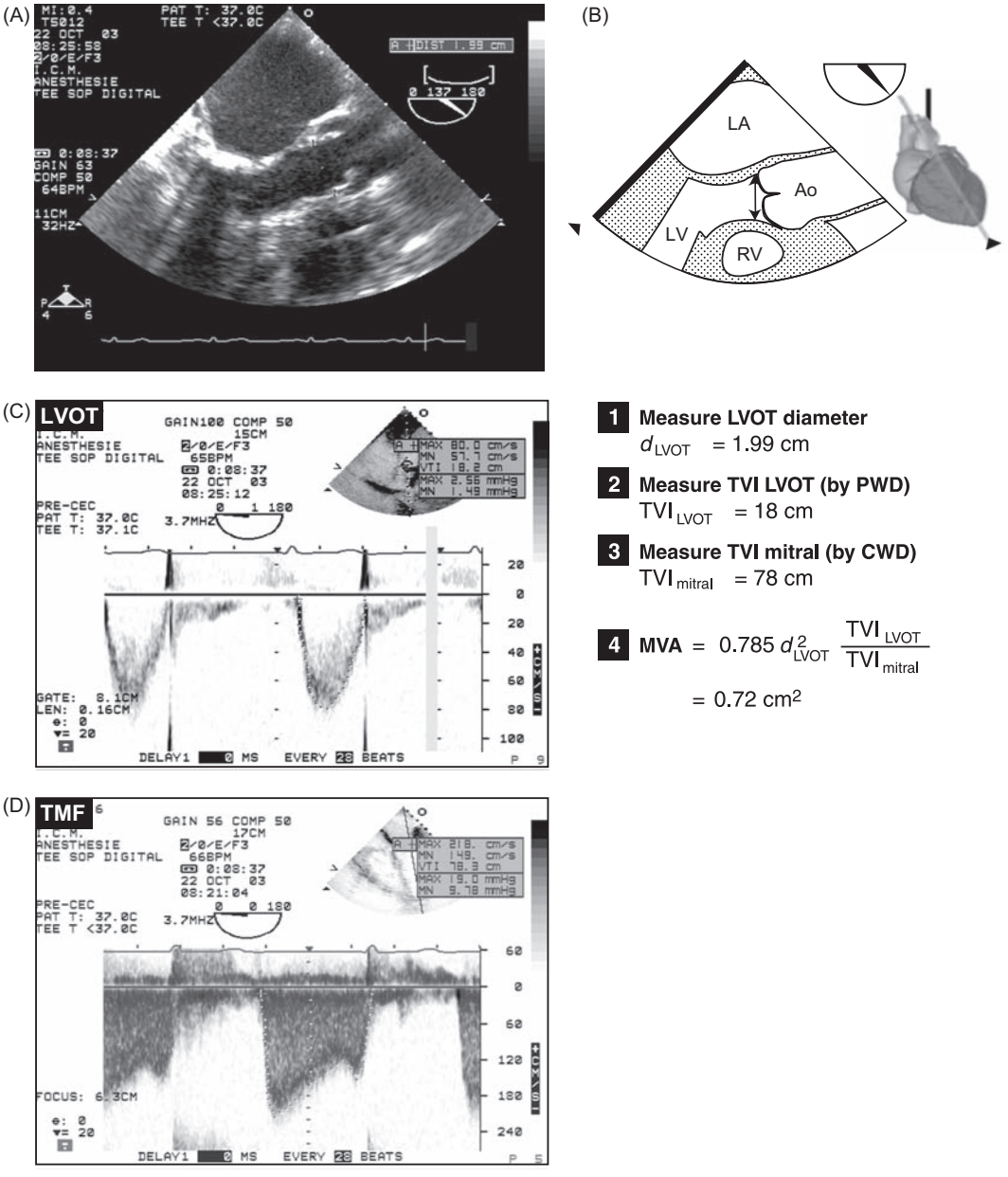

Figure 17.34 Calculation of the mitral valve area (MVA) using the continuity equation. (A, B) The left ventricular outflow tract (LVOT) diameter is measured from the mid-esophageal long-axis view at 135°. (C) To complete the calculation of the stroke volume, the LVOT time velocity integral (TVI) is obtained by pulsed-wave Doppler (PWD) examination from a deep transgastric view at 0° (or alternatively from a basal transgastric view at 110°). (D) The MVA is calculated by dividing the stroke volume by the TVI of the mitral valve, which is given by continuous-wave Doppler (CWD) examination through the mitral valve from the mid-esophageal view (Ao, aorta; LA, left atrium; LV, left ventricle; RV, right ventricle; TMF, transmitral flow).

stenotic MVA. The angle between the two mitral leaflets must also be measured for the necessary correction factor $\alpha/180$ in MS.

The PISA method appears to provide valve area estimates which are at least as accurate as the traditional echocardiographic methods with accuracy preserved in atrial fibrillation (55). Because this method applies the continuity equation with flow parameters measured on a single valve, the presence of other valve disease such as AR should not affect its accuracy (56).

Table 17.8 Summary of Perioperative Evaluation of Mitral Stenosis

Global appearance of the heart chambers (large LA, small LV)
Valve morphology
Presence of calcification
Leaflet decreased mobility
Leaflet thickening
Involvement of subvalvular apparatus
Evaluation of associated MR
Evaluation of the severity of mitral stenosis
Diastolic pressure gradient (maximal and mean)
MVA by PHT method
MVA by the continuity equation
MVA by PISA method (better when concomitant MR or AR)
Measurement of the left atrial dimensions
Detailed examination of the left atrium and left atrial appendage to exclude atrial thrombus
Examination of the atrial septum to exclude ASD
Evaluation of RV dimensions and systolic function
Evaluation of concomitant valvular disease (aortic and tricuspid)
Quantification of tricuspid regurgitation for estimation of right-sided pressures

Note: AR, aortic regurgitation; ASD, atrial septal defect; LA, left atrium; MVA, mitral valve area; PHT, pressure half-time; PISA, proximal isovelocity surface area.

The approach to MS is summarized in Table 17.8. In summary, mitral valve pathology is an area where TEE plays a critical role in the evaluation of the mechanism and also the related complications that can alter most, if not all of the other cardiac structures.

ACKNOWLEDGMENT

Dr. Saint-Pierre has received a grant from the Royal College of Physicians and Surgeons of Canada.

REFERENCES

1. Zoghbi WA, Enriquez-Sarano M, Foster E et al. Recommendations for evaluation of the severity of native valvular regurgitation with two-dimensional and Doppler echocardiography. J Am Soc Echocardiogr 2003; 16:777–802.
2. Kumar N, Kumar M, Duran CM. A revised terminology for recording surgical findings of the mitral valve. J Heart Valve Dis 1995; 4:70–75.
3. Lambert AS, Miller JP, Merrick SH et al. Improved evaluation of the location and mechanism of mitral valve regurgitation with a systematic transesophageal echocardiography examination. Anesth Analg 1999; 88:1205–1212.
4. Carpentier AF, Lessana A, Relland JY et al. The "physio-ring": an advanced concept in mitral valve annuloplasty. Ann Thorac Surg 1995; 60:1177–1185.
5. Poortmans G, Schupfer G, Roosens C, Poelaert J. Additional view of the mitral valve. Anesth Analg 2000; 91:494–495.
6. Mintz GS, Kotler MN, Segal BL, Parry WR. Two-dimensional echocardiographic recognition of ruptured chordae tendineae. Circulation 1978; 57:244–250.
7. Enriquez-Sarano M, Freeman WK, Tribouilloy CM et al. Functional anatomy of mitral regurgitation: accuracy and outcome implications of transesophageal echocardiography. J Am Coll Cardiol 1999; 34:1129–1136.
8. Durack DT, Lukes AS, Bright DK. New criteria for diagnosis of infective endocarditis: utilization of specific echocardiographic findings. Duke Endocarditis Service. Am J Med 1994; 96:200–209.
9. Li JS, Sexton DJ, Mick N et al. Proposed modifications to the Duke criteria for the diagnosis of infective endocarditis. Clin Infect Dis 2000; 30:633–638.
10. Tischler MD, Vaitkus PT. The ability of vegetation size on echocardiography to predict clinical complications: a meta-analysis. J Am Soc Echocardiogr 1997; 10:562–568.
11. Sanfilippo AJ, Picard MH, Newell JB et al. Echocardiographic assessment of patients with infectious endocarditis: prediction of risk for complications. J Am Coll Cardiol 1991; 18:1191–1199.
12. Khanderia BK. Suspected bacterial endocarditis: to TEE or not to TEE. J Am Coll Cardiol 1993; 21:222–224.
13. Birmingham GD, Rahko PS, Ballantyne F III. Improved detection of infective endocarditis with transesophageal echocardiography. Am Heart J 1992; 123:774–781.
14. Karalis DG, Bansal RC, Hauck AJ et al. Transesophageal echocardiographic recognition of subaortic complications in aortic valve endocarditis. Clinical and surgical implications. Circulation 1992; 86:353–362.
15. Daniel WG, Mugge A, Martin RP et al. Improvement in the diagnosis of abscesses associated with endocarditis by transesophageal echocardiography. N Engl J Med 1991; 324:795–800.
16. Duran CM, Gometza B, Saad E. Valve repair in rheumatic mitral disease: an unsolved problem. J Card Surg 1994; 9:282–285.
17. Marwick TH, Torelli J, Obarski T et al. Assessment of the mitral valve splitability score by transthoracic and transesophageal echocardiography. Am J Cardiol 1991; 68:1106–1107.
18. Wilkins GT, Weyman AE, Abascal VM et al. Percutaneous balloon dilatation of the mitral valve: an analysis of echocardiographic variables related to outcome and the mechanism of dilatation. Br Heart J 1988; 60:299–308.
19. Grayburn PA, Berk MR, Spain MG et al. Relation of echocardiographic morphology of the mitral apparatus to mitral regurgitation in mitral valve prolapse: assessment by Doppler color flow imaging. Am Heart J 1990; 119:1095–1102.

20. Nishimura RA, McGoon MD, Shub C et al. Echocardiographically documented mitral-valve prolapse. Long-term follow-up of 237 patients. N Engl J Med 1985; 313:1305–1309.
21. Zamorano J, Erbel R, Mackowski T et al. Usefulness of transesophageal echocardiography for diagnosis of mitral valve prolapse. Am J Cardiol 1992; 69:419–422.
22. Pini R, Devereux RB, Greppi B et al. Comparison of mitral valve dimensions and motion in mitral valve prolapse with severe mitral regurgitation to uncomplicated mitral valve prolapse and to mitral regurgitation without mitral valve prolapse. Am J Cardiol 1988; 62:257–263.
23. Cherian G, Tei C, Shah PM, Wong M. Diastolic prolapse in the flail mitral valve syndrome: a new observation providing differentiation from the mitral valve prolapse syndrome. Am Heart J 1982; 103:1074–1075.
24. Agricola E, Oppizzi M, De Bonis M et al. Multiplane transesophageal echocardiography performed according to the guidelines of the American Society of Echocardiography in patients with mitral valve prolapse, flail, and endocarditis: diagnostic accuracy in the identification of mitral regurgitant defects by correlation with surgical findings. J Am Soc Echocardiogr 2003; 16:61–66.
25. Stewart WJ, Currie PJ, Salcedo EE et al. Evaluation of mitral leaflet motion by echocardiography and jet direction by Doppler color flow mapping to determine the mechanisms of mitral regurgitation. J Am Coll Cardiol 1992; 20:1353–1361.
26. Mattingly TW, Parmley LF, Manion WC. Nonpenetrating traumatic injury of the heart. Circulation 1958; 18:371–396.
27. Simmers TA, Meijburg HW, de la Riviere AB. Traumatic papillary muscle rupture. Ann Thorac Surg 2001; 72:257–259.
28. Bonow RO, Carabello B, de LA Jr et al. Guidelines for the management of patients with valvular heart disease: executive summary. A report of the American College of Cardiology/American Heart Association Task Force on Practice Guidelines (Committee on Management of Patients with Valvular Heart Disease). Circulation 1998; 98:1949–1984.
29. Byram MT, Roberts WC. Frequency and extent of calcific deposits in purely regurgitant mitral valves: analysis of 108 operatively excised valves. Am J Cardiol 1983; 52:1059–1061.
30. Castello R, Lenzen P, Aguirre F, Labovitz AJ. Quantitation of mitral regurgitation by transesophageal echocardiography with Doppler color flow mapping: correlation with cardiac catheterization. J Am Coll Cardiol 1992; 19:1516–1521.
31. Helmcke F, Nanda NC, Hsiung MC et al. Color Doppler assessment of mitral regurgitation with orthogonal planes. Circulation 1987; 75:175–183.
32. Miyatake K, Izumi S, Okamoto M et al. Semiquantitative grading of severity of mitral regurgitation by real-time two-dimensional Doppler flow imaging technique. J Am Coll Cardiol 1986; 7:82–88.
33. Spain MG, Smith MD, Grayburn PA et al. Quantitative assessment of mitral regurgitation by Doppler color flow imaging: angiographic and hemodynamic correlations. J Am Coll Cardiol 1989; 13:585–590.
34. Kleinman JP, Czer LS, DeRobertis M et al. A quantitative comparison of transesophageal and epicardial color Doppler echocardiography in the intraoperative assessment of mitral regurgitation. Am J Cardiol 1989; 64:1168–1172.
35. Roberts BJ, Grayburn PA. Color flow imaging of the vena contracta in mitral regurgitation: technical considerations. J Am Soc Echocardiogr 2003; 16:1002–1006.
36. Hall SA, Brickner ME, Willett DL et al. Assessment of mitral regurgitation severity by Doppler color flow mapping of the vena contracta. Circulation 1997; 95:636–642.
37. Grayburn PA, Fehske W, Omran H et al. Multiplane transesophageal echocardiographic assessment of mitral regurgitation by Doppler color flow mapping of the vena contracta. Am J Cardiol 1994; 74:912–917.
38. Pu M, Griffin BP, Vandervoort PM et al. The value of assessing pulmonary venous flow velocity for predicting severity of mitral regurgitation: A quantitative assessment integrating left ventricular function. J Am Soc Echocardiogr 1999; 12:736–743.
39. Stewart WJ, Jiang L, Mich R et al. Variable effects of changes in flow rate through the aortic, pulmonary and mitral valves on valve area and flow velocity: impact on quantitative Doppler flow calculations. J Am Coll Cardiol 1985; 6:653–662.
40. Fisher DC, Sahn DJ, Friedman MJ et al. The mitral valve orifice method for noninvasive two-dimensional echo Doppler determinations of cardiac output. Circulation 1983; 67:872–877.
41. Rokey R, Sterling LL, Zoghbi WA et al. Determination of regurgitant fraction in isolated mitral or aortic regurgitation by pulsed Doppler two-dimensional echocardiography. J Am Coll Cardiol 1986; 7:1273–1278.
42. Lewis JF, Kuo LC, Nelson JG et al. Pulsed Doppler echocardiographic determination of stroke volume and cardiac output: clinical validation of two new methods using the apical window. Circulation 1984; 70:425–431.
43. Abascal VM, Wilkins GT, Choong CY et al. Echocardiographic evaluation of mitral valve structure and function in patients followed for at least 6 months after percutaneous balloon mitral valvuloplasty. J Am Coll Cardiol 1988; 12:606–615.
44. Gordon SP, Douglas PS, Come PC, Manning WJ. Two-dimensional and Doppler echocardiographic determinants of the natural history of mitral valve narrowing in patients with rheumatic mitral stenosis: implications for follow-up. J Am Coll Cardiol 1992; 19:968–973.
45. Michalis LK, Thomas MR, Smyth DW et al. Left atrial spontaneous echo contrast assessed by TEE in patients with either native mitral valve disease or mitral valve replacement. J Am Soc Echocardiogr 1993; 6:299–307.
46. Black IW, Hopkins AP, Lee LC, Walsh WF. Left atrial spontaneous echo contrast: a clinical and echocardiographic analysis. J Am Coll Cardiol 1991; 18:398–404.
47. Mugge A, Kuhn H, Nikutta P et al. Assessment of left atrial appendage function by biplane transesophageal echocardiography in patients with nonrheumatic atrial fibrillation:

identification of a subgroup of patients at increased embolic risk. J Am Coll Cardiol 1994; 23:599–607.
48. Tabata T, Oki T, Fukuda N, Iuchi A, Kawano T, Manabe K, Tanimoto M, Kageji Y, Sasaki M, Hama M, Ito S. Transesophageal pulsed Doppler echocardiographic study of pulmonary venous flow in mitral stenosis. Cardiology 1996; 87:112–118.
49. Nakatani S, Masuyama T, Kodama K et al. Value and limitations of Doppler echocardiography in the quantification of stenotic mitral valve area: comparison of the pressure half-time and the continuity equation methods. Circulation 1988; 77:78–85.
50. Firstenberg MS, Prior DL, Greenberg NL et al. Effect of cardiac output on mitral valve area in patients with mitral stenosis: validation and pitfalls of the pressure half-time method. J Heart Valve Dis 2001; 10:49–50.
51. Faletra F, Pezzano A Jr, Fusco R et al. Measurement of mitral valve area in mitral stenosis: four echocardiographic methods compared with direct measurement of anatomic orifices. J Am Coll Cardiol 1996; 28:1190–1197.
52. Kawahara T, Yamagishi M, Seo H et al. Application of Doppler color flow imaging to determine valve area in mitral stenosis. J Am Coll Cardiol 1991; 18:85–92.
53. Hatle L, Angelsen B, Tromsdal A. Noninvasive assessment of atrioventricular pressure half-time by Doppler ultrasound. Circulation 1979; 60:1096–1104.
54. Deng YB, Matsumoto M, Wang XF et al. Estimation of mitral valve area in patients with mitral stenosis by the flow convergence region method: selection of aliasing velocity. J Am Coll Cardiol 1994; 24:683–689.
55. Rifkin RD, Harper K, Tighe D. Comparison of proximal isovelocity surface area method with pressure half-time and planimetry in evaluation of mitral stenosis. J Am Coll Cardiol 1995; 26:458–465.
56. Ikawa H, Enya E, Hirano Y et al. Can the proximal isovelocity surface area method calculate stenotic mitral valve area in patients with associated moderate to severe aortic regurgitation? Analysis using low aliasing velocity of 10% of the peak transmitral velocity. Echocardiography 2001; 18:89–95.

18

Mitral Valve Replacement and Repair

ARSÈNE-J. BASMADJIAN, MICHEL PELLERIN
University of Montreal, Montreal, Canada

I. Types of Valve Prostheses 417
A. Mechanical Valves 418
B. Biological Tissue Valves 418
II. Transprosthetic Gradient 419
III. Prosthetic Valve Area 421
IV. Prosthetic Regurgitation 421
V. Multiplane TEE Evaluation 423
A. Two-Dimensional Evaluation 423
B. Transvalvular Prosthetic Regurgitation 428
C. Periprosthetic Regurgitation 429
D. Gradient Evaluation 432
VI. Surgical Indications of Mitral Valve Repair and Replacement 432
VII. TEE Evaluation After Mitral Valve Repair 432
VIII. Mitral Valve Repair 438
A. Cannulation and Extracorporeal Circulation (Video Loop) 438
B. Valve Analysis 439
C. Annuloplasty 439
IX. Posterior Leaflet Prolapse 441
A. Quadrangular Resection 441
B. Sliding Plasty of the Posterior Leaflet 441
C. Commissural Prolapse 441
D. Extensive Calcification of the Mitral Annulus 441
X. Anterior Leaflet Prolapse 442
A. Chordal Transfer 443
B. Artificial Goretex Chords 443
C. Papillary Muscle Shortening 444
D. Alferi Operation (Edge to Edge Repair) 444
E. Anterior Leaflet Resection 444
XI. Early Complications 444
A. Systolic Anterior Motion 444
B. Success of the Repair 444
References 444

I. TYPES OF VALVE PROSTHESES

The first successful artificial valve replacements were performed in the early 1960s (1). All prosthetic valves have a sewing ring which enables suture attachment to surrounding human tissue. They are mostly classified according to the material (biological tissue or mechanical) and the design of the occluder. Biological tissue valves are further divided on the basis of the presence (stented) or absence (stentless) of a structural support and upon the origin of the tissue, with homografts vs heterografts (porcine or bovine). Mechanical valves are distinguished by three main designs of occluders: ball-in-cage, tilting disk, and bileaflet, the latter being the most commonly implanted in the mitral position.

A. Mechanical Valves

As a group, mechanical prosthetic valves provide long durability with the disadvantage of requiring life-long anticoagulation (1–3). The *ball-in-cage valves* were the first mechanical valves implanted. The Starr–Edwards prosthesis (Fig. 18.1) represents the typical example of this design, and has the longest performance record (1). It consists of a metal cage holding a mobile silicone spherical Beal with a Teflon/polypropylene sewing ring. The ball valve represents a variation of the ball-in-cage, with the occluder consisting of a floating, mobile disk rather than a ball. While the Starr–Edwards ball-in-cage valve's best feature was its long track record of durability, its multiple disadvantages included high thrombogenicity requiring more intense anticoagulation, hemolysis, and a suboptimal intrinsic hydrodynamic profile with higher pressure gradient and obstruction of left ventricular outflow tract (LVOT) because of its bulky design.

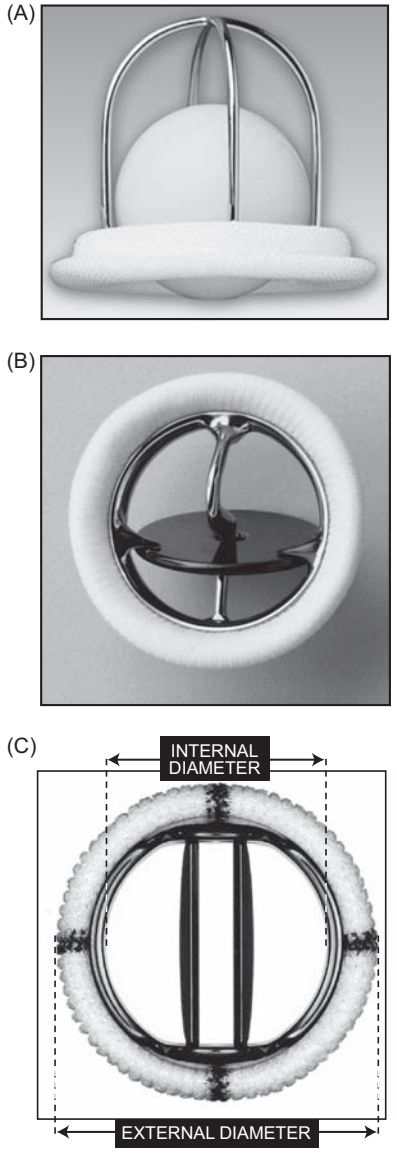

Figure 18.1 Starr–Edwards (Edwards Lifesciences LLC), Medtronic Hall (Copyright Medtronic, Inc.), and St. Jude Medical® (Copyright St. Jude Medical, Inc. 2002) mechanical mitral valve prostheses.

Tilting or pivoting disk valves consist of a single pyrolytic or carbon-coated circular disk suspended within a metal valve-housing with either a central hole or struts that permit tilting, with a polyester or Teflon sewing ring. By design, the maximum tilting angle varies between models from 55° to 70°: consequently, in open position, these valves have one larger (major) and one smaller (minor) orifice. Because a minimal clearance space between the moving parts is necessary to enable their unimpeded motion, small central and lateral (between the disk and the sewing ring) transvalvular regurgitant jets may normally be demonstrated on color flow imaging. The Bjork–Shiley, Lillehei–Kaster, Hall–Kaster, Medtronics Hall™ (Fig. 18.1), and Omniscience represent examples of single, tilting disk prostheses.

Bileaflet valves have two semicircular disks coated with pyrolytic carbon, mounted centrally on hinges. When they pivot open to approximately 70–80°, they reveal two equal semicircular (major) and one central slit-like (minor) orifices. As for the tilting disk valves, these prostheses normally present transvalvular converging as well as diverging regurgitant jets, at the periphery between the hemidisks and the sewing ring, and along the central closure line between the two hemidisks (4). The Carbomedics and the St. Jude Medical® valves (Fig. 18.1) are typical examples of bileaflet prostheses. The latter is the most commonly implanted bileaflet prosthetic valve worldwide.

Compared with ball-in-cage mechanical prostheses tilting disk and bileaflet valves have an improved hydrodynamic profile as they are less bulky, have a lower intrinsic pressure gradient and appear to present a lower thrombogenicity.

B. Biological Tissue Valves

In the mitral position, all biological tissue prostheses are currently mounted onto a flexible or semiflexible frame with struts (i.e. stented). Heterografts (or xenografts) designate a bioprosthesis made of nonhuman tissue, either glutaraldehyde-treated porcine aortic valve (AoV) such as the Carpentier–Edwards (Fig. 18.2), Hancock and Medtronic Intact prostheses, or reconstructed leaflets from bovine pericardium such as the Carpentier–Edwards Perimount™ (Fig. 18.2), Mitroflow, and Ionescu–Shiley valves. Homografts are made from human tissue, but they are no longer used in the mitral position because of their poor durability.

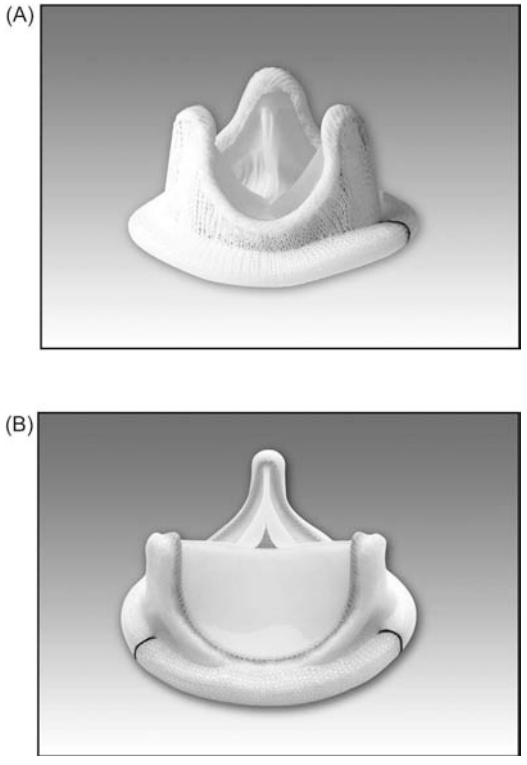

Figure 18.2 Carpentier–Edwards porcine and Carpentier–Edwards Perimount^{TM} (Edwards Lifesciences LLC) pericardial tissue mitral valve bioprostheses. (Courtesy of Edwards Lifesciences.)

While bioprostheses are advantageous as they do not require chronic anticoagulation, their lesser durability represents a significant drawback particularly in young patients or patients with chronic renal failure (1–4). They are most commonly used in patients with contraindications to anticoagulation or in older patients. These valves comprise of three leaflets which give them an interesting appearance during two-dimensional (2D) imaging resembling an AoV with triangular opening in the mitral position (Fig. 18.3). A functional mitral bioprosthetic leaflet usually appears as thin and pliable, with normal mobility, central flow, and trace or no regurgitation.

With time, biological valve leaflets and their annulus thicken and calcify, causing decreased mobility. Stenosis, regurgitation or a combination of both could then occur (Fig. 18.4). These can be demonstrated by 2D imaging, color-flow imaging and increased diastolic pressure gradient with continuous-wave (CW) Doppler.

II. TRANSPROSTHETIC GRADIENT

All mechanical or tissue prosthetic valves are hemodynamically restrictive compared with a normal native valve. This is reflected by the transprosthetic gradient which should be routinely measured with CW Doppler across the prosthesis during diastole. On color-flow imaging, normal flow through tissue valves appears central; in ball-in-cage mechanical

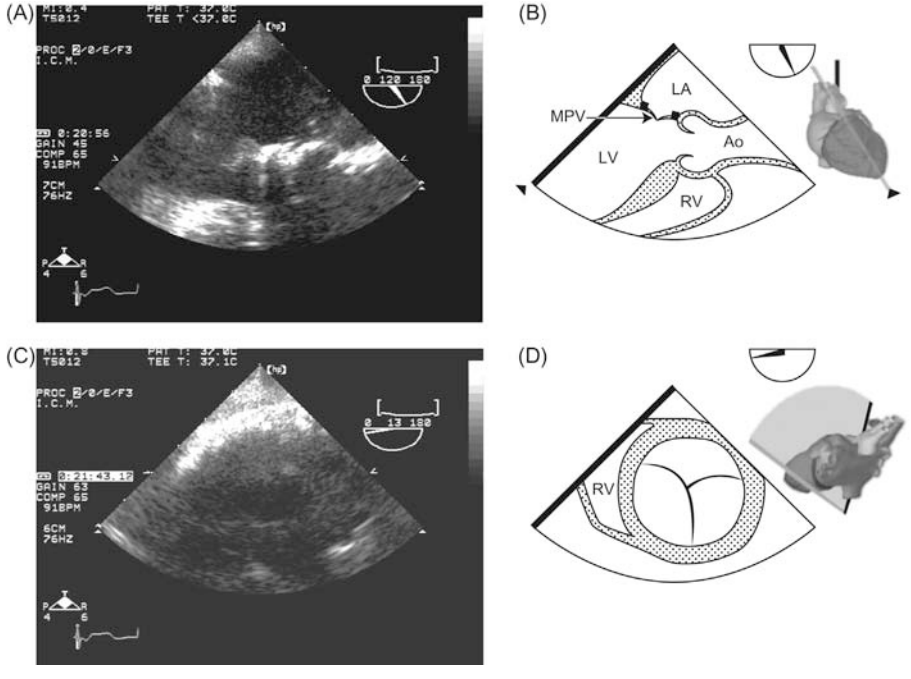

Figure 18.3 (A, B) Mid-esophageal long-axis view showing normal thickness and motion of the mitral bioprosthesis leaflets. (C, D) Transgastric view showing the three struts and three leaflets "en face" (Ao, aorta; LA, left atrium; LV, left ventricle; MPV, mitral prosthetic valve; RV, right ventricle).

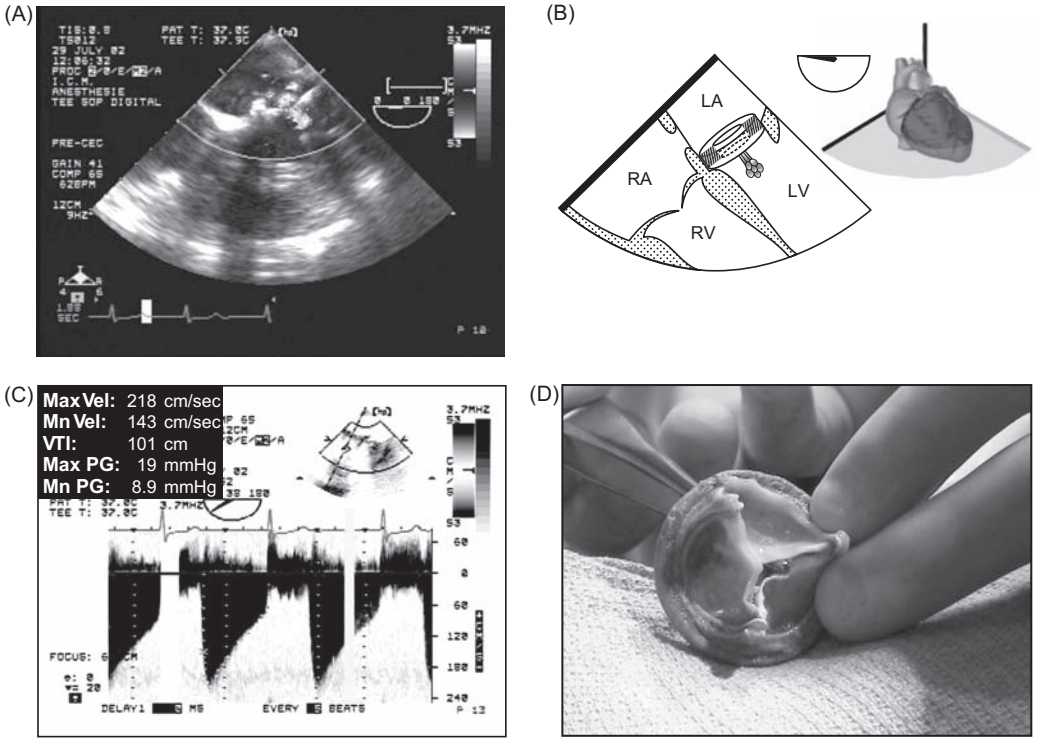

Figure 18.4 A 79-year-old woman was reoperated for bioprosthetic mitral valve stenosis and regurgitation. (A, B) A mid-esophageal four-chamber view shows the mitral regurgitant jet and acceleration through the orifice. (C) A mean pressure gradient of 8.9 mmHg is measured with continuous-wave Doppler. (D) Intraoperative examination of the valve revealed severe stenosis (LA, left atrium; LV, left ventricle; Max, maximum; Mn, mean; PG, pressure gradient; RA, right atrium; RV, right ventricle; Vel, velocity; VTI, velocity–time integral). (Photo D courtesy of Dr. Michel Pellerin.)

prostheses, it symmetrically curves around the ball while in tilting disk prostheses, color flow is seen through the three orifices. Two-dimensional and color flow imaging are used to guide the CW Doppler cursor in order to ensure optimal alignment of the ultrasound beam with the direction of the jet. The peak gradient is determined from the maximal Doppler flow velocity with the simplified Bernouilli equation: $P = 4v^2$ where P is the pressure in mmHg and v is the velocity in m/s. As for native mitral valves, the mean transprosthetic gradient is obtained, by tracing the diastolic CW Doppler signal (Fig. 18.5) which calculates the mean of the squared instantaneous velocities. Measurement of mean gradient is more important because it represents the gradient between the left atrium (LA) and the left ventricular (LV) throughout diastole.

The gradient evaluation must take into account the prosthetic valve type and size, as well as the heart rate (HR) and cardiac output (CO). In the adult population, the mitral transprosthetic gradient is, however, generally less dependent on the sewing ring size than for aortic prostheses. At normal heart rates, the normal mean diastolic gradient of mechanical mitral valves is 4–6 mmHg and for bioprostheses it is 3–5 mmHg. As with native valves, the gradient is increased with tachycardia. Pressure recovery may also be associated with increased gradient without intrinsic dysfunction. This is more commonly seen with AoV prostheses but can occasionally occur with mitral mechanical prostheses (5,6).

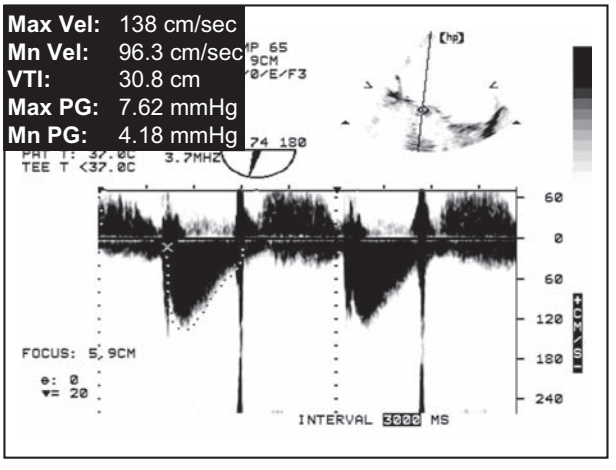

Figure 18.5 Measurement of the diastolic transvalvular gradient with continuous-wave Doppler in a functional bileaflet St. Jude mechanical prosthesis (Max, maximum; Mn, mean; PG, pressure gradient; Vel, velocity; VTI, velocity–time integral).

Transprosthetic pressure gradient represents the pressure difference between two chambers, proximally and distally to the prosthesis (in this case LA and LV). When flow must pass through a narrowed orifice, a prosthetic orifice in this case, pressure (potential energy) is transformed into kinetic energy (i.e. velocity) then back to potential energy with some loss in the form of heat which represents the pressure loss or gradient due to the narrowed orifice. Pressure recovery refers to the phenomenon where a certain degree of kinetic energy could return to pressure energy (5,6). Blood flow through the prosthesis accelerates more in the minor than in the major orifices. Doppler gradient estimation is dependent on the maximal velocity of red blood cells, which is found at the vena contracta. Generally, when measuring the pressure gradient across a prosthesis, the CW Doppler cursor should be positioned through the major orifice but inadvertent measurement through a minor orifice could result in overestimation of the true hemodynamic gradient, particularly in the smaller central slit-like minor orifice of a bileaflet mechanical prosthesis (Figs. 18.6 and 18.7) (5).

III. PROSTHETIC VALVE AREA

Manufacturers often report prosthetic valve areas based on the anatomic inner diameter of the sewing ring or on *in vitro* hemodynamic data. One should be aware that these areas do not necessarily reflect the true *in vivo* effective orifice area allowed by the valve, which is usually smaller. The prosthesis number usually represents the external diameter of the sewing ring [Fig. 18.1(C)]. The surgeon will generally try to implant the largest prosthesis for a given individual.

The pressure half-time (PHT) represents the time necessary for the maximal transvalvular gradient to reach half its initial value during diastolic filling (Fig. 18.8). The PHT is equal to $0.29 \times$ Deceleration Time. The mitral valve area (MVA) given by the formula $\text{MVA} = \text{PHT}/220$, has been validated for the native mitral valve in the absence of significant aortic insufficiency or left ventricular dysfunction. Unfortunately, this formula has not been validated for prosthetic valves and cannot be used to estimate their effective orifice area. Nevertheless, serial measurements of the PHT in prosthetic valves is useful in detecting valvular dysfunction prospectively, as it is usually <100 ms and will increase in cases of prosthesis obstruction or thrombosis. In the absence of significant (moderate or severe) aortic or mitral regurgitation (MR), effective prosthetic MVA is calculated using the continuity equation:

$$\text{MVA} = \text{Ao SV}/\text{MV TVI} \tag{18.1}$$

where Ao SV is the aortic stroke volume, equal to LVOT surface area $\times$ LVOT TVI (time–velocity integral) and MV TVI is mitral valve diastolic time–velocity integral. These measurements are easily performed with transthoracic echocardiography (TTE) and transesophageal echocardiography (TEE). However, the measurement of LVOT TVI by TEE is occasionally technically challenging because suboptimal transgastric windows may prevent adequate alignment of the pulsed-wave (PW) Doppler with the direction of flow in the LVOT, even with deep transgastric views at 0° or mid-transgastric views at $110–150^\circ$. Normal prosthetic MVAs range between 1.5 and 2.5 cm^2 (6,7).

IV. PROSTHETIC REGURGITATION

A CW Doppler sweep of the mitral valve prosthesis could demonstrate the presence of MR and a strong, dense regurgitant signal suggests a more severe degree of regurgitation. However, the evaluation of transvalvular and/or periprosthetic MR is most often better accomplished with color flow imaging. The sensitivity of this modality for detecting MR is rather low with transthoracic studies

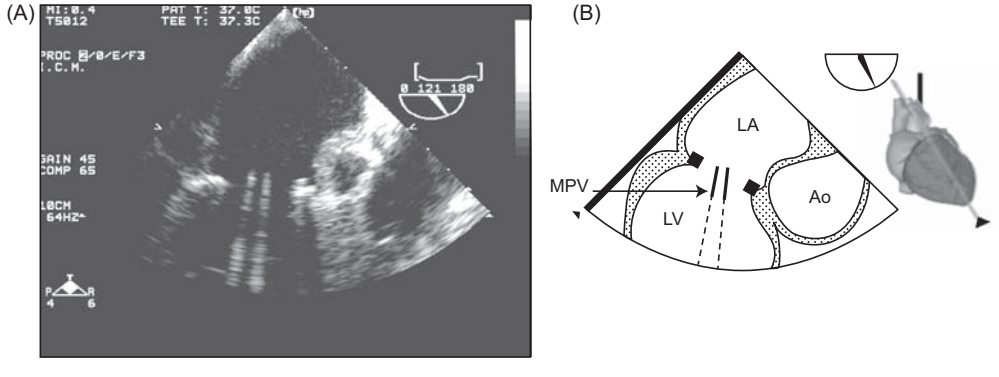

Figure 18.6 Mid-esophageal long-axis view showing the normal open position of the two hemidisks of a mitral mechanical bileaflet St. Jude prosthesis (Ao, aorta; LA, left atrium; LV, left ventricle; MPV, mitral prosthetic valve).

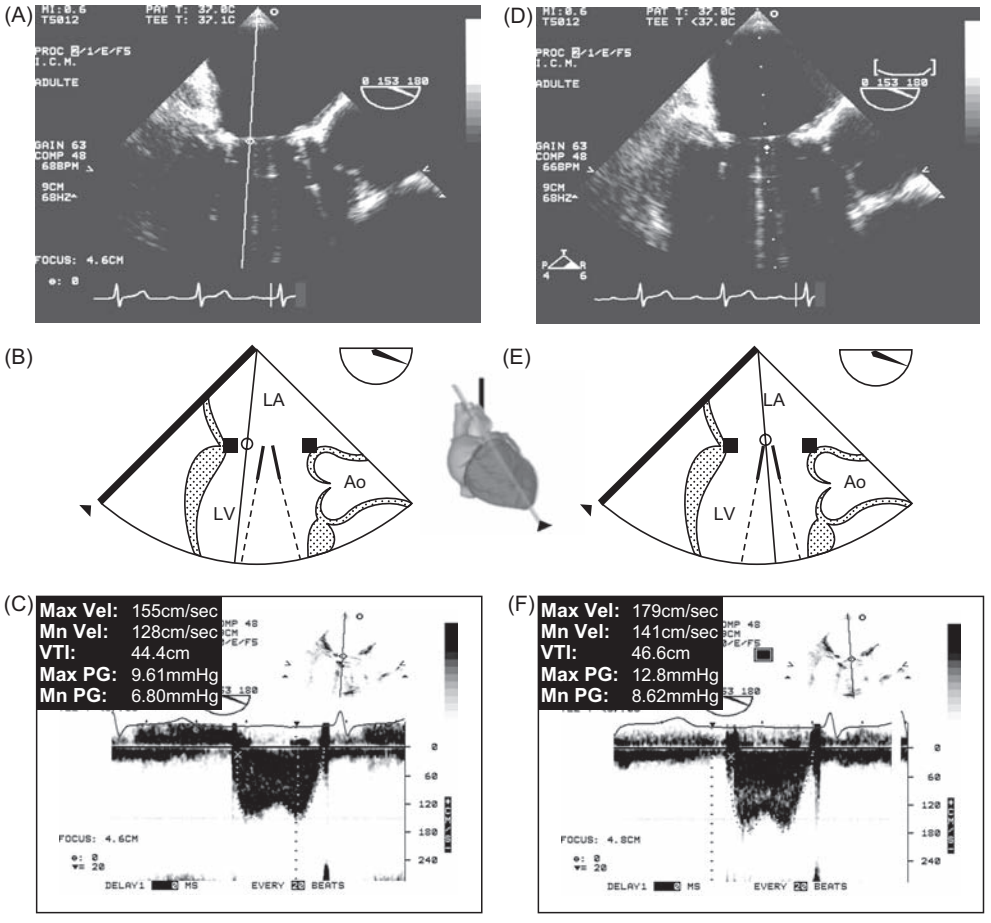

Figure 18.7 Mid-esophageal long-axis view of a patient with a normal bileaflet mechanical prosthetic valve. The Doppler cursor is positioned to measure pressure gradient (PG) measurement through the lateral, major orifice (A, B). The mean (Mn) PG is 6.8 mmHg (C). When the cursor samples velocities through the central minor orifice (D, E) of a bileaflet mechanical prosthetic valve, a higher PG is measured because of acceleration of blood flow through a smaller slit orifice. This is an example of pressure recovery. The heart rhythm and rate were identical in both conditions (Ao, aorta; LA, left atrium; LV, left ventricle; Max, maximum; Mn, mean; Vel, velocity; VTI, velocity–time integral).

because the regurgitant jets are hidden by the acoustic shadowing from the prosthetic material. Transesophageal echocardiography is ideally positioned to view these jets and has a near 100% sensitivity for MR detection as long as a systematic and meticulous evaluation is performed (8).

Prosthetic regurgitation can be divided into "intra"- or "transprosthetic" and "periprosthetic." While the latter is always pathological, the former can be further divided into functional or pathological. Normally functioning prosthetic valves, particularly mechanical, have a closing volume, that is a small and short regurgitant color flow Doppler signal visible in early systole. This corresponds to the small volume of blood displaced by the occluder as it moves in closed position and does not represent true regurgitation *per se.*

Bioprosthetic valves (Fig. 18.3) have no or very little intrinsic regurgitation. Ball-in-cage models should not have regurgitant jets whereas tilting-disk and bileaflet valves normally have an intrinsic "intraprosthetic" regurgitation of a small quantity ($\sim$5–15 mL/beat) which does not represent prosthetic dysfunction. Moreover, these normal intrinsic regurgitant jets have a functional antithrombotic effect, "washing out" the prosthesis occluder edges with each systole. As each mechanical disk prosthesis has a specific design, characteristic signature intrinsic regurgitant transvalvular jets are expected on color flow imaging. For instance, in bileaflet valves, the jets will form a converging pattern in the plane parallel to the central slit orifice as well as a diverging pattern in the plane perpendicular to it, at the periphery between disks and ring, particularly at the hinge points (Fig. 18.9) (4). The central orifice of the Medtronic Hall disk, through which it slides on the central strut, also explains its typical central regurgitant jet in addition to the jets at

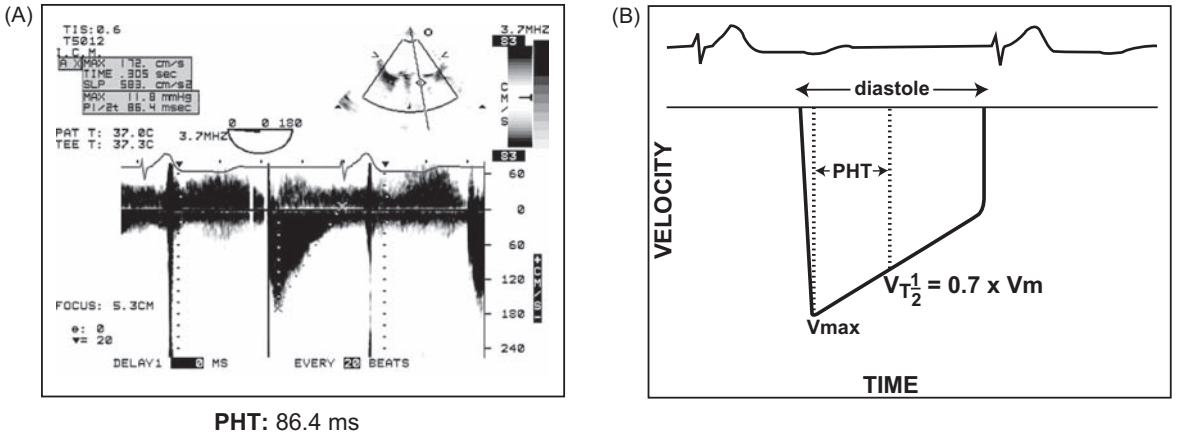

PHT: 86.4 ms

Figure 18.8 (A) Measurement by continuous-wave Doppler of the pressure half-time (PHT) in a functional mitral bileaflet St. Jude mechanical prosthesis. (B) The PHT corresponds to the time required for the pressure gradient to drop by half. The corresponding velocities are obtained through the simplified Bernoulli's equation (V_m, mean velocity; V_{max}, maximal velocity; $V_{T1/2}$, velocity half-time).

the periphery of the disk. Dysfunctional MR will be discussed in the following section.

V. MULTIPLANE TEE EVALUATION

Preoperative and immediate postoperative (pre- and post-cardiopulmonary bypass pump) evaluations should always be performed with a systematic approach (8). The echocardiographic examination should include the evaluation of other (native or prosthetic) valves as well as the evaluation of left ventricular size and global and regional function. Evaluation of prosthetic valve anatomy and function should include a full 2D imaging sweep, followed by color flow imaging and CW Doppler across the prosthesis and PW Doppler examination of the pulmonary veins.

A. Two-Dimensional Evaluation

Transesophageal echocardiography is the ideal tool for evaluating mitral prostheses. Two-dimensional evaluation involves real-time imaging in all imaging planes (0–180°) at the mid-eosophageal level. Rotation of the imaging angle at this level allows identification of the optimal imaging plane to observe the full motion of prosthetic valve occluders (leaflets, disks, or ball according to type). Machine settings should be adjusted to optimize the image. The depth should be adjusted to maximize the visualization of the prosthesis and the surrounding structures. Keeping the prosthesis in the center of the imaging display, systematic slow sweeps from one side of the sewing ring to the opposite in orthogonal views are important in picking up abnormal structures or flows not present in the middle of the prosthesis. The transgastric view must also be used to complete the evaluation of the ventricular side of the prosthesis and permit visualization and evaluation of the subvalvular apparatus and the LV, which is obscured by the prosthetic material at mid-esophageal level.

During 2D examination, a keen eye should look out for reduced occluder excursion, leaflet sticking, pannus, valve rocking, abscess, foreign bodies such as thrombus or vegetation, and, particularly in the immediate post-cardiopulmonary bypass (CPB) period, retained mitral valvular apparatus that could impede the free movement of the mobile components of the prosthetic valve.

During normal function, bileaflet mitral prostheses open and close symmetrically and generally in synchrony (Fig. 18.6). The puppet in the ball-in-cage prosthesis should have full to-and-fro excursion within the cage (Fig. 18.10). The mobile components should not remain held in either the open or closed position. However, asynchronous or incomplete movement of the occluder can be seen in the absence of prosthetic dysfunction in certain cases, for example, irregular heart rhythm (atrial fibrillation, multiple extrasystole, or ventricular pacing). In the immediate/early post-CPB period, abnormal movement of the prosthesis occluder could be present and disappear just a few minutes after reestablishing normal circulation and left ventricular function.

The identification of abnormal movement of the prosthesis occluder in the early post-CPB period in the operating room warrants immediate surgical reassessment and correction that sometimes simply consists of rotating the prosthesis within the sewing ring or resecting some "excess" subvalvular tissue (Figs. 18.11 and 18.12). This may prevent a late second look which represents a high-risk early reoperation.

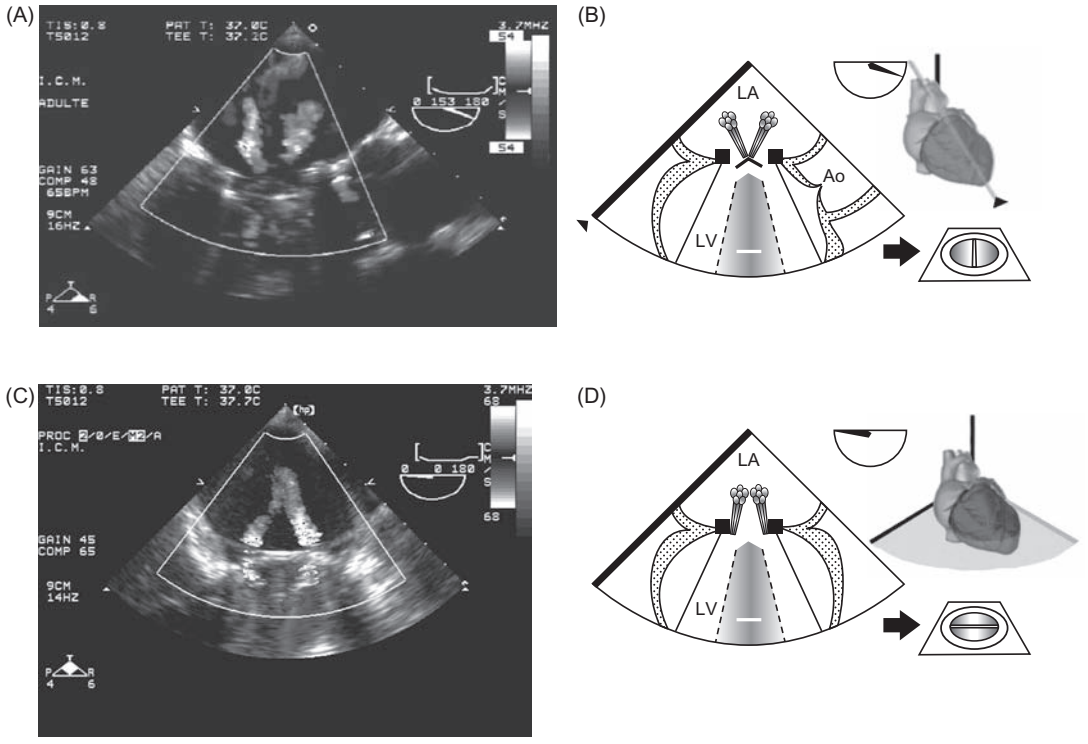

Figure 18.9 Mid-esophageal long-axis view and four-chamber view showing the normal signature of the diverging (A, B) and converging (C, D) regurgitant jets of a mitral mechanical bileaflet prosthesis. The diverging jets are seen when the view is perpendicular to the axis of the central slit orifice (Ao, aorta; LA, left atrium; LV, left ventricle).

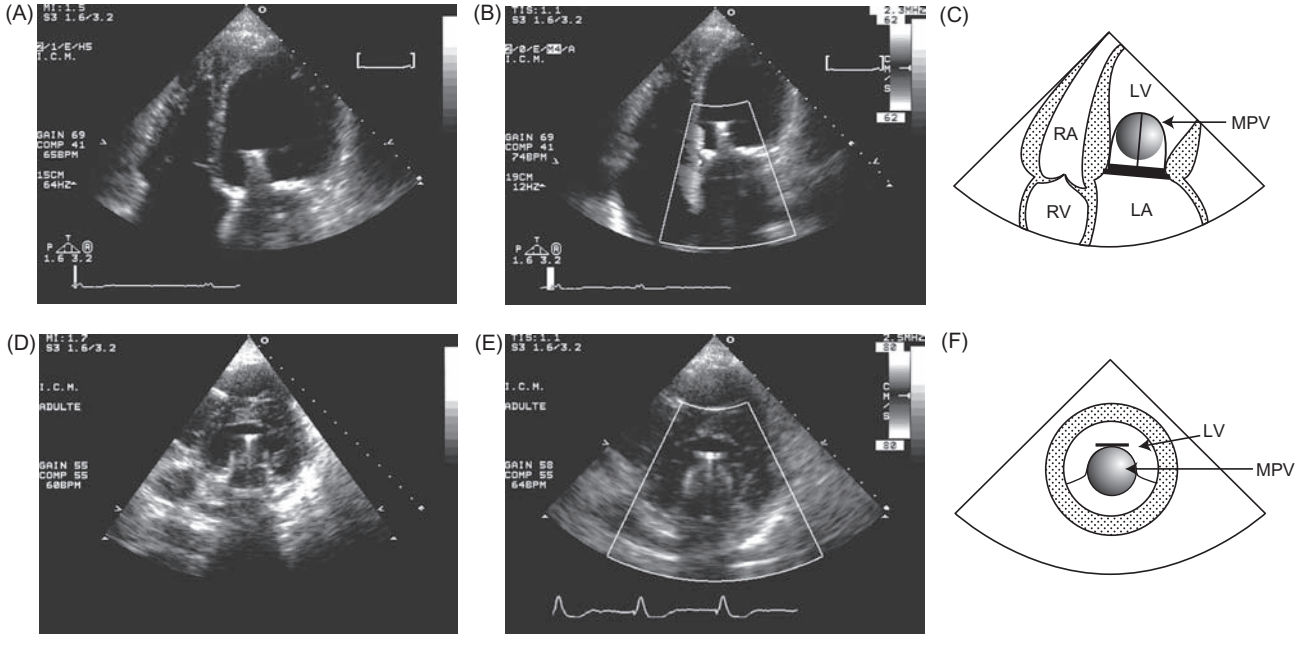

Figure 18.10 Transthoracic four-chamber (A–C) and short-axis (D–F) views of a functional Starr–Edwards ball-in-cage prosthesis (LA, left atrium; LV, left ventricle; MPV, mitral prosthetic valve; RA, right atrium; RV, right ventricle).

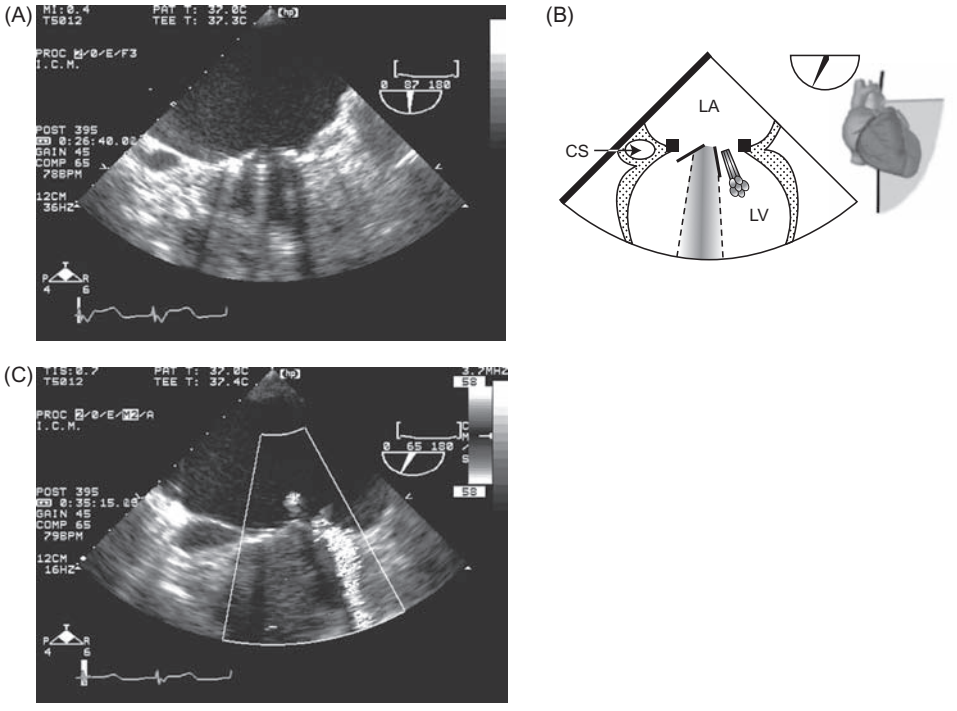

Figure 18.11 Mid-esophageal two-chamber view showing abnormal movement of the left hemidisc of a mitral mechanical bileaflet prosthesis (A, B). Of note, the right hemidisk has normal mobility while the other is immobile. This was noted introperatively just after cardiopulmonary bypass. (C) Color flow was present through only one major orifice while no flow is associated with the immobile hemidisk. (CS, coronary sinus; LA, left atrium; LV, left ventricle).

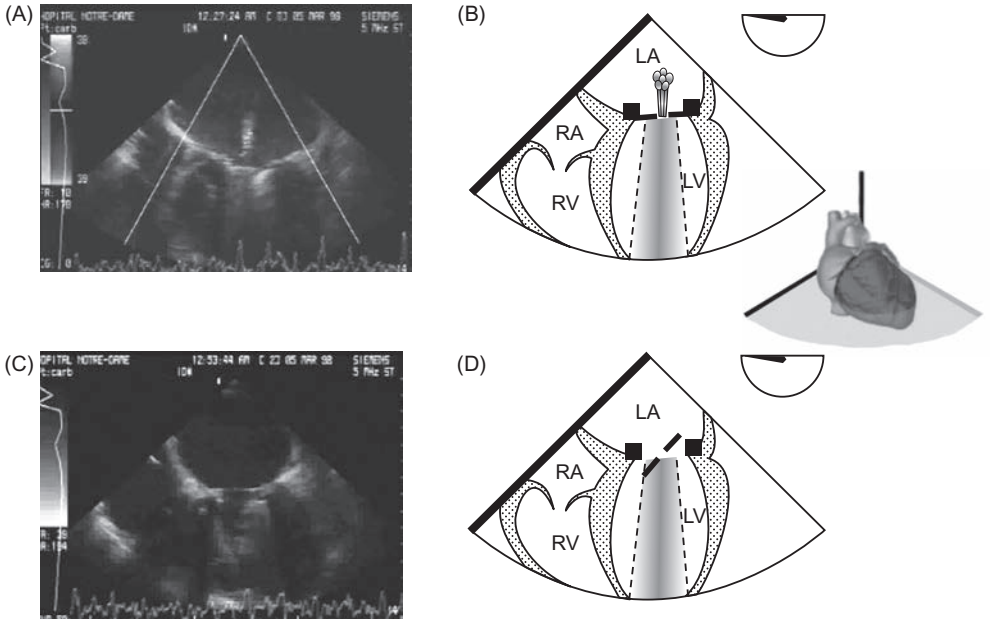

Figure 18.12 Severe pulmonary hypertension was noted during weaning from cardiopulmonary bypass (CPB) in a patient undergoing mitral valve replacement with a mitral valve tilting disk prosthesis. (A, B) The prosthesis was fixed in a closed position and only blood flowing through the central disk orifice could be seen both in systole and diastole. (C, D) CPB was reinstituted immediately. After rotation of the mitral prosthesis, normal motion was seen (LA, left atrium; LV, left ventricle; RA, right atrium; RV, right ventricle). (Courtesy of Dr. Jocelyne Maucotel.)

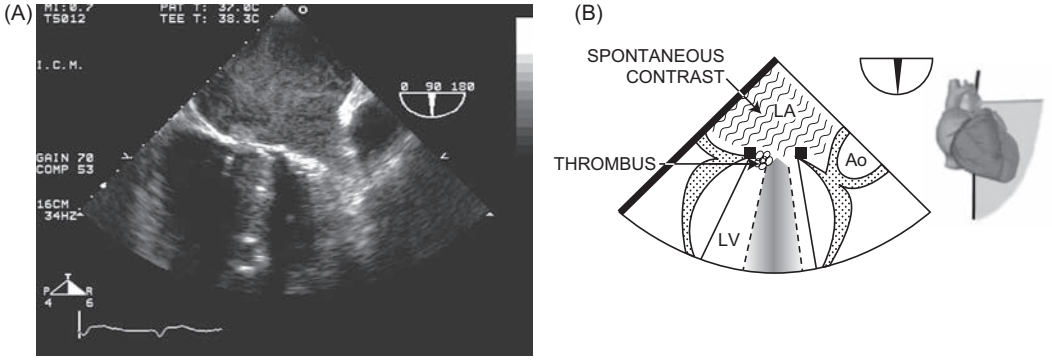

Figure 18.13 Mid-esophageal two-chamber view showing a thrombus protruding through one of the hemidisks of a mechanical bileaflet prosthesis during diastole. Spontaneous echo contrast due to stasis is noted in the left atrium (LA) (A, B) (Ao, aorta; LV, left ventricle).

Reduced excursion of the mobile components could be due to the presence of foreign bodies such as thrombus or vegetation, interfering excess subvalvular apparatus, abnormal tissue growth (pannus), or intrinsic prosthetic valve failure. Sometimes, the cause of dysfunction may not be readily obvious as with thrombus at the prosthetic hinge points. The only clue to prosthetic dysfunction may simply be abnormal disk motion or increased gradient. It is also important to remember that these abnormalities may be present intermittently. Therefore, prolonged careful 2D imaging is sometimes required.

Thrombus (Figs. 18.13 and 18.14) and vegetation (Fig. 18.15) generally appear as echo-dense irregular masses attached to a leaflet, the disk or to the sewing ring of the prosthesis. Their mobility and size are variable. These masses could be highly mobile and attached to the wall by a pedicle or fixed with a large base. Size could vary between a few millimetres to many centimetres in diameter. Masses could interfere with prosthetic function by causing obstruction, regurgitation, or a combination of both (Fig. 18.15).

Thrombus and vegetation can be very difficult to differentiate echocardiographically from one another. Certain clues within the clinical context may help to sort them out. The coexistence of spontaneous echo contrast, atrial fibrillation, a significantly dilated LA with subtherapeutic anticoagulation are more commonly associated with thrombus. Conversely, fever, weight loss, positive blood cultures and/or the identification of an abscess or a fistula (Fig. 18.15) make the diagnosis of vegetations more likely.

Abscesses are typically found at the level of the sewing ring, appearing as an echo-lucent area of variable dimension. To-and-fro flow within the abscess (Fig. 18.15) or periprosthetic regurgitation with annular dehiscence (Fig. 18.16) can be visualized. Spontaneous rupture of abscess may lead to perivalvular fistulae between various cardiac chambers. During all phases of the cardiac cycle, a normal prosthetic valve should move *en bloc* with the base of the ventricle to which it is sutured. Rocking represents abnormally exaggerated or independent motion of part of the sewing ring due to its dehiscence. Although

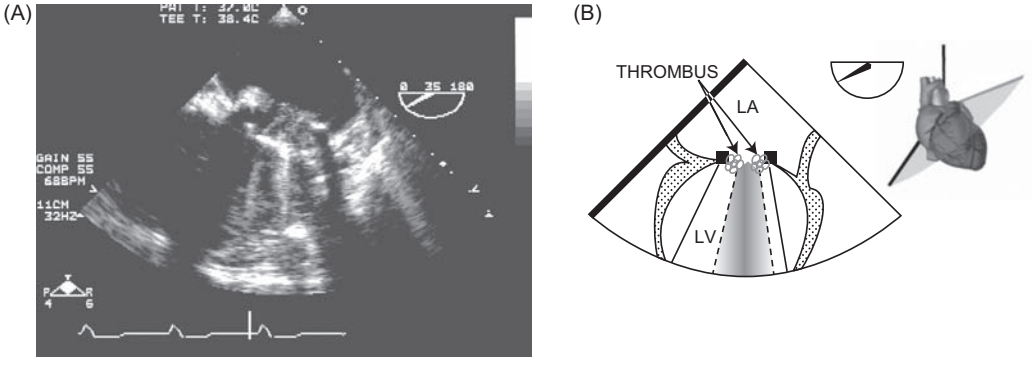

Figure 18.14 Mid-esophageal 35° view showing extensive thrombosis of a mechanical bileaflet prosthesis, with decreased mobility of the hemidisks. This patient was deemed a poor candidate for reoperation because of concomitant severe left ventricular dysfunction. The administration of an intravenous thrombolytic agent resulted in the disappearance of the trombus and the patient recovered uneventfully (LA, left atrium; LV, left ventricle).

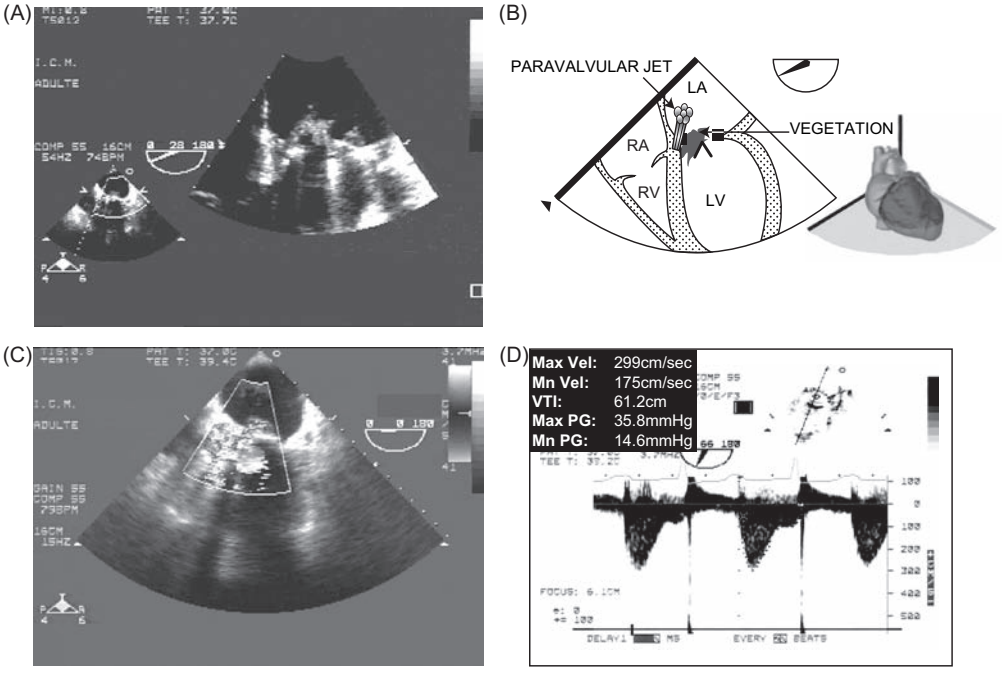

Figure 18.15 (A, B) Mid-esophageal 28° view showing two vegetations, one very large medially and a smaller one laterally, protruding through the orifices of a mechanical bileaflet prosthesis during both diastole and systole. (C) In the mid-esophageal four-chamber view, an associated color jet directed from the left ventricle (LV) to the left atrium (LA) during systole is consistent with a ruptured abscess and perivalvular fistula secondary to an infectious process. (D) Continuous-wave Doppler across the mechanical prosthesis demonstrates an increased transprosthetic pressure gradient (PG) due to the large obstructive vegetation (Max, maximum; Mn, mean; RA, right atrium; RV, right ventricle; Vel, velocity, VTI, velocity–time integral).

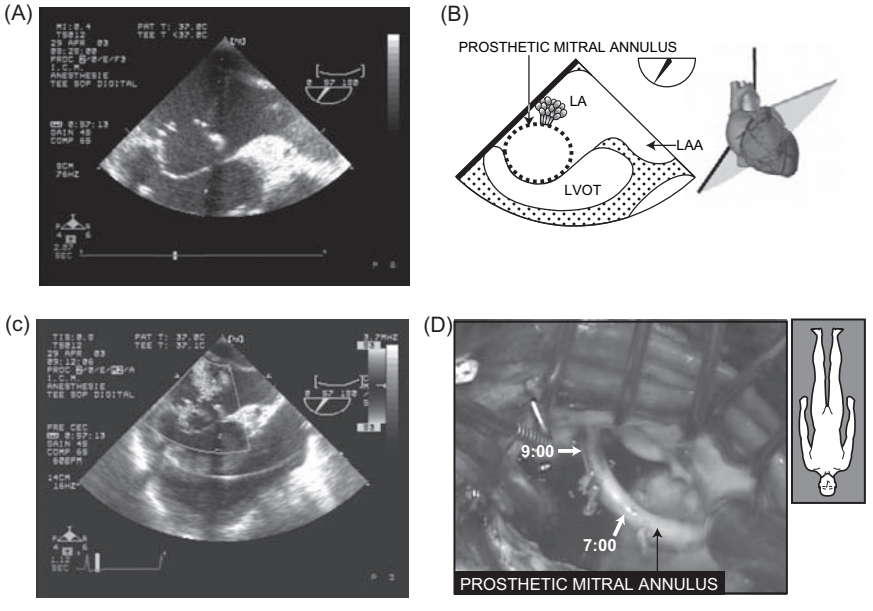

Figure 18.16 (A, B) Mid-esophageal 57° view of a 55-year-old man undergoing reoperation for dehiscence of an annuloplasty ring. (C) Severe para-annular mitral regurgitation is present on color flow imaging. (D) The intraoperative findings confirmed the 7–9 o'clock dehiscence (arrows) (LA, left atrium; LAA, left atrial appendage; LVOT, left ventricular outflow tract). (Photo D courtesy of Dr. Michel Pellerin.)

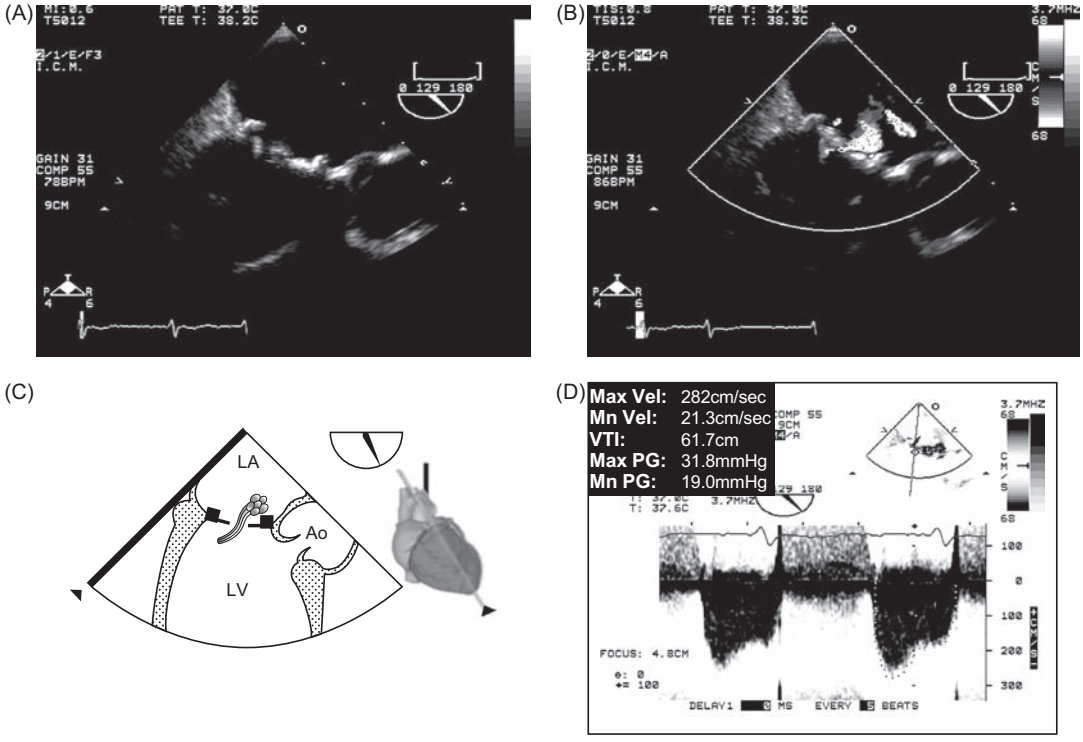

Figure 18.17 (A–C) Mid-esophageal long-axis view of a dysfunctional mitral bioprosthesis with thickened and calcified leaflets with reduced mobility. An ecccentric regurgitation jet is present. (D) The continuous-wave Doppler demonstrates a very high mean (Mn) diastolic pressure gradient (PG) of 19 mmHg with regurgitation through the dysfunctional mitral tissue prosthesis (Ao, aorta; LA, left atrium; LV, left ventricle; Max, maximum; VTI, velocity–time integral; Vel, velocity).

rupture of a suture due to degenerescence could be the cause, endocarditis and abscess should be ruled out.

The leaflets of a normal bioprosthesis should be thin and pliable. Thickening and calcification of the leaflets or the annulus can be demonstrated by 2D imaging. These degenerative changes decrease the mobility of the leaflets or may lead to fracture and tears of the cusps, with resulting stenosis and/or regurgitation detectable by color-flow imaging and CW Doppler (Fig. 18.17). Degenerative changes can also be seen in the cloth-covered model of the Starr–Edwards prosthesis (Figs. 18.18–18.20).

The presence of thrombus on bioprosthesis is much less common than with mechanical valves but can sometimes be seen (Fig. 18.21). Valve degenerescence or endocarditis may cause ring dehiscence and rocking with periprosthetic regurgitation. Endocarditis can also cause leaflet destruction and perforation with significant regurgitation.

B. Transvalvular Prosthetic Regurgitation

During TEE imaging, one must resist the urge to turn on the color flow imaging mode too soon without having properly performed a thorough 2D examination of all parts of the prosthesis. Similarly, during color flow imaging, the operator should not hesitate to turn off the color when a flow abnormality is found in order to understand its underlying anatomical basis.

Thrombus, vegetation, abnormal tissue growth (pannus), interfering residual subvalvular apparatus and intrinsic prosthetic valve failure (Fig. 18.22) could all be responsible for dysfunctional mitral prosthetic regurgitation. This type of regurgitation will usually be transvalvular or intraprosthetic, meaning that the regurgitation originates from within the prosthetic sewing ring, due to incomplete closure of one of the mobile components (Figs. 18.17 and 18.22). Intraprosthetic dysfunctional regurgitation is uncommon in the immediate postoperative period. When present with a mechanical prosthesis, it is generally associated with abnormal disk closure due to interfering residual subvalvular tissue or apparatus. This can often be immediately corrected by rotating the valve within the sewing ring. Early postoperative bioprosthetic valve regurgitation could arise from suture misplacement or improper sizing. In rare cases, an intrinsic bioprosthetic manufacturing problem could be responsible.

As mentioned previously, normal prosthetic valves may present a mild degree of intraprosthetic functional regurgitation characteristic of their valve design. On the other hand, pathologic intraprosthetic regurgitation will

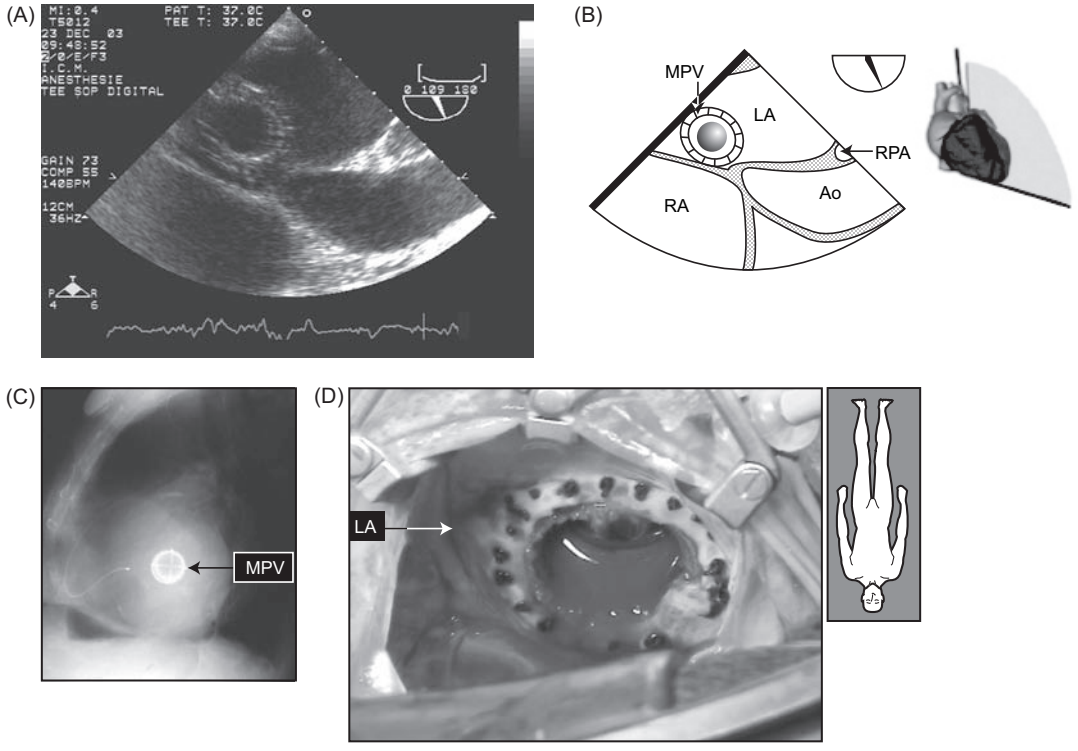

Figure 18.18 A 59-year-old man with a Starr–Edwards prosthetic valve in the mitral position. The echocardiographic appearance (A, B), radiologic (C), and intraoperative aspect through a left atriotomy (D) of the valve's ring are shown. Note that the valve orientation is modified by severe left atrial dilatation (Ao, aorta; LA, left atrium; MPV, mitral prosthetic valve; RA, right atrium; RPA, right pulmonary artery). (Photo D courtesy of Raymond Cartier.)

generally be $\geq 2/4$ or moderate to severe and could result from any of the abnormalities discussed in the 2D multiplane-TEE section earlier. It occurs within the prosthetic ring but could sometimes be difficult to differentiate from periprosthetic regurgitation. With thorough 2D and color-flow imaging examination from one side of the sewing ring to the other, in orthogonal planes will generally allow the localization of the origin of the jet and its cause. Indeed, careful observation of the location of the origin of the jet, the vena contracta and the proximal flow convergence in reference to the prosthetic ring will help to identify the type of regurgitation (i.e. intra- vs periprosthetic). The severity of regurgitation is graded as for native valves.

C. Periprosthetic Regurgitation

Periprosthetic regurgitation is a common cause of reoperation for prosthetic valve dysfunction. It is a dysfunctional regurgitant jet occurring outside the prosthetic sewing ring. It can appear as a result of a degenerative process or of endocarditis. Rarely, significant perivalvular regurgitation can be found at surgical closure in the operating room (OR).

One of the major indications and advantages of perioperative TEE is the identification of the presence, severity, and location of periprosthetic regurgitation in order to guide surgical intervention before CPB or to reduce the morbidity associated with this condition by allowing immediate diagnosis and correction after CPB, thus avoiding unnecessary reoperation.

The severity of perivalvular regurgitation is highly variable, ranging from a tiny suture leak to severe regurgitation associated with partial dehiscence. The identification and quantification of periprosthetic regurgitation requires a careful and systematic TEE evaluation. The prosthesis must be scanned in multiple angles with 2D and color-flow imaging. As mentioned above for intraprosthetic regurgitant jets, periprosthetic regurgitant jets should be sought with a thorough 2D and color-flow imaging examinations not only limited to a tomographical view through the middle of the prosthesis, but starting from the outside of one flank to the opposite aspect of the sewing ring. This should be done in at least two orthogonal views, but other angles better adapted to the examination of suspicious findings can be used. Moreover, this inspection at the plane of the valve should be complemented by a similar sweep above and below the prosthesis

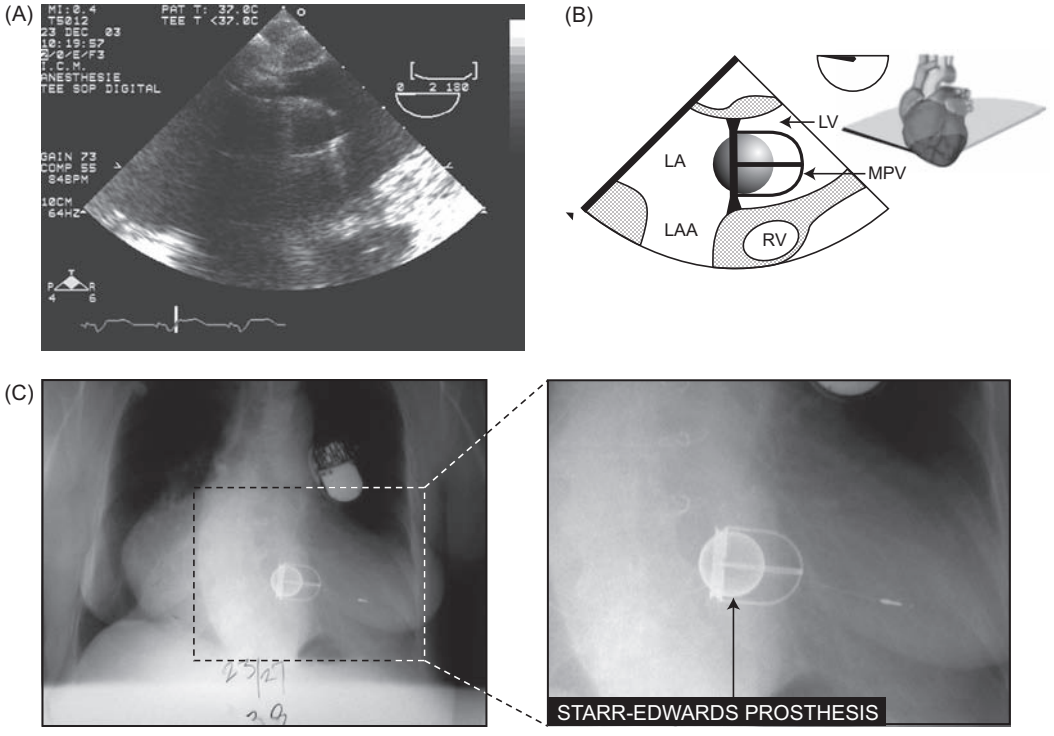

Figure 18.19 A 59-year-old man with a Starr–Edwards mechanical prosthesis in the mitral position. (A, B) The transgastric 0° view is altered secondary to the atrial dilatation. (C, D) Note the similar position of the prosthesis on the chest X-ray (LA, left atrium; LAA, left atrial appendage; LV, left ventricle; MPV, mitral prosthetic valve; RV, right ventricle).

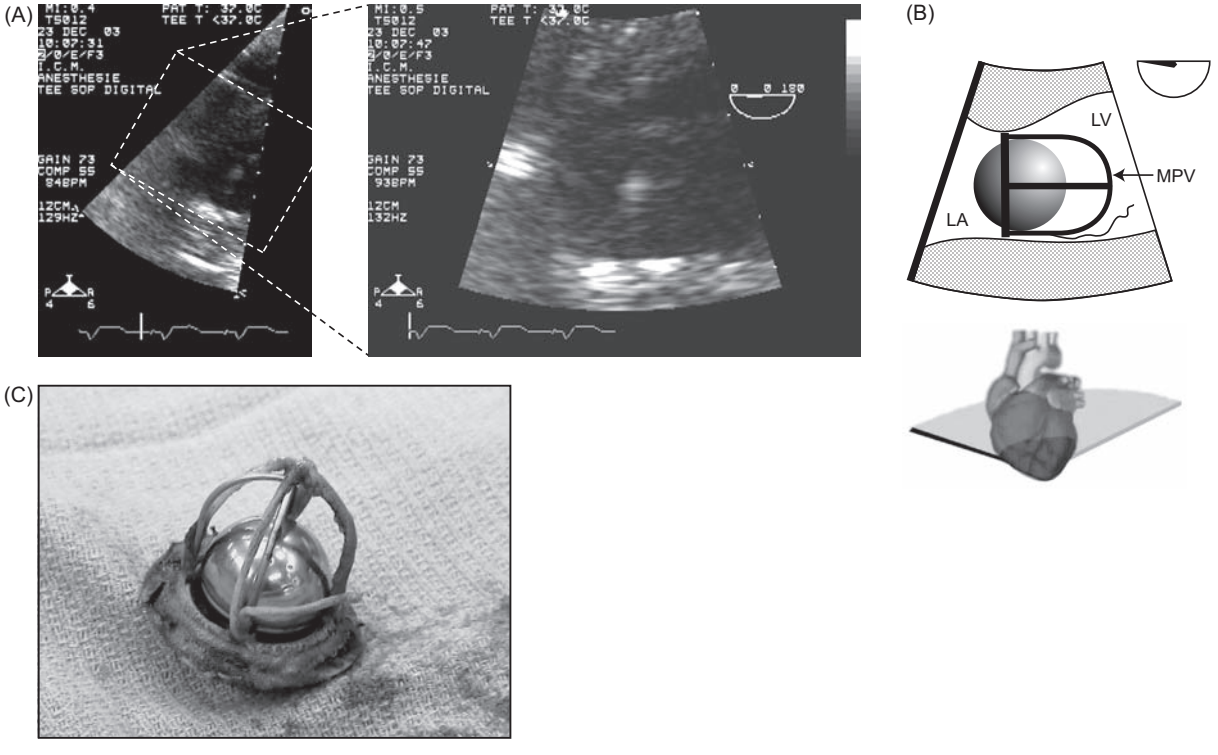

Figure 18.20 A 59-year-old man with a Starr–Edwards mechanical prosthesis in the mitral position. (A, B) Mobile material is seen in the transgastric view. The sheath over the prosthesis struts, which was a feature of the cloth-covered model 6310, is broken (C) (LA, left atrium; LV, left ventricle; MPV, mitral prosthetic valve). (Photo C courtesy of Dr. Raymond Cartier.)

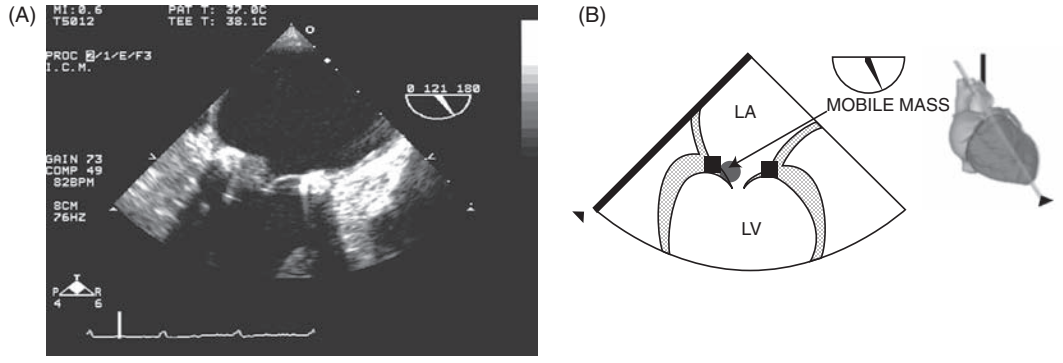

Figure 18.21 Mid-esophageal long-axis view showing a mobile mass attached to the posterior aspect of the sewing ring of a mitral bioprosthesis. This mass could represent a thrombus or a vegetation (Ao, aorta; LA, left atrium; LV, left ventricle).

level in order to improve the detection of perivalvular regurgitant jets or rocking of the sewing ring.

Localization of regurgitation can be reported in reference to neighbouring anatomical landmarks, such as the atrial septum, the AoV or the left atrial appendage (LAA). Others prefer to report jets following the polar coordinate system of a time-clock in reference to the surgeon's view (Figs. 18.23–18.26): at 0°, the left side of the display with the LA up or the side near the atrial septum corresponds to 12:00 on the clock; at 90°, the left side of the screen with the LA up corresponds to 03:00; and at 120°, the left side of the screen (opposite the AoV) corresponds to 04:00, while the LAA corresponds to 7:00 and the AoV to 10:00. For example, a periprosthetic leak extending between 0°—atrial septal side (i.e. left side of the imaging screen with LA up) and 60°—opposite the LAA at the left side of the screen corresponds to a regurgitation between 12:00 and 02:00 on the surgical field.

In transgastric views at 0°, the TEE probe could be angled to achieve a short-axis ("en-face") view (Fig. 18.27) of the mitral valve prosthesis. The site and extent of regurgitation can also be evaluated from this

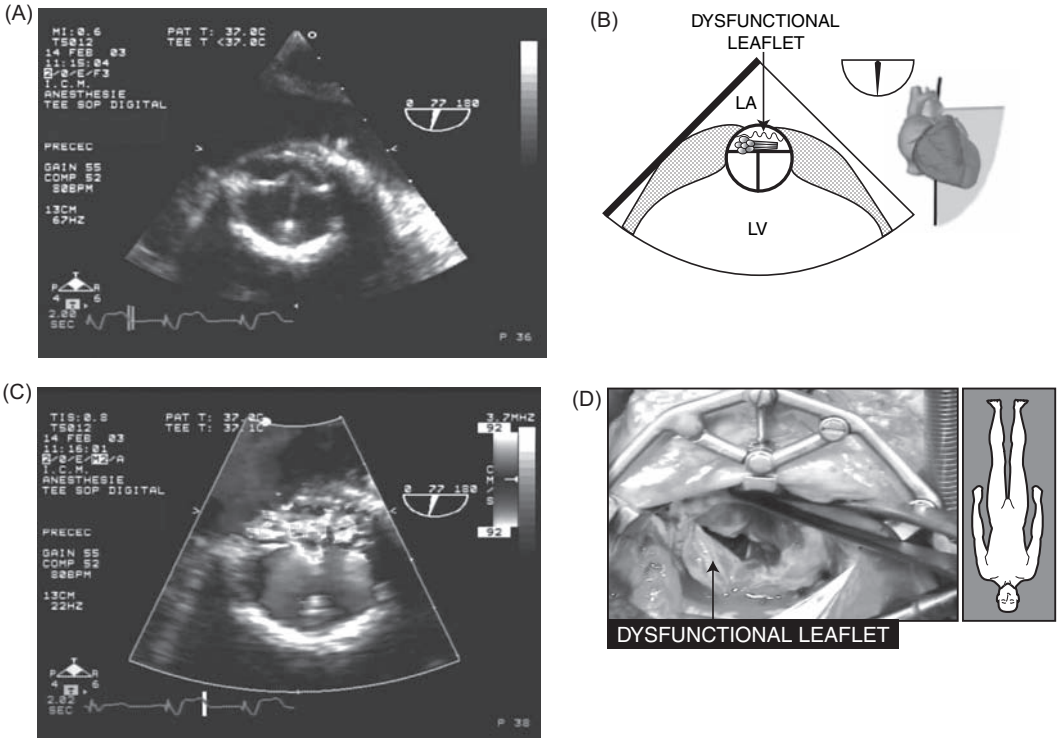

Figure 18.22 A 75-year-old woman scheduled for mitral bioprosthetic valve reoperation. (A–C) A torn leaflet resulted in severe mitral regurgitation. (D) Intraoperative findings (LA, left atrium; LV, left ventricle). (Photo D courtesy of Dr. Raymond Cartier.)

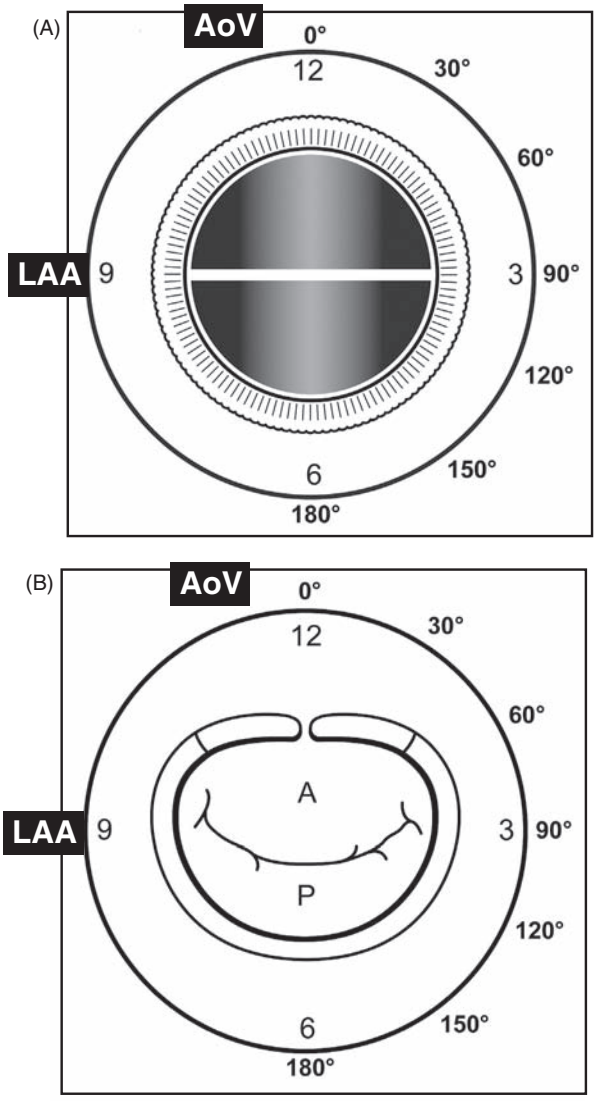

Figure 18.23 Correlation between the transesophageal echocardiographic angles (0–180°) and the surgeon's view for describing the localization of periprosthetic mitral regurgitant jets for mechanical prosthetic valves (A) or after annuloplasty (B). The bileaflet mitral prosthesis is shown here in anatomical position, that is, with the hemidisks in the same orientation as in a native valve. The left atrial appendage (LAA) is close to the 9 o'clock position and the aortic valve (AoV) close to the 12 o'clock position.

level by flexing the probe and slightly advancing or withdrawing the shaft.

The severity of regurgitation is graded as with native valves and based on the integrated evaluation of the regurgitant jet color Doppler surface area, the pulmonary venous systolic flow component on PW Doppler and the proximal flow convergence area (PISA). Several caveats must however be kept in mind: periprosthetic regurgitant jets often hug the left atrial wall (Coanda effect) and the jet area generally appears smaller than with central regurgitation. The quantification of periprosthetic MR by PISA method can also be used but has not been as well validated as for native valves. Finally, the severity of immediate postpump MR could be underestimated with color-flow imaging (see section on post mitral valve repair).

D. Gradient Evaluation

An abnormal increase in transprosthetic gradient (Figs. 18.15 and 18.17) can be secondary to incomplete opening of the mobile components most often due to thrombus, pannus or calcific degeneration, but can also result from the increased flow due to significant regurgitation. The measurement of deceleration time (DT) or PHT can prove very useful in distinguishing these two conditions. The DT and PHT will be prolonged with increased gradients due to thrombosis or degeneration whereas they will be within normal limits with severe regurgitation. The transvalvular diastolic gradient should be measured in the immediate post-CPB period to serve as baseline hemodynamics for future comparison and detection of prosthetic dysfunction. An approach to the evaluation of increased prosthetic gradient is shown in Fig. 18.28 (9).

VI. SURGICAL INDICATIONS OF MITRAL VALVE REPAIR AND REPLACEMENT

The American College of Cardiology and the American Heart Association established, in 1998, guidelines for the management of patients with valvular heart disease (10). The indications for mitral valve repair and replacement are shown in Tables 18.1–18.3. The level of evidence was discussed in Chapter 16.

VII. TEE EVALUATION AFTER MITRAL VALVE REPAIR

After surgical repair, the mitral valve often resembles a unileaflet valve with a large mobile and functional anterior leaflet and a fixed posterior leaflet (Fig. 18.29). The TEE evaluation of the mitral valve after repair should pay particular attention to residual MR. This regurgitation is generally within the annular ring and is usually eccentric. The causes include imperfect coaptation of the mitral leaflets, restricted leaflet motion, or residual prolapse. One should be leery of the severity of immediate postpump MR as color-flow imaging could underestimate this. Moreover, postop left ventricular function and systolic blood pressure (SBP) should be taken into consideration in the interpretation of the data: if left ventricular function or blood pressure (BP) are significantly reduced [i.e. left

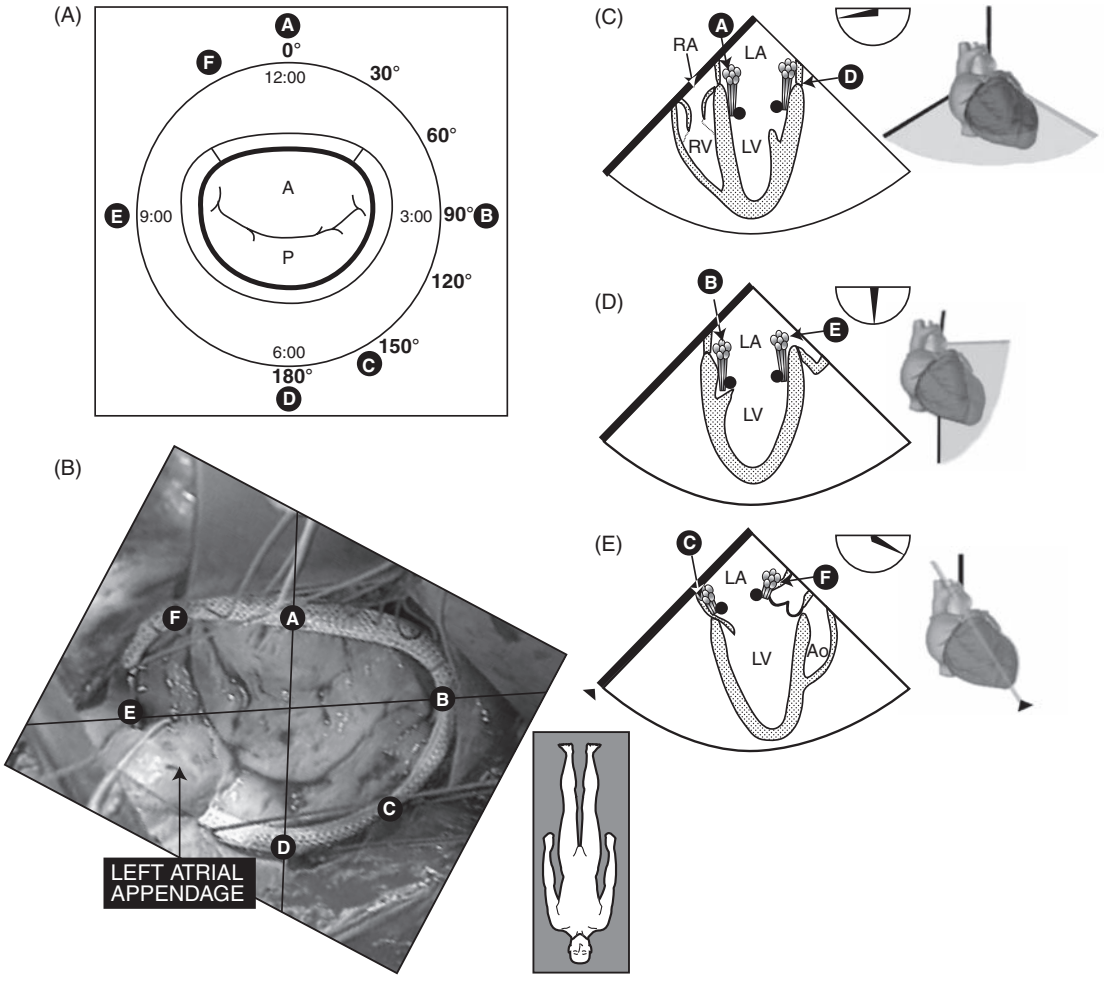

Figure 18.24 Localization of the para-annular jet using the transesophageal echocardiographic angles (0–180°) (A), the surgeon's view (B), and three mid-esophageal views (C–E). Note that the angle may vary $\pm 15^{\circ}$ (Ao, aorta; LA, left atrium; LV, left ventricle; RA, right atrium; RV, right ventricle).

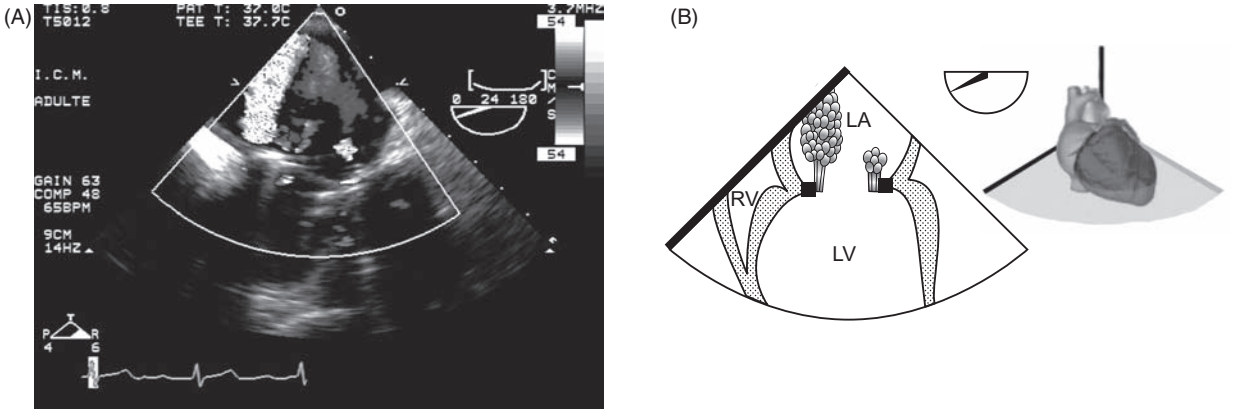

Figure 18.25 Mid-esophageal view with color-flow imaging showing a periprosthetic regurgitation (passing outside the sewing ring) as well as transvalvular prosthetic functional converging regurgitant jets. Periprosthetic leak shown here corresponds to 12:45 in the surgeon's view (LA, left atrium; LV, left ventricle; RV, right ventricle).

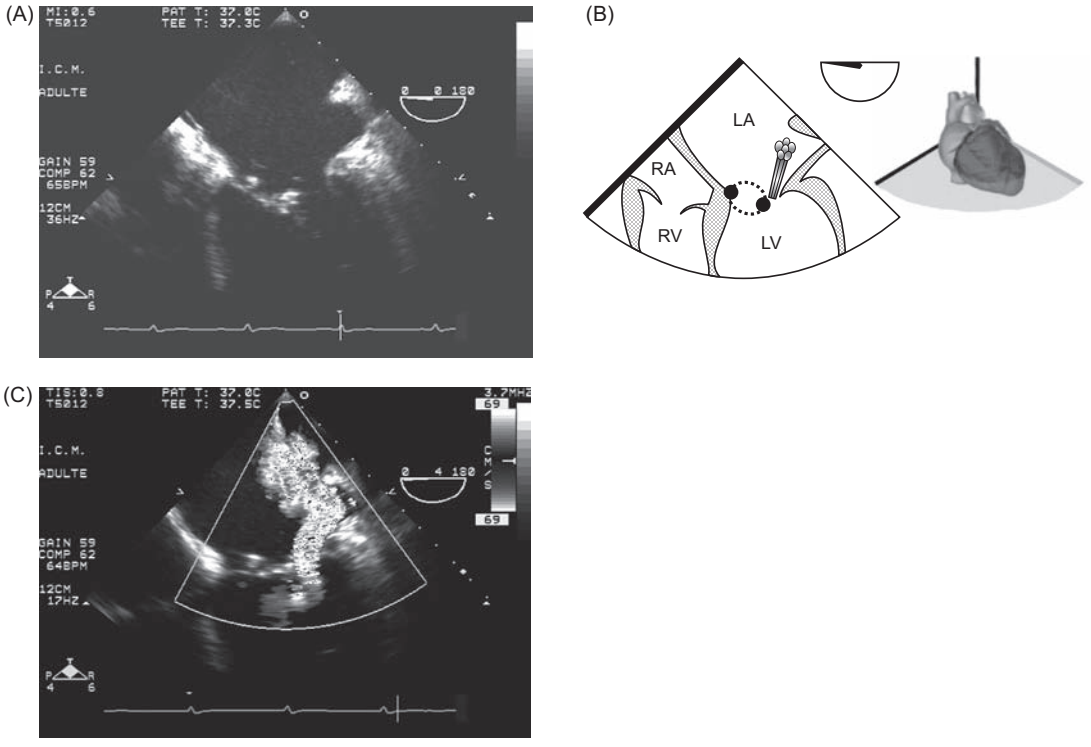

Figure 18.26 (A, B) Mid-esophageal four-chamber view showing annular dehiscence: the annular ring has moved in an apical direction away from the atrioventricular groove. (C) Note the important color regurgitant jet outside (lateral to) the annular ring. The location of periannular regurgitation jet corresponds to 06:00 in the surgeon's view (LA, left atrium; LV, left ventricle; RA, right atrium; RV, right ventricle).

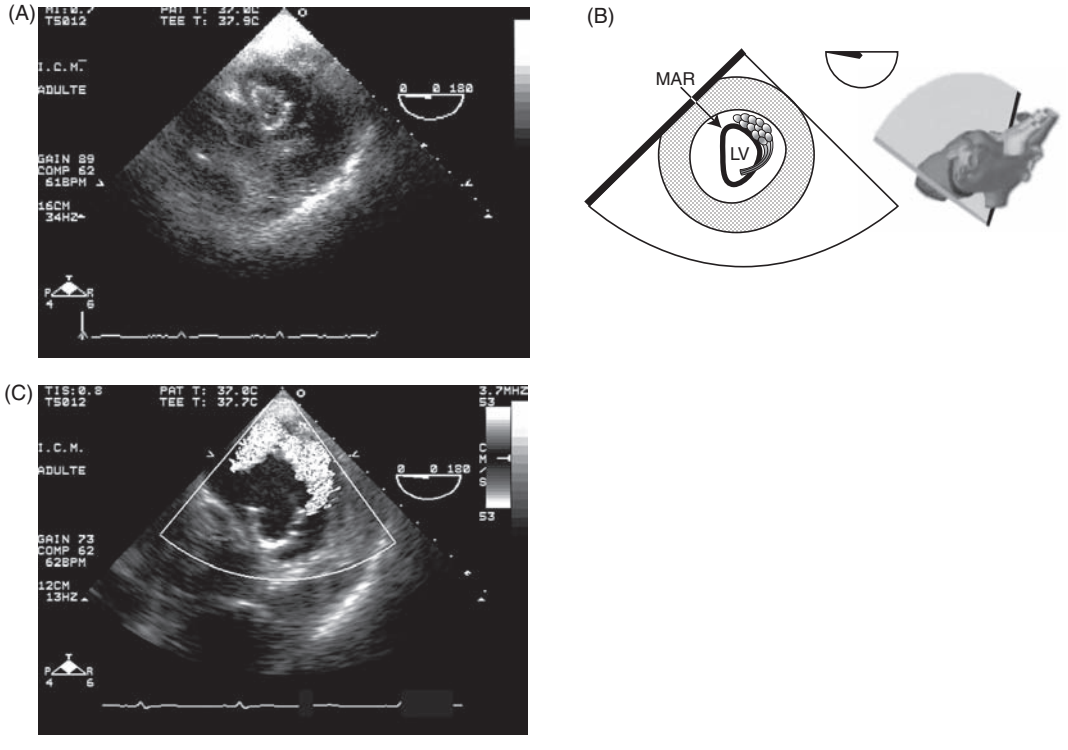

Figure 18.27 (A, B) Transgastric view of a patient with a mitral annuloplasty ring (MAR) with ring dehiscence. (C) Color Doppler interrogation shows severe posterior periannular mitral regurgitation. The color regurgitant jet appears clearly outside (lateral to) the MAR (LV, left ventricle).

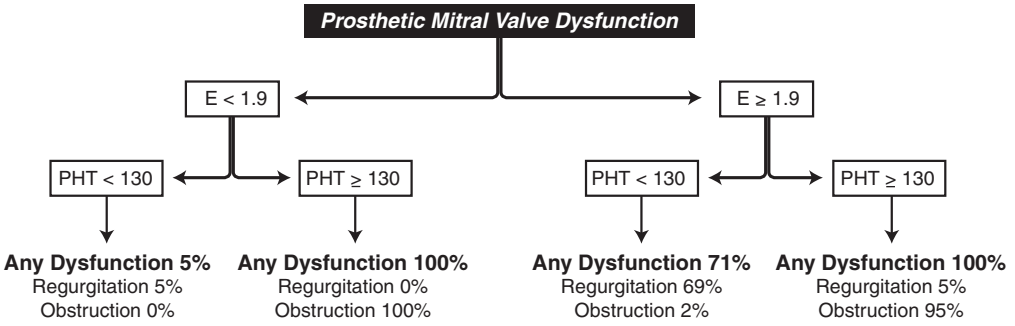

Figure 18.28 Approach to the evaluation of prosthetic valve dysfunction using the early or E component of the transmitral flow Doppler velocities and the measurement of pressure half-time (PHT). The percentage corresponds to the incidence found in the study population. [Adapted from Fernandes et al. (9).]

ventricular ejection fraction $\leq$40% or systolic arterial pressure (SAP) $\leq$100 mmHg], stimulation with vasopressors such as phenylephrine should be considered to reevaluate the severity of MR with higher loading conditions (see Chapter 17). Therefore, the evaluation of global and regional left ventricular function and review of the patient's hemodynamics should not be omitted.

Significant extra- or periannular leaks are uncommon after mitral valve repair but a search for their presence and evaluation of their severity should systematically be performed as with mitral valve replacement. In the long term, annular dehiscence with periannular leak is an infrequent condition and often results from degenerative disease or endocarditis.

Table 18.1 Recommendations for Mitral Valve Repair for Mitral Stenosis Indication

	Class
1. Patients with NYHA functional class III–IV symptoms, moderate or severe MS (mitral valve area <1.5 cm^2),[a] and valve morphology favorable for repair if percutaneous Mitral balloon valvotomy is not available	I
2. Patients with NYHA functional class III–IV symptoms, moderate or severe MS (mitral valve area <1.5 cm^2),[a] and valve morphology favorable for repair if a left atrial thrombus is present despite anticoagulation.	I
3. Patients with NYHA functional class III–IV symptoms, moderate or severe MS (mitral valve area <1.5 cm^2),[a] and a nonpliable or calcified valve with the decision to proceed with either repair or replacement made at the time of the operation	I
4. Patients in NYHA functional class I, moderate or severe MS (mitral valve area <1.5 cm^2),[a] and valve morphology favorable for repair who have had recurrent episodes of embolic events on adequate anticoagulation	IIb
5. Patients with NYHA functional class I–IV symptoms and mild MS	III

[a]The committee recognizes that there may be a variability in the measurement of mitral valve area and that the mean transmitral gradient, pulmonary artery wedge pressure, and pulmonary artery pressure at rest or during exercise should also be considered.
Note: MS, mitral stenosis; NYHA, New York Heart Association.
Source: Adapted from Bonow et al. (10).

Table 18.2 Recommendations for Mitral Valve Replacement for Mitral Stenosis

Indication	Class
1. Patients with moderate or severe MS (mitral valve area <1.5 cm^2)[a] and NYHA functional class III–IV symptoms who are not considered candidates for percutaneous balloon valvotomy or mitral valve repair	I
2. Patients with severe MS (mitral valve area <1 cm^2)[a] and severe pulmonary hypertension (pulmonary artery systolic pressure $>$60–80 mmHg) with NYHA functional class I–II symptoms who are not considered candidates for percutaneous balloon valvotomy or mitral valve repair	IIa

[a]The committee recognizes that there may be a variability in the measurement of mitral valve area and that the mean transmitral gradient, pulmonary artery wedge pressure, and pulmonary artery pressure should also be considered.
Note: MS, mitral stenosis; NYHA, New York Heart Association.
Source: Adapted from Bonow et al. (10).

Table 18.3 Recommendations for Mitral Valve Surgery in Nonischemic Severe Mitral Regurgitation

		Class
1.	Acute symptomatic MR in which repair is likely	I
2.	Patients with NYHA functional class II, III, or IV symptoms with normal LV function defined as ejection fraction >0.60 and end-systolic dimension <45 mm	I
3.	Symptomatic or asymptomatic patients with mild LV dysfunction, ejection fraction 0.50–0.60, and end-systolic dimension 45–50 mm	I
4.	Symptomatic or asymptomatic patients with moderate LV dysfunction, ejection fraction 0.30–0.50, and/or end-systolic dimension 50–55 mm	I
5.	Asymptomatic patients with preserved LV function and atrial fibrillation	IIa
6.	Asymptomatic patients with preserved LV function and pulmonary hypertension (pulmonary artery systolic pressure >50 mmHg at rest or >60 mmHg with exercise)	IIa
7.	Asymptomatic patients with ejection fraction 0.50–0.60 and end-systolic dimension <45 mm and asymptomatic patients with ejection fraction >0.60 and end-systolic dimension 45–55 mm	IIa
8.	Patients with severe LV dysfunction (ejection fraction <0.30 and/or end-systolic dimension >55 mm) in whom chordal preservation is highly likely	IIa
9.	Asymptomatic patients with chronic MR with preserved LV function in whom mitral valve repair is highly likely	IIb
10.	Patients with MVP and preserved LV function who have recurrent ventricular arrhythmias despite medical therapy	IIb
11.	Asymptomatic patients with preserved LV function in whom significant doubt about the feasibility of repair exists	III

Note: LV, left ventricular; MR, mitral regurgitation; NYHA, New York Heart Association.
Source: Adapted from Bonow et al. (10).

Systolic anterior motion (SAM) of the anterior mitral leaflet (11,12) may arise after mitral valve repair as a result of changes in the LV geometry and in the relationship between the LV, the mitral leaflets and the annulus. This is particularly prone to happen when the left ventricular function is hyperdynamic or under inotropic stimulation (Figs. 18.30–18.32) leading to variable degrees of subaortic dynamic obstruction and a late-peaking pressure gradient (13). While color-flow imaging will demonstrate the presence of flow acceleration and color aliasing in the LVOT, CW Doppler from the deep transgastric view should be properly aligned to estimate the severity of the dynamic gradient. Significant LVOT obstruction should be remedied by volume loading, down-titrating vasopressor and inotropic agents, or administrating β-blockers but sometimes requires reintervention. Left unrecognized, it can complicate postoperative management (see Chapter 10).

Mitral valve repair often causes a mild obstruction to diastolic flow and consequently a small gradient of 2–4 mmHg between the LA and the LV, which can be higher with tachycardia. The transmitral gradient should be measured with CW Doppler through the mitral flow during diastole. A regurgitant systolic signal noted during this evaluation should trigger the search for previously unsuspected MR. Transesophageal echocardiography evaluation of mitral valve repair for mitral stenosis (MS) (usually mitral commissurotomy) mostly

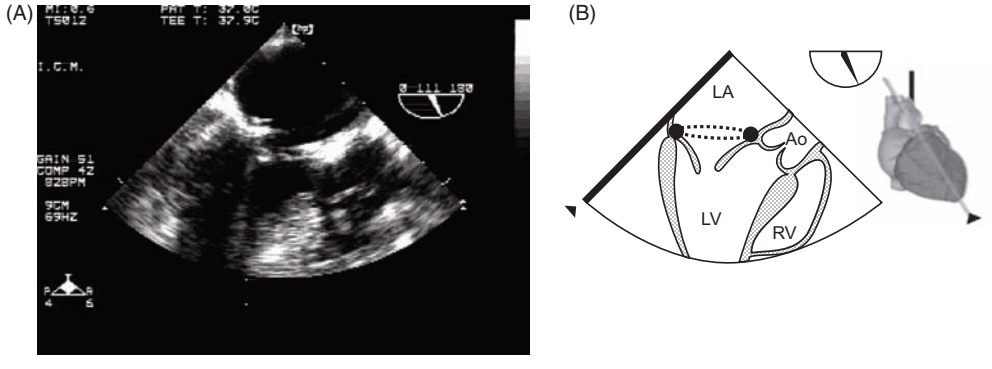

Figure 18.29 Mid-esophageal long-axis view showing normal function of the mitral valve immediately after annuloplasty. The annuloplasty ring is viewed transversely by the 2D tomographic plane and thus appears as two small echodensities at the base of the leaflets on the atrial side. This is sometimes mistaken for annular calcifications (Ao, aorta; LA, left atrium; LV, left ventricle; RV, right ventricle).

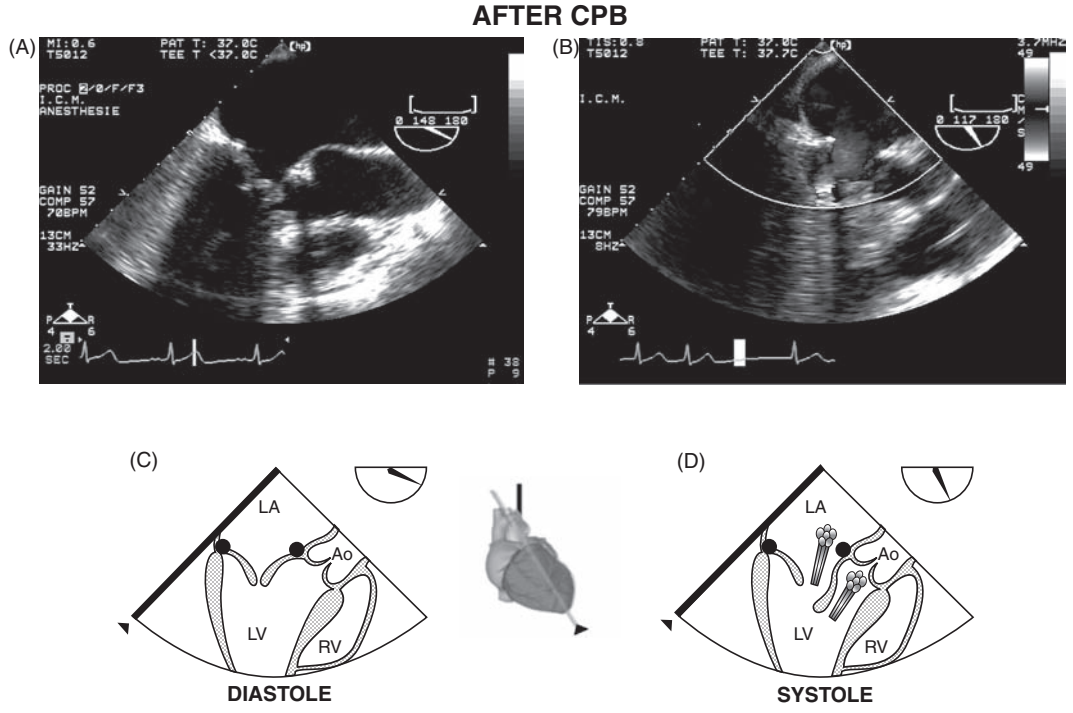

Figure 18.30 (A–D) Mid-esophageal long-axis view showing systolic anterior motion immediately after coming off cardiopulmonary bypass (CPB) for mitral valve repair (Ao, aorta; LA, left atrium; LV, left ventricle; RV, right ventricle).

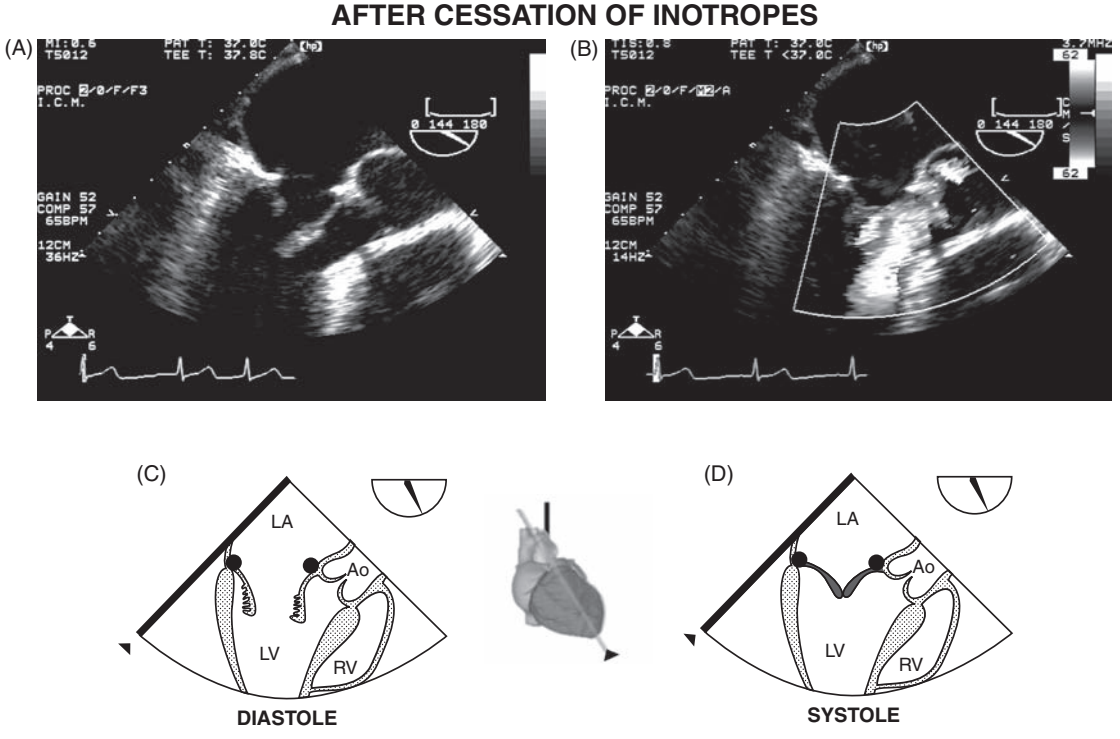

Figure 18.31 (A–D) Mid-esophageal long-axis view in the same patient (Fig. 18.30) after cessation of inotropes (Ao, aorta; LA, left atrium; LV, left ventricle; RV, right ventricle).

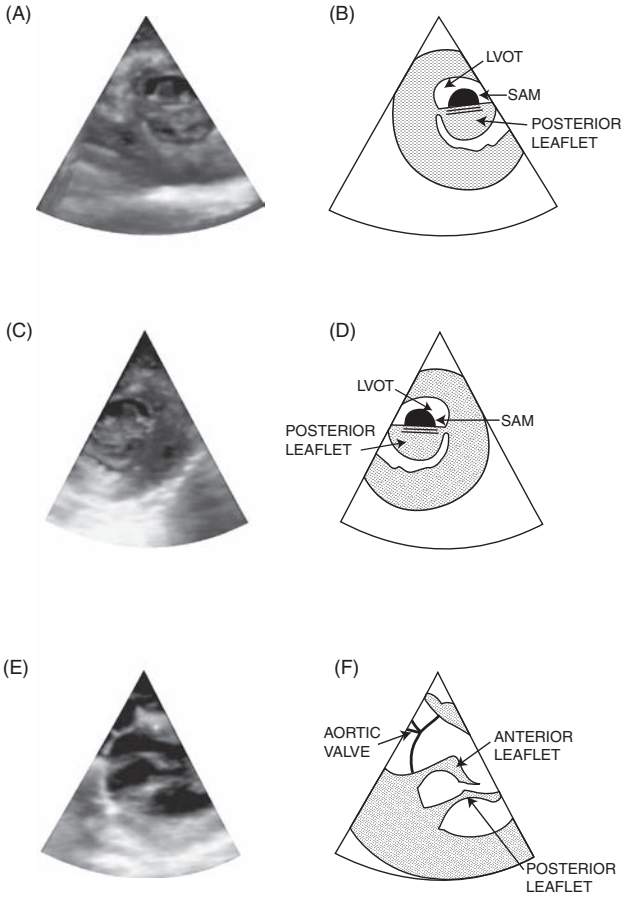

Figure 18.32 A 71-year-old man undergoing mitral valve repair who developed systolic anterior motion (SAM) of the mitral valve during weaning from bypass. Epiaortic 3D (A–D) and 2D views (E, F) were obtained demonstrating partial obstruction of the left ventricular outflow tract (LVOT). The long anterior mitral leaflet is seen displaced in the LVOT during systole. [With permission from Denault et al. (13).]

involves evaluation of valvular and subvalvular anatomy as well as measurement of the mean diastolic gradient and the search for regurgitation.

TEE is also useful after mitral valve repair or replacement for evaluation of deairing, excluding foreign material in the cardiac cavity (see Fig. 16.17), evaluation of left and right ventricular function and exclusion of *de novo* valvular or aortic disease and pleural effusions. The role of TEE in mitral valvular surgery is summarized in Table 18.4.

VIII. MITRAL VALVE REPAIR

Mitral valve reconstruction is the procedure of choice for MR. The issue of degenerative valve MR has been addressed by the pioneering work of Pr. Alain F Carpentier who is a world leader in the development and teaching of modern techniques of valve repair (14). The standardization of these techniques and the favorable long-term results have resulted in an exponential expansion of the indications for surgery of mitral insufficiency. The purpose of this section is to review and describe the contemporary surgical techniques used to correct severe MR.

The initial steps of the operation are important to establish the basis for precise reconstructive surgical techniques.

A. Cannulation and Extracorporeal Circulation (Video Loop)

After induction of general anesthesia, invasive cardiovascular monitoring, and multiplane TEE probe insertion, the mitral valve repair is classically performed through a median sternotomy. Mini-invasive approaches through the sternum or the right chest are becoming more popular as is robotic surgery (15).

The pericardium is then opened longitudinally to the right of the midline using electrocautery. Special attention is given to the careful midline division of the thymus gland at the superior part of the anterior mediastinum. Traction sutures are applied to the right and left superior pericardium in order to elevate and induce a right lateral rotation of the heart. These maneuvers will later facilitate the arterial and venous cannulations and the exposure of the mitral valve through the interatrial groove. Alternative exposures of the mitral valve include the various transseptal approaches. Systemic anticoagulation is achieved with intravenous heparin (3 mg/kg). Aortic purse-string sutures are completed on the ascending aorta (Ao) and the right atrium (RA). The Ao is then cannulated and the purse-string sutures are tied. Venous cannulas are inserted in the superior and inferior venae cava in order to drain the venous return to the membrane oxygenator (see Chapter 13). Double venous cannulation is preferred in order to avoid cerebral congestion due to superior venae cava distortion by the left atrial retractor that will be used for mitral valve exposure. A combined anterograde cardioplegia cannula and vent is inserted and secured in the ascending Ao. The final step is the introduction of the retrograde cardioplegia catheter in the coronary sinus through a stab incision in the RA. Perioperative TEE will confirm the position of the catheter in the coronary sinus. Activated clotting time (ACT) is monitored after heparin injection, a level of >400 s will permit the establishment of CPB at $2.2\,L/m^2$, the mechanical ventilation is then stopped and the Ao is cross-clamped followed by anterograde cold blood (4:1) cardioplegia infusion ($300\,cm^3$) in the aortic root. The LA is opened with a #15 scalpel blade and aspirated with the pump suction lines. Continuous retrograde cold blood cardioplegia is infused during the

Table 18.4 Summary of the Role of TEE in Patients Undergoing Mitral Valve Surgery

	Importance
Before the procedure	
See Table 13.1 for the role of TEE in cardiac surgery	
Evaluate left atrial dimension, presence of unsuspected thrombus in LA and LAA	Anticipation of difficult valve repair with possible modification of the surgical approach, removal of thrombus
Confirm the mechanism of mitral dysfunction (importance of loading conditions)	Confirmation of reparability or replacement
Evaluation of the severity of pulmonary hypertension and tricuspid regurgitation	Tricuspid annuloplasty may be considered with modification of the surgical approach
During CPB	
See Table 13.1	
After CPB	
See Table 13.1	
Evaluate result of repair or replacement	Early detection and correction of prosthetic dysfunction or suboptimal repair
Rule out SAM and LVOT obstruction	SAM will modify the medical approach and could lead to surgical reintervention
In the intensive care unit	
See Table 13.1	

Note: CPB, cardiopulmonary bypass; LA, left atrium; LAA, left atrial appendage; LVOT, left ventricular ourflow tract; SAM, systolic anterior motion; TEE, transesophageal echocardiography.

repair: perfusion pressure is maintained <40 mmHg to prevent myocardial edema. The left atrial retractor blades are positioned and pump aspirators are used to aspirate left atrial blood during surgery.

B. Valve Analysis

Mitral valve functional analysis is then performed. This is of critical importance in valve reconstruction, and should correlate with the perioperative TEE examination. There are three possible mechanisms responsible for MR: type 1—normal leaflet motion, type 2—increased leaflet motion, and type 3—restricted motion. Despite the fact that there are numerous possible valve lesions, they can always be categorized into these three functional groups.

Surgical valve analysis is then systematically performed with specifically designed hooks. The P1 scallop of the valve is taken as the reference point and delicately stretched with the left hand hook. The right hand hook will alternatively evaluate the posterior leaflet P2 and P3 scallops for prolapse or restriction which is defined as a coaptation plane above or below the plane of the native annulus of the mitral valve, respectively. Then, attention is given to the anterior leaflet A1, A2, and A3 scallops and finally to both anterolateral and posteromedian commissures defined by their fan shaped chords (Fig. 18.33).

Once the surgeon has determined the mechanism of MR, specific techniques of repair will be performed to correct the pathological valve.

C. Annuloplasty

The annuloplasty ring has four functions: (1) to restore normal annular geometry, (2) to prevent further annular dilation, (3) to decrease tension of sutures on mitral leaflets and annulus, and (4) to increase mitral valve coaptation surface. There are complete and incomplete annuloplasty rings (Fig. 18.34). All rings are associated with an excellent clinical outcome. In ischemic MR, experimental and clinical studies support the use of complete remodelling annuloplasties in order to provide circumferential support. In degenerative etiologies, posterior bands have been associated with good results, the anterior part of mitral annulus being naturally fixed by the left and right fibrous trigone and the aortic annulus.The ring size is selected with specifically designed templates which measure the intercommissural distance or the intertrigonal distance and the surface area of the anterior leaflet depending on the model of ring selected.

In degenerative MR, avoidance of an annuloplasty ring has been related to an increased recurrence rate of MR. However, in the case of an active acute bacterial endocarditis, a ring annuloplasty can be avoided in order to avoid

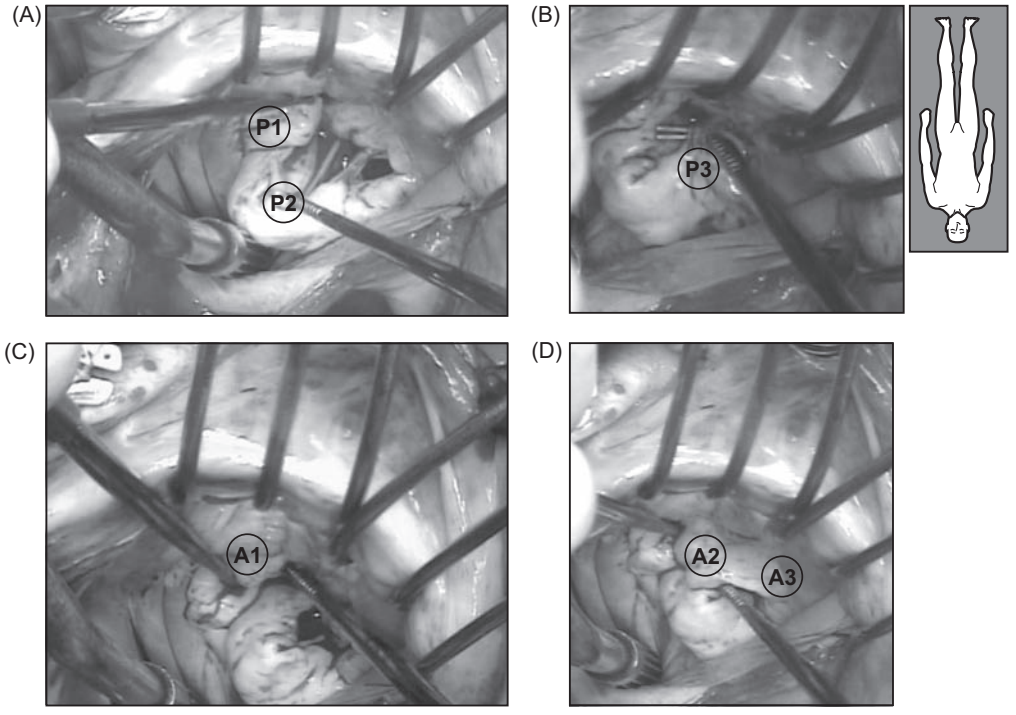

Figure 18.33 (A–D) Intraoperative examination of the mitral valve through a left atriotomy in a 71-year-old man with prolapse of P2 due to chordal rupture.

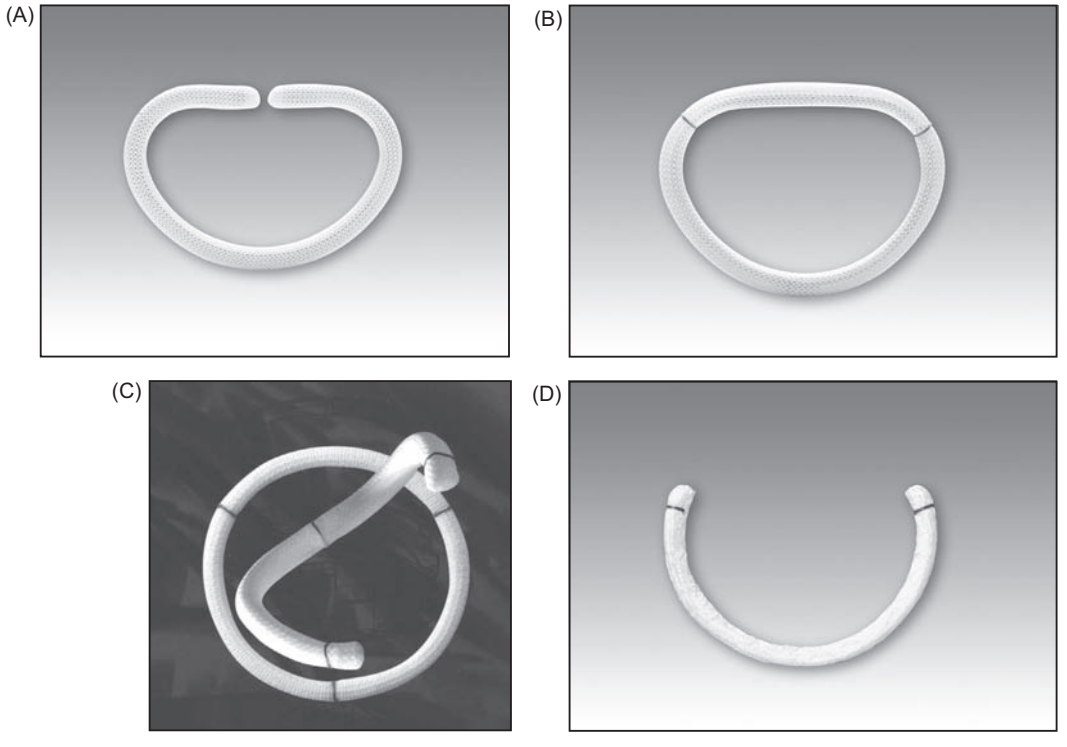

Figure 18.34 Various models of mitral annuloplasty rings: (A) Carpentier–Edwards, (B) Physioring, (C) Duran, and (D) Cosgrove–Edwards. (Courtesy of the manufacturers.)

the presence of foreign material. An autologous pericardial posterior band can alternatively be selected (16).

IX. POSTERIOR LEAFLET PROLAPSE

The posterior mitral valve leaflet is frequently involved in degenerative MR. Approximately 60% of cases of mitral valve prolapse are located on the middle scallop of the posterior leaflet (17).

A. Quadrangular Resection

The classic technique is to perform a quadrangular resection (Fig. 18.35) of the prolapsed segment. After resection of the diseased scallop, the native annulus is plicated with several figures of eight polyester braided 2-0 sutures. Finally, the leaflet remnants are reapproximated with simple everting matress sutures or double running 5-0 propylene monofilament sutures (Cardionyl, Peters, France). The valve is then tested with intraventricular saline injection. The plane of coaptation should be symmetric and no residual prolapse should be identified.

B. Sliding Plasty of the Posterior Leaflet

In some circumstances, the diseased portion is large and requires extensive resection accounting for $>50\%$ of the posterior leaflet. This should be recognized rapidly because it can be associated with an increased risk of SAM of the anterior mitral leaflet (AML).

A simple quadrangular resection could decrease the aortomitral angle, thereby propulsing, in systole, the anterior leaflet of the mitral valve towards the outflow tract of the LV. A sliding technique of the posterior leaflet should be used in order to plicate progressively the posterior ring and decrease the height of the posterior leaflet remnants (18) (see Chapter 10, Fig. 10.9).

First, the leaflet remnants are detached from the annulus of the mitral valve. The second step is to proceed with several (five to seven) 2-0 Ticron compression sutures. The number of plication sutures is variable in order to reapproximate the leaflets without tension. The goal of these sutures will be to progressively plicate the annulus in numerous locations. The leaflets are then reattached to the native annulus with a 4-0 Cardionyl running suture and sutured together with 5-0 Cardionyl sutures. The valve is then tested with saline injection and an appropriate annuloplasty ring is selected. These technical points will maintain the normal aorto-mitral angle (Fig. 18.36).

The posterior leaflet should be less than 2 cm after resection since excessive height is also linked with SAM. A slidding plasty associated with a bilateral triangular resection at the base of the leaflet remnants will correct the situation and avoid SAM (Fig. 18.36).

C. Commissural Prolapse

Commissural prolapse and perforations are frequently associated with bacterial endocarditis. The treatment of a pure prolapse is simple resection and suture. In some cases, a plication of the commissural area without resection is possible. For extensive commissural prolapse and cord rupture, chordal transfer can be used.

D. Extensive Calcification of the Mitral Annulus

Extensive calcification of the mitral annulus is occasionally encountered in degenerative MR. The calcifications are located on the posterior mitral annulus.

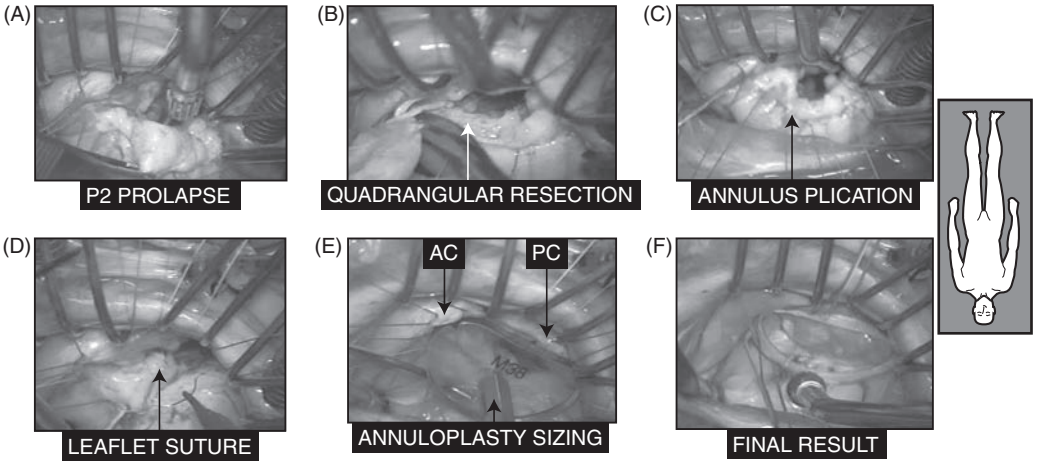

Figure 18.35 (A–F) Quadrangular resection: operative steps (see text for details).

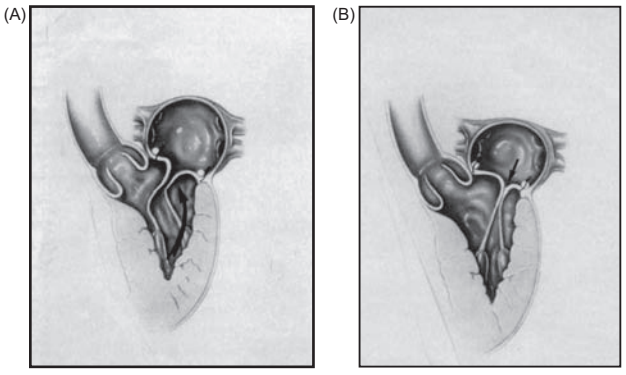

Figure 18.36 (A) Inverted flow closing the posterior leaflet, which pushes the anterior leaflet toward the left ventricular outflow tract. (B) After the sliding leaflet technique, the height of the posterior leaflet is reduced and the anterior leaflet closes away from the left ventricular outflow tract. [With permission from Jebara et al. (18).]

In >50% of cases the calcifications involve >50% of the annulus (Fig. 18.37) (19). The etiology of this condition is related to increased forces of tension on the posterior native annulus, induced by the increased surface area of the prolapsed leaflet. These repeated microtrauma generate fibrin deposition and progressive calcification of the annulus.

In addition to degenerative MR, aging and hypertension have been linked to mitral annulus calcification. For the echocardiographer and the surgeon this condition should be differentiated from rheumatic valve calcification which involves only the mitral valve leaflets and subvalvular apparatus. The clinical problem related to extensive annular calcifications is the difficulty in plicating the underlying native annulus when a posterior leaflet resection is necessary.

If a mitral valve repair is contemplated; a total decalcification of the mitral annulus should be performed (19). After standard resection of the prolapsed posterior leaflet, the posterior leaflet remnants need to be detached from the mitral annulus up to the commissural level if posterior calcification is complete. Decalcification is then accomplished. A sharp dissection plane is defined using a #15 blade scalpel and the resection of the calcified area is performed *en bloc* to avoid fragmentation. After completion of this step the LA is disconnected from the LV and the atrioventricular (AV) groove fat often becomes visible. The AV junction is then reconstructed using x-u stitches. The LA is used as a cuff to cover the left ventricular muscle. Alternatively if the tissues are fragile, an autologous pericardial patch is used to reconstruct the AV junction (20). After reconstruction of the AV junction, the steps of a sliding plasty are completed with proper annuloplasty ring selection.

X. ANTERIOR LEAFLET PROLAPSE

Anterior leaflet prolapse is encountered in ~20% of all cases of degenerative MR. It can be associated with posterior leaflet prolapse. The lesion should be suspected when the regurgitant jet is directed toward the posterior

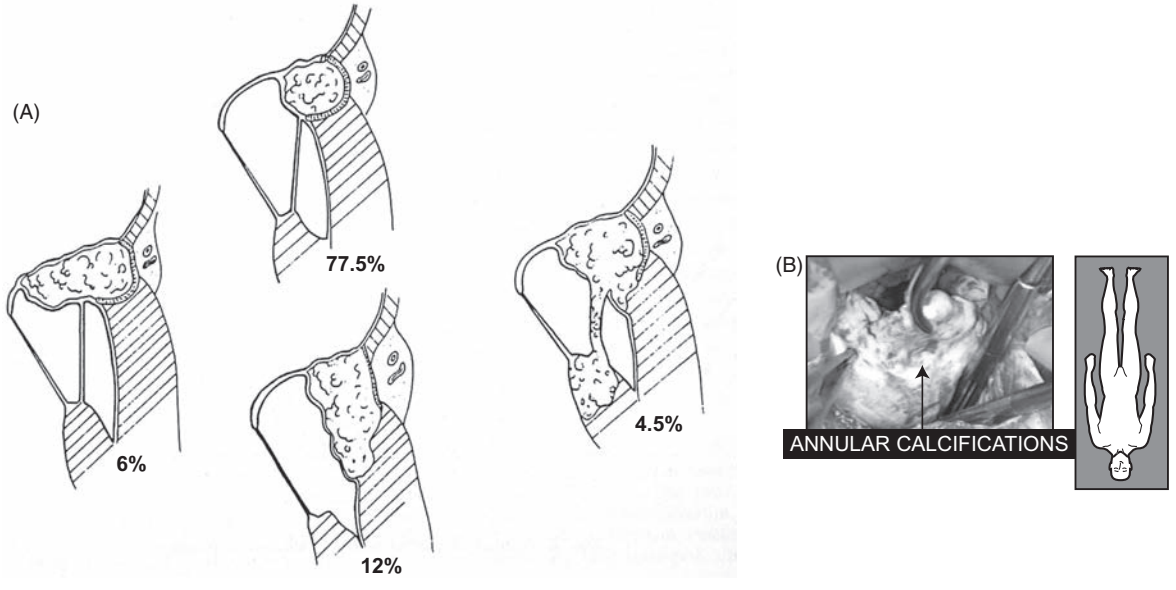

Figure 18.37 (A) Schematic representation of ventricular and leaflet extension of calcifications. Percentages represent frequency of intraoperative findings. (B) Intraoperative posterior annular calcifications through a left atriotomy. [With permission from Carpentier et al. (19).]

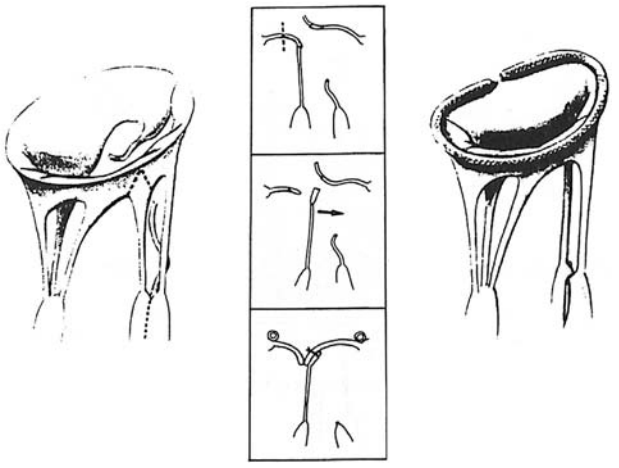

Figure 18.38 Repair of anterior leaflet prolapse due to chordal rupture, by transposition of mural leaflet chordae. [With permission of Carpentier (17).]

aspect of the LA. Repair of anterior lesions necessitates a mastery of surgical techniques.

A. Chordal Transfer

When ruptured chords are responsible for anterior leaflet prolapse, chordal transfer constitutes the treatment of choice (21). The advantage of this approach is the constant length of the transferred scallop. The scallop of the anterior leaflet is located and 2-0 Ticron traction sutures are placed on each side of the prolapsed area. A corresponding segment of the posterior leaflet is selected and traction sutures are also used to delimitate the surface area to be transferred. Then, two simple 4-0 Cardionyl sutures are applied directly on the lateral borders of the leaflet segment to be transferred. The diseased posterior leaflet will be excised (#15 blade scalpel) and transferred to the corresponding area of the anterior leaflet (Fig. 18.38). The 4-0 Cardionyl sutures are inserted on the edge of the anterior leaflet and tied to appose the transferred portion. Several 4-0 Cardionyl simple sutures are added to secure the repair. The posterior leaflet cleft is then repaired as in posterior resections. In a similar approach for limited prolapse, healthy anterior secondary chords can be transferred to the free margin of the anterior leaflet (17).

B. Artificial Goretex Chords

Synthetic chords can be used for diffuse anterior leaflet prolapse. This technique is now widely utilized with excellent long-term results. The anterior leaflet is assessed during valve analysis. A double armed 4-0 Goretex suture is passed through the papillary muscle and tied on Dacron pledgets. The two ends are then passed through the leaflet edge, at the site of ruptured or elongated chords from the ventricular side to the atrial side; then passed through the leaflet again and tied, using stay sutures on the posterior and anterior leaflet edges to assess proper length of the neo chordae (Fig. 18.39).

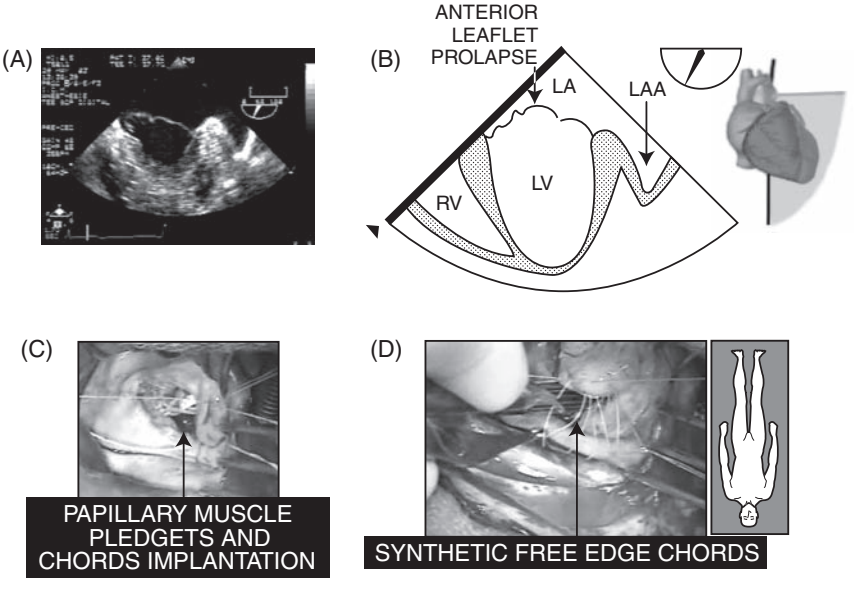

Figure 18.39 (A,B) Mid-esophageal 68° view of a patient with anterior leaflet prolapse. (C, D) Synthetic chords attached to the free edge are then implanted on the papillary muscle, preventing prolapse of the leaflet (LA, left atrium; LAA, left atrial appendage; LV, left ventricle; RV, right ventricle).

Multiple chords can be placed on both papillary muscles, in order to correct the leaflet pathology completely.

C. Papillary Muscle Shortening

This technique has been associated with an increased rate of late recurrence due to chordal erosion. A trench (half the length to be shortened) is made in the papillary muscle and a 4-0 Cardionyl suture is passed around the selected chordea to be shortened. The chord is then buried in the papillary muscle and, finally, the trench is closed with figure of eight stitches (Fig. 18.40) (21). An alternative technique to shorten numerous chords is to perform a wedge resection of the papillary muscle and to suture the parts close together with 4-0 Cardionyl simple sutures.

D. Alferi Operation (Edge to Edge Repair)

A central vertical pledgetted 2-0 Ticron suture can be applied occasionaly as a bail out procedure for anterior or bileaflet prolapse. This should never be used as a primary procedure and only added when no other option can be used. This technique has been associated with early reccurence of MR.

E. Anterior Leaflet Resection

Anterior leaflet resection has been abandoned as the primary treatment for prolapse. Extensive leaflet resection will decrease the surface area of coaptation and may lead to early failure of the procedure. An exception is the occasional rupture of a primary chord attached to the free margin of the anterior leaflet without any other valve lesion. A small wedge resection of the involved segment can then be performed if it represents $<10\%$ of the anterior surface of the anterior leaflet.

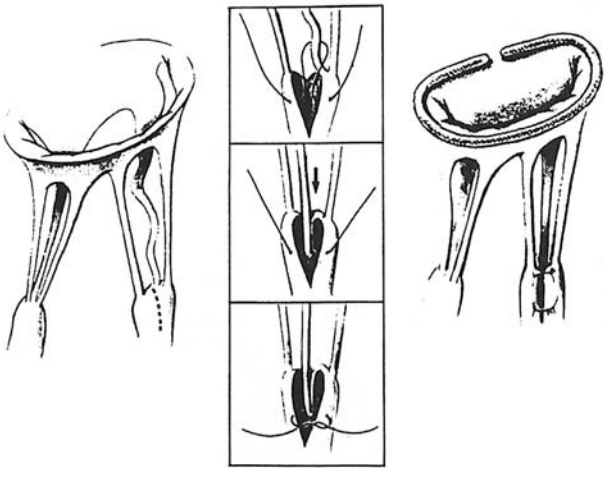

Figure 18.40 Repair of anterior leaflet prolapse due to chordal elongation, by a shortening plasty of the chordae. [With permission of Carpentier (17).]

XI. EARLY COMPLICATIONS

There are few early complications of mitral valve repair.

A. Systolic Anterior Motion

Systolic anterior motion leaflet of the mitral valve occurs at an incidence of $<6\%$. The consequence of this anterior displacement is a LVOT obstruction due to a sail effect of the anterior leaflet during systole. The physiopathology of this complication has been elucidated. Physiologically, the normal mitroaortic angle is $>110^\circ$, in some postoperative circumstances there will be a modification of the angle to $<90^\circ$ leading to an anterior displacement of the anterior leaflet causing obstruction and massive MR (Fig. 18.36).

Surgical risk factors are well known and include extensive posterior leaflet resection, a small LV and excess posterior valve tissue. Perioperative conditions have also been identified: such as a hyperdynamic LV, hypovolemia, and tachycardia (see Chapter 10). Prevention remains the best approach to SAM. A sliding plasty of the posterior leaflet is the most important single technique to consider (Fig. 18.36). Perioperative management includes optimal TEE monitoring, judicious preload adjustment, and avoidance of excessive inotropic agents.

B. Success of the Repair

Mitral valve reconstructive surgery for degenerative lesions is based on the critical knowledge of mitral anatomy. Long-term clinical evolution has been extensively reported. The freedom rate from reoperation at 30 years is low (21).

In conclusion, mitral valve reconstruction is now the procedure of choice for severe MR. Improvements in myocardial protection have allowed longer ischemic time to enable the repair of very complicated lesions. The better understanding of severe MR natural history, the standardization of surgical techniques, the excellent long-term postoperative clinical outcomes, together with the accurate identification of surgical candidates and the dedication to preserve the native mitral valve have resulted in an expansion of surgical indications to the asymptomatic patient before the onset of irreversible LV dysfunction.

REFERENCES

1. Braunwald E. Heart Disease: A Textbook of Cardiovascular Medicine. 5th ed. Philadelphia: W.B. Saunders, 1997.

2. ACC/AHA guidelines for the management of patients with valvular heart disease. A report of the American College of Cardiology/American Heart Association. Task Force on Practice Guidelines (Committee on Management of Patients with Valvular Heart Disease). J Am Coll Cardiol 1998; 32:1486–1588.
3. Hammermeister K, Sethi GK, Henderson WG et al. Outcomes 15 years after valve replacement with a mechanical versus a bioprosthetic valve: final report of the Veterans Affairs randomized trial. J Am Coll Cardiol 2000; 36:1152–1158.
4. Wilkins GT, Flachskampf FA, Weyman A. Echo-Doppler assessment of prosthetic heart valves. In: Weyman AE, ed. Principles and Practice of Echocardiography. Philadelphia: Lea & Febiger, 1994:1198–1237.
5. Solowiejczyk DE, Yamada I, Cape EG et al. Simultaneous Doppler and catheter transvalvular pressure gradients across St Jude bileaflet mitral valve prosthesis: *in vivo* study in a chronic animal model with pediatric valve sizes. J Am Soc Echocardiogr 1998; 11:1145–1154.
6. Weyman AE, Griffin B. Left ventricular outflow tract: The aortic valve, aorta, and subvalvular outflow tract. In: Weyman AE, ed. Principles and Practice of Echocardiography. Philadelphia: Lea & Febiger, 1994:498–574.
7. Dumesnil JG, Honos GN, Lemieux M, Beauchemin J. Validation and applications of mitral prosthetic valvular areas calculated by Doppler echocardiography. Am J Cardiol 1990; 65:1443–1448.
8. Shanewise JS, Cheung AT, Aronson S et al. ASE/SCA guidelines for performing a comprehensive intraoperative multiplane transesophageal echocardiography examination: recommendations of the American Society of Echocardiography Council for Intraoperative Echocardiography and the Society of Cardiovascular Anesthesiologists Task Force for Certification in Perioperative Transesophageal Echocardiography. J Am Soc Echocardiogr 1999; 12:884–900.
9. Fernandes V, Olmos L, Nagueh SF et al. Peak early diastolic velocity rather than pressure half-time is the best index of mechanical prosthetic mitral valve function. Am J Cardiol 2002; 89:704–710.
10. Bonow RO, Carabello B, de LA Jr et al. Guidelines for the management of patients with valvular heart disease: executive summary. A report of the American College of Cardiology/American Heart Association Task Force on Practice Guidelines (Committee on Management of Patients with Valvular Heart Disease). Circulation 1998; 98:1949–1984.
11. Freeman WK, Schaff HV, Khandheria BK et al. Intraoperative evaluation of mitral valve regurgitation and repair by transesophageal echocardiography: incidence and significance of systolic anterior motion. J Am Coll Cardiol 1992; 20:599–609.
12. Kronzon I, Cohen ML, Winer HE, Colvin SB. Left ventricular outflow obstruction: a complication of mitral valvuloplasty. J Am Coll Cardiol 1984; 4:825–828.
13. Denault A, Couture P, Pellerin M. Images in anesthesia: 3D systolic anterior motion of the mitral valve. Can J Anaesth 2004; 51:481.
14. Carpentier AF, Lessana A, Relland JY et al. The "physioring": an advanced concept in mitral valve annuloplasty. Ann Thorac Surg 1995; 60:1177–1185.
15. Loulmet DF, Carpentier A, Cho PW et al. Less invasive techniques for mitral valve surgery. J Thorac Cardiovasc Surg 1998; 115:772–779.
16. Dreyfus G, Serraf A, Jebara VA et al. Valve repair in acute endocarditis. Ann Thorac Surg 1990; 49:706–711.
17. Carpentier A. Cardiac valve surgery—the "French correction." J Thorac Cardiovasc Surg 1983; 86:323–337.
18. Jebara VA, Mihaileanu S, Acar C et al. Left ventricular outflow tract obstruction after mitral valve repair. Results of the sliding leaflet technique. Circulation 1993; 88:II30–II34.
19. Carpentier AF, Pellerin M, Fuzellier JF, Relland JY. Extensive calcification of the mitral valve anulus: pathology and surgical management. J Thorac Cardiovasc Surg 1996; 111:718–729.
20. Feindel CM, Tufail Z, David TE et al. Mitral valve surgery in patients with extensive calcification of the mitral annulus. J Thorac Cardiovasc Surg 2003; 126:777–782.
21. Braunberger E, Deloche A, Berrebi A et al. Very long-term results (more than 20 years) of valve repair with carpentier's techniques in nonrheumatic mitral valve insufficiency. Circulation 2001; 104:I8–I11.

19

Pulmonic and Tricuspid Valves

FRANÇOIS MARCOTTE, DENIS BOUCHARD
University of Montreal, Montreal, Canada

I. Normal Tricuspid and Pulmonic Valve Anatomy 447
II. Anatomical Manifestations of Valvular Lesions 450
A. Tricuspid Regurgitation 450
III. Endocarditis 455
A. Vegetations 455
B. Abscesses 458
IV. Rheumatic Valve Disease 458
A. Other Inflammatory Valvulopathies 458
V. Myxoid Degeneration 459
VI. Pulmonic Valve Disease 459
VII. Valve Repair, Tricuspid—Indications and Methods of Repair 460
A. Suture Annuloplasty, Complications, Failed Repair 462
B. Annuloplasty Rings 463
VIII. Valve Replacement 463
A. Tricuspid Valvectomy 465
B. Types of Valve Prosthesis 465
References 467

Transesophageal echocardiography (TEE) is only occasionally requested for the primary evaluation of tricuspid and pulmonic valve disease. This is, in part, because isolated tricuspid and pulmonic valve diseases are relatively uncommon in comparison with left-sided valvular heart disease. Furthermore, compared with the mitral and aortic valves, these structures are more anterior and located in the TEE far field, making their assessment perhaps more difficult. Nevertheless, as transthoracic echocardiography (TTE) does not always allow the optimal evaluation of the tricuspid and pulmonic valves, particularly during cardiac surgery, TEE may yield very useful informations complementary to TTE. Intraoperative TEE, typically done for the assessment of mitral and aortic valve (AoV) disease, provides a fairly accurate prediction of disease severity and pathology in $>95\%$ of cases in experienced hands (1). A TEE examination, oblivious to the presence of right-sided valve disease in the operating room, can lead to serious short- and long-term consequences for the patient. Right heart failure secondary to right-sided valvulopathies can be extremely difficult to treat medically and may ultimately lead to a reduced event-free survival (2,3).

I. NORMAL TRICUSPID AND PULMONIC VALVE ANATOMY

Situated in the crescentic, pyramid-shaped right ventricle (RV) which supports the low-pressure pulmonary circulation, the tricuspid valve (TV) is in the right ventricular inlet chamber or sinus, while the pulmonic valve (PV) is anterior and superior to the TV in the right ventricular outlet or conus (Fig. 19.1). Unlike the AoVs, the tricuspid

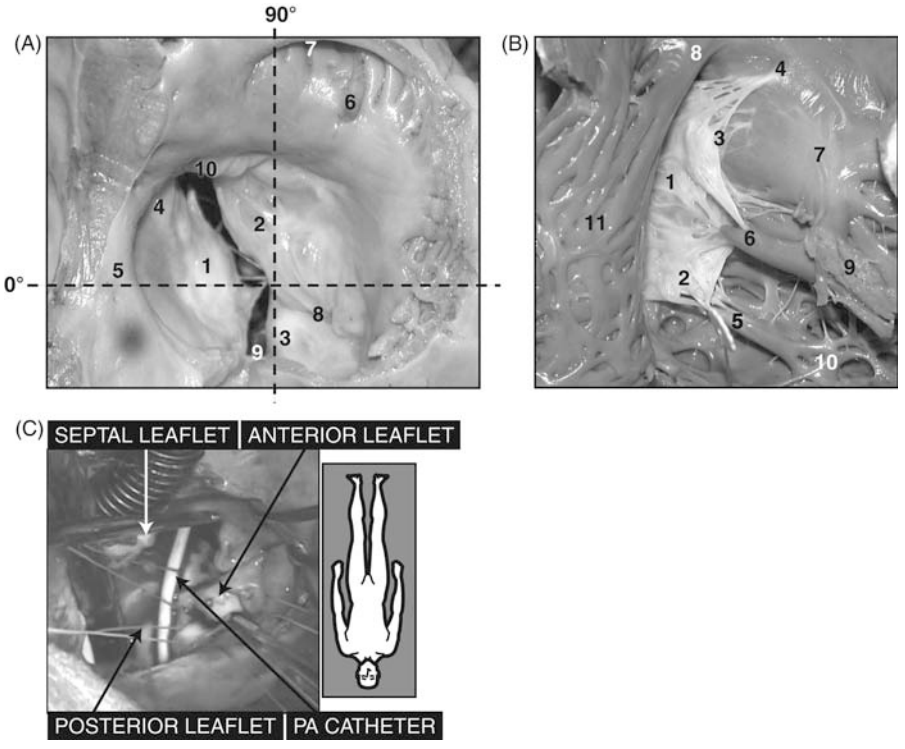

Figure 19.1 (A) Tricuspid valve seen from the right atrium. The 0–90° echocardiographic planes are shown (1, septal leaflet; 2, anterior leaflet; 3, inferior or posterior leaflet; 4, ventricular membranous septum; 5, atrial septum; 6, crista terminalis; 7, ostium of the right atrial appendage; 8, anteroinferior commissure; 9, inferior commissure; 10, anterosuperior commissure). (B) Tricuspid valve seen from the right ventricle (1, anterior leaflet; 2, inferior leaflet; 3, septal leaflet; 4, medial papillary muscle; 5, inferior papillary muscle; 6, anterior papillary muscle; 7, trabecula septomarginalis; 8, crista supraventricularis; 9, moderator band; 10, trabecular zone; 11, right ventricular free wall). (C) Intraoperative aspect of the tricuspid valve (PA, pulmonary artery). (Photos courtesy of Drs. Nicolas Dürrleman and Michel Pellerin.)

and pulmonic valves are anatomically discontiguous, separated by myocardium.

The TV is situated anterior, inferior and to the right of the mitral valve. It is composed of three leaflets, the septal, the anterior, and the posterior (or inferior). Each leaflet is supported by a papillary muscle with the right ventricular moderator band joining the septal and the anterior papillary muscles (Fig. 19.1). The TV has a large orifice, usually $>7\,cm^2$ and like its left-sided counterpart, requires the coordination of multiple structures for proper function as shown in Table 19.1 (4,5). Abnormalities affecting each of these components may in turn cause TV regurgitation and/or stenosis. The normal tricuspid annular circumference is 12–14 cm with a diameter of 3 cm (4). Normally, the tricuspid leaflet thickness is <3 mm.

The PV is situated anterior and to the left of the AoV (see Fig. 15.1). It has two posterior cusps (right and left) and one anterior cusp, in mirror image to the AoV cusps (Fig. 19.2). Proper PV function requires normal leaflet anatomy and support from the pulmonary artery and right ventricular outflow tract (RVOT).

Intraoperative TEE examination has been described and reviewed in a recent publication (6). From the recommended 20 views for performing a comprehensive TEE exam, seven views are particularly useful for the evaluation of the right-sided structures.

Basic TEE assessment of the right-sided valves begins with the mid-esophageal views which are typically used for valvular anatomy and atrial assessment. The four-chamber view at 0° reveals the TV anterior and septal leaflets (Fig. 19.3). In this view, the tricuspid annulus measures $\sim 28 \pm 5$ mm (7) or $16 \pm 3\,mm/m^2$ body surface area (BSA) (see Chapter 5).

The assessment of tricuspid flow is often hindered by its perpendicular direction to the ultrasound beam as well as occasional shadowing by the left-sided valves and the septum. In the basal view at 0°, by withdrawing the probe cranially, the PV is seen anteriorly and to the left of the ascending aorta while the pulmonary artery courses posteriorly. The RVOT diameter usually measures $\sim 27 \pm 4$ mm (7) or $15 \pm 2\,mm/m^2$ BSA.

Table 19.1 Components of Normal Tricuspid Valve Function

Structure	Pathological process
Right atrium	Right atrial dilatation
	Atrial septal defect
	Anomalous pulmonary venous return
	Right ventricular diastolic dysfunction
	Tumor protrusion through the annulus
Tricuspid annulus	Annular enlargement
Tricuspid leaflets and Chordae tendineae	Myxomatous degeneration
	Destruction by endocarditis
	Rheumatic heart disease
	Ebstein's anomaly
	Carcinoid tumor
	Anorectic drugs, ergot-derived drugs
	Radiation-induced scar
	Valve dysplasia
	Connective tissue disease
	Interference or damage by catheter or pacemaker wire
	Trauma from endomyocardial biopsy
	Unguarded tricuspid valve orifice
Atrioventricular septum	Septal defect producing septal leaflet cleft
	Septal aneurysm
Papillary muscles	Destruction by endocarditis
	Rupture from right ventricular infarction
	Damage from trauma
Right ventricle	Pressure overload
	Pulmonary hypertension
	Pulmonic valve stenosis
	Volume overload
	Atrial septal defect
	Pulmonic valve regurgitation
	Regional dysfunction
	Dysplasia
	Infarction
	Trauma
	Radiation injury
	Dilated cardiomyopathy
	Restrictive cardiomyopathy

As the probe is further withdrawn, shadowing from air in the tracheobronchial tree frequently precludes visualization of the pulmonary artery, especially the left branch. The assessment of the tricuspid and pulmonic valves thus frequently requires multiple views, as provided by multiplane imaging.

As the imaging plane is rotated to 30–70° and the probe is turned toward the right, the equivalent of the transthoracic parasternal short-axis view or right ventricular inflow–outflow view becomes visible (Fig. 19.4). Below the atrial septum and the AoV, the TV anterior and septal leaflets are seen, with tricuspid regurgitation (TR) shown by color flow imaging.

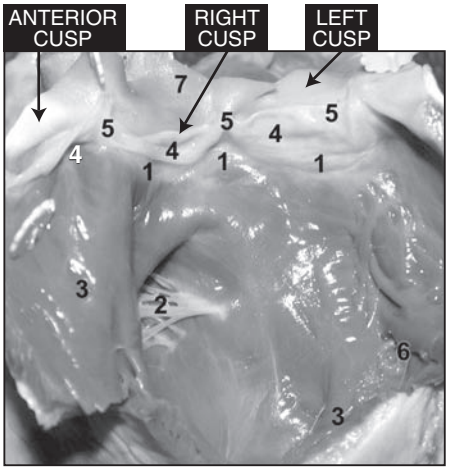

Figure 19.2 The pulmonic valve seen from a right ventriculotomy (1, pulmonary annulus; 2, septal leaflet of tricuspid valve; 3, right ventricle walls; 4, pulmonary cusps; 5, pulmonary commissures; 6, interventricular septum; 7, pulmonary artery). (Courtesy of Dr. Nicolas Dürrleman.)

Further rotation of the imaging plane to 90° in the mid- and high-esophageal views reveals the right ventricular infundibulum, the PV and the main pulmonary artery in a sagittal view of the heart (Fig. 19.5). Easy alignment of the ultrasound beam with the direction of the pulmonary artery flow makes this view particularly suited to Doppler interrogation of the PV.

At 120°, rightward rotation of the probe shaft yields the equivalent of a transthoracic parasternal long-axis RV inflow view which demonstrates the TV anterior and posterior leaflets and may be particularly useful to disclose a posteriorly directed TR jet by color flow imaging (Fig. 19.6).

The exam proceeds towards the transgastric views to demonstrate ventricular function and subvalvular atrioventricular (AV) apparatus anatomy. Further insertion of the probe from the mid-esophageal position first leads to the transitional (or gastroesophageal) view at 0° at the level of the coronary sinus displays the TV posterior and septal leaflets and is a useful view in the assessment of TR (Fig. 19.7). Further down, the transgastric view at 0° reveals the left and right ventricles side by side. This view may require some tilting of the probe in certain patients with unusual cardiac orientation (Fig. 19.8). The three leaflets of the TV can be seen "*en face*" when the RV is markedly dilated. More importantly, the right ventricular contractility and the ventricular septal curvature can be assessed in this view.

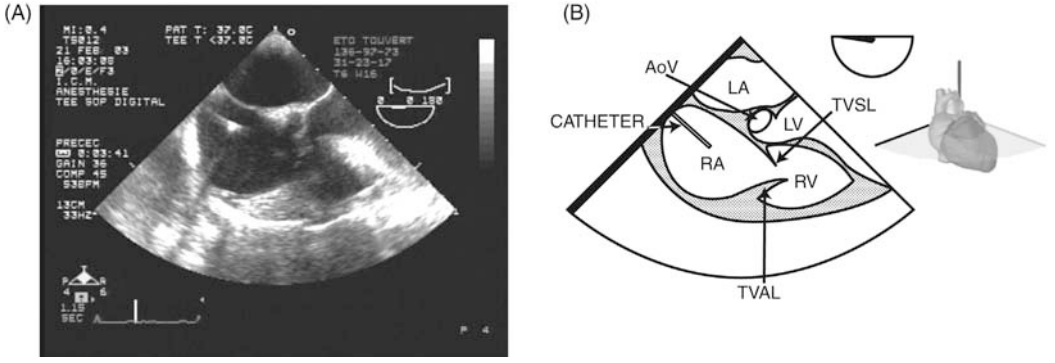

Figure 19.3 Mid-esophageal four-chamber view of the tricuspid valve (septal and anterior leaflets) in a 74-year-old man before coronary revascularization. A pulmonary artery catheter is seen in the right atrium (RA) (AoV, aortic valve; LA, left atrium; LV, left ventricle; RV, right ventricle; TVAL, tricuspid valve anterior leaflet; TVSL, tricuspid valve septal leaflet).

Rotation of the imaging plane to 60–90° with rightward rotation of the shaft past the plane of the ventricular septum reveals a right sagittal view with the right ventricular infundibulum and the subvalvar tricuspid apparatus (Fig. 19.9). The right ventricular outflow and the pulmonary trunk may be also visualized in the far field. Easy alignment of the ultrasound beam with the direction of the flow in this view is ideal for Doppler interrogation of the PV sub- and supravalvular velocities to diagnose stenosis.

A deeper transgastric view at 120° allows further visualization of the TV anterior and posterior leaflets and the subvalvar apparatus (Fig. 19.10).

II. ANATOMICAL MANIFESTATIONS OF VALVULAR LESIONS

A. Tricuspid Regurgitation

With the development of color flow imaging, TR has become a frequently disclosed finding and is seen in almost all individuals to same degree. Hemodynamically and echocardiographically significant TR, however, is usually associated with right-sided cardiac chamber enlargement, unless it is of acute onset (Fig. 19.11). Most commonly, TR is of functional origin and less commonly from structural tricuspid disease (9). Functional TR implies normal valve leaflet and usually results from right ventricular pressure overload from pulmonary hypertension or from right ventricular dysfunction.

Functional TR results mostly from dilatation of the mural annulus which supports the anterior and posterior leaflets, while there is little change in the septal annular dimensions (10,11). The mechanism of functional TR may also involve incomplete coaptation of the tricuspid leaflets as a result of the apical displacement of the tricuspid papillary muscles secondary to right ventricular dilatation and dysfunction. This is best appreciated in the four-chamber view (Fig. 19.3) (12). Significant TR is usually associated with dilatation of the tricuspid annulus diameter $>27\ \mathrm{mm/m^2}$ BSA (13). A diameter exceeding 30 mm is generally deemed enough to consider TV

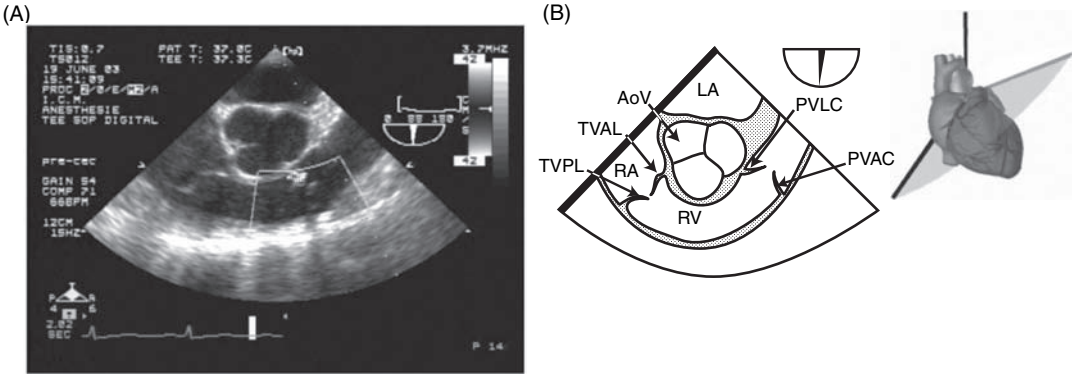

Figure 19.4 Mid-esophageal short-axis view of the right ventricular inflow and outflow tract showing both tricuspid and pulmonic valves (AoV, aortic valve; LA, left atrium; PVAC, pulmonic valve anterior cusp; PVLC, pulmonic valve left cusp; RA, right atrium; RV, right ventricle; TVAL, tricuspid valve anterior leaflet; TVPL, tricuspid valve posterior leaflet).

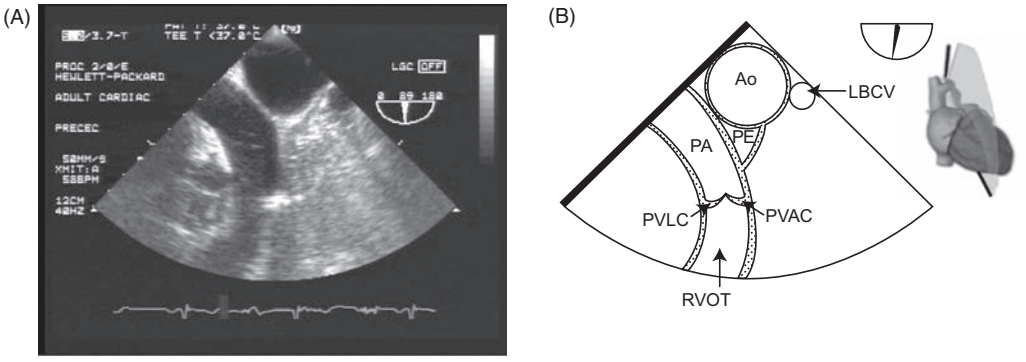

Figure 19.5 Upper esophageal sagittal view of the right ventricular outflow tract (RVOT) and pulmonic valve (Ao, aorta; LBCV, left brachiocephalic vein; PA, pulmonary artery; PE, pericardial effusion; PVAC, pulmonic valve anterior cusp; PVLC, pulmonic valve left cusp).

annuloplasty for significant TR in the setting of concomitant cardiac surgery (Fig. 19.12). A tricuspid annular dilatation >50 mm is associated with a lower likelihood of right ventricular function recovery following repair (14). Common causes of pulmonary hypertension leading to functional TR include left ventricular failure and mitral valve disease, both easily identified by TEE. Other causes are thromboembolic pulmonary vascular disease, autoimmune pulmonary vascular disease, and primary pulmonary hypertension (12,15).

Tricuspid regurgitation secondary to structural disease may implicate one of many mechanisms, such as leaflet

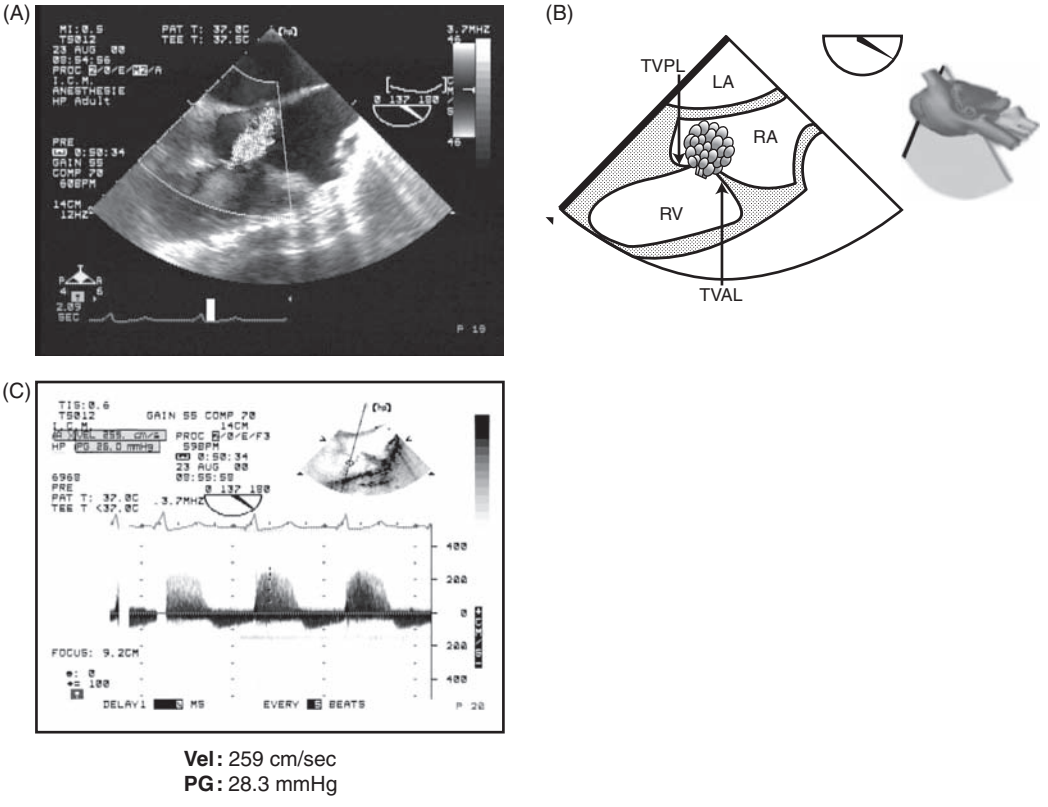

Figure 19.6 (A, B) Mid-esophageal 120° view with rightward rotation, demonstrating the anterior and posterior tricuspid leaflets, the right atrium (RA) and the atrial septum in a 77-year-old woman scheduled for tricuspid valve annuloplasty. (C) The peak systolic pressure gradient (PG) measured from the continuous-wave Doppler tricuspid regurgitant signal is 28.3 mmHg (LA, left atrium; RV, right ventricle; TVAL, tricuspid valve anterior leaflet; TVPL, tricuspid valve posterior leaflet; Vel, velocity).

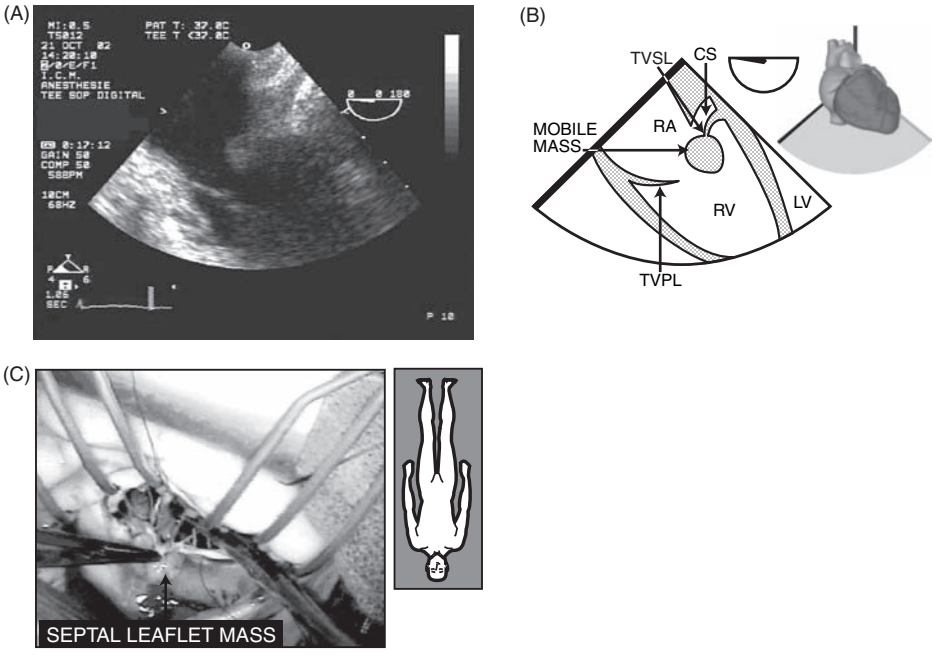

Figure 19.7 (A, B) Low esophageal four-chamber view of a 65-year-old woman who was operated on for a mass on the tricuspid valve. The posterior and septal leaflets of the tricuspid valve are shown. The mass is localised near the septal leaflet close to the coronary sinus (CS). (C) Intraoperative findings through a right atriotomy: on pathology, the mass was diagnosed as a fibroelastoma (LV, left ventricle; RA, right atrium; RV, right ventricle; TVPL, tricuspid valve posterior leaflet; TVSL, tricuspid valve septal leaflet). (Photo C courtesy of Dr. Pierre Pagé.)

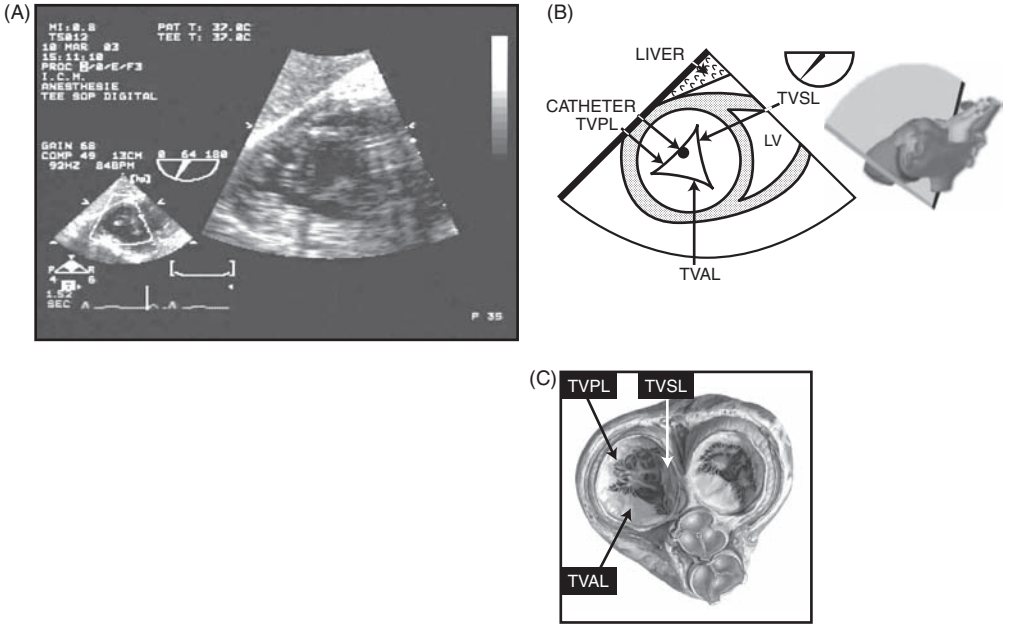

Figure 19.8 Tricuspid valve. (A, B) Modified transgastric basal view of the right ventricle showing the three leaflets of the tricuspid valve in a 50-year-old man before closure of an atrial septal defect and coronary revascularization. (C) Corresponding echocardiographic orientation (LV, left ventricle; TVAL, tricuspid valve anterior leaflet; TVPL, tricuspid valve posterior leaflet; TVSL, tricuspid valve septal leaflet). [Photo C with permission of Netter and Yonkman (8).]

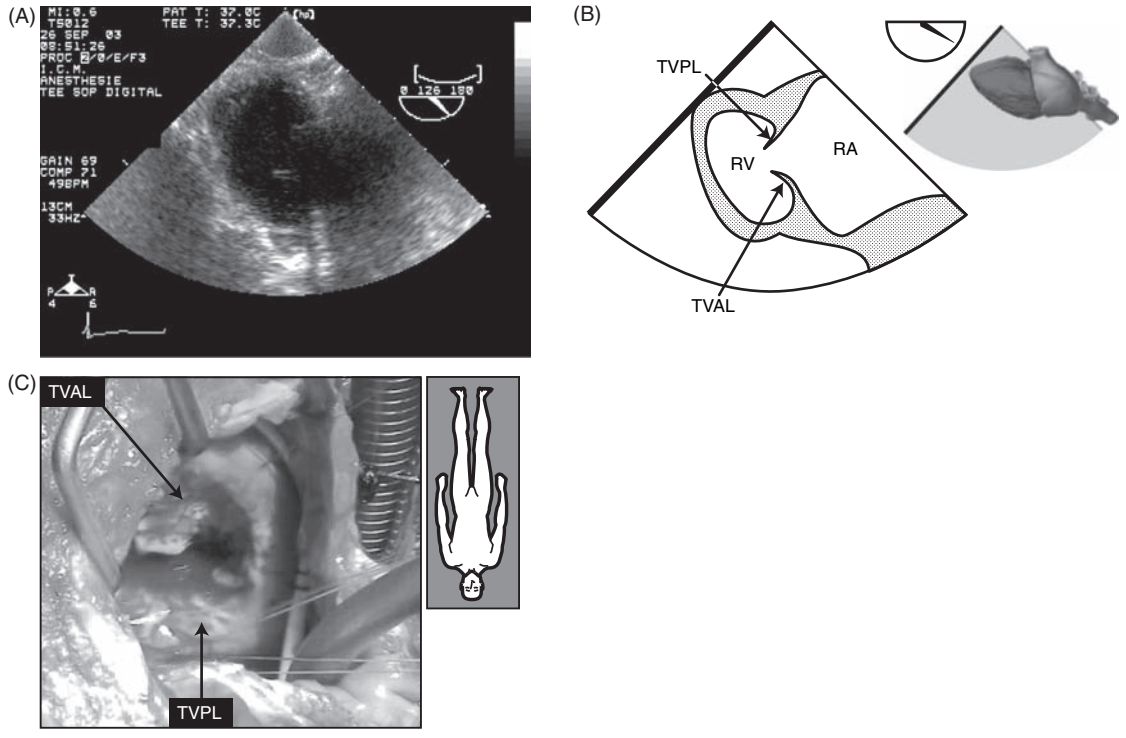

Figure 19.9 (A, B) Transgastric view at 90° of the right ventricle (RV) in a 70-year-old woman before tricuspid valve annuloplasty. The tricuspid valve posterior and anterior leaflets are seen in this view. (C) Intraoperative findings through a right atriotomy (RA, right atrium; TVAL, tricuspid valve anterior leaflet; TVPL, tricuspid valve posterior leaflet). (Photo C courtesy of Dr. Denis Bouchard.)

disease (e.g. endocarditis, rheumatic valvulitis, prolapse, and dysplasia), papillary muscle dysfunction or rupture (e.g. due to endocarditis, trauma or infarction), or interference with proper tricuspid leaflet motion (e.g. by a pacemaker wire or a RV catheter) (Fig. 19.11) (16). The most common causes of TV disease are listed in Table 19.1 (5,9).

Color flow imaging has become the principal method to grade regurgitation severity by echocardiography but few studies have looked at the assessment of right-sided valve regurgitation by TEE. A transthoracic TR jet color flow area $>9\,cm^2$ is deemed significant while a jet area $<4\,cm^2$ is viewed as mild (17). Color flow imaging depicts the displacement of red blood cells in the right atrium (RA) caused by the tricuspid regurgitant jet, typically as a mosaic, predominantly red-orange jet directed posteriorly towards the probe. Although the magnitude of hemodynamic entrainment of red blood cells is

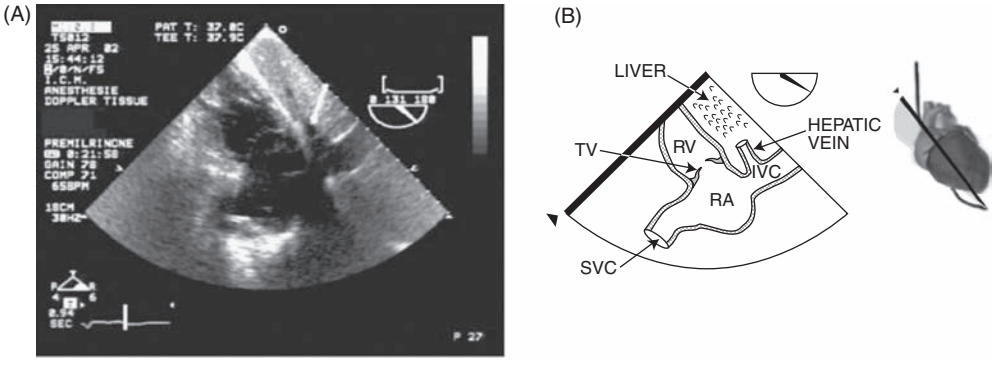

Figure 19.10 The deep transgastric long-axis view of the right ventricle (RV) is obtained to complete the evaluation of the right ventricular function. The tricuspid valve posterior and anterior leaflets are visualized in this 63-year-old woman scheduled for coronary revascularization (IVC, inferior vena cava; RA, right atrium; SVC, superior vena cava; TV, tricuspid valve).

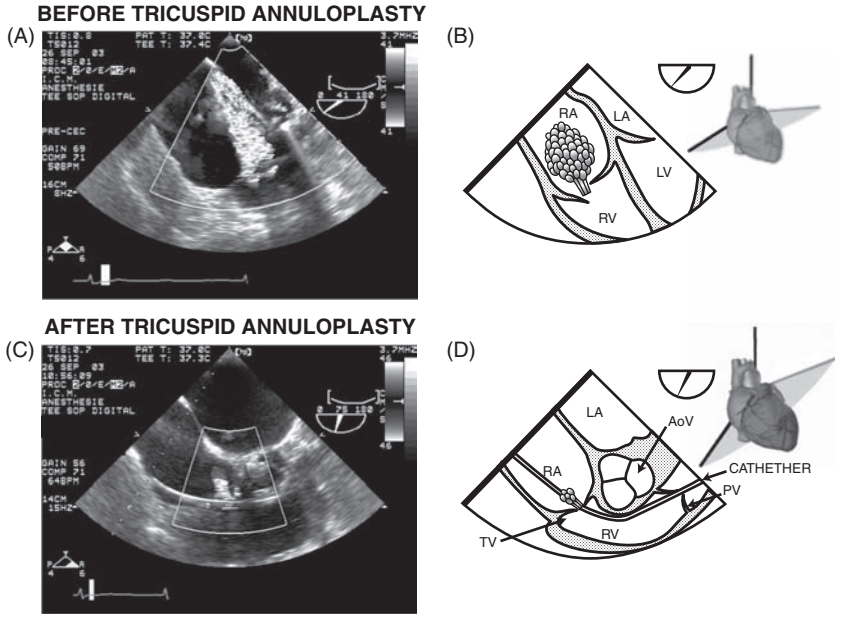

Figure 19.11 (A, B) Mid-esophageal four-chamber view showing tricuspid regurgitation in a 70-year-old woman before tricuspid valve (TV) annuloplasty. (C, D) Mid-esophageal right ventricular inflow-outflow view after repair, with only mild residual tricuspid regurgitation, around a pulmonary artery catheter (AoV, aortic valve; LA, left atrium; LV, left ventricle; PV, pulmonic valve; RA, right atrium; RV, right ventricle).

assumed to represent regurgitant volume, the severity of TR may not exactly correspond to the regurgitant color jet area, although it is generally proportional to it (Fig. 19.11). Some factors like jet eccentricity and shadowing from left-sided structures may limit the ability of regurgitant jet color flow area to grade TR. Regurgitation severity can be best correlated with the width of the color regurgitant jet, as a surrogate of the vena contracta, and to the presence of a large zone of proximal flow convergence. Tribouilloy et al. (18) reported that a vena contracta >6.5 mm best predicted severe TR, compared with regurgitant jet color flow area. While hepatic vein systolic flow reversal due to severe TR is easily demonstrated by TTE, the presence of this sign can be shown with TEE by the deep esophageal view at 0° or the transgastric view at 90° (Fig. 19.13) (19). Continuous-wave (CW) Doppler can be used to grade TR by weighing the amplitude of red blood cell displacement and right ventricular systolic pressure, thus providing information on whether TR etiology is based on normal or high pulmonary artery

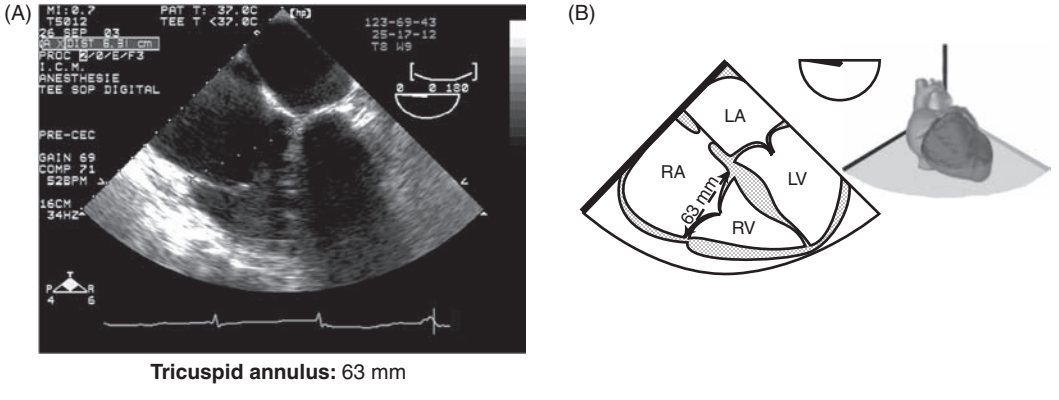

Figure 19.12 Mid-esophageal four-chamber view of a 70-year-old woman scheduled for tricuspid valve annuloplasty. The tricuspid valve annular diameter is 63 mm (LA, left atrium; LV, left ventricle; RA, right atrium; RV, right ventricle).

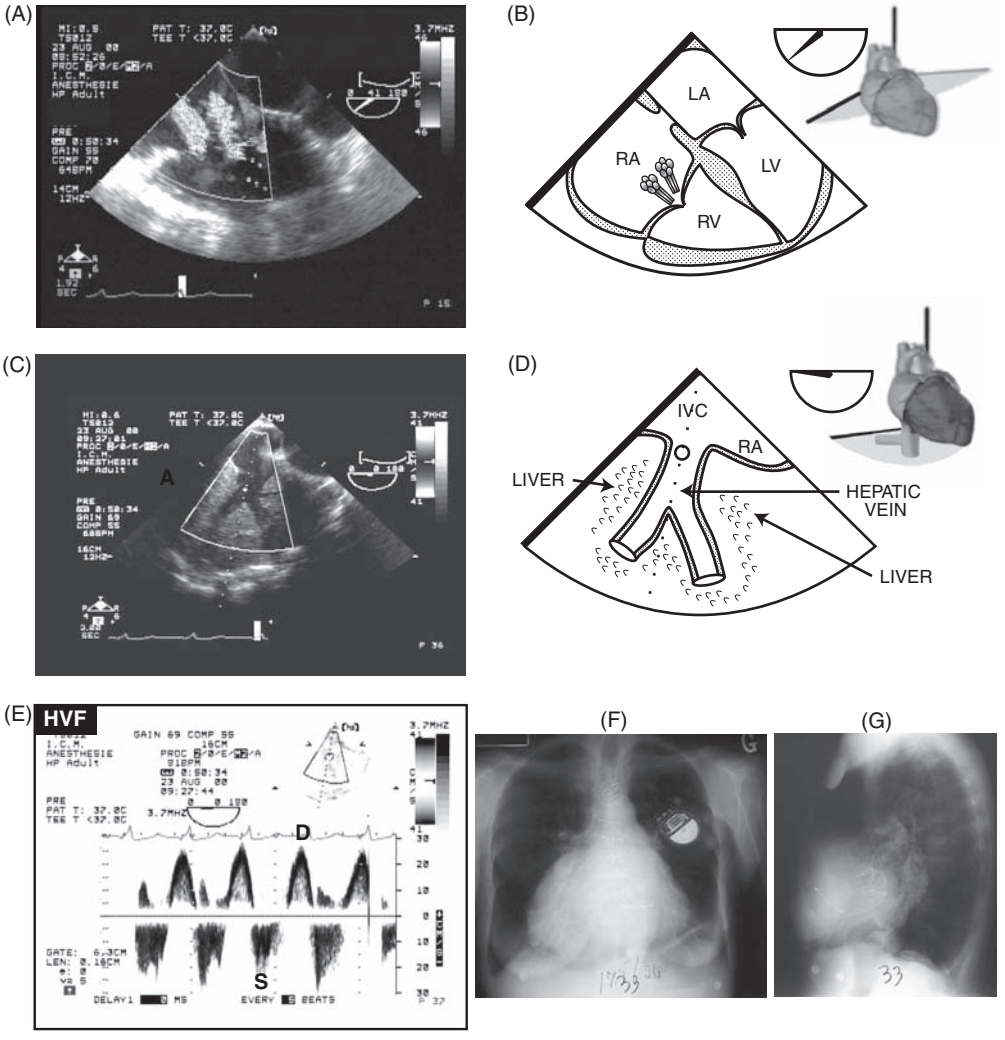

Figure 19.13 Severe tricuspid regurgitation in a 77-year-old woman before tricuspid annuloplasty. (A, B) Mid-esophageal four-chamber view. (C, D) Transgastric view with rotation towards the right showing dilated hepatic veins. (E) Corresponding pulsed-wave Doppler interrogation of the hepatic venous flow (HVF) with systolic flow reversal. (F, G) Chest radiography, note the abnormal right heart border consistent with dilated right-sided structures (IVC, inferior vena cava; LA, left atrium; LV, left ventricle; RA, right atrium; RV, right ventricle).

pressures. The American Society of Echocardiography's (ASE) published guidelines on the evaluation of TR are summarized in Tables 19.2 and 19.3 (20).

III. ENDOCARDITIS

A. Vegetations

Endocarditis of right-sided valves has become a common problem with the advent of intravenous access used in various forms of therapy and especially with individuals who use contaminated needles for intravenous drug abuse. The agents most often involved in right-sided endocarditis come from the skin flora, in particular staphylococci. Structural heart disease is not a prerequisite but is often present. Vegetations classically appear as a chaotically mobile echodense mass attached on the low-pressure aspect of a valve leaflet (Fig. 19.14). Thus TV vegetations are typically found on the atrial aspect of the valve, while PV vegetations are seen on the ventricular aspect of the valve. Most investigators found that the sensitivity of TTE and TEE for right-sided endocarditis and TR were similar. Transesophageal echocardiography provides a superior characterization of vegetation size and extent as well as a greater specificity for endocarditis (22,23). The mechanisms of TR caused by endocarditis

Table 19.2 Echocardiographic and Doppler Parameters Used in the Evaluation of Tricuspid Regurgitation Severity: Utility, Advantages, and Limitations

Parameter	Utility/advantages	Limitations
RV/RA/IVC size	Enlargement sensitive for chronic significant TR	Enlargement seen in other conditions
	Normal size virtually excludes significant chronic TR	May be normal in acute significant TR
TV leaflet alterations	Flail valve specific for significant significant TR	Other abnormalities do not imply TR
Paradoxical septal motion (volume overload pattern)	Simple sign of severe TR	Not specific for TR
Jet area—color flow	Simple, quick screen for TR	Subject to technical and hemodynamic factors. Underestimates severity in eccentric jets
Vena contracta width	Simple, quantitative, separates mild from severe TR	Intermediate values require further confirmation
PISA method	Quantitative	Validated in only a few studies
Flow quantitation—PWD	Quantitative	Not validated for determining TR regurgitant fraction
Jet profile—CWD	Simple, readily available	Qualitative, complementary data
Peak tricuspid E velocity	Simple, usually increased in severe TR	Depends on RA pressure and RV relaxation, TV area, and atrial fibrillation; Complementary data only
Hepatic vein flow	Simple Systolic flow reversal is sensitive for severe TR	Influenced by RA pressure, atrial fibrillation

Note: CWD, continuous-wave Doppler; EROA, effective regurgitant orifice area; IVC, inferior vena cava; PISA, proximal isovelocity surface area; PWD, pulsed-wave Doppler; RA, right atrium; RV, right ventricle; TV, tricuspid valve; TR, tricuspid regurgitation. [With permission of Zoghbi WA (20).]

include leaflet destruction or perforation, abnormal coaptation from chordal or papillary muscle rupture (9). A vegetation size >10 mm is associated with an increased likelihood of pulmonary emboli (24).

Infection of indwelling central venous catheters and permanent pacemakers also occasionally leads to right-sided endocarditis, which occurs in the face of valvular microtrauma caused by catheters, followed

Table 19.3 Echocardiographic and Doppler Parameters Used in Grading Tricuspid Regurgitation Severity

Parameter	Mild	Moderate	Severe
Tricuspid valve	Usually normal	Normal or abnormal	Abnormal/flail leaflet/poor coaptation
RV/RA/IVC size	Normal[a]	Normal or dilated	Usually dilated[b]
Jet area—central jets (cm^2)[c]	<5	5–10	>10
VC width (cm)[d]	Not defined	Not defined, but <0.7	>0.7
PISA radius (cm)[e]	<0.5	0.6–0.9	>0.9
Jet density and contour—CW	Soft and parabolic	Dense, variable contour	Dense, triangular with early peaking
Hepatic vein flow[f]	Systolic dominance	Systolic blunting	Systolic reversal

[a]Unless there are other reasons for RA or RV dilation. Normal 2D measurements from the apical four-chamber view: RV mediolateral end-diastolic dimension <4.3 cm, RV end-diastolic area $<35.5\ cm^2$, maximal RA mediolateral and superoinferior dimensions <4.6 and 4.9 cm respectively, maximal RA volume $<33\ mL/m^2$ (21).
[b]Exception: acute TR.
[c]At a Nyquist limit of 50–60 cm/sec. Not valid in eccentric jets. Jet area is not recommended as the sole parameter of TR severity due to its dependence on hemodynamic and technical factors.
[d]At a Nyquist limit of 50–60 cm/sec.
[e]Baseline shift with Nyquist limit of 28 cm/sec.
[f]Other conditions may cause systolic blunting (e.g. atrial fibrillation, elevated RA pressure).
Note: CWD, continuous-wave Doppler; IVC, inferior vena cava; RA, right atrium; RV, right ventricle; VC, vena contracta width. [With permission of Zoghbi WA (20).]

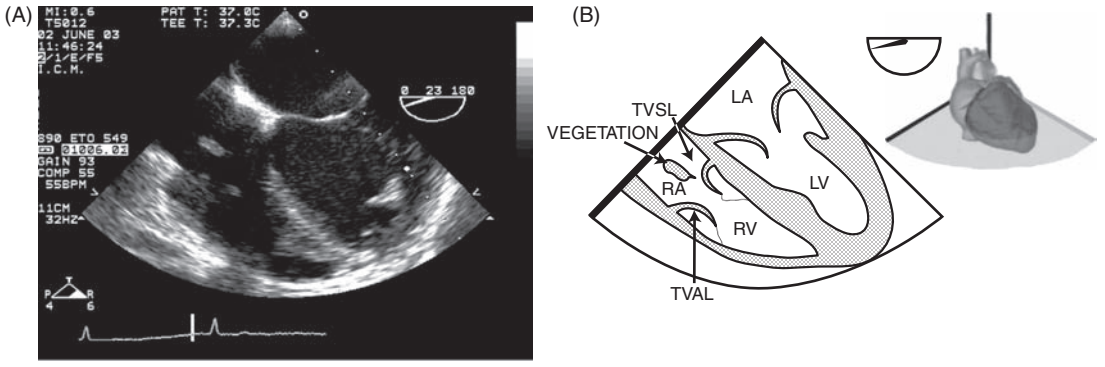

Figure 19.14 Mid-esophageal four-chamber view of a patient with endocarditis of the tricuspid valve. An echogenic mobile mass is seen between the tricuspid valve septal leaflet (TVSL) and the anterior leaflet (TVAL) (LA, left atrium; LV, left ventricle; RA, right atrium; RV, right ventricle).

by bacteremia (25). The identification of vegetation on foreign material can be challenging with TTE, as catheters often produce reverberations (26,27). Transesophageal echocardiography offers the advantage of a higher resolution to differentiate vegetation attachment to indwelling catheters or wires vs attachment to valves (26). Vegetations on pacemaker wires typically appear as sleeve-like with satellite vegetations on the TV associated in more than 2/3 of cases of pacemaker wire infections (26–29) (Fig. 19.15). Transesophageal echocardiography also offers the ability to visualize a greater catheter length including the superior vena cava using the sagittal 90–120° bicaval view. Importantly, the site of pacemaker or defibrillator infection may be in the pulse generator pocket, remote from the imaging capabilities of TEE and sometimes even missed by clinical examination (29). Thus, a negative TEE does not preclude the diagnosis of cardiac device infection. In cases with a high level of suspicion, evaluation of the pacemaker generator pocket with a computed tomography (CT) scan can complement the

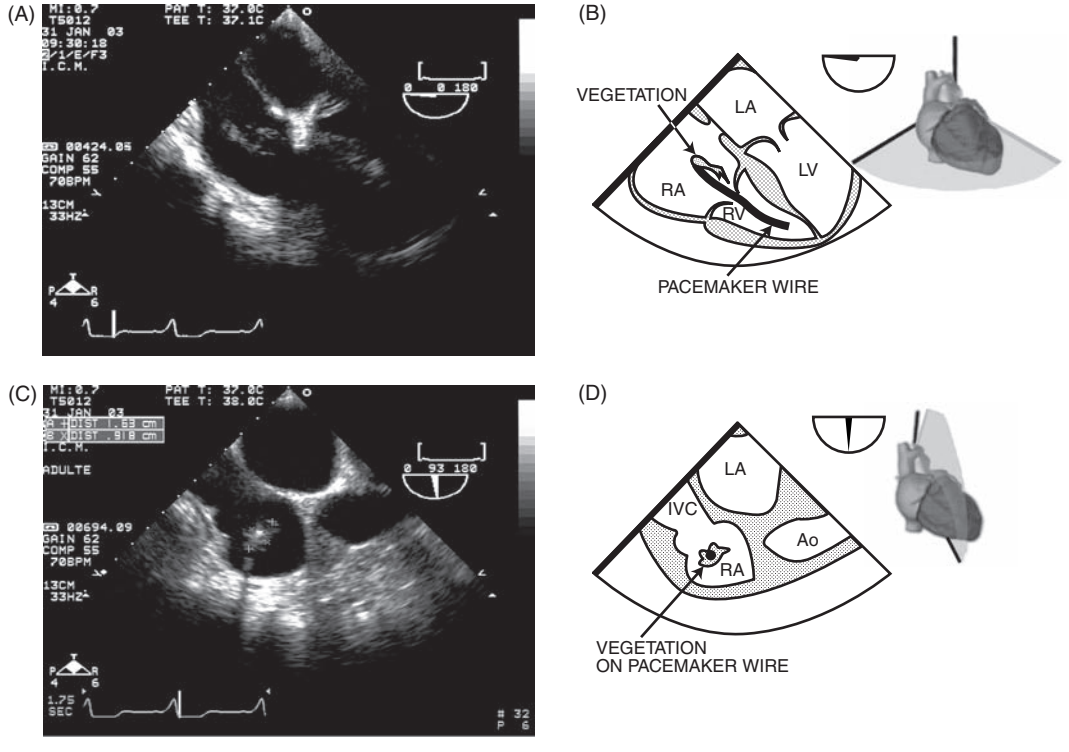

Figure 19.15 Echogenic material attached to a pacemaker wire seen in a mid-esophageal four-chamber (A, B) and 90° view (C, D) (Ao, aorta; IVC, inferior vena cava; LA, left atrium; LV, left ventricle; RA, right atrium; RV, right ventricle).

TEE, especially in febrile patients soon after device implantation (<12 weeks) (29). Almost all patients with proven or strongly suspected endocarditis on permanent pacemaker or defibrillator wires must have these surgically removed (25,26,29). The imaging specialist in the operating room is in a privileged position to confirm the diagnosis and rule out the presence of TV and right heart injury following the pacemaker lead extraction.

B. Abscesses

An abscess is an encapsulated collection of necrotic and infected debris. The most common site of a cardiac abscess is the aortic root in association with an AoV infection (30,31). Left and especially right AV groove abscesses are uncommon, insidious and associated with fistulous tracts and false aneurysm. They are more common in drug addiction-related endocarditis (31). A cardiac abscess appears typically as an oval or circular lesion containing different echo densities, reflecting solid, fluid, and gaseous necrotic contents. Transesophageal echocardiography has been shown to be superior to TTE in disclosing perivalvular abscess (31). One should bear in mind that the right coronary artery is surrounded by adipose tissue in the right AV groove and may appear as a small echo free space. This should not be mistaken for an abscess or tumor. Adipose tissue appears more homogeneous, echo-dense, and speckled, while a tricuspid abscess is usually associated with significant tricuspid leaflet infection, with a right ventricular to right atrial flow seen within an annular perforation by color flow imaging. The presence of a pulmonary root abscess is usually associated with a prosthetic valve or conduit and is extremely rare. The diagnosis is generally difficult to establish by TEE because of the anterior location of the pulmonary trunk in the far field from the esophagus. Often, CT or magnetic resonance imaging (MRI) is required to confirm the diagnosis.

IV. RHEUMATIC VALVE DISEASE

Over the last 30 years, cases of rheumatic fever have been on the decline, as a result of aggressive antibiotic treatment of streptococcal infections, however, rheumatic disease is still prevalent in regions of poor socio-economic status. Rheumatic tricuspid valvulitis seldom accounts for tricuspid involvement in rheumatic disease in Western countries (32). Most commonly, functional TR occurs due to right ventricular pressure overload and tricuspid annular dilatation as a result of pulmonary hypertension from rheumatic mitral stenosis (MS). Severe TR substantially reduces surgical following mitral valvuloplasty or replacement (33).

When rheumatic tricuspid valvulitis occurs, the most common result is leaflet retraction and thickening with chordal fusion and shortening causing TR. Less frequently, rheumatic valvulitis leads to commissural fusion in the closed position with diffuse fibrosis, causing tricuspid stenosis (TS) (9). The frequency of TS differs between reports, ranging between 5% and 38% of patients with rheumatic heart disease (4).

Two-dimensional diagnosis of TS rests on echocardiographic visualization of tricuspid leaflet thickening and restricted motion. Doppler echocardiography provides insight into TS severity with the typical flattening of the tricuspid E-wave slope and prolongation of the tricuspid deceleration slope. Mild to moderate TS produces mean gradients of 3–9 mmHg while severe TS is generally present with mean gradients >10 mmHg. The natural history of mild to moderate TS is generally benign and does not appear to benefit from surgery (1).

A. Other Inflammatory Valvulopathies

Another form of characteristically right-sided inflammatory valve disease is carcinoid heart disease. Carcinoid valvulitis is more commonly seen with small bowel carcinoid complicated by liver metastases, which produce high levels of circulating serotonin and systemic symptoms (e.g. flushing, bronchospasm and diarrhea). Serotonin stimulates plaque development on the TV and PV, leading to leaflet thickening and rigidity (9). Tricuspid regurgitation occurs in >90% of cases. Less commonly, ~20–30% of carcinoid heart disease cases are associated to TS, PV regurgitation, and stenosis. Unless an intracardiac right-to-left shunt is present, it is unusual for the left heart to be involved in carcinoid disease as serotonin and its metabolites are inactivated in the lung. The short-term prognosis of this disease was formerly quite grim but as a result of disease control by chemotherapy and with medium-term survival increasingly achieved, patients with significant right heart failure symptoms are occasionally referred for valve surgery.

Connolly et al. (34) reported a nonrandomized series of 26 patients operated on for carcinoid valve disease. All had severe TR and significant mixed PV disease with: (1) severe right heart failure symptoms; (2) controlled systemic disease; and (3) no concurrent severe medical problems. All patients underwent TV replacement, most had pulmonic valvectomy and in five, removal of endomyocardial metastases was carried out. The perioperative mortality was 35%, with a substantial number of deaths occurring as a result of right heart failure or uncontrolled postoperative bleeding. Survival of surgically treated patients was 40% at two years compared with 8% for medically treated patients. Furthermore, when PV disease was present, data from the same institution supports the use of PV replacement over simple valvectomy in reducing right ventricular dilatation (35). However, it is possible that carcinoid disease may accelerate bioprosthetic

tissue valve degeneration in the tricuspid and pulmonary positions (35).

V. MYXOID DEGENERATION

Degenerative myxoid or myxomatous valvular disease typically affects the mitral valve and tricuspid involvement most often consists of functional TR secondary to pulmonary hypertension. However, myxomatous tricuspid degeneration is rarely seen and is usually encountered in the setting of concomitant mitral valve disease. Inheritable disorders of connective tissue such as Marfan's disease may be a common link. Less is known about the three-dimensional geometry of the TV than that of the saddle-shaped mitral valve. The typical appearance of tricuspid leaflet prolapse is mid-systolic coaptation posterior to the annular plane with preserved tip coaptation. Chordal rupture is usually easily identified and causes significant leaflet malcoaptation with the leaflet tip typically pointing towards the RA, in association with severe eccentric TR directed opposite the diseased leaflet.

VI. PULMONIC VALVE DISEASE

Pulmonic valve assessment remains challenged by TEE, because of its anterior location relative to the esophagus in the far field (Figs. 19.16 and 19.17). In most cases other than endocarditis or inflammatory disease, PV disease is congenital in origin. Dome-shaped or bicuspid PV stenosis is a common entity with good survival (Fig. 19.18) (36). Most individuals with severe PV stenosis are treated in childhood by either percutaneous valvuloplasty or surgical valvotomy. Variable degrees of residual regurgitation may ensue, producing right ventricular dilatation when moderate or severe. The natural history of mild to moderate PV stenosis is benign and intervention is seldom required (36). Pulmonic valve regurgitation can occur as a result of valvular abnormalities or annular dilatation, the latter being either due to increased flow through the valve (e.g. by an intracardiac systemic-to-pulmonary shunt) or secondary to significant chronic pulmonary hypertension (Fig. 19.19). The use of short-axis and sagittal views is helpful to visualize native or prosthetic PVs. Demonstration of PV stenosis and regurgitation by Doppler and color flow is more easily done in the sagittal view at 90–100° (Fig. 19.5) where pulmonary flow is nearly parallel to the ultrasound beam. Pulmonary regurgitation appears as a blue, anteriorly directed color jet from the posteriorly situated pulmonary artery to the RV. Most jets are monochromic unless pulmonary hypertension is present. Severe PV regurgitation leads to right ventricular volume overload with dilatation and paradoxical septal motion and may ultimately cause right ventricular systolic dysfunction (see Chapter 9). This may, in turn, lead to symptoms like dyspnea and atrial or ventricular arrhythmias (21). The ASE published guidelines on the evaluation of PV regurgitation (20). They are summarized in Tables 19.4 and 19.5.

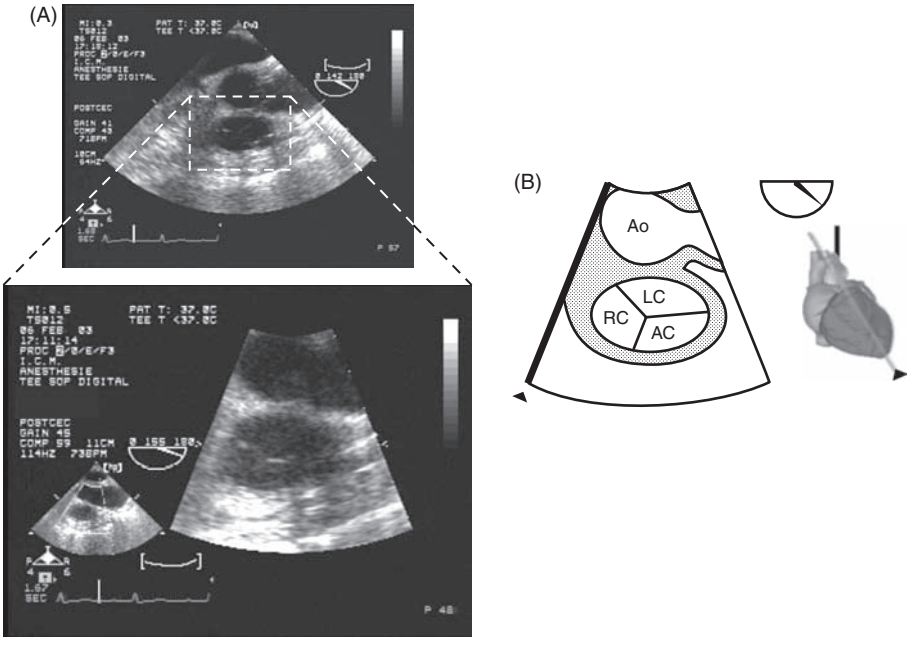

Figure 19.16 Mid-esophageal long-axis view at 142° showing a transverse view of a normal pulmonic valve (AC, anterior cusp; Ao, aorta; LC, left cusp; RC, right cusp).

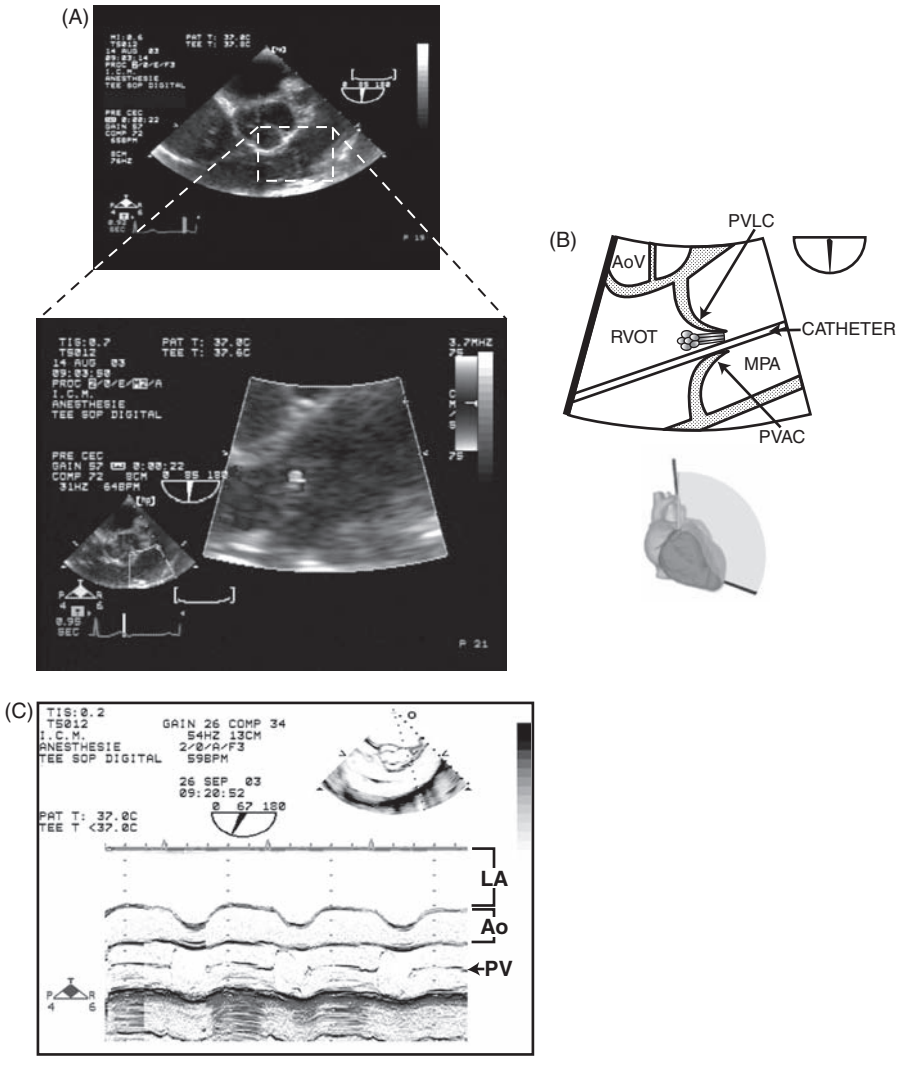

Figure 19.17 Normal pulmonic valve (PV) in a 23-year-old man undergoing mitral valve replacement. (A–C) Mid-esophageal 85° view. A small jet of PV regurgitation was present around the pulmonary artery catheter. (C) M-mode of a normal PV (Ao, aorta; AoV, aortic valve; LA, left atrium; MPA, main pulmonary artery; PVAC, pulmonic valve anterior cusp; PVLC, pulmonic valve left cusp; RVOT, right ventricular outflow tract).

VII. VALVE REPAIR, TRICUSPID—INDICATIONS AND METHODS OF REPAIR

The principal indication for TV repair is isolated moderate to severe TR, generally in the face of left-sided heart disease (37). For pure TV disease, surgery is generally performed for significant TR associated with right-sided heart failure. Tricuspid valve surgical repair, using an annuloplasty ring or a suture annuloplasty (by the technique of DeVega), is the technique of choice as it retains the valve leaflets and provides adequate coaptation by reducing the diameter of the TV annulus (10). Tricuspid valve replacement is the alternative and is performed when severe valve destruction has occurred or when previous TV repair has failed to relieve significant TR. Residual TR of moderate to severe magnitude on the postoperative TEE should probably be addressed by replacement of the valve or re-repair if the patient is stable enough.

Predictors of adverse survival following TV surgery include: severe TR as assessed echocardiographically, high preoperative New York Heart Association (NYHA) functional class, left ventricular systolic dysfunction, need for coronary revascularization and need for TV replacement (3). Transesophageal echocardiography plays an important role in evaluating the success of surgical repair and was found to influence the surgical plan in 10% of cases in a large single-center study of 401 patients. The presence of residual TR (10–15%) disclosed by

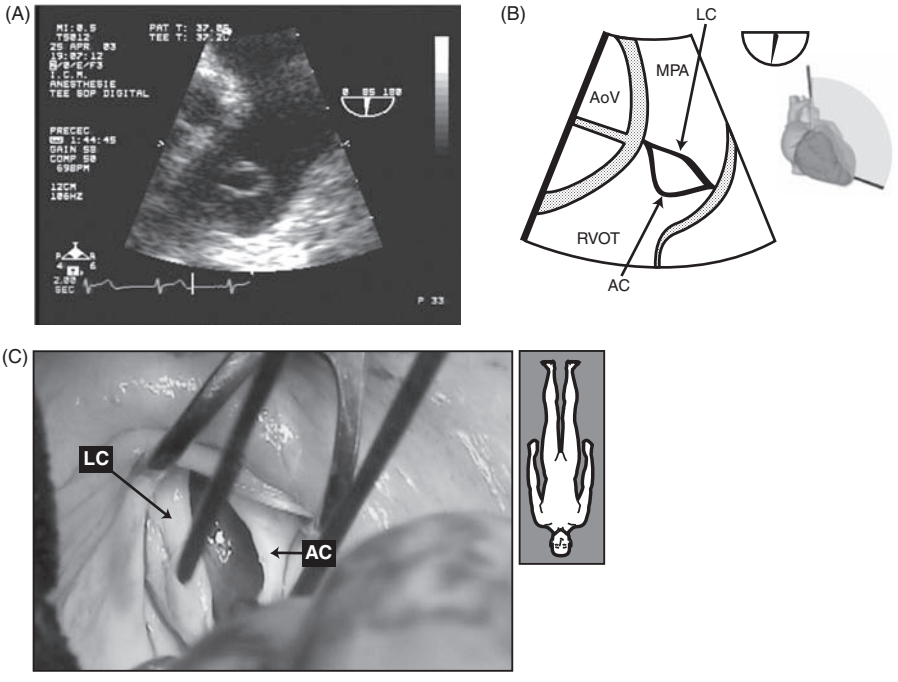

Figure 19.18 Bicuspid stenotic pulmonic valve in a 29-year-old man before open commisurotomy. (A, B) Mid-esophageal view at 85°. (C) Intraoperative findings (AoV, aortic valve; AC, anterior cusp; LC, left cusp; MPA, main pulmonary artery; RVOT, right ventricular outflow tract).

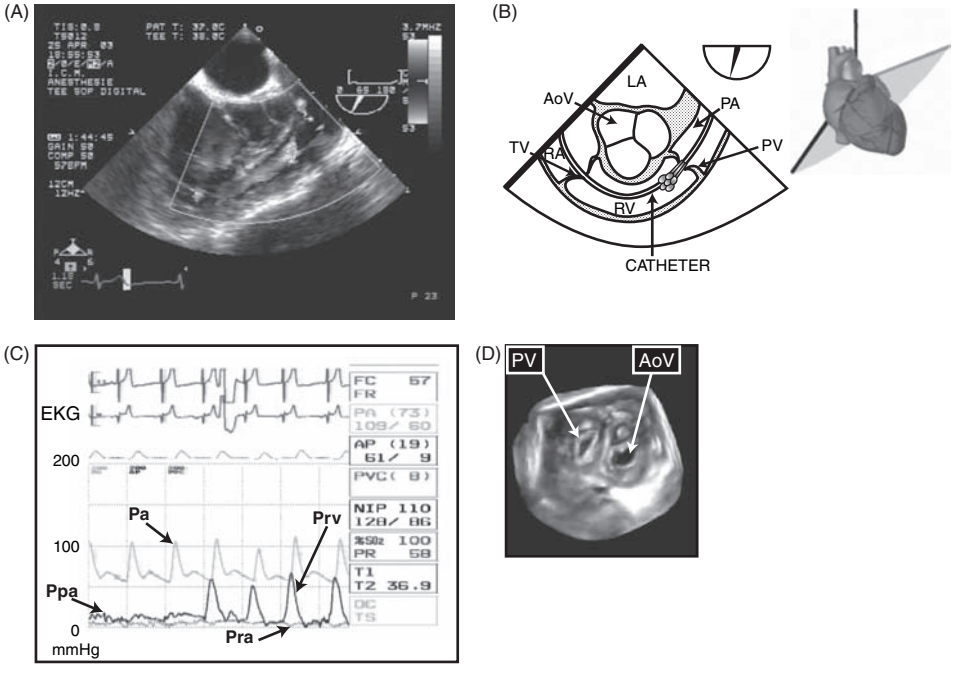

Figure 19.19 Bicuspid stenotic pulmonic valve (PV) in a 29-year-old man before open commisurotomy. (A, B) Mid-esophageal right ventricular inflow–outflow view showing with PV regurgitation. (C) The degree of PV stenosis is easily appreciated on the pulmonary artery catheter pressure tracing, note the gradient between the pulmonary artery pressure (Ppa) and the right ventricular pressure (Prv). The Prv was obtained through the paceport of the pulmonary artery (PA) catheter. (D) Three-dimensional echocardiogram of PV stenosis (AoV, aortic valve; EKG, electrocardiogram; LA, left atrium; Pa, arterial pressure; Pra, right atrial pressure; RA, right atrium; RV, right ventricle; TV, tricuspid valve). (Photo D courtesy of Philips.)

Table 19.4 Echocardiographic and Doppler Parameters Used in the Evaluation of Pulmonary Regurgitation Severity: Utility, Advantages, and Limitations

Parameter	Utility/advantages	Disadvantages
RV size	RV enlargement sensitive for chronic significant PR Normal size virtually excludes significant PR	Enlargement seen in other conditions
Paradoxical septal motion (volume overload pattern)	Simple sign of severe PR	Not specific for PR
Jet length—color flow	Simple	Poor correlation with severity of PR
Vena contracta width	Simple quantitative method that works well for other valves	More difficult to perform; requires good images of pulmonary valve; lacks published validation
Jet deceleration rate—CWD	Simple	Steep deceleration not specific for severe PR
Flow quantitation—PWD	Quantitates regurgitant flow and fraction	Subject to significant errors due to difficulties of measurement of pulmonic annulus and a dynamic RVOT; not well validated

Note: CWD, Continuous-wave Doppler; PWD, pulsed-wave Doppler; RV, right ventricle; PR, pulmonary regurgitation; RVOT, right ventricular outflow tract. [With permission of Zoghbi WA (20).]

intraoperative TEE has a controversial ability in predicting long-term mortality following valve surgery but predicts at least a reduced event-free survival (2,3).

A. Suture Annuloplasty, Complications, Failed Repair

The TV suture annuloplasty by the technique of DeVega is done with a 2.0 propylene suture button stressed with Teflon. A first suture line is started at the anteroseptal commissure and proceeds clockwise to a point just beyond the posteroseptal commissure (Fig. 19.20) (38). A second suture line is similarly run 2–3 mm above the first one. The sutures are then tied with Teflon over a 27 valve sizer in the annulus to prevent valvular stenosis (39). Significant residual TR following repair usually becomes clinically evident with symptoms of fatigue and signs of right-sided heart failure on long-term follow-up. Perioperative TEE may be useful in detecting residual problems following cardiac surgery. Indeed, right ventricular dimensions and systolic function remain important predictors of long-term success as the annuloplasty repair alone may not correct incomplete tricuspid leaflet closure in the setting of chronic right ventricular

Table 19.5 Echocardiographic and Doppler Parameters Used in Grading Pulmonary Regurgitation Severity

Parameter	Mild	Moderate	Severe
Pulmonic valve	Normal	Normal or abnormal	Abnormal
RV size	Normal[a]	Normal or dilated	Dilated[b]
Jet size by color Doppler[c]	Thin (usually <10 mm in length) with a narrow origin	Intermediate	Usually large, with a wide origin; may be brief in duration
Jet density and deceleration rate CWD[d]	Soft; slow deceleration	Dense; variable deceleration	Dense; steep deceleration early termination of diastolic flow
Pulmonary systolic flow compared to systemic flow—PWD[e]	Slightly increased	Intermediate	Greatly increased

[a]Unless there are other reasons for RV enlargement. Normal 2D measurements from the apical four-chamber view; RV mediolateral end-diastolic dimension <4.3 cm, RV end-diastolic area <35.5 cm^2.
[b]Exception: acute PR.
[c]At a Nyquist limit of 50–60 cm/sec.
[d]Steep deceleration is not specific for severe PR.
[e]Cut-off values for regurgitant volume and fraction are not well validated.
Note: CWD, continuous-wave Doppler; PR, pulmonary regurgitation; PWD, pulsed-wave Doppler; RA, right atrium; RF, regurgitant fraction; RV, right ventricle. [With permission of Zoghbi WA (20).]

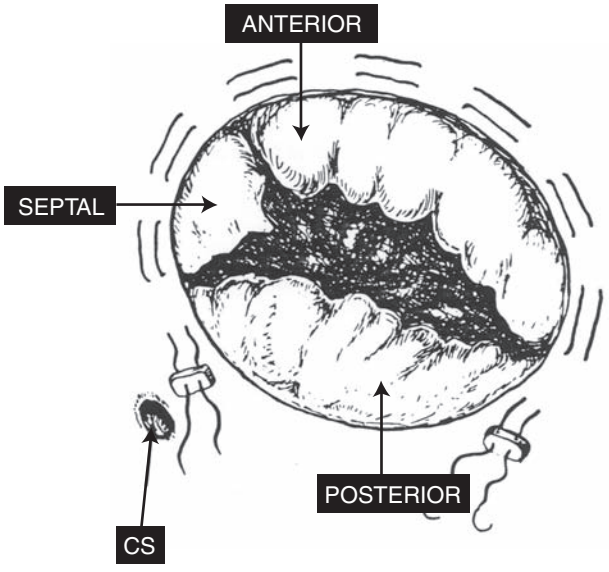

Figure 19.20 Double purse-string suture technique in DeVega's annuloplasty of the tricuspid valve (CS, coronary sinus). [Adapted with permission of Rabago et al. (38).]

remodeling. Dehiscence of a DeVega suture annuloplasty may appear on TEE as a horizontal linear echo-density running across the TV plane.

B. Annuloplasty Rings

Tricuspid annuloplasty rings appear on tomographic echo planes as two echodense annular structures located at the base of opposite leaflets on the atrial side of the valve, with variable acoustic shadowing (Fig. 19.21). Tricuspid leaflet mobility is expected to be somewhat reduced but stenosis is rare as the annular dimensions remain large. Tricuspid regurgitation or vegetation are usually easily demonstrated at 30–90° (Fig. 19.22), in the mid-esophageal, the transitional gastroesophageal, and the sagittal transgastric views.

VIII. VALVE REPLACEMENT

The American College of Cardiology and the American Heart Association established in 1998 guidelines for the

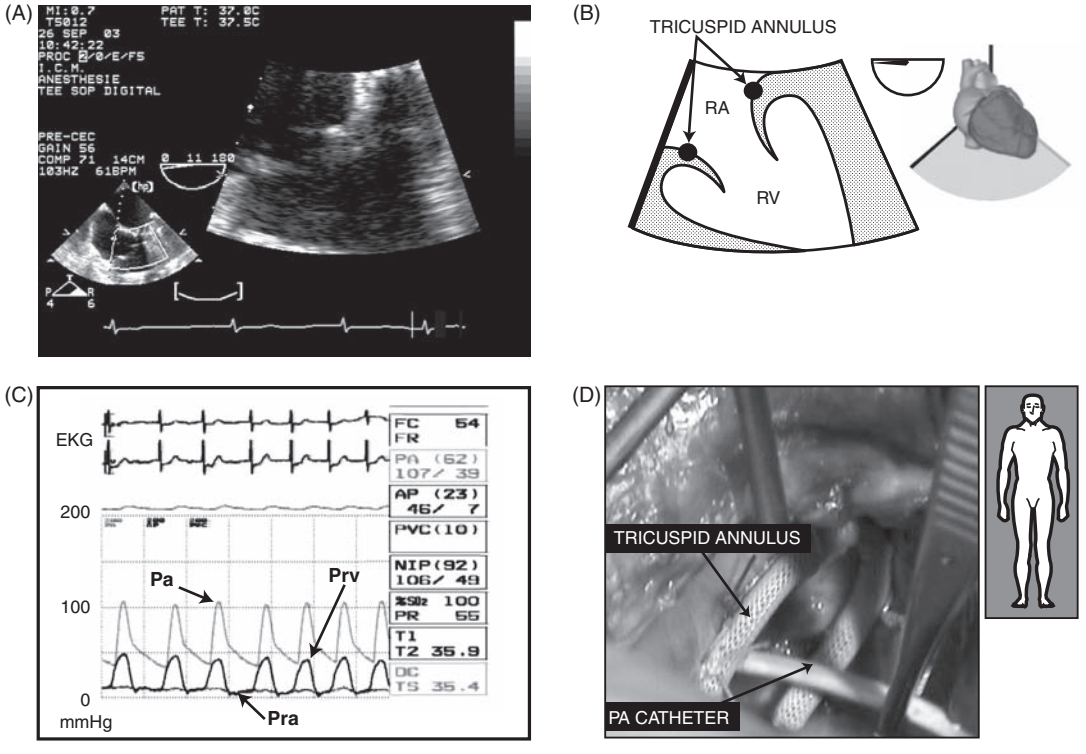

Figure 19.21 (A, B) Echocardiographic appearance of a tricuspid valve prosthetic annulus. (C) After the procedure no significant stenosis is present as demonstrated by the absence of a diastolic gradient across the tricuspid valve is confirmed on the simultaneous right atrial pressure (Pra) and right ventricular pressure (Prv) tracings obtained through the paceport of the pulmonary artery (PA) catheter. (D) Intraoperative findings (EKG, electrocardiogram; Pa, arterial pressure; RA, right atrium; RV, right ventricle). (Photo D courtesy of Dr. Denis Bouchard.)

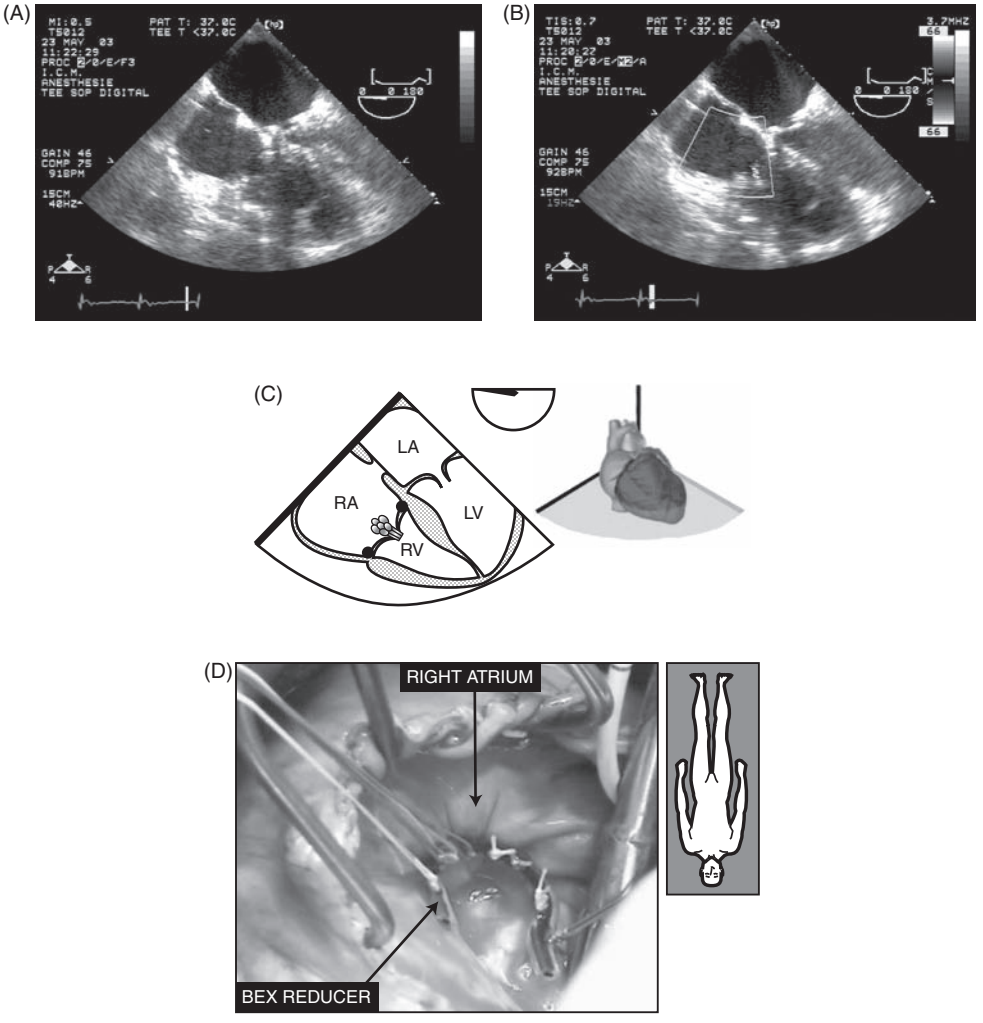

Figure 19.22 Tricuspid annuloplasty in a 56-year-old woman. (A–C) Mid-esophageal four-chamber view at 0° demonstrating the normal appearance of the prosthetic annulus. Mild residual tricuspid regurgitation was present postoperatively. (D) Intraoperative view of the Bex reducer on the anterior and septal leaflets (LA, left atrium; LV, left ventricle; RA, right atrium; RV, right ventricle). (Photo D courtesy of Dr. Louis P. Perrault.)

management of patients with valvular heart disease (40). The recommendations for tricuspid surgery are summarized in Table 19.6. The level of evidence for each indication was discussed in Chapter 16.

The surgical decision to replace the TV is usually made preoperatively on the basis of extensive leaflet disease. Such is the case in Ebstein's anomaly, mixed or predominantly stenotic degenerated calcified leaflets, or extensive destruction by endocarditis. However, TV replacement does carry a higher operative mortality compared with repair, partly because it is often performed in light of previous cardiac surgery. In a series from our Center spanning 20 years, mortality approached 22% with about the same percentage of patients also requiring permanent pacing. This underscores the close relationship of the tricuspid annulus to the conduction system (41).

Pulmonic valve replacement is increasingly performed especially in patients with previous repair of tetralogy of Fallot who present with right ventricular volume overload from severe PV regurgitation (21). It is also done with implantation of a heterologous aortic homograft in pulmonary position as part of the Ross procedure, a treatment for congenital aortic stenosis (AS) in childhood and adolescence. In this procedure, AoV replacement is done by transplanting the normal PV and root to the aortic position, thus avoiding the need for long-term anticoagulation while allowing the potential for the neoaortic valve to grow in children. Stenosis of the prosthetic heterologous aortic homograft in pulmonary position is a late complication (Fig. 19.23), sometimes difficult to diagnose by TTE alone.

Table 19.6 Recommendations for Surgery for Tricuspid Regurgitation

Indication	Class
1. Annuloplasty for severe TR and pulmonary hypertension in patients with mitral valve disease requiring mitral valve surgery	I
2. Valve replacement for severe TR secondary to diseased/abnormal tricuspid valve leaflets not amenable to annuloplasty or repair	IIa
3. Valve replacement or annuloplasty for severe TR with mean pulmonary artery pressure <60 mmHg when symptomatic	IIa
4. Annuloplasty for mild TR in patients with pulmonary hypertension secondary to mitral valve disease requiring mitral valve surgery	IIb
5. Valve replacement or annuloplasty for TR with pulmonary artery systolic pressure <60 mmHg in the presence of a normal mitral valve, in asymptomatic patients, or in symptomatic patients who have not received a trial of diuretic therapy	III

Note: TR, tricuspid regurgitation.
Source: Adapted from Bonow et al. (40).

A. Tricuspid Valvectomy

In the setting of significant endocarditis, total valvectomy is sometimes necessary and is surprisingly hemodynamically well tolerated initially. Once the infection is brought under control, a second stage procedure with tricuspid prosthetic valve implantation is performed to prevent wide-open TR progression to severe right heart failure. This technique has a definite place in the treatment of abceded tricuspid or PV endocarditis in intravenous drug abusers (42).

B. Types of Valve Prosthesis

Bioprosthesis have been the most commonly implanted valves in the tricuspid and pulmonic position, usually in the setting of refractory right-sided endocarditis. The need for chronic anticoagulation is avoided in subjects at high risk of bleeding or deemed unreliable to benefit overall from such therapy. Unfortunately, bioprosthetic valve failure occurs in $\sim$50% of patients at 10 years postoperatively and may require reoperation (43). Mechanical valve replacement offers greater durability but

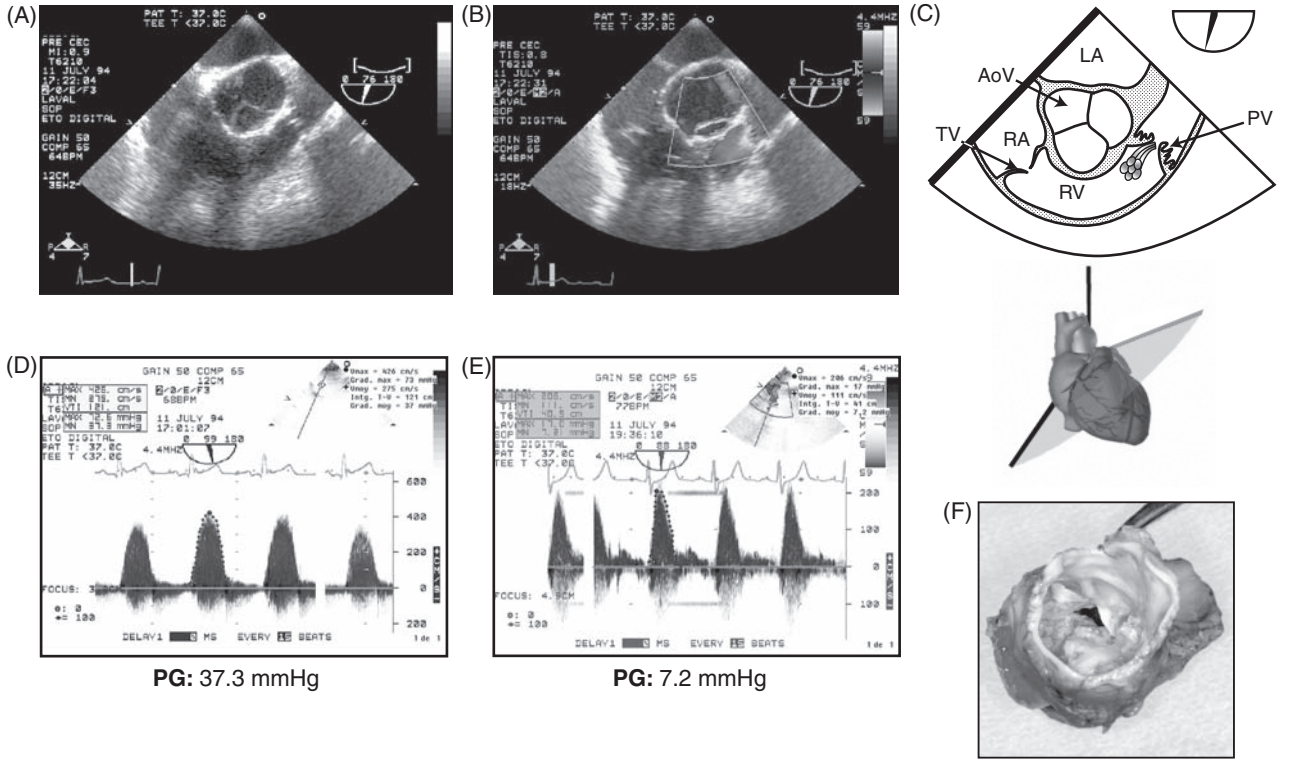

Figure 19.23 Reoperation for stenotic pulmonary homograft (from a Ross procedure initially for congenital aortic stenosis). (A–C) Mid-esophageal right ventricular inflow–outflow view of the thickened pulmonic valve (PV). (D, E) The pressure gradient (PG) across the PV decreased from 37.3 to 7.2 mmHg after the procedure. (F) Intraoperative findings showing the excised stenotic pulmonary homograft (AoV, aortic valve; LA, left atrium; RA, right atrium; RV, right ventricle; TV, tricuspid valve). (Courtesy of Drs. André Saint-Pierre, André Martineau, and Jean Perron from Hôpital Laval, Québec.)

requires chronic anticoagulation (44). This may not be any more a significant issue in patients with rheumatic or degenerative disease where mitral valve involvement and atrial fibrillation are commonly associated with TV pathology and warrant anticoagulation by themselves. However, mechanical prosthesis in tricuspid position prevents the implantation of endoventricular pacemaker leads in this group of patients in which atrioventricular block is common.

In view of the specific RV geometry, it was believed that the lower profile and the lesser procoagulant tendency of bioprosthesis in the setting of a low-pressure system would reduce thrombotic complications compared with mechanical valves. The poor performance of tilting-disk valves in the 1980s appeared to support this point but more recent data on the good long-term performance of the low-profile bileaflet mechanical valves may outweigh the risk of long-term tissue valve failure in patients likely to be reliable in taking anticoagulant therapy (45). A new approach has been the implantation of a mitral homograft in tricuspid position with adjustment of papillary muscle tension obtained by two ventriculotomy apertures through which each papillary muscle is inserted (46).

Transesophageal echocardiography assessment of TV prosthesis begins as for native valves in the mid-esophageal four-chamber view (Fig. 19.24). The presence of coexisting mitral and aortic prostheses requires the use of further views, in particular sagittal views, so that the acoustic shadowing from the left-sided prosthesis located more superoposteriorly than their right-sided counterparts are circumvented. The atrial aspect of the tricuspid

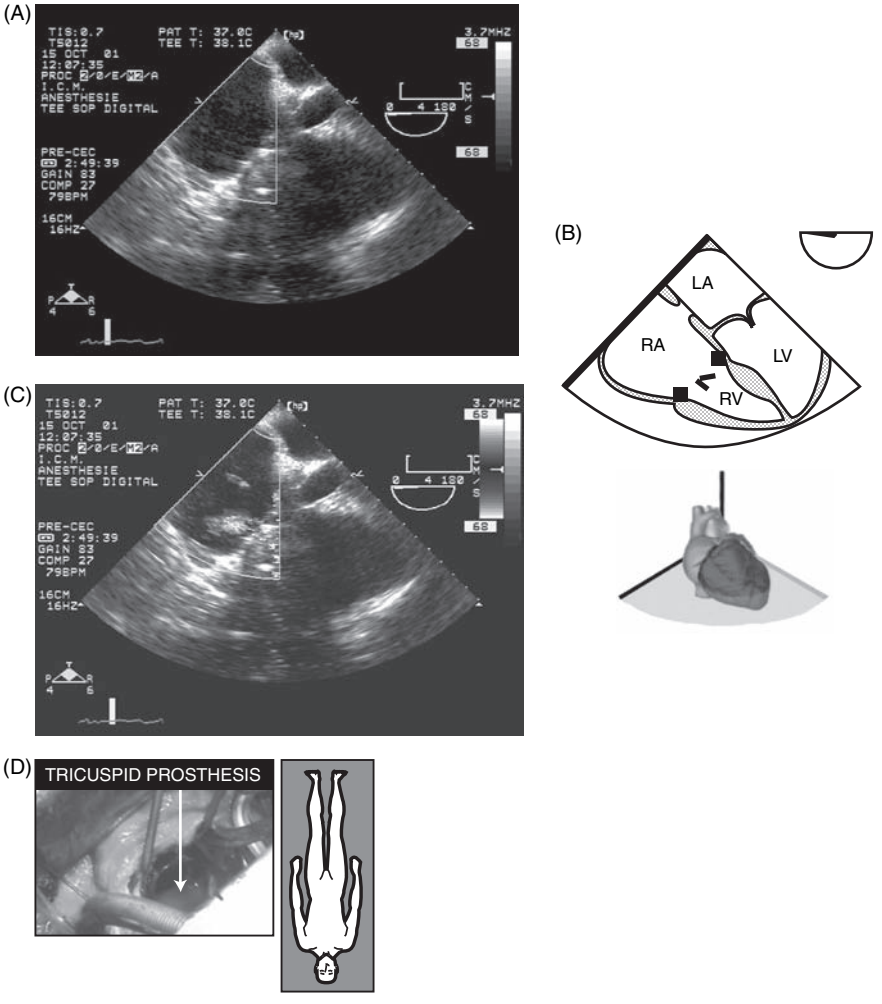

Figure 19.24 A 41-year-old man operated on for tricuspid bileaflet prosthetic valve dysfunction. (A–C) Mid-esophageal four-chamber-view showing dilated right atrium (RA) and right ventricle (RV). Mild tricuspid regurgitation is present. The lateral wall of the RV is obscured by acoustic shadowing from the tricuspid prosthesis. (D) Intraoperative findings, one of the hemidisks is fixed in the open position (LA, left atrium; LV, left ventricle). (Photo D Courtesy of Dr. Nancy Poirier.)

Table 19.7 Summary of the Role of TEE in Patients Undergoing Tricuspid Valve Surgery

Importance	
Before the procedure	
See Table 13.1 for the role of TEE in cardiac surgery	
Evaluate right atrial dimension	Anticipation of difficult valve repair with possible modification of the surgical approach
Evaluation of the severity of pulmonary hypertension and tricuspid regurgitation	Anticipate difficult separation from CPB
During CPB	
See Table 13.1	
After CPB	
See Table 13.1	
Evaluate result of repair or replacement	Early detection and correction of prosthetic dysfunction or suboptimal repair
Detect abnormal motion of PA catheter	The PA catheter could be accidentally entrapped during closure of the RA
In the intensive care unit	
See Table 13.1	

Note: CPB, cardiopulmonary bypass; PA, pulmonary artery; RA, right atrium; TEE, transesophageal echocardiography.

prosthesis can be shown with relative ease at 30–120° in the mid-esophageal and in the transitional gastroesophageal views. The transgastric views at 60–120° can also be used to inspect the diaphragmatic aspect of the TV. The normal tricuspid bioprosthesis has thin leaflets (2–4 mm) attached to three struts which protrude into the RV. Their appearance and movement resemble those of native leaflets. Mechanical bileaflet valve hemidiscs have a more linear aspect and produce characteristic linear acoustic reverberations pivoting within the annulus (Fig. 19.24). In the open position, the two hemidisks appear as two parallel lines, while in the closed position, they assume a wide-open V-shape against the prosthetic annulus.

Mechanical TV thrombosis should be ruled out when full range excursion of both hemidisks cannot be demonstrated (47). Even by TEE, thrombus within the prosthesis associated with decreased mobility of the occluder is sometimes difficult to establish. A search for perivalvular regurgitation should be done by color flow imaging in multiple imaging planes to describe the sector, site and width of the leak.

As for its native counterpart, the assessment of the pulmonary valve prosthesis suffers from the distance between the TEE in the esophagus and the anterior position of the pulmonary valve. In the absence of shadowing from the AoV, the pulmonary valve can be seen in the mid-esophageal short-axis view at 30–80° and sometimes in the sagittal transgastric view.

In conclusion, TEE is a useful modality in the evaluation and quantification of the tricuspid and pulmonic valves, and prosthetic dysfunction (Table 19.7). Its intraoperative use complements hemodynamic data from the pulmonary artery catheter and is likely to become an essential part of the postoperative evaluation of tricuspid and PV surgery.

REFERENCES

1. Chaliki HP, Click RL, Abel MD. Comparison of intraoperative transesophageal echocardiographic examinations with the operative findings: prospective review of 1918 cases. J Am Soc Echocardiogr 1999; 12(4):237–240.
2. King RM, Schaff HV, Danielson GK, Gersh BJ, Orszulak TA, Piehler JM et al. Surgery for tricuspid regurgitation late after mitral valve replacement. Circulation 1984; 70(3 Pt 2):I193–I197.
3. Bajzer CT, Stewart WJ, Cosgrove DM, Azzam SJ, Arheart KL, Klein AL. Tricuspid valve surgery and intraoperative echocardiography: factors affecting survival, clinical outcome, and echocardiographic success. J Am Coll Cardiol 1998; 32(4):1023–1031.
4. Roguin A, Rinkevich D, Milo S, Markiewicz W, Reisner SA. Long-term follow-up of patients with severe rheumatic tricuspid stenosis. Am Heart J 1998; 136(1):103–108.
5. Ammash NM, Warnes CA, Connolly HM, Danielson GK, Seward JB. Mimics of Ebstein's anomaly. Am Heart J 1997; 134(3):508–513.
6. Shanewise JS, Cheung AT, Aronson S, Stewart WJ, Weiss RL, Mark JB et al. ASE/SCA guidelines for performing a comprehensive intraoperative multiplane transesophageal echocardiography examination: recommendations of the American Society of Echocardiography Council for Intraoperative Echocardiography and the Society of Cardiovascular Anesthesiologists Task Force for Certification in Perioperative Transesophageal Echocardiography. J Am Soc Echocardiogr 1999; 12(10):884–900.
7. Cohen GI, White M, Sochowski RA, Klein AL, Bridge PD, Stewart WJ et al. Reference values for normal adult transesophageal echocardiographic measurements. J Am Soc Echocardiogr 1995; 8(3):221–230.
8. Netter FH, Yonkman FF, Ciba Pharmaceutical Company. Heart: a compilation of paintings on the normal and pathologic anatomy and physiology, embryology, and diseases. Summit, N. J: CIBA Pharmaceutical Company, 1978.
9. Hauck AJ, Freeman DP, Ackermann DM, Danielson GK, Edwards WD. Surgical pathology of the tricuspid valve: a study of 363 cases spanning 25 years. Mayo Clin Proc 1988; 63(9):851–863.

10. Yiwu L, Yingchun C, Jianqun Z, Bin Y, Ping B. Exact quantitative selective annuloplasty of the tricuspid valve. J Thorac Cardiovasc Surg 2001; 122(3):611–614.
11. Frater R. Tricuspid insufficiency. J Thorac Cardiovasc Surg 2001; 122(3):427–429.
12. Sagie A, Schwammenthal E, Padial LR, Vazquez de Prada JA, Weyman AE, Levine RA. Determinants of functional tricuspid regurgitation in incomplete tricuspid valve closure: Doppler color flow study of 109 patients. J Am Coll Cardiol 1994; 24(2):446–453.
13. Ubago JL, Figueroa A, Ochoteco A, Colman T, Duran RM, Duran CG. Analysis of the amount of tricuspid valve anular dilatation required to produce functional tricuspid regurgitation. Am J Cardiol 1983; 52(1):155–158.
14. Sugimoto T, Okada M, Ozaki N, Kawahira T, Fukuoka M. Influence of functional tricuspid regurgitation on right ventricular function. Ann Thorac Surg 1998; 66(6):2044–2050.
15. Enriquez-Sarano M, Rossi A, Seward JB, Bailey KR, Tajik AJ. Determinants of pulmonary hypertension in left ventricular dysfunction. J Am Coll Cardiol 1997; 29(1):153–159.
16. van Son JA, Danielson GK, Schaff HV, Miller FA Jr. Traumatic tricuspid valve insufficiency. Experience in thirteen patients. J Thorac Cardiovasc Surg 1994; 108(5): 893–898.
17. Shapira Y, Porter A, Wurzel M, Vaturi M, Sagie A. Evaluation of tricuspid regurgitation severity: echocardiographic and clinical correlation. J Am Soc Echocardiogr 1998; 11(6):652–659.
18. Tribouilloy CM, Enriquez-Sarano M, Bailey KR, Tajik AJ, Seward JB. Quantification of tricuspid regurgitation by measuring the width of the vena contracta with Doppler color flow imaging: a clinical study. J Am Coll Cardiol 2000; 36(2):472–478.
19. Kirkeby-Garstad I, Tromsdal A, Sellevold OF, Bjorngaard M, Bjella LK, Berg EM et al. Guiding surgical cannulation of the inferior vena cava with transesophageal echocardiography. Anesth Analg 2003; 96(5):1288–1293.
20. Zoghbi WA, Enriquez-Sarano M, Foster E, Grayburn PA, Kraft CD, Levine RA et al. Recommendations for evaluation of the severity of native valvular regurgitation with two-dimensional and Doppler echocardiography. J Am Soc Echocardiogr 2003; 16(7):777–802.
21. Gatzoulis MA, Balaji S, Webber SA, Siu SC, Hokanson JS, Poile C et al. Risk factors for arrhythmia and sudden cardiac death late after repair of tetralogy of Fallot: a multicentre study. Lancet 2000; 356(9234):975–981.
22. San Roman JA, Vilacosta I, Zamorano JL, Almeria C, Sanchez-Harguindey L. Transesophageal echocardiography in right-sided endocarditis. J Am Coll Cardiol 1993; 21(5):1226–1230.
23. Herrera CJ, Mehlman DJ, Hartz RS, Talano JV, McPherson DD. Comparison of transesophageal and transthoracic echocardiography for diagnosis of right-sided cardiac lesions. Am J Cardiol 1992; 70(9):964–966.
24. Robbins MJ, Frater RW, Soeiro R, Frishman WH, Strom JA. Influence of vegetation size on clinical outcome of right-sided infective endocarditis. Am J Med 1986; 80(2):165–171.
25. Rowley KM, Clubb KS, Smith GJ, Cabin HS. Right-sided infective endocarditis as a consequence of flow-directed pulmonary-artery catheterization. A clinicopathological study of 55 autopsied patients. N Engl J Med 1984; 311(18):1152–1156.
26. Klug D, Lacroix D, Savoye C, Goullard L, Grandmougin D, Hennequin JL et al. Systemic infection related to endocarditis on pacemaker leads: clinical presentation and management. Circulation 1997; 95(8):2098–2107.
27. Vilacosta I, Sarria C, San Roman JA, Jimenez J, Castillo JA, Iturralde E et al. Usefulness of transesophageal echocardiography for diagnosis of infected transvenous permanent pacemakers. Circulation 1994; 89(6):2684–2687.
28. Tighe DA, Tejada LA, Kirchhoffer JB, Gilmette P, Rifkin RD, Estes NA. Pacemaker lead infection: detection by multiplane transesophageal echocardiography. Am Heart J 1996; 131(3):616–618.
29. Victor F, De Place C, Camus C, Le Breton H, Leclercq C, Pavin D et al. Pacemaker lead infection: echocardiographic features, management, and outcome. Heart 1999; 81(1):82–87.
30. Arnett EN, Roberts WC. Valve ring abscess in active infective endocarditis. Frequency, location, and clues to clinical diagnosis from the study of 95 necropsy patients. Circulation 1976; 54(1):140–145.
31. Baumgartner FJ, Omari BO, Robertson JM, Nelson RJ, Pandya A, Pandya A et al. Annular abscesses in surgical endocarditis: anatomic, clinical, and operative features. Ann Thorac Surg 2000; 70(2):442–447.
32. Eichelberger JP, Meltzer RS. Right-sided valvular pathology and rheumatic fever. Curr Opin Cardiol 1994; 9(2):181–185.
33. Sagie A, Schwammenthal E, Newell JB, Harrell L, Joziatis TB, Weyman AE et al. Significant tricuspid regurgitation is a marker for adverse outcome in patients undergoing percutaneous balloon mitral valvuloplasty. J Am Coll Cardiol 1994; 24(3):696–702.
34. Connolly HM, Nishimura RA, Smith HC, Pellikka PA, Mullany CJ, Kvols LK. Outcome of cardiac surgery for carcinoid heart disease. J Am Coll Cardiol 1995; 25(2): 410–416.
35. Connolly HM, Schaff HV, Mullany CJ, Abel MD, Pellikka PA. Carcinoid heart disease: impact of pulmonary valve replacement in right ventricular function and remodeling. Circulation 2002; 106(12 suppl 1):I51–I56.
36. Nishimura RA, Pieroni DR, Bierman FZ, Colan SD, Kaufman S, Sanders SP et al. Second natural history study of congenital heart defects. Pulmonary stenosis: echocardiography. Circulation 1993; 87(suppl 2):I73–I79.
37. ACC/AHA guidelines for the management of patients with valvular heart disease. A report of the American College of Cardiology/American Heart Association. Task Force on Practice Guidelines (Committee on Management of Patients with Valvular Heart Disease). J Am Coll Cardiol 1998; 32(5):1486–1588.
38. Rabago G, Fraile J, Martinell J, Artiz V. Technique and results of tricuspid annuloplasty. J Card Surg 1986; 1(3):247–253.

39. Abe T, Tukamoto M, Yanagiya M, Morikawa M, Watanabe N, Komatsu S. DeVega's annuloplasty for acquired tricuspid disease: early and late results in 110 patients. Ann Thorac Surg 1989; 48(5):670–676.
40. Bonow RO, Carabello B, de LA Jr, Edmunds LH Jr, Fedderly BJ, Freed MD et al. Guidelines for the management of patients with valvular heart disease: executive summary. A report of the American College of Cardiology/American Heart Association Task Force on Practice Guidelines (Committee on Management of Patients with Valvular Heart Disease). Circulation 1998; 98(18): 1949–1984.
41. Do QB, Pellerin M, Carrier M, Cartier R, Hebert Y, Page P et al. Clinical outcome after isolated tricuspid valve replacement: 20-year experience. Can J Cardiol 2000; 16(4):489–493.
42. Arbulu A, Holmes RJ, Asfaw I. Tricuspid valvulectomy without replacement. Twenty years' experience. J Thorac Cardiovasc Surg 1991; 102(6):917–922.
43. Glower DD, White WD, Smith LR, Young WG, Oldham HN, Wolfe WG et al. In-hospital and long-term outcome after porcine tricuspid valve replacement. J Thorac Cardiovasc Surg 1995; 109(5):877–883.
44. Scully HE, Armstrong CS. Tricuspid valve replacement. Fifteen years of experience with mechanical prostheses and bioprostheses. J Thorac Cardiovasc Surg 1995; 109(6):1035–1041.
45. Singh AK, Feng WC, Sanofsky SJ. Long-term results of St. Jude Medical valve in the tricuspid position. Ann Thorac Surg 1992; 54(3):538–540.
46. Hvass U, Baron F, Fourchy D, Pansard Y. Mitral homografts for total tricuspid valve replacement: comparison of two techniques. J Thorac Cardiovasc Surg 2001; 121(3):592–594.
47. Shapira Y, Sagie A, Jortner R, Adler Y, Hirsch R. Thrombosis of bileaflet tricuspid valve prosthesis: clinical spectrum and the role of nonsurgical treatment. Am Heart J 1999; 137(4 Pt 1):721–725.

20

Heart Transplantation

PIERRE COUTURE, MICHEL CARRIER
University of Montreal, Montreal, Canada

I. Transesophageal Echocardiography and Heart Transplantation 471
II. Surgical Considerations 471
A. Standard Orthotopic Heart Transplantation 471
B. The Bicaval Technique 472
III. Transesophageal Echocardiography in the Perioperative Period 472
IV. Transesophageal Echocardiography in the Early Postoperative Period 475
A. Right Ventricular Remodeling, Tricuspid Regurgitation, and Abnormal Movement of the Ventricular Septum 475
B. Left Ventricular Mass and Mitral Valve Function 476
C. Left Ventricular Diastolic Function 476
D. Normal Echocardiographic Profile after Heart Transplantation 477
E. Abnormal Echocardiographic Findings Following Heart Transplantation 478
F. Detection of Acute Allograft Rejection and Coronary Artery Disease 479
V. Conclusion 480
References 480

I. TRANSESOPHAGEAL ECHOCARDIOGRAPHY AND HEART TRANSPLANTATION

Transesophageal echocardiography (TEE) plays an important role during the process of cardiac transplantation. Therefore, a clear understanding of the surgical procedure helps to provide key diagnostic information and appropriate monitoring parameters before, during and after the procedure.

II. SURGICAL CONSIDERATIONS

There are two techniques of orthotopic heart transplantation (OHT) currently used in clinical practice: the standard technique originally described by Lower and Shumway (1) and Shumway et al. (2) and the bicaval technique described by Dreyfus et al. (3) in 1991.

A. Standard Orthotopic Heart Transplantation

A standard anesthetic preparation for routine cardiac surgery is performed including the use of a TEE probe for monitoring. The right internal jugular vein is left undisturbed for later use for endomyocardial biopsies. A Swan–Ganz catheter is initially inserted to measure real time right ventricular and pulmonary artery pressure but will be pulled out during surgery. Both groins are prepared for emergency cannulation and initiation of cardiopulmonary bypass if needed.

A standard median sternotomy is performed. Following injection of heparin, standard canulation of the ascending aorta (Ao) and both vena cava is performed. Cardiopulmonary bypass (CPB) is initiated when the donor heart arrives in the operating room. Cross-clamping of the Ao is followed by standard removal of the recipient's failing heart leaving in place the posterior aspect of the left and right atria, and keeping as much as possible of the recipient's ascending Ao and pulmonary artery tissue. Mild systemic hypothermia is easily reached and maintained throughout surgery (34°C).

While the cardiectomy is performed, the donor heart is inspected and prepared in a cold bath saline solution. The integrity of the atrial septum is ensured and corrected if, for instance, a foramen ovale is detected. The tricuspid and mitral valve apparatus are also carefully inspected. Proper ligation of the superior vena cava is secured, the right atrial wall is opened from the inferior vena cava (IVC) to the right atrial appendage (RAA) and the left atrial wall is trimmed and prepared. The ascending Ao and the pulmonary artery are completely dissected and separated to facilitate proper exposure and suturing approach (Fig. 20.1).

The donor heart is brought into the thoracic cavity and the left atrial anastomosis is first performed with 3.0 polypropylene continuous sutures. Retrograde cardioplegia is administered through a catheter inserted in the coronary sinus by injection of a standard cold blood cardioplegic solution at a rate of 100–200 mL/min and application of ice slush onto the right ventricle (RV) to keep the heart as cold as possible during surgical implantation (4). The right atrial anastomosis (Fig. 20.2) is completed with 3.0 polypropylene sutures, but a small gap is left to allow the passage of the coronary sinus catheter up until both the pulmonary and aortic anastomoses are completed.

Donor and recipient pulmonary arteries are prepared, trimmed and anastomosed with a continuous 4.0 polypropylene suture.

Next, snares on both vena cava are released, the coronary sinus catheter is taken out, the operating table is put in the Trendelenburg position and the clamp on the ascending Ao is released. With gentle massage of the heart, air is evacuated from the left ventricle (LV) and from the ascending Ao through the suture line via the puncture done to inject the antegrade cardioplegic solution at the donor site. The hole created in the left atrial appendage (LAA) to decompress the LV during the harvest of the donor heart is closed with a 3.0 polypropylene suture.

The patient is weaned from the CPB after having obtained a heart rate averaging 100 beats/min with isoproterenol infusion and a good cardiac performance with systolic blood pressure (SBP) >90–100 mmHg. Atrial and aortic cannulae are removed while 500 mg of solumedrol is administered and protamine is injected. A Swan–Ganz catheter is reinserted through the pulmonary artery to monitor pulmonary artery pressure and cardiac output (CO). Two chest tubes are inserted in the mediastinum. Temporary pacing wires are sutured onto the RV. The sternum is then closed according to a standard technique.

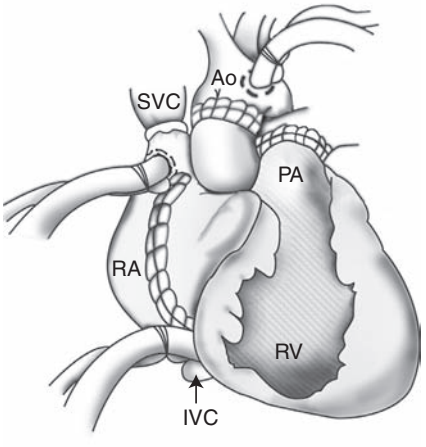

Figure 20.1 Classic biatrial technique of orthotopic heart transplantation (Ao, aorta; IVC, inferior vena cava; PA, pulmonary artery; RA, right atrium; RV, right ventricle; SVC, superior vena cava).

B. The Bicaval Technique

This method, using a different technique of cardiectomy and anastomoses has been proposed to minimize the problems arising from oversized posttransplant atria, such as stasis, spontaneous echo contrast and embolic complications. The right aspect of the left atrium (LA) is entered as for a routine mitral valve surgical approach. The incision is extended superiorly under the superior vena cava (SVC) and inferiorly under the IVC (Fig. 20.3). During excision of the right atrium (RA), generous portions of the SVC and IVC are left to facilitate donor and recipient anastomoses. The donor LA is anastomosed to the recipient LA as described in the standard method. The IVC and SVC are then anastomosed with 4-0 polypropylene suture. The rest of the procedure continues as described above for the standard approach to OHT.

III. TRANSESOPHAGEAL ECHOCARDIOGRAPHY IN THE PERIOPERATIVE PERIOD

Transesophageal echocardiography in adult cardiac surgery has expanded its role during cardiac transplantation from a useful intraoperative tool to an equally valuable perioperative monitoring tool. During the CPB weaning process,

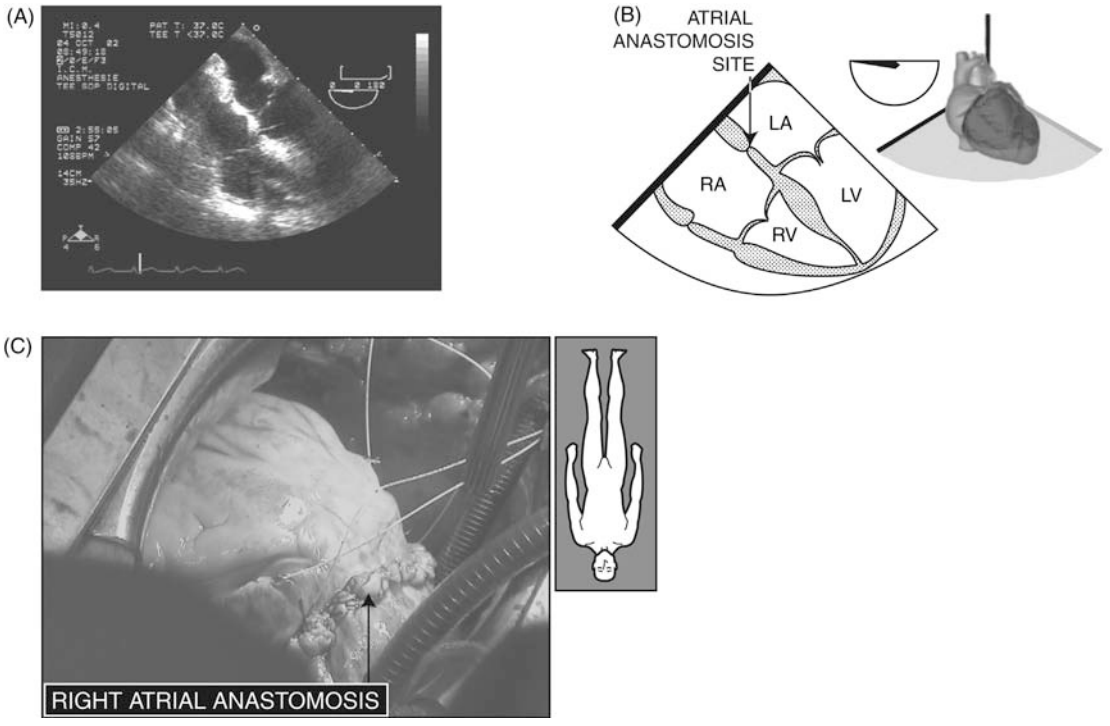

Figure 20.2 Atrial anastomosis in a 37-year-old man after cardiac transplantation. (A, B) Mid-esophageal four-chamber view. Note the thickened atrial anastomotic ridge. (C) Intraoperative view of the right atrial anastomotic line (LA, left atrium; LV, left ventricle; RA, right atrium; RV, right ventricle). (Courtesy of Dr. Denis Bouchard.)

TEE helps to define the etiology of hemodynamic instability, assess the efficacy of deairing procedures and confirm the integrity of surgical anastomosis in the posttransplantation period.

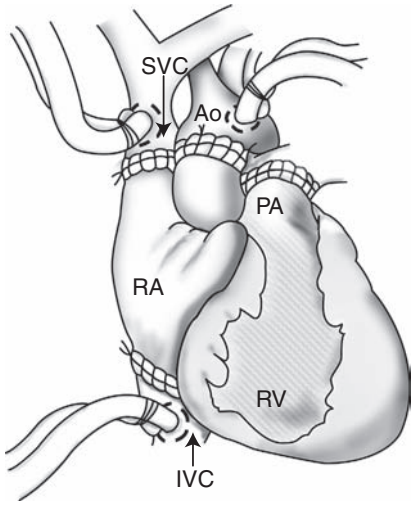

Figure 20.3 Bicaval technique when the donor right atrium is anastomosed to the superior and inferior vena cava (Ao, aorta; IVC, inferior vena cava; PA, pulmonary artery; RA, right atrium; RV, right ventricle; SVC, superior vena cava).

Hemodynamic instability after cardiac transplantation may arise from a single or multiple causes such as primary graft failure, hyperacute rejection, right ventricular dysfunction, hypovolemia, vasodilatation, tamponade, and right or left ventricular outflow tract (RVOT, LVOT) obstruction (Fig. 20.4).

Nonspecific graft failure is still the most common cause of death in the early postoperative period (5). Inadequate myocardial protection during the harvesting of the donor heart (role of cardioplegic solution, temperature, and duration of ischemia) and/or during transplantation lead to severe systolic dysfunction in the recipient. In rare instances, hyperacute rejection rather than insufficient myocardial protection may be responsible for the heart failure.

Right ventricular failure may occur in the recipient with pre-existing and underestimated pulmonary hypertension. Registry data from the International Society of Heart and Lung Transplantation show that, despite advances in perioperative management, right ventricular dysfunction accounts for 50% of all cardiac complications and 19% of early death after heart transplantation (Fig. 20.5). There is an approximately fourfold higher transplant mortality among patients with fixed pulmonary hypertension compared with patients without pulmonary hypertension (5). Pulmonary hypertension, defined as a pulmonary

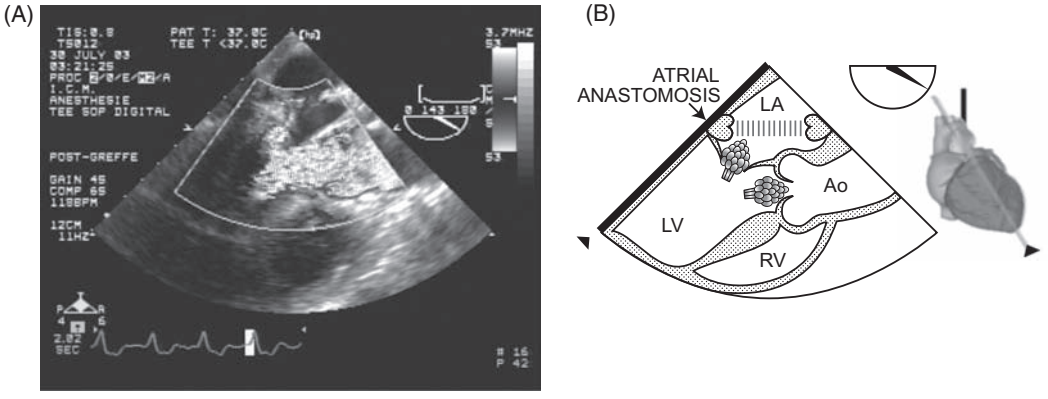

Figure 20.4 Mid-esophageal long-axis view of a 47-year-old man after cardiac transplantation. Note the flow acceleration in the left ventricular outflow tract upon weaning from cardiopulmonary bypass. Aliasing was also present at the level of the mitral valve most likely from the compressing effect of the edematous atrial anastomosis. This may simulate cor triatriatum (Ao, aorta; LA, left atrium; LV, left ventricle; RV, right ventricle).

vascular resistance (PVR) >480 dyne s/cm^5 or 6 Wood units, is currently considered as a contraindication to orthotopic cardiac transplantation. Patients with marked pulmonary hypertension (PVR >640 dyne s/cm^5 or 8 Wood units) should be considered for heart and lung transplantation and more recently long term left ventricular assistance followed with transplantation. To date, there have been no reports in the literature of a threshold beyond which donor right ventricular heart failure could occur which would constitute a clear contraindication to heart transplantation. A normal preoperative PVR does provide some potential protection from acute increase in PVR causing right ventricular failure after heart transplantation.

Organ preservation and CPB may have deleterious effects on ventricular function. Indeed CPB has been shown to cause an increase in PVR (5). Management of right ventricular failure after heart transplantation and the role for inhaled nitric oxide (NO) treatment has been recently reviewed (6).

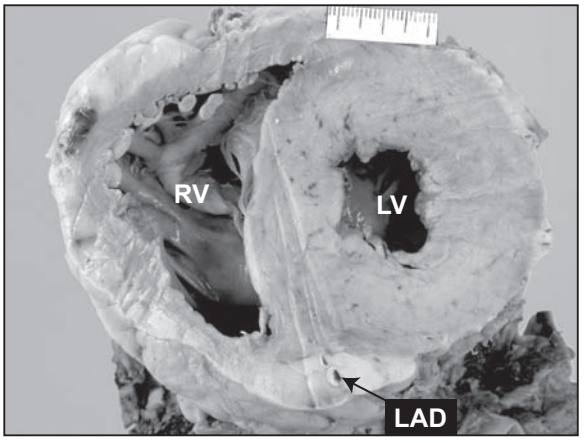

Figure 20.5 A 50-year-old man died from acute rejection after cardiac transplantation. The autopsy showed an hypertrophied left ventricle (LV) and a dilated right ventricle (RV) (LAD, left anterior descending). (Courtesy of Dr. Tack Ki Leung.)

Pericardial effusions are commonly observed in 85% of patients after cardiac transplantation (7). The loss of lymphatic drainage and the discrepancy in size between the new donor heart and the large remaining pericardial cavity are plausible explanations (8). Even if the pericardial effusions are common, rarely do they precipitate hemodynamic instability such as cardiac tamponade. While large but slowly accumulating pericardial effusions usually cause little hemodynamic impairment a loculated hematoma developing at a critical location may conversely cause acute cardiac tamponade (see Chapter 11). Thus, the relationship between the size of the effusion and the clinical outcome is likely to show a poor correlation (8). Most effusions are nearly, or completely, resolved by 30 days after surgery (7).

Transesophageal echocardiography is also useful to evaluate surgical anastomosis in the posttransplantation period (Fig. 20.6). The main pulmonary artery anastomosis appears as a suture ridge within the vessels. Stenosis should be ruled out by two-dimensional (2D) color flow imaging to detect turbulent flow and by continuous-wave (CW) Doppler to measure the systolic gradient across the anastomosis. The pulmonary artery catheter can also be used to document any gradient across the RV and the pulmonary artery (Fig. 20.7C) (9). The mid-esophageal long-axis or two-chamber view shows an elongated LA now composed of both donor and recipient atrial tissue (Fig. 20.8). The suture line within the left and right atria also appears predominantly as an echodense ridge (Fig. 20.6). Acquired cor triatriatum may develop secondary to infolding of the redundant tissue from excessive donor atrial tissue. Post-CPB examination should thus

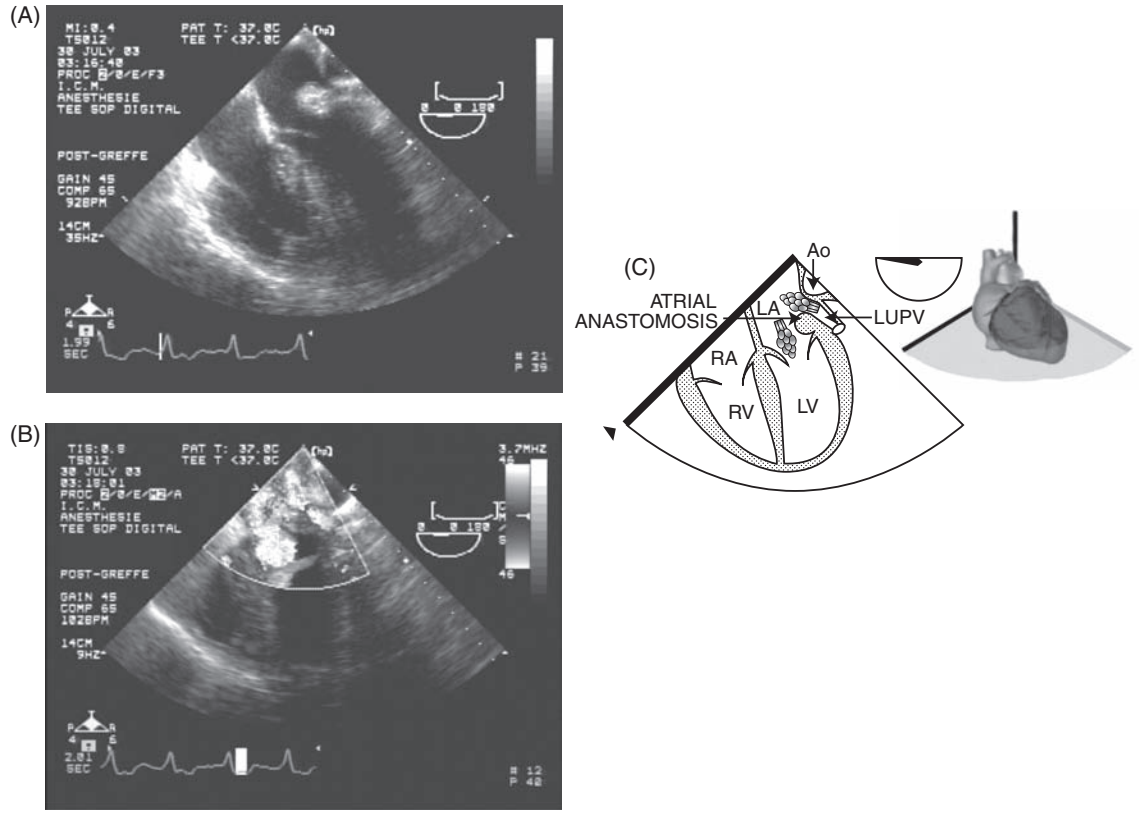

Figure 20.6 Mid-esophageal four-chamber view in a 47-year-old man after cardiac transplantation. The left atrial anastomotic site is edematous (A, B) with flow acceleration in the left upper pulmonary vein (LUPV) (C) (Ao, aorta; LA, left atrium; LV, left ventricle; RA, right atrium; RV, right ventricle).

include evaluation of the suture line for acquired cor triatriatum (Fig. 20.4).

IV. TRANSESOPHAGEAL ECHOCARDIOGRAPHY IN THE EARLY POSTOPERATIVE PERIOD

The early postoperative changes following heart transplantation include right ventricular remodeling, abnormal septal motion, increase in left ventricular mass, presence of pericardial fluid and abnormal left and right ventricular filling patterns (Fig. 20.9) (10).

A. Right Ventricular Remodeling, Tricuspid Regurgitation, and Abnormal Movement of the Ventricular Septum

The time course of the resolution of pulmonary hypertension (PHT) and right ventricular remodeling after orthotopic heart transplantation has been described by Bhatia et al. (11). In 24 patients with moderate PHT (mean pulmonary artery pressure <50 mmHg) after heart transplantation, the PHT resolved rapidly with the mean pulmonary artery pressure approaching normal values at two weeks after surgery. In parallel, the PVR had returned to normal in 80% of patients by one year. Patients with the highest preoperative PVR had the greatest decrease after the transplantation (ranging from 10% to 84%). Right and left heart filling pressure also decreased to a nadir in the upper normal range at two weeks after surgery and remained unchanged over one year of follow-up.

The donor RV remodels in response to recipient perioperative PHT. Initially enlarged, it dilates furthermore during the first month and subsequently returns to its immediate perioperative dimensions at one year after surgery (Fig. 20.10) (11). The RV wall thickness does not significantly increase probably because the PVR declines to normal level. Thus, at one year, while resting hemodynamics are normal, the donor RV remains enlarged probably as an adaptation to chronic volume overload. Tricuspid regurgitation (TR) is common after heart transplantation due to the afterload mismatch and right ventricular dilatation. The incidence of TR (grades 1–3) changes from 67% on day one after heart transplantation to 36% at one year. Nevertheless, TR is generally

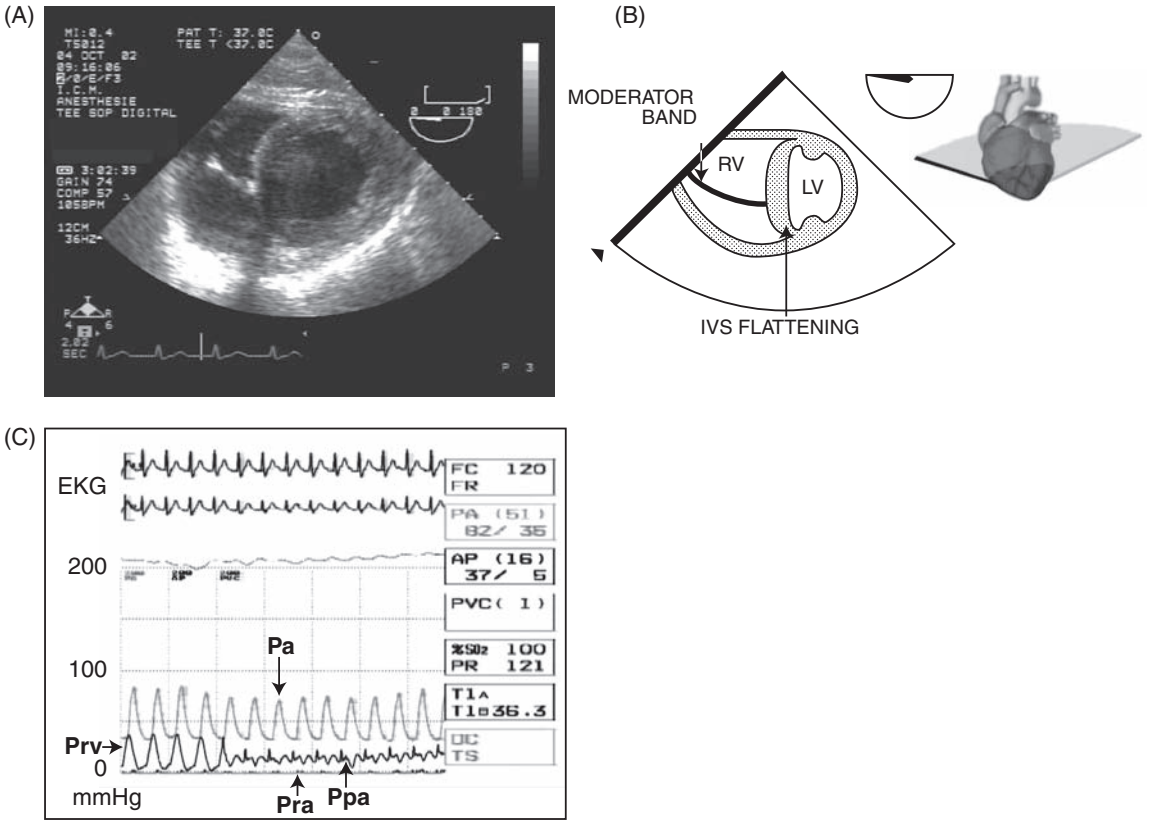

Figure 20.7 (A, B) Mid-papillary transgastric view of a 37-year-old man after cardiac transplantation. Mild right ventricular dilatation is present with a prominent moderator band. (C) A 10 mmHg systolic pressure gradient is present between the right ventricle (RV) and the pulmonary artery (EKG, electrocardiogram; IVS, interventricular septum; LV, left ventricle; Pa, arterial pressure; Ppa, pulmonary artery pressure; Pra, right atrial pressure; Prv, right ventricular pressure).

well tolerated and rarely of clinical significance (11). Finally, abnormal diastolic flattening of the ventricular septum was present in all patients immediately postoperatively (Fig. 20.7). This proportion decreased to 75% at one month and 42% at one year. This decline parallels the decrease in TR and RV dimensions. On the other hand, systolic paradoxical septal motion was uncommon, probably because the mean pulmonary artery pressure decreases significantly immediately after OHT (11).

B. Left Ventricular Mass and Mitral Valve Function

Left ventricular wall thickness and mass increase in the immediate postoperative period most likely from perioperative myocardial ischemia and edema. Systemic hypertension and side effects from cyclosporine and corticosteroid administration can further contribute to left ventricular mass augmentation seen at one year. Acute increase in myocardial thickness may also occur later with allograft rejection (Fig. 20.5) (8). Left ventricular contractility and contractile reserve appear to be normal after cardiac transplantation (12).

Mild to moderate mitral regurgitation (MR) has been reported to occur with a frequency ranging from 55% to 87% without major clinical implications (11,13). It usually occurs in a donor heart without structural abnormality of the mitral apparatus or left ventricular dysfunction. The MR may arise from biatrial enlargement which exerts tension on the posterior leaflet of the mitral valve and causes incomplete closure of the valve and annuloventricular disproportion (11). Moreover, the presence of both donor and recipient atria and sinus nodes results in asynchrone and inhomogenous atrial contraction, which may also play a role in the genesis of MR (11). Finally, MR can occur in association with LVOT obstruction.

C. Left Ventricular Diastolic Function

Diastolic function is also altered in the cardiac transplant recipient (in the absence of rejection) during the early postoperative period. Initial pulsed-wave (PW) Doppler

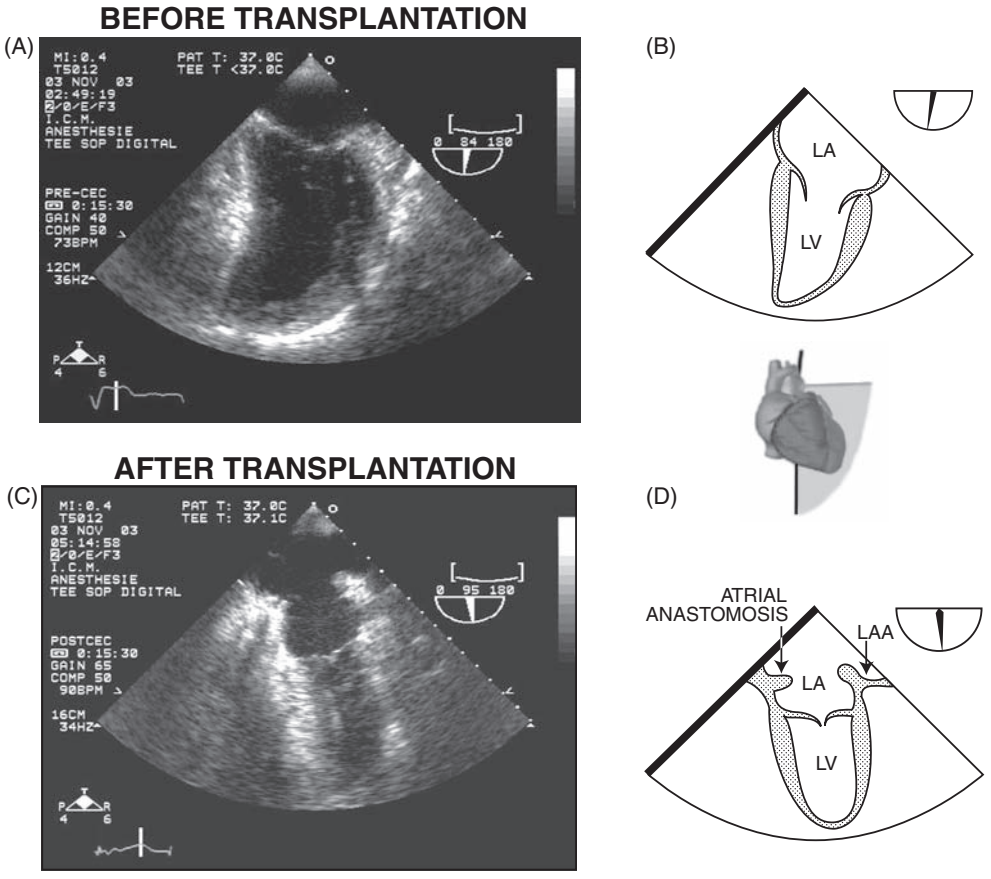

Figure 20.8 Mid-esophageal two-chamber view in a patient before (A, B) and after cardiac transplantation (C, D). The patient had end-stage hypertrophic cardiomyopathy. Note the left atrial suture anastomosis after the procedure and the increase in the anteroposterior size of the left atrium (LA) (LAA, left atrial appendage; LV, left ventricle).

examination of the mitral inflow shows a profile comparable to previously defined restrictive parameters (see Chapter 9); this evolves into a nonrestrictive pattern over a six weeks period leading to progressive improvement in postoperative diastolic function parameters and decrease in left heart filling pressures (14). The presence of recurrent or persistent severe diastolic dysfunction with restrictive filling within six months after transplantation is associated with a reduced late-term actuarial survival, independent of graft rejection (15).

Evidence suggests that retaining normal LA size and shape by using the bicaval technique promotes ventricular filling dynamics which more closely approximates normal physiology (8). Ventricular filling is influenced by the mechanical activity of residual recipient atrial tissue over that of the donor heart. In addition, "parasystolic" contraction of residual recipient atrial tissue also modifies the pulmonary venous flow: recipient atrial contraction occurring in late systole results in an increase in the diastolic component (D-wave); if it happens in early systole the systolic component (S-wave) is decreased. End-diastolic atrial contraction will increase the velocity observed during atrial reversal (AR wave) (10).

D. Normal Echocardiographic Profile after Heart Transplantation

One year after OHT, echocardiograms of recipients doing clinically well are characterized by increased left ventricular wall thickness and mass. Left ventricular dimensions, volumes and ejection fraction are within normal limits. Right ventricular wall thickness and cavity size are increased with preserved right ventricular systolic function. The transplanted heart also shows an anteromedial translational motion during systole. The atria of the transplanted heart have unique echocardiographic features. The anastomotic suture line is easily identified on 2D imaging as the waist of these hourglass-shaped atria (Fig. 20.8). This waist creates a natural point of subdivision within the native and donor atria. The markedly enlarged atrial volume results primarily from an increased long-axis

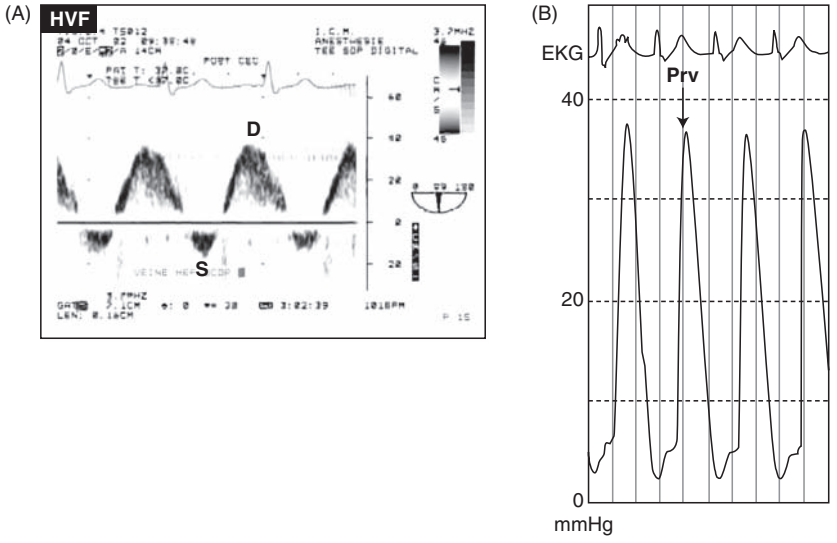

Figure 20.9 Hepatic venous flow (HVF) in a 37-year-old man after cardiac transplantation. (A) Note the inverted systolic waveform or S. (B) The right ventricular pressure (Prv) waveform obtained from the paceport is also abnormal with rapid increase in diastolic pressure consistent with abnormal right ventricular filling (EKG, electrocardiogram).

dimension (Fig. 20.8), although maximal width or short-axis dimension is also slightly larger than in controls (16). The increase in both donor and recipient atrial size is inversely correlated with survival (17).

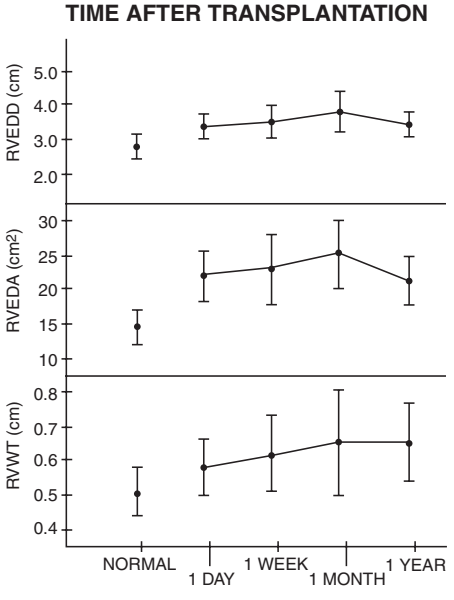

Figure 20.10 Serial right ventricular echocardiographic measurements after transplantation (± 1 SD) are compared with control values ($n = 10$). Shown are right ventricular end-diastolic dimensions (RVEDD in cm), right ventricular end-diastolic area (RVEDA in cm^2) and right ventricular wall thickness (RVWT in cm). [Adapted with permission from Bhatia et al. (11).]

E. Abnormal Echocardiographic Findings Following Heart Transplantation

The presence of the atrial suture line, with an increased atrial size with subcontractile portion of the recipient atrium and asynchrony between the donor and recipient atria contraction promotes stasis, which may account for the high prevalence of atrial spontaneous echo contrast (55%) as assessed with TEE. Left atrial thrombi were observed in 38% by TEE and are often missed by transthoracic echocardiography (TTE). Thrombi were located in the donor LAA (10/18), on the posterior wall of the LA (6/18), on the donor component of the atrial septum (1/18) and on the left atrial suture (1/18) (18). Thrombi occurred only in patients displaying spontaneous echocardiographic contrast. Episodes of arterial embolism were documented in 22 % of patients with both spontaneous echocardiographic contrast and left atrial thrombus (6% of heart transplantation recipients) (18). The use of the modified bicaval heart transplantation technique seems to decrease the incidence of this problem considerably (19).

Transesophageal echocardiography has also been found to be superior to TTE in demonstrating thickening of the atrial septum, bulging of the recipient and donor atrial septum, and shunt at the atrial level (18). It may identify uncommon patent foramen ovale after heart transplantation (20). Coronary fistula is another finding detected by TEE after heart transplantation. The incidence of this iatrogenic complication has been estimated between 5% and 15%, a 20-fold increase over the incidence of congenital coronary artery fistula. The increased incidence in this group is attributed to injury from

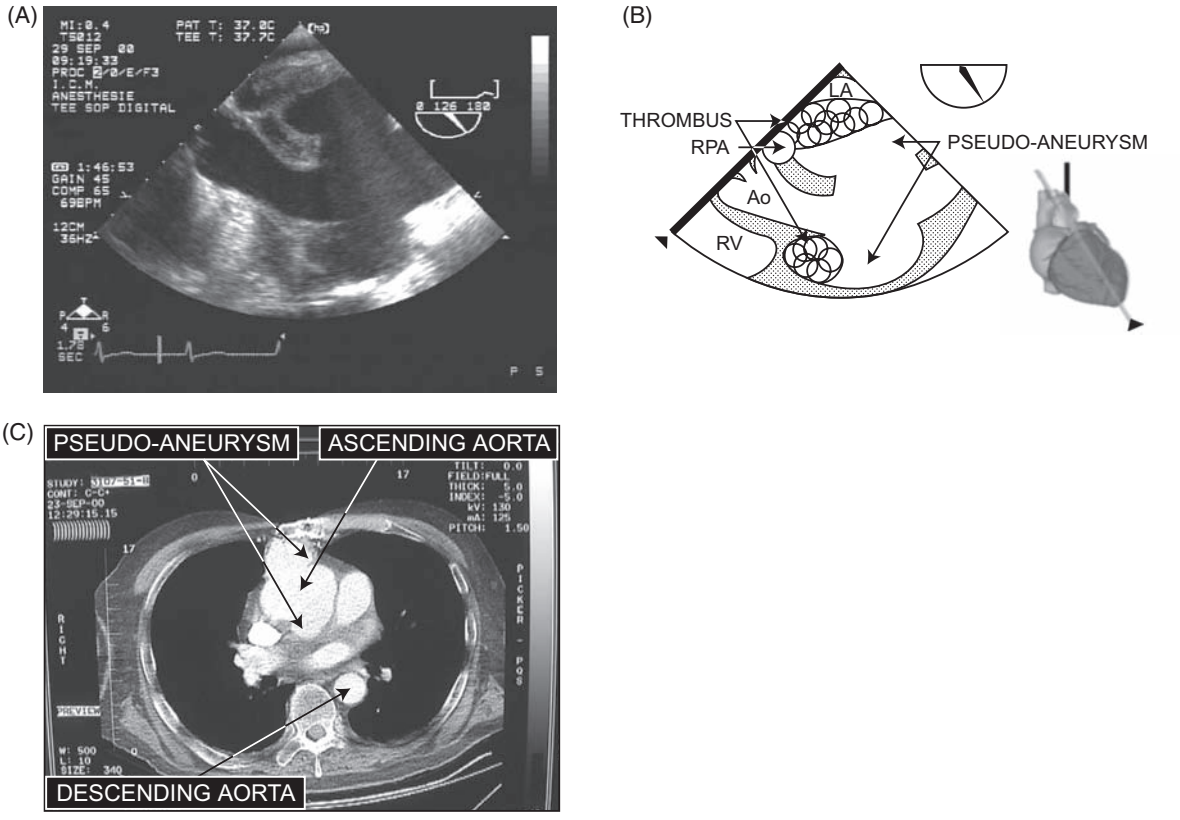

Figure 20.11 A 65-year-old man who developed an aortic pseudoaneurysm nine months after heart transplantation. (A, B) The pseudoaneurysm was located at the anastomotic site of the native aorta (Ao). Blood flow in the pseudoaneurysm was present. (C) Tomographic scan of the pseudoaneurysm with both posterior and anterior extension close to the sternal border (LA, left atrium; RPA, right pulmonary artery; RV, right ventricle).

multiple routine surveillance right ventricular endomyocardial biopsy procedures for detection of cardiac rejection, which frequently involves the right coronary artery (RCA). The vast majority of these fistulas communicate directly with the RV, are usually diagnosed by routine coronary angiography and are without hemodynamic significance (21). Finally pseudoaneurysm can occur after cardiac transplantation at any site of major vessel anastomosis (Fig. 20.11).

F. Detection of Acute Allograft Rejection and Coronary Artery Disease

Acute allograft rejection is common particularly in the first year after transplantation. It constitutes the most frequent cause of death during this period. Morphologic features suggestive of allograft rejection include an increase in myocardial mass due to inflammatory cell infiltration and myocardial edema (Fig. 20.5). However, as the addition of cyclosporin to the immunosuppressive medical regimen, cellular rejection is associated with less myocardial edema: the evaluation of ventricular systolic function and myocardial mass has thus become obsolete as a means of detecting early rejection. Doppler parameters of diastolic function have recently been used to detect acute rejection. It appears that moderate to severe rejection leads to a fall of at least 15% in the mitral deceleration or the isovolemic relaxation time. However, wide interpatient variability in Doppler variables renders isolated measurements cut-off less predictive. Each patient acting as their own control (from baseline) provides the basis for Doppler-based surveillance of allograft rejection. Currently, Doppler-derived parameters of diastolic function are used as an adjunct rather than a replacement for endomyocardial biopsy. Protocols now combine routine biopsies, with supplemental biopsy in the event of echocardiographic evidence of acutely restrictive physiology (8).

In patients who survive the first two years of transplantation, coronary artery disease constitutes an important cause of mortality. There is increasing interest in the ability of dobutamine stress echocardiography to predict adverse cardiac events in OHT recipients. A normal dobutamine stress echocardiography result is a very powerful determinant of a benign clinical course with a negative predictive value in excess of 90–95% (8).

Table 20.1 Role of TEE in Cardiac Transplantation

Before the procedure in patient with ventricular assist device (see Chapter 14)
Perioperative period:
Monitoring after cardiac surgery (see Chapter 13)
Deairing of all four cardiac cavities
Detection of stenotic anastomosis (pulmonary artery, pulmonary veins, inferior, and superior vena cava)
Detection of patent foramen ovale
Early and late postoperative period: evaluation of
Left and right systolic and diastolic function
Mitral and tricuspid valves
Atrial anastomosis, thrombus, spontaneous echocardiographic contrast
Presence of coronary fistula
Aneurysm and pseudoaneurysm of the large vessels anastomoses
If hemodynamic instability: detection of
Left and right ventricular acute systolic and diastolic dysfunction
Left and right ventricular outflow tract dynamic obstruction
Severe mitral or tricuspid regurgitation
Hypovolemia and vasodilatation
Cardiac tamponade from circumferential or loculated effusion

V. CONCLUSION

In summary, echocardiography may significantly contribute to the evaluation of patients at various stages of heart transplantation. During the initial perioperative period, it provides timely assessment of cardiac anatomy and physiology and bestows the opportunity to detect specific problems. Later, detection of allograft rejection and accelerated coronary artery disease benefits from the addition of this noninvasive diagnostic tool (Table 20.1).

REFERENCES

1. Lower RR, Shumway NE. Studies of the orthotopic homotransplantations of the canine heart. Surg Forum 1960; 11:18–23.
2. Shumway NE, Lower RR, Stofer RC. Transplantation of the heart. Adv Surg 1966; 2:265–284.
3. Dreyfus G, Jebara V, Mihaileanu S, Carpentier AF. Total orthotopic heart transplantation: an alternative to the standard technique. Ann Thorac Surg 1991; 52:1181–1184.
4. Carrier M, Leung TK, Solymoss BC et al. Clinical trial of retrograde warm blood reperfusion versus standard cold topical irrigation of transplanted hearts. Ann Thorac Surg 1996; 61:1310–1314.
5. Stobierska-Dzierzek B, Awad H, Michler RE. The evolving management of acute right-sided heart failure in cardiac transplant recipients. J Am Coll Cardiol 2001; 38:923–931.
6. Carrier M, Blaise G, Belisle S et al. Nitric oxide inhalation in the treatment of primary graft failure following heart transplantation. J Heart Lung Transplant 1999; 18:664–667.
7. Weitzman LB, Tinker WP, Kronzon I et al. The incidence and natural history of pericardial effusion after cardiac surgery—an echocardiographic study. Circulation 1984; 69:506–511.
8. Burgess MI, Bhattacharyya A, Ray SG. Echocardiography after cardiac transplantation. J Am Soc Echocardiogr 2002; 15:917–925.
9. Suriani RJ. Transesophageal echocardiography during organ transplantation. J Cardiothorac Vasc Anesth 1998; 12:686–694.
10. Durennes M. Échocardiographie transesophagienne chez le transplanté cardiaque. In: Cohena, édition Arnette, Échocardiographie Transoesophagienne en Cardiologie et en Anesthésie. 1992:265–279.
11. Bhatia SJ, Kirshenbaum JM, Shemin RJ et al. Time course of resolution of pulmonary hypertension and right ventricular remodeling after orthotopic cardiac transplantation. Circulation 1987; 76:819–826.
12. Borow KM, Neumann A, Arensman FW, Yacoub MH. Left ventricular contractility and contractile reserve in humans after cardiac transplantation. Circulation 1985; 71:866–872.
13. Angermann CE, Spes CH, Tammen A et al. Anatomic characteristics and valvular function of the transplanted heart: transthoracic versus transesophageal echocardiographic findings. J Heart Transplant 1990; 9:331–338.
14. StGoar FG, Gibbons R, Schnittger I et al. Left ventricular diastolic function. Doppler echocardiographic changes soon after cardiac transplantation. Circulation 1990; 82:872–878.
15. Ross HJ, Gullestad L, Hunt SA et al. Early Doppler echocardiographic dysfunction is associated with an increased mortality after orthotopic cardiac transplantation. Circulation 1996; 94:II289–II293.
16. Gorcsan J III, Snow FR, Paulsen W et al. Echocardiographic profile of the transplanted human heart in clinically well recipients. J Heart Lung Transplant 1992; 11:80–89.
17. Gudmundsson GS, Smull DL, Pisani BA et al. Increase in atrial size in long-term survivors of heart transplant. J Am Soc Echocardiogr 2003; 16:1043–1048.
18. Derumeaux G, Mouton-Schleifer D, Soyer R et al. High incidence of left atrial thrombus detected by transoesophageal echocardiography in heart transplant recipients. Eur Heart J 1995; 16:120–125.
19. Riberi A, Ambrosi P, Habib G et al. Systemic embolism: a serious complication after cardiac transplantation avoidable by bicaval technique. Eur J Cardiothorac Surg 2001; 19:307–311.
20. Ouseph R, Stoddard MF, Lederer ED. Patent foramen ovale presenting as refractory hypoxemia after heart transplantation. J Am Soc Echocardiogr 1997; 10:973–976.
21. Lowry RW, Young JB, Kleiman NS, Zoghbi WA. Transesophageal echocardiographic demonstration of right coronary artery-to-coronary sinus fistula in a heart transplant recipient. J Am Soc Echocardiogr 1993; 6:449–452.

21

Lung Transplantation

ANDRÉ Y. DENAULT, PASQUALE FERRARO
University of Montreal, Montreal, Canada

I. Role of TEE Before Lung Transplantation 481
II. Role of TEE During the Procedure 482
III. Role of TEE After the Procedure 483
IV. Role of TEE After Lung Transplant in the Intensive Care Unit 487
References 489

Transesophageal echocardiography (TEE) has, over the years, acquired an important role for patient monitoring in the operating room and in the intensive care unit (ICU) setting. Management of lung transplant recipients requires extensive monitoring, as hemodynamic and ventilatory changes during and after surgery can be critical and precipitous. The routine use of TEE during lung transplantation is considered a category II indication (1).

Lung transplantation has become a well-established treatment modality for patients with end-stage lung disease and respiratory failure. Indications for transplantation are varied and include three main groups of patients: obstructive lung disease (emphysema), septic lung disease (cystic fibrosis, bronchiectasis), restrictive lung disease (idiopathic pulmonary fibrosis), and pulmonary vascular disease (primary pulmonary hypertension, PPH). Patients who become transplant candidates have severely limited pulmonary capacity as well as varying degrees of right and left heart dysfunction depending on the underlying disorder and coexisting medical conditions. Successful lung transplantation, therefore, requires careful perioperative and intraoperative patient management of which TEE has become a cornerstone.

I. ROLE OF TEE BEFORE LUNG TRANSPLANTATION

The ability of TEE to assess the presence of pulmonary hypertension and right heart dysfunction in transplant candidates on a waiting list has been shown by Gorcsan et al. (2), Schenk et al. (3), and Bossone et al. (4). Interestingly, TEE also provided additional data that significantly altered surgical treatment in 25% of the 48 consecutive patients studied by Gorcsan et al. (2). At the time of the transplantation itself, the first role of TEE is to reassess the status of the right ventricular function. Indeed, between the time of the initial transplant eligibility evaluation to the lung transplantation itself, worsening of the respiratory function and the development of pulmonary hypertension and right ventricular failure is not uncommon. In patients with a mild degree of chronic obstructive lung disease (COLD), both right and left ventricular relaxation abnormalities are observed (5). As the disease progresses, these evolve towards a restrictive filling pattern which correlates with the severity of pulmonary hypertension. The diagnosis can be established using pulsed-wave (PW) Doppler examination of the tricuspid inflow as well as tissue

Doppler imaging of the tricuspid valve (TV) annulus (6). Right ventricular systolic dysfunction has also been shown to be associated with an abnormal hepatic venous systolic (S) wave (7). The use of a pulmonary artery catheter (PAC) for continuous pulmonary artery pressure measurement in conjunction with TEE is useful in this setting. The need for pharmacological support, ventilatory management and cardiopulmonary bypass (CPB) can thus be safely planned. In the authors' experience, the need for CPB varies from $<2\%$ for emphysema patients, 30% in patients with pulmonary fibrosis, to its systematic use in PPH patients.

II. ROLE OF TEE DURING THE PROCEDURE

During the procedure, TEE can be used to evaluate left and right systolic and diastolic function, to rule out the presence of an unexpected patent foramen ovale with a right-to-left shunt (8), to verify the integrity of the pulmonary vascular anastomoses (Fig. 21.1) and to exclude significant air embolus (1). The appearance of continuous air emboli observed by TEE at the end of a lung transplantation should prompt re-examination of the bronchial anastomosis integrity (9) (Fig. 21.2). Although the need for CPB varies greatly, all lung transplantations are performed with CPB on standby. In the absence of a formal indication for CPB such as the presence of PPH or an Eisenmenger's syndrome, surgeons have yet to agree on whether or not CPB should be routinely used (10,11). The need for CPB is difficult to establish preoperatively as reported by de Hoyos et al. (12) and Triantafillou et al. (13). In these two studies, parameters such as preoperative PaO_2, mean pulmonary artery pressure and pulmonary vascular resistance were not found to be reliable predictive indicators for the use of CPB. Intraoperatively however, the hemodynamic effects of pulmonary artery clamping as evaluated by TEE are extremely useful in establishing the need for CPB: echocardiographic signs of low cardiac output (CO) or severe right ventricular dysfunction such as right atrial and ventricular dilatation with paradoxical septal motion (Fig. 21.3) and reduced systolic excursion of the tricuspid annulus (see Chapter 9) help to determine precisely the need for circulatory support.

Using a 5.0 MHz biplane or multiplane TEE probe, a standard examination, including Doppler flow measurements, is performed in both the transverse and longitudinal planes. The examination should be repeated intraoperatively once the anastomoses have been completed. The presence of an arterial or pulmonary vein stenosis

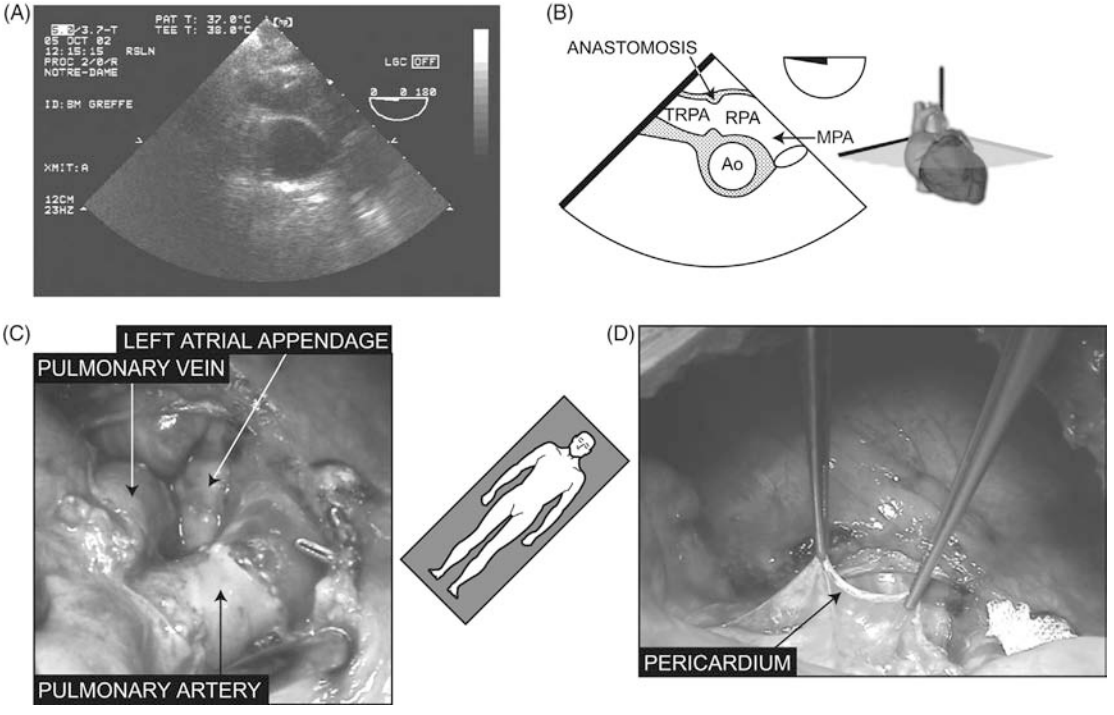

Figure 21.1 Pulmonary vascular anastomosis. (A, B) Right pulmonary artery (RPA) anastomosis in a 45-year-old man after lung transplantation, viewed through the upper mid-esophageal view at 0°. (C) Intraoperative left pulmonary artery anastomosis in a 55-year-old woman undergoing single left pulmonary transplantation. (D) After completing the anastomosis, the pericardium is closed. (Ao, aorta; MPA, main pulmonary artery; TRPA, transplanted right pulmonary artery).

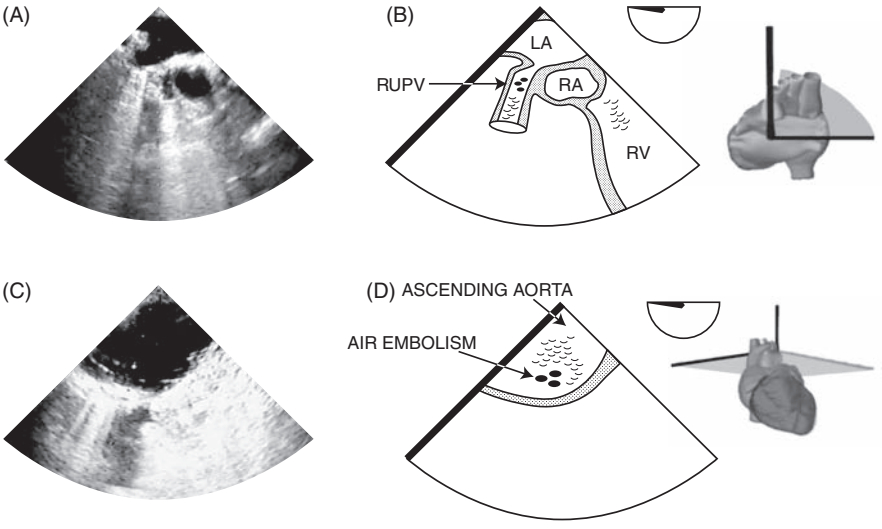

Figure 21.2 Presence of air embolism detected at the completion of the vascular anastomosis. Air bubbles are seen in the right upper pulmonary vein (RUPV) (A, B) and in the ascending aorta (C, D) (LA, left atrium; RA, right atrium; RV, right ventricle).

(Fig. 21.4) or thrombosis should be excluded by measuring the diameter of the donor and recipient vessels and if there are discrepancies, the corresponding pressure gradient. The pulmonary veins and left atrium (LA) should be carefully examined for the presence of thrombus, and if there are any, their size, precise location and associated flow abnormalities noted. The correction of such intraoperative findings are key in preventing life-threatening complications post-operatively (1,14). Figures 21.5–21.7 represent our approach in aquiring TEE 2D, Doppler data acquisition and hemodynamic evaluation of patients undergoing lung transplantation.

III. ROLE OF TEE AFTER THE PROCEDURE

Transesophageal echocardiography, whether used intraoperatively or postoperatively in the ICU, plays a valuable role in the assessment of arterial and veno-atrial anastomotic complications following lung transplantation. As reported by Griffith et al. (15), all too often, even the most experienced transplant surgeons may underestimate these anastomotic problems. Generally, TEE will easily display the right pulmonary artery (PA) anastomosis (Fig. 21.1) as well as those of the right upper and lower pulmonary veins to the LA. However, on the left, due to the location

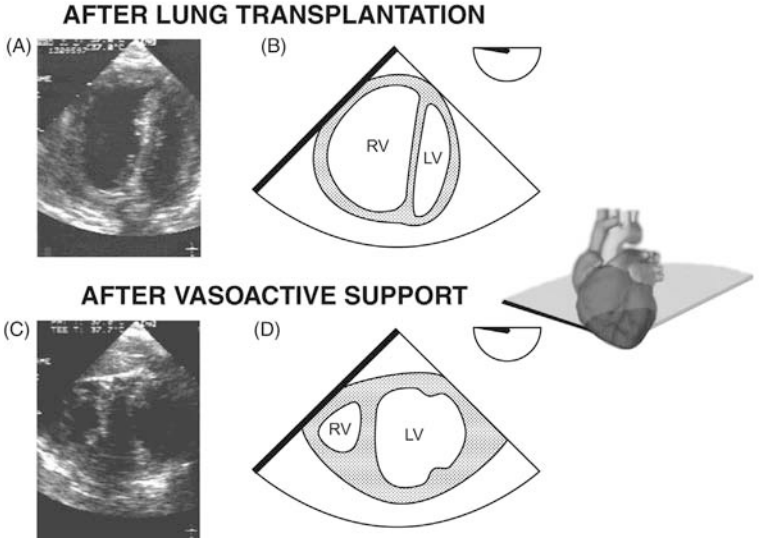

Figure 21.3 Bilateral lung transplantation complicated by transient right ventricular dysfunction. (A, B) On the transgastric view at 0°, significant dilatation of the right ventricle (RV) and paradoxical septal motion suggests RV failure, possibly secondary to clamping of the pulmonary artery or air embolisation in the right coronary artery. (C, D) Vasoactive support re-established RV size and normal septal motion (LV, left ventricle).

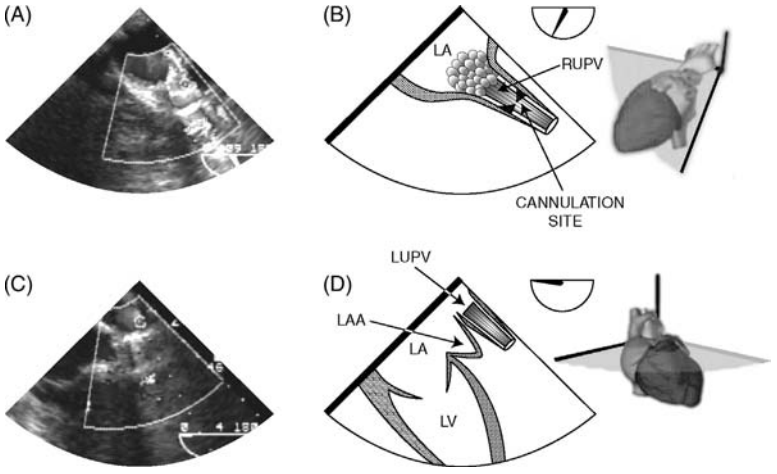

Figure 21.4 (A, B) Doppler evaluation of right upper pulmonary vein (RUPV) stenosis in a patient who underwent a repeated aortic valve procedure. A peak systolic velocity of 120 cm/sec is recorded with flow acceleration and aliasing in the RUPV. (C, D) In contrast, a velocity of 80 cm/sec with no aliasing is found in the left upper pulmonary vein (LUPV) (LA, left atrium; LAA, left atrial appendage; LV, left ventricle).

of the left hilum, the left PA anastomosis can only be identified in 71% of the cases (16) while the left lower pulmonary vein is usually not adequately visualized beyond the ostium. Figure 21.4 illustrates an example of a right pulmonary vein stenosis.

Pulmonary venous obstruction or thrombosis is generally associated with early graft failure and a high mortality rate (17–19). The true incidence of these venous anastomotic complications is however difficult to establish and is probably underestimated. Early series, such as the one from the Pittsburgh group, described only two venous anastomotic complications from a series of 134 transplant patients. This low rate of 1.5% was, however, based on clinical grounds and not systematic use of TEE. Later, reports from Hausmann (16) and Leibowitz (20) quoted rates varying from 9% to 29% when TEE was routinely used in consecutive patients.

In a more recent prospective study by Schulman et al. (21), the incidence of venous anastomotic complications was recorded at 15%, with 13 out of 87 consecutive

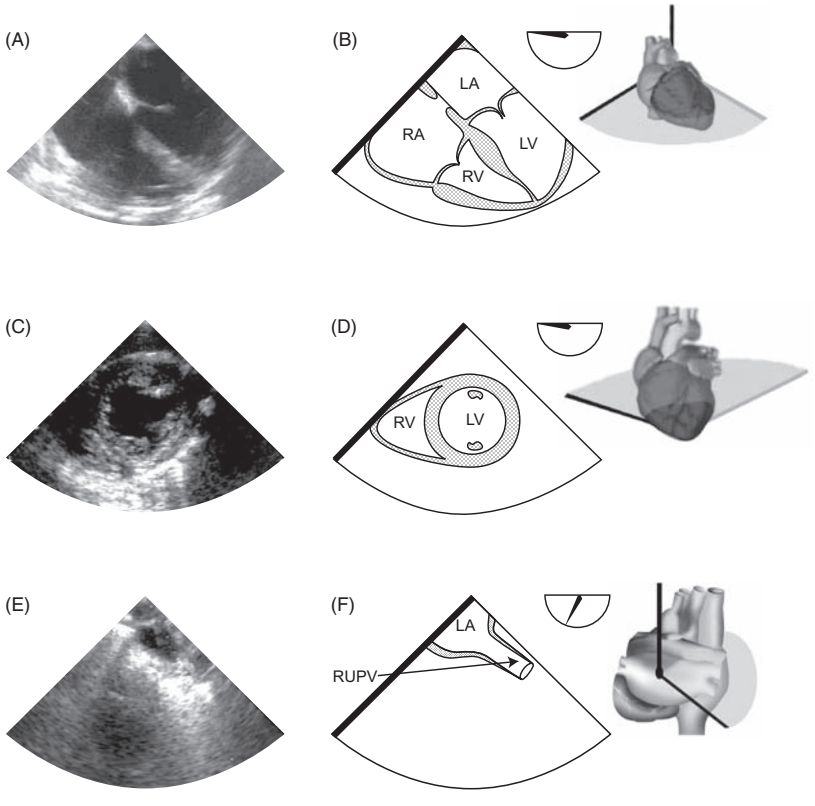

Figure 21.5 Suggested sequence of transesophageal echocardiographic systematic examination following bilateral lung transplantation in a 45-year-old man. After the evaluation of the anastomosis, left and right ventricular systolic function is assessed through the mid-esophageal four-chamber (A, B) and transgastric views (C, D). Left and right diastolic function is then assessed with pulsed-wave Doppler interrogation of the right (E, F) and left upper pulmonary veins, the mitral inflow as well as the hepatic veins (LA, left atrium; LV, left ventricle; RA, right atrium; RUPV, right upper pulmonary vein; RV, right ventricle).

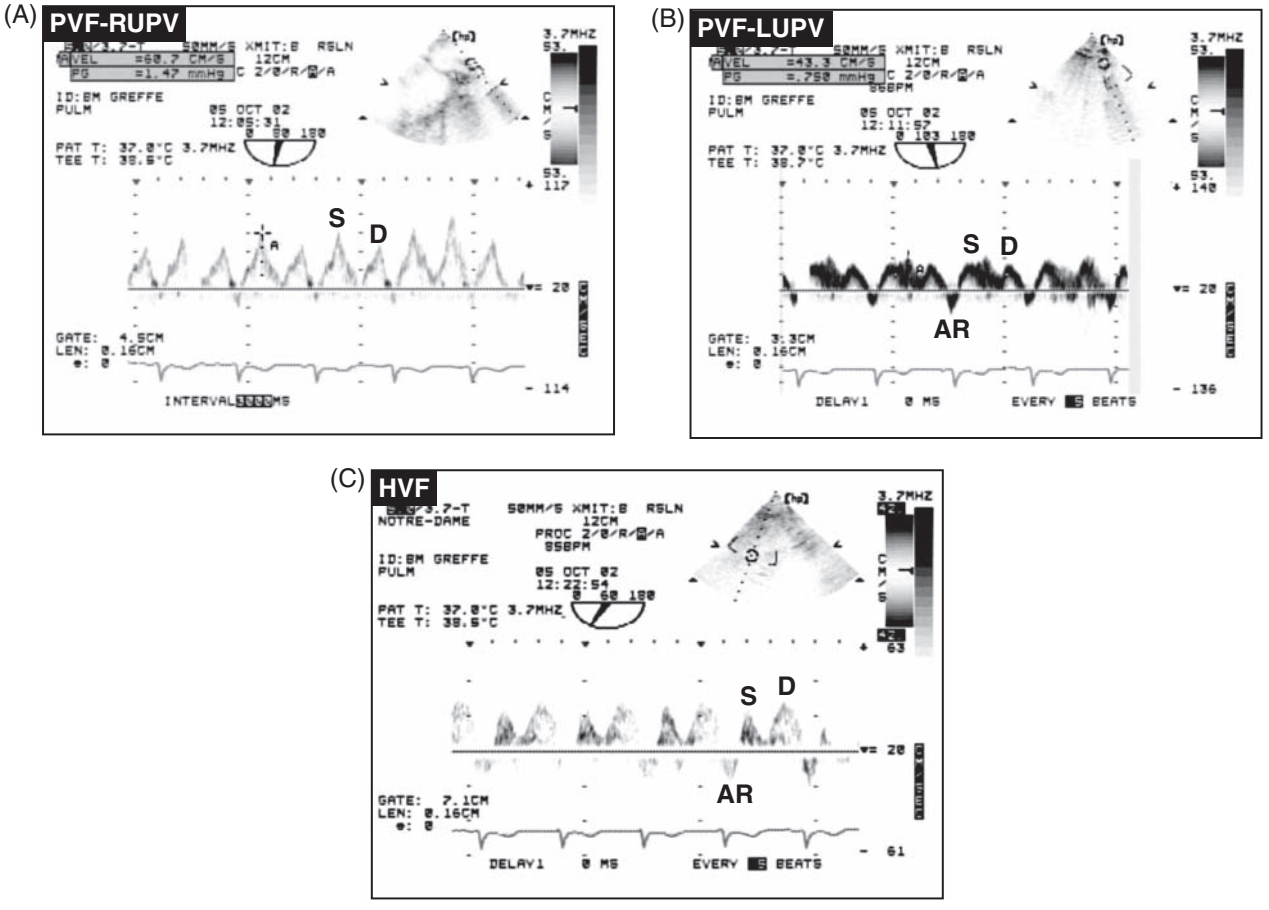

Figure 21.6 Suggested sequence for transesophageal echocardiographic systematic examination following bilateral lung transplantation in a 45-year-old man. The pulsed-wave Doppler profile of the right upper pulmonary vein (RUPV) (A) shows a systolic velocity of 60.7 cm/sec compared with 43.3 cm/sec in the left upper pulmonary vein (LUPV) (B). (C) Doppler examination of the hepatic vein shows abnormal diastolic flow predominance ($S/D < 1$) consistent with right ventricular diastolic dysfunction (AR, atrial reversal; HVF, hepatic venous flow; PVF, pulmonary venous flow).

transplant recipients diagnosed with a pulmonary vein thrombosis postoperatively. In 12 of the 13 cases, the thrombosis was localized in the upper lobe veins of the transplanted lung. The thrombi had a mean width of 0.9 ± 0.4 cm, with a mean pulmonary venous flow velocity of 127 ± 23 cm/sec. The mortality in the presence of this complication was significant, with five of the 13 patients (38.5%) dying postoperatively. The incidence of the complication was similar regardless of the side of the transplant or the use of CPB. Transesophageal echocardiography was thought to be helpful by obviating the need for angiography.

Complications involving the PA anastomosis occur far less frequently. Indeed, from a surgical technical standpoint, this anastomosis is less difficult to accomplish while abnormalities are usually easily detected early intraoperatively. Clark et al. (22) reported five cases of stenosis (two RPAs, three LPAs) from a series of 109 transplantations. Despite three surgical revisions of the PA anastomosis, all five patients ultimately died in the early postoperative period. Griffith et al. (15) also described fives cases of PA anastomotic complications, for a rate of 3.7%, in his review of 134 transplant recipients. Three of the five patients underwent reoperation and revision of the PA anastomosis. The author noted that excessive length of the donor PA and/or the recipient PA can create distortion or kinking of the anastomosis leading to reduced blood flow and thrombosis. This situation may arise particularly when an oversized lung is placed in a small chest during single lung transplantation. In the immediate postoperative period, both TEE and the PAC are useful to quantitate the severity of the pulmonary anastomosis (Fig. 21.7).

In our own experience with 158 lung transplantations over a seven year period (1997–2004), we have not encountered any vascular anastomotic complications

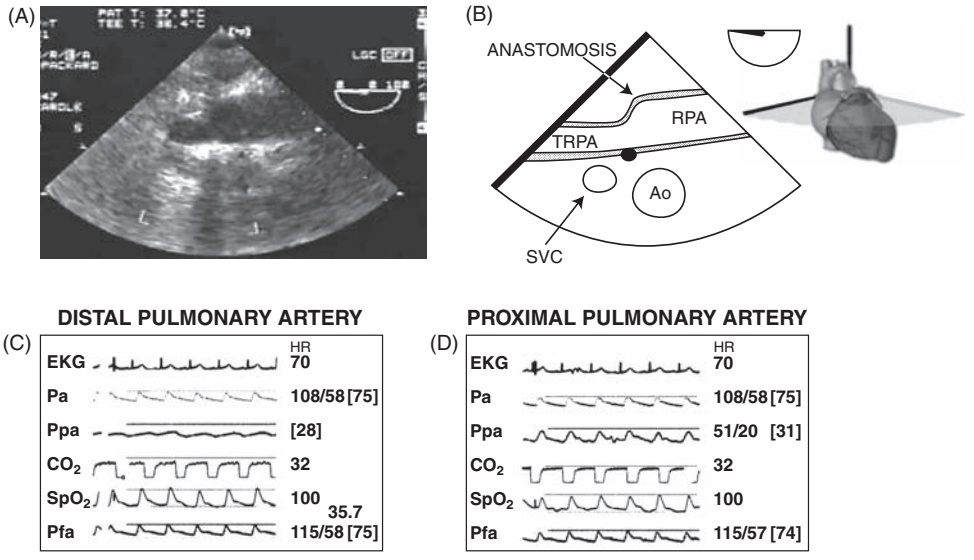

Figure 21.7 Quantification of a pulmonary artery stenotic anastomosis in a 65-year-old woman after right lung transplantation. (A, B) On the upper mid-esophageal view at 0°, a reduction in the diameter between the native and the donor right pulmonary artery (RPA) is seen. The hemodynamic severity of this finding is easily assessed by pulmonary artery catheter pullback from a distal (C) to a proximal position (D) to the anastomosis: a mean pressure gradient of 3 mmHg (31 mmHg − 28 mmHg) is found (Ao, aorta; CO_2, end-tidal carbon dioxide from capnography; EKG, electrocardiogram; Pa, arterial pressure (from radial artery); Pfa, arterial pressure from femoral artery; Ppa, pulmonary artery pressure; SpO_2, saturation from pulse oximetry; SVC, superior vena cava; TRPA, transplanted right pulmonary artery).

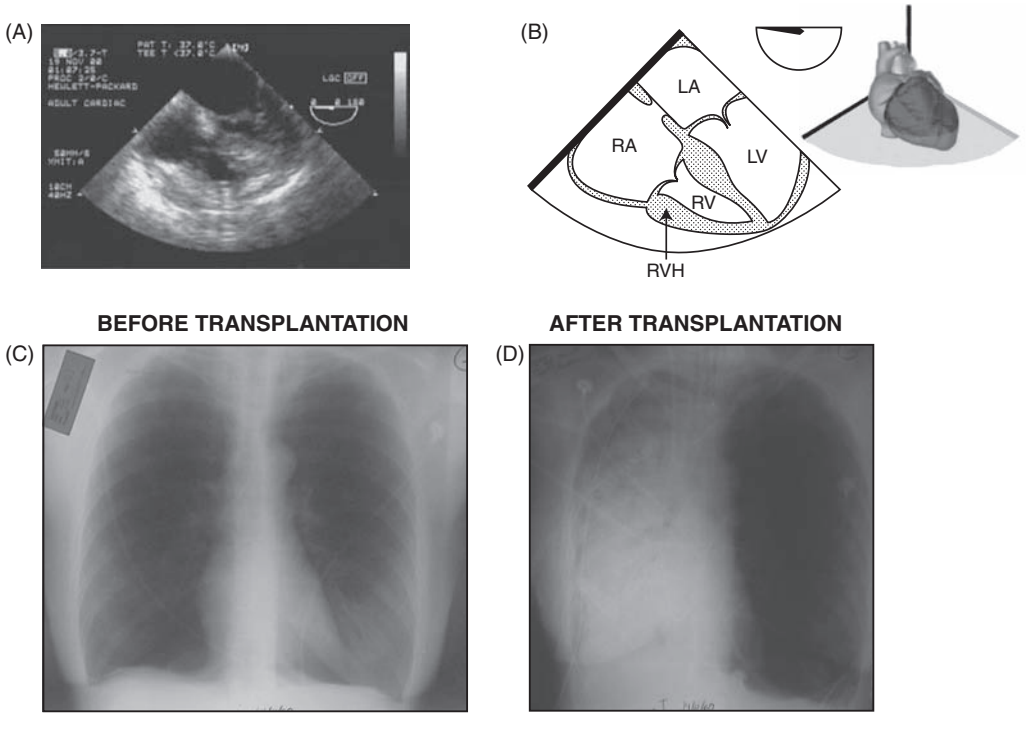

Figure 21.8 Hemodynamic instability following single lung transplantation in a 53-year-old woman with end-stage emphysema. (A, B) The mid-esophageal four-chamber view at 0° shows right ventricular hypertrophy (RVH) and abnormal tricuspid annular motion. She remains hemodynamically unstable despite administration of norepinephrine at 25 μg/min and displays severe hypoxia from right-sided ischemic reperfusion injury, as evident on the chest radiographs (C, D) (LA, left atrium; LV, left ventricle; RA, right atrium; RV, right ventricle).

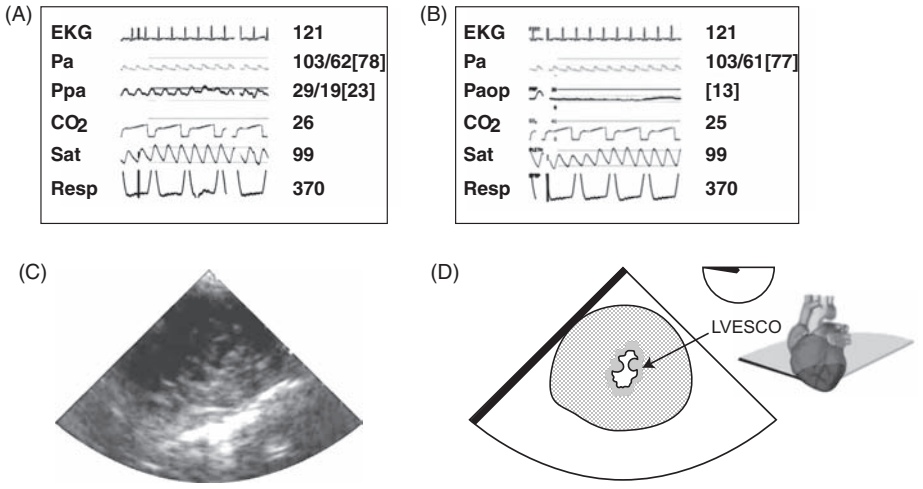

Figure 21.9 Hemodynamic instability following single lung transplantation in a 53-year-old woman with end-stage emphysema. (A, B) Invasive hemodynamic monitoring shows a heart rate of 121 beats/min, an arterial blood pressure (Pa) of 103/62 mmHg, a pulmonary artery pressure (Ppa) of 29/19 mmHg with a pulmonary artery occluded (wedge) pressure (Paop) of 13 mmHg. The central venous pressure was 14 mmHg (not shown). The capnographic waveform (CO_2) is typical of a single lung transplant with the initial normal waveform from the transplanted lung followed by the ascending phase III typical of obstructive disease. Respiratory variation of the saturation (Sat) signal from the pulse oximeter is seen. (C, D) Despite relatively normal filling pressures, left ventricular end-systolic cavity obliteration (LVESCO) is found on the transgastric mid-papillary view at 0°. The patient improved with intravenous fluid administration (EKG, electrocardiogram; Resp, respiration).

postoperatively. We believe that careful tailoring of the vascular structures on both the recipient and donor side as well as a meticulous surgical technique with the use of intraoperative TEE may account for these excellent results.

IV. ROLE OF TEE AFTER LUNG TRANSPLANT IN THE INTENSIVE CARE UNIT

Transesophageal echocardiography also plays an essential role in the postoperative care of lung transplant recipients in the ICU. The early post-operative course of these patients is frequently characterized by hemodynamic, radiographic and gas exchange abnormalities. Despite improved preservation techniques in recent years, severe ischemia–reperfusion injury (IRI) is still prevalent in 10% of patients following transplantation (Fig. 21.8). This injury is usually associated with abundant frothy sputum from the endotracheal tube, a PaO_2/FiO_2 ratio < 100, diffuse alveolar infiltrates on the side of the graft and hemodynamic instability. The differential diagnosis includes acute allograft rejection, cardiogenic pulmonary edema, noncardiogenic pulmonary edema other than IRI, sepsis and vascular anastomotic complications. Transesophageal echocardiography in this setting is useful in excluding the etiologies listed earlier and in confirming the diagnosis of IRI suggested by the clinical history and the hemodynamic profile obtained from a PA catheter. More interestingly, continuous TEE monitoring helps to assess the response to therapy (Fig. 21.9) and determine the need for more invasive support such as extra-corporeal membrane oxygenation (ECMO).

During ECMO, based on the American Society of Anesthesiology–Society of Cardiovascular Anesthesiology (ASA–SCA) guidelines (1), TEE is considered a category I indication (see Chapter 14). Transesophageal echocardiography can help to evaluate ventricular recovery, assist in cannula positioning and exclude the presence of intracardiac clot before initiating the weaning process

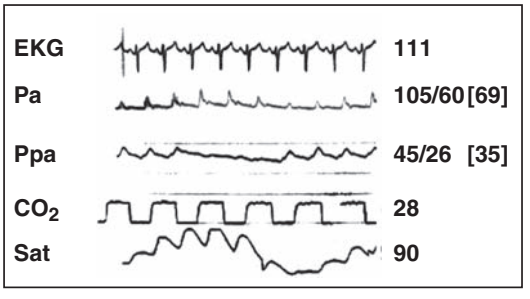

Figure 21.10 Hemodynamic instability in a 65-year-old woman following single lung transplantation. Fluctuation of the arterial pressure (Pa) or pulsus paradoxus coincident with the pulse oximetry signal (Sat), followed later by the pulmonary artery (Ppa) signal suggests tamponade. (CO_2, end-tidal CO_2; EKG, electrocardiogram). [With permission of Denault et al. (25).]

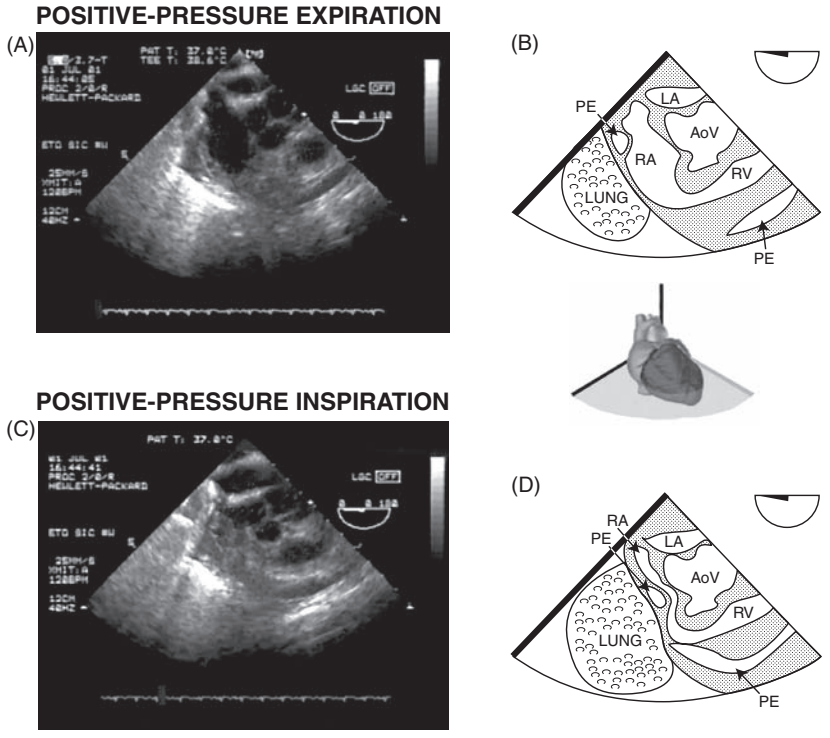

Figure 21.11 (A, B) Truncated mid-esophageal four-chamber view during positive-pressure expiration: the right atrial cavity is seen with two small pericardial effusions. (C, D) During positive-pressure inspiration, collapse of the right atrial cavity is seen. (AoV, aortic valve; LA, left atrium; PE, pericardial effusion; RA, right atrium; RV, right ventricle). [Adapted with permission from Denault et al. (25).]

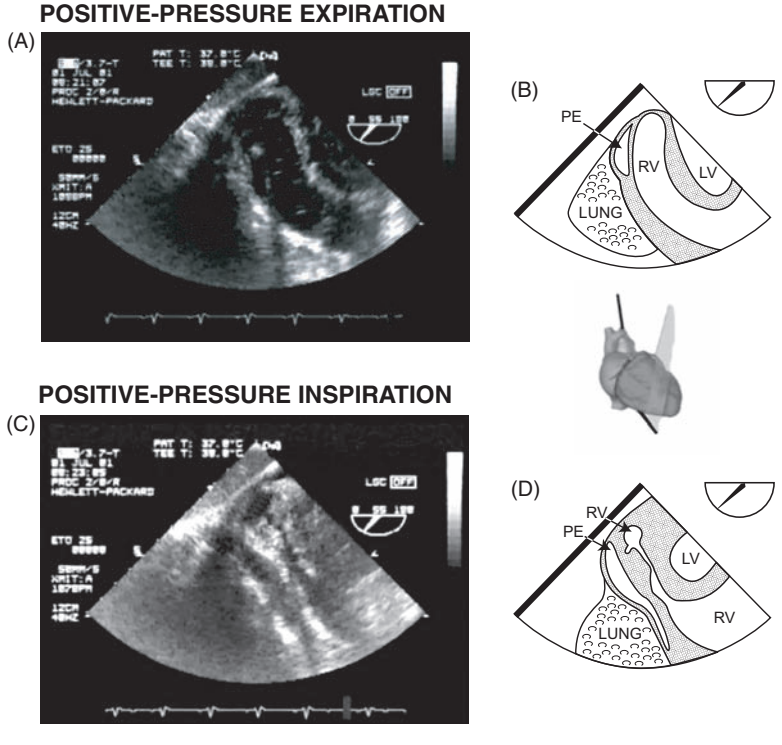

Figure 21.12 (A, B) Transgastric right ventricular outflow tract (RVOT) view at 55° during positive-pressure expiration. (C, D) During positive-pressure inspiration, collapse of the RVOT is observed with a small pericardial effusion (PE) (LV, left ventricle; RV, right ventricle). [Adapted with permission from Denault et al. (25).]

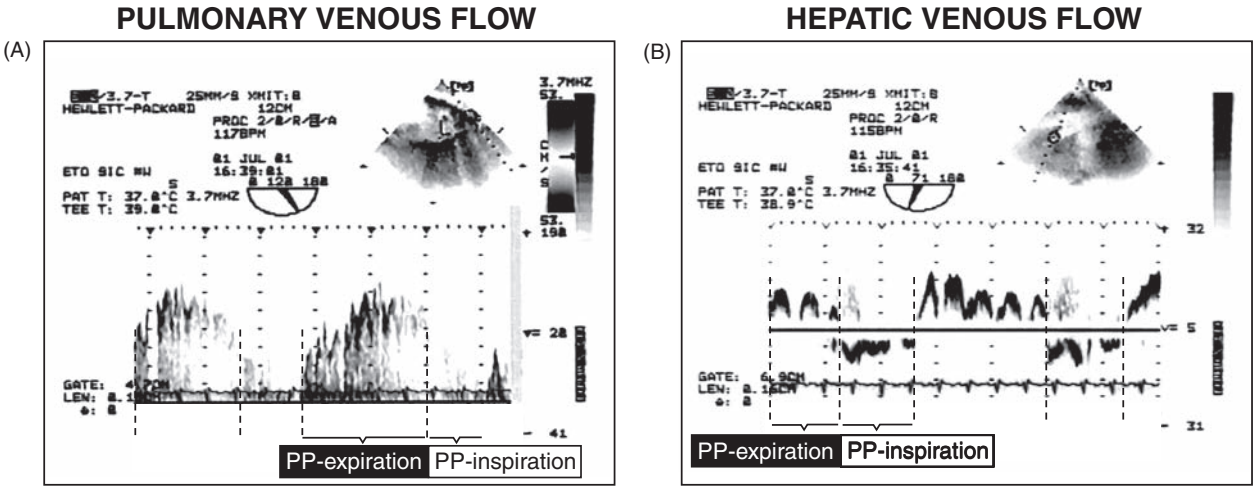

Figure 21.13 Pulsed-wave Doppler examination of the right upper pulmonary vein (A) and the hepatic vein (B). Cyclic fluctuation of the Doppler signal is seen with positive-pressure (PP) ventilation. [Adapted with permission of Denault et al. (25).]

(23,24). The exact timing and the type of ECMO required can also be facilitated by TEE findings. Generally, when both right and left ventricular function is preserved, the use of venovenous ECMO is sufficient, but with severe right or left ventricular dysfunction, venoarterial ECMO may be more appropriate. We recently reported a case in which continuous TEE in the ICU not only helped establish the indication for venoarterial ECMO in a transplant recipient with severe IRI, but also facilitated monitoring of the patient while on ECMO and guided the authors through a successful weaning 4 days later (25).

Other complications diagnosed with TEE following lung transplantation include left (26) and right ventricular dynamic outflow tract obstruction (27) precipitated by suboptimal preload, increased inotropy and right ventricular hypertrophy (28), as well as thoracic tamponade (Figs. 21.10–21.13) (25).

In summary, TEE is a promising diagnostic and monitoring modality in lung transplantation and is likely to become a routine part of this life-saving procedure (Table 21.1).

Table 21.1 Role of TEE in Lung Transplantation

Before the procedure
Evaluation of left and right ventricular and valvular function
Estimation of pulmonary artery pressure
Perioperative period
If performed under CPB: see Chapter 13
Deairing of all four cardiac cavities
Ruling out stenotic anastomosis (pulmonary artery, pulmonary veins)
Ruling out patent foramen ovale
Early and late postoperative period:
Left and right ventricular and valvular function assessment
Arterial and atrial anastomosis evaluation
If hemodynamic instability
Ruling out left and right ventricular systolic and diastolic function
Arterial or venous anastomotic obstruction
Left and right ventricular outflow tract obstruction
Hypovolemia and vasodilatation
Air embolism
Thoracic tamponade
If ECMO required: see Chapter 14

Note: CPB, cardiopulmonary bypass; ECMO, extracorporeal membrane oxygenation.

REFERENCES

1. Practice guidelines for perioperative transesophageal echocardiography. A report by the American Society of Anesthesiologists and the Society of Cardiovascular Anesthesiologists Task Force on Transesophageal Echocardiography. Anesthesiology 1996; 84:986–1006.
2. Gorcsan J III, Edwards TD, Ziady GM et al. Transesophageal echocardiography to evaluate patients with severe pulmonary hypertension for lung transplantation. Ann Thorac Surg 1995; 59:717–722.
3. Schenk P, Globits S, Koller J et al. Accuracy of echocardiographic right ventricular parameters in patients with different end-stage lung diseases prior to lung transplantation. J Heart Lung Transplant 2000; 19:145–154.
4. Bossone E, Paciocco G, Iarussi D et al. The prognostic role of the ECG in primary pulmonary hypertension. Chest 2002; 121:513–518.
5. Ozer N, Tokgozoglu L, Coplu L, Kes S. Echocardiographic evaluation of left and right ventricular diastolic function in patients with chronic obstructive pulmonary disease. J Am Soc Echocardiogr 2001; 14:557–561.

6. Caso P, Galderisi M, Cicala S et al. Association between myocardial right ventricular relaxation time and pulmonary arterial pressure in chronic obstructive lung disease: analysis by pulsed Doppler tissue imaging. J Am Soc Echocardiogr 2001; 14:970–977.
7. Mishra M, Swaminathan M, Malhotra R et al. Evaluation of right ventricular function during CABG: transesophageal echocardiographic assessment of hepatic venous flow versus conventional right ventricular performance indices. Echocardiography 1998; 15:51–58.
8. Sukernik MR, Mets B, Bennett-Guerrero E. Patent foramen ovale and its significance in the perioperative period. Anesth Analg 2001; 93:1137–1146.
9. Denault AY, Couture P, McKenty S et al. Perioperative use of transesophageal echocardiography by anesthesiologists: impact in noncardiac surgery and in the intensive care unit (L'utilization perioperatoire de l'echocardiographie transoesophagienne par les anesthesiologistes: les repercussions en chirurgie non cardiaque et a l'unite des soins intensifs). Can J Anaesth 2002; 49:287–293.
10. Marczin N, Royston D, Yacoub M. Pro: lung transplantation should be routinely performed with cardiopulmonary bypass. J Cardiothorac Vasc Anesth 2000; 14:739–745.
11. McRae K. Con: lung transplantation should not be routinely performed with cardiopulmonary bypass. J Cardiothorac Vasc Anesth 2000; 14:746–750.
12. de Hoyos A, Demajo W, Snell G et al. Preoperative prediction for the use of cardiopulmonary bypass in lung transplantation. J Thorac Cardiovasc Surg 1993; 106:787–795.
13. Triantafillou AN, Pasque MK, Huddleston CB et al. Predictors, frequency, and indications for cardiopulmonary bypass during lung transplantation in adults. Ann Thorac Surg 1994; 57:1248–1251.
14. Michel-Cherqui M, Brusset A, Liu N et al. Intraoperative transesophageal echocardiographic assessment of vascular anastomoses in lung transplantation. A report on 18 cases. Chest 1997; 111:1229–1235.
15. Griffith BP, Magee MJ, Gonzalez IF et al. Anastomotic pitfalls in lung transplantation. J Thorac Cardiovasc Surg 1994; 107:743–753.
16. Hausmann D, Daniel WG, Mugge A et al. Imaging of pulmonary artery and vein anastomoses by transesophageal echocardiography after lung transplantation. Circulation 1992; 86:II251–II258.
17. Huang YC, Cheng YJ, Lin YH et al. Graft failure caused by pulmonary venous obstruction diagnosed by intraoperative transesophageal echocardiography during lung transplantation. Anesth Analg 2000; 91:558–560.
18. Sarsam MA, Yonan NA, Beton D et al. Early pulmonary vein thrombosis after single lung transplantation. J Heart Lung Transplant 1993; 12:17–19.
19. Shah AS, Michler RE, Downey RJ et al. Management strategies for pulmonary vein thrombosis following single lung transplantation. J Card Surg 1995; 10:169–178.
20. Leibowitz DW, Smith CR, Michler RE et al. Incidence of pulmonary vein complications after lung transplantation: a prospective transesophageal echocardiographic study. J Am Coll Cardiol 1994; 24:671–675.
21. Schulman LL, Anandarangam T, Leibowitz DW et al. Four-year prospective study of pulmonary venous thrombosis after lung transplantation. J Am Soc Echocardiogr 2001; 14:806–812.
22. Clark SC, Levine AJ, Hasan A et al. Vascular complications of lung transplantation. Ann Thorac Surg 1996; 61:1079–1082.
23. Katz WE, Jafar MZ, Mankad S et al. Transesophageal echocardiographic identification of a malpositioned extracorporeal membrane oxygenation cannula. J Heart Lung Transplant 1995; 14:790–792.
24. Smith C, Bellomo R, Raman JS et al. An extracorporeal membrane oxygenation-based approach to cardiogenic shock in an older population. Ann Thorac Surg 2001; 71:1421–1427.
25. Denault A, Ferraro P, Couture P et al. Transesophageal echocardiography monitoring in the intensive care department: the management of hemodynamic instability secondary to thoracic tamponade after single lung transplantation. J Am Soc Echocardiogr 2003; 16:688–692.
26. Murtha W, Guenther C. Dynamic left ventricular outflow tract obstruction complicating bilateral lung transplantation. Anesth Analg 2002; 94:558–559.
27. Gorcsan J III, Reddy SC, Armitage JM, Griffith BP. Acquired right ventricular outflow tract obstruction after lung transplantation: diagnosis by transesophageal echocardiography. J Am Soc Echocardiogr 1993; 6:324–326.
28. Kirshbom PM, Tapson VF, Harrison JK et al. Delayed right heart failure following lung transplantation. Chest 1996; 109:575–577.

22

Liver Transplantation

FRANÇOIS PLANTE
University of Montreal, Montreal, Canada

STÉPHANE BUSQUE
Stanford University, Palo Alto, California, USA

I. The Liver Transplantation Procedure 491
A. Preanhepatic Stage 491
B. Anhepatic Stage 492
C. Postanhepatic Stage 492
II. Role of Transesophageal Echocardiography 492
A. Preoperatively 493
1. Hepatopulmonary Syndrome 493
2. Portopulmonary Hypertension 493
3. Pericardial and Pleural Effusions 494
4. Cardiomyopathy 494
B. Intraoperatively 494
References 495

I. THE LIVER TRANSPLANTATION PROCEDURE

Orthotopic liver transplantation (OLT) involves the replacement of the recipient's liver by the donor graft in its normal anatomical location. There are three distinct stages during OLT, each characterized by hemodynamic, metabolic, and hematological phenomena.

A. Preanhepatic Stage

The preanhepatic stage begins with the skin incision and ends with the completion of the hepatic vascular dissection. Several problems may occur.

1. *Hypotension*. Preload may decrease for many reasons: First, surgical bleeding may occur due to portal hypertension with intra-abdominal and parietal venous dilation. Second, a preexisting coagulopathy may worsen due to blood replacement, lack of hepatic production of coagulation factors, platelets consumption or dilution, and ongoing hypothermia causing more blood loss. Lack of clearance of plasminogen activators due to ongoing hepatic dysfunction can accentuate fibrinolysis and aggravate the bleeding diathesis. Third, insensible fluid loss and formation of a third space due to a large wound will reduce the effective circulating volume. Finally, drainage of ascites, compression or torsion of major blood vessels, low systemic vascular resistance, preexisting right and left cardiac dysfunction worsened with arrhythmia from electrolyte disturbances, and acid–base abnormalities can also contribute to hemodynamic instability.
2. *Hypothermia* may develop from heat loss, administration of cold fluids, skin vasodilation from anesthetic agents and lack of heat production by the liver.

3. *Hypocalcemia* most commonly originates from citrate toxicity from the blood products. This can also contribute to the decrease in blood pressure.
4. *Hypoglycemia* results from decreased glucose production by the liver glycogenolysis.
5. *Metabolic acidosis* occurs secondary to impaired hepatic clearance of acidotic products.
6. *Reduced urine output* can be caused with hypotension, hypovolemia, fluid retention from stress hormones, and the hepatorenal syndrome.

B. Anhepatic Stage

The anhepatic stage begins with the occlusion of the suprahepatic vena cava, the infrahepatic vena cava, the portal vein, and the hepatic artery. An alternative procedure, called the piggy-back, preserves the retrohepatic vena cava: the liver is mobilized off the vena cava and only the hepatic veins are occluded during the anhepatic stage avoiding the drastic hemodynamic effects of caval occlusion (1).

In this stage, the problems described in the previous stage may worsen. Occlusion of the inferior vena cava dramatically reduces the venous return. It also produces congestion of the infracaval venous system which, in turn, may cause intestinal and renal congestion. A venovenous bypass using heparin-coated tubing connected to a vortex pump may be used to decompress both the portal vein and the inferior vena cava through the axillary vein (2).

The vena cava anastomosis is performed first. The hyperkaliemic preservation solution (Viaspan^{TM}) is flushed out of the graft with a colloid or crystalloid solution. The portal vein anastomosis is completed and the graft then reperfused. As a result, a cold, acidotic, hyperkaliemic fluid containing metabolically active byproducts is released from the graft into the systemic circulation. Hypotension, peaked T waves and dysrhythmias (blocks, asystole) may ensue, causing the so-called post-reperfusion syndrome (PRS). Its duration is usually short but may require aggressive resuscitation (Fig. 22.1).

C. Postanhepatic Stage

The postanhepatic stage usually has less potential for complications than the previous stages. The new liver gradually corrects the metabolic abnormalities. The hepatic artery and biliary anastomosis are performed.

II. ROLE OF TRANSESOPHAGEAL ECHOCARDIOGRAPHY

Transesophageal echocardiography (TEE) may be useful in many instances as patients with liver failure are at risk of altered cardiopulmonary condition (Table 22.1).

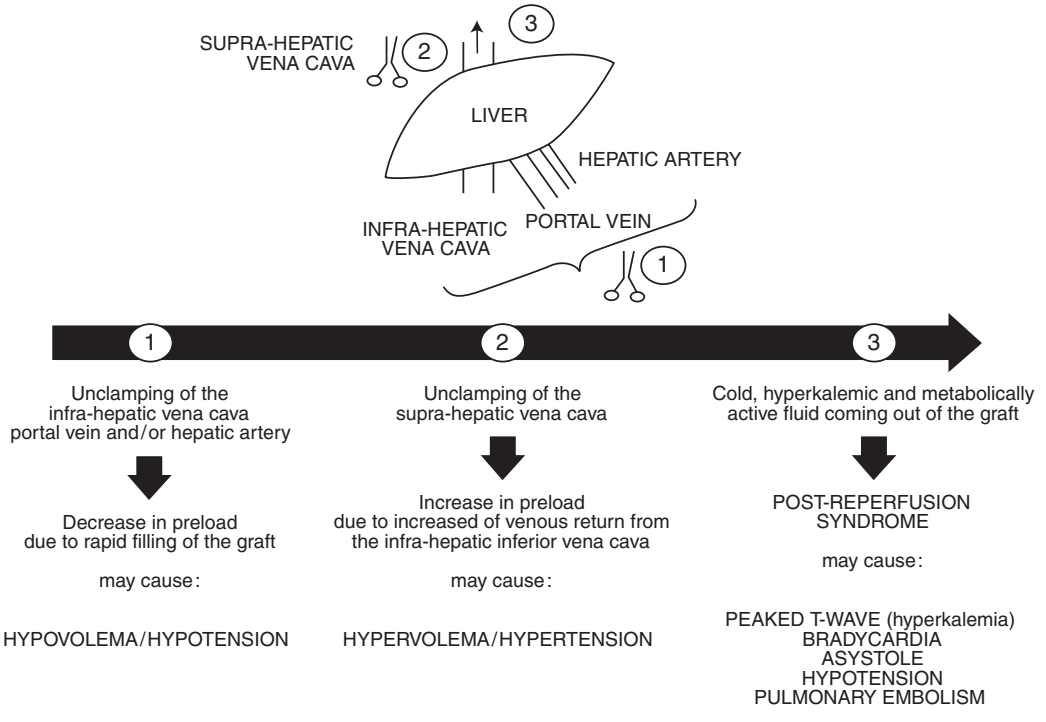

Figure 22.1 Unclampings of vascular anastomosis and hemodynamic consequences.

Table 22.1 Associated Cardiac and Hepatic Disorders

Heart diseases affecting the liver
Mild alterations of liver function tests in heart failure
Cardiogenic IH and its variants
CLF and congestive (cardiac) cirrhosis
Liver diseases affecting the heart
Hepatopulmonary syndrome
PPHTN in liver cirrhosis
Pericardial effusion in cirrhosis
Cirrhotic cardiomyopathy
High-output failure caused by intrahepatic arteriovenous fistulae in the noncirrhotic liver
Cardiac and hepatic disorders with joint etiology
Infectious and parasitic, metabolic, immune and vasculitic, toxic

Note: CLF, congestive liver fibrosis; IH, ischemic hepatitis; PPHTN, portopulmonary hypertension.
Source: With permission from Naschitz et al. (3).

A. Preoperatively

Hemodynamically, OLT is one of the most stressful surgeries for patients and a challenge for the anesthesiologist. Consequently, preoperative assessment of the cardiac function is of prime importance to ensure the best outcome possible. The patient with compensated end-stage liver failure usually presents a hyperdynamic state characterized by high cardiac output (CO), normal ejection fraction (EF), low systemic vascular resistance, and elevated heart rate. More specifically, anomalies due to the hemodynamic consequences of hepatic failure on the systemic and pulmonary circulation include: hepatopulmonary syndrome, plexogenic pulmonary hypertension, pericardial effusion, cardiomyopathy, and high-output heart failure caused by arteriovenous shunts.

1. Hepatopulmonary Syndrome

Symptomatic hepatopulmonary syndrome (HPS) occurs in ~15% of patient with end-stage liver failure (3) and may be reversed by OLT. Liver disorder provokes an imbalance between vasoconstricting and vasodilating mediators, as well as between hepatic factors controlling the endothelial cell growth: consequently, pulmonary capillary vessels grow and dilate. During their passage through the dilated pulmonary capillaries, red blood cells do not optimally pick up diffused oxygen in a patient breathing room air. Diffusion/perfusion mismatch causes hypoxemia. When the patient goes from a supine to an upright position, blood flow is increased in the lung bases, exacerbating hypoxemia. Orthodeoxia is defined as arterial desaturation accentuated in the upright position and improved by recumbence. This is often accompanied by platypnea, defined as dyspnea which is worse in the upright position and relieved by recumbence (Fig. 22.2).

Contrast-enhanced echocardiography with intravenous injection of agitated saline is the current gold standard for detection of pulmonary vascular dilations (3). Bubbles are usually trapped in the pulmonary circulation capillaries and are not seen in the left cardiac chambers. If an intracardiac shunt exists (such as an atrial septal defect), contrast bubbles will appear in the left atrium (LA) within three beats after their appearance the right atrium (RA). In the case of HPS, contrast will appear in the LA after four to six beats.

2. Portopulmonary Hypertension

Although not a common disease in liver failure, portopulmonary hypertension (PPHTN) can severely affect the outcome of OLT. The mechanisms are unknown. The severity appears to be related to the duration of portal hypertension and as in the case of HPS, substances not

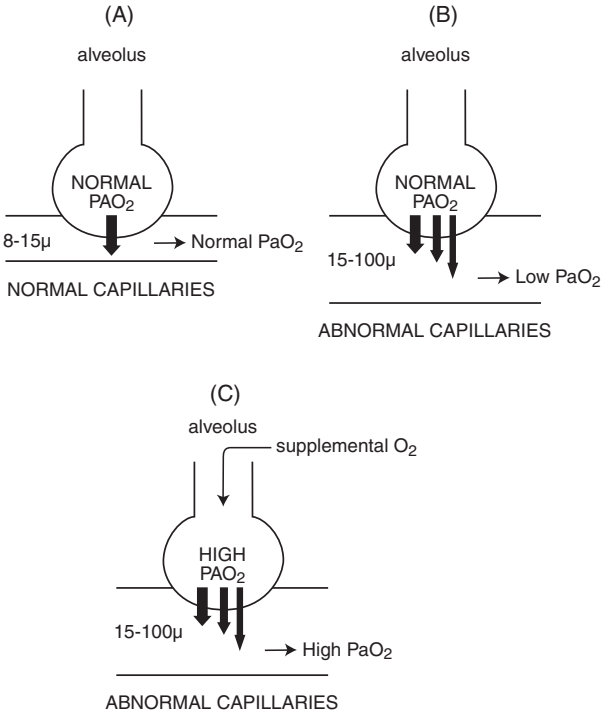

Figure 22.2 Anomalies of the vascular pulmonary bed in the hepatopulmonary syndrome. Compared with normal capillaries and alveolus (A), in the hepatopulmonary syndrome capillaries become dilated and blood does not receive diffused oxygen in a patient breathing room air causing hypoxemia (B). If the patient goes from a supine to a standing position, blood flow is increased at the lung base exacerbating hypoxemia and causing orthodeoxia and platypnea. As this is improved by supplemental oxygen, it represents severe diffusion-perfusion mismatch rather than true shunting (C). (PaO_2, oxygen partial pressure).

cleared by the liver (coming from the splanchnic blood) might cause those vascular changes.

On echocardiography, the diagnosis of PPHTN should be considered in the presence of signs of pulmonary hypertension such as dilated RA or ventricle, pulmonary valvular insufficiency, or abnormal ventricular septal curvature towards the left ventricle (LV).

3. Pericardial and Pleural Effusions

Pericardial and pleural effusions due to fluid retention are frequently seen in decompensated liver disease and echocardiography is a useful tool to assess the presence of pericardial effusion in those patients.

4. Cardiomyopathy

The hyperdynamic state imposes an increased left ventricular work (4). As previously mentioned, OLT presents one of the most important hemodynamic stressful procedure. Therefore, preoperative assessment of the LV function before the procedure is a mandatory part of the work-up.

B. Intraoperatively

Transesophageal echocardiography can be used during OLT for assessment of left and right ventricular filling, left and right ventricular global function (ejection fraction), detection of ischemia, regional wall motion abnormalities, and monitoring of embolic phenomenon.

Right ventricular (RV) failure may account for some of the hemodynamic instability during OLT (4). Furthermore, as pulmonary hypertension may also be present in many of the OLT patients, rapid shifts in intravascular volume with transfusions and clamping of vessels may be poorly tolerated by the RV. As central venous pressure (CVP) is an incomplete and unreliable method for monitoring right ventricular preload and function, TEE provides useful information on right ventricular filling pressure, global function and response to therapy.

As with CVP for the RV, the pulmonary capillary wedge pressure (PCWP) presents several shortcomings as an indicator of LV volumes. Measurement of end-diastolic volume with TEE is a better reflection of left ventricular preload. During OLT, TEE has shown significant changes in end-systolic and end-diastolic volumes without changes in ejection fraction. This suggests that left ventricular function was maintained and that hypovolemia was the most likely cause of hypotension (5).

Patients with end-stage liver disease may present myocardial ischemia. During OLT, the development of abnormal segmental wall motion indicative of myocardial ischemia has been described (5,6), probably from coronary emboli. Patients with HPS are at risk for paradoxical embolization through dilated pulmonary vessels with subsequent arterial occlusions in the coronary and cerebral circulation (7). Reperfusion of the new liver carries not only fluid thought to be responsible for the PRS syndrome, but also embolic material into the systemic circulation. As the surgeon's hands move near the TEE probe to carry out the unclampings, it is difficult to maintain a stable view of the heart and to find out exactly how the heart behaves during the few seconds following graft reperfusion. After reperfusion, the recipient frequently presents increased systemic vasodilatation with ensuing hypotension requiring vasopressors.

Although left ventricular global systolic function is maintained (8), some patients may present diastolic dysfunction after reperfusion. The LV filling pressures are higher after reperfusion while the end-diastolic volume is not changed significantly. This change in left ventricular compliance may be due to toxic effects related to the graft fluid or cardiac edema secondary to massive volume infusion of blood products, crystalloids, and colloids. Transesophageal echocardiography is also useful in making the diagnosis of pulmonary embolism and fresh thrombus formation in the RV after reperfusion (Fig. 22.3) (9).

Flow obstruction at the supra hepatic venal caval anastomosis can be assessed by two-dimensional TEE,

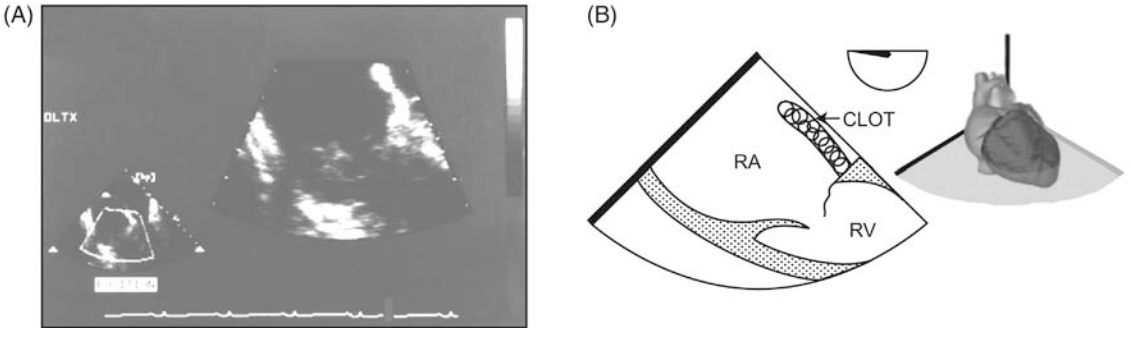

Figure 22.3 Mid-esophageal four-chamber view in a 44-year-old man undergoing liver transplantation: within 5 min after reperfusion, a large thrombus in the right atrium (RA) is seen attached to the tricuspid valve (RV, right ventricle). [Adapted with permission from Gologorsky et al. (9).]

but the permeability of the hepatic artery and portal vein is best assessed by color flow imaging (10–12).

The clinical impact of 100 TEE examinations during liver transplantation was reported by Suriani et al. (13). In their experience, unanticipated findings during the initial TEE examination, as well as the evaluation of intraoperative events resulted in a major impact on patient management in 11% of patients. Despite the increased prevalence of esophageal varices in liver failure patients, only one OLT recipient suffered from upper gastrointestinal bleeding. This suggests that the benefits of TEE in liver transplantation outweigh the risks and that TEE may become important, if not essential, as a monitoring tool in patients undergoing this procedure.

REFERENCES

1. Busque S, Esquivel CO, Concepcion W, So SK. Experience with the piggyback technique without caval occlusion in adult orthotopic liver transplantation. Transplantation 1998; 65:77–82.
2. Shaw BW Jr, Martin DJ, Marquez JM et al. Venous bypass in clinical liver transplantation. Ann Surg 1984; 200:524–534.
3. Naschitz JE, Slobodin G, Lewis RJ et al. Heart diseases affecting the liver and liver diseases affecting the heart. Am Heart J 2000; 140:111–120.
4. Ellis JE, Lichtor JL, Feinstein SB et al. Right heart dysfunction, pulmonary embolism, and paradoxical embolization during liver transplantation. A transesophageal two-dimensional echocardiographic study. Anesth Analg 1989; 68:777–782.
5. de la Morena G, Acosta F, Villegas M et al. Transesophageal echocardiographic evaluation of left ventricular function during orthotopic liver transplantation. Transplant Proc 1993; 25:1832.
6. Steltzer H, Blazek G, Gabriel A et al. Two-dimensional transesophageal echocardiography in early diagnosis and treatment of hemodynamic disturbances during liver transplantation. Transplant Proc 1991; 23:1957–1958.
7. Gronert GA, Messick JM Jr, Cucchiara RF, Michenfelder JD. Paradoxical air embolism from a patent foramen ovale. Anesthesiology 1979; 50:548–549.
8. Kuo PC, Schroeder RA, Vagelos RH et al. Volume-mediated pulmonary responses in liver transplant candidates. Clin Transplant 1996; 10:521–527.
9. Gologorsky E, De Wolf AM, Scott V et al. Intracardiac thrombus formation and pulmonary thromboembolism immediately after graft reperfusion in 7 patients undergoing liver transplantation. Liver Transpl 2001; 7:783–789.
10. Bjerke RJ, Mieles LA, Borsky BJ, Todo S. The use of transesophageal ultrasonography for the diagnosis of inferior vena caval outflow obstruction during liver transplantation. Transplantation 1992; 54:939–941.
11. De Wolf AM, Scott VL, Kang Y et al. Hepatic venous outflow obstruction during hepatic resection diagnosed by transesophageal echocardiography. Anesthesiology 1994; 80:1398–1400.
12. Rumi MN, Schumann R, Freeman RB et al. Acute transjugular intrahepatic portosystemic shunt migration into pulmonary artery during liver transplantation. Transplantation 1999; 67:1492–1494.
13. Suriani RJ, Cutrone A, Feierman D, Konstadt S. Intraoperative transesophageal echocardiography during liver transplantation. J Cardiothorac Vasc Anesth 1996; 10:699–707.

23

Intracavitary Contents

MARIA DI LORENZO, ROBERT AMYOT, RÉAL LEBEAU, CLAUDE SAUVÉ
University of Montreal, Montreal, Canada

I. Normal Variant 497
A. Embryological Remnants 498
B. Anatomical Structures 498
1. Atrial Appendages 498
2. Transverse Sinus 499
3. Intraventricular Bands and Chords 500
C. Lipomatous Infiltration of the Heart 500
D. Anomalous Left Superior Vena Cava 502
II. Atrial Septal Aneurysm 503
III. Primary Cardiac Neoplasm 503
A. Benign Cardiac Tumors 504
1. Myxomas 504
2. Fibromas 505
3. Rhabdomyomas 505
4. Lipomas 505
5. Papillary Fibroelastomas and Lambl's Excrescences 506
6. Hemangiomas 508
B. Malignant Cardiac Tumors 508
1. Thymomas 508
2. Lymphomas 508
3. Angiosarcomas 509
4. Rhabdomyosarcomas 510
5. Primary Extraskeletal Osteosarcomas 510
6. Mesotheliomas 511
IV. Noncardiac Neoplasm Invading the Heart 511
V. Calcified Structures 512
VI. Extracardiac Masses 512
A. Pericardial Cyst 512
B. Miscellaneous 512
VII. Intussusception of the Left Atrial Appendage 512
VIII. Intracardiac Thrombi 513
A. Left Ventricular Thrombus 513
B. Left Atrial Thrombus 513
C. Left Atrial Thrombus in Patients in Sinus Rhythm 516
D. Right Atrial Thrombus 517
E. Right Ventricular Thrombi 517
F. Biventricular Thrombi 517
IX. Man-Made Objects in the Heart 517
X. Vegetations 517
A. Echocardiographic Appearance of a Vegetation 519
XI. Patent Foramen Ovale 521
A. Ultrasound Contrast Technique 522
References 522

I. NORMAL VARIANT

Transesophageal echocardiography (TEE) has become a powerful clinical tool that offers a wide range of diagnostic capabilities. It is, however, important to acknowledge its limitations. Although the improvement in image quality heightens our ability to detect cardiac masses,

echocardiography still cannot define the histologic composition of these masses.

Information about the size, location, origin, site of attachment, consistency, mobility of a mass, as well as associated heart disease can lead to a differential diagnosis that will suggest the most likely diagnosis. Using both clinical data and echocardiographic findings can then lead to the best therapeutic approach.

A. Embryological Remnants

Previous knowledge of normal variants is necessary in order to recognize pathologic masses within the heart. A number of masses within the right atrium (RA) are in fact remnants of the sinus venosus. They are developmental structures that have regressed to various degrees leaving behind structures such as the Chiari network and the Eustachian valve and should not be mistaken for pathological masses. Their potential for catheter entrapment, embolization, and arrhythmias should be recognized.

The sinus venosus is a venous collector that evolves into a common atrium early in gestation. The smaller left valve usually resorbs completely while the larger right valve, which separates the RA into two chambers, can persist to variable degrees. In the rare cases where little regression of the right valve of the sinus venosus occurs, a fibrous band remains, extending from the inferior to the superior vena cava (SVC), leading to the condition also known as cor triatriatum dexter. This is a rare congenital anomaly where a complete septation of the RA results in two chambers: a superomedial and inferolateral compartments. In certain cases, this septation can cause obstruction to flow.

More commonly, a more advanced but still incomplete resorption of the right valve gives rise to a Chiari network (see Fig. 6.22). Found in 2–3% of normal hearts at autopsy, this perforated membranous remnant of the valve of the coronary sinus (CS) appears as a delicate, highly mobile, serpentine filamentous structure within the RA, originating from the junction of the inferior vena cava (IVC) with the RA and extending to the atrial septum or to the opening of the CS. Its undulations appear random and unrelated to valve motion. The Chiari network is seldom clinically important. Rarely, it can act as a nidus of thrombus formation. It can be associated with a patent foramen ovale. It is important to recognize this anatomical variant to avoid misdiagnosing a flail tricuspid leaflet, a tricuspid valve (TV) vegetation, or a pedunculated tumor or thrombus.

The Eustachian valve is another embryological remnant of the right valve of the sinus venosus. It is particularly useful in the fetal life to direct blood from the IVC into the left atrium (LA) via the patent foramen ovale (PFO) (see Fig. 6.21). This valve can be at times very large and is best seen at the base of the heart at 90° in the longitudinal axis. It is located at the junction of the IVC and the RA and shows variable length and mobility. Rarely, it can be the site of infective endocarditis (Fig. 23.1) (1).

A left cor triatriatum (Fig. 23.2) is an uncommon congenital anomaly. It is an embryologic remnant consisting of a fibromuscular diaphragm separating the LA in two chambers. The posterosuperior proximal chamber usually receives the pulmonary veins while the anteroinferior chamber contains the mitral orifice and the left atrial appendage (LAA). Communication between the two chambers can be free, absent, or obstructed to variable degrees. The severity of symptoms correlates with the degree of obstruction. Complete thrombosis of one of the chambers simulating a left atrial myxoma has been reported (2).

B. Anatomical Structures

1. *Atrial Appendages*

The right atrial appendage (RAA) is an irregular pyramidal structure with a broad-based opening into the RA. It has

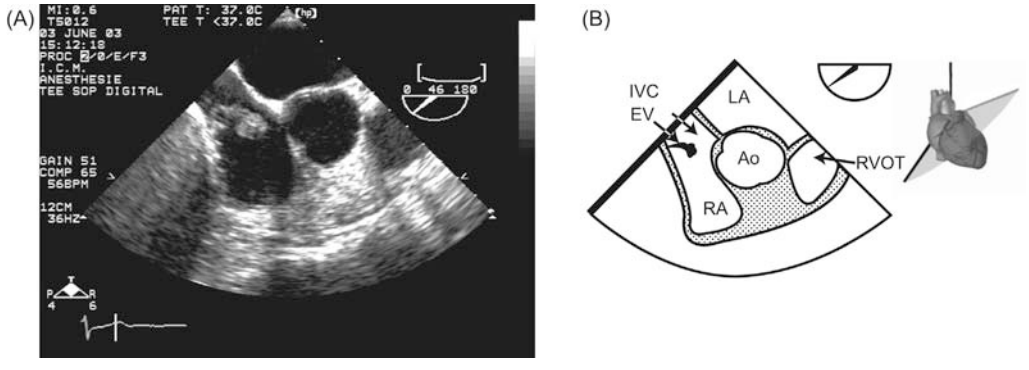

Figure 23.1 A 47-year-old woman diagnosed with pacemaker endocarditis. Following removal of the pacing wire, echodense vegetations were seen at the tip of the Eustachian valve (EV) (Ao, aorta; IVC, inferior vena cava; LA, left atrium; RA, right atrium; RVOT, right ventricular outflow tract).

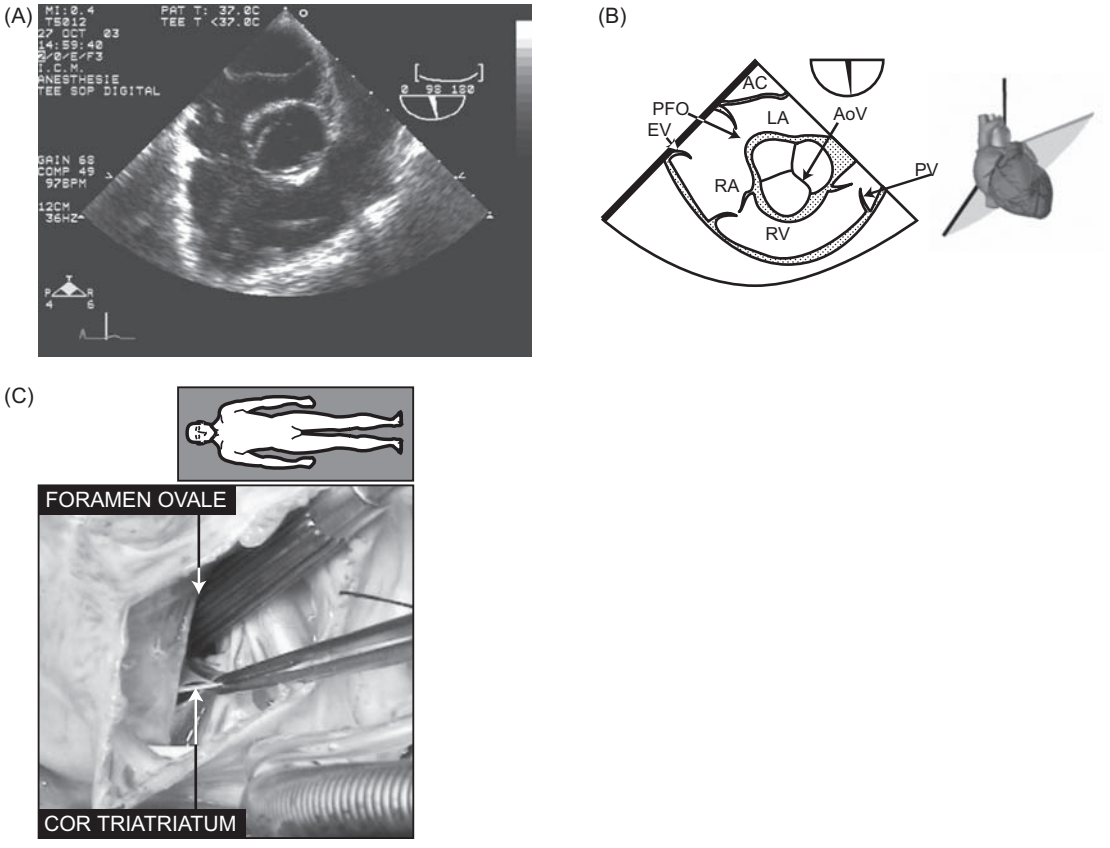

Figure 23.2 (A, B) Mid-esophageal 98° view of a classic cor triatriatum scheduled for repair in a 49-year-old woman. Note the presence of an Eustachian valve (EV). (C) Intraoperative view through a right atriotomy of the cor triatriatum (AC, atrial chamber; AoV, aortic valve; LA, left atrium; PFO, patent foramen ovale; PV, pulmonic valve; RA, right atrium; RV, right ventricle). (Photo C courtesy of Nancy Poirier.)

readily visible prominent trabeculations known as pectinate muscles, which could be confused with thrombus or tumor (see Fig. 6.17).

The LAA is classically described as a triangular-shaped cavity. In fact, it is multilobulated in >80% of cases. The trabeculations or pectinate muscles are confined to the body of LAA and may occasionally appear to cross the lumen. Less prominent than in the RAA, they can nevertheless reach a few millimeters in length (see Fig. 6.16). These trabeculations could also be mistaken for pathological masses.

Left atrial appendage size, shape, and degree of lobulation, as well as the size of the pectinate muscles vary significantly among individuals. The presence of atrial fibrillation and atrial dilatation also influences the size and shape of the LAA (3). Multiplane probes allow a more complete assessment of LAA structure by scanning from an angle of 0–180°. The ostium and the body of the LAA is best visualized in the mid-esophageal views at 0–60° (see Fig. 4.4), but inspection of accessory lobes often requires checking orthogonal views at 90–150°.

A ridge of tissue known as the "Q-tip" represents a partition between the LAA and left superior pulmonary vein. It is narrower at its base and becomes wider at the tip. It should not be confused with a tumor although the free edge of the "Q-tip" has been reported as a site of attachment of tumors such as fibroelastomas or myxomas (4). Careful inspection of the "Q-tip" with regard to its homogeneity, shape, consistency, mobility, as well as the clinical setting can help differentiate this normal structure from a pathological mass arising at its tip (Figs. 23.3 and 23.4)

2. *Transverse Sinus*

Near the LAA can be found the transverse sinus (see Fig. 6.26), a recess of the pericardium seen between the ascending aorta (Ao), the main pulmonary trunk and the LA. The transverse sinus is best imaged at the base of the heart in a short-axis view between the LA and its appendage. Occasionally, fatty infiltration of the pericardium, or even thrombus in the transverse sinus, may look as a thrombus sitting in the main LAA body or one

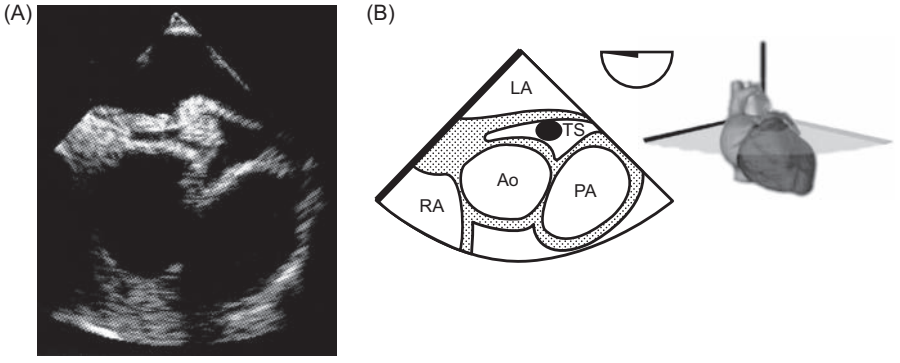

Figure 23.3 Fatty tissue in the transverse sinus (TS) (Ao, aorta; LA, left atrium; PA, pulmonary artery; RA, right atrium). [With permission of Oh et al. (5).]

of its accessory lobes (Fig. 23.5). Rarely, partial absence of the pericardium gives rise to an abnormally large LAA which cannot be completely visualized.

3. Intraventricular Bands and Chords

The moderator band is a structure located at the apical third of the right ventricle (RV), extending from the lateral free wall to the septum. This prominent muscular trabeculation or ridge found only in the RV, is best visualized in the mid-esophageal four-chamber view. Multiple muscle bundles along the endocardial surface of the RV are also frequently present, giving it its typical trabeculated appearance. When hypertrophied, these ventricular trabeculae can become so prominent in the RV that they may be confused with pathological masses (Fig. 23.6).

False tendons or aberrant bands or chords are fibrous structures crossing the left ventricular cavity with or without coexisting heart disease. Unlike true chordae tendinae which originate from papillary muscles, these ectopic chordae appear as linear echo-dense structures extending either from free wall to free wall or from free wall to the ventricular septum. They are anatomic variants of no clinical significance (Fig. 23.7).

C. Lipomatous Infiltration of the Heart

Accumulation of fibro-fatty tissue can occur in several locations within the heart. The diagnosis of lipomatous hypertrophy of the atrial septum is made when its wall thickness is >15 mm. The thickened atrial septum shows a rather homogenous and bright echogenicity. Because the fibro-fatty infiltration spares the fossa ovalis, the atrial septum has the typical appearance of a dumb-bell (Fig. 23.8). This is a benign finding requiring no specific treatment. However, infiltration of the atrial septum by tumors or Hodgkin's lymphoma has also been described. The concomitant presence of a pericardial effusion, abnormal thickening of the walls of the Ao, the pulmonary veins or other adjacent structures as well as an inhomogeneous echotexture or a suspicion of a coin lesion within the septum makes the diagnosis of benign lipomatous infiltration less likely (6).

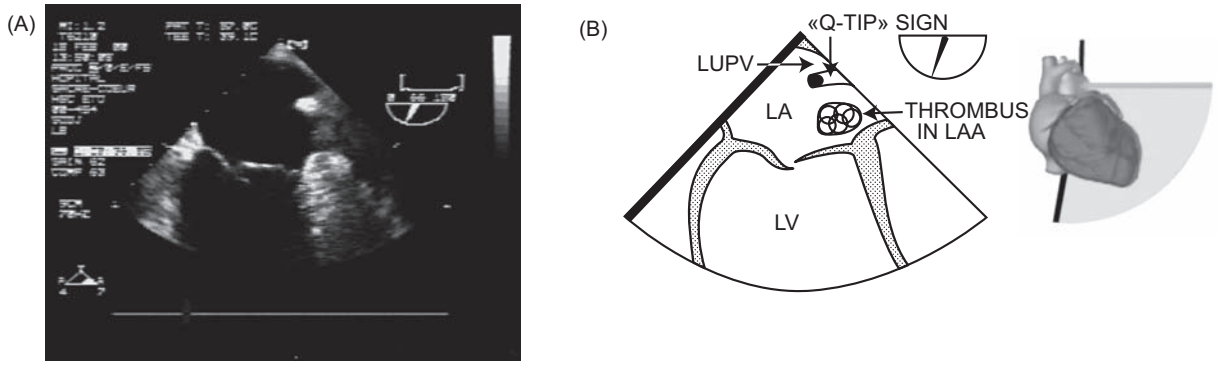

Figure 23.4 Mid-esophageal 66° view of the left ventricle (LV) showing the "Q-tip" sign or appearance of the junction of the left atrial appendage (LAA) and left upper pulmonary vein (LUPV). Note also the thrombus in the LAA (LA, left atrium).

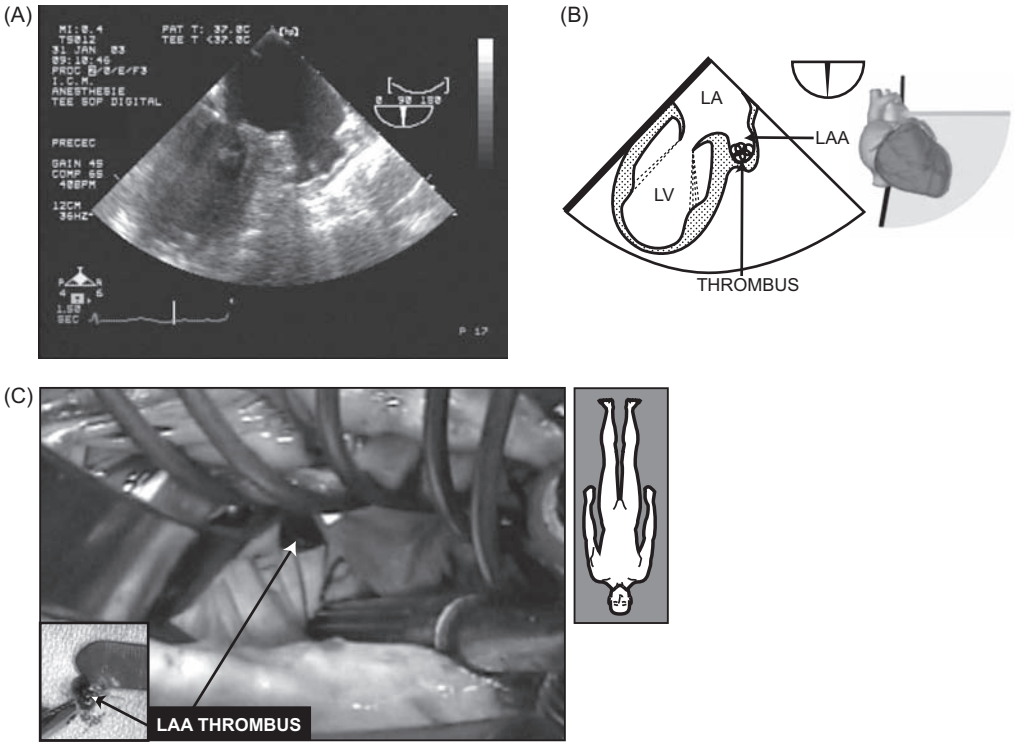

Figure 23.5 (A, B) A 63-year-old woman is scheduled for mitral and tricuspid valve surgery. A mid-esophageal view was suggestive of a thrombus in the left atrial appendage (LAA). (C) Upon opening the left atrium (LA) a small thrombus was seen and removed (LV, left ventricle).

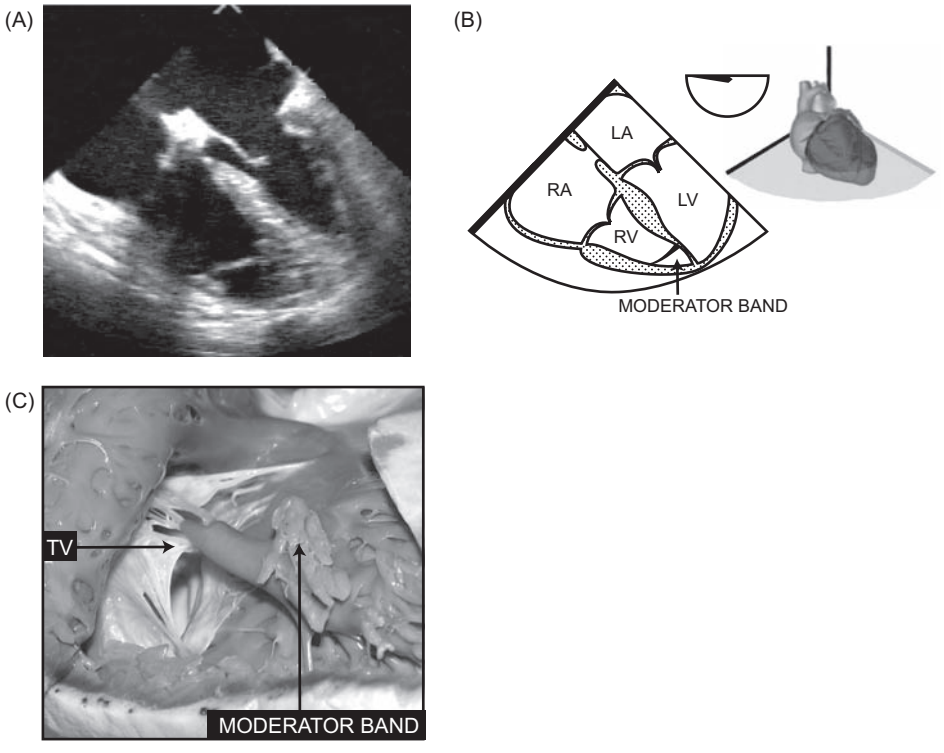

Figure 23.6 Moderator band. (A, B) Dilatation of the right ventricle (RV) facilitates visualization of the moderator band in this four-chamber view of the heart. Note the densely trabeculated aspect of the right ventricular apex. (C) Anatomical aspect of the moderator band (LA, left atrium; LV, left ventricle; RA, right ventricle; TV, tricuspid valve). (Photo C courtesy of Dr. Nicolas Dürrleman.)

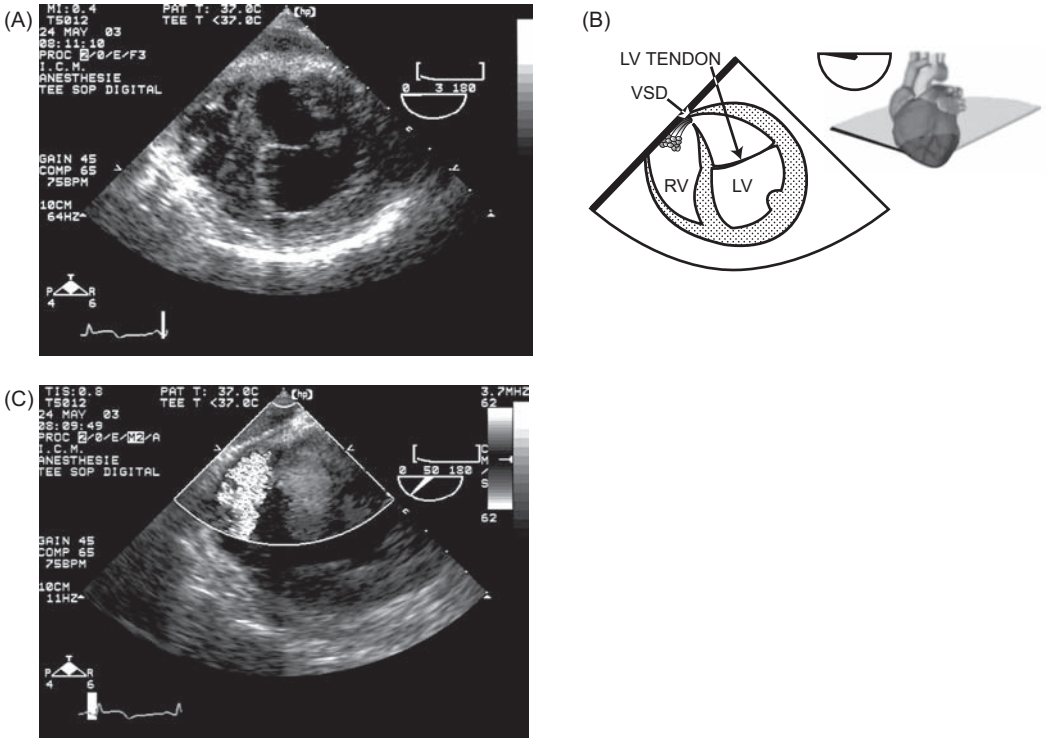

Figure 23.7 (A, B) Transgastric mid-papillary view in a 67-year-old woman with a ventricular septal defect (VSD). Note the left ventricular tendon seen close to the VSD. (C) A left-to-right shunt was present (LV, left ventricle; RV, right ventricle).

Significant lipomatous infiltration can also occur around the tricuspid annulus, simulating a mass effect. Periaortic fat accumulation, mostly around the descending Ao needs to be differentiated from thrombus filling a false lumen.

D. Anomalous Left Superior Vena Cava

A persistent left SVC can be found in 0.3–0.5% of normal individuals and in 3–10% of patients with other congenital anomalies (7). It is visualized between the left upper pulmonary vein and the LAA. The left SVC drain to the LA, or to the RA via the CS which secondarily will appear dilated. The diagnosis of a left SVC draining in the CS can be made by injecting agitated saline in the left upper extremity. The microbubbles are first seen in the left SVC and the CS followed by opacification of the RA. The recognition of the presence of a left SVC is important as cannulation of the CS may have significant different consequences in patients undergoing pulmonary

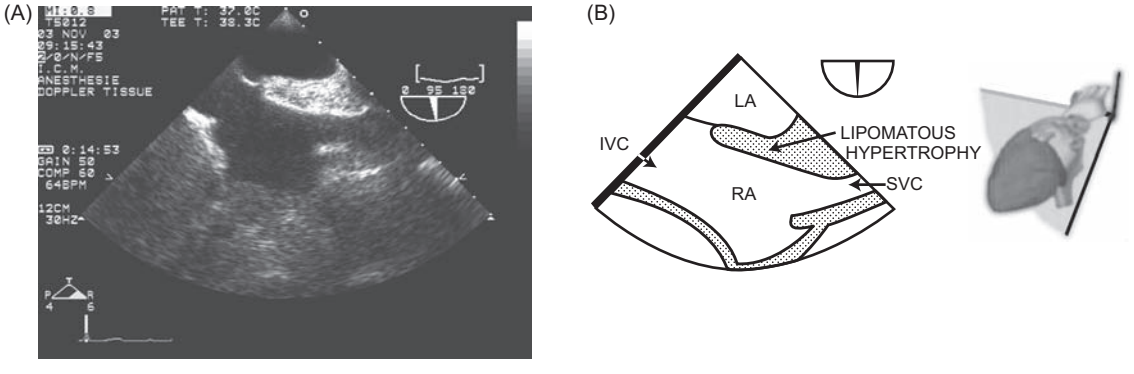

Figure 23.8 Lipomatous hypertrophy of the interatrial septum (IVC, inferior vena cava; LA, left atrium; RA, right atrium; SVC, superior vena cava).

artery catheterization, pacemaker insertion, or when cardioplegia is given into the CS (see Fig. 6.23).

II. ATRIAL SEPTAL ANEURYSM

The presence of an atrial septal aneurysm is found in 1% of adults at autopsy. The redundancy of the atrial septum may present as a fixed protruding bulge or a mobile aneurysm. By definition, the deviation of the septum from the median plane should exceed at least 11 mm while the base of the aneurysm should measure at least 15 mm (8). In the case of mobile aneurysms, the excursion of the septum measured from the extreme right to the extreme left should reach at least 15 mm. When the atrial septal aneurysm is fixed, the septum is usually deviated towards the atrium with the lower atrial pressure. Mobile atrial septal aneurysms exhibit a phasic excursion alternatively to the right and to the left as the pressure gradient between the two atria varies according to respiration and the phase of the cardiac cycle. Atrial septal aneurysms are usually found in the area of the fossa ovalis. In many cases, these aneurysms represent an incidental finding (Fig. 23.9). They have been associated with an increased risk of embolic events as thrombus may form within the concavity of the aneurysm. Some degree of shunt can be seen in up to 90% of cases with the theoretical associated risk of paradoxical embolus: therefore the presence of a shunt at the atrial level should always be sought (8). This is particularly important in young patients presenting with unexplained peripheral or cerebral emboli. The best view for identifying an atrial septal aneurysm by TEE is the bicaval long-axis view at the level of the atrial septum at an angle of 90–110°. The atrial septal aneurysm can also be visualized in the mid-esophageal four-chamber view at 0° (Fig. 23.9).

III. PRIMARY CARDIAC NEOPLASM

Tumors in the heart most often represent metastases from other primary neoplasms, while primary cardiac tumors are much less common with a prevalence of 0.02% reported in a large autopsy series (9). Benign tumors account for 75% of all primary cardiac tumors, three times as frequent as malignant tumors. Myxoma, the most common benign tumor, has an incidence of ~0.5 per million population per year. On the other hand, the majority of malignant primary cardiac tumors are constituted by sarcomas. While tumors involving the heart may be intracavitary, intramural, or extracardiac, most atrial tumors present as an intracavitary mass, whereas ventricular tumors are more commonly intramural (Fig. 23.10).

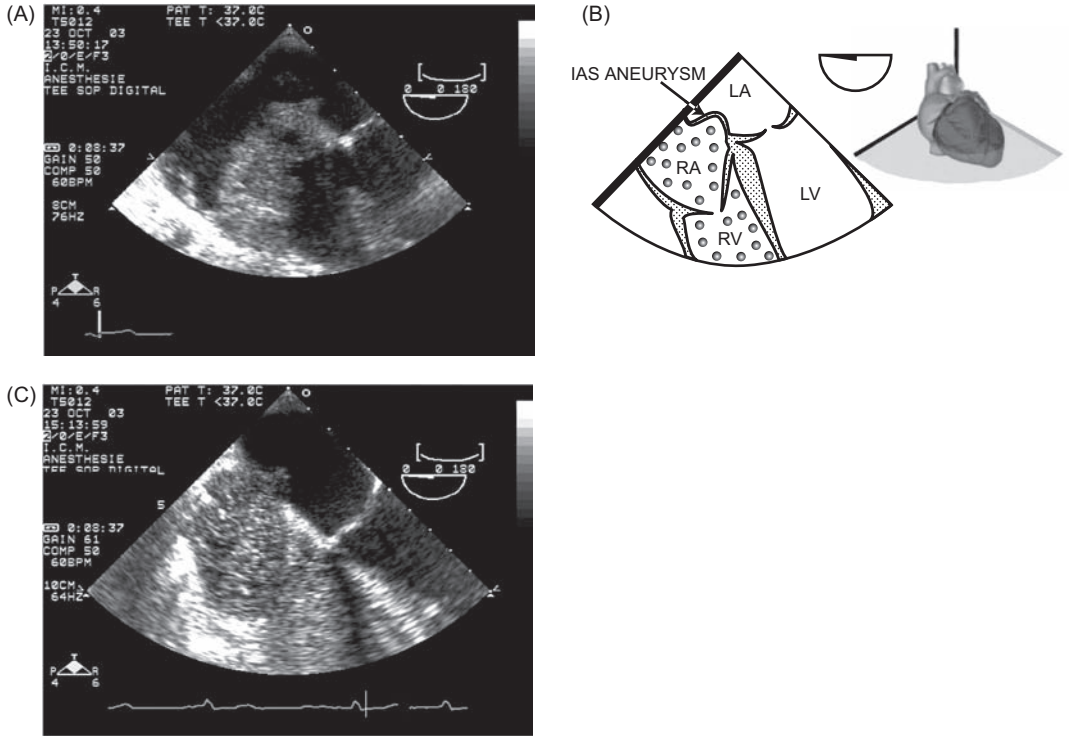

Figure 23.9 (A, B) A 57-year-old woman with atrial septal aneurysm. (C) A contrast study was obtained to rule out suspected interatrial communication (IAS, interatrial septum; LA, left atrium; LV, left ventricle; RA, right atrium; RV, right ventricle).

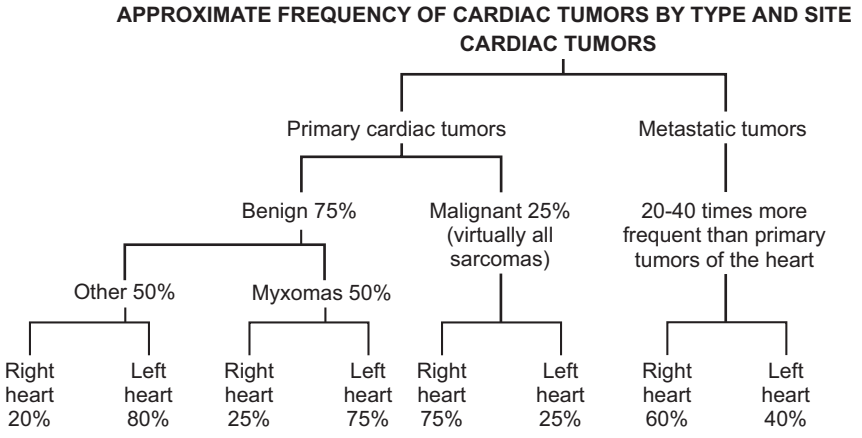

Figure 23.10 Classification of cardiac tumors. [Adapted with permission from Gopal et al. (9).]

A. Benign Cardiac Tumors

1. Myxomas

Myxomas constitute nearly 50% of all histologically benign tumors of the heart. They are usually pedunculated, polypoid, and friable. Some may have a smooth surface and may be round. These tumors generally have a jellylike, globular appearance. Echo-free spaces may be present within the mass, corresponding to areas of hemorrhage or necrosis. Areas of calcification can also be seen. At the time of diagnosis, myxomas have an average size of 4–8 cm but have been known to reach up to 15 cm.

Approximately 75% of cardiac myxomas classically involve the LA, presenting as a mobile echogenic mass found in the body of the LA, usually attached to the atrial septum by a stalk in the region of the fossa ovalis (Figs. 23.11 and 23.12). An additional 10% arise from other sites within the LA including the posterior, the anterior wall or the LAA. Most of the remainder of myxomas originate from the RA; the right or left ventricle (LV) is implicated in ~5% of the series. Some cases, arising from the mitral valve and the IVC, have also been reported. The diagnosis may be difficult to establish when the stalk is short and difficult to visualize, when the tumor is not very mobile or when the myxoma arises from an atypical location (9,10).

Transesophageal echocardiography is highly sensitive to detect left atrial tumors and is particularly useful in delineating the attachment or the stalk of the tumor, a significant contribution to narrowing the differential diagnosis. Beside accurate description of the size, shape, location, and attachment of the myxoma, TEE can also evaluate the degree of mitral inflow obstruction by the mass. Tumors with a long pedicle can be seen moving back and forth through the mitral orifice during the cardiac cycle.

Right atrial myxomas tend to be broader-based than left-sided tumors and involve a larger area of the atrial wall or septum. Ventricular myxomas may originate from the ventricular septum with either a pedunculated or sessile appearance.

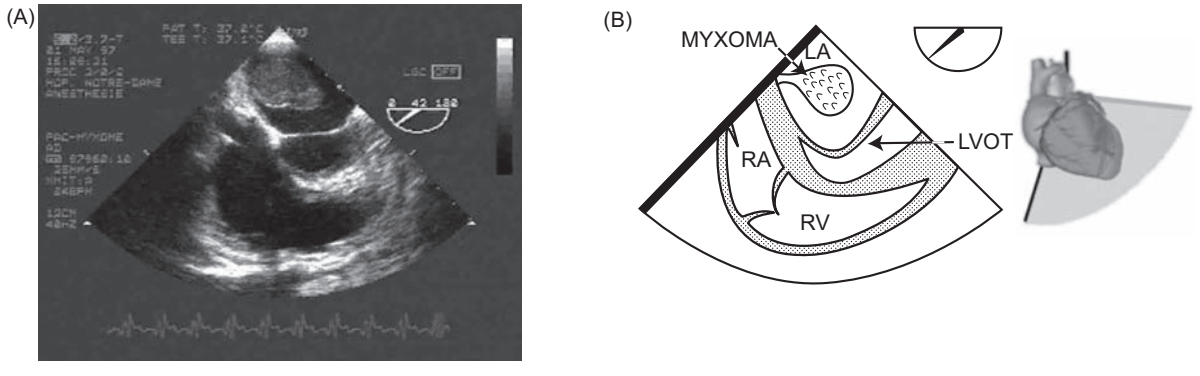

Figure 23.11 Mid-esophageal 42° view of a left atrial myxoma before surgical resection. Note that the pedicle of the myxoma is attached to the interatrial septum (LA, left atrium; LVOT, left ventricular outflow tract; RA, right atrium; RV, right ventricle).

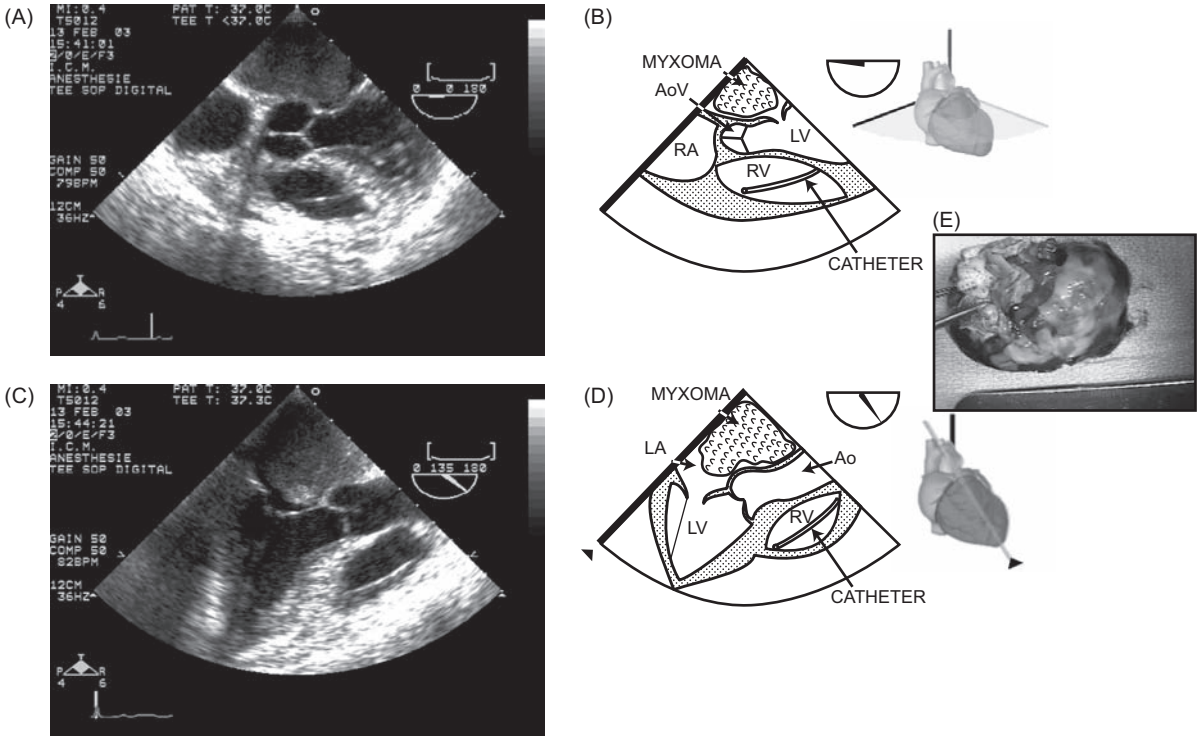

Figure 23.12 (A–D) Mid-esophageal views of a 61-year-old woman with a large left atrial myxoma occupying almost all the atrial cavity. (E) Intraoperative aspect (Ao, aorta; AoV, aortic valve; LA, left atrium; LV, left ventricle; RA, right atrium; RV, right ventricle).

Multiple tumors can be found in the same chamber or in different chambers. As multifocal myxomas have been reported in up to 5% of patients, a complete examination of all four chambers is mandatory. The most common pattern is biatrial. Recurrence of tumors after surgical resection has been reported in 5–14% of cases, at the site of the original tumor, at multiple intracardiac sites, or even at extracardiac sites (10–12). Serial follow-up echocardiographic studies are, therefore, recommended after surgical treatment.

2. *Fibromas*

Nearly all cardiac fibromas present as a solitary mass involving the ventricular myocardium, frequently in the septum, the apex or the LV free wall. Sometimes, they grow within the LV cavity and interfere with filling. On two-dimensional (2D) echocardiography, they are recognized as a large mass of echoes well demarcated from the surrounding myocardium by multiple calcifications (Fig. 23.13) (5), which may be difficult to differentiate from a solitary rhabdomyoma. When located at the apex, they can mimic the apical form of hypertrophic cardiomyopathy. Cardiac fibromas can occur in patients of all ages and sexes. They are more frequent in children, being the second most common primary cardiac tumor in the pediatric age group (10–12).

3. *Rhabdomyomas*

Rhabdomyomas represent the most common benign cardiac tumors in infants and children. It is uncommon to find them at the atrial level as they tend to occur in the ventricles. No cases of rhabdomyomas attached to the valves have been reported. Most patients have multiple tumors occurring with nearly equal frequency in the RV and LV, including the ventricular septum. They can be intramural or intracavitary. Rhabdomyomas can present as a solitary intramural echodense mass in the ventricular septum or the LV free wall. A strong association between rhabdomyomas and tuberous sclerosis have been described (11,12).

4. *Lipomas*

Cardiac lipomas occur most frequently in the LV or the RA but can be seen throughout the heart including the pericardium. Rarely, they have also been found attached to the valves. These benign tumors occur at all ages and are seen with equal frequency in men and women. Cardiac lipomas can be subendocardial and have a sessile appearance. They can also present as a large subepicardial pedunculated mass. Approximately 25% of lipomas are completely intramyocardial. Compared with LV myxomas, lipomas are less mobile and generally more echodense but the

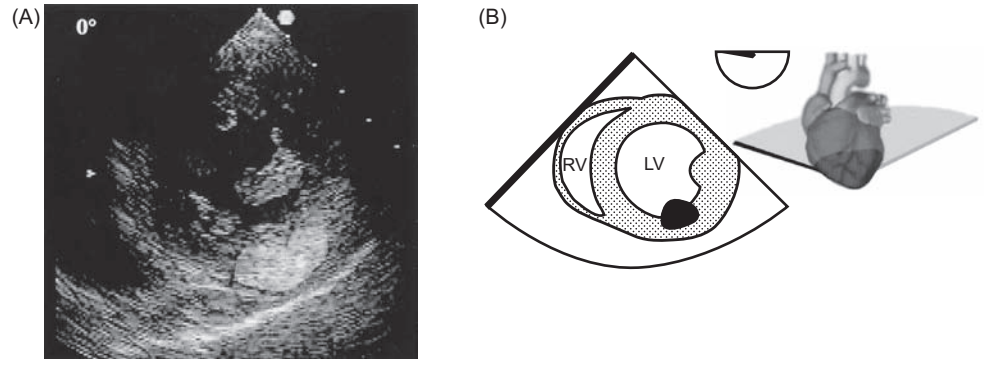

Figure 23.13 Transgastric mid-papillary view of a left ventricular cardiac fibroma (LV, left ventricle; RV, right ventricle). [With permission from Churchill Livingstone Inc. (13).]

echocardiographic diagnosis of a lipoma remains difficult as it can mimic myxomas, fibromas, papillary fibroelastomas, and thrombi. Magnetic resonance imaging (MRI) may help confirm the fatty nature of the tumor (11,12).

5. *Papillary Fibroelastomas and Lambl's Excrescences*

Papillary fibroelastomas or papillomas are benign tumors that are clinically important because of their potential for systemic embolization. They represent a small fraction of all primary cardiac tumors but are the most common type of primary valve tumor. They can still be found anywhere in the heart (Figs. 23.14 and 23.15) and have been described in atypical locations such as the LAA (14). They can occur in any age group although they are most common in patients >60 years of age, usually affecting the aortic valve (AoV). Fibroelastomas tend to arise in areas of endocardial damage such as the sites of valvular sclerosis, rheumatic heart disease, or cardiac surgery.

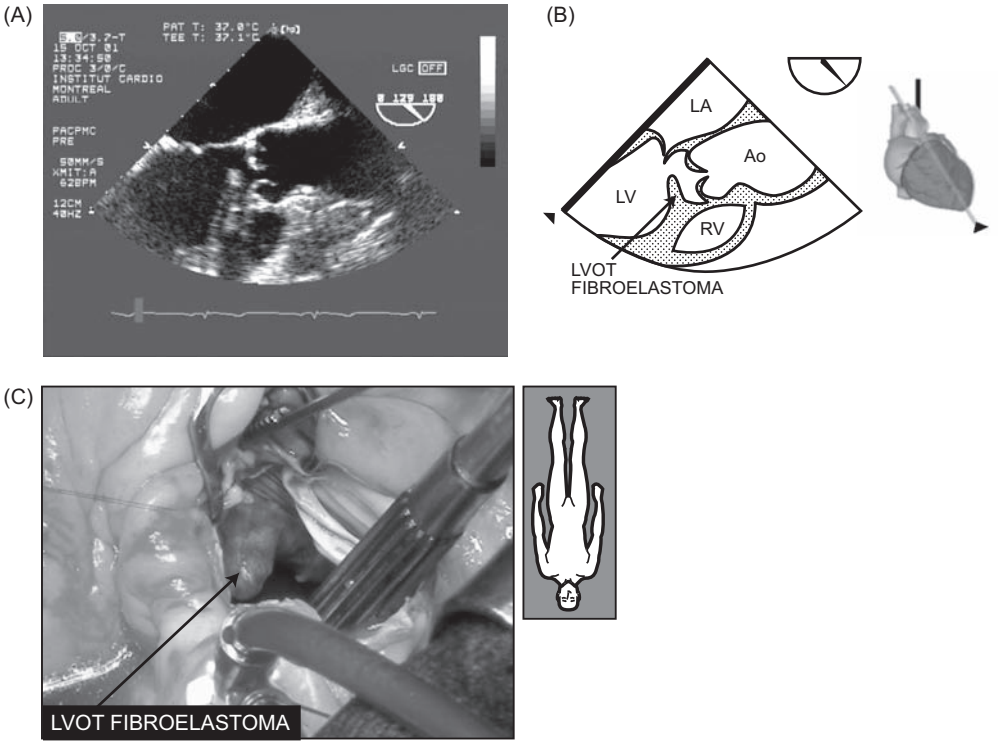

Figure 23.14 (A, B) A 72-year-old man scheduled for coronary revascularization was found to have a mobile mass attached to the left ventricular outflow tract (LVOT). (C) Intraoperative findings. The pathological diagnosis was a papillary fibroelastoma (Ao, aorta; LA, left atrium; LV, left ventricle; RV, right ventricle). (Photo C courtesy of Dr. Pierre Pagé.)

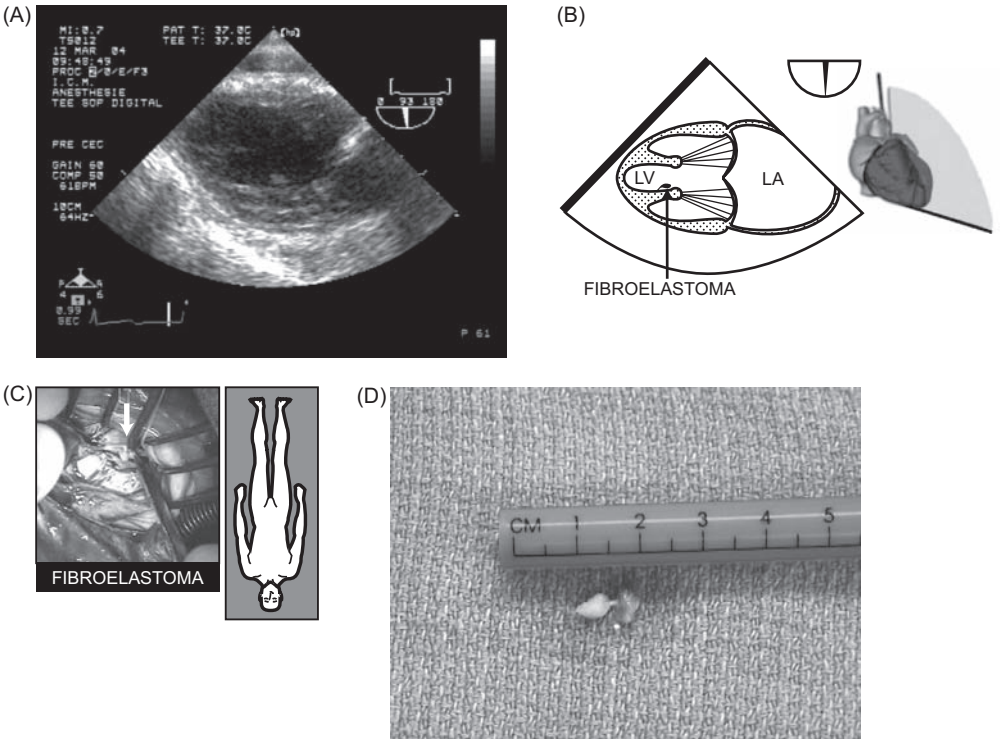

Figure 23.15 (A, B) Transgastric long-axis view in a 65-year-old woman scheduled for mitral valve repair. An incidental fibroelastoma attached to the anterior papillary muscle is found. (C, D) Intraoperative aspect (LA, left atrium; LV, left ventricle). (Photos C and D courtesy of Dr. Michel Pellerin.)

When the atrioventricular valves are affected the tumor is usually attached on the atrial surface. When present on the semilunar valves, the tumor appears on either the ventricular or the arterial surface.

A typical papillary fibroelastoma appears on echocardiography as a small pedunculated, homogeneous, well-demarcated mobile mass attached by a small stalk (Fig. 23.15). Located at the mid portion or body of the valve, the stalk usually has a broader base than a Lambl's excrescence (Fig. 23.16).

As the resolution of echocardiography improves, so does the sensitivity of TEE in detecting intracardiac masses. Subtle structures can be seen and be confused with tumors or vegetations.

Most important of these are Lambl's excrescences or valvular strands (Fig. 23.16), which prevalence increases with age. They consist of connective tissue with an elastin-like center, likely due to degenerative changes of the valves. They have not been clearly associated with embolic events (15). They are more commonly seen

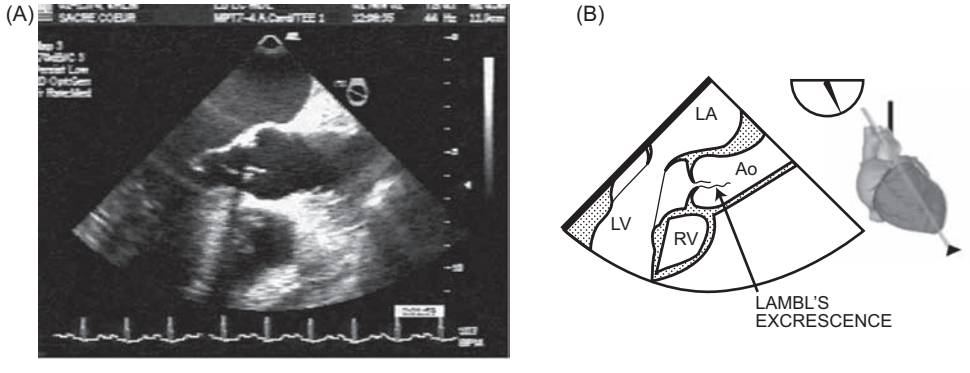

Figure 23.16 Mid-esophageal long-axis view showing a Lambl's excrescence (Ao, aorta; LA, left atrium; LV, left ventricle; RV, right ventricle). (Courtesy of Dr. François Beïque.)

attached to the free edge of the AoV cusps or to the ventricular surface of the cusps. They can also be found on the atrial surface of the mitral valve. They can reach several millimeters in length but are usually very thin. Their independent random motion particularly when they are long mimics the appearance of filamentous vegetations and without the clinical context, the echocardiographic differentiation between the two may be difficult. The distinction between the Lambl's excrescence and a fibroelastoma can also be difficult.

Lambl's excrescences are also often detected on prosthetic valves in asymptomatic patients, in the absence of infection. Higher or harmonic frequencies and better temporal resolution make them increasingly common findings.

6. Hemangiomas

Hemangiomas are benign proliferations of endothelial cells which form channels containing blood. These tumors can be intramural or intracavitary and can occur anywhere in the heart or pericardium, but are more common in the right-sided cardiac chambers. They are usually solitary but multiple tumors can occur. The finding of a solitary, sessile mass with echo-lucent areas associated with a pericardial effusion favors the diagnosis of a hemangioma rather than a myxoma or rhabdomyoma (Fig. 23.17). Potential complications reported include chamber compression, ventricular outflow tract obstruction, pericardial effusion from rupture of the tumor, compression of the coronaries, and arrhythmias (16).

B. Malignant Cardiac Tumors

1. Thymomas

Thymomas are mainly tumors of the anterior mediastinum. They often present as an extracardiac mass compressing a cardiac chamber. When no evidence of mediastinal involvement can be found, the pericardium can be deemed the primary site of origin (Fig. 23.18).

2. Lymphomas

Primary lymphomas of the heart, also known as lymphosarcomas, involve only the heart and the pericardium. They have been found in patients ranging from 14 months to 84 years of age but are extremely rare. An increased incidence of cardiac lymphomas has been noted in patients with acquired immunodeficiency syndrome and in transplant recipients under immunosuppressive therapy. Lymphomas may involve various cardiac

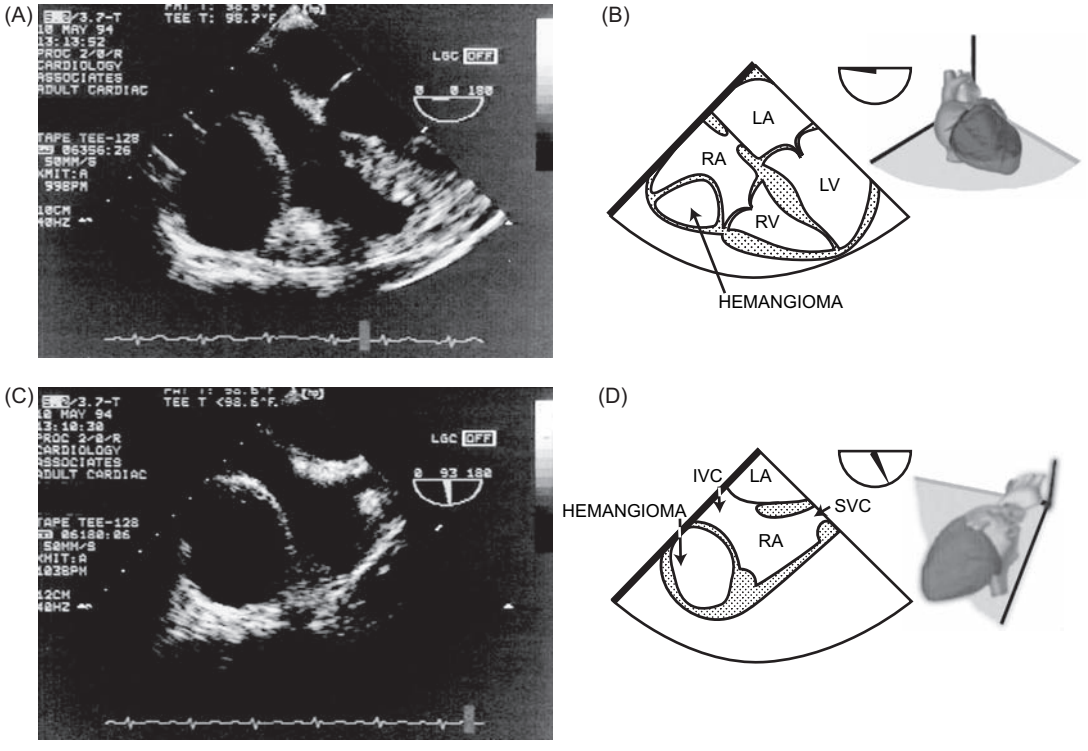

Figure 23.17 Cardiac hemangioma. Mid-esophageal four-chamber view (A, B) and 93° view (C, D) showing a large echo-lucent unilocular mass causing partial compression of the right atrium (RA). Somewhat vague, curvilinear echodensity is seen within the mass, possibly representing trabeculum within the hemangioma (IVC, inferior vena cava; LA, left atrium; LV, left ventricle; RV, right ventricle; SVC, superior vena cava). [Adapted with permission from Landolphi et al. (17).]

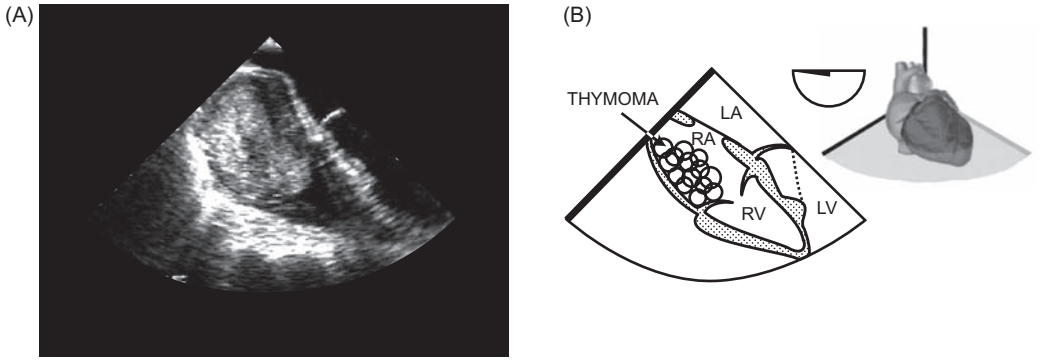

Figure 23.18 Mid-esophageal four-chamber view of a 40-year-old male with a mass in the right atrium (RA) which was a recurrent thymoma. He presented few months before with a large mediastinal mass and the diagnosis of a thymoma was made at that time (LA, left atrium; LV, left ventricle; RV, right ventricle).

sites but right-sided involvement is more frequent. Pericardial invasion is common. Myocardial infiltration can be diffuse or different, with multiple intracavitary nodules sometimes filling the LV apex resembling a thrombus. They can also mimic hypertrophic cardiomyopathy with thickening of the ventricular septum and lateral free wall (Fig. 23.19) (6,11,12).

3. Angiosarcomas

Malignant cardiac tumors are predominantly sarcomas, most commonly angiosarcomas and rhabdomyosarcomas. Angiosarcoma occur predominantly in men and 80% originate in the RA (Figs. 23.20 and 23.21) giving rise to large mural masses that invade the pericardium, the venae cavae

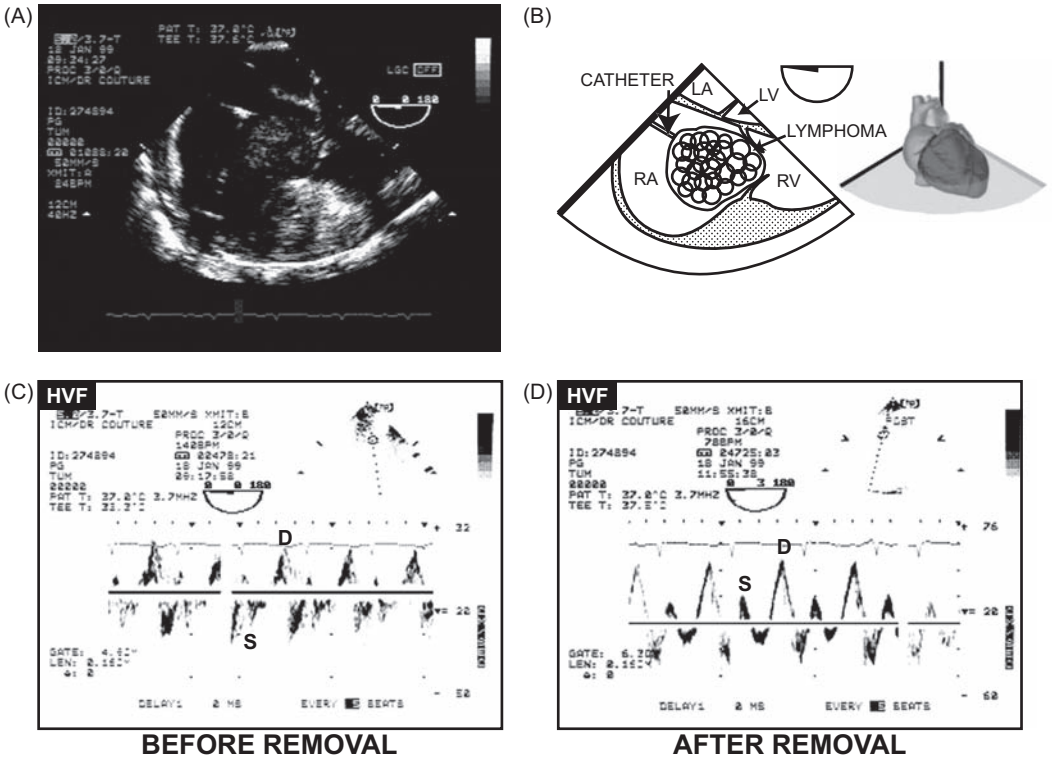

Figure 23.19 (A, B) Mid-esophageal four-chamber view of a 62-year-old man with a right cardiac mass obstructing the tricuspid atrioventricular junction and infiltrating the tricuspid lateral annulus. (C) Hepatic venous flow (HVF) Doppler examination: systolic flow reversal is seen before removal. (D) Change to systolic flow attenuation after removal (LA, left atrium; LV, left ventricle; RA, right atrium; RV, right ventricle).

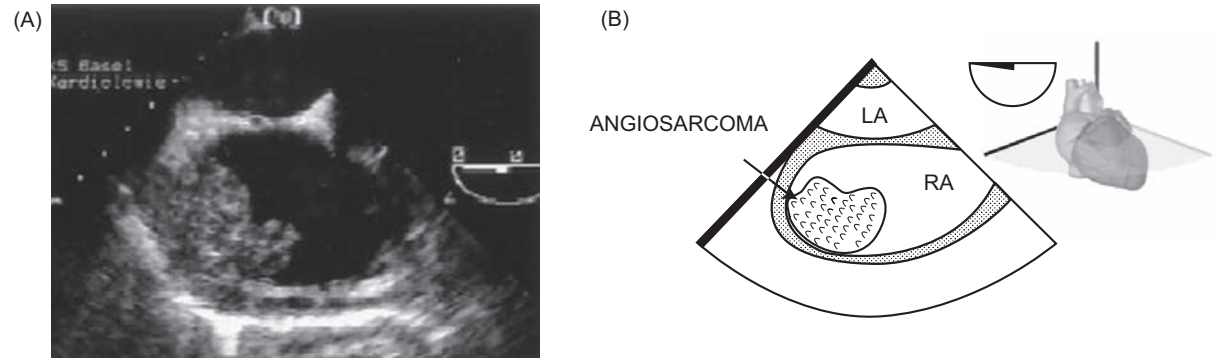

Figure 23.20 Mid-esophageal view of a right atrial angiosarcoma in a 52-year-old man (LA, left atrium; RA, right atrium). [Adapted with permission of Keller et al. (18).]

or the TV (18). Extensive involvement of the pericardium resulting in constriction or hemopericardium is seen in 30–40% of cases (11,12).

4. Rhabdomyosarcomas

Rhabdomyosarcomas are the second most common primary sarcoma of the heart occurring in 25% of cases in patients <20 years of age. They can arise in any cardiac chamber and can be multiple. Local pericardial and valvular invasion is frequent. They always develop intramurally but grow into adjacent cardiac chambers (11,12).

5. Primary Extraskeletal Osteosarcomas

Within the heart, primary extraskeletal osteosarcomas commonly arise from the LA, usually on the posterior

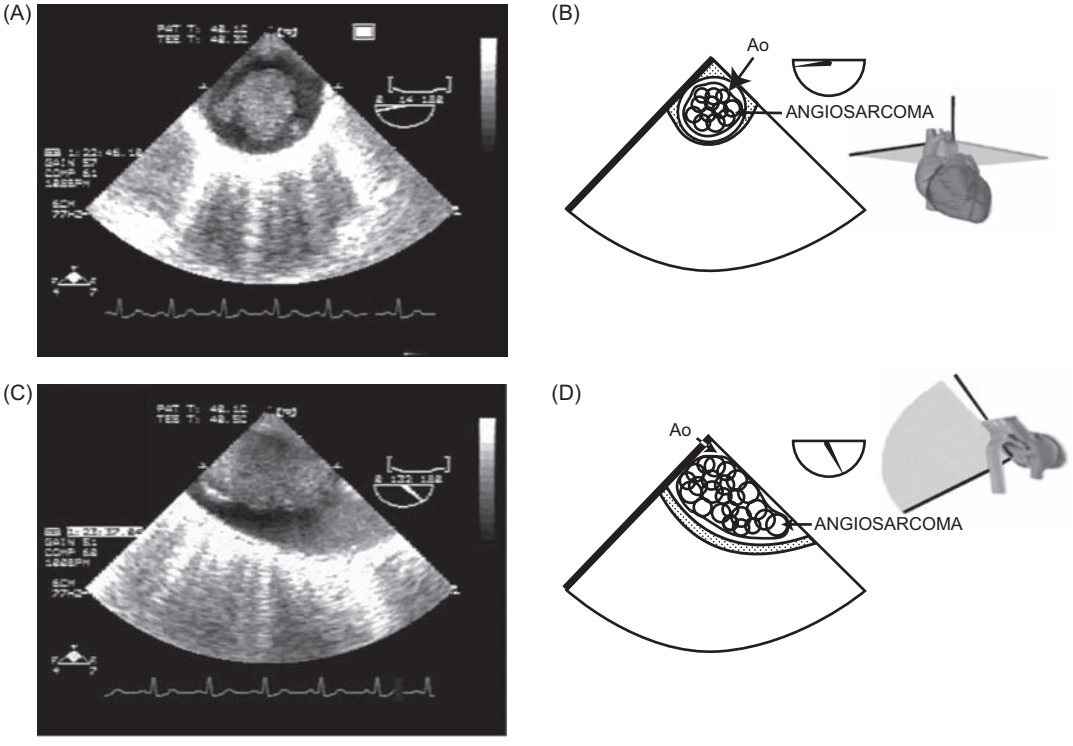

Figure 23.21 Upper-esophageal aortic view in a 55-year-old woman referred to the echo lab for investigation of recurrent transient ischemic attacks. A large mass was found in the aortic arch (A, B) and proximal descending aorta (Ao) (C, D). Surgical removal was complicated with multiple emboli to the lower limbs. Biopsy revealed an angiosarcoma.

wall close to the insertion of the pulmonary veins on the LA. These tumors can be mobile and prolapse into the mitral orifice at times. They can be differentiated from a myxoma by their site of attachment and their extension into the pulmonary veins. These tumors have also been described in the RA and RV. Metastatic osteosarcomas are more common. They can affect multiples sites within the heart. These tumors are often calcified, a useful feature for the diagnosis (11,12).

6. *Mesotheliomas*

Mesotheliomas represent the third most common malignant tumor of the heart and pericardium. They arise from the visceral or parietal pericardium and are more common in men than women. The majority of pericardial mesotheliomas diffusely covers the parietal and visceral pericardium encasing the heart. Solitary or localized ones are extremely rare. Mesotheliomas invade adjacent structures, including the heart but only superficially. This may help to differentiate between mesotheliomas and primary sarcomas as the latter can also invade the pericardium but almost always displays a large intramyocardial or intracavitary content (11,12).

IV. NONCARDIAC NEOPLASM INVADING THE HEART

Invasion of the heart by metastatic tumors occurs 20–40 times more frequently than with primary cardiac tumors. Approximately 10% of patients with malignant neoplasm have cardiac metastases but only a small fraction of these patients have clinical evidence of such metastases. The most common neoplasms that produce cardiac metastases are lung tumors in men and breast cancer in women. Lymphomas, leukemias, and melanomas are also often metastatic to the heart via hematogenous spread. Malignant tumors from every organ and tissue type have been reported to metastasize to the heart, with the exception of primary tumors of the central nervous system.

In most patients, clinical symptoms are the result of pericardial effusion, neoplastic thickening of the pericardium, or both. Wall thickening or protrusion of a tumor mass into a cardiac chamber, often producing obstruction, may be seen. Lung tumors such as bronchogenic carcinomas can invade the heart through the pulmonary veins. Renal cell carcinomas, hepatomas, and uterine leiomyomas may all extend along the IVC into the RA (Fig. 23.22).

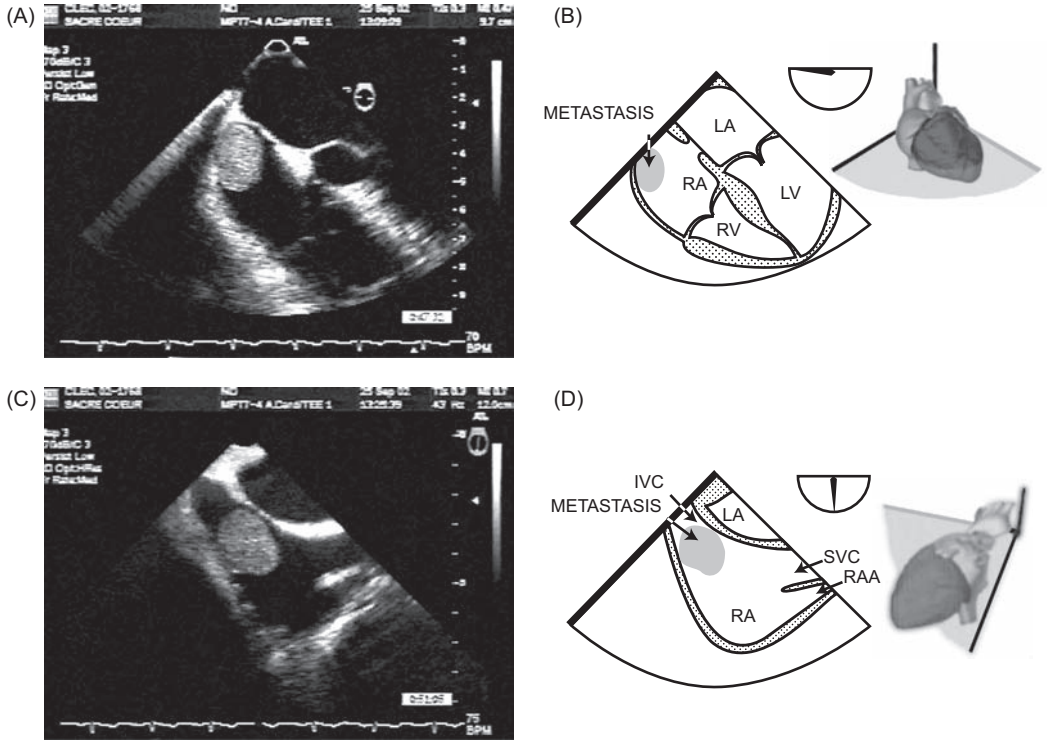

Figure 23.22 (A–D) Mid-esophageal four-chamber and bicaval view of a 60-year-old woman with a history of metastatic breast cancer. She presented with increasing dyspnea and right heart failure. A large mass was seen in the right atrium (RA) (IVC, inferior vena cava; LA, left atrium; LV, left ventricle; RAA, right atrial appendage; RV, right ventricle; SVC, superior vena cava).

V. CALCIFIED STRUCTURES

Calcified cardiac structures can be recognized by their bright, highly echogenic appearance associated with acoustic shadowing. Calcifications are not limited to the annular or submitral areas as they are frequently seen extending throughout the base of the heart to involve both the mitral and AoVs. Annular calcifications are usually immobile and this immobility together with the location and the bright appearance of the calcifications are helpful in differentiating these masses from pathological tumors.

Calcification of the mitral apparatus is commonly associated with mitral regurgitation (MR) and sometimes with some degree of mitral inflow obstruction. Caseous calcification is a rare form of mitral annular calcification (19) (see Fig. 17.13). It appears as a large, round mass containing a central area of echo-lucencies. Misdiagnosis of this structure as myocardial abscess or tumor has led to cardiotomy in certain cases. Absence of systemic symptoms would favor the diagnosis of caseous calcification especially if located posteriorly and associated with dense calcification.

Extensive calcifications of the mitral apparatus has been described in patients on chronic dialysis. The calcifications can extend to the papillary muscles and to the base of the mitral leaflets. They have also been described extending in the LA as unusual projecting nodules or excrescences (Fig. 23.23). Large calcific areas can also occur at the crux in the intervalvular fibrosa (20).

VI. EXTRACARDIAC MASSES

A. Pericardial Cyst

Pericardial cysts are uncommon intrathoracic masses. They are usually detected on chest X-ray in asymptomatic patients. The cysts are more commonly located at the right heart border and ~8% of them may project into the anterosuperior or the posterior mediastinum. Their dimensions range from 1 to 15 cm in diameter. They sometimes have a multilobular appearance and occasionally communicate with the pericardial cavity. Echocardiography reveals a spherical cystic echo-free space contiguous to the heart (see Fig. 11.23) and can, therefore, help to rule out other tumors such as lipomas, lymphangiomas, leiomyomas, benign and malignant teratomas, mesotheliomas, thymomas, and sarcomas (21). Aneurysms of saphenous venous bypass graft can also be similar in appearance (Fig. 23.24) (22).

B. Miscellaneous

Various extracardiac masses may compress the heart. A large thrombus compressing the right or left cardiac chambers are occasionally diagnosed in patients after cardiac surgery. As the usual clinical findings of cardiac tamponade may be absent and the localized cardiac compression may be missed by transthoracic echocardiography (TTE), TEE is required when the diagnosis is suspected in the hemodynamically unstable postoperative patient (see Chapter 11). Hiatal and diaphragmatic hernia, hepatic cyst, lung tumor, esophageal hematoma (Fig. 23.25), and aortic aneurysm have been also described as an extracardiac mass impinging on the heart.

VII. INTUSSUSCEPTION OF THE LEFT ATRIAL APPENDAGE

Immediately following cardiac surgery, the finding of a new left atrial mass not present previously on the preoperative study has been reported as the result of an invagination of the LAA into the LA (Fig. 23.26). The long-term consequences of this phenomenon, if not corrected intraoperatively, remain unknown (23).

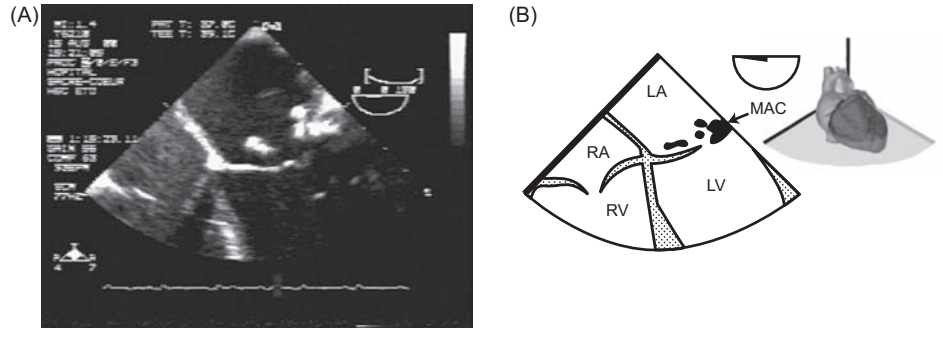

Figure 23.23 Mid-esophageal four-chamber view showing extensive calcification of the mitral valve annulus projecting into the left atrium (LA) in a patient on chronic hemodialysis (LV, left ventricle; MAC, mitral annular calcification; RA, right atrium; RV, right ventricle).

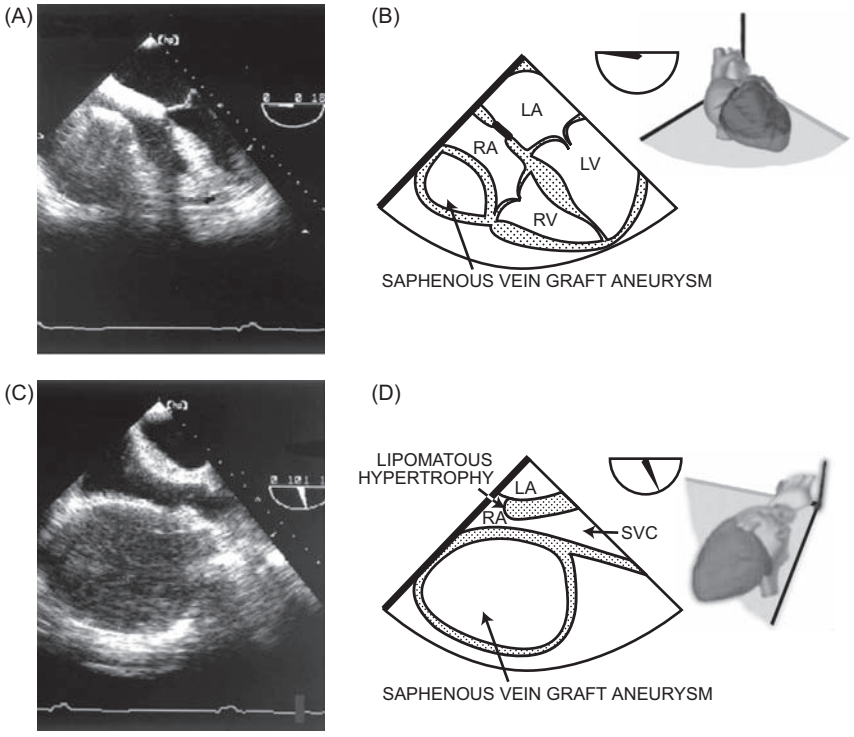

Figure 23.24 Saphenous vein graft aneurysm. Mid-esophageal four-chamber (A, B) and 101° view (C, D) showing a large circular mass compressing the right atrium (RA) in a patient with previous coronary artery bypass surgery. The saphenous vein graft seems to be filled with thrombus-like material (LA, left atrium; LV, left ventricle; RV, right ventricle; SVC, superior vena cava). [Adapted from Bansal (22).]

VIII. INTRACARDIAC THROMBI

A. Left Ventricular Thrombus

Left ventricular thrombi occur in conditions associated with stasis of blood and/or regional wall motion abnormalities such as severe left ventricular systolic dysfunction, myocardial infarction, or left ventricular aneurysm. Echocardiographically, it appears as a mass superimposed on and interrupting the normal endocardial contour of a myocardium wall with severely decreased contractility. These thrombi are most often located at the akinetic or dyskinetic apex of the LV (see Figs. 8.22 and 8.23). The diagnosis is further supported by the presence of associated spontaneous echo contrast (SEC), an indicator of decreased blood flow velocity, described as dynamic smoke-like echoes with a characteristic swirling or layering pattern. Larger and more pedunculated thrombi are easier to identify than sessile thrombi. Thrombi which protrude into the left ventricular cavity, are freely mobile with an irregular shaggy border and are more likely to embolize. The differential diagnosis of left ventricular thrombus includes benign and malignant tumors, transducer-related artifacts as well as a variety of normal cardiac structures such as prominent papillary muscles (Fig. 23.27), trabeculations and false tendons. Filling of the apex of a normal LV without regional wall abnormality can be seen in patients with the hypereosinophilic syndrome, the apical form of hypertrophic cardiomyopathy or in patients with malignancies and hypercoagulable state. Primary lymphoma of the heart can also fill the apex of the LV.

B. Left Atrial Thrombus

Left atrial and LAA thrombi are associated with stasis of blood in the LA (Figs. 23.4 and 23.5). Predisposing factors in the formation of LA thrombi include atrial fibrillation, mitral valve disease (especially rheumatic mitral valve stenosis), left atrial and LAA enlargement and the presence of prosthetic mitral valves. As for left ventricular thrombus, the presence of SEC favors the diagnosis of a thrombus when a mass is found in the LA (Fig. 23.28). Left atrial SEC is seen in $>50\%$ of patients with atrial fibrillation and in $>80\%$ of those with atrial fibrillation and LAA thrombi (24). Right atrial SEC is seen in only

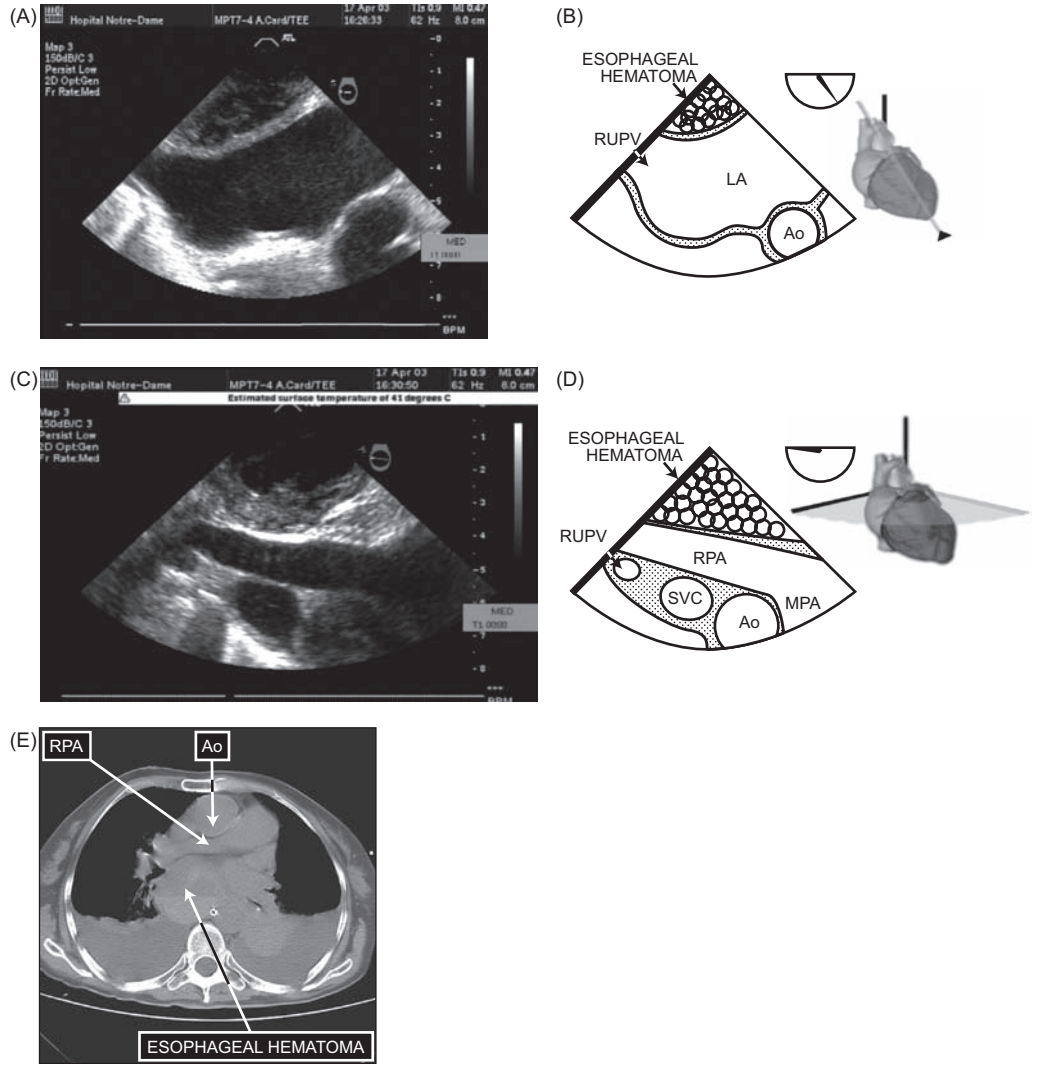

Figure 23.25 Upper-esophageal views of a 64-year-old woman anticoagulated for atrial fibrillation who developed a retrocardiac inhomogeneous mass behind the left atrium (LA) (A, B) and the right pulmonary artery (RPA) (C, D). (E) The computed tomography scan confirmed that the mass was a spontaneous esophageal hematoma (Ao, aorta; MPA, main pulmonary artery; SVC, superior vena cava; RUPV, right upper pulmonary vein). (Photos A–C courtesy of Dr. Pierre Laramée.)

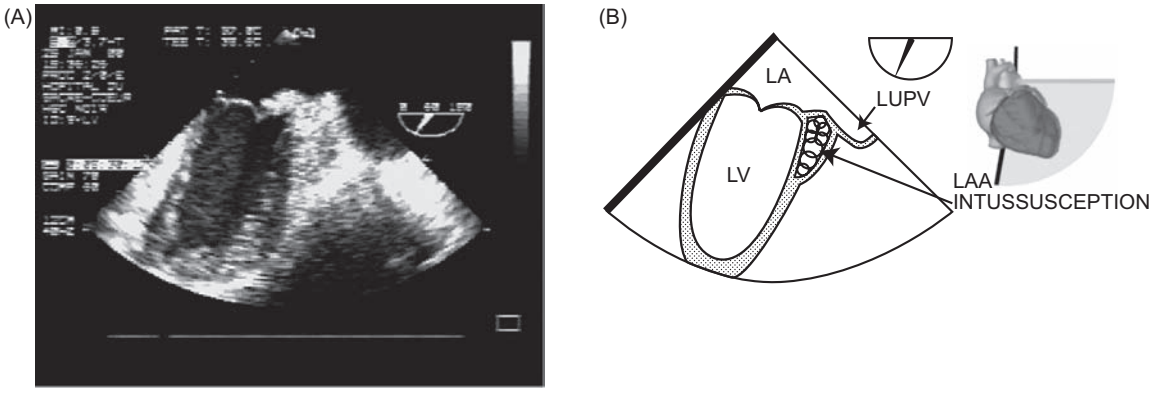

Figure 23.26 Intussusception of the left atrial appendage (LAA) after coronary revascularization. The preoperative examination was normal (LA, left atrium; LUPV, left upper pulmonary vein; LV, left ventricle).

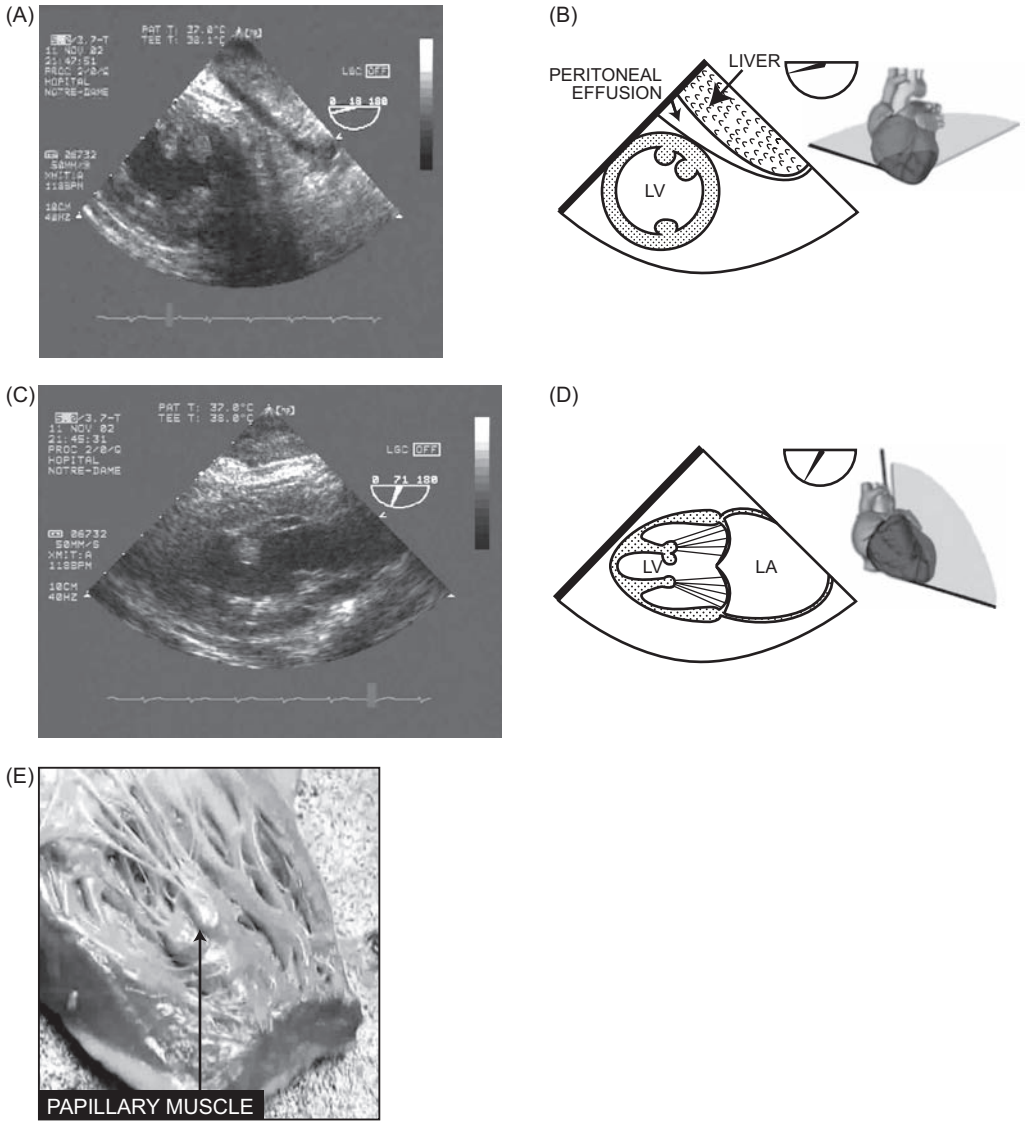

Figure 23.27 A 38-year-old man with end-stage Crohn's disease complicated with respiratory insufficiency, renal failure, and sepsis. (A, B) The transgastric mid-papillary view reveals the presence in the left ventricle (LV) of a mobile mass close to the posterior–medial papillary muscle. (C, D) The mobile mass was also seen at 71°. (E) The patient died from multiorgan failure and the autopsy revealed the presence of a double-headed papillary muscle (LA, left atrium). (Photo E courtesy of Dr. Tack Ki Leung.)

14% of patients with atrial arrhythmias referred for TEE prior to cardioversion (25).

The texture of a large thrombus in the LAA, which has an acoustic density different from the adjacent structures and the blood pool, may be helpful in distinguishing it from either pectinate muscles or the muscular walls of the LAA. The thrombus appears as a relatively well-circumscribed echo-dense mass with a defined border that has asynchronous motion with the underlying heart wall throughout the cardiac cycle. Left atrial appendage thrombus can sometimes appear as an ill-defined echogenic mass or sludge-like mass in the early stage of thrombus formation where the thrombus is in a more gelatinous form. When attached to the left atrial wall, it usually has a broad-based attachment and can be seen in several views (Fig. 23.29). Less commonly, the atrial thrombus may be attached to the mitral orifice, especially when rheumatic mitral stenosis (MS) is present or to the atrial anastomosis on the suture line after cardiac transplantation (see Fig. 14.9). Rarely, the thrombus may be free-floating, appearing as a left atrial ball thrombus (26).

The differential diagnosis of left atrial thrombus includes myxoma, fibroelastoma, other tumors and artifacts (see Fig. 6.3). The clinical setting often aids in the

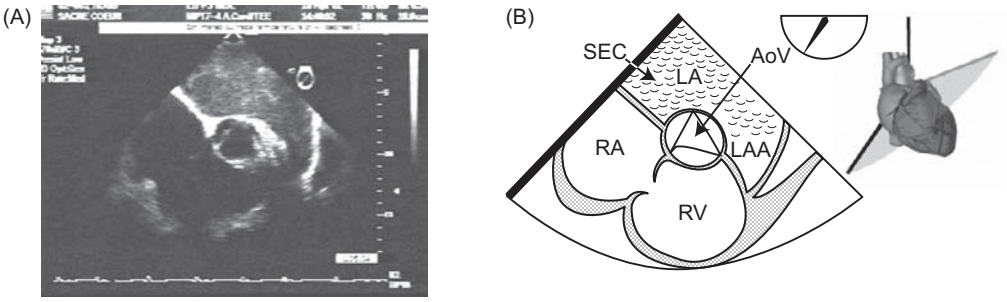

Figure 23.28 Mid-esophageal short-axis view in a patient with chronic atrial fibrillation demonstrating the presence of a significant amount of spontaneous echocontrast (SEC) in a dilated left atrium (LA) (AoV, aortic valve; LAA, left atrial appendage; RA, right atrium; RV, right ventricle).

diagnosis. The presence of SEC and the lack of septal wall attachment favor the diagnosis of a thrombus rather than a tumor.

C. Left Atrial Thrombus in Patients in Sinus Rhythm

Left atrial thrombus is usually detected in association with atrial arrhythmias and is uncommon in the presence of sinus rhythm. Thus, the yield of TEE in detecting left atrial thrombus in unselected patients in sinus rhythm is low. The incidence of left atrial thrombus and sinus rhythm was ~0.1% in a recent cohort of more than 20,000 TEE examinations (27). This low frequency is further supported by the rare occurrence of SEC in the LA in patients with sinus rhythm. Patients in whom left atrial thrombus is detected in sinus rhythm are characterized by the presence of significant left ventricular

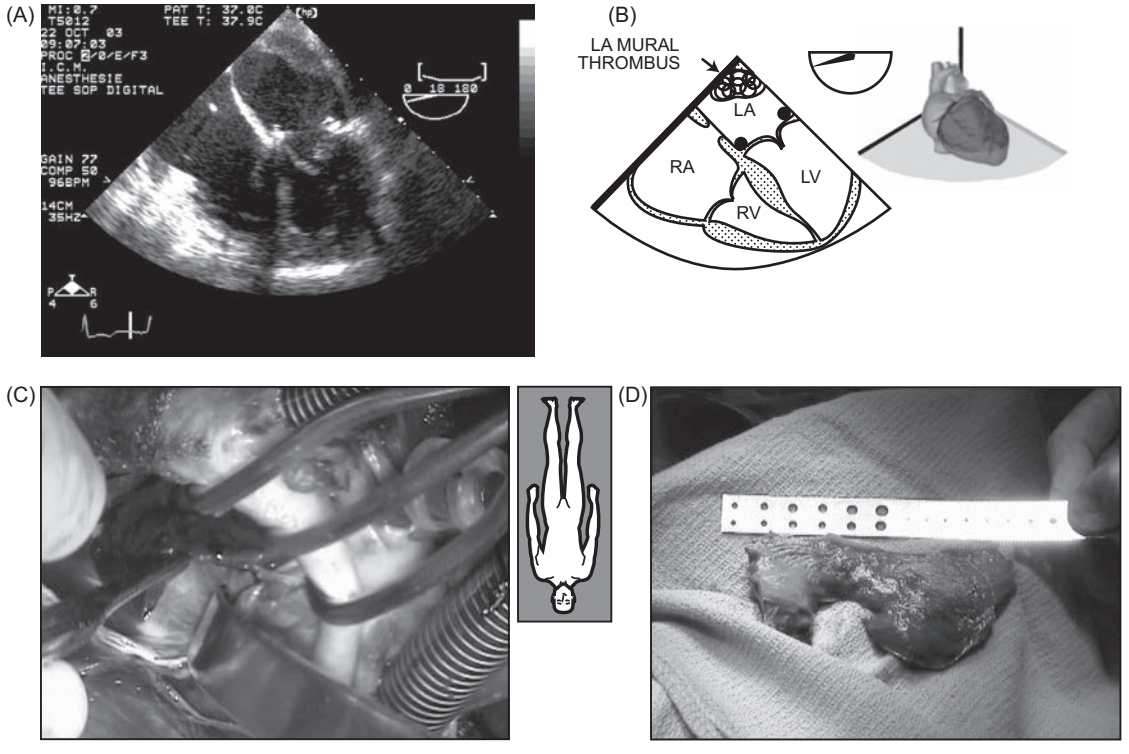

Figure 23.29 (A, B) Mid-esophageal four-chamber view of a left atrial mural thrombus which appeared after mitral valve repair and Maze procedure in a 78-year-old woman with atrial fibrillation. (C, D) Intraoperative fndings through a left atriotomy (LA, left atrium; LV, left ventricle; RA, right atrium; RV, right ventricle). (Photos C and D courtesy of Dr. Michel Pellerin.)

dysfunction, MS or previous episodes of paroxysmal atrial fibrillation. The latter is suspected when Doppler interrogation of the LAA orifice yields velocities <40 cm/sec, suggestive of poor contractility and increased probability of thrombus formation. These features define a group of patients in sinus rhythm who are at higher risk for left atrial thrombus formation.

D. Right Atrial Thrombus

Right atrial thrombi often originate from venous thromboemboli migrating through the right heart. Patients present with acute cor pulmonale secondary to pulmonary embolus (see Fig. 9.40). The migrating nature of a thrombus in transit may be demonstrated by the finding of additional clots in the SVC, the RV and the right ventricular outflow tract (RVOT), as well as the main pulmonary trunk and the right and left pulmonary branches. A thrombus in transit can also be seen crossing a patent foramen ovale and reaching the left-sided cardiac chambers and the systemic circulation as a paradoxical embolus.

Thrombus formation *in situ* in the RA also occurs in conditions associated with blood stasis or endocardial damage, such as in patients with right atrial dilatation, atrial arrhythmias, cardiomyopathies, or after right heart manipulation (Fig. 23.30). Thrombi *in situ* may also form on foreign bodies present in the RA including central venous and Swan–Ganz pulmonary artery catheters, transvenous pacing electrodes and ventriculoatrial shunts for hydrocephalus.

E. Right Ventricular Thrombi

Right ventricular thrombi are rarely diagnosed clinically. Besides conditions associated with decreased blood flow including right ventricular infarction, right ventricular failure and cor pulmonale, they have been also reported in patients with endomyocardial fibroelastosis, cardiomyopathy and hypercoagulable states. The differential diagnosis with other tumors is helped by the clinical context.

F. Biventricular Thrombi

Biventricular thrombi are quite rare and have been described in dilated cardiomyopathy and severe biventricular systolic dysfunction as well as in patients with a hypercoagulable state (Fig. 23.31) (28).

IX. MAN-MADE OBJECTS IN THE HEART

Intracardiac catheters are the most common objects seen in the heart and typically appear as a sharply defined linear intracardiac echo-density (see Chapter 13). Central venous catheters are a well-known nidus for infection and thrombosis. Careful examination should be performed to rule out the presence of superimposed thrombus, vegetation, and cardiac perforation. Echocardiography has become standard in the imaging of a venous catheter placed in the SVC or RA. Transesophageal echocardiography has been shown to be superior to TTE for diagnosis of right heart and SVC lesions (29). Other foreign bodies including pacemaker wires, atrial septal occluding prosthesis (Fig. 23.32), and embolized vena cava umbrella can be easily recognized by the echogenic appearance characteristic of their design. They can also become a nidus for thrombus formation or vegetations which can persist even after removal of the foreign object.

X. VEGETATIONS

Echocardiographic detection of a mass suggestive of vegetation has become an important criteria in the clinical diagnosis of endocarditis. Complications of endocarditis

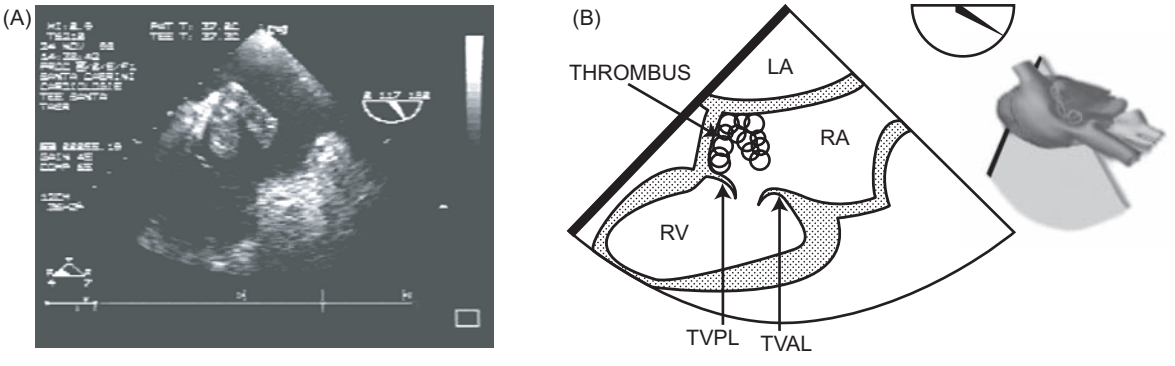

Figure 23.30 Mid-esophageal 117° right ventricular view demonstrating a right atrial "popcorn-like" thrombus in transit in a patient 2 weeks after revascularization (LA, left atrium; RA, right atrium; RV, right ventricle; TVAL, tricuspid valve anterior leaflet; TVPL, tricuspid valve posterior leaflet).

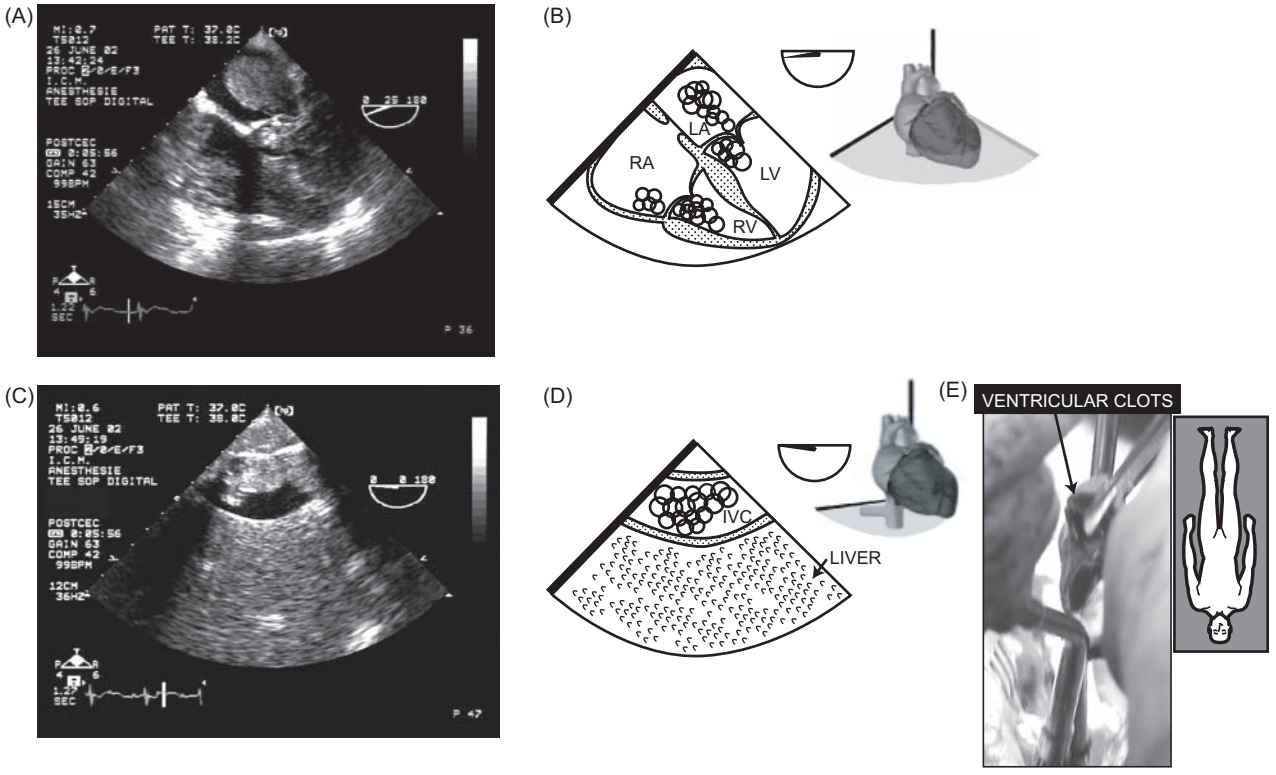

Figure 23.31 A 73-year-old man reoperated for an aortic pseudoaneurysm developed an acute hypercoagulable state after cardiac surgery. Clots were found in the left atrium (LA), left ventricle (LV), right atrium (RA), right ventricle (RV) (A, B), and inferior vena cava (IVC) (C, D). (E) Intraoperative aspect of the ventricular clots.

such as periannular abscess, prosthetic valve dehiscence, leaflet perforation, and fistula are best seen by TEE and help confirm the diagnosis and dictate important management decisions. Compared with TTE or monoplane transducers, multiplane TEE probes have improved diagnostic accuracy particularly with regard to prosthetic valves and abscess formation. The sensitivity of TEE imaging for the detection of vegetations approximates 100% on native valves and 86–94% for prosthetic valves while its specificity ranges from 88% to 100%. False negative echocardiographic studies have been seen in the case of disappearance by embolization of the infected material, inadequate visualization due to acoustic shadowing or with minute vegetation size falling below the resolution range of TEE. When both transthoracic and transesophageal studies are normal, the negative predictive value is 95% and therefore, a single negative transesophageal study alone is insufficient to rule out infective

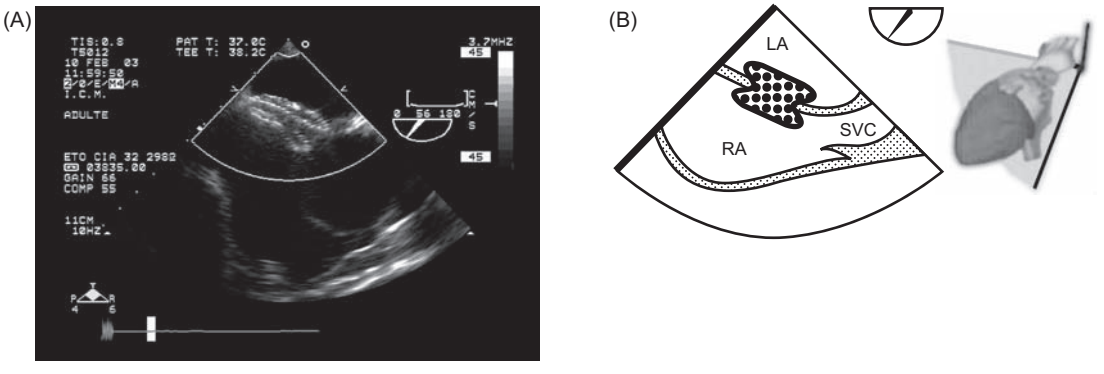

Figure 23.32 Mid-esophageal bicaval view of an atrial septal defect occluder device (LA, left atrium; RA, right atrium; SVC, superior vena cava). (Courtesy of Dr. Francois Marcotte.)

endocarditis. Thus, TEE should be repeated within 7–10 days if the clinical findings strongly suggest the diagnosis of endocarditis (30).

Finding a mass on a valve is not necessarily specific of active infectious endocarditis. Non-infectious endocarditis also occurs in Libman–Sacks (lupus) and marantic (paraneoplastic) endocarditis. Endocarditis secondary to granulomatous disease and scleroderma has also been described. The non-infectious vegetations secondary to an inflammatory process tend to be sessile without independent motion whereas marantic vegetations may appear identical to infectious vegetations (30).

A. Echocardiographic Appearance of a Vegetation

The morphologic features of vegetations vary depending on the nature of the offending organism, the state of the involved valve and the activity of the disease. Vegetations can appear either as a discrete, sessile mass closely adherent to the valve, as pedunculated, friable clumps that prolapse freely or as an elongated fibrous thickened strand (see Figs. 17.11 and 17.12). Fungal infections commonly give rise to larger vegetations which are less likely to cause significant leaflet destruction than bacterial vegetations. Tricuspid valve vegetations are generally larger than those located on the left heart.

In acute endocarditis, the classic vegetation appears as a circumscribed, pedunculated echogenic mass arising from the leaflet tip with varying degrees of independent motion. Active vegetations typically appear soft and friable, as opposed to chronic healed vegetations which are more echo-dense and fixed as they become fibrotic and calcified. Successful treatment of infectious endocarditis may not result in complete disappearance and resolution of the vegetation.

Vegetations can vary in size from a few millimeters or less to several centimeters and their appearance may dramatically change between studies because of growth, embolization, or valvular disruption. A complex appearance with cystic components may develop with certain vegetations, particularly those attached to foreign bodies (Fig. 23.33). As vegetations typically occur at sites of endothelial damage due to impinging flow jets or on already structurally abnormal valves, their appearance is influenced by the underlying valvular disorder. In fact, the greater the degree of valvular deformity before infection, the more difficult the vegetation is to define. Extensive calcification may cause important shadowing and mask the presence of small vegetation.

The mitral valve is more frequently involved in infective endocarditis than any other valve. The vegetations may involve any of its leaflets and are most often located on the atrial surface of the valve. Infection of both mitral leaflets is not uncommon. Seeding of the chordae tendinae or the anterior mitral leaflet from an infected AoV can also occur. Mitral valve vegetations must be differentiated from a variety of other disorders affecting the valve including myxomatous degeneration which cause thickening of both leaflets and increased echogenicity simulating endocarditis. When there is associated leaflet prolapse or chordal rupture, the similarity may be even more striking. Primary leaflet tumor such as fibroelastoma or myxoma may also at times be impossible to differentiate from vegetations.

The AoV is a common site of involvement in bacterial endocarditis. Combined infection of both aortic and mitral valves is also frequently observed. Predisposing factors in AoV endocarditis include rheumatic deformity of the valve leaflets, bicuspid AoV, and degeneration and calcification of the aortic cusps frequently seen in the elderly. Aortic vegetation appears as a mass attached to the ventricular surface of the cusps, in the outflow tract during diastole and prolapsing forward through the annulus during systole. Aortic vegetations characteristically involve the body or the free edges of the valve cusps. They are commonly focal and may involve one or two of the cusps. Endocarditis of the AoV can be complicated by the development of an abscess which appears initially as a periaortic asymmetric ill-defined thickening and swelling in

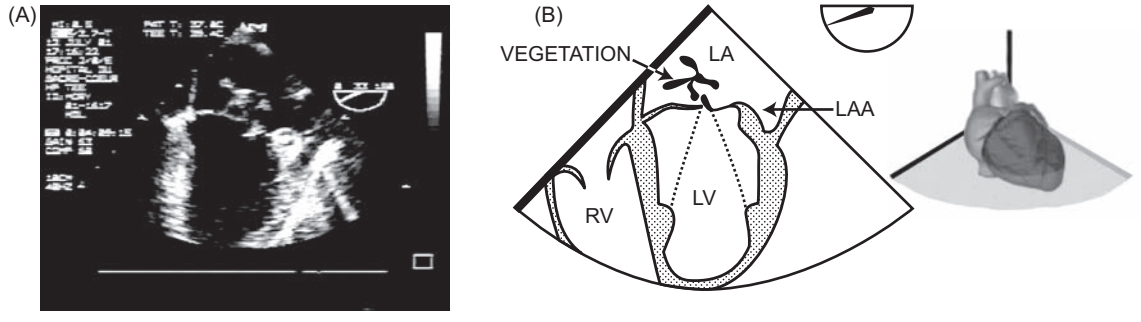

Figure 23.33 Mid-esophageal 33° view of an intravenous drug user with endocarditis. Note the large complex vegetation on the atrial side of the mitral valve (LA, left atrium; LAA, left atrial appendage; LV, left ventricle; RV, right ventricle).

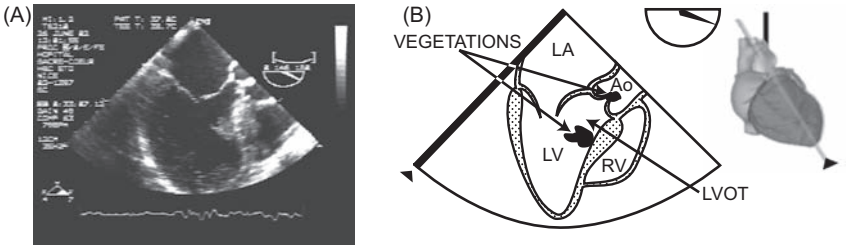

Figure 23.34 A 60-year-old woman who presented with a pneumococcal meningitis. Mid-esophageal long-axis view revealed a vegetation on the aortic valve as well as a mass attached to the basal interventricular septum where the jet of aortic regurgitation is directed. The multilobulated appearance is suggestive of a vegetation (Ao, aorta; LA, left atrium; LV, left ventricle; LVOT, left ventricular outflow tract; RV, right ventricle).

which coalescing echo-free spaces gradually evolve into a newly formed cavity (see Fig. 15.31). Once a pseudoaneurysm has clearly formed, the presence of blood flow in and out of the cavity can be seen with color flow imaging. The examination of AoV endocarditis should thus warrant a careful evaluation of the periaortic area and the posterior mitral annulus (Figs. 23.34 and 23.35).

Tricuspid valve endocarditis is usually an acute rather than a subacute process. Staphylococcus aureus is the most common infecting organism, since predisposing factors include intravenous drug abuse, infected catheters and virulent skin infection. In contrast to left-sided valves, infective endocarditis among intravenous drug users occurs on a structurally normal valve. Tricuspid vegetations generally appear as large echodense masses which disrupt the usual smooth contour of the TV (see Figs. 19.14 and 19.15). Vegetative growth may occur on the atrial surface, the leaflet margins, or the ventricular surface. Significant leaflet destruction and rupture of the chordae tendinea are common (30).

The pulmonic valve (PV) is the least commonly involved in infective endocarditis. It usually occurs in patients with congenital heart disease such as pulmonic stenosis (PS), patent ductus arteriosus, tetralogy of Fallot or ventricular septal defect (VSD). As mentioned previously, vegetations develop on areas of endothelial damage by impinging flow jets. Thus, in patients with VSD, vegetations can appear at the site of the jet lesion on the endocardium of the RV.

Vegetations on prosthetic valves are typically more difficult to detect than those involving native valves, as visualization of their components and specific design often requires specific angulations, complicated even more by acoustic shadowing from prosthetic material. The presence of both mitral and aortic prostheses is particularly challenging, as the aortic prosthesis obscures the mitral valve in transthoracic imaging while the opposite occurs with transesophageal imaging. The advent of multiplane transesophageal transducers has been particularly helpful in enabling observation from multiple viewing positions

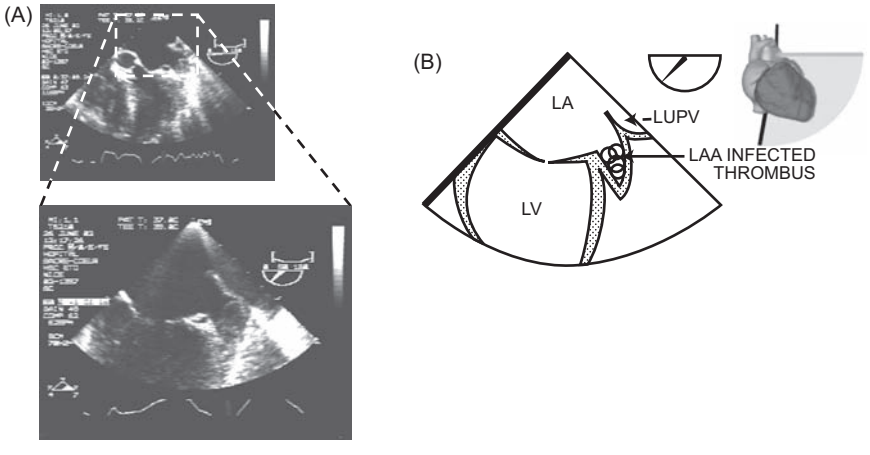

Figure 23.35 Mid-esophageal views of a 60-year-old woman with pneumococcal meningitis and endocarditis. A repeat transesophageal echocardiographic exam (TEE) revealed a new mass in the left atrial appendage (LAA), not seen on the first TEE done seven days before. The multilobulated appearance of the mass, the absence of atrial fibrillation and the ongoing bacteremia suggested the presence of a new source of infection. An infected thrombus was surgically removed (LA, left atrium; LUPV, left upper pulmonary vein; LV, left ventricle).

and angles to detect the presence of vegetations. Infection involving mechanical prosthetic valves usually begins in the perivalvular area at the annular insertion site and later extends along the struts where it may interfere with the motion of the occluder. Echocardiographically, the smooth contour of the ring may appear thickened, a finding sometimes difficult to differentiate from thrombus or pannus formation. When >40% of the sewing ring is involved by the infectious process, loosening of the sutures leads to dehiscence and rocking of the prosthesis. In bioprosthetic valves, in addition to similar involvement of the sewing ring, the infection may also deform and destroy the tissue cusps (11).

XI. PATENT FORAMEN OVALE

The prevalence of patent foramen ovale (PFO) is higher in patients with unexplained cerebrovascular accidents (CVA) than in the general population (up to 75% vs 25–30%). Furthermore, patients with PFO and previous CVA have a risk of recurrent events in the range of 1.7–4.7% per year. The presence of an atrial septal aneurysm or a Chiari network is associated with a higher prevalence of significant PFO. Recent studies have demonstrated that a larger PFO size as measured by 2D echocardiography is associated with an increased risk of stroke (8,31). Transesophageal echocardiography is the most useful and reliable tool to detect the presence of a PFO (see Fig. 24.6). The size of the PFO is assessed semiquantitatively by observing the number of contrast microbubbles injected through a peripheral vein crossing from RA to LA through the PFO. A large shunt is deemed present when more than 20 microbubbles enter the LA in fewer than three beats. The ability to detect the PFO and its degree of right-to-left shunting is influenced not only by the size of the orifice, but also by the quality of the contrast agent (mixture of agitated saline and blood, dosage, route of administration), the position of the patient and the use of adequate provocative maneuvers (such as the Valsalva maneuver). Color Doppler flow is initially used to assess the direction of flow from the IVC towards the fossa ovalis and the direction of the shunt, if present, both at rest and with provocative maneuvers. The injection of agitated saline contrast through a peripheral vein is also used both at rest and with provocative maneuvers to differentiate a resting PFO vs a provocable one. Provocative maneuvers are designed to induce a sudden inversion of the RA–LA pressure gradient to open up the membrane of the fossa ovalis: enhanced right-to-left shunt is noted

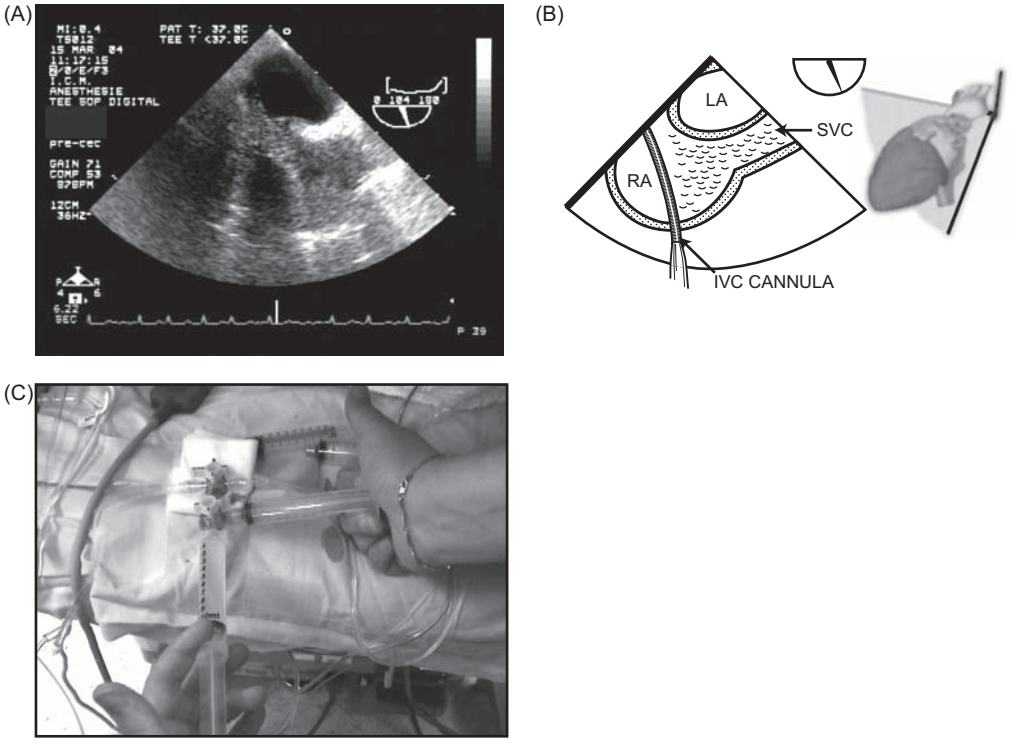

Figure 23.36 Intraoperative contrast examination. (A, B) Mid-esophageal bicaval view during a contrast study to rule-out the presence of a patent foramen ovale. Note the inferior vena cava (IVC) cannula inserted prior to cardiopulmonary bypass. (C) A two-syringe system was used (LA, left atrium; RA, right atrium; SVC, superior vena cava).

upon the release phase of the Valsalva maneuver, or in intubated patients, upon the release of significant positive pressure ventilation. The presence of a PFO may, however, be missed if the esophageal acoustical windows are poor with a small LA or frequent air swallowing. Elevated left atrial pressure may also prevent the passage of bubble from RA to LA. Improperly performed the Valsalva maneuver may sometimes also be insufficient to mobilize and open up the membrane of the fossa ovalis due to excessive sedation used during the TEE. The appearance of microbubbles from RA to LA may also occur in other conditions than PFO, such as atrial septal defect (ASD) or arteriovenous pulmonary connection where contrast can sometimes be seen entering the LA via one or more pulmonary veins (8,24,31).

Routine examination to rule out PFO during cardiac surgery should be strongly considered. Indeed, surgical closure might be contemplated particularly if significant right-to-left shunting through a PFO could potentially occur postoperatively such as with the use of ventricular assist device or in patients at risk for right ventricular failure. Definitive recommendations on the management based on clinical trials are, however, still pending (32).

A. Ultrasound Contrast Technique

The ultrasound contrast technique is done by injecting agitated normal saline via an antecubital vein to opacify the right cardiac chambers with microbubbles. The technique requires two syringes attached to a three-way stopcock while the third port is attached to the intracath introduced into the antecubital vein. One syringe is filled with 5–10 mL of normal saline and 0.5 mL of air and is attached to one port of the stopcock. The other syringe is empty and attached to the second port.

The ultrasound contrast solution is generated by forcefully passing the mixture of air and saline back and forth between the two syringes several times (Fig. 23.36). The well-aerated solution is immediately injected in the antecubital vein while the atrial septum is being imaged. Elevation of the upper extremity can speed the arrival of the bolus into the right cardiac chambers. Immediate passage of microbubbles into the LA occurs in the presence of a shunt and if the right atrial pressure, at some point during the cardiac cycle, exceeds the left atrial pressure (24). In the absence of a significant right-to-left shunt the microbubbles are usually trapped in the lung capillaries and are not seen in the left-sided cardiac chambers. Rarely, few microbubbles manage to go through the lung circulation and reach the LA through the pulmonary veins, but they do so after several heart beats. In the presence of a significant left-to-right shunt, the passage of unopacified blood into a RA full of microbubbles creates a negative or reverse contrast effect.

In summary, the diagnosis of abnormal intracavitary material is one of the most powerful applications of TEE in clinical practice and in the operating room. Such abnormalities can appear in numerous medical conditions and in both cardiac and noncardiac surgeries. The impact of such observations can lead to important alteration in the medical and surgical management of these patients.

REFERENCES

1. Sawhney N, Palakodeti V, Raisinghani A et al. Eustachian valve endocarditis: a case series and analysis of the literature. J Am Soc Echocardiogr 2001; 14:1139–1142.
2. Ridha M, Sequeira RF, Bilsker M et al. Thrombosed chamber of cor-triatriatum mimicking left atrial tumor (case report). Echocardiography 2001; 18:617–618.
3. Yao SS, Meisner JS, Factor SM et al. Assessment of left atrial appendage structure and function by transesophageal echocardiography: a review. Echocardiography 1998; 15:243–256.
4. Agostini F, Click RL. More than just the "Q-tip sign." J Am Soc Echocardiogr 2001; 14:832–833.
5. Oh JK, Seward JB, Tajik AJ. The Echo Manual. 2nd ed. Philadelphia: Lippincott-Raven, 1999.
6. Miller A, Mukhtar O, Aaluri SR et al. Two- and three-dimensional TEE differentiation of lymphoma involving the atrial septum from lipomatous hypertrophy. Echocardiography 2001; 18:205–209.
7. Pai RG. Echocardiographic features of persistent left superior vena cava. Echocardiography 1999; 16:435–436.
8. Kerut EK, Norfleet WT, Plotnick GD, Giles TD. Patent foramen ovale: a review of associated conditions and the impact of physiological size. J Am Coll Cardiol 2001; 38:613–623.
9. Gopal AS, Stathopoulos JA, Arora N et al. Differential diagnosis of intracavitary tumors obstructing the right ventricular outflow tract. J Am Soc Echocardiogr 2001; 14:937–940.
10. Goldman JH, Foster E. Transesophageal echocardiographic (TEE) evaluation of intracardiac and pericardial masses. Cardiol Clin 2000; 18:849–860.
11. Weyman AE. Principles and Practice of Echocardiography. 2nd ed. Philadelphia: Lea & Febiger, 1994.
12. McAllister HA Jr, Hall RJ, Cooley DA. Tumors of the heart and pericardium. Curr Probl Cardiol 1999; 24:57–116.
13. Roelandt J, Pandian NG. Multiplane Transesophageal Echocardiography. New York: Churchill Livingstone, 1996.
14. Sidhu JS, Harries M, Senior R. Papillary fibroelastoma of the left atrial appendage. J Am Soc Echocardiogr 2001; 14:838–839.
15. Roldan CA, Shively BK, Crawford MH. Valve excrescences: prevalence, evolution and risk for cardioembolism. J Am Coll Cardiol 1997; 30:1308–1314.
16. Chrissos DN, Agelopoulos NG, Garyfallos DJ, Stergiopoulou PD. Follow-up of an unresectable hemangioma in the heart. Echocardiography 1998; 15:239–242.

17. Landolphi DR, Belkin RN, Hjemdahl-Monsen CE, LaFaro RJ. Cardiac cavernous hemangioma mimicking pericardial cyst: atypical echocardiographic appearance of a rare cardiac tumor. J Am Soc Echocardiogr 1997; 10:579–581.
18. Keller DI, Hunziker P, Buser P. Biopsy of right atrial angiosarcoma guided by transesophageal echocardiography. J Am Soc Echocardiogr 2002; 15:475–477.
19. Harpaz D, Auerbach I, Vered Z et al. Caseous calcification of the mitral annulus: a neglected, unrecognized diagnosis. J Am Soc Echocardiogr 2001; 14:825–831.
20. Madu EC, D'Cruz IA, Wall B et al. Transesophageal echocardiographic spectrum of calcific mitral abnormalities in patients with end-stage renal disease. Echocardiography 2000; 17:29–35.
21. Antonini-Canterin F, Piazza R, Ascione L et al. Value of transesophageal echocardiography in the diagnosis of compressive, atypically located pericardial cysts. J Am Soc Echocardiogr 2002; 15:192–194.
22. Bansal RC. Echocardiographic diagnosis of an asymptomatic aneurysm of a saphenous vein graft. J Am Soc Echocardiogr 2002; 15:661–664.
23. Roberson DA, Arcillia R, Sachsteder W. Transesophageal echocardiographic diagnosis of intussusception of the left atrial appendage. Echocardiography 1993; 10:619–622.
24. Otto CM. The Practice of Clinical Echocardiography. Philadelphia: W.B. Saunders, 1997.
25. Bashir M, Asher CR, Garcia MJ et al. Right atrial spontaneous echo contrast and thrombi in atrial fibrillation: a transesophageal echocardiography study. J Am Soc Echocardiogr 2001; 14:122–127.
26. Feigenbaum H. Echocardiography. 5th ed. Philadelphia: Lea & Febiger, 1994.
27. Agmon Y, Khandheria BK, Gentile F, Seward JB. Clinical and echocardiographic characteristics of patients with left atrial thrombus and sinus rhythm: experience in 20,643 consecutive transesophageal echocardiographic examinations. Circulation 2002; 105:27–31.
28. Wongpraparut N, Apiyasawat S, Jacobs LE, Kotler MN. Biventricular thrombi. Echocardiography 2001; 18:619–620.
29. Shapiro MA, Johnson M, Feinstein SB. A retrospective experience of right atrial and superior vena caval thrombi diagnosed by transesophageal echocardiography. J Am Soc Echocardiogr 2002; 15:76–79.
30. Ryan EW, Bolger AF. Transesophageal echocardiography (TEE) in the evaluation of infective endocarditis. Cardiol Clin 2000; 18:773–787.
31. Schuchlenz HW, Weihs W, Beitzke A et al. Transesophageal echocardiography for quantifying size of patent foramen ovale in patients with cryptogenic cerebrovascular events. Stroke 2002; 33:293–296.
32. Sukernik MR, Mets B, Bennett-Guerrero E. Patent foramen ovale and its significance in the perioperative period. Anesth Analg 2001; 93:1137–1146.

24

Congenital Heart Disease

JEAN-MARC CÔTÉ, DANY CÔTÉ, ALAIN CLOUTIER
Laval University, Quebec City, Canada

I. Introduction 525
II. Unoperated Congenital Heart Defects 526
A. Septation Defects 526
1. Atrial Septal Defect 526
2. Ventricular Septal Defect 528
3. Atrioventricular Septal Defect 535
4. Patent Ductus Arteriosus 538
B. Tricuspid Valve Anomaly 539
1. Ebstein's Anomaly of the Tricuspid Valve 539
C. Right Ventricular Outflow Tract Anomaly 540
1. Pulmonary Stenosis (Subvalvular, Valvular, Supravalvular) 540
2. Tetralogy of Fallot 541
D. Left Atrial Anomaly 542
1. Cor Triatriatum 542
E. Mitral Valve Anomalies 543
1. Mitral Valve Stenosis 543
2. Cleft Mitral Valve 545
F. Aortic Valve Anomaly 546
1. Bicuspid Aortic Valve, Congenital Aortic Valve Stenosis 546
2. Supra- and Subvalvular Aortic Stenosis 546
G. Coarctation of the Aorta 547
III. Previously Repaired Congenital Heart Defects 548
A. Tetralogy of Fallot 548
B. Transposition of the Great Arteries 549
C. Complex Single Ventricle 550
References 552

I. INTRODUCTION

There are two basic categories of congenital heart disease in adults (1). The first includes the defects that have been unrecognized in childhood but were diagnosed in the adult because of a newly developed symptomatology or as an incidental finding during an investigation for another reason. Coarctation of the aorta (Ao) and ostium secundum atrial septal defect (ASD) are examples of this category. It also includes patients with a previously diagnosed congenital cardiac malformation that did not previously require a surgical repair such as the bicuspid aortic valve (AoV) in childhood that evolved to a significant aortic stenosis (AS) in the adult.

The second category involves patients surviving to adulthood with a previously diagnosed and operated congenital heart defect, such as the patient with operated tetralogy of Fallot or transposition of the great arteries.

The comprehensive echocardiographic evaluation of the adult with suspected or known congenital heart

defect should include detailed and systematic analysis of intra- and extracardiac structures. The segmental echocardiographic analysis of the heart requires definition of the various cardiac segments and components: 1—visceral situs, 2—venoatrial connection (systemic and pulmonary veins), 3—atrial situs (solitus, inversus, ambiguous), 4—atrioventricular connection (concordant, discordant, double inlet, straddling, absent), 5—ventriculoarterial connection (concordant, discordant, double outlet, single outlet), 6—septae (atrial, ventricular), 7—atrioventricular and semilunar valves, 8—ventricular outflows, and 9—great arteries (2) (Table 24.1).

In practice, this begins by the evaluation of the venous connections (vena cava and pulmonary veins), atrial anatomy (right and left atria), atrioventricular valves, ventricles, outflow tracts, semilunar valves, and proximal portion of the great arteries. The right and left sides of the heart can be examined in parallel or in sequence, as long as the evaluation is complete.

II. UNOPERATED CONGENITAL HEART DEFECTS

A. Septation Defects

1. Atrial Septal Defect

Significant ASD is usually recognized in childhood and managed either by surgical closure or, more recently, by percutaneous closure using one of the available devices. Many of the defects, however, may evolve unrecognized in childhood and be diagnosed only in adulthood. Symptoms or signs that will usually prompt diagnosis in the adult are shortness of breath, exercise intolerance, right heart failure, atrial arrhythmias, or a cardiac murmur. The left-to-right shunt at the atrial level causes right ventricular volume overload with right ventricular and atrial dilatation in diastole (Fig. 24.1) and increased right ventricular ejection volume in systole with dilated pulmonary arterial bed. There are four recognized types of ASD: ostium secundum (fossa ovalis), ostium primum, sinus venosus, and coronary sinus (Fig. 24.2).

The ostium secundum (fossa ovalis) type is the most common type of ASD (Figs. 24.3 and 24.4). It usually lies close to the center of the inter-atrial septum occupying part, or all, of the fossa ovalis. It is caused by exaggeration of the normal resorption of the septum primum, leading to the absence of the part normally covering and closing the fossa ovalis lying on the left side of the atrial septum [Fig. 24.2(B)]. This must be differentiated from a patent foramen ovale (PFO or "*Trou de Botal*"): in 20% of the adult population, the septum primum is complete but does not fuse with the septum secundum to obliterate the foramen ovale [Fig. 24.2(A)]. Patency of the foramen ovale can be demonstrated anatomically with a probe (Fig. 24.5). A shunt can be elicited with a Valsalva maneuver (Figs. 24.6 and 24.7). It usually has no consequences

Table 24.1 Definitions of the Different Cardiac Segments and Components

Cardiac segments and connections	Definition
Visceroatrial situs	Spatial positioning of abdominal organs and morphological right and left atria
Solitus (normal)	Morphologic right atrium, liver and IVC to the right Morphologic left atrium, stomach, spleen, and descending aorta to the left
Inversus	The opposite of solitus
Ambiguous	Atrial situs undiagnosed with median liver
Atrioventricular connection	The connection between the atria and the ventricles
Concordant	Morphologic right atrium connected to the morphologic right ventricle and morphologic left atrium connected to the morphologic left ventricle
Discordant	Morphologic right atrium connected to the morphologic left ventricle and morphologic left atrium connected to the morphologic right ventricle
Double inlet	The two atrioventricular valves are connected to the same ventricle
Straddling	The subvalvular apparatus of one atrioventricular valve is connected to both sides of the interventricular septum
Absent	Atresia of one atrioventricular valve
Ventriculoarterial connection	Connection between the ventricles and the great arteries
Concordant	Morphologic right ventricle connected to the pulmonary artery and the morphologic left ventricle connected to the aorta
Discordant	Morphologic right ventricle connected to the aorta and morphologic left ventricle connected to the pulmonary artery
Double outlet	Aorta and pulmonary artery connected to the same ventricle, most commonly the right ventricle
Single outlet	Atresia of one great artery or fusion of the two (truncus arteriosus)

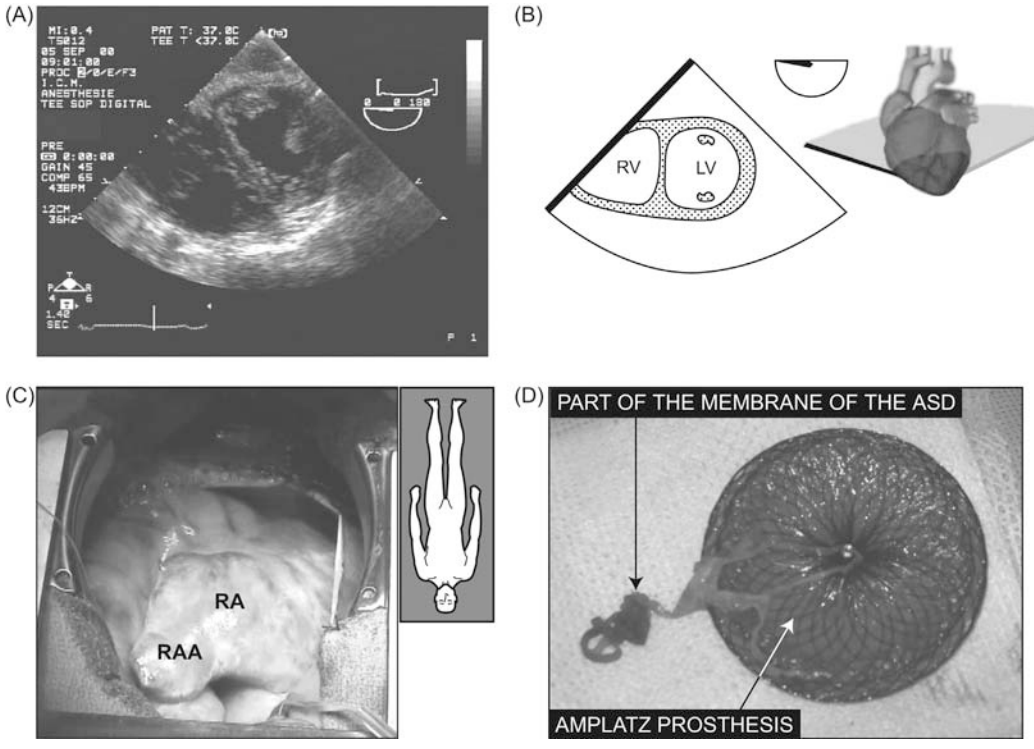

Figure 24.1 A 54-year-old woman undergoing repair of an atrial septal defect (ASD) after unsuccessful percutaneous treatment with an Amplatz closure device. (A, B) Transgastric view of the right ventricle (RV) and left ventricle (LV) showing right ventricular dilatation and a "D-shaped" LV due to the flattened curvature of the ventricular septum. (C) Intraoperative aspect demonstrating dilatation of the right atrium (RA). (D) Failure of the Amplatz prosthesis was secondary to a multifenestrated ASD. Part of the fenestrated ASD was excised with the prosthesis (RAA, right atrial appendage). (Photos C and D courtesy of Drs. Nancy Poirier and Reda Ibrahim.)

unless it is involved in a paradoxical emboli. Some authors, however, suggest that it should be closed if found in a patient in whom a cardiac surgical procedure is performed (2).

The sinus venosus ASD involves an interatrial communication at the superior and posterior aspect of the atrial septum adjacent to the superior vena cava (SVC) [Fig. 24.2(C)]. It is often associated with a partial anomalous pulmonary venous connection of one or more of the right pulmonary veins to the junction of the SVC and the right atrium (RA) (Figs. 24.8 and 24.9). Rarely a connection between the right lower pulmonary vein and the inferior vena cava (IVC) can occur.

The ostium primum, (also called partial atrioventricular) septal defect, is the consequence of an endocardial cushion defect with a resulting communication at the lower and posterior aspect of the interatrial septum at the level of the atrioventricular valves (Fig. 24.10). The defect usually also involves a cleft in the anterior leaflet of the mitral valve (Figs. 24.11 and 24.12).

Finally, the coronary sinus defect is a rare but well-recognized type of ASD located around the orifice of an unroofed coronary sinus in association with a persistent left SVC. Left-to-right shunt occurs as left atrial blood goes to the RA via the unroofed coronary sinus (Fig. 24.13).

Transesophageal Echocardiography in ASD (Table 24.2)

Atrial septal defects can be demonstrated very easily with transesophageal echocardiography (TEE) using a combination of the mid-esophageal four-chamber view (Fig. 24.6), AoV short-axis view (Fig. 24.6), and bicaval view (Fig. 24.4) (5). The location and the anatomical size of the defect with the amount of surrounding tissue in the rim of the defect (ridges) should be determined. The shunt and its direction(s) can be visualized with color Doppler and will usually be from left to right, because pressure in the left atrium (LA) is usually higher than in the RA (Fig. 24.4). Contrast echocardiography, using intravenous injection of agitated normal saline, opacifies the right-sided cardiac chambers and may sometimes demonstrate the unopacified jet of the left-to-right shunt. As the microbubbles of agitated saline are usually trapped in the pulmonary circulation, none is seen in the

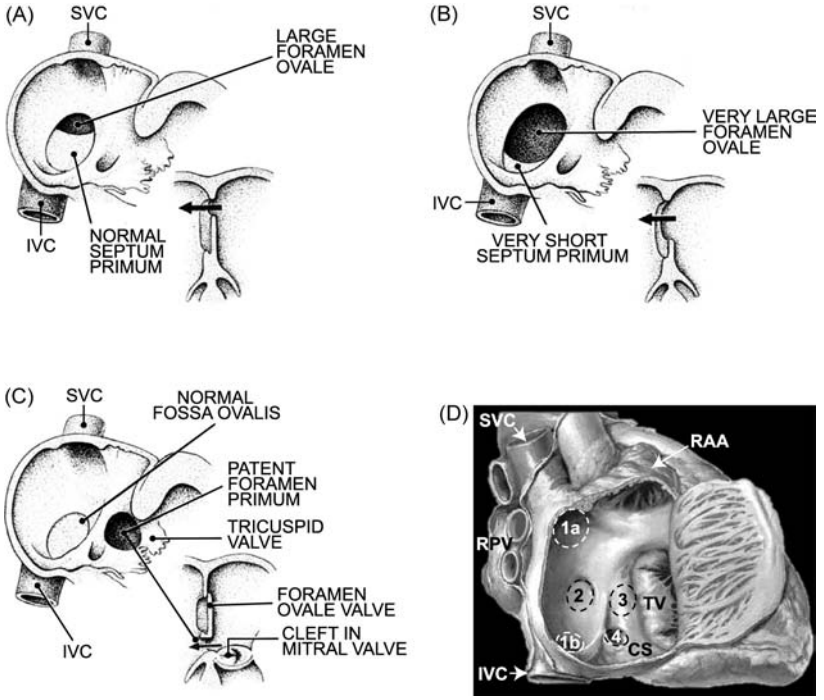

Figure 24.2 Patent foramen ovale (PFO) and various types of atrial septal defects (ASD). (A) Patent foramen ovale. (B) Large ostium secundum ASD resulting from the absence of a large portion of the septum primum covering the fossa ovalis. (C) Endocardial cushion defect with ostium primum ASD. The normal fossa ovalis is covered by the septum primum. Also shown is the frequently associated cleft in the anterior mitral leaflet. (D) Comparative location of the types of ASD: 1a—sinus venosus ASD (superior), 1b—sinus venosus ASD (inferior), 2—ostium secundum ASD, 3— ostium primum ASD, 4— coronary sinus (CS) ASD (IVC, inferior vena cava; RAA, right atrial appendage; RPV, right pulmonary veins; SVC, superior vena cava; TV, tricuspid valve). [Reproduced with permission from Moore and Persaud (3). Adapted with permission from Netter and Yonkman (4).]

left cardiac chambers, unless there is a right-to-left shunt. The potential of paradoxical embolus may be assessed by transiently increasing right atrial pressure above that in the LA (Fig. 24.6): this is best performed during the release phase of a forceful Valsalva maneuver with a deep rapid inspiratory effort or using positive-pressure ventilation in the operating room (OR). The magnitude of left-to-right shunting through the ASD and the volume overload can be inferred from the degree of right cardiac chamber enlargement. More quantitative assessment of the amount of shunting at the atrial level may be performed by measuring the Qp/Qs ratios from transgastric views at 60–90° [for the right ventricular outflow tract (RVOT) or the main pulmonary artery] and 90–120° [for the left ventricular outflow tract (LVOT) or Ao].

Before considering treatment with percutaneous prosthesis implantation or surgical closure, associated congenital lesions must also be ruled out. For ostium secundum ASD, this includes atrial septal aneurysms, mitral valve prolapse, and mitral regurgitation (MR). Ostium primum ASD may be accompanied by a cleft anterior mitral valve leaflet, best confirmed from the transgastric basal 0° "*en face*" transverse view of the mitral valve; a 135° mid-esophageal long-axis view will also reveal the abnormal ventricular septal attachments of a cleft anterior mitral leaflet, occasionally associated with partial left ventricular subaortic outflow obstruction. The MR from an abnormal mitral leaflet can sometimes only be diagnosed after the ASD closure (see Chapter 17; part I Fig. 17.22). Sinus venosus ASD are often accompanied by anomalous right upper and/or lower pulmonary venous return to the RA or the SVC. Finally, the coronary sinus ASD is found in the setting of complex congenital heart disease and may be associated with a left persistent SVC.

2. *Ventricular Septal Defect*

Ventricular septal defects (VSDs) are the most common congenital cardiac anomalies identified in infancy. In adults with congenital heart defects, VSD accounts for ~10% of all cases. The VSD with significant left-to-right shunt usually presents early in life with failure to thrive, pulmonary hypertension and signs of heart failure. The shunts will be diagnosed early and operated

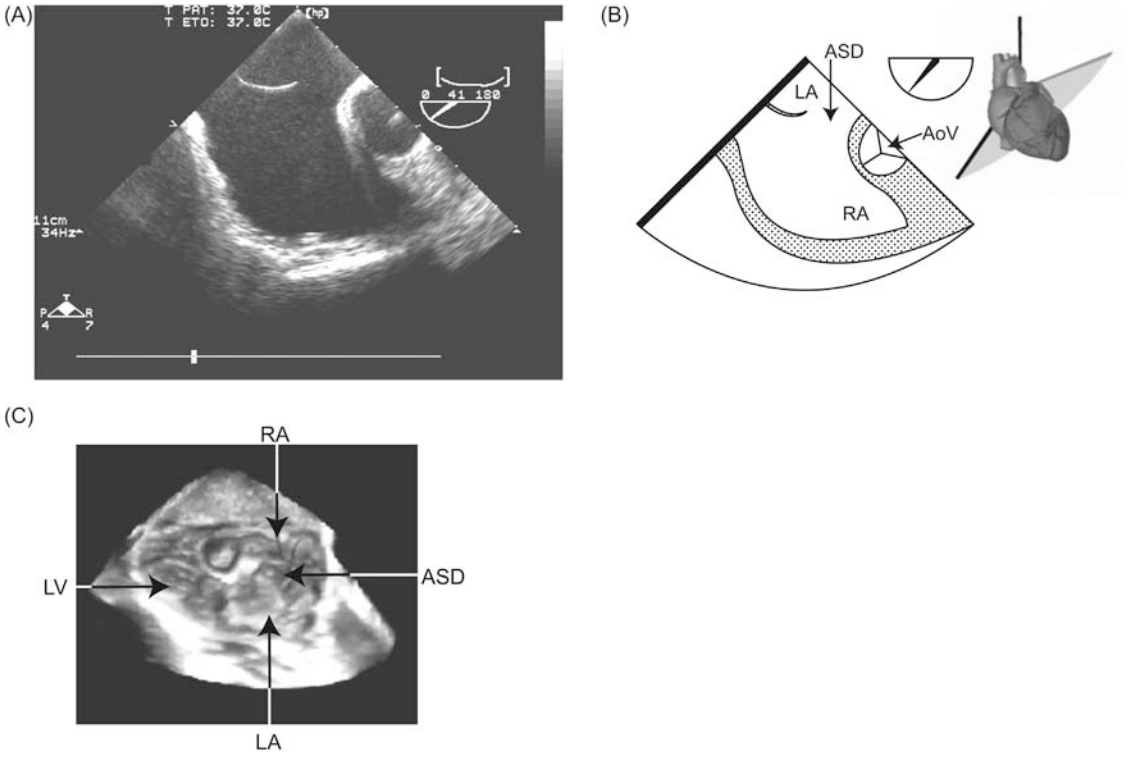

Figure 24.3 Ostium secundum atrial septal defect (ASD). (A, B) Mid-esophageal aortic valve short-axis view. (C) Three-dimensional echocardiographic view of an ASD (AoV, aortic valve; LA, left atrium; LV, left ventricle; RA, right atrium). (Photo C courtesy of Philips.)

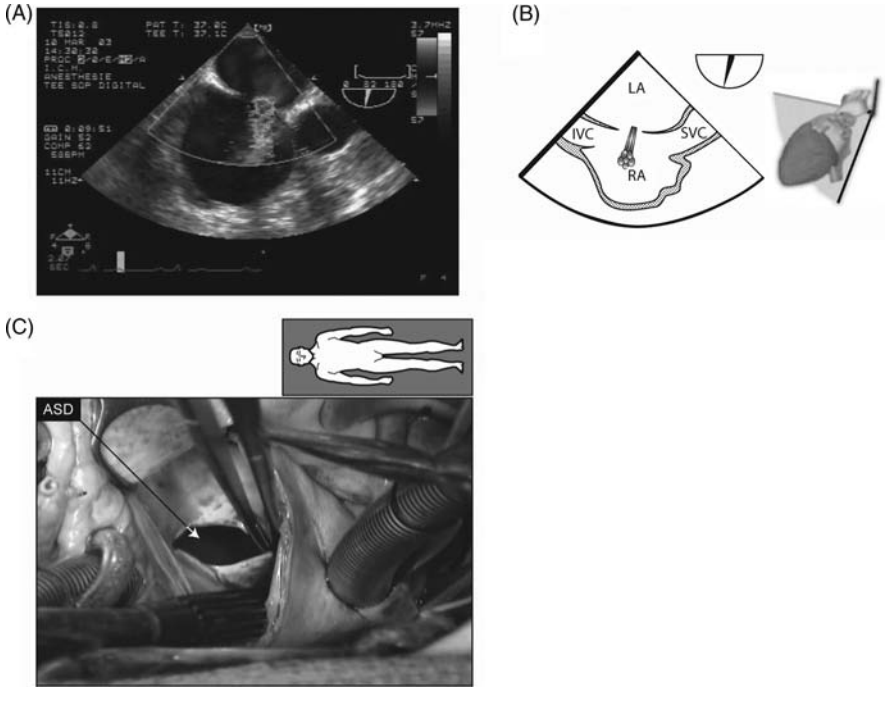

Figure 24.4 Ostium secundum atrial septal defect (ASD) in the mid-portion of the atrial septum diagnosed in a 50-year-old man undergoing coronary revascularization. (A, B) Mid-esophageal 82° view. The color flow Doppler shows the left-to-right shunt. (C) Intraoperative aspect of the ASD (IVC, inferior vena cava; LA, left atrium; RA, right atrium; SVC, superior vena cava). (Photo C courtesy of Dr. Michel Carrier.)

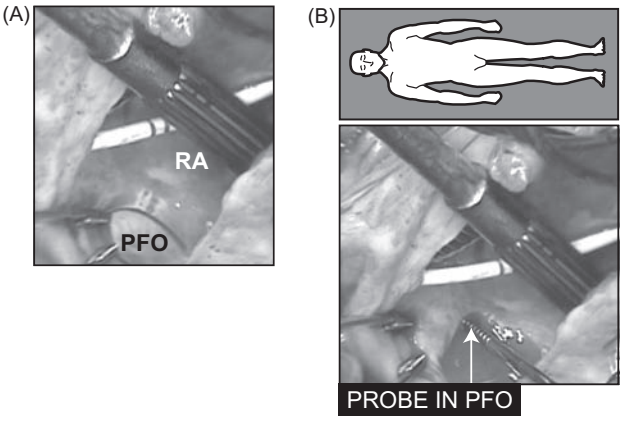

Figure 24.5 Intraoperative view through a right atriotomy of a patent foramen ovale (PFO) diagnosed and closed intraoperatively in a 67-year-old man undergoing tricuspid annuloplasty. (A) Baseline: the fossa ovalis is visible at the lower part of the image. A suction device and a Swan–Ganz catheter are also visible in the right atrium (RA). (B) Upon mild pressure on the fossa ovalis with a surgical probe, blood appears in the RA, coming from the left atrium through the PFO. (Courtesy of Dr. Michel Pellerin.)

on before the development of irreversible obstructive pulmonary artery disease. On the other hand, VSDs which persist unoperated to adult life are usually small in size, are associated with a restrictive left-to-right shunt and not accompanied with pulmonary hypertension. Morphologically, the ventricular septum is divided in four components: (1) membranous, (2) inlet, (3) muscular trabecular, and (4) outlet or infundibular septum (see Chapter 4, Fig. 4.16). The VSDs are classified according to their location as follows: (1) perimembranous, (2) inlet, (3) muscular, or (4) outlet VSDs (Fig. 24.14).

The most common defect, the perimembranous type, is located near the tricuspid septal leaflet, just beneath the right and noncoronary aortic cusps in the LVOT (Figs. 24.15 and 24.16). The small membranous portion of the ventricular septum itself is divided into an atrioventricular portion above and an interventricular portion below the insertion of the septal tricuspid leaflet. The presence of a septal aneurysm has been associated with a high incidence of spontaneous defect closure (Fig. 24.15).

Inlet VSDs, also termed atrioventricular canal defects, are located in the posterior or inlet septum and lie in

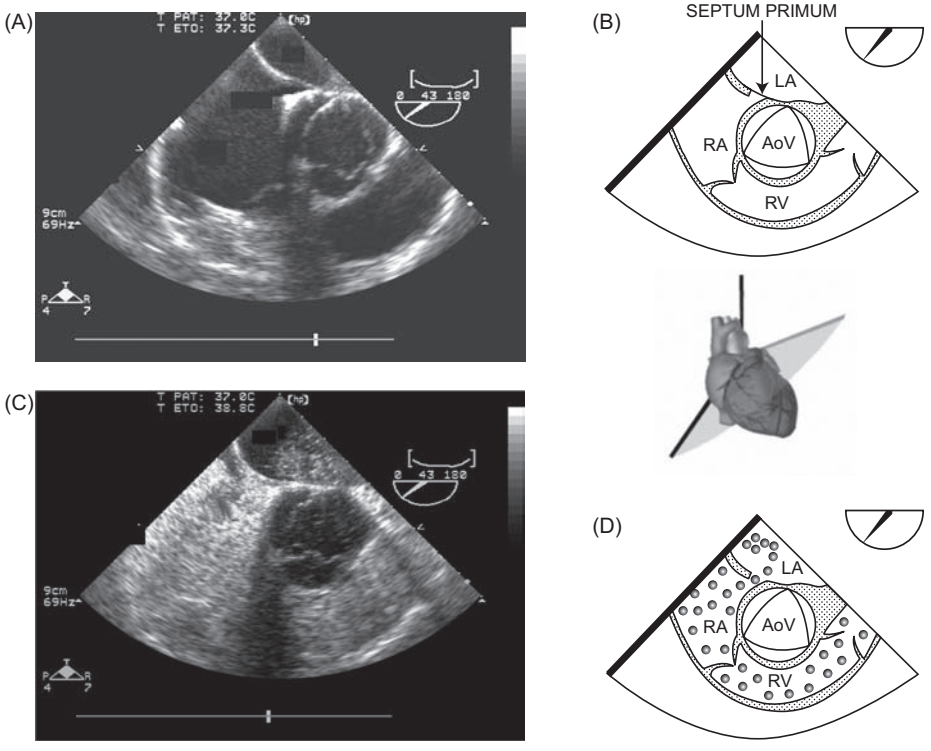

Figure 24.6 Patent foramen ovale (PFO) demonstrated by contrast echocardiography. (A, B) Mid-esophageal aortic valve (AoV) short-axis view showing at baseline an apparently intact atrial septum, with a thin septum primum near the AoV. (C, D) Opacification of the right-sided cardiac chambers by intravenous injection of agitated normal saline. During the release phase of the Valsalva maneuver, microbubbles are seen crossing to the left atrium (LA) through a PFO (RA, right atrium; RV, right ventricle).

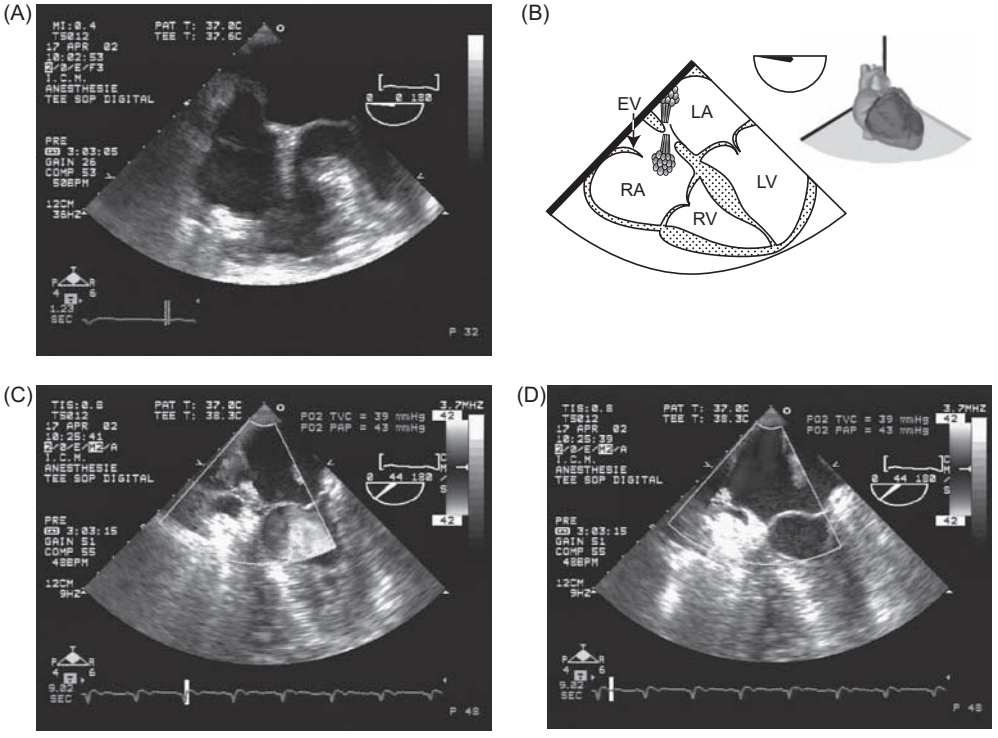

Figure 24.7 (A, B) Mid-esophageal views in an 82-year-old man with a patent foramen ovale associated with the presence of a prominent Eustachian valve (EV). (C, D) Varying right-to-left and left-to-right shunting is shown upon the different phases of positive-pressure ventilation. An increase in the oxygen partial pressure (PO_2) from the right atrium (RA) (39 mmHg) to the pulmonary artery (43 mmHg) is observed (LA, left atrium; LV, left ventricle; RV, right ventricle).

close proximity to the atrioventricular valves. Echocardiographically, these defects are recognized by the fact that both atrioventricular valves insert at the same level instead of the normal offset and inferior position of the tricuspid leaflets. These defects are usually large and do not close spontaneously, requiring surgical repair in the young.

Small muscular (trabecular) VSD may persist to adult life, but are usually very small, without significant shunt. The VSD can be seen with color Doppler anywhere along the trabecular (central or apical) part of the interventricular septum (Fig. 24.17). These defects are rarely significant enough to require surgical closure.

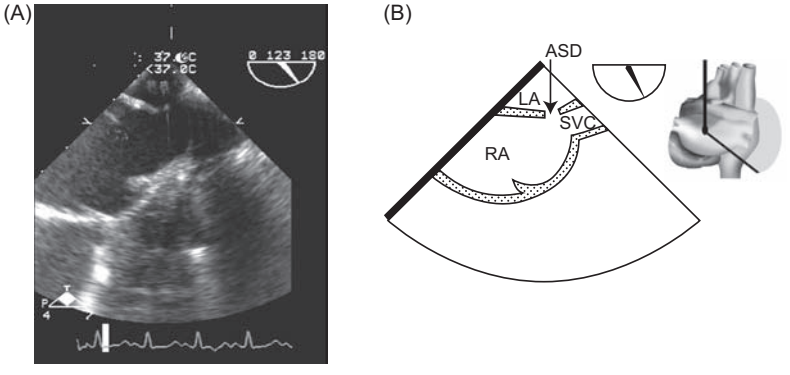

Figure 24.8 Mid-esophageal bicaval view showing a sinus venosus atrial septal defect (ASD). Note the gap between the upper part of the atrial septum and the superior vena cava (SVC). The right pulmonary veins are often anomalously connected to the SVC at its junction with the right atrium (RA) (LA, left atrium).

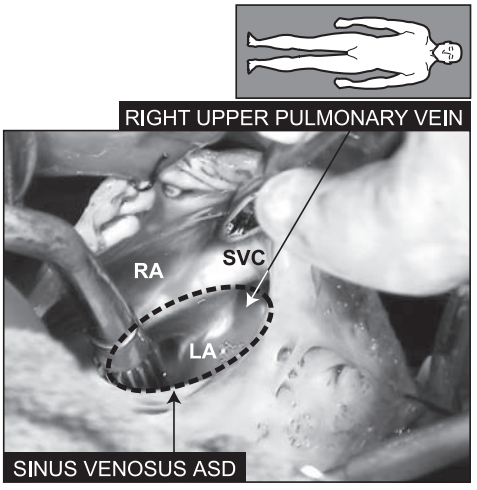

Figure 24.9 A 48-year-old man is scheduled for closure of a sinus venosus atrial septal defect (ASD). The right pulmonary veins are here connected to the left atrium (LA) and can be seen through the ASD (RA, right atrium; SVC, superior vena cava). (Courtesy of Dr. Nancy Poirier.)

Outlet VSDs are also referred to as supracristal, infundibular, conal, doubly committed, or subarterial ventricular defects. They lie proximal to the right coronary cusp and pulmonic valve (PV) in the LVOT ceiling, are usually large and do not close spontaneously (Fig. 24.18). They are often associated with prolapse of the right aortic cusp due to decreased structural aortic valvular support or damage from a high velocity impinging jet.

The VSDs persisting to adulthood are usually relatively small, and restrictive, that is, with a systolic pressure gradient between the left and right ventricles (LV, RV). Surgical management will be required if there is volume overload or if complications have developed, mainly bacterial endocarditis, or aortic cusp prolapse into the VSD with development of significant aortic regurgitation (AR) (6).

Transesophageal Echocardiography for VSD (Table 24.2)

Because of the complex anatomical characteristics of the ventricular septum due to its longitudinal twisting

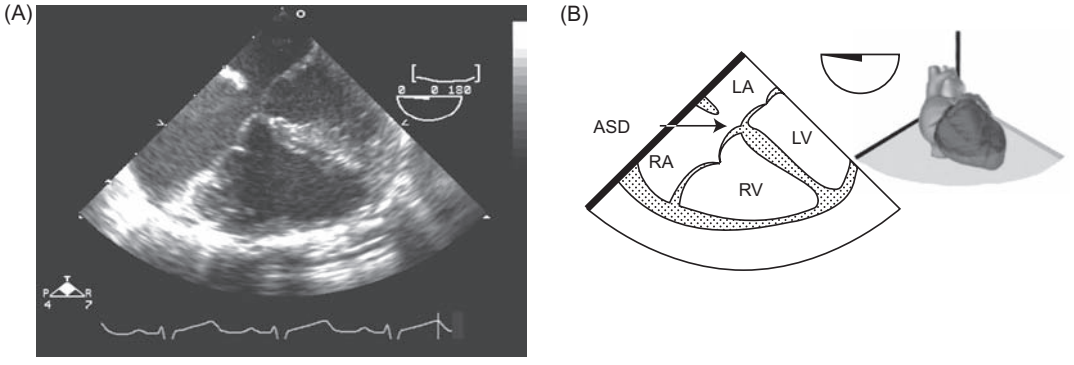

Figure 24.10 Ostium primum atrial septal defect (ASD). Mid-esophageal four-chamber view showing, in addition to the ASD, the insertion of the two atrioventricular valves at the same level on the superior aspect of the ventricular septum (LA, left atrium; LV, left ventricle; RA, right atrium; RV, right ventricle).

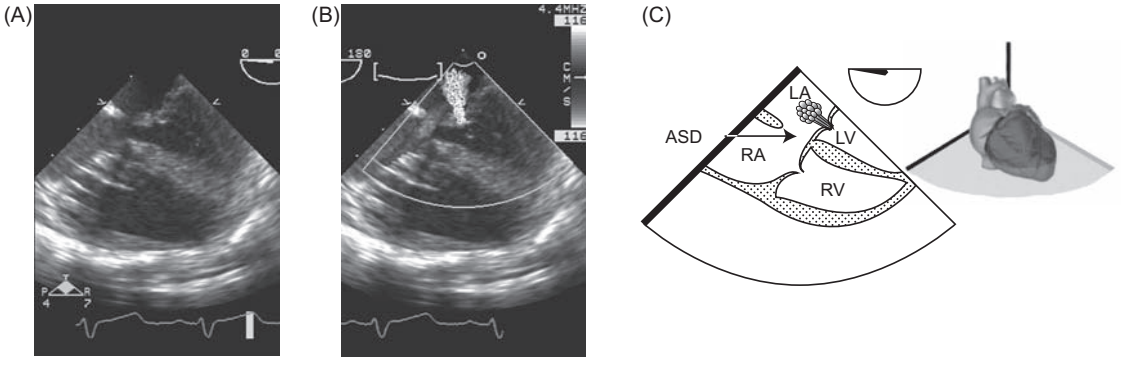

Figure 24.11 Ostium primum atrial septal defect (ASD) with a cleft anterior mitral valve leaflet. (A) Mid-esophageal four-chamber view: the lower part of the atrial septum is missing near the insertion of the atrioventricular valves. (B, C) Color-flow Doppler shows left-to-right shunting at the atrial level as well as left atrioventricular valve regurgitation through a cleft in the anterior leaflet (LA, left atrium; LV, left ventricle; RA, right atrium; RV, right ventricle).

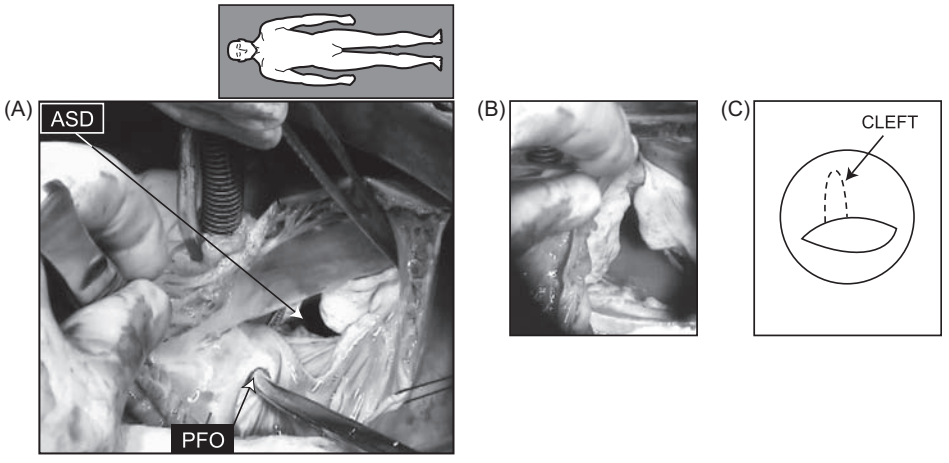

Figure 24.12 Surgical view through a right atriotomy in a 60-year-old man with an ostium primum atrial septal defect (ASD), a patent foramen ovale (PFO) (A) and a cleft anterior mitral leaflet (B, C). (Courtesy of Dr. Nancy Poirier.)

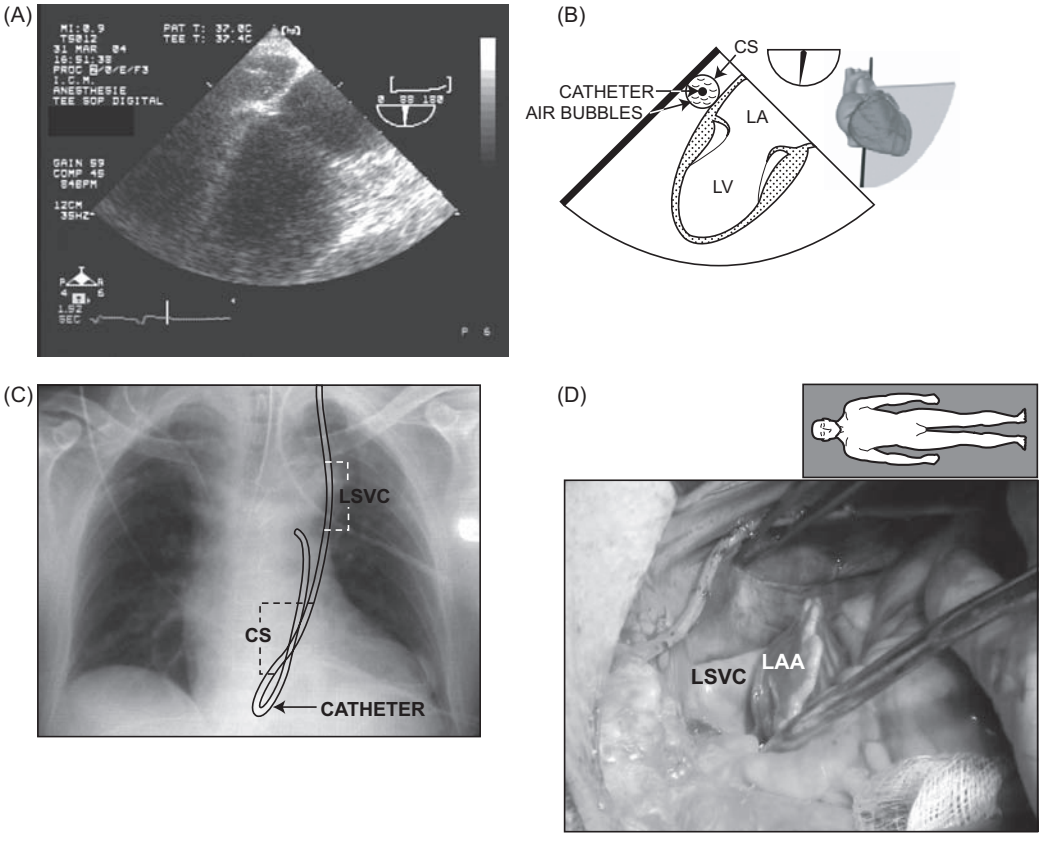

Figure 24.13 Persistent left superior vena cava (LSVC), incidentally found in a 74-year-old man undergoing cardiac surgery. (A, B) The diagnosis is evoked by a dilated coronary sinus (CS) in which a pulmonary artery (PA) catheter and air bubbles are visible. (C) Post-operative chest X-ray, confirming that the PA catheter was inadvertently inserted through the LSVC and the CS, then proceeding normally in the right atrium, the right ventricle and the PA. (D) Intraoperative view, showing the LSVC adjacent to the left atrial appendage (LAA) (LA, left atrium; LV, left ventricle). (Courtesy of Dr. Raymond Cartier.)

Table 24.2 Recommended TEE Views and Multiplane Angles to Image Various Congenital Cardiac Malformations

Malformation	View	Multiplane angle range (°)
ASD	Mid-esophageal	
	Four-chamber	0–20
	Aortic valve short-axis	30–60
	Bicaval	80–110
VSD	Mid-esophageal	
	Four-chamber	0–20
	Aortic valve short-axis	30–60
	Aortic valve long-axis	120–160
	Transgastric	
	Short-axis	0–30 (trabecular)
PDA	Upper esophageal aortic	90
	Mid-esophageal	
	RV outflow	60–90
AV canal defect (AVSD, endocardial cushion defect)	Mid-esophageal	
	Four-chamber view	0–20
	Aortic valve long-axis	120–160
	Transgastric	
	Basal short-axis (cleft mitral valve)	0–20
	Long-axis	90–110
Ebstein's anomaly	Mid-esophageal	
	Four-chamber view	0–20
	Transgastric	
	Long-axis view of TV	60–90
Pulmonary stenosis	Mid- and upper-esophageal	
	RV outflow	0–90
Tetralogy of Fallot	Mid-esophageal	
	Four-chamber	0–20
	Aortic valve short-axis	30–60
	Aortic valve long-axis	120–160
	RV outflow	60–90
Cor triatriatum	Mid-esophageal	
	Four-chamber	0–20
	Two-chamber	80–100
Mitral valve stenosis	Mid-esophageal	
	Four-chamber	0–20
	Two-chamber	80–100
	Long-axis	120–160
	Transgastric	
	Basal short-axis	0–25
	Long-axis	80–100
Cleft mitral valve	Mid-esophageal	
	Four-chamber	0–20
	Two-chamber	80–100
	Transgastric	
	Basal short-axis	0–20
Aortic valve stenosis	Mid-esophageal	
	Aortic valve short-axis	30–60
	Aortic valve long-axis	120–160
	Transgastric	
	Long-axis	90–120
Subvalvular aortic stenosis	Mid-esophageal	
	Five-chamber	0–20
	Aortic valve long-axis	120–160

(*continued*)

Table 24.2 *Continued*

Malformation	View	Multiplane angle range (°)
	Transgastric	
	Long-axis	90–120
Supravalvular aortic stenosis	Mid-esophageal	
	Aortic valve short-axis	30–60
	Aortic valve long-axis	120–160
	Transgastric	
	Long-axis	90–120
Coarctation of the aorta	Upper esophageal	
	Aortic arch long-axis	0
	Aortic arch short-axis	90
Postoperative tetralogy of Fallot	Mid-esophageal	
	Four-chamber	0–20
	Aortic valve short-axis	30–60
	Aortic valve long-axis	120–160
	RV outflow	60–90
Transposition of the great arteries	Mid-esophageal	
	Four-chamber	0–20
	Bicaval	80–110
	Aortic valve short-axis	30–60
	Aortic valve long-axis	120–160
	Transgastric	
	Basal and mid short-axis	0–20
Complex single ventricle	Mid-esophageal	
	Four-chamber	0–20
	Bicaval	80–110
	Aortic valve short-axis	30–60
	Aortic valve long-axis	120–160
	RV outflow	60–90
	Transgastric	
	Basal and mid short-axis	0–20

Note: RV, right ventricular; TEE, transesophageal echocardiography; TV, tricuspid valve.

structure, complete TEE evaluation of the interventricular septum using one tomographic view is inadequate and always requires imaging in multiple complementary planes (Fig. 24.14), which should at least include the mid-esophageal four-chamber (Fig. 24.15), and the AoV short- and long-axis views (Fig. 24.16). The precise location, extension, and size of the VSD should be first determined with the combination of two-dimensional (2D) echocardiography, color, and spectral Doppler modalities. The measurement of a significant interventricular shunt pressure gradient between the LV and RV (Figs. 24.17 and 24.18) will define the VSD as restrictive. The importance of the VSD may also be reflected by its repercussions on the size of the right and the left cardiac chambers. In a significant VSD with Eisenmenger's physiology, right ventricular dimensions and systolic function should be measured as well as the level of pulmonary artery pressure (see Chapter 5).

Other associated lesions should be sought depending on the location of the VSD. The AoV should be systematically examined in outlet VSD and the degree and mechanism of AR carefully assessed.

3. Atrioventricular Septal Defect

Between the fourth and eighth-week of gestation, fusion of the growing endocardial cushions with the muscular portion of the ventricular septum and the right and the left ridges of the bulbus cordis results in the division of the single ventricle into two separate ventricles. If the endocardial cushions fail to fuse, development of the atrioventricular valves, the lower portion of the atrial septum and the upper portion of the ventricular septum will be deficient, leading to the atrioventricular septal defect. This condition is also referred to as atrioventricular canal defect, canal-type VSD or endocardial cushion defect. The complete form of endocardial cushion defect will create a large atrial septal defect, a large inlet ventricular septal defect and a common atrioventricular valve (Fig. 24.19). The latter consists of five leaflets: the

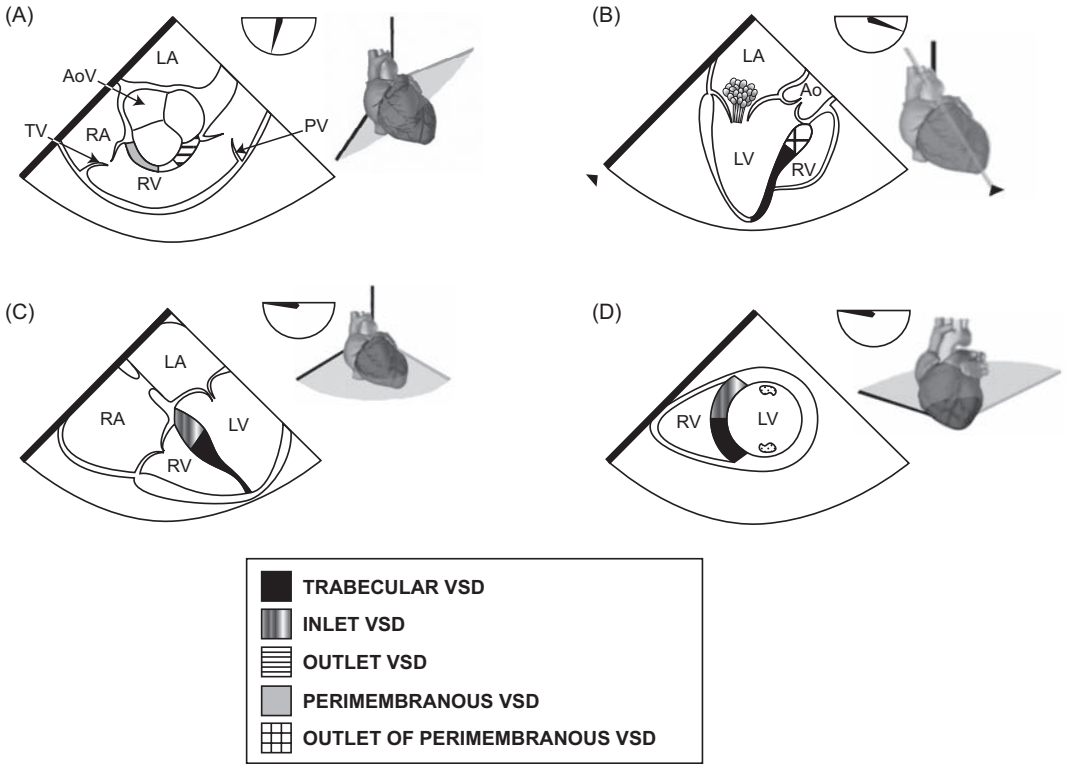

Figure 24.14 Classification of ventricular septal defects (VSD) according to their localisation. (A) Right ventricular inflow–outflow view. (B) Mid-esophageal long-axis view. (C) Mid-esophageal four-chamber view (D) Transgastric view (Ao, aorta; AoV, aortic valve; LA, left atrium; LV, left ventricle; PV, pulmonic valve; RA, right atrium; RV, right ventricle; TV, tricuspid valve).

normal left posterior mitral valve, the anterior and posterior tricuspid leaflets, and the remaining two, the anterosuperior and posteroinferior leaflets which straddle the atrial and ventricular septa and may be attached to the top of the ventricular septum by short chordae tendinae. The common valvular orifice may have an undivided common orifice or be divided into two orifices by a tongue of tissue that connects the bridging leaflets. The variable attachment of the atrioventricular valve to the cardiac septae results in different levels of intracardiac shunting (atrial, ventricular, ventriculoatrial). Various forms of partial endocardial cushion defects have been described depending upon the presence of interatrial or interventricular communication. When the interventricular

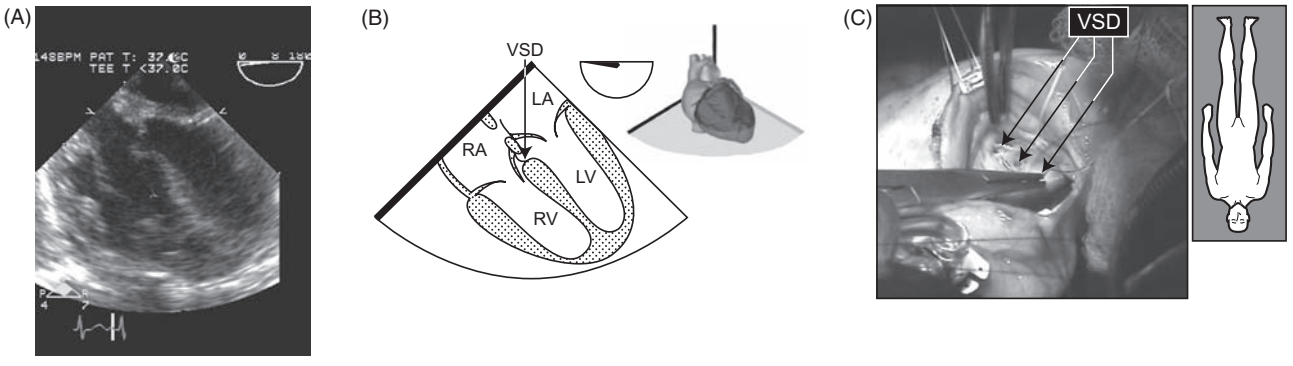

Figure 24.15 (A, B) Perimembranous ventricular septal defect (VSD). The mid-esophageal four-chamber view shows an aneurysmal membranous septum bulging towards the right ventricle (RV) at the upper part of the interventricular septum (arrow). (C) Intraoperative aspect of three small perimembranous VSD in a 54-year-old man (LA, left atrium; LV, left ventricle; RA, right atrium). (Photo C courtesy of Dr. Denis Bouchard.)

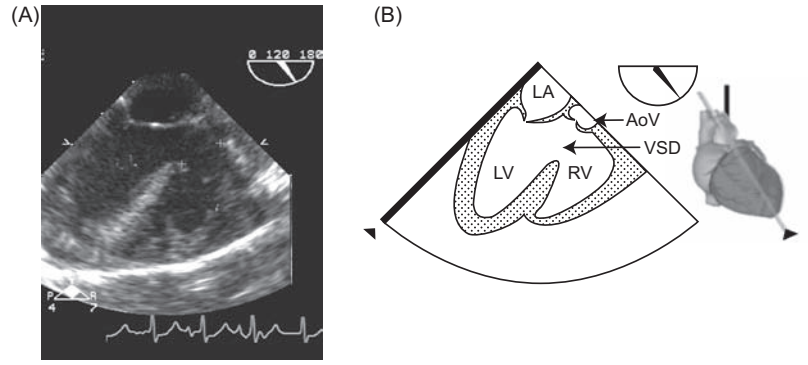

Figure 24.16 Mid-esophageal long-axis view showing a large nonrestrictive membranous ventricular septal defect (VSD) (AoV, aortic valve; LA, left atrium; LV, left ventricle; RV, right ventricle).

communication is large and nonrestrictive, massive shunting leads to pulmonary hypertension, obstructive pulmonary vascular disease, and early heart failure, requiring surgical repair. On the other hand, when the VSD is small or absent as in the partial form with only an interatrial communication resulting in an ostium primum ASD and a cleft anterior mitral leaflet (Fig. 24.12), the diagnosis is sometimes made at an older age.

TEE in Atrioventricular Septal Defect (Table 24.2)

The echocardiographic evaluation should focus on the following points: the type and extent of intracardiac shunting, the atrioventricular valve morphology, assessment of the commitment of the atrioventricular junction to the underlying ventricular myocardium, assessment of ventricular size (in certain cases, the ventricles are unequal in

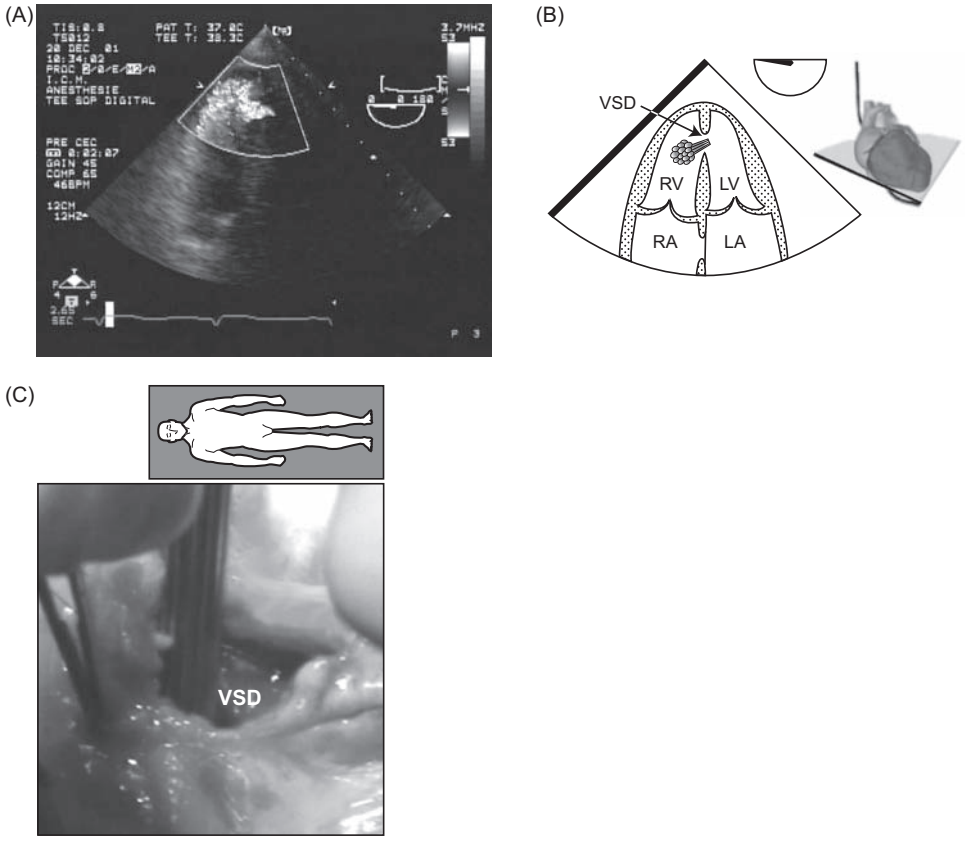

Figure 24.17 Trabecular muscular ventricular septal defect (VSD). (A, B) Deep transgastric view, showing a left-to-right shunt on the color Doppler examination. (C) Intraoperative findings (LA, left atrium; LV, left ventricle; RA, right atrium; RV, right ventricle).

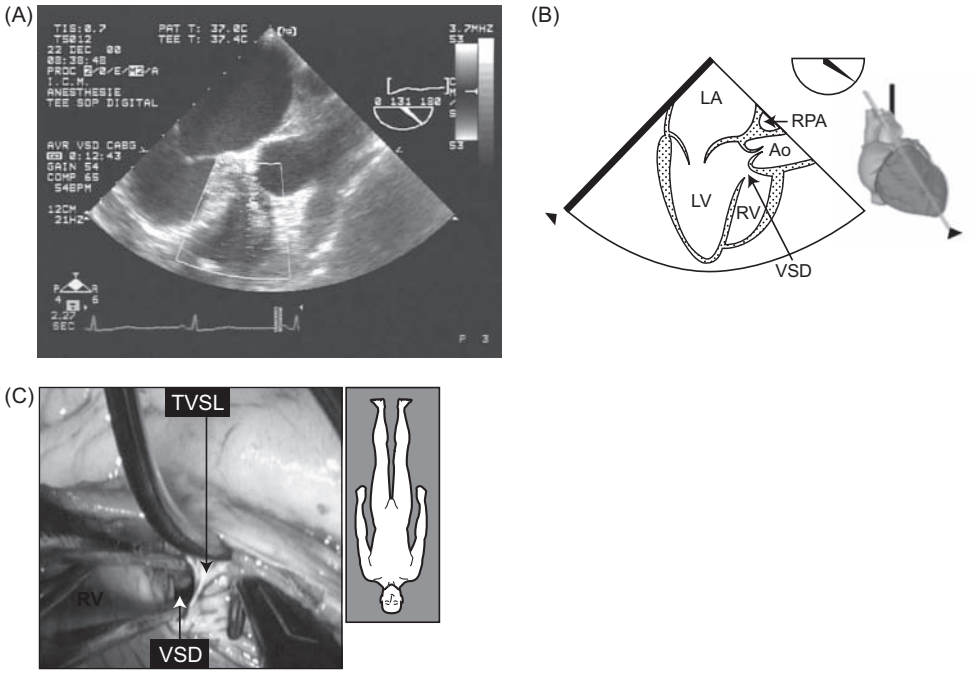

Figure 24.18 (A, B) Infundibular or subarterial membranous ventricular septal defect (VSD) seen using color Doppler in a mid-esophageal long-axis view. (C) Intraoperative view from the opened pulmonary artery (Ao, aorta; LA, left atrium; LV, left ventricle; RPA, right pulmonary artery; RV, right ventricle; TVSL, tricuspid valve septal leaflet). (Courtesy of Dr. Nancy Poirier.)

size and the defect is said to be unbalanced), and identification of associated lesions, such as tetralogy of Fallot, double outlet RV, anomalous pulmonary venous connection, pulmonary stenosis (PS), or atresia. Postoperative assessment includes detection of residual shunting, atrioventricular valve regurgitation, potential atrioventricular valve stenosis or LVOT obstruction. The view that allows the best images of this anomaly is the mid-esophageal four-chamber view (Fig. 24.19). A cleft anterior mitral valve may be more easily visualized in the transgastric short-axis view at the mitral valve level at 0°.

4. *Patent Ductus Arteriosus*

The ductus arteriosus serves, during fetal life, as a communication between the pulmonary artery and the Ao and normally closes after birth. As it fibroses, it becomes the ligamentum arteriosum. The patient with a persistently patent ductus arteriosus (PDA) thus has a communication

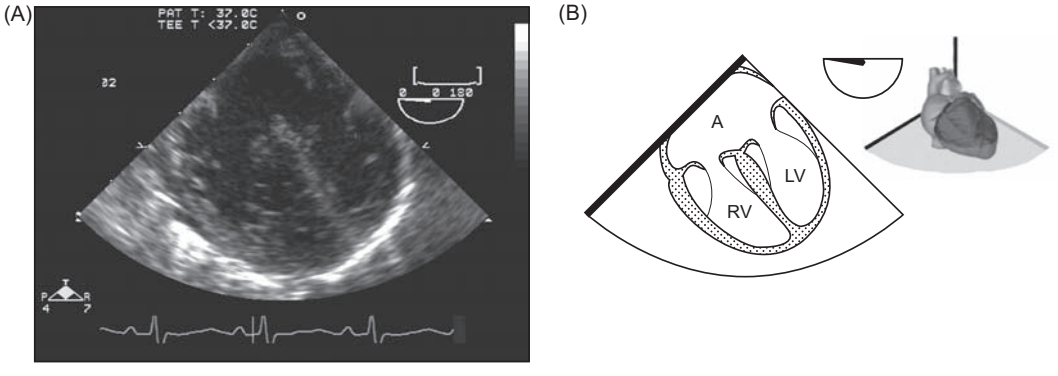

Figure 24.19 Atrioventricular septal defect in diastole showing a large defect at the center of the heart and balanced right ventricle (RV) and left ventricle (LV) (A, atrium).

between the high-pressure Ao and the lower-pressure pulmonary artery leading to a left-to-right shunt past the right ventricular level. Therefore, the volume overload will result in dilatation of the pulmonary vessels, the left cardiac chambers and the Ao, but not the RA or RV. Significant PDA will present early in life with heart failure symptoms and pulmonary hypertension. On the other hand, a smaller PDA may remain unrecognized for years and be incidentally discovered during a work-up for other medical problems. Moderate shunt will cause decreased exercise tolerance and may predispose to the development of pulmonary hypertension and right heart failure. Closure of a PDA can be performed percutaneously by an interventional cardiologist with insertion of a device (coils, Amplatz device, or Rashkin device). The alternate approach is surgical and requires a left thoracotomy or it can be performed using video-assisted thoracoscopic surgery.

TEE in Ductus (Table 24.2)

As the ductus arteriosus courses in front of the trachea and above the left main bronchus draining most often to the superior aspect of the left side of the pulmonary artery bifurcation, adequate visualization of the duct is frequently difficult. Starting from the four-chamber view at 0°, pullback of the probe higher in the esophagus reveals dilatation of the main, right and left pulmonary arteries with presence of an abnormal turbulent shunt flow from the PDA. The PDA may also occasionally be visualized "from above" in the high esophageal aortic views at 90° with rotation of the probe towards the right: left-to-right continuous color flow is then seen from the transverse aorta to the main pulmonary artery.

B. Tricuspid Valve Anomaly

1. Ebstein's Anomaly of the Tricuspid Valve

The classic findings in Ebstein's anomaly of the tricuspid valve (TV) include a large sail-like anterior leaflet and apically displaced septal and posterior leaflets (Fig. 24.20) (7–9). Apical displacement must exceed (8 mm/m^2) in adults. As a consequence of this displacement, the right heart is composed of three parts: the RA, the atrialized portion of the RV, and the functional RV which includes the trabecular and outlet RV. The septal and posterior leaflets of the TV are displaced from the atrioventricular junction and usually display impaired mobility because of short chordae, tethering, thickening, and fibrosis (Fig. 24.21). Tricuspid regurgitation (TR) is usually present in varying degrees and the regurgitant jet can be traced to the coaptation level in the distal right ventricular

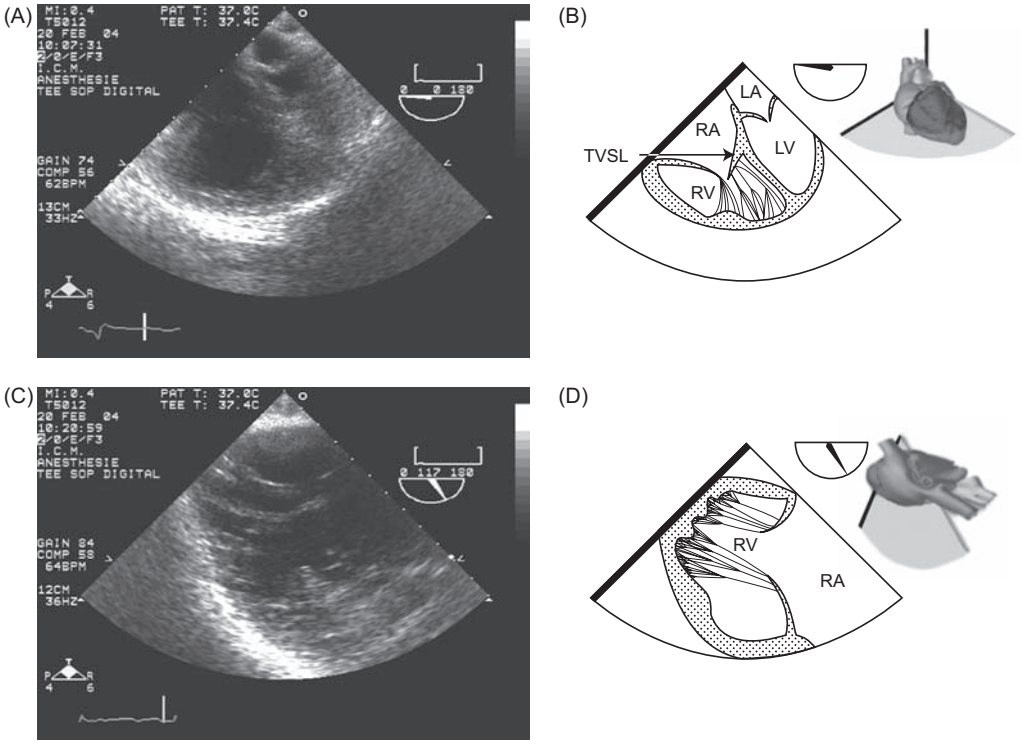

Figure 24.20 A 62-year-old woman with Ebstein's anomaly. (A, B) Mid-esophageal view: the insertion of the tricuspid valve septal leaflet (TVSL) is displaced towards the apex, with atrialization and dilatation of part of the right ventricular inflow. (C, D) Transgastric 117° view. Note the obvious trabeculations of the dilated right ventricle (RV) (LA, left atrium; LV, left ventricle; RA, right atrium).

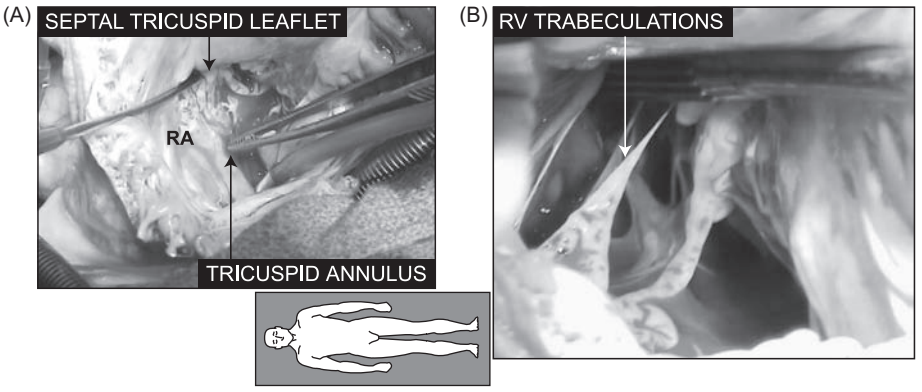

Figure 24.21 Intraoperative views of an Ebstein's anomaly in a 62-year-old woman (same patient as in Fig. 24.20). (A) The origin of the tricuspid septal leaflet is displaced apically in relation to the normal position of the tricuspid annulus (RA, right atrium). (B) Prominent abnormal trabeculations, resulting from noncompaction of the right ventricle (RV). (Photos C and D courtesy of Dr. Nancy Poirier.)

chamber. Tricuspid stenosis is occasionally seen as well. Tricuspid annular dilatation is the rule and can be severe. The severity of the Ebstein's anomaly is described as the ratio between the functional RV and the combined area of both the RA and atrialized RV. A ratio inferior to 35% is associated with a poor prognosis. Other characteristic features include a dilated or aneurysmal RVOT, obstruction due to a redundant anterior TV leaflet, and altered geometry of the LV with regional (inferoseptal) dysfunction. The left ventricular function may be difficult to evaluate by echocardiography because of the paradoxical motion of the interventricular septum and the crescentic shape of the LV due to bulging of the interventricular septum to the left. An interatrial septal defect or patent foramen ovale, is a frequent associated finding, such that contrast administration should be part of the examination. Although the Ebstein's anomaly is more often isolated, mitral valve prolapse, pulmonary stenosis, and VSD can also be present. Finally, Ebstein's anomaly is occasionally part of the corrected transposition of the great arteries.

TEE in Ebstein (Table 24.2)

The features of Ebstein's anomaly are best demonstrated with the mid-esophageal four-chamber view: (1) degree of apical displacement of the origin of the TV septal leaflet from the atrioventricular junction, (2) the location of leaflet coaptation within the right ventricular cavity, (3) the presence and severity of TR and/or stenosis, and (4) the integrity of the TV leaflet and subvalvular apparatus to assess its suitability for repair vs replacement. Evaluating the latter also benefits from the transgastric longitudinal views of the TV at 60–90°, which can also add useful information about the presence and morphology of obstructive lesions within the infundibulum and the PV. Associated congenital lesions such as ASD and PS are best demonstrated with the appropriate views for those lesions. While TEE can be useful preoperatively to confirm the diagnosis and document associated lesions, in the immediate postoperative period following valve replacement and/or right heart plication procedures, TEE should be aimed at evaluating residual stenosis or regurgitation and confirming the adequate function of the implanted prosthesis.

C. Right Ventricular Outflow Tract Anomaly

1. Pulmonary Stenosis (Subvalvular, Valvular, Supravalvular)

Valvular PS is the most common form of RVOT obstruction; it is almost always congenital in origin, and is found in ~10% of adults with congenital heart defects (see Chapter 19; Fig. 19.18). Typically, the stenotic pulmonic valve presents as a dome-shaped structure with thin, pliable tissue and a narrow opening at the apex. In 10–15% of the cases, the valve is dysplastic with thickened and immobile cusps. When the systolic pressure gradient is moderate (50–79 mmHg) to severe (>80 mmHg) or the patient is symptomatic, percutaneous balloon valvuloplasty is recommended. Results are normally good except for dysplastic valves which often require a valvotomy. Assessment by echocardiography should include morphologic examination of the valve, determination of annular size, severity of obstruction, sizing of the main pulmonary artery and its branches, documentation of right ventricular dilatation and/or hypertrophy, and other associated congenital lesions.

Subvalvular or infundibular stenosis is usually associated with other anomalies, especially VSD and tetralogy of Fallot. A separate but similar entity is the double-chamber RV with mid-cavitary obstruction, often from a prominent moderator band, frequently associated also with a VSD.

Supravalvular stenosis is rarely an isolated occurence. It may be part of a tetralogy of Fallot or the William's syndrome, Noonan's syndrome, Allagyl's syndrome (arteriohepatic dysplasia), or the congenital rubella syndrome.

Moderate to severe sub- and supravalvar stenosis can only be relieved surgically.

TEE in RVOT Obstruction (Table 24.2)

Transesophageal echocardiography evaluation preoperatively must confirm the diagnosis, demonstrate the severity of the obstruction and identify associated anomalies. The RVOT is best visualized with the mid- and upper-esophageal right ventricular outflow views (see Chapter 19, Fig. 19.17). Transgastric views centered on the right heart may help to determine the gradient, usually at 90–120°. Postoperatively, after reconstruction of the RVOT with a pericardial patch or repair with a conduit or a homograft, TEE should identify residual stenosis and surgically induced PV regurgitation.

2. Tetralogy of Fallot

The tetralogy of Fallot is one of the most common complex congenital cardiac malformations found in adults. (1) The primary anomaly underlying this malformation is an anterocephalad deviation of the outlet septum, resulting in RVOT obstruction which is usually infundibular, but can also be valvular or supravalvular. The other components of the tetralogy are secondary to the hypoplastic infundibulum and anterior and rightward displacement of the conal septum. (2) As the latter is no longer aligned with the trabecular septum, an anterior malalignment subaortic VSD is present and usually nonrestrictive. (3) The AoV is displaced anteriorly and to the right following the conal septum, overriding the trabecular septum (Fig. 24.22). (4) Right ventricular hypertrophy is secondary to the systemic pressure in the RV due to the nonrestrictive VSD. The severity of the disease depends largely on the degree of narrowing of the infundibulum, ranging from mild hypoplasia with good antegrade flow through the RVOT with mild cyanosis, to complete atresia of the infundibulum with no antegrade flow to the pulmonary arteries. The patient is then dependent on pulmonary blood flow coming either from aortopulmonary collaterals or from a PDA. Collaterals may originate anywhere in the arterial system but usually arise from the descending Ao and the transverse arch. Other associated features include additional muscular VSDs, anomalous coronary arteries, right aortic arch, PDA, aortic root dilation, and ASD. The major coronary artery anomalies include a prominent right conal artery, or an anterior descending coronary originating from the right coronary artery.

Adults presenting with a tetralogy of Fallot can be separated into three groups (10): (1) the patients who

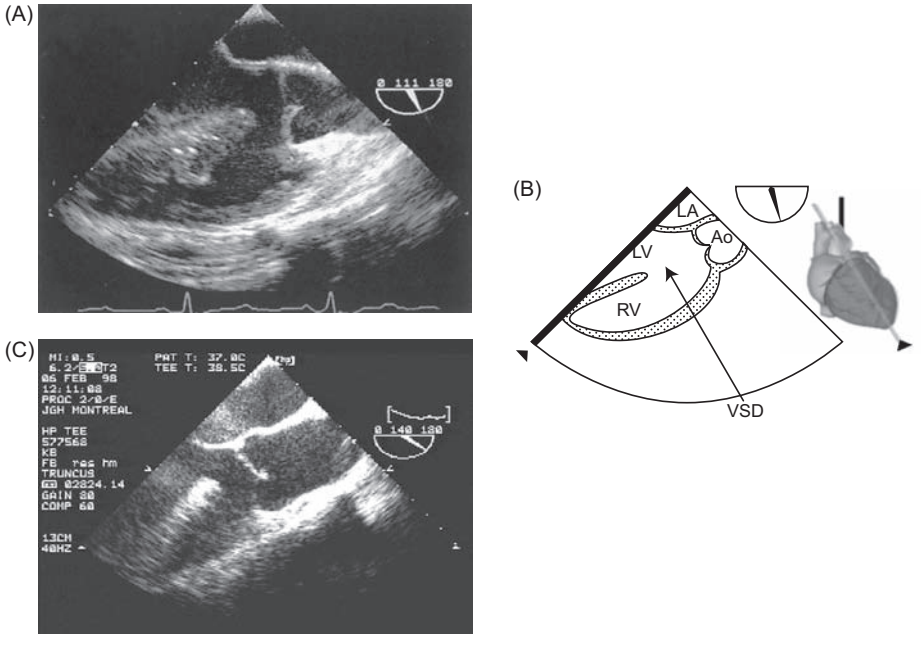

Figure 24.22 (A, B) Tetralogy of Fallot. Mid-esophageal long-axis view, showing a ventricular septal defect (VSD) and the aortic root overriding the ventricular septum. (C) Truncus arteriosus: note the similarity with tetralogy of Fallot. There is however a separate origin for the pulmonary artery in the tetralogy abnormality (Ao, aorta; LA, left atrium; LV, left ventricle; RV, right ventricle). [Photo A, modified with the permission from Miller-Hance et al. (1) and Photo C courtesy of Dr. François Béïque.]

previously underwent a corrective procedure in infancy or childhood who survived to adulthood; (2) the patients with an unoperated form of tetralogy of Fallot, either the unusual patient with mild RVOT obstruction, or the patient with an extreme form of tetralogy with aortopulmonary collaterals; and (3) the patients who underwent a palliative surgery anteriorly in childhood and who reach adulthood without having undergone corrective surgery. The types of palliation includes: Blalock–Taussig shunt or modification (subclavian artery to pulmonary artery shunt), Waterston shunt (ascending Ao to right pulmonary artery), Potts shunt (descending Ao to left pulmonary artery), central interposition tube graft, infundibulum resection (Brock), or pulmonary valvotomy, RV to pulmonary artery conduit without VSD closure or partial closure of the VSD.

TEE in Tetralogy of Fallot (Table 24.2)

The role of preoperative echocardiography in nonoperated tetralogy of Fallot is mainly to evaluate the level and severity of the RVOT obstruction, demonstrate the size of the VSD, and rule out aortic valve incompetence sometimes associated with aortic root dilatation. Distal pulmonary arteries and coronary arteries are better evaluated with angiography. The large nonrestrictive perimembranous VSD is best visualized in the mid-esophageal four-chamber view and AoV short- and long-axis views (Fig. 24.22). The appearance is similar to a truncus arteriosus and is differentiated by the identification of a separate origin of the pulmonary artery. The direction of the shunt can also be evaluated using color flow mapping. Other shunts either at the atrial level or in the trabecular ventricular septum should be ruled out. The RVOT is best visualized with the upper- and mid-esophageal right ventricular outflow views.

The immediate postoperative echocardiographic evaluation should attempt at detecting residual RVOT obstruction and shunt through the VSD, demonstrating regurgitation of either the native pulmonary valve or the valved conduit or homograft. Evaluation of TR is important and can also be used to evaluate the RV systolic pressure. This should be completed by the evaluation of RV function, size and thickness, LV function, and aortic valve competence.

D. Left Atrial Anomaly

1. Cor Triatriatum

Cor triatriatum sinister is a rare congenital cardiac malformation involving the LA, resulting embryologically from failure of the common pulmonary vein to become incorporated into the LA. The incomplete absorption leaves a fibromuscular membrane dividing the left atrial chamber into a proximal compartment (the atrial accessory chamber) receiving the pulmonary veins and a distal compartment or true left atrial chamber, which most often contains the fossa ovalis and the left atrial appendage. The size of the communicating hole(s) between the proximal and the distal chambers determines the clinical picture. The degree of obstruction varies from being barely detectable

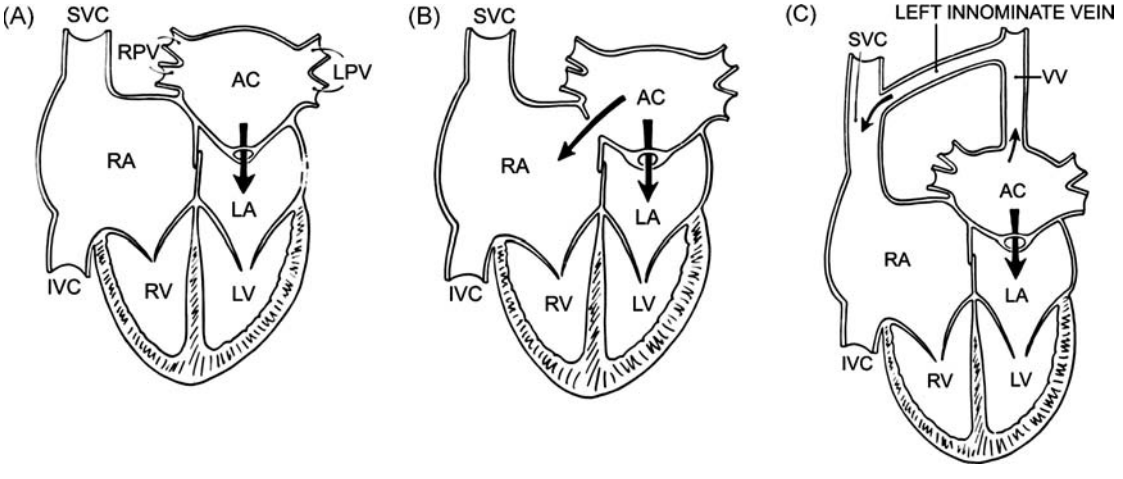

Figure 24.23 Variants of cor triatriatum sinister where the atrial accessory chamber (AC) communicates with the left atrium (LA). (A) Classic cor triatriatum. The atrial AC receives the right pulmonary veins (RPV) and the left pulmonary veins (LPV). The only outlet for pulmonary venous blood is the orifice of the fibromuscular transatrial membrane. (B) Cor triatriatum with anomalous connection between the atrial AC and the right atrium (RA). This communication decompresses the atrial AC and results in a left-to-right shunt at the atrial level. (C) Cor triatriatum with anomalous pulmonary venous connection. Here the accessory AC is decompressed by way of a vertical vein (VV) to the left innominate vein (IVC, inferior vena cava; LV, left ventricle; RA, right atrium; RV, right ventricle; SVC, superior vena cava). [Adapted with permission from (11).]

to causing severe inflow obstruction and pulmonary venous congestion. There are many anatomic variations of that defect (Figs. 24.23–24.25). The atrial accessory chamber may communicate only with the LA [Fig. 24.23(A)], with both LA and RA [Fig. 24.23(B)], or only with the RA, either directly through an ASD [Fig. 24.24(A)] or through an anomalous venous connection [Fig. 24.24(B)]. In the incomplete anomaly (Fig. 24.25), so-called subtotal cor triatrial, the accessory atrial chamber receives part of the pulmonary veins and connects either to the LA or to the RA. The other veins connect either normally to the LA or abnormally to the RA through an anomalous vein.

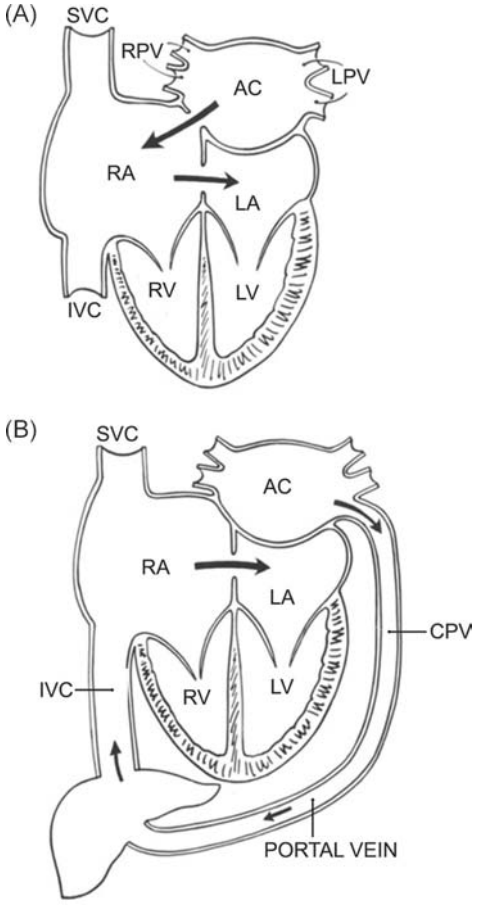

Figure 24.24 Variants of cor triatriatum sinister, where the atrial accessory chamber (AC) does not communicate with left atrium (LA). (A) the atrial AC communicates with the right atrium (RA). Blood reaches the true LA via a patent foramen ovale (PFO) or an atrial septal defect (ASD). (B) The atrial AC connects with a common pulmonary vein (CPV) which reaches the portal vein. Pulmonary venous blood traverses the hepatic vascular bed and the inferior vena cava (IVC) and ultimately reaches the LA through a PFO or an ASD. (LV, left ventricle; RV, right ventricle; SVC, superior vena cava). [Adapted with permission from (11).]

The physiopathological consequences of the cor triatriatum sinister is directly related to the degree of obstruction through the transatrial fibromuscular membrane between the atrial accessory chamber and the true LA, as well as to the presence of additional connections. It may remain unrecognized if there is no obstruction and no connection with the RA. On the other hand, in the presence of a narrow orifice causing severe inflow obstruction, significant pulmonary venous congestion leads to pulmonary artery hypertension. Cyanosis may coexist if there is right-to-left shunt from the RA to the distal LA (Fig. 24.24). In severe forms, the diagnosis is usually made early in infancy and surgically corrected. Nonobstructive forms can be diagnosed as an incidental finding in adults during an echocardiographic study (Fig. 24.26).

TEE in Cor Triatriatum Sinister (Table 24.2)

Due to its very close proximity with the LA and pulmonary veins, TEE is ideally suited for the characterisation of cor triatriatum sinister. The fibromuscular membrane is classically seen coursing transversely in the LA in the mid-esophageal four- and two-chamber views (Fig. 24.26). The diagnosis requires documentation that the atrial accessory chamber does receive the pulmonary veins while the left atrial proper chamber includes both the foramen ovale and the left atrial appendage (LAA). However, if the proximal chamber includes the ostium of the LAA or communicates with the atrial septal defect, the diagnosis of a supravalvular mitral ring should rather be considered. The connection of each pulmonary vein should be identified to rule out anomalous venous drainage in these patients. Other anomalous connections should also be identified, such as an ASD connecting with the proximal atrial accessory chamber.

E. Mitral Valve Anomalies

The normal mitral valve has an anterior (aortic) and a posterior (mural) leaflet. The two commissures of these leaflets are subtended by the posteromedial and anterolateral papillary muscles and chordae tendineae. The congenital anomalies of the mitral valve most frequently encountered include congenital mitral stenosis (MS) (including the parachute mitral valve), an isolated cleft in the mitral valve and the double-orifice mitral valve. The anomalies that will be discussed here are the congenital mitral valve stenosis and the isolated cleft of the mitral valve.

1. Mitral Valve Stenosis

Obstructions to left ventricular inflow include congenital MS with two papillary muscles, parachute mitral valve, supravalvular mitral ring, and cor triatriatum (see preceding text) (12).

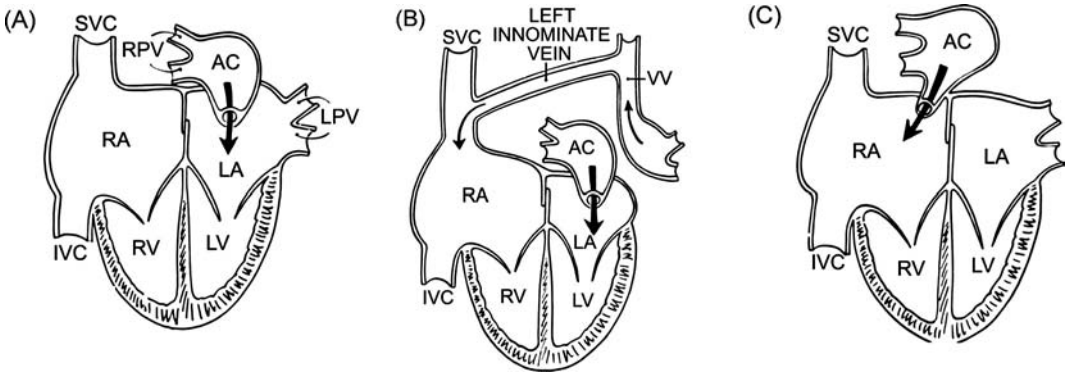

Figure 24.25 Variants of cor triatriatum sinister: subtotal cor triatriatum. (A) The atrial accessory chamber (AC) receives the right pulmonary veins (RPV) and communicates via a stenotic opening to the left atrium (LA), while the left pulmonary veins (LPV) connect normally to the LA. (B) Subtotal connection of the RPV to the LA by means of a stenotic opening and of the LPV to the right atrium (RA) via a vertical vein (VV) and the left innominate vein. (C) Subtotal connection of the RPV to the RA via a stenotic opening, while the LPV is normally connected to the LA (IVC, inferior vena cava; LV, left ventricle; RV, right ventricle; SVC, superior vena cava). [Adapted with permission from (11).]

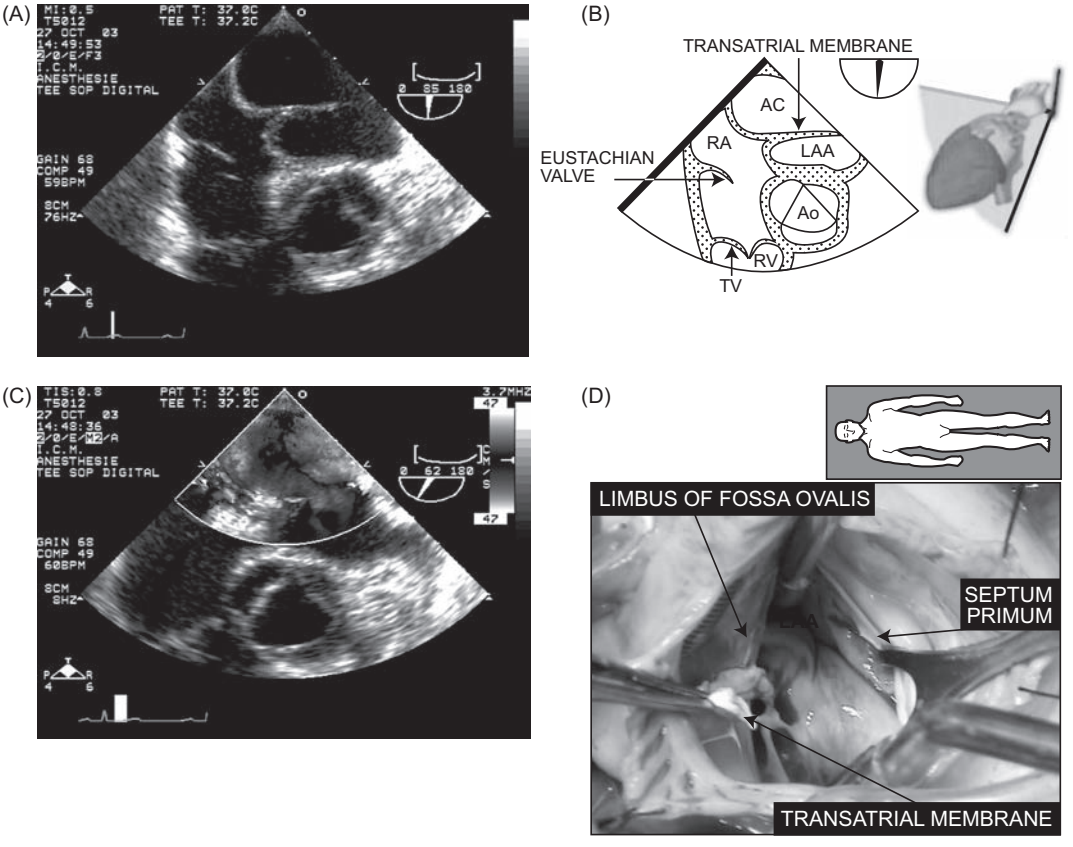

Figure 24.26 Classic cor triatriatum sinister with a Eustachian valve in a 49-year-old woman scheduled for repair. (A, B) Mid-esophageal views: a fibromuscular membrane courses between the atrial septum and the junction of the left upper pulmonary vein (LUPV) and the left atrial appendage (LAA). The atrial accessory chamber (AC) receives the LUPV. (C) A left-to-right shunt through a patent foramen ovale is present. (D) Intraoperative views: the fibromuscular diaphragm has a thin Swiss cheese slice appearance (Ao, aorta; RA, right atrium; RV, right ventricle; TV, tricuspid valve). (Photo D courtesy of Dr. Nancy Poirier.)

Congenital MS can be classified according to which component of the mitral valve apparatus is abnormal, including leaflets, annulus, chordae, or papillary muscles (13). Most cases, however, involve variable combinations of structural anomalies, including annulus hypoplasia, thickened rolled leaflet margins, commissural fusion, shortened and thickened chordae tendineae, fibrous obliteration of the interchordal spaces (Fig. 24.27), abnormal chordal insertion, papillary muscle hypoplasia, and decreased interpapillary muscle distance or fusion. Echocardiographically, the mitral valve leaflets appear thickened, dysplastic, and echo-dense; they move poorly and dome during LV diastolic filling. The subvalvular mitral apparatus similarly presents an echo-dense, crowded appearance.

The parachute mitral valve represents about half of the MS diagnosed in pediatric patients (Fig. 24.27). It is characterized by insertion of all the chordae tendineae into a single papillary muscle group. The mitral valve leaflets also appear dense, with restricted motion. The chordae are generally shortened and thickened. The anatomy of the papillary muscles is highly variable. A single papillary muscle in the LV, the hallmark of this lesion, may be identified in the four-chamber view, the transgastric short- and long-axis views. The parachute mitral valve is often associated with other anomalies which constitute the Shone's syndrome, that is, a supravalvular mitral ring, subaortic stenosis, and coarctation of the aorta.

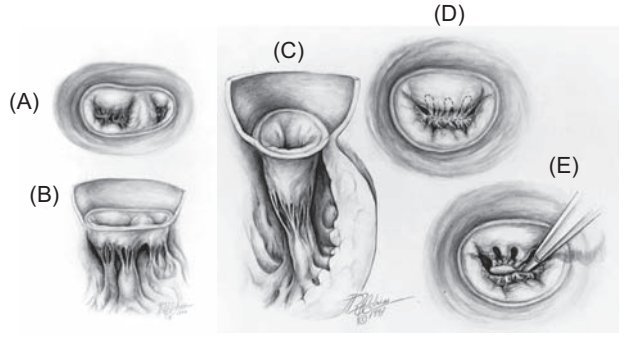

Figure 24.27 (A, B) Double-orifice mitral valve: (A) left atrial and (B) cut-away atrioventricular views: More commonly, the smaller of the two orifices is in the right lateral position; the degree of stenosis is variable. (C–E) Stenotic parachute mitral. (C) Cut-away atrioventricular view: a single papillary muscle or fused papillary muscles usually arise from the posterior left ventricular wall. (D) Left atrial views: the dotted lines show the areas of proposed leaflet fenestrations and papillary muscle incision to open the ventricular inlet. Leaflet fenestrations are performed to maximize unrestricted blood flow into the left ventricle during diastole while preserving enough valvular tissue for effective coaptation during systole. (E) The fused papillary muscle is being incised to facilitate valvular mobility. [With permission from Zias et al. (13).]

Nearly 70% of parachute mitral valves are associated with a supravalvular mitral ring while 60% present a significant diastolic pressure gradient.

The supravalvular mitral ring rarely occurs as an isolated finding. In most instances, other anomalies are found such as parachute mitral valve, subaortic stenosis, or coarctation of the aorta. A supravalvular ring is also found with 20% of congenital MS with two anatomical papillary muscles. It originates from a collection of connective tissue arising from the atrial surface of the mitral leaflets and consequently encroaches on the mitral valve orifice. It may be closely adherent to the anterior mitral valve leaflet. The ring itself causes a significant obstruction in only 10% of cases. In the other case, the ring does not add significant obstruction to the associated mitral valve stenosis.

TEE in Mitral Stenosis (Table 24.2)

The mitral valve is best evaluated with the mid-esophageal four- and two-chamber, and long-axis views using 2D and color-flow imaging, as well as Doppler determination of mitral inflow diastolic pressure gradient. The transgastric views can also help to better evaluate the subvalvular apparatus.

2. Cleft Mitral Valve

This rare anomaly of the mitral valve, often associated with significant MR, usually involves the anterior leaflet but cases affecting the posterior leaflet have also been reported (Figs. 24.11 and 24.12). Attachments of the chordae tendineae arising from the margins of the cleft to the ventricular septum may cause LVOT obstruction. The most commonly associated congenital cardiac anomalies include ASD, VSD, and transposition of the great arteries.

TEE in Cleft Mitral Valve (Table 24.2)

The TEE plane which best demonstrates the cleft anterior leaflet is the transgastric basal short-axis view of the LV at the level of the mitral valve. The cleft appears as a break in the continuity of the anterior leaflet which divides it into a medial and a lateral portion. In true cleft of the mitral valve, the cleft is pointing towards the LVOT while the atrioventricular septum is intact and the TV is normally inserted lower than the mitral valve. In contrast, in atrioventricular septal defects, the so-called "mitral valve cleft" constituted by the space between the anterior and posterior bridging leaflets rather points medially towards the inlet ventricular septum (Fig. 24.11). Incomplete cleft or mitral valve defect can also be seen (see Fig. 17.22).

F. Aortic Valve Anomaly

1. *Bicuspid Aortic Valve, Congenital Aortic Valve Stenosis*

The bicuspid AoV is the most common congenital anomaly in adults. It occurs in approximately 2–3% of the general population (see Chapter 15). Initially, the bicuspid valve functions normally without much stenosis and with minimal regurgitation. However, early fibrocalcific changes develop with time and can progress to significant stenosis and/or regurgitation. Frequent associated anomalies include VSD and coarctation of the Ao. The anomaly may also exist in the context of the multiple left-sided obstructive lesions in the Shone's complex with parachute mitral valve.

Cross-sectional examination of the bicuspid valve in the closed position (diastole) shows in most cases two equal or nearly equal cusps (Fig. 24.28). Occasionally, the cusps are unequal in size with an eccentric commissure. The larger cusp may display a raphe as a remnant of the embryonic fusion between the two cusps. In the closed position, the presence of a raphe gives the false impression that the valve has three cusps. However, in systole, the valve opens only along two of the closure lines and will not separate at the site of the raphe. Hence, the number of cusps in the AoV is best determined during systole rather than diastole.

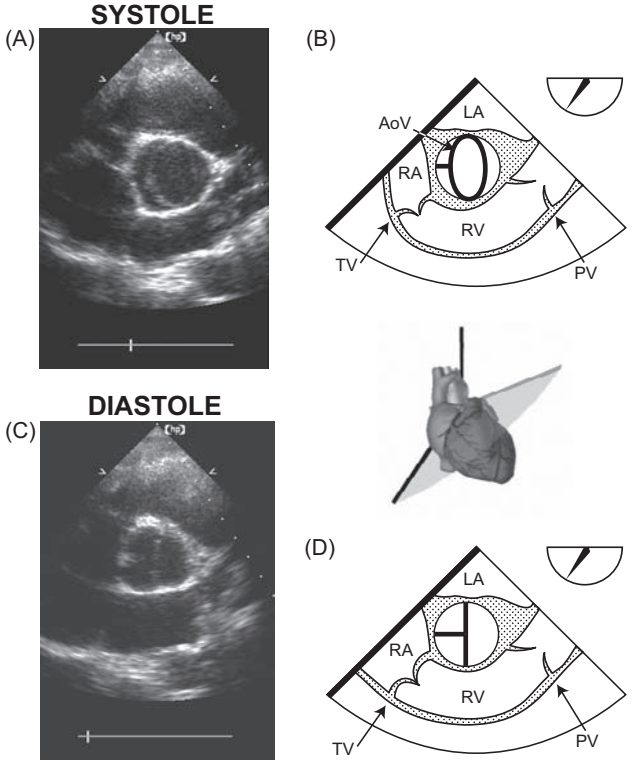

Figure 24.28 Bicuspid aortic valve. (A, B) In systole, the aortic orifice is oval rather than normally triangular, with commissure at 12 and 6 o'clock. (C, D) In diastole, a raphe at 9 o'clock falsely gives the appearance that the aortic valve (AoV) has three cusps (LA, left atrium; PV, pulmonic valve; RA, right atrium; RV, right ventricle; TV, tricuspid valve).

TEE in Aortic Valve Stenosis (Table 24.2)

The valve should be evaluated in multiple planes, mainly the mid-esophageal AoV short- (Fig. 24.28) and long-axis views. The operator should pay particular attention to the valve morphology, the number of cusps, their mobility, the annular size, and the origin of the coronary arteries with regard to the sinuses of Valsalva. Associated features may include left ventricular hypertrophy and poststenotic dilatation of the ascending Ao (see Chapter 15; Fig. 15.16). Color flow Doppler readily identifies AoV regurgitation and assists in the evaluation of its severity. A quantitative evaluation of the degree of outflow obstruction can be obtained by Doppler echocardiography. The transgastric long-axis or deep transgastric view provides optimal alignment of the ultrasound beam with the aortic flow for recording of the subvalvular (V_1) and maximal (V_2) velocities (see Chapter 15; Fig. 15.13). Using the modified Bernoulli equation, estimates of the peak instantaneous and mean pressure gradients across the stenotic AoV can be obtained from Doppler recordings. Perioperative TEE evaluation will also involve evaluation of the PV in patients undergoing repair with a pulmonary autograft or Ross procedure. The PV should be evaluated to determine its size to ensure adequate match and to rule out significant pulmonary regurgitation or stenosis.

2. *Supra- and Subvalvular Aortic Stenosis*

Subvalvular Aortic Stenosis

Fixed, nondynamic subaortic stenosis is classified into three categories: membranous, fibromuscular, and tunnel types. The first two types consist of a discrete membranous diaphragm or fibromuscular ring encircling the LVOT (see Chapter 15, Fig. 15.18). The ridge may be found in close proximity to the AoV or may be located several millimeters below the valve level (Fig. 24.29). The high velocity jet from the subaortic stenosis may damage the aortic cusps and lead to significant valvular regurgitation. The third type consists of a long tunnel-like narrowing just beneath the base of the aortic valve.

TEE in Subvalvular Aortic Stenosis (Table 24.2)

The mid-esophageal long-axis view of the LVOT at 135° provides adequate definition of the subaortic obstruction and evaluation of AoV competence (see Chapter 15, Fig. 15.18). The deep transgastric long-axis view allows evaluation of the systolic peak and mean pressure gradient.

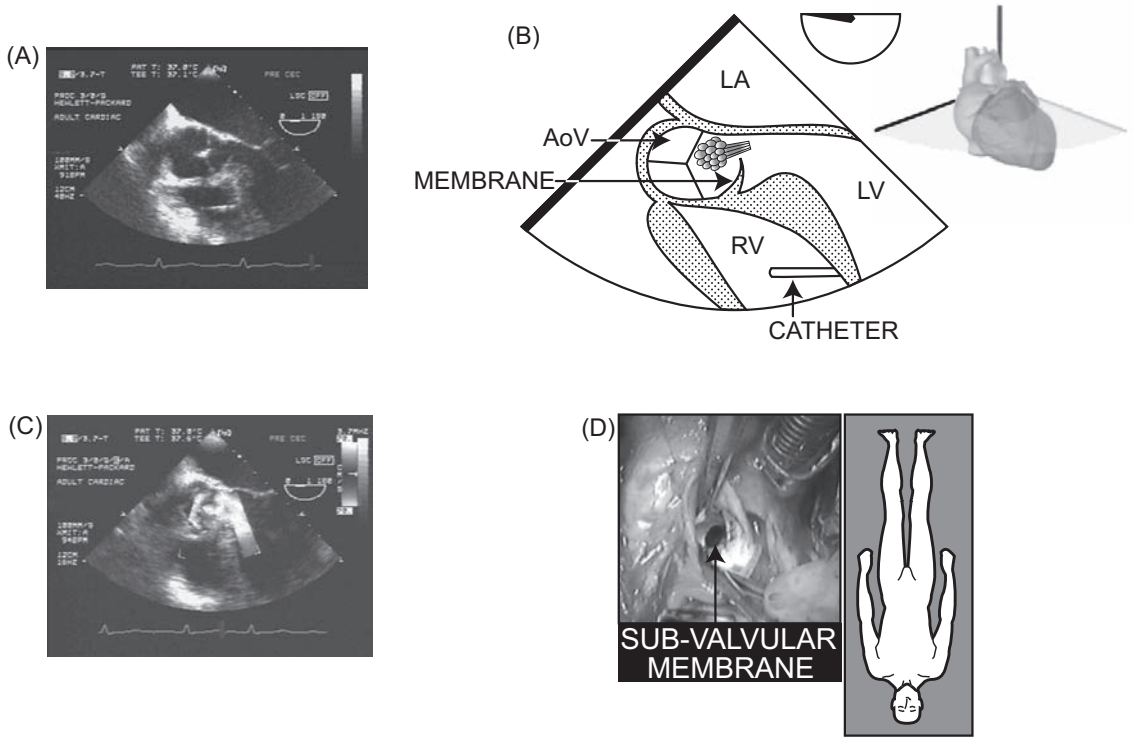

Figure 24.29 Subvalvular aortic stenosis before coronary bypass. (A, B) Mid-esophageal five-chamber view at 0°: a membrane seems present in the left ventricular outflow tract. (C) Color Doppler shows flow acceleration close to the membrane. (D) Intraoperative findings (AoV, aortic valve; LA, left atrium; LV, left ventricle; RV, right ventricle). [Courtesy of Dr. Louis Normandin.]

Postoperative TEE should document the adequacy of the resection, as well as the integrity of the neighboring ventricular septum, aortic, and mitral valves which may have been injured because of their proximity with the resected area.

Supravalvular Aortic Stenosis

Supravalvular AS denotes obstructive constriction of the ascending Ao above the AoV (see Chapter 15, Fig. 15.17). This anomaly is commonly (30–40% of cases) associated with the William's syndrome (elfin facies) and often involves other areas of vascular stenosis, such as peripheral pulmonary artery stenosis, coarctation of the aorta, or renal artery stenosis. The obstructing ring is situated above the AoV and the sinuses of Valsalva. The edge of the obstructing tissue may impinge upon a sinus of Valsalva compromising flow to the coronary ostia. The obstruction may be localized, virtually membranous or may extend diffusely into the ascending Ao (Fig. 24.30). The aortic cusps are often thickened and distorted and aortic regurgitation is common but rarely severe.

The physiology is comparable to that of valvular stenosis except that coronary blood flow may be under increased pressure and the coronary ostia may be obstructed. Surgery is undertaken in patients with symptoms or with a mean pressure gradient >50 mmHg. Patch angioplasty of the ascending Ao is usually undertaken plus coronary ostial angioplasty when necessary.

TEE in Supravalvular Aortic Stenosis (Table 24.2)

The diagnosis is easily made by echocardiography. The TEE mid-esophageal aortic long-axis view (see Chapter 15; Fig. 15.17) demonstrates the supravalvular narrowing and allows precise evaluation of the aortic cusps anatomy (Table 24.2). Aortic regurgitation can be easily demonstrated. The mid-esophageal AoV short-axis view may reveal the coronary ostia narrowing or obstruction in some cases. Continuous-wave Doppler through the aortic valve and ascending aorta using the deep transgastric long-axis view allows determination of the left ventricular-aorta gradient. Associated aortic coarctation and stenosis of brachiocephalic arteries are more easily demonstrated with transthoracic echocardiography (TTE) using the suprasternal view, or with aortography and magnetic resonance imaging (MRI).

G. Coarctation of the Aorta

Coarctation of the Ao is a narrowing of the Ao usually at the level of the ligamentum arteriosus. It is usually discrete

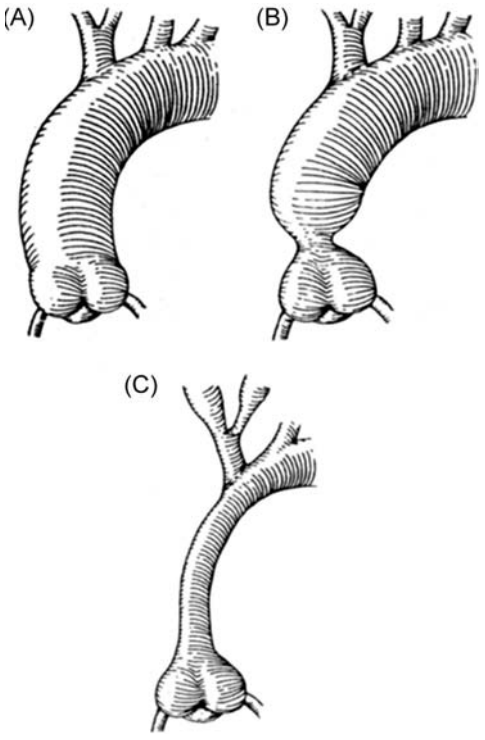

Figure 24.30 Anatomic types of supravalvular aortic stenosis. (A) Normal aorta. (B) Focal supravalvular stenosis. (C) Tubular supravalvular stenosis. Note the concomitant obstruction in the innominate and common carotid arteries as they arise from the aortic arch. Other arterial obstructions, such as coarctation of the aorta, renal artery stenosis, and pulmonary artery stenosis, are found in some patients. [Reproduced with permission from (14).]

but can be associated with diffuse hypoplasia of the aortic arch and isthmus. Coarctation is considered "simple" when it is discrete and without major intracardiac lesions. This is the form most commonly diagnosed *de novo* in teenagers and adults (Fig. 24.31). In contrast, "complex" aortic coarctation is usually diagnosed in infancy and is associated with other important intracardiac anomalies, mainly VSD, subvalvular AS, and valvular AS. The coarctation is hemodynamically significant in the presence of right arm hypertension and a peak pull-back gradient of >20 mmHg across the coarctation during catheterization. However, minimal or no pressure gradient may be encountered in the presence of significant collateral circulation. Associated cardiovascular anomalies include: bicuspid AoV in close to 85%, intracranial berry aneurysms of the circle of Willis in 3–5% and anomalies of the brachiocephalic circulation such as anomalous origin of the right subclavian artery in 5%. Other anomalies include collaterals involving the internal mammary arteries anteriorly and the intercostal arteries posteriorly as well as VSD and aortic medial disease in the paracoarctation area and in the ascending Ao.

TEE in Coarctation (Table 24.2)

The best echocardiographic window to visualize a coarctation is the transthoracic suprasternal notch view. It provides 2D imaging of the obstruction and allows acquisition of the Doppler-derived pressure gradient across the area of narrowing. Severe coarctation is suggested by high-velocity flow in systole with a gradient that persists in diastole. Abnormal flow will be found distally in the abdominal Ao. Multiplane TEE evaluation can provide helpful 2D information about the area of obstruction which is usually apparent just below the aortic arch past the origin of the left subclavian artery. In the upper-esophageal short-axis view at 0° the coarctation will appear as a narrowing of the cross-sectional area with a variable degree of hypoplasia proximally and dilatation distally. The long-axis view at 90° provides additional insight about the length and morphology of the coarctation (Fig. 24.31). However, in either views, Doppler determination of pressure gradient is frequently difficult due to inadequate alignment of the ultrasound beam with the blood flow. Hence, preoperative MRI or biplane aortography may be required to complete the evaluation in adults. Postsurgical evaluation includes determination of residual narrowing, recurrent obstruction or aneurysmal formation.

III. PREVIOUSLY REPAIRED CONGENITAL HEART DEFECTS

A. Tetralogy of Fallot

Tetralogy of Fallot has been described in detail earlier in this chapter. We will focus mainly on the patient with tetralogy of Fallot who previously underwent a complete repair in infancy and has survived to adulthood. Over the years, many situations may develop in the operated patient which warrant reintervention. These include: 1—residual VSD with a shunt greater than 1.5:1.2, 2—residual pulmonary stenosis with elevation of right ventricular pressure to two-thirds or more of the systemic pressure, 3—severe pulmonary regurgitation associated with progressive right ventricular enlargement, TR, significant atrial, or ventricular arrhythmias and worsening exercise intolerance, 4—significant AR associated with symptoms and left ventricular enlargement and dysfunction, 5—aortic root enlargement, and 6—large RVOT aneurysm (15–17).

TEE in Operated Tetralogy of Fallot (Table 24.2)

When previously operated patients with tetralogy of Fallot need reoperation, the preoperative TEE evaluation is performed mainly to evaluate atrioventricular valve competence, RV and LV size and function, RVOT size, residual RVOT obstruction, and pulmonary regurgitation. The presence of aortic root dilatation, AoV regurgitation,

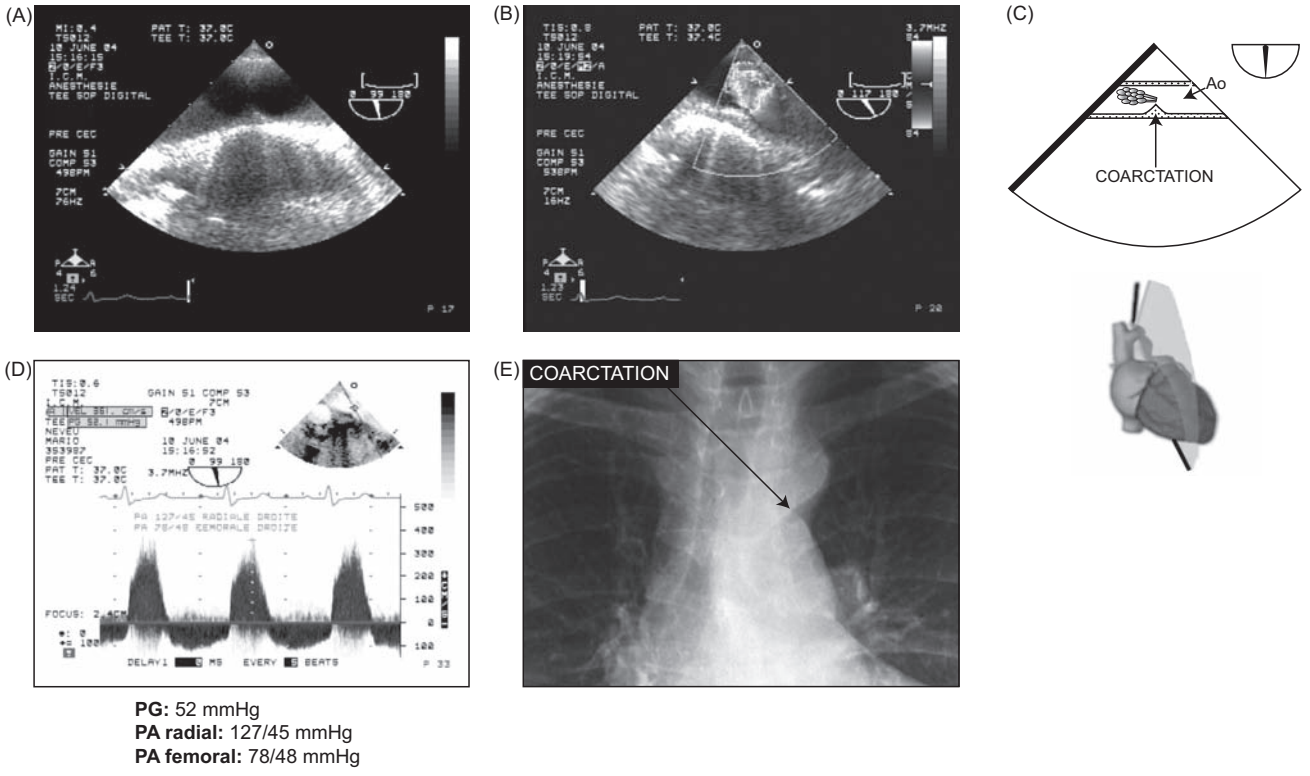

Figure 24.31 Aortic coarctation in a 48-year-old man with bicuspid aortic valve scheduled for valve replacement. (A–C) The aortic coarctation with color Doppler aliasing is seen in a 99° view of the ascending aorta (Ao). (D) The pressure gradient (PG) was 52 mmHg. This is close to the 49 mmHg PG obtained using the systolic radial to femoral arterial pressure (Pa) difference. (E) Chest X-ray of the patient. Note the aortic indentation (the "3" sign) typical of the coarctation.

and residual VSD should also be ruled out or confirmed. These patients are also at risk for developing atrial fibrillation and endocarditis. The most useful TEE views include the mid-esophageal AoV short- and long-axis views, the mid-esophageal four-chamber view, and the mid-esophageal RVOT view. The immediate postoperative TEE evaluation will examine the result of the surgery and the need for further repair.

B. Transposition of the Great Arteries

In transposition of the great arteries (TGA), there is atrioventricular concordance and ventriculoarterial discordance. Physiologically, the systemic venous return is directed back to the Ao, whereas the pulmonary venous return is directed back to the pulmonary arteries. The majority of the transposition are "simple" with no other major anomalies, while the others are more complex and are associated with anomalies such as VSD and/or pulmonary obstruction. Most patients present with cyanosis soon after birth. Unoperated TGA is lethal with 90% mortality in the first year of life. Nearly all patients seen in adolescence or adulthood will have had surgery. The most common previous procedure in patients who are now adults was the atrial switch operation. Crafting an intra-atrial baffle made of a prosthetic patch (original Mustard procedure), supplemental pericardial tissue (modified Mustard procedure), or atrial tissue (Senning procedure), systemic venous return is redirected at the atrial level to the subpulmonary morphologic LV while pulmonary venous blood is rerouted to the subaortic morphologic RV, thus achieving physiological correction. With this repair, the morphologic RV has to support the high pressures of the systemic circulation.

Starting in the late 1980s, the atrial switch operation has progressively been replaced by the arterial switch operation which consists of switching the great arteries and translocating the coronary arteries to the neoaorta (Fig. 24.32) (18). The theoretical advantage of this repair lies in the morphologic LV being the systemic ventricle.

The Rastelli operation addressed patients with a VSD and pulmonary stenosis. Blood is redirected at the ventricular level by tunnelling the left ventricular outflow to the Ao and a valved conduit connects the RV to the pulmonary arteries. The morphologic LV supports the systemic circulation.

Long-term postoperative sequelae will vary according to the type of operation performed. Long-term recognized

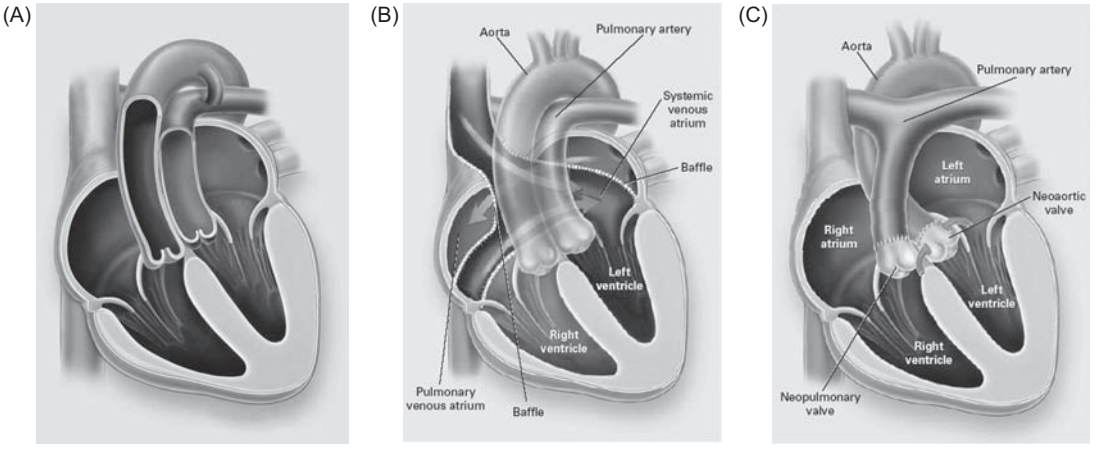

Figure 24.32 D-Transposition of the great arteries (TGA). (A) The aorta is connected to the right ventricle while the pulmonary artery is connected to the left ventricle. Therefore, systemic venous blood returns to the right atrium, from which it goes to the right ventricle and then back to the systemic circulation through the aorta. Pulmonary venous blood returns to the left atrium, from which it goes to the left ventricle and then to the pulmonary artery. Survival is possible only if there is a communication between the two parallel circuits, such as with a patent ductus arteriosus. (B) The "atrial switch" operation: a baffle is created in the atria, so that blood returning from the systemic venous circulation is diverted into the left ventricle and then the pulmonary artery (blue arrows), whereas blood returning from the pulmonary venous circulation is directed into the right ventricle and then the aorta (red arrow). (C) The "arterial switch" operation: the pulmonary artery and ascending aorta are transected above the semilunar valves and coronary arteries, are then switched (neoaortic and neopulmonary valves). [With permission from Brickner et al. (18).]

sequelae in patients who underwent an atrial switch operation include: right (systemic) ventricular dysfunction, significant TR, symptomatic bradycardia, tachycardia, or sick sinus syndrome. Other potential late complications include obstruction of the SVC or IVC venous pathways, baffle leak resulting in significant left-to-right or right-to-left shunting, progressive left ventricular outflow subpulmonary obstruction (19,20). Some of those sequelae are best approached by percutaneous interventions: balloon angioplasty and stent insertion for baffle obstruction or occlusion devices for baffle leaks. Other sequelae such as atrioventricular valve regurgitation, subpulmonary, obstruction, or ventricular dysfunction require surgery. The patient with a failing RV and severe TV regurgitation may be considered for heart transplantation.

Late complications of the arterial switch procedure include significant RVOT obstruction, myocardial ischemia from coronary artery obstruction, and neoaortic valve regurgitation (21). Those complications need to be approached surgically. Rastelli patients may develop right ventricular to pulmonary artery conduit obstruction, subaortic obstruction across the left ventricular-aorta tunnel, VSD and pulmonary branch stenosis.

TEE in Operated Transposition of the Great Arteries (Table 24.2)

The TEE examination of operated TGA should include evaluation of ventricular function, atrioventricular valve competence, obstruction of the pulmonary or the systemic venous pathways (baffle), and baffle leakage. These anomalies can be seen using a combination of the mid-esophageal four-chamber and bicaval views. Transesophageal echocardiography can also be used to guide catheter closure of baffle leaks or as a pre- and postoperative tool to assist the surgeon in the repair.

C. Complex Single Ventricle

Patients with a single ventricle have either a single anatomical ventricle made up of a single pouch of undeterminate origin or, more commonly, a functionally single ventricle with one well-formed ventricle accompanied by a second underdeveloped or rudimentary ventricle (Fig. 24.33). The atria can be solitus, inversus or ambiguous. The atrioventricular connection consists of a common valve or two separate valves, one patent and the other atretic. The well-developed ventricular chamber can be of the left or right ventricular type. The ventriculoarterial connection can be concordant or discordant, or the great arteries can arise from the same ventricle and be either patent or stenotic. The most common types of single ventricle of left ventricular morphology consist of tricuspid atresia, pulmonary atresia with intact ventricular septum and double inlet LV (Fig. 24.33). The most common single RV is the hypoplastic left heart syndrome (Fig. 24.34).

Physiologically, the patient with a single ventricle may display restricted pulmonary blood flow with cyanosis or obstructed systemic arterial flow with heart failure and

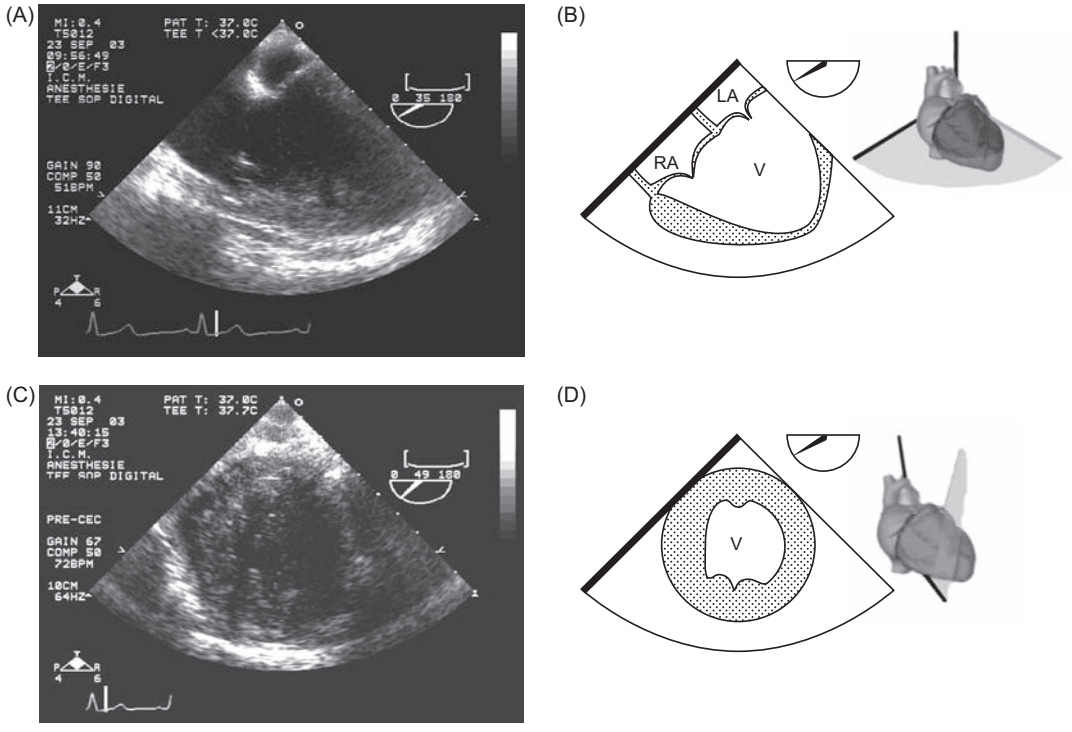

Figure 24.33 Double inlet left ventricle in a 38-year-old woman who previously underwent a Blalock procedure. (A, B) Mid-esophageal view. The two atrioventricular valves (tricuspid and mitral) open in a single ventricle (V). (C, D) Transgastric view. Note the thickened septal part of the ventricle (LA, left atrium; RA, right atrium).

low cardiac output. Those with unobstructed great arteries develop pulmonary overcirculation with reduction of the pulmonary vascular resistance. A minority of patients present a well-balanced circulation with some degree of pulmonary stenosis preventing excessive pulmonary blood flow.

Adults with a single ventricle are separated into two groups: first, a group of patients who either never required surgery because of an acceptable well-balanced physiology or who have undergone one or several palliative (non-Fontan) surgical procedures. The latter include the Glenn's bidirectional cavopulmonary connection and a variety of other aortopulmonary shunts such as the Blaloch–Taussig subclavian to pulmonary artery branch shunt, the Pott's anastomosis of the anterior wall of the Ao to the posterior wall of the left pulmonary artery and the Waterston shunt between the ascending Ao and the right pulmonary artery. The other group includes patients who have undergone a repair where the systemic venous return is diverted to the pulmonary artery circulation without passing through a subpulmonary ventricle, a principle which is now known as the Fontan procedure.

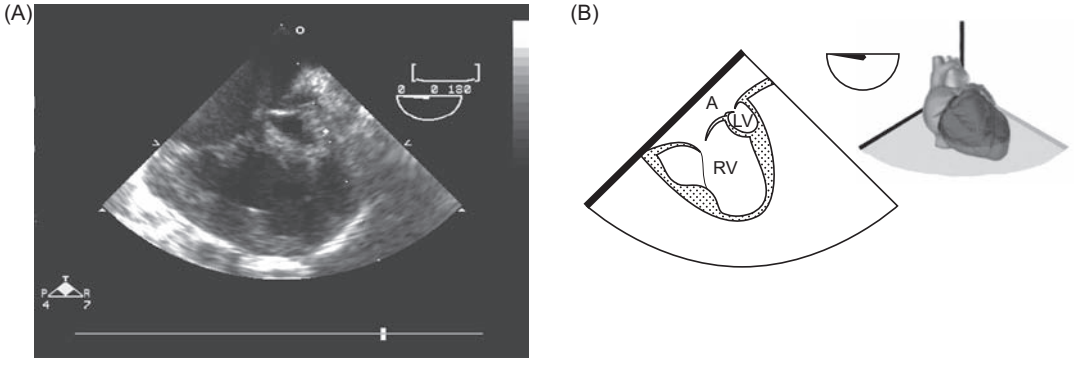

Figure 24.34 Mid-esophageal view of a hypoplastic left heart. Note the small left ventricle (LV) and the large right ventricle (RV). The image was obtained as a preoperative evaluation for a third stage Fontan procedure (A, atrium).

The non-Fontan adult with a single ventricle will require surgery in the presence of significant functional limitation, cyanosis (resting oxygen saturation $<90\%$), dilated systemic ventricle from volume overload, and paradoxical embolism. Surgical options include performing a bidirectional Glenn, a bidirectional Glenn with additional pulmonary blood flow through a native pulmonary artery with valvular stenosis or pulmonary artery banding or the addition of a small aortopulmonary shunt, and Fontan procedure. Numerous variants to the Fontan approach have been described. The most frequently encountered are the direct RA to pulmonary artery connection, the total cavopulmonary connection (with SVC to pulmonary artery and IVC to pulmonary artery through an intra-atrial tunnel), the extracardiac conduit (SVC to pulmonary artery and IVC to pulmonary artery through an external conduit), and RA to RV through a valved conduit when right ventricular size and function are adequate.

Table 24.3 Role of TEE in Congenital Heart Disease Surgery

Before the procedure
Systematic analysis of intra- and extra-cardiac structures (see Table 24.2)
Evaluation of the anomalies and their impact on bi-ventricular function
Evaluation of all four cardiac valves
Ruling-out associated congenital anomalies (e.g. persistent left superior vena cava)
Contrast examination and shunt calculation (see Chapter 5)
Before the procedure in patient with ventricular assist device (see Chapter 14)
Perioperative period
Monitoring during cardiac surgery (see Chapter 13)
Ruling out stenotic or regurgitant anastomosis
Detection of residual shunts
Deairing of all (four) cardiac cavities
Ruling out patent foramen ovale with color Doppler and contrast study
Early and late postoperative period: systematic evaluation of
Left and right ventricular systolic and diastolic function
Valvular (all four valves) integrity and function
Vascular anastomosis, thrombus, spontaneous echocardiographic contrast
Aneurysm and pseudoaneurysm of anastomosis
In the advent of hemodynamic instability: identification of
Obstruction of the anastomosis
Left and right ventricular systolic and diastolic function
Left and right ventricular outflow tract dynamic or fixed obstruction
Severe mitral or tricuspid regurgitation
Hypovolemia
Cardiac tamponade (circumferential or loculated)

Patients with a previous Fontan procedure may also require surgical reintervention (22,23) for the following indications: (1) residual ASD with right-to-left shunt and symptomatic cyanosis, (2) significant atrioventricular valve regurgitation, (3) obstruction in the Fontan conduit, (4) development of venous collateral channels or pulmonary arteriovenous malformations, (5) development of sustained atrial flutter or fibrillation, (6) protein-losing enteropathy, (7) pulmonary venous obstruction, and (8) heart block or sick sinus syndrome requiring a pacemaker.

The Fontan "redo" procedures vary from the original Fontan procedure to more modern approaches with total cavopulmonary connection or extracardiac conduit.

TEE in Complex Single Ventricle (Table 24.2)

Adults with a single ventricle requiring surgical repair must undergo a complete hemodynamic and angiographic evaluation of the aortic arch, coronary, and pulmonary arteries, as well as the state of the distal vascular bed. The goal of a thorough perioperative TEE examination is mainly to evaluate ventricular function, atrioventricular competence or adequacy of the atrioventricular valve repair, semilunar valve function and competence, and pulmonary venous blood flow, and to exclude the presence of thrombus.

In summary, the role of TEE in congenital heart disease surgery, both in the pediatric and adult population, has been expanding. The preoperative characterisation of the anomaly and its consequences and the evaluation of the postoperative results are important roles of TEE, as summarized in Table 24.3.

REFERENCES

1. Miller-Hance WC, Silverman NH. Transesophageal echocardiography (TEE) in congenital heart disease with focus on the adult. Cardiol Clin 2000; 18:861–892.
2. Sukernik MR, Mets B, Bennett-Guerrero E. Patent foramen ovale and its significance in the perioperative period. Anesth Analg 2001; 93:1137–1146.
3. Moore KL, Persaud TVN. The Developing Human: Clinically Oriented Embryology. 5th ed. Philadelphia: WB Saunders, 1993.
4. Netter FH, Yonkman FF, Ciba Pharmaceutical Company. Heart a compilation of paintings on the normal and pathologic anatomy and physiology, embryology, and diseases. Summit, NJ: CIBA Pharmaceutical Company, 1978.
5. Shanewise JS, Cheung AT, Aronson S et al. ASE/SCA guidelines for performing a comprehensive intraoperative multiplane transesophageal echocardiography examination: recommendations of the American Society of Echocardiography Council for Intraoperative Echocardiography and

the Society of Cardiovascular Anesthesiologists Task Force for Certification in Perioperative Transesophageal Echocardiography. Anesth Analg 1999; 89:870–884.
6. Therrien J, Dore A, Gersony W et al. Canadian Cardiovascular Society Consensus Conference 2001 update: recommendations for the management of adults with congenital heart disease—Part I. Can J Cardiol 2001; 17:940–959.
7. Fram D, Missri J, Therrien ML. Assessment of Ebstein's anomaly and its surgical repair using transesophageal two-dimensional echocardiography and Doppler color flow mapping. Echocardiography 1991; 8:367–371.
8. Frescura C, Angelini A, Daliento L, Thiene G. Morphological aspects of Ebstein's anomaly in adults. Thorac Cardiovasc Surg 2000; 48:203–208.
9. Oechslin E, Buchholz S, Jenni R. Ebstein's anomaly in adults: Doppler-echocardiographic evaluation. Thorac Cardiovasc Surg 2000; 48:209–213.
10. Therrien J, Gatzoulis M, Graham T et al. Canadian Cardiovascular Society Consensus Conference 2001 update: recommendations for the management of adults with congenital heart disease—Part II. Can J Cardiol 2001; 17:1029–1050.
11. Moss AJ, Adams FH, Emmanouilides GC. Moss and Adams Heart Disease in Infants, Children, and Adolescents Including the Fetus and Young Adult. 5th ed. Baltimore: Williams & Wilkins, 1995.
12. Banerjee A, Kohl T, Silverman NH. Echocardiographic evaluation of congenital mitral valve anomalies in children. Am J Cardiol 1995; 76:1284–1291.
13. Zias EA, Mavroudis C, Backer CL et al. Surgical repair of the congenitally malformed mitral valve in infants and children. Ann Thorac Surg 1998; 66:1551–1559.
14. Nadas AS, Fyler DC. Nadas' Pediatric Cardiology. Philadelphia: Hanley & Belfus, 1992.
15. Murphy JG, Gersh BJ, Mair DD et al. Long-term outcome in patients undergoing surgical repair of tetralogy of Fallot. N Engl J Med 1993; 329:593–599.
16. Oechslin EN, Harrison DA, Harris L et al. Reoperation in adults with repair of tetralogy of fallot: indications and outcomes. J Thorac Cardiovasc Surg 1999; 118:245–251.
17. Therrien J, Warnes C, Daliento L et al. Canadian Cardiovascular Society Consensus Conference 2001 update: recommendations for the management of adults with congenital heart disease—Part III. Can J Cardiol 2001; 17:1135–1158.
18. Brickner ME, Hillis LD, Lange RA. Congenital heart disease in adults. Second of two parts. N Engl J Med 2000; 342:334–342.
19. Gelatt M, Hamilton RM, McCrindle BW et al. Arrhythmia and mortality after the Mustard procedure: a 30-year single-center experience. J Am Coll Cardiol 1997; 29:194–201.
20. Mee RB. Severe right ventricular failure after Mustard or Senning operation. Two-stage repair: pulmonary artery banding and switch. J Thorac Cardiovasc Surg 1986; 92:385–390.
21. Haas F, Wottke M, Poppert H, Meisner H. Long-term survival and functional follow-up in patients after the arterial switch operation. Ann Thorac Surg 1999; 68:1692–1697.
22. Driscoll DJ, Offord KP, Feldt RH et al. Five- to fifteen-year follow-up after Fontan operation. Circulation 1992; 85:469–496.
23. Fontan F, Kirklin JW, Fernandez G et al. Outcome after a "perfect" Fontan operation. Circulation 1990; 81:1520–1536.

25

Indications for Perioperative Transesophageal Echocardiography

ANDRÉ MARTINEAU, MARIE ARSENAULT
Laval University, Quebec City, Canada

I. Review of Published Practice Guidelines 556
II. Category I: Supported by the Strongest Evidence of Expert Opinion 557
A. Hemodynamic Disturbances 557
B. Valve Repair 557
C. Congenital Heart Disease 558
D. Thoracic Aortic Dissections, or Disruptions 559
1. Traumatic Thoracic Aortic Disruption 559
2. Aortic Dissection 560
E. Hypertrophic Obstructive Cardiomyopathy 560
F. Endocarditis 561
G. Unstable ICU Patients with Unexplained Hemodynamic Disturbances, Suspected Valve Disease, or Thromboembolic Problems 561
H. Pericardial Window Procedures 561
I. Evaluation of Complex Valve Replacements Requiring Homografts or Coronary Reimplantation such as the Ross Procedure 561
J. Placement of Intracardiac Devices and Monitoring of Their Position During Minimally Invasive Surgery or Other Cardiac Surgical Intervention 562
III. Category II: Supported by Weaker Evidence and Expert Consensus 562
A. Patients with Increased Risk of Myocardial Ischemia/Infarction 562
B. Patients with Increased Risk of Hemodynamic Disturbances 563
C. Assessment of Patients with Suspected Acute Thoracic Dissection, Aneurysm, or Disruptions 563
D. Assessment During Valve Replacement 563
E. Assessment and Repair of Cardiac Aneurysms 563
F. Evaluation of Removal of Cardiac Masses 563
G. Detection of Foreign Bodies 564
H. Detection of Air Emboli During Cardiotomy, Heart Transplant, and Upright Neurosurgical Procedures 564
I. Intracardiac Thrombectomy 564
J. Pulmonary Embolectomy 564
K. Suspected Cardiac Trauma 564
L. Detection of Aortic Atheromatous Disease or Other Sources of Aortic Emboli 565
M. Evaluation of Pericardial Surgery 565
N. Evaluation of Anastomotic Sites During Heart and/or Lung Transplantation 565
O. Assessment of Residual Duct Flow After Interruption of Patent Ductus Arteriosus 565
P. Evaluation of Myocardial Perfusion, Coronary Artery Anatomy, Graft Patency 565
IV. Category III: Little Current Scientific or Expert Support 565
A. Repair of Cardiomyopathies (Other than Hypertrophic Obstructive Cardiomyopathy) 565

B. Uncomplicated Endocarditis During Noncardiac Surgery 566
C. Monitoring of Emboli During Orthopedic Procedures 566
D. Assessment of Repair of Thoracic Aortic Injuries 566
E. Uncomplicated Pericarditis 566
F. Evaluation of Pleuropulmonary Disease 566
G. Monitoring of Cardioplegia Administration 566
H. Monitoring Placement of Intra-Aortic Balloon Pumps 566
I. Automatic Implantable Cardiac Defibrillators 566
J. Pulmonary Artery Catheters 566
V. Conclusion 566
References 566

Perioperative echocardiography is widely used in most cardiac surgery centers in North America and around the world and has become a standard of care for many patients. Intraoperative echocardiography (IOE) is widely used because it provides information that significantly influences clinical management and improves clinical outcome. Several recent series have documented the usefulness of IOE in adult cardiac surgery (1–5). The new information obtained with IOE was examined and its impact on anesthetic or surgical management studied. In adult cardiac surgery, the incidence of new information ranged from 12.8% to 38.6% while the impact on treatment ranged from 9.7% to 14.6% (Table 25.1).

The use of IOE has also become routine in many pediatric cardiac surgery centers. Epicardial echocardiography was used before the availability of small multiplane transesophageal echocardiography (TEE) probes. Recent studies demonstrated the value of pediatric intraoperative TEE for the detection of residual defects, after cardiopulmonary bypass (CPB) which ranged from 4.4% to 12.8% (6–10) (Table 25.2).

These retrospective studies confirm the clinical perception that IOE provides new information on cardiac pathology in a significant number of patients and that this frequently results in management changes. However, intraoperative TEE is not without risks as it has been associated with postoperative morbidity and complications such as swallowing dysfunction, dysphagia, esophageal ulcerations, and rupture. Therefore, the indication for performing an intraoperative TEE must be carefully evaluated and weighed against the risks. Perioperative TEE should be performed by, or in close collaboration with, a physician with advanced TEE training.

I. REVIEW OF PUBLISHED PRACTICE GUIDELINES

In 1996, a task force of the American Society of Anesthesiologsts/Society of Cardiovascular Anesthesiologists (ASA/SCA) published their practice guidelines for perioperative TEE (12). The recommendations of the task force address indications, the clinical settings in which TEE should be considered and the proficiency, and cognitive and technical skills expected from the anesthesiologist who performs perioperative TEE. The guidelines were evidence-based and focused on the effectiveness of perioperative TEE in improving clinical outcomes. The literature search conducted at that time retrieved 1844 articles of which 588 were considered relevant to the perioperative context.

The recommendations in this document were divided into three categories based on the strength of supporting evidence, or expert opinion, that the technology improved clinical outcomes.

Category I are indications supported by the strongest evidence of expert opinion: TEE is frequently useful in improving clinical outcomes and is often indicated, depending on individual circumstances (e.g. patient risk and practice settings).

Category II are indications supported by weaker evidence and expert consensus: TEE may be useful in

Table 25.1 Usefulness of Intraoperative Echocardiography in Adult Cardiac Surgery

Author (ref)	Year	*N*	New information (%)	Change in management (%)
Click et al. (3)	2000	3245	15	14
Couture et al. (4)	2000	851	—	14.6
Michel-Cherqui et al. (5)	2000	203	12.8	10.8
Mishra et al. (1)	1998	5016	22.9	—
Sutton and Kluger (2)	1998	238	38.6	9.7

Table 25.2 Usefulness of Intraoperative Echocardiography in Pediatric Cardiac Surgery

Author (ref)	Year	*N*	Residual defects (%)
Rosenfeld et al. (8)	1998	86	12.8
Sheil and Baines (9)	1999	200	10.5
Stevenson (6)	1995	667	6.6
Ungerleider et al. (7); Cheitlin et al. (11)	1995	1000	4.4

improving clinical outcomes, depending on individual circumstances, but appropriate indications are less certain.

Category III are indications in situations where the use of TEE has so far little current scientific or expert support: TEE is infrequently useful in improving clinical outcomes and appropriate indications are uncertain (Table 25.3).

These recommendations refer to clinical problems rather than to individual patients who often have more than one reason for needing a perioperative TEE. Physicians must integrate these multiple variables in assessing a patient's need for TEE.

In 1997, the American Heart Association (AHA) and American College of Cardiology (ACC) published their general guidelines for the clinical application of echocardiography (13). In 2000, the AHA/ACC task force was reconvened to update those guidelines and the American Society of Echocardiography (ASE) was invited to participate. It was then decided to include a section on intraoperative echocardiography. In preparation for this section, 118 additional articles related to intraoperative use of echocardiography were identified (Daniel M Thys, Update indications on TEE. Annual Comprehensive Review & TEE Update: Clinical Decision Making in the Cardiac Surgery Patient. San Diego, CA, 2003). The indications for IOE provided in these new guidelines are based on the initial 1996 ASA/SCA guidelines as well as on the newest data (Table 25.4).

These ACC/AHA/ASE guidelines published in 2003 utilize a new standard classification system: (11) (Table 25.5). In this Chapter, we review the indications for perioperative TEE according to the 1996 ASA/SCA guidelines (12) as well as the newest indications as classified in the ACC/AHA/ASE 2003 guidelines (11).

II. CATEGORY I: SUPPORTED BY THE STRONGEST EVIDENCE OF EXPERT OPINION

Transesophageal echocardiography is frequently useful in improving clinical outcomes in category I settings and is often indicated, depending on individual circumstances (e.g. patient risk and practice setting).

A. Hemodynamic Disturbances

Intraoperative evaluation of acute, persistent, and life threatening hemodynamic disturbances in which ventricular function and its determinants are uncertain and have not responded to treatment is a category I indication to use TEE.

The use of TEE has been described extensively for the evaluation of hemodynamic and global ventricular function (see Chapter 9). It has been used to estimate standard hemodynamic variables [e.g. filling pressure, cardiac output (CO)] that are normally obtained by invasive techniques such as pulmonary artery catheterization, to quantify cardiac dimensions, estimate ejection fraction, intracardiac flow rates, and overall cardiac performance. Such measurements are available in the operating room (OR) or in the intensive care unit (ICU) (12).

Rapidly detecting acute hemodynamic disturbances during surgery improves clinical outcome. Transesophageal echocardiography is an excellent tool to identify quickly the hemodynamic problem [e.g. hypovolemia, myocardial depression, left ventricular outflow tract (LVOT) obstruction], and to suggest appropriate therapy (e.g. volume expansion, use or cessation of inotropic therapy) (see Chapter 9, Fig. 9.10).

B. Valve Repair

Valve repair is a category I indication for the use of intraoperative TEE whereas valve replacement is a category II (see following sections). The potential benefits of TEE evaluation during valve surgery are not limited to valve assessment. Hemodynamic disturbances are common, and TEE may be especially useful in weaning the patient from CPB (see Chapter 18, Fig. 18.30). Transesophageal echocardiography can also detect trapped air and facilitate venting procedures.

During mitral valve repair, TEE is useful to evaluate the anatomy of the valve and the mechanism of regurgitation. However, as intraoperative hemodynamics can differ significantly from these in the awake state due to anesthesia, special care should be taken to optimize the patient's filling pressures as well as systemic blood pressure (BP) while assessing valvular regurgitations in the OR (before and after the procedure) (see Chapter 17, Fig. 17.23). Performing a comprehensive preoperative TEE in the non anesthetized patient before surgery will help overcome these problems, avoid unexpected findings, give more time to discuss the case with the surgical team and plan the surgical procedure.

Two recent studies have confirmed the usefulness of intraoperative TEE for the assessment of residual regurgitation after mitral valve repair.

Table 25.3 Quick Reference Guide: Indications for Perioperative TEE (12)

Category	Indications
I	Supported by the strongest evidence or expert opinion; TEE is frequently useful in improving clinical outcomes in these settings and is often indicated, depending on individual circumstances (e.g. patient risk and practice setting):
	Intraoperative evaluation of acute, persistent and life-threatening hemodynamic disturbances in which ventricular function and its determinants are uncertain and have not responded to treatment
	Intraoperative use in valve repair
	Intraoperative use in congenital heart surgery for most lesions requiring cardiopulmonary bypass
	Intraoperative use in repair of hypertrophic obstructive cardiomyopathy
	Intraoperative use for endocarditis when preoperative testing was inadequate or extension of infection to perivalvular tissue is suspected
	Preoperative use in unstable patients with suspected thoracic aortic aneurysm, dissection, or disruption who need to be evaluated quickly
	Intraoperative assessment of aortic valve function in repair of aortic dissection with possible aortic valve involvment
	Intraoperative evaluation of pericardial window procedures
	Use in Intensive Care Unit for unstable patients with unexplained hemodynamic disturbances, suspected valve disease, or thromboembolic problems (if other tests or monitoring techniques have not confirmed the diagnosis or patients are too unstable to undergo other tests).
II	Supported by weaker evidence and expert consensus; TEE may be useful in improving clinical outcomes in these settings and is often indicated, depending on individual circumstances, but appropriate indications are less certain.
	Perioperative use in patients with increased risk of myocardial ischemia or infarction
	Perioperative use in patient with hemodynamic disturbances
	Intraoperative assessment of valve replacement
	Intraoperative assessment of repair of cardiac aneurysms
	Intraoperative evaluation of removal of cardiac tumors
	Intraoperative detection of foreign bodies
	Intraoperative detection of air emboli during cardiotomy, heart transplant operations, and upright neurosurgical procedures
	Intraoperative use during intracardiac thrombectomy
	Intraoperative use during pulmonary embolectomy
	Intraoperative use for suspected cardiac trauma
	Preoperative assessment of patients with suspected acute thoracic aortic dissections, aneurysms, or disruption
	Intraoperative use during repair of thoracic aortic dissections without suspected aortic valve involvment
	Intraoperative detection of aortic atheromatous disease or other sources of aortic emboli
	Intraoperative evaluation of pericardiectomy, pericardial effusion or evaluation of pericardial surgery
	Intraoperative evaluation of anastomotic sites during heart and/or lung transplantation
	Monitoring placement and function of assist devices.
III	Little current scientific or expert support: TEE is infrequently useful in improving clinical outcomes in these settings, and appropriate indications are uncertain.
	Intraoperative evaluation of myocardial perfusion, coronary artery anatomy, or graft patency
	Intraoperative use during repair of cardiomyopathies other than hypertrophic obstructive cardiomyopathy
	Intraoperative use for uncomplicated endocarditis during non-cardiac surgery
	Intraoperative monitoring for emboli during orthopedic procedures
	Intraoperative assessment of repair of thoracic aortic injuries
	Intraoperative use for uncomplicated pericarditis
	Intraoperative evaluation of pleuropulmonary diseases
	Monitoring placement of intraaortic balloon pumps, automatic implantable cardiac defibrillators, or pulmonary catheters
	Intraoperative monitoring of cardioplegia administration.

C. Congenital Heart Disease

Surgery for most congenital heart lesions requiring CPB in adults or children is a category I indication for intraoperative TEE, including pre-CPB and post-CPB imaging. Several studies have documented the utility of intraoperative TEE in congenital heart disease, particularly for the detection of residual defects after CPB (6–9) (Table 25.2).

Use of TEE is contraindicated in children when available probes are too large for the child's size. Epicardial

Table 25.4 Updated Indications for Intraoperative Echocardiography (13)

Class	Indications
I	1. Evaluation of acute, persistent, and life-threatening hemodynamic disturbances in which ventricular function and its determinants are uncertain and have not responded to treatment. 2. Surgical repair of valvular lesions, hypertrophic obstructive cardiomyopathy, and aortic dissection with possible aortic valve involvement. 3. Evaluation of complex valve replacements requiring homografts or coronary reimplantation such as Ross procedure. 4. Surgical repair of most congenital heart lesions that require cardiopulmonary bypass. 5. Surgical interventions for endocarditis when preoperative testing was inadequate or extension to perivalvular tissue is suspected. 6. Placement of intracardiac devices and monitoring of their position during port-access and other cardiac surgical interventions. 7. Evaluation of pericardial window procedures in patient with posterior or loculated pericardial effusions.
IIa	1. Surgical procedures in patients with increased risk of myocardial ischemia, myocardial infarction, or hemodynamic disturbances. 2. Evaluation of valve replacement, aortic atheromatous disease, the Maze procedure, cardiac aneurysm repair, removal of cardiac tumors, intracardiac thrombectomy, and pulmonary embolectomy. 3. Detection of air emboli during cardiotomy, heart transplant operations, and upright neurosurgical procedures.
IIb	1. Evaluation of suspected cardiac trauma, repair of acute aortic dissection without valvular involvment, and anastomotic sites during heart and/or lung transplantation. 2. Evaluation of regional myocardial function during and after off-pump CABG procedures. 3. Evaluation of pericardiectomy, pericardial effusions, and pericardial surgery. 4. Evaluation of myocardial perfusion, coronary anatomy, or graft patency. 5. Dobutamine stress testing to detect inducible demand ischemia or to predict functional changes after myocardial revascularization. 6. Assessment of residual duct flow after interruption of patent ductus arteriosus.
III	1. Surgical repair of uncomplicated secundum atrial septal defect.

echocardiography can provide a useful alternative in those cases. New multiplane pediatric probes are available and should be used whenever possible following the manufacturer's recommendations. While epicardial echocardiography was used most commonly in earlier years, the use of TEE has increased with the development of smaller TEE probes. Before using TEE in a child, one must remember that in addition to the usual potential adverse effects of TEE, small children face the added risks of hemodynamic and/or respiratory compromise, which are more common in patients weighing <3 kg or when a nonpediatric sized probe is used. Greene et al. (14) evaluated the safety of TEE in pediatric cardiac surgery by performing an endoscopic examination of the esophagus following TEE after removal of the probe in 50 patients undergoing repair of congenital cardiac defects. In 32/50 patients, mild mucosal injury was observed but none resulted in long term feeding or swallowing difficulties (14).

Table 25.5 Definition of Classification (11): The ACC/AHA/ASE 2003 Guidelines Utilize the Following Classification System for Indications

Class	Definition
I	Conditions for which there is evidence and/or general agreement that a given procedure or treatment is useful and effective.
II	Conditions for which there is conflicting evidence and/or divergence of opinion about the usefulness/efficacy of a procedure or treatment.
IIa	Weight of evidence/opinion is in favor of usefulness/efficacy.
IIb	Usefulness/efficacy is less well established by evidence/opinion.
III	Conditions for which there is evidence and/or general agreement that the procedure/treatment is not useful/effective and in some cases may be harmful.

D. Thoracic Aortic Dissections, or Disruptions

1. Traumatic Thoracic Aortic Disruption

Preoperative or intraoperative TEE can play an important role in the early detection of aortic injuries. In trauma patients with suspected aortic injuries, hemodynamic shock often precludes the performance of diagnostic tests before the patient is taken to surgery. The reported sensitivity and specificity of TEE in the emergent preoperative assessment of suspected aortic trauma is 100%

and 94–100%, respectively (12) (see Chapter 12, Fig. 12.31).

In the context of chest trauma, other investigators have reported sensitivity and specificity for detection of traumatic aortic rupture ranging from 63% to 100% and 84% to 100%, respectively (15).

Transesophageal echocardiography cannot consistently visualize the superior ascending aorta (Ao) and aortic arch branch vessels (TEE's "blind spot"), which are unfortunately frequent sites of traumatic aortic injury. Thus the role of TEE in the diagnostic evaluation of chest trauma patients remains undefined. When the hemodynamic status of the patients allows it, other imaging modalities such as computed tomography (CT) scanning, magnetic resonance imaging (MRI) or angiography must be used. The task force believes that the early detection of undiagnosed traumatic aortic disruption improves clinical outcomes because of the life-threatening nature of such injuries (12). However, there is little evidence that the use of TEE in this setting improves clinical outcome. Therefore the preoperative assessment of suspected thoracic aortic trauma is a category II indication for TEE.

In unstable patients who need to be treated urgently, TEE has a category I indication because it allows a more expedient examination than other preoperative imaging procedures.

Assessing the repair of thoracic aortic injuries is a category III indication for intraoperative TEE (1).

2. *Aortic Dissection*

Aortic dissection can be detected by TEE with a high degree of accuracy and is the diagnostic test of choice in many institutions for suspected aortic dissections. The ascending Ao, aortic arch and descending thoracic Ao can be examined with excellent resolution as these structures are close to the high-frequency transducer. Importantly, a small segment of the superior ascending Ao cannot be visualized using TEE owing to the interposition of the air filled trachea and bronchus. The sensitivity of monoplane and biplane TEE for the diagnosis of aortic dissection has been reported to be 97–100% with a specificity that has ranged from 77% to 100%. The use of multiplane TEE is associated with sensitivities and specificities of 98–100% and 94–95%, respectively. The sensitivity and specificity of TEE compares favorably with those of other imaging modalities including aortography, CT, and MRI (see Chapter 12).

In addition to diagnosis, TEE can determine the extent of dissection, differentiate between the true and false lumen, identify thrombus within the false lumen, identify the site of intimal tear, and assess aortic valve (AoV) involvement. The TEE exam will quickly identify regional wall motion abnormalities associated with coronary involvement in proximal ascending aortic dissections as well as involvement of arch vessels. Additionally, TEE can detect signs of aortic rupture, such as pericardial effusion, pleural effusion, or mediastinal hematoma, which may significantly alter surgical therapy. Aortic complications after repair may also be detected.

Associated aortic abnormalities, such as intramural hematoma (see Chapter 12, Fig. 12.29) and penetrating aortic ulcers can also be diagnosed by TEE. The TEE findings appear to have high sensitivity and specificity for the detection of intramural hematoma, but the diagnostic accuracy in the detection of penetrating aortic ulcers is unclear. In the largest series of 12 patients, penetrating ulcers were identified by TEE in 83% of patients.

The intraoperative use of TEE for assessing AoV function when patients undergo repair of aortic dissection with possible AoV involvement is a category I indication (12). Transesophageal echocardiography provides information about the functional status of the AoV. It has also been used to diagnose other conditions accompanying aortic dissection and aneurysm including bicuspid AoV, quadricuspid AoV, and others. Aortic valve repair and aortic complications after repair can also be assessed.

E. Hypertrophic Obstructive Cardiomyopathy

Septal myectomy (Morrow procedure) for the treatment of symptomatic hypertrophic obstructive cardiomyopathy is a category I indication for either epiaortic echocardiography (EE) or TEE assessments.

Preoperative TEE will help characterize LVOT anatomy and septal thickness, measure LVOT gradient and determine mitral valve abnormalities and degree of regurgitation. Careful evaluation of septal morphology and thickness will help the surgeon to determine the amount of septal muscle to be removed (see Chapter 10, Fig. 10.1). Echocardiographic assessment also facilitates weaning from CPB, and enables intraoperative detection of iatrogenic septal defects or residual systolic anterior motion of the anterior leaflet of the mitral valve.

After myectomy, residual LVOT gradient and mitral regurgitation (MR) may warrant a return under CBP for further myectomy or mitral valve repair/replacement (see Chapter 18). Iatrogenic ventricular septal defects (VSDs) (see Chapter 10, Fig. 10.13), papillary muscle lacerations and coronary to left ventricular fistulae may also be identified. In difficult cases, epicardial echocardiography may be an alternative and obviate the need for invasive measurement of residual gradient by cardiac needle puncture.

The largest series focusing on the usefulness of TEE for hypertrophic obstructive cardiomyopathy (HOCM) in 256 patients was published by Ommen et al. (16). In their series, prebypass TEE revealed unexpected findings in 17% of patients and resulted in an alteration of the surgical plan in 9%. Postbypass TEE revealed unexpected results in 7% and prompted further surgical procedures in 4%. The

authors recommended TEE monitoring for all septal myectomies for HOCM.

The 1996 ASA/ASC task force believed that the echocardiographic confirmation of the adequacy of HOCM surgery improves clinical outcomes based, in part, on natural history data suggesting poorer outcomes for patients with persistent hemodynamic compromise from HOCM (12).

The ACC/AHA/ASE 2003 echocardiography practice guidelines consider TEE monitoring for surgical repair of HOCM as a category I indication.

F. Endocarditis

Intraoperative use of TEE for endocarditis is a category I indication when preoperative testing is inadequate or extension of infection to perivalvular tissue is suspected (12).

Although its accuracy in detecting endocarditis outside the OR is well established, there is little evidence beyond case reports that the use of intraoperative TEE is more accurate in detecting endocarditis or improves clinical outcomes (12). Before the patient enters the OR, either the transthoracic echocardiography (TTE) or the TEE should be performed to help plan the surgery and avoid unexpected intraoperative findings.

Beyond the accepted applications of intraoperative TEE during valve surgery, there is little role for TEE in evaluating endocarditis during surgery, unless preoperative testing was inadequate, extension to perivalvular tissue is suspected or the patient required urgent surgery.

Noncardiac surgery in patients with uncomplicated endocarditis is a category III indication for intraoperative TEE.

The complications of infective endocarditis, including abscess formation (see Chapter 15, Fig. 15.31), leaflet diverticula, leaflet perforation, fistula tracts, and pseudoaneurysm formation are better detected by TEE than TTE. Regarding abscess formation, the specificity of both techniques exceeds 90%. The sensitivity regarding abscess cavity was 28% for TTE and 87% for TEE.

Transesophageal echocardiography is especially effective with prosthetic mitral valves, as acoustic shadowing hinders visualization of the atrial aspect by TTE. Therefore TEE must be combined with TTE but may even supplant TTE in patients with valve prosthesis who present with signs and symptoms of endocarditis.

G. Unstable ICU Patients with Unexplained Hemodynamic Disturbances, Suspected Valve Disease, or Thromboembolic Problems

Unexplained hemodynamic disturbances, suspected valve disease, or thromboembolic problems in unstable ICU patients is a category I indication for TEE if the other tests or monitoring techniques have failed to confirm the diagnosis or if patients are too unstable to undergo other tests.

In this setting, TEE can provide essential information that alters patient management of myocardial function, valve function, and volume status, which is critical in evaluating the patient with unexplained hypotension or unexplained pulmonary edema.

Some studies have reported that TEE detected information not seen by TTE in 44–59% of ICU patients. Information provided by TEE examinations is reported to change therapy in 17–48% of critical care patients (17).

The TTE images obtained in the ICU can be inadequate because of poor acoustic penetration, limited windows from surgical bandages and drains, mechanical ventilation, and an inability to position patients properly. Recent technological advances such as harmonic imaging and contrast imaging have improved TTE image quality significantly and decreased the number of nondiagnostic studies. In urgent situations and in acutely unstable patients, TEE may nevertheless remain a first option. The presence of massive or proximal pulmonary emboli can be diagnosed by TEE (see Chapter 9, Fig. 9.40). Potential complications of myocardial infarction, including left ventricular dysfunction, papillary muscle rupture with severe MR (see Chapter 8, Fig. 8.20) and myocardial rupture (free wall or ventricular septum), may be identified. TEE can also detect right-to-left intracardiac shunting through a patent foramen ovale, which may occur in ventilated patients requiring high levels of pressure support and right ventricular dysfunction.

H. Pericardial Window Procedures

Intraoperative evaluation of pericardial window procedures is a category I indication for perioperative TEE. There is some evidence suggesting that perioperative TEE is more sensitive than TTE in detecting pericardial effusions (mostly loculated effusions), but there is little evidence beyond case reports that such findings, during or after surgery, result in improved clinical outcomes. Perioperative TEE is clinically beneficial if it detects pericardial tamponade and avoids serious hemodynamic sequelae. This application is important when effusions cannot be detected easily by other means such as TTE (see Chapter 11, Fig. 11.9). Clinical experience suggests that posterior or loculated pericardial effusions that are easily missed by the surgeon may develop in the patients treated with pericardial windows.

I. Evaluation of Complex Valve Replacements Requiring Homografts or Coronary Reimplantation such as the Ross Procedure

In this context, TEE is a category I indication and is useful to evaluate valve function and ventricular function before surgery and it may also modify the surgical approach.

Coming off bypass, TEE is used to guide deairing of the heart, to evaluate coronary perfusion and ventricular function and to assess transvalvular gradients and regurgitations. Proximal segments of the left main and right coronary arteries can often be visualized and assessed for flow and patency.

J. Placement of Intracardiac Devices and Monitoring of Their Position During Minimally Invasive Surgery or Other Cardiac Surgical Intervention

The role of TEE has been evaluated in minimally invasive cardiac surgery. Applebaum et al. (18) reported that TEE facilitated the placement of intravascular catheters during port-access surgery, thereby avoiding the use of fluoroscopy. Fluoroscopy was only useful as an aide to TEE for the placement of coronary sinus catheters. Falk et al. (19) observed that TEE was particularly useful for monitoring the placement and positioning of the endoaortic clamp that is used in these procedures. The same benefits were reported by Schulze et al. (20).

Kort et al. (21) examined the role of TEE in 153 patients undergoing minimally invasive AoV replacement. Postbypass mild aortic regurgitation (AR) was observed in two patients and mild in 18 patients. The regurgitation was paravalvular in eight of these patients.

In patients undergoing coronary bypass without CPB, Moises et al. (22) detected 31 new regional wall motion abnormalities (RWMA) during 48 coronary artery clampings. At the time of chest closure, 16 segments had partially recovered and five of these had not recovered. Seven days later, the RWMA persisted in the five without recovery and in two with partial recovery. These patients had more clinical events in the postoperative period.

In minimally invasive valve surgery, Secknus et al. (23) noted intracardiac air in all patients. New left ventricular dysfunction was more common in patients with extensive air detected by TEE. Second CPB runs were required in 6% of patients.

During off-pump coronary artery bypass surgery, TEE is useful in assessing global left ventricular function during grafting, regional left ventricular function before, during and after grafting and position-related mitral and tricuspid insufficiency.

Transesophageal echocardiography is useful during port-access procedures to evaluate the severity of aortic atheromatosis, the competence of the AoV and the atrial septum. It is also useful for the placement of the coronary sinus catheter, pulmonary vent femoral venous and arterial canula, and endoaortic clamp. Throughout the procedure TEE will be used to monitor left and right ventricular function, and to detect intracardiac air.

Monitoring the placement and function of ventricular assist devices is also a class I indication of TEE according to the 2003 AHA/ACC guidelines (11). This aspect is discussed in details in Chapter 14.

III. CATEGORY II: SUPPORTED BY WEAKER EVIDENCE AND EXPERT CONSENSUS

Transesophageal echocardiography may be useful in improving clinical outcomes in these settings, depending on individual circumstances, but appropriate indications are less certain.

A. Patients with Increased Risk of Myocardial Ischemia/Infarction

An increased risk of myocardial ischemia or infarction during the perioperative period is a category IIa indication for perioperative TEE. An increased risk may occur because of associated conditions (e.g. history of previous myocardial ischemia or coronary artery disease, left ventricular dysfunction, dysrhythmias), procedure (e.g. coronary artery bypass graft (CABG), operations on the great vessels or that involve aortic cross-clamping, noncardiac intrathoracic surgery, upper abdominal procedures), or clinical setting (e.g. anticipated duration of surgery).

Hemodynamic and other physiologic stresses during the perioperative period increase the risk of perioperative myocardial ischemia, especially among patients with coronary artery disease, multiple risk factors for coronary artery disease and peripheral vascular disease. Traditional methods for monitoring myocardial ischemia during surgery, such as a continuous electrocardiogram, have limited sensitivity in the early detection of tissue injury. Wall motion abnormalities generally precede electrocardiogram changes during myocardial ischemia (24). There is good evidence that the development of regional ventricular dysfunction during surgery increases the risk of developing perioperative myocardial infarction and sudden death.

Although there is little direct evidence that TEE detection of myocardial ischemia improves clinical outcome, the task force believes that indirect evidence can be extrapolated from non TEE studies showing that the early treatment of myocardial ischemia and MI improves survival (12). Intraoperative detection of ischemia permits corrective interventions including alterations in surgery, anesthetic management and postoperative triage, which can prevent perioperative complications (see Chapter 8, Fig. 8.23).

In one study that involved 584 intraoperative interventions, TEE was the single most important factor that guided decision making in 98 instances (17%) (25).

In high risk CABG, Savage et al. (26) observed that at least one major surgical management alteration and one major anesthetic/hemodynamic change were initiated because of TEE findings in 33% and 51% of patients, respectively.

B. Patients with Increased Risk of Hemodynamic Disturbances

An increased risk of hemodynamic disturbances during the perioperative period is a category IIa indication for perioperative TEE. Increased risk may occur because of conditions associated with the patient (e.g. congestive heart failure, valvular heart disease, abdominal aortic aneurysm, preeclampsia, trauma, burn injuries), procedure (e.g. vascular surgery, CPB, extensive tumor resection, liver transplantation, total hip replacement), or clinical setting (e.g. difficulties in inserting central venous pressure catheters, inability to estimate blood loss) (12).

C. Assessment of Patients with Suspected Acute Thoracic Dissection, Aneurysm, or Disruptions

This topic was already discussed in previous sections as in many patients TEE may have a category I indication.

The intraoperative use of TEE for the repair of thoracic aortic dissections without involvement of the AoV is a category II indication. If valvular involvement is suspected, it becomes a category I indication. The preoperative assessment of suspected aortic trauma is a category II indication.

D. Assessment During Valve Replacement

Nowrangi et al. (27) reviewed the impact of intraoperative TEE in patients undergoing aortic valve replacement (AVR) for aortic stenosis (AS). They reviewed the clinical data of 383 patients and observed that 54 patients had mitral valve replacement (MVR) at the time of the AVR. In six patients, MVR was not planned but was performed on the basis of the IOE findings. In 25 patients, MVR was cancelled because of IOE findings.

The clinical impact of routine IOE were studied prospectively in 300 patients by Ionescu et al. (28). In two patients undergoing AVR, significant MR detected by IOE resulted in MVR and in one patient undergoing MVR, AR resulted in AVR.

Intraoperative findings must be interpreted with caution because of the altered hemodynamic state in the OR which may affect valvular performance, transvalvular gradients and regurgitation. Preoperative TTE and/or TEE in the awake patient should be performed and analyzed in combination with the intraoperative findings.

Morehead et al. (29) have studied the significance of paravalvular jets detected by TEE after valve replacement. In 27 patients, multiple jets were detected after valve replacement. They were more common and larger in the mitral position and after insertion of mechanical valves. Reversal of anticoagulation with protamine reduced the incidence and size of the jets in all patients (see Chapter 16, Fig. 16.11). The outcome of mild periprosthetic regurgitation identified by IOE was also studied by O'Rourke et al. (30). Of 608 patients undergoing isolated aortic or MVR, 113 were found to have trivial or mild periprosthetic regurgitation at surgery. While the observation was benign in most patients, four patients were found to have progression of regurgitation by late TTE.

E. Assessment and Repair of Cardiac Aneurysms

Intraoperative TEE during aneurysmectomy can play an important role in evaluating the adequacy of repair and, occasionally, in detecting previously unsuspected abnormalities (e.g. pseudoaneurysms, thrombi) (see Chapter 8, Fig. 8.28). Patients with cardiac aneurysms typically have advanced ischemic heart disease and associated hemodynamic complications, and TEE is often useful in evaluating these problems. Patients with cardiac aneurysms who undergo cardiac surgery often have difficulty weaning from CBP, and TEE monitoring of hemodynamic function is often helpful in withdrawing extracorporal circulatory support.

Assessing surgical repair of cardiac aneurysms is a category II indication for intraoperative TEE (see Chapter 10, Fig. 10.22) (12).

F. Evaluation of Removal of Cardiac Masses

There is some evidence that intraoperative TEE may be more accurate than TTE testing in characterizing the anatomy of some cardiac tumors and cardiac extensions of pulmonary or renal tumors, but there is little evidence beyond case reports that this information, or the use of TEE during resection, results in improved clinical outcomes.

In many cases, the information that TEE provides about the location and anatomy of intracardiac tumors to plan incision and excision techniques can be obtained before surgery by careful preoperative testing (including preoperative TEE) (see Chapter 23, Fig. 23.12). Either TTE or TEE performed before the surgery outside the OR will allow optimal surgical planning and comparison with other imaging techniques. If preoperative evaluation is adequate, the most important role for intraoperative TEE is determining whether a mass has embolized and the new location of the mass, often prompting the need

for further exploration or a change in the surgical procedure. The removal of cardiac masses is a category II indication for intraoperative TEE.

G. Detection of Foreign Bodies

The ability of intraoperative TEE to locate bullet fragments, mobile calcium plaques (see Chapter 16, Fig. 16.17) and medical devices (e.g. catheter fragments) is reported, but there is no evidence regarding its impact on clinical outcomes. The yield of intraoperative TEE in detecting foreign bodies is likely to be low in most settings, but it may have greater utility at centers with a high incidence of gunshot injuries. The detection of foreign bodies is a category II indication for intraoperative TEE.

H. Detection of Air Emboli During Cardiotomy, Heart Transplant, and Upright Neurosurgical Procedures

Intraoperative TEE can detect air bubbles in 8–60% of patients undergoing neurosurgery and 11–79% of patients undergoing cardiac surgery (see Chapter 9, Fig. 9.42). Current evidence is inadequate, however, to determine whether these emboli increase the risk of neurologic complications or whether intraoperative TEE monitoring for air emboli improves clinical outcomes.

Transesophageal echocardiography is an extremely sensitive test for air (bubbles as small as 2 μm usually can be detected) but the clinical significance of these bubbles is unclear. Animal studies suggest that air entrainment >1 cm^3/kg increases the risk of neurologic complications, but the threshold value for safe air volumes in humans is uncertain. The task force believes that patients benefit when TEE detects air during cardiotomy and neurosurgical procedures (12). During cardiotomy, venting procedures before cessation of CPB can eliminate retained air, and the task force believes that such measures decrease the patient's risk of embolic neurologic events, right ventricular failure due to right coronary artery embolization (see Chapter 16, Fig. 16.18) and myocardial ischemia. Transesophageal echocardiography offers similar benefits during sitting craniotomies, especially if the patients have not been screened preoperatively for patent foramen ovale (12). Patent foramen ovale appears to be a risk factor for stroke, and intraoperative maneuvers can induce intracardiac pressure changes that open probe-patent defects to permit paradoxical emboli.

Transesophageal echocardiography is the only intraoperative tool for detecting these abnormalities; few other tests can detect air and sources of right-to-left shunt as accurately. Use of TEE during upright neurosurgical procedures may increase the risk of vocal cord injury, although this risk may be reduced by proper technique and equipment (31).

The detection of air emboli during cardiotomy and heart transplant is a category II indication for using intraoperative TEE. It should also be considered for patients undergoing upright neurosurgical procedures (category II).

I. Intracardiac Thrombectomy

Intraoperative TEE can detect intracardiac thrombi in 2–10% of patients undergoing cardiac surgery, often exposing thrombi that were not apparent on preoperative TTE, but there is little evidence beyond case reports that the detection or evacuation of these clots results in improved clinical outcomes (see Chapter 23, Fig. 23.31).

In patients scheduled for thrombectomy, a pre-CPB echocardiographic examination can prevent an unnecessary operation if it determines that the thrombus has already embolized. Intracardiac thrombectomy is a category II indication for pre-CPB TEE.

J. Pulmonary Embolectomy

Case reports have described the use of perioperative TEE to detect pulmonary emboli and evaluate treatment, but there is little evidence regarding its impact on clinical outcomes.

The task force (1996) believes that perioperative TEE is especially useful during pulmonary embolectomy to evaluate hemodynamic status and detect residual emboli. The opinion of the task force, based on perioperative TEE monitoring, is that ~30% of embolectomy procedures fail to remove all emboli completely. These residual emboli are potentially harmful to the patient and the use of TEE to detect them intraoperatively may therefore be beneficial (12).

Transesophageal echocardiography may also be useful to determine the cause of acute hemodynamic disturbances, such as those resulting from pulmonary emboli, but it is not necessary for all patients with known or suspected pulmonary emboli (see Chapter 9, Fig. 9.40). Pulmonary embolectomy is a category II indication for using TEE.

K. Suspected Cardiac Trauma

The role of intraoperative and postoperative TEE in detecting unrecognized traumatic injuries to the heart has been described, but there is otherwise little evidence that TEE improves the clinical outcome of cardiac trauma patients (12).

Routine use of TEE for evaluating cardiac trauma is predicated on the availability of TEE equipment and qualified staff at trauma units. Unsuspected injuries could be detected during surgery if TEE is performed

intraoperatively. The need to return for further surgery and the risk of complications might thereby be reduced by intraoperative TEE, but this hypothesis needs to be confirmed through further research. Suspected cardiac trauma is a category II indication for perioperative TEE.

L. Detection of Aortic Atheromatous Disease or Other Sources of Aortic Emboli

Approximately 1–5% of patients suffer strokes during CPB, and the presence of atheromatous aortic ulcers is considered a major risk factor. Palpation of the Ao is not known to be sensitive, but TEE has been shown to allow detection of aortic atheromas. The detection of aortic atheromatous disease or other sources of aortic emboli is a category II indication for intraoperative TEE.

Intraoperative TEE and epivascular echocardiography are capable of detecting aortic atheromatous disease, but it is unclear whether its detection improves clinical outcomes. Atheromatous disease of the ascending Ao is noted in 9% of elderly patients and results in a change in therapy in 8–17% of patients (12).

The relationship between the severity of aortic atheromatous disease and postoperative dysfunction has been established previously. Choudary et al. (32) documented severe atheromatous disease in 12 of 126 patients undergoing CABG. Protruding atheromas were significantly more common in patients over 60 years of age. Out of four patients with grade V atheromas, two developed right hemiplegia postoperatively. To determine the optimal method to detect ascending aortic atheromas intraoperatively, manual palpation, TEE, and epiaortic scanning were compared in 100 patients (33). Age older than 70 years and hypertension were significant risk factors for severe ascending atheromas. Epiaortic scanning was found to be superior to both manual palpation and TEE.

M. Evaluation of Pericardial Surgery

Transesophageal echocardiography may be helpful in evaluating constrictive pericarditis and pericardiectomy procedures (see Chapter 11, Fig. 11.17). Evaluating the effectiveness of pericardiectomy constitutes a category II indication, but uncomplicated pericarditis is a category III indication.

N. Evaluation of Anastomotic Sites During Heart and/or Lung Transplantation

Some studies suggest that TEE is more sensitive than TTE in screening heart donor patients and more accurate than pulmonary capillary wedge pressure measurements in detecting hemodynamic disturbances during transplant surgery. Postoperative studies have demonstrated its ability to evaluate cardiac allograft function and detect thrombotic obstruction and stenoses in patients with lung transplants (see Chapter 21, Fig. 21.7).

Anastomotic integrity can be accurately assessed by TEE using two-dimensional (2D) or Doppler modalities (see Chapter 21, Fig. 21.6). Hemodynamic benefits of TEE during major organ transplant surgery are especially important. Evaluating anastomotic sites during heart and/or lung transplantation is a category II indication for intraoperative TEE.

O. Assessment of Residual Duct Flow After Interruption of Patent Ductus Arteriosus

The efficacy of intraoperative TEE in reducing the incidence of residual ductal flow after video-assisted thoracoscopy interruption of a patent ductus arteriosus (PDA) was studied by Lavoie et al. (34). In two of 30 consecutive patients (mean age 2.4 years; mean weight 11.2 kg), intraoperative TEE detected residual flow after placement of the vascular clip, requiring placement of a second clip. At one-month follow-up, three patients presented residual duct flow.

P. Evaluation of Myocardial Perfusion, Coronary Artery Anatomy, Graft Patency

Use of perioperative TEE to evaluate myocardial perfusion, coronary anatomy, or graft patency are category III indications. The argument for using TEE is strengthened when ECG monitoring cannot provide accurate information, such as patients with conduction disorders or in procedures that interfere with ECG lead placement. The argument for using TEE is weakened when clinical factors (e.g. pre-existing regional ventricular dysfunction) limit the accuracy of wall motion interpretation.

IV. CATEGORY III: LITTLE CURRENT SCIENTIFIC OR EXPERT SUPPORT

Conditions for which there is evidence and/or general agreement that the procedure/treatment is not useful/effective and in some cases may be harmful (11).

A. Repair of Cardiomyopathies (Other than Hypertrophic Obstructive Cardiomyopathy)

Hypertrophic obstructive cardiomyopathy repair is a category I indication for either EE or TEE assessment. Use of intraoperative TEE for other cardiomyopathies is however a category III indication.

B. Uncomplicated Endocarditis During Noncardiac Surgery

Noncardiac surgery in patients with uncomplicated endocarditis is a category III indication for intraoperative TEE.

C. Monitoring of Emboli During Orthopedic Procedures

Intraoperative TEE can detect embolized air or medullary contents in 30–62% of patients undergoing total hip replacement and, after tourniquet deflation, in 27–100% of patients undergoing knee arthroplasty. There is little evidence, however, that this information results in improved clinical outcomes (12). In practice, TEE detection of emboli during orthopedic procedures often prompts clinical interventions (e.g. replacing tourniquets) but the ultimate benefit to the patient of these maneuvers is uncertain. Monitoring for emboli during orthopedic procedures is a category III indication for intraoperative TEE.

D. Assessment of Repair of Thoracic Aortic Injuries

Assessing the repair of thoracic aortic injuries is a category III indication for intraoperative TEE. Other indications for TEE in aortic disease have been discussed in previous sections.

E. Uncomplicated Pericarditis

Uncomplicated pericarditis is a category III indication for TEE, as previously mentioned.

F. Evaluation of Pleuropulmonary Disease

There is no direct evidence that intraoperative TEE is accurate in detecting pleural or pulmonary parenchymal disease, or that such monitoring results in improved clinical outcomes. Pleural effusions and atelectatic lungs are sometimes identified (see Chapter 11, Fig. 11.7). The evaluation of pleuropulmonary disease is a category III indication for perioperative TEE.

G. Monitoring of Cardioplegia Administration

Monitoring cardioplegia administration is a category III indication for intraoperative TEE (12). In contrast, in the 2003 ACC/AHA/ASE guidelines, placement of intracardiac devices and monitoring of their position during port-access and other cardiac surgical procedures have become a class I indication. Positioning of a coronary sinus cannula is now one of these new class I indications of TEE monitoring.

H. Monitoring Placement of Intra-Aortic Balloon Pumps

Although the positioning of an intra-aortic balloon pump can be optimized by the use of TEE, this is a category III indication because it can be done properly and safely without TEE.

I. Automatic Implantable Cardiac Defibrillators

Implantation of a cardiac defibrillator is a category III indication for TEE. Hemodynamic disturbances may however occur in such patients and TEE may then become useful.

J. Pulmonary Artery Catheters

It is also a category III indication. TEE may be useful in patients with hemodynamic instability not responding to treatment based on pulmonary artery catheter data.

V. CONCLUSION

The indications for TEE are reviewed periodically after investigation of new procedures and documentation of outcome data. In the meantime, the ACC/AHA/ASE 2003 guidelines (11) are a useful tool to help the physician in making decisions and improving patient care.

REFERENCES

1. Mishra M, Chauhan R, Sharma KK et al. Real-time intraoperative transesophageal echocardiography—how useful? Experience of 5,016 cases. J Cardiothorac Vasc Anesth 1998; 12:625–632.
2. Sutton DC, Kluger R. Intraoperative transoesophageal echocardiography: impact on adult cardiac surgery. Anaesth Intensive Care 1998; 26:287–293.
3. Click RL, Abel MD, Schaff HV. Intraoperative transesophageal echocardiography: 5-year prospective review of impact on surgical management. Mayo Clin Proc 2000; 75:241–247.
4. Couture P, Denault AY, McKenty S et al. Impact of routine use of intraoperative transesophageal echocardiography during cardiac surgery. Can J Anaesth 2000; 47:20–26.
5. Michel-Cherqui M, Ceddaha A, Liu N et al. Assessment of systematic use of intraoperative transesophageal echocardiography during cardiac surgery in adults: a prospective study of 203 patients. J Cardiothorac Vasc Anesth 2000; 14:45–50.

6. Stevenson JG. Role of intraoperative transesophageal echocardiography during repair of congenital cardiac defects. Acta Paediatr Suppl 1995; 410:23–33.
7. Ungerleider RM, Kisslo JA, Greeley WJ et al. Intraoperative echocardiography during congenital heart operations: experience from 1,000 cases. Ann Thorac Surg 1995; 60:S539–S542.
8. Rosenfeld HM, Gentles TL, Wernovsky G et al. Utility of intraoperative transesophageal echocardiography in the assessment of residual cardiac defects. Pediatr Cardiol 1998; 19:346–351.
9. Sheil ML, Baines DB. Intraoperative transoesophageal echocardiography for paediatric cardiac surgery—an audit of 200 cases. Anaesth Intensive Care 1999; 27:591–595.
10. Sloth E, Pedersen J, Olsen KH et al. Transoesophageal echocardiographic monitoring during paediatric cardiac surgery: obtainable information and feasibility in 532 children. Paediatr Anaesth 2001; 11:657–662.
11. Cheitlin MD, Armstrong WF, Aurigemma GP et al. ACC/AHA/ASE 2003 guideline update for the clinical application of echocardiography: summary article: a report of the American College of Cardiology/American Heart Association Task Force on Practice Guidelines (ACC/AHA/ASE Committee to Update the 1997 Guidelines for the Clinical Application of Echocardiography). Circulation 2003; 108:1146–1162.
12. Practice guidelines for perioperative transesophageal echocardiography. A report by the American Society of Anesthesiologists and the Society of Cardiovascular Anesthesiologists Task Force on Transesophageal Echocardiography. Anesthesiology 1996; 84:986–1006.
13. Cheitlin MD, Alpert JS, Armstrong WF et al. ACC/AHA Guidelines for the Clinical Application of Echocardiography. A report of the American College of Cardiology/American Heart Association Task Force on Practice Guidelines (Committee on Clinical Application of Echocardiography). Developed in colloboration with the American Society of Echocardiography. Circulation 1997; 95:1686–1744.
14. Greene MA, Alexander JA, Knauf DG et al. Endoscopic evaluation of the esophagus in infants and children immediately following intraoperative use of transesophageal echocardiography. Chest 1999; 116:1247–1250.
15. Otto CM. The Practice of Clinical Echocardiography. Philadelphia: W.B. Saunders, 1997.
16. Ommen SR, Park SH, Click RL et al. Impact of intraoperative transesophageal echocardiography in the surgical management of hypertrophic cardiomyopathy. Am J Cardiol 2002; 90:1022–1024.
17. Denault AY, Couture P, McKenty S et al. Perioperative use of transesophageal echocardiography by anesthesiologists: impact in noncardiac surgery and in the intensive care unit (L'utilisation perioperatoire de l'echocardiographie transoesophagienne par les anesthesiologistes: les repercussions en chirurgie non cardiaque et a l'unite des soins intensifs). Can J Anaesth 2002; 49:287–293.
18. Applebaum RM, Cutler WM, Bhardwaj N et al. Utility of transesophageal echocardiography during port-access minimally invasive cardiac surgery. Am J Cardiol 1998; 82:183–188.
19. Falk V, Walther T, Diegeler A et al. Echocardiographic monitoring of minimally invasive mitral valve surgery using an endoaortic clamp. J Heart Valve Dis 1996; 5:630–637.
20. Schulze CJ, Wildhirt SM, Boehm DH et al. Continuous transesophageal echocardiographic (TEE) monitoring during port-access cardiac surgery. Heart Surg Forum 1999; 2:54–59.
21. Kort S, Applebaum RM, Grossi EA et al. Minimally invasive aortic valve replacement: echocardiographic and clinical results. Am Heart J 2001; 142:476–481.
22. Moises VA, Mesquita CB, Campos O et al. Importance of intraoperative transesophageal echocardiography during coronary artery surgery without cardiopulmonary bypass. J Am Soc Echocardiogr 1998; 11:1139–1144.
23. Secknus MA, Asher CR, Scalia GM et al. Intraoperative transesophageal echocardiography in minimally invasive cardiac valve surgery. J Am Soc Echocardiogr 1999; 12:231–236.
24. Clements FM, de Bruijn NP. Perioperative evaluation of regional wall motion by transesophageal two-dimensional echocardiography. Anesth Analg 1987; 66:249–261.
25. Bergquist BD, Bellows WH, Leung JM. Transesophageal echocardiography in myocardial revascularization: II. Influence on intraoperative decision making. Anesth Analg 1996; 82:1139–1145.
26. Savage RM, Lytle BW, Aronson S et al. Intraoperative echocardiography is indicated in high-risk coronary artery bypass grafting. Ann Thorac Surg 1997; 64:368–373.
27. Nowrangi SK, Connolly HM, Freeman WK, Click RL. Impact of intraoperative transesophageal echocardiography among patients undergoing aortic valve replacement for aortic stenosis. J Am Soc Echocardiogr 2001; 14:863–866.
28. Ionescu AA, West RR, Proudman C et al. Prospective study of routine perioperative transesophageal echocardiography for elective valve replacement: clinical impact and cost-saving implications. J Am Soc Echocardiogr 2001; 14:659–667.
29. Morehead AJ, Firstenberg MS, Shiota T et al. Intraoperative echocardiographic detection of regurgitant jets after valve replacement. Ann Thorac Surg 2000; 69:135–139.
30. O'Rourke DJ, Palac RT, Malenka DJ et al. Outcome of mild periprosthetic regurgitation detected by intraoperative transesophageal echocardiography. J Am Coll Cardiol 2001; 38:163–166.
31. Sukernik MR, Mets B, Bennett-Guerrero E. Patent foramen ovale and its significance in the perioperative period. Anesth Analg 2001; 93:1137–1146.
32. Choudhary SK, Bhan A, Sharma R et al. Aortic atherosclerosis and perioperative stroke in patients undergoing coronary artery bypass: role of intra-operative transesophageal echocardiography. Int J Cardiol 1997; 61:31–38.
33. Sylivris S, Calafiore P, Matalanis G et al. The intraoperative assessment of ascending aortic atheroma: epiaortic imaging is superior to both transesophageal echocardiography and direct palpation. J Cardiothorac Vasc Anesth 1997; 11:704–707.
34. Lavoie J, Javorski JJ, Donahue K et al. Detection of residual flow by transesophageal echocardiography during video-assisted thoracoscopic patent ductus arteriosus interruption. Anesth Analg 1995; 80:1071–1075.

Index

Abnormal diastolic function, 198–201
Abnormal left ventricular function, 192–193
  acute vs. chronic etiology, 192–193
  problems confounding diagnosis, 193
  transesophageal echocardiographic evaluation, 193
Abnormal right ventricular function, 193–198
  importance, 193–194
  transesophageal echocardiography findings, 194–198
Abscesses
  endocarditis, 389–390
Absent, 526
Accelerating flow
  mitral valve orifice, 38
Acoustic impedance, 6
  mismatch, 7, 8
Acoustic shadowing, 127, 128
Acquired aortic valve stenosis, 334–336
Acute aortic dissection, 274, 278
Acute mitral regurgitation, 395, 404
  mid-esophageal two-chamber view, 398
Acute thoracic dissection
  patient assessment, 563
Acute tricuspid regurgitation, 232
Air detection, 308
Air embolism, 212
Alferi operation
  Goretex anterior leaflet prolapse, 444
Aliasing, 26–27, 123–124
  color Doppler
    mitral stenosis, 125
  color reversal, 38
  computer sampling, 27
  movie image, 26
  prevention, 34
  pulsed-wave Doppler signal, 125
Ambiguous, 526
American College of Cardiology (ACC), 363
  classification guidelines, 559
American Heart Association (AHA), 363
  classification guidelines, 559
American Society of Anesthesiologists, 286, 316
American Society of Echocardiography (ASE), 90, 158, 167, 186, 383, 455
  classification guidelines, 559
  Devereux method, 107
A mode. *See* amplitude (A) mode
Amplitude (A) mode, 12
Amyloidosis, 237
  transthoracic subcostal view, 237
Anastomotic site evaluation
  heart and/or lung transplantation, 565
Anesthetic drugs, 295–300
Aneurysms
  aortic
    classification, 271
    frequency and distribution, 271
  aortic dilation, 270–272
  apical
    mid-esophageal four-chamber view, 180
  ascending aortic
    long axis and short-axis view, 272
  atrial septal, 503
  basal inferior ventricular
    mid-esophageal two-chamber view, 179
  cardiac
    repair and assessment, 563
  differences, 181
  left ventricular, 178–179
  mid-esophageal short-axis view, 273
  saphenous vein graft, 513
  thoracic aortic
    TEE, 271
  Valsalva, 271–272, 273
Angiosarcomas, 509–510
Angle dependence, 6
Annular ring
  mid-esophageal four-chamber view, 434
Annuloplasty ring, 463
  mid-esophageal view, 427
Anterior chordal rupture, 175
Anterior leaflet, 400
  prolapse, 442–444
    chordal transfer, 443
    mid-esophageal view, 443
    repair, 443, 444
Anterior mitral valve leaflets, 394
Anterior myocardial infarction, 176
Anterior tricuspid leaflets
  mid-esophageal view, 451
Antero-basal left ventricular pseudoaneurysm, 180
Antibioprophylaxis
  TEE, 147
Aorta, 261–282. *See also* ascending aorta
  anatomical considerations, 261–262
  coarctation, 547–548, 549
  echocardiographic examination, 264
  mid-esophageal short-axis view, 265
  short and long axis view, 267
  short-axis view, 270
  transverse sinus, 136
  traumatic rupture, 279–280
  upper esophageal short axis view, 76
  upper esophageal view, 265

Aortic aneurysm
classification, 271
frequency and distribution, 271
Aortic arch, 264–265
epiaortic probe imaging, 269
and right pulmonary artery
transverse plane transtracheal image, 151
upper esophageal view, 79, 267
Aortic atheromatosis
assessment techniques, 270
classification, 263
Aortic atheromatous disease
detection, 565
Aortic atherosclerosis, 266–270
cardiac surgery, 266–270
echocardiographic findings, 270
Aortic cannula
aortic mid-esophageal view, 293
Aortic cusps
mid-esophageal short-axis view, 333
Aortic dilation
aneurysms, 270–272
Aortic dissection, 268, 272–279, 295, 560
acute, 274, 278
aortic intramural hematoma, 278–279
ascending
mid-esophageal long-axis view, 276
associated complications, 277–278
classification, 274–276, 278
clinical background, 272–274
computed tomography scan, 294
diagnosis, 277
femoral arterial cannula, 304
imaging modalities and diagnostic accuracy, 276–277
low esophageal long-axis view, 276
Aortic hematoma
mid-esophageal short-axis view, 280
Aortic injury
short and long-axis view, 281
Aortic prosthesis
transesophageal echocardiogram, 373
Aortic pseudoaneurysm, 518
Aortic regurgitation, 349, 371
echocardiographic and Doppler parameters, 359
etiology, 349–350
mid-esophageal view, 196
mitral valve fluttering, 206
periprosthetic, 374
qualitative parameter, 358
quantification, 350–359
CW Doppler and pressure half-time, 356–357
effective regurgitant orifice, 354–356
flow reversal, 352
jet height/LVOT height, 350–352
regurgitant fraction, 352–354
short-axis jet area/LVOT area, 352
vena contract, 356–357
quantitative parameter, 358
application, 360
surgical indications, 364, 365
Aortic root
mid-esophageal long-axis view, 332
Aortic stenosis (AS), 215, 334–340
aortic valve, 85
bicuspid
dilatation aortic, 340
cardiac surgery, 344
etiology, 334–338
mid-esophageal long-axis view, 341
quantitative assessment, 338–349
aortic valve area, 342–349
flow velocity ratio, 342
M-mode, 342–349
pressure gradient, 338–342
surgical indications, 364
Aortic valve, 85, 329–360
anatomy, 329–334
anomaly, 546–547
aortic regurgitation, 85
aortic stenosis, 85
basal short-axis view, 82
basal transgastric longitudinal view, 356
basal transgastric view, 339
bicuspid, 352, 546
congenital aortic valve stenosis, 546
bicuspid bi-commissural, 335
bicuspid unicommissural, 334
bioprosthesis endocarditis, 366
classification, 348
closure, 322
congenital anomalies, 331–332
Doppler interrogation, 34
echocardiographic imaging, 332–334
long-axis view, 351
mid-esophageal
five-chamber view, 337
long axis view, 347, 353
M-mode view, 349
short-axis spilt screen view, 355
short-axis view, 331, 339, 345, 346, 350
normal anatomy, 329–331
off-axis view, 337
replacement, 275, 292, 297, 354, 367, 368, 372, 376, 378, 393
algorithm evaluation, 379
left ventricular outflow tract obstruction, 207
mid-esophageal long-axis view, 411
surgical indications, 363
stenosis, 350
acquired, 334–336
asymptomatic patients, 363–364
cardiac surgery patients, 364–365
surgical indications, 363–365
symptomatic patents, 364
surgery
avoiding patient-prosthesis mismatch, 365–368
echocardiography, 369–377
cardiopulmonary bypass, 370
before operation, 369–370
postoperative period, 377–380
left ventricular dysfunction patients, 368–369
operation type, 365
perioperative evaluation, 363–380
TEE role, 380
surgical anatomical view, 158
Apical aneurysm
mid-esophageal four-chamber view, 180
Apical ball thrombus, 177
Apical VSD
mid-esophageal four-chamber view, 174
transgastric view, 173
Array configurations, 43
Arterial cannulation, 302–304
Arterial cardiopulmonary bypass
pressure-area
arterial and left ventricular, 307
Arteries, 72–77
transposition, 549–550
Artifacts, 37, 121–129
Ascending aorta, 86, 263
aortic dissection, 303
linear artifacts, 122
mid-esophageal long-axis view, 76, 242, 262, 264
reverberation, 122
upper esophageal short-axis view, 100
Ascending aortic aneurysm
mid-esophageal long axis and upper esophageal short-axis view, 272
Ascending aortic dissection
mid-esophageal long-axis view, 276
Atherosclerotic ascending aorta
surgical strategy, 280–282
Atrial appendages, 498
Atrial cavity
left atrial myxoma, 505
Atrial reversal (AR), 73, 86
Atrial septal aneurysm, 503
Atrial septal defect, 144, 321, 526–528, 527
mid-esophageal view, 407
bicaval, 518
Atrial septum
left atrium, 67
lipomatous hypertrophy, 132

Atrial thrombus, 132
Atrioventricular connection, 526
Atrioventricular septal defect, 535–538, 538
Atrioventricular valves
  schematic drawing, 385
Attenuation, 9–10
  components, 10

Ball-in-cage prosthesis, 424
Ball-in-cage valves, 418
Ball thrombus
  apical, 177
Basal inferior ventricular aneurysm
  mid-esophageal two-chamber view, 179
Basal ventricular septal defect
  mid-esophageal four-chamber view, 174
Baseline shift, 137–138
Beam focusing, 47
Benign cardiac tumors, 504–508
Bentall procedure, 288
Bernoulli equation, 342
Biatrial technique
  orthotopic heart transplantation, 472
Bicaval technique, 472, 473
Bicuspid aortic stenosis
  dilatation aortic, 340
Bicuspid aortic valve, 352, 546
  congenital aortic valve stenosis, 546
Bicuspid bi-commissural aortic valve, 335
Bicuspid stenotic pulmonic valve, 461
Bicuspid unicommissural aortic valve, 334
Bilateral lung transplantation, 483
  transesophageal echocardiographic systematic examination, 485
Bilateral pleural effusion, 246
Bileaflet mechanical prosthetic valve
  mid-esophageal pressure gradient, 422
Bileaflet prosthetic valve dysfunction, 466
Biological effects, 141–144
  intensity measurement and quantification, 144
Biological tissue valves, 418–419
Bioprosthetic mitral valve stenosis and regurgitation, 420
Biventricular function evaluation, 195
Biventricular thrombi, 517
Blood flow, 108
Body surface area
  2-D cardiac structures, 96
Bridge to recovery device, 315
Bridge to transplant device, 315
Brightness (B) mode, 12
Brockenbrough-Braunwald phenomenon, 218

Calcified structures, 512
Canadian Consensus Conference on Heart Valve Surgery, 368
Carbomedics, 418
Carbon dioxide embolism, 211
Cardiac aneurysms
  repair and assessment, 563
Cardiac appendages, 69
Cardiac chambers, 64–65
  and great vessels
    normal pressures, 83
Cardiac cycle phases, 81–83
Cardiac disorders, 493
Cardiac hemangioma, 508
Cardiac masses
  removal evaluation, 563
Cardiac output, 115–116
Cardiac physiology
  cardiopulmonary bypass, 291–300, 304–310
  hypothermia, hemodilution, and nonpulsatile flow, 304
  myocardial perfusion and cardioplegia, 304
Cardiac septae, 65–69
Cardiac surgery
  echocardiography, 285–310
  intraoperative echocardiography, 556
    usefulness, 557
  TEE role, 310
Cardiac tamponade, 242–252
  2-D echocardiographic features, 248–250
  Doppler features, 250
Cardiac transplantation
  acute rejection, 474
  atrial anastomosis, 473
  mid-esophageal
    four-chamber view, 475
    long-axis view, 474
    two-chamber view, 477
  mid-papillary transgastric view, 476
  pseudoaneurysm, 479
  right ventricular echocardiographic measurements, 478
  TEE role, 480
Cardiac trauma, 564–565
Cardiac tumors
  classification, 504
Cardiogenic shock
  left ventricular dysfunction, 202
Cardiographic infusion
  aortic and mitral valve regurgitation, 305
Cardiomyopathy, 215–238
  dilated, 227–234
  dilated ischemic
    diastolic dysfunction, 231
    mid-esophageal four-chamber view, 235
    transgastric mid-papillary view, 229
  hypertrophic, 223
    obstructive, 343, 560–561
  hypertrophic septal
    mid-esophageal long-axis view, 217
  repair, 565
  restrictive and infiltrative, 234–238
  transesophageal echocardiography, 494
Cardioplegia cannula
  bicaval view, 290
Cardiopulmonary bypass (CPB)
  devices used, 286–291
  mean pulmonary outflow tract velocities, 115
  mid-esophageal long-axis view, 437
  pulmonary hypertension, 425
  surgery, 193
Cardiotomy
  air emboli detection, 564
Carpentier
  functional classification, 399
Catheters
  central venous, 286
  CS, 289–291
  intracardiac, 286
  mediastinal
    pleural fluid drainage, 286–287
Cavitation, 143
Central acceleration zone
  pulmonary artery, 38
Central venous catheters, 286
Centrifugal pumps, 317–319, 322
  cardiac transplantation, 323
Chamber compression
  hematoma, 250–251
Chiari network, 133, 134, 498
Chordal rupture, 394, 396
Circumference fiber shortening, 106
Cleft mitral valve, 545–546
Color-coded mapping, 38
Color Doppler, 31–37
  aliasing
    mitral stenosis, 125
  flow, 135–138, 221
  LVOT, 65
  principle, 33
Color flow Doppler
  jet area mapping, 397
Color flow imaging, 33
  mid-esophageal view, 433

Color jet area, 402
Commissural prolapse, 441
Complex single ventricle, 550
Complications, 141–155
Concordant, 526
Congenital aortic valve stenosis
  bicuspid aortic valve, 546
Congenital cardiac malformations, 534–535
Congenital heart defects, 526–548
  repaired, 548–552
Congenital heart disease, 525–552, 558–559
  surgery
    TEE role, 552
Constrictive pericarditis, 252–258, 255, 256, 257
  echocardiographic findings, 252
  restrictive cardiomyopathy, 253–258, 257
  and restrictive cardiomyopathy differences, 236–237
Continuity equation, 411, 421
  and mass conservation principle, 116
  method
    valvular areas, 116
Continuous wave (CW) Doppler, 27–30, 401
  flow, 32
  left ventricular apex, 321
  mitral regurgitation, 344
  pressure half-time, 423
Controlled bypass, 291–295
Coronary artery
  anatomy
    evaluation, 565
  disease
    acute allograft rejection, 479–480
  distribution and flow, 157–158
  imaging
    coronary vasodilator reserve, 181–182
Coronary distribution
  transesophageal echocardiographic view, 161
  transgastric echocardiographic view, 161
Coronary revascularization, 165, 275
  aortic and mitral valve replacement, 377
  LVOT, 506
  mid-esophageal four-chamber view, 450
  right ventricular outflow tract obstruction, 208
Coronary sinus (CS), 87
  catheter, 289–291
  lower esophageal view, 75
  low-esophageal four-chamber view, 103
  visualization, 289
Cor triatriatum, 542–543
  variants, 542
Cor triatriatum sinister
  Eustachian valve, 544
  variants, 543
Crohn's disease, 515

Damping material
  role, 45
Descending aorta, 263–264
  deep esophageal view, 99
  hematoma, 279
  short-axis view, 269
Descending aorta-flow reversal
  and aortic regurgitation, 86
Destination therapy, 315
Devereux method
  ASE, 107
Diastolic dysfunction, 169
  cardiopulmonary bypass, 201
  echocardiographic classification, 200
Diastolic function
  assessment, 308
Diastolic pressure gradient, 409
Diastolic transvalvular gradients
  measurement, 420
Diastolic waves, 73
Dicom standard, 21
Dilatation aortic
  bicuspid aortic stenosis, 340
Dilated ascending aorta
  distal view, 266
Dilated cardiomyopathy, 227–234
  clinical features, 228
  echocardiographic features, 228–233
    chambers dilation, 228
    diastolic dysfunction, 230
    secondary findings, 230–233
    ventricular systolic dysfunction, 229–230
  epidemiology, 227–228
  noncompacted LV, 233–234
    anatomical features, 233–234
    clinical features, 233
    echocardiographic features, 234
    epidemiology, 233
  nontransplant surgery, 234
  transthoracic apical four-chamber view, 232
Dilated ischemic cardiomyopathy
  diastolic dysfunction, 231
  mid-esophageal four-chamber view, 235
  transgastric mid-papillary view, 229
Discordant, 526
Disk-shaped transducer, 43
Dobutamine, 301
Doppler, 108–119. *See also* pulsed-wave Doppler
  aliasing
    mitral stenosis, 125
  clinical applications, 36
  color, 31–37
  color flow
    jet area mapping, 397
  continuous and pulsed-wave, 27–30
  continuous wave (CW), 27–30, 401
    left ventricular apex, 321
    mitral regurgitation, 344
    pressure half-time, 423
  effect, 23–25
    target motion, 24
  flow, 135–138, 221
  flow profiles
    normal and abnormal physiology, 81–87
  formula, 25
  high-PRF PW, 27
  interrogation
    aortic valve, 34
  jet area mapping
    color flow, 397
  LVOT, 65
  principle, 33
  schematic spectrum, 108
  shift, 25
  tissue imaging, 37
  ultrasound
    beam, 338
    clinical applications, 39
    principles, 23–39
  velocities
    normal values, 109
Doppler, Johann Christian, 23
Double inlet, 526
Double inlet left ventricle, 551
Double-orifice mitral valve, 545
Double outlet, 526
Double purse-string suture technique, 463
Duchenne dystrophy, 236
Dynamic range compression, 17
Dynamic reception focus, 48
Dysfunctional mitral bioprosthesis
  mid-esophageal long-axis view, 428

Ebstein's anomaly, 539
  intraoperative views, 540
  tricuspid valve, 539–540
Echocardiographic findings, 405–406

Echocardiographic parameters
fluid loading, 190
Echocardiography
indications, 559
patent foramen ovale, 530
Echo-free spaces, 133–135
Echogenic material, 457
Echo machines
high-PRF, 30
Echo train, 13
Effective regurgitant orifice, 403
Ehlers-Danlos syndrome, 349
Ejection fraction, 103–104
mitral annular motion relationship, 186
Ejection fraction (EF)
calculation, 105
Electrical safety, 144
Electrocardiogram (ECG), 90
volume and pressure relationship, 187
Electrocauter artifact, 128
Electrocautery, 127
Electron, 41
Electronic scanning and phasing differences, 49
Embryological remnants, 498
Endocarditis, 388–390, 560–561
abscesses, 389–390
Duke criteria, 389
intravenous drug user, 519
pneumococcal meningitis, 520
vegetation, 389
Energy conservation principle
and pressure difference, 108–110
Epiaortic scanning, 265–266
Epicardial fat, 246
Epinephrine, 300
Equipment, 141–155
biological effects, 141–144
contraindications, 146
health personnel concerns, 155
patient evaluation before procedure, 144–146
contraindications, 146
indications, 144–145
and personnel, 144
Esophageal intubation, 149–151
Eustachian valve, 132–133, 134
cor triatriatum sinister, 544
mid-esophageal view, 499
Extracardiac masses, 512
Extraskeletal osteosarcomas, 510–511

Fallot tetralogy, 541–542, 548–549
False tendons, 129–130
Fiberoptic laryngoscope
TEE probe, 151
Fibromas, 505
Flow mapping, 31
Flow patterns
color, 36
Flow profiles, 35
Fluid loading
hemodynamic parameters, 190
Focusing, 45–49
Food and Drug Administration, 315
Foreign bodies
detection, 564
Fractional area change, 105–106
measurement, 107
Fractional shortening (FS), 104
calculation, 105
Frame rate
width, 19
Fraunhofer zone, 46
Frequency, 137
Frequency shift
velocity range, 27
Fresnel zone, 46

Gain, 136–137
Gain control, 16
Ghosting, 124
artifacts, 124
phenomenon, 123
Global function
left ventricular assessment, 306
stroke volume
cardiac output, and cardiac index, 105
systolic changes, 162–165
Global systolic ventricular function, 165–167
Global ventricular function
and hemodynamics, 185–212
Glutaraldehyde exposition, 155
Goretex anterior leaflet prolapse
Alferi operation, 444
Goretex chords, 443–444
papillary muscle shortening, 444
resection, 444
Goretex chords, 443–444
Gradient evaluation, 432
Graft patency
evaluation, 565
Great arteries
transposition, 549–550
Great vessels
upper esophageal view, 67

Harmonic imaging principle, 53
Health personnel concerns, 155
Heart
fibrous skeleton, 333
lipomatous infiltration, 500–502
man-made objects, 517
movements
schematic representation, 92
noncardiac neoplasms, 511–512
two-dimensional four-chamber view, 53
Heart transplantation, 471–480
bicaval orthotopic biatrial technique, 472
normal echocardiographic profile, 477–478
Heart valve
systole and diastole atria removed, 330
Hemangiomas, 508
Hematoma
chamber compression, 250–251
Hemochromatosis, 238
Hemodynamic(s)
and global ventricular function, 185–212
Hemodynamic disturbances, 557
patients, 563
Hemodynamic parameters
fluid loading, 190
Hepatic disorders, 493
Hepatic vein, 86
lower esophageal view, 74
Hepatic venous flow (HVF), 36, 478
Hepatopulmonary syndrome
transesophageal echocardiography, 493
Human soft tissue ultrasound
velocity, 25
Hydraulic principle, 113
Hypertension and hemodynamic derangement
causes, 201–209
Hypertrophic cardiomyopathy, 215–227
anatomical features, 216
clinical features, 216
echocardiographic features, 218–223
diastolic function, 222–223
Doppler and color flow imaging, 221–222
M-mode and 2-D imaging, 218–221
epidemiology, 215–216
monitoring therapy, 223–227
obstructive, 343, 560–561
outflow tract obstruction pathophysiology, 216–218
Hypertrophic septal cardiomyopathy
mid-esophageal long-axis view, 217
Hypertrophy, 223
Hypocalcemia, 492
Hypoglycemia, 492
Hypoplastic left heart
mid-esophageal, 551

Hypotension, 491
Hypothermia, 491
Hypovolemia
  Doppler indices summary, 192

Image features and artifacts, 121–129
Image generation, 50
Image quality, 50–54
  contrast resolution, 51–52
  detail resolution, 50–51
  resolution, 50–53
  temporal resolution, 52–53
Imaging
  artifacts and pitfalls, 121–138
  B mode, 12
  C mode, 14
  color flow, 33
    mid-esophageal view, 433
  3D, 14
  Doppler, 14
  duplex, 14
  maximal
    depth, 18
  M mode, 14
  A mode, 11–12
  planes, 56–64
  principle
    harmonic, 53
  ultrasound frequency, 11
Infection control, 141, 154–155
Inferior myocardial infarction
  right ventricle diastolic function, 197
  right ventricle systolic function, 197
Inferior vena cava (IVC), 69
  cardioplegia cannula, 291
  lower esophageal view, 74, 100
Infiltrative cardiomyopathy, 234–238
Inflammatory valvulopathies
  rheumatic valve disease, 458
Inhalation agents, 296–299
Inotropes
  mid-esophageal long-axis view, 437
Instrumentation, 14–16, 25–26
  transducers, 14
    scan converters, 16
    transmitting/receiving electronics, 15
Integrated approach, 404–405
Intensity measurement and quantification
  biological effects, 144
Intensive care unit and cardiac surgery, 223–224
Interatrial septum, 189
  lipomatous hypertrophy, 502
Internal mammary dissection, 302
Interventricular septum wall thickness (IVST), 107
Intraaortic balloon counterpulsation, 316–317
Intraaortic balloon pump, 316
  aorta, 317
  effect, 319
  hemodynamic and Doppler profile, 318
Intracardiac catheters, 286
Intracardiac devices and monitoring surgery placement, 562
Intracardiac pressures, 110–113
Intracardiac thrombectomy, 564
Intracardiac thrombi, 513–517
Intracavitary contents, 497–522
  anatomical structures, 498
  variant, 497–503
Intravenous anesthetic agents
  diastolic function, 299–300
  systolic function, 300
Intraventricular bands and chords, 500
Inversus, 526
Irregular flow
  velocity spectrum, 32
Ischemia ventricular function, 157–182
  anatomy and function, 157–162
  complications and associated findings, 171–181
Ischemic mitral valvular disease, 392–394
Isoproterenol
  maximum pressure gradient, 228
Isovolumic relaxation time (IVRT), 169

Jet area mapping
  color flow Doppler, 397
Jet width, 398

Lambl's excrescence
  mid-esophageal long-axis view, 507
Lambl's excrescences
  papillary fibroelastomas, 506–508
Laminar flow
  spectral curve, 31
  spectral display, 32
Leading and trailer edge, 90
Leaflet extension
  schematic representation, 442
Leaflet prolapse
  Goretex anterior, 443–444
Left anterior descending artery
  septal branches, 162
Left anterior descending (LAD) coronary, 157
Left atrial anomaly, 542–543
Left atrial appendage (LAA), 71
  intussusception, 512–513, 514
  mid-esophageal view, 60, 102, 500
  pectinate muscles, 131
  pulsed-wave Doppler examination, 408
  thrombus, 233
Left atrial myxoma
  atrial cavity, 505
  mid-esophageal view, 504
Left atrial pressure, 113
  estimation, 231
  mitral regurgitation, 114
Left atrial thrombus, 513–516
  sinus rhythm patients, 516–517
Left atrium (LA)
  atrial septum, 67
  mid-esophageal four-chamber view, 98
  mid-esophageal two-chamber view, 60
  retrocardiac inhomogenous mass, 514
Left main coronary artery (LMCA)
  anatomical view, 159
  angiographic view, 159
  echocardiographic view, 159
  upper esophageal short-axis view, 75
Left superior vena cava (LSVC), 133–134, 135, 287, 500–502, 533
Left upper pulmonary vein (LUPV), 32, 69
  mid-esophageal view, 71, 101
Left ventricle (LV)
  aneurysm, 178–179
  and aortic pressure, 226
  apex
    continuous-wave Doppler, 321
  assist device, 320, 323
    outlet cannula positioning, 326
  cardiac fibroma
    transgastric mid-papillary view, 506
  contractile function
    valve function, 309–310
  diameter, 97
  diastolic dysfunction, 194, 198–200, 203
    brain heart syndrome, 203
    diagnosis and classification, 201
  diastolic function, 476–477
  dysfunction
    cardiogenic shock, 202
  elastance, 300
  end-diastolic pressure, 112–114
  end-systolic cavity, 189
  function, 186–192
    mid-esophageal view, 163

global function
assessment, 306
inflow, 83–84
abnormal relaxation, 83
restrictive filling, 83–84
mid-esophageal long-axis view, 61
pressure change
time measurement, 195
pressure–volume relationship, 187
load and function changes, 187
pseudoaneurysm
antero-basal, 180
short-axes diameters
transgastric mid-papillary view, 97
spatial orientation, 94
systolic dysfunction, 194
systolic function
evaluation, 196
tamponade, 248
thrombus, 176–177, 513
time indices measurement, 106
transgastric mid-papillary echocardiographic view, 63
transgastric view, 63
Left ventricular outflow tract (LVOT), 35, 86
coronary revascularization, 506
flow acceleration, 225
gradient, 222
mid-esophageal long-axis view, 98, 346
obstruction, 192, 204–206, 223
aortic valve replacement, 207
pulsed-wave Doppler interrogation, 81
transgastric view, 81
Linear fissure
TEE probe, 148
Lipomas, 505–506
Lipomatous hypertrophy, 133
atrial septum, 132
interatrial septum, 502
Liver transplantation, 491–495
mid-esophageal four-chamber view, 494
procedure, 491–492
anhepatic stage, 492
postanhepatic stage, 492
preanhepatic stage, 491–492
Longitudinal waves, 4
momentum, 2
Lung transplantation, 481–489
hemodynamic instability, 486, 487
TEE role, 481–482, 489
after procedure, 483–487
intensive care unit, 487–489
during procedure, 482–483
transesophageal echocardiographic systematic examination, 485
Lymphomas, 508–509

Malignant cardiac tumors, 508–511
Mapping
color-coded, 38
jet area
color flow Doppler, 397
standard color, 29
Marfan's syndrome, 349
Mass conservation principle
and continuity equation, 116
Maximal imaging depth, 18
Mechanical bileaflet prosthesis
diastole, 426
mid-esophageal view, 426, 427
Mechanical circulatory assistance
TEE role, 315–327
Mechanical index
transmitting power, 5
Mechanical mitral valve prostheses, 418
Mechanical valves, 418–419
Mediastinal catheter
pleural fluid drainage, 286–287
Mesotheliomas, 511
Metabolic acidosis, 492
Metastatic breast cancer
mid-esophageal four-chamber and bicaval view, 511
Mirror images, 124–125
Miscellaneous, 512
Mitral and tricuspid annular diameters, 101
Mitral annular velocities (MAV)
tissue Doppler, 171
Mitral annuloplasty rings
transgastric view, 434
various models, 440
Mitral annulus
extensive calcification, 441–442
Mitral bioprosthesis
dysfunctional
mid-esophageal long-axis view, 428
mid-esophageal long-axis view, 431
Mitral bioprosthesis leaflets
mid-esophageal long-axis view, 419
Mitral bioprosthetic valve
reoperation, 431
Mitral mechanical bileaflet prosthesis
mid-esophageal long-axis view, 421, 424
mid-esophageal two-chamber view, 425
Mitral regurgitation (MR), 36, 400
acute, 395, 404
mid-esophageal two-chamber view, 398
continuous-wave Doppler, 344
etiology, 388
left atrial pressure, 114
mid-esophageal view, 196
severity score, 401
Mitral stenosis, 405–409
associated findings, 406
color Doppler aliasing, 125
evaluation summary, 413
pressure half-time, 410
quantitative echocardiographic evaluation, 409
and regurgitation, 406
severity, 409
Mitral valve, 83, 383–413
basal transgastric view, 80
deep transgastric view, 338
double-orifice, 545
echocardiographic and anatomical representation, 386, 387
echocardiographic representation, 388, 389
intraoperative examination, 440
mid-esophageal four-chamber view, 80, 386
mid-esophageal long-axis view, 436
mid-esophageal two-chamber view, 389
mitral stenosis, 83
regurgitation, 83
reoperation, 290
surgical and intraoperative view, 384
Mitral valve annulus
calcification, 512
Mitral valve anomalies, 543–546
Mitral valve area, 409
calculation, 412
continuity equation, 410–411
planimetry, 409
pressure half-time, 409–410
proximal flow convergence, 411
Mitral valve fluttering
aortic regurgitation, 206, 210
Mitral valve function
left ventricular mass, 476
Mitral valve inflow
Doppler interrogation, 33
Mitral valve leaflets
anterior and posterior, 394
Mitral valve lesions
anatomical manifestations, 384–395
examination, 384–388
Mitral valve regurgitation, 397
mechanism and quantification, 395

Mitral valve repair, 394, 417–444
annuloplasty, 439
cannulation and extracorporeal circulation, 438
recommendations, 435
mitral stenosis indications, 435
right ventricular diastolic function, 207
surgical indications, 432
TEE evaluation, 432–438
transgastric long-axis view, 507
valve analysis, 439
video loop, 438
Mitral valve replacement, 392, 393, 417–444
early complications, 444
repair success, 444
mid-esophageal long-axis view, 309
surgical indications, 432
Mitral valve stenosis, 408, 543–545
bioprosthetic, 420
and regurgitation, 420
Mitral valve surgery
recommendations, 436
TEE role, 439
Mitral valve valvuloplasty
echocardiographic score, 407
Moderator band, 132
right ventricle, 501
Moderator bond, 133
Modified Simpson's biplane method, 103
Motion (M) mode imaging, 12, 90–108
centerline method, 92–93
chamber dimensions, volume calculations, 101–104
edge recognition, 90
global function, 104–105
hypertrophic cardiomyopathy
echocardiographic features, 218–221
measurements and calculations, 93–101
referencing centroids, 91–92
timing, 90–91
wall thickness, mass, stress, 106–108
Multiple reflections and acoustic shadowing, 124
Multiple TEE evaluation, 423–432
Myocardial infarction
anterior, 176
VSD, 172
Myocardial ischemia, 201–204
Myocardial ischemia/infarction
risk, 562–563
Myocardial performance index (MPI)
measurement, 194
Myocardial perfusion
evaluation, 565
Myocardial rupture, 179–181
Myocardial segmental identification, 158–159
Myxoid degeneration, 390–392, 459
lesion complexity, 392
Myxomas, 504–505

Native aortic valve, 329–360
Native valves
physiologic regurgitation, 135–136
Near-field clutter, 125, 126
Nonanesthetic drugs
cardiac surgery, 300–302
Noncardiac neoplasms
heart, 511–512
Nonrestrictive membranous ventricular septal defect, 537
Nonspecular reflections, 7
Nonsurgical septal ablation, 224–225
Nontransplant surgery
dilated cardiomyopathy, 234
Normal anatomy and flow, 56–87
complete examination, 56–81
anatomy and physiology, 64–81
Normal right and left ventricular function, 186–192
base descent and segmental contraction, 186
pressure–volume relationship, 186–192
Normal right and left ventricular morphology, 186
Normal segmental function, 159–162
Novacor system
mid-esophageal four-chamber view, 324
Nyquist limit, 34

Operating room (OR) maintenance, 154
Orthotopic heart transplantation, 471–472
biatrial technique, 472
Ostium primum atrial septal defect, 532
cleft anterior mitral valve leaflet, 532
surgical view, 533
Ostium secundum atrial septal defect, 529
Overall gain control, 16

Pacemaker endocarditis, 498
Papillary fibroelastomas
Lambl's excrescences, 506–508
Papillary muscle dysfunction
mitral regurgitation evaluation, 173–176
Para-annular jet
localization, 433
Patent ductus arteriosus, 538–539
Patent foramen ovale (PFO), 69, 321, 521–522, 528
echocardiography, 530
intraoperative view, 530
mid-esophageal view, 531
Pathogen destruction, 155
Patient-prosthesis mismatch, 367, 369
Pectinate muscles, 130–132
LAA, 131
RA, 131
Penn Convention, 90
Percutaneous alcohol septal ablation, 226
Pericardial cyst, 258, 512
esophageal view, 258
Pericardial effusion (PE), 241, 243–244, 253
and cardiac tamponade, 242–252
epicardial fat and pleural fluid differences, 243–244
localization, 245
location, volume, and nature, 243
Pericardial fluid
percutaneous drainage, 254
Pericardial sac, 243
Pericardial surgery
evaluation, 565
Pericardial tissue mitral valve bioprosthesis, 419
Pericardiectomy, 255
Pericardiocentesis, 324
surgical drainage assessment, 251–252
Pericarditis
Doppler criteria, 256
Pericardium, 241–259
congenital absence, 259
intraoperative view, 242
Periprosthetic regurgitation, 429–432
Permembranous ventricular septal defect, 536
Persistence, 20
Phasing and scanning differences, 49
Phenylephrine, 303
Phillips Medical Systems, 54
Phosphodiesterase inhibitors, 302
Picture archiving and communication systems (PACS), 21
Piezo, 41
Piezoelectric principle, 41–42
pressure, 42
Pneumococcal meningitis, 520
endocarditis, 520
Point septal separation
transthoracic parasternal view, 230
Position emission tomography (PET), 168

Positive-end expiratory pressure (PEEP), 299
Positive inotropic drugs, 300
Positive-pressure expiration
  truncated mid-esophageal four-chamber view, 488
Positive-pressure ventilation
  Doppler transmitral flow, 296
Posterior leaflet
  inverted flow, 442
  mid-esophageal four-chamber view, 391
  sliding pasty, 441
Posterior leaflet prolapse, 441–442
Posterior mitral valve leaflets, 394
Posterior tricuspid leaflets
  mid-esophageal view, 451
Posteromedial papillary muscle rupture, 175, 399
Preload assessment, 306–308
Pressure
  cardiac chambers and great vessels, 83
Pressure half-time
  continuous-wave Doppler, 423
  factors affecting, 410
  mitral stenosis, 410
  valvular areas, 116–117
Pressure–volume relationship
  afterload, 190–191
  contractility and ventricular performance, 191–192
  normal right and left ventricular function, 186–192
  preload, 187–190
Primary cardiac neoplasm, 503
Probe maintenance, 154–155
Prophylaxis planification, 146–147
Prosthesis
  ball-in-cage, 424
Prosthetic color Doppler flow, 137
Prosthetic mitral valve replacement, 179
Prosthetic regurgitation, 421–423
Prosthetic valve
  area, 421
  bileaflet
    dysfunction, 466
  bileaflet mechanical
    mid-esophageal pressure gradient, 422
  dysfunction, 435
  effective orifice area, 369
  physiologic regurgitation, 135–136
Protamine, 309
Provocative testing, 405
Proximal ascending aorta
  upper esophageal view, 77
Proximal flow acceleration convergence zone, 38
Proximal flow convergence, 117–118
Proximal isovelocity surface area, 401–403
Pseudoaneurysm
  antero-basal left ventricular, 180
  aortic, 518
  cardiac transplantation, 479
  left ventricular
    antero-basal, 180
Pulmonary artery, 87
  pressure, 111–112
  and right ventricular diastolic pressure, 112
  stenotic anastomosis quantification, 486
  systolic pressure, 110
Pulmonary artery end-diastolic pressure (PAEDP), 113
Pulmonary embolectomy, 564
Pulmonary hypertension, 210
  cardiopulmonary bypass, 425
  midsystolic pulmonary valve closure, 206–209
Pulmonary regurgitation
  echocardiographic and Doppler parameters
    evaluation, 462
    grading, 462
Pulmonary stenosis, 540–541
Pulmonary thromboembolism, 209–211
Pulmonary vascular anastomosis, 482
Pulmonary vein, 86
Pulmonary venous flow (PVF), 398
  changes, 405
  S-wave, 169
Pulmonic valve (PV), 80, 85–86, 447–467
  disease, 459–460
  endocarditis, 450–458
    abscesses, 455–458
    vegetation, 455–458
  mitral valve replacement, 460
  pulmonic regurgitation, 85
  pulmonic stenosis, 85–86
  right ventriculostomy, 449
  transverse view, 459
Pulsatile blood pumps, 319–326
Pulse, 12
Pulsed Doppler wave characteristics, 18
Pulsed ultrasound
  parameters, 17
Pulsed wave (PW), 32
  technology, 30
Pulsed-wave Doppler, 27–30, 33
  examination, 489
  interrogation, 73, 84
    LUPV, 70
    PA, 85
    PV, 85
    transmitral valve flow, 191
  signal, 79
    aliasing, 125
  TMF, 166, 168
Pulse repetition frequency (PRF), 18, 25

Quadrangular resection, 441
Quadricuspid valve, 336
Quantitative echocardiography, 89–119

Range ambiguity, 125–126
Reduced urine output, 492
Refraction, 7, 8, 126–127
Refraction phenomenon, 9
Regional left ventricular function assessment, 306
Regurgitant aortic valve
  continuous-wave Doppler interrogation, 357
Regurgitant pressure half-time, 358
Regurgitant volume, 403–404
  and fractions, 118
Relative ultrasound intensity, 10
Residual duct flow
  assessment, 565
Resolution
  types, 51
Restrictive and infiltrative cardiomyopathy, 234–238
  clinical findings, 234–235
  definition, 234
  echocardiographic features, 235–236
Restrictive cardiomyopathy
  constrictive pericarditis, 257
  and constrictive pericarditis differences, 236–237
Retrocardiac inhomogenous mass
  left atrium, 514
Revascularization
  mid-esophageal short-axis view, 143
  normal diastolic function, 170
Reverberation, 37, 121–123
  ascending aorta, 122
Rhabdomyomas, 505
Rhabdomyosarcomas, 510
Rheumatic heart disease, 406
Rheumatic valve disease, 458–459
  inflammatory valvulopathies, 458
Rheumatoid valve disease, 390
Right atrial angiosarcoma
  mid-esophageal view, 510
Right atrial appendage
  mid-esophageal long-axis view, 70
Right atrial collapse, 250
Right atrial pressure (RAP), 112
  echocardiographic estimation, 113

Right atrial thrombus, 517
mid-esophageal right ventricular view, 517
Right atrium (RA)
lower esophageal view, 75
mid-esophageal four chamber view, 98
mid-esophageal four-chamber view, 509
mid-esophageal long-axis view, 70
pectinate muscles, 131
tricuspid valve, 448
Right coronary artery (RCA), 157
anatomical view, 160
angiographic view, 160
echocardiographic view, 160
intraoperative view, 160
upper esophageal short axis view, 76
Right lower pulmonary vein
mid-esophageal view, 73
Right pulmonary artery
transverse plane transtracheal image, 151
Right systolic ventricular systolic pressure
tricuspid regurgitation, 111
Right upper and lower pulmonary veins
mid-esophageal views, 102
Right upper pulmonary vein
Doppler evaluation, 484
mid-esophageal view, 72
Right ventricle
mid-esophageal echocardiographic view, 66
mid-esophageal short-axis view, 66
Right ventricle (RV)
apical short-axis view, 164
basal short-axis view, 164
deep transgastric long-axis view, 453
lower esophageal view, 75
mid-esophageal four-chamber view, 62, 97
mid-esophageal short-axis view, 99
mid short-axis view, 164
moderator band, 501
short-axis transgastric view, 164
transgastric longitudinal view, 293
transgastric view, 64, 453
Right ventricle contractile function
valve function, 309–310
Right ventricle diastolic dysfunction, 200–201, 204
algorithm, 204
cardiac revascularization, 205
off-pump bypass surgery, 205, 206
Right ventricle diastolic function
evaluation, 197
inferior myocardial infarction, 197
mitral valve repair, 207
Right ventricle dysfunction, 299
Right ventricle function, 186–192
assessment, 308
mid-esophageal view, 163
Right ventricle infarction, 177
Right ventricle inflow and outflow
mid-esophageal short-axis view, 99
Right ventricle inflow and outflow tract
mid-esophageal short-axis view, 450
Right ventricle ischemic dysfunction, 178
Right ventricle systolic dysfunction
transgastric view, 199
Right ventricle systolic function
evaluation, 197, 198
inferior myocardial infarction, 197
Right ventricle systolic pressure, 110, 112
Right ventricle thrombi, 517
Right ventricular outflow tract (RVOT), 64
anomaly, 540–543
obstruction, 206, 208, 210
coronary revascularization, 208
transverse sinus, 137
upper esophageal sagittal view, 451
Royal College of Physicians and Surgeons of Canada, 413

Safety, 141–155
Saphenous vein graft aneurysm, 513
Sarcoidosis, 237–238
Scanning, 45–49
epiaortic, 265–266
and phasing differences, 49
ultrasound system, 13
Scattering, 7, 8
Schematic Doppler spectrum, 108
Sector depth, 138
Sector scan
width, 19
Segmental systolic function changes, 167–169
Segmental ventricular function, 157–182
Septal motion
transgastric mid-papillary view, 91, 93
Septation defects, 526–539
Shadowing, 127
Shear waves, 2
Shunt fractions, 118–110
Side lobes, 127–129, 129
Signal processing and display, 16–17
display, 17
image resolution, 17
time gain control, 16
Simpson's biplane method
left ventricular volumes measurement, 104
Sine qua non condition, 320
Single outlet, 526
Single photon emission computed tomography (SPECT), 168
Single plane area-length method, 103
Sinus venosus atrial septal defect, 532
Sinus venosus septal defect
mid-esophageal view, 531
Society of Cardiovascular Anesthesiologists, 316
Soft tissue ultrasound velocity, 25
Solitus, 526
Speckle reflection, 7
Spectral display, 30–31
curve construction, 30
flow reversal, 28
Specular reflection, 6–7
Spontaneous echo contrast, 305
Spontaneous echocontrast, 516
St. Jude Medical, 418
Standard color mapping, 29
Standard Convention, 90
Starr–Edwards mechanical prosthesis
mitral position, 430
Starr–Edwards prosthetic valve, 429
Stenotic pulmonary homograft, 465
Straddling, 526
Stroke volume (SV), 165
and cardiac output, 115–116
global function
cardiac output, and cardiac index, 105
Structure misinterpretation, 129–133
Subaortic membrane
mid-esophageal long-axis view, 342
Subvalvular aortic stenosis
coronary bypass, 547
Superior vena cava (SVC), 69, 292
deep transgastric view, 73
mid-esophageal bicaval view, 286
Supra and subaortic stenosis, 336–338
Supra and subvalvular aortic stenosis, 546–547
Supravalvular aortic stenosis
anatomic types, 548
Surgical septal myectomy, 225–227
Suture annuloplasty
complications and failed repair, 462–463
Suture technique
double purse-string, 463
S-wave pulmonary venous flow, 169
Synthetic catecholamines, 301–302

Systematic transesophageal echocardiography examination and imaging planes, 56–64
four-chamber view, 61
image display, 57
structures, 57–61
TEE probe, 56–57
thoracic aorta, 62–64
transgastric view, 61–62
Systolic anterior motion (SAM), 220, 438, 444
mid-esophageal long-axis view, 370
obstruction, 223
risk assessment, 224
Systolic changes
global function, 162–165
Systolic time intervals, 105
Systolic ventricular function
global, 165–167
Systolic waves, 73

Tamponade, 249
mechanical ventilation, 251
respiratory changes, 252
Tamponade patients
ventricular changes, 251
Thermal bioeffect, 142
Thermal index (TI)
transmitting power, 6
Thermal safety, 143
Thoracic aorta
short-axis view, 78
Thoracic aortic aneurysms
TEE, 271
Thoracic aortic dissections, 559–560
Thoracic dissection
acute
patient assessment, 563
Thoratec system, 327
Three-dimensional echocardiography, 53
Thrombotic pulmonary emboli, 211
Thrombus
left atrial appendage, 233
Thymomas, 508
Tilting disk prostheses, 418
Time gain compensation (TGC), 15
Time-of-flight, 13
Tissue Doppler
MAV, 166, 171
Tissue harmonic imaging, 53
Tissue injury
temperature elevations, 142
Tissue properties
temperature increases, 142
Trabecular muscular ventricular septal defect, 537
Trabeculations, 129
Transducer
dynamic relationship, 46
Transducer arrays, 50
Transducer classifications, 49–50
Transducer Doppler mode, 29
Transducer operations, 43–49
image generation, 49
ultrasound energy emission, 44
Transducers, 41–54
examples, 43
opening frequencies, 52
Transducer structure, 42–43
assembly and array, 43
Piezoelectric element, 42–43
Transducer technology
recent and future, 53–54
Transesophageal echocardiography (TEE), 119, 146, 220, 373, 375, 484, 492–495
angles
correlation, 432
antibioprophylaxis, 147
ascending aorta, 281
assist devices description, 315–316
cardiomyopathy, 494
complications, 151–154, 152
congenital heart disease surgery, 552
diagnostic tool, 262–263
equipment, 145
evidence, 557–562, 562–565
export support, 565
general approach, 145
guidelines review, 556–557
heart transplantation, 471
surgical considerations, 471
hepatopulmonary syndrome, 493
images, 58
and imaging planes, 56–64
indications, 555–565
intraoperatively, 495
intraoperative monitoring, 147
monitoring
aortic and mitral valve replacement, 152
monitoring and patient position, 147
patient evaluation and preparation, 146
pericardial and pleural effusions, 494
perioperative period, 472–475
portopulmonary hypertension, 493–494
postoperative period, 475–480
right ventricular remodeling, 475–476
preoperatively, 493–494
probe
buckling, 149
cleaning and disinfection, 155
control knobs, 149
fiberoptic laryngoscope, 151
hypoxia management algorithm, 153
insertion, 153
inspection, 147–149
lateral insertion, 151
linear fissure, 148
lubricant, 150
orientation, 57
protective covers, 155
quick reference guide, 558
sedative agents, 148
thoracic aorta and aortic arch vessels, 263
views, 59
Transesophageal multiple transducer, 43
Transesophageal probe manipulation
graphic display, 56
Transgastric right ventricular outflow tract, 488
Transient ischemic attacks
upper-esophageal aortic view, 510
Transmitral flow
pulsed-wave Doppler, 166
Transmitral flow (TMF)
pulsed-wave Doppler, 166, 168
Transprosthetic gradient, 419–421
Transthoracic echocardiography
measurement methods, 95
Transthoracic echocardiography (TTE), 145
Transtricuspid flow (TTF), 36
Transtricuspid inflow
Doppler changes, 256
Transvalvular pressure gradient
transgastric longitudinal view, 375
Transvalvular pressure gradients
evaluation, 374
Transvalvular prosthetic regurgitation, 428–429
Transverse aorta
upper esophageal view, 79
Transverse pericardium sinus, 134–135
Transverse sinus, 136, 498
aorta, 136
fatty tissue, 500
RVOL, 137
Transverse waves, 2
Traumatic mitral valve injury, 394
Traumatic rupture
aorta, 279–280
Traumatic thoracic aortic disruption, 559–560
Tricuspid and pulmonic valve
anatomy, 447–450
Tricuspid annular diameters, 101
Tricuspid annuloplasty, 464
Tricuspid atrioventricular junction
mid-esophageal four-chamber view, 509

Tricuspid leaflets
anterior and posterior
mid-esophageal view, 451
Tricuspid regurgitation, 450–455, 455
acute, 232
echocardiographic and Doppler parameters, 456
mid-esophageal four-chamber view, 454
right systolic ventricular systolic pressure, 111
surgery
echocardiographic and Doppler parameters, 456
recommendations, 465
Tricuspid valve, 84–85, 447–467
annuloplasty
mid-esophageal four-chamber view, 454
anomaly, 539–540
Ebstein's anomaly, 539–540
endocarditis, 450–458
abscesses, 455–458
vegetation, 455–458
function
components, 449
low esophageal four-chamber view, 452
mid-esophageal four-chamber view, 457
mid-esophageal view, 84
prosthetic annulus
echocardiographic appearance, 463
right atrium, 448
surgery, 501
TEE role, 467
transgastric basal view, 452
Tricuspid vulvectomy, 465
Trou de Botal, 526
Turbulent flow
spectral curve, 31
Two dimensional cardiac structures
body surface area, 96
Two dimensional echocardiographic features
cardiac tamponade, 248–250
Two dimensional evaluation, 423–428
Two dimensional imaging, 90–108
centerline method, 92–93
chamber dimensions, volume calculations, 101–104
echocardiographic features
hypertrophic cardiomyopathy, 218–221
edge recognition, 90
global function, 104–105
measurements and calculations, 93–101
referencing centroids, 91–92
timing, 90–91
wall thickness, mass, stress, 106–108

Ultrasound
characteristics
different mediums, 8
contrast technique, 522
energy emission
electrical impulse mode generation, 44
electrical matching, 45
frequency bandwidth, 44–45
impedance matching, 45
operating frequency, 44
transducer damping, 45
human soft tissue
velocity, 25
imaging
matrix representation, 14
modes, 12
period
amplitude versus time, 2
principles, 1–21
compression and rarefaction, 1–3
depth, 19
factors, 17–20
frame line numbers, 18
frame rate and time generation, 18
frequency, 3
pixels, 20
propagation speed, 3
pulsing characteristics, 17
temporal resolution, 20
wavelength, 3
properties
air, 4
fat, 4
materials, 4
muscle, 4
skull bone, 4
scanning system, 13
transducer concept, 42
wave properties, 4–6
amplitude, 4
compression and catching up, 23
density versus distance, 2
generation, 2
generation and transmission, 44
intensity, 4–6
parameters, 3
power, 4
pressure, 4
Ultrasound beam, 45–49
components, 46
focusing, 46–48
mechanical methods, 48
time delay patterns, 48
image scanning, 49
main beam, 46
side lobes, 48–49
structure, 46
Unicommissural unicuspid aortic valve
mid-esophageal
short-axis view, 335

Valsalva aneurysms, 271–272, 273
Valves, 77–81. *See also* specific valves
ball-in-cage, 418
disease
unstable ICU patients, 561
lesions
functional manifestations, 395–413
prosthesis, 417–419
types, 465–467
repair, 557–558
methods and indications, 460–462
replacement, 463–467
aortic and mitral, 393
assessment, 563
Valvular areas, 116–117
Valvular lesions
anatomical manifestations, 450–455
Vascular anastomosis, 492
air embolism, 483
Vascular clamp placement, 287–289
Vascular pulmonary bed
anomalies, 493
Vegetation, 517–521
mobility score, 390
Veins, 69–72
Velocity scale
and baseline shift, 137–138
Vena cava
mid-esophageal bicaval view, 100
Vena contracta, 398
moderate mitral regurgitation, 403
Ventricular and leaflet extension
schematic representation, 442
Ventricular assist devices, 317–326
TEE role, 325
Ventricular dilatation, 177–178
Ventricular function
and hemodynamics, 185–212
Ventricular septal defect (VSD), 172–173, 227, 528–535
apical
mid-esophageal four-chamber view, 174
transgastric view, 173
classification, 536
infundibular or subarterial, 538
myocardial infarction, 172
transgastric mid-papillary view, 502

Ventricular septum
classification, 68
examination, 68
Ventricular trabeculations, 130
Ventriculoarterial connection, 526
Vents and venous canulation, 291
Venturi effect, 336
Vessels
upper esophageal view, 67
Visceroatrial situs, 526
Volume loading
echocardiographic and hemodynamic effect, 191
Volumetric flow calculations, 113–116
Wall motion score index (WMSI), 167
Wall motion scoring system, 164
Wall stress, 107–108
Wavelength, 3. *See also* ultrasound, wave properties
Windowing, 21

about the book...

The first illustrative guide to follow the published objectives of the American National Board of Echocardiography perioperative TEE certification examination, this reference explores the role of transesophageal echocardiography and its relation with other monitoring and imaging modalities in the operating room, intensive care unit and catheterization laboratory.

Unlike any other source on the subject, this reference examines the impact of perioperative transesophageal echocardiography using several individualized examples based on authors' experience. The manual provides tables summarizing key features and criteria useful for clinical interpretation of TEE data and presents echocardiographic images alongside annotated diagrams detailing various structures as well as information on 3D cardiac imaging plane orientation. Perspectives from several specialties including those of the anesthesiologist, cardiologist, cardiac surgeon and critical care physician are included.

An invaluable study tool and reference, this handbook is accompanied by a companion **DVD-ROM** containing 857 videoclips not only of the echocardiographic examination, but also with the corresponding live hemodynamic pressure tracings, intraoperative surgical views and anatomical specimens, along with 3D animation depicting the orientation of the tomographic plane obtained with the transesophageal echocardiographic probe.

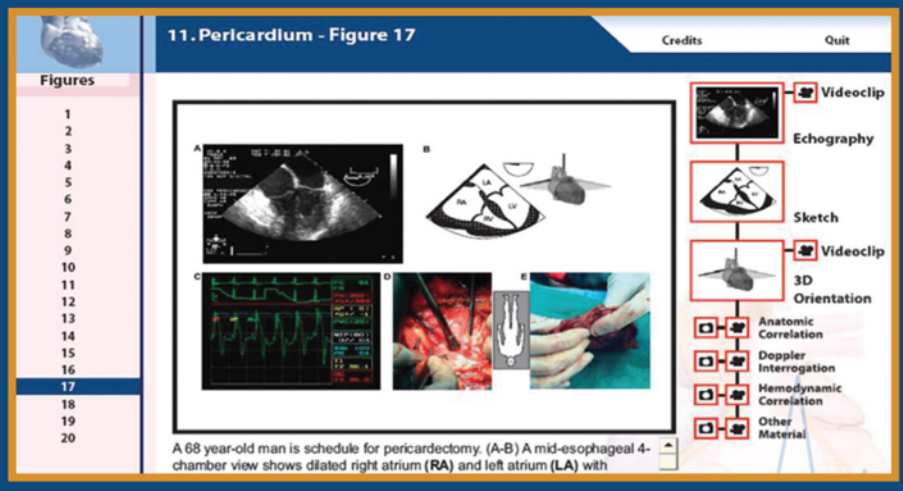

about the editors...

ANDRÉ Y. DENAULT is a Quebec Health Care Foundation Scientist and Director of the Cardiac Anesthesia Fellowship Program Montreal Heart Institute, Université de Montréal, Québec, Canada, as well as a Critical Care Physician, Centre Hospitalier de l'Université de Montréal, Québec, Canada. He received his M.D. degree from the Université de Montréal, Québec, Canada.

PIERRE COUTURE is Head of the Department of Anesthesia, Montreal Heart Institute, Université de Montréal, Québec, Canada. He received his M.D. degree from the Université de Montréal, Québec, Canada.

JEAN BUITHIEU is the Director of Echocardiography and Non-invasive Cardiovascular Imaging, McGill University Health Center, Montréal, Québec, Canada. He received his M.D. degree from the Université de Montréal, Québec, Canada.

JEAN-CLAUDE TARDIF holds the Canadian Institute of Health Research and Pfizer chair in atherosclerosis and is the Director of the Montreal Heart Institute Research Center, Université de Montréal, Québec, Canada. He received his M.D. degree from the Université de Montréal, Québec, Canada.

Printed in the United States of America

Taylor & Francis
Taylor & Francis Group
www.taylorandfrancisgroup.com

270 Madison Avenue
New York, NY 10016

2 Park Square, Milton Park
Abingdon, Oxon OX14 4RN, UK

DK2985
ISBN 0-8247-2353-8
90000
9 780824 723538